Karlsruhe Institute of Technology

Lab Rotation Reports

On the determination of Total Water Storage based on monthly gravity field solutions from the GRACE gravity field mission and from GLDAS data

Kurt Seitz und Hansjörg Kutterer

KIT SCIENTIFIC WORKING PAPERS 270

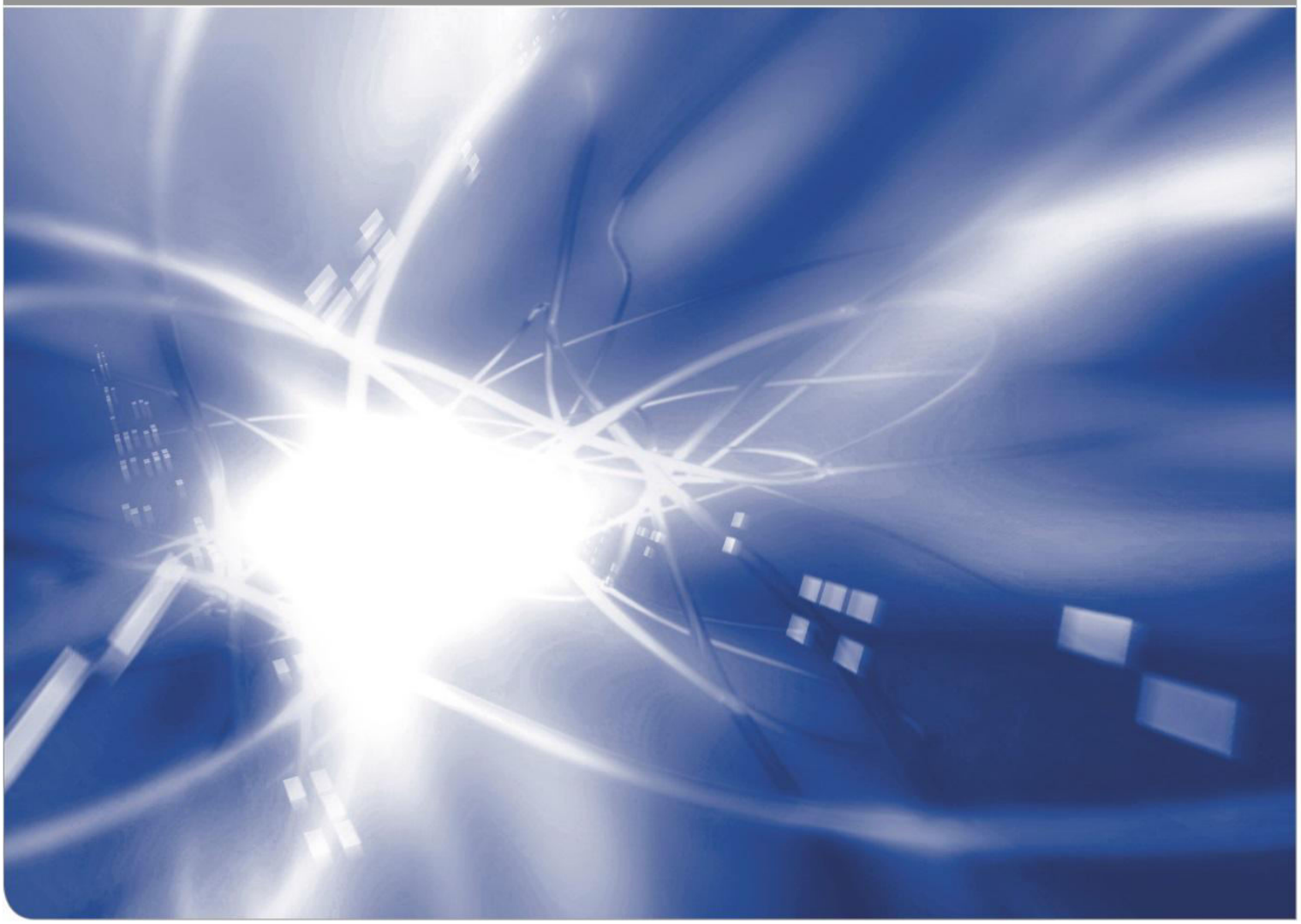

Geodetic Institute, Karlsruhe Institute of Technology,
Englerstraße 7, D-76128 Karlsruhe, Germany

Geodetic Institute (GIK)
Englerstraße 7
76128 Karlsruhe
www.gik.kit.edu

Impressum

Karlsruher Institut für Technologie (KIT)
www.kit.edu

This document is licensed under the Creative Commons Attribution – Share Alike 4.0 International License (CC BY-SA 4.0): https://creativecommons.org/licenses/by-sa/4.0/deed.en

ISSN: 2194-1629
KIT Scientific Working Papers
Issue Number 270
ISSN: 2194-1629
DOI: 10.5445/IR/1000191188

Online: June 2026

Preface to these student papers

The Earth system is subject to various temporal changes. The changes associated with mass transport on or beneath the Earth surface can be studied by monitoring the Earth's gravitational field. Satellite-based geodetic sensors offer the possibility of recording both temporal and spatial mass fluctuations. Gravity field models based on space borne observations of the Gravity Recovery and Climate Experiment (GRACE and GRACE-FO) missions are provided as monthly solutions by at least four evaluation centers as spherical harmonic models up to d/o 96. In particular, spherical harmonic models are available from CSR (Center for Space Research), GFZ (Helmholtz Center Potsdam – German Research Center for Geosciences) and JPL (NASA Jet Propulsion Laboratory). A mean model based on these is a statistical combination named COST-G. The CSR provides Total Water Storage (TWS) grids based on the mascon approach, ready to use. They can be obtained in release 6, with different order of de-striping (DDK-filter, 1, 2, ... , 8, unfiltered) from the International Center for Global Earth Models (ICGEM) website (http://icgem.gfz-potsdam.de/series). In addition, components of the total water balance are available on discrete grids at different spatial and temporal resolutions through the Global Land Data Assimilation System (GLDAS). It ingests satellite- and ground-based observational data products.

The Geodetic Institute (GIK) and the Institute of Photogrammetry and Remote Sensing (IPF) at the Karlsruhe Institute of Technology (KIT) collaborate closely in teaching and research. The master's degree program **Remote Sensing and Geoinformatics** is offered at GIK and IPF. The curriculum includes two **Lab Rotations**. The Module Handbook (https://www.bgu.kit.edu/english/3101.php) states for the Lab Rotations:
Competence Goal The student will gain insight into lab work and learn to work in a self-organized manner. Furthermore, the student will deepen his or her knowledge in the topic of choice and will then be better qualified to select the topic and research groups that best suit his or her personal interests.
Content The student works on a selected topic in one of the research groups of the involved institutes. Lab rotations at external institutions are allowable. The selection of the topic is made in agreement with the supervisor and the student. The student familiarizes himself or herself with the topic, carries out the lab work, and prepares a report.

This compilation comprises the results of Lab Rotations carried out at the chair of Geodetic Earth System Science between April 2025 and June 2026. They deal with the determination of Total Water Storage (TWS) based on monthly gravity field solutions from the GRACE(-FO) gravity field mission and from GLDAS data (Global Land Data Assimilation System).
Studies were conducted on the impact of DDK filters. Solutions from various services were also compared. Changes in groundwater levels were analyzed using GRACE and GLDAS data. The studies were conducted on a global scale as well as at the continental and regional levels.

The task creator for these Lab Rotations was Prof. Hansjörg Kutterer.
The work was supervised by Dr.-Ing. Kurt Seitz.

Kurt Seitz and Hansjörg Kutterer

June 2026

Contents

Characterizing Drought Using GRACE Data at two different altitudes **1**
Aleena Sajan Abbas

Analysis of Terrestrial Water Storage Variations across the Continent of Australia Using GRACE and GLDAS Monthly Solutions **25**
Pratheeksh Suresh Babu

Investigation of the heavy rainfall event in Germany in spring 2024 using GRACE-FO monthly solutions **47**
Ananthan Pushpa Balan

Study on the inverse Tesseroid method in TWS calculation **63**
Ananthan Pushpa Balan

Comparison of Various Spherical Harmonic and Mascon Solutions and Their Quality Assessment with Respect to Nepal Region **93**
Sudur Bhattarai

Accounting for VLM Signal in Level-2 GRACE Product **127**
Sudur Bhattarai

Groundwater monitoring over the continent of Africa **151**
Anugrah John Jojy

Ground water monitoring over the continent of South-America **167**
Ignatious Jose

Groundwater monitoring over the continent of Australia **221**
Athulya Jyothy

Monitoring Ice Mass Loss over Greenland based on GRACE Monthly Solutions **241**
Nabhan Karimbil

Investigation of the time series of the Earth's center of mass based on TWS variations in terms of 1st order spherical harmonic coefficients **265**
Maike Li

Groundwater Storage Estimation by Combining GRACE and GLDAS Data across the Continent Africa **285**
Vishnu Njaneswar

Comparison of GRACE DDK Filters for Terrestrial Water Storage **325**
Vishnu Prakash

Analysis of Terrestrial Water Storage Variations in the Murray-Darling Basin, Australia, Using GRACE and GLDAS Monthly Solutions **351**
Anujith Gopal Venugopal Prameela

Investigations on the El Niño event 2015-2016 based on GRACE **379**
Rahul Rajeev

Influence of DDK Filtering on GRACE Monthly Solutions for TWS Time Series using Europe as an Example **397**
Sharath Sunil Ravi

Spatial Comparison of GRACE-derived TWS and GLDAS During California Drought Periods **427**
Adersh Kolappurath Remesan

Evaluation of Global Geopotential Models (GGMs) using GNSS/Levelling Data in the State of Baden-Württemberg **447**
Adersh Kolappurath Remesan

Investigation of Very Low-Degree Potential Coefficients in Relation to Total Water Storage (TWS) from GRACE Data **467**
Amal Kareeem Abdul Salam

Inverse Tesseroid Approach based on Potential and Gravity **493**
Amal Kareeem Abdul Salam

Investigation on the El Niño event 2015-2016 based on GRACE **529**
Abhijith Puthenveetil Sangeeth

Study on TWS Changes in India using GRACE-FO Level-2 Products from CSR **545**
Aravind Santhosh

Monitoring Ice Mass Loss over Antarctica based on GRACE Monthly Solutions **561**
Iwin Scaria

How does the Variation of the Total Water Storage affect the Earth's Center of Mass **585**
Jacob Sebastian

Determination of terrestrial water storage (TWS) in the Amazon Basin from GRACE and SLR data . **601**
Jacob Sebastian

Impact of Himalayan Glacier Melt on Groundwater Storage in Northern India **641**
Shincy Sebastian

Characterizing hydrological mass variations across the continent of Africa by GRACE-FO and GLDAS data **667**
Akhil Sunny

Study on Groundwater Changes in Spain and Italy using GRACE, GRACE-FO and GLDAS Data . . **695**
Swathy Suresh

Total Water Storage Dynamics in the Amazon Basin: GRACE and GLDAS Comparison (2003–2016) **721**
Unni Udayan

Assessing Loading Effects and Signal Leakage in GRACE-based TWS Estimation over the Amazon Basin (2003- 2016) **745**
Unni Udayan

Characterizing Drought Using GRACE Data at two different altitudes

Aleena Sajan Abbas[1]

1 Remote Sensing and Geoinformatics Master of Science (M.Sc.), KIT, Germany
E-Mail: usfoz@student.kit.edu

Abstract

This study uses monthly GRACE gravity field solutions over India to describe how water storage changes during droughts. We used the DDK2 filter to process and decorrelate CSR spherical harmonic products. This helped reduce north-south striping and make geophysically relevant signals stronger (Kusche, 2007; Landerer and Swenson, 2012). Spherical harmonic synthesis and a Regularized inversion method is used to find terrestrial water storage (TWS) anomalies and estimate changes in regional mass. To find out how the recovered signal changes with altitude, TWS fields were looked at at two different heights. This made it possible to compare how the signal changes with height and how stable large-scale drought signatures are with height. The findings demonstrate a consistent seasonal cycle characterized by pre-monsoon depletion and monsoon-season recharging, alongside interannual variations that signify intervals of persistent storage deficit pertinent to drought progression. Both altitude evaluations have the main regional patterns, but higher-altitude fields have a smoother spatial structure and lower anomaly amplitudes, which is expected, if shorter-wavelength components were less strong (Wouters et al., 2014). The study shows that GRACE-derived TWS is useful for describing regional droughts, but it also points out its limitations, such as low spatial resolution, leakage, and edge effects. These limitations mean that the data must be interpreted at basin to sub-national scales and carefully masked near the edges of the study area.

Keywords GRACE · Inverse Tesseroid Approach · India

1 Introduction

Drought is a common hydroclimatic risk that affects agriculture, ecosystems, and water security, especially in areas with a lot of monsoons, like India. Precipitation-based indicators characterize meteorological drought; however, water availability and social implications are more directly associated with changes in stored water within the land system. Terrestrial water storage (TWS) is the combined storage of groundwater, soil moisture, surface water, and snow, it gives a physically relevant way to keep track of how droughts change and recover on a regional scale.
The Gravity Recovery and Climate Experiment (GRACE) mission watches how the Earth's gravity changes over time because of changes in the mass of the Earth system. These changes in gravity over land may mostly be seen as changes in water mass, which makes it possible to estimate monthly TWS anomalies (Tapley et al., 2004; Wahr et al., 1998). India is chosen as the study location because it has a significant seasonal hydrological cycle that

KIT Scientific Working Papers
Issue Number 270
ISSN: 2194-1629
DOI: 10.5445/IR/1000191188
Online: June 2026

This document is licensed under the Creative Commons Attribution – Share Alike 4.0 International License (CC BY-SA 4.0):
https://creativecommons.org/licenses/by-sa/4.0/deed.en

is governed by the summer monsoon. Monthly GRACE gravity field solutions are used to find geographical and temporal patterns of TWS anomalies across India. This helps look at storage deficits and recharge phases that are important for understanding drought.
The analysis utilizes monthly CSR spherical harmonic products that have been processed with the DDK2 decorrelation filter. This filter minimizes correlated errors and north–south striping and makes it easier to understand regional signals. Two complimentary methods are employed, spherical harmonic synthesis to convert the filtered spherical harmonic coefficients into gridded fields, and a regularized inversion approach to estimate regional mass changes within the Indian domain. The most important part of this study is the assessment of recovered fields at two distinct altitudes (500km and 200km), which discusses the impact of the evaluation height on the amplitude, spatial smoothness and resilience of anomaly-related signals, attributable to the attenuation of short-wavelength components with increasing distance from the Earth (Landerer and Swenson, 2012).
The goals of this work are to use DDK2 filtering to handle CSR GRACE spherical harmonic solutions. Spherical harmonic synthesis and a regularized inversion framework are used to find monthly TWS anomalies over India. Then, the TWS fields that were recovered are compared at two different heights. Finally, the seasonal and yearly TWS changes over India are looked at in light of how droughts form and end, taking into consideration problems with spatial resolution, leakage, and edge effects.

2 Theoretical Aspects

This section summarizes about the theoriticala spects that explains how mass changes based on gravity data, how noise and signal behave at different spatial scales, and how to use spherical harmonic coefficients to describe GRACE gravity data. Also, regularization and the inverse tesseroid approach are added. These turn gravity anomalies into very accurate Total Water Storage (TWS) forecasts.

2.1 Principle of GRACE Satellite Gravimetry

The GRACE mission focus on measuring tiny variations in Earth's gravity field that generally occur due to the movement of water or other masses across planet's surface. Here, it uses 2 identical satellites flying 500km above the earth's surface, 220 km apart. When the first satellite passes over a region with higher mass such as more groundwater, it pulls a little closer to Earth, and thus there will be a slight change in distance between the satellites. These distance variations are recorded continuously, and this is how GRACE detects a change in distribution of masses in earth system (Tapley et al., 2004). These variations in gravity are mostly caused by natural processes such as evaporation, rainfall, change in soil moisture, and groundwater use. Therefore, GRACE provides a useful approach for studying TWS and its changes over time (Wahr et al., 1998; Tapley et al., 2004).

2.2 Spherical Harmonic Synthesis (SHS)

Spherical harmonic expansion is a mathematical technique that can be used to define the Earth's gravity field. Using this method, the gravitational potential is given as a set of numbers called Stokes coefficients C_{lm} and S_{lm}. Each pair of these coefficients represents the contribution of a particular wavelength (represented by degree l and order m) to the Earth's total gravity field.

$$V(P) = \frac{GM}{r} \sum_{n=0}^{\infty} \left(\frac{R}{r}\right)^n \sum_{m=0}^{n} (\bar{C}_{nm} \cos m\lambda + \bar{S}_{nm} \sin m\lambda) \bar{P}_{nm}(\sin \varphi) \tag{2.1}$$

where,
GM : Geocentric gravitational constant
R : Radius of the reference sphere.

$\bar{C}_{nm}, \bar{S}_{nm}$: Fully normalized spherical harmonic coefficients of degree n and order m
$\bar{P}_{nm}$: Fully normalized Legendre functions of degree n and order m.

The spatial distribution of the Earth's gravity field is described by the spherical harmonic coefficients $\bar{C}_{nm}$ and $\bar{S}_{nm}$ (Wahr et al., 1998). Lower degrees show changes in mass on a large scale, while higher degrees show changes in mass on a smaller scale. GRACE Level-2 data gives these coefficients as monthly solutions, which makes it possible to look at changes in the gravity field over time. Changes in the coefficients, which mostly reflect mass redistribution processes such as variations in terrestrial water storage, are the source of gravity field anomalies for potential synthesis and mass inversion.

2.3 Filtering and Noise Reduction (DDK2 Filter)

The raw gravity data from GRACE, which are given as spherical harmonic coefficients, often have noise that looks like long "north-south stripes" on the maps. This happens when the connected satellites make small errors in their measurements. There are different ways to filter out this noise and make the data easier to read. The DDK2 filter was utilized in this study; these filters are used to get rid of striping effects and make GRACE data decorrelated. They use spatial smoothing and statistical weighting to reduce related errors while maintaining a true geophysical signal as accurate as possible. The DDK2 filter improves the GRACE data and makes potential fields clearer and more reliable for further processing. Filtering can make a signal weaker, but there was no extra scaling correction used here because the DDK2-filtered data gives solid and reliable results for studies in the areas on which they are based (Kusche, 2007).

2.4 Degree Variance and Error Degree Variance

The errors in the spherical harmonic coefficients of the gravity field solutions introduce uncertainties in the mass changes estimated from GRACE. Variance propagation is commonly analysed in the spectral (degree) domain to examine how these errors vary across spatial scales. The degree variance, defined as the sum of the squared spherical harmonic coefficients over all orders m for a given degree l, indicates how the signal energy is distributed across spherical harmonic degrees (Wahr et al., 1998).

$$\sigma_n^2 = \sum_{m=0}^{n} \left(\bar{C}_{nm}^2 + \bar{S}_{nm}^2\right) \tag{2.2}$$

The degree variance (Figure 2.1(blue)) describes how the gravity signal is spread out across different spatial wavelengths. Lower degrees mean long-wavelength mass changes, while higher degrees mean shorter spatial scales. The error-degree variance can also be used to describe the spectral distribution of measurement noise. GRACE solutions usually show a crossover between signal and noise at intermediate degrees. This is because noise gets stronger as the degree goes up, while signal power is stronger at low degrees.

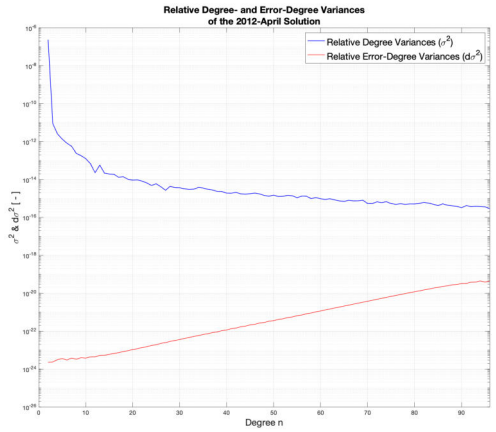

(a) April 2012

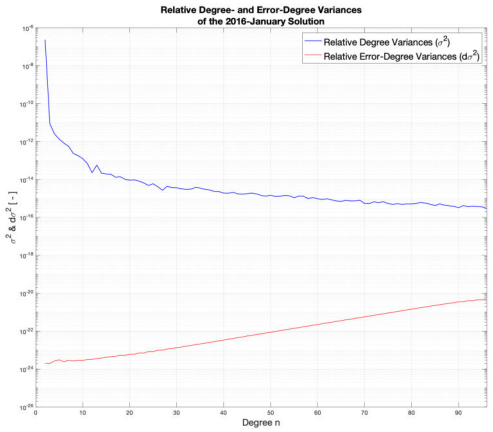

(b) April 2016

Figure 2.1: Degree and error degree variance of GRACE spherical harmonic coefficients for April 2012 and April 2016.

In addition to the signal degree variance, The error-degree variance is calculated using the formal uncertainty of the spherical harmonic coefficients that accompany the GRACE Level-2 solutions (Figure 2.1(red)).The error-degree variance is defined as:

$$\sigma^2_{C_n} = \sum_{m=0}^{n} \left(\sigma^2_{\bar{C}_{nm}} + \sigma^2_{\bar{S}_{nm}} \right) \tag{2.3}$$

The distribution of measurement noise over spherical harmonic degrees is explained by the error-degree variance. Noise has a greater impact on coefficients with higher degrees because it often increases with degree. It is feasible to identify the spectral region where the noise is significant and where the gravity signal is stronger by comparing degree variance and error-degree variance (Kusche, 2007).

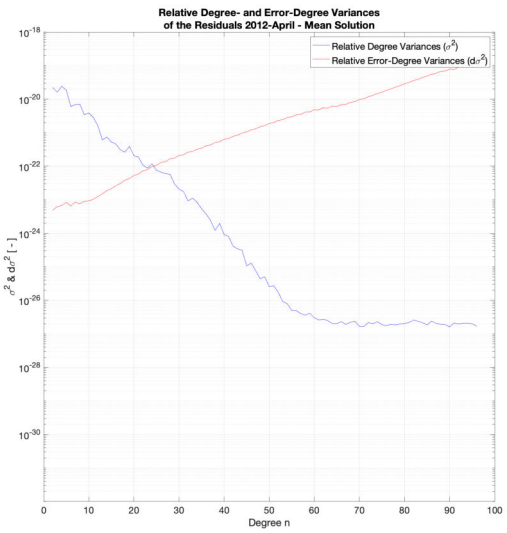

(a) April 2012

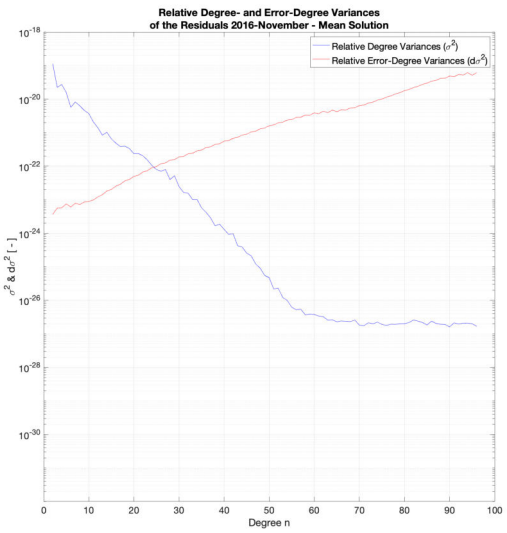

(b) April 2016

Figure 2.2: Error Degree variance of GRACE spherical harmonic coefficients for April 2012 and April 2016.

2.5 Inverse Tesseroid Approach and L-curve Regularization

The inverse tesseroid method uses the gravity potential that GRACE measures to find out how the surface mass changes. A tesseroid is a small, curved 3D block that is defined by its latitude, longitude, and radius. It makes the curve of the Earth easier to see than rectangular prisms do (Heck and Seitz, 2007). This method shows the possible effects of all the tesseroids at satellite altitude as a straight line. There is a link between them that looks like this:

$$\mathbf{y} = \mathbf{A}\mathbf{x} + \mathbf{e} \tag{2.4}$$

where **y** is the observed gravitational potential, **A** is the design or Jacobi matrix, **x** is the vector of unknown mass changes, and **e** represents the measurement errors. The gravitational influence of each tesseroid is based on the spherical harmonic coefficients that come from GRACE data. Each tesseroid is a localized mass element. This makes it possible to figure out how much mass varies because of different geophysical phenomena, like water storage problems, glacier mass loss, and groundwater depletion(Landerer and Swenson, 2012; Heck and Seitz, 2007). The method lets you estimate mass changes with great accuracy by breaking the Earth's surface into these small parts. This is important for studies on climate change and its effects on water. Tesseroids allow for a more thorough and precise picture of how mass is spread out than simpler models do. This makes this method very useful for both little and large studies of how mass changes over time.

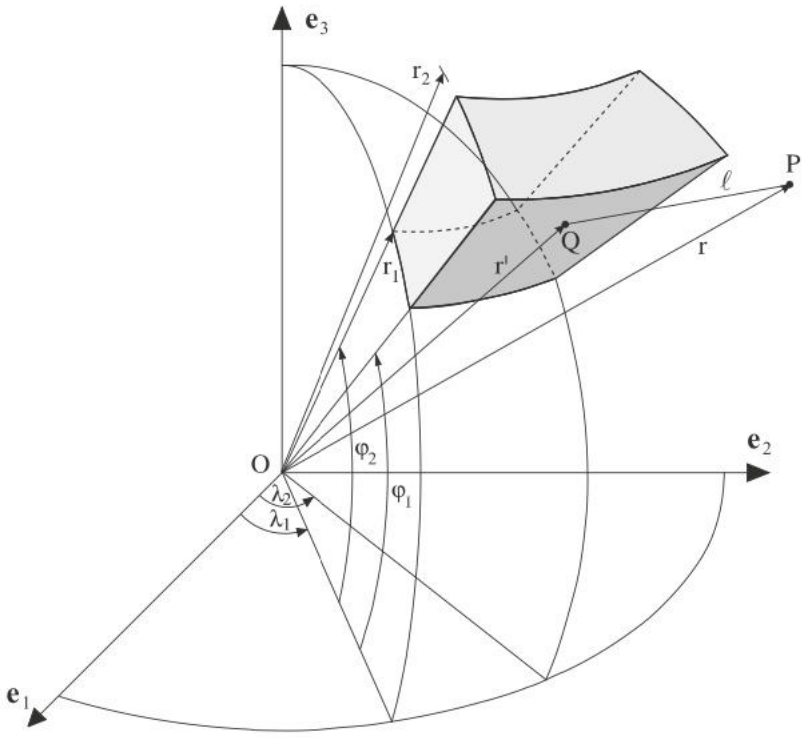

Figure 2.3: Geometry of a spherical tesseroid (Heck and Seitz, 2007)

This figure illustrates the geometry of a tesseroid, which is a curved volume element defined by latitude, longitude, and radial boundaries. This representation properly accounts for Earth's curvature and forms the basis for forward modelling of the gravitational potential used in the inverse tesseroid approach.

The inverse tesseroid formulation is an ill-posed problem, which means that small errors in the observed gravitational potential can make surface mass estimates unstable. Tikhonov regularization is used to find a stable and

physically meaningful solution by putting a smoothness requirement on the model parameters (Hansen, 1999). The regularized inverse problem is written as:

$$\min_{\mathbf{x}} \left(\|\mathbf{A}\mathbf{x} - \mathbf{y}\|_2^2 + \lambda^2 \|\mathbf{x}\|_2^2 \right) \tag{2.5}$$

where $\mathbf{y}$ denotes the observed gravitational potential anomalies, $\mathbf{A}$ is the sensitivity matrix relating tesseroid mass changes to the potential observations, $\mathbf{x}$ represents the unknown surface mass variations, and λ is the regularization parameter. The parameter λ controls the trade-off between fitting the GRACE observations and enforcing solution smoothness.

The L-curve criterion, which is often used in geodetic inverse problems and GRACE-based mass change studies, is used to find the best value because it gives an objective balance between data misfit and model norm (Hansen, 1992).

The two L-curve plots below show how the regularization parameter changes with altitude (500 km and 200 km) in 2014. The corner of the L-curve is the best regularization parameter since it balances how well the data fit and how smooth the solution is.

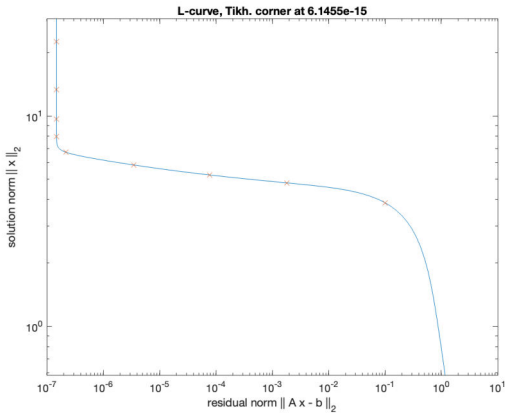

(a) Observation-grid at 500 km height

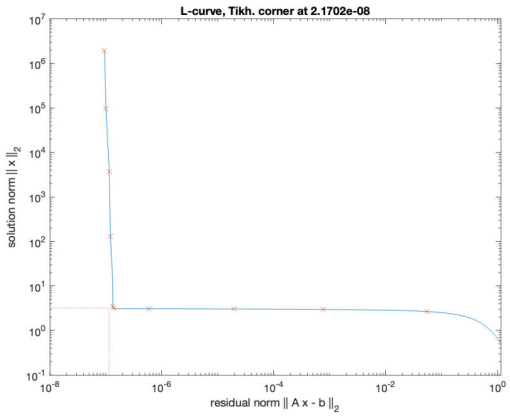

(b) Observation-grid at 200 km height

Figure 2.4: (a) shows L-curve for at an altitude of 500 km for the month of October, 2013. (b) shows L-curve for at an altitude of 200 km for the month of October, 2013.

These figures show how the regularization parameter changes with height, which affects the solution norms. The L-curve shows that at higher altitudes, the sensitivity to minor changes in mass goes down, which means that the sensitivity to big mistakes goes up.

2.6 Computation of TWS Anomalies and Drought Interpretation

The monthly TWS anomaly maps based on reversed results show how much the amount of water has changed from the long-term average. Positive anomalies mean that storage is getting better or bigger, while negative anomalies mean that it is getting smaller and going into drought. We can find out when droughts start, how long they last, and how bad they are by looking at TWS anomalies in the Indian region and their time series (Asoka et al., 2017). Previous research has shown a correlation between the decline of TWS in India and lack of summer precipitation along with excessive groundwater extraction. It is easier to understand how people and the weather affect the development of droughts when you use GRACE-derived TWS data and information about the region's hydrology (Long et al., 2013).

3 Study Area and Data

This study is about India, country that depends on rains for most of its water supply and uses groundwater for many other things. This makes India very vulnerable to drought. This help us to know how bad and how long droughts are by looking at changes in India's total water storage (TWS).
The study period included a major drought from 2012 to 2016. Using satellite data ,it make sense and more convinient to learn about how droughts start, get worse, and end during this time.
This study uses datas from the CSR Release-06 (RL06) dataset, focusing on the monthly Level-2 gravity readings. These values are the coefficients for spherical harmonics with degrees and orders up to 96. The DDK2 filter cleans up the data by getting rid of noise and striped patterns. The gravitational potential fields are calculated and put them on a 30' × 30' grid at heights of 200 km and 500 km. These numbers are used by the inverse tesseroid method to figure out how India's TWS changes from month to month.

4 Methodology

This section talks about the processing chain that is used to get monthly changes in Total Water Storage (TWS) over India during the 2012–2016 drought from GRACE CSR geopotential coefficients (DDK2-filtered). It also compares the results of synthesizing the gravitational potential at 500 km and 200 km altitude on a $30' \times 30'$ grid, and then estimating TWS using an inverse tesseroid approach with L-curve–based regularization.

4.1 Data selection and study region

Monthly GRACE Level-2 gravity field models come with fully-normalized spherical harmonic coefficients. GRACE is made to send monthly gravity data from low Earth orbit, which lets scientists keep an eye on how mass moves over time (Tapley et al., 2004). According to the task requirements, the analysis uses DDK2-filtered CSR potential coefficients for the Indian region from 2012 to 2016 (maximum degree/order

4.2 Temporal anomalies of spherical harmonic coefficients

Monthly GRACE Level-2 gravity fields are given as fully normalized spherical harmonic coefficients $\bar{C}_{nm}(t)$ and $\bar{S}_{nm}(t)$, which show the Earth's external gravitational potential (Tapley et al., 2004; Wahr et al., 1998). To isolate the time-variable component, monthly coefficients were transformed into residual (anomalous) coefficients by subtracting a reference mean field calculated over

$$\Delta\bar{C}_{nm}(t) = \bar{C}_{nm}(t) - \left\langle \bar{C}_{nm} \right\rangle_{(\ldots)}, \qquad \Delta\bar{S}_{nm}(t) = \bar{S}_{nm}(t) - \left\langle \bar{S}_{nm} \right\rangle_{(\ldots)}. \tag{4.1}$$

These residual coefficients form the input for the subsequent filtering and spherical harmonic synthesis steps used to derive gridded TWS anomalies.

4.3 Spherical harmonic synthesis of potential anomalies at two altitudes

The residual coefficients were employed to generate gridded gravitational potential anomalies $\Delta V(\theta, \lambda, t)$ by assessing the spherical harmonic expansion at two radii, corresponding to two synthesis heights: (i) 500 km (indicative of GRACE's orbital altitude) and (ii) 200 km (for sensitivity comparison) (Tapley et al., 2004). This created two monthly potential-anomaly grids, $\Delta V_{500}(t)$ and $\Delta V_{200}(t)$, which were inverted independently to see how the height of the synthesis affected the recovered hydrological signal.

4.4 Inverse Tesseroid Approach

A tesseroid-based forward modeling approach was used to connect the gravitational potential anomalies from GRACE to changes in surface mass across India. The study area was divided into tesseroids that matched the $30' \times 30'$ analytical grid. Tesseroids are three-dimensional elements bounded by latitude/longitude grid lines and radial surfaces, making them suitable for gravity forward modelling in spherical Earth geometry (Heck and Seitz, 2007). Each tesseroid represents a surface mass element with constant water density, and the mass variations are expressed as equivalent water height (EWH).
For each month of the 2012–2016 study period, the gravitational potential anomalies synthesized at 500 km and 200 km altitude were used as input to the forward model. The tesseroid sensitivities were computed using the standard tesseroid potential formulation and were used to construct the forward modelling operator required for the subsequent regularized inversion and the comparison of the two-altitude solutions (Baur and Sneeuw, 2011). Consistent with the task assumption, the modeled temporal and spatial variations are attributed to mass transport within the Indian region, while remaining contributions are treated as residual errors.

4.5 Regularized inversion for monthly TWS estimation

The connection between the synthesized gravitational potential anomalies and the unknown changes in the tesseroid mass constitutes an ill-conditioned inverse problem, meaning that even small observation errors can lead to unstable solutions. Therefore, a zero-order Tikhonov regularization was applied to derive stable monthly estimates of surface mass change (expressed as EWH). The regularized solution was obtained by minimizing a functional that balances the fit to the GRACE-derived potential anomalies with the smoothness and energy of the solution vector (Hansen, 2000; Baur and Sneeuw, 2011).
The inversion was performed independently for the two synthesis heights (500 km and 200 km) for each month from 2012 to 2016, yielding two monthly TWS anomaly fields that can be compared to assess how the evaluation height affects the recovered drought signal.

4.6 Selection of the regularization parameter using the L-curve

The level of regularization controls the trade-off between overfitting noise and oversmoothing the true hydrological signal. The regularization parameter was selected using the L-curve criterion, which identifies an optimal compromise between the residual norm and the solution norm by locating the corner of the L-shaped curve in log–log space (Hansen, 1999, 2000). This selection was applied for the monthly inversions to ensure a stable and consistent time series.

4.7 Post-processing and drought characterization

The inverted monthly solutions were transformed into gridded TWS anomalies in water-equivalent units and compiled into (i) monthly spatial maps over India and (ii) an area-mean TWS anomaly time series calculated using latitude-dependent area weighting. The progression of the drought from 2012 to 2016 was subsequently analyzed using the temporal behaviour of TWS anomalies, focusing on the onset, severity, and duration of prolonged negative storage intervals. The time series and spatial patterns derived from the 500 km and 200 km solutions were compared to assess the sensitivity of drought estimates to synthesis height (Landerer and Swenson, 2012).

5 Results and Discussion

This section shows the results of the inverse tesseroid technique and spherical harmonic synthesis. Throughout the study, monthly gravitational potential fields and corresponding Total Water Storage (TWS) estimates exhibit consistent spatial trends. When we look at the results at different computation altitudes, we can only see small

differences. This shows that the method used is stable. The results indicate that the synthesis and inversion processes accurately depict the temporal variations in mass distribution across India during the drought.

5.1 Monthly Gravitational Potential Anomalies

Time-varying changes in the Earth's gravity potential are described by the monthly gravitational potential anomaly model derived from GRACE observations (Wahr et al., 1998; Tapley et al., 2004). The model represents the gravity effect of mass redistribution, mainly due to changes in water storage, relative to a reference level. It is obtained by spherical harmonic synthesis of the monthly Level-2 coefficients after applying the DDK2 decorrelation filter (Kusche, 2007). The resulting potential anomaly field represents the observed signal that is used as input for the inverse tesseroid method to estimate Total Water Storage (TWS) anomalies.

The monthly solution used to construct the potential anomaly model is evaluated through a spectral quality check using the two degree–order maps shown in Figure 4.These plots display the formal uncertainties of the spherical harmonic coefficients (both C_{nm} and S_{nm}) as a function of degree n and order m. For most months in the period 2012–2016, the uncertainty pattern is smooth and approximately symmetric, with relatively small uncertainties at low degrees (large spatial scales) and increasing uncertainty towards higher degrees and orders (smaller spatial scales). This regular behaviour (e.g., July 2013) indicates a stable monthly gravity field solution, and the corresponding potential anomaly model is therefore expected to be dominated by physically meaningful, large-scale signals.

In contrast, a small number of months exhibit an unusual pattern (e.g., February 2015), where the degree–order distribution becomes irregular and patchy, and the uncertainty structure is no longer smooth. This behaviour suggests the presence of enhanced noise and/or residual artefacts, such as increased correlated errors or reduced solution quality for that month. Although filtering reduces striping effects, such anomalous spectral behaviour may still propagate into the synthesized potential anomaly model as enhanced short-wavelength variability (Landerer and Swenson, 2012). These plots therefore justify why most monthly solutions are considered reliable, while a few months should be interpreted with greater caution in the analysis of potential anomalies and subsequent inversion.

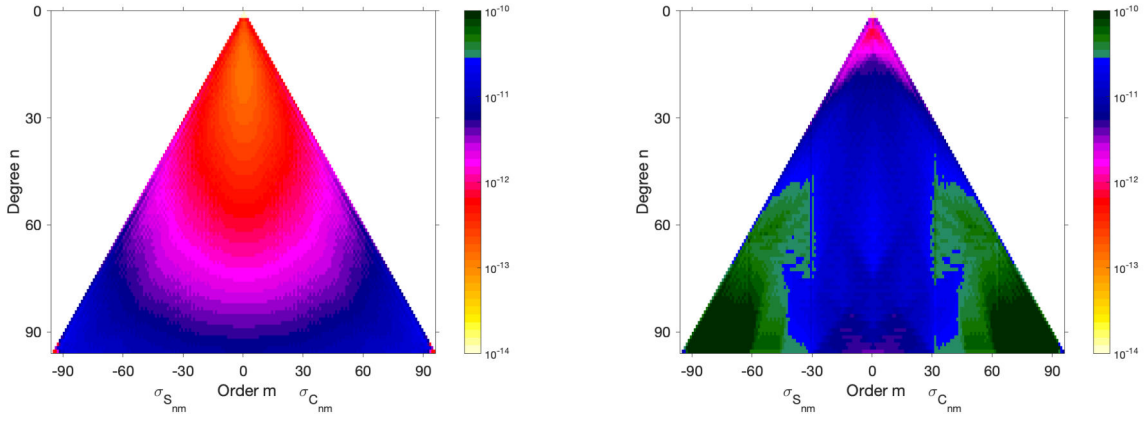

(a) July 2013

(b) February 2015

Figure 5.1: Accuracy of monthly GRACE spherical harmonic coefficients. Panel (a): regular (July 2013) behaviour. Panel (b): anomalous (February 2015) spectral behaviour.

5.2 Relative accuracy

Relative accuracy is used to assess the internal consistency of the GRACE spherical harmonic solutions rather than the absolute magnitude of the formal errors. It evaluates whether the uncertainties of the cosine coefficients $\sigma_{C_{nm}}$ and sine coefficients $\sigma_{S_{nm}}$ behave in a comparable manner across spherical harmonic degree n and order m.

Since both coefficient types describe the same physical gravity signal with different phase components, a stable and well-balanced solution is expected to show similar error propagation for $\sigma_{C_{nm}}$ and $\sigma_{S_{nm}}$ (Wahr et al., 1998; Tapley et al., 2004).

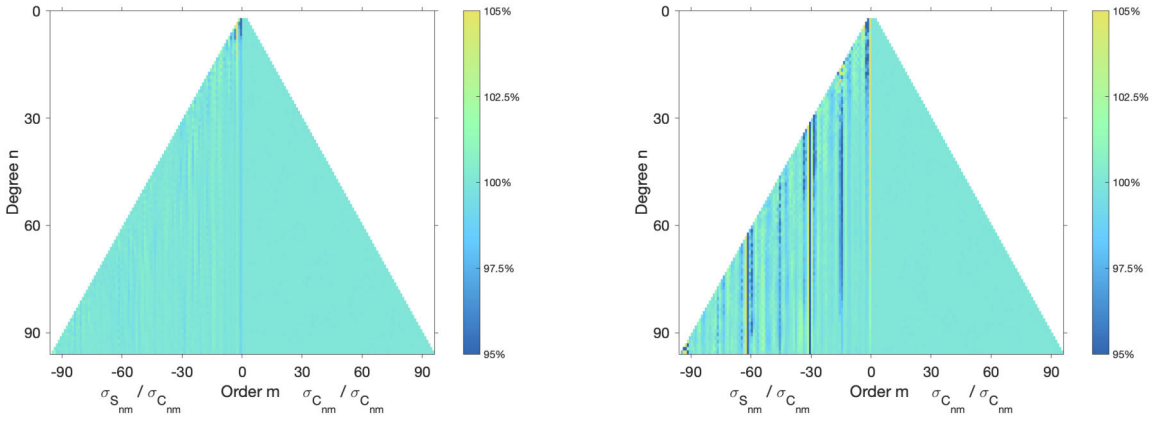

(a) May 2013 (b) February 2015

Figure 5.2: Relative accuracy maps of GRACE spherical harmonic coefficients ($\sigma_{S_{nm}}/\sigma_{C_{nm}}$) for two example months, shown as a function of degree n and order m.

In the recovery of GRACE gravity fields, several orbit-related effects influence the error characteristics of the spherical harmonic coefficients. These include resonant orbit disturbances, secular perturbations, orbit tilting, and linear or periodic effects associated with the satellite ground-track repeat cycle. Resonant effects can occur when specific temporal mass variations interact with the satellite orbit at particular frequencies, leading to enhanced sensitivity at certain degrees or orders. Although such effects may introduce structured error patterns – especially at higher degrees – they generally affect sine and cosine coefficients in a similar way due to their common observation geometry. From an error-propagation perspective, the formal uncertainties of $\sigma_{C_{nm}}$ and $\sigma_{S_{nm}}$ are derived from the same observation system and orbit configuration. When the error-propagation equations are formulated and simplified, the ratio between the uncertainties of the sine and cosine coefficients approaches unity. Therefore, relative accuracy values close to 100% indicate balanced error propagation and represent a key indicator of internally consistent monthly gravity field solutions (Wahr et al., 1998).

Across the full set of monthly solutions analysed in this study, the relative accuracy remains close to 100% for most degrees and orders, confirming the overall stability of the GRACE Level-2 solutions used for potential synthesis. The two example maps shown in Figure 5.1 illustrate typical results of this analysis. In both cases, the majority of the degree–order domain exhibits near-unity values, indicating that neither the sine nor cosine coefficients dominate the error structure.

Small deviations from 100% appear as narrow, order-dependent bands, particularly at higher degrees (Wouters et al., 2014). This behaviour is expected because higher degrees correspond to shorter spatial wavelengths, where GRACE measurement noise and residual correlated errors are more pronounced. The similarity of the relative accuracy patterns between the two example months demonstrates that these deviations are systematic and noise-related rather than indicative of solution failure. Overall, the relative accuracy analysis supports the reliability of the filtered monthly solutions used in this study, while also highlighting that short-wavelength features should be interpreted with appropriate caution in subsequent potential modelling and inversion.

5.3 Geoid Undulations

The integrated effect of mass redistribution within the Earth system is reflected in the geoid undulation, which is the height variation of an equipotential surface of the Earth's gravitational field in relation to a reference ellipsoid (Heiskanen and Moritz, 1967). Large-scale changes in terrestrial water storage, as opposed to short-wavelength

geological features, are the primary cause of temporal fluctuations in geoid undulations in the context of GRACE. In order to connect the spectral gravity field solutions to the resulting inversion for surface mass fluctuations, the undulation fields thus offer a crucial intermediate product.

5.3.1 Spatial scale discussion (2015)

The residual geoid undulation fields across India is visualized in Figure 5.3 for a few months in 2015. They are characterized by smooth spatial patterns dominated by large-scale features because of GRACE's poor spatial resolution and the use of decorrelation filtering (Tapley et al., 2004; Kusche, 2007). The undulation fields' overall structure is consistent over the months under analysis, indicating that regional-scale mass signals predominate over short-wavelength variability.

Despite this general homogeneity, monthly changes in the geoid undulations' sign and amplitude are seen, suggesting a temporal redistribution of mass within the hydrological system. Seasonal hydrological processes that modify land water storage are mostly to blame for these variations. Furthermore, the lack of distinct spatial gradients suggests that regional-scale mass shifts, rather than localized effects, are primarily recorded by the GRACE-derived undulations.

The combined effects of mass redistribution within the Earth system are demonstrated by geoid undulation, which is the height fluctuation of an equipotential surface of the Earth's gravitational field with respect to a reference ellipsoid (Heiskanen and Moritz, 1967). In GRACE observations, large-scale changes in terrestrial water storage, rather than static geological formations, are the primary drivers of temporal variations in geoid undulations. As a result, for surface mass fluctuations, the undulation fields offer a physically significant intermediate product connecting the spherical harmonic gravity field solutions to the ensuing inversion.

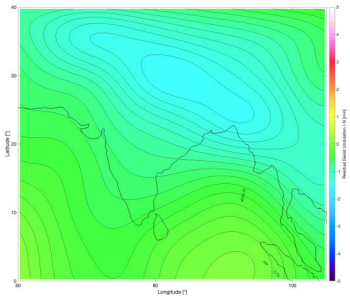

(a) January 2015

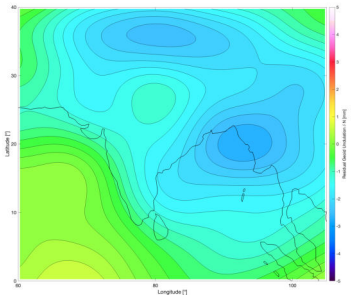

(b) February 2015

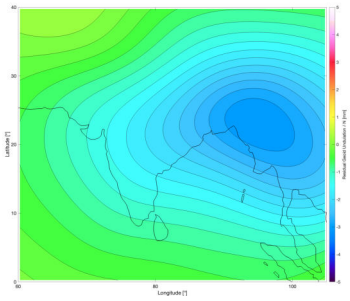

(c) March 2015

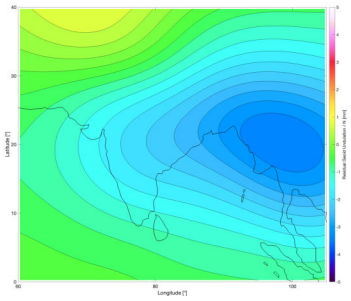

(d) April 2015

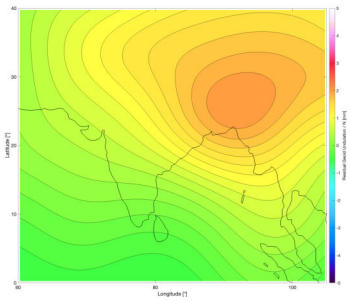

(e) July 2015

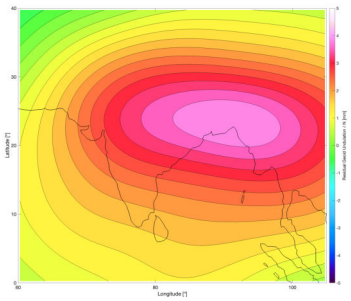

(f) August 2015

Figure 5.3: Monthly residual geoid undulations over India derived from GRACE CSR RL06 solutions for selected months in 2015.

5.3.2 Seasonal scale discussion (August, 2012–2016)

August is used to analyze the seasonal behavior of geoid undulations since it is the peak month of the Indian summer monsoon and may thus be used to emphasize mass redistribution driven by hydrology (Wahr et al., 1998; Asoka et al., 2017). The remaining geoid undulation fields for August 2012, 2014, 2015, and 2016 are displayed in Figure 5.4. The seasonal comparison does not include data for August 2013 since they are absent from the GRACE dataset.

The August geoid undulation fields, which are characterized by smooth anomalies with broad wavelength structures, show persistent large-scale spatial patterns over the Indian subcontinent over the years under analysis. This behavior is expected given GRACE's poor spatial resolution and the use of decorrelation filtering, which highlights regional-scale mass fluctuations and reduces short-wavelength noise (Tapley et al., 2004; Kusche, 2007). Similar anomaly patterns are consistent from year to year, suggesting that seasonal hydrological processes, rather than sporadic or localized influences, control the primary signal.

There are clear interannual variations in anomaly amplitude and spatial extent despite the general homogeneity in spatial organization. Differences in groundwater recharge, soil moisture storage, and monsoon intensity between

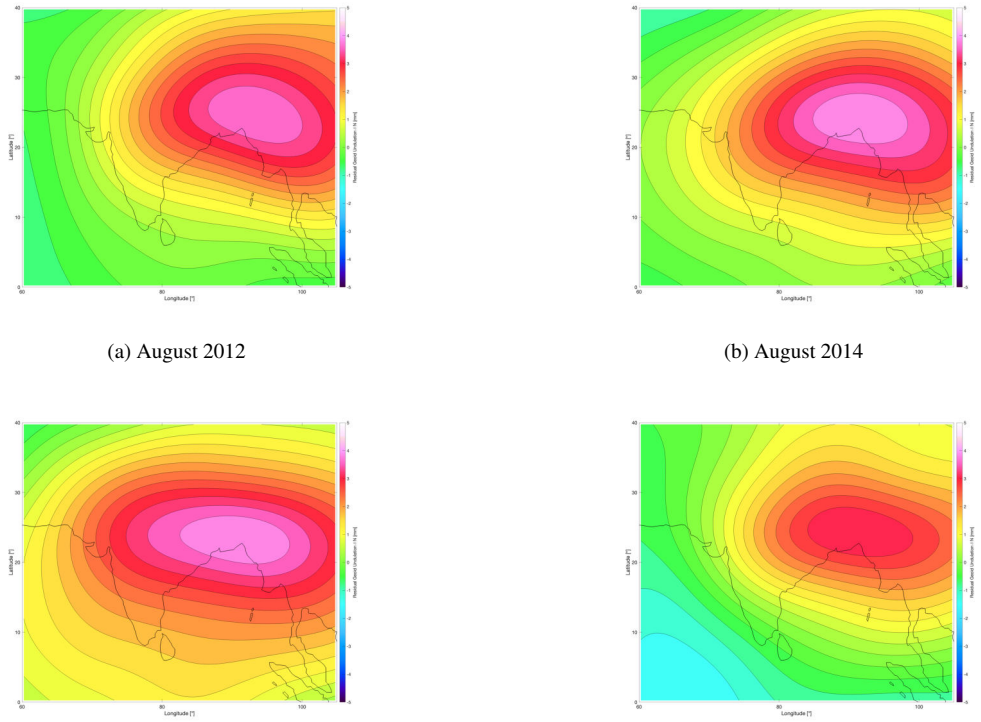

(a) August 2012

(b) August 2014

(c) August 2015

(d) August 2016

Figure 5.4: Seasonal (August) residual geoid undulations over India derived from GRACE CSR RL06 solutions for selected years.

years are reflected in variations in the strength and distribution of positive geoid undulations. Stronger positive anomaly years are associated with more seasonal mass buildup during the monsoon season, while weaker or more diffuse patterns indicate relatively lower hydrological loading.

Since the other years continuously exhibit the distinctive monsoon-related gravity response, the lack of August 2013 has no bearing on how the seasonal signal should be interpreted. Large-scale, periodic hydrological mass fluctuations over India are reliably captured by the GRACE-derived geoid undulations, as evidenced by the continuity of the observed patterns before and after 2013.

Overall, the August geoid undulation maps show that GRACE can resolve seasonal mass redistribution at regional scales, but they also highlight the importance of interpreting these findings in terms of broad hydrological signals rather than short-wavelength spatial features (Wouters et al., 2014).

5.3.3 Temporal Trend of Geopotential Variations at 500 km Altitude

From 2012 to 2016, Figure 5.5 shows how the mean and root mean square (RMS) geopotential changed over time at a height of 500 km. Periodic mass redistribution processes are shown by the mean geopotential time series, which has a strong seasonal signal with recurring peaks and minima. They mostly happen because of large-scale hydrological cycles, such as changes in yearly water storage and the movement of continental mass, which control the gravity signal at this height (Wahr et al., 1998; Tapley et al., 2004).

Not only does the mean geopotential change with the seasons, but it also changes slightly from year to year, which suggests that the mass distribution will experience longer-term changes. The RMS geopotential time series demonstrates how the geopotential field changes over space as a whole and has higher values when the mass changes more quickly. The relationship between peaks in the RMS values and extremes in the mean geopotential shows that seasonal mass redistribution changes the average signal and makes the signal more different in different places (Wouters et al., 2014).

In general, the results show that at an altitude of 500 km, large-scale, seasonally changing mass signals have a major effect on the geopotential field, while features with shorter wavelengths are much less affected. This behavior aligns with the diminished sensitivity of higher-altitude measurements to minor mass fluctuations. Appendix A shows the geopotential trends at 200 km altitude, where shorter spatial wavelengths are more noticeable, for comparison.

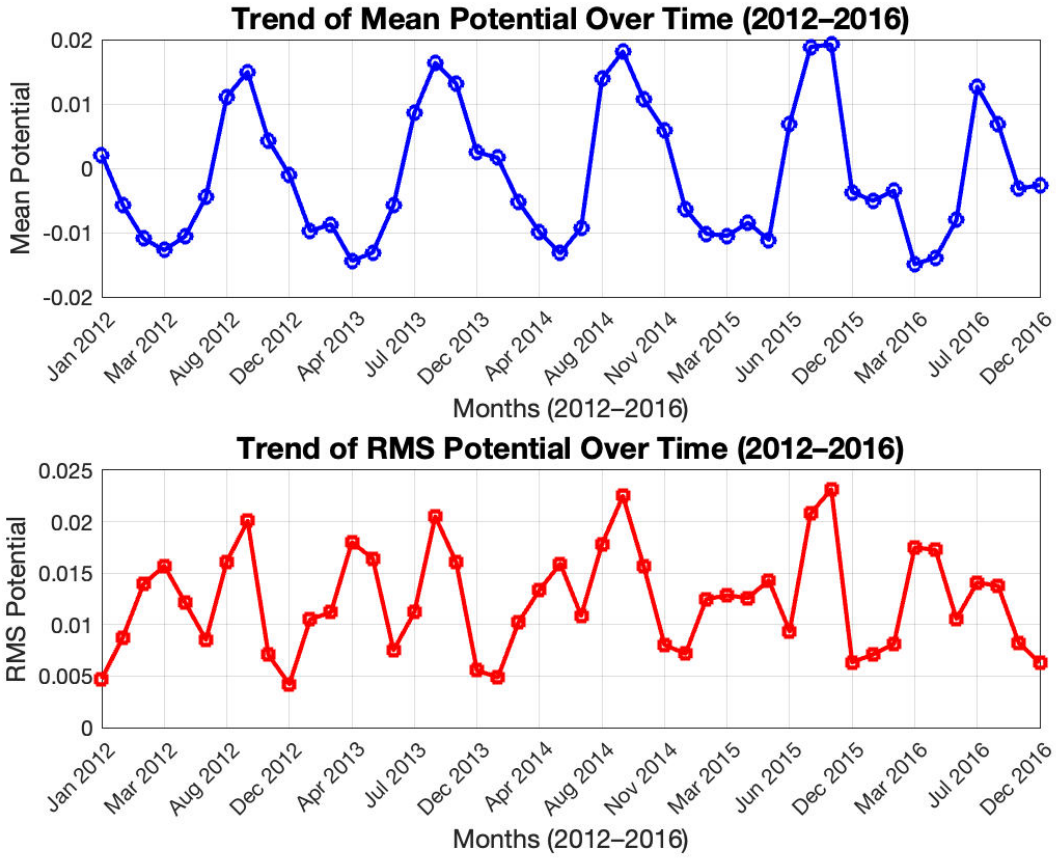

Figure 5.5: Temporal trend of mean and RMS geopotential at 500 km altitude for the period 2012–2016.

5.4 Total Water Storage (TWS)

Here, GRACE-derived Total Water Storage (TWS) anomalies are analysed here to investigate hydrological mass variations over India,as described in the methodology Section 3.6. The following results focus on the spatial and temporal behaviour of TWS anomalies, highlighting both intra-annual variability and seasonal characteristics relevant to drought development.

5.4.1 Monthly TWS variations in 2015 (Spatial-scale analysis)

The following maps show monthly GRACE-derived TWS anomalies over India for selected months in 2015.

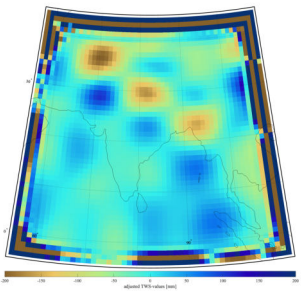

(a) January

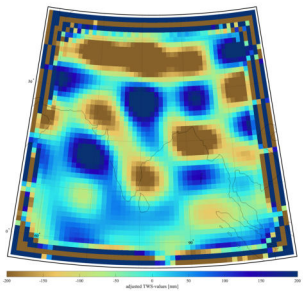

(b) February

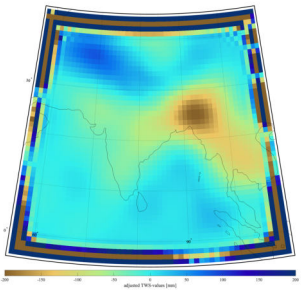

(c) March

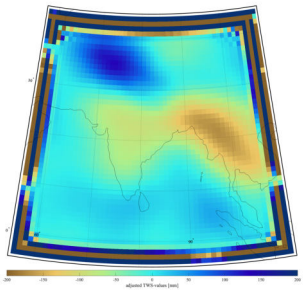

(d) April

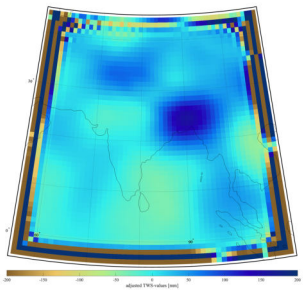

(e) July

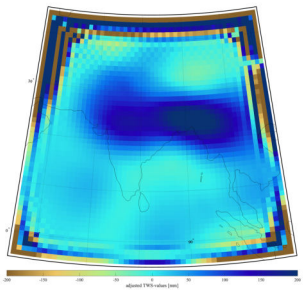

(f) August

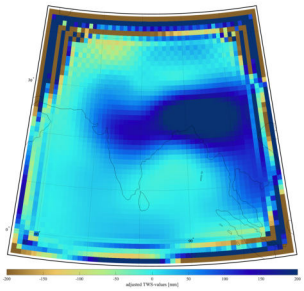

(g) September

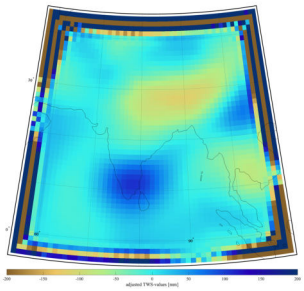

(h) December

Figure 5.6: Monthly Total Water Storage (TWS) anomalies over India for selected months in 2015 derived from GRACE data using the inversion approach.

The monthly TWS anomaly maps from GRACE reveal a clear seasonal change in water storage over India in 2015. The beginning of the year had conditions that were mostly neutral, then there was a notable rise in storage during the monsoon season, and finally, by the end of the year, storage started to go back down (Fig. 5.6). The spatial patterns match what we expect to happen during the yearly hydrological cycle: drawdown before the monsoon (mostly caused by evapotranspiration and the use of groundwater and surface water) and recharging during the monsoon (caused by rainfall and soaking across the whole basin) (Rodell et al., 2009; Asoka et al., 2017). This is most clear from July to September.

From January to April, most of the domain has only small anomalies, but other areas have much larger ones. In March and April, some portions of the study area show signs of pre-monsoon depletion, while other parts stay near to neutral. This shows how different parts of India have different amounts of water storage variations. The February map shows more small-scale patchiness than the January map. This is probably because of the blocky look and the alternating positive and negative cells. This month should be looked at more in terms of large-scale trends than small-scale details (Landerer and Swenson, 2012; Long et al., 2013).

The monsoon months (July–September) have the most coherent and physically interpretable signal. Here, a large positive anomaly forms and grows over large areas of the region, showing that the region gains net storage during the wet season. The positive signal's spatial range and amplitude grow from July to August/September. This is in line with the accumulation of water in soil moisture, surface water, and groundwater throughout the wet season (Asoka et al., 2017). By December, the anomaly field is weaker and more mixed again. This suggests that we are moving into the post-monsoon depletion phase, where the water that was stored throughout the wet season is being lost through evaporation and usage.

Finally, some things at the domain margins (such a colored frame and sharp gradients near the edges) show edge effects or leakage and show how hard it is for GRACE-based inversions to find sharp spatial boundaries. So, the maps are best for figuring out patterns on a regional scale, not on small, isolated areas. These findings require a comparison with independent hydrological data (e.g., GLDAS rainfall/runoff/soil moisture or basin-averaged time series) to enhance the physical interpretation of the deduced storage variations.

Some features at the edges of the domain, including a colorful frame and steep gradients near the edges, show that there are edge effects or leaks.GRACE looks at the gravity field on large spatial scales, and the inversion happens on a limited tesseroid domain. Because of this, signals from inside and outside the domain cannot be properly separated. As a result, the solution tends to show leakage (true signals spreading across the boundary) near the edges, especially where regularization enforces smoothness. Also, having less data support near the boundary can make the model setup (domain extent, regularization strength, and filtering) more sensitive, which can cause boundary artifacts that are easy to see. So, interpretation should look at big, connected regional patterns (such the positive anomalies related to the monsoon in July–September) instead of small patches that are next to the edge (Long et al., 2013; Wouters et al., 2014).

5.4.2 Event-focused TWS anomalies during 2012–2016 (August, 2012-2016)

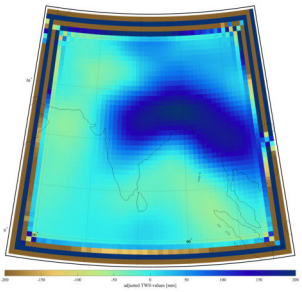

(a) August 2012

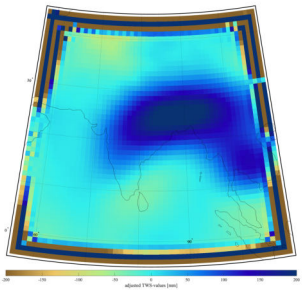

(b) August 2014

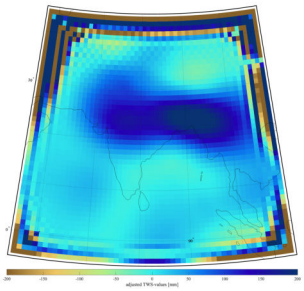

(c) August 2015

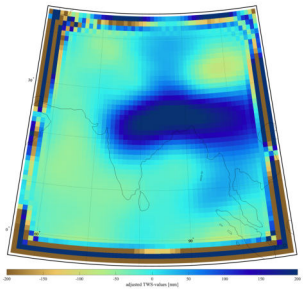

(d) August 2016

Figure 5.7: Event-focused TWS anomalies over India for August (2012–2016) derived from CSR GRACE spherical harmonic solutions using DDK2 filtering and the inversion framework.

August TWS anomaly maps for several years between 2012 and 2016 are compared to show how things changed from year to year during the peak monsoon season (some months and years are missing since the GRACE record is incomplete). In all available August epochs, the most noticeable characteristic is a huge positive TWS anomaly band over northern India. This is in line with recharge caused by the monsoon and storage accumulation at the basin level. After DDK2 filtering and the effective spatial resolution of GRACE-based products, the strongest signals show up as broad, smooth anomalies on a size of hundreds of kilometers (Kusche, 2007; Tapley et al., 2004).

In August 2012 (shown in Fig. 5.7) , there was a clear positive anomaly over the northern to north-central sector, and weaker anomalies over peninsular India. The spatial structure of 2014 (August) is comparable, but the high-amplitude core seems to be a little smaller than it was in 2012. This suggests that storage gains are either smaller or more confined to a specific area at the same time of year. The year 2015 August has the biggest and strongest positive anomaly of the years presented, with the northern belt getting bigger and stronger. This means that the recovered field has a stronger large-scale storage signal this month than it did in the other August images (within the limits of GRACE resolution and filtering). The northern positive ring is still there in August 2016, but the anomaly looks more limited and weaker overall. Compared to 2015, bigger areas are moving toward near-neutral values.

The August comparison shows that the seasonal monsoon imprint is still there, but the amount and area of recovered storage gains changes a lot from year to year. This is an important aspect to remember when looking at the drought development and recovery stages from GRACE-derived TWS (Asoka et al., 2017; Long et al., 2013; Wouters et al., 2014).

5.4.3 Statistical Characteristics of TWS Variability at 500 km Altitude (2012–2016)

Figure 5.8 shows how statistical Total Water Storage (TWS) data changed over time at an altitude of 500 km from 2012 to 2016. Using GRACE-based inversion data, the figure shows the monthly mean, standard deviation, minimum, and maximum TWS values. This gives a quick look at both the overall trend and the changes in TWS over time.

The mean TWS time series has amplitude changes that are not very big compared to the extremes. This suggests that large positive and negative anomalies are averaged out at this height. On the other hand, the maximum and lowest TWS values change a lot from season to season, which is due to substantial differences in water flow caused by monsoon-driven recharge and dry-season depletion. The repeated pattern of extremes shows that moving water storage over the Indian subcontinent is the most important thing that happens (Rodell et al., 2009; Asoka et al., 2017).

The standard deviation follows a distinct seasonal pattern and goes more when there is more hydrological activity, which means that TWS anomalies are more spread out in space. Peaks in the standard deviation generally happen at the same time as very high or very low values, which means that big hydrological events have a big effect on geographical variability (Long et al., 2013). In general, the results show that observations at higher altitudes smooth out short-wavelength signals but strongly capture TWS variability that is large-scale and driven by the seasons. This makes them good for climatological and long-term hydrological studies (Wouters et al., 2014). Appendix A shows the TWS statistics for 200 km altitude, which are more sensitive to shorter spatial wavelengths.

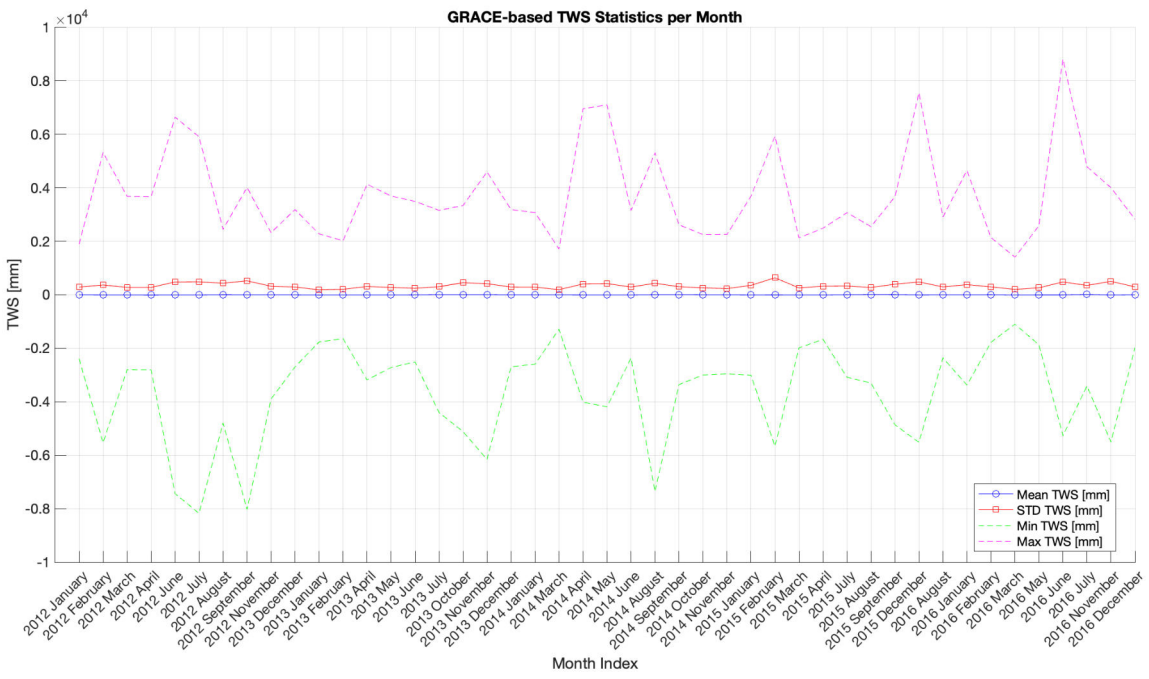

Figure 5.8: Monthly mean, standard deviation, minimum, and maximum Total Water Storage (TWS) anomalies at 500 km altitude for the period 2012–2016 derived from GRACE data.

5.5 Two-altitude comparison

To assess the sensitivity of the retrieved GRACE-derived TWS anomalies to evaluation altitude, the monthly fields were calculated at two altitudes (200 km and 500 km). This comparison is physically important because altering the evaluation altitude generates an upward extension of the gravity field: elevated altitudes generally diminish short-

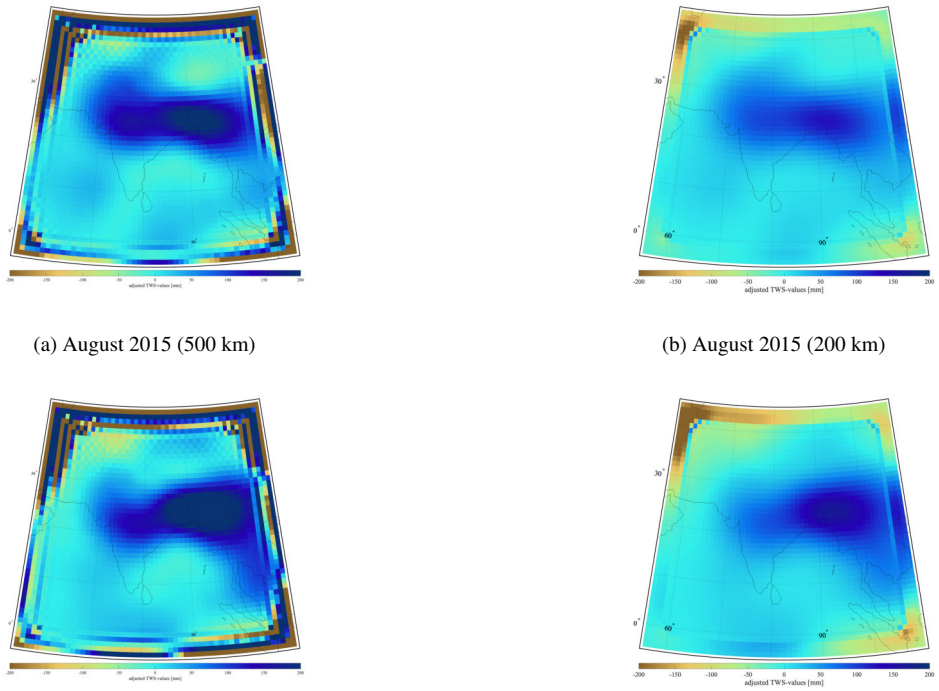

(a) August 2015 (500 km)

(b) August 2015 (200 km)

(c) September 2015 (500 km)

(d) September 2015 (200 km)

Figure 5.9: Two-altitude comparison of GRACE-derived TWS anomalies over India.

wavelength signals, resulting in smoother fields with diminished amplitudes, while stable large-scale hydrological patterns are expected to persist (Wahr et al., 1998; Wouters et al., 2014).
So, the comparison of altitudes is a straightforward way to verify for robustness. If the primary anomaly centers and their sign stay the same at both 200 km and 500 km, the signal can be seen as stable on a regional level. There should be differences mainly in amplitude and smoothness. The 500 km fields should have weaker extremes and structures that are more spatially coherent (Tapley et al., 2004; Landerer and Swenson, 2012). On the other hand, small patches that only show up at 200 km, especially near the domain boundary, are more likely to be affected by residual noise, leakage, or edge effects, thus they should be taken with caution. The comparison reveals that 500 km gives a conservative and robust representation adequate for climatological drought evaluation, while 200 km is more sensitive to localized variability but also more prone to leakage and boundary artifacts.

5.5.1 Spatial impact of altitude

The spatial maps at 200 km and 500 km demonstrate that the primary TWS anomaly structures in India are maintained at various altitudes. The broad-scale anomaly distribution (sign and approximate spatial extent) stays the same in both months. This means that the patterns we see are caused by long-wavelength mass variations that GRACE can see clearly after DDK2 filtering. But the 500 km fields look smoother, with less steep local gradients and lower peak values than the 200 km charts. This behavior is in line with the fact that higher-degree components are less strong at higher altitudes, which shows that the higher-altitude representation reduces smaller-scale variability (Wouters et al., 2014; Landerer and Swenson, 2012).
The 200 km maps indicate regional differences that are a little clearer near the Indian landmass boundary. However, the 500 km maps show these differences less clearly. This means that some of the higher-frequency changes at lower altitudes may be caused by leakage and boundary effects, especially where there are strong changes from land to ocean or land to mountain (Long et al., 2013). The fact that the dominant large-scale anomaly pattern is the

same at both altitudes confirms that the key hydrological signal is strong, while the smaller-scale details should be considered with caution.

5.5.2 Interpretation and link to edge effects

The two-altitude comparison is also an effective method to find edge effects and spatial leakage. Because GRACE doesn't have very good spatial resolution and the filtering used makes noise go away at the expense of spatial information, signal spreading across the research area mask can affect anomalies that are close to the domain boundary (Wahr et al., 1998; Kusche, 2007). At lower altitudes (200 km), these impacts can be more pronounced as sharper transitions. At higher altitudes (500 km), the extra smoothing makes this less sensitive. So, when the two altitudes agree, it makes more sure about conclusions on a regional scale (like seasonal depletion and recovery patterns). On the other hand, when the two altitudes don't agree, it's likely because of a mix of leakage, filtering artifacts, and the fact that spherical-harmonic fields can't show sharp boundaries very well (Tapley et al., 2004; Landerer and Swenson, 2012).
In general, the altitude comparison shows that the timing and spatial footprint of the main TWS anomaly features stay the same, but the amplitude and apparent small-scale structure change depending on the evaluation altitude. This result is expected and backs up the idea that the two-altitude results can be used as complementary views. The 200 km fields keep more spatial detail, while the 500 km fields give a conservative, smoother picture of the same regional hydrological signal.

5.6 Overall Interpretation of GRACE-Derived Drought Characteristics

In conclusion, the findings show that Total Water Storage (TWS) anomalies obtained from GRACE give a clear and physically accurate picture of how the Indian drought has changed over time. The start of drought conditions is reflected by the formation of widespread negative TWS anomalies following periods of reduced monsoon recharge, while the amplitude and spatial breadth of these anomalies indicate the severity of water storage deficiencies. There have been negative TWS anomalies for several months in a row, which shows that GRACE can fix long-term droughts rather than short-term changes in water flow.
Temporal TWS data and geographical anomaly patterns always show that the seasons are strongly controlled by monsoon-driven recharge and dry-season depletion. Negative anomalies are more noticeable and more spatially coherent in years with weaker recharge, whereas years with larger monsoon influence show partial or full recovery of terrestrial water storage. These differences highlight how hydrological processes on a larger scale control the spread of droughts over the Indian subcontinent (Rodell et al., 2009; Asoka et al., 2017).
The two-altitude comparison backs up the strength of the discovered drought signals even further. The 200 km results keep more spatial complexity and are more sensitive to localized variability. However, the prevailing large-scale anomaly patterns are reliably repeated at 500 km with less amplitude and a smoother structure. This agreement shows that the main features of drought are caused by mass redistribution on a regional scale and are not caused by evaluation altitude, filtering, or boundary effects. This supports their use for regional and climatological drought assessment (Landerer and Swenson, 2012; Wouters et al., 2014).

6 Conclusion and Outlook

The study utilized DDK2 filtering to process CSR GRACE spherical harmonic solutions across India and subsequently generated monthly terrestrial water storage (TWS) anomalies by spherical harmonic synthesis and regularized inversion. The intermediate results (potential anomalies and geoid undulations) exhibited distinct and physically coherent seasonal patterns, demonstrating that the preprocessing and filtering reduced correlated noise while maintaining the predominant large-scale hydrological signal (Kusche, 2007).

The TWS fields that were created showed a significant seasonal cycle caused by the monsoon and consistent interannual variability during the time studied. Monthly maps that focused on specific events showed clear changes in the severity and spatial extent of anomalies between years. The two-altitude evaluation (200 km and 500 km) was used as an extra robustness check: the primary anomaly centers and their sign stayed mostly the same, but the higher-altitude fields were smoother and had lower amplitudes, which is expected from short-wavelength components losing energy (Wahr et al., 1998). In general, the consistency between processing stages and evaluation heights supports the idea that the main patterns show consistent changes in water storage over India on a regional scale. The data also show some of the known problems with GRACE-based products, such as low spatial resolution, leakage, and edge effects, especially around domain boundaries and steep land-ocean transitions. Future enhancements should concentrate on minimizing leakage and edge effects (for instance, scale-factor/forward-modelling adjustments and enhanced masking) and on measuring uncertainty by evaluating sensitivity to filter strength (DDK), regularization, and inversion configuration (Landerer and Swenson, 2012). To better connect the observed anomalies to the development and recovery of drought in India, the interpretation can be improved by comparing GRACE-derived TWS with independent hydro-climate datasets, such as GLDAS components and precipitation.

Acknowledgement

I would like to express my sincere gratitude to Dr.-Ing. Kurt Seitz for his guidance, valuable suggestions, and continuous support throughout the course of this study. His expertise in satellite gravimetry and geodetic data analysis was instrumental in shaping this work.

I also thank the Karlsruhe Institute of Technology (KIT) for providing the academic environment, computational resources, and research facilities required for this study. The gravity field data used in this work were obtained from publicly available GRACE monthly gravity field solutions, which enabled the analysis of terrestrial water storage variations presented in this report.

Finally, I would like to thank my colleagues and peers for their helpful discussions and support during the preparation of this report.

References

Asoka, A., Gleeson, T., Wada, Y., and Mishra, V. (2017): Relative contributions of monsoon precipitation and groundwater abstraction to drought severity in India. *Nature Geoscience* 10:109–117.

Baur, O. and Sneeuw, N. (2011): Assessing Greenland Ice Mass Loss by Means of Point-Mass Modeling: A Viable Methodology. *Journal of Geodesy* 85:607–615. DOI: 10.1007/s00190-011-0463-1.

Hansen, P. C. (1992): Analysis of Discrete Ill-Posed Problems by Means of the L-Curve. *SIAM Review* 34(4):561–580. DOI: 10.1137/1034115.

Hansen, P. C. (1999): The L-curve and its use in the numerical treatment of inverse problems. 1999.

Hansen, P. C. (2000): The L-curve and its use in the numerical treatment of inverse problems. In: *Computational Inverse Problems in Electrocardiology*. Ed. by P. Johnston. WIT Press, pp. 119–142.

Heck, B. and Seitz, K. (2007): A comparison of the tesseroid, prism and point-mass approaches for mass reductions in gravity field modelling. *Journal of Geodesy* 81:121–136.

Heiskanen, W. A. and Moritz, H. (1967): Physical Geodesy. W. H. Freeman & Co., San Francisco, USA.

Kusche, J. (2007): Approximate decorrelation and non-isotropic smoothing of time-variable GRACE-type gravity field models. *Journal of Geodesy* 81(11):733–749. DOI: 10.1007/s00190-007-0143-3.

Landerer, F. W. and Swenson, S. C. (2012): Accuracy of scaled GRACE terrestrial water storage estimates. *Water Resources Research* 48(4). DOI: 10.1029/2011WR011453.

Long, D., Longuevergne, L., and Scanlon, B. R. (2013): Global analysis of drought and flood in GRACE terrestrial water storage anomalies. *Hydrology and Earth System Sciences* 17:4475–4490.

Rodell, M., Velicogna, I., and Famiglietti, J. S. (2009): Satellite-based estimates of groundwater depletion in India. *Nature* 460:999–1002. DOI: 10.1038/nature08238.

Tapley, B. D., Bettadpur, S., Watkins, M., and Reigber, C. (2004): The gravity recovery and climate experiment: Mission overview and early results. *Geophysical Research Letters* 31(9):1–4. DOI: 10.1029/2004GL019920.

Wahr, J., Molenaar, M., and Bryan, F. (1998): Time variability of the Earth's gravity field: Hydrological and oceanic effects and their possible detection using GRACE. *Journal of Geophysical Research: Solid Earth* 103(B12):30205–30229.

Wouters, B., Bonin, J. A., Chambers, D. P., Riva, R. E., Sasgen, I., and Wahr, J. (2014): GRACE, time-varying gravity, Earth system dynamics and climate change. *Reports on Progress in Physics* 77(11):116801.

Appendix

A Appendices

A.1 Supplementary Time-Series Statistics at 200 km Altitude

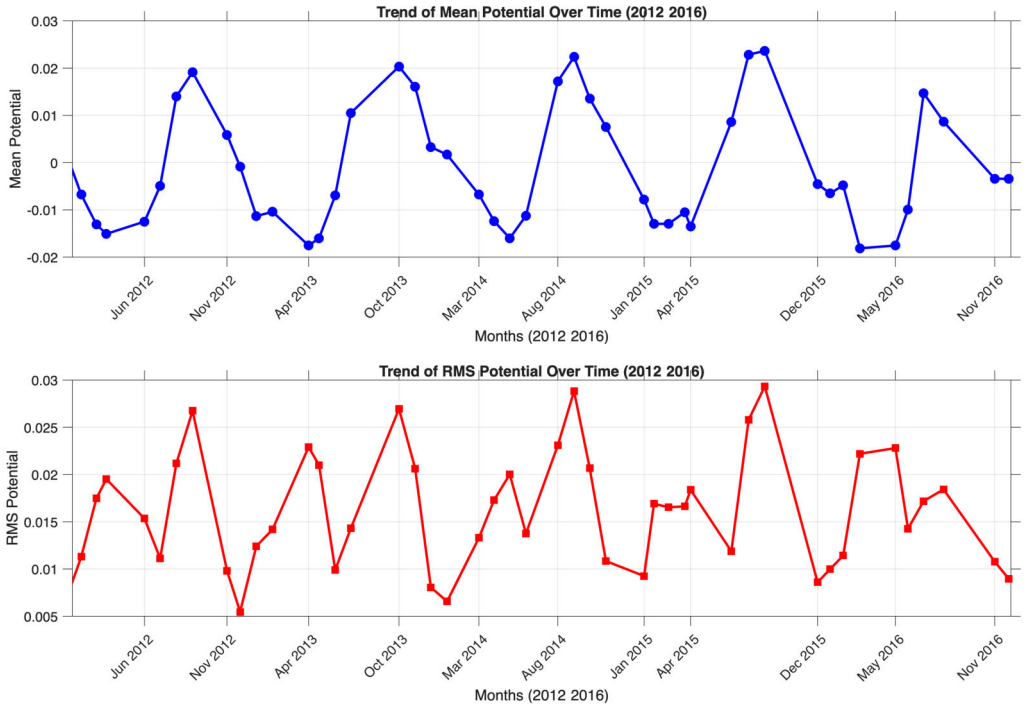

Figure A.1: Temporal evolution of the mean and root mean square (RMS) geopotential at 200 km altitude for the period 2012–2016. Compared to the 500 km results presented in the main text, the 200 km time series shows enhanced sensitivity to shorter spatial wavelengths while preserving the dominant seasonal signal.

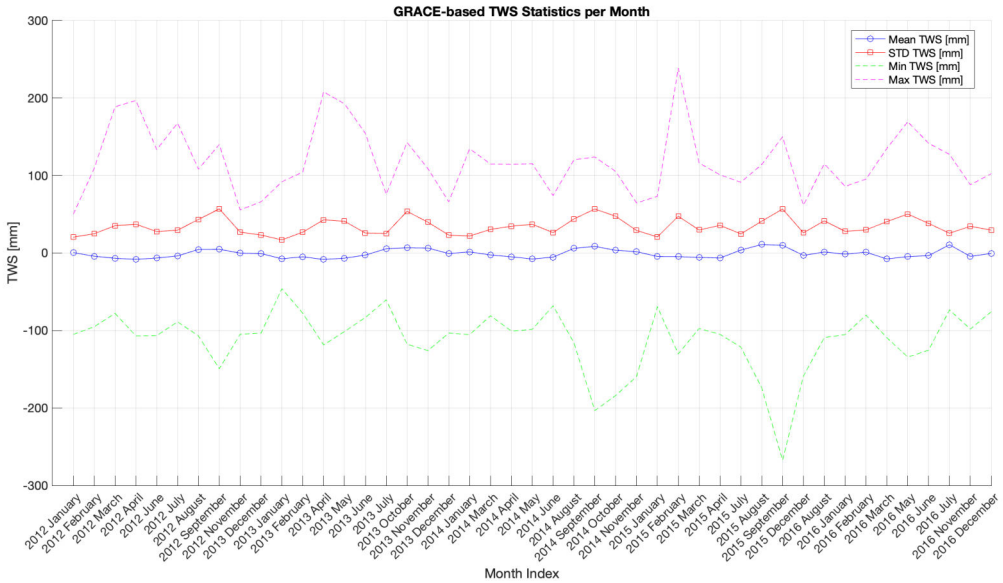

Figure A.2: This Figure contains time-series analyses of geopotential and Total Water Storage (TWS) statistics derived from GRACE and measured at an altitude of 200 km. These results add to the analysis at 500 km altitude that was mentioned about in the main text and show that shorter spatial wavelengths are more sensitive.

Analysis of Terrestrial Water Storage Variations across the Continent of Australia Using GRACE and GLDAS Monthly Solutions

Pratheeksh Suresh Babu[1]

1 Remote Sensing and Geoinformatics Master of Science (M.Sc.), KIT, Germany
E-Mail: ufrgw@student.kit.edu

Abstract

This study assesses terrestrial water storage (TWS) variability across Australia by integrating GRACE / GRACE-FO gravity field observations with GLDAS hydrological model outputs for the period 2003-2024. Monthly spherical harmonic solutions were processed via the Wahr approach to derive Equivalent Water Height (EWH) anomalies, enabling characterization of large-scale storage changes. To mitigate correlated errors and enhance gravity field quality, DDK filtering was applied, with the DDK5-filtered products selected for subsequent analyses.

GRACE-derived TWS anomalies exhibit pronounced spatial and temporal variability driven by climatic and hydrological processes across the continent. April 2011 is identified as a representative wet period, displaying widespread positive storage anomalies and elevated water accumulation, while October 2020 marks a relative dry period with reduced storage conditions. The contrasting hydrological states demonstrate the capability of GRACE/GRACE-FO observations to capture continental-scale TWS fluctuations and their response to evolving climate conditions.

Incorporation of GLDAS hydrological variables provides deeper insight into the individual storage components contributing to observed TWS changes. The joint analysis of GRACE/GRACE-FO and GLDAS datasets enables estimation of groundwater storage anomalies, facilitating the investigation of subsurface water dynamics across Australia. Overall, results underscore the effectiveness of satellite gravimetry coupled with land-surface modeling for monitoring TWS variability at continental scales.

The study offers a framework for understanding hydroclimatic variability and groundwater dynamics, supporting future water resource assessment and management across Australia. Outlooks include advancements in filtering, leakage corrections, and alternative GRACE products (e.g., mascon solutions), the integration of additional hydrological datasets, regional basin-scale investigations, and the extension to ongoing GRACE-FO observations to monitor long-term trends under changing climates. The methodologies herein are transferable to other regions facing significant water stress, contributing to drought assessment and climate impact studies at continental and basin scales.

Keywords GRACE · DDK5 · GLDAS · Total Water Storage (TWS) · Australia

KIT Scientific Working Papers
Issue Number 270
ISSN: 2194-1629
DOI: 10.5445/IR/1000191188
Online: June 2026

This document is licensed under the Creative Commons Attribution – Share Alike 4.0 International License (CC BY-SA 4.0):
https://creativecommons.org/licenses/by-sa/4.0/deed.en

1 Introduction

Terrestrial water storage (TWS) is a fundamental component of the Earth's hydrological system, representing the total amount of water stored on and beneath the land surface. It includes groundwater, soil moisture, surface water, snow and ice, as well as water stored in vegetation. Variations in terrestrial water storage are closely linked to droughts, floods, groundwater depletion, seasonal rainfall variability, and long-term climate-driven hydrological changes (Syed et al., 2008). Monitoring these variations is particularly important for Australia, where water availability exhibits strong spatial and temporal variability. Large parts of the continent are frequently affected by prolonged droughts, irregular precipitation patterns, and extreme hydrological events. Consequently, analysing terrestrial water storage variations across Australia provides valuable insights into regional water availability and large-scale mass redistribution within the Earth system.

The Gravity Recovery and Climate Experiment (GRACE) mission and its successor, GRACE Follow-On (GRACE-FO), provide a unique satellite-based approach for monitoring terrestrial water storage changes at continental and global scales (Tapley et al., 2004). Rather than measuring water directly, these missions observe temporal variations in the Earth's gravity field caused by mass redistribution within the Earth system. Monthly gravity field solutions are provided in the form of spherical harmonic coefficients by several processing centres, including the Center for Space Research (CSR), the Helmholtz Centre for Geosciences (GFZ, 2026), and the Jet Propulsion Laboratory (JPL). In this study, GRACE and GRACE-FO Level-2 monthly solutions from CSR are used, specifically DDK5 filtered products up to degree and order 96. A mean gravity field is first computed as a reference model, and monthly deviations from this reference field are subsequently transformed into terrestrial water storage anomalies using the methodology proposed by Wahr et al. (1998). This approach establishes a relationship between temporal gravity field variations and surface mass redistribution while accounting for the elastic response of the solid Earth through load Love numbers.

The resulting terrestrial water storage anomalies are expressed as Equivalent Water Height (EWH), which represents the observed mass change as an equivalent thickness of water distributed over the Earth's surface. Positive EWH values indicate an increase in water storage relative to the reference period, whereas negative values indicate water loss. One of the major advantages of GRACE observations is their ability to capture the integrated response of all terrestrial water storage components, including groundwater, soil moisture, surface water, and vegetation water. However, because GRACE measures only the total water storage signal, it cannot directly distinguish between individual hydrological components.

To support the interpretation of GRACE-derived water storage variations, data from the Global Land Data Assimilation System (GLDAS) are incorporated into the analysis (Rodell et al., 2004). GLDAS is a land surface modelling framework developed by NASA that combines meteorological forcing data, satellite observations, and land surface models to simulate hydrological and energy balance processes. In this study, GLDAS Version 2.1 monthly products are used to obtain information on soil moisture, runoff, canopy water storage, and other relevant hydrological variables. These datasets provide physically meaningful estimates of near-surface water storage components and enable a more detailed interpretation of the GRACE-derived total water storage signal. Furthermore, groundwater storage anomalies can be estimated indirectly by subtracting GLDAS-derived surface water storage components from the total terrestrial water storage observed by GRACE.

The study area considered in this report is the Australian continent. Australia is particularly suitable for terrestrial water storage investigations because of its pronounced climatic variability and frequent occurrence of hydrological extremes. Northern Australia experiences seasonal monsoonal rainfall, whereas central and western Australia are dominated by arid and semi-arid environments. Eastern and southeastern Australia are characterised by intensive agricultural activity and substantial water demand, making these regions highly sensitive to both droughts and flood events. The strong climatic and hydrological contrasts across the continent provide an excellent opportunity to investigate large-scale water storage dynamics using satellite gravimetry and land surface model data.

The analysis covers the period from 2003 to 2024, encompassing the main GRACE mission, the transition period between GRACE and GRACE-FO, and the recent GRACE-FO observation era. Based on the obtained results, April 2011 was selected as a representative wet period because it exhibited strong positive terrestrial water storage anomalies across large parts of Australia. These conditions were associated with the intense 2010–2011 La Niña event, which resulted in above-average rainfall and widespread flooding across the continent. In contrast, October 2020 was selected as a representative dry period because it exhibited comparatively low terrestrial water storage conditions and widespread storage depletion. The comparison between these two contrasting hydrological states provides valuable insight into the magnitude and spatial distribution of water storage variability across Australia.
The primary objective of this study is to analyse and visualise terrestrial water storage variations across Australia using GRACE and GRACE-FO monthly gravity field solutions together with GLDAS hydrological data. The analysis includes the computation of terrestrial water storage anomalies, the generation of spatial maps, and the investigation of temporal variability through regional monthly averages. Particular emphasis is placed on comparing GRACE-derived terrestrial water storage with GLDAS-derived hydrological components and estimating groundwater storage variations from the combined datasets. Through the investigation of contrasting wet and dry periods, this study aims to improve the understanding of continental-scale hydrological variability and demonstrate the capability of satellite gravimetry for monitoring water storage changes across Australia.

2 Theoretical Aspects

The analysis of terrestrial water storage variations from satellite gravimetry requires an understanding of the Earth's gravity field, its representation through spherical harmonics, and the relationship between gravity field changes and surface mass redistribution. This chapter introduces the theoretical concepts underlying the GRACE and GRACE-FO missions, the derivation of Equivalent Water Height (EWH) using the approach of Wahr et al. (1998), and the hydrological information provided by the GLDAS land surface model. These concepts form the basis for the methodology and interpretation of the results presented in this study.

2.1 Earth's Gravity Field and Mass Redistribution

The Earth's gravity field is not constant but varies in response to the redistribution of mass within the Earth system. Changes in terrestrial water storage, including groundwater, soil moisture, surface water, and ice mass, alter the Earth's mass distribution and consequently modify the gravity field. These gravity variations can be detected by satellite missions and used to infer hydrological changes over large spatial scales.
Since water represents one of the most dynamic mass components of the Earth system, monitoring gravity field variations provides valuable information about continental-scale water storage dynamics. In regions experiencing floods, droughts, or groundwater depletion, the associated mass changes produce measurable gravity anomalies that can be observed from space.

$$V(P) = \frac{GM}{r} \sum_{n=0}^{\infty} \left(\frac{R}{r}\right)^n \sum_{m=0}^{n} (\bar{C}_{nm} \cos m\lambda + \bar{S}_{nm} \sin m\lambda) \bar{P}_{nm}(\sin \varphi) \tag{2.1}$$

where,
GM : Geocentric gravitational constant
R : Radius of the reference sphere.
$\bar{C}_{nm}, \bar{S}_{nm}$: Fully normalised spherical harmonic coefficients of degree n and order m
$\bar{P}_{nm}$: Fully normalised Legendre functions of degree n and order m.

2.2 GRACE and GRACE-FO Monthly Gravity Solutions

The Gravity Recovery and Climate Experiment (GRACE) mission was launched (Tapley et al., 2004) in March 2002. It was a joint mission of NASA and the German Aerospace Center (DLR). The mission consisted of two satellites flying approximately 220 km apart in the same orbit. By continuously measuring small variations in the distance between the satellites using a K-band microwave ranging system, GRACE was able to detect changes in the Earth's gravity field caused by mass redistribution.

Following the successful completion of the original mission in 2017, the GRACE Follow-On (GRACE-FO) mission was launched in 2018 to continue the observation record. Together, GRACE and GRACE-FO provide more than two decades of continuous observations of global mass transport processes.

Monthly gravity field solutions are generated by several processing centres, including the Center for Space Research (CSR), the German Research Centre for Geosciences (GFZ), and the Jet Propulsion Laboratory (JPL). These solutions are provided in the form of spherical harmonic coefficients and represent temporal variations in the Earth's gravity field. In this study, CSR Release 06 monthly solutions filtered with DDK5 filter are used for the analysis of terrestrial water storage changes across Australia..

2.3 Spherical Harmonic Representation and Gravity Field Variations

GRACE monthly gravity field solutions are represented by normalized spherical harmonic coefficients $\bar{C}_{nm}$ and $\bar{S}_{nm}$, where n denotes the spherical harmonic degree and m denotes the order. Lower degrees represent large-scale gravity field structures, while higher degrees describe progressively smaller spatial features.

Coefficients representing the mean (reference) model are calculated as:

$$\bar{C}_{nm} = \frac{1}{T}\sum_{t=1}^{T} C_{nm}(t), \qquad \bar{S}_{nm} = \frac{1}{T}\sum_{t=1}^{T} S_{nm}(t) \tag{2.2}$$

The resulting coefficient differences

$$\Delta C_{nm}(t) = C_{nm}(t) - \bar{C}_{nm}, \qquad \Delta S_{nm}(t) = S_{nm}(t) - \bar{S}_{nm} \tag{2.3}$$

represent temporal gravity field variations caused by changes in mass distribution. Before these coefficients can be transformed into terrestrial water storage changes, their quality and spectral characteristics must be evaluated.

Figure 2.1 presents the accuracy behaviour of the spherical harmonic coefficients and their associated degree variances for a representative monthly solution. Panels (a) and (b) illustrate the formal and relative accuracies of the coefficients, while panels (c) and (d) show the corresponding degree variance statistics. The figure demonstrates that coefficient uncertainties generally increase with spherical harmonic degree, reflecting the reduced signal-to-noise ratio at shorter spatial wavelengths. Such analyses are important for assessing the quality of the gravity field solutions and motivate the application of filtering techniques before further processing.

2.4 Equivalent Water Height from GRACE Observations

The transformation of gravity field anomalies into terrestrial water storage variations follows the methodology proposed by Wahr et al. (1998). Under the assumption that temporal gravity field changes are primarily caused by surface mass redistribution, variations in the spherical harmonic coefficients can be related to changes in terrestrial water storage.

The resulting storage anomalies are commonly expressed as Equivalent Water Height (EWH), which represents the thickness of a hypothetical water layer producing the observed gravity change. Positive EWH values indicate an increase in terrestrial water storage relative to the reference period, whereas negative values indicate water loss.

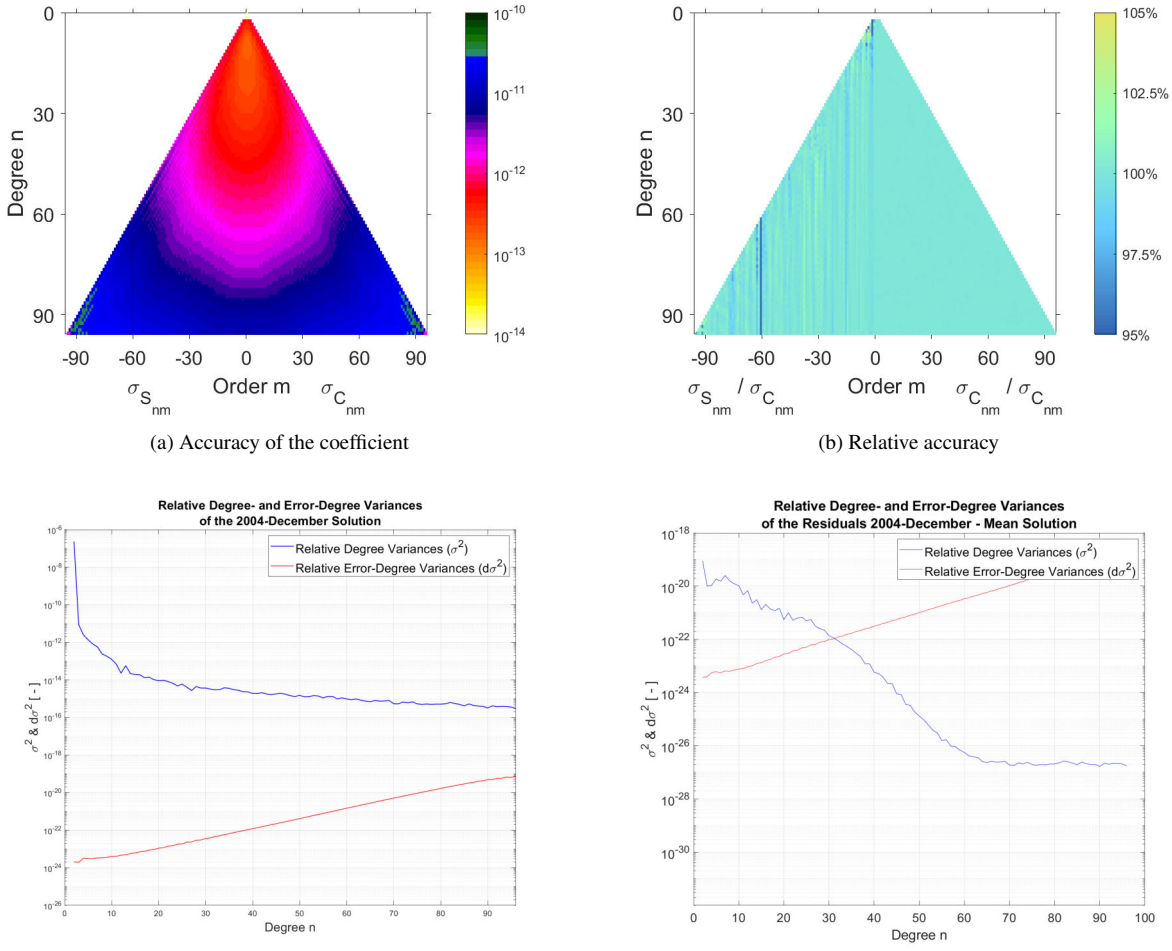

(a) Accuracy of the coefficient

(b) Relative accuracy

(c) Degree and Error Degree variance

(d) Degree and Error Degree variance of the relative model

Figure 2.1: Accuracy behaviour of the spherical harmonic coefficients and degree and error degree variance for the December 2004 GRACE-FO solution.

An important aspect of the transformation is the inclusion of load Love numbers, which account for the elastic response of the solid Earth to surface loading. This ensures that both the direct gravitational effect of mass redistribution and the indirect effect of Earth's deformation are incorporated into the final storage estimates.

$$\Delta h(\varphi,\lambda) = \frac{a\rho_e}{3\rho_w}\sum_{n=0}^{N}\sum_{m=0}^{n}\frac{2n+1}{1+k_n}\bar{P}_{nm}(\sin\varphi)\left[\Delta\bar{C}_{nm}\cos(m\lambda)+\Delta\bar{S}_{nm}\sin(m\lambda)\right] \tag{2.4}$$

The resulting EWH grids provide a physically meaningful representation of terrestrial water storage variations and form the basis for the subsequent spatial and temporal analyses.

2.5 Global Land Data Assimilation System (GLDAS)

The Global Land Data Assimilation System (GLDAS) is a land surface modelling framework developed by NASA to simulate terrestrial hydrological and energy balance processes at the global scale. GLDAS integrates satellite observations, ground-based measurements, and meteorological forcing data within physically based land surface models to produce spatially and temporally consistent estimates of hydrological variables.

In this study, GLDAS Version 2.1 outputs generated by the Noah Land Surface Model were utilised. The selected variables include soil moisture storage, canopy water storage, and runoff-related components, which represent major contributors to terrestrial water storage. These variables provide valuable information for interpreting the

integrated water storage signal observed by GRACE/GRACE-FO and for assessing the contribution of individual hydrological components to total water storage variability.
Unlike GRACE/GRACE-FO, which measures changes in total terrestrial water storage, GLDAS provides estimates of individual storage components within the hydrological cycle. Consequently, the combined use of GRACE/GRACE-FO and GLDAS enables a more comprehensive assessment of hydrological variability across Australia and facilitates the estimation of groundwater storage variations through the separation of surface and subsurface water storage components.

2.6 Groundwater Storage Estimation

GRACE/GRACE-FO observations represent integrated terrestrial water storage variations, whereas GLDAS provides estimates of individual hydrological storage components. Consequently, groundwater storage variations can be estimated using a residual approach in which the GLDAS-derived storage components are subtracted from the total terrestrial water storage signal obtained from GRACE/GRACE-FO observations.

$$\Delta GW = \Delta TWS_{\mathrm{GRACE}} - (\Delta SM + \Delta RO + \Delta SWE + \Delta CW) \tag{2.5}$$

where ΔGW denotes groundwater storage anomaly, $\Delta TWS_{\mathrm{GRACE}}$ represents the total terrestrial water storage anomaly derived from GRACE/GRACE-FO observations, ΔSM denotes soil moisture storage anomaly, ΔRO represents runoff storage anomaly, ΔSWE denotes snow water equivalent anomaly, and ΔCW represents canopy water storage anomaly.
The resulting groundwater storage anomalies provide valuable information about subsurface water dynamics and support the investigation of groundwater contributions to terrestrial water storage variability across Australia. By combining GRACE/GRACE-FO observations with GLDAS hydrological variables, it becomes possible to distinguish groundwater-related changes from variations occurring within the near-surface components of the hydrological cycle.

3 Data

The analysis of terrestrial water storage variations across Australia requires the integration of satellite gravimetry observations and hydrological model data. In this study, monthly gravity field solutions from the GRACE and GRACE-FO missions are combined with land surface hydrological variables from the Global Land Data Assimilation System (GLDAS). While GRACE provides observations of total terrestrial water storage changes resulting from mass redistribution within the Earth system, GLDAS supplies information on individual hydrological storage components that support the interpretation of the observed gravity-derived signals. Together, these datasets enable the investigation of long-term water storage dynamics and groundwater variability across the Australian continent.

3.1 Study Area

Australia, the world's sixth-largest continent, covers an area of approximately 7.7 million km² and exhibits substantial climatic and hydrological diversity. The continent ranges from tropical environments in the north to temperate regions in the south, while much of the interior is characterized by arid and semi-arid conditions. Due to its geographical location and climate variability, Australia experiences pronounced fluctuations in precipitation, evapotranspiration, runoff, and groundwater recharge.
The continent has been affected by several major hydrological extremes during the past two decades, including prolonged droughts, intense rainfall events, and widespread flooding. These events significantly influence terrestrial water storage and make Australia an ideal study region for investigating large-scale water storage variations using satellite gravimetry. The strong spatial and temporal variability of water resources across the continent pro-

vides an excellent opportunity to evaluate the capability of GRACE and GLDAS datasets to monitor hydrological changes.

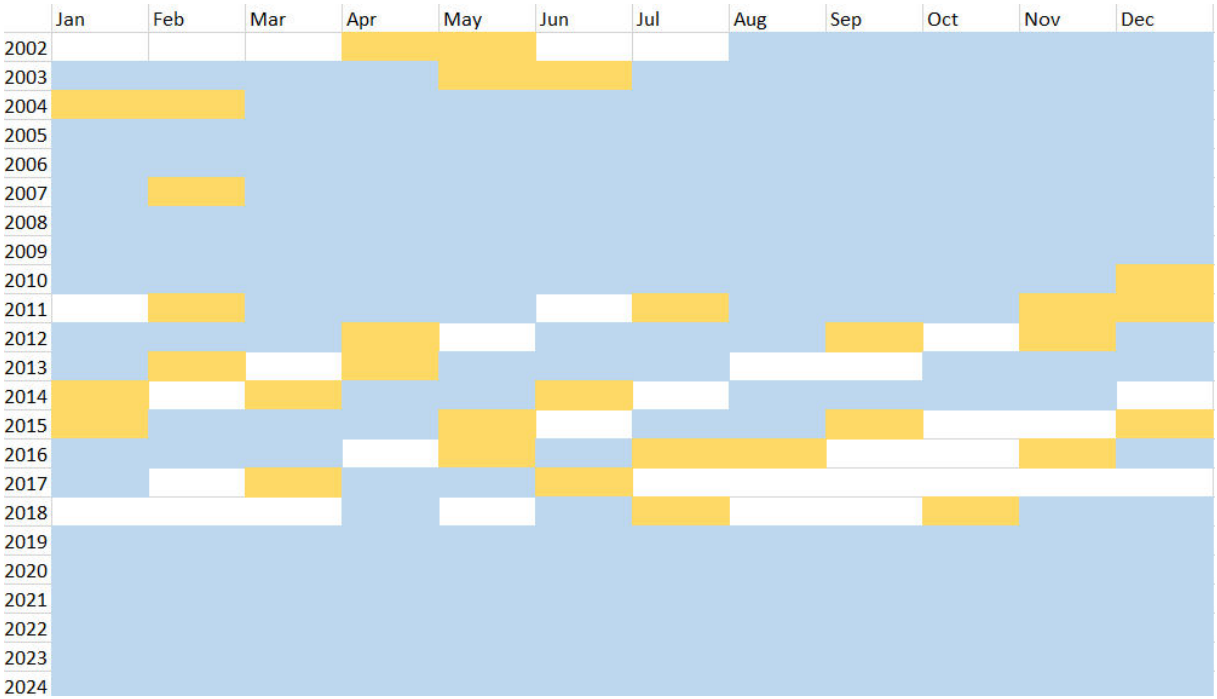

Figure 3.1: Availability of GRACE and GRACE-FO monthly data from 2002 to 2024. Blue indicates fully available data, yellow indicates partially available data, and white cells represent missing data.

3.2 GRACE and GRACE-FO Data

The primary dataset used in this study consists of monthly gravity field solutions derived by CSR from the GRACE and GRACE-FO satellite missions (ICGEM, 2026). GRACE operated from 2002 to 2017 and was followed by the GRACE Follow-On mission, launched in 2018 to ensure continuity in global gravity field observations. The availability of GRACE and GRACE-FO monthly data used in this study is illustrated in Figure 3.1. Both missions measure temporal variations in the Earth's gravity field caused by mass redistribution processes occurring within the atmosphere, oceans, cryosphere, and terrestrial hydrological system.

Monthly gravity field solutions were obtained from the Center for Space Research (CSR) and accessed through the International Centre for Global Earth Models (ICGEM, 2026). The data are provided as Level-2 spherical harmonic coefficients up to degree and order 96. To minimize correlated errors and striping artefacts that commonly affect GRACE solutions, DDK5 decorrelation filtered solutions are used.

Monthly gravity field anomalies were computed relative to a mean reference model and subsequently transformed into Equivalent Water Height (EWH), which serves as a measure of terrestrial water storage change.

3.3 GLDAS Data

To complement the GRACE observations, hydrological model outputs from the Global Land Data Assimilation System (GLDAS) Version 2.1 were employed. GLDAS is developed by NASA and combines satellite observations, ground-based measurements, and meteorological forcing data within physically based land surface models to simulate water and energy fluxes at the global scale.

This study utilizes outputs from the Noah Land Surface Model, which provides monthly estimates of several hydrological storage components. The selected variables include soil moisture storage within different soil layers,

canopy water storage, and runoff-related components. These variables represent important contributors to terrestrial water storage and provide valuable information for interpreting the GRACE-derived water storage anomalies. Unlike GRACE, which measures the integrated response of all terrestrial water storage components, GLDAS provides information on individual hydrological processes. Consequently, the combined analysis of both datasets allows for a more comprehensive assessment of water storage dynamics and supports the estimation of groundwater storage variations across Australia.

3.4 Selection of Representative Wet and Dry Periods

To investigate the spatial behaviour of terrestrial water storage under contrasting hydrological conditions, representative wet and dry periods were selected from the analysed time series. The selection was based on the magnitude of the observed terrestrial water storage anomalies derived from the GRACE dataset and supported by the corresponding GLDAS hydrological conditions.

April 2011 was identified as the representative wet period, exhibiting strong positive terrestrial water storage anomalies across large parts of Australia. The elevated storage conditions observed during this period reflect substantial water accumulation within surface and subsurface reservoirs and provide an example of a hydrologically wet state.

In contrast, October 2020 was selected as the representative dry period due to the occurrence of comparatively low terrestrial water storage conditions. The reduced storage levels observed during this period indicate significant water deficits and represent a hydrologically dry state.

The comparison of these two contrasting periods provides valuable insight into the response of terrestrial water storage and groundwater systems to changing climatic and hydrological conditions. Furthermore, these periods serve as reference cases for the detailed spatial and temporal analyses presented in the Results and Discussion chapter.

4 Methodology

This study combines GRACE/GRACE-FO gravity field observations with GLDAS hydrological model outputs to investigate terrestrial water storage variations across Australia during the period 2003-2024. The methodological framework consists of the derivation of terrestrial water storage anomalies from monthly gravity field solutions, the processing of hydrological storage components from GLDAS, and the subsequent estimation of groundwater storage variations. The overall workflow adopted in this study is illustrated in Figure 4.1.

4.1 Derivation of Terrestrial Water Storage from GRACE

Monthly gravity field solutions from the CSR Release 06 dataset were used as the primary source of information on terrestrial water storage variability. The data are provided as spherical harmonic coefficients up to degree and order 96 and describe temporal variations in the Earth's gravity field resulting from mass redistribution processes. A mean reference gravity field was first established from all available monthly solutions. Monthly gravity field anomalies were subsequently computed relative to this reference model following the procedure described in Section 2.3. To reduce correlated errors and striping artefacts commonly present in GRACE solutions, the DDK5 decorrelation filter (Kusche, 2007; Kusche et al., 2009) were applied prior to further processing.

The filtered gravity field anomalies were transformed into Equivalent Water Height (EWH) using the formulation of Wahr et al. (1998) presented in Section 2.4. This transformation relates temporal gravity field variations to surface mass redistribution and enables the estimation of terrestrial water storage anomalies. The resulting coefficients were synthesised onto a regular spatial grid covering Australia, producing monthly maps of terrestrial water storage variations.

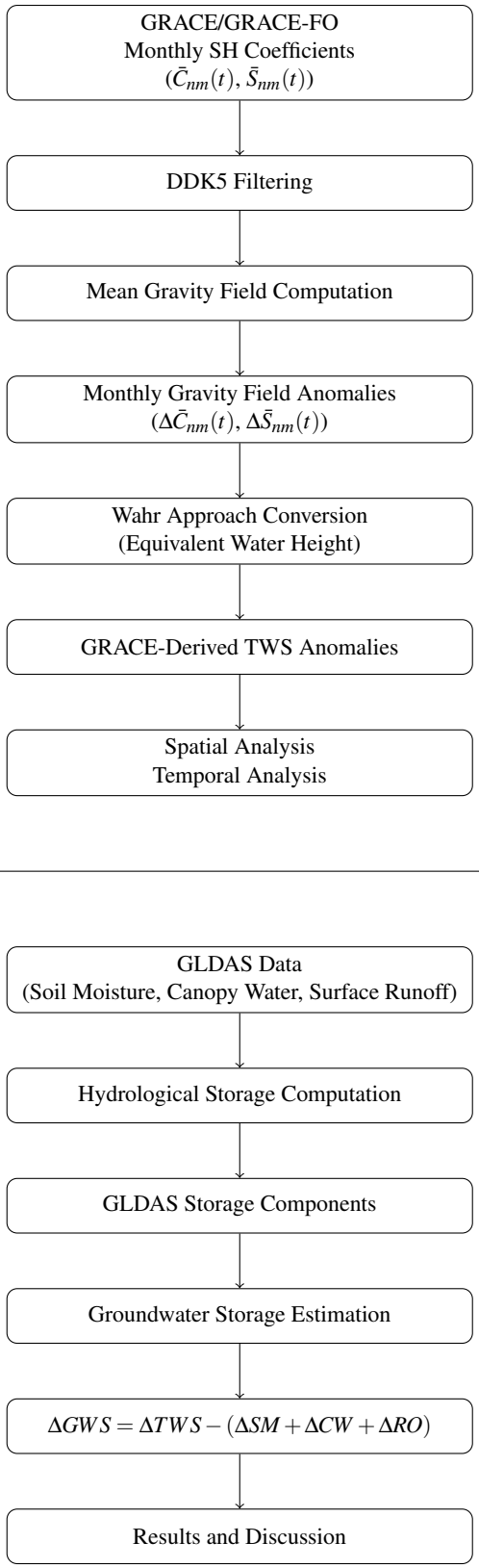

Figure 4.1: Methodological workflow for GRACE/GRACE-FO and GLDAS processing used in this study.

4.2 Processing of GLDAS Data

To support the interpretation of the GRACE-derived terrestrial water storage anomalies, monthly outputs from GLDAS Version 2.1 were analysed. The Noah Land Surface Model was selected because it provides spatially and temporally consistent estimates of major hydrological storage components.
The selected variables include soil moisture storage, canopy water storage, and runoff-related components. These variables were extracted for the Australian continent and processed over the same observation period as the GRACE dataset. All variables were converted into comparable units to facilitate a consistent comparison with the GRACE-derived Equivalent Water Height data. The processed GLDAS variables were subsequently used to investigate the contribution of individual hydrological storage components to the observed terrestrial water storage variations.

4.3 Groundwater Storage Estimation

The groundwater storage anomaly is estimated using a residual approach in which GRACE/GRACE-FO derived terrestrial water storage anomalies are combined with hydrological storage components obtained from GLDAS. Since GRACE measures the integrated mass change of all terrestrial water storage components, groundwater storage cannot be observed directly. Therefore, the surface and near-surface water storage components simulated by GLDAS are subtracted from the total water storage anomaly to isolate the groundwater contribution (Yin et al., 2020) as defined in Equation (2.5).
The GLDAS-derived components represent hydrological storage variations occurring within the land surface and near-surface water balance system, including soil moisture, runoff, snow water equivalent, and canopy water storage. By removing these contributions from the GRACE-derived terrestrial water storage signal, the residual component can be interpreted as groundwater storage anomaly (Tangdamrongsub et al., 2018; Rodell et al., 2009).
For Australia, the contribution of snow water equivalent is generally very small and can often be considered negligible compared with soil moisture and groundwater variations. Consequently, groundwater storage changes are primarily controlled by the interaction between total water storage, soil moisture storage, runoff, and canopy water storage. The resulting groundwater anomalies provide valuable insight into subsurface water dynamics and their contribution to terrestrial water storage variability across Australia.

4.4 Spatial and Temporal Analysis

The processed GRACE/GRACE-FO and GLDAS datasets were analysed using both spatial and temporal approaches to investigate variations in terrestrial water storage and groundwater storage across Australia. Spatial analyses were performed through the generation of monthly maps illustrating the distribution of terrestrial water storage and groundwater storage anomalies. These maps provide insight into the spatial patterns and regional differences in water storage variations across the continent.
Temporal analyses were conducted using monthly mean time series to examine seasonal and interannual variability throughout the study period from 2003 to 2024. The time series were used to identify long-term trends, periods of water storage accumulation, and periods of storage depletion associated with hydrological and climatic variability. Particular emphasis was placed on the comparison of contrasting hydrological conditions represented by April 2011 and October 2020. Based on the derived terrestrial water storage anomalies, April 2011 was identified as a representative wet period associated with widespread positive storage anomalies, whereas October 2020 was selected as a representative dry period marked by pronounced storage depletion across large parts of Australia. These two months were analysed in detail to investigate the response of terrestrial water storage and groundwater systems under contrasting climatic conditions.
In addition to the wet and dry period analysis, long-term variations in terrestrial water storage were evaluated over the entire observation period. The combined spatial and temporal analyses provide a comprehensive assessment of

water storage dynamics across Australia and facilitate the interpretation of hydrological variability observed across the continent during the study period.

5 Results and Discussion

This chapter presents and discusses the results obtained from the analysis of GRACE/GRACE-FO gravity field observations and GLDAS hydrological model outputs over Australia during the period 2003–2024. Terrestrial water storage anomalies derived from GRACE/GRACE-FO observations are first examined to evaluate the effects of the applied filtering techniques and to investigate their spatial and temporal variability across the continent. The GRACE-derived results are subsequently compared with hydrological storage components obtained from GLDAS, enabling a more comprehensive assessment of terrestrial water storage dynamics and groundwater variability.
Particular emphasis is placed on the analysis of contrasting hydrological conditions represented by April 2011 and October 2020, which were identified as representative wet and dry periods, respectively. These periods provide valuable insight into the response of Australia's hydrological system under markedly different climatic conditions and support the interpretation of long-term water storage variability across the study area.

5.1 Terrestrial Water Storage Variations Derived from GRACE

The DDK5-filtered GRACE solutions were used to investigate terrestrial water storage variability across Australia. The resulting Equivalent Water Height anomalies provide a spatial representation of water storage changes and reflect the combined influence of surface water, soil moisture, and groundwater variations (Kim et al., 2024).

5.1.1 Spatial Distribution of TWS Anomalies

The spatial distributions reveal considerable seasonal and interannual variability in terrestrial water storage across Australia. During 2011, widespread positive anomalies are observed over large parts of the continent, indicating enhanced water storage conditions associated with increased recharge and water accumulation. In contrast, the year 2020 exhibits comparatively weaker positive anomalies and localized storage deficits, reflecting reduced water availability in several regions. These contrasting patterns demonstrate the strong influence of climatic variability on terrestrial water storage dynamics. The monthly evolution of TWS anomalies for the representative wet and dry years is presented in Figures 5.6 and 5.7, providing a detailed overview of how storage conditions evolved throughout 2011 and 2020, respectively.

5.1.2 Wet Period Analysis: April 2011

April 2011 was selected as the representative wet period because it exhibits the strongest positive terrestrial water storage anomalies observed during the study period (Tapley et al., 2019). The spatial anomaly pattern indicates substantial water accumulation across large parts of Australia, reflecting enhanced recharge and increased storage within surface water bodies, soil moisture reservoirs, and groundwater systems. As illustrated in Figure 5.1a, the widespread extent and magnitude of the positive anomalies highlight the exceptional hydrological conditions that prevailed during this period and confirm its significance as one of the wettest phases within the study period.

5.1.3 Dry Period Analysis: October 2020

October 2020 was selected as the representative dry period because it exhibits significantly reduced terrestrial water storage conditions relative to the long-term mean. Compared with April 2011, both the magnitude and spatial extent of positive anomalies are considerably diminished, indicating lower water availability and reduced recharge across large parts of Australia. As shown in Figure 5.1b, the predominance of weak positive anomalies and localized negative values reflects widespread storage depletion, highlighting the strong contrast between wet and dry hydrological conditions observed during the study period.

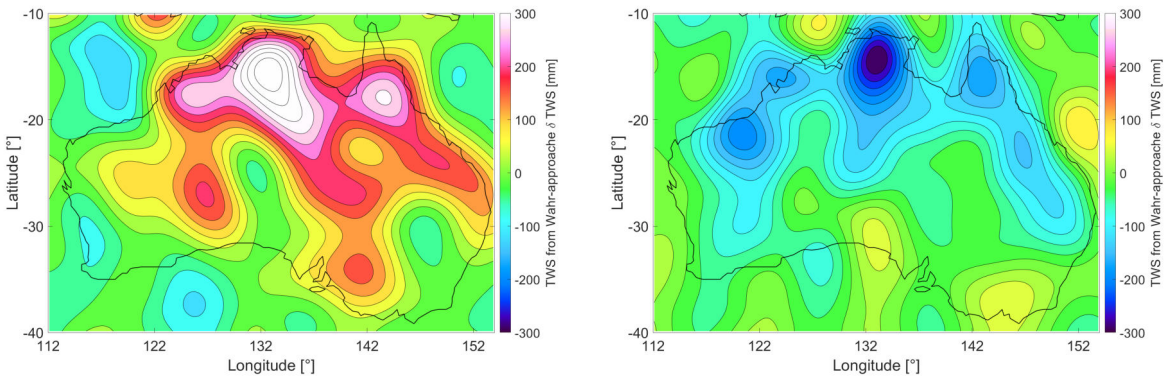

(a) TWS anomaly April 2011 (Wet Season)

(b) TWS anomaly October 2020 (Dry Season)

Figure 5.1: TWS anomaly for Wet and Dry month. (Range is ±300 mm)

5.1.4 Interannual Variability of Terrestrial Water Storage

The interannual analysis reveals pronounced variability in terrestrial water storage throughout the study period. April generally exhibits positive storage conditions associated with enhanced recharge and water accumulation, whereas October commonly corresponds to periods of reduced storage. The strongest positive anomalies are observed during April 2011, while October 2020 represents one of the most pronounced low-storage conditions identified within the analysed period. The long-term evolution of April and October terrestrial water storage patterns is presented in Figures 5.8, 5.9, 5.10 and 5.11, which illustrate the spatial variability of storage conditions across both the GRACE (2003–2017) and GRACE-FO (2018–2024) observation periods and highlight the contrasting hydrological behaviour between wet and dry years.

5.1.5 Statistical Characteristics of TWS

Statistical indicators including minimum, maximum, mean, RMS, and standard deviation were analysed to evaluate the temporal behaviour of terrestrial water storage across Australia. Figure 5.2 illustrates the evolution of these parameters throughout the study period and reveals substantial fluctuations associated with changing hydrological conditions. Periods characterised by elevated maximum values and increased variability generally correspond to enhanced water storage conditions, whereas lower minimum values indicate episodes of storage depletion. The observed temporal variations confirm the dynamic nature of terrestrial water storage and provide quantitative support for the spatial patterns identified in the preceding analyses.

5.2 Hydrological Storage Variations Derived from GLDAS

To support the interpretation of the GRACE-derived terrestrial water storage anomalies, hydrological storage components obtained from GLDAS were analysed over the same observation period. Unlike GRACE, which provides integrated water storage observations, GLDAS represents individual hydrological storage components and therefore provides additional insight into the processes contributing to the observed storage variations.

5.2.1 Wet and Dry Period Analysis

The GLDAS-derived hydrological variables indicate enhanced storage conditions during the wet period of April 2011 and comparatively reduced storage conditions during October 2020. Figures 5.3 presents the spatial distribution of soil moisture and total runoff for April 2011 at both global and regional scales. Elevated soil moisture values are observed across large parts of Australia, indicating favourable recharge conditions and increased water availability. Although runoff exhibits regional variability, the overall patterns suggest enhanced hydrological activity during this period. These observations are consistent with the strong positive terrestrial water storage anomalies

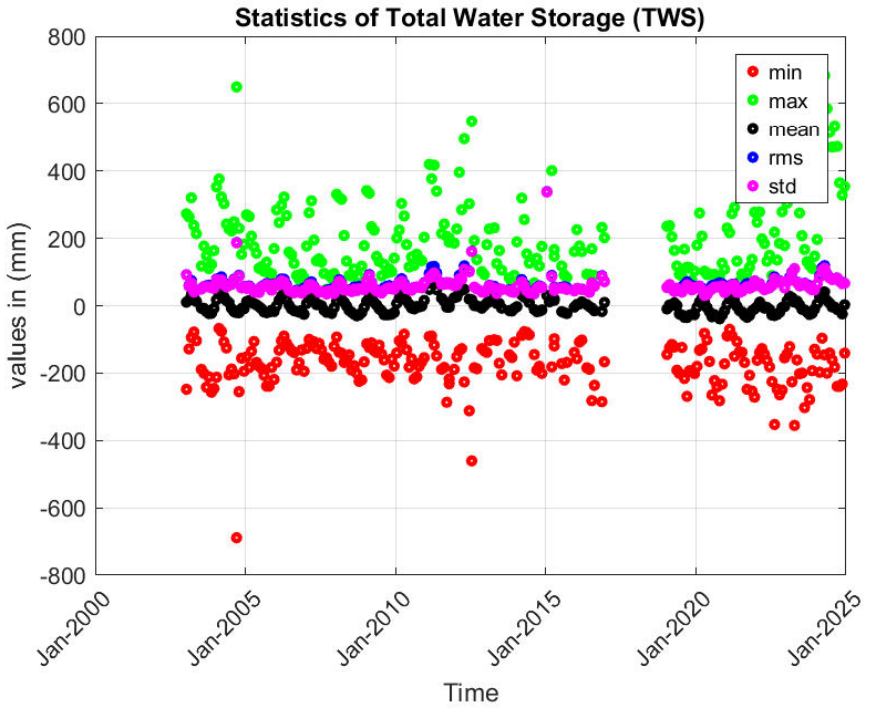

Figure 5.2: Statistics of Total Water Storage(TWS) based on DDK5

derived from GRACE and provide additional insight into the hydrological processes contributing to the observed storage increase.

The corresponding GLDAS-derived storage conditions for the dry period are illustrated in Figure 5.4. Compared with April 2011, lower soil moisture levels and reduced runoff activity are observed across several regions of Australia, indicating diminished recharge and reduced water availability. The spatial patterns are consistent with the reduced terrestrial water storage anomalies identified from GRACE observations and reflect the hydrological response to prolonged dry conditions during October 2020.

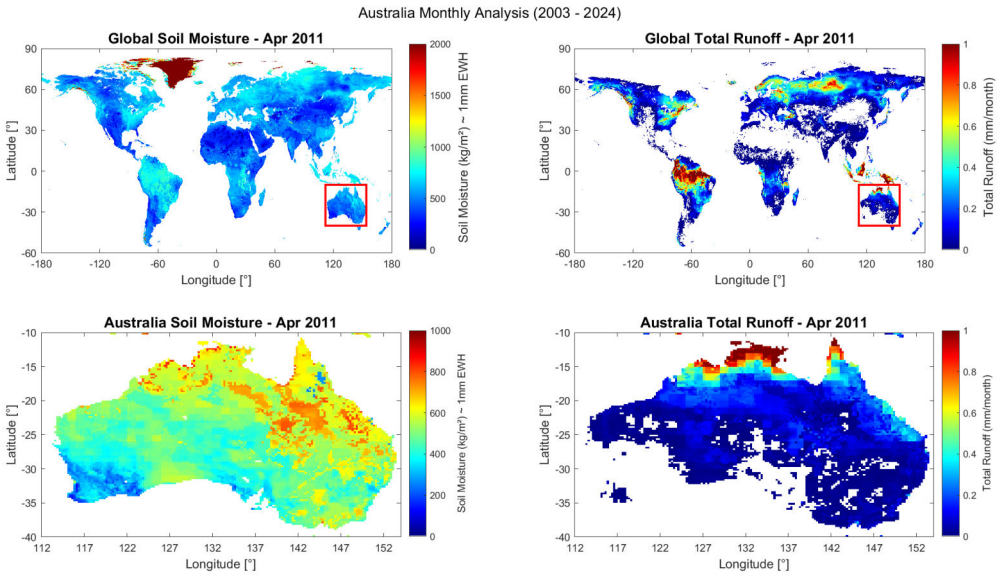

Figure 5.3: GLDAS Storage Distribution – April 2011

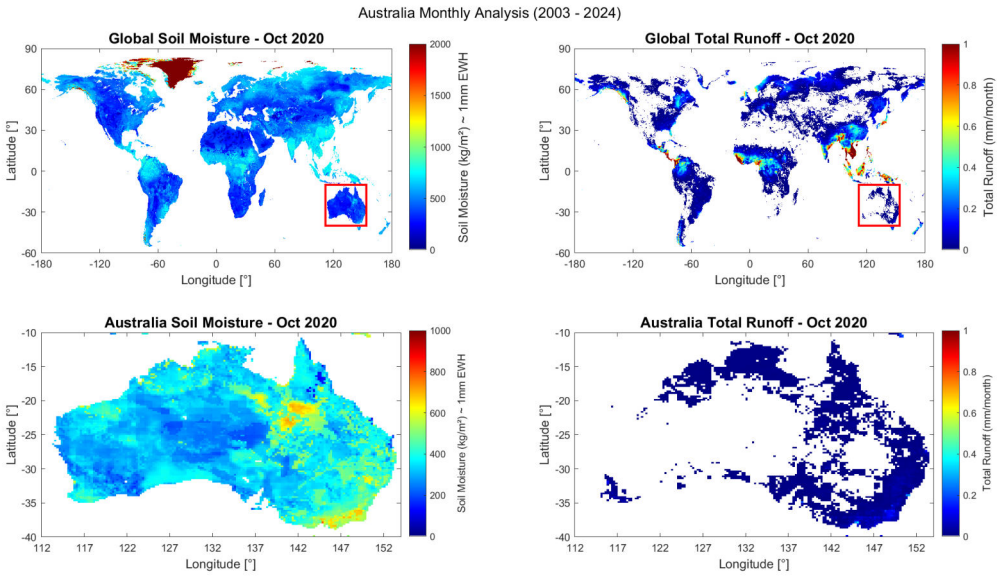

Figure 5.4: GLDAS Storage Distribution – October 2020

5.2.2 Interannual Variability of GLDAS Storage

The temporal variability of GLDAS-derived soil moisture storage is illustrated in Figure 5.5. The time series reveals pronounced seasonal fluctuations across all soil layers, reflecting the response of soil moisture to changing climatic and hydrological conditions throughout the study period. Variability is particularly evident within the deeper soil layers, which exhibit longer-term changes associated with recharge and water storage processes. Periods of increased soil moisture generally correspond to enhanced terrestrial water storage conditions observed by GRACE, whereas reduced soil moisture levels coincide with periods of water deficit. These results highlight the important contribution of soil moisture dynamics to the overall variability of terrestrial water storage across Australia.

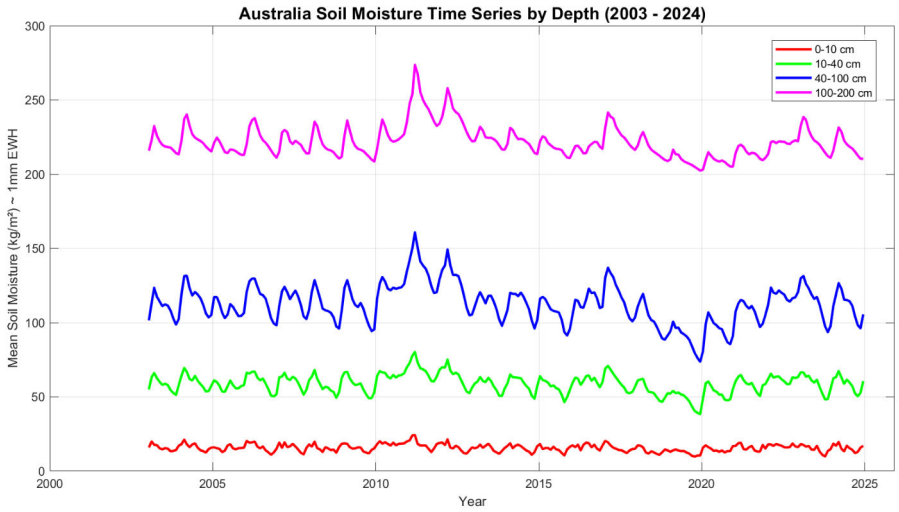

Figure 5.5: Australia Soil Moisture By Depth Time Series from 2003 to 2024

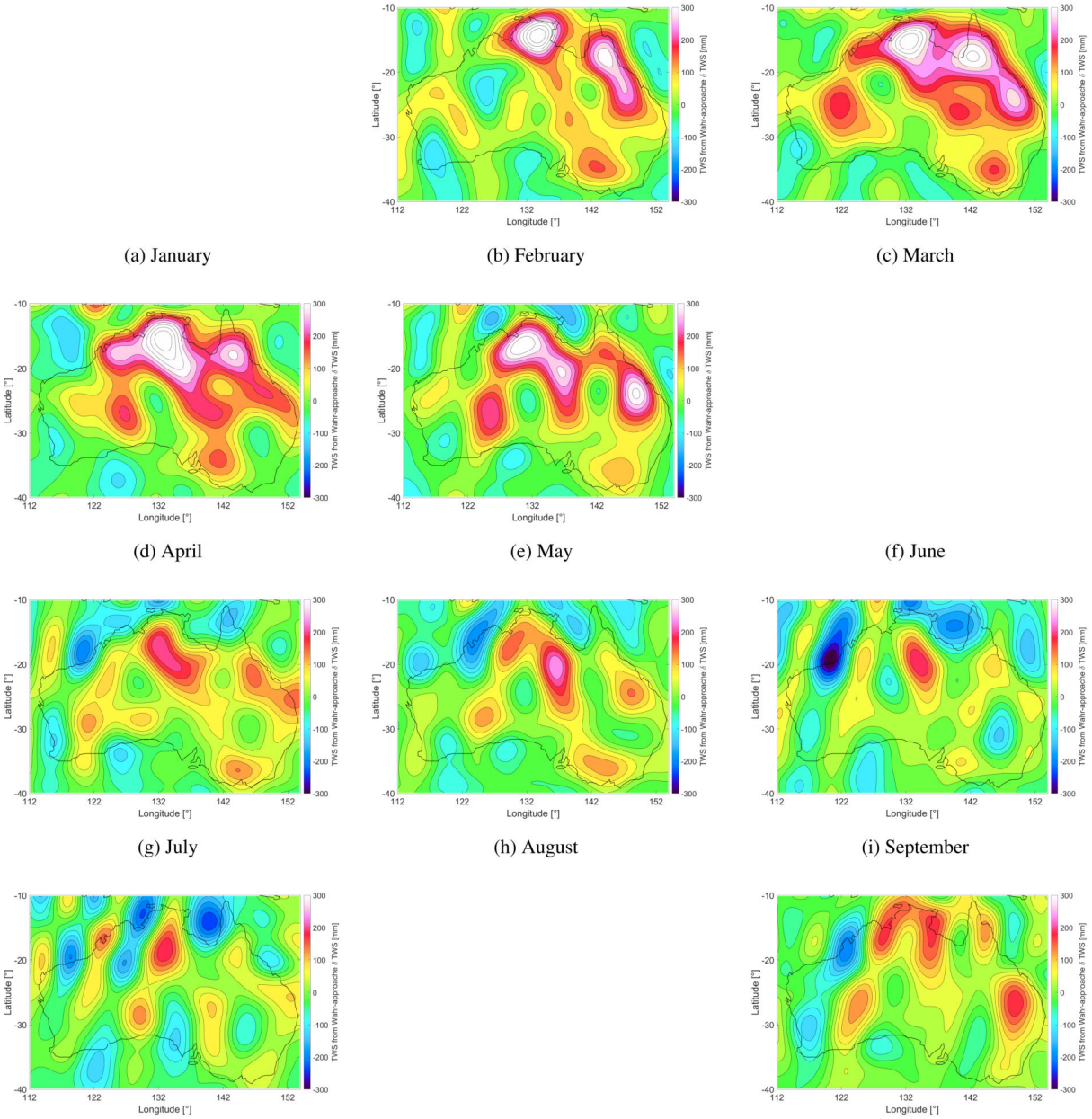

(a) January (b) February (c) March

(d) April (e) May (f) June

(g) July (h) August (i) September

(j) October (k) November (l) December

Figure 5.6: TWS in 2011 based on DDK5. (Range is ±300 mm)

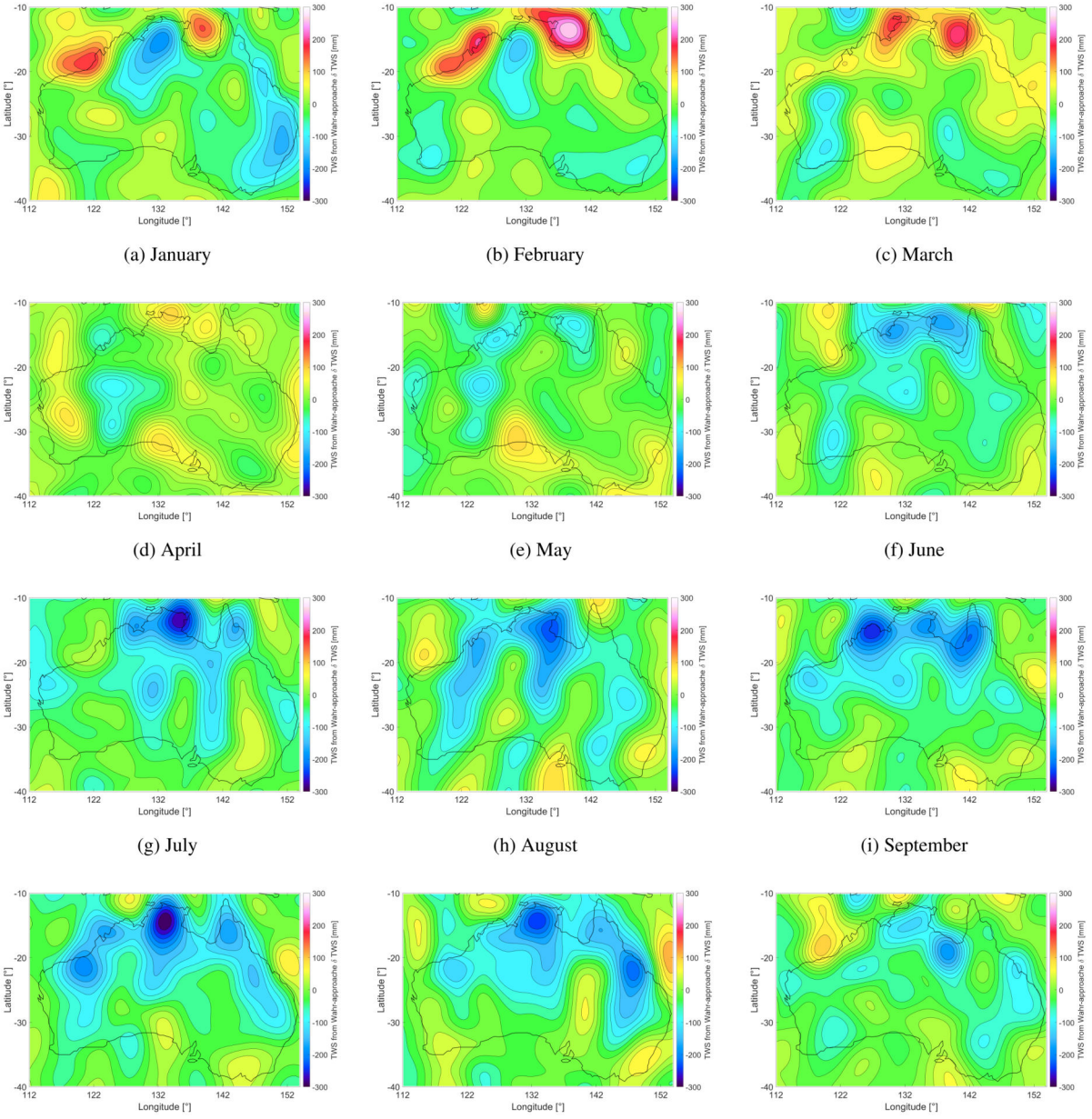

(a) January (b) February (c) March

(d) April (e) May (f) June

(g) July (h) August (i) September

(j) October (k) November (l) December

Figure 5.7: TWS in 2020 based on DDK5. (Range is ±300 mm)

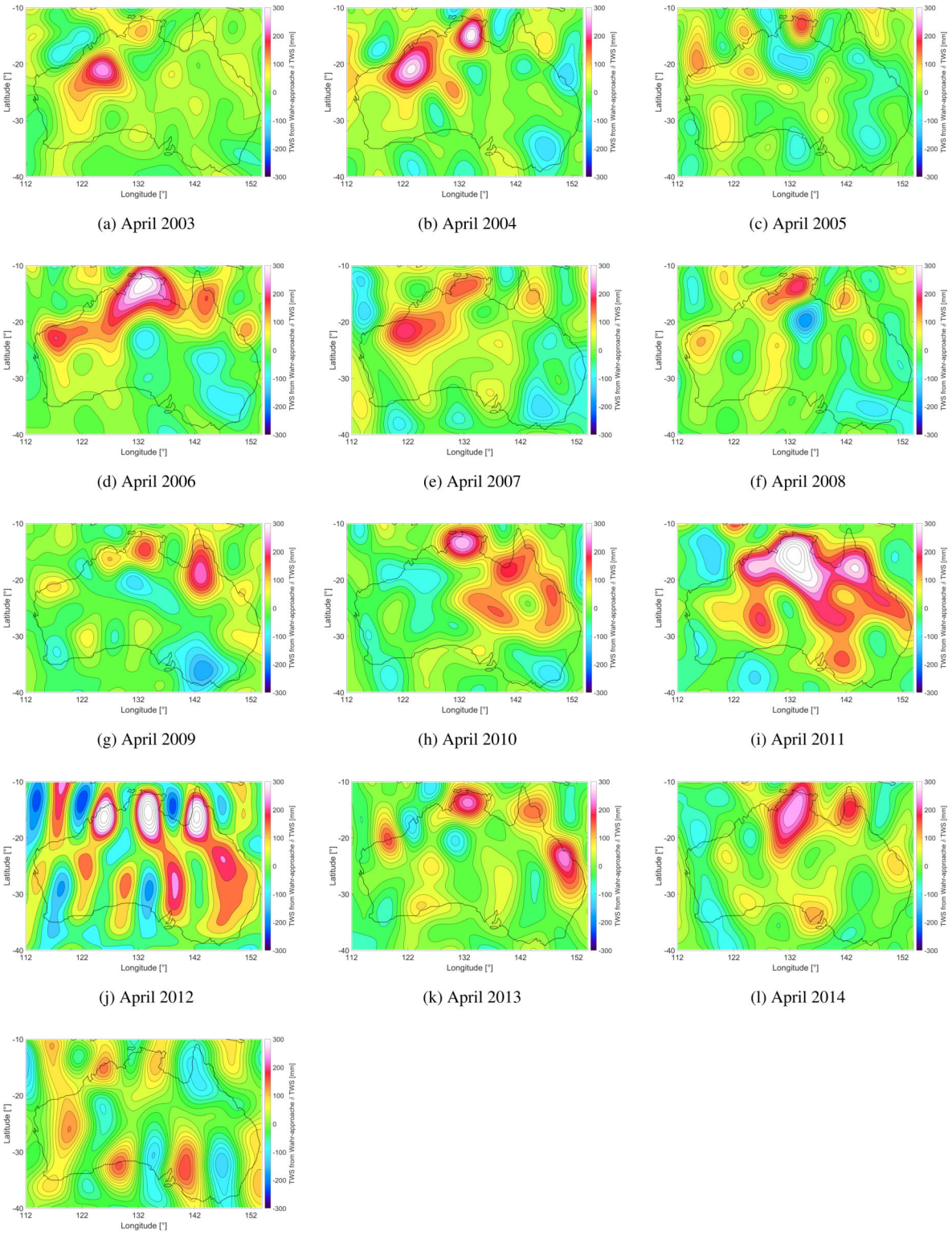

(a) April 2003 (b) April 2004 (c) April 2005

(d) April 2006 (e) April 2007 (f) April 2008

(g) April 2009 (h) April 2010 (i) April 2011

(j) April 2012 (k) April 2013 (l) April 2014

(m) April 2015 (n) April 2016 (o) April 2017

Figure 5.8: TWS in April from 2003 to 2017 based on DDK5 GRACE mission. (Range is ±300 mm)

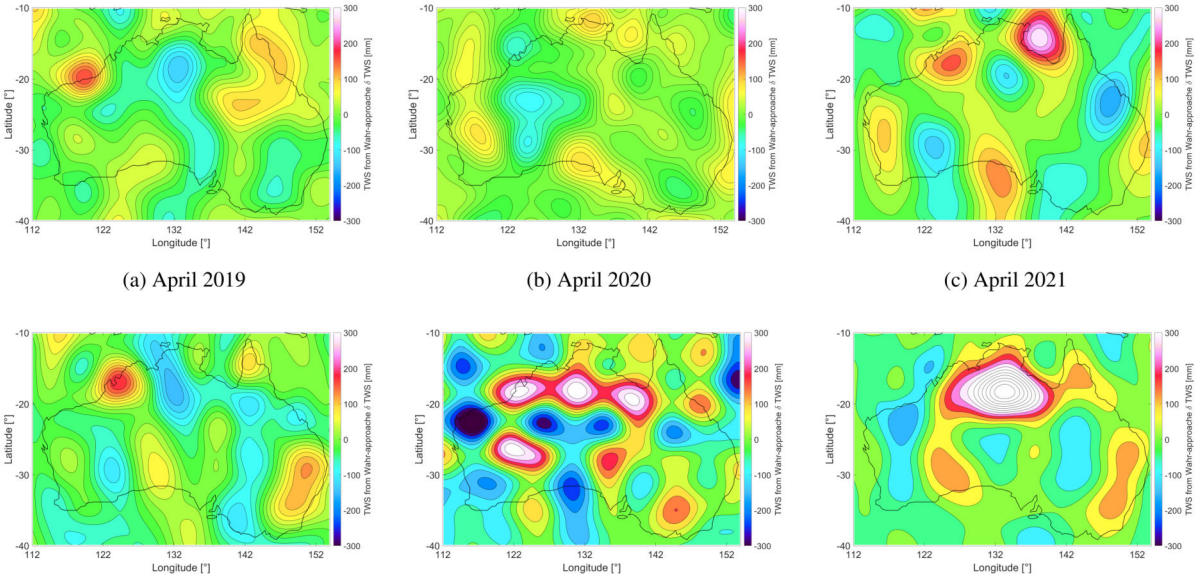

(a) April 2019 (b) April 2020 (c) April 2021

(d) April 2022 (e) April 2023 (f) April 2024

Figure 5.9: TWS in April from 2019 to 2024 based on DDK5 GRACE-FO mission. (Range is ±300 mm)

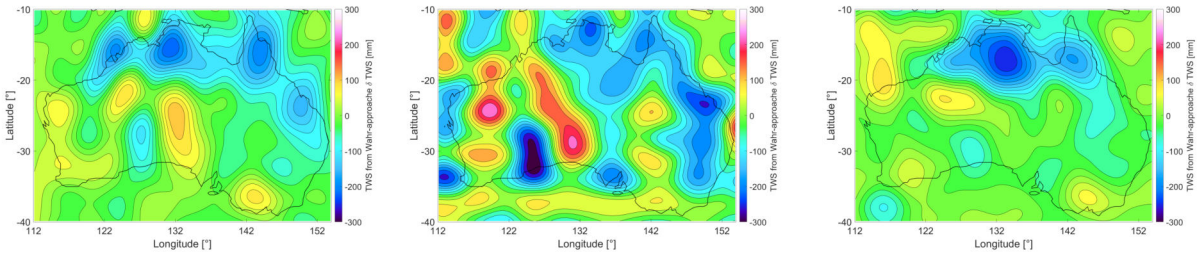

(a) October 2003

(b) October 2004

(c) October 2005

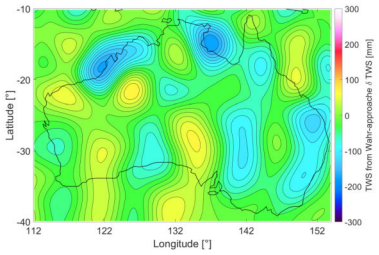

(d) October 2006

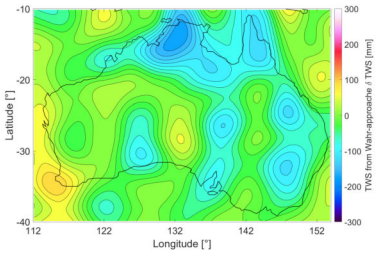

(e) October 2007

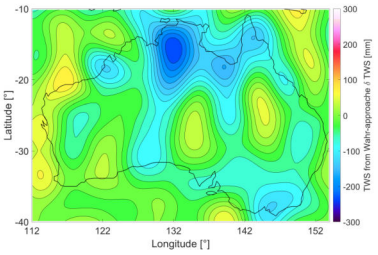

(f) October 2008

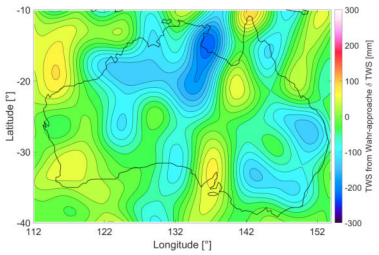

(g) October 2009

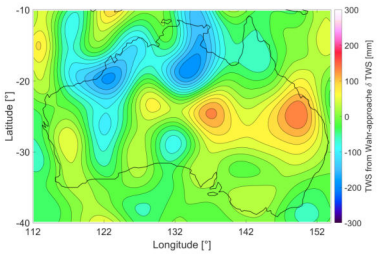

(h) October 2010

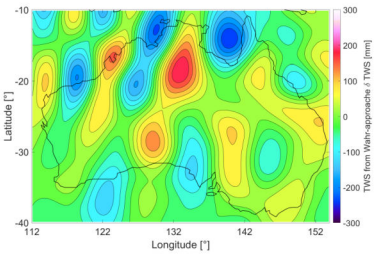

(i) October 2011

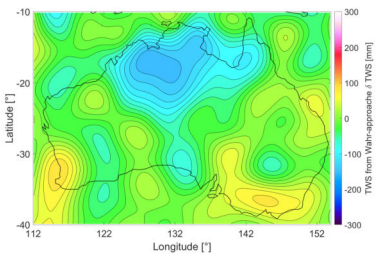

(k) October 2013

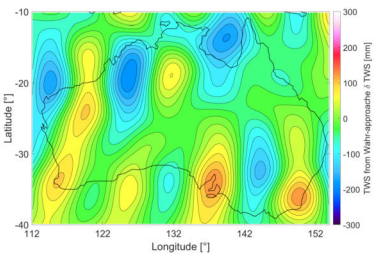

(l) October 2014

(j) October 2012

(m) October 2015

(n) October 2016

(o) October 2017

Figure 5.10: TWS in October from 2003 to 2017 based on DDK5 GRACE mission. (Range is ±300 mm)

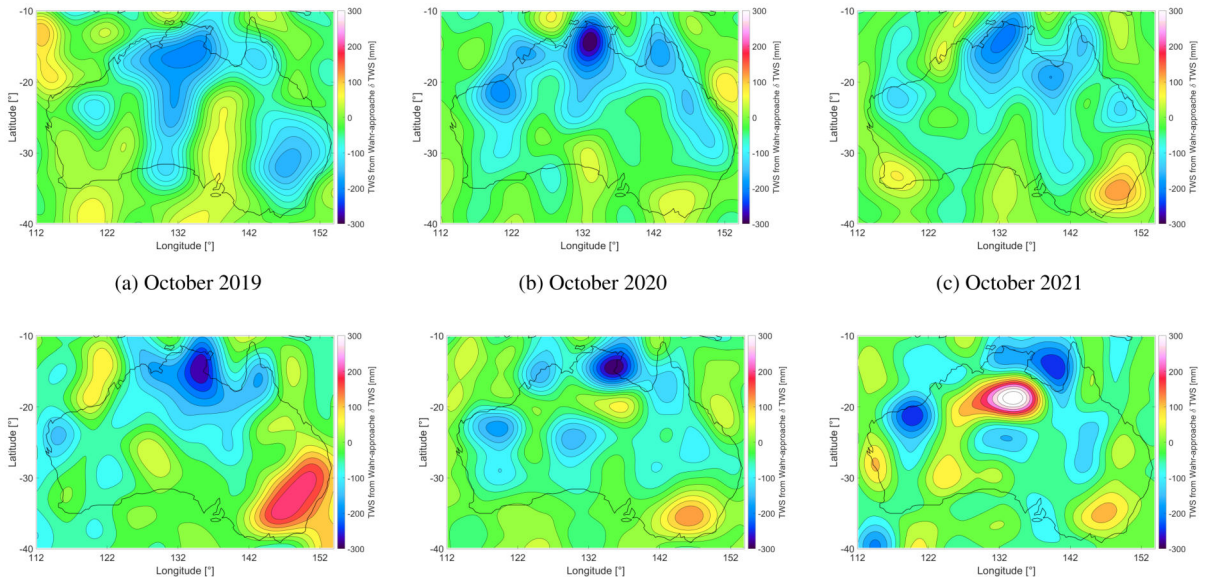

(a) October 2019 (b) October 2020 (c) October 2021

(d) October 2022 (e) October 2023 (f) October 2024

Figure 5.11: TWS in October from 2019 to 2024 based on DDK5 GRACE-FO mission. (Range is ±300 mm)

6 Conclusion

This study investigated terrestrial water storage (TWS) variations across Australia using GRACE and GRACE-FO gravity field observations and GLDAS hydrological model outputs for the period 2003–2024. Monthly spherical harmonic solutions were processed using the Wahr approach to derive Equivalent Water Height (EWH) anomalies, enabling the assessment of large-scale water storage changes across the continent. To reduce correlated errors and improve the quality of the gravity field solutions, DDK filtering was applied, and the DDK5-filtered results were selected for subsequent analyses.

The GRACE-derived TWS anomalies revealed pronounced spatial and temporal variability throughout the study period, reflecting the strong influence of climatic and hydrological processes on water storage conditions across Australia. April 2011 was identified as a representative wet period, characterized by widespread positive storage anomalies and enhanced water accumulation, whereas October 2020 represented a dry period with comparatively reduced storage conditions. The comparison of these contrasting hydrological states demonstrated the capability of GRACE and GRACE-FO observations to capture large-scale water storage fluctuations and their response to changing climatic conditions.

The incorporation of GLDAS hydrological variables provided additional insight into the individual storage components contributing to the observed TWS variations. Furthermore, the integration of GRACE and GRACE-FO and GLDAS datasets enabled the estimation of groundwater storage anomalies, supporting the investigation of subsurface water dynamics across Australia.

Overall, the results demonstrate the effectiveness of satellite gravimetry and land surface modelling for monitoring terrestrial water storage variability at continental scales. The combined use of GRACE and GRACE-FO and GLDAS data provides a valuable framework for understanding hydrological variability and groundwater dynamics, thereby supporting future water resource assessment and management efforts across Australia.

7 Outlook

Future research could further improve the accuracy and spatial resolution of terrestrial water storage estimates by incorporating advanced filtering techniques, leakage corrections, and alternative GRACE products such as mascon solutions. The integration of additional hydrological datasets, including precipitation, evapotranspiration, and in-situ groundwater observations, would provide a more comprehensive understanding of the processes controlling water storage variability.

Further investigation of regional-scale hydrological behaviour within major Australian river basins could provide valuable insight into local groundwater dynamics and climate-related impacts on water resources. In addition, extending the analysis using future GRACE-FO observations will enable the continuous monitoring of terrestrial water storage trends and support the assessment of long-term hydrological changes under evolving climatic conditions.

The methodologies applied in this study can also be extended to other regions experiencing significant water stress, thereby contributing to improved water resource management, drought assessment, and climate impact studies at continental and basin scales.

Acknowledgement

The author would like to express his sincere gratitude to Prof. Dr. Kurt Seitz for his invaluable guidance, continuous support, and constructive feedback throughout the course of this lab rotation. His expertise, insightful discussions, and encouragement were instrumental in the successful completion of this study.

The author is also grateful to the Geodetic Institute (GIK), Karlsruhe Institute of Technology (KIT), for providing an excellent academic environment and the computational resources required for conducting this research.

Furthermore, the author acknowledges the International Center for Global Earth Models (ICGEM) for providing access to GRACE and GRACE-FO gravity field products, and the NASA Goddard Earth Sciences Data and Information Services Center (GES DISC) for making the Global Land Data Assimilation System (GLDAS) datasets publicly available.

References

GFZ (2026): GRACE-FO – Gravity Recovery and Climate Experiment Follow-On Mission. German Research Centre for Geosciences (GFZ). Accessed: 2026-04-06. URL: https://www.gfz.de/en/section/global-geomonitoring-and-gravity-field/projects/grace-fo-gravity-recovery-and-climate-experiment-follow-on-mission.

ICGEM (2026): International Centre for Global Earth Models (ICGEM): Gravity field and GRACE/GRACE-FO products hosted at the German Research Centre for Geosciences (GFZ). Accessed: 2026-04-06. URL: https://icgem.gfz-potsdam.de/.

Kim, J.-S., Seo, K.-W., Kim, B.-H., Ryu, D., Chen, J., and Wilson, C. (2024): High-resolution terrestrial water storage estimates from GRACE and land surface models. *Water Resources Research* 60(2):e2023WR035483.

Kusche, J. (2007): Approximate decorrelation and non-isotropic smoothing of time-variable GRACE-type gravity field models. *Journal of Geodesy* 81(11):733–749. DOI: 10.1007/s00190-007-0143-3.

Kusche, J., Schmidt, R., Petrovic, S., and Rietbroek, R. (2009): Decorrelated GRACE time-variable gravity solutions by GFZ, and their validation using a hydrological model. *Journal of Geodesy* 83:903–913. DOI: 10.1007/s00190-009-0308-3.

Rodell, M., Houser, P. R., Jambor, U., Gottschalck, J., Mitchell, K. E., Meng, C.-J., Arsenault, K., Cosgrove, B. A., Radakovich, J. D., Bosilovich, M. G., Entin, J. K., Walker, J. P., Lohmann, D., and Toll, D. L. (2004): The Global Land Data Assimilation System. *Bulletin of the American Meteorological Society* 85(3):381–394. DOI: 10.1175/BAMS-85-3-381.

Rodell, M., Velicogna, I., and Famiglietti, J. S. (2009): Satellite-based estimates of groundwater depletion in India. *Nature* 460:999–1002. DOI: 10.1038/nature08238.

Syed, T. H., Famiglietti, J. S., Rodell, M., Chen, J., and Wilson, C. R. (2008): Analysis of terrestrial water storage changes from GRACE and GLDAS. *Water Resources Research* 44:W02433. DOI: 10.1029/2006WR005779.

Tangdamrongsub, N., Han, S.-C., Tian, S., Müller Schmied, H., Sutanudjaja, E. H., Ran, J., and Feng, W. (2018): Evaluation of groundwater storage variations estimated from GRACE data assimilation and state-of-the-art land surface models in Australia and the North China Plain. *Remote Sensing* 10(3):483.

Tapley, B. D., Watkins, M. M., Flechtner, F., et al. (2019): Contributions of GRACE to understanding climate change. *Nature Climate Change* 9:358–369. DOI: 10.1038/s41558-019-0456-2.

Tapley, B. D., Bettadpur, S., Watkins, M., and Reigber, C. (2004): The gravity recovery and climate experiment: Mission overview and early results. *Geophysical Research Letters* 31(9):1–4. DOI: 10.1029/2004GL019920.

Wahr, J., Molenaar, M., and Bryan, F. (1998): Time variability of the Earth's gravity field: Hydrological and oceanic effects and their possible detection using GRACE. *Journal of Geophysical Research: Solid Earth* 103(B12):30205–30229.

Yin, W., Li, T., Zheng, W., Hu, L., Han, S.-C., Tangdamrongsub, N., Šprlák, M., and Huang, Z. (2020): Improving regional groundwater storage estimates from GRACE and global hydrological models over Tasmania, Australia. *Hydrogeology Journal* 28(5):1809–1825.

Investigation of the heavy rainfall event in Germany in spring 2024 using GRACE-FO monthly solutions

Ananthan Pushpa Balan[1]

1 Remote Sensing and Geoinformatics Master of Science (M.Sc.), KIT, Germany
E-Mail: ubxll@student.kit.edu

Abstract

This study analyzes the variations of total water storage (TWS) in Germany using GRACE-FO data from 2019 to 2025 to assess the detectability of the 2024 Southern Germany flood event. A comparison of decorrelation filters shows that filter choice strongly influences the results. The DDK2 filter yields a clean, low-noise signal but with substantial attenuation due to strong smoothing (equivalent to a 340 km filter radius). In contrast, the DDK8 filter preserves higher signal amplitudes but introduces pronounced striping noise, complicating interpretation of spatial anomalies. For the Spring 2024 flood, the signal is largely undetectable in standard DDK2-filtered monthly solutions. Despite the extreme precipitation reported by Mohr et al. (2024), the short duration of the event and the limited extent of southern Germany caused the gravitational anomaly to smooth below the DDK2 detection threshold. These findings highlight current satellite gravimetry limitations in monitoring short-term, localized hydrological extremes. Future work could explore mascon solutions or integrate GRACE-FO data with hydrological models to improve downscaling and detection of localized events.

Keywords GRACE-FO · Rainfall Event in Germany

1 Introduction

Extreme hydro-meteorological events, such as droughts and floods, have become increasingly frequent in Central Europe in recent years. Most notably, in late May and early June 2024, Southern Germany – specifically the states of Bavaria and Baden-Württemberg – was impacted by a severe heavy rainfall event. This event was triggered by a "Vb-cyclone" weather pattern named Orinoco, which transported warm, moist air from the Mediterranean over the Alps. This resulted in extreme precipitation accumulation, with some stations recording up to 130–150 mm within 48 hours, and localized peaks reaching 255 mm within 120 hours (Mohr et al., 2024). While the hydrological impact was devastating on the ground, leading to disaster declarations in multiple districts, the detection of such short-duration, spatially concentrated events poses a specific challenge for satellite gravimetry. The Gravity Recovery and Climate Experiment Follow-On (GRACE-FO) mission monitors the Earth's time-variable gravity field, providing a unique capability to quantify changes in Total Water Storage (TWS). TWS represents the vertically integrated sum of all water storage components, including soil moisture, groundwater, surface water, and snow (Zhang et al., 2023). Unlike optical or radar remote sensing which observes surface extent, GRACE-FO detects

KIT Scientific Working Papers
Issue Number 270
ISSN: 2194-1629
DOI: 10.5445/IR/1000191188
Online: June 2026

This document is licensed under the Creative Commons Attribution – Share Alike 4.0 International License (CC BY-SA 4.0):
https://creativecommons.org/licenses/by-sa/4.0/deed.en

the mass change associated with the water volume. However, the detection of flood signals is often constrained by the satellite's spatial resolution and the temporal averaging of the data over monthly intervals, which can attenuate the signal of flash floods (Zhang et al., 2023) A critical step in deriving TWS from GRACE-FO Level-2 spherical harmonic coefficients is the application of post-processing filters to remove correlated errors, commonly known as "striping". The DDK decorrelation filters, developed by Kusche et al. (2009), are the standard method for this purpose. However, the choice of filter strength involves a trade-off between noise reduction and signal preservation. For example, the DDK2 filter applies strong smoothing (equivalent to a $\approx$ 340 km Gaussian filter), which effectively suppresses noise but may dampen local flood signals. Conversely, the DDK8 filter is weaker; it retains higher signal amplitude but allows more noise to remain in the solution (Kusche et al., 2009). This lab rotation report focuses on the analysis of Total Water Storage variations over Germany for the period of 2019 to 2025. The primary objective is to evaluate whether the heavy rainfall event of spring 2024 left a detectable footprint in the monthly GRACE-FO solutions. Using GFZ Level-2 data, Spherical Harmonic Synthesis (SHS) was performed to calculate TWS time series. A comparative analysis was conducted between DDK2 and DDK8 filtered datasets to determine if the weaker filtering of DDK8 allows for the detection of the flood signal that might be smoothed out by the stronger DDK2 filter.

2 Theoretical Aspects

Theoretical Aspects The analysis of mass transport within the Earth system, specifically the variation in terrestrial water storage, relies on the theoretical framework of satellite gravimetry and spherical harmonic synthesis. This section outlines the fundamental principles of determining Total Water Storage (TWS) from GRACE-FO coefficients and the theoretical basis for the decorrelation filters (DDK) used in this study.

2.1 Principles of Satellite Gravimetry and TWS

The primary observable of the GRACE and GRACE-FO missions is the inter-satellite distance change between two co-orbiting satellites. These distance variations are caused by the Earth's heterogeneous gravity field acting on the satellites. By removing signals from atmospheric mass, ocean tides, and solid earth tides, the residual time-variable gravity field is largely attributed to changes in Terrestrial Water Storage (TWS) (Zhang et al., 2023).
TWS represents the vertically integrated sum of all water storage components stored on and beneath the land surface:

$$TWS = SoilMoisture + Groundwater + SurfaceWater + Snow \tag{2.1}$$

As noted by Zhang et al. 2023, GRACE-FO provides a unique capability to detect flood events by measuring the "water storage capacity deficit," although the detection is physically limited by the spatial resolution and temporal averaging (monthly solutions) of the satellite data.

2.2 Spherical Harmonic Synthesis (SHS)

Spherical harmonics are given in Equation (2.2). Spherical Harmonic Synthesis is the forward computation of a function on the sphere from a series of surface spherical harmonics (Tsoulis, 1999). The spherical harmonic coefficients derived from GRACE level-2 data is used to express the gravity field of Earth.

$$V(P) = \frac{GM}{r} \sum_{n=0}^{\infty} \left(\frac{R}{r}\right)^n \sum_{m=0}^{n} (\bar{C}_{nm} \cos m\lambda + \bar{S}_{nm} \sin m\lambda) \bar{P}_{nm}(\sin \varphi) \tag{2.2}$$

where,
GM : Geocentric gravitational constant
R : Radius of the reference sphere.

$\bar{C}_{nm}, \bar{S}_{nm}$: Fully normalised spherical harmonic coefficients of degree n and order m
$\bar{P}_{nm}$: Fully normalised Legendre functions of degree n and order m.

2.3 spherical harmonic coefficients

The time-variable component of the gravity field is provided as fully normalized spherical harmonic coefficients $(\bar{C}_{nm}, \bar{S}_{nm})$ To derive surface mass density anomalies (such as TWS) in terms of equivalent water height (EWH), a Spherical Harmonic Synthesis is performed
Following the methodology described in standard geodetic literature and applied in Kusche et al. 2009, the relationship between the surface mass density

$$\Delta\sigma(\phi,\lambda) = \frac{3a\rho_{\text{ave}}}{\rho_w} \sum_{n=0}^{N} \sum_{m=0}^{n} \frac{2n+1}{1+k_n} \bar{P}_{nm}(\sin\phi) \left[\Delta\bar{C}_{nm}\cos(m\lambda) + \Delta\bar{S}_{nm}\sin(m\lambda)\right] \tag{2.3}$$

Where: where a is the mean Earth radius, ρ_{ave} denotes the average density of the Earth, k_n are the load Love numbers accounting for the elastic deformation of the Earth, and $\bar{P}_{nm}$ are the fully normalized associated Legendre functions.

2.4 Degree and Error Degree Variances

To evaluate the spectral content of the gravity field solutions and the quality of the observations, degree variances and error degree variances are analyzed. These metrics quantify the power of the signal and the noise as a function of the spherical harmonic degree n.
The **signal degree variance** (σ_n^2) represents the average power of the gravitational anomalies at a specific degree n. It is calculated by summing the squares of the fully normalized spherical harmonic coefficients $(\bar{C}_{nm}, \bar{S}_{nm})$ over all orders m:

$$\sigma_n^2 = \sum_{m=0}^{n} (\bar{C}_{nm}^2 + \bar{S}_{nm}^2) \tag{2.4}$$

Conversely, the **error degree variance** $(\delta\sigma_n^2)$ quantifies the uncertainty associated with these coefficients. It is derived using the standard deviations $(\sigma_{\bar{C}_{nm}}, \sigma_{\bar{S}_{nm}})$ provided in the GFZ Level-2 data:

$$\delta\sigma_n^2 = \sum_{m=0}^{n} (\sigma_{\bar{C}_{nm}}^2 + \sigma_{\bar{S}_{nm}}^2) \tag{2.5}$$

In satellite gravimetry, the signal power typically decreases with increasing degree n, while the error power increases exponentially due to the attenuation of the gravitational signal at orbital altitude (Wahr et al., 1998).
The intersection of these curves indicates the resolution limit where noise begins to dominate, necessitating the use of filtering methods such as the DDK decorrelation filters (Kusche et al., 2009).

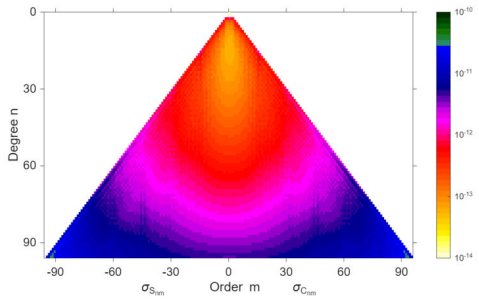

(a) Accuracy of Coefficients

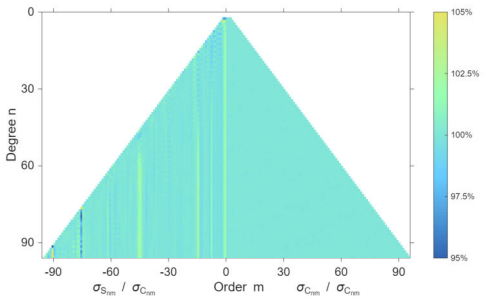

(b) relative Accuracy of Coefficients

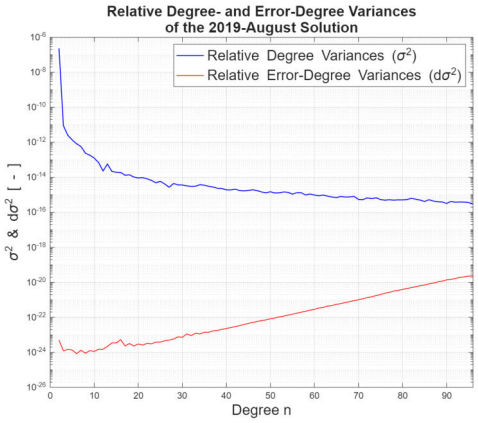

(c) Degree and Error Degree Varianz

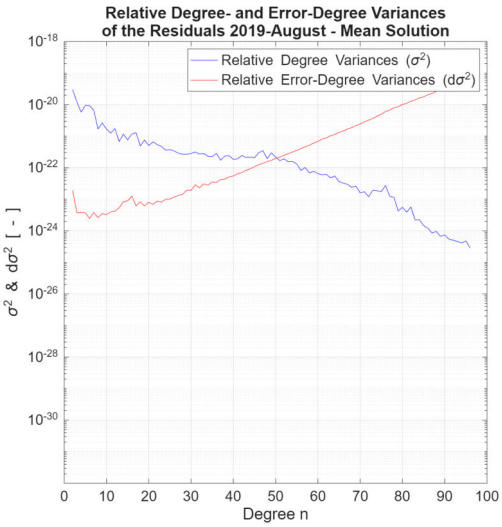

(d) Relative Degree and Error Degree Varianz

Figure 2.1: Accuracy of GRACE-FO GFZ coefficients (August 2019).

2.5 Correlated Errors and Decorrelation Filtering (DDK)

A major challenge in using GRACE-FO Level-2 data is the presence of correlated errors, which manifest as north-south oriented "stripes" in the spatial maps. These errors arise from the specific orbital geometry of the satellite pair and the under-sampling of high-frequency mass variations (Kusche et al., 2009). Standard isotropic Gaussian filters can suppress this noise but often result in significant signal attenuation and leakage, "smearing" local signals into the surrounding areas. To address this, DDK decorrelation filters are employed. As derived by Kusche et al. (2009), these filters are based on a non-isotropic regularization approach that accounts for the error covariance structure of the GRACE solutions. The filter kernel is designed to suppress the correlated noise (stripes) while preserving the signal in the east-west direction more effectively than isotropic filters. The strength of the DDK filter determines the trade-off between noise reduction and spatial resolution: DDK2: This is a relatively strong filter. According to Kusche et al. (2009), DDK2 has smoothing radius of approximately 340 km (equivalent harmonic degree ≈ 60. It provides a very clean signal with minimal striping but strongly attenuates localized peaks, such as flash floods in small basins. DDK8: This filter applies a weaker regularization. While not explicitly detailed in the original table of Kusche et al. (2009), DDK8 follows the same theoretical construction but with a lower smoothing parameter. It allows for higher spatial resolution (retaining more signal amplitude) but permits a higher level of residual striping noise to remain in the final TWS maps. This study compares these two filter strengths to determine if the weaker filtering of DDK8 allows for the detection of the spatially concentrated 2024 Germany flood event, which may be oversmoothed by the DDK2 filter.

3 Data

This study utilizes satellite gravimetry data to derive terrestrial water storage anomalies, alongside in-situ hydro-meteorological data to validate specific flood events. The primary timeframe of analysis spans from January 2019 to June 2025, with a specific focus on the heavy rainfall event of spring 2024.

3.1 GRACE-FO Level-2 Data (GFZ)

The core dataset consists of monthly time-variable gravity field solutions from the Gravity Recovery and Climate Experiment Follow-On (GRACE-FO) mission. The data were obtained from the German Research Centre for Geosciences (GFZ) archive (ICGEM, 2026). The data are provided as Level-2 (GSM) products, consisting of fully normalized spherical harmonic coefficients $(\bar{C}_{nm}, \bar{S}_{nm})$ representing the Earth's gravity potential. Unlike Level-3 data (which are pre-gridded), Level-2 coefficients require spherical harmonic synthesis to derive physical mass changes.

- Temporal Resolution: Monthly solutions were selected to analyze long-term trends and seasonal variations in Total Water Storage (TWS).
- Filtering: To mitigate the characteristic north-south "striping" noise inherent in GRACE-FO solutions, the coefficients were post-processed using DDK decorrelation filters. As described by Kusche et al. (2009), these filters utilize error covariance matrices to suppress correlated noise while preserving signal amplitude better than isotropic Gaussian filters.
  - DDK2: A strong filter (equivalent to $\approx 340\,\text{km}$ spatial smoothing) used to minimize noise.
  - DDK8: A weaker filter used to retain higher spatial resolution, allowing for a comparative analysis of signal sensitivity regarding the 2024 flood event.

3.2 Spectral Characteristics and Error Structure

To assess the quality and spectral content of the raw data, the coefficients and their formal errors are visualized in a triangular matrix format

- Structure: The vertical axis of the triangle represents the spherical harmonic degree (n), which corresponds to spatial resolution. The horizontal axis represents the order (m).
- Signal vs. Noise: As illustrated in the coefficient triangles generated for this study (see Fig. 5.1), the geophysical signal is concentrated at lower degrees (long wavelengths). However, the formal errors (σ) typically increase with higher degrees ($n > 30$).
- Justification for Filtering: This spectral visualization confirms that at high degrees, the solution is dominated by correlated errors, which manifest as north-south "striping" in spatial maps. This necessitates the application of decorrelation filters to suppress high-frequency noise while preserving the physical hydrological signal.

3.2.1 Hydrological and Meteorological Validation Data

To validate the TWS anomalies derived from satellite data, particularly for the flood event in Southern Germany, ground-based meteorological data were referenced.

- Precipitation Data: The primary reference for the flood event is the forensic disaster analysis by CEDIM (2025) and Mohr et al. (2024). This report utilizes data from the Deutscher Wetterdienst (DWD) network (DWD, 2025), specifically RADOLAN (Radar Online Adjustment) data.

- Event Specifics: The data confirms that between May 30 and June 3, 2024, a Vb-cyclone system caused extreme precipitation in Southern Germany (Bavaria and Baden-Württemberg). Station data recorded precipitation sums of up to 177 mm in 48 hours (Schrobenhausen) and 255.6 mm in 120 hours (Buchenberg-Kreuzthal) (Mohr et al., 2024).
- River Discharge: The report also references discharge data (HQ values), noting that water levels in Danube tributaries (e.g., Günz, Mindel, Schmutter) exceeded the 100-year flood markers (HQ100), providing the necessary ground truth to evaluate the sensitivity of the GRACE-FO DDK2 and DDK8 solutions.

4 Methodology Overview

The processing workflow to derive Total Water Storage (TWS) anomalies and detect the 2024 flood event involved three primary stages: post-processing of spherical harmonic coefficients, spherical harmonic synthesis (SHS), and comparative time-series analysis. All numerical computations were performed using the MATLAB computing environment.

4.1 Decorrelation Filtering

To address the issue of correlated high-frequency noise (striping) inherent in the GRACE-FO Level-2 data, a filtering step was applied prior to synthesis. Unlike isotropic Gaussian filters, which smooth signals uniformly in all directions, anisotropic decorrelation filters (DDK) were employed to preserve the north-south signal structure while suppressing error stripes.
Following the strategy defined by Kusche et al. 2009, the full error covariance matrix of the gravity field solutions was utilized. Two distinct filter strengths were applied to the same dataset (2019–2025) to evaluate signal sensitivity:

- DDK2: A strong filter configuration. As detailed in Kusche et al. 2009, this filter corresponds to an isotropic Gaussian smoothing radius of approximately 340 km. It was selected to produce a high-precision, low-noise baseline, albeit with potential attenuation of localized flood signals.
- DDK8: A weaker filter configuration. This was selected to retain higher spectral resolution, theoretically allowing for the detection of smaller spatial anomalies such as the regional flooding in Southern Germany, at the cost of higher residual noise.

4.2 Spherical Harmonic Synthesis (SHS) and TWS Computation

After filtering, the spherical harmonic coefficients were converted into physical mass anomalies on the Earth's surface by applying Wahr et al. (1998). This process, known as Spherical Harmonic Synthesis, was computed using the standard equation for surface mass density in terms of Equivalent Water Height (EWH).
The synthesis was performed on a $1^\circ \times 1^\circ$ grid over the region of Germany. To isolate the TWS anomaly ΔTWS

4.3 Time Series Extraction and Flood Detection

Finally, spatially averaged time series were extracted for the German territory for the period January 2019 to June 2025. The analysis focused on comparing the amplitude differences between the DDK2 and DDK8 solutions. The specific objective was to identify a peak in May/June 2024 corresponding to the heavy rainfall event reported by Mohr et al. (2024). The analysis examines whether the weaker DDK8 filter preserves a distinct flood signal that is otherwise smoothed out by the stronger DDK2 filter, thereby testing the limits of GRACE-FO's detectability for short-duration extreme events.

5 Results and Discussion

The analysis of GRACE-FO Level-2 data over Germany (2019–2025) reveals distinct differences in Total Water Storage (TWS) estimates depending on the post-processing filter applied. This section compares the spatial and temporal characteristics of the DDK2 and DDK8 solutions and evaluates their ability to detect the hydrological extreme event of Spring 2024.

5.1 Spatial Filter Performance (DDK2 vs. DDK8)

The spatial distribution of the mean TWS and signal variance demonstrates the trade-off between noise suppression and signal preservation described by Kusche et al. (2009)

- DDK2 Results: As shown in the generated spatial maps 5.1, the DDK2 filter produces a highly smoothed gravity field. The contours are regular, and the north-south "striping" errors are effectively removed. However, the signal amplitude is visibly attenuated. This aligns with the theoretical smoothing radius of approximately 340 km for DDK2 (Kusche et al., 2009, Table 1) which inevitably suppresses localized mass variations smaller than this footprint.
- DDK8 Results: In contrast, the DDK8 spatial maps (5.2f) exhibit higher spatial variability. While the signal amplitude (max/min values) is higher, significant north-south striping artifacts are visible. This confirms that the weaker regularization of DDK8 allows correlated errors to propagate into the final solution, making it difficult to distinguish between geophysical mass changes and orbital noise artifacts in a single monthly snapshot.

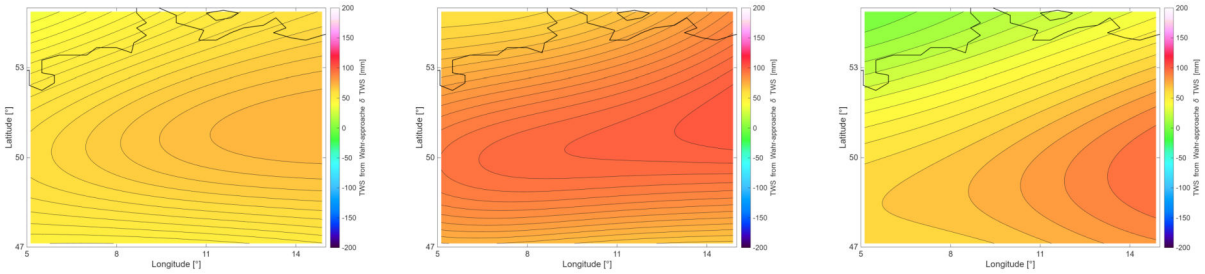

(a) Januany (b) February (c) March

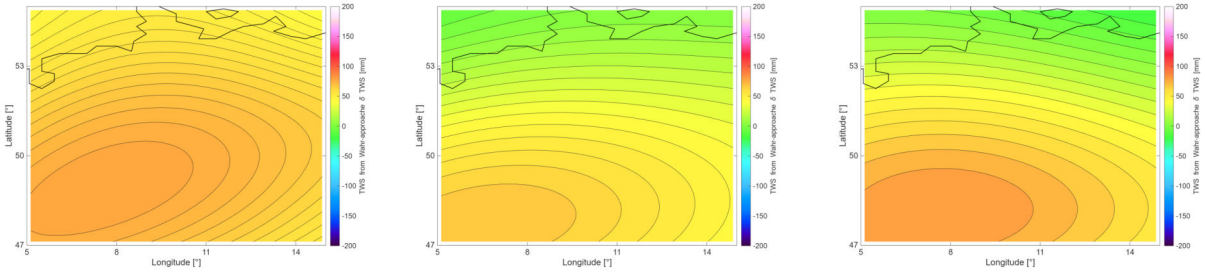

(d) April (e) May (f) June

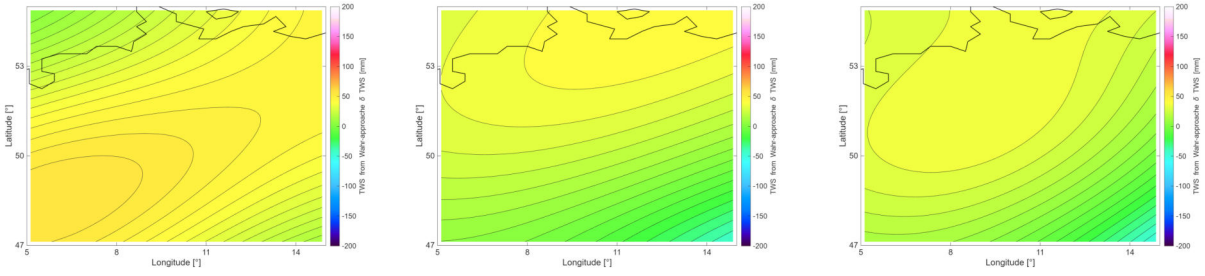

(g) July (h) August (i) September

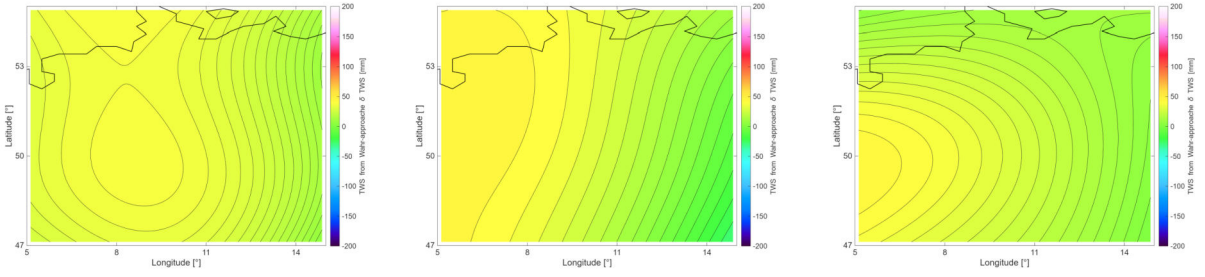

(j) October (k) November (l) December

Figure 5.1: Equivalent water height DDK2 in 2024.

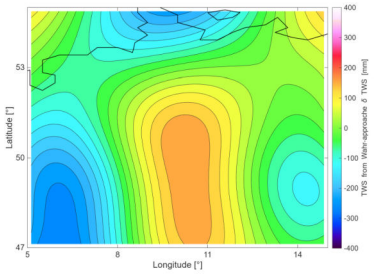

(a) Januany

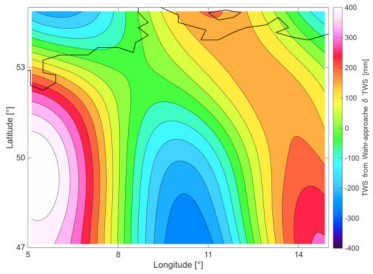

(b) February

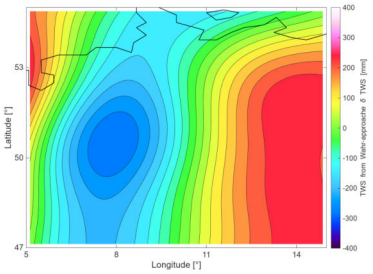

(c) March

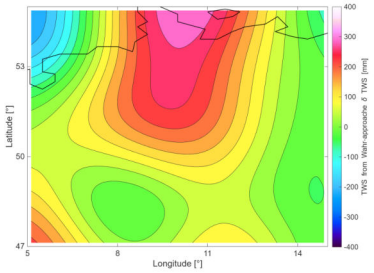

(d) April

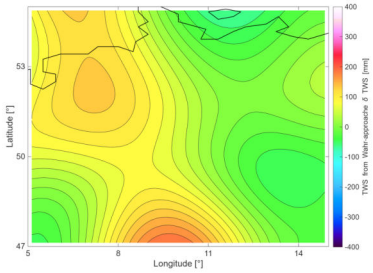

(e) May

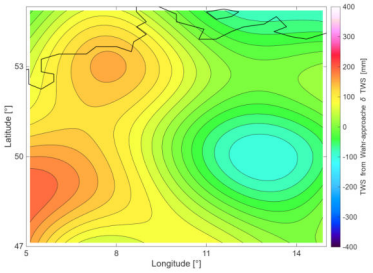

(f) June

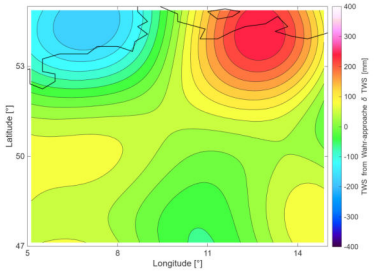

(g) July

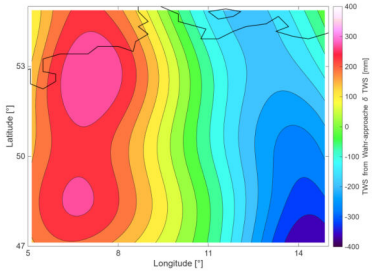

(h) August

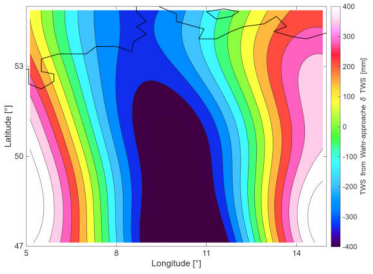

(i) September

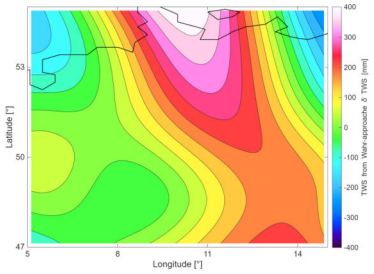

(j) October

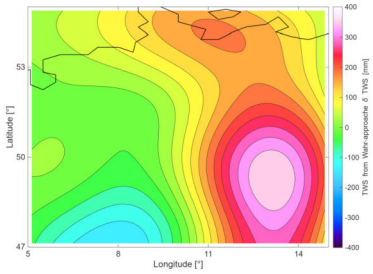

(k) November

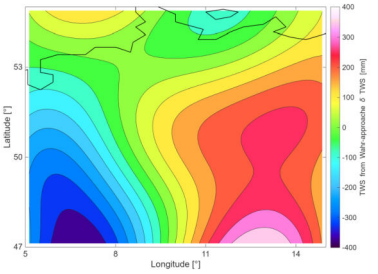

(l) December

Figure 5.2: Equivalent water height DDK8 in 2024.

5.2 Time Series Analysis and Signal Attenuation

The extracted time series for the German territory (Figures 5.1 and 5.2) quantify the temporal evolution of TWS.

- Amplitude Differences: Comparing the "Max" and "Min" curves of the two datasets, the DDK8 solution consistently shows a larger range of equivalent water height (EWH) than DDK2. The DDK2 time series appears dampened. This suggests that the stronger DDK2 filter causes signal leakage, where the water mass signal is "smeared" into surrounding areas, reducing the peak values observed over the study area.
- Seasonal Trends: Both filters successfully capture the seasonal hydrological cycle, with TWS maxima typically occurring in late winter/early spring and minima in late summer.

5.3 Detection of the Spring 2024 Flood Event

The primary objective was to identify the heavy rainfall event of late May/early June 2024 documented by (Mohr et al., 2024).

- Analysis of DDK2 Filtered Solutions Figure 5.3 presents the monthly EWH variations for 2024 derived using the DDK2 filter. The resulting maps are characterized by a high degree of smoothness. The contours (isolines) form coherent, large-scale patterns that evolve gradually from month to month, reflecting the seasonal hydrological cycle.
  - Noise Suppression: The strong regularization of the DDK2 filter (approx. 340 km smoothing radius) effectively removes the north-south "striping" errors.
  - Flood Detection (May/June 2024): Looking specifically at panels (e) May and (f) June, the maps show a generalized transition in water storage. However, distinct, localized anomalies corresponding to the extreme flooding in Southern Germany (Bavaria/Baden-Württemberg) are not clearly resolvable. The flood event, described by (Mohr et al., 2024) as a concentrated heavy rainfall event, appears to have been spatially "smeared" into the broader regional signal. The magnitude of the anomaly is dampened, preventing the identification of the specific flood location.

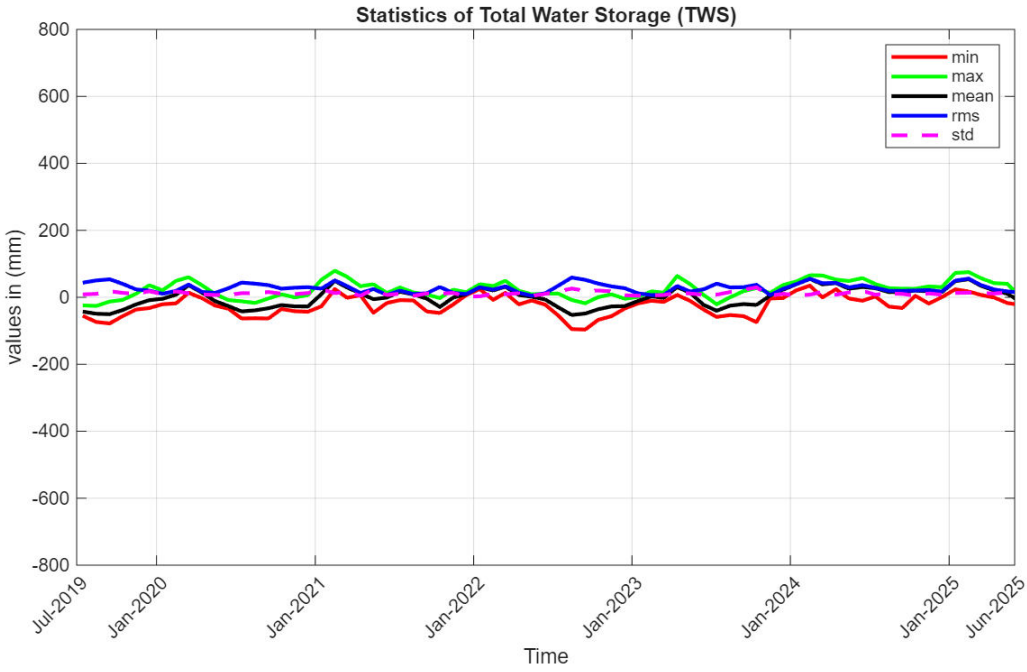

Figure 5.3: Statistics of total water storage from DDK2 filter from 2019 to 2025

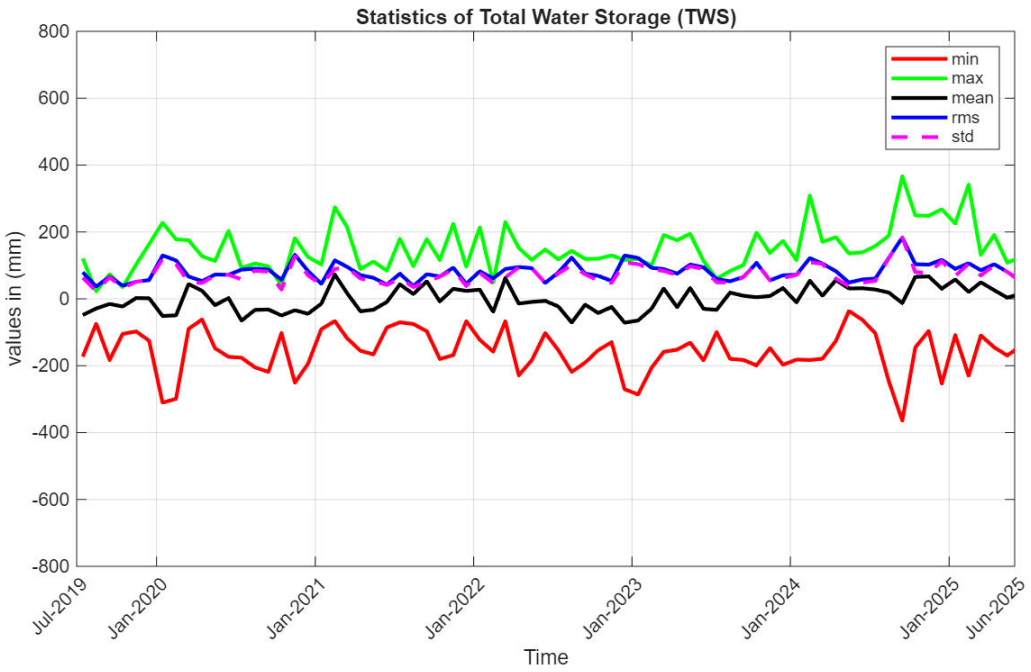

Figure 5.4: Statistics of total water storage from DDK8 filter from 2019 to 2025

- Analysis of DDK8 Filtered Solutions displays the same time period processed with the weaker DDK8 filter. The difference in visual quality is striking.
- Analysis of DDK8 Filtered Solutions Figure 5.4 presents the monthly EWH variations for 2024 derived using the DDK8 filter.
  - Signal and Noise: The maps exhibit much higher signal amplitudes (as indicated by the deep blue and red color saturation) compared to DDK2. However, the solutions are dominated by strong, vertical north-south striping artifacts.
  - Signal and Noise: The maps exhibit much higher signal amplitudes (as indicated by the deep blue and red color saturation) compared to DDK2. However, the solutions are dominated by strong, vertical north-south striping artifacts.
- Meteorological Ground Truth: According to Mohr et al. (2024), precipitation accumulations reached up to 255 mm in 120 hours in Southern Germany.
- GRACE-FO Observation: In the DDK2 time series, a distinct, sharp peak corresponding to this magnitude is not clearly observable in June 2024. The curve remains relatively consistent with the seasonal trend.
- Interpretation: The lack of a strong signal in the DDK2 solution can be attributed to two factors:
  - Spatial Resolution: The flood was spatially concentrated in Bavaria and Baden-Württemberg. The 340 km smoothing radius of the DDK2 filter Kusche et al. 2009 is larger than the core flood area, causing the signal to be averaged out with drier surrounding regions.
  - Temporal Averaging: As noted by Zhang et al. 2023, GRACE-FO provides monthly averages. Since the extreme event lasted only 5 days (May 30–June 3), the water mass increase was likely diluted when averaged over the entire month of June, unlike longer-duration floods which accumulate over weeks.

While the DDK8 time series shows higher variability in 2024, the presence of high-frequency noise (as seen in the spatial stripes in Figure 5.2) makes it risky to interpret the peaks as a definitive flood signal without further external validation.

5.4 Spatial Undulation and Signal Morphology

To further investigate the spatial characteristics of the water storage anomalies, the undulation of the TWS signal – representing the spatial morphology of the mass change – was analyzed for 2024. A comparison between Figure 5.5 (DDK2) and Figure 5.6 (DDK8) provides visual evidence of how filtering affects the signal structure during the flood period.

- Analysis of DDK2 Undulations Figure 5.5 illustrates the undulation of TWS using the DDK2 filter. The isolines (contour lines) exhibit a high degree of smoothness and regularity across all months.
  - Signal Coherence: The transitions between high and low anomalies are gradual, indicating that the DDK2 filter ($\approx$ 340 km smoothing) has successfully suppressed high-frequency spatial noise.
  - May/June 2024 (Panels k, l in Figure 5.1): During the flood months, the undulation pattern shows a broad, large-scale increase in water mass (shift in color gradient). However, the isolines remain widely spaced and smooth. This confirms that the specific, localized "peak" of the Southern Germany flood has been spatially smoothed into a broader regional signal, making it difficult to pinpoint the event's epicenter.

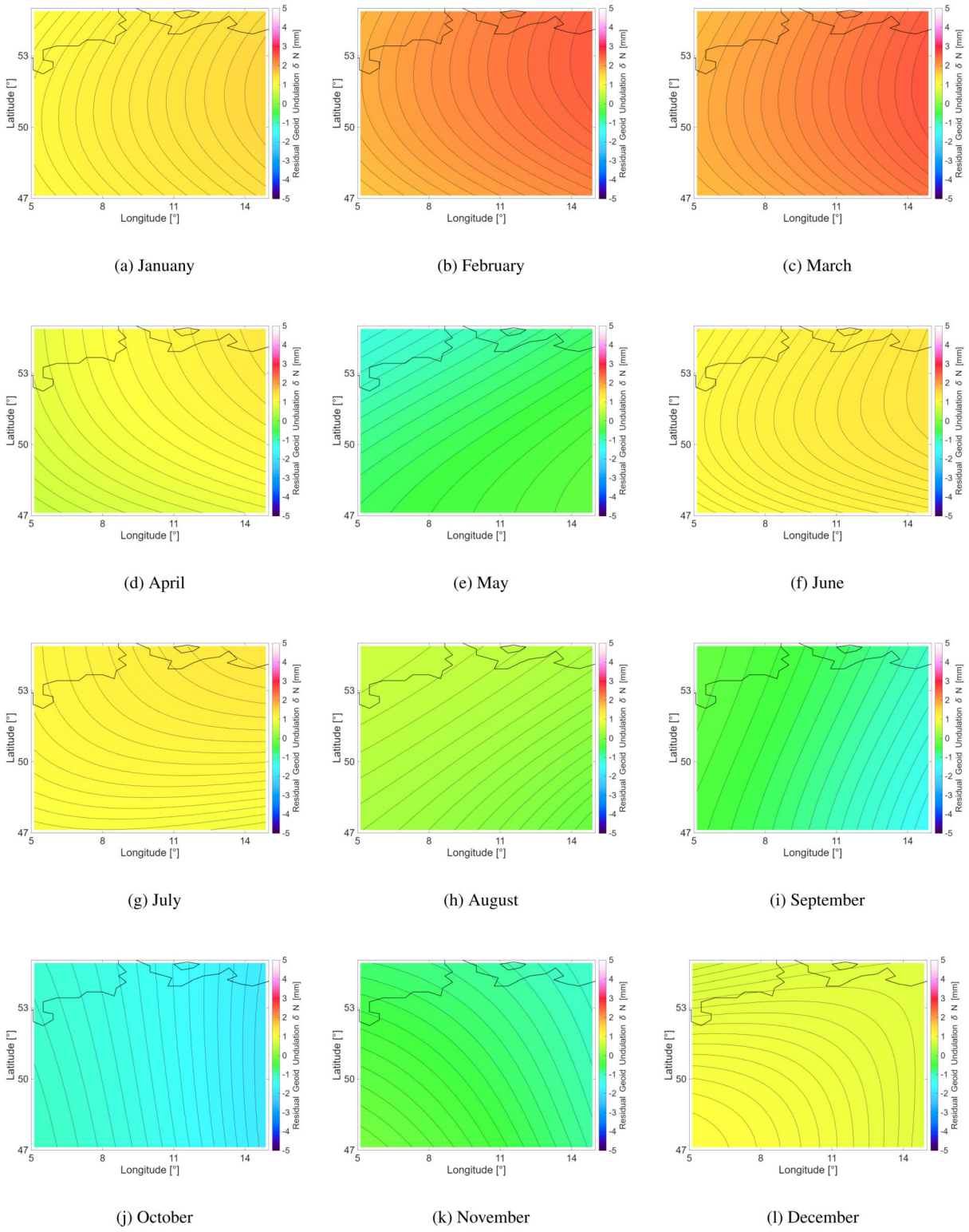

(a) Januany (b) February (c) March

(d) April (e) May (f) June

(g) July (h) August (i) September

(j) October (k) November (l) December

Figure 5.5: Geoid Undulation change due to TWS change using DDK2 filter in 2024 (±5 mm).

- Analysis of DDK8 Undulations Figure 5.6 displays the results using the weaker DDK8 filter. The morphology of the isolines differs significantly from the DDK2 solution.
  - Analysis of DDK8 Undulations Figure 5.6 displays the results using the weaker DDK8 filter. The morphology of the isolines differs significantly from the DDK2 solution.

* Striping Artifacts: Unlike the unfiltered solutions, the DDK8 filter yields a smooth spatial pattern similar to that of DDK2. This indicates that the correlated errors are effectively suppressed, rather than being amplified during the downward continuation to the sphere in the north-south direction. This is the visual signature of correlated error striping discussed by Kusche et al. (2009).
* Sensitivity vs. Noise: While DDK8 theoretically preserves more signal amplitude (sensitivity), the undulation maps reveal that this signal is heavily contaminated. In May (k) and June (l) in Figure 5.6, the undulations are chaotic. While there are areas of higher intensity, the "striping" effect distorts the isolines to such a degree that a clear hydrological boundary for the flood cannot be reliably drawn.

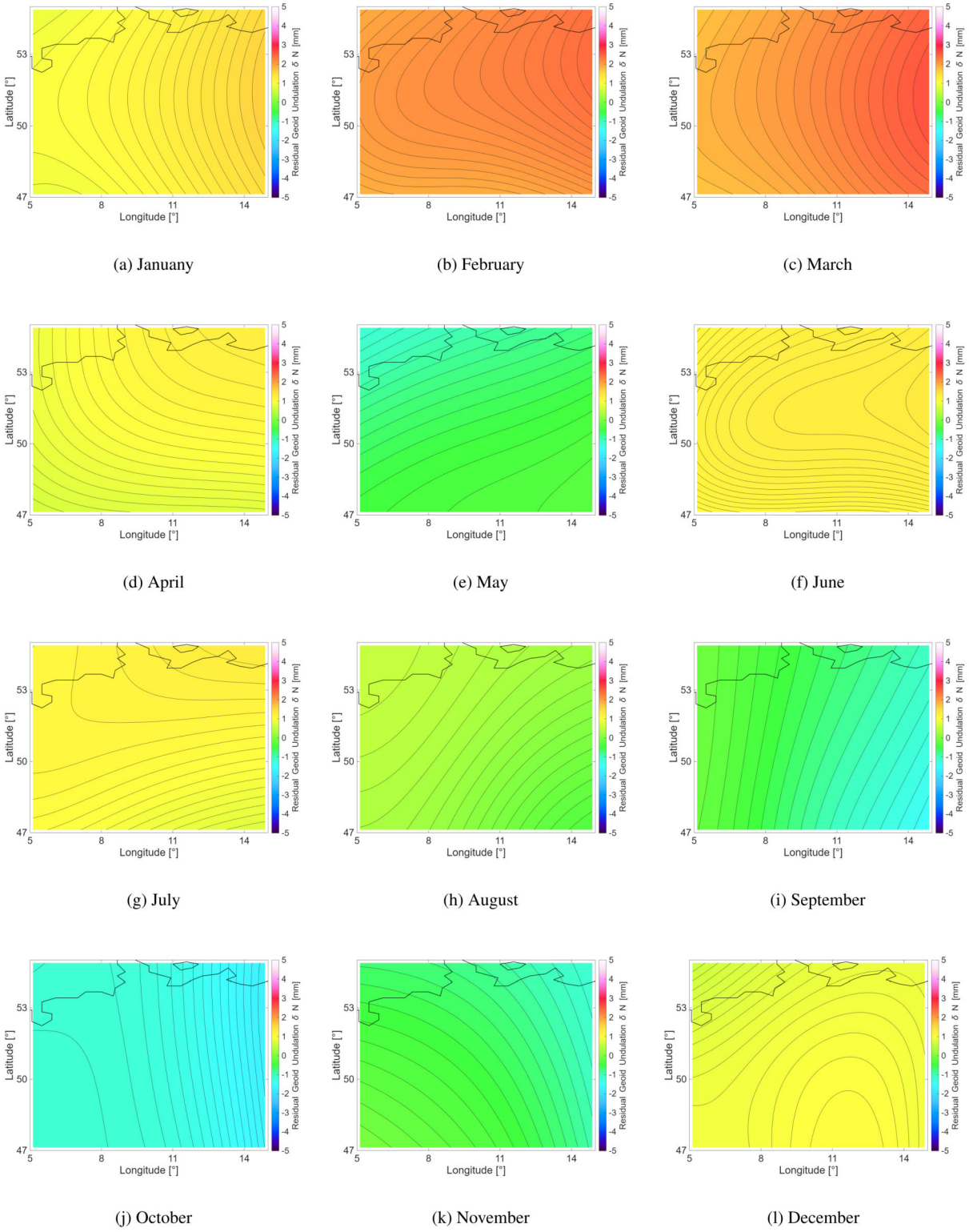

(a) Januany (b) February (c) March

(d) April (e) May (f) June

(g) July (h) August (i) September

(j) October (k) November (l) December

Figure 5.6: Geoid Undulation change due to TWS change using DDK8 filter in 2024 (±5 mm).

6 Conclusion and Outlook

This study analyzed the Total Water Storage (TWS) variations over Germany using GRACE-FO satellite data from 2019 to 2025 to assess the detectability of the 2024 Southern Germany flood event. The comparison between decorrelation filters confirmed that the choice of filter significantly dictates the results. The DDK2 filter provided a

clean, error-free signal but resulted in significant signal attenuation due to its strong smoothing (equivalent to a filter radius of 340 km). The DDK8 filter retained higher signal amplitudes but introduced substantial striping noise, complicating the interpretation of spatial anomalies. Regarding the specific event of Spring 2024, the analysis indicates that the flood signal was largely undetectable in the standard DDK2-filtered monthly solutions. Despite the extreme precipitation reported by Mohr et al. (2024), the short duration of the event (flash flood dynamics) and its spatial confinement to Southern Germany meant that the gravitational anomaly was smoothed below the detection threshold of the DDK2 filter. This highlights the limitations of current satellite gravimetry in monitoring short-term, localized hydrological extremes, as discussed by Zhang et al. (2023) Future work could focus on using mascon solutions or integrating GRACE-FO data with hydrological models to improve the downscaling of such localized events.

Acknowledgement

The author wishes to express sincere gratitude to Prof. Kurt Seitz and the team at the Geodätisches Institut (GIK), Karlsruhe Institute of Technology (KIT) for their continuous guidance, academic support, and for providing the necessary computational resources and laboratory facilities through- out the duration of this study. Their expertise and encouragement were invaluable in shaping the direction and quality of this research.
The author also gratefully acknowledges the International Centre for Global Earth Models (ICGEM), GFZ German Research Centre for Geosciences (2023) for supplying the GRACE spherical harmonic datasets used in this work. The author further acknowledges the support and motivation received from colleagues and fellow students within the Remote Sensing and Geoinformatics programme at KIT, whose discussions and insights enriched the understanding of the scientific challenges involved.

References

CEDIM (2025): Center for Disaster Management and Risk Reduction Technology (CEDIM). Accessed: 2025-12-16. URL: https://cedim.kit.edu/english/index.php.

DWD (2025): Deutscher Wetterdienst (DWD). Accessed: 2025-12-16. URL: https://icgem.gfz-potsdam.de/sp/01_GRACE/GFZ/GFZ%20Release%2006.1%20(GFO)/96x96.

ICGEM (2026): International Centre for Global Earth Models (ICGEM): Gravity field and GRACE/GRACE-FO products hosted at the German Research Centre for Geosciences (GFZ). Accessed: 2026-04-06. URL: https://icgem.gfz-potsdam.de/.

Kusche, J., Schmidt, R., Petrovic, S., and Rietbroek, R. (2009): Decorrelated GRACE time-variable gravity solutions by GFZ, and their validation using a hydrological model. *Journal of Geodesy* 83:903–913. DOI: 10.1007/s00190-009-0308-3.

Mohr, S., Daniell, J. E., Ehret, U., Küpfer, K., Ludwig, P., Mühr, B., Rosenberg, S., Schäfer, A. M., Wilhelm, J., and Kunz, M. (2024): CEDIM Forensic Disaster Analysis Group (FDA): Außergewöhnliche Niederschläge und Hochwasser in Süddeutschland im Juni 2024. German. Tech. rep. 12.11.35; LK 01. KIT. DOI: 10.5445/IR/1000171441.

Tsoulis, D. (1999): Spherical harmonic computations with topographic/isostatic coefficients. Tech. rep. IAPG/FESG No. 3. Munich, Germany: Institut für Astronomische und Physikalische Geodäsie, Technische Universität München.

Wahr, J., Molenaar, M., and Bryan, F. (1998): Time variability of the Earth's gravity field: Hydrological and oceanic effects and their possible detection using GRACE. *Journal of Geophysical Research: Solid Earth* 103(B12):30205–30229.

Zhang, J., Liu, K., and Wang, M. (2023): Flood detection using Gravity Recovery and Climate Experiment (GRACE) terrestrial water storage and extreme precipitation data. *Earth System Science Data* 15(2):521–540. DOI: 10.5194/essd-15-521-2023. URL: https://essd.copernicus.org/articles/15/521/2023/.

Study on the inverse Tesseroid method in TWS calculation

Ananthan Pushpa Balan[1]

1 Remote Sensing and Geoinformatics Master of Science (M.Sc.), KIT, Germany
E-Mail: ubxll@student.kit.edu

Abstract

This study investigates the estimation of terrestrial water storage (TWS) anomalies over Europe in 2024 using data from the GRACE-FO mission. Building on the pioneering role of GRACE in enabling global-scale quantification of TWS, the research aims to improve the spatial representation of TWS by addressing known error sources such as striping effects and correlated noise. A comparative analysis is conducted between the frequency-domain Wahr approach and a space-domain inverse tesseroid method, using GRACE-FO Level-2 spherical harmonic products (Release 6.3, DDK5 filter) as the data basis.

The Wahr approach is used to establish a reference TWS solution that successfully captures seasonal hydrological mass variations across Europe. To evaluate the inverse tesseroid method, gravitational potentials are forward-modeled at three different altitudes h (0 km, 200 km, and 500 km) and subsequently inverted via least-squares adjustment to recover surface TWS. A residual analysis is performed to assess the mathematical stability and convergence behavior of the inversion.

The results demonstrate that increasing synthesis altitude leads to significant attenuation of the gravitational signal, with high-frequency spatial details diminishing at satellite height. At ground level (0 km), the inverse tesseroid method achieves near-perfect agreement with the reference solution, confirming its high accuracy under minimal signal decay conditions. However, at higher altitudes (200 km and 500 km), the inversion becomes increasingly ill-posed, resulting in loss of spatial resolution and the emergence of artifacts such as striping and ringing. Despite achieving near-zero residuals and thus mathematical convergence, the reconstructed TWS fields at high altitudes deviate substantially from physical reality.

In conclusion, while the inverse tesseroid method is highly effective for near-surface applications, its use at satellite altitudes is fundamentally limited by the ill-posed nature of downward continuation. Future research should focus on advanced regularization techniques to stabilize the inversion and enhance the physical reliability of high-altitude TWS estimations.

Keywords GRACE · Inverse Tesseroid Approach

1 Introduction

The Earth system is highly dynamic, subject to continuous temporal changes driven predominantly by mass transport processes within the atmosphere, oceans, and continental hydrosphere. Monitoring the Earth's time-variable gravitational field via satellite-based geodetic sensors, such as the Gravity Recovery and Climate Experiment

KIT Scientific Working Papers
Issue Number 270
ISSN: 2194-1629
DOI: 10.5445/IR/1000191188
Online: June 2026

This document is licensed under the Creative Commons Attribution – Share Alike 4.0 International License (CC BY-SA 4.0):
https://creativecommons.org/licenses/by-sa/4.0/deed.en

(GRACE) and its successor GRACE Follow-On (GRACE-FO), offers an unprecedented global perspective on these spatial and temporal mass fluctuations (Humphrey et al., 2023). The primary hydrological quantity obtainable from these missions is the variation in Terrestrial Water Storage (TWS), which serves as a crucial indicator of the global water cycle, climate dynamics, and regional water availability (Long et al., 2013). Traditionally, TWS variations are derived from the released Level-2 fully normalized Spherical Harmonic Coefficients (SHCs) using a well-established frequency-domain approach introduced by Wahr et al. (1998). However, because unconstrained GRACE/GRACE-FO Level-2 products suffer from high-frequency noise and distinct north-south correlated striping errors caused by the satellite's polar orbit, spatial filtering is a mandatory step before converting potential changes to TWS (Qian et al., 2022). Consequently, anisotropic decorrelation filters (Kusche, 2007), such as the DDK filter family (e.g., DDK5), are routinely applied to balance the suppression of high-frequency noise while retaining the maximum possible physical signal (Qian et al., 2022). While the frequency-domain (Wahr et al., 1998) approach is the standard procedure, alternative spatial-domain methods can be formulated as an inverse problem of forward modeling, which is particularly advantageous for regional applications. One highly effective spatial-domain method utilizes tesseroids (spherical prisms). Bounded by geographical grid lines (longitude and latitude) and surfaces of constant height, tesseroids are naturally suited to account for the Earth's curvature in global and regional gravity field modeling (Heck and Seitz, 2007). In the inverse tesseroid approach, a grid of gravitational potential values is synthesized from the satellite data, and an iterative least-squares adjustment is performed to reconstruct the TWS information by estimating the unknown heights of the modeled tesseroidal mass bodies (Grombein et al., 2013). The central focus of this Lab Rotation is the investigation of the differences between TWS results obtained via the traditional Wahr approach (frequency domain) and the inverse tesseroid approach (space domain). A critical parameter in the inverse tesseroid method is the vertical position of the data grid where the potential changes are synthesized. Therefore, the primary research question of this study is how the altitude of this synthesized grid affects the estimation of TWS. To address this, the study focuses on the European continent over a time period spanning from 2019 to 2025. Using MATLAB, GFZ GRACE-FO monthly solutions filtered with the DDK5 filter were processed. In the inverse tesseroid workflow, the data was synthesized at three distinct satellite/evaluation heights: 500 km, 200 km, and 0 km (surface level). The synthesized potential values act as observations in an ill-posed least-squares adjustment, requiring Tikhonov regularization to stabilize the normal equations and successfully estimate the TWS (Uieda and Barbosa, 2016). Furthermore, to provide an in-depth interpretation of the connection between the modeled TWS and the gravity field, additional parameters including gravitational potential, geoid undulation, degree variances, and error spectra were calculated. By comparing the spatial and spectral analysis of the TWS generated at different heights against the standard Wahr approach, this report aims to provide a thorough discussion on the reliability, accuracy, and physical characteristics of the inverse tesseroid method for regional hydrological mass variation modeling.

2 Theoretical Aspects

Several fundamental concepts play an essential role in the conversion of time-variable gravity field models into Total Water Storage (Long et al., 2013). While traditional methods operate in the frequency domain, modern regional analyses utilize space-domain parameterizations such as tesseroids. This section outlines the mathematical formulations of the Spherical Harmonic Synthesis (Wahr approach) and the Inverse Tesseroid method, where the height of individual tesseroids is estimated through least-squares adjustment.

2.1 Spherical Harmonic Synthesis (SHS)

The gravitational potential $V(P)$ is usually represented in the global basis of spherical harmonic as expressed in Equation (2.1) (Heiskanen and Moritz, 1967). Spherical Harmonic Synthesis (SHS) is the forward computation of

a function on the sphere from a given set of coefficients $\bar{C}_{nm}$ and $\bar{S}_{nm}$. The spherical harmonic coefficients derived from GRACE level-2 data is used to express the gravity field of Earth,

$$V(P) = \frac{GM}{r} \sum_{n=0}^{\infty} \left(\frac{R}{r}\right)^n \sum_{m=0}^{n} (\bar{C}_{nm} \cos m\lambda + \bar{S}_{nm} \sin m\lambda) \bar{P}_{nm}(\sin \varphi) \tag{2.1}$$

where,
GM : Geocentric gravitational constant
R : Radius of the reference sphere.
$\bar{C}_{nm}, \bar{S}_{nm}$: Fully normalised spherical harmonic coefficients of degree n and order m
$\bar{P}_{nm}$: Fully normalised Legendre functions of degree n and order m
$r(P) = r_E + h_P$
$h_P = \{500 \text{ km}, 200 \text{ km}, 0 \text{ km}\}$.
The Level-2 monthly gravity field solutions from the GRACE and GRACE-FO missions are provided as fully normalized Spherical Harmonic Coefficients (SHCs), denoted as $\bar{C}_{nm}$ and $\bar{S}_{nm}$ (Humphrey et al., 2023). Spherical Harmonic Synthesis (SHS) is the forward mathematical computation that projects these frequency-domain coefficients back into the spatial domain on a spherical surface. In the traditional Wahr approach (Wahr et al., 1998), the calculation of TWS is performed directly in the frequency domain. The Earth's mass redistributions are modeled as an infinitely thin spherical surface layer, allowing a direct analytical conversion from the SHCs to equivalent water height (EWH) (Wahr et al., 1998; Humphrey et al., 2023).
To derive Total Water Storage (TWS) from these potential changes, the conventional Wahr approach is applied. In this frequency-domain method, the gravity field variations are assumed to be caused by a thin layer of mass redistribution at the Earth's surface. The spherical harmonic coefficients of the gravity field are converted into surface mass density coefficients, effectively yielding TWS anomalies expressed as Equivalent Water Height (EWH). This relies on applying load Love numbers (k_n) to account for the elastic deformation of the solid Earth under the hydrological load.
In contrast, the spatial-domain approach proposed in this study requires synthesizing the physical gravity field functionals – specifically the gravitational potential and geoid undulation – on discrete regional grids. To investigate the height dependence of the inverse method, the SHS is evaluated at three different radial altitudes: $h = 0$ km (Earth's surface), $h = 200$ km, and $h = 500$ km (approximate satellite altitude).

2.2 Degree Variance And Error Degree Variance

The degree variance quantifies the amplitudes of the spherical harmonic coefficients, which vary across different degrees. The sum of the squared coefficients expresses the overall energy in the signal as shown in Equation (2.2). Figure 2.1 shows the degree and error degree variances calculated from Equations (2.2) and (2.3). There is a higher degree variance at lower degrees, and the value decreases as the degree (n) increases. This shows that there is a higher concentration of signal power at lower degrees compared to higher degrees.

$$C_n^2(\bar{C}_{nm}, \bar{S}_{nm}) = \sum_{m=0}^{n} (\bar{C}_{nm}^2 + \bar{S}_{nm}^2) \tag{2.2}$$

$$\sigma C_n^2(\sigma\bar{C}_{nm}, \sigma\bar{S}_{nm}) = \sum_{m=0}^{n} (\sigma\bar{C}_{nm}^2 + \sigma\bar{S}_{nm}^2) \tag{2.3}$$

This helps to understand the distribution of signal intensity through the frequency range. Degree variance for the coefficients obtained for this study has been analysed, which shows that the signal has higher energy in the long wavelength part and it drops in shorter wavelength part of the signal. The plots for degree variance for all the

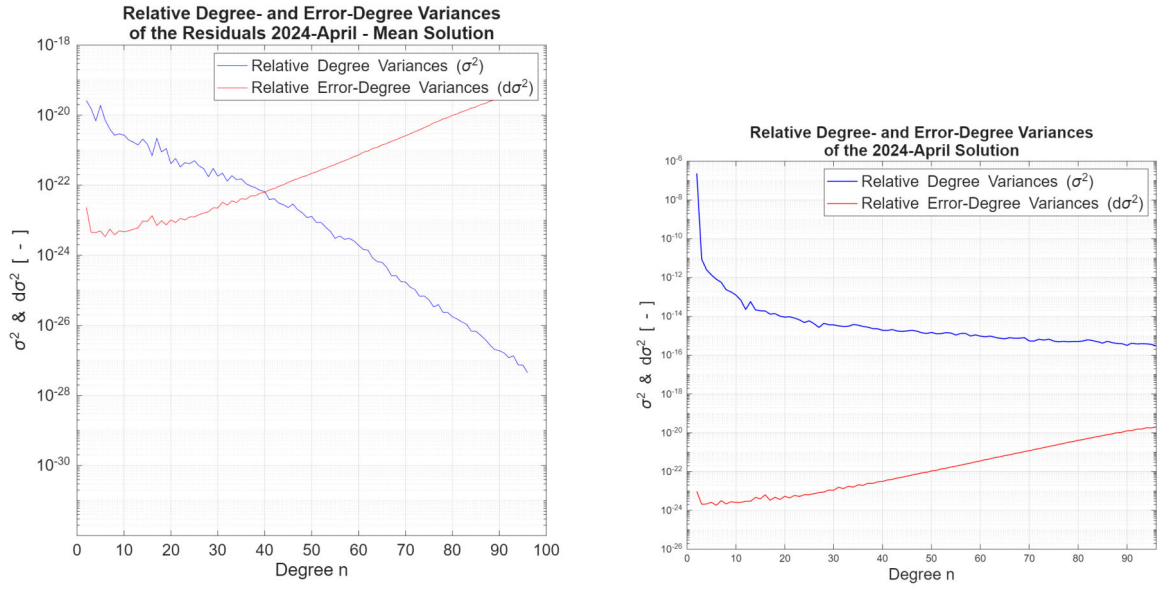

(a) Relative Degree Variance And Error Degree Variance

(b) Degree Variance And Error Degree Variance

Figure 2.1: Degree and error Degree Variances, April 2024.

months are similar with marginal variations, so an example plot for April, 2024 is shown in Figure 2.1. The degree variance is non dependent on altitude of P.

2.3 Mass discretization using Tesseroids

Tesseroids are three dimensional shapes of constant height bounded by longitudinal planes (λ_1, λ_2), latitudinal cones (φ_1, φ_2), and concentric spherical caps (r_1, r_2) as shown in Figure 2.2.
Newton's Integral can be applied on the tesseroids to derive gravitational potential values V of a solid volume Ω.

$$V(r,\varphi,\lambda) = G\rho \iiint_{\Omega} \frac{1}{l} d\Omega = G\rho \int_{\lambda_1}^{\lambda_2} \int_{\varphi_1}^{\varphi_2} \int_{r_1}^{r_2} \frac{r'^2 cos\varphi'}{l} dr' d\varphi' d\lambda' \tag{2.4}$$

$$l(P,Q) = \sqrt{r^2 + r'^2 - 2rr' cos\psi} \tag{2.5}$$

$$\cos\psi = \sin\varphi \sin\varphi' + \cos\varphi \cos\varphi' \cos(\lambda' - \lambda) \tag{2.6}$$

G : Newton's gravitational constant
ρ : density function at running integration point (Q).
l : Euclidean distance between the computation point $P(r,\varphi,\lambda)$ and the running integration point $Q(r',\varphi',\lambda')$
ψ : Angle between the points P and Q.
Newton' integral as mentioned in Equation (2.4) cannot be solved analytically in the case of tesseroids due presence of elliptical integrals. Taylor series expansion can be used for best possible solution. The Taylor point $(r_0,\varphi_0,\lambda_0)$ for the series expansion is set at the geometrical centre of each tesseroid for maximum efficiency in calculation of potentials (Heck and Seitz, 2007).

$$r_0 = \frac{(r_1 + r_2)}{2}; \quad \varphi_0 = \frac{(\varphi_1 + \varphi_2)}{2}; \quad \lambda_0 = \frac{(\lambda_1 + \lambda_2)}{2} \tag{2.7}$$

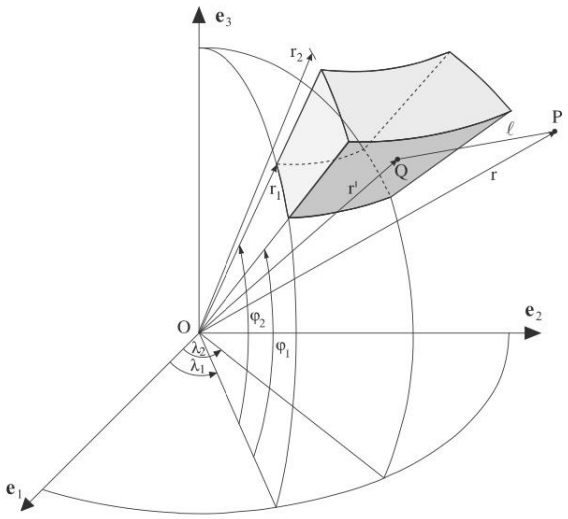

Figure 2.2: Geometry of a spherical tesseroid (Heck and Seitz, 2007)

The integrand in equation (2.4) which represents the kernel $K(r',\varphi',\lambda')$, upon taylor expansion forms Equation (2.9). The coefficients K_{ijk} denotes the partial derivatives of integration kernel.

$$K(r',\varphi',\lambda') = \sum_{i,j,k} K_{ijk}(r'-r_0)^i(\varphi'-\varphi_0)^j(\lambda'-\lambda_0)^k \tag{2.8}$$

From above equations, gravitational potential of a tesseroid with constant density can be formulated as:

$$v(r,\varphi,\lambda) = G\rho\Delta r\Delta\varphi\Delta\lambda\left[K_{000} + \frac{1}{24}(K_{200}\Delta r^2 + K_{020}\Delta\varphi^2 + K_{002}\Delta\lambda^2) + O(\Delta^4)\right] \tag{2.9}$$

with even powers of coefficient K as the odd terms cancel out due to the position of Taylor point being at the geometric centre of the tesseroid (Heck and Seitz, 2007). The Taylor expansion terms in the order of four and above are neglected, which is represented by $O(\Delta^4)$. Here,

$$\Delta r = r_2 - r_1; \quad \Delta\varphi = \varphi_2 - \varphi_1; \quad \Delta\lambda = \lambda_2 - \lambda_1\ . \tag{2.10}$$

2.4 The Inverse Tesseroid Method

The primary objective of this study is the inverse modeling of TWS using tesseroids. In this approach, the height (or radial thickness, Δr) of the water column in each tesseroid is treated as the unknown variable representing TWS. The workflow begins by synthesizing the GRACE-FO potential values δV using SHS on a specified regional grid over Europe. Crucially, the altitude of the computation gridpoints P_{ij} alters the characteristics of the synthesized potential.

In this study, the forward modeling Equations (2.9) of the tesseroids are inverted to solve for TWS. The synthesized potential values (calculated at 0 km, 200 km, and 500 km Height) act as the "observations" L. A uniform grid of tesseroids over Europe with a constant density of freshwater (ρ=1000 kg/m^3) is assumed. The unknown parameters x to be estimated are the radial height variations Δr of each tesseroid, which directly represent the TWS anomalies (Grombein et al., 2013). Because gravity inversion is an ill-posed and non-unique problem, a direct least-squares adjustment will suffer from numerical instability. Therefore, Tikhonov regularization is implemented to constrain the inversion and ensure a stable, smooth solution (Uieda and Barbosa, 2016).

The resulting linear system is formulated evaluating the potential at high altitude (e.g., 500 km) results in a smoother, attenuated signal due to the upward continuation effect, whereas evaluating at the surface (0 km) yields a sharper but potentially noisier signal. These synthesized potential values serve as the pseudo-observations (vec-

tor L) in the inversion process. A system of linear equations is formulated where the design matrix A maps the unknown radial height changes of the tesseroid bodies (vector) to the observed potential values. Because the observation grid (e.g. $1^\circ \times 1^\circ$) and the unknown tesseroid grid (e.g. $2^\circ \times 2^\circ$) often result in an overdetermined system, the unknowns are estimated using a least-squares adjustment:

$$\hat{x} = (A^T PA)^{-1} A^T PL \tag{2.11}$$

where P is the weight matrix of the observations.
Instead of minimizing only the residual $\|Ax - L\|_2^2$, a regularization term is introduced to "smooth" the solution or to constrain its norm. The resulting minimization problem is given by:

$$\hat{x}_\lambda = \arg\min_x \left(\|Ax - L\|_2^2 + \lambda \|Rx\|_2^2 \right) \tag{2.12}$$

- $\|Ax - L\|_2^2$: The data fidelity term (residual), which ensures that the solution x satisfies the equation $Ax \approx L$ in the least-squares sense.
- $\lambda \|Rx\|_2^2$: The regularization term (penalty term), which stabilizes the solution.
- $\lambda > 0$: The regularization parameter (Tikhonov parameter). It determines the trade-off between fitting the data and the smoothness of the solution.
- R: The regularization matrix. Often, $R = I$ (identity matrix), which leads to minimizing the ℓ_2-norm of x.

2.4.1 Special Case: Standard Tikhonov Regularization ($R = I$)

If $R = I$ (standard ridge regression), the closed-form solution to the optimization problem is:

$$\hat{x}_\lambda = (A^T A + \lambda I)^{-1} A^T L, \qquad P = I \tag{2.13}$$

- $A^T A$: The matrix arising from the normal equations.
- λI: The addition of λ times the identity matrix ensures that $(A^T A + \lambda I)$ is invertible, even if $A^T A$ is singular or ill-conditioned.

and λ is the Tikhonov regularization parameter. Regularization is strictly necessary because downward continuation (especially inverting potential from 500 km down to the surface) is an ill-posed mathematical problem that dramatically amplifies high-frequency noise Uieda and Barbosa (2016). The optimal regularization parameter for each altitude was determined using the L-curve method, plotting the solution norm $\|\hat{x}\|_2$ against the residual norm $\|A\hat{x} - L\|_2$ to find the optimal corner point representing the best trade-off between data fit and model smoothness.

2.5 The GRACE/GRACE-FO Observational Concept

The Gravity Recovery and Climate Experiment (GRACE) and its successor, GRACE Follow-On (GRACE-FO), operate on the principle of satellite-to-satellite tracking. Twin satellites flying in a low Earth polar orbit ($h \approx 500$ km) continuously measure minute variations in their inter-satellite distance (≈ 220 km) caused by the gravitational pull of underlying mass anomalies –predominantly driven by the hydrological cycle (Humphrey et al., 2023). While GRACE utilized a K-band microwave ranging system, GRACE-FO achieves even higher precision using a Laser Ranging Interferometer (LRI). These highly precise ranging observations, combined with GPS and accelerometer data, are processed by evaluation centers (e.g., GFZ, CSR, JPL) into Level-2 products. These products represent the Earth's time-variable gravity field as fully normalized Spherical Harmonic Coefficients (SHCs), denoted as $\bar{C}_{nm}, \bar{S}_{nm}$ (Humphrey et al., 2023).

3 Data

To investigate the recovery of Terrestrial Water Storage (TWS) using the frequency-domain Wahr et al. (1998) approach and the spatial-domain inverse tesseroid approach, appropriate time-variable gravity field models are required. This section details the acquisition, characteristics, and pre-processing of the satellite gravity data utilized in this study. The level-2 data used in this study is the monthly solutions from GRACE-FO mission. It includes fully normalized spherical harmonic coefficients that assist in the computation of gravitational potential of the Earth, generated by release 6.1 of GFZ (2026).

3.1 GRACE-FO Level-2 Monthly Solutions

The primary dataset utilized in this analysis consists of Level-2 monthly gravity field solutions from the Gravity Recovery and Climate Experiment Follow-On (GRACE-FO) mission. These Level-2 products represent the Earth's time-variable gravity field as sets of fully normalized Spherical Harmonic Coefficients (SHCs) Humphrey et al. (2023). Specifically, the models employed are the Release 6.3 (RL06.3) monthly solutions generated by the Helmholtz Centre Potsdam – GFZ German Research Centre for Geosciences. These datasets are publicly accessible and were downloaded via the International Centre for Global Earth Models (ICGEM, 2026). The time period selected for this study spans from 2019 to 2025. This temporal range provides a comprehensive dataset to capture seasonal and inter-annual mass variations across the target region. The spatial scope of the investigation is restricted to the European continent, necessitating the synthesis of the global SHCs onto regional spatial grids.

3.2 Filtering and Noise Reduction (DDK5 Filter)

The raw, unconstrained Level-2 SHC products inherently suffer from spatial and temporal noise. Because of the polar orbital configuration and the along-track ranging measurements of the GRACE-FO satellites, the derived gravity models exhibit high-frequency errors and strong correlations between certain spherical harmonic coefficients. In the spatial domain, these errors manifest as prominent north-south oriented stripes (Qian et al., 2022). To effectively isolate the hydrological signals from this satellite-induced noise, spatial filtering is a mandatory processing step before any TWS computation. For this study, the DDK5 decorrelation filter, provided directly via the ICGEM platform, was applied to the GRACE-FO SHCs. The DDK filtering scheme utilizes (Kusche et al., 2009) a formal error covariance matrix to anisotropically smooth the data. This approach optimally balances the suppression of high-degree noise and correlated striping errors while retaining as much of the true geophysical signal (such as water mass variations) as possible (Qian et al., 2022).

3.3 Synthesized Data Grids for the Inverse Tesseroid Method

While the traditional Wahr approach derives TWS directly from the filtered SHCs in the frequency domain, the inverse tesseroid method requires regional spatial grids of gravity field functionals as its input observations. Using MATLAB scripts, the DDK5-filtered SHCs were used to synthesize the residual gravitational potential (δV) and geoid undulation over the European grid. Because the primary research question of this study is how the altitude of the observation grid affects the estimated TWS in the spatial domain, the synthesis was performed at three distinct radial height:

- $h = 0$ km (the Earth's reference surface
- $h = 200$ km (an intermediate altitude)
- $h = 500$ km (approximating the actual satellite orbital altitude)

These synthesized potential grids serve as the primary observational data L in the system of normal equations for the inverse tesseroid method (Grombein et al., 2013). Additionally, calculations of degree variances and error spectra were extracted from the data to evaluate signal intensity and error propagation across the frequency spectrum.

3.4 TWS Anomalies (TWSA)

It is important to note that the data processed in this study represents Terrestrial Water Storage Anomalies (TWSA) rather than absolute total water storage. GRACE and GRACE-FO measure temporal changes in the gravity field relative to a long-term mean (baseline) state. Therefore, the resulting data grids – whether calculated via the Wahr approach or the inverse tesseroid method – reflect the surplus or deficit of water mass (e.g., changes in groundwater, soil moisture, and snowpack) during a specific month compared to the long-term average (Humphrey et al., 2023).

4 Methodology Overview

The central objective of this lab rotation is to investigate and compare the Terrestrial Water Storage (TWS) anomalies derived from two distinct methodologies: the traditional frequency-domain approach (Wahr approach) and the spatial-domain inverse tesseroid approach. To achieve this, a comprehensive data processing workflow was implemented in MATLAB. The study focuses on the European continent for the period spanning from 2019 to 2025, utilizing DDK5-filtered GRACE-FO Level-2 products.

The residual gravitational potential δV values can be projected in a 1°x1° grid on the earth surface, separately for altitudes of computation point P. Spherical harmonic coefficients can be applied in Equation (2.1) to perform Spherical Harmonic Synthesis as shown in Figure 5.3 at the height of ground level. The discretized mass elements known as tesseroids possess uniform surface panels $(\Delta\varphi, \Delta\lambda)$ with constant density where the radial component Δr is assumed to create residual gravitational potential δV. Thus the residual potential can be expressed in terms of Δr, as shown in Equation (4.1), which is used to develop the design matrix A.

$$\delta V(r,\varphi,\lambda) = G\rho\Delta\varphi\Delta\lambda \sum_k \Delta r_k \left[K_{000} + \frac{1}{24}(K_{200}\Delta r^2 + K_{020}\Delta\varphi^2 + K_{002}\Delta\lambda^2) + O(\Delta^4) \right]_k \tag{4.1}$$

Potential values derived through synthesis are introduced as observations L in Equation (4.1) for least squares adjustment. The vector of unknowns represent the radial height change Δr of tesseroid bodies. Here, the observation vector L is of size [m x 1], unknowns vectors x is of size $[nx1]$ and the design matrix A of size $[mxn]$, such that $m > n$ to ensure a over determined system of equations (Baur and Sneeuw, 2011). So the observations from synthesis is derived for a grid of 1°x1° spatial resolution at computation point P, while the unknowns Δr at Q is calculated for a spatial grid of 2°x2°. The regularized solution for the unknownΔr_k can solved from Equation (2.13).

Table 4.1: Tikhonov (optimum) Regularization parameter for all observations.

Month in 2024	0 km	200 km	500 km
January	0.0053749	0.9579e-05	2.4057e-08
April	0.0050584	1.3382e-05	3.3610e-08
July	0.0052821	1.5818e-05	3.3610e-08
October	0.0065521	2.2099e-05	2.8435e-08

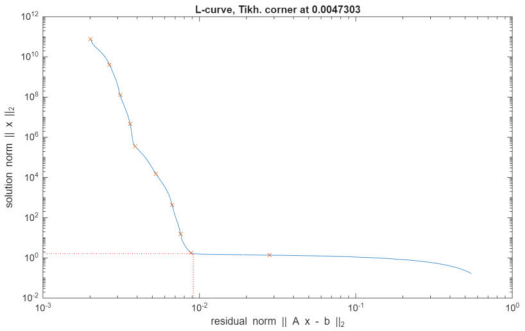

(a) $H = 0$ km

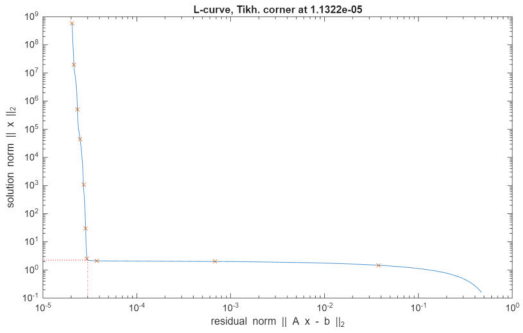

(b) $H = 200$ km

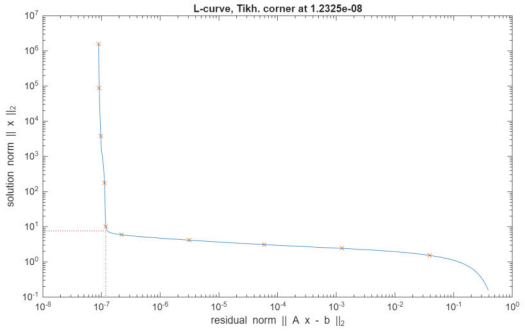

(c) $H = 500$ km

Figure 4.1: **(a)** shows L-curve for P at an altitude of Ground level for the month of May, 2024. **(b)** shows L-curve for P at an altitude of 200 km for the month of May, 2024. **(c)** shows L-curve for P at an altitude of 500 km for the month of May L-curve for several months has been included in Appendix A.1

4.1 The Frequency-Domain (Wahr) Approach

To establish a baseline for comparison, TWS was first calculated using the traditional analytical method in the frequency domain. In this method, the DDK5-filtered Spherical Harmonic Coefficients (SHCs) are directly converted into mass anomalies represented as Equivalent Water Height (EWH). This mathematical conversion relies on the assumption that Earth's mass redistributions occur within an infinitely thin layer at the surface. By applying the appropriate load Love numbers to account for the elastic yielding of the solid Earth, the variations in the spherical harmonic coefficients are directly translated into TWS grids (Wahr et al., 1998; Humphrey et al., 2023). The TWS fields generated using this standard approach serve as the absolute reference against which the spatial-domain inverse tesseroid method is evaluated.

4.2 Forward Synthesis and Spectral Analysis

The first major step in the spatial-domain approach is Spherical Harmonic Synthesis (SHS). Using the filtered GRACE-FO SHCs, the residual gravitational potential δV values can be projected in a 1°x1° spatial grid covering the European continent. To systematically address the primary research question – how the height of the synthesized grid of potential changes affects the estimated TWS – the synthesis was executed at three distinct radial observation altitudes:

- $h = 0$ km (the Earth's reference surface
- $h = 200$ km (an intermediate altitude)
- $h = 500$ km (approximating the actual satellite orbital altitude)

The Earth's reference surface. Generating these distinct grids simulates observations at different proximities to the mass sources, allowing for the assessment of signal attenuation over distance Grombein et al. (2013). Simultaneously, a spectral analysis was conducted in MATLAB to map the connection between TWS and the gravity field. The degree variances and error degree variances were calculated to evaluate the signal-to-noise ratio and track how the signal energy is distributed across the frequency spectrum (Qian et al., 2022).

4.3 The Inverse Tesseroid Approach

Once the potential grids at the three designated heights were synthesized, the problem was framed as a spatial-domain inversion. To accurately account for the Earth's curvature over the European continent, the topographic water mass layer was discretized into three-dimensional spherical prisms known as tesseroids Heck and Seitz (2007) For the parameterization of the forward model:

- The mass elements, discretized by tesseroids, were defined by longitudinal and latitudinal boundaries matching the 1°x1° grid.
- Each tesseroid was assigned a constant density of liquid freshwater ($\rho = 1000$ kg m^{-3}).
- The unknown parameters to be estimated were the radial height changes of the tesseroids (Δr_k), which directly correspond to the desired TWS values (Grombein et al., 2012).

Because the Newton's volume integral for a tesseroid, given in Equation (2.4), cannot be solved analytically, the integration kernel was approximated using a Taylor series expansion. The Taylor-point was set at the geometrical center of each tesseroid to maximize computational efficiency and cause the odd-order terms to cancel out (Heck and Seitz, 2007). These linearized forward modeling equations were used to populate the design matrix A.

5 Results and Discussion

The results obtained from spherical harmonic synthesis of coefficients and derived estimates of TWS through inversion techniques has been included in this section. The estimated heights of tesseroids has been refined using adjustment and regularization techniques. The potential values derived using Equation (4.1) is compared to the potential of synthesis to analyze its deviation.

5.1 Baseline Terrestrial Water Storage and Potential (Wahr Approach)

The analysis of Total Water Storage (TWS) variations over the European continent for the year 2024 was initially conducted using the frequency-domain Wahr approach. Figure 5.1 illustrates the monthly TWS anomalies derived directly from the GRACE spherical harmonic coefficients (filtered with DDK5). A distinct seasonal hydrological cycle is visible across Europe: positive TWS anomalies (mass excess) are predominant during the spring months (March, April) due to winter precipitation and snow accumulation, while significant negative anomalies (mass deficit) are observed during the late summer and autumn months (August to October), reflecting the depletion of water storage due to evaporation and reduced rainfall.
Figure 5.2 presents the corresponding gravitational potential anomalies δv for the same period. These results serve as the reference baseline to evaluate the performance of the space-domain inverse tesseroid approach at various altitudes.

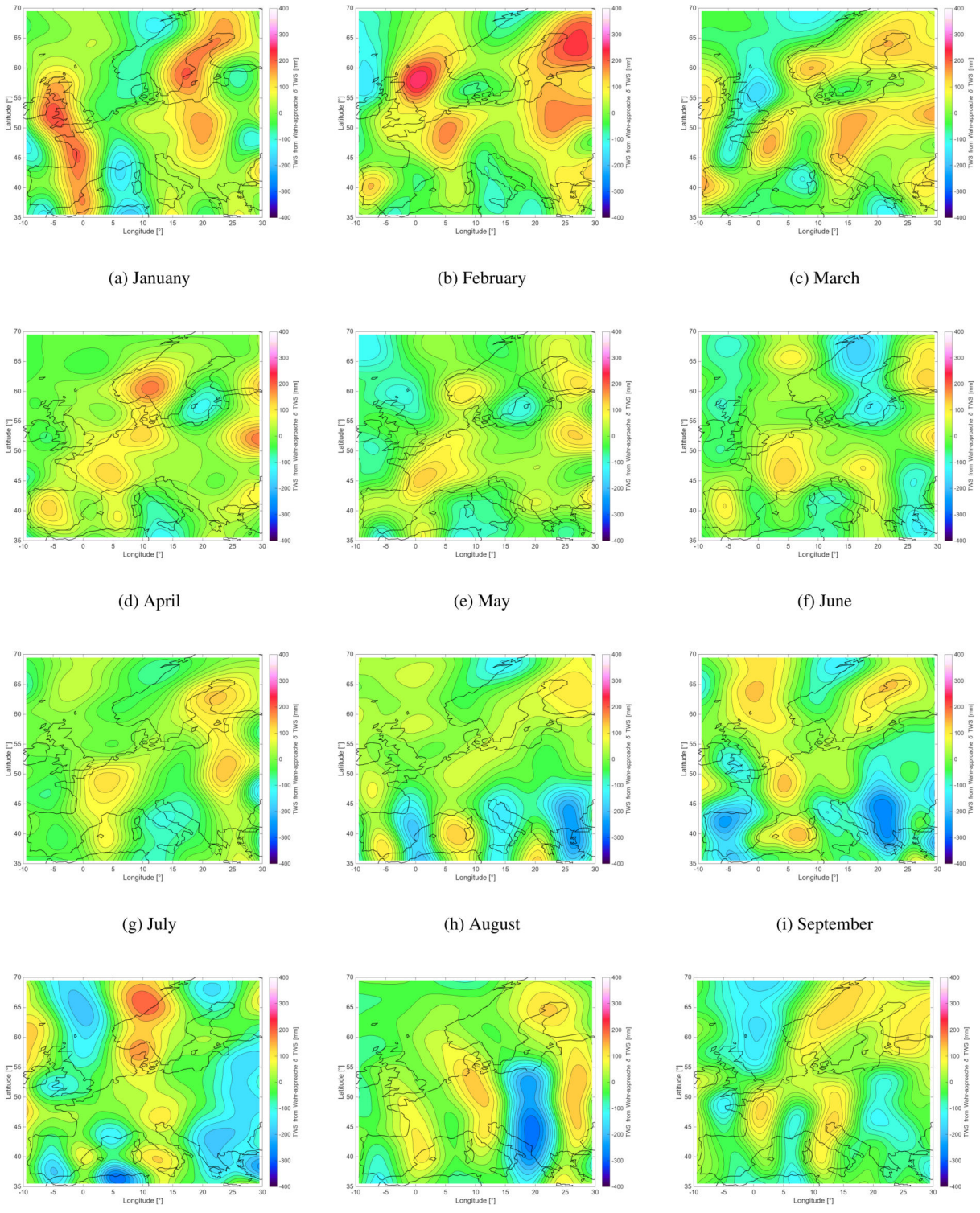

(a) Januany (b) February (c) March

(d) April (e) May (f) June

(g) July (h) August (i) September

(j) October (k) November (l) December

Figure 5.1: Terrestrial water storage over Europe in 2024 based on the Wahr approach. Range is $\pm$ 400 mm.

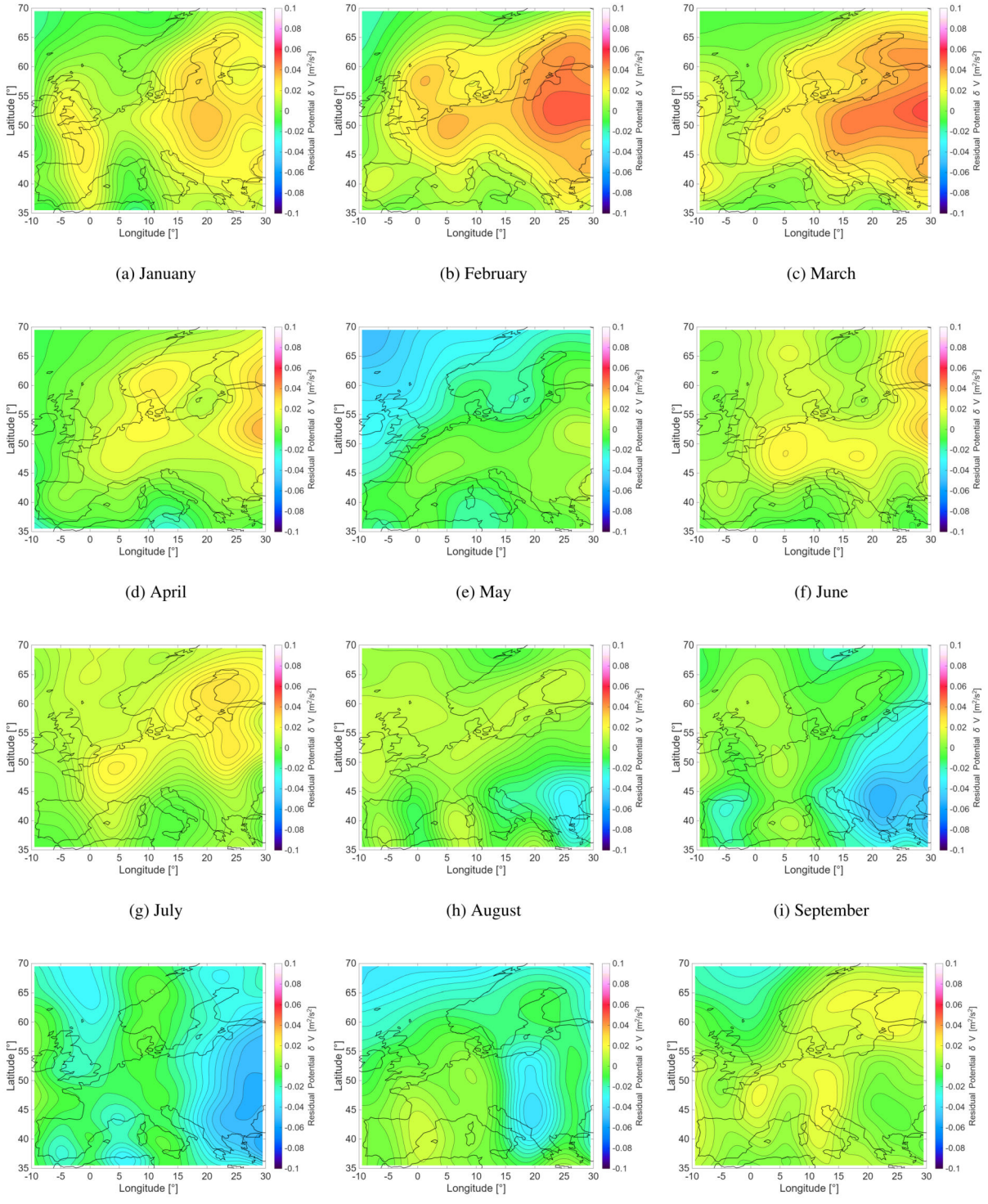

(a) Januany (b) February (c) March

(d) April (e) May (f) June

(g) July (h) August (i) September

(j) October (k) November (l) December

Figure 5.2: Synthesized potential over Europe in 2024 on the ground level. Range is $\pm$ 0.1 $m^2 s^{-2}$.

5.2 Synthesis of Gravitational Potential at Varying Altitudes ($h = 0$ km, 200 km, 500 km)

A primary research question of this study is how the altitude of the synthesized grid affects the subsequent TWS estimation. To investigate this, the gravitational potential was synthesized at three different heights: ground level (0 km), 200 km, and 500 km (satellite altitude). As observed in Figures 5.3, 5.4, 5.5 altitude has a profound impact on the spatial resolution and amplitude of the gravitational potential. At ground level (Figure 5.3), the potential retains high-frequency spatial details and sharp gradients, closely mirroring the underlying localized mass distributions. As the synthesis height increases to 200 km (Figure 5.4) and 500 km (Figure 5.5), the gravitational potential becomes increasingly smoothed and the signal amplitude is significantly attenuated. This is consistent with Newton's law of gravitation, where the gravitational effect of a mass anomaly decays inversely with distance. At 500 km, the high-frequency regional hydrological signals merge into broader, low-frequency patterns.

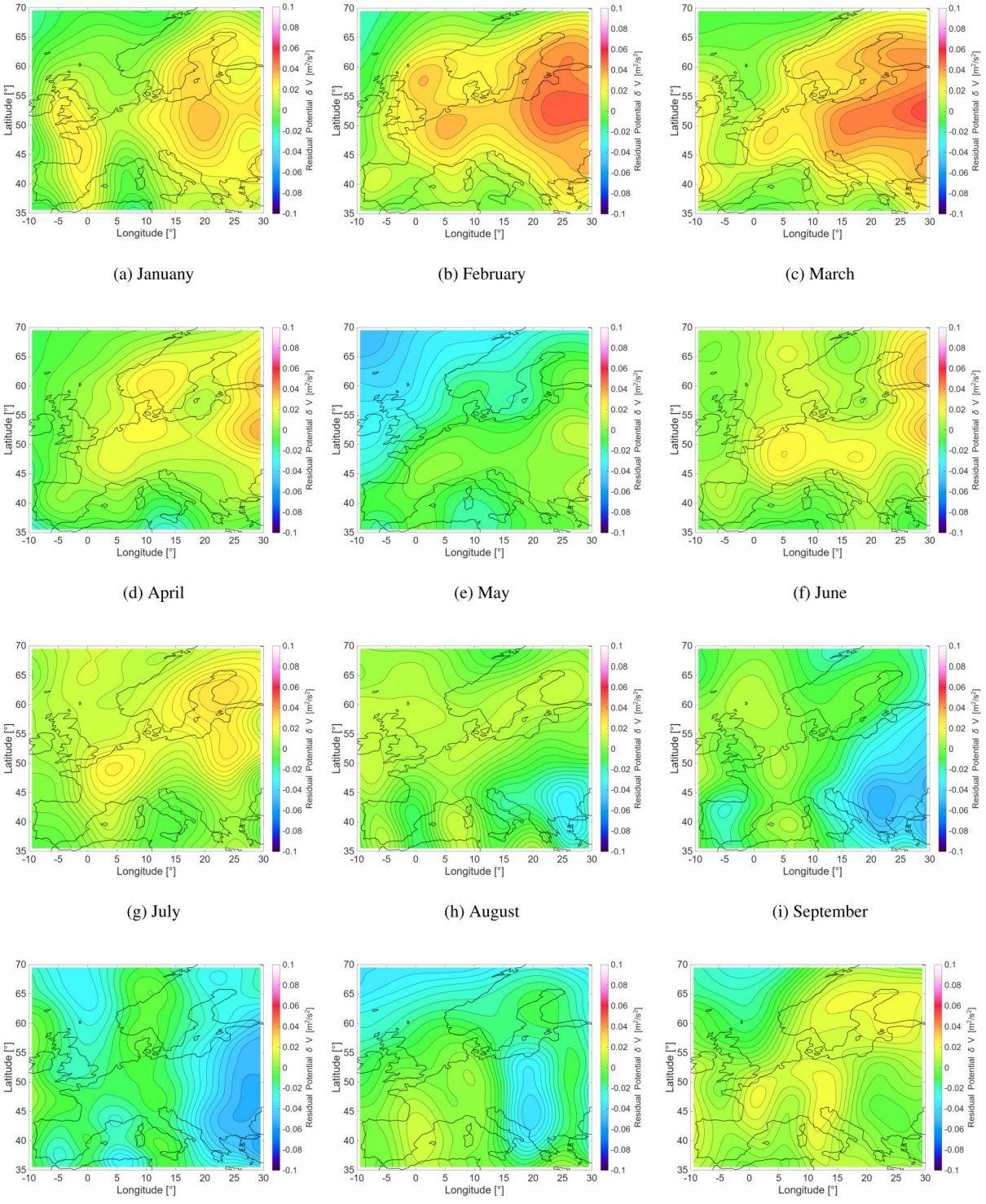

(a) Januany (b) February (c) March

(d) April (e) May (f) June

(g) July (h) August (i) September

(j) October (k) November (l) December

Figure 5.3: Synthesized potential over Europe at $h = 0$ km (ground level) in 2024. Range is $\pm$ 0.1 m^2s^{-2}.
(Remark: This Figure is for completeness and is identical to Figure 5.2)

.

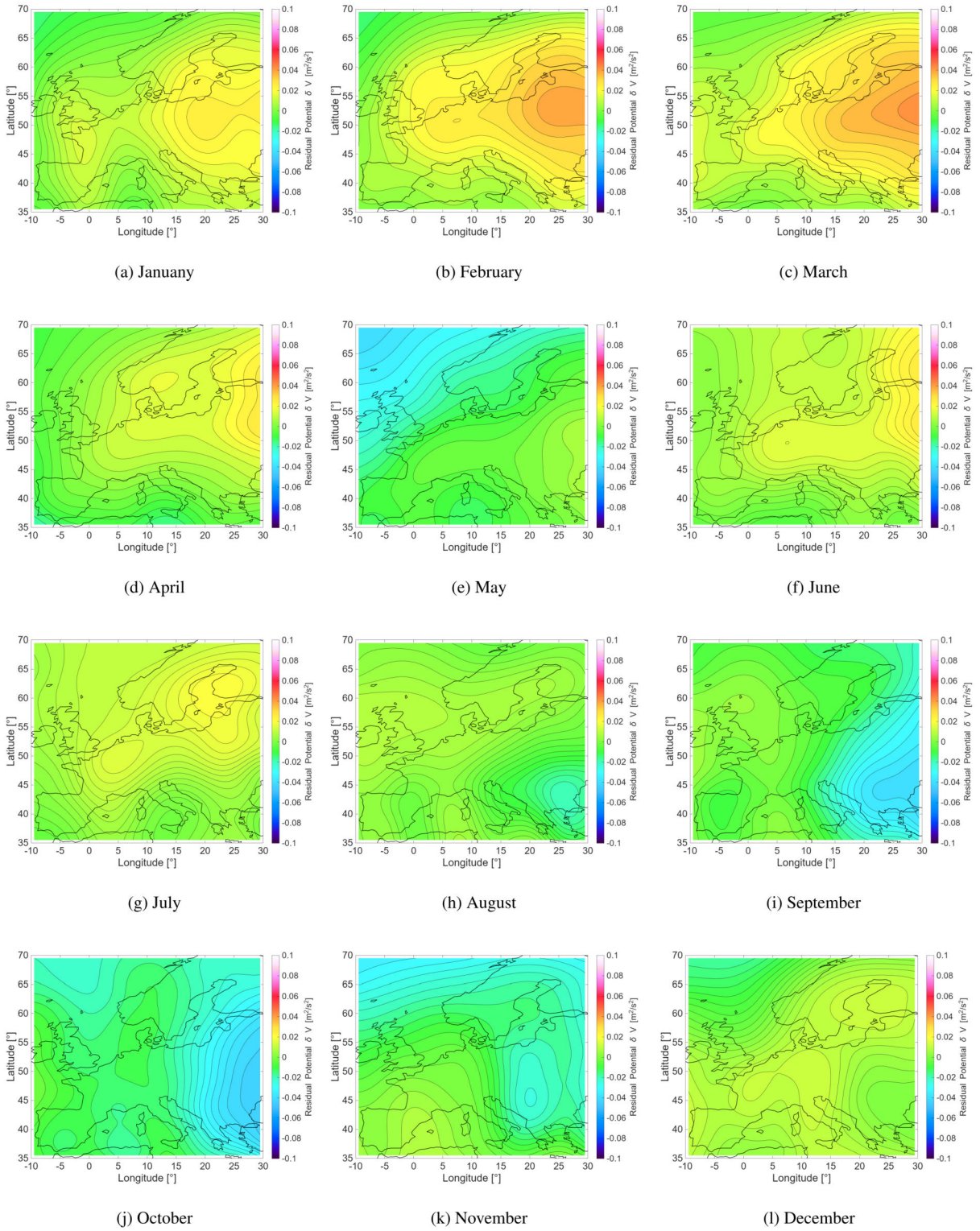

(a) Januany (b) February (c) March

(d) April (e) May (f) June

(g) July (h) August (i) September

(j) October (k) November (l) December

Figure 5.4: Synthesized potential over Europe at $h = 200$ km in 2024. Range is $\pm$ 0.1 $m^2 s^{-2}$.

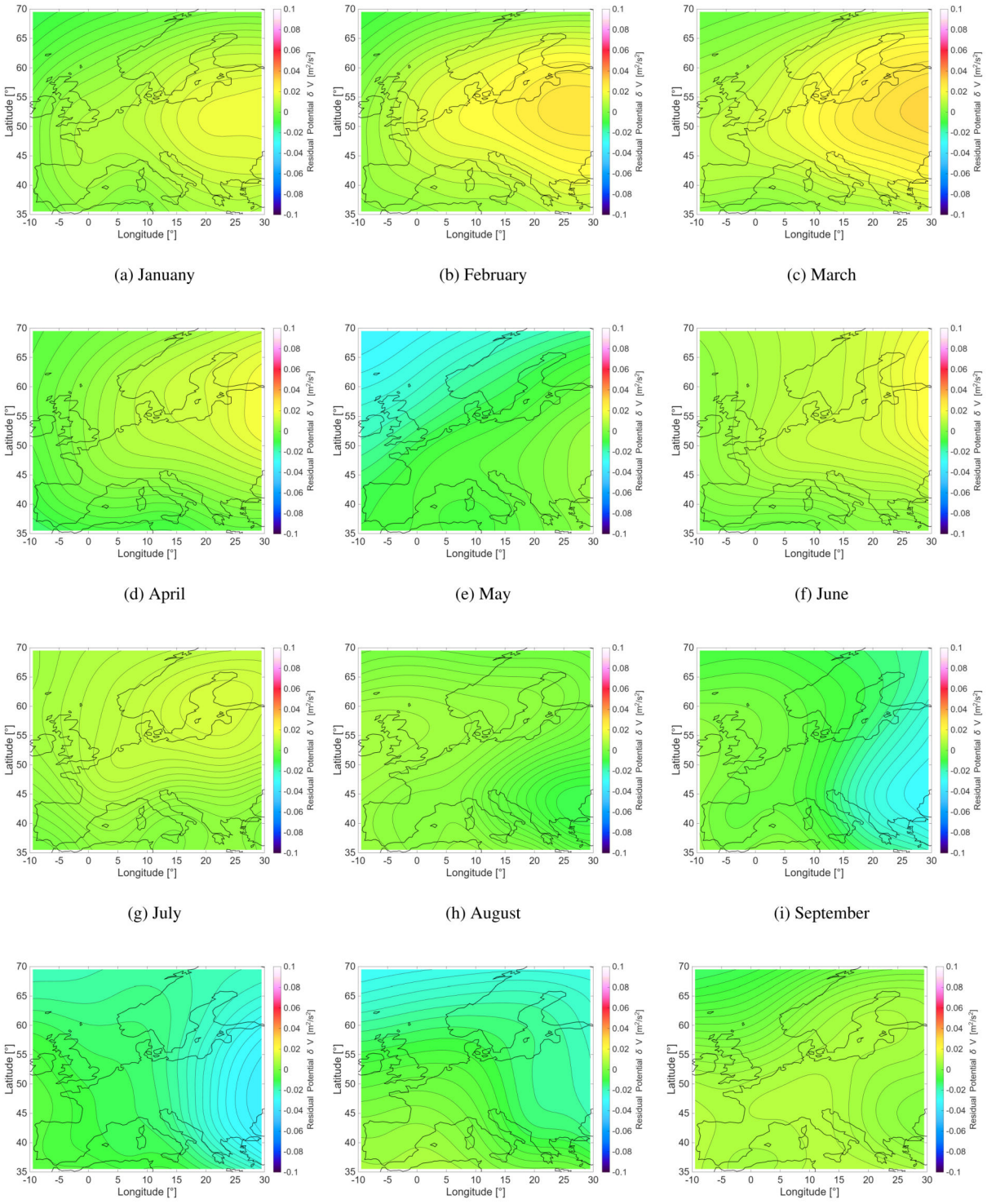

(a) Januany (b) February (c) March

(d) April (e) May (f) June

(g) July (h) August (i) September

(j) October (k) November (l) December

Figure 5.5: Synthesized potential over Europe at $h = 500$ km in 2024. Range is $\pm$ 0.1 $m^2 s^{-2}$.

5.3 Model Assessment: Reconstructed Potential and Residual Analysis

To assess the mathematical convergence of the tesseroid inversion, the reconstructed potentials (Figures 5.6, 5.7, 5.8) were calculated from the newly estimated TWS and compared against the original synthesized potentials to yield the residuals (Figures 5.9, 5.10, 5.11). The residual maps represent the post-adjustment discrepancies ($v = Ax - L$). For all three heights (0 km, 200 km, and 500 km), the potential residuals are extremely small. Their

range is ± 0.005 $m^2 s^{-2}$, indicating that the least-squares adjustment converged successfully from a mathematical standpoint. However, the juxtaposition of near-zero potential residuals (Figure 5.11) with a highly distorted TWS map at 500 km (Figure 5.6) perfectly illustrates the challenge of the inverse problem. It proves that while the algorithm can find a TWS distribution that perfectly matches the smoothed 500 km potential, this mathematical solution does not necessarily represent the true physical hydrological reality without highly optimized, altitude-specific regularization strategies.

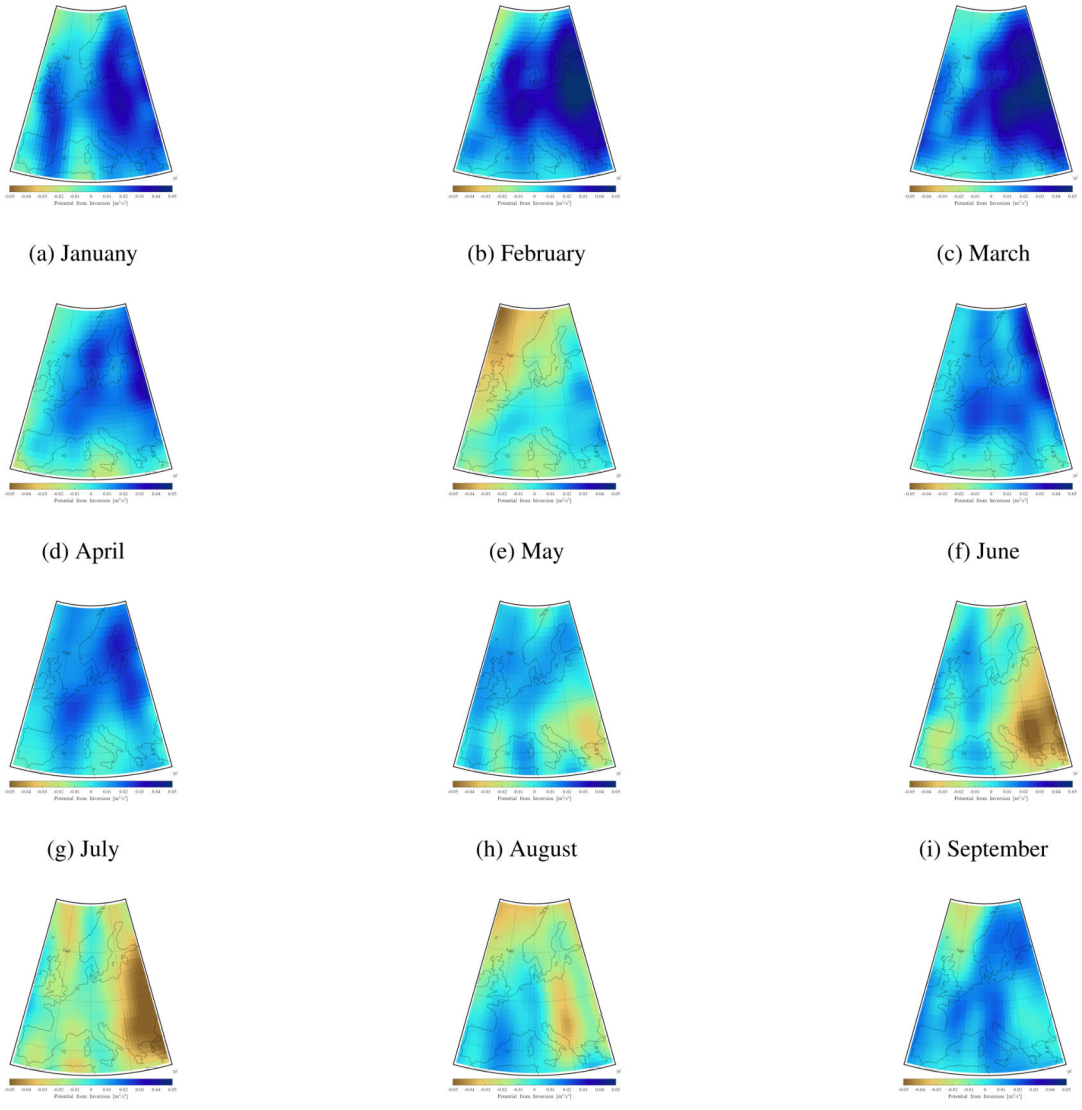

(a) Januany (b) February (c) March

(d) April (e) May (f) June

(g) July (h) August (i) September

(j) October (k) November (l) December

Figure 5.6: Potential from the solved tesseroids (forward modelling) using Height $h = 0$ km, DDK5 filter, in 2024. Range is $\pm$ 0.05 $m^2 s^{-2}$.

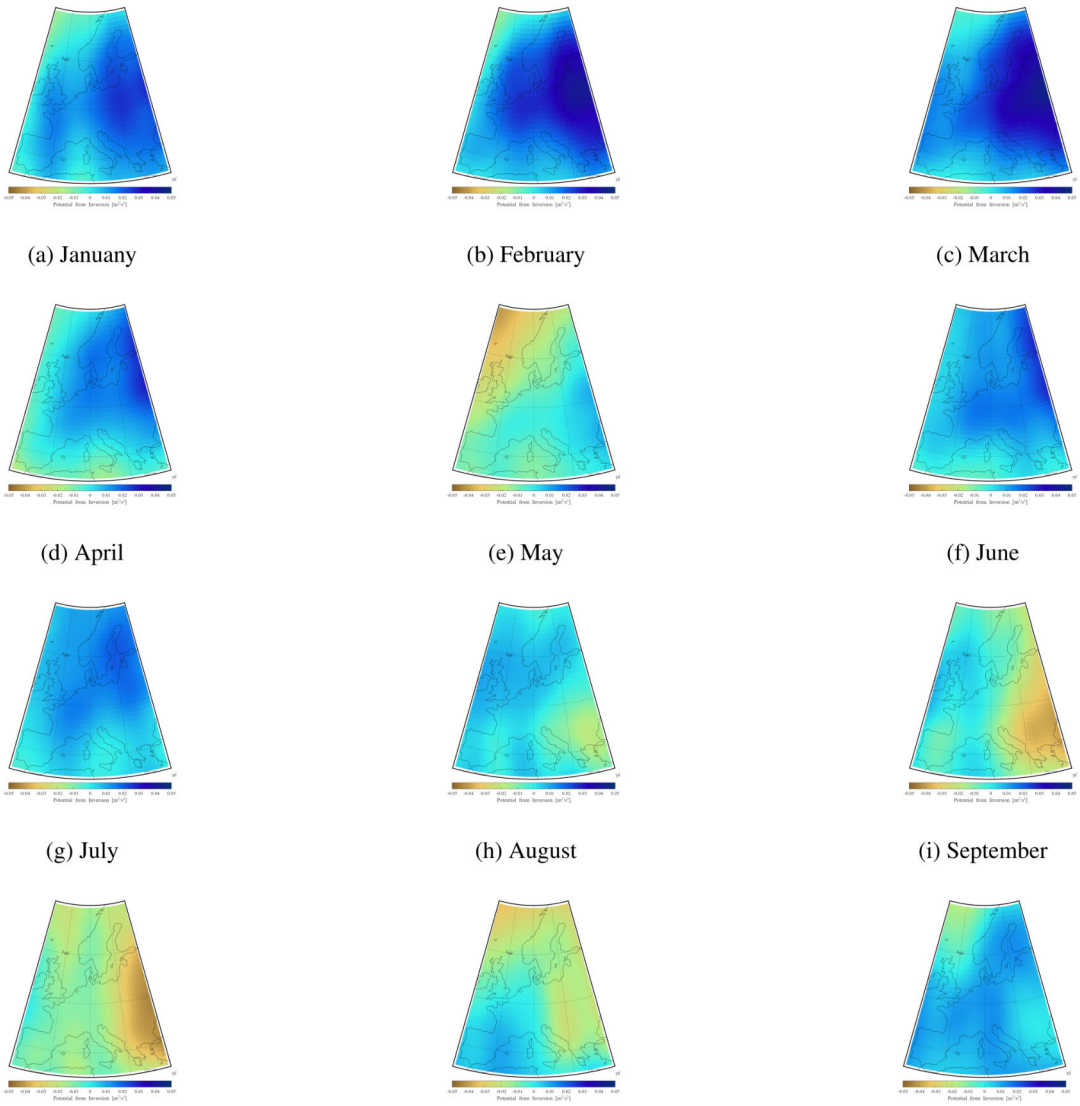

(a) Januany (b) February (c) March

(d) April (e) May (f) June

(g) July (h) August (i) September

(j) October (k) November (l) December

Figure 5.7: Potential from the solved tesseroids (forward modelling) using Height $h = 200$ km, DDK5 filter, in 2024. Range is $\pm$ 0.05 $m^2 s^{-2}$.

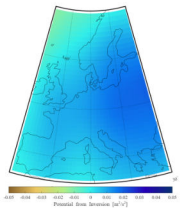

(a) Januany

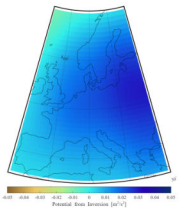

(b) February

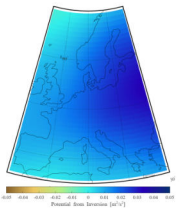

(c) March

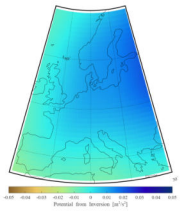

(d) April

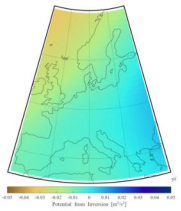

(e) May

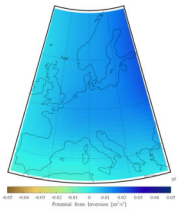

(f) June

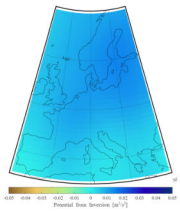

(g) July

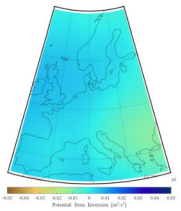

(h) August

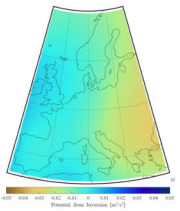

(i) September

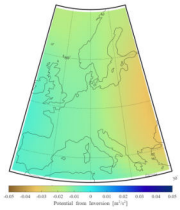

(j) October

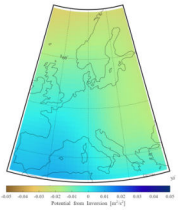

(k) November

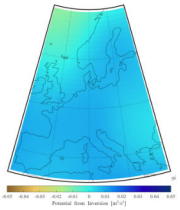

(l) December

Figure 5.8: Potential from the solved tesseroids (forward modelling) using Height $h = 500$ km, DDK5 filter, in 2024. Range is $\pm$ 0.05 $m^2 s^{-2}$.

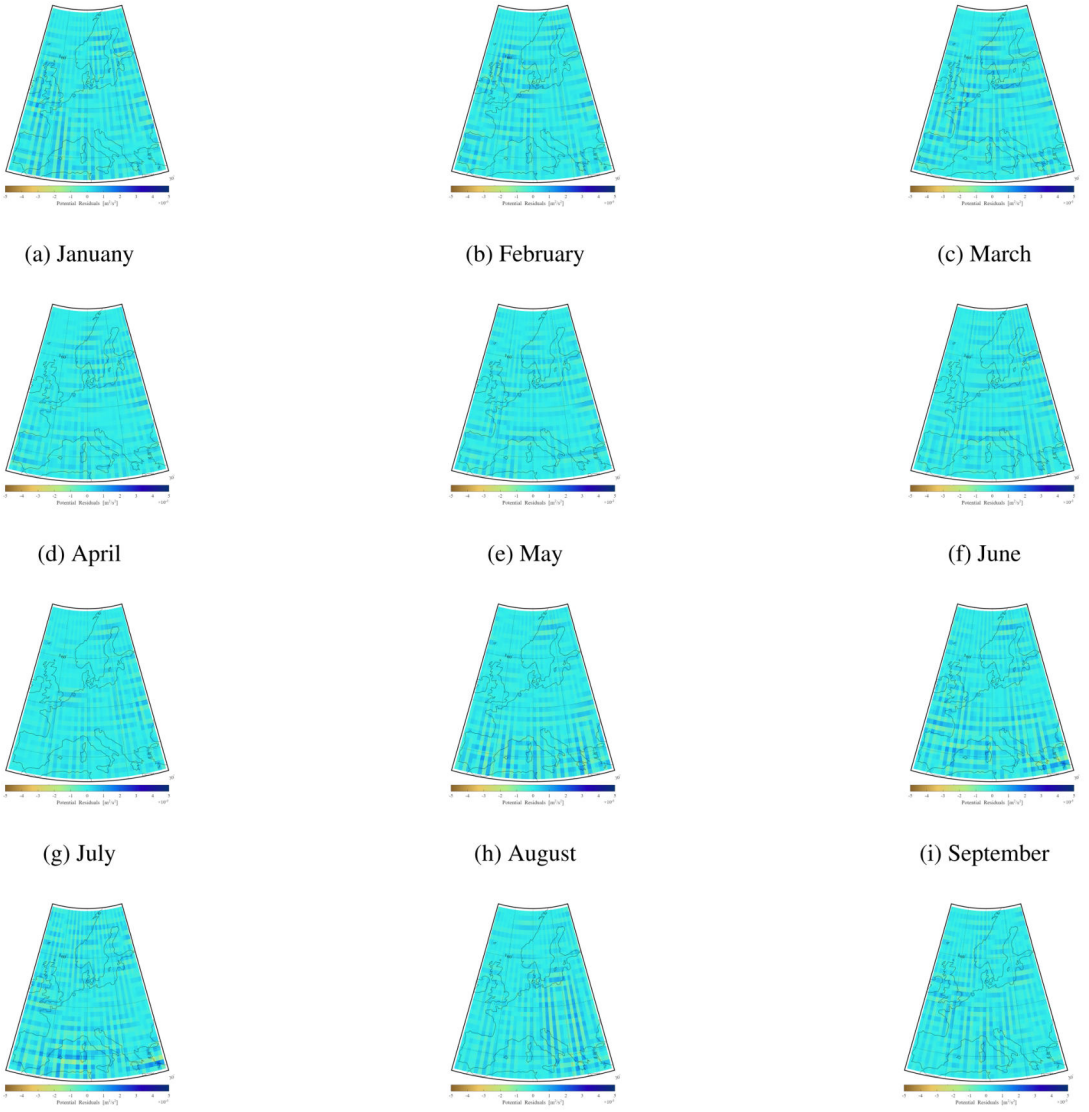

(a) Januany (b) February (c) March

(d) April (e) May (f) June

(g) July (h) August (i) September

(j) October (k) November (l) December

Figure 5.9: Residual Potential Analysis using Height $h = 0$ km, DDK5 filter, in 2024. Range is $\pm$ 0.005 $m^2 s^{-2}$.

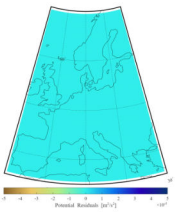

(a) Januany

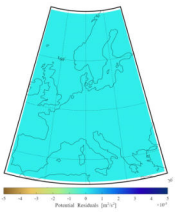

(b) February

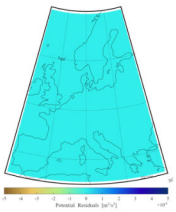

(c) March

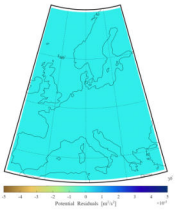

(d) April

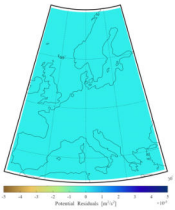

(e) May

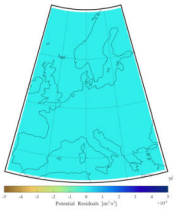

(f) June

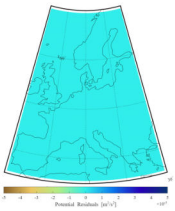

(g) July

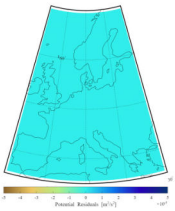

(h) August

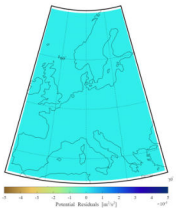

(i) September

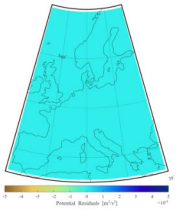

(j) October

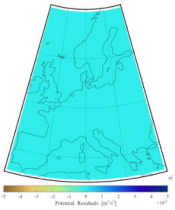

(k) November

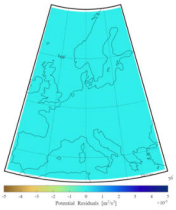

(l) December

Figure 5.10: Residual Potential Analysis using Height $h = 200$ km, DDK5 filter, in 2024. Range is $\pm$ 0.005 $m^2 s^{-2}$.

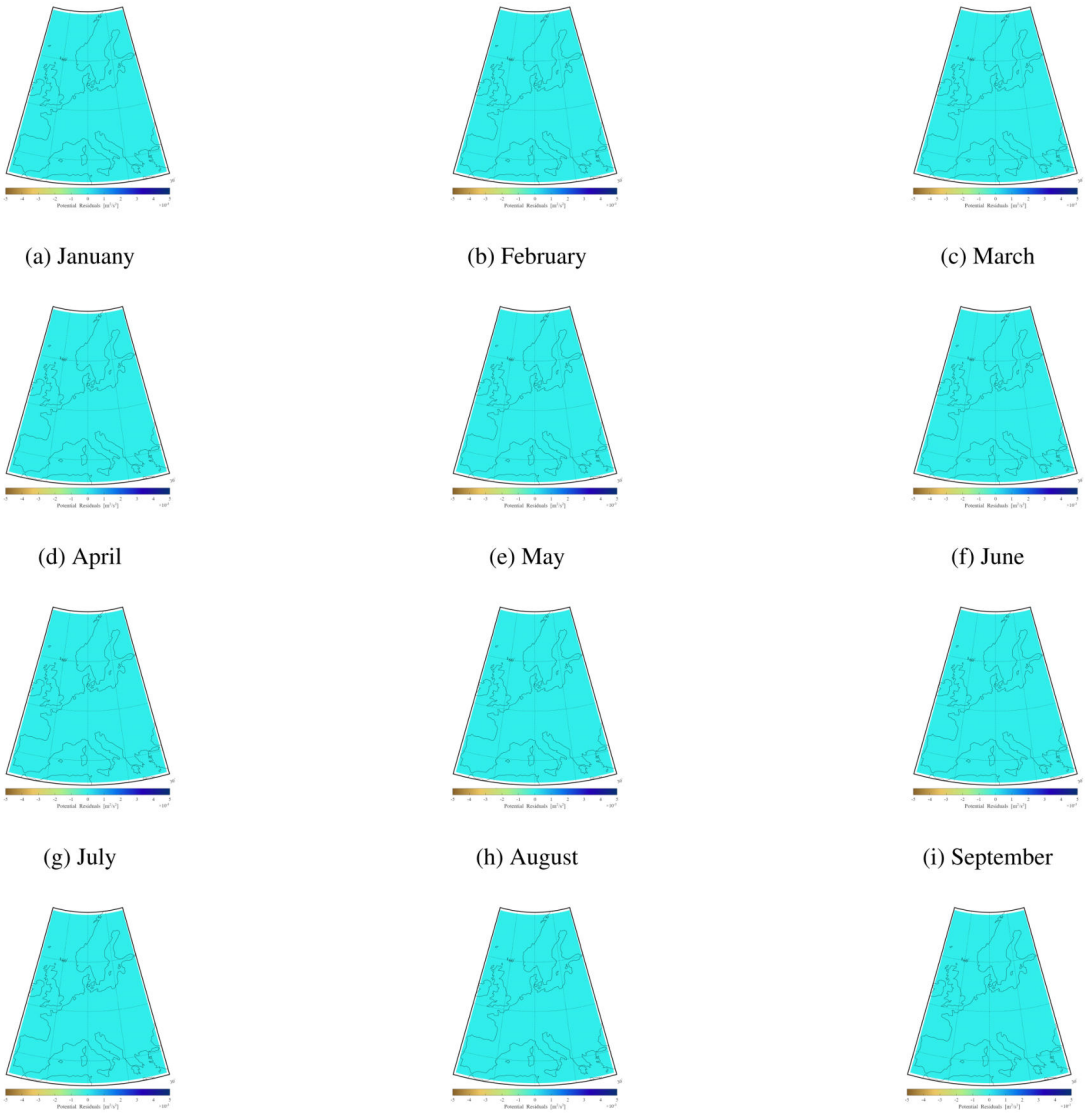

(a) Januany (b) February (c) March

(d) April (e) May (f) June

(g) July (h) August (i) September

(j) October (k) November (l) December

Figure 5.11: Residual Potential Analysis using Height $h = 500$ km, DDK5 filter, in 2024. Range is $\pm$ 0.005 $m^2 s^{-2}$.

5.4 Inverse Modeling: Recovering TWS using the Tesseroid Method

The synthesized potentials at the three altitudes were subsequently inverted in the space domain using the tesseroid method to estimate TWS. The inversion relies on an iterative least-squares adjustment with Tikhonov regularization. The estimated TWS at ground level (Figure 5.12) shows excellent agreement with the reference TWS calculated via the Wahr approach (Figure 5.1). The spatial patterns, amplitudes, and seasonal variations are accurately recovered. This demonstrates that when the observation height is zero, the inverse tesseroid method is highly effective and numerically stable. However, as the inversion height increases, the quality of the recovered TWS degrades. The TWS inverted from 200 km (Figure 5.13) begins to show signs of spatial blurring. The inversion from 500 km (Figure 5.14) exhibits severe signal degradation, characterized by distinct vertical striping and ringing artifacts. This degradation occurs because downward continuation (recovering surface mass from high-altitude potential) is a severely ill-posed mathematical problem. High-frequency signals that were attenuated at 500 km are buried in the noise level. Consequently, the regularization parameter required to stabilize the normal equations heavily smooths the true signal while inadvertently amplifying numerical noise, leading to the observed striping effects.

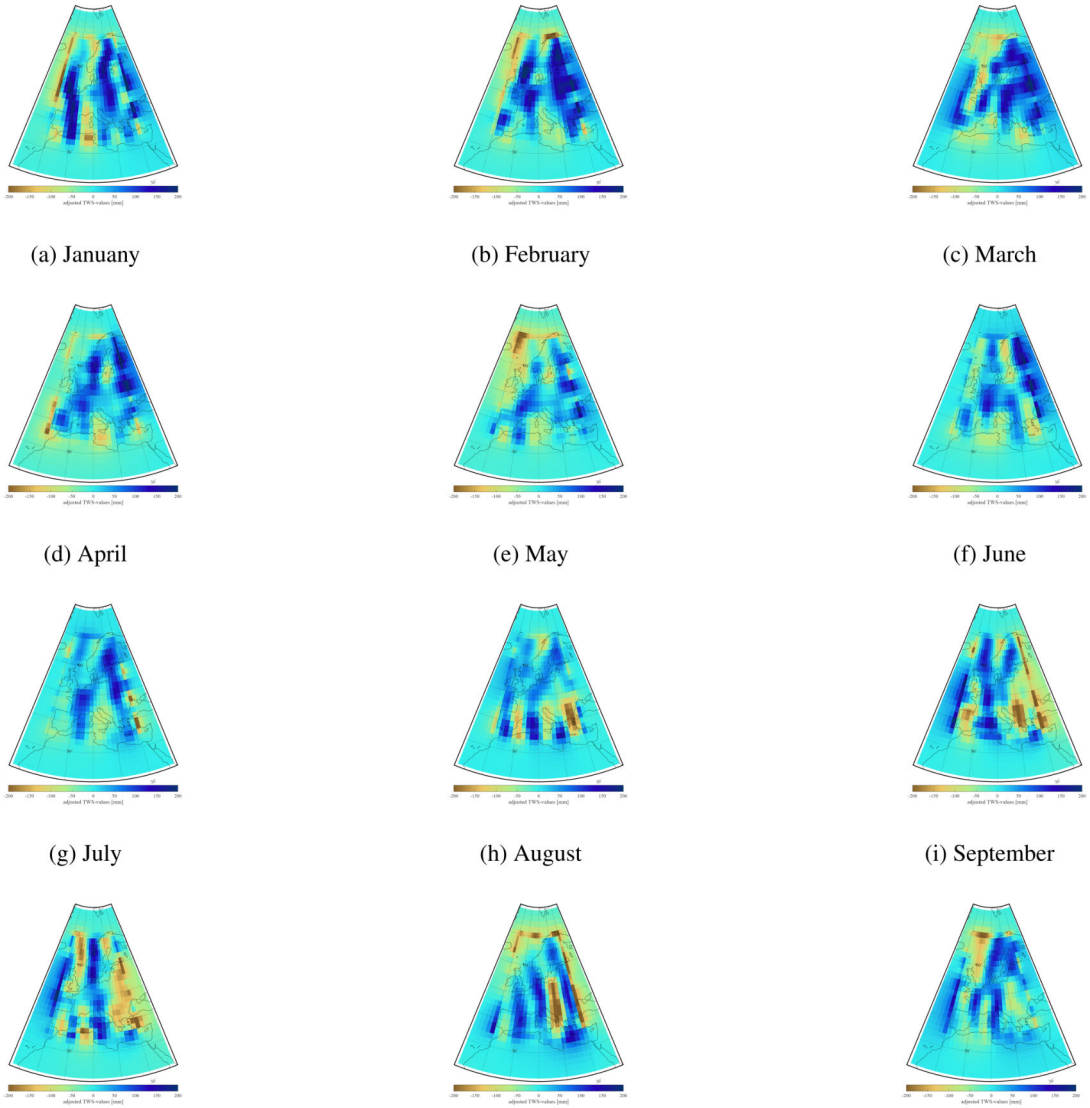

(a) Januany (b) February (c) March

(d) April (e) May (f) June

(g) July (h) August (i) September

(j) October (k) November (l) December

Figure 5.12: Terrestrial water storage using Height $h = 0$ km, DDK5 filter, in 2024. Range is $\pm$ 200 mm.

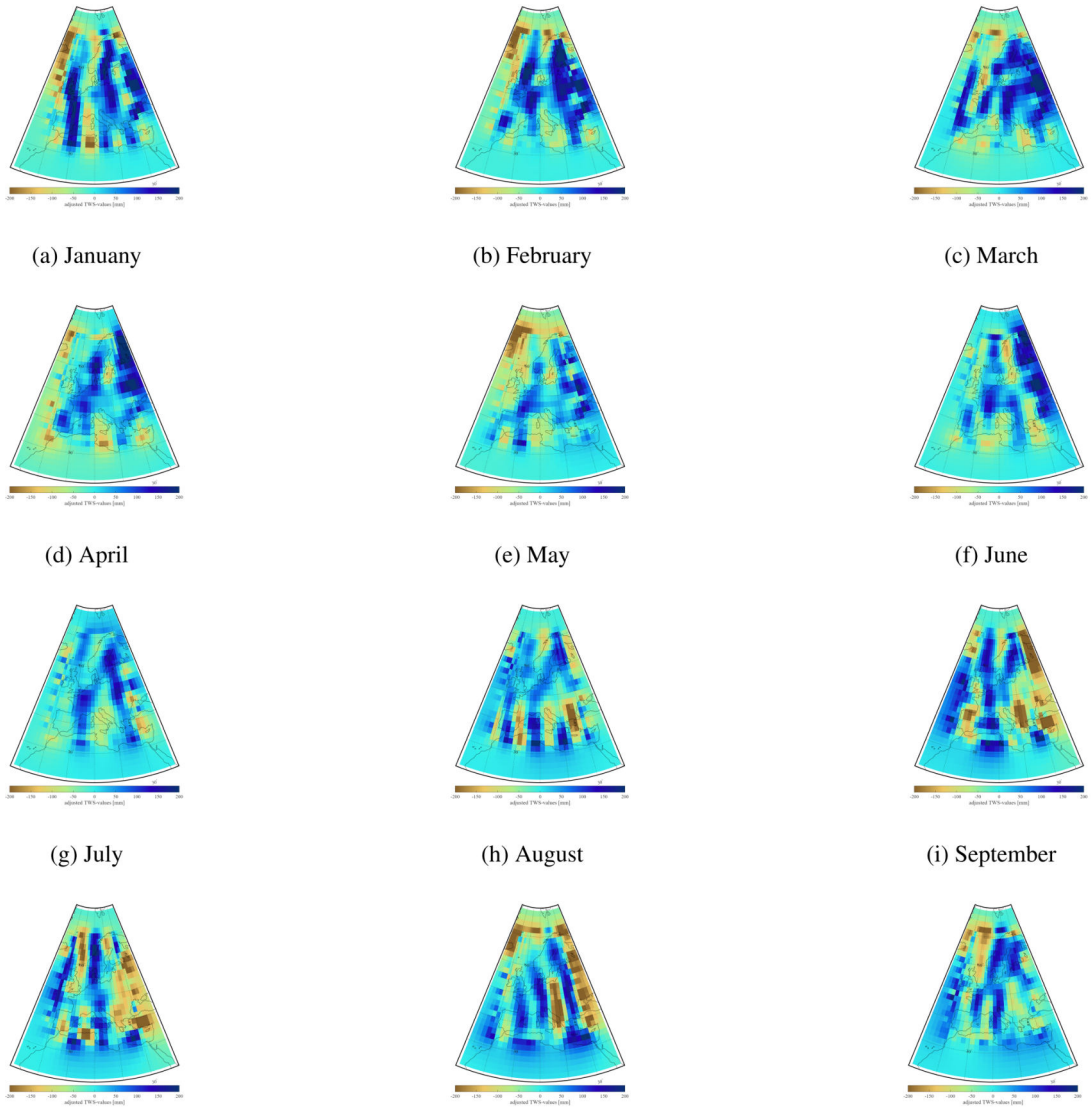

(a) Januany (b) February (c) March

(d) April (e) May (f) June

(g) July (h) August (i) September

(j) October (k) November (l) December

Figure 5.13: Terrestrial water storage using Height $h = 200$ km, DDK5 filter, in 2024. Range is $\pm$ 200 mm.

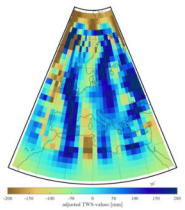

(a) January

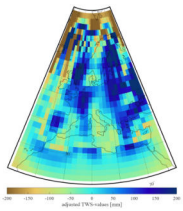

(b) February

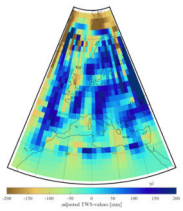

(c) March

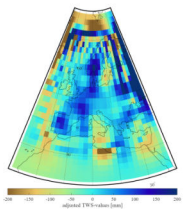

(d) April

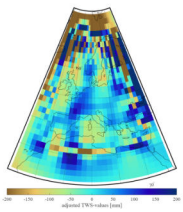

(e) May

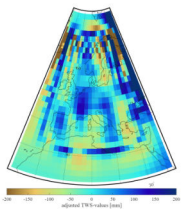

(f) June

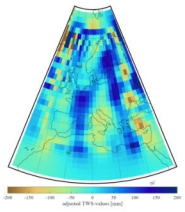

(g) July

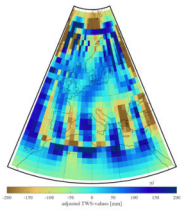

(h) August

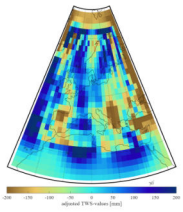

(i) September

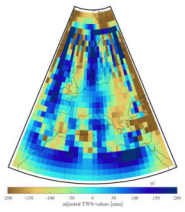

(j) October

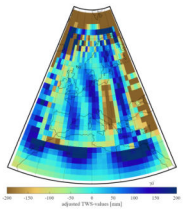

(k) November

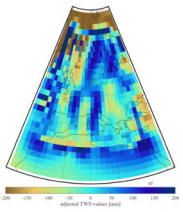

(l) December

Figure 5.14: Terrestrial water storage using Height $h = 500$ km, DDK5 filter, in 2024. Range is $\pm$ 200 mm.

6 Conclusion and Outlook

GRACE mission is the pioneer mission that allowed reliable quantification of TWS in a global scale.
A more precise depiction of TWS can be achieved by eliminating the striping effect observed in the results.
Successor mission for GRACE is expected to adopt a mission architecture that could considerably reduce undesirable errors such as the correlation errors (Massotti et al., 2022).
This study investigated the differences between the frequency-domain approach (Wahr et al., 1998) and the space-domain inverse tesseroid method (Heck and Seitz, 2007; Grombein et al., 2012) for calculating Total Water Storage (TWS) anomalies over the European continent for the year 2024. Using GRACE-FO Level-2 spherical harmonic products (Release 6.3, DDK5 filter), a reference TWS baseline was established using the Wahr approach, which successfully captured the seasonal hydrological mass fluctuations across Europe. To rigorously evaluate the inverse tesseroid method, the gravitational potential was first forward-modeled (synthesized) at three distinct observation altitudes: 0 km (ground level), 200 km, and 500 km (satellite altitude). These synthesized potentials were subsequently inverted using a least-squares adjustment to recover the surface TWS. Finally, a residual analysis ($v = Ax - L$) was conducted to evaluate the mathematical convergence and stability of the inversion algorithm across these varying heights.

6.1 Main Findings and Conclusions

The primary research question of this lab rotation was to determine how the height of the synthesized grid of potential changes affects the estimated TWS. Based on the numerical experiments and visual analyses, the following conclusions are drawn:

- Impact of Altitude on Signal Synthesis: In the forward modeling phase, increasing the synthesis height from 0 km to 500 km resulted in severe attenuation of the gravitational potential signal. According to Newton's law of gravitation, the high-frequency spatial details of local hydrological masses naturally decay and merge into broader, low-frequency patterns at satellite altitudes.

- Performance of the Inverse Tesseroid Method at Ground Level (0 km): When the potential is synthesized at 0 km, the inverse tesseroid method performs exceptionally well. The recovered TWS shows a near-perfect spatial and amplitude agreement with the baseline Wahr approach. This confirms that the space-domain discretization using tesseroids is highly accurate when distance-related signal decay is not a factor.

- The Ill-Posed Nature of High-Altitude Inversion (200 km and 500 km): As the synthesis height increases, the inversion process degrades significantly. At 200 km, the recovered TWS begins to lose spatial sharpness. At 500 km, the recovered TWS suffers from severe degradation, characterized by distinct vertical striping and ringing artifacts. Because the inversion acts as a downward continuation – recovering surface mass from a smoothed, high-altitude potential – it is a severely ill-posed mathematical problem. The inversion algorithm struggles to differentiate between true high-frequency hydrological signals and numerical noise.

- Mathematical Convergence vs. Physical Reality: The residual analysis revealed an important characteristic of the inversion process. Even at 500 km, the potential residuals remained extremely close to zero, proving that the least-squares adjustment converged successfully from a mathematical standpoint. However, the highly distorted TWS map at 500 km demonstrates that a mathematically "perfect" fit to a smoothed potential does not equate to a physically accurate reconstruction of the water storage.

In conclusion, the inverse tesseroid method is a highly capable tool for space-domain TWS calculation, offering excellent precision at or near ground level. However, estimating TWS from potentials synthesized at satellite altitudes (e.g., 500 km) exposes the inherent limitations of downward continuation. To make high-altitude tesseroid inversion practically viable for hydrological studies, future research must focus on implementing highly optimized,

altitude-specific regularization strategies (such as rigorous L-curve parameter tuning) to suppress numerical noise amplification while preserving the true physical amplitude of the terrestrial water storage.

Acknowledgement

The author wishes to express sincere gratitude to Prof. Kurt Seitz and the team at the Geodätisches Institut (GIK), Karlsruhe Institute of Technology (KIT) for their continuous guidance, academic support, and for providing the necessary computational resources and laboratory facilities through- out the duration of this study. Their expertise and encouragement were invaluable in shaping the direction and quality of this research. The author also gratefully acknowledges the International Centre for Global Earth Models (ICGEM), GFZ German Research Centre for Geosciences (2026) for supplying the GRACE spherical harmonic datasets used in this work. The availability of high-quality global gravity field products made the detailed analysis of Terrestrial Water Storage (TWS) variations in Europe. Special thanks are extended to the developers and maintainers of the GLDAS and Surface Model, whose openly accessible hydrological datasets contributed significantly to the comparative analysis carried out in this research. The author further acknowledges the support and motivation received from colleagues and fellow students within the Remote Sensing and Geoinformatics program at KIT, whose discussions and insights enriched the understanding of the scientific challenges involved

A Appendices

A.1 L-curve of regularization parameter 2024

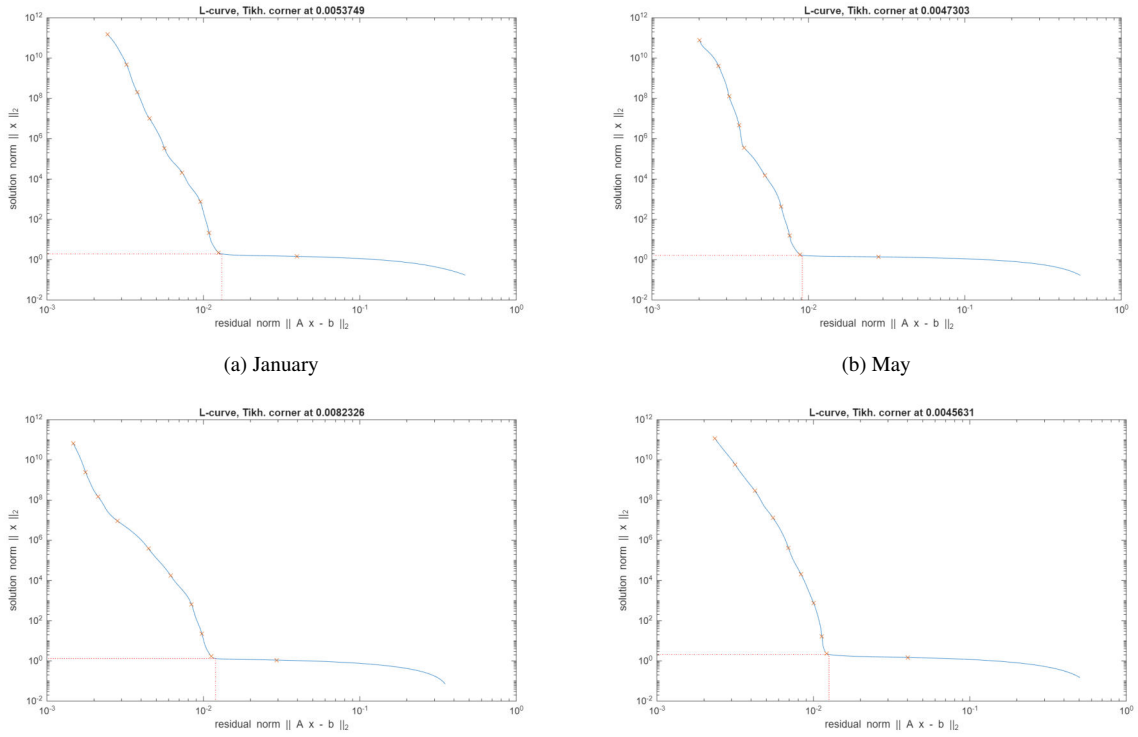

(a) January (b) May

(c) August (d) November

Figure A.1: L-curves for *P* at altitude Ground Level

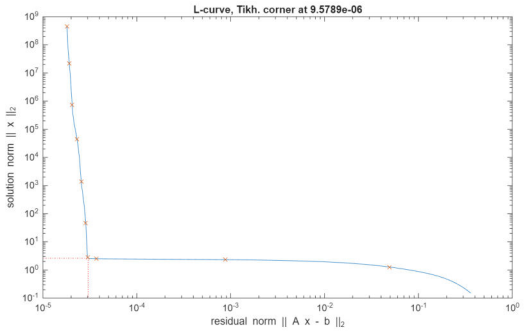

(a) January

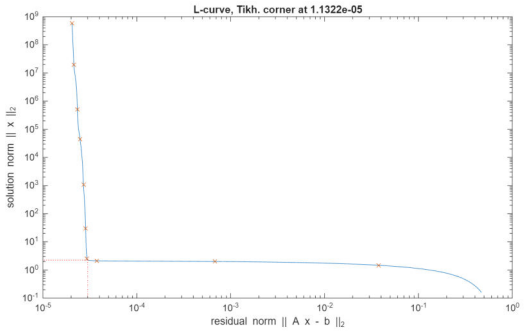

(b) May

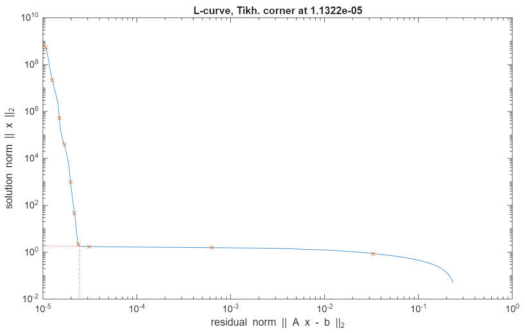

(c) August

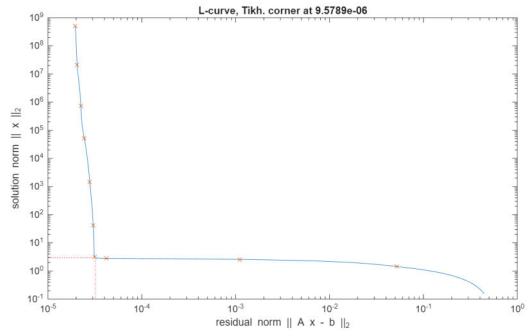

(d) November

Figure A.2: L-curves for P at altitude at 200 km

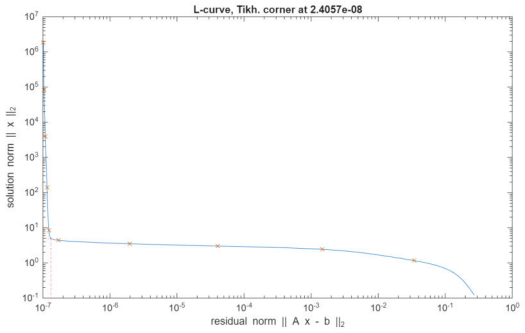

(a) January

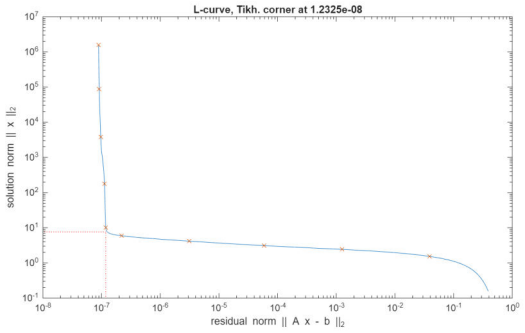

(b) May

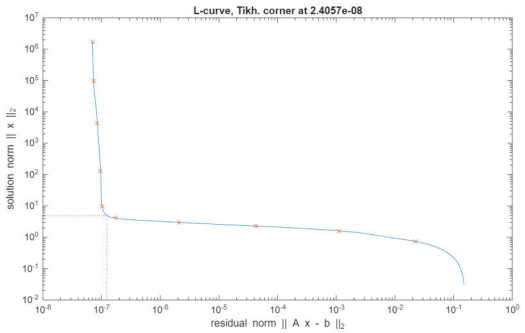

(c) August

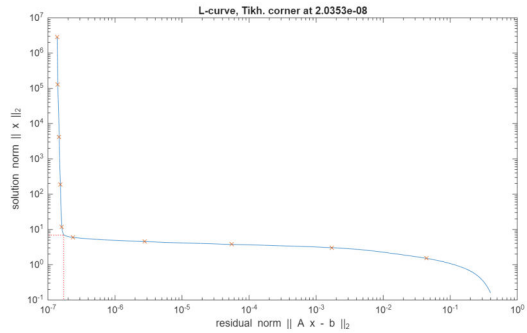

(d) November

Figure A.3: L-curves for P at altitude at 500 km

References

Baur, O. and Sneeuw, N. (2011): Assessing Greenland ice mass loss by means of point-mass modeling: a viable methodology. *Journal of Geodesy* 85(9):607–615. ISSN: 0949-7714. DOI: 10.1007/s00190-011-0463-1.

GFZ (2026): GRACE-FO – Gravity Recovery and Climate Experiment Follow-On Mission. German Research Centre for Geosciences (GFZ). Accessed: 2026-04-06. URL: https://www.gfz.de/en/section/global-geomonitoring-and-gravity-field/projects/grace-fo-gravity-recovery-and-climate-experiment-follow-on-mission.

Grombein, T., Seitz, K., Awange, J. L., and Heck, B. (2012): Detection of hydrological mass variations by means of an inverse tesseroid approach. Poster presentation at the European Geosciences Union General Assembly (EGU 2012), Vienna, Austria, 22.–27. April 2012. DOI: 10.5445/IR/1000162814.

Grombein, T., Seitz, K., and Heck, B. (2013): Optimized formulas for the gravitational field of a tesseroid. *Journal of Geodesy* 87(7):645–660. ISSN: 0949-7714. DOI: 10.1007/s00190-013-0636-1.

Heck, B. and Seitz, K. (2007): A comparison of the tesseroid, prism and point-mass approaches for mass reductions in gravity field modelling. *Journal of Geodesy* 81(2):121–136. DOI: 10.1007/s00190-006-0094-0.

Heiskanen, W. A. and Moritz, H. (1967): Physical Geodesy. W. H. Freeman & Co., San Francisco, USA.

Humphrey, V., Rodell, M., and Eicker, A. (2023): Using satellite-based terrestrial water storage data: A review. *Surveys in Geophysics* 44(5):1489–1517. DOI: 10.1007/s10712-022-09754-9.

ICGEM (2026): International Centre for Global Earth Models (ICGEM): Gravity field and GRACE/GRACE-FO products hosted at the German Research Centre for Geosciences (GFZ). Accessed: 2026-04-06. URL: https://icgem.gfz-potsdam.de/.

Kusche, J. (2007): Approximate decorrelation and non-isotropic smoothing of time-variable GRACE-type gravity field models. *Journal of Geodesy* 81(11):733–749. DOI: 10.1007/s00190-007-0143-3.

Kusche, J., Schmidt, R., Petrovic, S., and Rietbroek, R. (2009): Decorrelated GRACE time-variable gravity solutions by GFZ, and their validation using a hydrological model. *Journal of Geodesy* 83:903–913. DOI: 10.1007/s00190-009-0308-3.

Long, D., Longuevergne, L., and Scanlon, B. R. (2013): Global analysis of drought and flood in GRACE terrestrial water storage anomalies. *Hydrology and Earth System Sciences* 17:4475–4490.

Massotti, L., Bulit, A., Daras, I., Dominguez, B. C., Carraz, O., Hall, K., Heliére, A., March, G., Martimort, P., Rodrigues, G., et al. (2022): Next generation gravity mission design activities within the mass change and geoscience international constellation. In: Sensors, Systems, and Next-Generation Satellites XXVI, vol. 12264. SPIE, pp. 6–17.

Qian, N., Chang, G., Gao, J., Shen, W., and Yan, Z. (2022): Adaptive DDK Filter for GRACE Time-Variable Gravity Field with a Novel Anisotropic Filtering Strength Metric. *Remote Sensing* 14(13). ISSN: 2072-4292. DOI: 10.3390/rs14133114. URL: https://www.mdpi.com/2072-4292/14/13/3114.

Uieda, L. and Barbosa, V. C. (2016): Fast nonlinear gravity inversion in spherical coordinates with application to the South American Moho. *Geophysical Journal International* 208(1):162–176. DOI: 10.1093/gji/ggw390.

Wahr, J., Molenaar, M., and Bryan, F. (1998): Time variability of the Earth's gravity field: Hydrological and oceanic effects and their possible detection using GRACE. *Journal of Geophysical Research: Solid Earth* 103(B12):30205–30229.

Comparison of Various Spherical Harmonic and Mascon Solutions and Their Quality Assessment with Respect to Nepal Region

Bhattarai, Sudur

Remote Sensing and Geoinformatics Master of Science (M.Sc.), KIT, Germany

E-Mail: uhkmj@student.kit.edu

Abstract

The Gravity Recovery and Climate Experiment (GRACE) revolutionized the study of Earth's gravity field by providing observations of water storage variations with unprecedented accuracy. Unlike traditional techniques – such as localized ground-based measurements, hydrologic modeling, and electromagnetic based methods – GRACE captures water mass redistribution across land, atmosphere, and oceans, including subsurface changes. Its successor, GRACE-FO, further enhances the ability to analyze seasonal, long-term, and decadal trends in water storage, offering critical insights for water resource management and policy-making.

GRACE data processing relies on two primary approaches: spherical harmonic (SH) solutions and mascon solutions. While SH solutions defined globally are represented as coefficient series, suffer from challenges like north-south striping and signal leakage – requiring extensive filtering; mascon solutions provide localized mass anomaly estimates on a predefined grid, incorporating geophysical constraints to mitigate leakage effects through various regularization techniques.

This study compares SH and mascon solutions in assessing terrestrial water storage (TWS) over the Nepal region using exploratory time-series analysis, time-series decomposition, and regional spatiotemporal mapping - including the mean state map, variability map, seasonal cycle map, Hovmöller-latitude-longitude map, and linear trend map; in terms of interpreting total water storage anomalies. Our findings reveal that mascon solutions effectively capture temporal changes in TWS, whereas SH solutions tend to underestimate mass variations after Gaussian smoothing that attenuates the real geophysical signals and induces leakage effects over the Nepal region from nearby signals, resulting in reduced resolution of the localized features in the region, which itself has the size smaller than the inherent spatial resolution of GRACE of about 300-400 km.

A comprehensive quality assessment confirms that mascon solutions (GSFC, JPL, and their mean) consistently outperform SH solutions (ITSG, JPL, CSR, and their mean) across all evaluation metrics (R, RMSE, Bias, and MAE). Among the mascon solutions, the mean mascon solution exhibits the best performance, with the highest correlation (0.944), lowest RMSE (4.723 cm), lowest MAE (2.916 cm), and a minor positive bias (0.409 cm). These results establish the mean mascon solution as the most suitable GRACE solution for studying TWS in Nepal, while the GSFC mascon solution serves as the secondary option.

Keywords GRACE · GRACE-FO · Total Water Storage (TWS) · SH Solution · North-South Stripping · Gaussian Filtering · Leakage Effects · Mascon Solutions · Nepal

Graphical Abstract

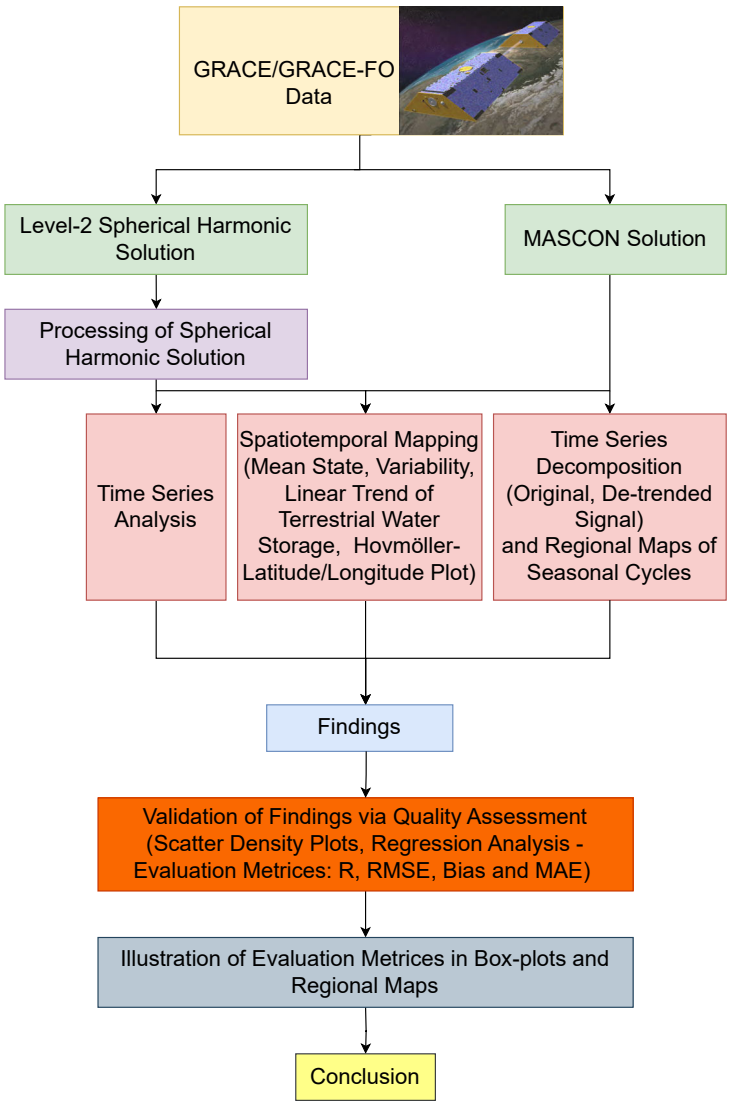

KIT Scientific Working Papers
Issue Number 270
ISSN: 2194-1629
DOI: 10.5445/IR/1000191188
Online: June 2026

This document is licensed under the Creative Commons Attribution – Share Alike 4.0 International License (CC BY-SA 4.0):
https://creativecommons.org/licenses/by-sa/4.0/deed.en

1 Introduction

This section explains some background aspects of GRACE/GRACE-FO and primary approaches to GRACE data processing. Additionally, the existing statements of problems, objectives, scope, and limitations with respect to this study will be further clarified.

1.1 Background

Recognizing the need for a more comprehensive approach to monitoring Earth's water cycle, NASA and the German Aerospace Center (DLR) collaborated to develop the Gravity Recovery and Climate Experiment (GRACE) mission, launched on March 17, 2002 (NASA Jet Propulsion Laboratory, 2016; European Space Agency (ESA), 2025). GRACE introduced a revolutionary method for studying Earth's water cycle by measuring minute changes in the planet's gravitational field caused by water mass redistribution over land, atmosphere, and oceans (NASA Jet Propulsion Laboratory, 2016).

GRACE employed a unique twin-satellite configuration with a microwave ranging system to detect these gravitational variations (NASA Jet Propulsion Laboratory, 2016; European Space Agency (ESA), 2025). This innovative approach allowed scientists to track changes in ice sheets, groundwater, ocean currents, and other components of the water cycle with unprecedented accuracy and global coverage (European Space Agency (ESA), 2025).

GRACE's primary objective was to provide high-resolution monthly global maps of Earth's gravity field and surface mass changes (NASA Jet Propulsion Laboratory, 2016). This capability addressed the limitations of previously introduced techniques (localized ground-based measurements, hydrologic modeling, and electromagnetic-based measurements) by offering observations of water storage variations, including those occurring beneath the Earth's surface (NASA Jet Propulsion Laboratory, 2006). The mission's success in balancing the water cycle budget for entire continents, as demonstrated in South America, highlighted its transformative impact on hydrological studies (NASA Jet Propulsion Laboratory, 2006).

The GRACE mission, followed by GRACE-FO in 2018, has significantly advanced our understanding of Earth's changing freshwater landscape, with profound implications for climate change research and water resource management (Tapley et al., 2019). By providing a truly global perspective on water cycle dynamics, GRACE has enabled scientists to study seasonalities, long-term trends, and decadal variability in water storage, offering crucial insights for policy-making, resource planning and management (NASA Jet Propulsion Laboratory, 2016).

Two primary approaches have emerged for processing GRACE data: spherical harmonic (SH) solutions and mass concentration (mascon) solutions. Each method has its strengths and limitations, particularly when applied to regions like Nepal with complex topography, landforms, and varied seasonalities, moreover, with dynamic hydrological and tectonic behavior.

Spherical harmonic representations have been extensively used to represent the variations in the Earth's gravity field for decades (Chen et al., 2022). They represent the gravity field as a series of coefficients. The application of spherical harmonic solutions from GRACE/GRACE-FO data faces several challenges, such as north-south striping (Swenson and Wahr, 2006) and signal leakage (Kusche et al., 2009), especially near land-sea boundaries. These issues primarily stem from temporal aliasing (Wiese et al., 2011b) and the design of satellite orbits and tracking systems (Wiese et al., 2011a), including factors like inclination, altitude, inter-satellite distance, and the co-planar low-low satellite-to-satellite tracking system. Conventional approaches for addressing these problems include empirical smoothing (Wahr et al., 1998), de-striping (Swenson and Wahr, 2006), and regularization techniques (Save et al., 2012). While these approaches are generally effective in preserving signals and reducing noise, it's crucial to recognize that eliminating stripes also reduces the genuine geophysical signals (Han et al., 2005; Yi and Sneeuw, 2022; Zhou et al., 2023) and induces leakage effect (Chen et al., 2021; Klees et al., 2008) in the coastal zones. Additionally, the effectiveness of de-striping is significantly influenced by signal characteristics such as size, shape, and orientation (Watkins et al., 2015). It's noteworthy that the impact of aliasing errors can

be mitigated through the combination of gravity satellite formations in optimal constellation configurations (Yan et al., 2024) or by recovering the temporal gravity field at higher temporal resolutions (Yan et al., 2023).
The so-called mass concentration (mascon) solutions serve as an alternative for representing the GRACE data and mass anomalies. A mascon corresponds to a small, predefined region on the Earth's surface, for instance, a 3° rectangular grid cell. Mascon solution does not represent a global gravity field like spherical harmonic solutions, but rather it quantifies mass anomalies at the local level. Using 'mascon' solutions, one can implement geophysical constraints much more easily. These a priori constraints help to filter out noise from the GRACE/GRACE-FO observations at the Level-2 processing step, which is a much more rigorous approach than the empirical post-processing filtering applied to land and ocean grids derived from spherical harmonics (Wiese et al., 2018). Furthermore, mascon products are also easier to use in general as they do not need to be spatially filtered (smoothed) during postprocessing. This is because some (geophysically motivated) spatial information is explicitly guiding the retrieval of the mascon solution, thus greatly reducing the spatial noise patterns (Humphrey et al., 2023).

1.2 Statements of Problems

Analyzing and interpreting GRACE and GRACE-FO data over the Nepal region is extremely challenging due to the following reasons:

i. The limited size of the Nepal region compared to GRACE's inherent spatial resolution of approximately 300-400 km.

ii. The presence of high noise levels in the gravimetric data, such as striping patterns, and bias; necessitates robust filtering, which induces leakage effects. Hence, for instance, strong gravitational signals from groundwater abstraction in the Ganges Plain and Tibetan Plateau may likely leak into the Nepal signal.

1.3 Objectives

The specific objective and general objectives of this study are further explained in this section.

1.3.1 Specific Objective

i. To compare various mascon solutions and SH solutions from different GRACE data providers and their quality assessment with respect to reference CSR mascon solution, in terms of interpreting terrestrial water storage for Nepal region.

1.3.2 General Objectives

i. To evaluate the strengths and limitations of mascon and SH solutions in capturing terrestrial water storage (TWS) dynamics in the region with complex topography.

ii. To interpret the result of GRACE data via SH analysis and mascon analysis on the interpretation of total water storage anomaly in mountainous areas like Nepal.

iii. To investigate the potential advantages of mascon solutions over spherical harmonic which requires various processing methods.

iv. To provide insights that could inform the selection of appropriate GRACE data products, among the various products in the case of Nepal region.

1.4 Scope and Limitations of the Study

This section covers the scope and limitations of the study.

1.4.1 Scope

i. To grasp the satellite gravimetric signal content relative to the noise level of GRACE products over a small Nepal region.

ii. Illustration to download, process, and compare different mascons solutions and SH solutions from different GRACE providers.

iii. To perform exploratory data analysis, both statistical and visual, on time series and regional maps from mascons and SH solutions.

iv. Evaluation of the performance of different GRACE solutions in capturing seasonality and long-term trends in TWS for the Nepal region.

v. Investigation of the differences in processing strategies of the various mascon solutions, as well as for SH solutions, as documented in the literature.

vi. To obtain a spectrum of perspectives for the stability (or rather instability) of the basic GRACE products for small areas like Nepal from the exploratory data analysis.

1.4.2 Limitations

i. Grasped satellite gravimetric signal content relative to the noise level of GRACE products over the Nepal region does not apply corrections for the induced leakage effects as a result of strong filtering.

ii. Coarse spatial resolution of GRACE data (approximately 300-400 km), which may limit the ability to capture fine-scale hydrological processes in Nepal's diverse terrain.

iii. Monthly temporal resolution of GRACE data, which may not capture rapid changes or short-term events in the landscape of the Nepal region.

iv. TWS is not disaggregated into individual water storage components under this research, which requires additional data or modeling.

v. GRACE products are not validated against ground-based in-situ observations for comparison.

vi. Segregation of anthropogenic and climate-driven changes in TWS is not done under this research.

2 Theoretical Aspects

Several theoretical aspects were reviewed before diving into the generation of the results for the comparison of the various mascon solutions and SH solutions via scientific papers and reports.

2.1 GRACE Concepts and its Principles

The fundamental principle behind the GRACE satellite mission is to measure the time-variable mass anomalies in the gravity field of the Earth (Humphrey et al., 2023), with their key observations of Satellite-to-Satellite Tracking (SST) in low–low and high–low mode (Murböck et al., 2023), from which total water storage anomaly (in other words: terrestrial water storage or equivalent water height used interchangeably in the literature, which refer to the same thing) can be detected (Tapley et al., 2004; Wahr et al., 2004).
Terrestrial water storage (TWS) is a dynamic component of the hydrological cycle (Girotto and Rowland, 2019), which can be defined as the summation of all water stored above and below the land surface. This includes surface waters, soil moisture, groundwater, snow and ice, and water stored in biomass (Girotto and Rowland, 2019; Humphrey et al., 2023).

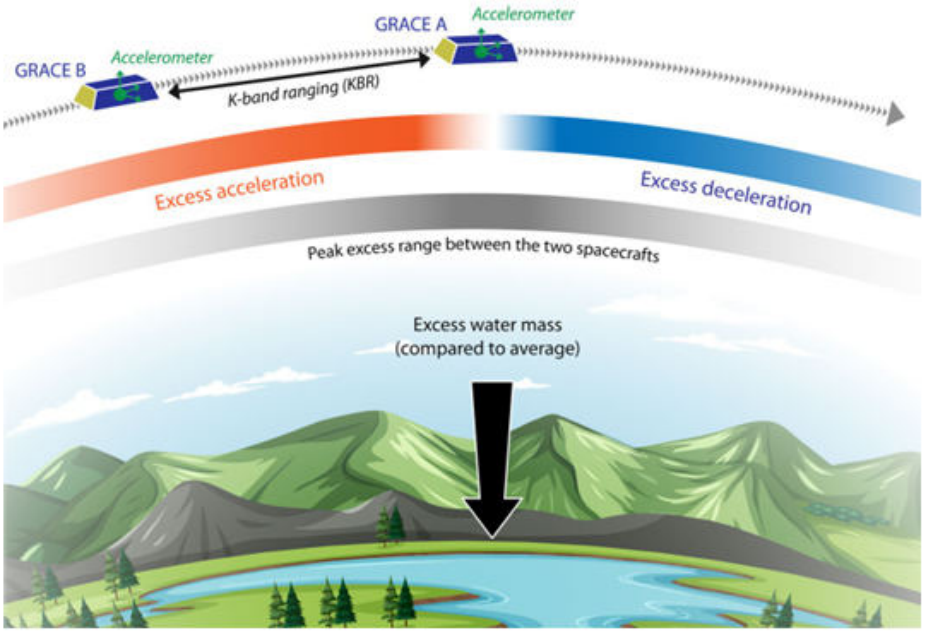

Figure 2.1: Measurement principle of the GRACE showing the twin satellite separated by the distance of approximately 220 km, at an altitude of about 500 km in tandem orbit (Humphrey et al., 2023).

The insight into the measurement principle of the GRACE satellite mission is given by Figure 2.1. During the trajectory of the GRACE satellites, whenever the satellite passes through the region with an excess mass, the gravitational attraction is stronger, causing the leading satellite to accelerate towards the positive mass anomaly. Consequently, the separation between the satellites increases until the trailing satellite catches up. These variations in the distance between the satellites can be used to infer the time-variable mass changes at the Earth's surface at the local, regional or at global level at the end (Humphrey et al., 2023).

GRACE estimates mass anomalies relative to the long-term average gravity field (Humphrey et al., 2023), which is saturated from the monthly solutions, to produce the anomaly map (Girotto and Rowland, 2019). In other words, GRACE provides estimates of total water storage anomalies $(\mathrm{TWSA} = \mathrm{TWS} - \overline{\mathrm{TWS}})$. Neither the total amount of TWS nor its long-term average $\overline{\mathrm{TWS}}$ can be measured with GRACE (Humphrey et al., 2023).

To measure the total water storage anomalies with GRACE satellites, they are equipped with three-dimensional accelerometers to measure atmospheric drag and other non-gravitational accelerations (ESA, 2025). The range between the two satellites is measured with a K-band microwave with a precision of about 1 μm. This range can be detected with the precision of nanometers with a laser interferometer instrument in the case of GRACE Follow-On (Hauk, 2023; GFZ, 2026). GPS receivers and star cameras are used for precise orbit determination and attitude control, enabling accurate gravitational field measurements (eoPortal, 2023; ESA, 2025).

The monthly analysis of the range and range-rate measurements between the two satellites provides the temporal variations (i.e., anomalies) of the gravity field (Girotto and Rowland, 2019; Humphrey et al., 2023). GRACE estimates the terrestrial water storage anomalies in the form of two solutions, namely spherical harmonic solutions and mascon solutions.

2.2 Spherical Harmonic Modeling

A short-arc approach presented in Chen et al. (2019) was reviewed to understand the basic principles behind the SH solutions. Furthermore, the theoretical aspects of TWS, along with the processing scheme used to derive it during this lab rotation, are elaborated in the following sections.

2.2.1 Basic Principle of the Spherical Harmonic Solution

From GRACE satellite observations (i.e., orbit, inter-satellite range rate, attitude, and acceleration data) in order to determine monthly spherical harmonic coefficients $\boldsymbol{u}$, short-arc approach is explained here, where the observation equations for both orbits and inter-satellite range-rates are summarized in the following form (Chen et al., 2021):

$$\boldsymbol{v} = \boldsymbol{A}\boldsymbol{x} - \boldsymbol{y} \tag{2.1}$$

in which $\boldsymbol{x} = (\delta\boldsymbol{u}^T \delta\boldsymbol{a}^T \delta\boldsymbol{b}^T)^T$ denotes the vector of parameters to be estimated, containing the spherical harmonic coefficients $\delta\boldsymbol{u} = (\ldots \delta C_{nm} \quad \delta S_{nm} \ldots)^T$ and accelerometer calibration parameters $\delta\boldsymbol{a}$ as well as boundary parameters $\delta\boldsymbol{b}$; $\boldsymbol{v} = \left(\boldsymbol{v}_{\boldsymbol{rA}}^T, \boldsymbol{v}_{\boldsymbol{rB}}^T, \boldsymbol{v}_{\dot{\boldsymbol{\rho}}}^T\right)^T$ is the correction vector to the measurements of both twin orbits (GRACE A and GRACE B) and inter-satellite range rate $\dot{\boldsymbol{\rho}}$; $\boldsymbol{A}$ is the design matrix regarding $\boldsymbol{x}$; and $\boldsymbol{y}$ is the residual vector by subtracting reference orbits and range-rates from their observations. Using the weighted least squares method by minimizing the criterion $\Phi = \boldsymbol{v}^T\boldsymbol{P}\boldsymbol{v}$, we can easily derive the normal equation regarding the parameters to be solved as follows:

$$\boldsymbol{A}^T\boldsymbol{P}\boldsymbol{A}\boldsymbol{x} = \boldsymbol{A}^T\boldsymbol{P}\boldsymbol{y} \tag{2.2}$$

in which $\boldsymbol{P}$ is the weight matrix for measurements (orbits and range-rates) constructed according to the postfit residuals of measurements (Chen et al., 2019). Before solving the spherical potential coefficients, the local parameters $\delta\boldsymbol{w} = (\delta\boldsymbol{a}^T \delta\boldsymbol{b}^T)^T$, including accelerometer and boundary parameters, should be eliminated from the normal equation. To eliminate the local parameters, we rewrite the normal Eq. (2.2) as follows:

$$\begin{bmatrix} \boldsymbol{N}_{\boldsymbol{uu}} & \boldsymbol{N}_{\boldsymbol{uw}} \\ \boldsymbol{N}_{\boldsymbol{uw}}^{\boldsymbol{T}} & \boldsymbol{N}_{\boldsymbol{ww}} \end{bmatrix} \begin{bmatrix} \delta\boldsymbol{u} \\ \delta\boldsymbol{w} \end{bmatrix} = \begin{bmatrix} \boldsymbol{Y}_{\boldsymbol{u}} \\ \boldsymbol{Y}_{\boldsymbol{w}} \end{bmatrix} \tag{2.3}$$

where $\boldsymbol{N}_{\boldsymbol{uu}}$, $\boldsymbol{N}_{\boldsymbol{uw}}$, and $\boldsymbol{N}_{\boldsymbol{ww}}$ are the block matrices of $\boldsymbol{A}^T\boldsymbol{P}\boldsymbol{A}$ regarding the potential harmonic parameters $\delta\mathbf{u}$ and the local parameters $\delta\mathbf{w}$; $\mathbf{Y}_u$ and $\mathbf{Y}_w$ are the sub vectors of $\boldsymbol{A}^T\boldsymbol{P}\boldsymbol{y}$. Eliminating the local parameters from the normal Eq. (2.3) leads to the following reduced normal equation regarding the potential harmonic coefficients:

$$\left(\boldsymbol{N}_{\boldsymbol{uu}} - \boldsymbol{N}_{\boldsymbol{uw}}\boldsymbol{N}_{\boldsymbol{ww}}^{-1}\boldsymbol{N}_{\boldsymbol{uw}}^{T}\right)\delta\boldsymbol{u} = \boldsymbol{Y}_{\boldsymbol{u}} - \boldsymbol{N}_{\boldsymbol{uw}}\boldsymbol{N}_{\boldsymbol{ww}}^{-1}\boldsymbol{Y}_{\boldsymbol{w}}\,. \tag{2.4}$$

The reduced normal Eq. (2.4) can be further simplified as:

$$\overline{\boldsymbol{N}}_{\boldsymbol{uu}}\delta\boldsymbol{u} = \overline{\boldsymbol{Y}}_{\boldsymbol{u}}\,, \tag{2.5}$$

where $\overline{\boldsymbol{N}}_{\boldsymbol{uu}}$ is the unconstrained normal matrix regarding the potential harmonic coefficients; and $\overline{\boldsymbol{Y}}_{\boldsymbol{u}}$ is the right-hand vector. The reduced normal Eq. (2.5) is the basis for developing the regularized spherical harmonic solution, which is not under the scope of this lab rotation. But, note that the regularized spherical harmonic coefficients greatly improve the spatial resolutions and reduce the signal leakage problem inherited in the unconstrained spherical harmonic solutions, and the resulting solutions after regularization have a quality comparable with the constrained mascon solutions, which takes into account the spatial constraints and considers various regularization approaches (Chen et al., 2021; Wang et al., 2023)

2.2.2 Terrestrial Water Storage Change from Spherical Harmonic Solutions

The grace gravity signal describes the monthly mass changes, which can be expressed in terms of equivalent water height using the spherical harmonic coefficient as described by Wahr et al. (1998):

$$h(\theta,\lambda,\boldsymbol{u}) = \frac{a}{3}\frac{\rho_{\text{ave}}}{\rho_w}\sum_{l=0}^{N_{\max}}\frac{2l+1}{1+k_l}\sum_{m=0}^{l}\left[\left(C_{lm}-\overline{C}_{lm}\right)\cos(m\lambda) + \left(S_{lm}-\overline{S}_{lm}\right)\sin(m\lambda)\right]\overline{P}_{lm}(\cos\theta) \tag{2.6}$$

where h is the equivalent water height at a given grid point; θ and λ are the corresponding co-latitude and longitude at that grid point; $\mathbf{u} = (C_{nm}\ S_{nm})^{\mathrm{T}}$ is the vector of the potential harmonic coefficients complete to degree and order $N_{\max}$ for a particular month.
$\overline{\boldsymbol{u}} = (\ldots \overline{C}_{lm} \quad \overline{S}_{lm} \ldots)^T$ denotes the vector of reference potential coefficients; a denotes the semi-major radius of the Earth; ρ_{ave} and ρ_w stand for the mean densities of the Earth (5,517 kg/m^3) and water (1,000 kg/m^3), respectively; $\overline{P}_{lm}$ is the normalized associated Legendre function for degree l and order m; and k_l is the l-th load Love number. For more information about the derivation of the equivalent water height, see Appendix A.
However, the equivalent water height, thus obtained from an unconstrained harmonic solution is noisy and corrupted by the north-south striping noises, which necessitates the robust filter, as a result of which induces leakage effects. To mitigate this leakage effect, introducing the geophysical constraints as implemented in mascon solutions can improve the spherical harmonic solutions and can invariably improve the resulting equivalent water height.

2.2.3 Processing of TWS from Spherical Harmonic Solutions

The scheme of the data processing used in this lab rotation to quantify terrestrial water storage (TWS) from GRACE Level-2 SH products is shown in Figure 2.3. The processing includes the following:

- The degree-1 coefficients (Geocenter) are added to the GRACE fields to consider the movement of the Earth's center of mass, relative to the modeled atmosphere and ocean degree 1 coefficients (e.g., GAC and GAD) via Technical Note-13 (Swenson et al., 2008), to include the effects of the barystatic sea level fingerprint in the ocean mass contribution to degree-1 (Sun et al., 2016).

- The lowest-degree zonal harmonic coefficients, $C_{2,0}$ and $C_{3,0}$ are replaced by the coefficients derived from Satellite Laser Ranging (SLR) data via Technical Note TN-14 (Loomis et al., 2020).

- The long-term, i.e. 2004–2010 mean of the SHs ($\overline{C}_{lm}, \overline{S}_{lm}$) are subtracted as a representative of the static gravity field to calculate the total mass anomalies.

Thus obtained spherical harmonic solution, when employed to derive the map of TWS (cf. Figure 2.2), is corrupted by north-south striping and no clear signal can be viewed over medium and low latitudes. This is due to the correlated noise at higher degrees, which arises from the geometric configuration of the polar-type GRACE satellite mission (Chen et al., 2021). Additionally, temporal aliasing caused by imperfect background models and the sampling frequency introduces errors into the solutions. Furthermore, the GRACE-FO level-2 SH coefficients are affected by instrument noise, resulting from orbital errors, star camera issues, accelerometer data, and noise in the K-band ranging system. These errors appear as distinct North-South striping patterns (Swenson and Wahr, 2006; Chen et al., 2021; Wahr et al., 2006). In order to further investigate any geophysical signal from the solutions, such noises need to be removed or suppressed in the solutions. There is a trade-off between resolution and noise, meaning that higher (or lower) degrees of spherical harmonic coefficients result in larger (or smaller) errors during mission design. To reduce the noise, a straightforward approach would be to truncate the spherical harmonic series around degrees 20–30. However, for applications requiring high spatial resolution, such as hydrology, the monthly results tend to contain significant noise.

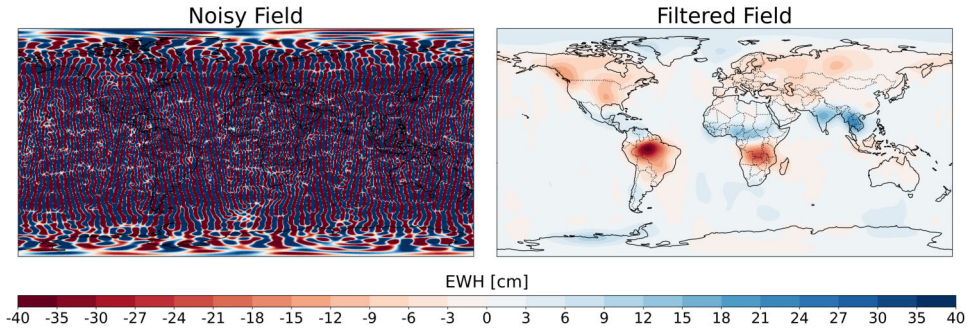

Figure 2.2: Illustrative example of TWS obtained before and after filtering. Gaussian Filter at 500 km is used to filter the original noisy TWS field from the GRACE satellite mission. The dataset used is the CSR spherical harmonic solution for October 2006. Units of Equivalent Water Height (EWH): cm.

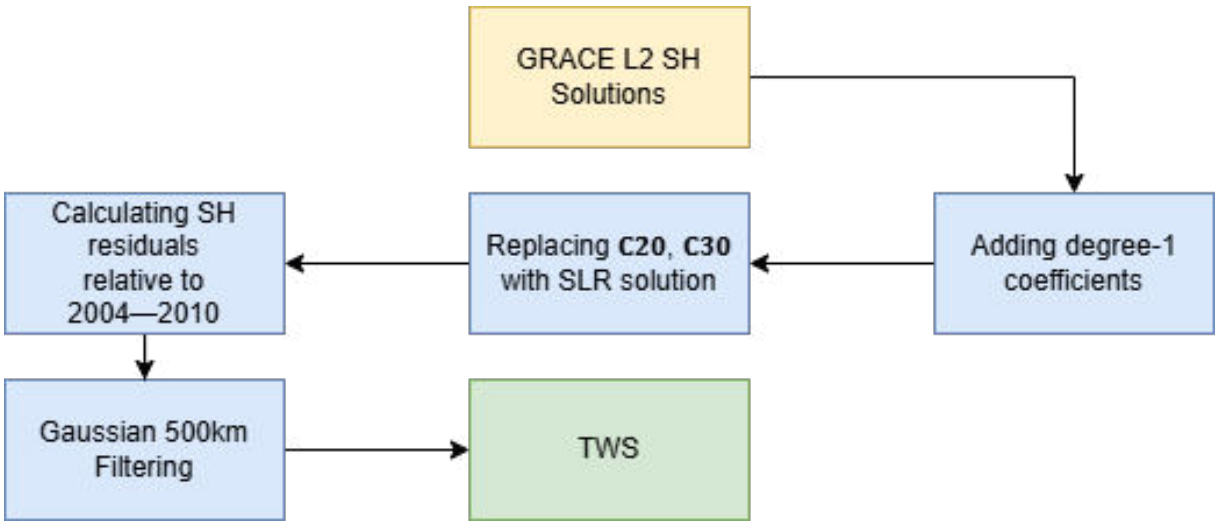

Figure 2.3: Flowchart for obtaining Terrestrial Water Storage (TWS) from GRACE Level-2 Spherical Harmonic (SH) solutions in this Lab Rotation.

Several filters have been developed to reduce or suppress the noise in the GRACE/GRACE-FO solutions.Wahr et al. (1998) utilized the low-pass isotropic Gaussian Smoothing operator developed by Jekeli (1981) as the spatial filter. The idea of the Jekeli (1981) was further extended to develop into an anisotropic version by Han et al. (2005) and Zhang et al. (2009). Other examples of the spectral filter include the Wiener filter (Klees et al., 2008; Sasgen et al., 2006), the DDK filter (Kusche, 2007; Kusche et al., 2009) and the regularization filter (Devaraju and Sneeuw, 2017). Swenson and Wahr (2006) developed a de-striping filter by smoothing the spherical harmonic coefficients for a particular order m with a polynomial of order p using least squares estimation. Following Swenson and Wahr (2006) several filters have been developed which investigate such a pattern in the unconstrained solutions (Chambers, 2006; Chen et al., 2007; Duan et al., 2009). These filters are mostly followed by a spatial filter like a Gaussian filter to reduce the remaining noise. Other categories of filters include temporal filters such as the Empirical Orthogonal Function(EOF) filter (Schrama et al., 2007; Wouters and Schrama, 2007), the stochastic filter (Wang et al., 2016), the SSA filter (Prevost et al., 2019), the least square filter (Crowley and Huang, 2020). The temporal filters regard the north-south striping as the white/stochastic noise and suggest that this random signal can be identified as the time information grows (Yi and Sneeuw, 2022). It is noteworthy to mention that users can freely choose a suitable filter based on the demand of their application.

Here, we apply a Gaussian filter at 500 km (spatial filter) to suppress the overwhelming north-south striping noises. The filter radius is chosen based on the hit-and-trial method to mitigate the noise at the global scale. Although the filter has succeeded in dampening most of the noise by reducing stripes (while some stripes still exist), it has induced leakage effects, as a consequence of the spatial convolution operation during the spectral analysis or

transformation. Supporting Chen et al. (2021) and Klees et al. (2008) we can perceive the leakage effects near the coastline of Greenland as shown in Figure 2.2.
In this lab rotation, we deliberately exclude further leakage effects analysis and its correction. Furthermore, ellipsoidal corrections, corrections for tidal aliasing error, and GIA (Glacial Isostatic Adjustment) corrections to eliminate the post-glacial rebound effects have been grossly underestimated. But, note that these corrections aid in improving the final results. SH solution, hereafter, referred to the solutions after incorporating the corrections and filtering as mentioned in the flowchart in Figure 2.3.
Incorporating spatial constraints from mascon modeling into spherical harmonic modeling through regularization methods can improve the spherical harmonic gravity field solution, considering signal leakage effects and remaining striping noise, even after robust smooth filtering of the spherical harmonic models (Chen et al., 2021).
However, the user-friendly mascon products (Save et al., 2016; Loomis et al., 2019; Watkins et al., 2015) during the inversion of mascons make use of a priori information on the parameter uncertainties that can be derived from ancillary geophysical observations/models, geographic boundaries, and temporal correlation to suppress the noise and recover the signal intensity (Yi and Sneeuw, 2022).

2.3 Mascon Modeling

To understand the theoretical aspects of mascon modeling, Wang et al. (2024) was reviewed, which gives us the way to calculate the gravitational disturbances δg_i, that is, the pseudo-observations using the unfiltered GRACE/Grace-FO spherical harmonic coefficients (SHCs), as follows:

$$\delta g_i = g(r,\lambda_i,\varphi_i) = -\frac{GM}{r^2}\sum_{l=1}^{l_{\max}}\left(\frac{a}{r}\right)^l \frac{l+1}{1+k_l}\sum_{m=0}^{l} P_{lm}(\sin\varphi_i)\left(\Delta C_{lm}\cos m\lambda_i + \Delta S_{lm}\sin m\lambda_i\right) \tag{2.7}$$

where (r, λ_i, φ_i) are the geocentric distance, longitude and latitude of the ith point at a given satellite altitude, a represents the Earth's mean radius given in the SHCs model used, $r = a$ + 500 km, G is the gravitational constant and M is the mass of the Earth. l and m are the degree and order of the SHCs, and the maximum degree is denoted by $l_{\max}$. k_l indicates the load Love number for degree l and the linear-interpolation values from Wahr et al. (1998) are adopted. P_{lm} is the fully normalized associated Legendre function, and ΔC_{lm} and ΔS_{lm} denote the SHCs with the mean value over the study period removed.
The fundamental mascon model as per Baur and Sneeuw (2011) is given by:

$$y = Ax + \Delta \tag{2.8}$$

where, $\mathbf{y} = (\delta\mathbf{g}_1,\ldots,\delta\mathbf{g}_n)^\top$ is the n - vector of observations, $\boldsymbol{A}$ denotes the $n \times t$ design matrix and the ijth element can be derived via Newton's law of gravitation by considering the corresponding ellipsoidal correction (Save, 2020; Ditmar, 2018):

$$A(i,j) = \frac{G(r - d(\theta_j)r\cos\Psi_{i,j})}{(d(\theta_j)^2 + r^2 - 2d(\theta_j)r\cos\Psi_{i,j})^{\frac{3}{2}}} \tag{2.9}$$

where $\psi_{i,j}$ is the spherical distance between the ith space location and the jth mascon point, θ_j denotes the co-latitude of the jth mascon point,

$$d(\theta_j) = \frac{a(1-f)}{\sqrt{1 - e^2\sin(\theta_j)^2}} \tag{2.10}$$

represents the radial distance of the jth mascon point from the centre of the ellipsoid, and f and e represent the ellipsoid flattening and eccentricity, respectively. $\boldsymbol{x}$ is a vector of t mass variations to be estimated, and Δ is the random error vector with a zero mean and a covariance matrix of $\sigma_0^2\boldsymbol{P}^{-1}\cdot\sigma_0^2$ is the variance of the unit weight, and the weight matrix $\boldsymbol{P}$ is obtained through the inversion of the covariance matrix, which is derived via the law of error propagation from the full covariance matrix of the monthly GRACE/GRACE-FO solutions (Chen et al.,

2016); notably, deriving the weight matrix in such a way can significantly improve the accuracy of the mascon solutions (Ran et al., 2018).
Eq. (2.8) is ill-conditioned, it is usually solved with the Tikhonov regularization method, where the solution is derived by minimizing the following cost function (Wang et al., 2023):

$$\Phi(\boldsymbol{x}) = (\boldsymbol{y} - \boldsymbol{A}\boldsymbol{x})^T \boldsymbol{P} (\boldsymbol{y} - \boldsymbol{A}\boldsymbol{x}) + \alpha \boldsymbol{x}^T \boldsymbol{R}\boldsymbol{x} \tag{2.11}$$

where α indicates the regularization parameter ($\alpha > 0$) and $\boldsymbol{R}$ is the symmetric regularization matrix. On the right hand side of Eq. (2.11), the first term represents how well the mascons fit the temporal geopotential anomalies derived from the unfiltered SHCs, and the second term denotes the total signal variance of the mascons.
Mascon solutions from various GRACE providers implement distinct regularization methods to address the ill-conditioned problem described in Eq. (2.8), which will be discussed in detail in Section 3.

3 Dataset Description

In order to make the comparison of the mascon solutions and SH solutions, three global mascons from CSR (Save et al., 2016), GSFC (Loomis et al., 2019) and JPL (Watkins et al., 2015) are used.
The CSR mascon solutions can be downloaded from https://www2.csr.utexas.edu/grace/RL06_mascons.html,
the GSFC mascon solutions from https://earth. gsfc.nasa.gov/geo/data/grace-mascons
and JPL mascon solutions from https://grace.jpl.nasa.gov/data/get-data/jpl-global-mascons/.
The global mascon solutions from GSFC and JPL are directly derived from the GRACE Level-1B data, while the CSR mascon solution is derived from Level-2 GRACE SHCs up to degree and order 120 (Wang et al., 2023). For GSFC mascon modeling, the 1-arc-degree equal area values have been placed on an equal angle $0.5^\circ \times 0.5^\circ$ grid. While, CSR is modeled onto 1° near equal-area mass concentration blocks, placed onto $0.25^\circ \times 0.25^\circ$ grid and JPL estimates global, monthly gravity fields in terms of $3^\circ \times 3^\circ$ equal-area mass concentration blocks, placed on $0.5^\circ \times 0.5^\circ$ degree grid equal-area. All the mascon solutions take into account the following corrections: $C_{2,0}$ and $C_{3,0}$ coefficients replacement from TN-14 (Loomis et al., 2019, 2020), degree-1 (Geocenter) correction, GIA corrections. It is noted that all three GRACE mascon solutions use the global ICE-6G GIA model (Peltier et al., 2018) to remove the post-glacial effects. In order to reduce the leakage effects and improve the spatial resolution, different regularization matrices based on different approaches are used in various mascon solutions (Wang et al., 2023). As shown in Table 3.1, CSR uses filtered GRACE SHCs as the regularization matrix to estimate prior signal variances. Nonetheless, JPL and GSFC respectively computed the prior signal variances based on geophysical models and spatial/temporal correlated exponential function. Moreover, regarding the regularization approach, JPL used the sequential Kalman filter based on Bayesian estimation, GSFC employed the iterative solution with an empirical damping parameter, and CSR used the Tikhonov regularization using the L-ribbon approach.
Regarding the spherical harmonic solutions, three spherical harmonic solutions from ITSG (Mayer-Gürr et al., 2018; Kvas et al., 2019), JPL, and CSR. The ITSG SH solutions was downloaded from ITSG (2025) (but can also be downloaded from ICGEM (2026)), the JPL SH solutions ICGEM 2026 and CSR SH solutions ICGEM 2026, respectively.

Table 3.1: Comparison of Various Mascon Solutions (Wang et al., 2023; Humphrey et al., 2023)

	CSR Mascon	**GSFC Mascon**	**JPL Mascon**
Coverage	global	global	global
Input data	GRACE SHCs	Level-1B data	Level-1B data
Mascon size	$1^\circ \times 1^\circ$	$1^\circ \times 1^\circ$	$3^\circ \times 3^\circ$
Grid size	$0.25^\circ \times 0.25^\circ$	$0.5^\circ \times 0.5^\circ$	$0.5^\circ \times 0.5^\circ$
Technique	1° near equal-area mass concentration blocks	1° equal-area mass concentration blocks	3° equal-area mass concentration blocks
Regularization Matrix	Filtered GRACE SHCs	Spatial/temporal correlated function	Geophysical models
Regularized method	Tikhonov regularization using the *L*-curve approach	Iterative solution with an empirical damping parameter	Bayesian estimation and sequential Kalman filter
GIA correction	ICE6G-D	ICE6G-D	ICE6G-D
Error assessment	no	Data-driven method	no

Various corrections to the SH solutions from different GRACE providers (ITSG, JPL, and CSR) are described in the Sub-section 2.2.3 (Processing of TWS from Spherical Harmonic Solutions).

4 Research Area

In order to conduct research with respect to the quality assessment of various products (solutions) from different GRACE providers through comparison of these solutions, we took Nepal region as our research area as shown in Figure 4.1. Nepal is a landlocked country in South Asia, situated between India and China. It occupies an area of 147,516 km^2, with a length of about 800 km from east to west and a width ranging from 150 to 250 km from north to south. It is located between two major basins, namely the Brahmaputra basin on the northern and eastern side and the Indo-Gangetic (IG) basin on the southern side.

Nepal can be divided into three main geographical regions:

1)Himalayan Region: This region contributes to glacial mass balance studies in the Brahmaputra basin

2) Mid Hill Region: Includes the Mahabharat range (1,500-2,700 m) and valleys

3)Terai Region: The southernmost strip, an extension of the Gangetic plain, with elevations ranging from 60 to 305 meters.

Moreover, Nepal's unique position at the intersection of these major basins, which itself has the Himalayas, glaciers, and major perennial river basins like Koshi, Gandaki, Karnali, and monsoon rivers; lies in a tectonically active region, makes it a critical area for hydrological and solid Earth studies using GRACE data, offering insights into total water storage changes dynamics, including monthly changes (averages), long-term trend, seasonality and linear trend.

From now on, all analysis will be done based on this research area.

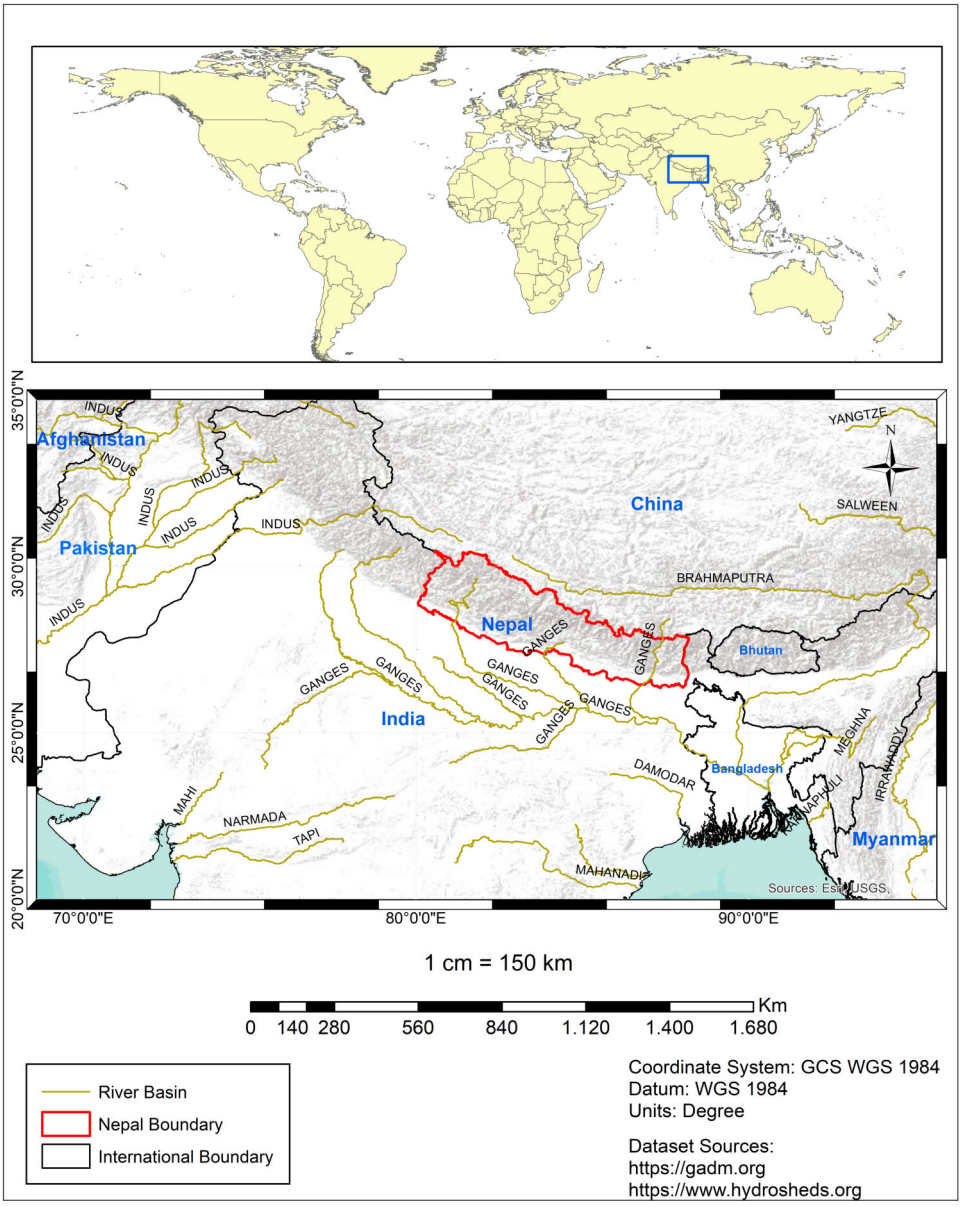

Figure 4.1: Map showing the Nepal region as the study area along with Indo-Gangetic Brahmaputra (IGB) basin.

5 Results and Discussions

To make a comparison of the mascon solutions and spherical harmonic solutions, various analyses are done in the following sub-sections with respect to the Nepal region, in terms of interpreting the terrestrial water storage. The mass anomalies appear blockier, and more concentrated in the mascon solution than in the spherical harmonic solution as shown in Figure 5.1. This is because of the capability of the mascon solutions to quantify the local mass anomaly signals in small, predefined regions, unlike the spherical harmonic solution, which itself is defined globally and are representations of the global gravity field. The inherent overwhelming north-south striping noises, when removed using the robust Gaussian smoothing filter (500 km), attenuate the real geophysical signals, as a result of the induced signal leakage from the IGB basin into the Nepal region, in the case of the SH solutions. This reduces the resulting spatial resolution of the spherical harmonic solutions, with respect to the mass change estimates.

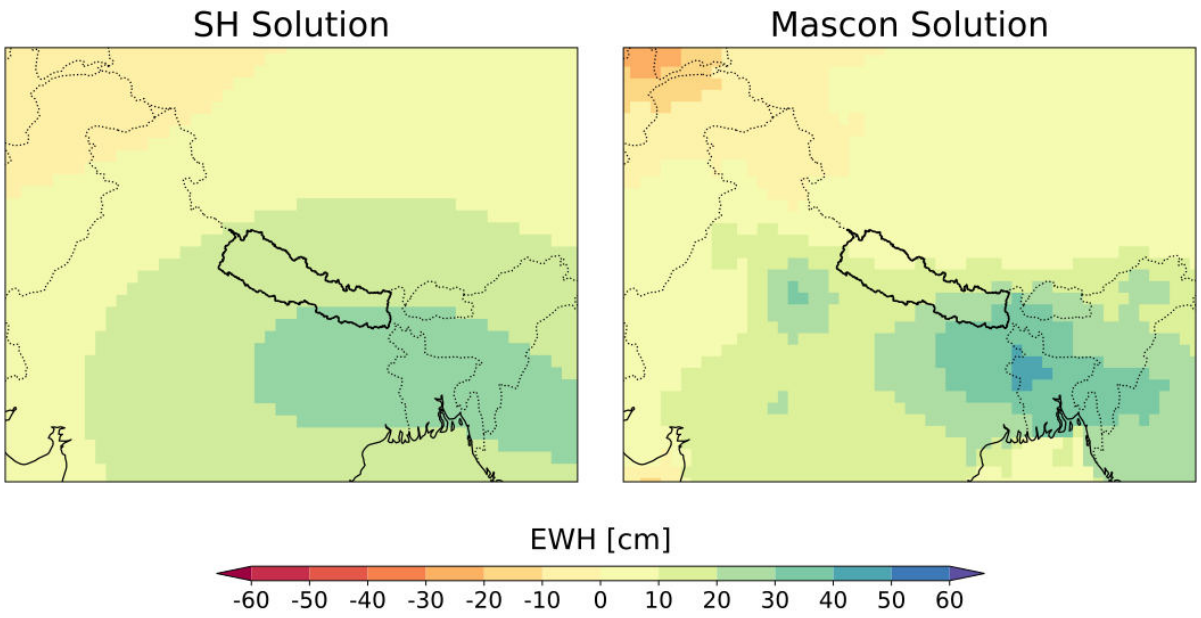

Figure 5.1: Exemplary Plot of TWS from GRACE satellite mission for Nepal Region using SH Solutions in the left plot and Mascon Solution in the right plot. Nepal region is annotated with a dark black color on the map. The dataset used is CSR spherical harmonic solutions in the first plot and CSR Mascon Solutions in the second plot, both for August 2008. In August 2008, eastern Nepal experienced heavy rainfall, as a result of the Indian monsoon (Reddy et al., 2008) which caused positive equivalent water height values in the eastern Nepal region as illustrated here. Units of Equivalent Water Height: cm.

5.1 Total Water Storage Deficits

For instance, we have a time series of EWH based on GSFS mascons for Nepal region, c.f. Figure 5.2 (top). All the parts of the time series that manifest the water storage deficiency can represent a potential drought period from the perspective of drought identification. Therefore, a baseline is needed to quantify the occurrence and severity of water storage deficits. One common approach to quantify this baseline is through climatology (Thomas et al., 2014). We can compute the monthly climatology for the GRACE EWH time series for the Nepal region by averaging the values for each month of the GRACE mission's record. To simplify, all Januaries in the 20-year record are averaged; the same is done for all months. Then, to quantify the deficiencies, we subtract the climatology from the GRACE EWH time series (Figure 5.2 (middle)). We call the result EWH anomalies, the negative values of which represent the water storage deficits. The red region in the Figure 5.2 (bottom) indicates the potential drought period in the Nepal region, which may be due to various natural and anthropogenic factors, including changing climate, variability in El Niño Southern Oscillation (ENSO) cycle, melting of the glaciers in the Himalayan region due to rising global temperature, ground-water depletion, and alarming deforestation due to rapid urbanization. Furthermore, the potential drought indicated by the red regions agrees more with Sharma et al. (2021). Moreover, the end of the year 2017 measured the record-high drought across the time scale from April 2002 to April 2022, which is in agreement with Shrestha et al. (2024).

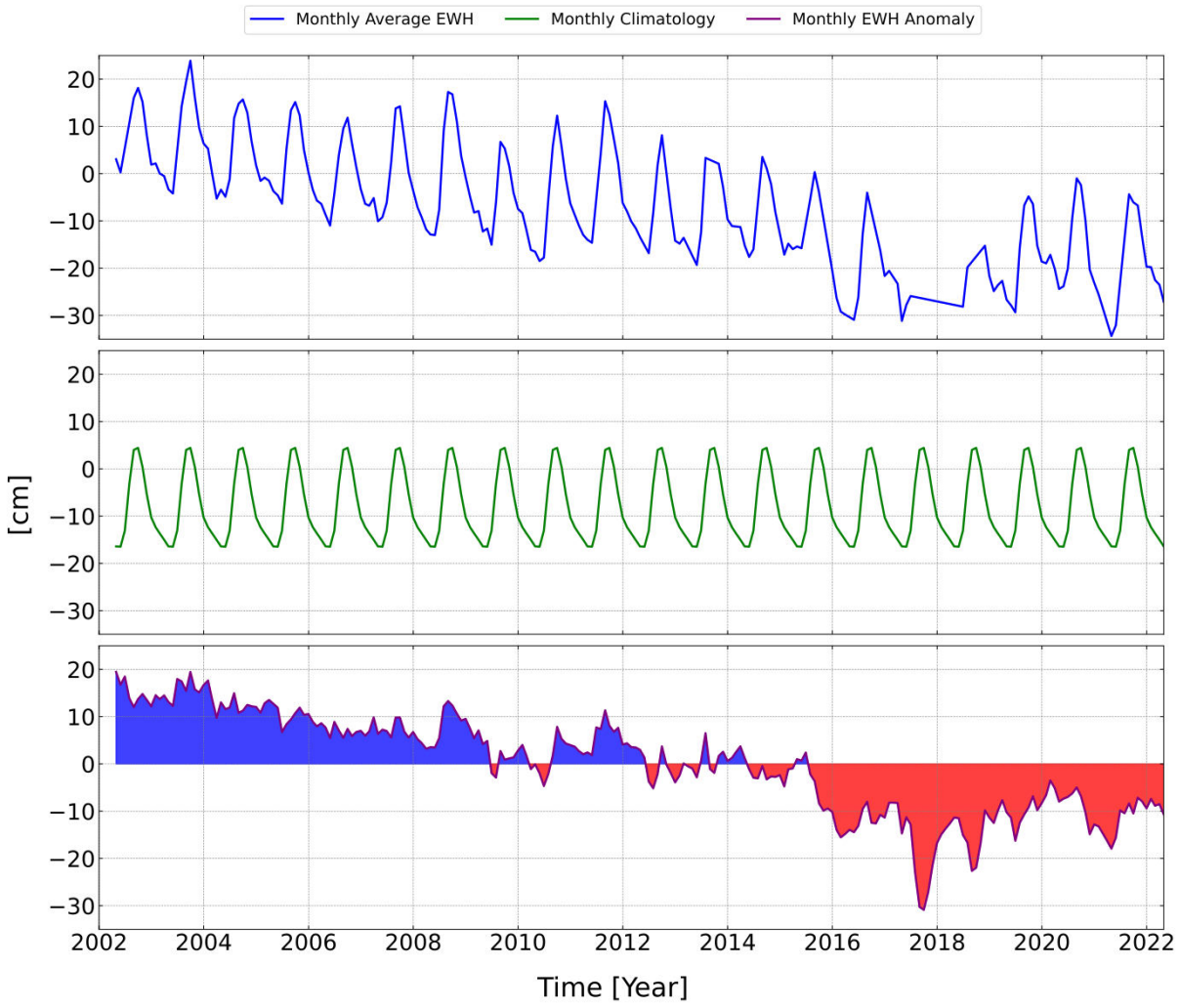

Figure 5.2: Exemplary plot showing top: Monthly Average EWH time series, middle: Climatology time series, and bottom: Monthly EWH anomaly over Nepal region from April 2002 to April 2022. Dataset used: GSFC Mascon solution.

Monthly EWH anomalies plot for all the datasets will be explained in the following sub-section 5.2 which analyzes the time series of the equivalent water height across the time scale, with respect to the Nepal region from April 2002 to April 2022.

5.2 Temporal Analysis across the Timescales

The region (i.e., Nepal) averaged time-series plot for monthly EWH, 3-month simple moving averages; and also the linear trend of the EWH across the time-scales from April 2002 to April 2022, with respect to Nepal region is shown in Figure 5.3. Furthermore, mean mascon solutions and mean spherical harmonic (SH) solutions are developed, where mean mascon solutions are obtained by the average of the GSFC, JPL, and CSR mascon solution over the mentioned time period in the dimension (and coordinates) latitude, longitude, and time, and mean SH solutions are obtained by the average of ITSG, JPL, and CSR SH solutions over the same time period in the same dimensions (and coordinates).

As explained in the sub-section Total Water Storage Deficits 5.1, monthly anomaly curves give us insight into the water deficit, further explaining the potential drought period over the Nepal region within the time period spanning from April 2002 to April 2022. A 3-month simple moving average (SMA) simply averages the consecutive 3-month's equivalent water height values. The slope of the trend curve gives the trend of equivalent water height changes, quantified with the unit cm/year. Here, in this plot in Figure 5.3, the trend is significant at 95%

confidence level. Fitting a linear trend to the given sets of temporal EWH data corresponding to various GRACE data providers is summarized in Table 5.1.

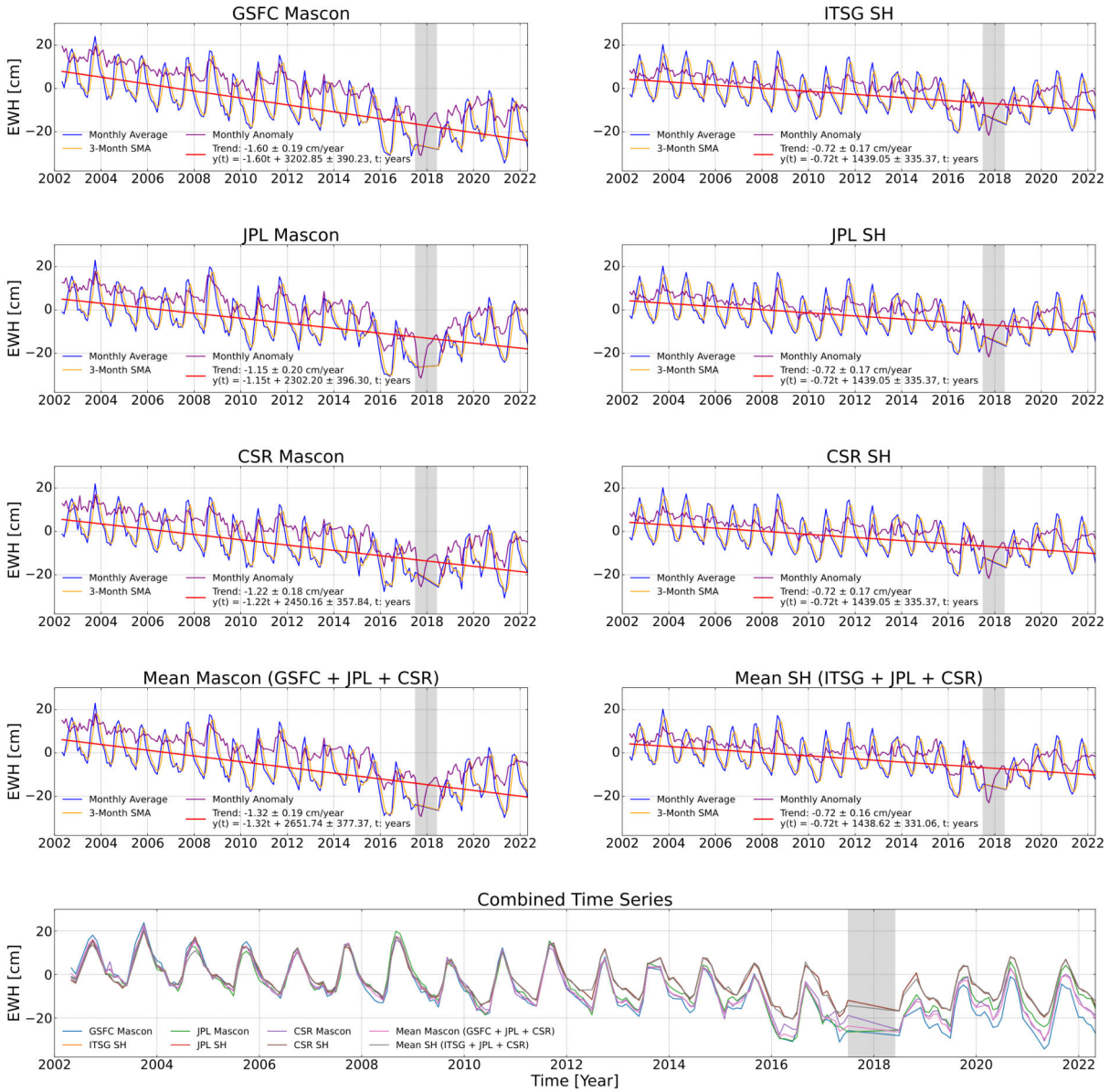

Figure 5.3: Time Series of TWS from April 2002 to April 2022, using Mascon Solutions in the first column and SH solution in the second column for Nepal Region. The combined time series is plotted in the last row. Mean Mascon solutions are obtained by the average of the GSFC, JPL, and CSR mascon solution over the time period April 2002 to April 2022 in the dimension (and coordinates) latitude, longitude, and time. Similarly, Mean SH solutions are obtained by the average of ITSG, JPL, and CSR SH solutions over the same time period in the same dimensions (and coordinates). The 11-month gap between GRACE and GRACE-FO is shown in grey. Units of EWH: cm.

Here, fitting a linear trend to the given sets of temporal EWH is quantified in terms of slope, intercept, correlation, and standard error. The linear trend of TWS in the Nepal region is assessed by the slope. While the intercepts give us insight into the starting water levels. The correlation coefficient measures the actual strength and direction of the linear relationship between time and EWH. The standard error measures the average distance that the observed EWH values deviate from the fitted linear regression line. It's a measure of the model's accuracy in cm.

From Table 5.1, it can be seen that GSFC has the strongest trend (-1.596 ± 0.19 cm/yr) and highest correlation (-0.724) with a comparable minimum standard error (0.098). JPL and CSR show similar trends (-1.147 to -1.221 cm/yr) but with a slightly lower correlation. The mean of all three mascon datasets smooths out any biases and has a linear trend of -1.312 cm/yr. All the spherical harmonic solutions have the minimum trend with the minimum

coefficient of correlation, corresponding to the linear regression of the temporal EWH data; due to the fact that SH solutions themselves have large inherent noises in the form of north-south stripping and due to leakage effects. The negative slope with respect to the linear regression of the temporal EWH data in all datasets supports the long-term loss in terrestrial water storage across the Nepal region, which can be attributed to the glacier melt, groundwater depletion, or changes in monsoon precipitation. Mascon solutions (GSFC, JPL, CSR, mean mascon) show a stronger and more negative trend than SH solutions, meaning they likely capture regional changes better with minimum standard error that supports the credibility of the captured trends. The minimum standard error of the spherical harmonic solutions, relative to the mascon solutions, indicates lower variability due to signal smoothing as a result of Gaussian filtering. Higher intercept values suggest initially greater water storage levels, while lower values suggest already reduced storage.

Table 5.1: Summary of fitting a linear trend to the given sets of temporal EWH data

Datasets Used	**Slope** (95%) [cm/yr]	**Intercept** (95%) [cm]	**Correlation Coefficient**	**Standard Error** [cm]
GSFC (Mascon)	-1.596 ± 0.19	3202.846 ± 390.23	-0.724	0.098
JPL (Mascon)	-1.147 ± 0.20	2302.203 ± 396.30	-0.596	0.100
CSR (Mascon)	-1.221 ± 0.18	2450.164 ± 357.84	-0.658	0.090
Mean (Mascon)	-1.312 ± 0.19	2651.738 ± 377.37	-0.668	0.095
ITSG (SH)	-0.717 ± 0.17	1439.055 ± 335.37	-0.481	0.085
JPL (SH)	-0.717 ± 0.17	1439.055 ± 335.37	-0.481	0.085
CSR (SH)	-0.717 ± 0.17	1439.055 ± 335.37	-0.481	0.085
Mean (SH)	-0.716 ± 0.16	1438.620 ± 331.06	-0.485	0.084

In general, all the mascon solutions show almost the same behavior in terms of recording TWS across the mentioned time period for Nepal. The little bit of difference in the curves among the mascon solutions stems from the fact that the modeling techniques and the regularization approaches followed by the various mascon solutions are different (c.f Dataset Description section 3, for more detail). While all the spherical harmonic solutions share identical behavior, in terms of interpreting TWS. This is because, all SH solutions are applied the same corrections, and the same Gaussian filter at 500 km as shown in the above flowchart in the Figure 2.3.
Furthermore,from Figure 5.3 it can be noted that the regularized mascon solutions consistently have higher linear trend estimates than the filtered spherical solution, which is mainly attributed to the effect of Gaussian filtering, which also attenuates some real geophysical signal corresponding to terrestrial water storage changes. Furthermore, the spherical harmonic solution underestimates the mass changes, as shown clearly in the plot of the monthly average EWH, resulting monthly EWH anomaly and 3-month SMA of EWH. With the improved spatial resolution, mascon solutions, which are defined at a predefined region, can capture the dynamic temporal behavior in the total water storage changes, happening at the regional level, which can be demonstrated through the plots of the mascon solutions.

5.3 Spatiotemporal Analysis of Terrestrial Water Storage

The mean state and variability of TWS are analyzed and discussed in the following sections. Additionally, the influence of TWS at the latitude–longitude level, as well as the spatial distribution of its linear trend, are further examined and discussed.

5.3.1 Mean State and Variability of Terrestrial Water Storage

Map of the mean state of TWS, in the case of the mascon solutions, are better able to capture the local spatial features than in the case of spherical harmonic solutions in Figure 5.4. The inability of the spherical harmonic solutions is due to the fact that the spherical harmonic solutions are defined on the global scale that it could not resolve the local spatial features, because of the smaller size of the Nepal Region. The lower values of the equivalent

water height in the southern and eastern parts of Nepal in mascon solutions indicate declining precipitation and rising temperature that hint at the potential drought, and groundwater depletion, in the local area of Nepal region. Similarly, the variability captured in the mascon solutions in the context of the Nepal region can be attributed to several compounding stressors: monsoonal rainfall shifts (International, 2021), unsustainable groundwater use (Wang et al., 2013), climate-induced glacier loss (Nepal et al., 2021), and land degradation (International, 2021). While spherical harmonic solutions could not capture the variability in TWS anomalies. Moreover, the signal leakage effects over the southern Terai area of the Nepal region from IG basin can be seen, which to a small extent introduces the variability in that region.

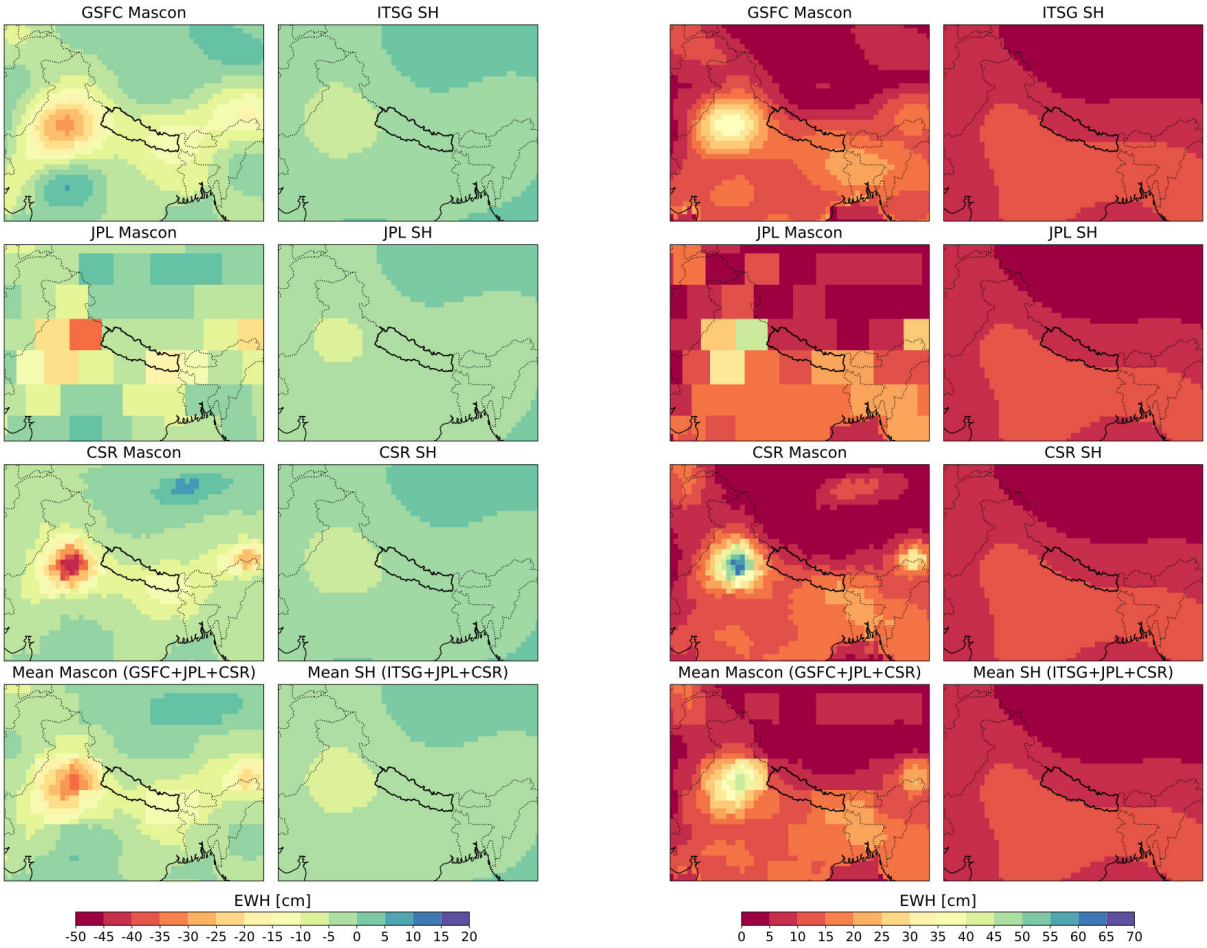

Figure 5.4: **Left:** Mean State and **Right:** Variability of TWS for the Nepal region over the entire time period from April 2002 to April 2022.

To study further the dynamics of TWS anomalies across the time scales from April 2002 to April 2022 on latitude-longitude level, Figure 5.5 gives further insight. It can be seen that it supports the region-averaged time series of EWH in Figure 5.3, as we can note the fairly decreasing trend of the EWH in both latitude and longitude level in Figure 5.5. To cite an example, at 30.50° North latitude, the EWH recorded was 40 cm in April 2002 and decreased to -40 cm in April 2022, if analyzed JPL Mascon dataset. Similarly, 28.25° North and 26° North latitude experienced a decreasing trend of EWH over these 20 years, which can be seen in both SH and mascon solutions. At 88.50° East longitude, the EWH was recorded to be somewhere around -5 cm in April 2002, which decreased to -40 cm in April 2022, when analyzed JPL mascon solution. The values of EWH got similarly decreased at 85.67°, 80° East longitude in 20 years time-span which is visible in both mascon and SH solution. More importantly, we can see mascon solutions capturing the intense decreasing trend, while the SH solutions become less sensitive in this regard.

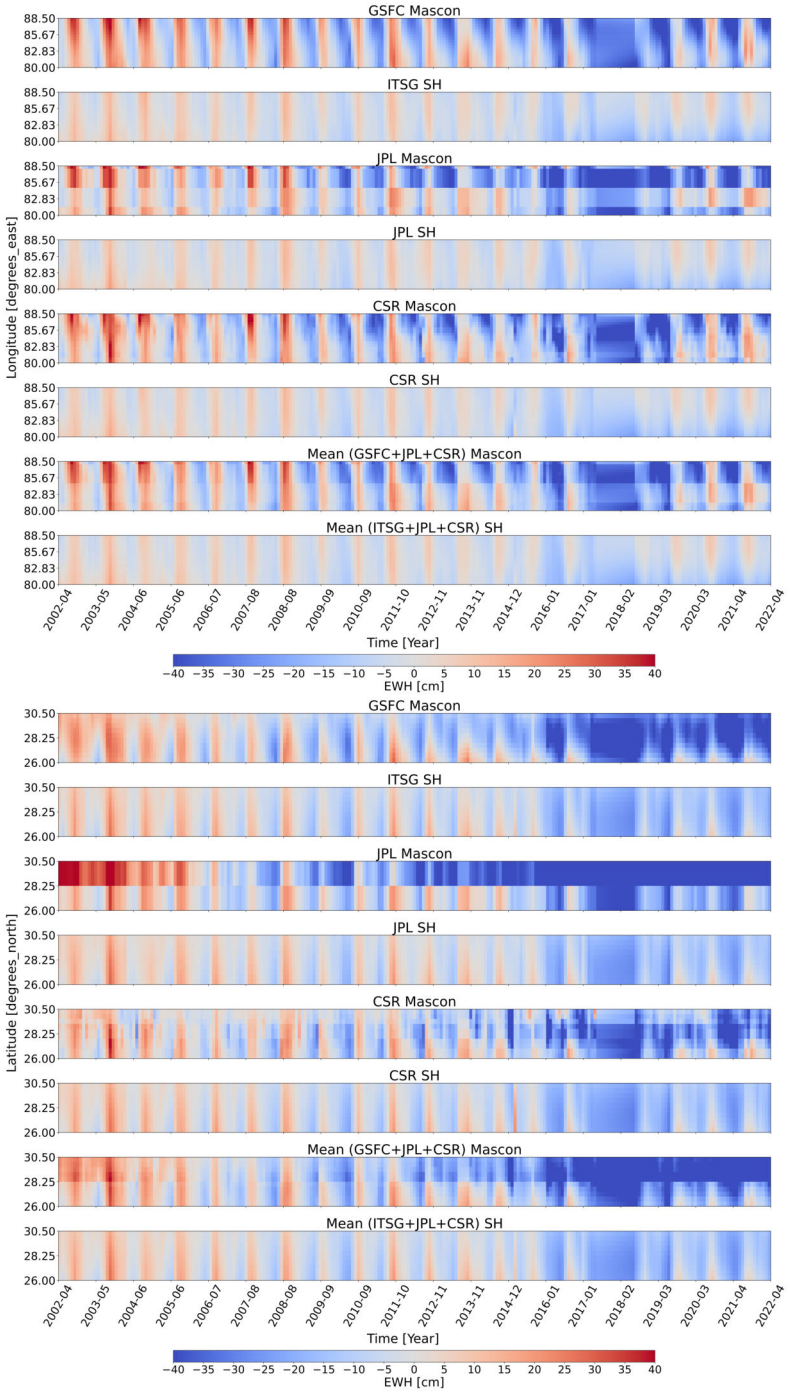

Figure 5.5: **Top:** Hovmöller-Longitude plot and **Buttom:** Hovmöller-Latitude plot of TWS for the Nepal region over the entire time period from April 2002 to April 2022.

5.3.2 Linear Trend of Terrestrial Water Storage

The spatial distribution of the time-averaged linear trend of the TWS across the Nepal region (c.f. Figure 5.6) is much extent aligned with the result (from 2002-2012) from Wang et al. (2013). Also, here spherical harmonic solutions undermine the mass changes, and hence the spatial distribution of the linear trend in the demonstrated map. The mascon plot illustrated here shows that the eastern and western parts of Nepal have significant negative linear trends, while that is only visible in the western part of Nepal region in SH solutions.

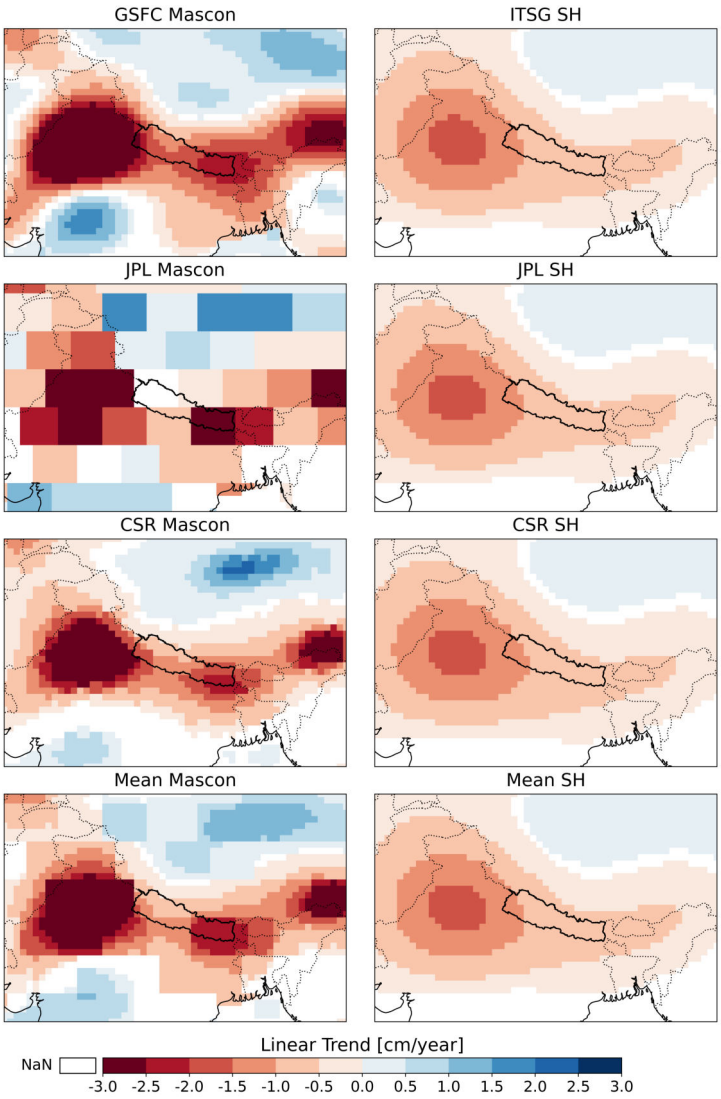

Figure 5.6: Linear Trend of TWS for Nepal region over the entire time period April 2002 to April 2022. NaN values are shown in white color which indicates that the linear trend is not statistically significant at a 95% significant level. Units of Linear Trend: cm/year.

5.4 Time Series Decomposition of Terrestrial Water Storage

The original GRACE TWS signal can be decomposed into long-term trends, seasonality signals, and residual components by implementing the seasonal decomposition of time series by LOESS (STL) approach. LOESS (Locally Estimated Scatterplot Smoothing) is a non-parametric regression technique used to model complex relationships in data by fitting local polynomial models to subsets of the data. It is particularly effective for time series decomposition methods like STL, and the equation for this approach is as follows (Scanlon et al., 2016):

$$S_{\text{total}} = S_{\text{long-term}} + S_{\text{seasonality}} + \text{Residuals} \tag{5.1}$$

where S_{total} is the original signal, $S_{\text{long-term}}$ is the long-term trend, $S_{\text{seasonality}}$ is the seasonality signal and Residuals is the residual component.

Decomposing the time series allows researchers to evaluate how well each method (SH and Mascon approach) captures specific components, e.g., long-term trends, seasonal cycles, and residuals. Mascon solutions capture the linear trend, long-term trend, and seasonality better than SH solutions across the time scales as shown in Figure 5.7. SH solutions underestimate the mass anomalies because of the robust filtering effect needed to smooth the inherent errors, while mascon solutions have a good ability to capture the mass transport across the time span. The decreasing long-term trend hints at the water deficits across the time scales in the Nepal region. High

fluctuations in seasonality result from the high variations in the seasonal cycle, which can be attributed to several natural and anthropogenic factors. Natural factors include shrinking of glaciers, glacial lakes, rising of global temperature, suppression of the precipitation due to Indian monsoon, changes in El Niño–La Niña oscillations (Wang et al., 2013). Anthropogenic factors include intense groundwater abstraction, deforestation, and rapid urbanization.

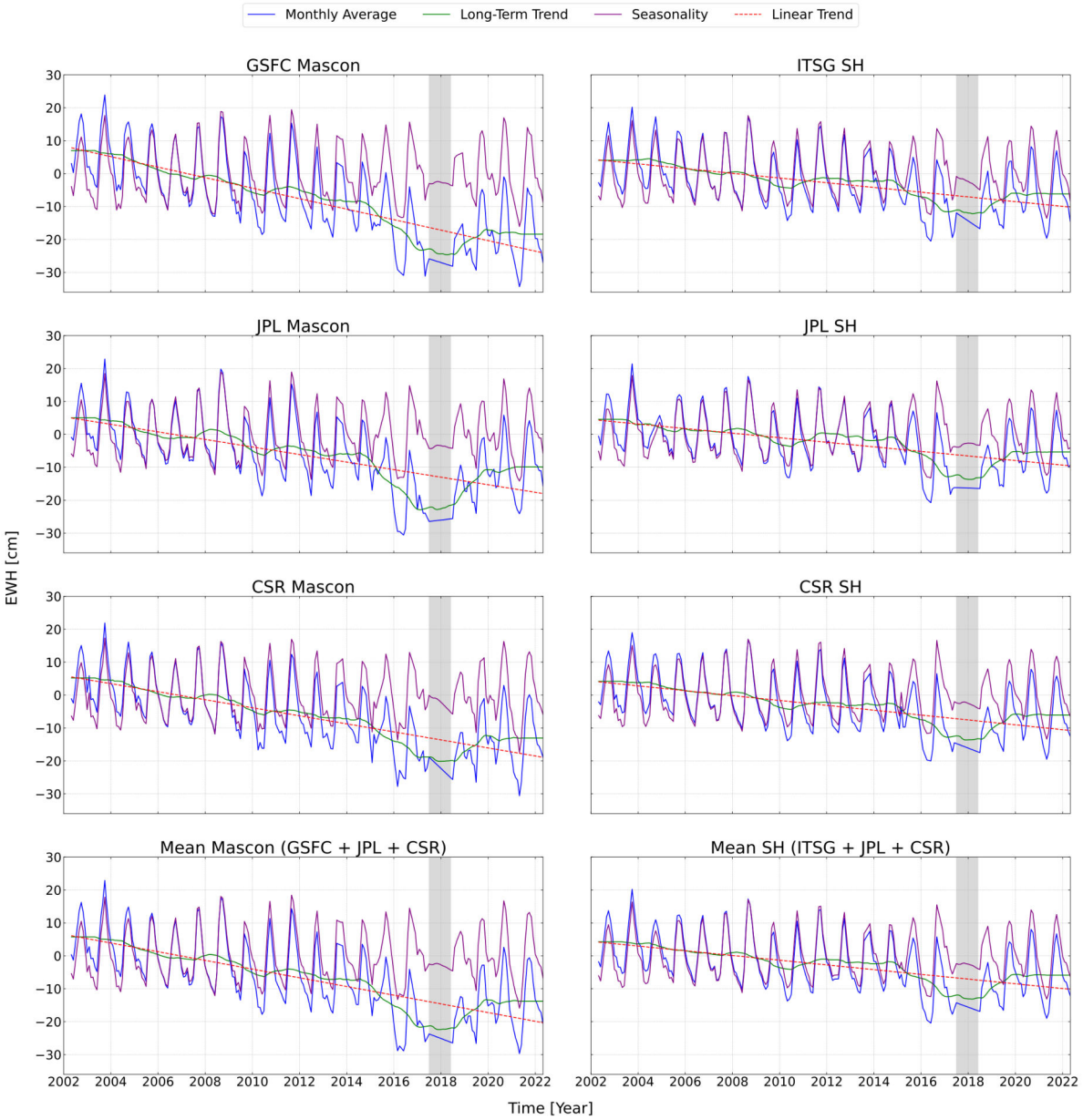

Figure 5.7: Time Series Decomposition of TWS using Mascon Solutions in the first column and SH solution in the second column, for Nepal region from April 2002 to April 2022. Long-term trend (or non-linear trend) is achieved by STL decomposition using the rolling window of 24 months. Detrended Time Series (seasonality plot) is obtained by the difference of the long-term trend of EWH from a monthly average EWH.

Furthermore, in theory, the residual component in Eq. (5.1) is set to zero (see Appendix sub-section B for more details). Therefore, de-seasonalized signal (residual plot, c.f. Figure B.1) is hereby neglected for further analysis with respect to the Nepal region.

5.5 Spatial Distribution of Seasonal Cycle of the Terrestrial Water Storage

It could be of interest to study the ongoing natural seasonal cycle, also study the effect of the monsoon rainfall and ongoing climate change, whose effects can be defined in the spatial distribution of the seasonal cycle of TWS as shown in Figure 5.8.

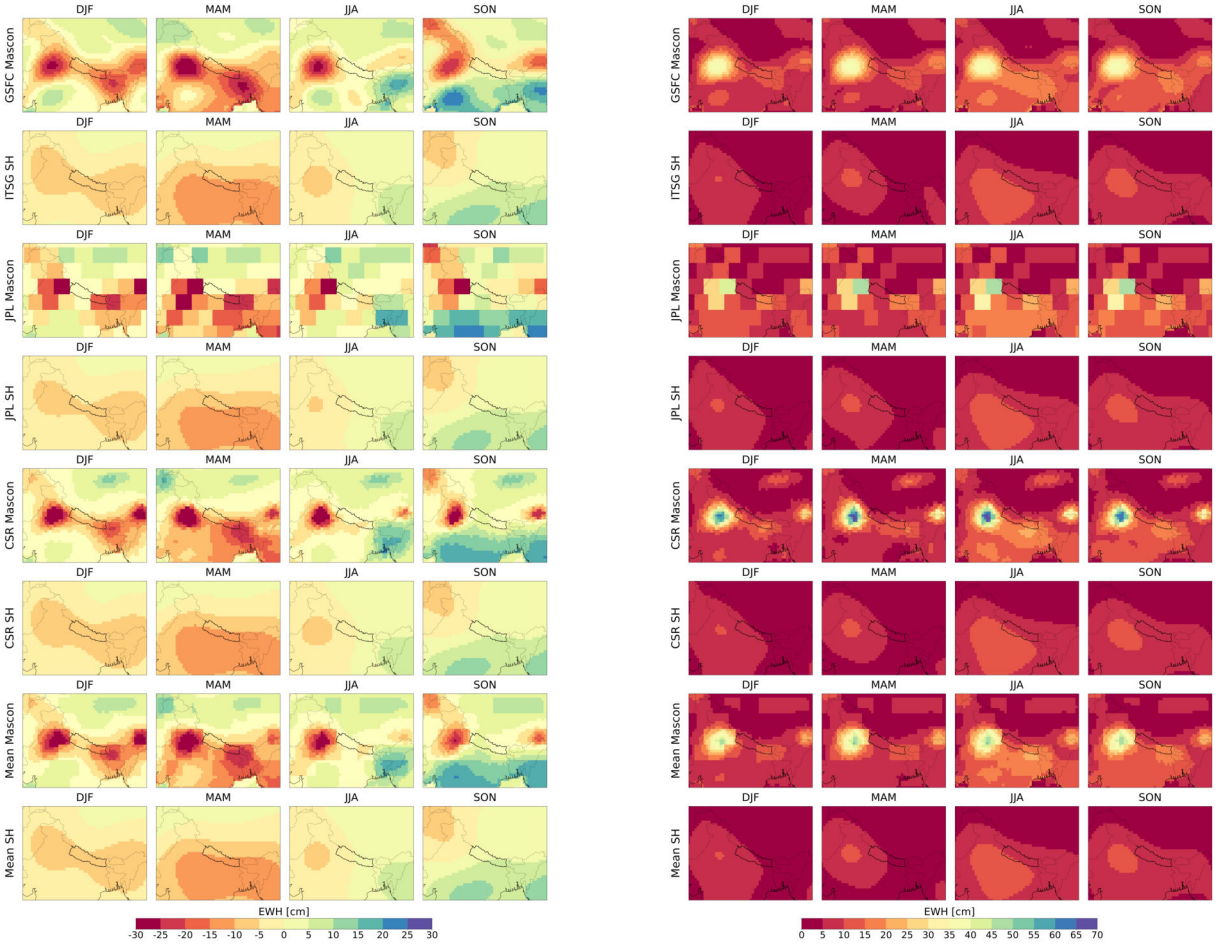

Figure 5.8: Seasonal Cycle of TWS for Nepal region over the entire time period: April 2002 to April 2022. Each row shows the **Left:** Seasonal Average **Right:** Seasonal Variability plot for the different datasets for the different three-month period. DJF, MAM, JJA, SON annotated on the top of each different plots indicates December January February season, March April May season, June July August season and September October November season respectively

The lower values of EWH during the winter (DJF) and spring (MAM), seen in both mascon solutions and spherical harmonic solutions, are due to the fact that the Nepal region remains dry during these seasons because of the reduced precipitation. The increase in these values seen in summer (JJA) and autumn (SON) is due to the monsoon rainfall and the monsoonal water recharge respectively. The monsoon creates pronounced wetness in the Nepal region during the rainy season, which spans from June to September. Furthermore, the Indian monsoon drives peak flow in the seasonal rivers during the rainy season. In general, the dynamics in the mass anomalies are apparently less captured in the SH solutions in comparison to mascon solutions, due to the damping of the original geophysical signals, as a result of the Gaussian smoothing filter.

Regarding the seasonal variability map, mascon solutions capture more variability than SH solutions across seasonal cycles, with dry winters and springs due to reduced precipitation, glacier retreat, and groundwater depletion; and wet summers and moist autumns due to monsoonal and monsoonal recharge, respectively.

5.6 Quality Assessment of Various GRACE Products

This study makes the comparison of the various mascon solutions and spherical harmonic solutions in assessing the ability of the products to interpret terrestrial water storage as shown in the scatter-density plot in Figure 5.9. For this, we employed several assessment metrics: Correlation Coefficient (R), Root Mean Square Error (RMSE), Bias, and Mean Absolute Error (MAE). Here we chose the CSR Mascon solution as the reference solution, because of the fact that CSR is modeled onto 1° near equal-area mass concentration blocks, placed onto the smallest $0.25° \times 0.25°$ grid, than other counterparts (JPL mascon and GSFC mascon) and all SH solutions, themselves have an inherited error. That's why the spherical solutions are not taken as the reference dataset.

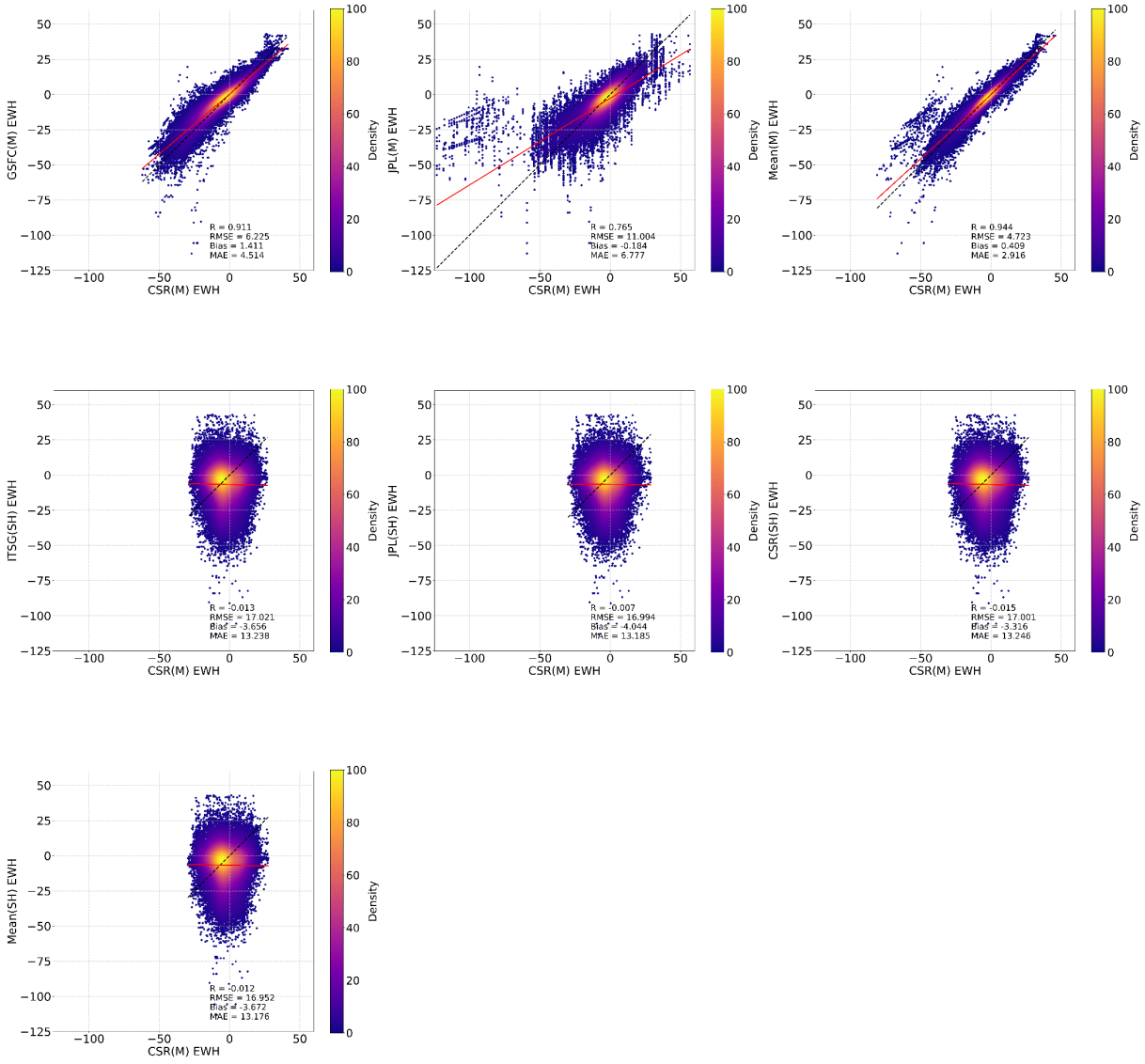

Figure 5.9: Scatter density plots of different solutions (mascon and spherical harmonics) with the reference CSR Mascon solutions for Nepal region over the entire time period April 2002 to April 2022. The reference EWH from CSR Mascon solutions in the X-axis is plotted against EWH from different mascon and/or spherical harmonic solutions in the Y-axis. The black line shows a 1:1 line while the red line shows the regression line in each subplot. The color bar shows the density of the scatter points.

The 1:1 line in scatter density plots refers to a theoretical line where the values on the x-axis (reference CSR Mascon solutions) exactly match the values on the y-axis (other GRACE solutions being compared) and the red regression line shows the actual relationship between the reference and the compared solution. The density of

scatter points (color bar) shows how frequently values cluster near or far from the 1:1 line. A "tighter" cluster around the 1:1 line suggests better agreement (lower RMSE/MAE and higher correlation).

The results of the comparison show that the mascon solutions, unlike the spherical harmonic solutions, show a "tighter" cluster around the 1:1 line when compared with reference CSR mascon solutions. This is due to the fact that we have a reference dataset itself a mascon product (CSR), and comparing it to other mascon solutions (JPL, GSFC, Mean Mascon) inherently reduces methodological discrepancies, leading to better agreement with the reference and hence a "tighter" cluster around the theoretical line. While with the SH solutions, it shares fundamentally different processing pipelines (c.f. Processing of Spherical harmonic Solutions 2.2.3) with the reference CSR mascon solutions, leading to more scattering from theoretical 1:1 line as shown in **Figure 5.9**.

The evaluation metrics (R, RMSE, Bias, and MAE) were obtained by the comparison of the reference solution and different compared solutions through linear regression, which shows the actual relationship between the solutions (reference vs. compared solutions). These metrics are well visualized in **Figure 5.10**.

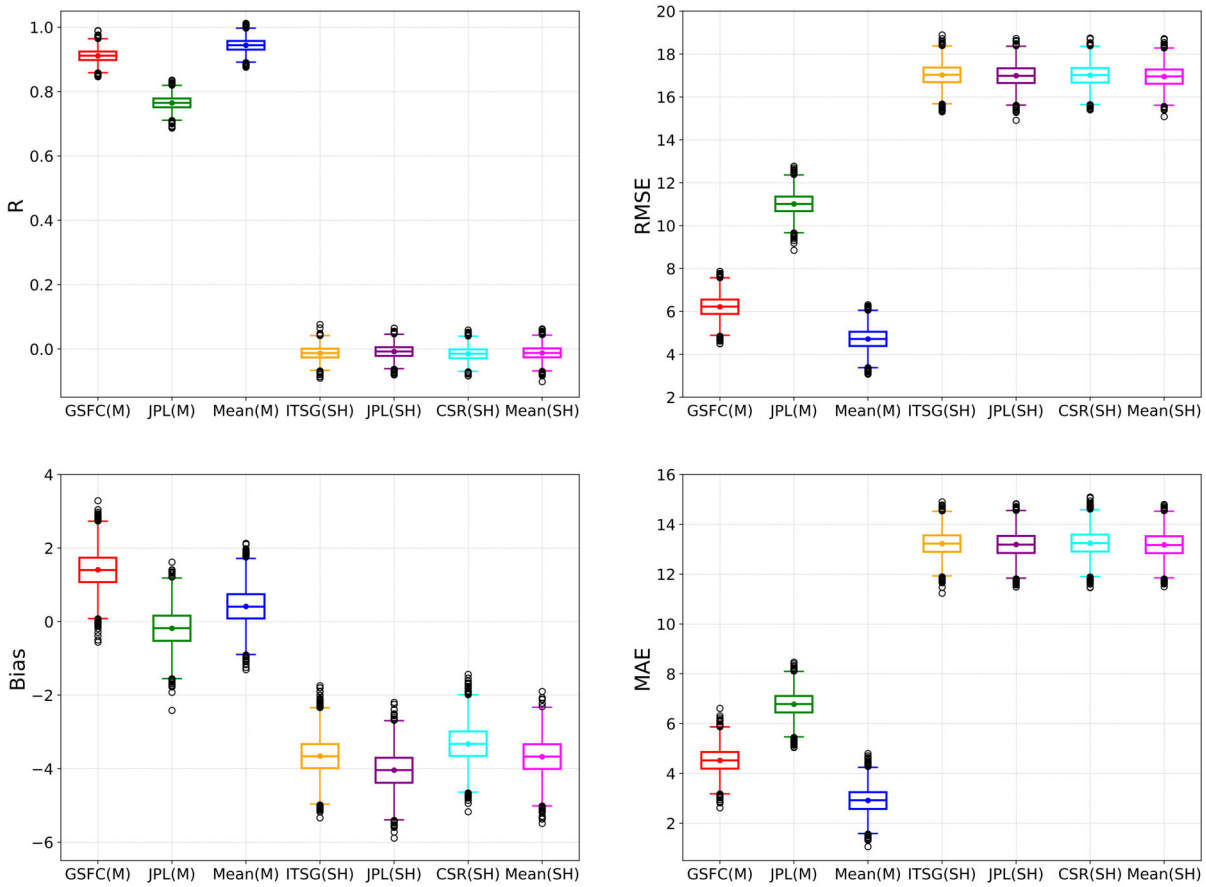

Figure 5.10: Box-whisker plot of the evaluation metrics, obtained by the comparison of the different solutions (mascon and/or spherical harmonics) with the reference CSR Mascon solutions for Nepal region, over the entire time period: April 2002 to April 2022 from Figure 5.9. The box-whisker plot for the different datasets wrt reference CSR mascon solutions are drawn in different colors. The circular patches on almost the middle of the box plot indicate the mean, while the median (0.50), first, and third quantiles are represented by the horizontal lines across the box. The whiskers represent the minimum and maximum values. GSFC(M) is to indicate the linear regression of GSFC Mascon Vs reference CSR Mascon, JPL(SH) shows the linear regression of JPL SH solutions and reference CSR mascon solution, and so on.

The result of the comparison of different solutions (mascons and/or SH) with reference CSR Mascon solutions, through linear regression, for Nepal region over the time-scales from April 2002 to April 2022 is further summarized in Table 5.2.

Table 5.2: Summary of statistical metrics

Parameters	GSFC (M)	JPL (M)	Mean (M)	ITSG (SH)	JPL (SH)	CSR (SH)	Mean (SH)
R	0.911	0.765	0.944	-0.013	-0.007	-0.015	-0.012
RMSE	6.225	11.004	4.723	17.021	16.994	17.001	16.952
Bias	1.411	-0.184	0.409	-3.656	-4.044	-3.316	-3.672
MAE	4.514	6.777	2.916	13.328	13.185	13.246	13.176
Legend	**Best in R**	**Best in RMSE**	**Overbiased**	**Underbiased**	**Best in MAE**		

Here, R measures how well the temporal variations in one solution correlate with the reference CSR mascon solution. The mascon solutions (GSFC, JPL, Mean) show strong positive correlations with the CSR mascon solution, with the Mean (M) solution having the highest correlation (0.944). This suggests that the temporal variations in TWS (e.g., seasonal water storage changes, tectonic signals, or glacial signals in the Nepal region) in these mascon solutions closely follow the patterns in the CSR mascon solution. The Mean (M) solution likely benefits from averaging multiple mascon solutions, reducing remaining inherent noise, and improving agreement. In contrast, the spherical harmonic solutions (ITSG, JPL, CSR, Mean) show very weak negative correlations (close to 0). This indicates that the SH solutions do not capture the same dynamics of mass changes as the CSR mascon solution. This could be due to differences in data-processing strategies. Moreover, mascon solutions are localized and better at capturing regional signals like those in Nepal (e.g., hydrological signals or Himalayan glacial signal), while SH solutions are global and may struggle with small-scale regional signals.

RMSE reflects the overall error in EWH estimates. The Mean (M) solution has the lowest RMSE (4.723 cm), indicating that its EWH values are, on average, the closest to the CSR mascon solution. This suggests that the Mean (M) solution provides the most accurate representation of water storage changes in Nepal compared to the CSR mascon solution. The JPL (M) solution has the highest RMSE among mascon solutions (11.004 cm), indicating larger discrepancies in EWH estimates. This could be due to differences in how JPL processes mascon data, such as different regularization or leakage corrections. The SH solutions have much higher RMSE values (around 16.9–17.0 cm), showing poorer agreement with the CSR mascon solution. This is likely because SH solutions are less effective at resolving localized mass changes in a tectonically active and hydrologically variable region like Nepal. The high RMSE suggests that SH solutions, when smoothed out attenuate the genuine regional geophysical signal.

Bias indicates systematic overestimation or underestimation of EWH. Positive bias (e.g., GSFC (M) at 1.411 cm) means the solution overestimates EWH compared to the CSR mascon solution, while negative bias (e.g., JPL (M) at -0.184 cm) means it underestimates EWH. Among mascon solutions, GSFC (M) has the largest positive bias (1.411 cm) followed by Mean (M), suggesting it consistently overestimates terrestrial water storage anomalies in Nepal. This could be due to differences in how GSFC handles leakage from surrounding regions (e.g., IGB) or its regularization approach. The SH solutions all show significant negative bias (ranging from -3.316 to -4.044 cm), meaning they consistently underestimate EWH. This underestimation could result from the SH solutions' inability to capture localized mass changes in Nepal, possibly due to robust smoothing to reduce overwhelming north-south striping noise.

MAE measures the average absolute deviation in EWH. The Mean (M) solution has the lowest MAE (2.916 cm), suggesting that Mean (M) solution has the smallest overall discrepancies in capturing water storage changes for the Nepal region. The JPL (M) solution has a higher MAE (6.777 cm) among mascon solutions, indicating larger absolute errors compared to GSFC (M) and Mean (M). The SH solutions have much higher MAE values (around 13.1–13.3 cm), again highlighting their poorer performance in capturing the EWH variations in Nepal. The Mean (SH) solution has the lowest MAE among SH solutions (13.176 cm), but this is still much higher than the mascon solutions, indicating that SH solutions are less reliable for this region.

To visually understand the above discussions, these analyses are demonstrated in Figure 5.11 in the form of the regional map, which further illustrates that mascon solutions' ability to capture the regional mass changes signals (e.g., monsoon-derived water storage change signals, Himalayan glacier signal, tectonic signals) in the Nepal region.

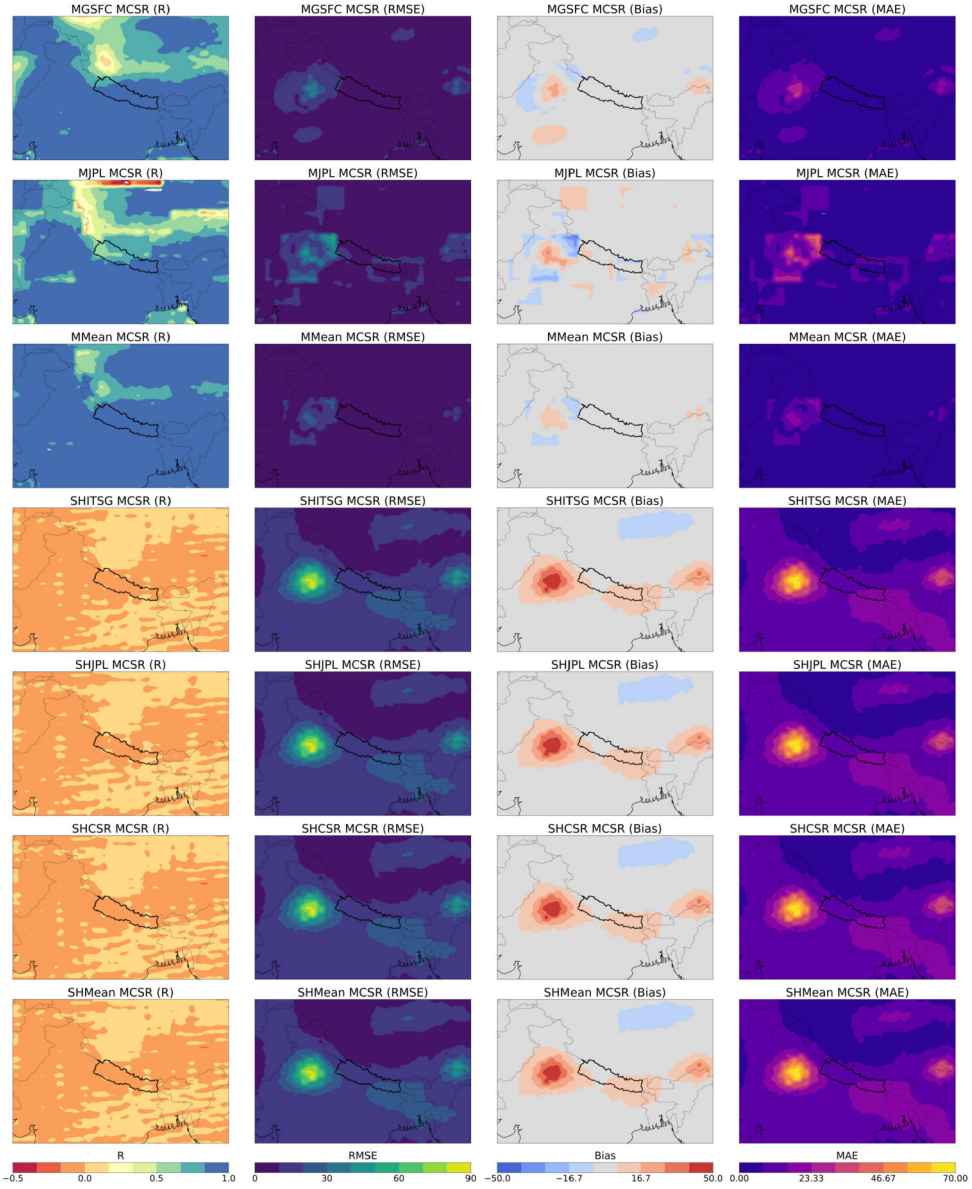

Figure 5.11: Regional Map for Nepal region obtained by the plotting of the regression evaluation metrices (R, RMSE, Bias and MAE) achieved by the comparison of the different solutions (mascon and/or spherical harmonics) with the reference CSR Mascon solutions over the entire time period April 2002 to April 2022. Each column indicates the plot for different evaluation metrices. First column is used to plot the map obtained for correlation coefficient achieved by the comparison of different solutions with reference CSR mascon solutions. Second column is used to plot the map obtained for RMSE achieved by the comparison of different solutions with reference CSR mascon solutions. Third column is used to plot the map obtained for Bias achieved by the comparison of different solutions with reference CSR mascon solutions. Fourth column is used to plot the map obtained for MAE achieved by the comparison of different solutions with reference CSR mascon solutions.

6 Conclusion

We compared various spherical harmonic (SH) and Mascon solutions from different GRACE data providers over the period from April 2002 to April 2022. Our analysis assessed the quality of these products relative to the CSR Mascon solution. Using exploratory time-series analysis, time-series decomposition, and spatiotemporal mapping

– including the mean state map, variability map, seasonal cycle map, Hovmöller-latitude-longitude map, and linear trend map — we evaluated the ability of Mascon solutions to capture temporal changes in total water storage anomalies over Nepal.

Our findings indicate that mascon solutions, which are defined over small, predefined regions, effectively capture regional variations in mass anomalies across different time scales. In contrast, SH solutions fail to represent these changes because they are globally defined and cannot resolve localized gravimetric signals in the Nepal region, whose size is itself smaller relative to the inherent spatial resolution of GRACE of about 300 – 400 km. Additionally, SH solutions are affected by significant north-south striping noise, requiring smoothing filters that attenuate real geophysical signals and introduce leakage effects. For instance, strong gravimetric signals from groundwater abstraction in the Ganges Plain or the Tibetan Plateau may leak into the Nepal region, reducing spatial resolution and accuracy.

To validate these observations, we conducted a quality assessment of the different solutions, confirming that SH solutions tend to underestimate mass changes. Our evaluation metrics show that Mascon solutions (GSFC, JPL, and Mean) consistently outperform SH solutions (ITSG, JPL, CSR, and Mean) across all criteria. This reinforces our findings that Mascon solutions are more sensitive to regional mass changes (e.g. monsoon-driven water storage changes, Himalayan glacier signals, tectonic signals) and, therefore, better suited for localized studies in complex areas like Nepal.

Among the Mascon solutions, the Mean mascon solution performed best overall, exhibiting the highest correlation (0.944), the lowest RMSE (4.723 cm), and the lowest MAE (2.916 cm). It also showed a small positive bias (0.409 cm), indicating a slight overestimation of TWS. Based on these findings, we conclude that the Mean mascon solution — computed as the average of the GSFC, JPL, and CSR mascon solutions over latitude, longitude, and time — is the most suitable choice for studying total water storage anomalies and their temporal changes in Nepal. The GSFC mascon solution serves as a secondary option for regional studies.

7 Further Research

The evaluation metrics and conclusions obtained in this study provide us an opportunity to understand the observations we made, through further investigation at a deeper level. One potential research could be exploring the poorer performance of SH solutions in capturing localized mass dynamics in the Nepal region. This could be due to excessive Gaussian smoothing applied to mitigate overwhelming north-south striping noise, which obscures regional TWS signals; truncation at lower degrees (e.g., degree 96 in GRACE data, as done here), which limits the resolution of localized signals; or leakage of nearby signals from the IGB basin into Nepal. We do not really know the exact reason, so this could be the one possible further research. This raises further interest in developing an improved SH filtering approach by selecting an optimal degree SH series and implementing advanced leakage correction methods through the regularization techniques, such as the Vishwakarma method (Vishwakarma et al., 2017). Then resulting constrained SH solutions can have the quality comparable with the mascon solutions.

Additionally, in all the observations from the above analysis, we have seen that TWS is quantified in terms of EWH. However, it remains unclear how much each component of the dynamic hydrological cycle contributes to TWS. This is because satellite gravimetry alone cannot separate terrestrial water storage changes from surface gravity signals (e.g., glacier, hydrological signals) and solid Earth signals without incorporating external information — such as GNSS data to constrain and improve solid Earth signal estimation, or hydrological models to isolate hydrological components. This limitation of the GRACE satellite mission presents a valuable research opportunity to separate surface gravity signals from solid Earth signals, thereby offering new insights for monitoring glacier mass changes in the Himalayas, or in the Nepal region using time-variable gravity data from the GRACE satellite mission. Last but not least, the contribution of the seasonal monsoon to water storage dynamics in the Nepal region can be further assessed.

Acknowledgement

Firstly, I would like to express my genuine gratitude to my (Co-supervisor) Examiner, Dr.-Ing. Kurt Seitz. Without him, this journey of the Lab Rotation in Physical Geodesy would not have been possible. From my early days at university during his lectures to reaching out to Prof. Nico Sneeuw at the Geodetic Institute of Stuttgart (GIS), University of Stuttgart through video calls and mail, on my behalf before I began my Lab Rotation at GIS, he has been a remarkable mentor and supporter for me. Moreover, during the process of generating results, he guided me both theoretically and practically.
Secondly, I extend my heartfelt thanks to Prof. Dr.-Ing. Nico Sneeuw for his insightful guidance, motivating feedback, and support in shaping a coherent research story with the data I had. His directions on how to proceed with the research were invaluable. I am deeply grateful to him for providing me with the opportunity to undertake a lab rotation at GIS, University of Stuttgart.
Thirdly, I would like to express my gratitude to my local supervisor, Dr. Yixiati Dilixiati, for his valuable input and feedback on my results during our weekly meetings at GIS.
Furthermore, I would like to thank Prof. Hansjörg Kutterer for granting permission to undertake this lab rotation as part of the RSGI course.
Additionally, I would like to acknowledge Dr.-Ing. Michael Mayer for his valuable suggestions and counseling on administrative matters as an excellent student advisor.
I also wish to thank the following data providers for granting open access to their data:

- Mascon Solutions - GSFC, CSR, JPL
- Spherical Harmonic Solutions - ITSG, CSR, JPL
- River basins data – hydrosheds.org
- Shapefile data – gadm.org

I would like to remember my grandmother (*Hajuraa*) for her continuous selfless love and blessings. My acknowledgements would not be complete without expressing my heartfelt thanks to my parents and my brother for giving me the opportunity to pursue my dream of obtaining research-level education in Germany.
Lastly, I want to thank all the wonderful individuals who, directly or indirectly, contributed to this work and supported me in reaching this stage of my academic journey.

Appendix

A Terrestrial Water Storage from Spherical Harmonics

GRACE and GRACE-FO measure the Earth's gravity field (commonly described by geoid), which can be quantified by the (geo)potential V, given by the following relation (Wahr et al., 1998):

$$V(r,\theta,\lambda) = \frac{GM}{a}\sum_{l=0}^{N_{max}}\sum_{m=0}^{l}\left(\frac{a}{r}\right)^{l+1}\overline{P}_{lm}(\cos\theta)\Big\{C_{lm}\cos(m\lambda)+S_{lm}\sin(m\lambda)\Big\} \tag{A.1}$$

where G is Newton's Gravitational constant, M is the total mass of the Earth, a represents the mean radius of the Earth, r is the radial distance, θ and λ are co-latitude and longitude respectively. $\overline{P}_{lm}$ are fully normalized Legendre polynomials of degree l and order m while C_{lm} and S_{lm} are fully normalized spherical harmonic coefficients.
Besides the static gravity potential Eq. (A.1), GRACE/GRACE-FO provides valuable insight into the time variable gravity information represented by the change in the spherical harmonic coefficients. This variability can be seen as either the change in V from one time to the other, or the difference with respect to a time average of V. We considered the latter form of the interpretation and removed the long-term mean of the spherical harmonic coefficients from the monthly values. These residual spherical harmonic coefficients are denoted by ΔC_{lm} and ΔS_{lm}, which are related to the density redistribution ($\Delta\rho(r,\theta,\lambda)$) occurring on and in the Earth:

$$\begin{pmatrix}\Delta C_{lm}\\ \Delta S_{lm}\end{pmatrix} = \frac{3}{4\pi a\rho_{\text{ave}}(2l+1)}\iiint_V \Delta\rho(r,\theta,\lambda)\overline{P}_{lm}(\cos\theta)\times\left(\frac{r}{a}\right)^{l+2}\begin{Bmatrix}\cos(m\lambda)\\ \sin(m\lambda)\end{Bmatrix}\sin\theta\, d\theta\, d\lambda\, dr \tag{A.2}$$

where ρ_{ave} is the average density of the Earth (= 5,517 kg/m^3). ΔC_{lm} = C_{lm} - $\overline{C}_{lm}$; ΔS_{lm} = C_{lm} - $\overline{C}_{lm}$. We assume that most of the mass redistribution takes place within a thin layer of thickness H, including those portions of the atmosphere, oceans, ice-caps, and below groundwater storage with significant mass fluctuations. Moreover, we pretend that a thin layer consists of water. This is a meaningful assumption in handling hydrological signals, but special care must be taken when handling glacier signals and tectonic signals. When H is thin enough (i.e. $(l_{max}+2)H/a << 1$) then $(\frac{r}{a})^{l+2}$ will be approximately equal to 1 and by replacing the volume integral $\Delta\rho$ by the surface integral $\Delta\sigma$, Eq. (A.2) becomes:

$$\begin{Bmatrix}\Delta C_{lm}\\ \Delta S_{lm}\end{Bmatrix} = \frac{3}{4\pi a\rho_{\text{ave}}(2l+1)}\int_\Omega \Delta\sigma(\theta,\lambda)\overline{P}_{lm}(\cos\theta)\times\begin{Bmatrix}\cos(m\lambda)\\ \sin(m\lambda)\end{Bmatrix}\mathrm{d}\Omega \tag{A.3}$$

The surface mass density change ($\Delta\sigma$) can be expressed in terms of the *Equivalent Water height (EWH)* which can be given as follows (Wahr et al., 1998) as mentioned in Eq. (2.6) by Eq. (A.4) :

$$h(\theta,\lambda,u) = \frac{a\rho_{\text{ave}}}{3\rho_w}\sum_{l=0}^{N_{\max}}\frac{2l+1}{1+k_l}\sum_{m=0}^{l}\overline{P}_{lm}(\cos\theta)\left[\Delta C_{lm}\cos(m\lambda)+\Delta S_{lm}\sin(m\lambda)\right] \tag{A.4}$$

B Deseasonalized Time Series

After the original TWS signal is detrended and the resulting detrended signal is deseasonalized, there are still errors prevalent in the signal, which are called residuals. Residual analysis helps identify errors or anomalies in the solutions caused by inherent noise, weather influences, or processing artifacts. In a normal case scenario, the higher positive spikes in the residual plot give preliminary tentative ideas about the flooding events in a certain region, while the higher negative spikes in the plot result from extreme events like drought. But, note that residual signals here are not physically meaningful, which themselves are on the order of 10^{-15} (c.f. Figure B.1), so here the residual signal is neglected for further analysis, and in theory, we have reduced the residuals to zero in Eq. (5.1).

Figure B.1: Deseasonalized Time Series (Residual Plot) of TWS using Mascon Solutions in the first column and SH solution in the second column, for the Nepal region from April 2002 to April 2022. The deseasonalized time series is obtained by subtracting the sum of the long-term trend and detrended time series of EWH (from Figure 5.7).

References

Baur, O. and Sneeuw, N. (2011): Assessing Greenland Ice Mass Loss by Means of Point-Mass Modeling: A Viable Methodology. *Journal of Geodesy* 85:607–615. DOI: 10.1007/s00190-011-0463-1.

Chambers, D. P. (2006): Evaluation of new GRACE time-variable gravity data over the ocean. *Geophysical Research Letters* 33(17). DOI: 10.1029/2006GL027296.

Chen, J., Cazenave, A., Dahle, C., et al. (2022): Applications and Challenges of GRACE and GRACE Follow-On Satellite Gravimetry. *Surveys in Geophysics* 43:305–345. DOI: 10.1007/s10712-021-09685-x.

Chen, J. L., Wilson, C. R., Tapley, B. D., and Grand, S. (2007): GRACE detects coseismic and post seismic deformation from the Sumatra-Andaman earthquake. *Geophysical Research Letters* 34(13). DOI: 10.1029/2007GL030356.

Chen, Q., Shen, Y., Chen, W., Francis, O., Zhang, X., Chen, Q., et al. (2019): An optimized short-arc approach: Methodology and application to develop refined time series of Tongji-Grace2018 GRACE monthly solutions. *Journal of Geophysical Research: Solid Earth* 124:6010–6038. DOI: 10.1029/2018JB016596.

Chen, Q., Shen, Y., Kusche, J., Chen, W., Chen, T., and Zhang, X. (2021): High-resolution GRACE monthly spherical harmonic solutions. *J. Geophys. Res. Solid Earth* 126:e2019JB018892. DOI: 10.1029/2019JB018892.

Chen, T., Shen, Y., and Chen, Q. (2016): Mass Flux Solution in the Tibetan Plateau Using Mascon Modeling. *Remote Sensing* 8(5):439. DOI: 10.3390/rs8050439.

Crowley, J. W. and Huang, J. (2020): A least-squares method for estimating the correlated error of GRACE models. *Geophys J Int* 221(3):1736–1749. DOI: 10.1093/gji/ggaa104.

Devaraju, B. and Sneeuw, N. (2017): The polar form of the spherical harmonic spectrum: implications for filtering grace data. *Journal of Geodesy* 91(12):1475–1489. DOI: 10.1007/s00190-017-1037-7.

Ditmar, P. (2018): Conversion of time-varying Stokes coefficients into mass anomalies at the Earth's surface considering the Earth's oblateness. *Journal of Geodesy* 92:1401–1412. DOI: 10.1007/s00190-018-1128-0.

Duan, X., Guo, J., Shum, C., and Van Der Wal, W. (2009): On the postprocessing removal of correlated errors in GRACE temporal gravity field solutions. *Journal of Geodesy* 83(11):1095–1106. DOI: 10.1007/s00190-009-0327-0.

eoPortal (2023): GRACE (Gravity Recovery And Climate Experiment). Accessed: March 15, 2025. URL: https://www.eoportal.org/satellite-missions/grace#eop-quick-facts-section.

ESA (2025): GRACE Objectives – European Space Agency (ESA). Accessed: March 15, 2025. URL: https://earth.esa.int/eogateway/missions/grace/objectives.

European Space Agency (ESA) (2025): GRACE Mission Objectives. ESA Earth Observation Gateway. Accessed: 29 Jan. 2025. URL: https://earth.esa.int/eogateway/missions/grace/objectives.

GFZ (2026): GRACE-FO – Gravity Recovery and Climate Experiment Follow-On Mission. German Research Centre for Geosciences (GFZ). Accessed: 2026-04-06. URL: https://www.gfz.de/en/section/global-geomonitoring-and-gravity-field/projects/grace-fo-gravity-recovery-and-climate-experiment-follow-on-mission.

Girotto, M. and Rowland, M. (2019): Terrestrial Water Storage. In: *Earth Resources and Remote Sensing*. GSFC-E-DAA-TN72619. NASA Technical Report, Public Distribution. NASA Goddard Space Flight Center.

Han, S.-C., Shum, C. K., Jekeli, C., Kuo, C.-Y., Wilson, C., and Seo, K.-W. (2005): Non-isotropic filtering of GRACE temporal gravity for geophysical signal enhancement. *Geophysical Journal International* 163(1):18–25. DOI: 10.1111/j.1365-246X.2005.02756.x.

Hauk, M. (2023): The Influence of LRI Observations on GRACE-FO Gravity Field Models. Accessed: March 15, 2025. URL: https://www.globalwaterstorage.info/en/the-influence-of-lri-observations-on-grace-fo-gravity-field-models.

Humphrey, V., Rodell, M., and Eicker, A. (2023): Using satellite-based terrestrial water storage data: A review. *Surveys in Geophysics* 44(5):1489–1517. DOI: 10.1007/s10712-022-09754-9.

ICGEM (2026): International Centre for Global Earth Models (ICGEM): Gravity field and GRACE/GRACE-FO products hosted at the German Research Centre for Geosciences (GFZ). Accessed: 2026-04-06. URL: https://icgem.gfz-potsdam.de/.

International, W. (2021): Nepal Water Resources Profile Overview. Accessed March 25, 2025. URL: https://winrock.org/wp-content/uploads/2021/08/Nepal_Country_Profile_Final.pdf.

ITSG (2025): Institute for Geodesy – TU Graz. Accessed: 2025-12-16. URL: https://www.tugraz.at/institute/ifg/downloads/gravity-field-models/itsg-grace2018.

Jekeli, C. (1981): Modifying Stokes's function to reduce the error of geoid undulation computations. *Journal of Geophysical Research* 86(B8):6985–6990. DOI: 10.1029/JB086iB08p06985.

Klees, R., Revtova, E., Gunter, B., Ditmar, P., Oudman, E., Winsemius, H., and Savenije, H. (2008): The design of an optimal filter for monthly GRACE gravity models. *Geophysical Journal International* 175(2):417–432. DOI: 10.1111/j.1365-246X.2008.03922.x.

Kusche, J. (2007): Approximate decorrelation and non-isotropic smoothing of time-variable GRACE-type gravity field models. *Journal of Geodesy* 81(11):733–749. DOI: 10.1007/s00190-007-0143-3.

Kusche, J., Schmidt, R., Petrovic, S., and Rietbroek, R. (2009): Decorrelated GRACE time-variable gravity solutions by GFZ, and their validation using a hydrological model. *Journal of Geodesy* 83:903–913. DOI: 10.1007/s00190-009-0308-3.

Kvas, A., Behzadpour, S., Ellmer, M., Klinger, B., Strasser, S., Zehentner, N., and Mayer-Gürr, T. (2019): ITSG-Grace2018: Overview and evaluation of a new GRACE-only gravity field time series. *Journal of Geophysical Research: Solid Earth* 124. DOI: 10.1029/2019JB017415.

Loomis, B. D., Luthcke, S. B., and Sabaka, T. J. (2019): Regularization and error characterization of GRACE mascons. *Journal of Geodesy* 93(9):1381–1398. DOI: 10.1007/s00190-019-01252-y.

Loomis, B. D., Rachlin, K. E., Wiese, D. N., Landerer, F. W., and Luthcke, S. B. (2020): Replacing GRACE/GRACE-FO ΔC_{20} with satellite laser ranging: Impacts on Antarctic Ice Sheet mass change. *Geophysical Research Letters* 47:e2019GL085488. DOI: 10.1029/2019GL085488.

Mayer-Gürr, T., Behzadpur, S., Ellmer, M., Kvas, A., Klinger, B., Strasser, S., and Zehentner, N. (2018): ITSG-Grace2018 - Monthly, Daily and Static Gravity Field Solutions from GRACE. DOI: 10.5880/ICGEM.2018.003. URL: http://doi.org/10.5880/ICGEM.2018.003.

Murböck, M., Abrykosov, P., Dahle, C., Hauk, M., Pail, R., and Flechtner, F. (2023): In-Orbit Performance of the GRACE Accelerometers and Microwave Ranging Instrument. *Remote Sensing* 15(3):563. DOI: 10.3390/rs15030563. URL: https://doi.org/10.3390/rs15030563.

NASA Jet Propulsion Laboratory (2006): NASA Satellites Find Balance in South America's Water Cycle. NASA JPL News. Accessed: 29 Jan. 2025. URL: https://www.jpl.nasa.gov/news/nasa-satellites-find-balance-in-south-americas-water-cycle/.

NASA Jet Propulsion Laboratory (2016): Applications Plan for the Gravity Recovery And Climate Experiment (GRACE) Missions: GRACE, GRACE-FO, and Future Missions. GRACE Website. Accessed: 29 Jan. 2025. URL: https://grace.jpl.nasa.gov/internal_resources/114/.

Nepal, S., Pradhananga, S., Shrestha, N. K., Kralisch, S., Shrestha, J. P., and Fink, M. (2021): Space–time variability in soil moisture droughts in the Himalayan region. *Hydrology and Earth System Sciences* 25(4):1761–1777. DOI: 10.5194/hess-25-1761-2021.

Peltier, W. R., Argus, D. F., and Drummond, R. (2018): Comment on "An Assessment of the ICE-6G_C (VM5a) Glacial Isostatic Adjustment Model" by Purcell et al. *Journal of Geophysical Research: Solid Earth* 123(2):2019–2028. DOI: 10.1002/2016JB013844.

Prevost, P., Chanard, K., Fleitout, L., Calais, E., Walwer, D., van Dam, T., and Ghil, M. (2019): Data adaptive spatio-temporal filtering of GRACE data. *Geophysical Journal International* 219(3):2034–2055. DOI: 10.1093/gji/ggz409.

Ran, J., Ditmar, P., Klees, R., et al. (2018): Statistically optimal estimation of Greenland Ice Sheet mass variations from GRACE monthly solutions using an improved mascon approach. *Journal of Geodesy* 92:299–319. DOI: 10.1007/s00190-017-1063-5.

Reddy, D., Kumar, D., Saha, D., and Mandal, M. (2008): The 18 August 2008 Kosi river breach: an evaluation. *Current Science* 95(12):1668–1671. URL: http://www.indiaenvironmentportal.org.in/files/The%2018%20August%202008%20Kosi%20river%20breach.pdf.

Sasgen, I., Martinec, Z., and Fleming, K. (2006): Wiener optimal filtering of GRACE data. *Studia Geophysica et Geodaetica* 50(4):499–508. DOI: 10.1007/s11200-006-0031-y.

Save, H., Bettadpur, S., and Tapley, B. D. (2016): High resolution CSR GRACE RL05 mascons. *J. Geophys. Res. Solid Earth* 121:7547–7569. DOI: 10.1002/2016JB013007.

Save, H., Bettadpur, S., and Tapley, B. (2012): Reducing errors in the GRACE gravity solutions using regularization. *Journal of Geodesy* 86:695–711. DOI: 10.1007/s00190-012-0548-5.

Save, H. (2020): CSR GRACE and GRACE-FO RL06 Mascon Solutions v02. DOI: 10.15781/cgq9-nh24.

Scanlon, B. R., Zhang, Z., Save, H., Wiese, D. N., Landerer, F. W., Long, D., Chen, J., Wolock, D. M., Conway, B. D., and Winester, D. (2016): Global evaluation of new GRACE mascon products for hydrologic applications. *Water Resources Research* 52(12):9412–9429. DOI: 10.1002/2016WR019494.

Schrama, E. J., Wouters, B., and Lavallée, D. A. (2007): Signal and noise in Gravity Recovery and Climate Experiment (GRACE) observed surface mass variations. *Journal of Geophysical Research: Solid Earth* 112(B8). DOI: 10.1029/2006JB004882.

Sharma, S., Hamal, K., Khadka, N., Shrestha, D., Aryal, D., and Thakuri, S. (2021): Drought characteristics over Nepal Himalaya and their relationship with climatic indices. *Meteorological Applications* 28(n/a):e1988. DOI: 10.1002/met.1988. URL: https://doi.org/10.1002/met.1988.

Shrestha, A., Dhakal, N. R., Lamsal, P. C., and Regmi, B. (2024): Water crises in a water-rich country: case studies from Nepal. *Water Policy* 21(4):826–842. DOI: 10.2166/wp.2024.040. URL: https://iwaponline.com/wp/article/21/4/826/66987/Water-crises-in-a-water-rich-country-case-studies.

Sun, Y., Riva, R., and Ditmar, P. (2016): Optimizing estimates of annual variations and trends in geocenter motion and J2 from a combination of GRACE data and geophysical models. *Journal of Geophysical Research: Solid Earth* 121. DOI: 10.1002/2016JB013073.

Swenson, S., Chambers, D., and Wahr, J. (2008): Estimating geocenter variations from a combination of GRACE and ocean model output. *Journal of Geophysical Research: Solid Earth* 113(B8):B08410. DOI: 10.1029/2007JB005338.

Swenson, S. and Wahr, J. (2006): Post-processing removal of correlated errors in GRACE data. *Geophysical Research Letters* 33(8):L08402. DOI: 10.1029/2005GL025285.

Tapley, B. D., Watkins, M. M., Flechtner, F., et al. (2019): Contributions of GRACE to understanding climate change. *Nature Climate Change* 9:358–369. DOI: 10.1038/s41558-019-0456-2.

Tapley, B. D., Bettadpur, S., Ries, J. C., Thompson, P. F., and Watkins, M. M. (2004): GRACE Measurements of Mass Variability in the Earth System. *Science* 305(5683):503–505. DOI: 10.1126/science.1099192.

Thomas, A. C., Reager, J. T., Famiglietti, J. S., and Rodell, M. (2014): A GRACE-based water storage deficit approach for hydrological drought characterization. *Geophysical Research Letters* 41(5):1537–1545. DOI: 10.1002/2014GL059323.

Vishwakarma, B. D., Horwath, M., Devaraju, B., Groh, A., and Sneeuw, N. (2017): A data-driven approach for repairing the hydrological catchment signal damage due to filtering of GRACE products. *Water Resources Research* 53:9824–9844. DOI: 10.1002/2017WR021150.

Wahr, J., Molenaar, M., and Bryan, F. (1998): Time variability of the Earth's gravity field: Hydrological and oceanic effects and their possible detection using GRACE. *Journal of Geophysical Research: Solid Earth* 103(B12):30205–30229.

Wahr, J., Swenson, S., and Velicogna, I. (2006): Accuracy of GRACE mass estimates. *Geophysical Research Letters* 33(6):L06401. DOI: 10.1029/2005GL025305.

Wahr, J., Swenson, S., Zlotnicki, V., and Velicogna, I. (2004): Time-variable gravity from GRACE: First results. *Geophysical Research Letters* 31(L11501):1–4. ISSN: 1944-8007. DOI: 10.1029/2004GL019779.

Wang, L., Davis, J. L., Hill, E. M., and Tamisiea, M. E. (2016): Stochastic filtering for determining gravity variations for decade-long time series of GRACE gravity. *J Geophys Res Solid Earth* 121(4):2915–2931. DOI: 10.1002/2015JB012650.

Wang, S., Yoon, J., Gillies, R. R., and Cho, C. (2013): What Caused the Winter Drought in Western Nepal during Recent Years? *Journal of Climate* 26(21):8241–8256. DOI: 10.1175/JCLI-D-12-00800.1.

Wang, W., Shen, Y., Chen, Q., and Chen, T. (2023): One-degree resolution mascon solution over Antarctic derived from GRACE Level-2 data. *Frontiers in Earth Science* 11:1129628. DOI: 10.3389/feart.2023.1129628.

Wang, W., Shen, Y., Chen, Q., and Wang, F. (2024): High-resolution mascon solutions reveal glacier-scale mass changes over the Greenland Ice Sheet from 2002 to 2022. *Geophys. J. Int.* 236:494–515. DOI: 10.1093/gji/ggad439.

Watkins, M. M., Wiese, D. N., Yuan, D. N., Boening, C., and Landerer, F. W. (2015): Improved methods for observing Earth's time variable mass distribution with GRACE using spherical cap mascons. *Journal of Geophysical Research: Solid Earth* 120:2648–2671. DOI: 10.1002/2014JB011547.

Wiese, D. N., Nerem, R. S., and Han, S.-C. (2011a): Expected improvements in determining continental hydrology, ice mass variations, ocean bottom pressure signals, and earthquakes using two pairs of dedicated satellites for temporal gravity recovery. *Journal of Geophysical Research* 116:B11405. DOI: 10.1029/2011JB008375.

Wiese, D., Yuan, D., Boening, C., Landerer, F., and Watkins, M. (2018): JPL GRACE Mascon Ocean, Ice, and Hydrology Equivalent Water Height Release 06 Coastal Resolution Improvement (CRI) Filtered Version 1.0. PO.DAAC, CA, USA. Version 1.0. Dataset accessed [2025-03-19] at http://dx.doi.org/10.5067/TEMSC-3MJC6. DOI: 10.5067/TEMSC-3MJC6.

Wiese, D. N., Visser, P., and Nerem, R. S. (2011b): Estimating low resolution gravity fields at short time intervals to reduce temporal aliasing errors. *Advances in Space Research* 48(6):1094–1107. ISSN: 0273-1177. DOI: 10.1016/j.asr.2011.05.027. URL: https://www.sciencedirect.com/science/article/pii/S0273117711003929.

Wouters, B. and Schrama, E. J. (2007): Improved accuracy of GRACE gravity solutions through empirical orthogonal function filtering of spherical harmonics. *Geophysical Research Letters* 34(23). DOI: 10.1029/2007GL032098.

Yan, Z. et al. (2024): Optimal Design of a Third Pair of Gravity Satellites to Augment Two Existing Polar Pairs to Enhance Earth's Temporal Gravity Field Recovery. *IEEE Journal of Selected Topics in Applied Earth Observations and Remote Sensing* 17:14145–14160. DOI: 10.1109/JSTARS.2024.3437744.

Yan, Z., Ran, J., Xiao, Y., Xu, Z., Wu, H., Deng, X.-L., et al. (2023): The temporal improvement of Earth's mass transport estimated by coupling GRACE-FO with a Chinese polar gravity satellite mission. *Journal of Geophysical Research: Solid Earth* 128:e2023JB027157. DOI: 10.1029/2023JB027157.

Yi, S. and Sneeuw, N. (2022): A novel spatial filter to reduce north–south striping noise in GRACE spherical harmonic coefficients. *Journal of Geodesy* 96:23. DOI: 10.1007/s00190-022-01614-z.

Zhang, Z.-Z., Chao, B. F., Lu, Y., and Hsu, H.-T. (2009): An effective filtering for GRACE time-variable gravity: fan filter. *Geophysical Research Letters* 36(17):L17311. DOI: 10.1029/2009GL039459.

Zhou, H., Wang, P., Tang, L., and Luo, Z. (2023): A new GRACE filtering approach based on iterative image convolution. *Journal of Geophysical Research: Solid Earth* 128:e2023JB026553. DOI: 10.1029/2023JB026553.

Accounting for VLM Signal in Level-2 GRACE Product

Bhattarai, Sudur
Remote Sensing and Geoinformatics Master of Science (M.Sc.), KIT, Germany
E-Mail: uhkmj@student.kit.edu

Abstract
The Gravity Recovery and Climate Experiment (GRACE) observes time-variable gravity signals that represent mass transport within various compartments of the Earth system, including the atmosphere, ocean, Terrestrial Water Storage (TWS) components, and the solid Earth. The signals attributable to the atmosphere and ocean are already removed by GRACE data processing centers during the conversion of satellite raw data to theLevel-2 Spherical Harmonic (SH) GRACE monthly products to avoid aliasing of these signals. However, the secular solid Earth signals associated with Vertical Land Motion (VLM) remain embedded in the GRACE SH products and must be corrected to obtain accurate TWS estimates. This VLM signal can be more precisely constrained using observations from the Global Navigation Satellite System (GNSS). In this study, multiple data-driven workflows are proposed for incorporating VLM correction into the SH product to derive the improved TWS fields, also referred to as VLM-corrected GRACE Equivalent Water Height (EWH) fields here. Theoretical analyses are made on each of these workflows to recommend a consistent way of the VLM correction in the GRACE EWH field. These workflows are further implemented in the regional case studies to demonstrate how such workflows affect the VLM-corrected GRACE EWH fields. Finally, recommendations for the consistent and accurate treatment of VLM signals in the GRACE Level-2 product for end users are provided. Last but not least, the scaling approach is used to scale the attenuated EWH field due to the leakage problem inherent in the SH solution in this research work, which is proposed to be improved in further research work.

Keywords GRACE · GRACE-FO · Total Water Storage (TWS) · SH Solution · North-South Stripping · Gaussian Filtering · Leakage Effects · Mascon Solutions · Nepal

1 Introduction

This section provides the background concepts on the GRACE and VLM, along with the objectives of this research work.

1.1 Background

The Gravity Recovery and Climate Experiment (GRACE) mission, launched on 17 March 2002, has revolutionized the understanding of large-scale mass transport in the Earth system by providing time-variable gravity field solutions from 2002 to 2017, and this record has been extended by the GRACE Follow-On (GRACE-FO) mission, operating since 22 May 2018. These gravimetric observations have been an important source of information for

KIT Scientific Working Papers
Issue Number 270
ISSN: 2194-1629
DOI: 10.5445/IR/1000191188
Online: June 2026

This document is licensed under the Creative Commons Attribution – Share Alike 4.0 International License (CC BY-SA 4.0):
https://creativecommons.org/licenses/by-sa/4.0/deed.en

several disciplines of Earth system sciences. It enables global monitoring of the terrestrial water cycle, including changes in groundwater, soil moisture, snow, and surface water, which were previously poorly constrained at basin to continental scales (Tapley et al., 2019; Rodell and Reager, 2023). This novel observation has enabled the detection and monitoring of hydrological extremes such as droughts and floods and revealed long-term trends in regional water availability that are highly relevant for water-resources management. It has also facilitated the quantification of ongoing glacier mass loss in Antarctica, Greenland, and other glaciers worldwide. Beyond the hydrosphere and cryosphere, GRACE captures gravity signals associated with solid Earth processes, including Glacial Isostatic Adjustment (GIA) and postseismic deformation following great earthquakes, which contribute to the Vertical Land Motion (VLM) signal independently constrained by Global Navigation Satellite System (GNSS) observations (Wu et al., 2010; Tapley et al., 2019; Bhattarai, 2026). It is to be further noted that the signals attributable to the atmosphere and ocean are already removed by processing centers during the conversion of satellite raw data to SH coefficients to avoid aliasing of these signals. A portion of the solid Earth signal in the GRACE data coming from GIA, and various non-GIA sources contributing to the VLM signal, must undergo VLM correction from the GRACE signal to get reliable estimates on Terrestrial Water Storage, TWS (here interchangeably referred to as the VLM corrected GRACE EWH field/signal throughout the report). This VLM corrected GRACE signal can only provide reliable estimates later on the glacier/ice mass balances (Liu and Pail, 2025; Bhattarai, 2026) and barystatic sea level change.

1.2 GRACE Concepts and its Principles

The fundamental principle behind the GRACE satellite mission is to measure the time-variable mass anomalies in the gravity field of the Earth (Humphrey et al., 2023), with their key observations of Satellite-to-Satellite Tracking (SST) in low–low and high–low mode (Murböck et al., 2023), from which total water storage anomaly (in other words: terrestrial water storage) can be detected (Tapley et al., 2004; Wahr et al., 2004).
Terrestrial water storage (TWS) is a dynamic component of the hydrological cycle (Girotto and Rowland, 2019), which can be defined as the summation of all water stored above and below the land surface. This includes surface water, soil moisture, groundwater, snow, ice, glaciers, and water stored in biomass (Girotto and Rowland, 2019; Humphrey et al., 2023).

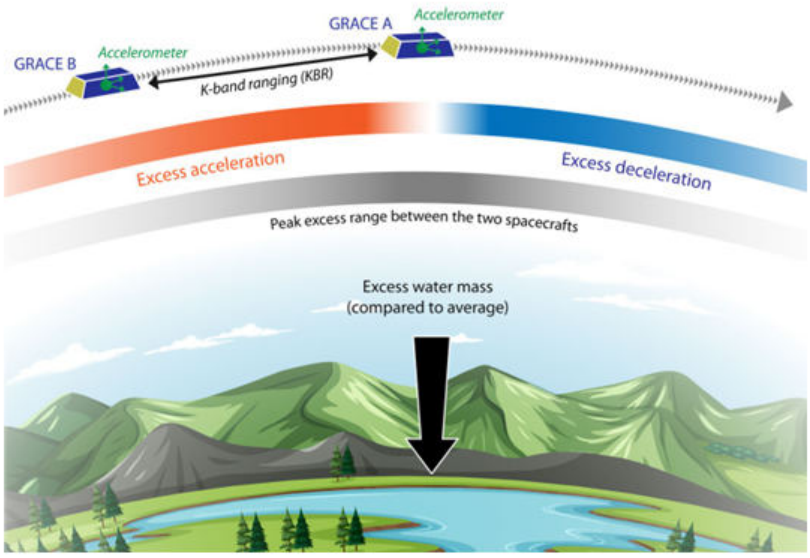

Figure 1.1: Measurement principle of the GRACE showing the twin satellite separated by the distance of approximately 220 km, at an altitude of about 500 km in tandem orbit (Humphrey et al., 2023). Please see an animation on GRACE/-FO working principle for more details.

The insight into the measurement principle of the GRACE satellite mission is given by Figure 1.1. During the trajectory of the GRACE satellites, whenever the satellite passes through the region with an excess mass, the gravitational attraction is stronger, causing the leading satellite to accelerate towards the positive mass anomaly. Consequently, the separation between the satellites increases until the trailing satellite catches up. These variations in the distance between the satellites can be used to infer the time-variable mass changes at the Earth's surface at the local, regional, or global level at the end (Humphrey et al., 2023).
GRACE estimates mass anomalies relative to the long-term average gravity field (Humphrey et al., 2023), which is saturated from the monthly solutions, to produce the TWS anomaly map (Girotto and Rowland, 2019). In other words, GRACE provides estimates of total water storage anomalies $(\mathrm{TWSA} = \mathrm{TWS} - \overline{\mathrm{TWS}})$. Neither the total amount of TWS nor its long-term average ($\overline{\mathrm{TWS}}$) can be measured with GRACE (Humphrey et al., 2023).
To measure the total water storage anomalies with GRACE satellites, they are equipped with three-dimensional accelerometers to measure atmospheric drag and other non-gravitational accelerations (ESA, 2025). The range between the two satellites is measured with a K-band microwave interferometer with a precision of about $1\mu m$. This range can be detected with the precision of nanometers with a laser ranging instrument in the case of GRACE Follow-On (Hauk, 2023; GFZ, 2026). GPS receivers and star cameras are used for precise orbit determination and attitude control, enabling accurate gravitational field measurements (eoPortal, 2023; ESA, 2025).
The monthly analysis of the range and range-rate measurements between the two satellites provides the temporal variations (i.e., anomalies) of the gravity field (Girotto and Rowland, 2019; Humphrey et al., 2023). GRACE estimates the terrestrial water storage anomalies in the form of different solutions.

1.3 GRACE Solutions

Two primary solutions have emerged for processing GRACE data: spherical harmonic (SH) solutions and mass concentration (mascon) solutions. SH representations have been extensively used to represent the variations in the Earth's gravity field for decades (Chen et al., 2022). They represent the gravity field as a series of Stokes coefficients. The so-called low-degree and low-order coefficients of these spherical harmonics represent large-scale features, like the Earth's oblateness, while higher-degree and higher-order coefficients represent increasingly finer spatial scale features. There is an upper limit to the number of coefficients that can be robustly estimated with a given set of GRACE measurements. With a month's worth of GRACE measurements, it is generally accepted that one can reliably estimate spherical harmonic coefficients up to a degree and order of at least 60. This number puts a hard limit on the resulting spatial resolution of the mass change estimates, at about 330×330 km^2. At the higher degree/order 120, with the aim of including more detailed spatial features, resolution would be about 160 km after including a higher number of less robust coefficients. This will, as a result, increase the uncertainty of the solution and lead to a much higher level of noise (Humphrey et al., 2023).
The application of the SH solutions from GRACE/-FO data faces north-south striping problems (Swenson and Wahr, 2006). These issues primarily stem from temporal aliasing (Wiese et al., 2011b) and the design of satellite orbits and tracking systems (Wiese et al., 2011a), including factors like inclination, altitude, inter-satellite distance, and the co-planar low-low satellite-to-satellite tracking system. Conventional approaches for addressing these problems include empirical smoothing (Wahr et al., 1998), de-striping (Swenson and Wahr, 2006), applying non-isotropic smoothing by approximate decorrelation and regularization kernels (Kusche, 2007), and regularization techniques (Save et al., 2012). While these approaches are generally effective in preserving signals and reducing noise, it's crucial to recognize that eliminating stripes also reduces the genuine geophysical signals (Han et al., 2005; Yi and Sneeuw, 2022; Zhou et al., 2023) and induces a leakage effect (Chen et al., 2021; Klees et al., 2008) in the coastal zones. Additionally, the effectiveness of de-striping is significantly influenced by signal characteristics such as size, shape, and orientation (Watkins et al., 2015). It's noteworthy that the impact of aliasing errors can be mitigated through the combination of gravity satellite formations in optimal constellation configurations (Yan et al., 2024) or by recovering the temporal gravity field at higher temporal resolutions (Yan et al., 2023).

The so-called mass concentration (mascon) solutions serve as an alternative for representing the GRACE data and mass anomalies. A mascon corresponds to a small, predefined region on the Earth's surface, for instance, a 3° rectangular grid cell. Mascon solution does not represent a global gravity field like spherical harmonic solutions, but rather it quantifies mass anomalies at the local level. Using 'mascon' solutions, one can implement geophysical constraints much more easily. These a priori constraints help to filter out noise from the GRACE/-FO observations at the Level-2 processing step, which is a much more rigorous approach than the empirical post-processing filtering applied to land and ocean grids derived from spherical harmonics (Wiese et al., 2018). Furthermore, mascon products are also easier to use in general as they do not need to be spatially filtered (smoothed) during postprocessing. This is because some (geophysically motivated) spatial information is explicitly guiding the retrieval of the mascon solution, thus greatly reducing the spatial noise patterns (Humphrey et al., 2023). However, it is to be further noted that the VLM correction in the GRACE signal is limited to only the SH solution with respect to this Lab Rotation-II.

1.4 Vertical Land Motion

Vertical Land Motion (VLM) is the uplift and subsidence of the Earth's surface relative to a fixed reference point, such as mean sea level or a stable geodetic benchmark (CSD, 2026). It is the vertical displacement of the ground caused by various natural and human-induced processes.

One of the primary natural causes of VLM is Glacial Isostatic Adjustment (GIA), which is the Earth's crust rebounding in response to the melting of massive ice sheets since the Last Glacial Maximum (LGM) about 21,000 years ago. This ongoing process causes land previously compressed by ice to slowly rise, sometimes exceeding uplift rates of 10 millimeters per year in formerly glaciated regions. Similarly, other regions may experience subsidence as the Earth adjusts to changes in mass distribution, for example, by loading/unloading of ice and water (CSD, 2026). Tectonic activity is another major driver, as the movement and interaction of tectonic plates induce vertical displacements. Around plate boundaries, seismic and volcanic events can cause sudden vertical shifts (coseismic VLM) of tens of centimeters, followed by post-seismic adjustments over years to decades. Interseismic periods exhibit slower VLM on the order of millimeters per year caused by accumulated tectonic stresses. Mantle convection and internal Earth dynamics also contribute to vertical motion at longer time-scales and larger spatial extents (Pfeffer et al., 2017). Human activities significantly influence VLM, especially through the extraction of groundwater, oil, and gas. Removing subsurface fluids causes sediment compaction, resulting in land subsidence, which can lead to local VLM rates much higher than natural uplift processes. This is particularly critical in urban and deltaic regions where heavy groundwater use accelerates sinking (Pfeffer et al., 2017; Hensel et al., 2024; NASA, 2025). Other contributors include sediment deposition and erosion, which affect land elevation, particularly in deltaic environments. Sediment accumulation increases load, causing subsidence, while erosion removes the load, potentially leading to uplift (Hensel et al., 2024). Therefore, VLM captures a broader spectrum of natural and anthropogenic deformation processes – including, but not limited to, the GIA signal alone.

Quantifying VLM requires sophisticated techniques. Geodetic methods, such as Global Navigation Satellite System (GNSS), provide highly precise measurements of ground elevation changes over time. Continuous GNSS stations offer long-term records of absolute vertical motion relative to the Earth's center of mass. This offers a direct delineation of land movement (CSD, 2026). Interferometric Synthetic Aperture Radar (InSAR) is another powerful tool, using satellite radar images taken at different times to detect ground surface deformation over large areas with millimeter-scale precision. InSAR is particularly effective at mapping spatial patterns of subsidence or uplift associated with groundwater extraction, mining, or volcanic activity (Hensel et al., 2024). Traditional surveying techniques and tide gauges also provide valuable, albeit often less spatially extensive, data. Tide gauges measure sea level relative to the land surface at a specific point; comparing tide gauge records with independent measurements of absolute sea level (e.g., from satellite altimetry) allows for the isolation of the local VLM signal (CSD, 2026; Pfeffer et al., 2017).

1.5 Objectives of This Lab Rotation Research Work

The specific objective and general objectives of this study are further explained in this section.

1.5.1 Specific Objective

i. To document the consistent treatment of accounting VLM signal in GRACE product and to examine the errors arising from inconsistent VLM treatment.

1.5.2 General Objectives

i. To correct the leakage problem in the SH solution, which resulted from the truncation of the SH series expansion, and applied Gaussian filter to suppress the remaining noise.
ii. To discuss the limitations of this Lab Rotation research work and outline directions for future research building on this work.

2 Data Used

The Level-2 SH solutions from (JPL, 2026), that are available for the time spans April 2002 through March 2016, are used in this study. The JPL SH solutions are computed using the classical variation approach (or dynamic approach). The SH solutions up to degree and order (d/o) 96 in this work are used. Also, the interpolated Vertical Land Motion (VLM) dataset produced by the Nevada Geodetic Laboratory (NGL, 2026) is utilized. This dataset provides global VLM rates, excluding Greenland and Antarctica, derived through GPS imaging, based on a comprehensive compilation of uniformly processed GPS solutions aligned to the International Terrestrial Reference Frame (ITRF) (see Hammond et al. (2021), for more details). The VLM rates estimated by NGL represent the combined contributions of GIA and non-GIA processes, including tectonic uplift, post-glacial rebound signals, and the elastic response to contemporary surface mass changes.

3 Theoretical Aspects

This section presents the theories on the synthesis of the SH solution, SH analysis, along with the post-processing workflow applied to this solution to derive the VLM corrected GRACE field. The theories on the various possible workflows of the VLM correction in the GRACE field are also discussed here.

3.1 Synthesis of Spherical Harmonic Solutions

Spherical Harmonic Synthesis (SHS) is the forward computation of a function on or outside a sphere (of radius a) from a series of surface spherical harmonics (Heiskanen and Moritz, 1967). In geodesy, these SH solutions are expressed in terms of SH coefficients, which can be further synthesized in terms of surface mass density at geocentric co-latitude θ and longitude λ as described by Wahr et al. (1998) and Ditmar (2018):

$$\Delta\sigma(\theta,\lambda) = \frac{M_E}{4\pi a^2} \sum_{n=2}^{N} \sum_{m=0}^{n} \frac{2n+1}{1+k_n} \bar{P}_{nm}(\cos\theta) \left(\Delta\bar{C}_{nm}\cos(m\lambda) + \Delta\bar{S}_{nm}\sin(m\lambda)\right), \tag{3.1}$$

where M_E is Earth's mass (5.9722×10^{24} kg), a is the Earth's equatorial radius (6,378,137 m), N is the maximum spherical harmonic degree in the exploited GRACE data product (which is 96 in this study). $\bar{P}_{nm}$ are fully normalized associated Legendre functions of argument $\cos\theta$ at degree n and order m. $\Delta\bar{C}_{nm}$ and $\Delta\bar{S}_{nm}$ are the Stokes coefficient anomalies in respect to a reference solution as mentioned in Section 1.2. k_n are load Love numbers accounting for the change in gravity caused by the load-induced VLM (Wahr et al., 1998); for example, the elastic load Love numbers are computed by Han and Wahr 1995 for the Earth model PREM (Preliminary Reference Earth model).

Because the GRACE twin satellites are unable to observe degree-1 Stokes coefficients, the spherical harmonic expansion in Eq. (3.1) begins from degree 2. It is worth noting that the surface mass density unit kg/m^2 and mm equivalent water height (mm water equivalent) are numerically identical. For more information about the derivation of the equivalent height, see Appendix A.

3.2 Spherical Harmonic Analysis

Spherical Harmonic Analysis (SHA) inverts surface data on a sphere into the SH coefficients representing harmonic functions like Earth's gravity field. Regarding the land-uplift signal, Purcell et al. (2011) provides a relationship to transform the geometric uplift dr measured by GNSS into an equivalent gravity signal observed by GRACE, expressed in terms of Stokes coefficients in the SH domain:

$$\left\{ \begin{array}{c} \Delta\bar{C}_{nm} \\ \Delta\bar{S}_{nm} \end{array} \right\} = \frac{1}{4\pi} \frac{1}{a} \frac{k'_n}{h'_n} \sum_{i=1}^{I} \sum_{j=1}^{J} dr(\theta^i, \lambda^j) \bar{P}_{nm}(\cos\theta^i) \left\{ \begin{array}{c} \cos(m\lambda^j) \\ \sin(m\lambda^j) \end{array} \right\} \sin\theta^i \Delta\theta \Delta\lambda, \tag{3.2}$$

where the ratio k'_n/h'_n defines how changes in the geopotential are related to vertical displacements in the viscoelastic context. The parameters I and J are the numbers of longitudes and latitudes in the spatial grid, while $\Delta\theta$ and $\Delta\lambda$ denote the grid resolutions in latitude and longitude. Here, the conversion between long-term (secular) uplift rates and their corresponding gravity effects is assumed to be valid for the entire vertical deformation signal – also referred to as the VLM signal – measured by GNSS (only on land).

3.3 Post-processing of Spherical Harmonic Solutions

The scheme of the data post-processing used in this lab rotation to quantify VLM corrected GRACE EWH field-/signal from Level-2 SH solution is shown in Figure 3.1. The processing includes the following:

- The degree-1 coefficients (Geocenter) are added to the GRACE field to consider the movement of the Earth's center of mass, relative to the modeled atmosphere and ocean degree-1 coefficients (e.g., GAC and GAD) via Technical Note-13 (Swenson et al., 2008), to include the effects of the barystatic sea level fingerprint in the ocean mass contribution to degree-1 (Sun et al., 2016).

- The lowest degree zonal harmonic coefficients, C_{20} and C_{30} are replaced by the coefficients derived from Satellite Laser Ranging (SLR) data via Technical Note TN-14 (Loomis et al., 2020).

- The long-term, i.e., 2004-2010 mean of the SHs is subtracted as a representative of the static gravity field to get the residual SH coefficients (Vishwakarma et al., 2022).

Thus obtained spherical harmonic solution, when employed to derive the map of the GRACE EWH field (cf. Figure 3.2), is corrupted by north-south striping, and no clear signal can be viewed over medium and low latitudes. This is due to the correlated noise at higher degrees, which arises from the geometric configuration of the polar-type GRACE satellite mission (Chen et al., 2021). Additionally, temporal aliasing caused by imperfect background models and the sampling frequency introduces errors into the solution. Furthermore, the GRACE-FO level-2 SH coefficients are affected by instrument noise, resulting from orbital errors, star camera issues, accelerometer data, and noise in the K-band ranging system. These errors appear as distinct north-south striping patterns (Swenson and Wahr, 2006; Chen et al., 2021; Wahr et al., 2006). In order to further investigate any geophysical signal from the solution, such noises need to be removed or suppressed in the solution. There is a trade-off between resolution and noise, meaning that higher (or lower) degrees of spherical harmonic coefficients result in larger (or smaller) errors during mission design. To reduce the noise, a straightforward approach would be to truncate the spherical harmonic series around degrees 20–30. However, for applications requiring high spatial resolution, such as hydrology, glaciology and solid Earth dynamics, the monthly results tend to contain significant noise.

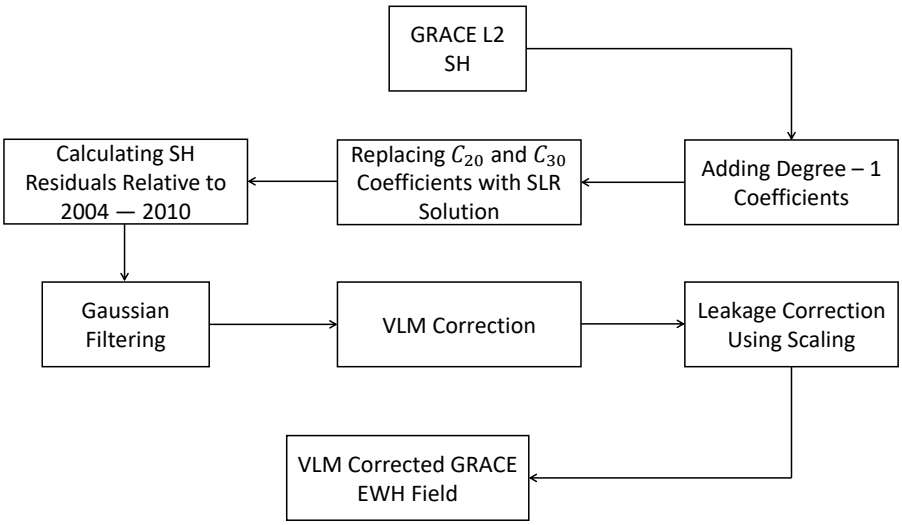

Figure 3.1: General workflow to obtain VLM corrected GRACE EWH field/signal from the GRACE Level-2 solution used.

Several filters have been developed to reduce or suppress the noise in the GRACE/-FO solutions. Wahr et al. (1998) utilized the low-pass isotropic Gaussian smoothing operator developed by Jekeli (1981) as the spatial filter. The idea of the Jekeli (1981) was further extended to develop into an anisotropic version by Han et al. (2005) and Zhang et al. (2009). Other examples of the spectral filter include the Wiener filter (Klees et al., 2008; Sasgen et al., 2006), the Deterministic Decorrelation Kernel (DDK) filter (Kusche, 2007; Kusche et al., 2009), and the regularization filter (Devaraju and Sneeuw, 2017). Swenson and Wahr (2006) developed a de-striping filter by smoothing the spherical harmonic coefficients for a particular order m with a polynomial of order p using least squares estimation. Following Swenson and Wahr (2006) several filters have been developed which investigate such a pattern in the unconstrained solutions (Chambers, 2006; Chen et al., 2007; Duan et al., 2009). These filters are mostly followed by a spatial filter like a Gaussian filter to reduce the remaining noise. Other categories of filters include temporal filters such as the Empirical Orthogonal Function (EOF) filter (Schrama et al., 2007; Wouters and Schrama, 2007), the stochastic filter (Wang et al., 2016), the

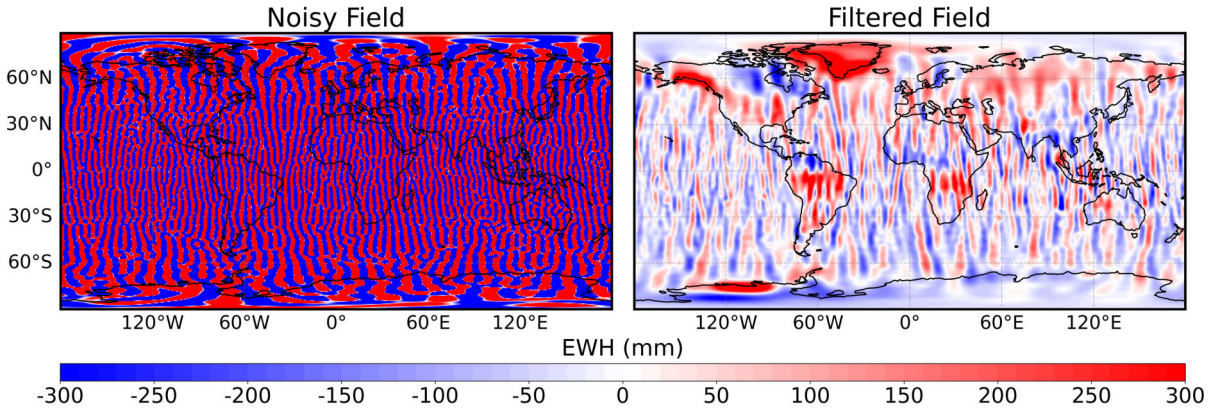

Figure 3.2: Illustrative example of GRACE EWH field expressed in mm EWH obtained before and after filtering. Left panel: Noisy field is obtained with 0 km Gaussian filtering, while the filtered field (right panel) is obtained with 300 km Gaussian filtering. The shown EWH field has not been corrected for leakage, and no VLM correction has been applied. Dataset used: JPL SH solution for the time period April 2002.

SSA filter (Prevost et al., 2019), or the least square filter (Crowley and Huang, 2020). The temporal filters regard the north-south striping as the white/stochastic noise and suggest that this random signal can be identified as the

time information grows (Yi and Sneeuw, 2022). It is noteworthy to mention that users can freely choose a suitable filter based on the demands of their application.

Here, a Gaussian smoothing filter is applied to suppress the overwhelming north-south striping noises in this study. Gaussian smoothing – being a linear operation – is more straightforward to evaluate in contrast to other filters. The Gaussian low-pass filtering is typically implemented by applying predetermined weights to each SH coefficient, followed by the inversion of these coefficients to get the EWH field in the spatial domain. Thus, the consequence at the end is the filtering of the EWH field in the spatial domain.

Following Jekeli (1981), the Gaussian-filtered field can be expressed by modifying Eq. (3.1) as follows (Wahr et al., 1998):

$$\Delta\sigma(\theta,\lambda) = \frac{M_E}{4\pi a^2}\sum_{n=2}^{N}\frac{2n+1}{1+k_n}\sum_{m=0}^{n} W_n \bar{P}_{nm}(\cos\theta)\left(\Delta\bar{C}_{nm}\cos(m\lambda)+\Delta\bar{S}_{nm}\sin(m\lambda)\right), \tag{3.3}$$

where $W_n = W_n(R)$ is the normalized Gaussian weighting function (with a maximum weight of 1), dependent on a chosen averaging radius (R).

The degree dependent weights W_n reduces contributions from high-degree and order SH coefficients. The same weight W_n is applied to all orders of SH coefficients at each degree (n), equivalent to spatial domain convolution with a circular Gaussian-shaped filter. Radius R corresponds to the distance at which the convolution operator drops to half of its peak value (Wahr et al., 1998). Gaussian weights as functions of degree $\boldsymbol{n}$ and radius (R) are defined recursively:

$$\begin{aligned} W_0 &= 1, \\ W_1 &= \frac{1+e^{-2b}}{1-e^{-2b}} - \frac{1}{b}, \\ W_{n+1} &= -\frac{2n+1}{b}\cdot W_n + W_{n-1} \end{aligned} \tag{3.4}$$

$$b = \frac{\ln(2)}{1-\cos(R/a)}. \tag{3.5}$$

It should be noted that Eq. (3.4) and Eq. (3.5) are similar to Eqs. 32 – 34 of Wahr et al. (1998), but differ in normalization by a factor of 2.

In this study, the SH series is truncated at degree and order 96, which corresponds to an approximate spatial resolution of 200 km at the equator. These SH series are further applied with Gaussian filtering to suppress the remaining noises after truncation, with a filter radius of 300 km to comply with the so-called gain/scale factors that are used to restore the attenuated signals (detailed below), which, as a result, reduces the effective spatial resolution of the GRACE gravity field to about 300 km at the equator.

Since GRACE suffers from vertical resolution, it is unable to disentangle the mass-change signals arising from solid Earth processes from those associated with terrestrial water storage variations. Moreover, the cumulative effects of all solid Earth processes are intrinsically incorporated into the GRACE observations. To obtain an accurate representation of terrestrial water storage variability, these solid Earth contributions must be removed through appropriate correction procedures.

3.4 Various Possible Workflows of Accounting for VLM Correction in GRACE EWH Field

In this section, the various workflows for applying VLM correction to remove the solid Earth signal from the GRACE Level-2 product are presented. Within the scope of this study, these workflows are tested using the JPL Level-2 product; however, it should be noted that they are also applicable to other GRACE Level-2 datasets as well. In particular, different workflows for correcting the secular component of the GRACE EWH field are evaluated by accounting for VLM in multiple ways (as described below), as illustrated in the Figures 3.3 – 3.6, given that

only secular VLM estimates are available rather than a monthly VLM time series from the GNSS data used. Furthermore, the potential errors arising from the inconsistent treatment of VLM within this GRACE product are examined.

In **option (A)** (Figure 3.3), the secular VLM Stokes coefficients ($\Delta\dot{\bar{C}}_{VLM,nm}$ and $\Delta\dot{\bar{S}}_{VLM,nm}$) are respectively subtracted from secular GRACE Stokes coefficients ($\Delta\dot{\bar{C}}_{nm}$ and $\Delta\dot{\bar{S}}_{nm}$) in the SH domain; with an assumption that all the solid Earth signals captured by the secular GRACE Stokes coefficients are captured by the secular VLM Stokes coefficients. Thus obtained secular VLM corrected GRACE Stokes coefficients when using Eq. (3.3) dropping k_n give the VLM corrected GRACE estimates in terms of the secular trend. On the other side, the monthly non-secular GRACE EWH field is computed as explained by Bhattarai (2026), whereby the monthly detrended GRACE Stokes are computed and Eq. (3.3) is used keeping k_n (Wahr et al., 1998) to capture the non-secular solid Earth signal induced by contemporary surface load. For the non-secular part, VLM has to be eliminated one way or the other, as a monthly VLM solution is not available. Then, a very reasonable assumption can be invoked that only the non-secular contemporary surface loading would induce non-secular monthly VLM. Thus, the non-secular GRACE EWH field, i.e., $\Delta\tilde{\sigma}(\theta,\lambda,t)$ (obtained by the same ways in all options), is added to the monthly EWH field generated from the VLM corrected secular GRACE EWH field from option (A), i.e., ($\Delta\dot{\sigma}_a(\theta,\lambda)$) to obtain a time variable monthly VLM corrected GRACE EWH field given by:

$$\Delta\sigma_A(\theta,\lambda,t) = \Delta\dot{\sigma}_a(\theta,\lambda)\cdot(t-t_0) + \Delta\tilde{\sigma}(\theta,\lambda,t), \tag{3.6}$$

where t is any epoch of time, while t_0 is the reference time period (epoch), say 2006-12-31, for the baseline time period adopted here (from 2004-01 to 2010-12) in this research work. However, it is to be noted that this option (A) for the VLM correction in the GRACE EWH field requires expertise to process data in the SH domain at the user-end and provides no flexibility to the users who wish to process data in the spatial domain.

Therefore, options (B), (C), and (D) are opted for by Level-3 users, who wish to correct VLM in the GRACE EWH field in the spatial domain.

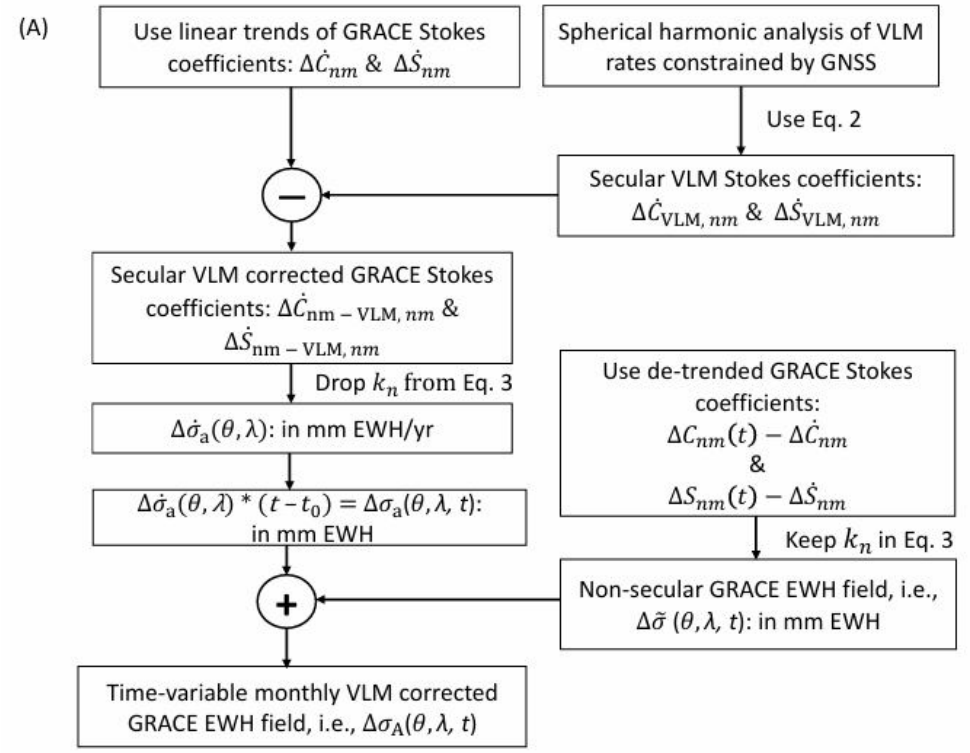

Figure 3.3: Option (A) of accounting VLM signal in GRACE products. In the flowchart, t is any epoch of time, while t_0 is the reference time period, say 2006-12-31, for the baseline time period we adopted here (from 2004-01 to 2010-12) in this research work.

Option (B) (Figure 3.4) is similar to the workflow for the VLM correction in the GRACE EWH field as adopted by Bhattarai (2026), where secular VLM EWH field is obtained by keeping k_n in Eq. (3.3) (Wahr et al., 1998) using secular VLM Stokes coefficients. This secular VLM EWH field is subtracted from the secular GRACE EWH field (obtained by using secular GRACE Stokes coefficients, dropping k_n in Eq. (3.3)) to get the secular VLM corrected GRACE EWH field from option (B), i.e., $\Delta\dot{\sigma}_b(\theta,\lambda)$. Thus, the time-variable monthly VLM corrected GRACE EWH field from option (B) is obtained by:

$$\Delta\sigma_B(\theta,\lambda,t) = \Delta\dot{\sigma}_b(\theta,\lambda)\cdot(t-t_0) + \Delta\tilde{\sigma}(\theta,\lambda,t)\,. \tag{3.7}$$

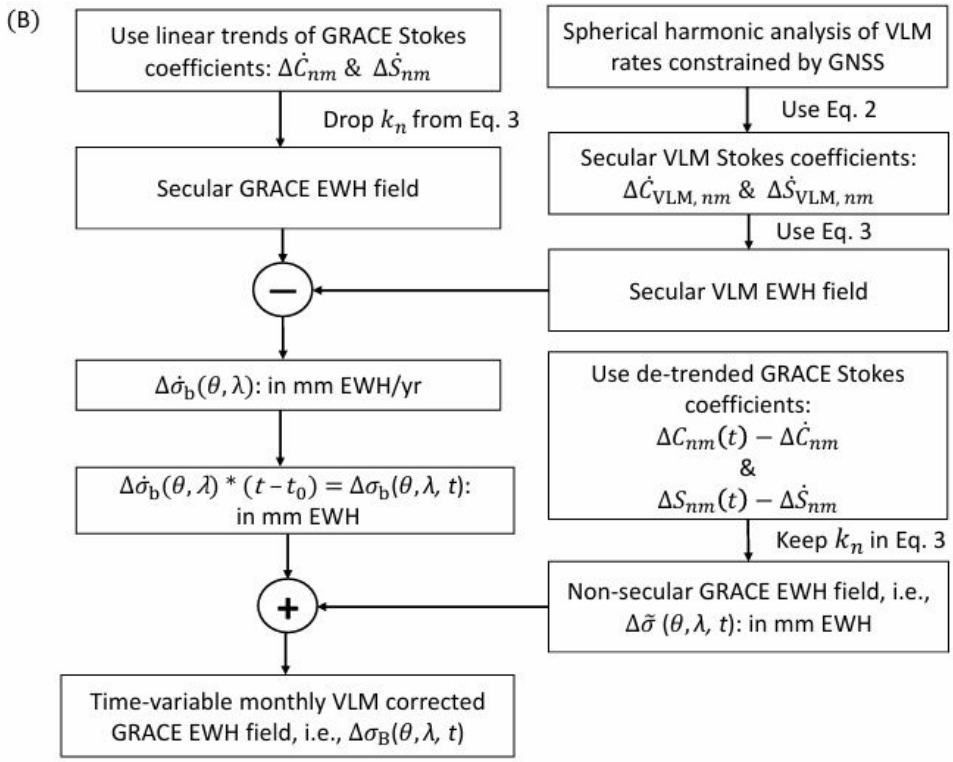

Figure 3.4: Option (B) of accounting VLM signal in GRACE products. In the flowchart, t is any epoch of time, while t_0 is the reference time period, say 2006-12-31, for the baseline time period we adopted here (from 2004-01 to 2010-12) in this research work.

In **option (C)** (Figure 3.5), secular VLM Stokes coefficients are plugged in Eq. (3.3), dropping k_n from the same equation to obtain secular VLM EWH field; while on the other page, the secular GRACE EWH field is computed, dropping k_n and plugging this secular GRACE Stokes coefficients in Eq. (3.3). Thus, the obtained secular VLM EWH field is subtracted from the secular GRACE EWH field as illustrated in option (C) in Figure 3.5 to get the VLM corrected secular GRACE EWH field. This VLM corrected secular GRACE EWH field is equivalent to the one computed by plugging secular VLM corrected GRACE Stokes coefficients, dropping k_n in Eq. (3.3) in option (A). The first VLM corrected secular GRACE EWH field is computed in the spatial domain, while the latter field in option (A) is computed by correcting the VLM signal in the SH domain to obtain a secular VLM corrected GRACE EWH field in the spatial domain. Then, the time-variable monthly VLM corrected GRACE EWH field is computed by adding the non-secular GRACE EWH field to the monthly EWH field obtained from the VLM corrected secular GRACE EWH field ($\Delta\dot{\sigma}_c(\theta,\lambda)$), as shown in the flowchart in the Figure 3.5 from option (C) as:

$$\Delta\sigma_C(\theta,\lambda,t) = \Delta\dot{\sigma}_c(\theta,\lambda)\cdot(t-t_0) + \Delta\tilde{\sigma}(\theta,\lambda,t)\,. \tag{3.8}$$

As secular VLM corrected GRACE EWH field from option (A) and option (C) are equivalent, and the non-secular GRACE EWH field is computed in the same ways in all the options; time variable monthly VLM corrected GRACE EWH field from option (A) and (C) are thus equivalent.

In **option (D)** (Figure 3.6), we follow everything as we do in option (B), except using k_n, when plugging the secular GRACE Stokes coefficients in Eq. (3.3) to get the Secular GRACE EWH field. Thus, the time-variable monthly VLM corrected GRACE EWH field from option (D) is given by:

$$\Delta\sigma_D(\theta,\lambda,t) = \Delta\dot{\sigma}_d(\theta,\lambda)\cdot(t-t_0) + \Delta\tilde{\sigma}(\theta,\lambda,t)\,, \tag{3.9}$$

where, $\Delta\dot{\sigma}_d(\theta,\lambda)$ is the secular VLM corrected GRACE EWH field from the option (D).

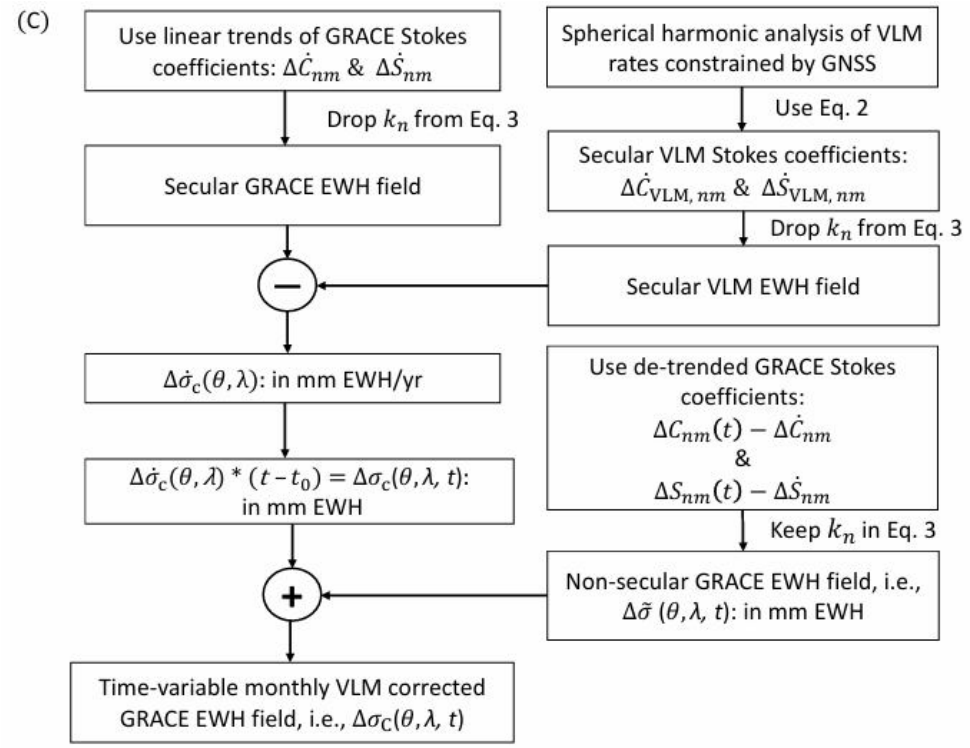

Figure 3.5: Option (C) of accounting VLM signal in GRACE products. In the flowchart, t is any epoch of time, while t_0 is the reference time period, say 2006-12-31, for the baseline time period we adopted here (from 2004-01 to 2010-12) in this research work.

Thus obtained time-variable monthly VLM corrected GRACE EWH field (terrestrial water storage signal) from the different options as shown in Figure 3.3-Figure 3.6 suffers from the signal attenuation due to the GRACE mission's limited spatial resolution, truncation of spherical harmonics (up to degree and order 96), and the spatial filtering applied to Level-2 GSM Stokes coefficients. Moreover, continental water storage signals can leak into adjacent oceanic and surrounding regions, which significantly attenuates water storage signals within the region of interest. In addition, the surrounding signals can possibly leak into the region of interest. This spatial leakage poses a particular challenge when estimating the mass change signal, which, as a result, may bias the estimates. To obtain reliable mass change estimates from GRACE observations, these leakage effects must be mitigated.
While this scaling factor was previously applied only to option (B) by Bhattarai (2026), in this study, its application is extended to all time-variable monthly VLM corrected GRACE EWH field obtained from all options. This gridded scaling factor developed using the Community Land Model Version 4 hydrological model (CLML4, 2026).

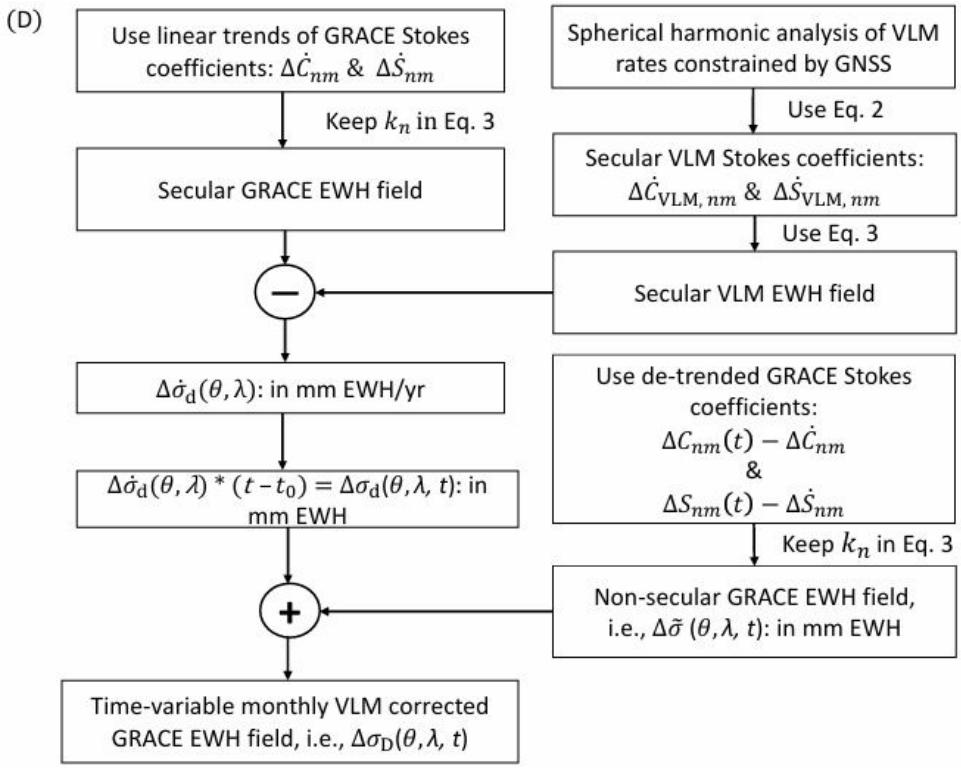

Figure 3.6: Option (D) of accounting VLM signal in GRACE products. In the flowchart, t is any epoch of time, while t_0 is the reference time period, say 2006-12-31, for the baseline time period we adopted here (from 2004-01 to 2010-12) in this research work.

The illustration of the gridded gain/scaling factor developed by Landerer and Swenson 2012, true mass, apparent mass, and leakage mass using this scale factor is shown in Figure 3.7. It is to be noted that the VLM correction workflow is used as shown in the option (B) to correct the VLM signal in the GRACE EWH field in this plot. The reason to use this VLM correction workflow is further demonstrated in the sub-section 4.1.

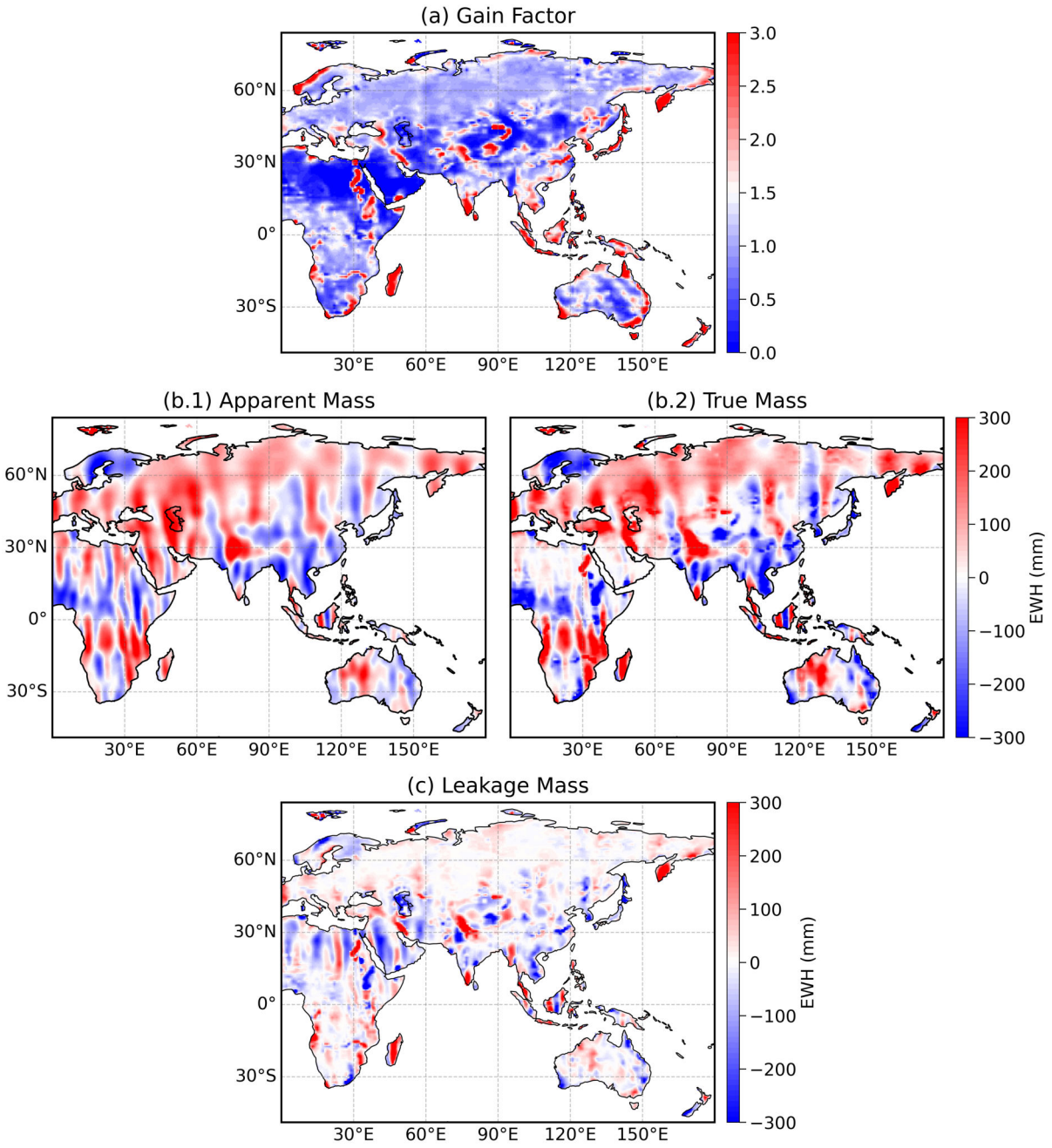

Figure 3.7: (a) Applied gain/scaling factor in this research work (top row). (b.1) Apparent mass with the VLM correction workflow from option B, as shown in Figure 3.4; while (b.2) is obtained by multiplying the gain factor shown in panel (a) with apparent mass (b.1). Panel (c) shows the difference between (b.2) and (b.1) and is termed as leakage mass. The mass in panels (b1) and (b2) is based on JPL SH solutions for April 2002.

4 Results and Discussion

In this section, the errors due to inconsistent VLM correction with respect to the correct way for the consistent VLM correction are presented through regional case studies.

4.1 Errors Due to Inconsistent VLM Correction

In this sub-section, each option of the VLM correction in the GRACE EWH field as shown in the flowchart in the Figures 3.3-3.6 is diagnosed, then a consistent way of accounting for the VLM signal in the GRACE EWH field is suggested. To illustrate the error due to the inconsistent treatment of VLM, the Level-2 SH solution from the JPL and the VLM rates published by NGL are taken. All the post-processing workflow for the SH solution is followed as explained in Section 3.3.

Here, why option (B) is the correct way for the consistent treatment of the VLM signal in the GRACE Level-2 product is explained first, followed by why other options fail to consistently account for the VLM signal. Cautions should be taken to make VLM correction in the GRACE solution, because GNSS captures almost all the solid Earth processes. On one hand and on the other hand, the vertical deformation due to the contemporary surface loading is already accounted for in the "secular" GNSS-constrained VLM solution and hence in secular VLM Stokes coefficients. Thus, it is justified to model the secular GRACE Stokes coefficients assuming the concept of the rigid Earth as described in Bhattarai (2026) without modeling k_n. To model the non-secular VLM signal, k_n has to be included to transform secular VLM Stokes coefficients to secular VLM EWH field. Moreover, if it is assumed that the (long-term) solid Earth signal, for example, Glacial Isostatic Adjustment (GIA) signal, is modeled by $\Delta\dot{C}_{nm}$ and $\Delta\dot{S}_{nm}$, then a reasonable assumption can be invoked that $\Delta C_{nm}(t) - \Delta\dot{C}_{nm}$ and $\Delta S_{nm}(t) - \Delta\dot{S}_{nm}$ models the non-secular signal as described in Bhattarai 2026. Therefore, option (B) is the correct way for the consistent treatment of the VLM signal in the SH products.

Option (A) and option (C), which give the same time-variable monthly VLM corrected GRACE EWH field, fail to correct for the contemporary loading due to the VLM trend (CLVT). The VLM correction done in the SH domain fails to correct CLVT, as secular VLM Stokes coefficients ($\Delta\dot{C}_{VLM,nm}$, $\Delta\dot{S}_{VLM,nm}$) are directly subtracted from secular GRACE Stokes coefficients ($\Delta\dot{C}_{nm}$, $\Delta\dot{S}_{nm}$) without modeling (correcting) CLVT. This introduces bias in the time-variable monthly VLM corrected GRACE EWH field (i.e., $\Delta\sigma_A(\theta,\lambda,t)$) from option (A). On one hand, and on the other hand, k_n, which characterizes CLVT is dropped from Eq. (3.3) when modeling secular VLM Stokes coefficients to get secular VLM EWH field in option (C); thus obtained (biased) secular VLM EWH field is subtracted from secular GRACE EWH field, resulting in the biased VLM corrected secular GRACE EWH field and subsequently time-variable monthly VLM corrected GRACE EWH field, i.e., $\Delta\sigma_C(\theta,\lambda,t)$.

In option (D), everything is the same as the workflow that is followed in option (B), except keeping k_n in Eq. (3.3) when modeling the secular GRACE Stokes coefficients. This consequently biases the secular GRACE EWH field estimates, as the vertical deformation due to the contemporary surface loading arising from the secular GRACE Stokes coefficients is already accounted for in the secular VLM rates and hence in the secular VLM Stokes coefficients. Therefore, keeping k_n in Eq. (3.3) when modeling the secular GRACE Stokes coefficients to get the secular GRACE EWH field gives an extra contemporary surface loading due to the secular GRACE EWH field, which fails to be corrected for.

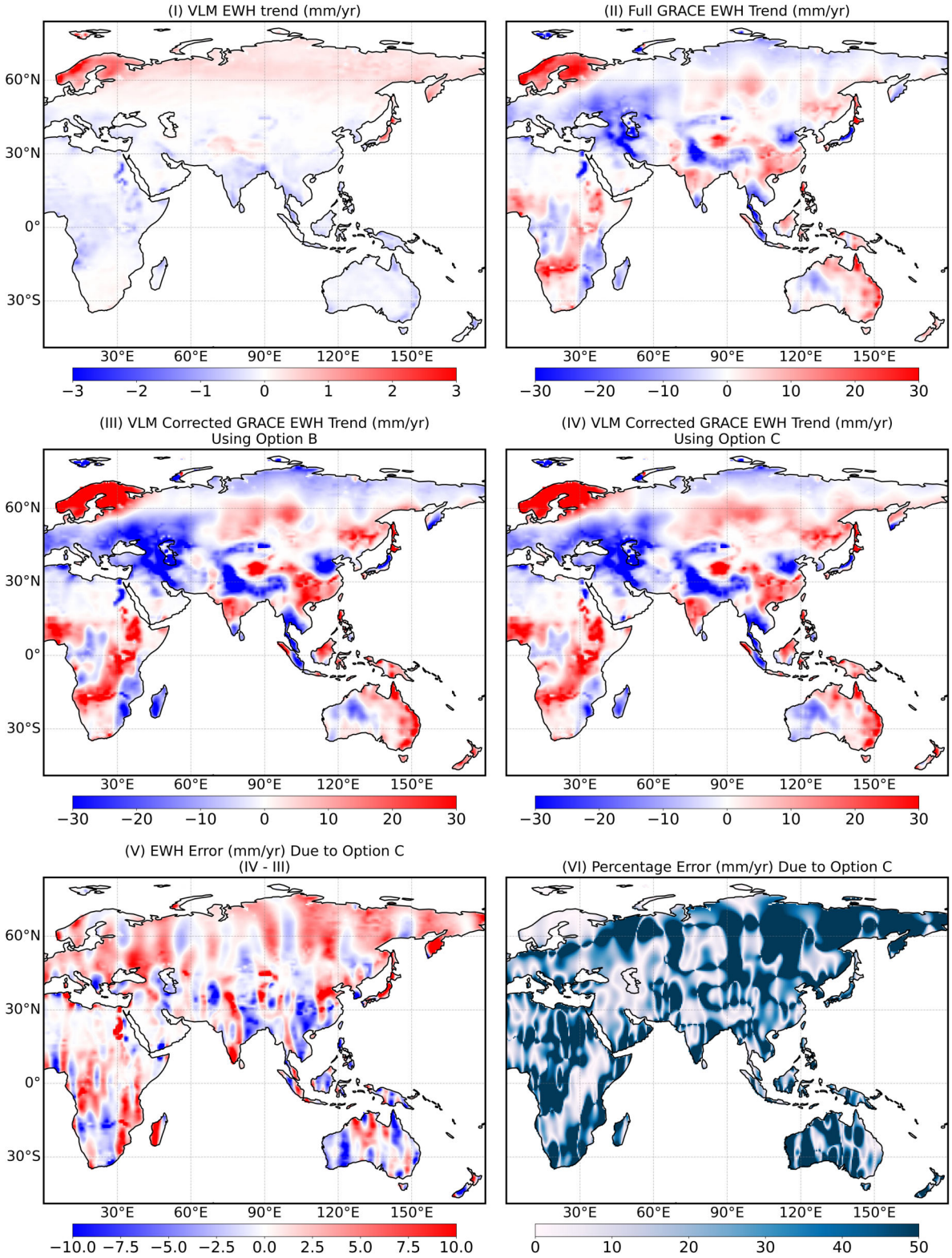

Figure 4.1: Panel (I) shows the VLM EWH in mm/yr using VLM rates published by NGL; panel (II) shows total mass change trend as detected by GRACE in mm/yr; panel (III) shows VLM corrected GRACE EWH trend in mm/yr from option (B); panel (IV) shows VLM corrected GRACE EWH trend in mm/yr from option (C); panel (V) shows the EWH error in mm/yr, obtained by subtracting panel (III) from panel (IV); and panel (VI) shows the percentage error (mm/yr) due to option (C). All the subplots are leakage corrected using the scaling factor from Landerer and Swenson 2012.

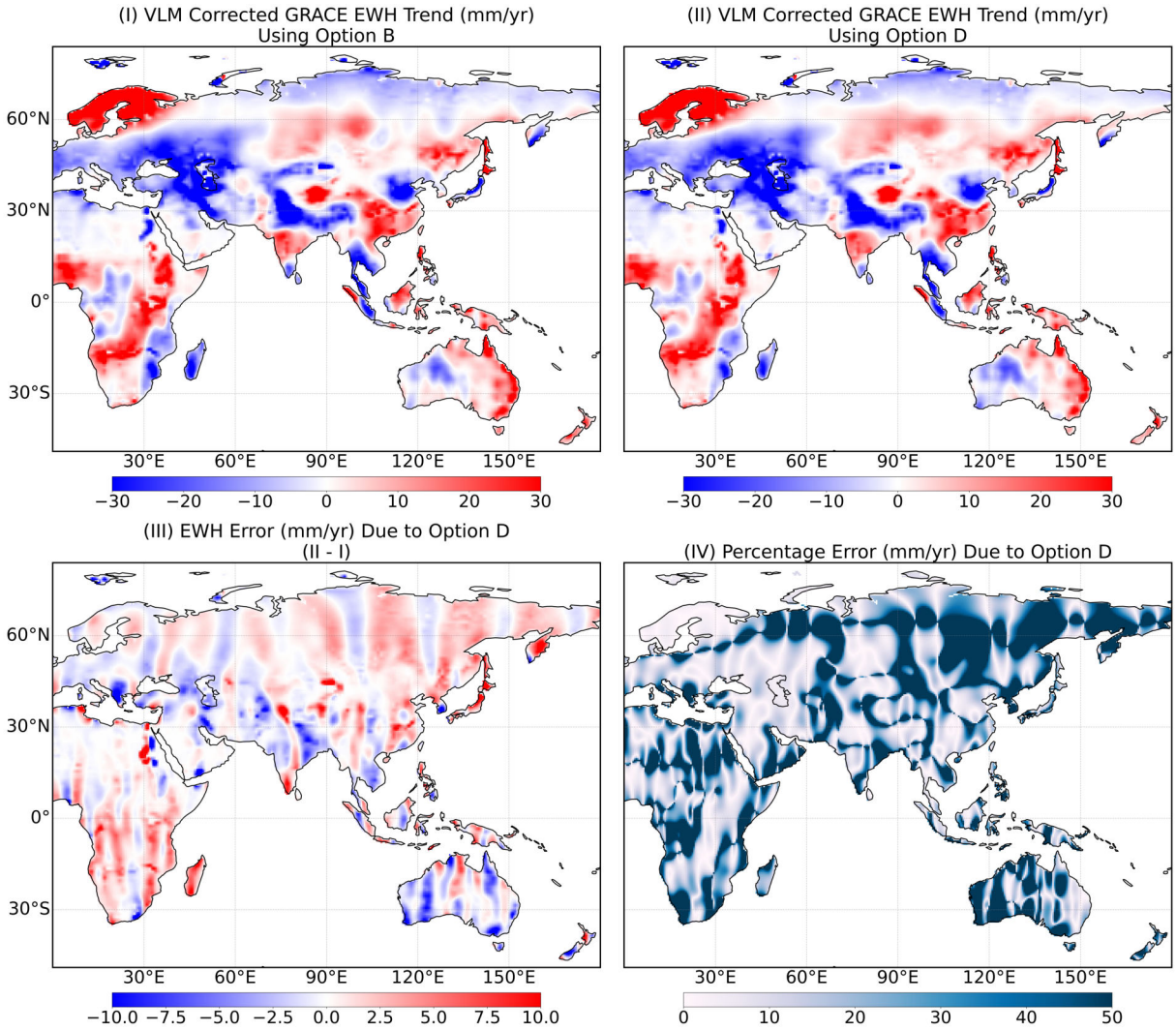

Figure 4.2: Panel (I) shows VLM corrected GRACE EWH trend in mm/yr from option (B); panel (II) shows VLM corrected GRACE EWH trend in mm/yr from option (D); panel (III) shows the EWH error in mm/yr, obtained by subtracting panel (I) from panel (II); and panel (IV) shows the percentage error (mm/yr) due to option (D). All the subplots are leakage corrected using the scaling factor from Landerer and Swenson (2012).

Each lat-lon grid containing the monthly EWH time series is decomposed into an intercept, a linear trend, a semiannual signal, and an annual signal using least-squares regression. Here, linear trends from the GRACE and the VLM EWH field (which is already expressed in secular trend) are used. The difference between the VLM corrected GRACE EWH trend obtained from options (B) and (C) is not negligible, which is quantified as the error due to option (C) and is shown in panel V of Figure 4.1. In the same figure, Panel (I) shows the VLM EWH trend, panel (II) shows GRACE EWH trend, panel (III) shows the VLM corrected GRACE EWH trend using option (B), panel (IV) shows the VLM corrected GRACE EWH trend using option (C) and the percentage error due to same option (C) is shown in panel (VI).

Similarly, the difference between the VLM corrected GRACE EWH trend obtained from options (B) and (D) is not negligible and is shown in panel (III) of Figure 4.2, which is quantified as the error due to option (D). In the same figure, Panel (I) shows the VLM corrected GRACE EWH trend using option (B), panel (II) shows the VLM corrected GRACE EWH trend using option (D) and the percentage error due to same option (D) is shown in panel

(IV). It is to be further noted that the VLM corrected GRACE EWH trend in panel (III) of Figure 4.1 and the VLM corrected GRACE EWH trend in panel (I) of Figure 4.2 is the same. The percentage error is computed as:

$$|E_{\%}|(\theta,\lambda) = \left| \frac{EWH_{\text{error}}(\theta,\lambda)}{EWH_{\text{correct}}(\theta,\lambda)} \right| \times 100\%\,, \tag{4.1}$$

where it has to be noted that the $EWH_{\text{error}}(\theta,\lambda)$ is different due to the VLM correction workflow due to options (C) and (D), while $EWH_{\text{correct}}(\theta,\lambda)$ is the one followed using option (B).

In Bhattarai (2026) the study area was HMA. It is extended for Switzerland to derive the glacier mass change estimates using the VLM correction workflow from option (B). Thus, obtained glacier mass loss estimates, i.e., -0.6 ± 0.097 Gt yr^{-1}, is consistent with glacier mass loss estimates of -0.3 ± 1.6 Gt yr^{-1} for the period 2002–2016 reported by Wouters et al. 2019, who applied GIA and Little Ice Age (LIA) corrections as part of the solid Earth correction but did not account for tectonic vertical deformation. It is also in agreement with the estimate of -0.7 ± 0.4 Gt yr^{-1} reported by Liu and Pail 2025 for the period 2002–2023, who used a mascon fitting approach and applied a regional VLM data developed for the Swiss Alpine region by Sánchez et al. 2018) to correct for VLM signals in the GRACE data.

Table 4.1: Error due to the inconsistent treatment of VLM on the estimates of regional mass change rates. The interpolated VLM published by NGL (2026) is being used.

Region	**VLM corrected GRACE mass change estimates from option C and D**	**Error**	**VLM corrected GRACE mass change estimates from Literature**
High Mountain Asia (HMA)	-19.873 Gt yr^{-1} (from option C)	0.773 Gt yr^{-1} (Underestimated from option C)	-20.646 $\pm$ 2.626 Gt yr^{-1} Bhattarai 2026
–	-17.786 Gt yr^{-1} (from option D)	2.860 Gt yr^{-1} (Underestimated from option D)	
Switzerland	-0.532 Gt yr^{-1} (from option C)	0.068 Gt yr^{-1} (Underestimated from option C)	-0.600 $\pm$ 0.097 Gt yr^{-1} Liu and Pail 2025
–	-0.647 Gt yr^{-1} (from option D)	-0.047 Gt yr^{-1} (Overestimated from option D)	

Also, the area-weighted averages of the error due to VLM correction workflows from options (C) and (D) for two regions: (i) High Mountain Asia (HMA) and (ii) Switzerland, along with the correct area-weighted averages obtained from option (B), are computed and are shown in Table 4.1.

It is found that, following the VLM correction workflow as described in option (C), the VLM-corrected GRACE signal for the HMA region would be underestimated by approximately 4%, whereas the same signal would be underestimated by roughly 14% under the workflow outlined in option (D). Similarly, in the Switzerland region, the VLM-corrected GRACE signal would be underestimated by about 11% when using option (C), but would be overestimated by approximately 8% with option (D). This further demonstrates the importance of consistent VLM treatment in the GRACE Level-2 product. The error here is a function of the load Love number (k_n), which can be clearly understood from Figure 3.3 – Figure 3.6.

It is important to note that these mass change estimates from the different options may vary depending on the specific SH data post-processing workflow employed and the approach adopted for leakage correction for these regions. Assessing the impact of these methodological variations on these regions remains an open question that demands further investigation. Furthermore, the magnitude of mass change estimates obtained from the different options, and the resulting errors due to inconsistent treatment of the VLM signal in the GRACE EWH field, vary across the topographical settings, as variations in topography induce differing solid Earth elastic deformation

responses, which are characterized by k_n. Also, the VLM corrected GRACE mass change estimates, and the resulting error due to inconsistent VLM treatment may induce some minor differences in the magnitude with the use of the different Level-2 SH solution from different GRACE data processing centers, which should be further investigated.

5 Conclusion and Outlook for Further Research

Correcting the VLM signal is essential to accurately determine the terrestrial water storage signal (here explained as the VLM corrected GRACE EWH field/signal) from GRACE data. Here, in this study, the various workflows of the VLM correction in the GRACE EWH field are diagnosed; the errors due to the inconsistent VLM correction are discussed, and the correct way for accounting for the VLM signal in the Level-2 GRACE products is suggested. Using the JPL GRACE Level-2 SH product and the VLM rates published by NGL, it is shown that the VLM correction workflow, as described in option (D), can lead to an underestimation of the VLM corrected GRACE EWH signal by 2.860 $\mathrm{Gt\,yr^{-1}}$ in the HMA region and an underestimation of 0.773 $\mathrm{Gt\,yr^{-1}}$ through option (C) for the same region. Similarly, the VLM corrected GRACE EWH signal, as described in option (C), can lead to an underestimation of 0.068 $\mathrm{Gt\,yr^{-1}}$, while the same signal can be overestimated by -0.047 $\mathrm{Gt\,yr^{-1}}$ from option (D) over the Switzerland region. Therefore, users should carefully account for the VLM signal in the GRACE Level-2 SH product.

In this study, the gridded scaling factor developed by Landerer and Swenson 2012 is used, exploiting the CLM4 hydrological model to scale the attenuated EWH field for the leakage correction in the spatial domain as used by Bhattarai (2026). Since this scale factor does not account for the dynamic component of the glaciers, it generates the open question about its accuracy for the leakage correction, which needs to be validated. This further motivates the development of a more comprehensive scaling factor by combining the ice-component from ICESat or CryoSat altimetry with the CLM4 hydrological model-based EWH field; thereby representing all major components of the water–ice budget, as explained in Bhattarai (2026). Last but not least, as suggested in this study, the correct and consistent treatment of the VLM signal in the GRACE EWH field using Level-2 SH solution further opens the door to exploring the correct way for the consistent accounting of the VLM signal in the Level-3 mascon product.

Acknowledgement

I extend my heartfelt thanks to my supervisor/examiner, Dr.-Ing. Kurt Seitz, for giving me the freedom to explore independently further on the VLM correction I did in the GRACE Level-2 SH solution in my Master's Thesis research work. Moreover, I am thankful for his constructive feedback on my results and preliminary manuscript report on LR-II. Similarly, I would like to thank Prof. Dr.-Ing. Hansjörg Kutterer for granting me permission to do this Lab Rotation research work under his chair. Also, I would like to remember Dr. Surendra Adhikari for providing me with the theoretical foundation for the proper accounting of the VLM signal in the GRACE Level-2 SH in my Master's Thesis; on the basis of the Thesis work, this research came to my mind, and today I did this work independently. Lastly, I am thankful to various data providers for granting open access to their datasets.

Appendix

A Terrestrial Water Storage from Spherical Harmonics

GRACE/-FO measure the Earth's gravitational field, which can be quantified by the gravitational potential V, given by the following relation (Heiskanen and Moritz, 1967):

$$V(r,\theta,\lambda) = \frac{GM}{a}\sum_{n=2}^{N}\sum_{m=0}^{n}\left(\frac{a}{r}\right)^{n+1}\bar{P}_{nm}(\cos\theta)\Big\{\bar{C}_{nm}\cos(m\lambda)+\bar{S}_{nm}\sin(m\lambda)\Big\}, \tag{A.1}$$

where G is Newton's Gravitational constant, M is the total mass of the Earth, a represents the mean equatorial radius of the Earth, r is the radial geocentric distance, θ and λ are co-latitude and longitude respectively. N is the maximum SH degree in the exploited GRACE data product (which is 96 in this study). $\bar{P}_{nm}$ are fully normalized Legendre polynomials of degree n and order m, while $\bar{C}_{nm}$ and $\bar{S}_{nm}$ are fully normalized SH coefficients. It is to be further noted that the GRACE twin satellites are unable to observe degree-1 Stokes coefficients, the spherical harmonic expansion in Eq. (A.1) begins at degree 2.

Besides the static gravitational potential Eq. (A.1), GRACE/-FO provides valuable insight into the time variable gravitational information represented by the change in the SH coefficients. This variability can be seen as either the change in V from one epoch to the other, or the difference with respect to a time average of V. The latter form of the interpretation is considered here, and the long-term mean of the SH coefficients from the monthly values is removed. Thus obtained residual SH coefficients are denoted by $\Delta\bar{C}_{nm}$ and $\Delta\bar{S}_{nm}$, which are related to the density redistribution $\Delta\rho(r,\theta,\lambda)$ occurring on and in the Earth, as explained in Wahr et al. (1998):

$$\begin{pmatrix}\Delta\bar{C}_{nm}\\ \Delta\bar{S}_{nm}\end{pmatrix} = \frac{3}{4\pi a\rho_{\text{ave}}(2n+1)}\iiint_V \Delta\rho(r,\theta,\lambda)\bar{P}_{nm}(\cos\theta)\times\left(\frac{r}{a}\right)^{n+2}\begin{Bmatrix}\cos(m\lambda)\\ \sin(m\lambda)\end{Bmatrix}\sin\theta\, d\theta\, d\lambda\, dr, \tag{A.2}$$

where ρ_{ave} is the average density of the Earth (= 5,517 kg/m^3). $\Delta\bar{C}_{nm} = \bar{C}_{nm} - \bar{C}_{nm}^{\text{mean}}$; $\Delta\bar{S}_{nm} = \bar{S}_{nm} - \bar{S}_{nm}^{\text{mean}}$. Most of the mass redistribution takes place within a thin layer of thickness H, including those portions of the atmosphere, oceans, ice-caps, and below groundwater storage with significant mass fluctuations. Moreover, it is pretended that this thin layer consists of a signal coming from the surface mass distribution. When H is thin enough, i.e., $(N+2)H/a << 1$) then $(\frac{r}{a})^{n+2}$ will be approximately equal to 1 and by replacing the volume integral $\Delta\rho$ by the surface integral $\Delta\sigma$, Eq. (A.2) becomes:

$$\begin{Bmatrix}\Delta\bar{C}_{nm}\\ \Delta\bar{S}_{nm}\end{Bmatrix}_{\text{surface mass}} = \frac{3}{4\pi a\rho_{\text{ave}}(2n+1)}\int_\Omega \Delta\sigma(\theta,\lambda)\bar{P}_{nm}(\cos\theta)\begin{Bmatrix}\cos(m\lambda)\\ \sin(m\lambda)\end{Bmatrix}d\Omega. \tag{A.3}$$

Eq. (A.3) describes the contribution to the geoid from the direct gravitational attraction of the surface mass. That surface mass also loads and deforms the underlying solid Earth, which causes an additional geoid contribution, subsequently contributing to the GRACE EWH field:

$$\begin{Bmatrix}\Delta\bar{C}_{nm}\\ \Delta\bar{S}_{nm}\end{Bmatrix}_{\text{solid Earth}} = \frac{3k_n}{4\pi a\rho_{\text{ave}}(2n+1)}\int_\Omega \Delta\sigma(\theta,\lambda)\bar{P}_{nm}(\cos\theta)\begin{Bmatrix}\cos(m\lambda)\\ \sin(m\lambda)\end{Bmatrix}d\Omega, \tag{A.4}$$

The total contribution to the GRACE EWH field is the sum of Eq. (A.3) and Eq. (A.4):

$$\begin{Bmatrix}\Delta\bar{C}_{nm}\\ \Delta\bar{S}_{nm}\end{Bmatrix} = \begin{Bmatrix}\Delta\bar{C}_{nm}\\ \Delta\bar{S}_{nm}\end{Bmatrix}_{\text{surface mass}} + \begin{Bmatrix}\Delta\bar{C}_{nm}\\ \Delta\bar{S}_{nm}\end{Bmatrix}_{\text{solid Earth}}. \tag{A.5}$$

The change in GRACE EWH (in mm) is similar to the surface mass density change ($\Delta\sigma$), which can then be expressed as in Wahr et al. (1998):

$$\Delta\sigma(\theta,\lambda) = \frac{a\,\rho_{\text{ave}}}{3}\sum_{n=2}^{N}\sum_{m=0}^{n}\frac{2n+1}{1+k_n}\bar{P}_{nm}(\cos\theta)\left(\Delta\bar{C}_{nm}\cos(m\lambda)+\Delta\bar{S}_{nm}\sin(m\lambda)\right). \tag{A.6}$$

Eq. (A.6) is similar to Eq. (14) derived by Wahr et al. (1998). Moreover, this Eq. (A.6) is similar to the Eq. (3.1) which is used in this Lab Rotation, to expressed the terms of the Earth's mass.

Dividing the surface density $\Delta\sigma(\theta,\lambda)$, which represents the equivalent water height (EWH), by the density of water ρ_w the height of EWH results:

$$TWS = \Delta r(\theta,\lambda) = \frac{a}{3}\frac{\rho_{\text{ave}}}{\rho_{\text{w}}}\sum_{n=2}^{N}\sum_{m=0}^{n}\frac{2n+1}{1+k_n}\bar{P}_{nm}(\cos\theta)\left(\Delta\bar{C}_{nm}\cos(m\lambda)+\Delta\bar{S}_{nm}\sin(m\lambda)\right). \tag{A.7}$$

B Time Series of the VLM Corrected GRACE EWH Field

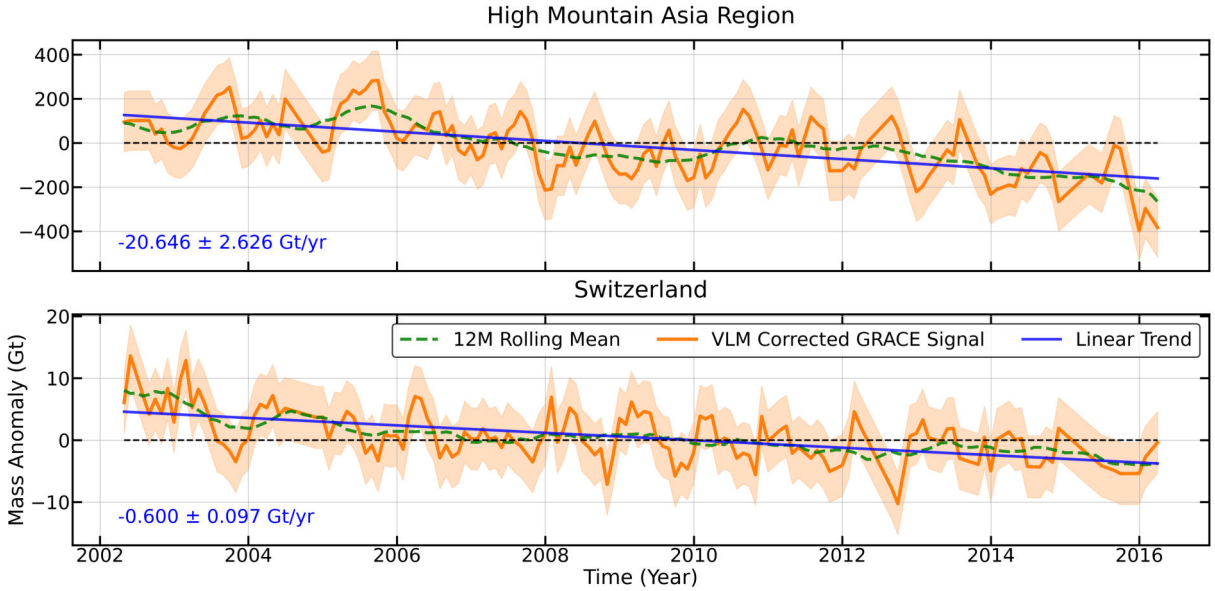

Figure B.1: Time series of the VLM-corrected GRACE signal obtained using JPL SH solution from VLM correction workflow as described in option (B) for the High Mountain Asia (HMA) region and Switzerland over April 2002– March 2016. The orange curve represents the monthly VLM corrected GRACE signal, while the green dashed line denotes the 12-month rolling mean of this signal which captures the annual signal. The blue line indicates the linear trend, obtained as the straight-line component of a least-squares fit to the VLM corrected GRACE signal that also includes annual and semi-annual sinusoidal terms to represent seasonality. The reported trend value corresponds to the slope of this straight line (in Gt/yr), and the quoted trend uncertainties are based on the $\pm 2\sigma$ uncertainty of the fitted slope, approximating a 95% confidence interval. The shaded orange uncertainty envelope represents $\pm 2\sigma$ of the residuals between the observed monthly anomalies and the fitted curve. Note that the y-axis ranges differ between the subplots to make the time series readable. Unit of Mass anomaly in y-axis: Gt.

References

Bhattarai, S. (2026): Monitoring the Changing Mass of Glaciers in High Mountain Asia Region During the GRACE Satellite Mission (2002 – 2016). MA thesis. Karlsruhe Institute of Technology.

Chambers, D. P. (2006): Evaluation of new GRACE time-variable gravity data over the ocean. *Geophysical Research Letters* 33(17). DOI: 10.1029/2006GL027296.

Chen, J., Cazenave, A., Dahle, C., et al. (2022): Applications and Challenges of GRACE and GRACE Follow-On Satellite Gravimetry. *Surveys in Geophysics* 43:305–345. DOI: 10.1007/s10712-021-09685-x.

Chen, J. L., Wilson, C. R., Tapley, B. D., and Grand, S. (2007): GRACE detects coseismic and post seismic deformation from the Sumatra-Andaman earthquake. *Geophysical Research Letters* 34(13). DOI: 10.1029/2007GL030356.

Chen, Q., Shen, Y., Kusche, J., Chen, W., Chen, T., and Zhang, X. (2021): High-resolution GRACE monthly spherical harmonic solutions. *J. Geophys. Res. Solid Earth* 126:e2019JB018892. DOI: 10.1029/2019JB018892.

CLML4 (2026): Vertical Land Motion (VLM) dataset. available on a $1^\circ \times 1^\circ$ grid. URL: http://grace.jpl.nasa.gov/ (visited on 02/03/2026).

Crowley, J. W. and Huang, J. (2020): A least-squares method for estimating the correlated error of GRACE models. *Geophys J Int* 221(3):1736–1749. DOI: 10.1093/gji/ggaa104.

CSD (2026): Vertical Land Movement (VLM), Climate Sustainability Directory. https://climate.sustainability-directory.com/term/vertical-land-movement/. Accessed: 12 February 2026. URL: https://climate.sustainability-directory.com/term/vertical-land-movement/.

Devaraju, B. and Sneeuw, N. (2017): The polar form of the spherical harmonic spectrum: implications for filtering grace data. *Journal of Geodesy* 91(12):1475–1489. DOI: 10.1007/s00190-017-1037-7.

Ditmar, P. (2018): Conversion of time-varying Stokes coefficients into mass anomalies at the Earth's surface considering the Earth's oblateness. *Journal of Geodesy* 92:1401–1412. DOI: 10.1007/s00190-018-1128-0.

Duan, X., Guo, J., Shum, C., and Van Der Wal, W. (2009): On the postprocessing removal of correlated errors in GRACE temporal gravity field solutions. *Journal of Geodesy* 83(11):1095–1106. DOI: 10.1007/s00190-009-0327-0.

eoPortal (2023): GRACE (Gravity Recovery And Climate Experiment). Accessed: March 15, 2025. URL: https://www.eoportal.org/satellite-missions/grace#eop-quick-facts-section.

ESA (2025): GRACE Objectives – European Space Agency (ESA). Accessed: March 15, 2025. URL: https://earth.esa.int/eogateway/missions/grace/objectives.

GFZ (2026): GRACE-FO – Gravity Recovery and Climate Experiment Follow-On Mission. German Research Centre for Geosciences (GFZ). Accessed: 2026-04-06. URL: https://www.gfz.de/en/section/global-geomonitoring-and-gravity-field/projects/grace-fo-gravity-recovery-and-climate-experiment-follow-on-mission.

Girotto, M. and Rowland, M. (2019): Terrestrial Water Storage. In: *Earth Resources and Remote Sensing*. GSFC-E-DAA-TN72619. NASA Technical Report, Public Distribution. NASA Goddard Space Flight Center.

Hammond, W. C., Blewitt, G., Kreemer, C., and Nerem, S. (2021): Global vertical land motion for studies of sea level rise. *Journal of Geophysical Research: Solid Earth* 126(7):e2021JB022355. DOI: 10.1029/2021JB022355.

Han, D. and Wahr, J. (1995): The viscoelastic relaxation of a realistically stratified Earth, and a further analysis of postglacial rebound. *Geophysical Journal International* 120(2):287–311. DOI: 10.1111/j.1365-246X.1995.tb01819.x.

Han, S.-C., Shum, C. K., Jekeli, C., Kuo, C.-Y., Wilson, C., and Seo, K.-W. (2005): Non-isotropic filtering of GRACE temporal gravity for geophysical signal enhancement. *Geophysical Journal International* 163(1):18–25. DOI: 10.1111/j.1365-246X.2005.02756.x.

Hauk, M. (2023): The Influence of LRI Observations on GRACE-FO Gravity Field Models. Accessed: March 15, 2025. URL: https://www.globalwaterstorage.info/en/the-influence-of-lri-observations-on-grace-fo-gravity-field-models.

Heiskanen, W. A. and Moritz, H. (1967): Physical Geodesy. W. H. Freeman & Co., San Francisco, USA.

Hensel, P., Stamps, D. S., and Duda, J. (Dec. 2024): GPS Campaign Surveys for Estimating Vertical Land Motion to Inform Coastal Management. Webinar – National Geodetic Survey Webinar Series. PDF file, 61 pages. URL: https://www.ngs.noaa.gov/web/science_edu/presentations_library/files/vertical_land_motion.pdf.

Humphrey, V., Rodell, M., and Eicker, A. (2023): Using satellite-based terrestrial water storage data: A review. *Surveys in Geophysics* 44(5):1489–1517. DOI: 10.1007/s10712-022-09754-9.

Jekeli, C. (1981): Modifying Stokes's function to reduce the error of geoid undulation computations. *Journal of Geophysical Research* 86(B8):6985–6990. DOI: 10.1029/JB086iB08p06985.

JPL (2026): Level-2 SH solutions. URL: https://podaac.jpl.nasa.gov/GRACE?sections=data (visited on 02/01/2026).

Klees, R., Revtova, E., Gunter, B., Ditmar, P., Oudman, E., Winsemius, H., and Savenije, H. (2008): The design of an optimal filter for monthly GRACE gravity models. *Geophysical Journal International* 175(2):417–432. DOI: 10.1111/j.1365-246X.2008.03922.x.

Kusche, J. (2007): Approximate decorrelation and non-isotropic smoothing of time-variable GRACE-type gravity field models. *Journal of Geodesy* 81(11):733–749. DOI: 10.1007/s00190-007-0143-3.

Kusche, J., Schmidt, R., Petrovic, S., and Rietbroek, R. (2009): Decorrelated GRACE time-variable gravity solutions by GFZ, and their validation using a hydrological model. *Journal of Geodesy* 83:903–913. DOI: 10.1007/s00190-009-0308-3.

Landerer, F. W. and Swenson, S. C. (2012): Accuracy of scaled GRACE terrestrial water storage estimates. *Water Resources Research* 48(4). DOI: 10.1029/2011WR011453.

Liu, S. and Pail, R. (2025): The glacier changes in the Alps from the GRACE and GRACE follow-on missions (2002–2023). *Journal of Geophysical Research: Earth Surface* 130:e2024JF008182. DOI: 10.1029/2024JF008182.

Loomis, B. D., Rachlin, K. E., Wiese, D. N., Landerer, F. W., and Luthcke, S. B. (2020): Replacing GRACE/GRACE-FO ΔC_{20} with satellite laser ranging: Impacts on Antarctic Ice Sheet mass change. *Geophysical Research Letters* 47:e2019GL085488. DOI: 10.1029/2019GL085488.

Murböck, M., Abrykosov, P., Dahle, C., Hauk, M., Pail, R., and Flechtner, F. (2023): In-Orbit Performance of the GRACE Accelerometers and Microwave Ranging Instrument. *Remote Sensing* 15(3):563. DOI: 10.3390/rs15030563. URL: https://doi.org/10.3390/rs15030563.

NASA (2025): Subsidence. Regional Sea Level – NASA Sea Level Change Portal. URL: https://sealevel.nasa.gov/understanding-sea-level/regional-sea-level/subsidence/ (visited on 11/24/2025).

NGL (2026): Vertical Land Motion (VLM) dataset. University of Nevada, Reno (UNR). URL: https://geodesy.unr.edu/vlm.php/ (visited on 02/03/2026).

Pfeffer, J., Spada, G., Mémin, A., Boy, J.-P., and Allemand, P. (July 2017): Decoding the origins of vertical land motions observed today at coasts. *Geophysical Journal International* 210(1):148–165. DOI: 10.1093/gji/ggx142.

Prevost, P., Chanard, K., Fleitout, L., Calais, E., Walwer, D., van Dam, T., and Ghil, M. (2019): Data adaptive spatio-temporal filtering of GRACE data. *Geophysical Journal International* 219(3):2034–2055. DOI: 10.1093/gji/ggz409.

Purcell, A., Dehecq, A., Tregoning, P., Potter, E. K., McClusky, S. C., and Lambeck, K. (2011): Relationship between glacial isostatic adjustment and gravity perturbations observed by GRACE. *Geophysical Research Letters* 38(18):L18307. DOI: 10.1029/2011GL048624.

Rodell, M. and Reager, J. T. (2023): Water cycle science enabled by the GRACE and GRACE-FO satellite missions. *Nature Water* 1:47–59. DOI: 10.1038/s44221-022-00005-0. URL: https://doi.org/10.1038/s44221-022-00005-0.

Sánchez, L., Völksen, C., Sokolov, A., Arenz, H., and Seitz, F. (2018): Present-day surface deformation of the Alpine region inferred from geodetic techniques. *Earth System Science Data* 10(3):1503–1526. DOI: 10.5194/essd-10-1503-2018.

Sasgen, I., Martinec, Z., and Fleming, K. (2006): Wiener optimal filtering of GRACE data. *Studia Geophysica et Geodaetica* 50(4):499–508. DOI: 10.1007/s11200-006-0031-y.

Save, H., Bettadpur, S., and Tapley, B. (2012): Reducing errors in the GRACE gravity solutions using regularization. *Journal of Geodesy* 86:695–711. DOI: 10.1007/s00190-012-0548-5.

Schrama, E. J., Wouters, B., and Lavallée, D. A. (2007): Signal and noise in Gravity Recovery and Climate Experiment (GRACE) observed surface mass variations. *Journal of Geophysical Research: Solid Earth* 112(B8). DOI: 10.1029/2006JB004882.

Sun, Y., Riva, R., and Ditmar, P. (2016): Optimizing estimates of annual variations and trends in geocenter motion and J2 from a combination of GRACE data and geophysical models. *Journal of Geophysical Research: Solid Earth* 121. DOI: 10.1002/2016JB013073.

Swenson, S., Chambers, D., and Wahr, J. (2008): Estimating geocenter variations from a combination of GRACE and ocean model output. *Journal of Geophysical Research: Solid Earth* 113(B8):B08410. DOI: 10.1029/2007JB005338.

Swenson, S. and Wahr, J. (2006): Post-processing removal of correlated errors in GRACE data. *Geophysical Research Letters* 33(8):L08402. DOI: 10.1029/2005GL025285.

Tapley, B. D., Watkins, M. M., Flechtner, F., et al. (2019): Contributions of GRACE to understanding climate change. *Nature Climate Change* 9:358–369. DOI: 10.1038/s41558-019-0456-2.

Tapley, B. D., Bettadpur, S., Watkins, M., and Reigber, C. (2004): The gravity recovery and climate experiment: Mission overview and early results. *Geophysical Research Letters* 31(9):1–4. DOI: 10.1029/2004GL019920.

Vishwakarma, B. D., Horwath, M., Groh, A., and Bamber, J. L. (2022): Accounting for GIA signal in GRACE products. *Geophysical Journal International* 228(3):2056–2060. DOI: 10.1093/gji/ggab464.

Wahr, J., Molenaar, M., and Bryan, F. (1998): Time variability of the Earth's gravity field: Hydrological and oceanic effects and their possible detection using GRACE. *Journal of Geophysical Research: Solid Earth* 103(B12):30205–30229.

Wahr, J., Swenson, S., and Velicogna, I. (2006): Accuracy of GRACE mass estimates. *Geophysical Research Letters* 33(6):L06401. DOI: 10.1029/2005GL025305.

Wahr, J., Swenson, S., Zlotnicki, V., and Velicogna, I. (2004): Time-variable gravity from GRACE: First results. *Geophysical Research Letters* 31(L11501):1–4. ISSN: 1944-8007. DOI: 10.1029/2004GL019779.

Wang, L., Davis, J. L., Hill, E. M., and Tamisiea, M. E. (2016): Stochastic filtering for determining gravity variations for decade-long time series of GRACE gravity. *J Geophys Res Solid Earth* 121(4):2915–2931. DOI: 10.1002/2015JB012650.

Watkins, M. M., Wiese, D. N., Yuan, D. N., Boening, C., and Landerer, F. W. (2015): Improved methods for observing Earth's time variable mass distribution with GRACE using spherical cap mascons. *Journal of Geophysical Research: Solid Earth* 120:2648–2671. DOI: 10.1002/2014JB011547.

Wiese, D. N., Nerem, R. S., and Han, S.-C. (2011a): Expected improvements in determining continental hydrology, ice mass variations, ocean bottom pressure signals, and earthquakes using two pairs of dedicated satellites for temporal gravity recovery. *Journal of Geophysical Research* 116:B11405. DOI: 10.1029/2011JB008375.

Wiese, D., Yuan, D., Boening, C., Landerer, F., and Watkins, M. (2018): JPL GRACE Mascon Ocean, Ice, and Hydrology Equivalent Water Height Release 06 Coastal Resolution Improvement (CRI) Filtered Version 1.0. PO.DAAC, CA, USA. Version 1.0. Dataset accessed [2025-03-19] at http://dx.doi.org/10.5067/TEMSC-3MJC6. DOI: 10.5067/TEMSC-3MJC6.

Wiese, D. N., Visser, P., and Nerem, R. S. (2011b): Estimating low resolution gravity fields at short time intervals to reduce temporal aliasing errors. *Advances in Space Research* 48(6):1094–1107. ISSN: 0273-1177. DOI: 10.1016/j.asr.2011.05.027. URL: https://www.sciencedirect.com/science/article/pii/S0273117711003929.

Wouters, B. and Schrama, E. J. (2007): Improved accuracy of GRACE gravity solutions through empirical orthogonal function filtering of spherical harmonics. *Geophysical Research Letters* 34(23). DOI: 10.1029/2007GL032098.

Wouters, B., Gardner, A. S., and Moholdt, G. (2019): Global glacier mass loss during the GRACE satellite mission (2002–2016). *Frontiers in Earth Science* 7:96. DOI: 10.3389/feart.2019.00096.

Wu, X., Heflin, M. B., Schotman, H., Ivins, E. R., Fukumori, I., Sutterley, T. C., Sabadini, R., Sella, G. F., van der Wal, W., Peltier, W. R., Drummond, R., and Moore, A. W. (2010): Simultaneous estimation of global present-day water transport and glacial isostatic adjustment. *Nature Geoscience* 3(9):642–646. DOI: 10.1038/ngeo938. URL: https://doi.org/10.1038/ngeo938.

Yan, Z. et al. (2024): Optimal Design of a Third Pair of Gravity Satellites to Augment Two Existing Polar Pairs to Enhance Earth's Temporal Gravity Field Recovery. *IEEE Journal of Selected Topics in Applied Earth Observations and Remote Sensing* 17:14145–14160. DOI: 10.1109/JSTARS.2024.3437744.

Yan, Z., Ran, J., Xiao, Y., Xu, Z., Wu, H., Deng, X.-L., et al. (2023): The temporal improvement of Earth's mass transport estimated by coupling GRACE-FO with a Chinese polar gravity satellite mission. *Journal of Geophysical Research: Solid Earth* 128:e2023JB027157. DOI: 10.1029/2023JB027157.

Yi, S. and Sneeuw, N. (2022): A novel spatial filter to reduce north–south striping noise in GRACE spherical harmonic coefficients. *Journal of Geodesy* 96:23. DOI: 10.1007/s00190-022-01614-z.

Zhang, Z.-Z., Chao, B. F., Lu, Y., and Hsu, H.-T. (2009): An effective filtering for GRACE time-variable gravity: fan filter. *Geophysical Research Letters* 36(17):L17311. DOI: 10.1029/2009GL039459.

Zhou, H., Wang, P., Tang, L., and Luo, Z. (2023): A new GRACE filtering approach based on iterative image convolution. *Journal of Geophysical Research: Solid Earth* 128:e2023JB026553. DOI: 10.1029/2023JB026553.

Groundwater monitoring over the continent of Africa

Anugrah John Jojy[1]

1 Remote Sensing and Geoinformatics Master of Science (M.Sc.), KIT, Germany
E-Mail: udwab@student.kit.edu

Abstract

This study demonstrates that a processing chain integrating spherical harmonic synthesis of GRACE monthly gravity field solutions with conversion to equivalent water height via the Wahr et al. (1998) approach effectively captures water storage changes across Africa from 2003 to 2024. Comparing DDK3 and DDK5 filtered solutions (Kusche, 2007), both filters reproduce the main hydrological signals but exhibit a trade-off between spatial resolution and noise reduction. DDK3 yields stronger smoothing and more effective stripe mitigation, yielding smoother fields, while DDK5 preserves more regional detail at the expense of slightly higher residual noise. Key months illustrate hydrological extremes and recovery: April 2010 shows a positive total water storage (TWS) anomaly aligned with wet conditions, August 2016 reveals widespread negative anomalies indicating storage depletion during a drought, March 2020 suggests partial recovery and redistribution, and October 2022 highlights recent variations during the GRACE-FO era, consistent across multiple figures. An analysis with GLDAS indicates soil moisture as the dominant land-surface storage contributor, with runoff contributing a smaller, seasonally variable signal; the discrepancy between GRACE-derived TWS and GLDAS storage points to subsurface influences, including groundwater variability, particularly during extreme periods when near-surface models cannot fully explain GRACE-observed changes. Diagnostics of degree variance underscore the necessity of filtering and show that higher-degree terms are increasingly noise-dominated, supporting the use of DDK filtering to emphasize robust large-scale patterns. In general, the GRACE-GLDAS framework provides a reliable approach to assess continental-scale water storage dynamics and groundwater changes throughout Africa. The study highlights the value of combining GRACE/GRACE-FO data with GLDAS for surface and subsurface analysis and outlines future directions, including the integration of GRACE-FO data for recent years, exploration of alternative filtering and leakage-correction methods, region-specific basin analyzes, and the incorporation of additional hydrological models and in-situ observations to improve groundwater understanding.

Keywords GRACE · GLDAS · Total Water Storage (TWS) · Africa

KIT Scientific Working Papers
Issue Number 270
ISSN: 2194-1629
DOI: 10.5445/IR/1000191188
Online: June 2026

This document is licensed under the Creative Commons Attribution – Share Alike 4.0 International License (CC BY-SA 4.0):
https://creativecommons.org/licenses/by-sa/4.0/deed.en

1 Introduction

Tracking terrestrial water storage (TWS) is critical for comprehending hydrological processes, managing water resources, and evaluating climate-related changes in vulnerable areas. The African continent, in particular, faces significant climatic variability, a strong reliance on groundwater, and limited in-situ monitoring infrastructures, which makes satellite gravimetry an essential method for large-scale water assessments. The Gravity Recovery and Climate Experiment (GRACE) and its successor, GRACE-FO, deliver monthly gravity field data that reflect mass redistribution within the Earth's system. Changes in these gravity fields can be translated into variations in TWS, providing a unique opportunity to analyze groundwater dynamics over extensive spatial and temporal ranges. To achieve accurate estimates of mass change, it is crucial to minimize the noise associated with spherical harmonic coefficients, particularly the north-south "striping" errors typical of GRACE data.
To tackle this issue, decorrelation and smoothing filters are applied to the original gravity solutions. In this research, DDK3 and DDK5 filters, originating from the DDK family of Wiener-type filters, are utilized to diminish correlated noise while maintaining geophysically significant signals. DDK3 functions as a stronger filtering option, yielding smoother fields but with some diminishment of small-scale variability, while DDK5 uses a gentler filter, retaining more regional detail at the expense of slightly heightened noise. Comparing the results from both filters allows for an evaluation of how groundwater estimates are sensitive to the selection of regularization strength. After filtering, the TWS anomalies derived from gravity measurements are further refined by eliminating contributions from soil moisture, snow, and runoff, based on outputs from the Global Land Data Assimilation System (GLDAS). This separation isolates groundwater storage anomalies, which cannot be directly observed through GRACE alone.
By combining observations from GRACE/GRACE-FO with GLDAS model components, this study examines spatial and temporal groundwater fluctuations across Africa from January 2003 to December 2024. The merged dataset facilitates the evaluation of long-term trends, identification of regional anomalies, and analysis of hydrological responses to climatic extremes such as droughts and periods of heavy rainfall. The investigation enhances the understanding of water availability on a continental scale and underscores the significance of satellite gravimetry in monitoring groundwater in regions lacking sufficient data. Ultimately, the comparison of DDK3- and DDK5-filtered products sheds light on the reliability of groundwater estimates and the balance between noise reduction and signal preservation in GRACE-based hydrological research.

2 Theoretical Aspects

The basis of this research is grounded in the representation and analysis of Earth's gravitational field through spherical harmonic coefficients obtained from the GRACE and GRACE-FO missions. These coefficients reflect variations in mass both on and inside the Earth and can be converted into spatial representations of terrestrial water storage (TWS) anomalies. However, the initial GRACE data includes correlated errors, particularly in the form of longitudinal striping, necessitating the use of decorrelation and smoothing techniques such as DDK3 and DDK5. These filtering methods employ Wiener optimal filtering principles to strike a balance between noise reduction and the preservation of the signal. Once filtering is completed, the gravity-derived signals are associated with hydrological mass changes based on the theory of load Love numbers, which quantify the Earth's elastic response to mass loads at the surface. Groundwater storage is then isolated by removing non-groundwater components using hydrological models like GLDAS. Collectively, these theoretical components create a framework for translating gravity field measurements into significant estimates of groundwater variability on a continental scale.

2.1 Spherical Harmonic Synthesis (SHS)

The representation of the gravitational potential of the Earth in Spherical harmonics are given in Equation (2.1). Spherical Harmonic Synthesis is the forward computation of a function on the sphere from a series of surface

spherical harmonics (Tsoulis, 1999). The spherical harmonic coefficients derived from GRACE level-2 data is used to express the gravity field of Earth.

$$V(P) = \frac{GM}{r} \sum_{n=0}^{\infty} \left(\frac{R}{r}\right)^n \sum_{m=0}^{n} (\bar{C}_{nm} \cos m\lambda + \bar{S}_{nm} \sin m\lambda) \bar{P}_{nm}(\sin \varphi) \tag{2.1}$$

where,
GM : Geocentric gravitational constant
R : Radius of the reference sphere.
$\bar{C}_{nm}, \bar{S}_{nm}$: Fully normalised spherical harmonic coefficients of degree n and order m
$\bar{P}_{nm}$: Fully normalised Legendre functions of degree n and order m.

In order to establish the geodetic foundation for representing the Earth's gravity field with spherical harmonics, this research draws on the traditional principles of physical geodesy outlined by Heiskanen and Moritz (1967). Their framework provides the mathematical groundwork for depicting the Earth's gravitational potential through spherical harmonics and associated Legendre functions, which serves as the theoretical underpinning for contemporary satellite gravimetry and the analysis of GRACE gravity field results.

2.2 Degree Variance And Error Degree Variance

Degree variance analysis offers insights into how the power of gravitational signals is spread across various spherical harmonic degrees. The degree variance measures the impact of each degree on the overall gravity field signal, proving useful for pinpointing the dominant spatial scales of mass variability. Lower degrees relate to large-scale phenomena, whereas higher degrees correspond to smaller-scale features that tend to be more affected by noise.
Alongside the signal degree variance, the error degree variance is calculated using the formal uncertainties associated with the spherical harmonic coefficients included in the GRACE solutions. The error degree variance facilitates the evaluation of noise characteristics in the gravity field estimates and aids in identifying the degree range where the signal-to-noise ratio significantly declines.
In this research, both the degree variance and error degree variance are examined for individual monthly solutions as well as for filtered datasets. This assessment allows for an evaluation of how effective the implemented DDK filters are in reducing noise while still maintaining hydrologically relevant signals.
The degree variance quantifies the contribution of each spherical harmonic degree to the total gravity field signal. It is defined as:

$$C_n^2(\bar{C}_{nm}, \bar{S}_{nm}) = \sum_{m=0}^{n} (\bar{C}_{nm}^2 + \bar{S}_{nm}^2) \tag{2.2}$$

Degree variance analysis allows an assessment of the dominant spatial scales of the observed signal, where lower degrees correspond to large-scale mass variations and higher degrees represent smaller-scale features.
The error degree variance is computed using the formal uncertainties of the spherical harmonic coefficients:

$$\sigma_{n,\mathrm{err}}^2 = \sum_{m=0}^{n} \left(\sigma_{\bar{C}_{nm}}^2 + \sigma_{\bar{S}_{nm}}^2\right), \tag{2.3}$$

where $\sigma_{\bar{C}_{nm}}$ and $\sigma_{\bar{S}_{nm}}$ denote the standard deviations of the spherical harmonic coefficients. The comparison between degree variance and error degree variance provides insight into the signal-to-noise ratio as a function of spherical harmonic degree and allows an evaluation of the effectiveness of the applied filtering.

2.3 Wahr Approach

The method for converting variations in the gravity field from GRACE into changes in surface mass in this research is based on the approach developed by Wahr et al. (1998). This method creates a linear correlation between changes over time in the Earth's gravitational field and integrated mass variations at the surface of the Earth.

$$\bar{D}^c_{nm} = \frac{a}{3}\frac{\rho_M}{\rho_w}\frac{2n+1}{1+k_n}\Delta\bar{C}_{nm}, \qquad \bar{D}^s_{nm} = \frac{a}{3}\frac{\rho_M}{\rho_w}\frac{2n+1}{1+k_n}\Delta\bar{S}_{nm} \tag{2.4}$$

The mean density of Earth is given by ρ_M. Density of water is given by ρ_w.
By utilizing degree-dependent load Love numbers k_n, the Wahr method incorporates the elastic response of the solid Earth to loading at the surface, facilitating the conversion of spherical harmonic gravity anomalies into equivalent water height (EWH). Consequently, the EWH obtained from GRACE encapsulates variations in total terrestrial water storage, which includes contributions from soil moisture, surface water, snow, ice, and groundwater. The EWH is expressed by the use of Equation (2.5) in surface Spherical Harmonics :

$$EWH = a\sum_{n=0}^{\infty}\sum_{m=0}^{n}(\bar{D}^c_{nm}\,\cos m\lambda + \bar{D}^s_{nm}\,\sin m\lambda)\bar{P}_{nm}(\sin\varphi) \tag{2.5}$$

Due to its consistent physical treatment of mass loading and Earth deformation, the Wahr method has established itself as the standard approach for hydrological studies using GRACE and GRACE-FO data.

2.4 Components of TWS

The EWH which is derived from GRACE observations include all the hydrological components. The individual components are Soil moisture(SM), Groundwater, Surface runoff (SRO)and Subsurface runoff (SSRO), Equivalent snowmelt (ESM) and Canopy. These components are given by GLDAS database except Groundwater:

$$TWS_{GLDAS} = SM + SRO + SSRO + ESM + Canopy \tag{2.6}$$

3 Data

In the following subsections describes the used datasets GRACE and GLDAS. A mask specific to continental Africa, based on a shapefile, is applied to both the GRACE and GLDAS datasets to confine the analysis to the African land region, excluding oceanic and non-relevant areas.

3.1 GRACE And GRACE-FO

The main dataset utilized in this research comprises monthly gravity field solutions from GRACE and GRACE-FO, presented in spherical harmonic format. Solutions sourced from the chosen processing center are utilized up to degree and order 96. The study spans from January 2003 to December 2024. Prior to spatial synthesis, two decorrelation filters, DDK3 and DDK5 processed by the GFZ (GeoForschungsZentrum, Potsdam), are applied to the gravity field coefficients. The respective datasets are downloaded from the ICGEM (2026) web page.

3.2 GLDAS

To aid in the interpretation of TWS derived from GRACE data, hydrological model data from the Global Land Data Assimilation System (GLDAS) Noah land surface model is employed (Rodell et al., 2004). It is downloaded from GLDAS (2025). Monthly GLDAS NOAH-025 products, featuring a spatial resolution of 0.25°, are examined. The hydrological components considered encompass soil moisture at four depth layers (0–10 cm, 10–40 cm, 40–100 cm, and 100–200 cm), as well as surface runoff, subsurface runoff, snowmelt equivalent, and canopy water storage.

4 Results

The TWS maps generated from GRACE data show marked spatial and temporal differences across Africa. Seasonal patterns linked to precipitation are distinctly observable, revealing strong wet-season indicators in tropical regions and less variability in arid zones. When comparing DDK3 and DDK5 filtered outcomes, DDK3 provides stronger smoothing and more effective stripe reduction, resulting in smoother fields, whereas DDK5 preserves more regional detail but may retain slightly higher noise.
Continental mean TWS time series show notable interannual fluctuations and long-term trends throughout the study duration. The components of water storage derived from GLDAS primarily consist of soil moisture, with runoff playing a smaller yet seasonally significant role. The contributions of snow and canopy water are minimal across the majority of Africa.
Variations in groundwater storage calculated as the difference between GRACE and GLDAS indicate considerable long-term changes, especially in areas experiencing significant climatic variability and heavy water usage. The contrasts between GRACE and GLDAS emphasize the crucial role of groundwater in total water storage changes and illustrate the limitations of land surface models in accurately depicting subsurface water dynamics.
The uncertainty analysis reveals that higher-degree signals are more susceptible to noise, highlighting the need for appropriate filtering. The combined application of DDK3 and DDK5 offers a comprehensive framework for analyzing both regional detail and large-scale trends.

4.1 Assessment of SHS results

The TWS time series over Africa (2003–2024), derived from GRACE data and computed using the Wahr technique, demonstrates significant seasonal changes along with interannual variations. The extreme values in minimum, maximum, and RMS statistics, which are presented in Figures 4.5 and 4.6, do not appear to be evenly distributed over time but are rather concentrated in certain years linked to large-scale hydroclimatic anomalies. These extremes can be reliably identified in both DDK3 and DDK5 filtered solutions, although their intensity and spatial representation vary between the two filtering methods. To demonstrate the effectiveness of spherical harmonic synthesis and the related filtering methods, specific months from the years 2010, 2016, 2020, and 2022 have been selected. The year 2010 is characterized by notably strong positive anomalies in terrestrial water storage, making it an excellent example for evaluating the spatial accuracy of the synthesis. Conversely, 2016 reflects a significant drought period, emphasizing how the gravity field reacts to large-scale mass loss. The years 2020 and 2022 are included to illustrate recovery following extreme events and the recent variability observed with GRACE-FO, respectively, which permits an evaluation of the reliability and consistency of the SHS results across various hydrological conditions and mission phases.

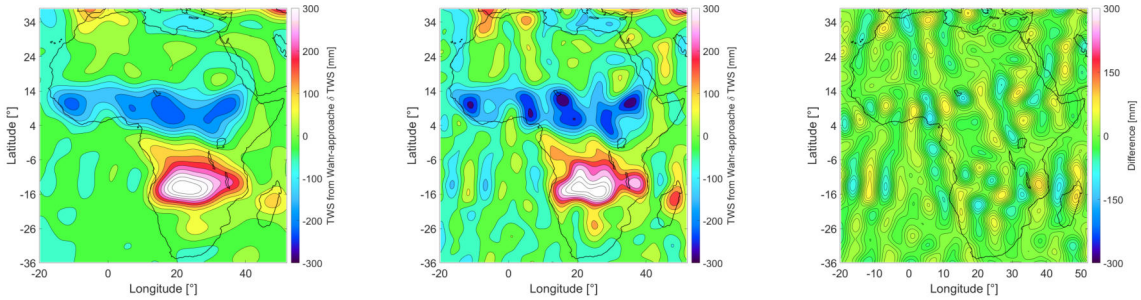

(a) DDK3 APRIL 2010 (b) DDK5 APRIL 2010 (c) DDK3-DDK5

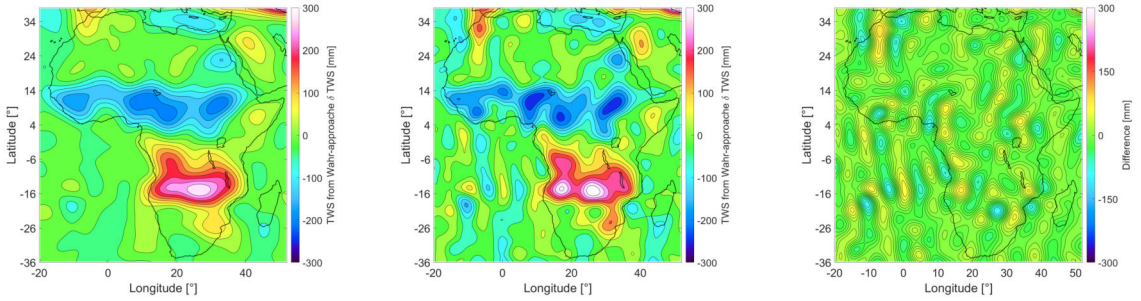

(d) DDK3 MAY 2010 (e) DDK5 MAY 2010 (f) DDK3-DDK5

Figure 4.1: GRACE-derived EWH anomalies over Africa for April and May 2010, illustrating a strong positive hydrological anomaly. Results are shown for DDK3 and DDK5 filtering.

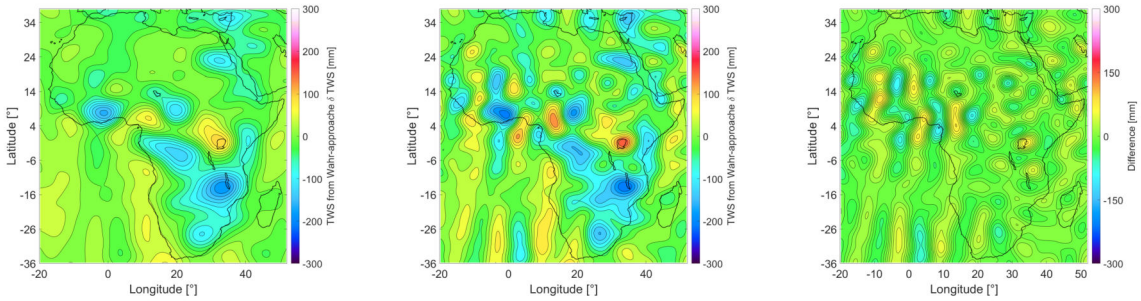

(a) DDK3 JULY 2016 (b) DDK5 JULY 2016 (c) DDK3-DDK5

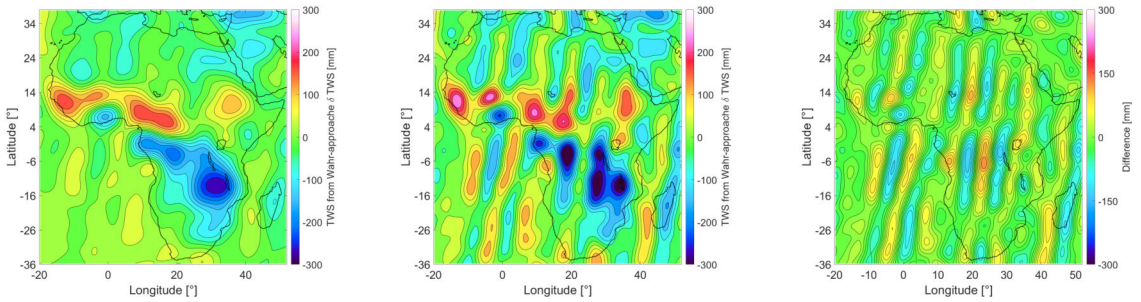

(d) DDK3 AUGUST 2016 (e) DDK5 AUGUST 2016 (f) DDK3-DDK5

Figure 4.2: GRACE-derived EWH anomalies over Africa for July and August 2016, highlighting widespread terrestrial water storage depletion during a major drought period.

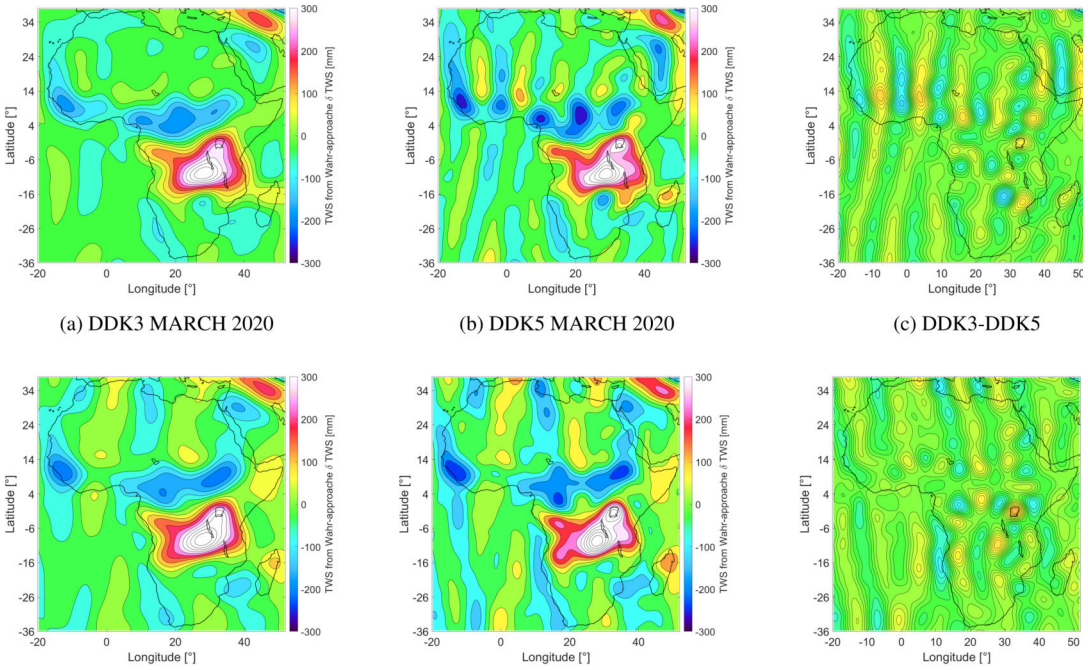

(a) DDK3 MARCH 2020 (b) DDK5 MARCH 2020 (c) DDK3-DDK5

(d) DDK3 APRIL 2020 (e) DDK5 APRIL 2020 (f) DDK3-DDK5

Figure 4.3: GRACE-derived EWH anomalies for March and April 2020, showing partial recovery of terrestrial water storage following the 2015–2016 drought.

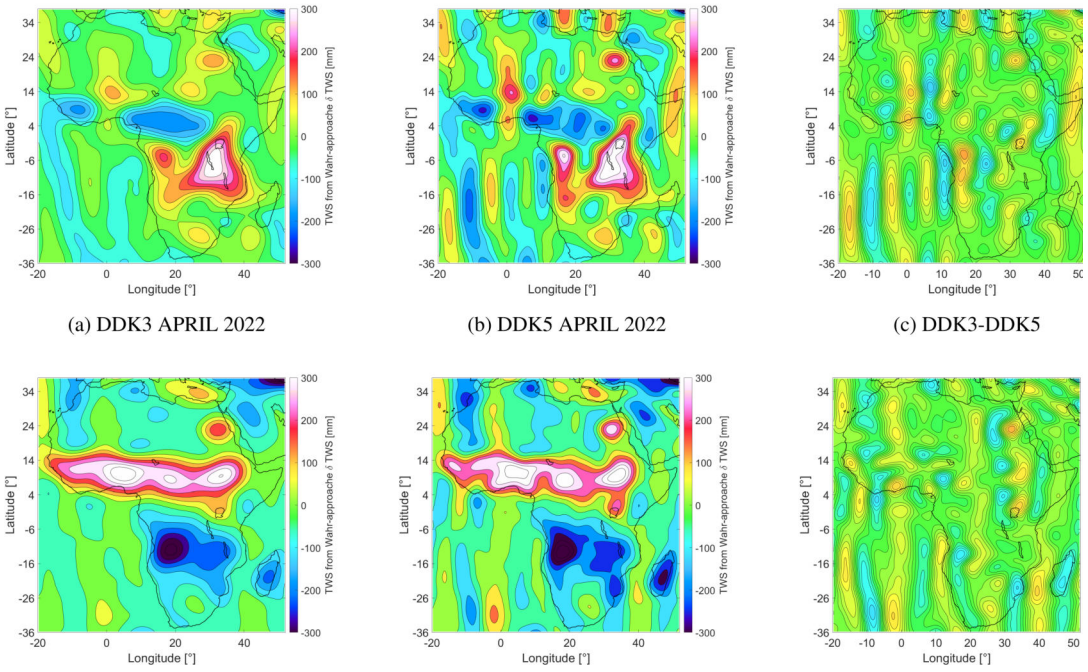

(a) DDK3 APRIL 2022 (b) DDK5 APRIL 2022 (c) DDK3-DDK5

(d) DDK3 OCTOBER 2022 (e) DDK5 October 2022 (f) DDK3-DDK5

Figure 4.4: GRACE-derived EWH anomalies over Africa for April and October 2022, illustrating recent variability. Results are shown for DDK3 and DDK5 filtering.

Table 4.1: Statistics over the months for TWS values (mm)

Months in 2010	Minimum	Maximum	Mean	RMS	STD
April	-90.8	96.9	-0.1	26.6	26.6
May	-83.5	82.1	0.1	23.02	23.0
Months in 2016	Minimum	Maximum	Mean	RMS	STD
July	-87.1	93.9	-0.2	22.8	22.8
August	-127.9	141.9	-0.7	37.5	37.5
Months in 2020	Minimum	Maximum	Mean	RMS	STD
March	-112.6	104.1	-0.6	29.4	29.4
April	-82.1	123.2	-0.1	24.8	24.8
Months in 2022	Minimum	Maximum	Mean	RMS	STD
April	-123.1	131.2	1.6	37.5	37.5
October	-107.5	113.5	-0.4	33.9	33.9

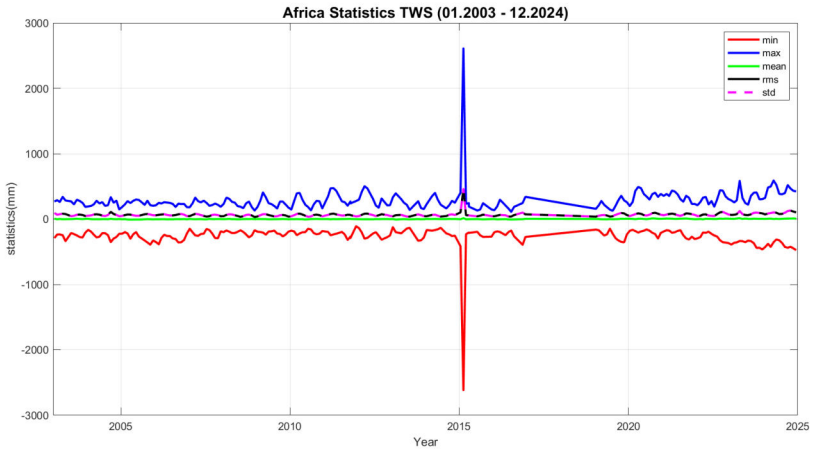

Figure 4.5: Africa-mean GRACE-derived TWS anomalies (2003–2024) computed using the Wahr approach. Results for DDK3 filter.

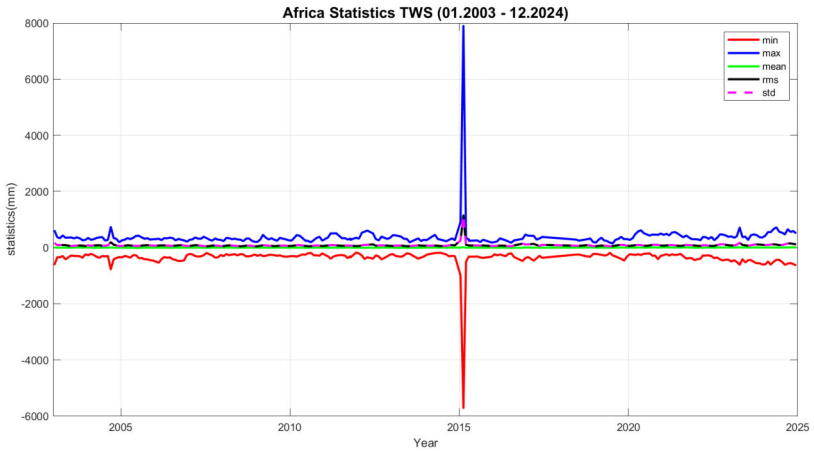

Figure 4.6: Africa-mean GRACE-derived TWS anomalies (2003–2024) computed using the Wahr approach. Results for DDK5 filter.

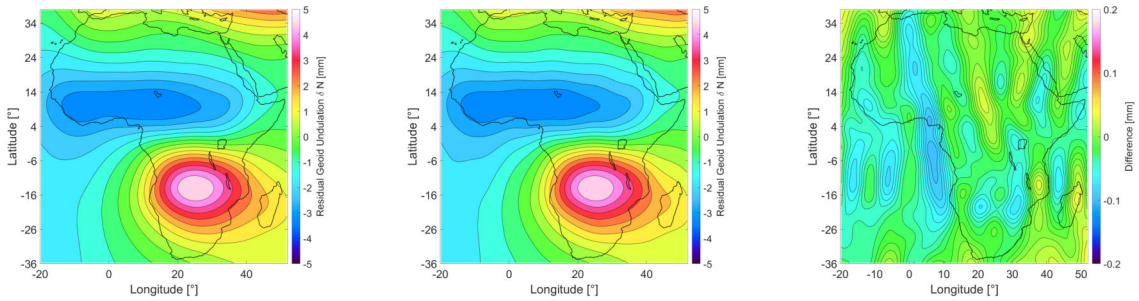

Figure 4.7: GRACE-derived geoid undulation anomalies over Africa for April 2010, computed using the Wahr approach

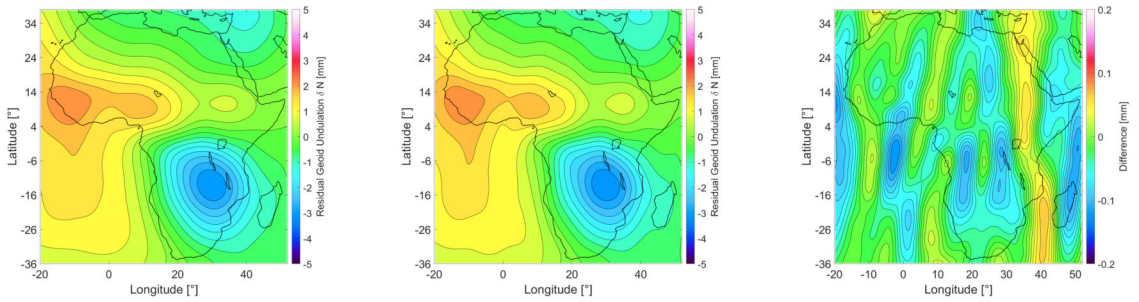

Figure 4.8: Geoid undulation anomalies over Africa for August 2016, illustrating the geodetic response to large-scale terrestrial water storage depletion during a drought period.

4.2 GLDAS Results

The analysis based on GLDAS reveals significant seasonal and interannual fluctuations in terrestrial water storage components across Africa for the period from 2003 to 2024. Soil moisture is the primary contributor to the overall GLDAS water storage signal, with the upper and mid-soil layers (0–100 cm) displaying the most pronounced seasonal variation. While runoff adds a smaller yet distinctly seasonal signal, especially in humid and equatorial areas, snow melt and canopy water make minimal contributions across much of the continent. The spatial patterns and time series generated from GLDAS demonstrate clear wet and dry cycles that align well with variations in TWS derived from GRACE, though the level of variability is less intense due to the model's lack of an explicit groundwater component.

4.2.1 Monthly Runoff Maps

Monthly runoff maps are presented for April 2010, August 2016, March 2020, and October 2022, illustrating wet, drought, recovery, and current hydrological situations, respectively are shown in Figures 4.9 to 4.12. These specific months were chosen to emphasize differences in surface and subsurface runoff reactions under varying hydroclimatic conditions across Africa. The month October 2022 is included to represent recent hydrological conditionsduring the GRACE-FO mission phase.

4.2.2 Monthly Spatial Maps

Monthly spatial maps are shown for the same months (April 2010, August 2016, March 2020, and October 2022) to maintain consistency with the runoff analysis in Figures 4.13 to 4.20. The chosen months enable a clear depiction of the spatial distribution of soil moisture and total runoff at global and continental levels, allowing for a comparative evaluation across different hydrological conditions.

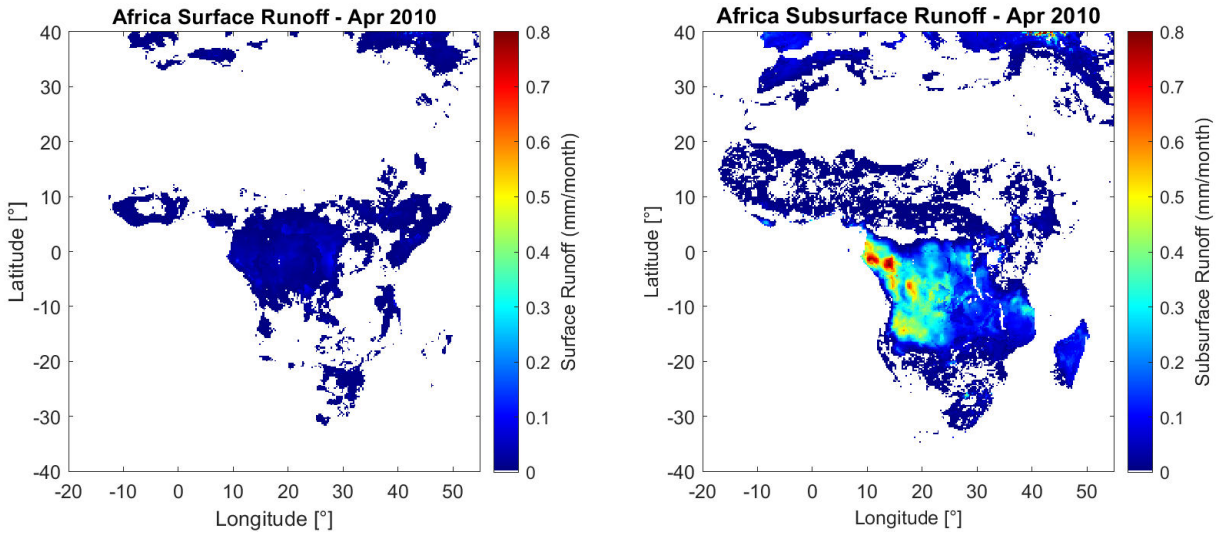

Figure 4.9: April 2010 - Wet extreme

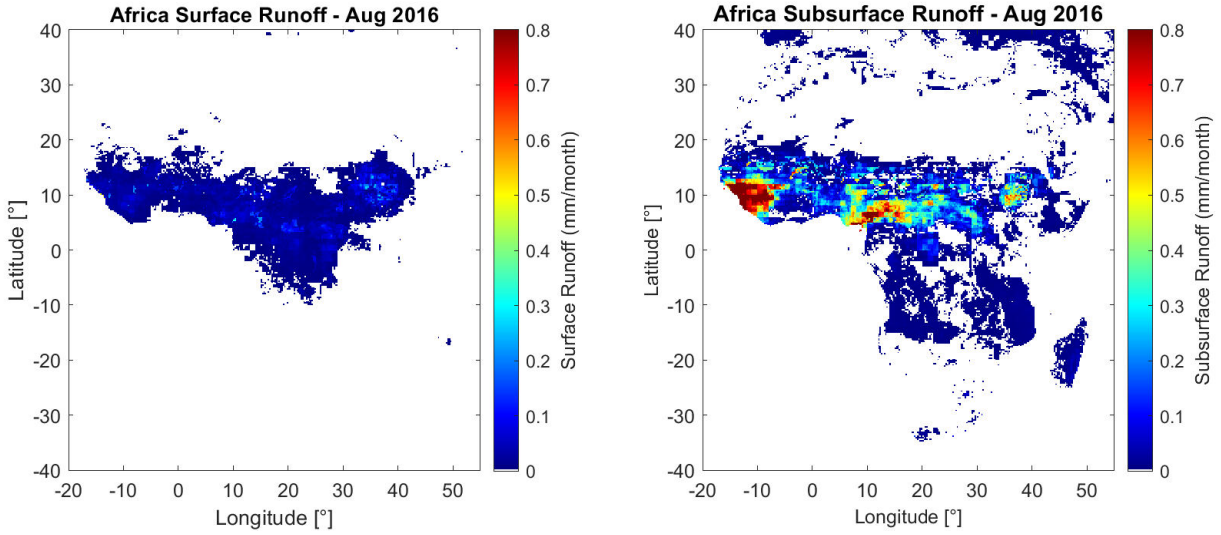

Figure 4.10: August 2016 - Drought extreme

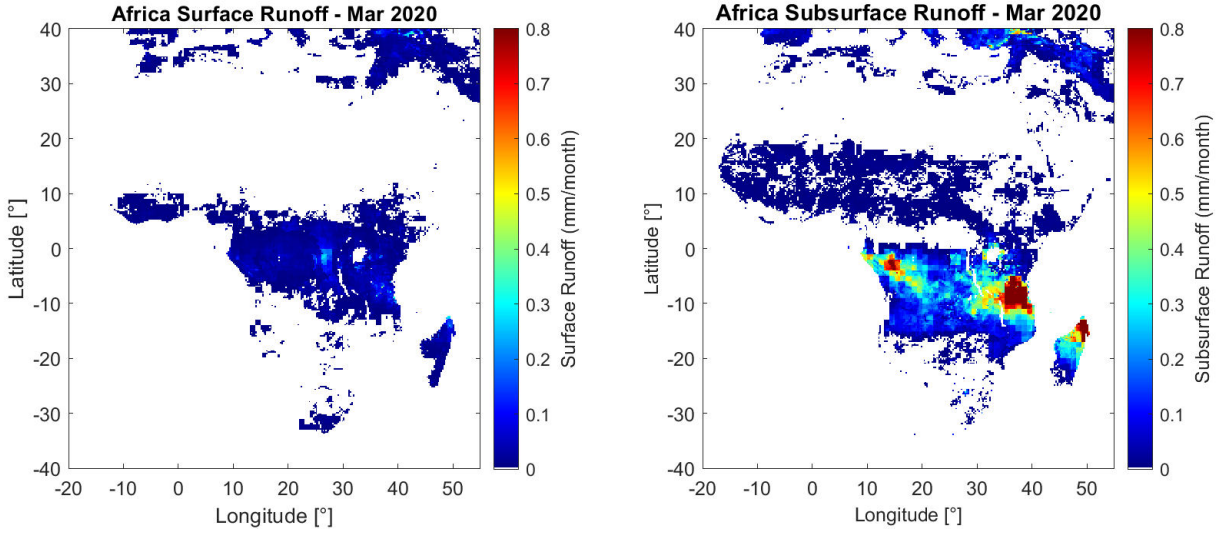

Figure 4.11: March 2020 Recovery phase

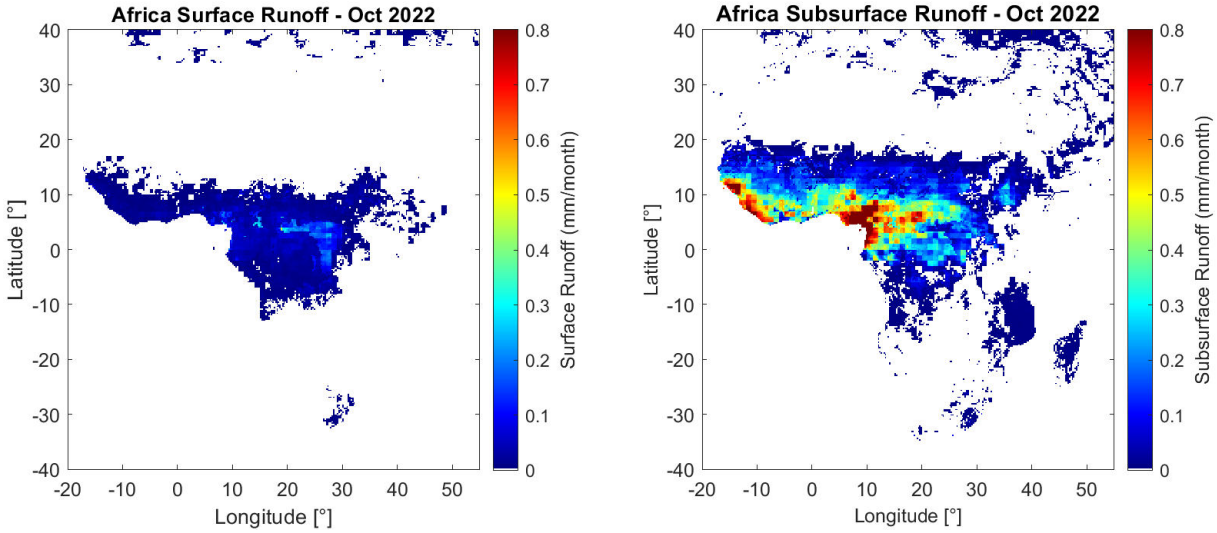

Figure 4.12: October 2022 - Recent variability

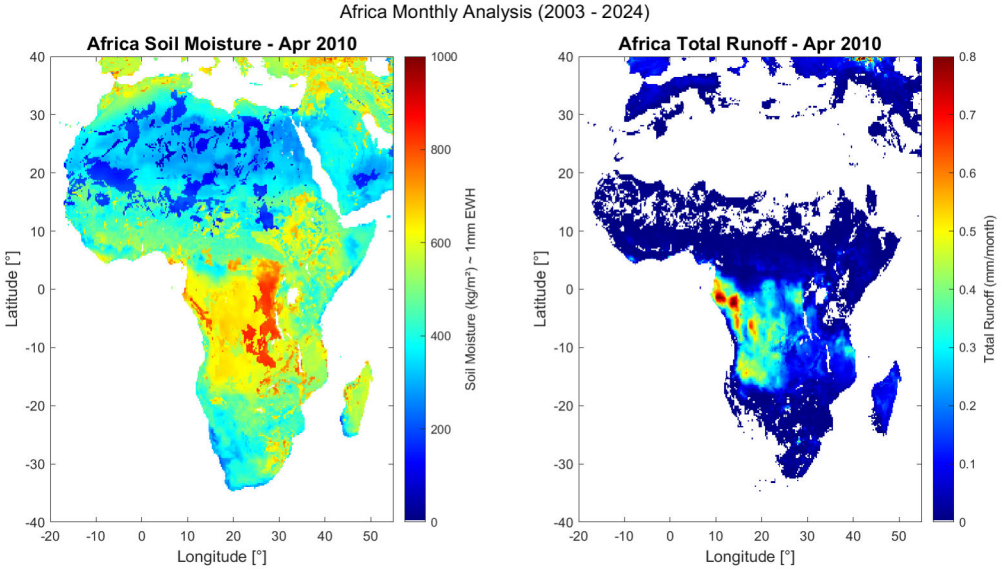

Figure 4.13: Africa Soil Runoff - 2010 April

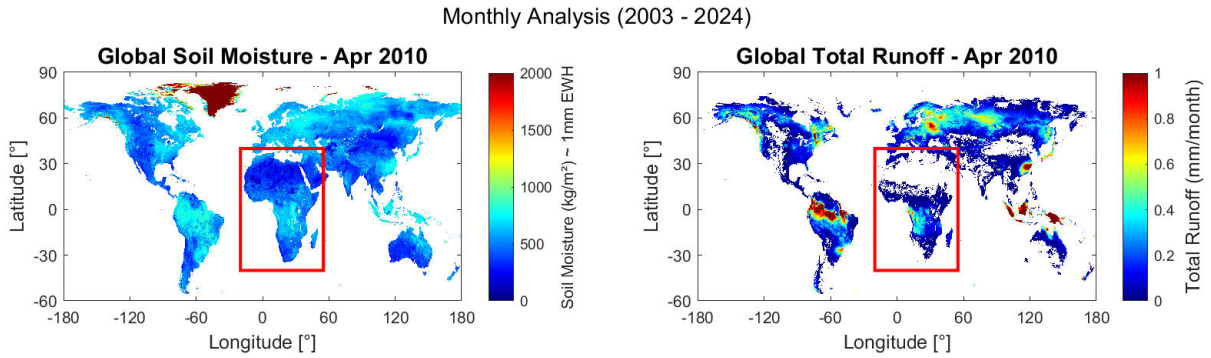

Figure 4.14: Global Soil Runoff - 2010 April

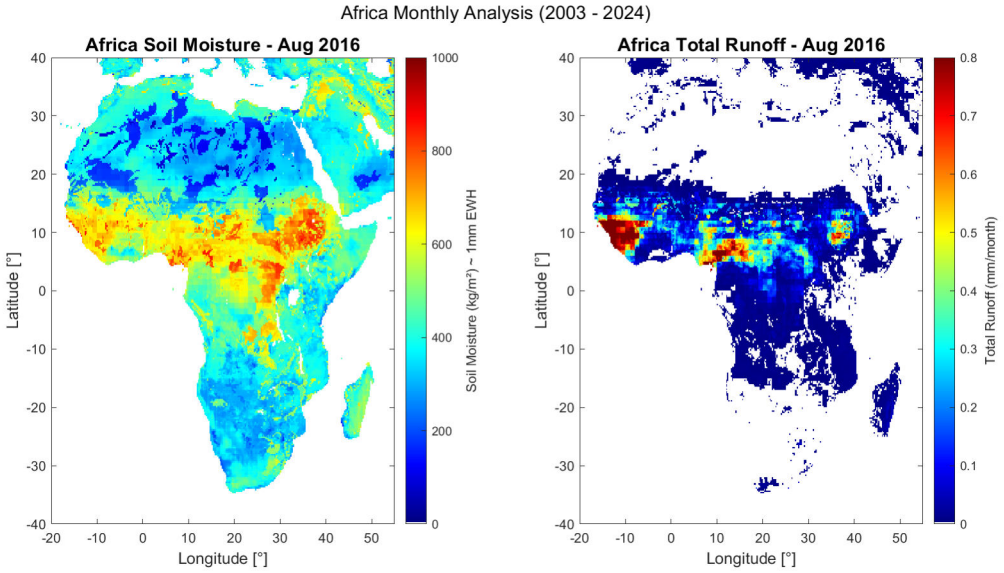

Figure 4.15: Africa Soil Runoff - 2016 August

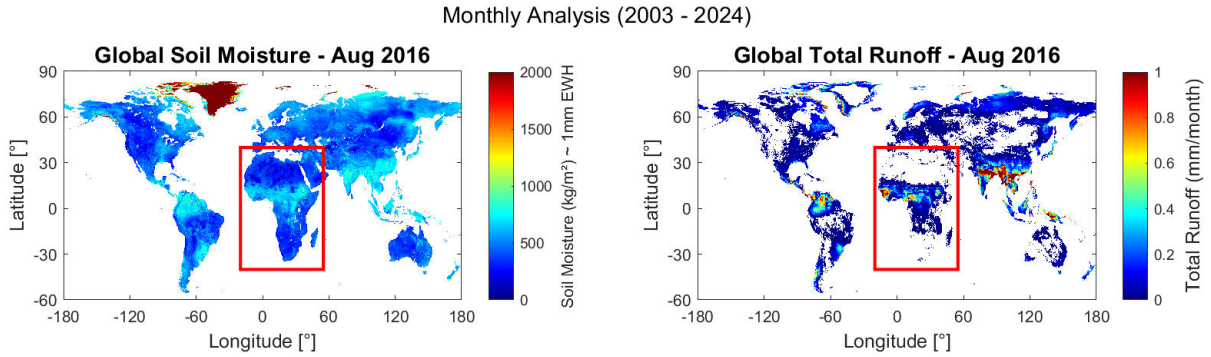

Figure 4.16: Global Soil Runoff - 2016 August

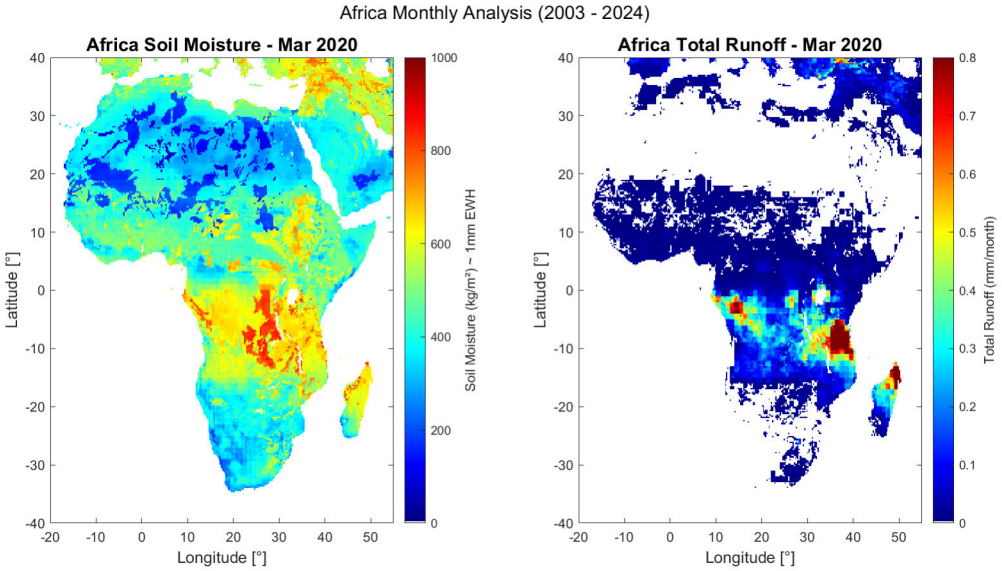

Figure 4.17: Africa Soil Runoff - 2020 March

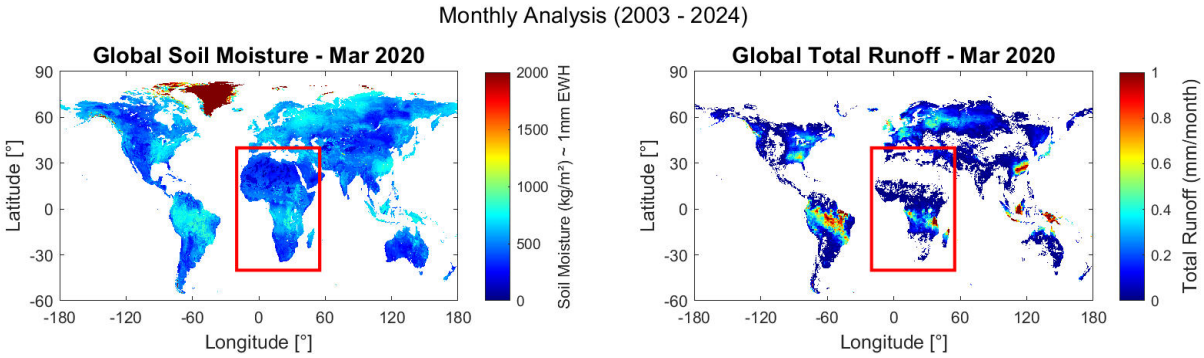

Figure 4.18: Global Soil Runoff - 2020 March

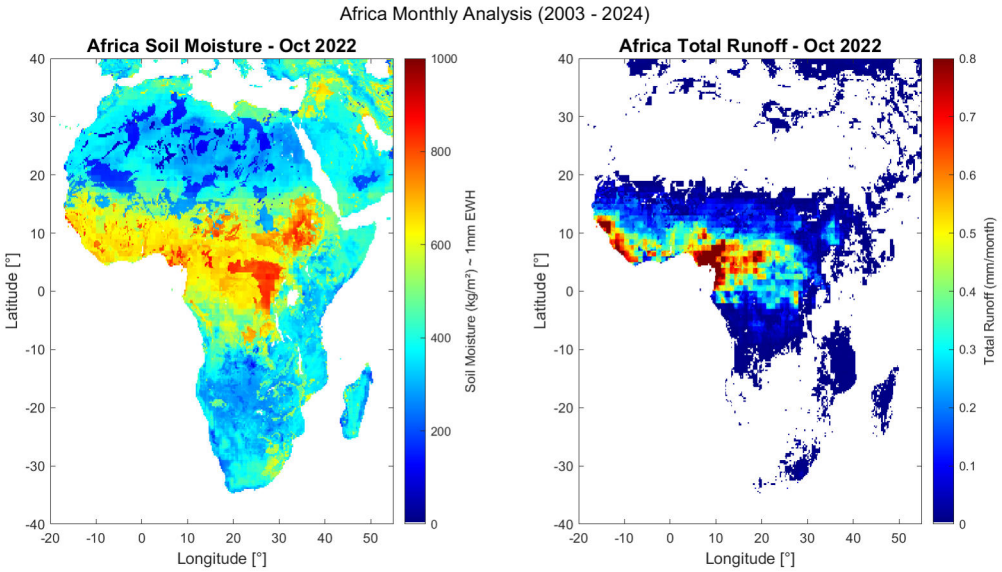

Figure 4.19: Africa Soil Runoff - 2022 October

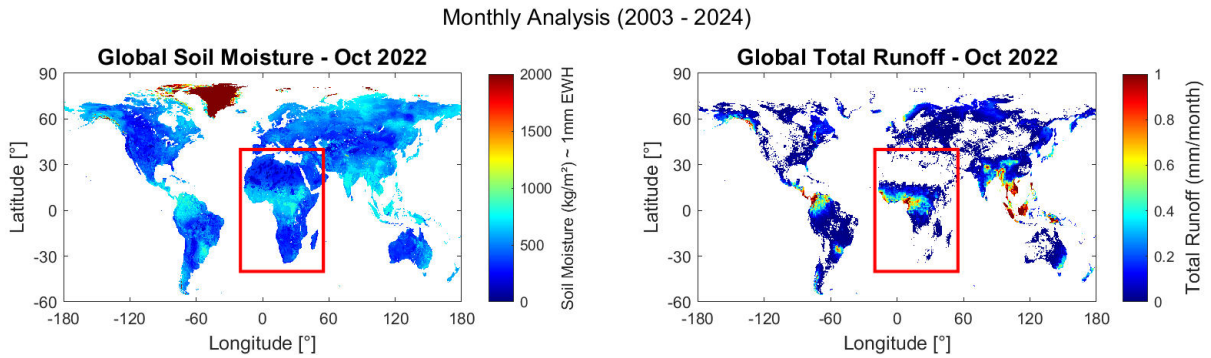

Figure 4.20: Global Soil Runoff - 2022 October

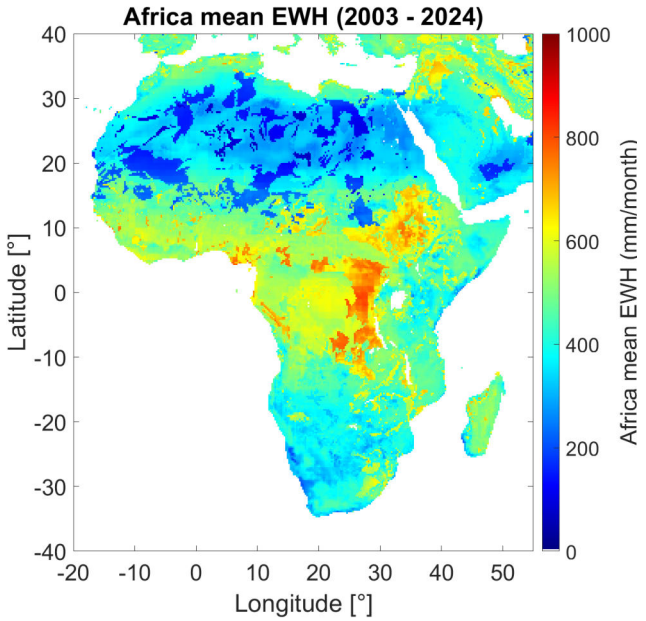

Figure 4.21: Africa-mean equivalent water height (EWH) derived from GLDAS NOAH-025 for the period January 2003 to December 2024.

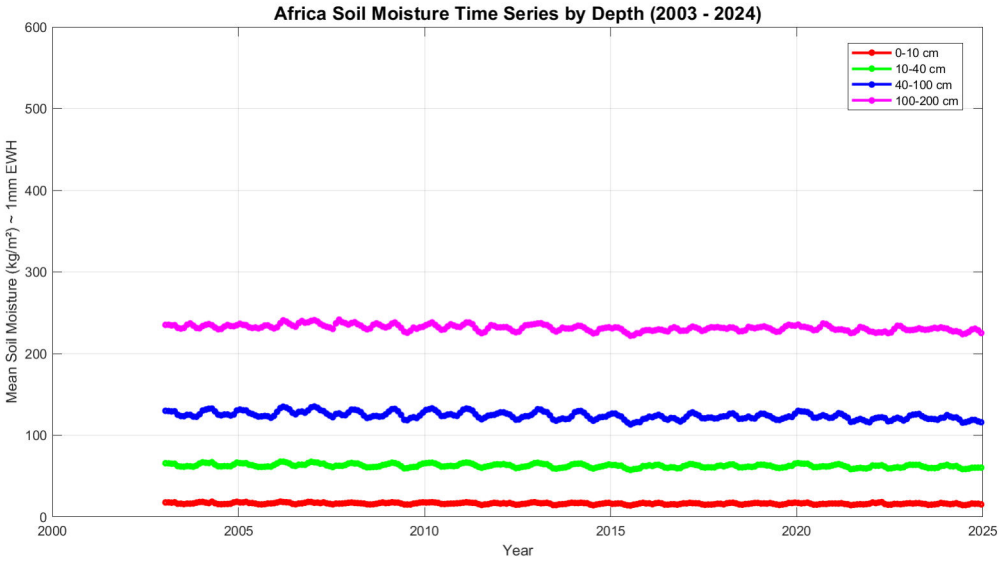

Figure 4.22: Africa Soil Moisture Time series by Depth

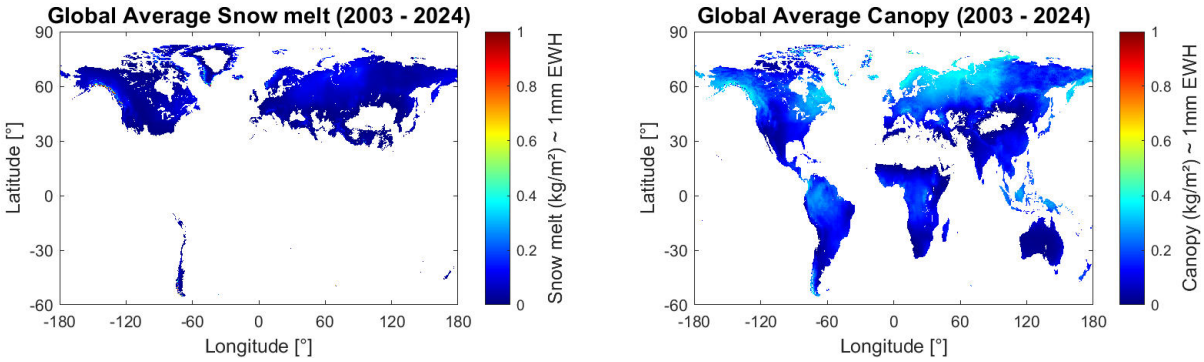

Figure 4.23: Global canopy average

5 Conclusion and Outlook

This research showcases the ability of GRACE and GRACE-FO satellite data to track variations in terrestrial water storage and groundwater across Africa. By combining GRACE data with outputs from the GLDAS hydrological model, a thorough evaluation of both surface and subsurface water dynamics is achieved. The analysis of various de correlation filters reveals a trade-off between diminishing noise and maintaining spatial resolution.

Future research could build on this work by utilizing GRACE-FO data for the most recent years, exploring different filtering methods and leakage correction approaches, and conducting region-specific investigations for particular river basins. Incorporating additional hydrological models and on-ground observations would significantly enhance the understanding of changes in groundwater storage.

Acknowledgement

I would like to extend my gratitude to Dr.-Ing. Kurt Seitz for his significant support and guidance throughout this lab rotation. His extensive knowledge and thoughtful suggestions played a crucial role in shaping the research and enhancing the report's quality. In addition to his advice, his assistance with code modifications and error corrections has expedited the progress of the report. His support has also increased my confidence for the upcoming lab rotations and thesis preparation. I am also grateful to Prof. Dr.-Ing. Hansjörg Kutterer for designing the task and clarifying the objectives, which provided a robust foundation for the research and its successful implementation. I would also like to recognize the assistance from Geodätisches Institut (GIK) for supplying the necessary resources and facilities. Furthermore, I acknowledge ICGEM (2026) for providing the data used in this study.

References

GLDAS (2025): GLDAS - Global Land Data Assimilation System. https://disc.gsfc.nasa.gov/datasets?keywords=GLDAS. Accessed: 2025-11-26.

Heiskanen, W. A. and Moritz, H. (1967): Physical Geodesy. W. H. Freeman & Co., San Francisco, USA.

ICGEM (2026): International Centre for Global Earth Models (ICGEM): Gravity field and GRACE/GRACE-FO products hosted at the German Research Centre for Geosciences (GFZ). Accessed: 2026-04-06. URL: https://icgem.gfz-potsdam.de/.

Kusche, J. (2007): Approximate decorrelation and non-isotropic smoothing of time-variable GRACE-type gravity field models. *Journal of Geodesy* 81(11):733–749. DOI: 10.1007/s00190-007-0143-3.

Rodell, M., Houser, P. R., Jambor, U., Gottschalck, J., Mitchell, K. E., Meng, C.-J., Arsenault, K., Cosgrove, B. A., Radakovich, J. D., Bosilovich, M. G., Entin, J. K., Walker, J. P., Lohmann, D., and Toll, D. L. (2004): The Global Land Data Assimilation System. *Bulletin of the American Meteorological Society* 85(3):381–394. DOI: 10.1175/BAMS-85-3-381.

Tsoulis, D. (1999): Spherical harmonic computations with topographic/isostatic coefficients. Tech. rep. IAPG/FESG No. 3. Munich, Germany: Institut für Astronomische und Physikalische Geodäsie, Technische Universität München.

Wahr, J., Molenaar, M., and Bryan, F. (1998): Time variability of the Earth's gravity field: Hydrological and oceanic effects and their possible detection using GRACE. *Journal of Geophysical Research: Solid Earth* 103(B12):30205–30229.

Ground water monitoring over the continent of South-America

Ignatious Jose[1]

1 Remote Sensing and Geoinformatics Master of Science (M.Sc.), KIT, Germany
E-Mail: uqrgk@student.kit.edu

Abstract

This study confirms that satellite gravimetry is a powerful tool for large-scale groundwater monitoring when appropriate filtering strategies are employed and surface hydrological contributions are carefully accounted for. The results emphasize methodological transparency and cautious interpretation of groundwater information derived from GRACE observations, particularly regarding signal leakage and attenuation induced by decorrelation filters. Looking forward, improving quantitative reliability requires explicit correction of leakage and filter-induced biases, with mascon-based GRACE solutions or region-specific leakage correction as promising approaches to preserve groundwater signals while reducing distortions. Extending uncertainty propagation to include the groundwater estimation step would enable formal error quantification for groundwater anomalies and enhance confidence in regional and temporal comparisons. Integrating alternative hydrological models and in-situ observations where available can constrain near-surface storage components and reduce ambiguity in separating groundwater from total water storage. At a regional scale, basin- or sub-regional analyses are essential to reveal heterogeneous groundwater trends potentially masked by continental averages, particularly in areas with intensive abstraction or pronounced climatic gradients. Finally, next-generation gravity missions with higher spatial resolution and lower correlated errors are expected to substantially enhance groundwater monitoring under increasing climatic variability and anthropogenic pressure, reinforcing satellite gravimetry as a core component of global groundwater assessment frameworks.

Keywords GRACE · Total Water Storage (TWS) · GLDAS · South-America

1 Introduction

In this study, the temporal variations of groundwater storage over the South American continent are investigated using satellite-based gravity data. The analysis is based on the Gravity Recovery and Climate Experiment (GRACE) and its successor mission GRACE Follow-On (GRACE-FO), which provide monthly solutions of the Earth's gravity field. These variations reflect the redistribution of mass within the Earth system, mainly related to hydrological processes such as precipitation, evaporation, and groundwater depletion (Wahr et al., 1998).
An integration of GRACE-derived Total Water Storage (TWS) data with the Global Land Data Assimilation System (GLDAS) is performed to estimate groundwater changes. Since GLDAS provides individual components of the water budget, including soil moisture, snow, and surface runoff, the groundwater storage is obtained by subtracting these from the GRACE-based TWS anomalies.

KIT Scientific Working Papers
Issue Number 270
ISSN: 2194-1629
DOI: 10.5445/IR/1000191188
Online: June 2026

This document is licensed under the Creative Commons Attribution – Share Alike 4.0 International License (CC BY-SA 4.0):
https://creativecommons.org/licenses/by-sa/4.0/deed.en

This approach enables a comprehensive assessment of continental-scale groundwater variability between 2012 and 2024. The resulting maps and time series provide insights into regional hydrological patterns, seasonal fluctuations, and long-term trends across diverse climatic zones in South America.

2 Theoretical Aspects

Several fundamental concepts play an important role in analysing the temporal and spatial variations of groundwater storage derived from satellite gravimetry. The GRACE and GRACE-FO missions provide monthly gravity field solutions in the form of spherical harmonic coefficients, which can be transformed to surface mass variations. The combination of these gravity-derived Total Water Storage (TWS) anomalies with hydrological model outputs from GLDAS enables the estimation of groundwater storage variations (GWS) across South America.

2.1 Spherical Harmonic Representation of the Gravity Field

The Earth's external gravitational potential V can be expressed as a series of fully normalised spherical harmonics as shown in Equation (1):

$$V(r,\varphi,\lambda) = \frac{GM}{r}\sum_{n=0}^{N}\left(\frac{R}{r}\right)^{n}\sum_{m=0}^{n}\left(\bar{C}_{nm}\cos m\lambda + \bar{S}_{nm}\sin m\lambda\right)\bar{P}_{nm}(\sin\varphi)\,, \tag{2.1}$$

where
GM : geocentric gravitational constant,
R : mean radius of the reference Earth,
$\bar{C}_{nm}, \bar{S}_{nm}$: fully normalised spherical harmonic coefficients of degree n and order m,
$\bar{P}_{nm}$: fully normalised associated Legendre functions.
The temporal variation in mass distribution on the Earth's surface is represented by changes in these coefficients in respect to a reference (mean) model, denoted as $\Delta\bar{C}_{nm}$ and $\Delta\bar{S}_{nm}$, between monthly GRACE solutions. These variations can be converted into equivalent surface mass anomalies using the formulation of Wahr et al.(1998)

2.2 Computation of Surface Mass Change

Surface mass variations are derived from spherical harmonic coefficients using the following relation:

$$\Delta\sigma(\theta,\lambda) = \frac{a\rho_E}{3}\sum_{n=0}^{N}\sum_{m=0}^{n}\frac{2n+1}{1+k_n}P_{nm}(\cos\theta)\left(\Delta C_{nm}\cos m\lambda + \Delta S_{nm}\sin m\lambda\right) \tag{2.2}$$

where a is the Earth's mean radius, ρ_E is the average density of the Earth, and k_n is the load Love number. The resulting surface mass density, $\Delta\sigma$, represents the Total Water Storage (TWS) anomaly at each grid point.

2.3 Estimation of Groundwater Storage

The GRACE-derived TWS represents the vertically integrated sum of all water components within the terrestrial column, expressed as:

$$\mathrm{TWS} = \mathrm{SM} + \mathrm{SW} + \mathrm{SN} + \mathrm{GWS}, \tag{2.3}$$

where SM denotes soil moisture, SW surface water, SN snow/ice, and GWS groundwater storage. Since GLDAS provides estimates of SM, SW, and SN, the groundwater component can be isolated by subtraction as:

$$\mathrm{GWS} = \mathrm{TWS}_{\mathrm{GRACE}} - (\mathrm{SM} + \mathrm{SW} + \mathrm{SN})_{\mathrm{GLDAS}}. \tag{2.4}$$

2.4 Filtering and Spatial Resolution

The GRACE spherical harmonic solutions contain correlated noise that appears as north–south stripes in the spatial domain. To mitigate this effect, decorrelation filters such as DDK2 and DDK5 are applied before synthesising the mass grids. These filters reduce noise while preserving geophysically meaningful signals. The filtered mass change coefficients are then transformed into a spatial grid with a resolution of $0.5^\circ \times 0.5^\circ$ to analyse regional variations across the South American continent.
This theoretical framework provides the basis for quantifying groundwater storage changes from GRACE and GLDAS datasets, allowing for the interpretation of large-scale hydrological variations and climate-induced water balance trends across South America.

3 Data

The Level-2 data used in this study consist of the monthly gravity field solutions from the GRACE and GRACE-FO missions and the corresponding hydrological parameters from the Global Land Data Assimilation System (GLDAS). The solutions are provided by the Jet Propulsion Laboratory (JPL,DDK2 and DDK5) as Release 6.1 products (GFZ German Research Centre for Geosciences, 2025) available through the International Centre for Global Earth Models (ICGEM).

3.1 Monthly Solutions from GES DISC for GLDAS

In addition, GLDAS land surface model outputs were obtained from the NASA Goddard Earth Sciences Data and Information Services Center (GES DISC) via the LDAS portal. The GLDAS datasets provide monthly gridded variables such as soil moisture, snow water equivalent, surface runoff, and subsurface runoff, at a spatial resolution of $0.5^\circ \times 0.5^\circ$. These data are used to represent the individual components of the terrestrial water balance. The total water storage anomalies (TWSA) derived from GRACE/GRACE-FO are compared with GLDAS-based estimates to isolate the groundwater storage variations over South America.The GLDAS data used in this study were obtained from the NASA Goddard Earth Sciences Data and Information Services Center (GES DISC) through the Land Data Assimilation System (LDAS) portal `https://ldas.gsfc.nasa.gov/gldas`. The specific product accessed was the GLDAS NOAH v2.1 monthly dataset with a spatial resolution of $0.5^\circ \times 0.5^\circ$, available at `https://disc.gsfc.nasa.gov/datasets/GLDAS_NOAH025_M_2.1/summary`.

3.2 Monthly Solutions from ICGEM for GRACE and GRACE-FO

The monthly solutions for Gravitational Potential are obtained from the GRACE and GRACE-FO missions, with data available from ICGEM's website. These solutions provide normalized spherical harmonic coefficients up to degree/order 96, which are essential for computing the gravitational potential of the Earth. To obtain these solutions, users can visit the ICGEM portal at `http://icgem.gfz-potsdam.de/series`, where data from different evaluation centers such as CSR, GFZ, and JPL are compiled.
For the TWS, filtered solutions like DDK2 and DDK5 are preferred for comparative studies, as they remove long-wavelength signals that may distort regional hydrological analyses (Kusche, 2007). The data from CSR, which provides ready-to-use TWS grids, is also available for download in different levels of de-striping.

4 Methodology

4.1 Objective and Data Sources

The primary objective of this project is to analyze the changes in Earth's water balance using data from the **GRACE** (Gravity Recovery and Climate Experiment) and **GLDAS** (Global Land Data Assimilation System) datasets for

the South American continent. The analysis focuses on estimating *Total Water Storage (TWS)* and its temporal dynamics by integrating satellite-based geodetic sensor data with hydrological model outputs.

4.2 GRACE Processing: From Potential Coefficients to TWS

Let $\overline{C}_{nm}(t), \overline{S}_{nm}(t)$ denote fully normalized SH coefficients at epoch t, referenced to (GM, R) and filtered by DDK.

Mean (reference) field and residuals. A multi-year mean model is formed and removed month-wise:

$$\Delta\overline{C}_{nm}(t) \;=\; \overline{C}_{nm}(t) - \langle \overline{C}_{nm} \rangle, \qquad \Delta\overline{S}_{nm}(t) \;=\; \overline{S}_{nm}(t) - \langle \overline{S}_{nm} \rangle. \tag{4.1}$$

Synthesis of the potential residuals on the ellipsoid.
For latitude φ, longitude λ, geocentric radius r , the disturbing gravitational potential residual is synthesized as

$$\Delta V(\varphi,\lambda,t) \;=\; \frac{GM}{r} \sum_{n=2}^{n_{\max}} \left(\frac{a}{r}\right)^n \sum_{m=0}^{n} \overline{P}_{nm}(\sin\varphi) \Big[\Delta\overline{C}_{nm}(t)\cos(m\lambda) + \Delta\overline{S}_{nm}(t)\sin(m\lambda)\Big]. \tag{4.2}$$

The (residual) geoid undulation follows as

$$\Delta N(\varphi,\lambda,t) = \frac{\Delta V(\varphi,\lambda,t)}{\gamma(\varphi)},$$

with $\gamma(\varphi)$ denoting the normal gravity on GRS80.

Scaling to equivalent water height (TWS)
Following the load-deformation theory (e.g. Wahr et al., 1998), residual mass loading (equivalent water height, EWH) is obtained by applying degree-wise scale factors $\alpha_n = \alpha_n(h_n, k_n)$ that depend on the load Love numbers (h_n, k_n):

$$\Delta D_{nm}(t) \;=\; \alpha_n \Delta\overline{C}_{nm}(t), \qquad \Delta E_{nm}(t) \;=\; \alpha_n \Delta\overline{S}_{nm}(t). \tag{4.3}$$

By comparing Eqs. (2) and (7), the degree-dependent scaling factor α_n is defined as

$$\alpha_n = \frac{a\rho_E}{3}\,\frac{2n+1}{1+k_n}. \tag{4.4}$$

Synthesizing on the sphere as a surface SH representation,

$$\mathrm{TWS}_{\mathrm{GRACE}}(\varphi,\lambda,t) \;=\; \sum_{n=2}^{n_{\max}} \sum_{m=0}^{n} \overline{P}_{nm}(\sin\varphi) \Big[\Delta D_{nm}(t)\cos(m\lambda) + \Delta E_{nm}(t)\sin(m\lambda)\Big]. \tag{4.5}$$

The equation (4.5) for calculating TWS follows from the equation (2.2).

4.3 GLDAS Processing: Water Storage Components

For each month t and grid cell, GLDAS components are read and aggregated.

Soil moisture (four layers).

$$W_{\mathrm{soil}}(t) \;=\; W_{0\text{–}10}(t) \;+\; W_{10\text{–}40}(t) \;+\; W_{40\text{–}100}(t) \;+\; W_{100\text{–}200}(t). \tag{4.6}$$

Runoff and other terms.

$$R_{\mathrm{tot}}(t) \;=\; R_{\mathrm{surf}}(t) + R_{\mathrm{sub}}(t), \qquad W_{\mathrm{SA}}(t) \;=\; W_{\mathrm{snow}}(t) + W_{\mathrm{canopy}}(t). \tag{4.7}$$

GLDAS total (no groundwater).

$$\mathrm{TWS}_{\mathrm{GLDAS}}(t) \;=\; W_{\mathrm{soil}}(t) + R_{\mathrm{tot}}(t) + W_{\mathrm{SA}}(t). \tag{4.8}$$

All GLDAS fields are aggregated to the South America mask and summarized by monthly spatial means and descriptive statistics (mean, std, min, max).

4.4 TWS–GLDAS Fusion and Groundwater Estimate

Assuming GLDAS captures the non-groundwater storage terms, a first-order estimate of groundwater storage anomalies (GWS) is obtained as the residual between GRACE-derived TWS and GLDAS sum:

$$\mathrm{GWS}(t) \;\approx\; \big\langle \mathrm{TWS}_{\mathrm{GRACE}}(\varphi,\lambda,t)\big\rangle_{\Omega} \;-\; \big\langle \mathrm{EWH}_{\mathrm{GLDAS}}(\varphi,\lambda,t)\big\rangle_{\Omega}, \tag{4.9}$$

where $\langle\cdot\rangle_{\Omega}$ denotes spatial averaging over the South America domain (same mask/grid). When desired, Eq. (4.9) can be evaluated per grid cell to obtain spatial GWS maps.

4.5 Uncertainty Characterization

This section describes the characterization of coefficient variances and their linear propagation into the gravitational potential. Let $\sigma^2(\bar{C}_{nm})$ and $\sigma^2(\bar{S}_{nm})$ denote the monthly variances of the fully normalized spherical harmonic coefficients.

$$\sigma_V^2(\varphi,\lambda) \;=\; \sum_{n=2}^{n_{\max}} \sum_{m=0}^{n} \left(\frac{\partial V}{\partial \overline{C}_{nm}}\right)^2 \sigma^2(\overline{C}_{nm}) + \left(\frac{\partial V}{\partial \overline{S}_{nm}}\right)^2 \sigma^2(\overline{S}_{nm}), \tag{4.10}$$

with partials directly read from Eq. (2.1). Undulation variances follow as $\sigma_N^2 = \sigma_V^2/\gamma^2$. (Implemented in the matlab code and mapped by `plot_vfp_potential_grid`/`plot_vfp_undulation_grid`.)

Signal and error degree variances

Signal degree variances and error degree variances are computed as follows:

$$S_n \;=\; \sum_{m=0}^{n} \Big(\Delta\overline{C}_{nm}^2 + \Delta\overline{S}_{nm}^2\Big), \qquad E_n \;=\; \sum_{m=0}^{n} \Big(\sigma^2(\overline{C}_{nm}) + \sigma^2(\overline{S}_{nm})\Big), \tag{4.11}$$

illustrating signal power vs. noise by degree (see `degreevariances` and `errordegreevariances`).

4.6 Implementation Flow

1. **Load & filter GRACE SH:** Read monthly $\overline{C}_{nm}, \overline{S}_{nm}$; rescale to common (GM, R); use the DDK5; form mean reference and residuals Eq.(4.1).

2. **Synthesize fields:** Compute residual potential Eq.(4.2), residual geoid undulation ΔN , and convert to TWS via Love-number scaling Eqs.(4.3–4.5) on a $0.5^\circ \times 0.5^\circ$ grid.

3. **GRACE statistics & diagnostics:** Map fields; compute variance propagation Eq.(4.10); degree/error-degree variances Eq.(4.11); export monthly statistics and time series.

4. **Load GLDAS:** Read monthly soil layers, runoff (surface/subsurface), snowmelt, canopy on 0.25° grid; mask South America.

5. **Aggregate GLDAS:** Sum layers Eqs.(4.6)–(4.8); compute monthly spatial means, ranges; produce spatial maps and time series.

6. **Fuse & estimate GWS:** Combine GRACE TWS and GLDAS totals to obtain groundwater anomalies via Eq. (4.9) (either spatial means or maps).

4.7 Parameter Choices and Notes

- **Ellipsoid and constants:**
  GRS80 with $a = 6378137$ m,
  $e^2 = 0.00669438$;
  gravity parameter $GM = 0.3986004415 \times 10^{15}$ m^{3}s^{-2}.
- **Spectral limits:** $n_{\max} = 96$; minimum degree $n_{\min} = 2$.
- **Filtering:** DDK5 (other DDK levels optional).
- **Grids:** GRACE synthesis on $0.5^\circ \times 0.5^\circ$; GLDAS native at 0.25°.
- **Outputs:** Monthly PNG maps (potential, undulation, TWS, VFP, DV/EDV), MAT files for all gridded fields, and text summaries of descriptive statistics.

4.8 Assumptions and Limitations

- Groundwater is inferred as a residual Eq.(4.9); biases in GLDAS components or leakage/striping residuals in GRACE propagate into GWS.
- Degree-wise scaling α_n depends on adopted load Love numbers; alternative sets lead to small but systematic differences in EWH amplitude.
- Coastline leakage and signal attenuation from filtering are not explicitly corrected here (no dedicated leakage-inversion or mascon constraint applied).

Abbreviations. EWH: Equivalent Water Height; TWS: Total Water Storage; GWS: Groundwater Storage; DV/EDV: (Error) Degree Variance; SA: South America.

5 Results and Discussions

The primary objective of the results presented in this chapter is to assess groundwater storage variability using GRACE gravity field observations. Since GRACE captures total terrestrial water storage, the applied filtering strategies and the comparison with GLDAS are used to isolate and interpret the groundwater-related component of the observed mass changes.
This section discusses the results obtained from the GRACE/GRACE-FO and GLDAS analyses for South America (15° N–60° S, 85° W–30° W). The focus lies on how different filtering strategies affect the spectral and spatial characteristics of GRACE-derived products and how these results compare with hydrological storage estimates from GLDAS

5.1 Spectral Behaviour of DDK2 and DDK5 Filtered Coefficients

To evaluate how different decorrelation filters affect the spectral properties of GRACE gravity field solutions, a set of degree-based diagnostics was computed for both DDK2 and DDK5 filtered spherical harmonic coefficients. The analysis focuses on degree variance, error degree variance, degree–order triangle representations, and coefficient accuracy for two representative epochs, April 2003 and April 2024. These quantities were selected because they allow a direct assessment of how signal energy and noise are distributed across spherical harmonic degrees and how effectively correlated errors are suppressed by the respective filters.

The results obtained using the DDK2 filter are shown in Figure 5.1, while Figure 5.2 presents the corresponding diagnostics for DDK5. The degree variance and error degree variance plots provide an overview of how spectral energy changes with increasing harmonic degree and therefore serve as a primary indicator of noise attenuation at smaller spatial scales. The degree–order triangle plots complement this information by visualising the distribution of coefficient amplitudes across degrees and orders, making striping patterns and anisotropic error structures directly visible. In addition, the coefficient accuracy maps illustrate the formal uncertainties associated with individual coefficients and offer further insight into the stability of the filtered solutions.

A comparison of the degree variance results in Figure 5.1(a–b) and Figure 5.2(a–b) shows that the DDK5 filter leads to a stronger reduction of high-degree signal energy than DDK2. This behaviour reflects a more aggressive suppression of short-wavelength noise. In contrast, the DDK2-filtered solutions retain higher energy at medium to high degrees, indicating that more small-scale signal content is preserved, albeit together with increased residual noise. This trade-off between noise reduction and signal preservation is also evident in the relative degree and error degree variance plots Figure 5.1(g–h) and Figure 5.2(g–h), where DDK2 consistently exhibits higher noise levels compared to DDK5.

Further differences between the two filters become apparent in the degree–order triangle representations Figure 5.1(c–d) and 5.2(c–d). The DDK2 results show more pronounced directional patterns and striping, suggesting incomplete removal of correlated errors. In contrast, the DDK5 solutions display a more homogeneous triangular structure, consistent with stronger regularisation. A similar tendency is observed in the coefficient accuracy maps Figure 5.1(e–f) and Figure 5.2(e–f), where DDK5 generally yields lower error amplitudes, particularly at higher degrees.

In general, these results demonstrate that DDK5 prioritizes spectral stability and noise suppression, while DDK2 preserves a larger fraction of short-wavelength signal content. The choice between the two filters therefore has a direct impact on the balance between spatial resolution and noise level, which is a critical consideration for subsequent spatial and hydrological analyses.

From a groundwater perspective, the spectral behaviour of the filtered coefficients is critical, as excessive smoothing may suppress groundwater signals that typically evolve at medium spatial scales, while insufficient filtering may introduce noise that obscures long-term groundwater trends.

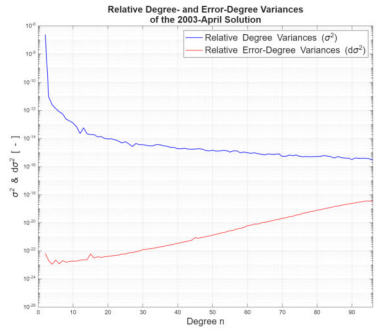

(a) Degree and Error degree Variance April 2003

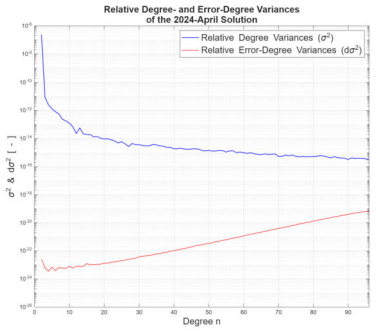

(b) Degree and Error degree Variance April 2024

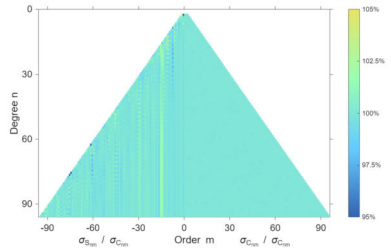

(c) Degree Order Triangle April 2003

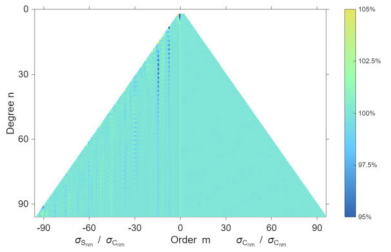

(d) Degree Order Triangle April 2024

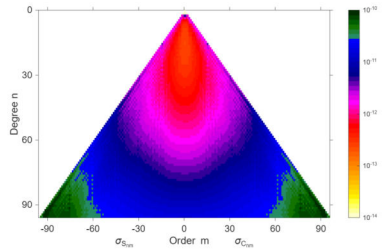

(e) Accuracy Of Coefficients April 2003

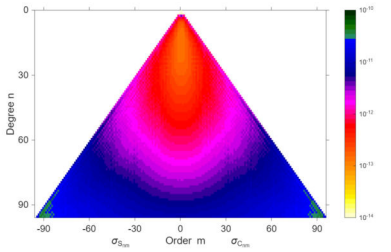

(f) Accuracy Of Coefficients April 2004

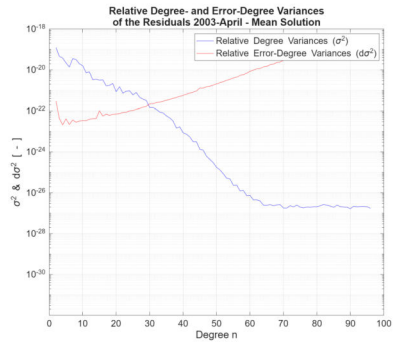

(g) Relative Degree and Error degree Variance April 2003

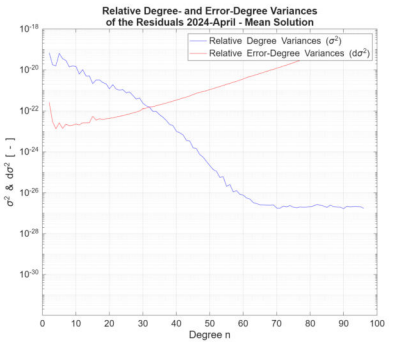

(h) Relative Degree and Error degree Variance April 2024

Figure 5.1: JPL DDK2 Coefficients

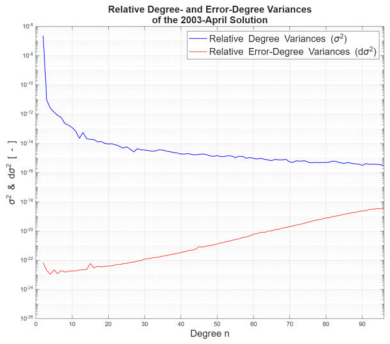

(a) Degree and Error degree Variance April 2003

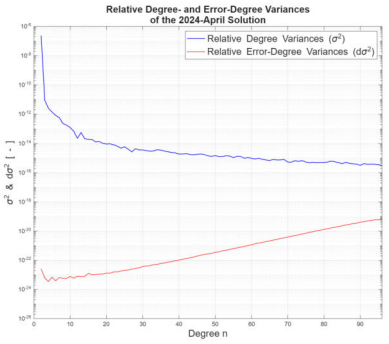

(b) Degree and Error degree Variance April 2024

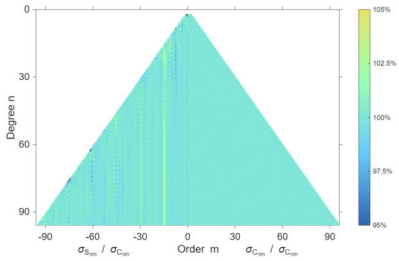

(c) Degree Order Triangle April 2023

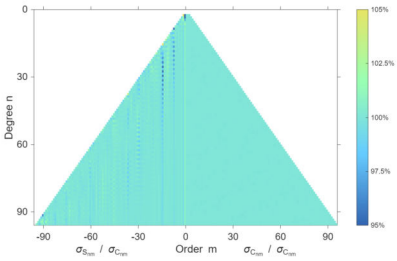

(d) Degree Order Triangle April 2024

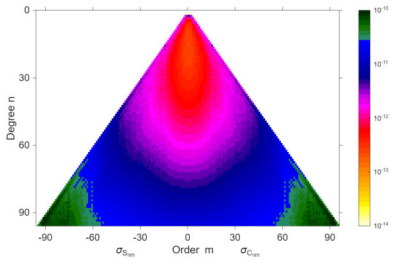

(e) Accuracy Of Coefficients April 2003

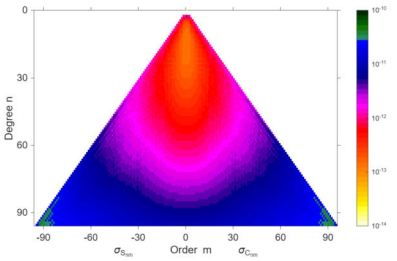

(f) Accuracy Of Coefficients April 2024

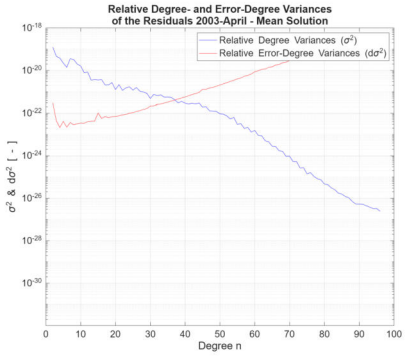

(g) Relative Degree and Error degree Variance April 2003

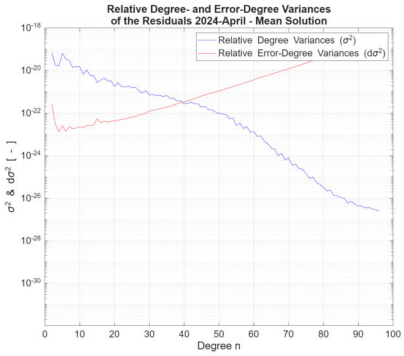

(h) Relative Degree and Error degree Variance April 2024

Figure 5.2: JPL DDK5 Coefficients

5.2 Spatial and Temporal Variations of Geoid Undulations and Equivalent Water Height Based on DDK2 and DDK5 Filtering

This subsection presents a comprehensive comparison of spatial and temporal variations in geoid undulations and Equivalent Water Height (EWH) derived from DDK2- and DDK5-filtered GRACE and GRACE-FO gravity field solutions. The analysis aims to assess how de-correlation filtering influences the representation of terrestrial water storage signals across different seasons, time periods, and mission phases.

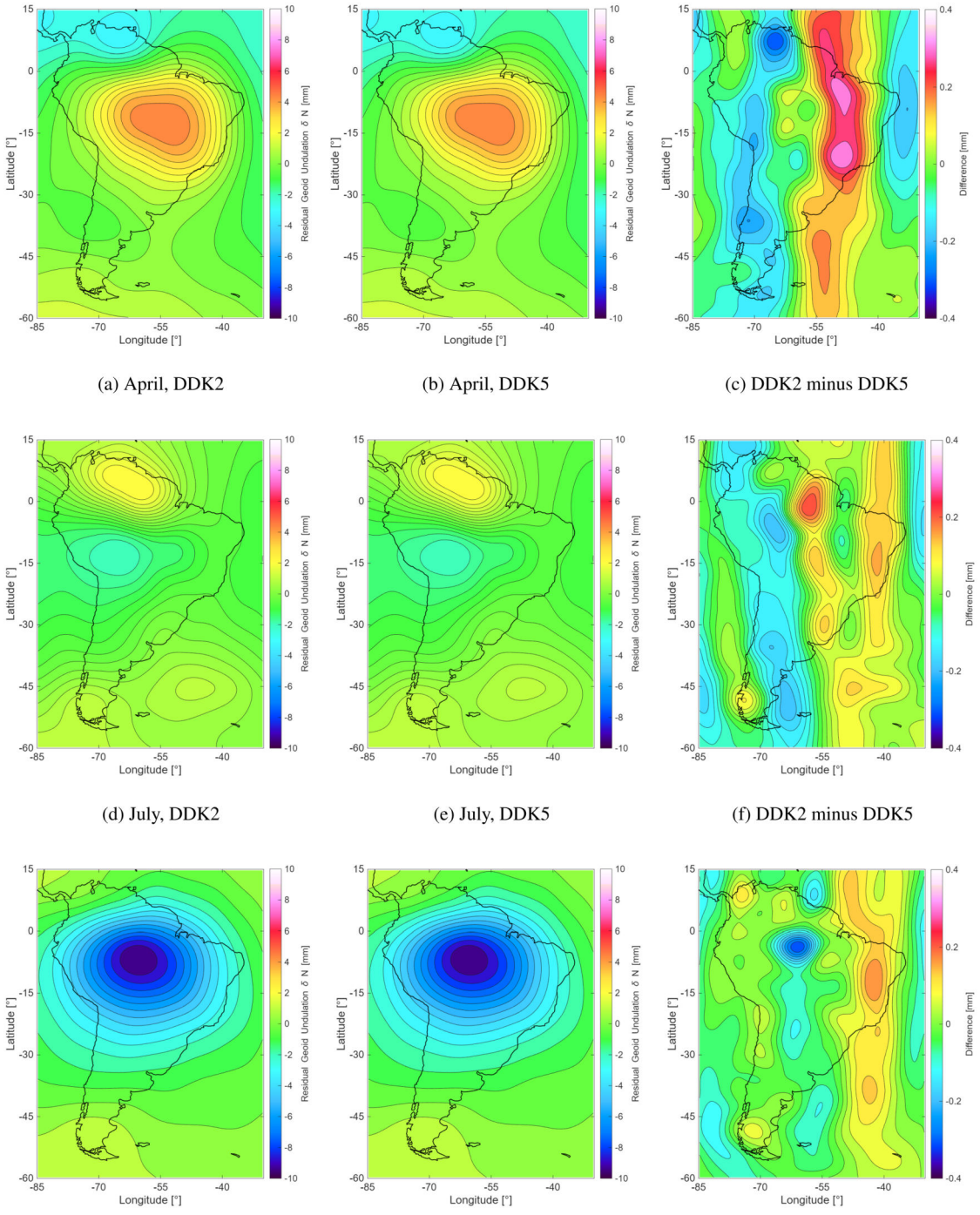

(a) April, DDK2 (b) April, DDK5 (c) DDK2 minus DDK5

(d) July, DDK2 (e) July, DDK5 (f) DDK2 minus DDK5

(g) October, DDK2 (h) October, DDK5 (i) DDK2 minus DDK5

Figure 5.3: Comparison of the Geoid Undulations based on JPL DDK2 vs DDK5 for the seasons in 2010

A direct comparison between DDK2 and DDK5-filtered solutions is first illustrated in Figure 5.3, which highlights the fundamental impact of filter choice on the spatial structure of geoid undulations. The DDK2 results exhibit stronger spatial gradients and more pronounced regional extrema, whereas the DDK5-filtered fields appear smoother and more spatially coherent, reflecting enhanced suppression of correlated noise.
Seasonal variability in geoid undulations during the GRACE mission period is shown in Figures 5.4 to Figure 5.7 and Figures 5.20 to Figures 5.23, covering April, October, and half-year intervals for the time spans 2005 and 2006–2011. Across all seasons, DDK2-filtered undulations display increased spatial variability and sharper local features, whereas DDK5-filtered results consistently show reduced short-wavelength structures and a clearer dominance of large-scale patterns. Despite these differences in spatial expression, the overall seasonal behaviour remains comparable between the two filtering approaches.
Corresponding variations in equivalent water height for the GRACE period are presented in Figures 5.8 to Figure 5.11 and Figures 5.24 to Figure 5.27. The EWH fields reflect integrated terrestrial water storage anomalies and exhibit pronounced seasonal contrasts between April and October. Similarly to the undulation results, the DDK2-derived EWH maps show larger anomaly amplitudes and stronger spatial contrasts, while DDK5 produces smoother anomaly distributions with reduced extremes. The temporal consistency of the patterns across multiple years indicates that the dominant hydrological signals are preserved under both filtering approaches, with differences primarily related to signal amplitude and spatial smoothness.
The analysis is extended to the GRACE-FO mission period using Figures 5.12 to Figure 5.15 and Figures 5.28 to Figure 5.31 for geoid undulations, and Figures 5.16 to Figure 5.19 and Figures 5.32 to Figure 5.35 for EWH. These figures demonstrate that the filter-dependent behaviour observed during the GRACE period persists in the GRACE-FO data. DDK2 continues to emphasise regional-scale variability and extrema, while DDK5 yields more stable and coherent spatial fields. Seasonal differences between April and October remain evident, and half-year aggregations further illustrate the persistence of large-scale signal structures over time.
Overall, the combined evaluation of geoid undulations and equivalent water height across multiple seasons, time spans, and mission phases confirms that decorrelation filter choice systematically affects the spatial detail and amplitude of GRACE-derived products. While DDK2 enhances short-wavelength variability and extremes, DDK5 provides a smoother and more consistent representation of continental-scale water storage variations. These differences form the basis for subsequent interpretation of long-term subsurface water storage behaviour.
The spatial patterns observed in GRACE-derived geoid undulations and equivalent water height represent integrated mass variations associated with terrestrial water storage. In regions with limited surface water storage, these signals are expected to be strongly influenced by groundwater contributions. The persistence and spatial coherence of both undulation and EWH patterns across seasons indicate that a substantial part of the observed signal is linked to subsurface water storage rather than short-term surface processes.

5.2.1 Results For Geoid Undulation Based On DDK2, GRACE

The Figure 5.3 shows GRACE-derived geoid undulations from JPL solutions filtered with DDK2 and DDK5 for April, July, and October 2010. Both filters reproduce consistent large-scale spatial patterns and seasonal variability. DDK2 preserves higher anomaly amplitudes and finer spatial features, while DDK5 yields smoother fields due to stronger noise suppression. The DDK2–DDK5 differences mainly reflect filter-induced effects rather than physical changes in the gravity field.

This section of figures presents geoid undulations derived from DDK2-filtered GRACE gravity field solutions. Figure 5.4 and Figure 5.5 illustrates the spatial patterns of April and October geoid undulations over South America for the period 2006–2011 and their interannual variability.

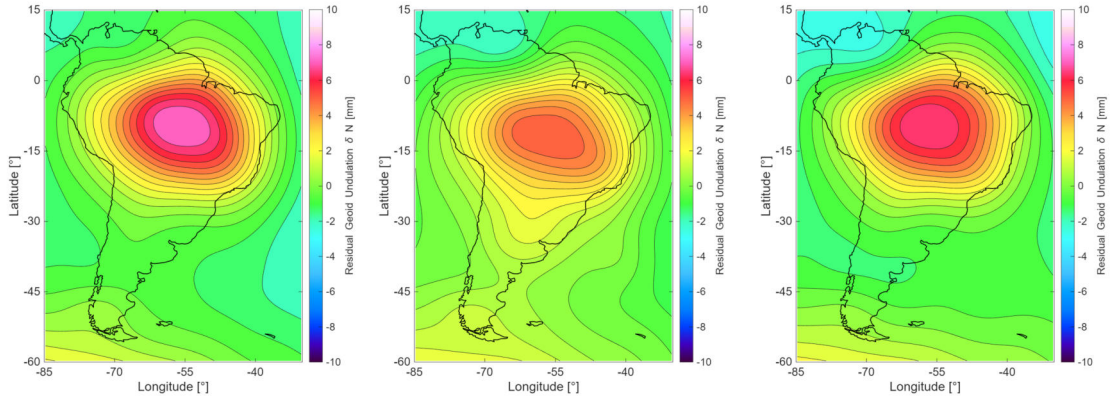

(a) 2006 (b) 2007 (c) 2008

(d) 2009 (e) 2010 (f) 2011

Figure 5.4: Variations of Geoid Undulations in April over the time span of 2006-2011

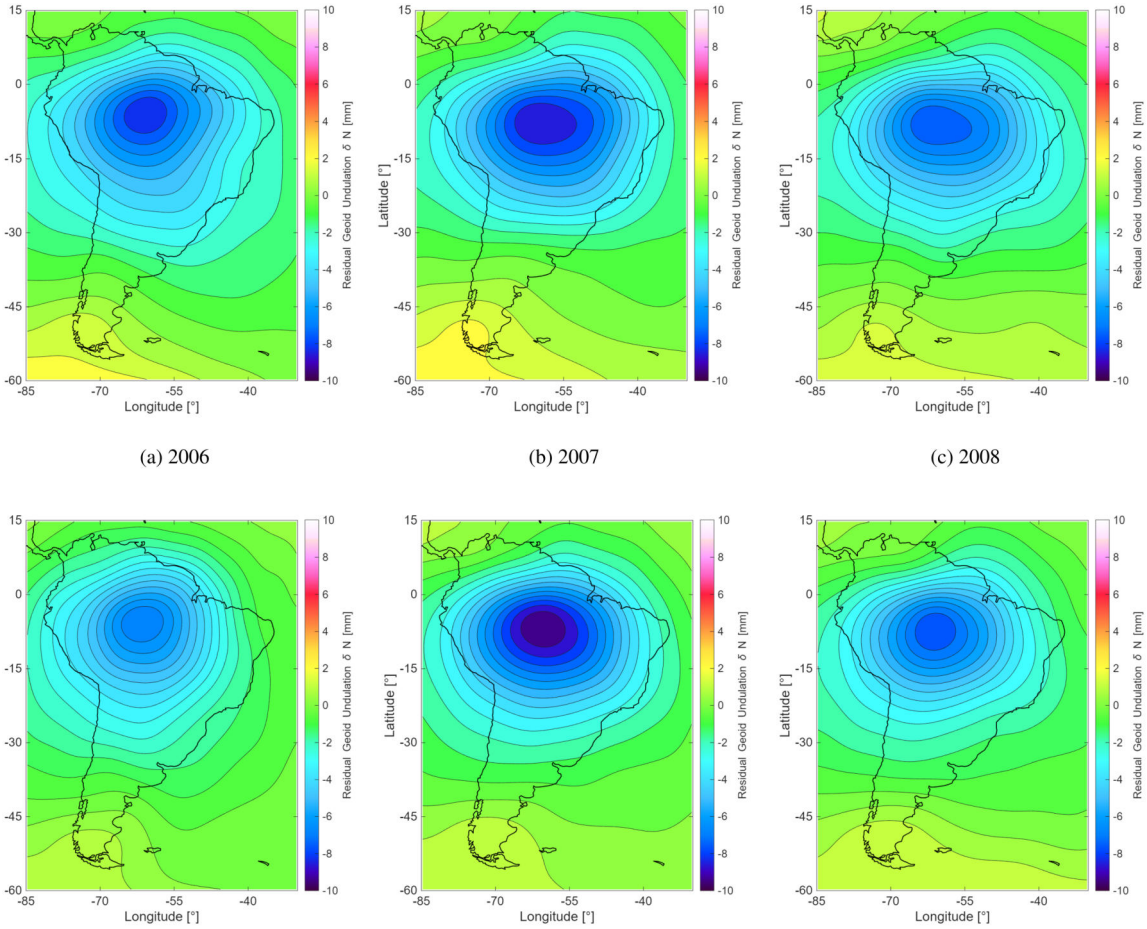

(a) 2006 (b) 2007 (c) 2008

(d) 2009 (e) 2010 (f) 2011

Figure 5.5: Variations of Geoid Undulations in October over the time span of 2006-2011

gure 5.6 shows the monthly variations of geoid undulations over South America from January to June 2005. The atial patterns and their temporal evolution reflect seasonal mass redistribution related to terrestrial water storage anges captured by GRACE observations.

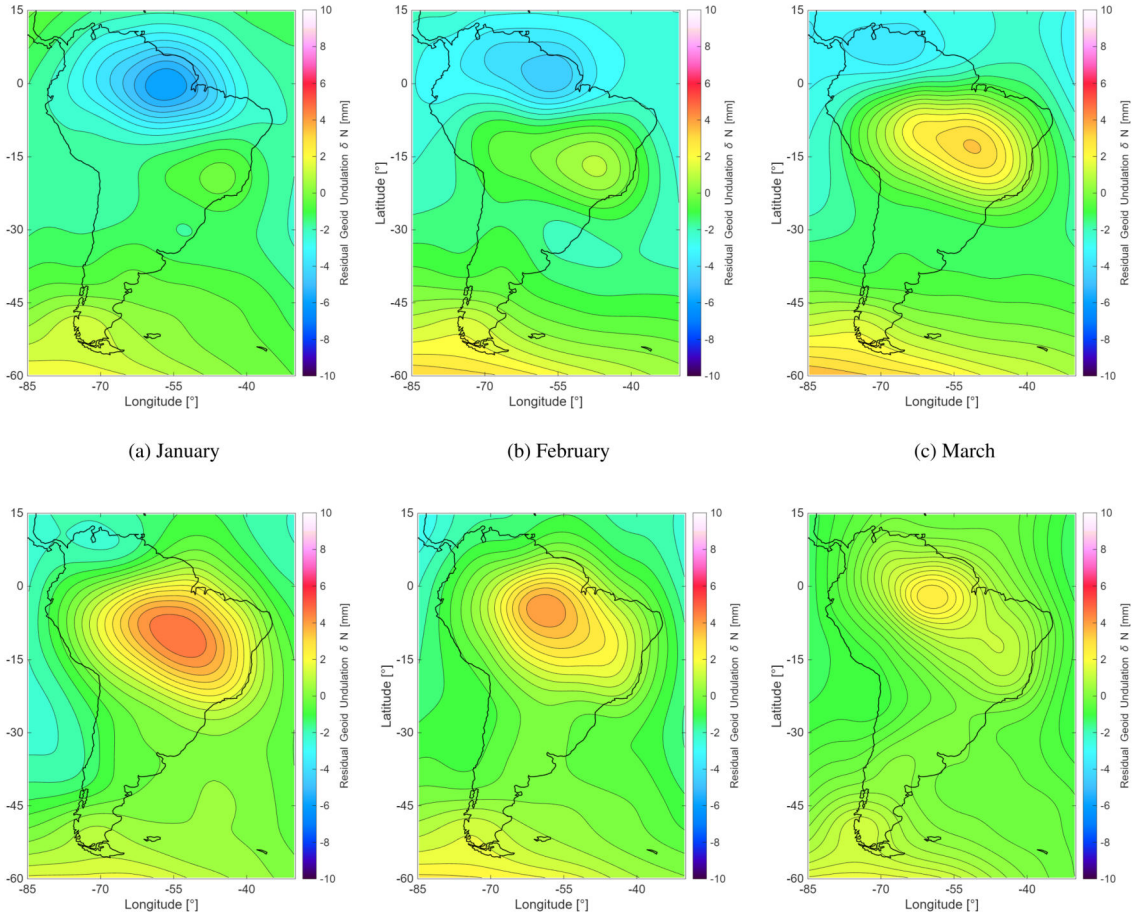

(a) January (b) February (c) March

(d) April (e) May (f) June

Figure 5.6: Variations of Geoid Undulations in 2005 (January - June)

Figure 5.7 shows the monthly evolution of geoid undulations from July to December 2005. In comparison with the first half of the year, the second half is characterised by more pronounced anomaly amplitudes and more spatially coherent patterns, indicating a seasonal shift in the mass distribution captured by the GRACE observations.

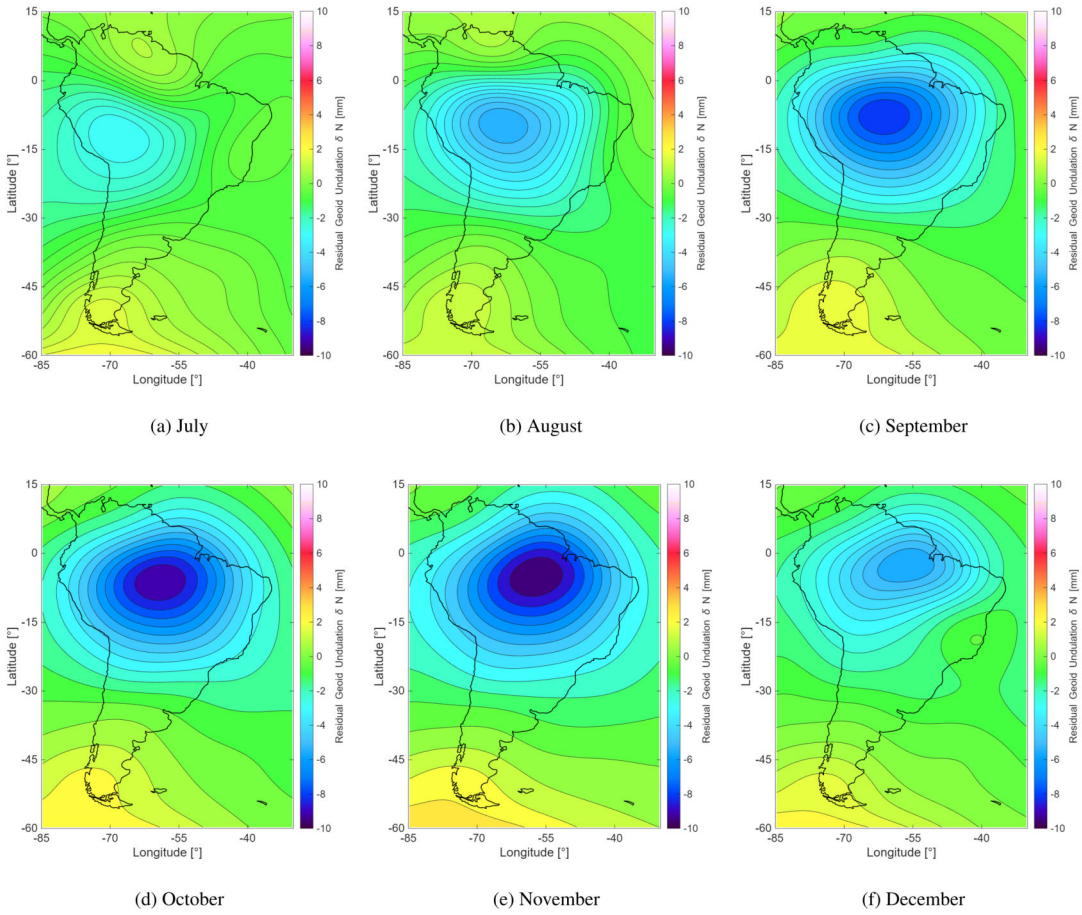

(a) July (b) August (c) September

(d) October (e) November (f) December

Figure 5.7: Variations of Geoid Undulations in 2005 (July - December)

5.2.2 Results For TWS Based On DDK2, GRACE

This section of figures presents the spatial distribution of Equivalent Water Height (EWH) derived from DDK2-filtered GRACE gravity field solutions. The EWH fields reflect mass-related surface deformation converted from spherical harmonic coefficients and serve as an integrated indicator of terrestrial water storage variability.
Figure 5.8 and Figure 5.9 shows the April and October EWH anomalies over South America for the period 2006–2011, highlighting the main spatial patterns and their interanual variability.

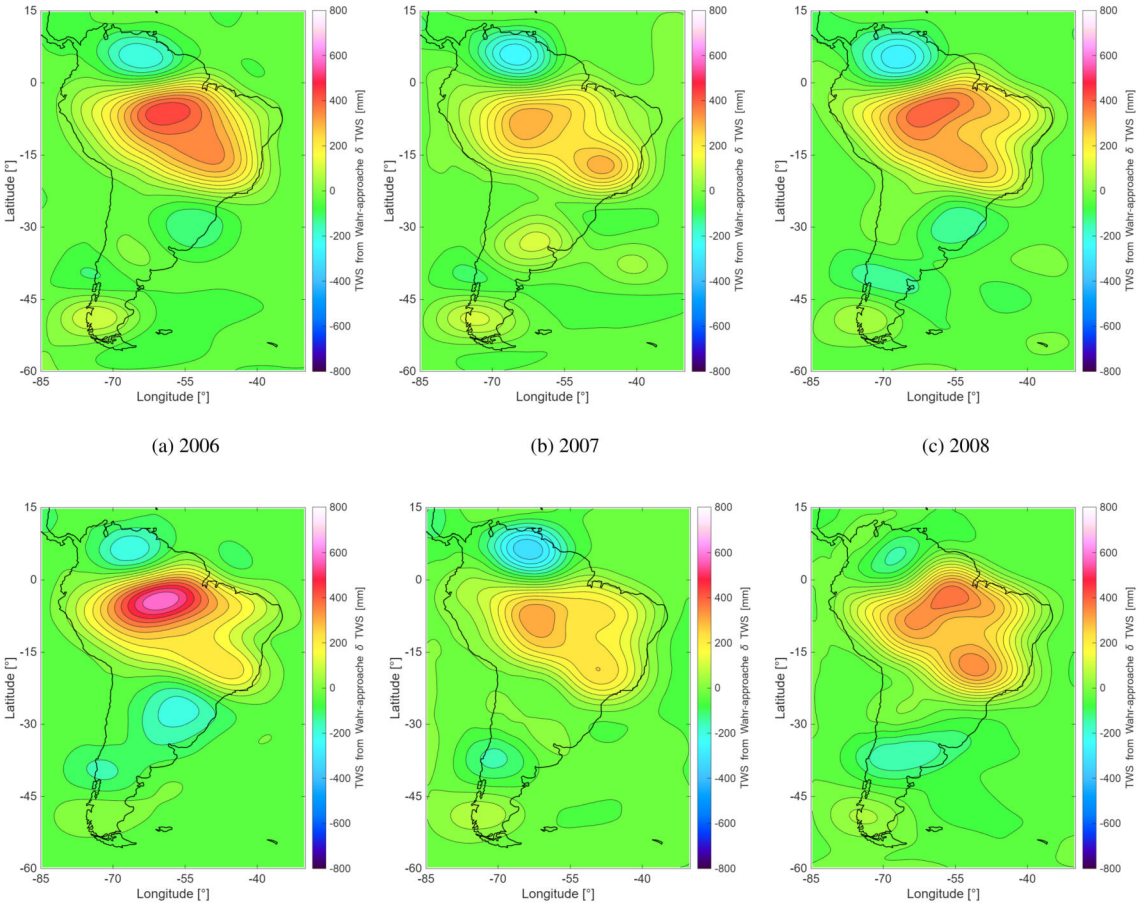

(a) 2006 (b) 2007 (c) 2008

(d) 2009 (e) 2010 (f) 2011

Figure 5.8: Variations of EWH in April over the time span of 2006-2011

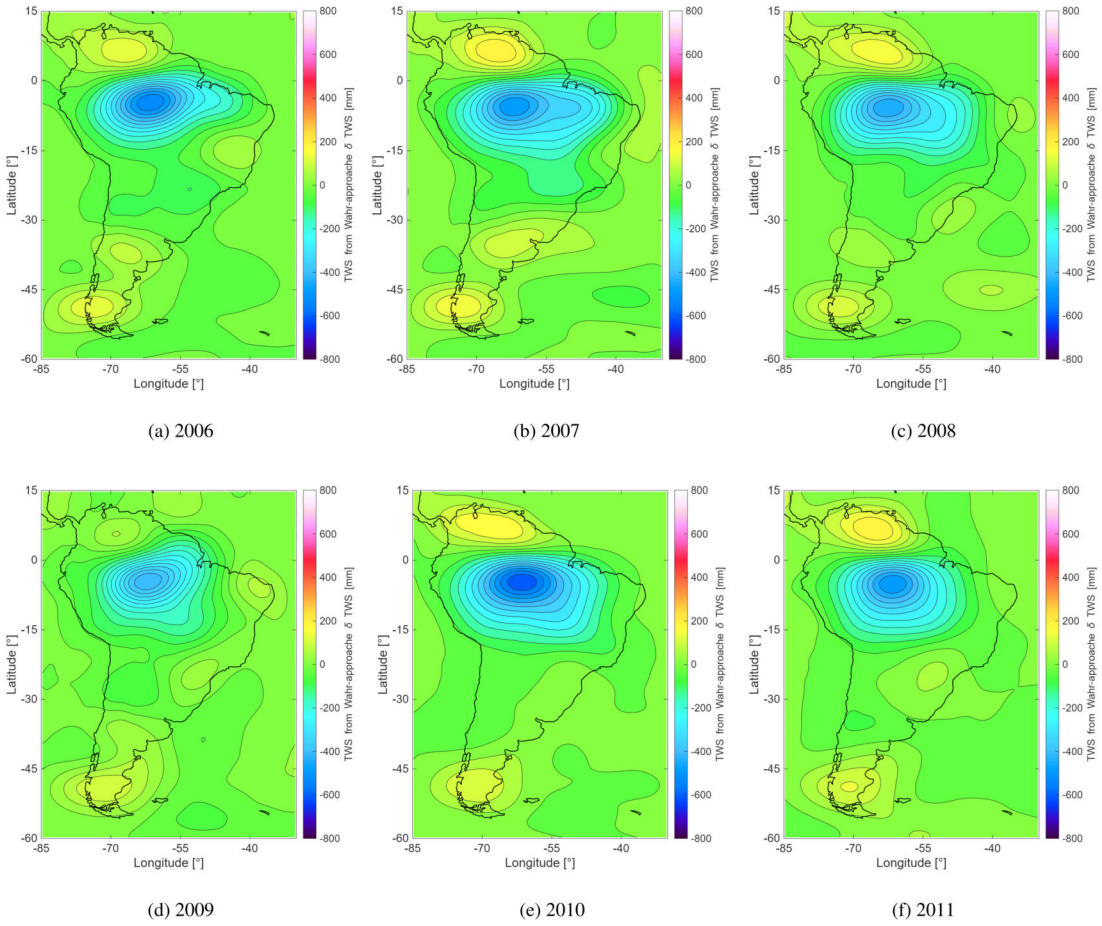

(a) 2006 (b) 2007 (c) 2008

(d) 2009 (e) 2010 (f) 2011

Figure 5.9: Variations of EWH in October over the time span of 2006-2011

Figure 5.10 presents the monthly variations of GRACE-derived Equivalent Water Height (EWH) over South America from January to June 2005. The maps show strong spatial variability and a clear seasonal evolution, with increasing anomaly amplitudes toward March–April followed by a redistribution and partial weakening in May and June. These patterns reflect seasonal changes in integrated terrestrial water storage captured by GRACE during the first half of the year.

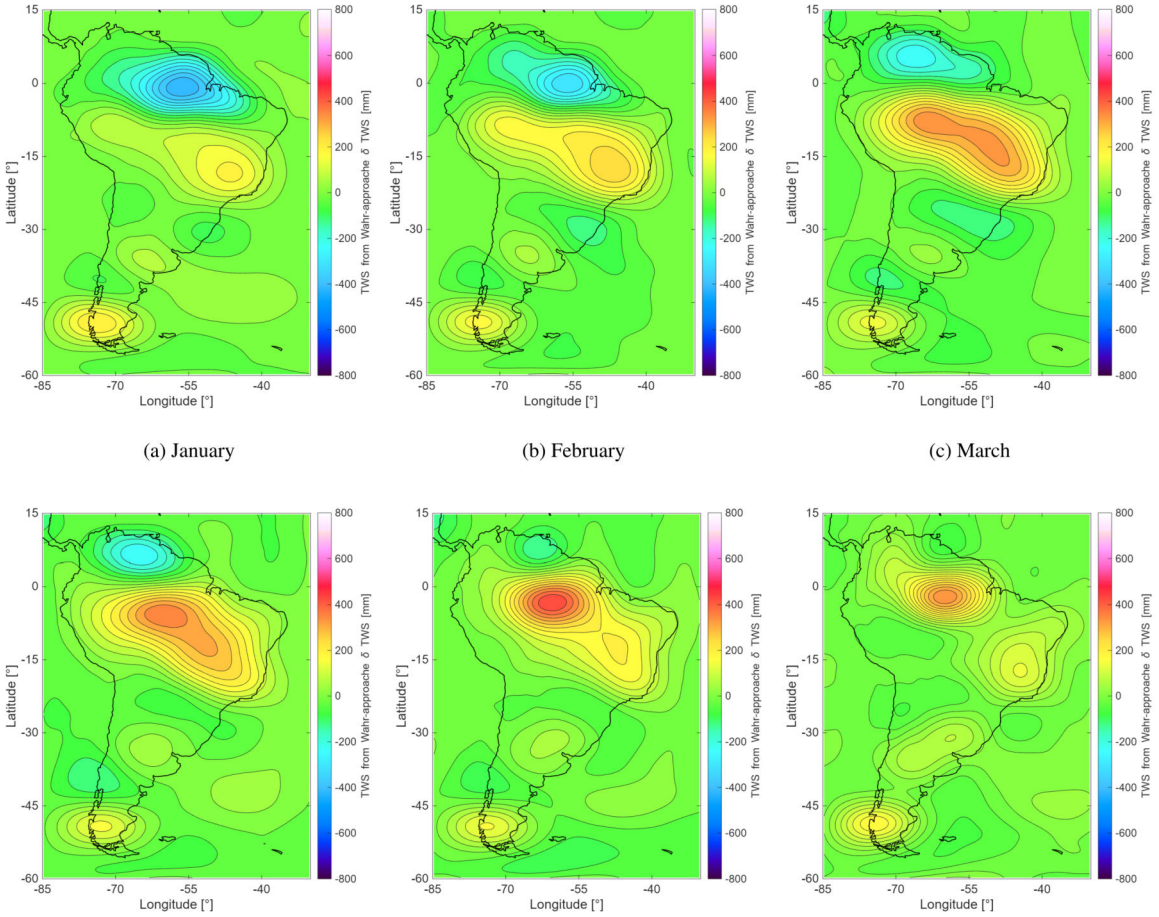

(a) January (b) February (c) March

(d) April (e) May (f) June

Figure 5.10: Variations of EWH in 2005 (January - June)

Figure 5.11 shows the monthly variations of GRACE-derived Equivalent Water Height (EWH) over South America from July to December 2005. Compared to the first half of the year, the second half is characterised by more spatially coherent negative anomalies and a clearer dominance of large-scale patterns, particularly between August and November. This contrast indicates a seasonal shift in integrated terrestrial water storage relative to January–June.

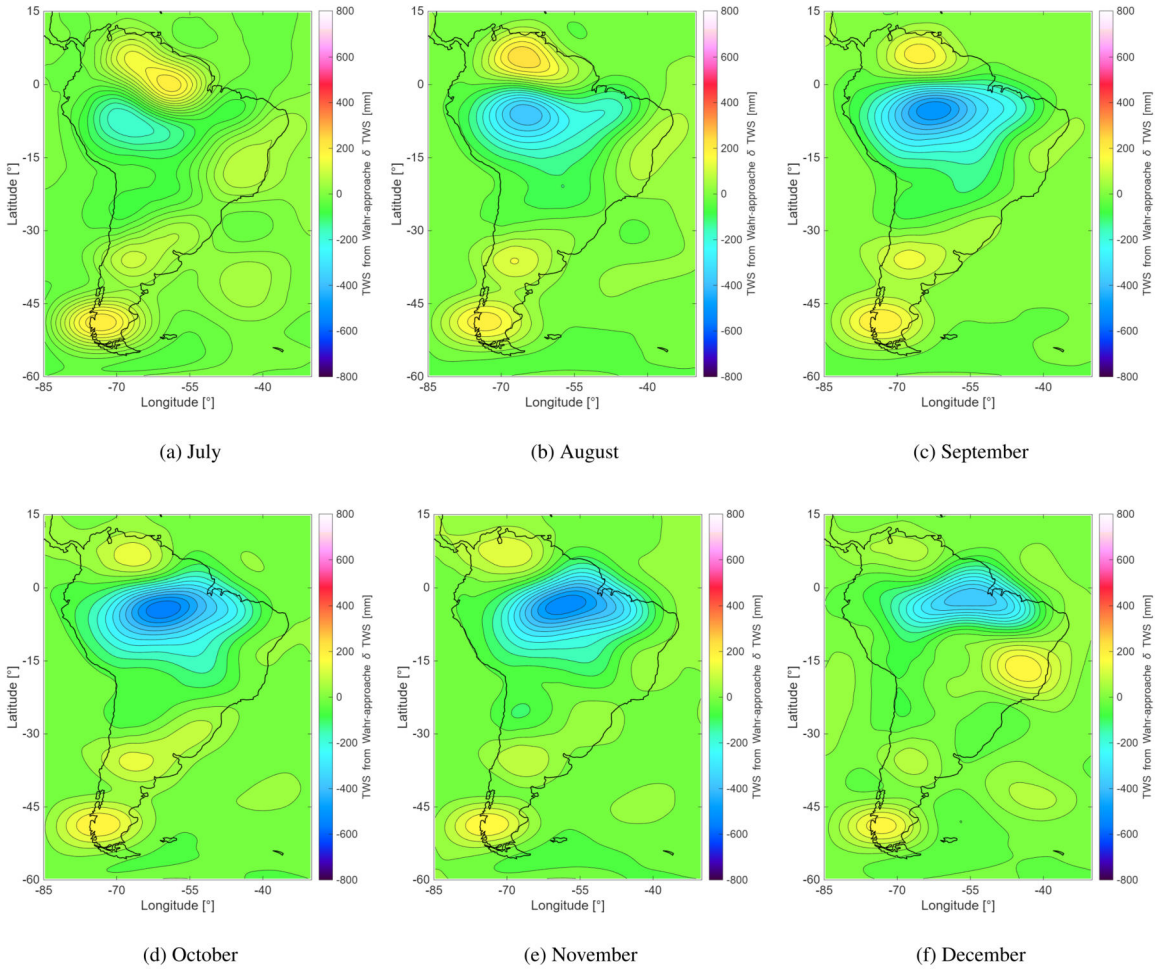

(a) July (b) August (c) September

(d) October (e) November (f) December

Figure 5.11: Variations of EWH in 2005 (July - December)

5.2.3 Results For Geoid Undulations Based On DDK2, GRACE-FO

This section of figures presents geoid undulations derived from DDK2-filtered GRACE-FO gravity field solutions. Figure 5.12 and Figure 5.13 illustrates the spatial patterns of April and October geoid undulations over South America for the period 2019–2024 and their interannual variability.

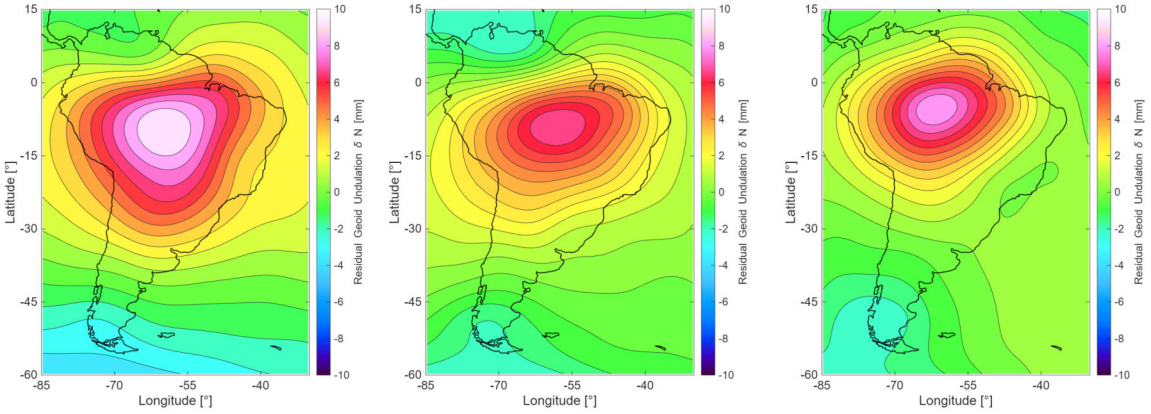

(a) 2019 (b) 2020 (c) 2021

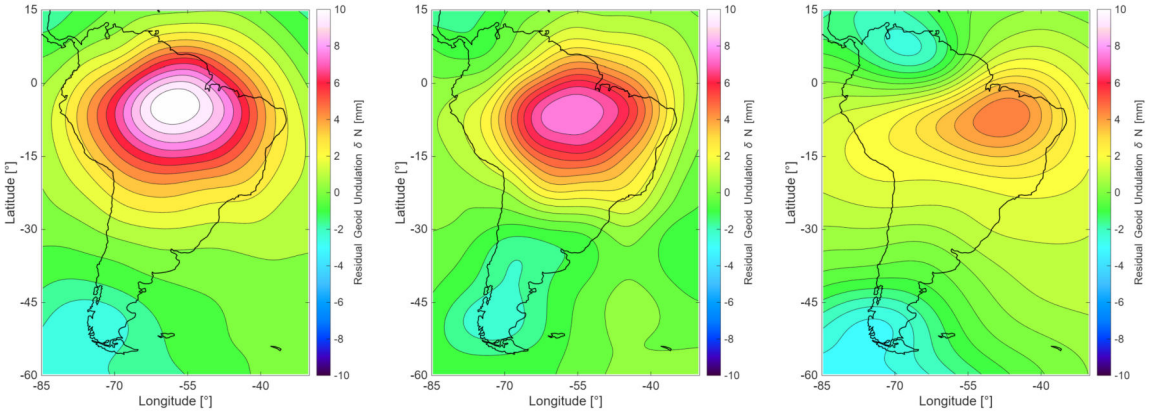

(d) 2022 (e) 2023 (f) 2024

Figure 5.12: Variations of Geoid Undulations in April over the time span of 2019-2024

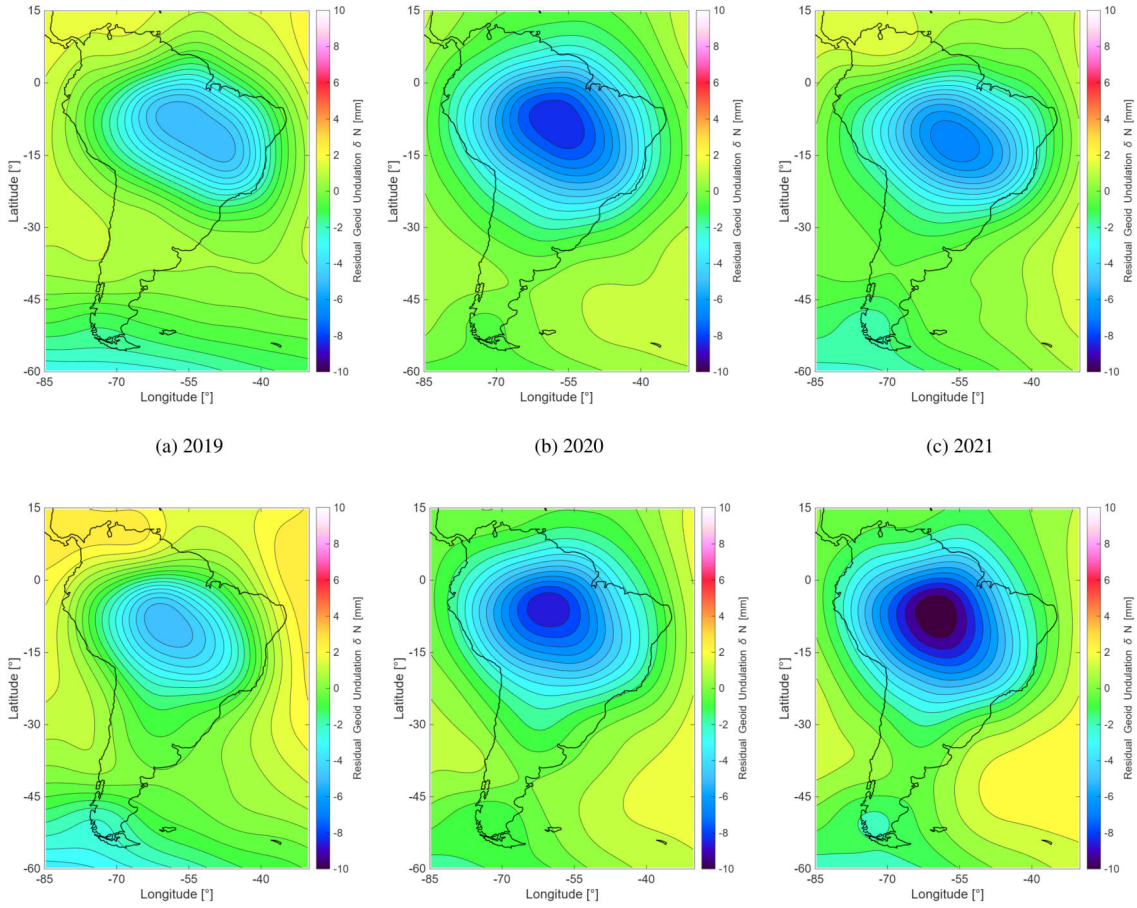

(a) 2019 (b) 2020 (c) 2021

(d) 2022 (e) 2023 (f) 2024

Figure 5.13: Variations of Geoid Undulations in October over the time span of 2019-2024

Figure 5.14 presents monthly geoid undulations derived from GRACE-FO observations. Compared to GRACE-based results, the large-scale spatial patterns remain consistent, indicating stable gravity-derived mass redistribution signals. This consistency supports the use of both missions for continuous analysis of terrestrial water storage and subsurface water variability.

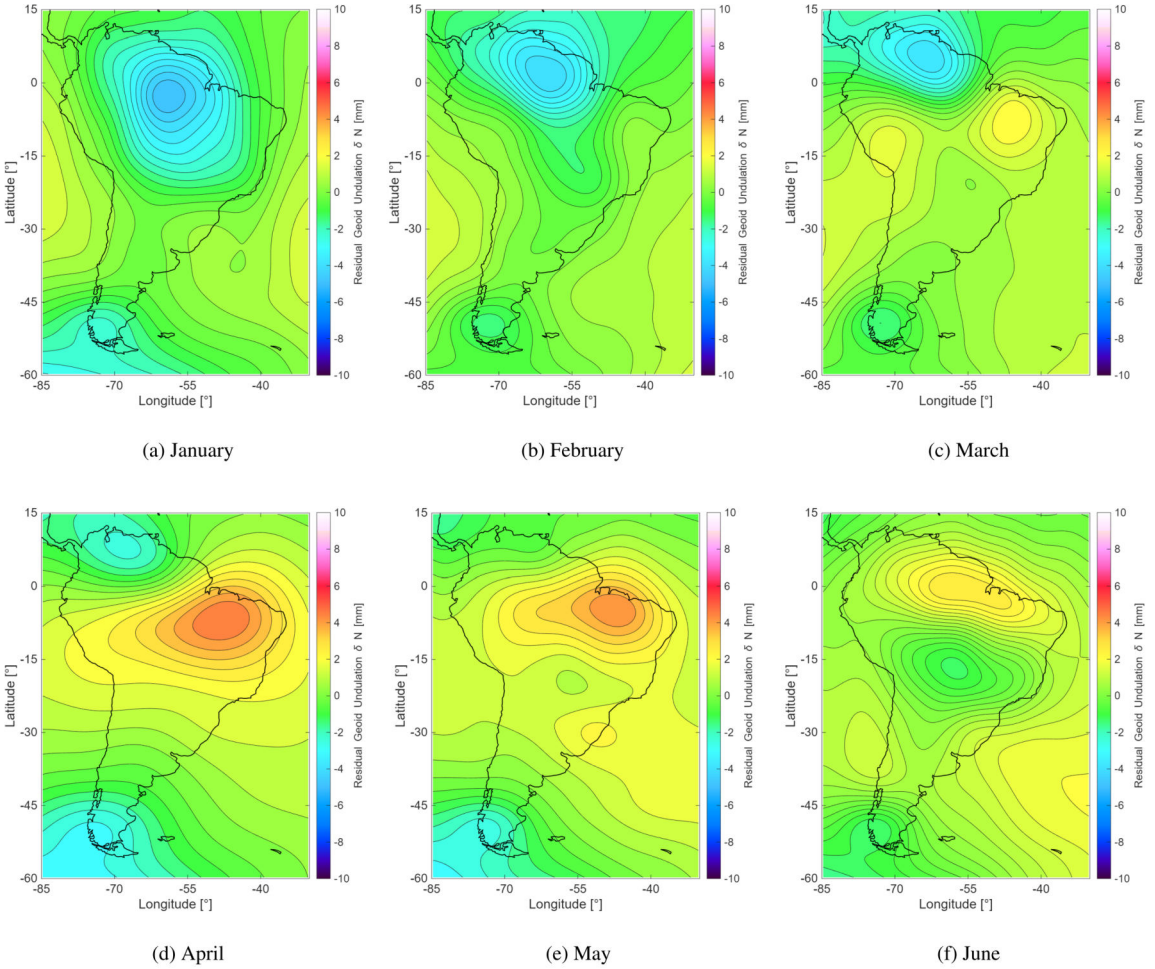

(a) January (b) February (c) March

(d) April (e) May (f) June

Figure 5.14: Variations of Geoid Undulations 2024 (January - June)

Figure 5.15 shows the monthly variations of geoid undulations from July to December 2024. Compared to the first half of the year, the second half is characterised by stronger anomaly amplitudes and more spatially coherent large-scale patterns, particularly during August–October. This seasonal contrast reflects a shift in the distribution of gravity-derived mass variations over the continent.

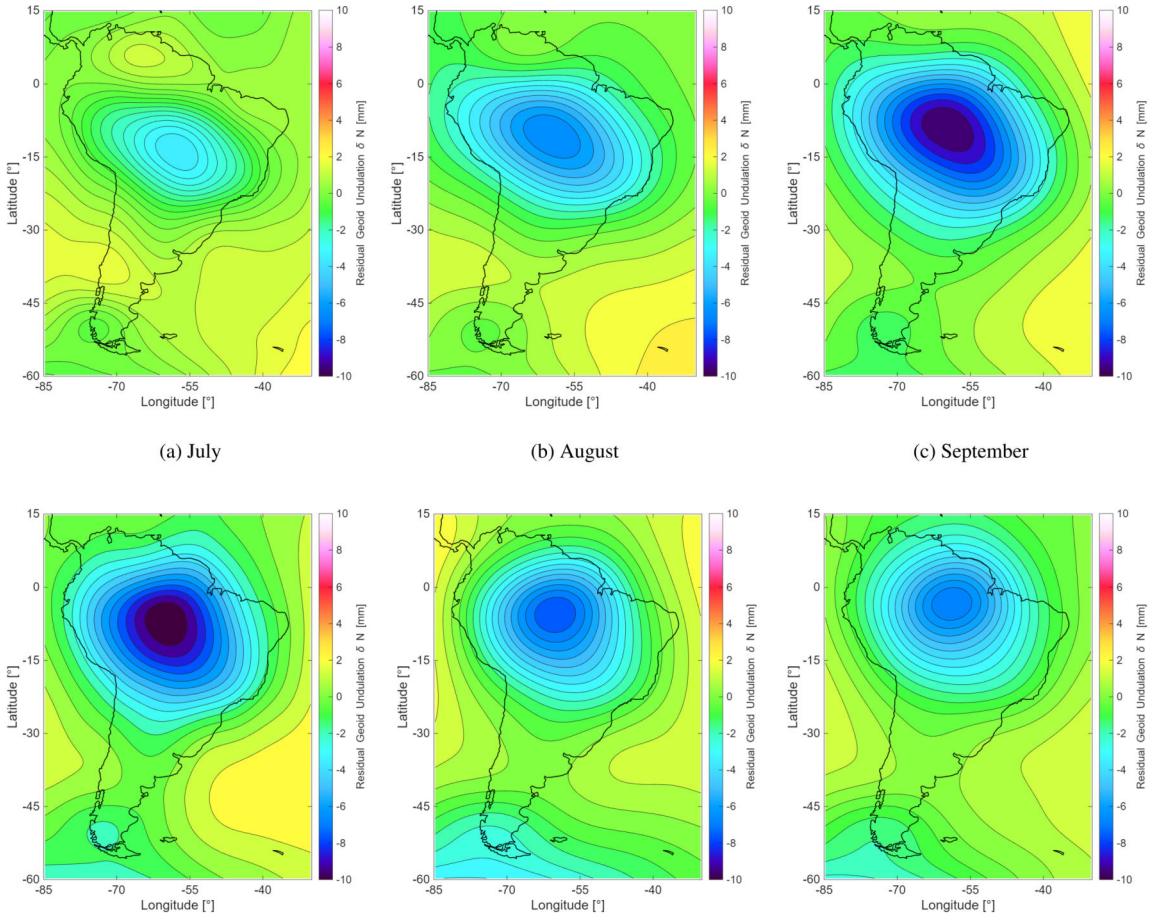

(a) July (b) August (c) September

(d) October (e) November (f) December

Figure 5.15: Variations of Geoid Undulations 2024 (July - December)

5.2.4 Results For TWS Based On DDK2, GRACE-FO

This section of figures presents the spatial distribution of Equivalent Water Height (EWH) derived from DDK2-filtered GRACE-FO gravity field solutions. The EWH fields reflect mass-related surface deformation converted from spherical harmonic coefficients and serve as an integrated indicator of terrestrial water storage variability. Figure 5.16 and Figure 5.17 shows the April and October EWH anomalies over South America for the period 2019–2024, highlighting the main spatial patterns and their interannual variability.

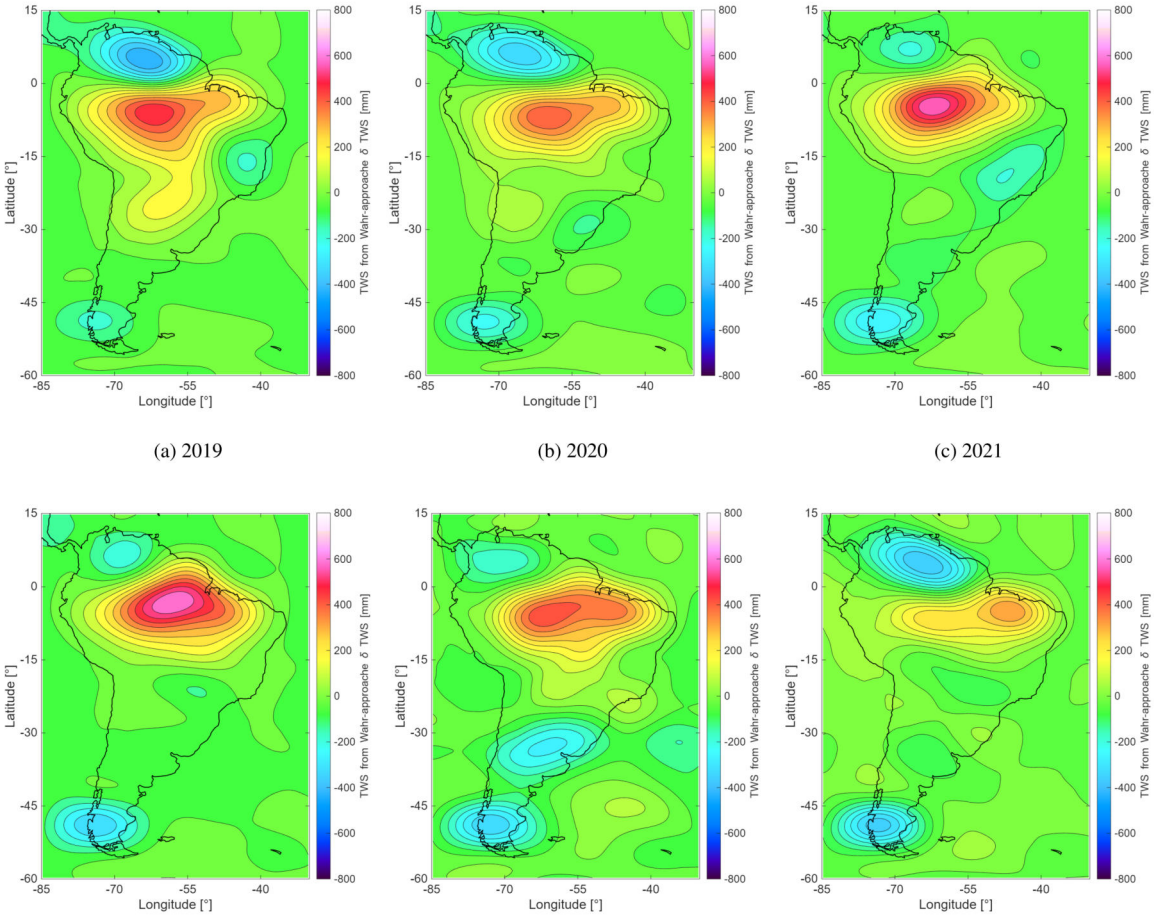

(a) 2019 (b) 2020 (c) 2021

Figure 5.16: Variations of EWH in April over the time span of 2019-2024

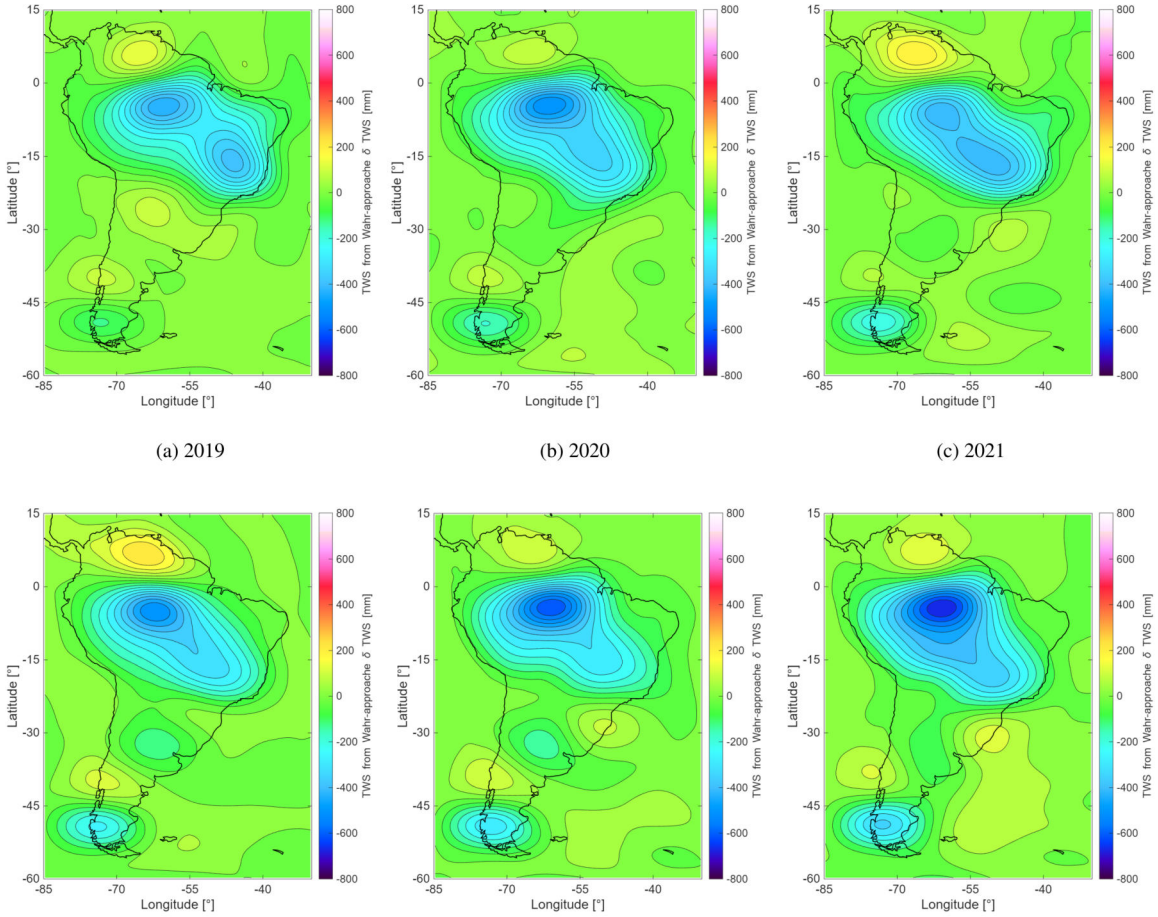

(a) 2019 (b) 2020 (c) 2021

(d) 2022 (e) 2023 (f) 2024

Figure 5.17: Variations of EWH in October over the time span of 2019-2024

Figure 5.18 shows the monthly variations of Equivalent Water Height (EWH) derived from GRACE-FO observations for January to June. Compared to GRACE-based EWH results, the overall large-scale spatial patterns remain consistent, while the GRACE-FO fields appear smoother with reduced short-wavelength variability. This indicates that GRACE-FO captures comparable integrated terrestrial water storage signals, allowing continuity in the analysis across both missions.

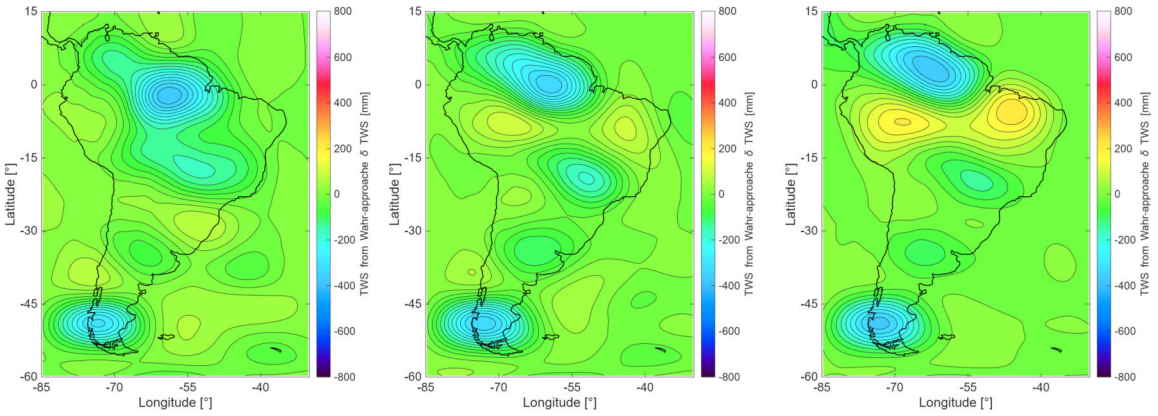

(a) January (b) February (c) March

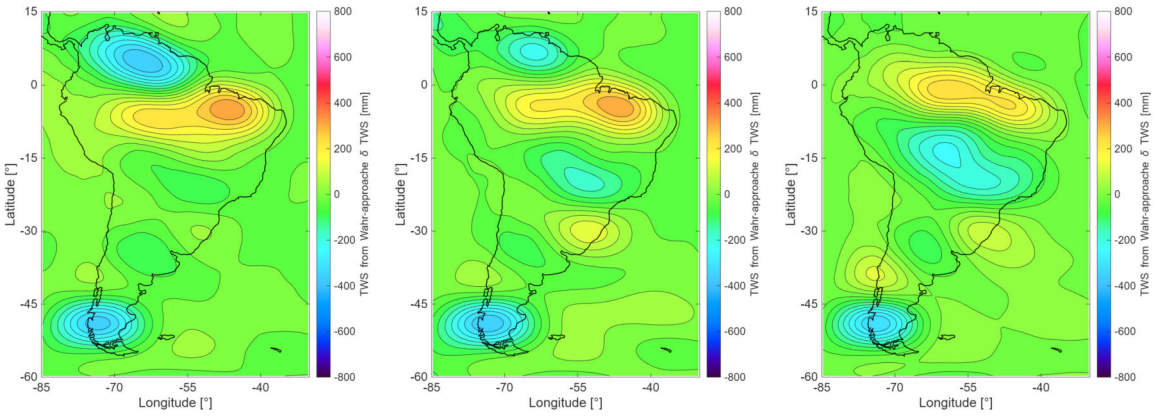

(d) April (e) May (f) June

Figure 5.18: Variations of EWH in 2024 (January - June)

Figure 5.19 shows the monthly variations of Equivalent Water Height (EWH) from July to December 2024. Compared to the first half of the year, the second half is characterised by more spatially coherent negative anomalies and a clearer dominance of large-scale patterns, particularly between August and October. This seasonal contrast indicates a redistribution of integrated terrestrial water storage relative to January–June.

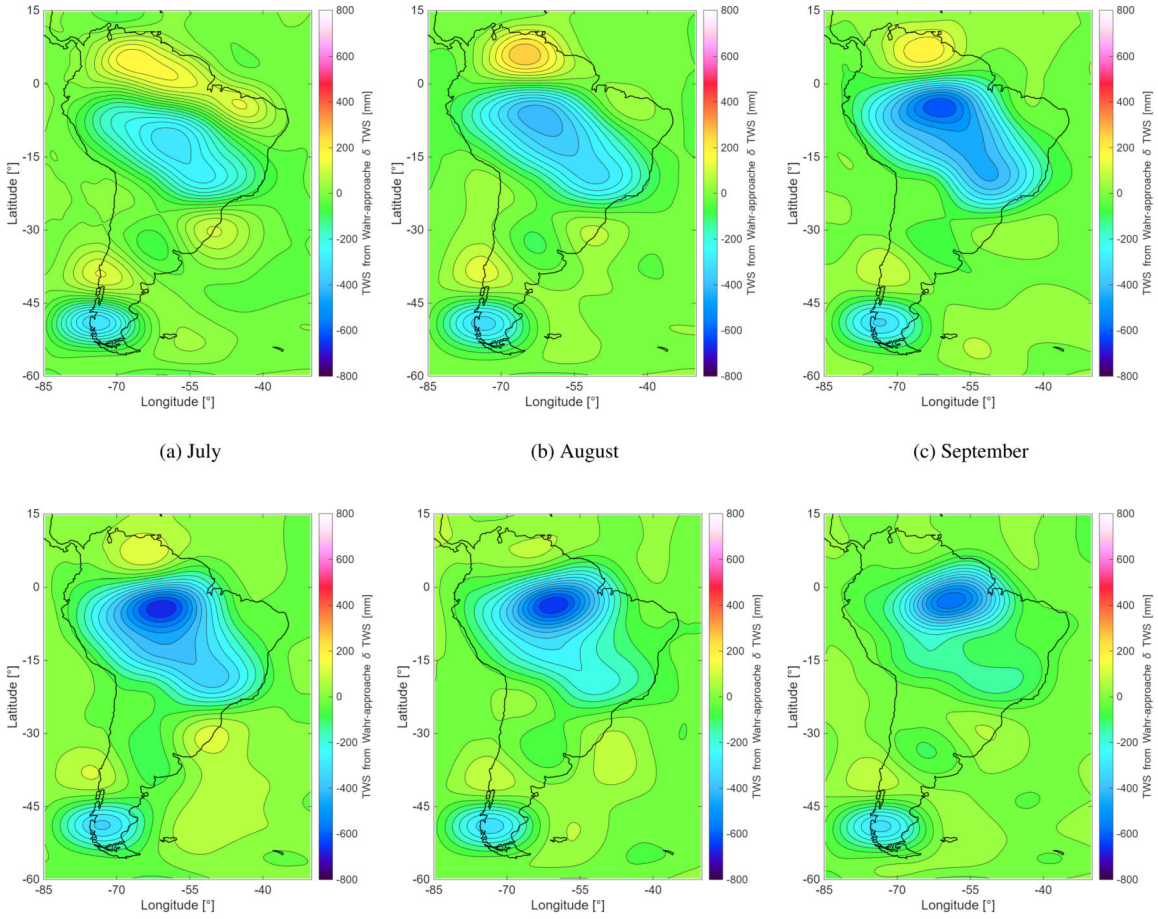

(a) July (b) August (c) September

(d) October (e) November (f) December

Figure 5.19: Variations of EWH in 2024 (July - December)

5.2.5 Results For Geoid Undulations Based on DDK5, GRACE

This section of figures presents geoid undulations derived from DDK5-filtered GRACE gravity field solutions. Figure 5.20 and Figure 5.21 illustrates the spatial patterns of April and October geoid undulations over South America for the period 2006–2011 and their interannual variability.

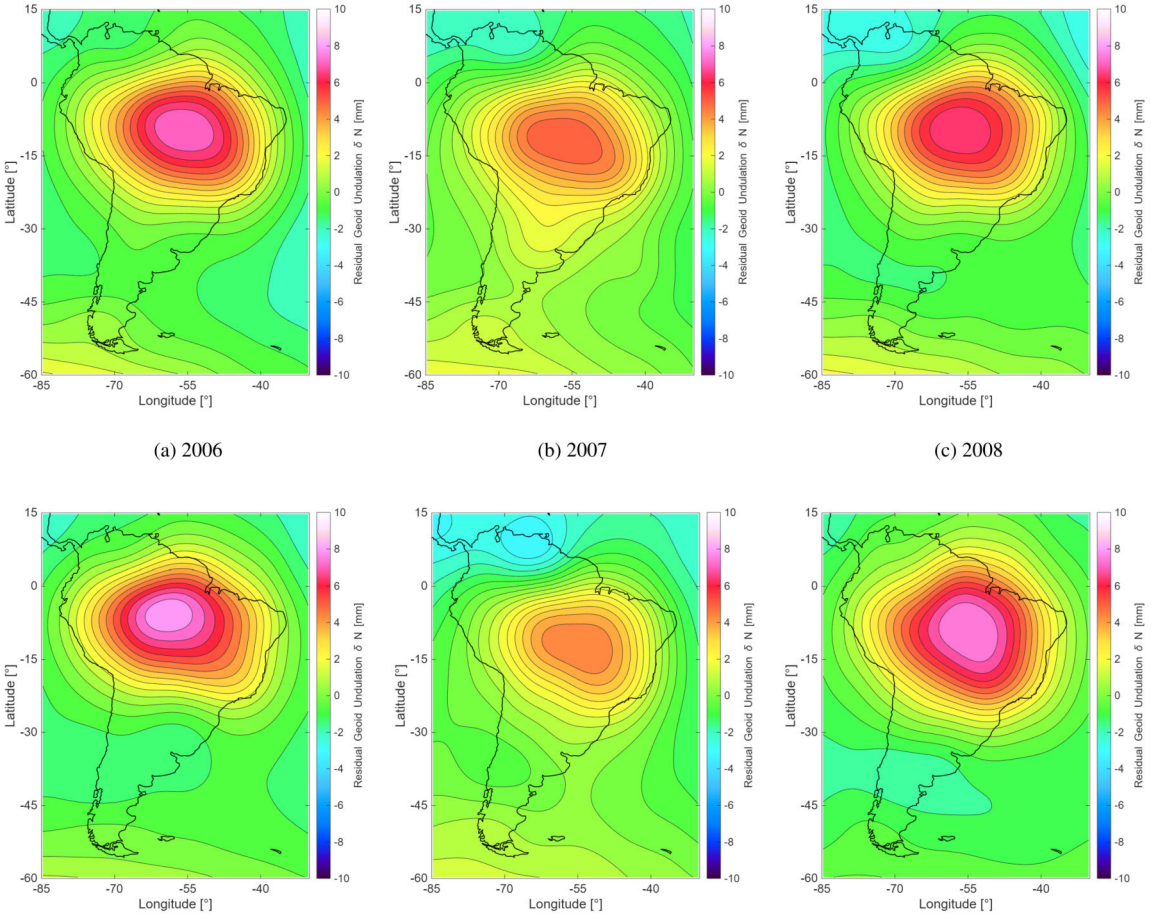

(a) 2006 (b) 2007 (c) 2008

(d) 2009 (e) 2010 (f) 2011

Figure 5.20: Variations of Geoid Undulations in April over the time span of 2006-2011

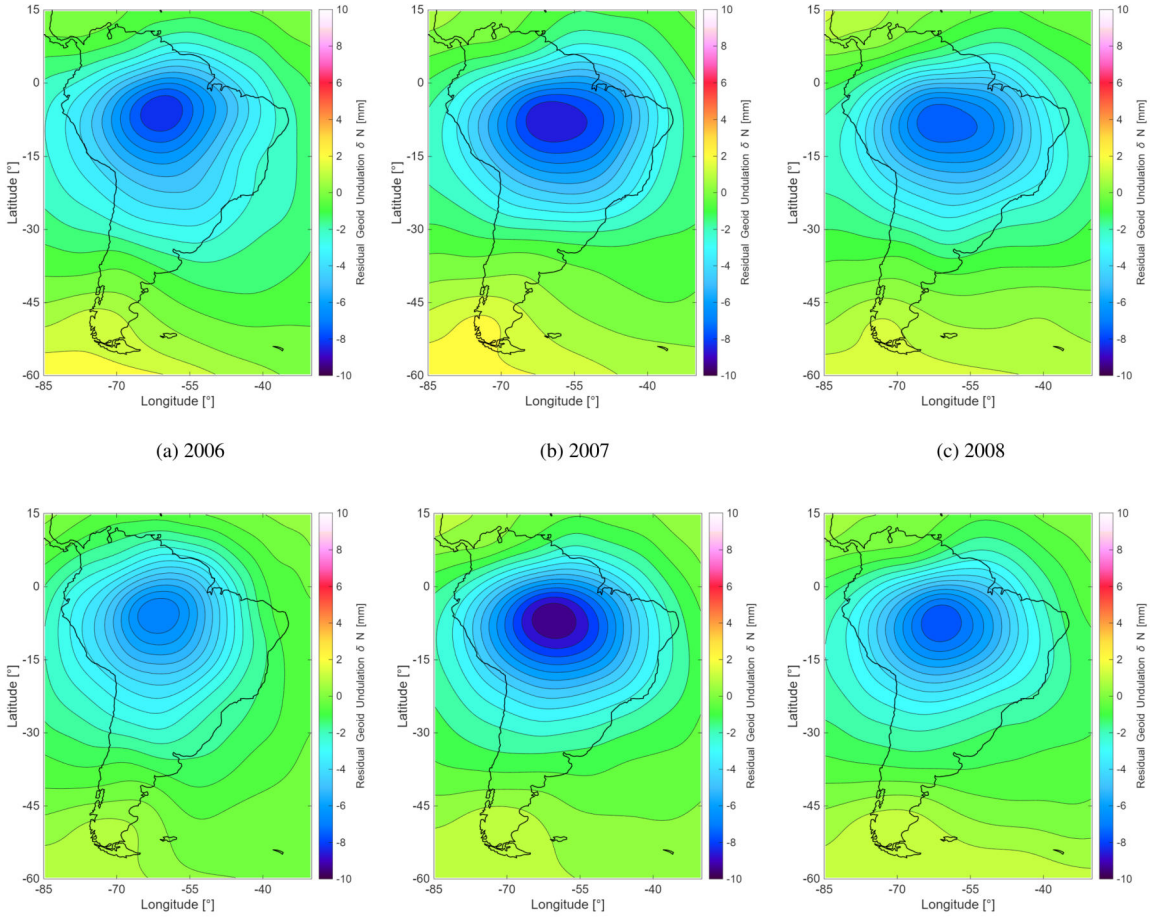

(a) 2006 (b) 2007 (c) 2008

(d) 2009 (e) 2010 (f) 2011

Figure 5.21: Variations of Geoid Undulations in October over the time span of 2006-2011

Figure 5.22 shows the monthly variations of geoid undulations for January to June 2005. In comparison with the corresponding GRACE observations for the same year, the spatial patterns and their seasonal evolution are consistent, with similar locations of anomaly centres and comparable large-scale gradients. Minor differences are mainly expressed in anomaly amplitude and spatial smoothness, reflecting methodological and filtering effects rather than changes in the underlying mass redistribution signal.

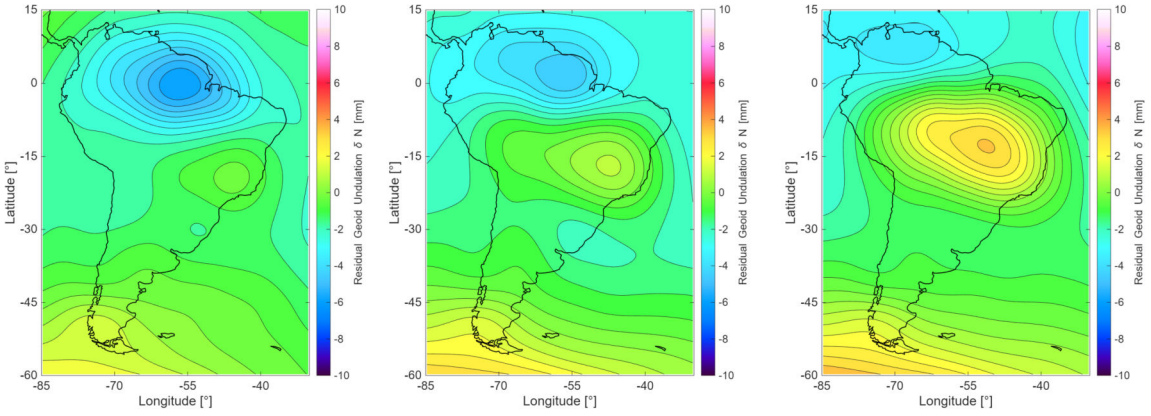

(a) January (b) February (c) March

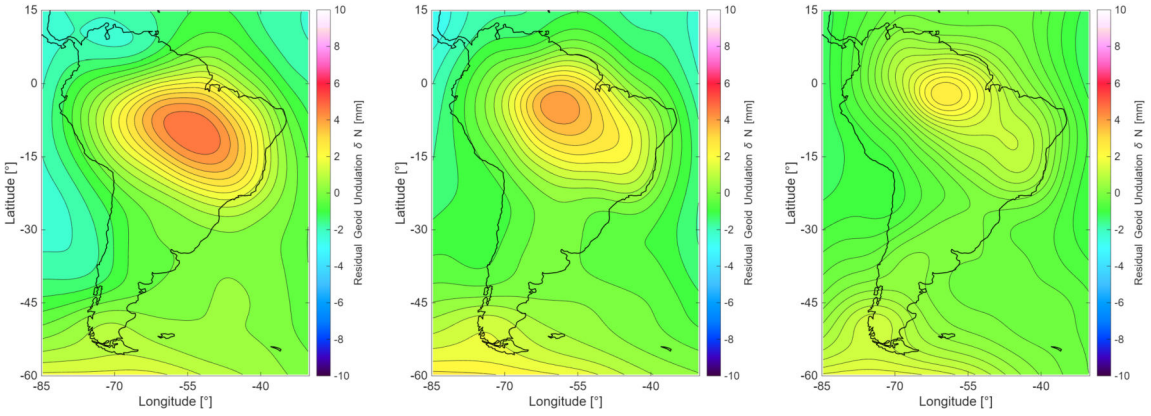

(d) April (e) May (f) June

Figure 5.22: Variations of Geoid Undulations in 2005 (January - June)

Figure 5.23 shows the monthly variations of geoid undulations from July to December 2005. In comparison with the corresponding GRACE observations for the same year, the spatial patterns and seasonal progression remain consistent, with comparable anomaly centres and large-scale gradients. Differences are mainly observed in the strength and smoothness of the anomalies, reflecting filtering and processing effects rather than changes in the underlying mass redistribution.

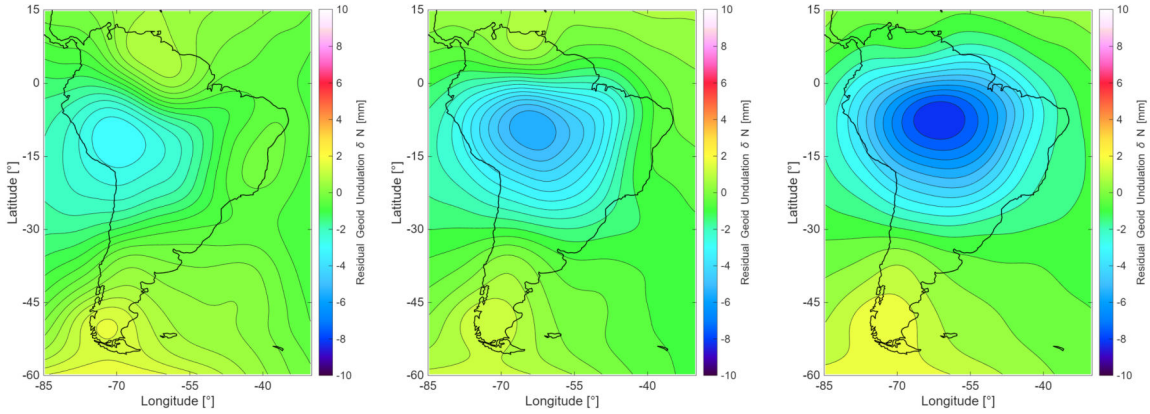

(a) July (b) August (c) September

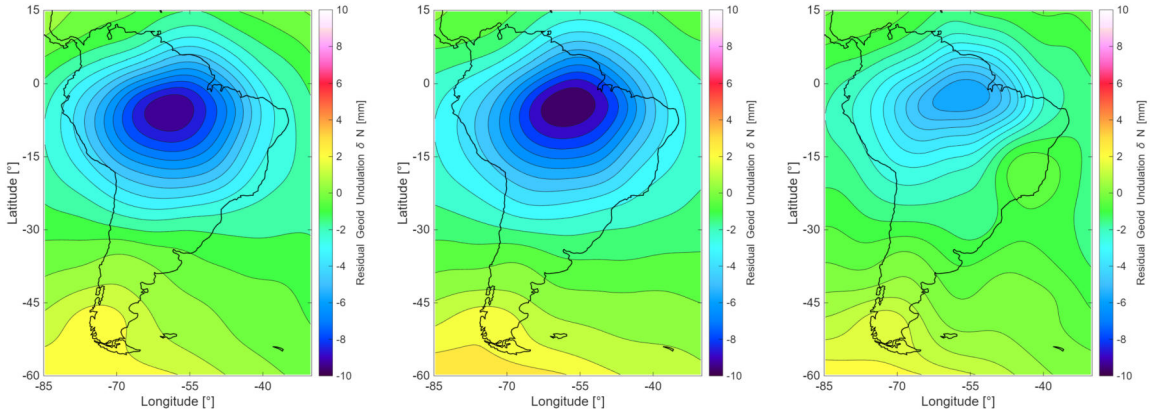

(d) October (e) November (f) December

Figure 5.23: Variations of Geoid Undulations in 2005 (July - December)

5.2.6 Results For TWS Based On DDK5, GRACE

This section of figures presents the spatial distribution of Equivalent Water Height (EWH) derived from DDK5-filtered GRACE gravity field solutions. The EWH fields represent integrated terrestrial water storage variations obtained from spherical harmonic coefficients and provide insight into large-scale mass redistribution over South America.

Figure 5.24 and Figure 5.25 shows the April and October EWH anomalies over South America for the period 2006–2011, highlighting the main spatial patterns and their interannual variability.

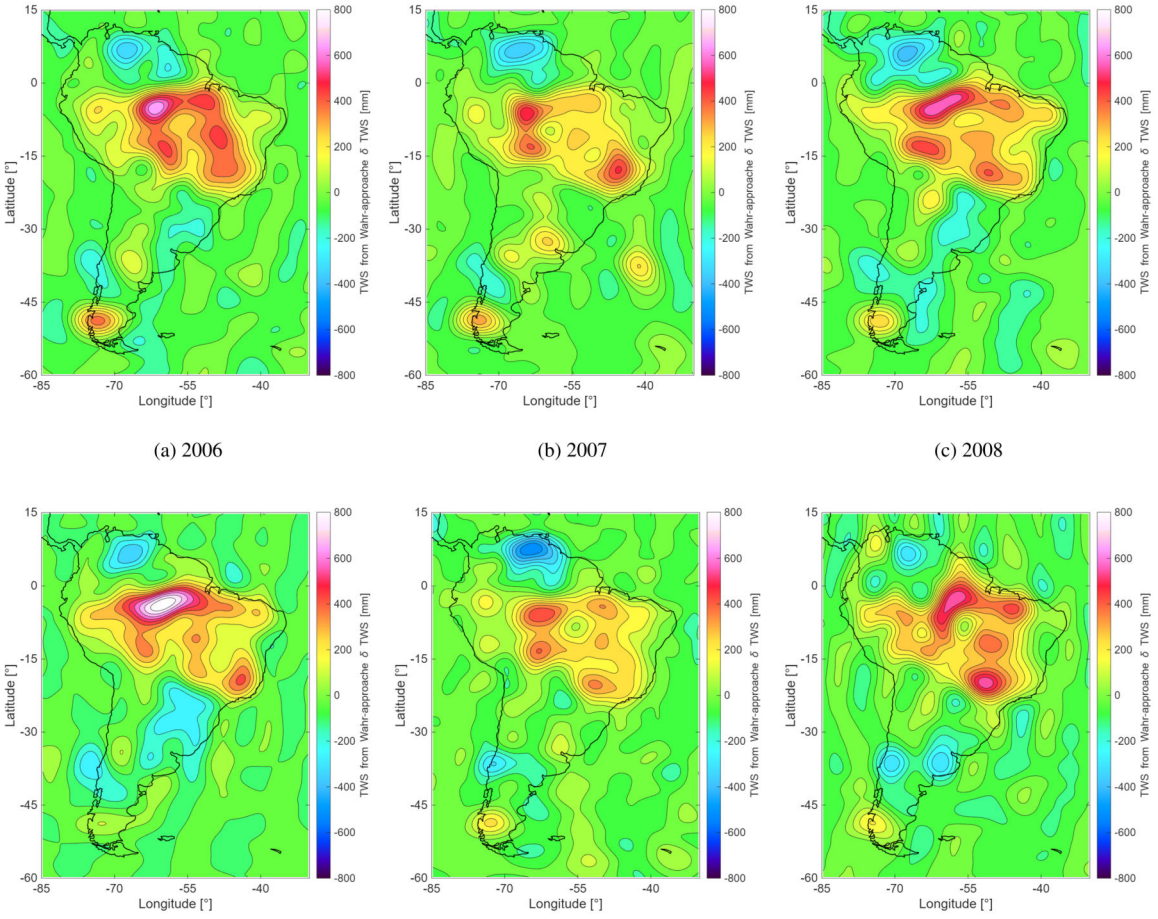

(a) 2006 (b) 2007 (c) 2008

(d) 2009 (e) 2010 (f) 2011

Figure 5.24: Variations of EWH in April over the time span of 2006-2011

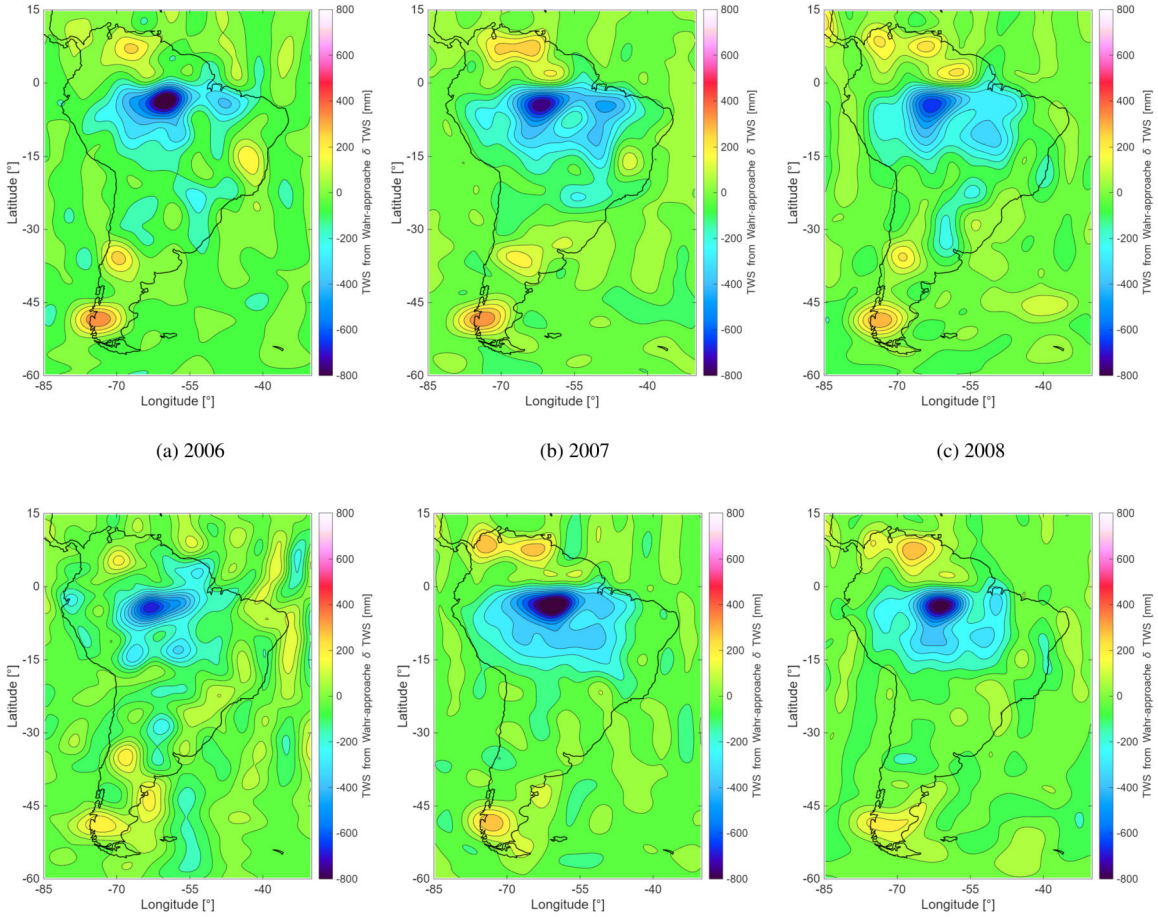

(a) 2006 (b) 2007 (c) 2008

(d) 2009 (e) 2010 (f) 2011

Figure 5.25: Variations of EWH in October over the time span of 2006-2011

Figure 5.26 shows the monthly variations of Equivalent Water Height (EWH) for January to June 2005. Compared to GRACE-based EWH observations, the large-scale spatial patterns and seasonal evolution are consistent, with similar regions of positive and negative anomalies. Differences are mainly observed in anomaly amplitude and spatial smoothness, reflecting filtering and processing effects rather than changes in the underlying terrestrial water storage signal.

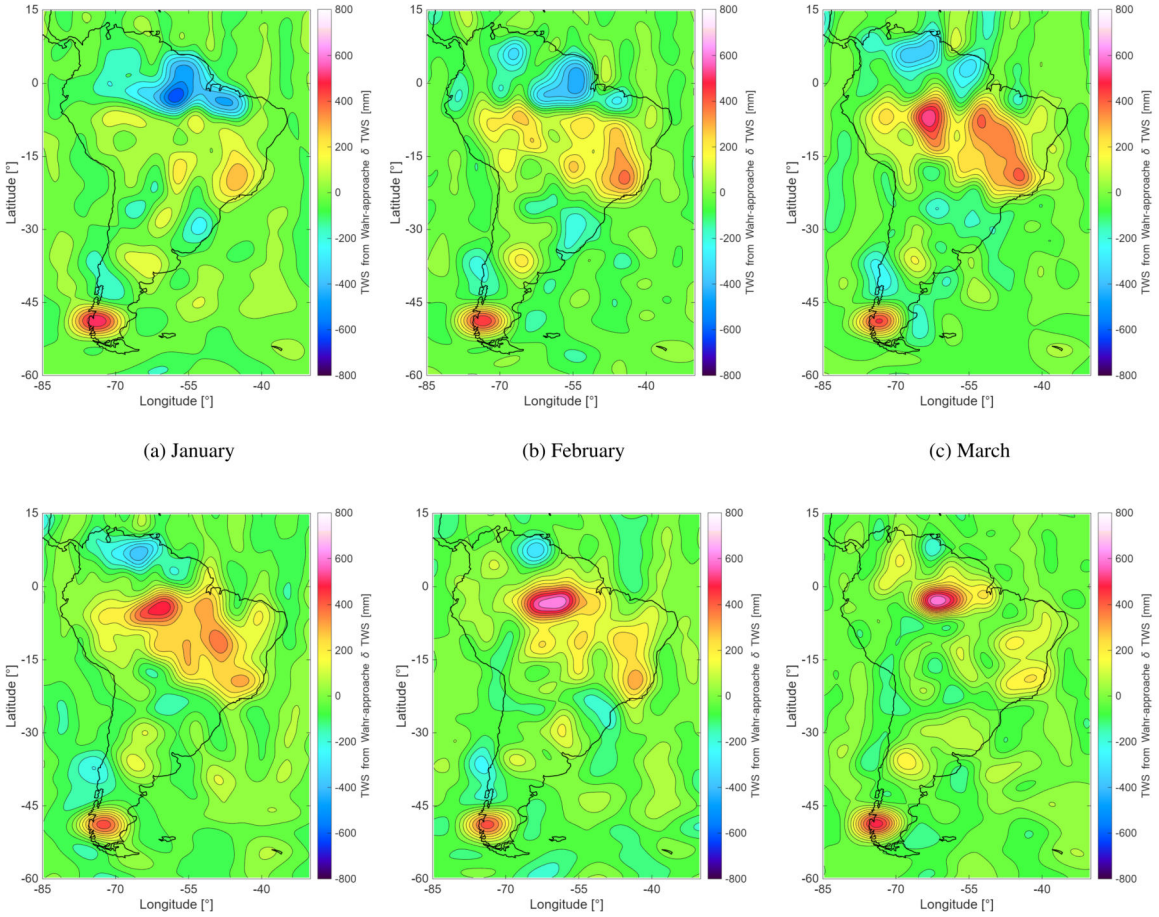

(a) January (b) February (c) March

(d) April (e) May (f) June

Figure 5.26: Variations of EWH in 2005 (January - June)

Figure 5.27 presents the monthly variations of Equivalent Water Height (EWH) from July to December 2005. In comparison with GRACE-based EWH observations, the spatial patterns and seasonal evolution remain consistent, with similar large-scale anomaly structures. Differences are mainly reflected in the magnitude and smoothness of the anomalies, which can be attributed to filtering and processing effects rather than changes in the underlying terrestrial water storage signal.

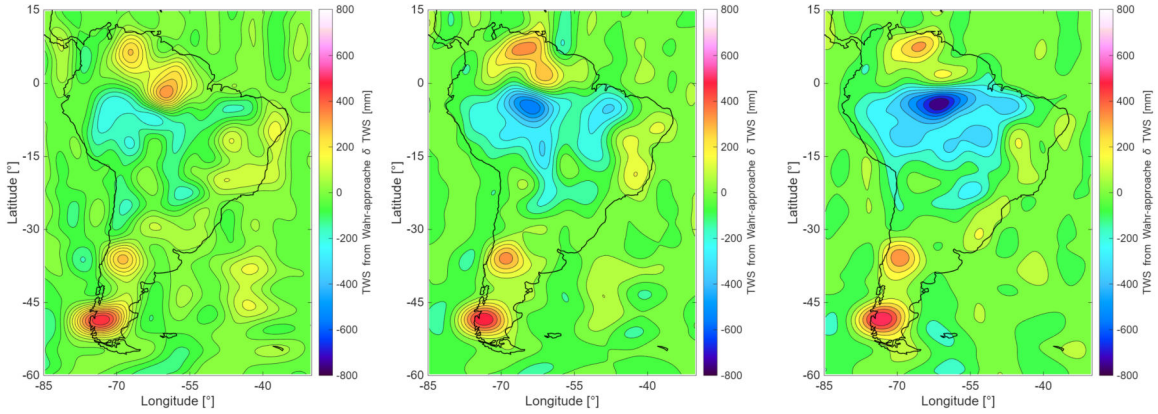

(a) July (b) August (c) September

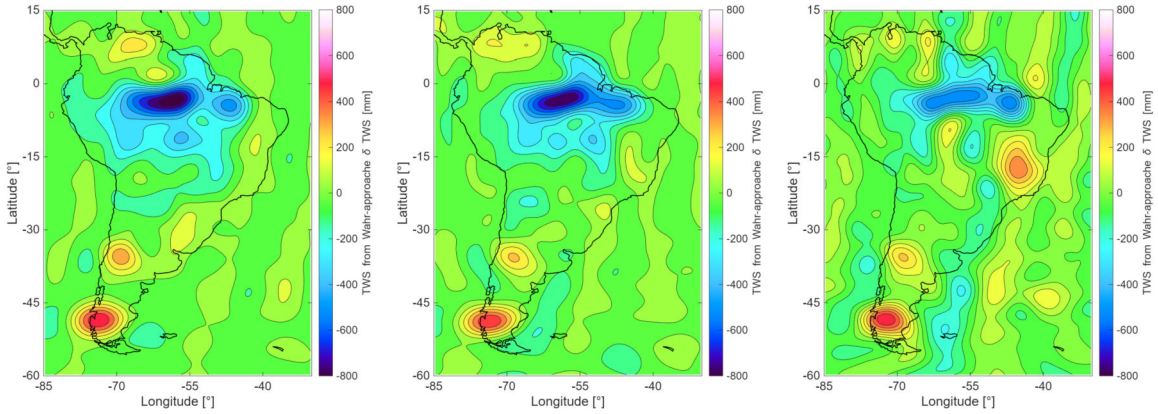

(d) October (e) November (f) December

Figure 5.27: Variations of EWH in 2005 (July - December)

5.2.7 Results For Geoid Undulations Based on DDK5, GRACE-FO

This section of figures presents geoid undulations derived from DDK5-filtered GRACE gravity field solutions. Figure 5.28 and Figure 5.29 illustrates the spatial patterns of April and October geoid undulations over South America for the period 2019-2024 and their interannual variability.

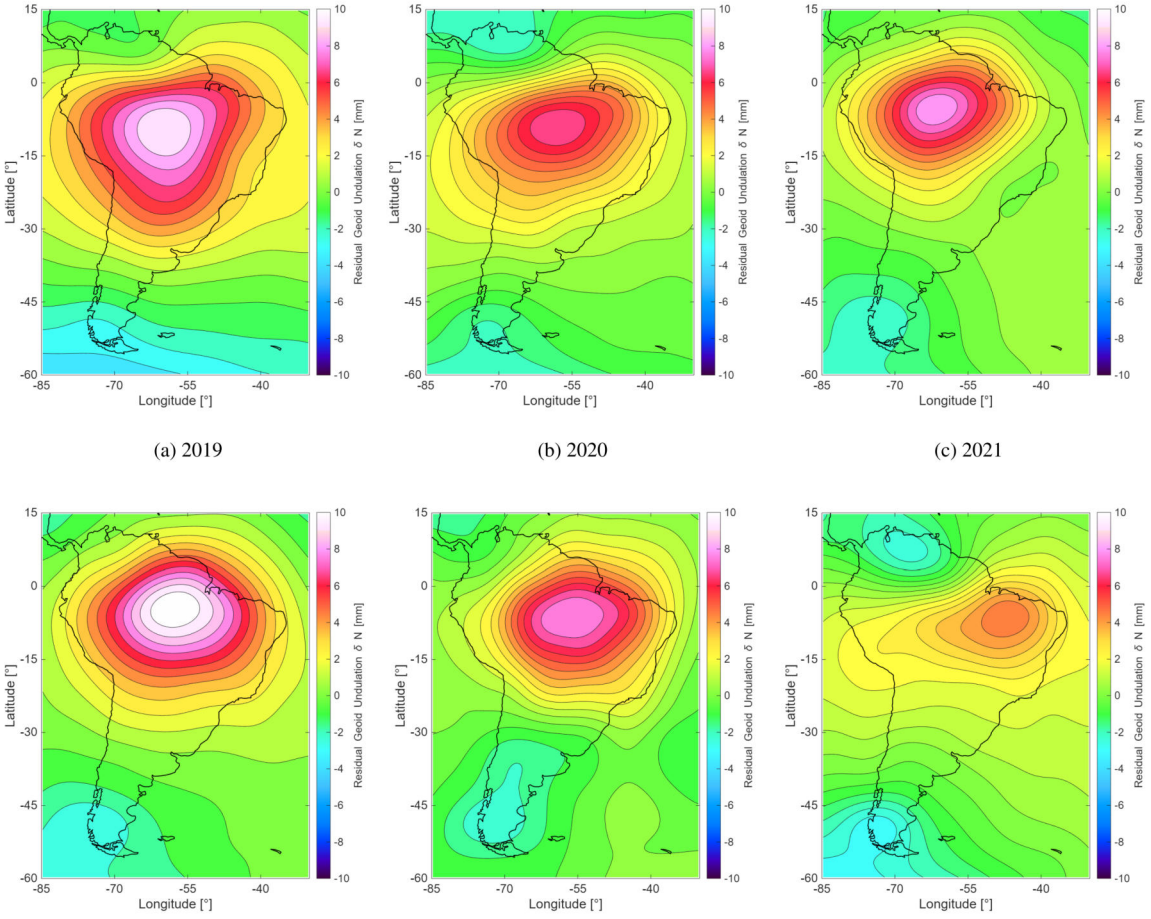

(a) 2019 (b) 2020 (c) 2021

(d) 2022 (e) 2023 (f) 2024

Figure 5.28: Variations of Geoid Undulations in April over the time span of 2019-2024

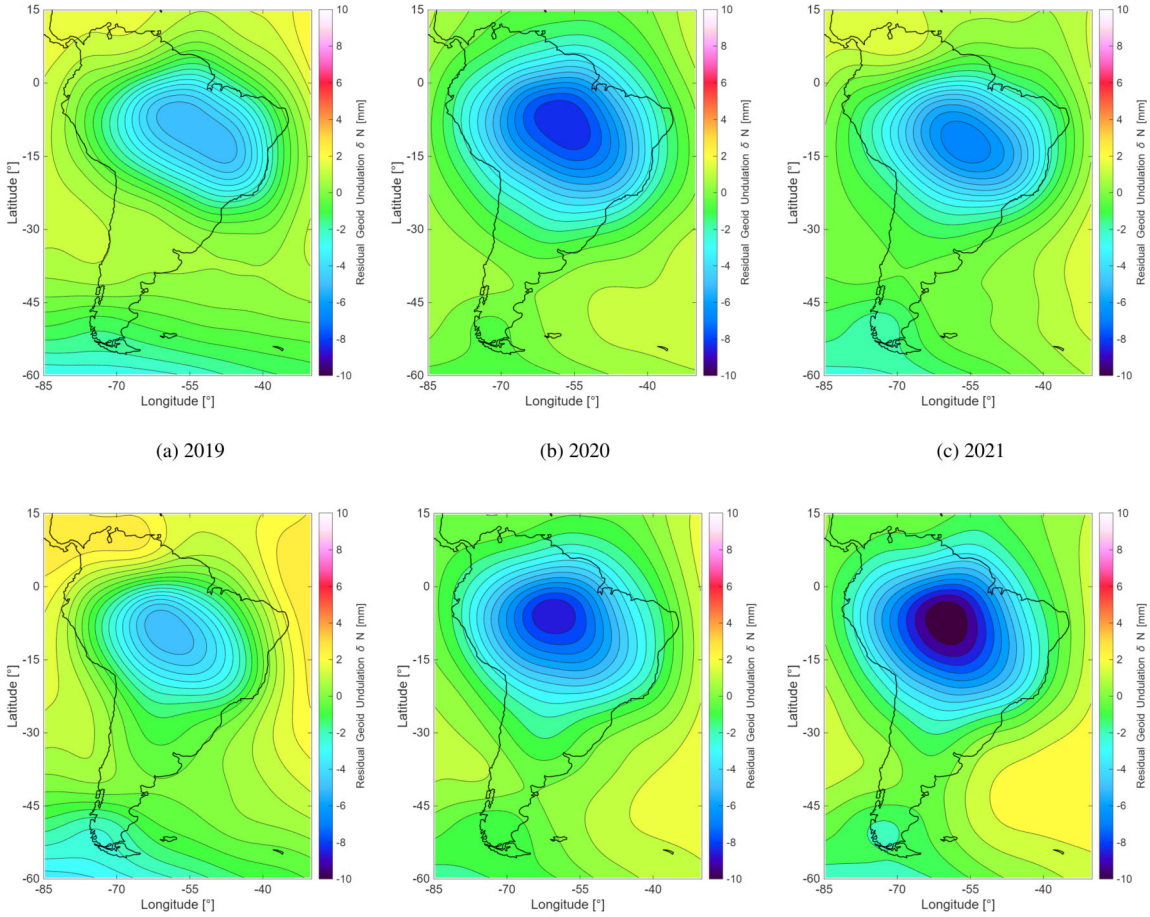

(a) 2019 (b) 2020 (c) 2021

(d) 2022 (e) 2023 (f) 2024

Figure 5.29: Variations of Geoid Undulations in October over the time span of 2019-2024

Figure 5.30 shows the monthly variations of geoid undulations from January to June 2024. In comparison with the corresponding GRACE observations for the same year, the spatial patterns and seasonal evolution are consistent, with similar locations of anomaly centres and large-scale gradients. Differences are mainly expressed in anomaly amplitude and spatial smoothness, reflecting filtering and processing effects rather than changes in the underlying mass redistribution.

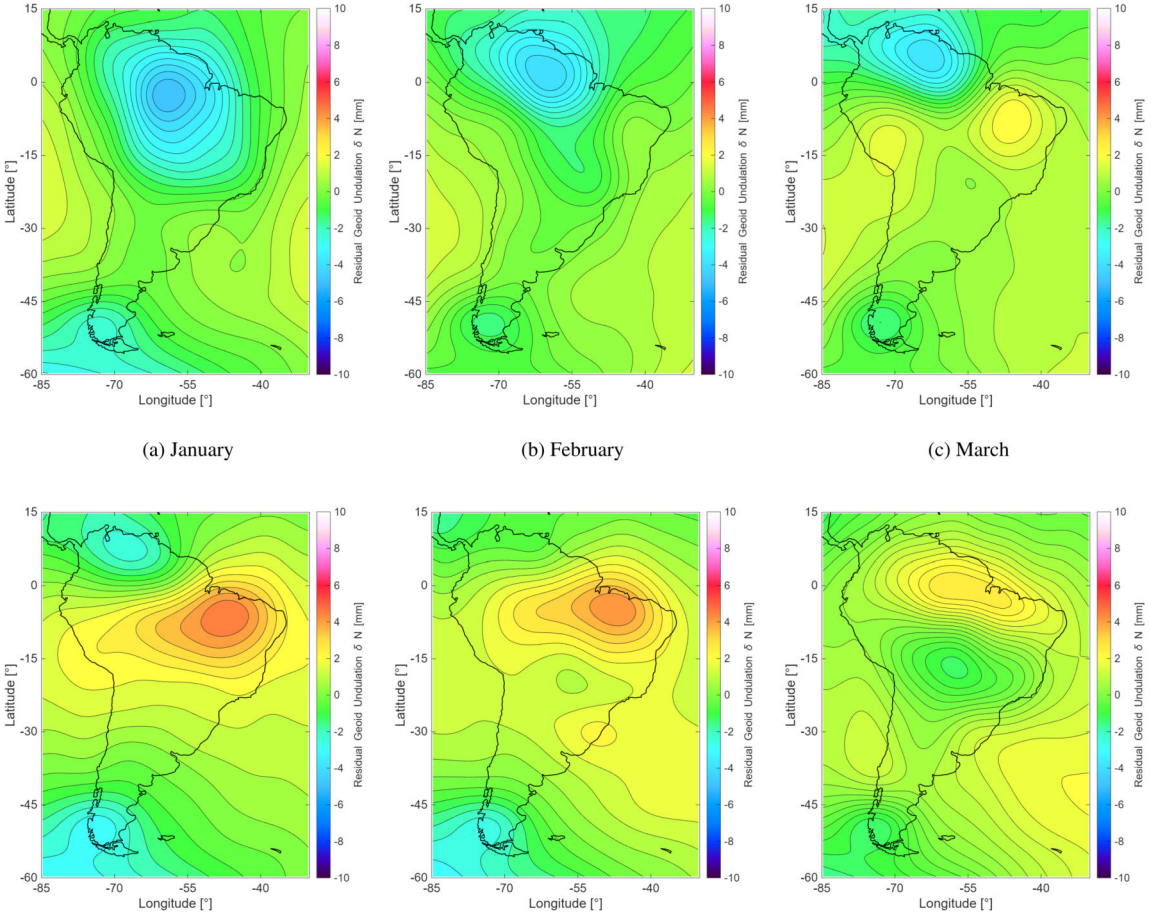

(a) January (b) February (c) March

(d) April (e) May (f) June

Figure 5.30: Variations of Geoid Undulations in 2024 (January - June)

Figure 5.31 presents the monthly variations of geoid undulations from July to December 2024. In comparison with the corresponding GRACE observations for the same year, the spatial patterns and seasonal progression remain consistent, with comparable large-scale gradients and anomaly centres. Differences are mainly observed in anomaly amplitude and spatial smoothness, reflecting filtering and processing effects rather than changes in the underlying mass redistribution signal.

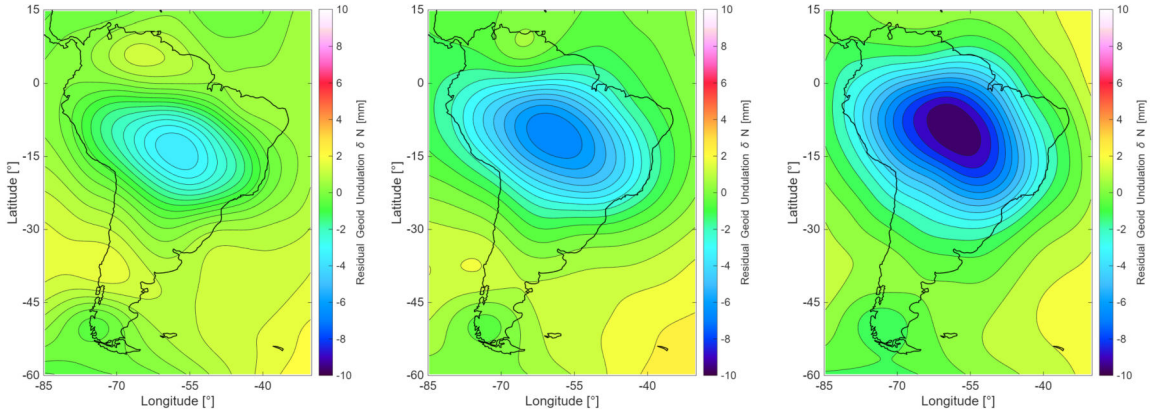

(a) July (b) August (c) September

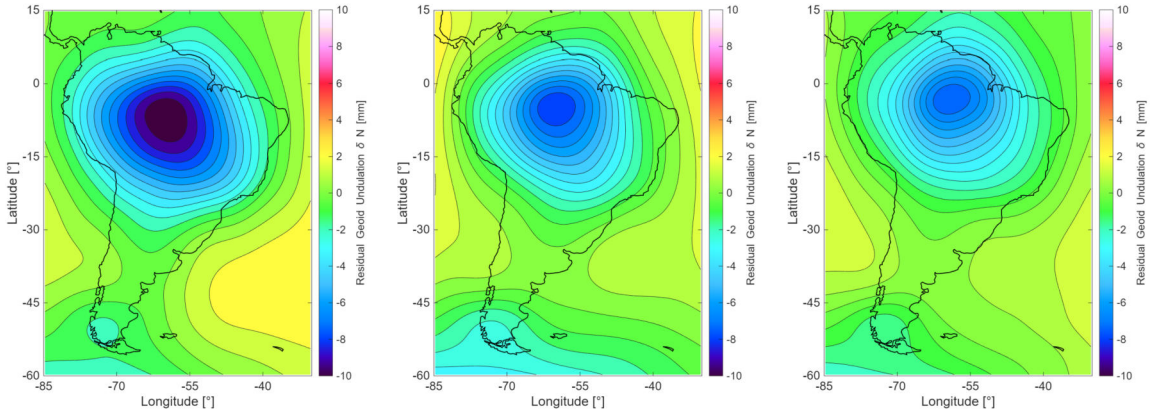

(d) October (e) November (f) December

Figure 5.31: Variations of Geoid Undulations in 2024 (July - December)

5.2.8 Results For TWS Based On DDK5, GRACE-FO

This section of figures presents the spatial distribution of Equivalent Water Height (EWH) derived from DDK5-filtered GRACE-FO gravity field solutions. The EWH fields represent integrated terrestrial water storage variations obtained from spherical harmonic coefficients and provide insight into large-scale mass redistribution over South America.

Figure 5.32 and Figure 5.33 shows April and October EWH anomalies over South America for the period 2019–2024, highlighting the main spatial patterns and their interannual variability.

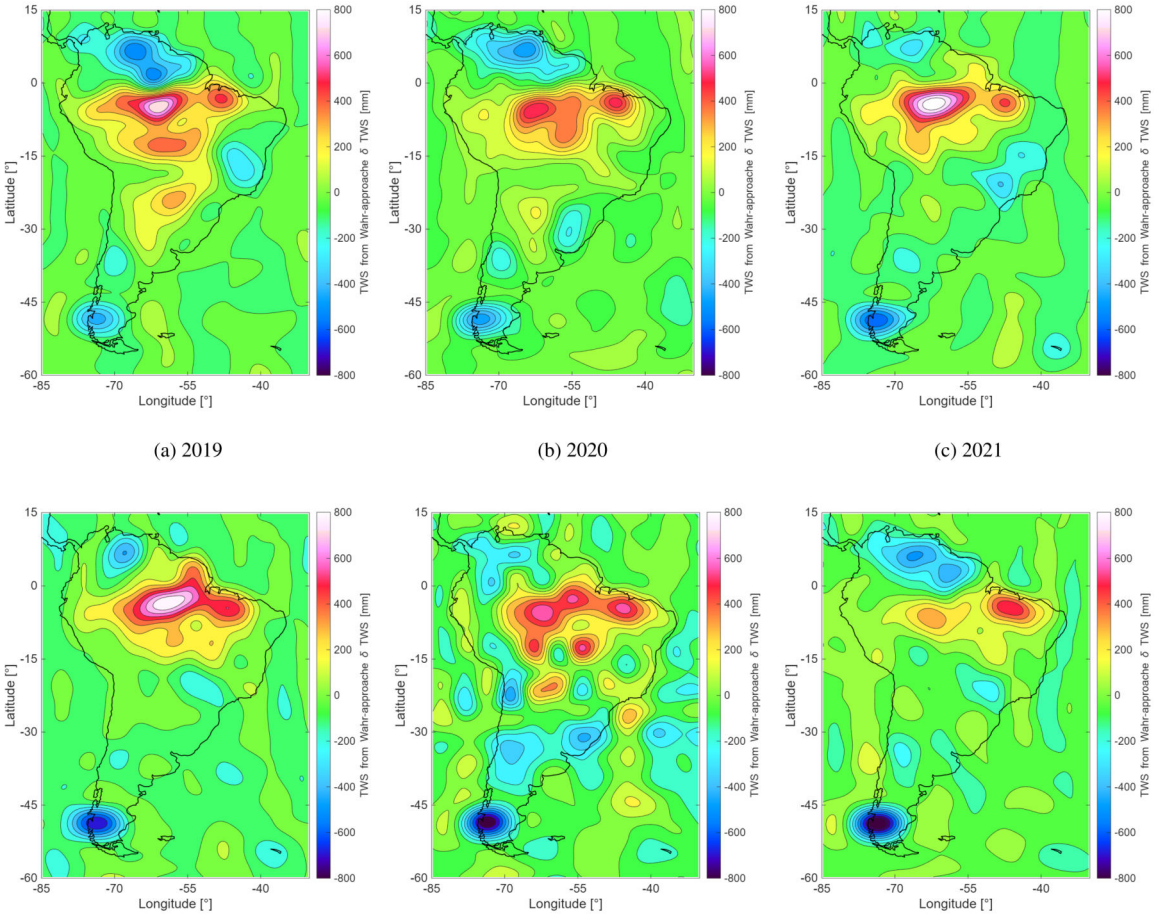

(a) 2019 (b) 2020 (c) 2021

Figure 5.32: Variations of EWH in April over the time span of 2019-2024

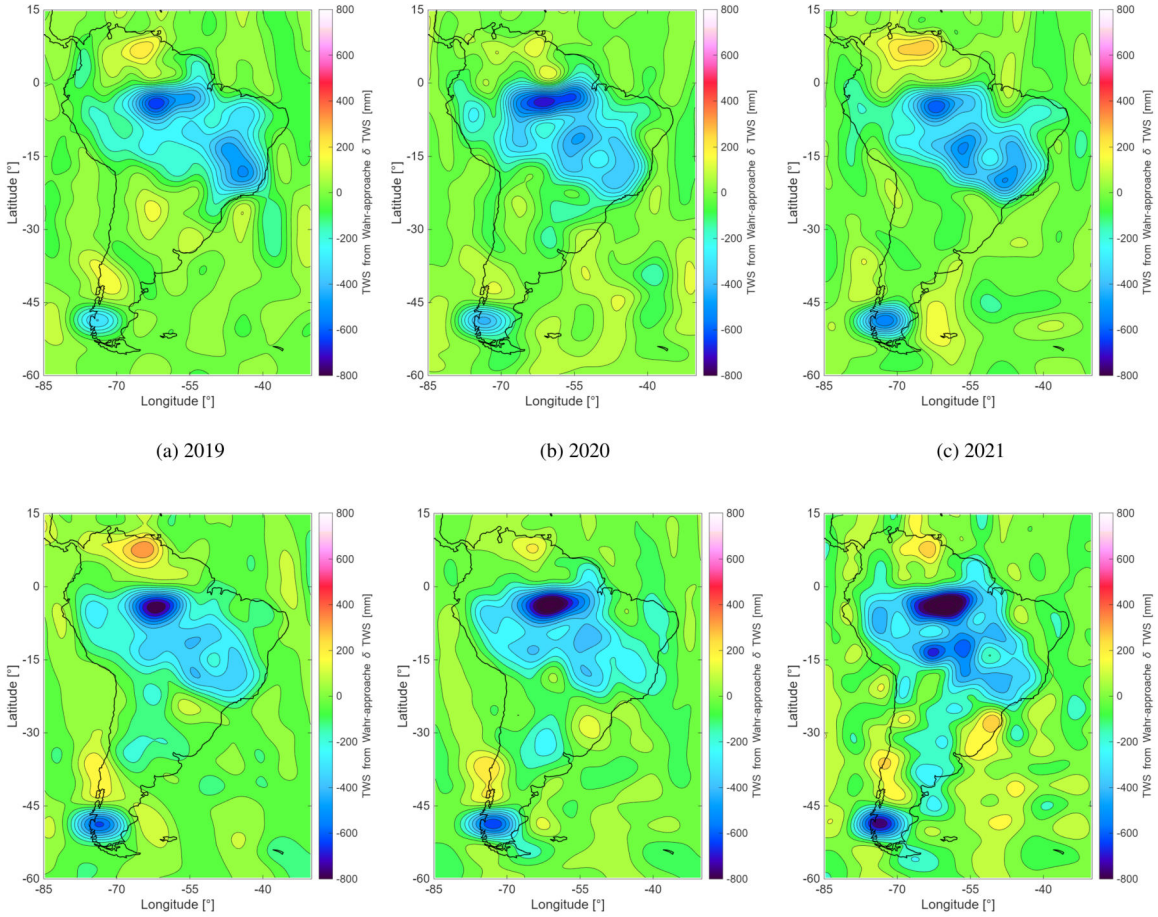

(a) 2019 (b) 2020 (c) 2021

(d) 2022 (e) 2023 (f) 2024

Figure 5.33: Variations of EWH in October over the time span of 2019-2024

Figure 5.34 depicts the monthly EWH variability from January to June 2024. Relative to GRACE observations from the same year, the large-scale spatial structure and seasonal progression are preserved, with comparable positive and negative anomaly patterns. Observed differences mainly concern anomaly magnitude and spatial smoothness and are attributable to filtering and processing effects.

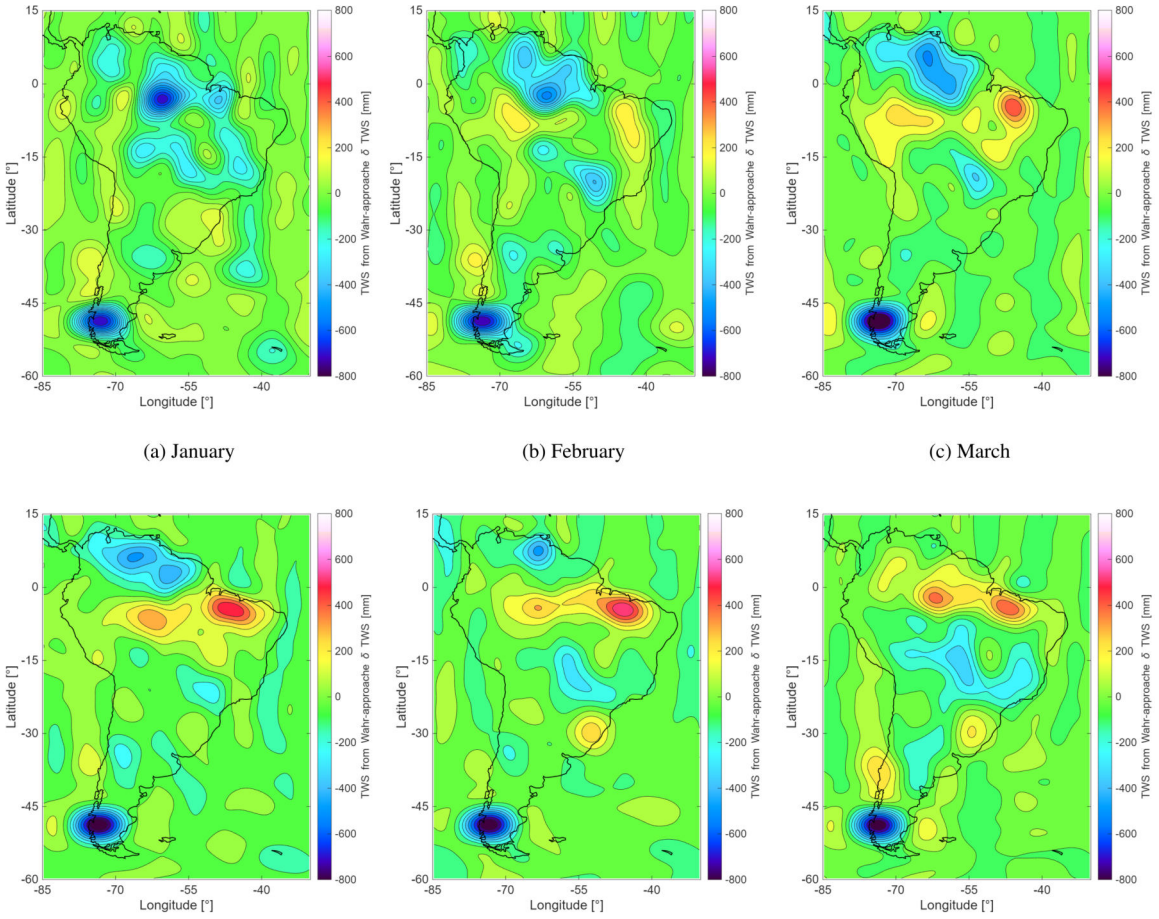

(a) January (b) February (c) March

(d) April (e) May (f) June

Figure 5.34: Variations of EWH in 2024 (January-June)

Figure 5.35 depicts the monthly EWH variability from July to December 2024. Relative to GRACE observations from the same year, the large-scale spatial patterns and seasonal progression remain consistent, while differences are mainly observed in anomaly magnitude and spatial smoothness due to filtering and processing effects.

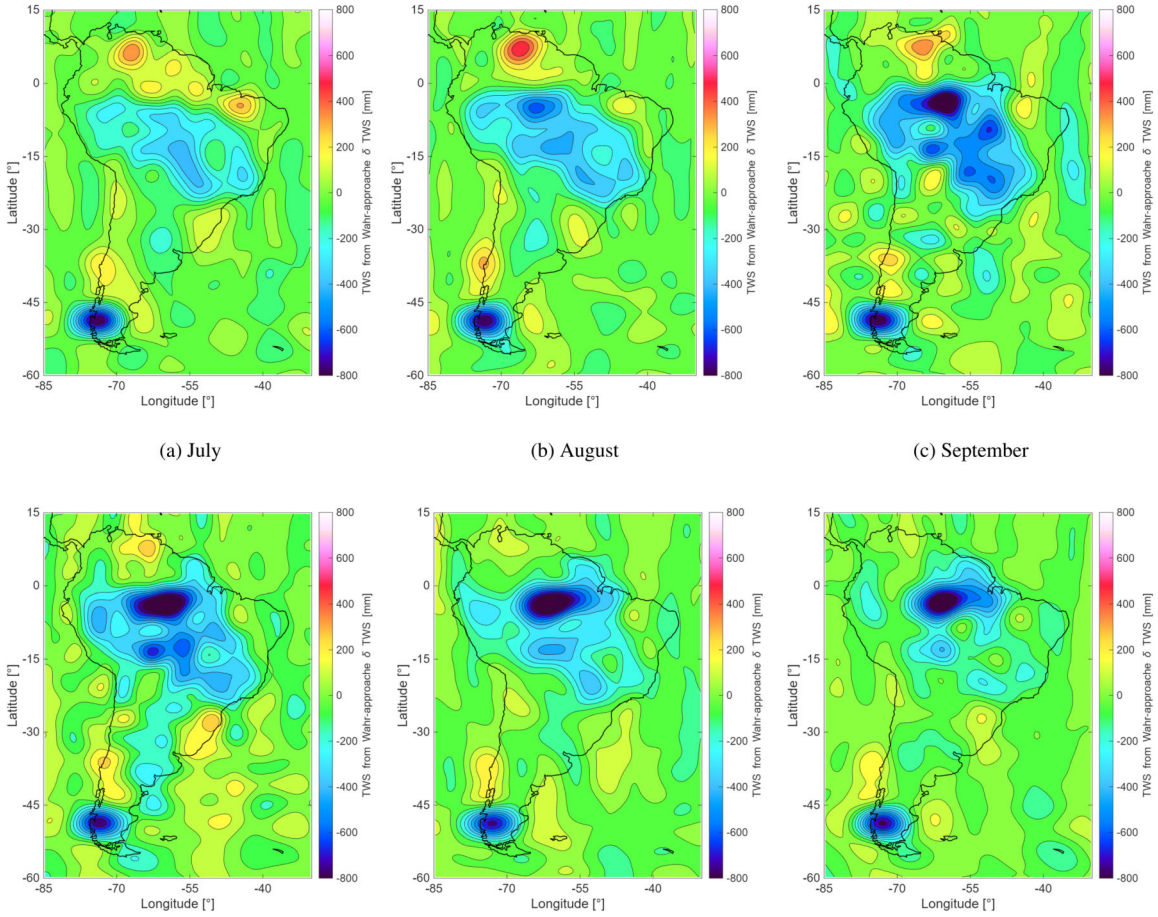

(a) July (b) August (c) September

(d) October (e) November (f) December

Figure 5.35: Variations of EWH in 2024 (July-December)

5.2.9 Monthly Total Water Storage Statistics

The monthly Total Water Storage (TWS) statistics show strong seasonal variability for both filtering approaches, while the mean TWS remains close to zero over the full period, reflecting the use of a mean reference field. DDK2 produces larger extrema than DDK5, indicating stronger signal preservation, whereas DDK5 yields smoother variations due to enhanced noise suppression. This comparison highlights the sensitivity of TWS amplitudes to the choice of decorrelation filter. Since GRACE-derived TWS represents integrated terrestrial water storage, its magnitude and temporal stability directly affect the groundwater anomalies obtained after removing near-surface components using GLDAS. The differences between DDK2 and DDK5 therefore influence not only TWS variability, but also the robustness of groundwater-related signals derived in the subsequent analysis.

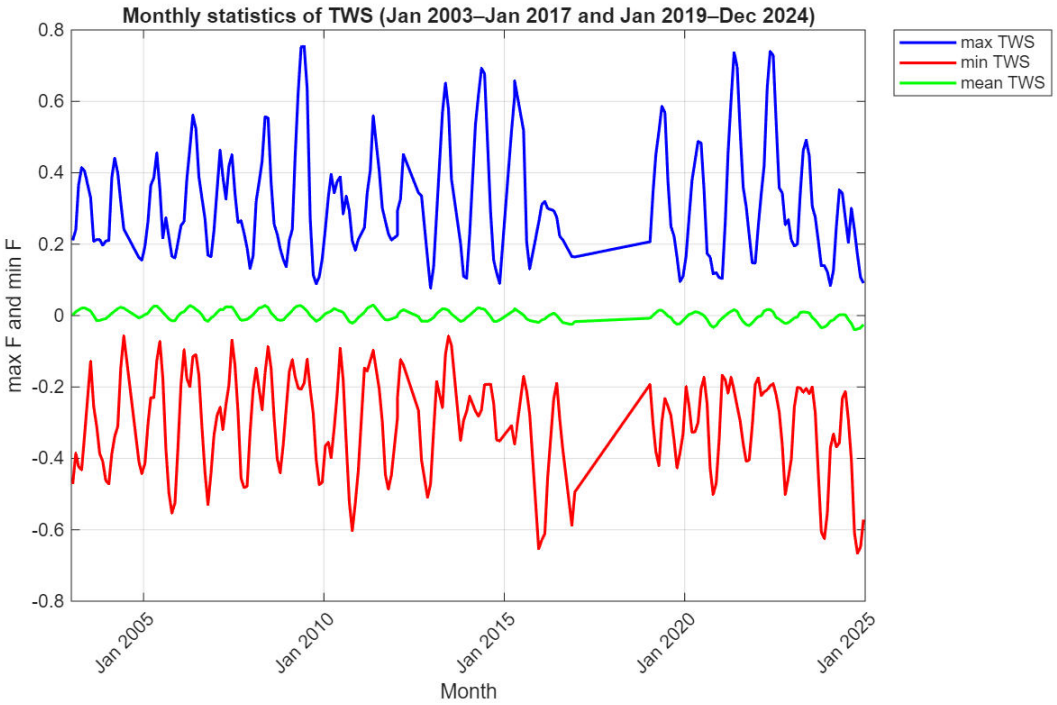

Figure 5.36: Statistics of TWH Based On DDK2

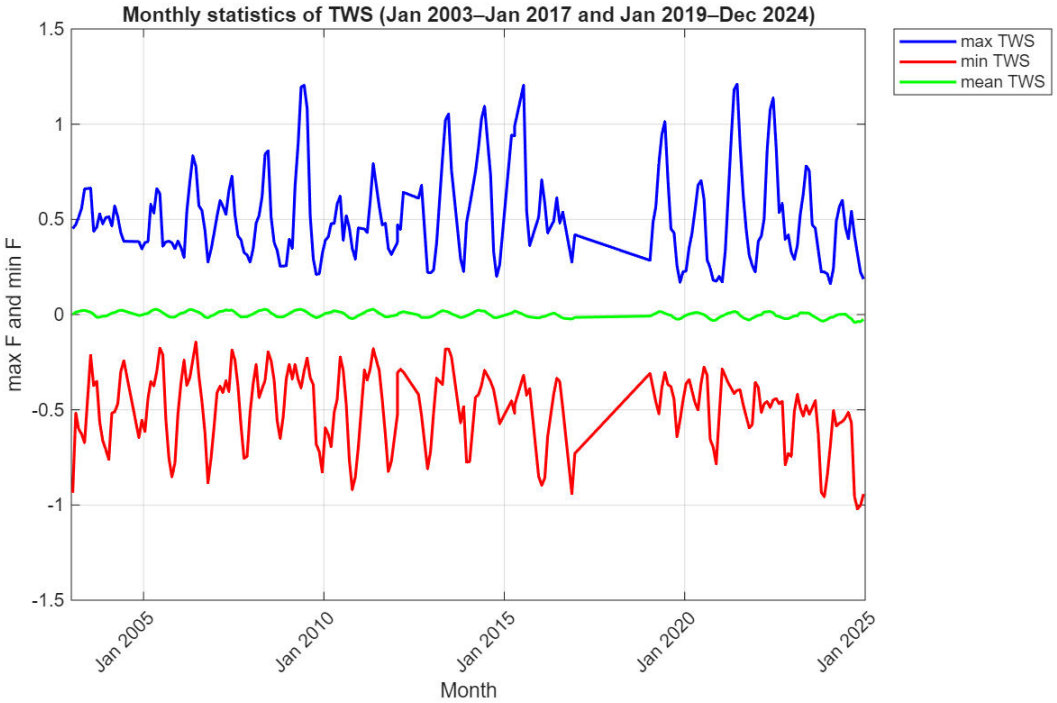

Figure 5.37: Statistics of TWH Based On DDK5

5.3 Hydrological Components and Temporal Variability from GLDAS and GRACE

This subsection presents the temporal and spatial characteristics of hydrological components derived from GLDAS and their relation to GRACE-based Equivalent Water Height (EWH) over South America. The aim is to quantify the contribution of near-surface water storage components and to provide a basis for interpreting integrated terrestrial water storage signals in subsequent groundwater analysis. Seasonal runoff behaviour is illustrated in Figure 5.41, which shows runoff patterns for selected seasons in 2010. The figure highlights pronounced seasonal variability, reflecting precipitation-driven surface hydrological processes. These variations are primarily associated with short-term surface responses and are expected to contribute to the seasonal component of total water storage rather than long-term subsurface storage.

The temporal evolution of GRACE-derived EWH over South America is presented in Figure 5.42 for the period 2003–2024. The time series includes contributions from snow water equivalent and canopy water storage and represents integrated terrestrial water storage variations. Pronounced seasonal oscillations are evident, superimposed on longer-term variations, indicating the combined influence of surface, near-surface, and subsurface water storage processes.

Further insight into near-surface water storage is provided by soil moisture time series shown in Figure 5.43, were variations are displayed separately for the four soil layers. The results indicate that soil moisture exhibits strong seasonal variability, particularly in the upper soil layers, while deeper layers show damped responses. This vertical differentiation highlights the limited depth sensitivity of soil moisture relative to deeper subsurface storage. The South American soil runoff time series for the period 2003–2024 Figure 5.44 shows strong seasonal behaviour with limited persistence over longer time scales, similar to the soil moisture results, reinforcing its role as a short-term hydrological component.

Global-scale reference fields derived from GLDAS are shown in Figure 5.38 to Figure 5.40. Figure 5.38 displays the global average EWH from GLDAS for the period 2003–2024, while Figure 5.39 presents the corresponding global distributions of canopy water storage and snow water equivalent. Figure 5.40 shows the global average soil moisture and total runoff over the same period. Together, these figures provide a climatological context for near-surface water storage components and illustrate their spatial heterogeneity and temporal variability. Finally, the long-term mean GRACE-derived EWH over South America for the period 2003–2024 is shown in Figure 5.45. This spatial representation reflects persistent large-scale terrestrial water storage patterns and serves as a reference against which temporal variations and residual groundwater-related signals can be evaluated.

Overall, the GLDAS-derived hydrological components are characterised by pronounced seasonal variability and limited long-term persistence, whereas the GRACE-derived EWH captures both seasonal and longer-term mass changes. This contrast forms the basis for separating near-surface hydrological contributions from deeper subsurface water storage in the subsequent groundwater analysis. In the context of groundwater assessment, the comparison between GRACE and GLDAS is particularly important. GLDAS primarily represents soil moisture and other surface or near-surface water components, while deeper groundwater storage is not explicitly modelled. Consequently, discrepancies between GRACE-derived total water storage and GLDAS estimates can be attributed largely to groundwater variability. The observed differences in magnitude and spatial smoothness therefore provide indirect evidence of groundwater storage changes across the study region.

5.3.1 Results Derived From GLDAS Data

Figure 5.41 shows the spatial distribution of surface and subsurface runoff over South America for selected months in 2010, representing different hydrological seasons. A clear seasonal signal is observed, with subsurface runoff consistently exhibiting higher magnitudes and wider spatial extent than surface runoff. In February 2010, corresponding to the wet season, both runoff components reach their maximum values, particularly over the Amazon basin and northern regions. Subsurface runoff dominates, indicating strong soil saturation and groundwater contributions under peak precipitation conditions. During May 2010, surface runoff decreases, while subsurface runoff

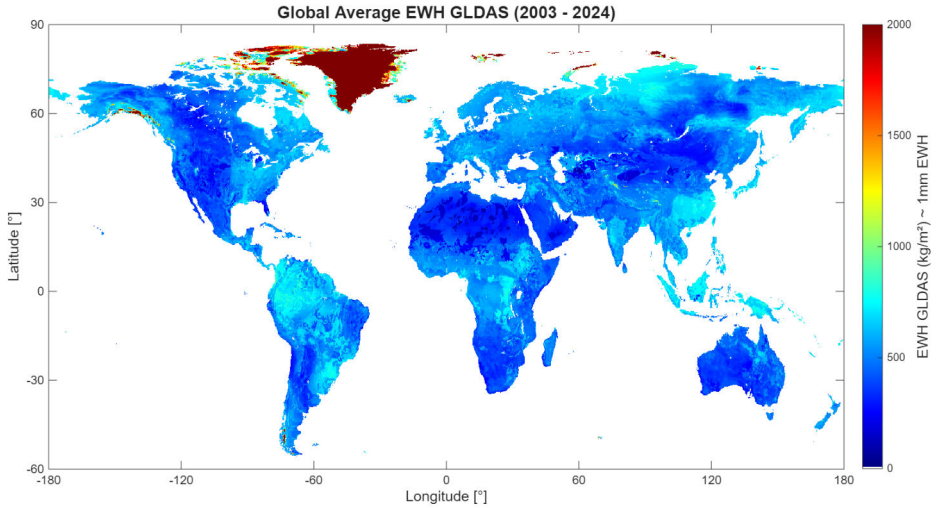

Figure 5.38: Global Average EWH GLDAS (2003 - 2024)

remains relatively elevated, reflecting a delayed hydrological response and continued release of stored subsurface water following the wet season. In August 2010, both surface and subsurface runoff are strongly reduced, with surface runoff nearly absent across most regions. This reflects dry-season conditions with limited precipitation and groundwater recharge. By November 2010, runoff increases again, especially in northern South America, marking the transition to the wet season. The subsurface runoff shows a more pronounced recovery than the surface runoff, indicating an early reactivation of subsurface hydrological processes. Overall, the seasonal comparison demonstrates that runoff dynamics in South America are strongly controlled by precipitation seasonality, with subsurface runoff dominating the hydrological response throughout the year. The delayed and persistent nature of subsurface runoff highlights the importance of soil and groundwater storage in regulating seasonal runoff variability.

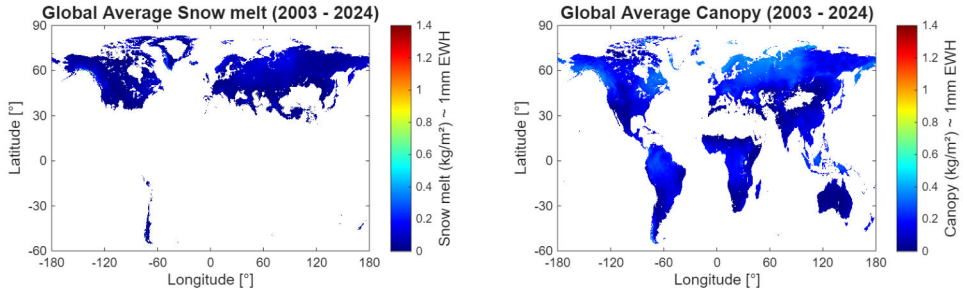

Figure 5.39: Global Average Canopy and Snow Water Equivalent (2003–2024)

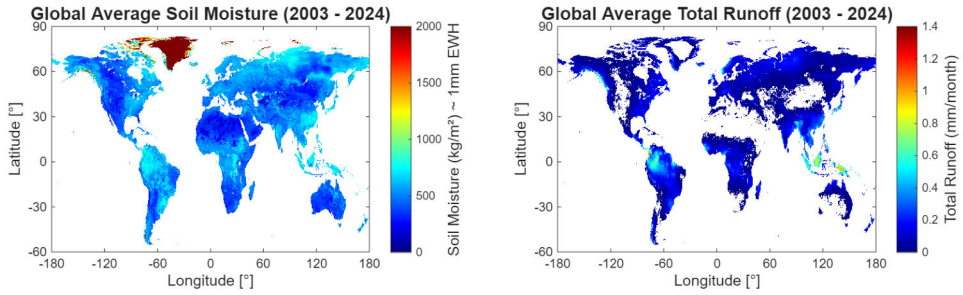

Figure 5.40: Global Average Soil Moisture and Total Runoff (2003–2024)

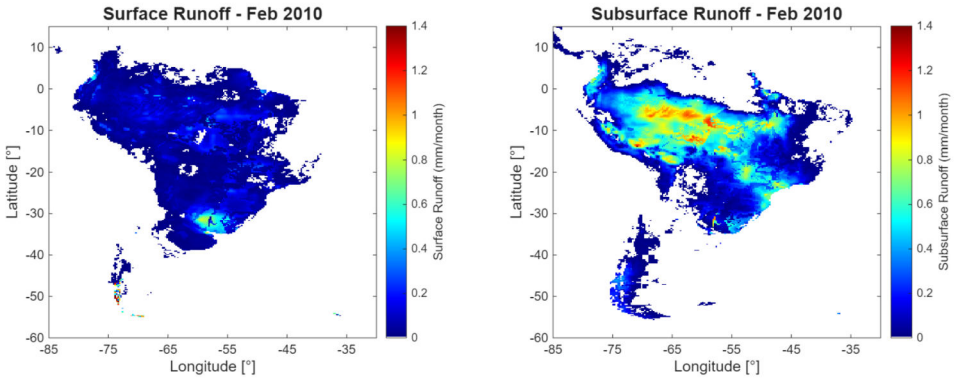

(a) Runoff in February 2010

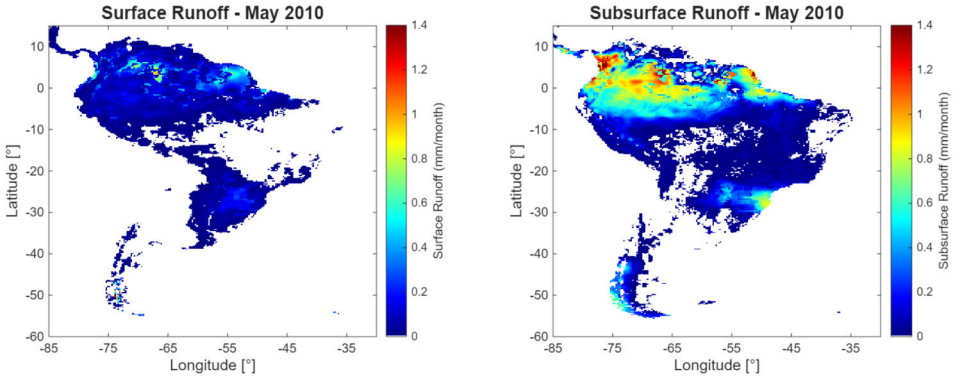

(b) Runoff in May 2010

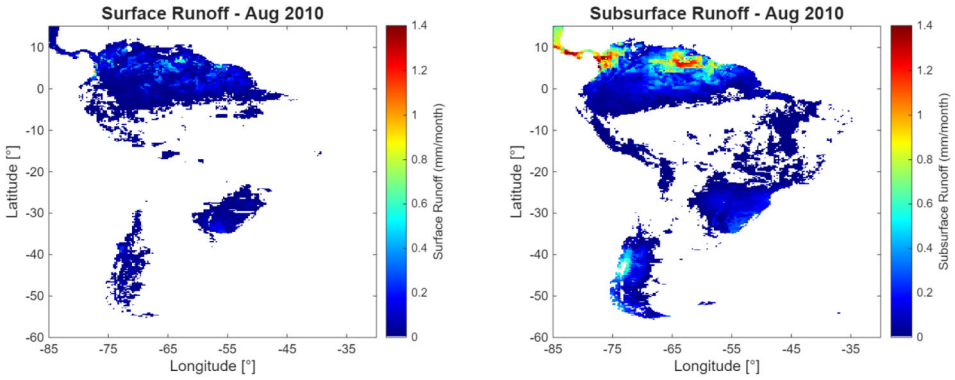

(c) Runoff in August 2010

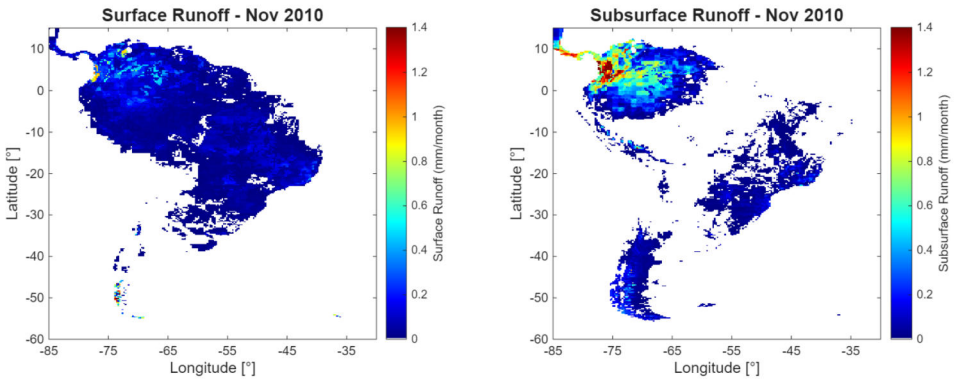

(d) Runoff in November 2010

Figure 5.41: Runoff during the seasons in 2010

Figure 5.39 shows the long-term global mean distribution of canopy water storage and snow water equivalent for the period 2003–2024 derived from GLDAS. The spatial patterns reflect climatological conditions,with higher snow storage in high-latitude and mountainous regions and enhanced canopy water in densely vegetated areas. These fields provide a reference for nearsurface water storage components considered in the separation of terrestrial water storage.

Figure 5.40 presents the global mean distribution of soil moisture and total runoff averaged over 2003–2024. Soil moisture exhibits strong regional variability associated with climate and land surface characteristics, while runoff patterns highlight major hydrological regimes. Together,these variables represent key surface and near-surface components of terrestrial water storage used for comparison with GRACE-derived estimates.

5.3.2 Mean TWS Distribution over South America (2003–2024)

Figure 5.45 illustrates the long-term mean equivalent water height (EWH) over South America for the period 2003–2024.The spatial distribution reflects persistent large-scale water storage patterns, with higher mean values in humid regions such as the Amazon basin and lower values in arid and semi-arid areas. This map provides a baseline representation of integrated terrestrial water storage against which temporal variations and groundwater-related anomalies are interpreted.

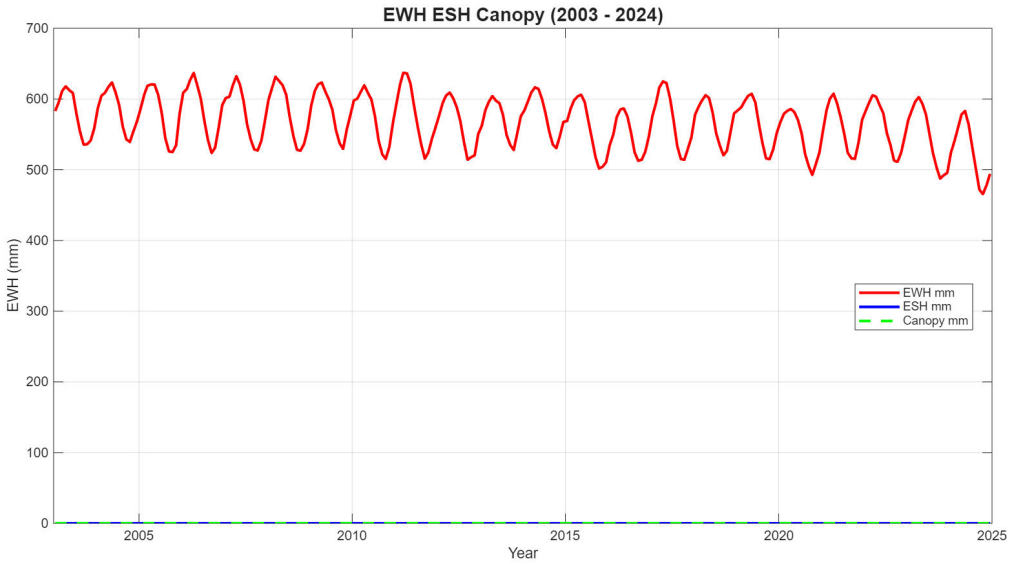

Figure 5.42: South America Equivalent Water Height (EWH) time series for the period 2003–2024, including contributions from snow water equivalent and canopy water storage.

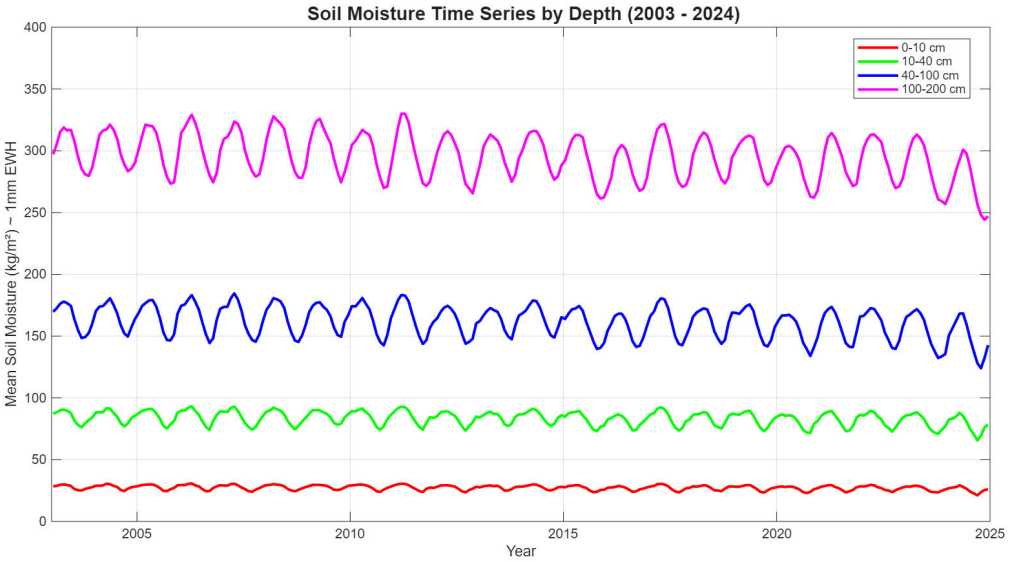

Figure 5.43: South America soil moisture time series for the period 2003–2024, shown separately for the four soil layers.

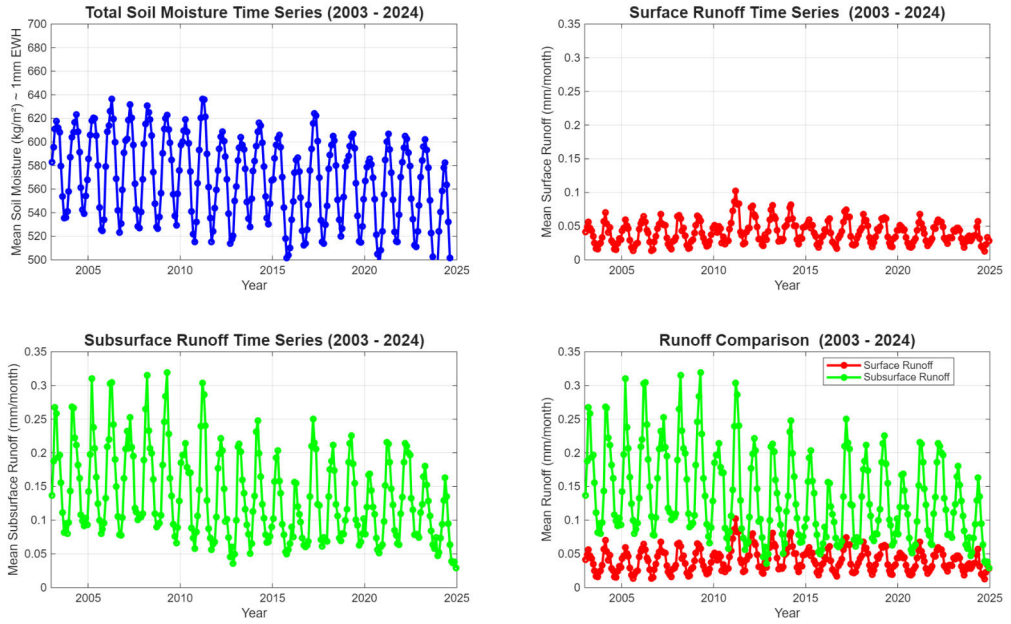

Figure 5.44: South America Soil Runoff Timeseries (2003 - 2024)

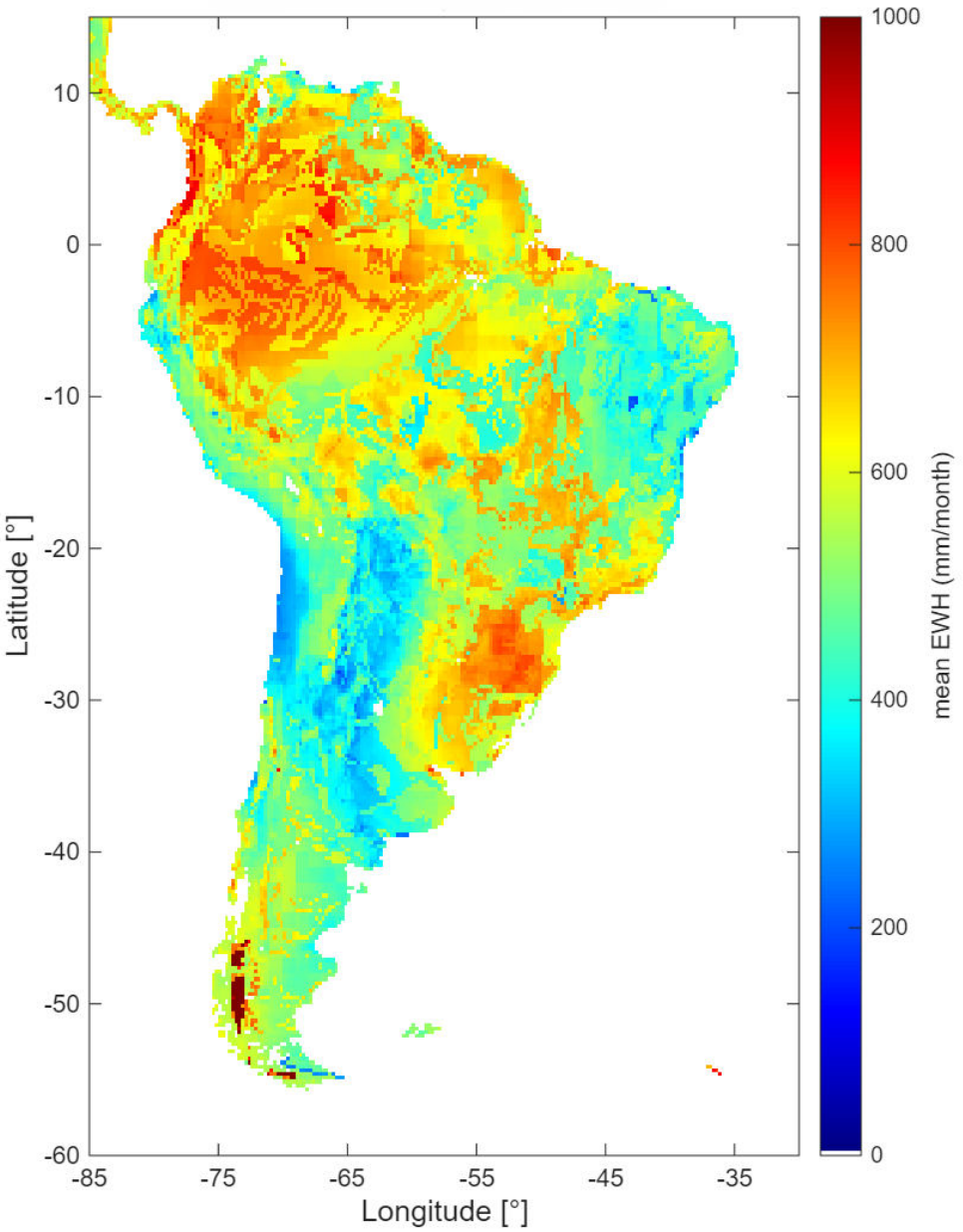

Figure 5.45: South America Mean EWH (2003 - 2024)

5.4 Estimation of Groundwater Storage Variability from GRACE–GLDAS Integration

This subsection presents the estimation of groundwater storage variability over South America by combining GRACE-derived equivalent water height (EWH) with hydrological components obtained from the GLDAS model. Since GRACE observes integrated terrestrial water storage, the groundwater contribution is inferred by subtracting near-surface water storage components represented by GLDAS from the total water storage signal.

The groundwater storage (GWS) is calculated as the residual between GRACE-derived total water storage and the sum of soil moisture, snow water equivalent, canopy water storage, and surface runoff obtained from GLDAS. This approach isolates subsurface water storage variations that are not explicitly modelled in land surface models and therefore provides indirect information on groundwater dynamics at large spatial scales.

The resulting groundwater time series exhibits pronounced seasonal variability superimposed on longer-term trends. Compared to surface and near-surface hydrological components, the groundwater signal shows a smoother

temporal evolution, reflecting the larger storage capacity and slower response of subsurface reservoirs. This behaviour is consistent with the expected characteristics of groundwater storage changes at the continental scale.
Spatially, groundwater-related anomalies derived from the GRACE–GLDAS residual display coherent large-scale patterns across South America. Regions characterised by limited surface water storage and strong climatic forcing show more persistent groundwater signals, while areas dominated by short-term hydrological processes exhibit weaker residuals. The spatial coherence of these patterns across multiple years supports their interpretation as groundwater-related mass changes rather than artefacts of surface hydrology.
Overall, the integration of GRACE and GLDAS data enables a first-order quantification of groundwater storage variability at continental scale. While uncertainties remain due to signal leakage, filtering effects, and limitations in hydrological modelling, the derived groundwater estimates provide valuable insight into long-term subsurface water storage dynamics and form the basis for further interpretation in the subsequent discussion.

5.5 Overall Discussion

The combined analysis of GRACE-derived geoid undulations, equivalent water height (EWH), and GLDAS hydrological components provides a coherent framework for assessing groundwater storage variability across South America. The results demonstrate that both the applied decorrelation filter and the treatment of near-surface hydrological processes play a decisive role in the interpretation of subsurface water storage signals derived from satellite gravimetry.
The comparison of DDK2- and DDK5-filtered GRACE and GRACE-FO products highlights a clear trade-off between signal preservation and noise suppression. While DDK2 retains stronger spatial gradients and larger anomaly amplitudes in both geoid undulations and EWH, it also exhibits residual striping and short-wavelength artefacts that complicate physical interpretation. DDK5, in contrast, produces smoother and more spatially coherent fields that consistently preserve large-scale seasonal and interannual variability. From a groundwater perspective, this stability is essential, as groundwater storage changes are expected to evolve gradually over time and to be expressed primarily at large spatial scales.
The analysis of GLDAS-derived hydrological components further clarifies the origin of the GRACE-observed signals. Soil moisture, canopy water storage, snow water equivalent, and runoff are characterised by pronounced seasonal variability and limited long-term persistence. These components dominate short-term fluctuations in terrestrial water storage but do not account for deeper subsurface storage processes. Their strong seasonal behaviour contrasts with the smoother and more persistent patterns observed in GRACE-derived EWH, indicating that a substantial fraction of the GRACE signal cannot be explained by near-surface hydrology alone.
By integrating GRACE and GLDAS data, groundwater storage variability is inferred as the residual component of total water storage after removal of near-surface contributions. The resulting groundwater signal exhibits coherent spatial patterns and a smoother temporal evolution than surface hydrological components, consistent with the physical characteristics of groundwater systems. The persistence of these patterns across both GRACE and GRACE-FO mission periods supports the interpretation that satellite gravimetry captures meaningful groundwater-related mass changes at the continental scale.
At the same time, the results underline the sensitivity of groundwater estimates to methodological choices. Filtering strength, signal leakage, and uncertainties in land surface modelling directly affect the magnitude and spatial expression of inferred groundwater anomalies. While the applied GRACE–GLDAS framework provides a robust first-order assessment of groundwater variability, the derived estimates should therefore be interpreted with appropriate caution, particularly at regional scales or when analysing short-term extremes.
Overall, this study demonstrates that GRACE and GRACE-FO satellite gravimetry, when combined with hydrological model outputs, offer valuable insight into large-scale groundwater storage dynamics. The findings confirm that careful filter selection and explicit consideration of surface hydrological components are essential for reliable

groundwater interpretation. This integrated approach forms a solid basis for future investigations of groundwater variability under changing climatic conditions and increasing anthropogenic pressure.

6 Conclusion

This research investigated groundwater storage variability over the South American continent using satellite gravimetry from the GRACE and GRACE-FO missions in combination with hydrological model outputs from GLDAS. Since GRACE observes vertically integrated terrestrial water storage, the central objective was to isolate and interpret groundwater-related mass changes by separating near-surface hydrological contributions and assessing the influence of decorrelation filtering on the derived signals.

A key outcome of this study is the demonstrated sensitivity of groundwater estimation to the choice of decorrelation filter. The comparison between DDK2 and DDK5 shows that while DDK2 retains stronger short-wavelength variability and produces larger anomaly amplitudes in both geoid undulations and equivalent water height (EWH), it is also affected by residual correlated noise and striping artifacts. These characteristics complicate the physical interpretation of changes in subsurface water storage. In contrast, the DDK5 filter provides smoother, more spatially coherent fields and a more stable spectral behaviour, which is better aligned with the expected large-scale and slowly evolving nature of groundwater storage.

Spatial and temporal analyses of geoid undulations and EWH reveal persistent large-scale patterns across seasons and mission phases, indicating that a substantial portion of the GRACE signal reflects long-term mass redistribution rather than short-term surface processes. When combined with GLDAS-derived soil moisture, runoff, canopy water storage, and snow water equivalent, it becomes evident that near-surface hydrological components are dominated by pronounced seasonal variability and limited long-term persistence. The systematic differences between GRACE-derived total water storage and GLDAS estimates therefore provide indirect but robust evidence of groundwater storage variability.

The resulting groundwater signal, obtained as the residual between GRACE and GLDAS, exhibits smoother temporal behaviour and coherent spatial structures consistent with the physical characteristics of groundwater systems at the continental scale. Although uncertainties related to filtering, signal leakage, and model limitations remain, the integrated GRACE–GLDAS framework applied in this study successfully captures meaningful groundwater-related mass changes across South America.

Overall, this work confirms that satellite gravimetry is a powerful tool for large-scale groundwater monitoring, provided that appropriate filtering strategies are applied and surface hydrological contributions are carefully taken into account. The findings underline the importance of methodological transparency and cautious interpretation when deriving groundwater information from GRACE observations.

7 Outlook

Future research should focus on improving the quantitative reliability of groundwater estimates derived from GRACE data. In particular, explicit correction of signal leakage and attenuation effects introduced by decorrelation filtering is essential. The use of mascon-based GRACE solutions or region-specific leakage correction techniques represents a promising pathway to better preserve groundwater-related signals while reducing filter-induced biases. Further advancements could be achieved by extending uncertainty propagation to explicitly include the groundwater estimation step. This would allow a formal quantification of errors associated with groundwater anomalies and improve confidence in regional and temporal comparisons. In addition, integrating alternative hydrological models or regional in-situ observations, where available, would help constrain near-surface storage components more effectively and reduce ambiguity in the separation of groundwater from total water storage.

From a spatial perspective, moving beyond continental averages toward basin-scale or sub-regional analyses would enable the investigation of heterogeneous groundwater trends that may be masked at larger scales. Such analyses are particularly relevant in regions subject to intensive groundwater abstraction or strong climatic gradients.
Looking ahead, next-generation gravity missions with improved spatial resolution and reduced correlated errors are expected to substantially enhance groundwater monitoring capabilities. These developments will be critical for tracking groundwater dynamics under increasing climatic variability and growing anthropogenic pressure, reinforcing the role of satellite gravimetry as a key component of global groundwater assessment frameworks.

Acknowledgement

The author express their sincere gratitude to Prof. Dr.-Ing. Hansjörg Kutterer for defining the topic of this lab rotation and for providing the academic framework within which this work was conducted. The author is particularly grateful to Dr.-Ing. Kurt Seitz for his continuous supervision, valuable guidance, and constructive feedback throughout the course of this study.
The author thanks the International Center for Global Earth Models (ICGEM) for providing access to the GRACE and GRACE-FO gravity field solutions, including the decorrelated DDK2 and DDK5 datasets used in this analysis. The authors also acknowledge the Global Land Data Assimilation System (GLDAS) for making the NOAH land surface model datasets available, which formed the basis for the analysis of the hydrological components.
Furthermore, the author thanks the Geodetic Institute at Karlsruhe Institute of Technology (KIT) for providing the necessary computational resources required for data processing and analysis.

References

Kusche, J. (2007): Approximate decorrelation and non-isotropic smoothing of time-variable GRACE-type gravity field models. *Journal of Geodesy* 81(11):733–749. DOI: 10.1007/s00190-007-0143-3.

Wahr, J., Molenaar, M., and Bryan, F. (1998): Time variability of the Earth's gravity field: Hydrological and oceanic effects and their possible detection using GRACE. *Journal of Geophysical Research: Solid Earth* 103(B12):30205–30229.

Groundwater monitoring over the continent of Australia

Athulya Jyothy[1]

1 Remote Sensing and Geoinformatics Master of Science (M.Sc.), KIT, Germany
E-Mail: uwpwn@student.kit.edu

Abstract

This study investigates Terrestrial Water Storage (TWS) and groundwater dynamics across the Australian continent for 2019-2024 using Level-2 monthly GRACE-FO solutions (GFZ/ICGEM) and GLDAS meteorological-hydrological outputs. The Wahr et al. (1998) approach was implemented in MATLAB to transform spherical harmonic potential coefficients into gridded Equivalent Water Height (EWH) maps, enabling robust capture of integrated mass transport over the continent in agreement with the framework described by Kim (2024). Filtering analyses comparing DDK2 and DDK5 demonstrate a trade-off between noise reduction and signal preservation; while DDK filters reduce longitudinal striping, results align with (Yang et al., 2013) and highlight the need for regional-scale evaluation to identify reliable TWS anomalies when GRACE products diverge from land surface models. Groundwater signals were isolated by subtracting GLDAS-derived soil moisture and runoff from total GRACE-TWS, a vital step for reliable water-resource assessment in Australia's arid and semi-arid zones where groundwater buffers climatic extremes (Tangdamrongsub et al., 2018). Despite high-resolution gridding ($30' \times 30'$), the intrinsic $\sim$300 km spatial resolution of GRACE-FO remains a limitation for resolving localized storage changes within narrow drainage basins, corroborating (Youm, 2025) on challenges in estimating fine-scale hydrological variation with satellite gravimetry alone. The integrated methodology provides a clarified view of continental TWS and groundwater behavior, informing regional water management under changing climatic conditions.

Keywords GRACE · GLDAS · Total Water Storage (TWS) · Australia

KIT Scientific Working Papers
Issue Number 270
ISSN: 2194-1629
DOI: 10.5445/IR/1000191188
Online: June 2026

This document is licensed under the Creative Commons Attribution – Share Alike 4.0 International License (CC BY-SA 4.0):
https://creativecommons.org/licenses/by-sa/4.0/deed.en

1 Introduction

The Earth system is a dynamic environment subject to various temporal changes, many of which are associated with significant mass transport within its fluid envelopes and solid parts. These changes can be effectively monitored by studying variations in the Earth's gravitational field.The satellite-based geodetic sensors allow for the detection of both temporal and spatial mass fluctuations, from which monthly solutions for the time-varying gravitational potential are generated. Terrestrial Water Storage (TWS) is a critical component of this mass transport, particularly in arid and semi-arid environments. As stated by Tangdamrongsub et al. (2018), accurate knowledge of groundwater storage variation (ΔGWS) is essential for reliable water resource assessment in regions like Australia, where water storage is significantly affected by human activities and spatiotemporal climate variations. The challenge in managing these resources lies in the expense and scarcity of traditional mapping and the high spatial variability of groundwater systems (Tregoning et al., 2012). The launch of the Gravity Recovery and Climate Experiment (GRACE) in 2002 and its successor, GRACE Follow-On (GRACE-FO) in 2018, provided a unique tool to measure the integrated change in all components of the hydrological cycle (Kim, 2024). These missions quantify mass redistribution over the Earth's surface as Equivalent Water Height (EWH). However, a primary limitation of GRACE data is its coarse spatial resolution – approximately 300-400 km – which is often insufficient to capture rapid or localized hydrological variations, such as those found along narrow river channels (Youm, 2025). Furthermore, as noted by Yang et al. (2013), inconsistencies often exist between GRACE-born products and land surface models like the Global Land Data Assimilation System (GLDAS), necessitating an in-depth analysis to identify reliable measurements of TWS anomalies. To bridge these gaps, this study analyzes the time series of groundwater over the continent of Australia. Following the workflow established during this, the study focuses on the GRACE-FO period from 2019 to 2024. The analysis utilizes Level-2 monthly solutions provided by the GFZ German Research Centre for Geosciences and compiled by ICGEM. In accordance, the data was processed using different orders of de-striping (specifically DDK2 and DDK5 filters) to ensure a high-precision mean solution. The methodology involves using MATLAB-based scripts to perform Spherical Harmonic Synthesis (SHS). As described in Youm (2025) , this allows for the conversion of potential coefficients into surface mass distribution maps. By integrating GRACE-FO data with hydrological model outputs, the soil moisture, runoff, and ice contributions can be reduced from the TWS to solve for the groundwater component, which is not directly partitioned in GLDAS data. The objective of this report is to present the quantified storage dynamics of Australia, visualize the TWS changes through high-resolution spatial mapping, and provide a thorough discussion on the resulting hydrological trends observed during the analyzed six-year window.

2 Theoretical Aspects

Several fundamental concepts play an important role in the modelling of TWS.

2.1 Spherical Harmonic Synthesis (SHS)

Spherical harmonics are given in Equation (2.1). Spherical Harmonic Synthesis is the forward computation of a function on or outside the sphere from a series of surface spherical harmonics (Tsoulis, 1999; Heiskanen and Moritz, 1967). The spherical harmonic coefficients provided as GRACE level-2 data is used to express the gravity field of the Earth.

$$V(r,\varphi,\lambda) = \frac{GM}{r}\sum_{n=0}^{\infty}\left(\frac{R}{r}\right)^n \sum_{m=0}^{n}(\bar{C}_{nm}\ \cos m\lambda + \bar{S}_{nm}\ \sin m\lambda)\bar{P}_{nm}(\sin\varphi) \tag{2.1}$$

where,

GM : Geocentric gravitational constant

R : Radius of the reference sphere

$\bar{C}_{nm}, \bar{S}_{nm}$: Fully normalised spherical harmonic coefficients of degree n and order m
$\bar{P}_{nm}$: Fully normalised Legendre functions of degree n and order m.

2.2 Degree and error degree variances

The degree variance quantifies the amplitudes of the spherical harmonic coefficients, which vary across different degrees n and orders m. The sum of the squared coefficients per degree expresses the overall energy in the signal as shown in Equation (2.2). Figure 2.1 shows that there is a higher degree variance at lower degrees, and the value decreases as the degree n increases. This shows that there is a higher concentration of signal at lower degrees compared to higher degrees.

$$C_n^2(\bar{C}_{nm}, \bar{S}_{nm}) = \sum_{m=0}^{n} (\bar{C}_{nm}^2 + \bar{S}_{nm}^2). \tag{2.2}$$

This helps to understand the distribution of signal intensity through the frequency range. Degree variance for the coefficients obtained for this study has been analysed, which shows that the signal has higher energy in the long wavelength part and it drops in shorter wavelength part of the signal. The plots for degree variance for all the months are similar with marginal variations, so an example plot for January, 2021 is shown in Figure 1. The degree variance does not dependent on the position of the calculation point $P(r, \varphi, \lambda)$.

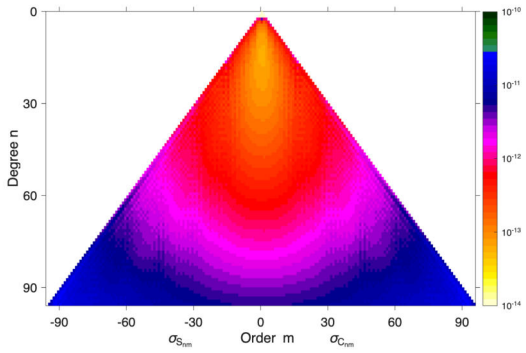

(a) Accuracy of the coefficient

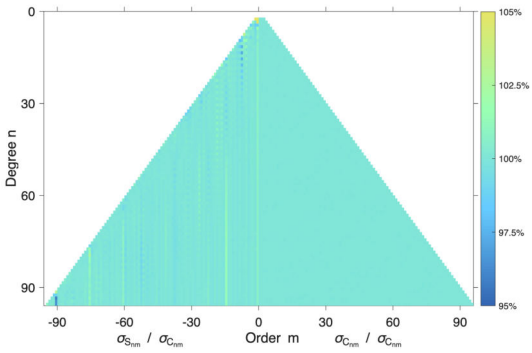

(b) Quotient of the accuracy

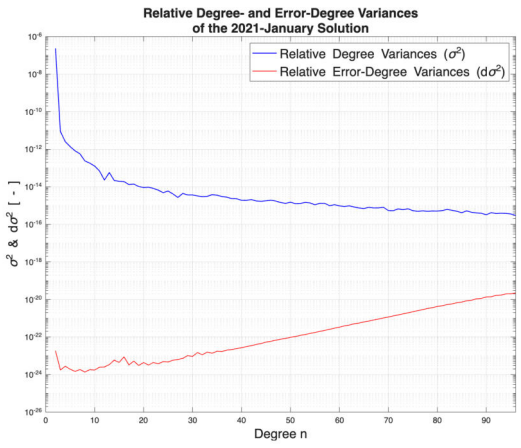

(c) Degree and error degree variance

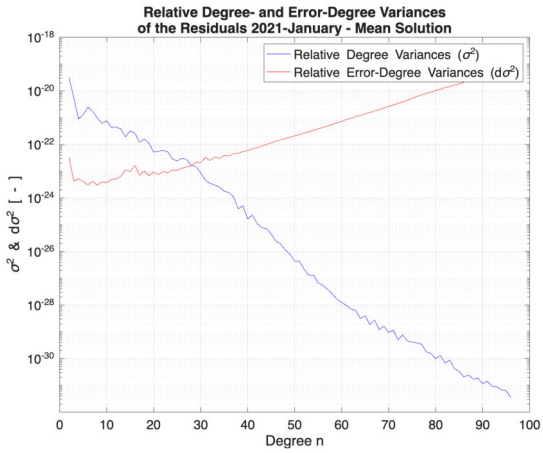

(d) Relative Degree and error degree variance

Figure 2.1: Accuracy of the potential coefficients January 2021

2.3 The Wahr Approach

The Wahr approach is the mathematical bridge that allows scientists to take dimensionless changes in the Earth's gravity field and calculate the actual weight of water on the ground. The core of the Wahr et al. (1998) theory is the

assumption that mass variations within the Earth system (like groundwater moving or ice melting) occur in a very thin layer relative to the Earth's mean radius. As stated in Kim (2024), if this layer is thin enough, the distance from the Earth's center to the mass is approximately equal to the Earth's radius . This allows for the direct conversion of geoid height changes into surface mass density. A critical part of the Wahr approach is acknowledging that the Earth is not a perfectly rigid rock. When a large volume of water accumulates over Australia, its weight causes the Earth's crust to sink slightly. This crustal deformation also changes the gravity signal. To correct for this, Wahr introduced the Load Love Numbers k_n . As referenced in Kim (2024), the potential coefficients must be scaled by the factor:

$$\frac{2n+1}{1+k_n} \tag{2.3}$$

This factor separates the gravity signal caused by the actual water from the signal caused by the Earth's crust bending under the weight of that water.

3 Data

The primary dataset used in this study consists of Level-2 monthly gravitational field solutions from the Gravity Recovery and Climate Experiment Follow-On (GRACE-FO) mission. These data were retrieved from the GFZ German Research Centre for Geosciences via the ICGEM (International Centre for Global Earth Models) web portal (ICGEM, 2026). The data basis includes all monthly solutions up to degree and order (d/o) 96. To mitigate the effects of longitudinal "stripping" errors common in GRACE data, this study utilizes the DDK2 and DDK5 filtered versions, which allow for comparative analysis of signal-to-noise ratios. To perform component separation, auxiliary hydrological data from the Global Land Data Assimilation System (GLDAS) were utilized. Following the approach of Tregoning et al. (2012), these data provide discrete grids of soil moisture and runoff, which are essential for isolating the groundwater signal from the Total Water Storage (TWS) observations.

3.1 GRACE

The primary data source consists of Level-2 monthly gravitational field solutions from the Gravity Recovery and Climate Experiment Follow-On (GRACE-FO) mission. These data were provided by the GFZ German Research Centre for Geosciences and accessed via the ICGEM (International Centre for Global Earth Models) web portal. The study utilizes spherical harmonic models up to degree and order (d/o) 96. These models are provided as a set of fully normalized potential coefficients ($\bar{C}_{nm}, \bar{S}_{nm}$). According to Kim (2024), these coefficients represent the integrated change in mass of all components of the hydrological cycle. To ensure data quality, the coefficients were processed using DDK de-striping filters, both DDK2 and DDK5 filtered versions were utilized to reduce the characteristic north-south "stripping" noise while preserving the hydrological signal. They are related to the mean model ($\bar{C}^{\circ}_{nm}, \bar{S}^{\circ}_{nm}$) to get ($\Delta\bar{C}_{nm}, \Delta\bar{S}_{nm}$).

3.2 GLDAS

The Global Land Data Assimilation System (GLDAS) is a sophisticated terrestrial modeling framework developed jointly by NASA and the National Oceanic and Atmospheric Administration (NOAA). To isolate the groundwater component, auxiliary data from GLDAS were incorporated. GLDAS provides high-resolution fields of land surface states by ingesting satellite and ground-based observations. In this study, GLDAS outputs (such as soil moisture and runoff) are used to perform component separation. As explained by Tangdamrongsub et al. (2018), GRACE-derived TWS represents an integrated vertical column; therefore, contributions from soil moisture, snow, and surface water must be estimated via models like GLDAS (Rodell et al., 2004; NASA, 2022) to solve for the residual groundwater storage variation (ΔGWS), which states that groundwater is not directly available in GLDAS and must be calculated by reducing these other contributions from the GRACE TWS. GLDAS is a system that ingests satellite- and ground-based observational data products to generate high-resolution fields of land surface

states and fluxes. The primary reason for incorporating GLDAS data into this study is to overcome the inherent limitation of GRACE-FO observations. While GRACE-FO provides an integrated measure of Total Water Storage (TWS), it cannot distinguish between different vertical layers of the hydrological compartments. For the analysis of Australia between 2019 and 2024, GLDAS data provides the necessary spatial maps of soil moisture and surface runoff. By aligning the $30' \times 30'$ regional grid of the GRACE-FO synthesis with GLDAS outputs, the groundwater fluctuations across the continent's diverse climatic zones, ranging from the tropical north to the arid interior of Australia, can be quantify and visualize.

4 Methodology Overview

4.1 Data Pre-processing and Filtering

The downloaded potential coefficients $(\bar{C}_{nm}, \bar{S}_{nm})$represent variations in the Earth's geopotential. According to Yang et al. (2013), processing methods vary between research centers, requiring careful alignment. In this study, we adopted the DDK de-striping filters (DDK2 and DDK5) to suppress high-frequency noise. A mean solution was first calculated from the initial data basis to serve as a reference for subsequent monthly variations.

4.2 Mathematical Transformation to EWH

To convert dimensionless potential coefficients into TWS expressed as Equivalent Water Height (EWH), the transformation described by Wahr et al. (1998) is applied. The relationship between geoid change and surface mass density is defined by the formula:

$$\Delta TWS(\varphi,\lambda) = \frac{R\rho_e}{3\rho_w} \sum_{n=0}^{N} \sum_{m=0}^{n} \frac{2n+1}{1+k_n} \bar{P}_{nm}(\sin\varphi) \left(\Delta\bar{C}_{nm}\cos m\lambda + \Delta\bar{S}_{nm}\sin m\lambda\right) . \tag{4.1}$$

The mean density of the Earth is denoted by ρ_e, and the mean density of water by ρ_w, respectivly.

4.3 Spherical Harmonic Synthesis (SHS) and Gridding

The converted potential coefficients were projected into the space domain using MATLAB. Following the parameters, TWS variations were synthesized on a regional grid over Australia with a spatial resolution of $30' \times 30'$. As highlighted by Youm (2025), this synthesis is critical because it allows for localized analysis of mass changes that are otherwise smoothed in global gravity solutions.

4.4 Separation of Groundwater Storage (GWS)

Since GRACE observes the integrated total mass change, the groundwater component must be isolated by removing other hydrological variables. Based on Tangdamrongsub et al. (2018), the large-scale ΔGWS is derived by subtracting soil moisture, surface water, and snow contributions (from GLDAS) from the total GRACE-derived EWH. The mathematical expression used in this study is

$$\Delta GWS = \Delta TWS - (\Delta_{\text{SoilMoisture}} + \Delta_{\text{Runoff}} + \Delta_{\text{Ice}}) . \tag{4.2}$$

5 Results and Discussion

The results obtained from spherical harmonic synthesis of coefficients and derived estimates of TWS using the Wahr approach (Wahr et al., 1998), as well as the GLDAS results, have been included in this section.

5.1 GRACE Results

5.1.1 DDK2 Results (Smoothed Filtering)

The DDK2 filter provides a more heavily smoothed representation of mass variations, which is effective for identifying broad regional trends while sacrificing some fine-scale spatial detail.

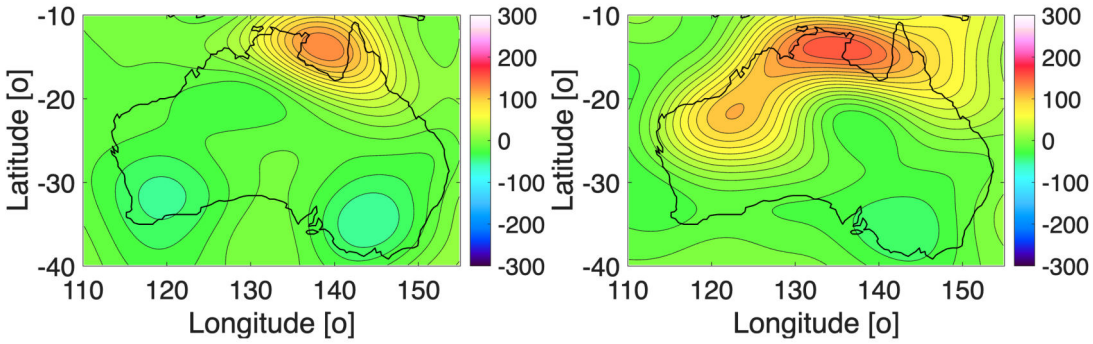

(a) January

(b) February

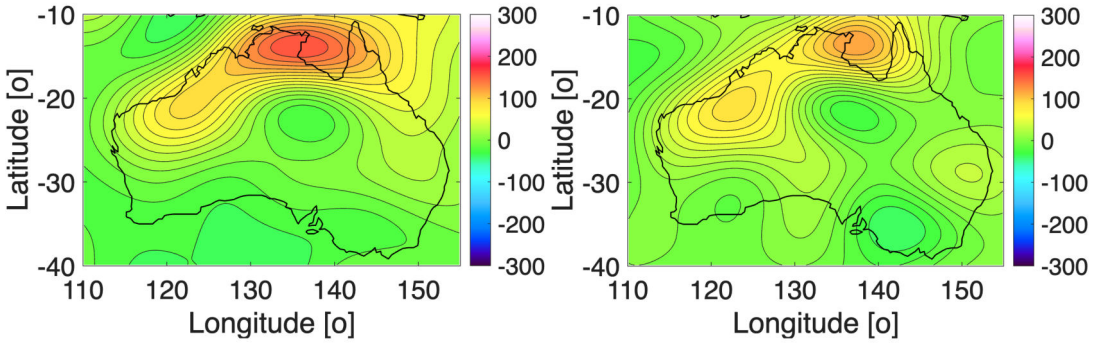

(c) March

(d) April

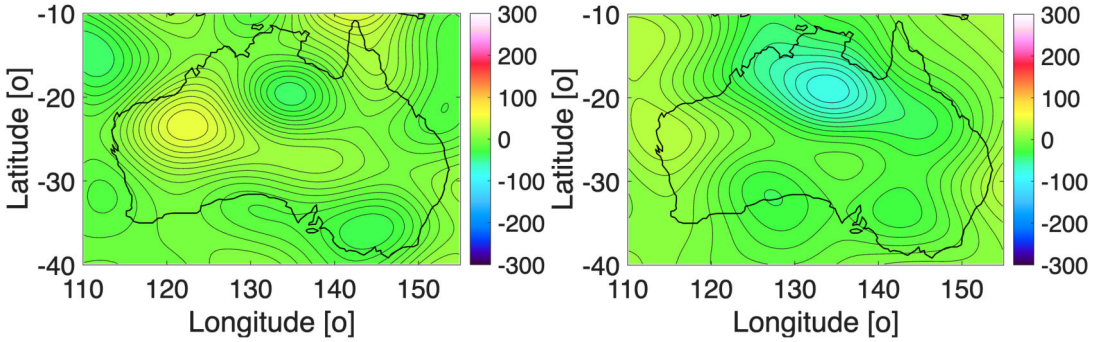

(e) May

(f) June

Figure 5.1: TWS-DDK2 for January to June 2021 (range is ±300 mm).

5.1.2 Monthly Variation in 2021

As shown in Figures 5.1 and 5.2, the monthly TWS progression for 2021 using DDK2 reveals a continent-wide transition. The first quarter (January–March) is dominated by positive EWH anomalies in Northern Australia. According to Tangdamrongsub et al. (2018), this spatial pattern is typical of the strong seasonal rainfall induced by the tropical monsoon in the north.

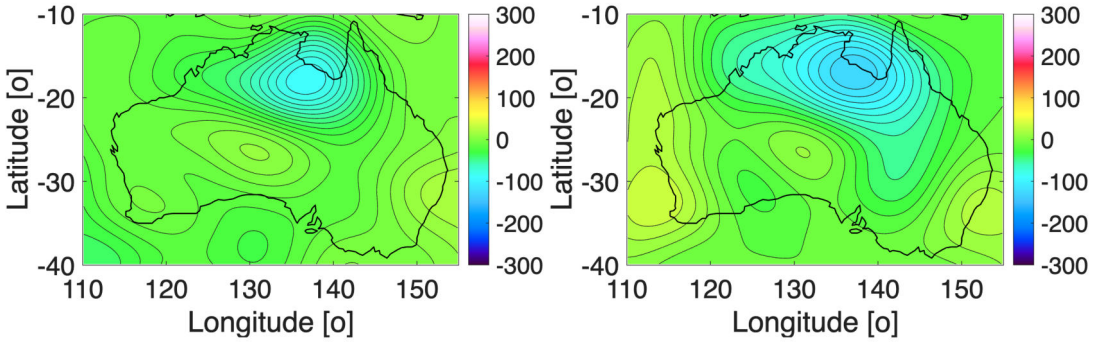

(a) July

(b) August

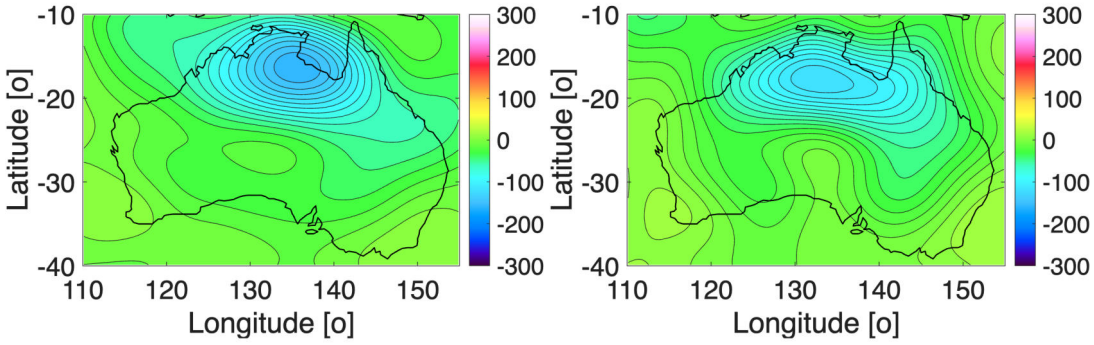

(c) September

(d) October

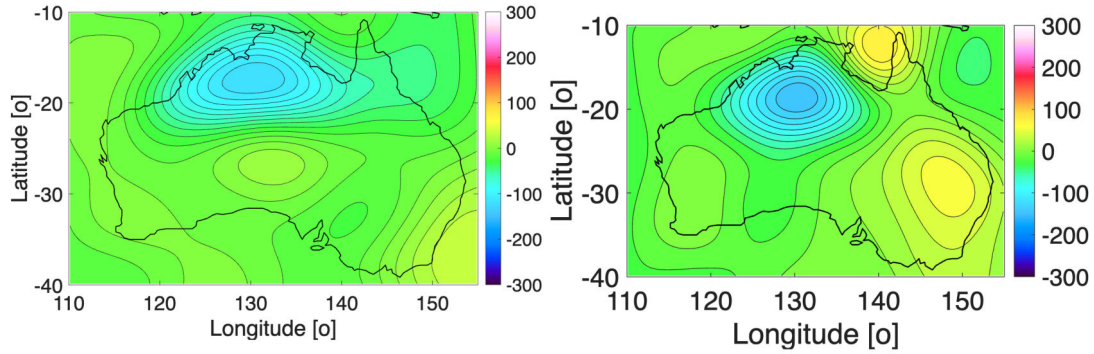

(e) November

(f) December

Figure 5.2: TWS-DDK2 for July to December 2021 (range is ±300 mm).

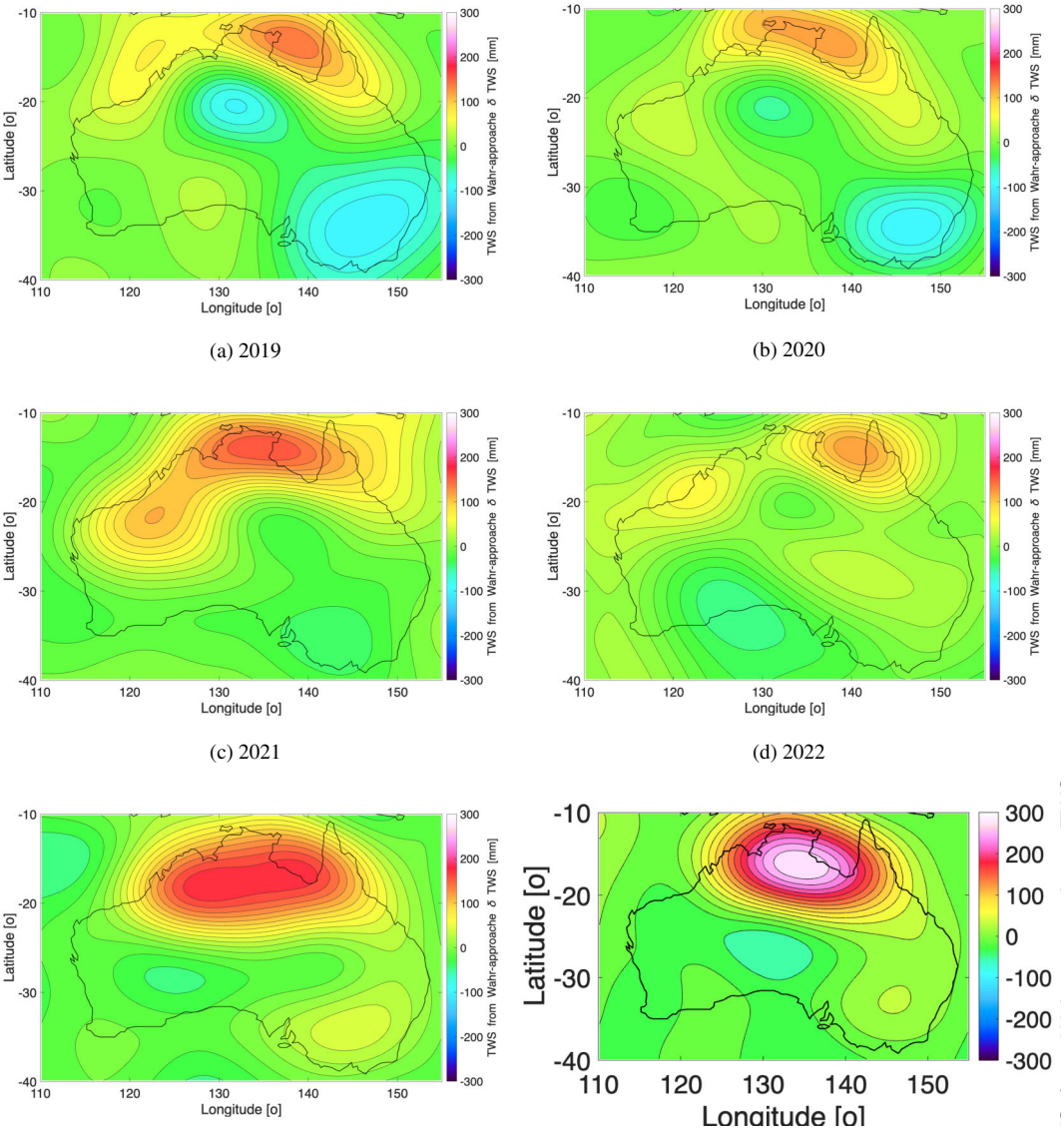

(a) 2019

(b) 2020

(c) 2021

(d) 2022

(e) 2023

(f) 2024

Figure 5.3: TWS-DDK2 for February 2019 to 2024 (range is ±300 mm).

5.1.3 Inter-annual February Analysis (2019–2024)

Comparing the month of February across the six-year span (Figure 5.3), DDK2 highlights a significant "drastic variation." 2019-2020: Low mass concentration, indicative of the severe drought conditions previously noted in the Murray-Darling and Western basins (Tregoning et al., 2012). 2021-2022: A sharp peak in water storage, with the EWH signature appearing as a broad, smooth positive anomaly across the top end of the Northern Territory.

5.1.4 DDK5 Results (High-Resolution Filtering)

The DDK5 filter allows for higher spatial resolution, enabling the detection of more localized mass changes, though it is more susceptible to residual noise.

5.1.5 Monthly Variation in 2021

In Figures 5.4 and 5.5, the TWS-DDK5 maps for 2021 show a more "textured" distribution of mass. In February and March 2021, the anomalies are not just broad blobs but show higher intensity concentrations along specific

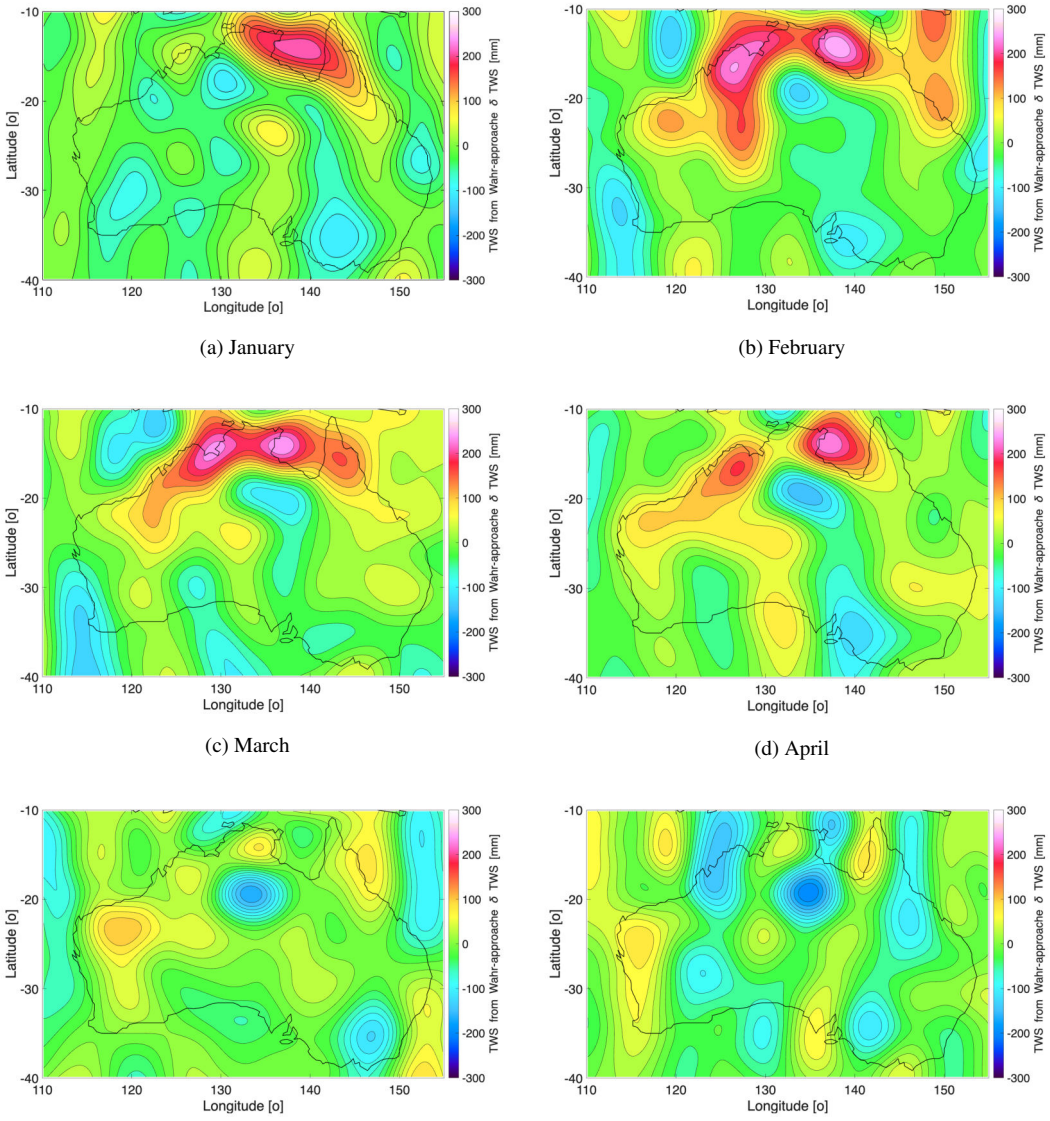

(a) January

(b) February

(c) March

(d) April

(e) May

(f) June

Figure 5.4: TWS-DDK5 for January to June 2021 (range is ±300 mm).

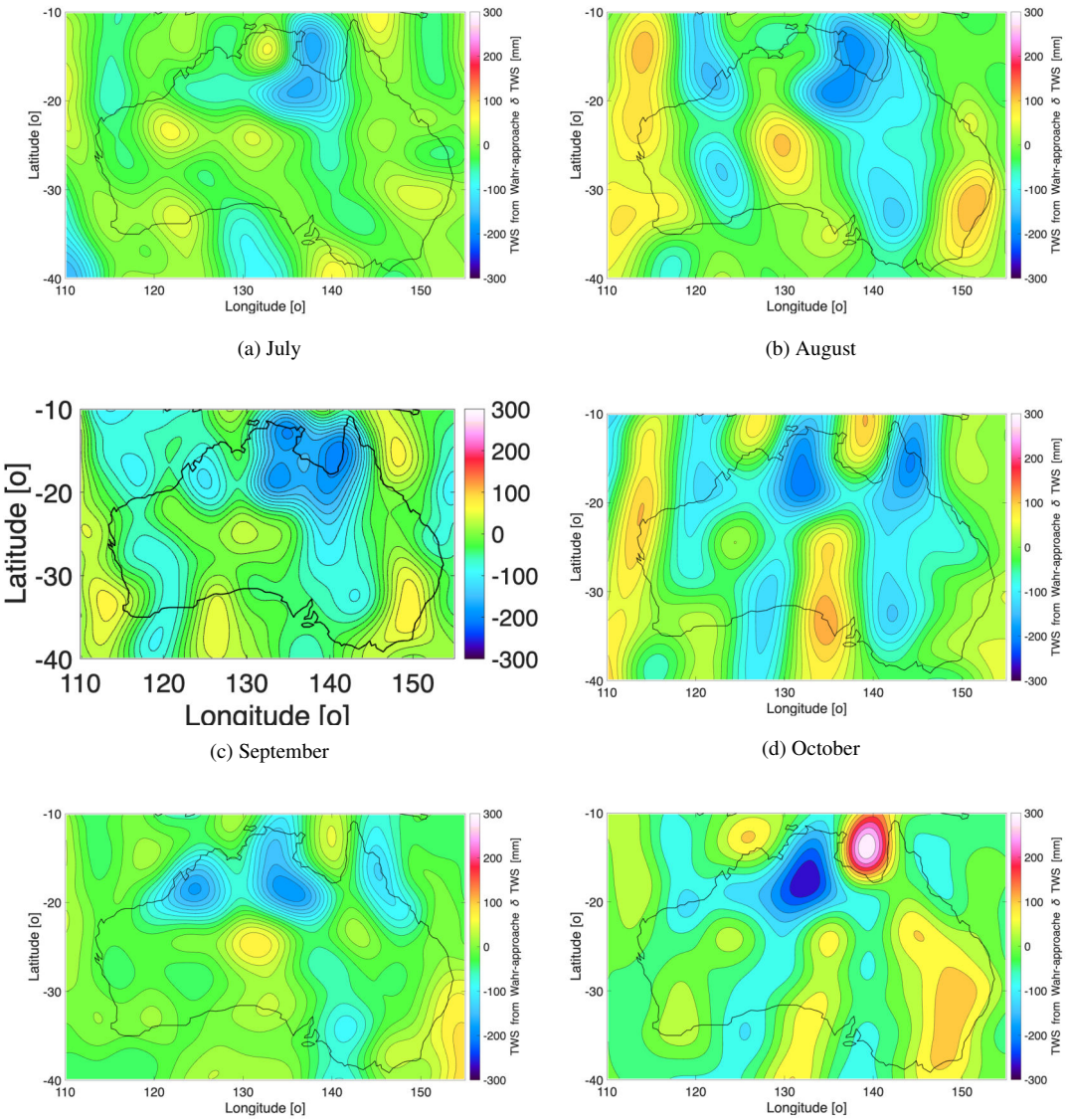

(a) July

(b) August

(c) September

(d) October

(e) November

(f) December

Figure 5.5: TWS-DDK5 for July to December 2021 (range is ±300 mm).

drainage systems. This aligns with the findings of Youm (2025), stating that higher-resolution modeling is required to capture mass variations concentrated along river channels that are otherwise smoothed out.

5.1.6 Inter-annual February Analysis (2019–2024)

The DDK5 results for February (Figure 5.6) show that the "drastic variations" in 2021 and 2022 were more localized than DDK2 suggested. Specifically, the peak in February 2022 shows intense mass concentration in the Kimberley and Carpentaria regions. As noted by Kim (2024), these spikes are often the result of La Niña-enhanced rainfall, which RU-Net and high-resolution filters can capture more precisely than global mean solutions.

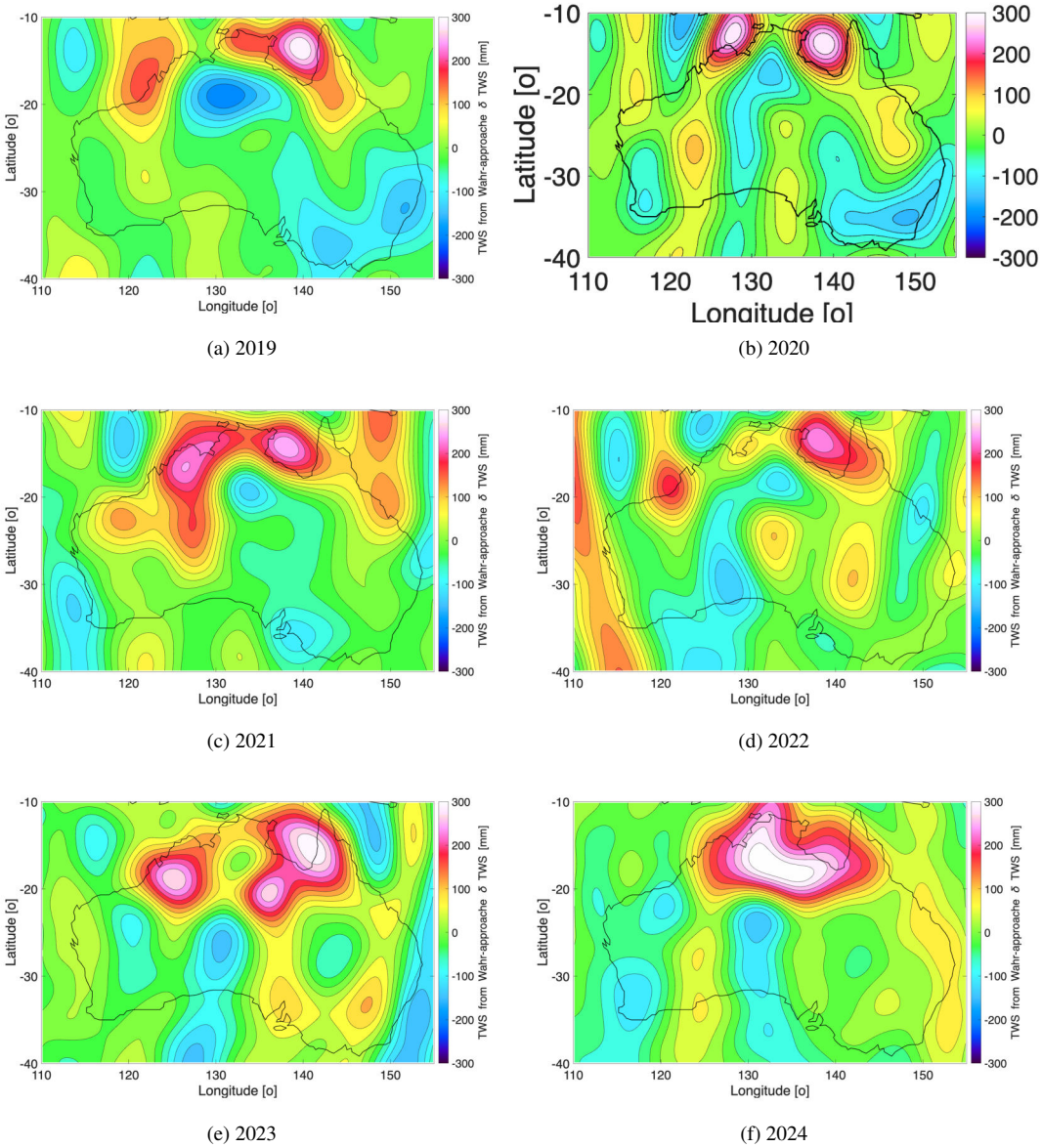

(a) 2019

(b) 2020

(c) 2021

(d) 2022

(e) 2023

(f) 2024

Figure 5.6: TWS-DDK5 for February 2019 to 2024 (range is ±300 mm).

5.2 Statistics Of TWS

5.2.1 Analysis of DDK2 Statistics (Smoothed)

The DDK2 filter is a "stronger" filter, which provides a more stable but smoothed result (see Figure 5.7). Signal Attenuation: In comparison to DDK5 (Figure 5.8), the DDK2 statistics show a reduced dynamic range. The "Max" peaks are generally lower, and the "Min" troughs are less deep. This is a result of the "smearing" effect described by Yang et al. (2013), where the filter distributes intense local mass changes over a wider area. Noise Reduction: The RMS and STD values for DDK2 are lower than those of DDK5. This indicates a "cleaner" dataset with fewer longitudinal stripping artifacts, which is preferable for studying long-term continental trends rather than monthly spikes.

5.2.2 Analysis of DDK5 Statistics (High-Resolution)

The DDK5 filter represents a "weaker" smoothing approach, designed to preserve localized hydrological signals (see Figure 5.8). Extreme Values: The "Max" values (green dots) show significant peaks, particularly in the

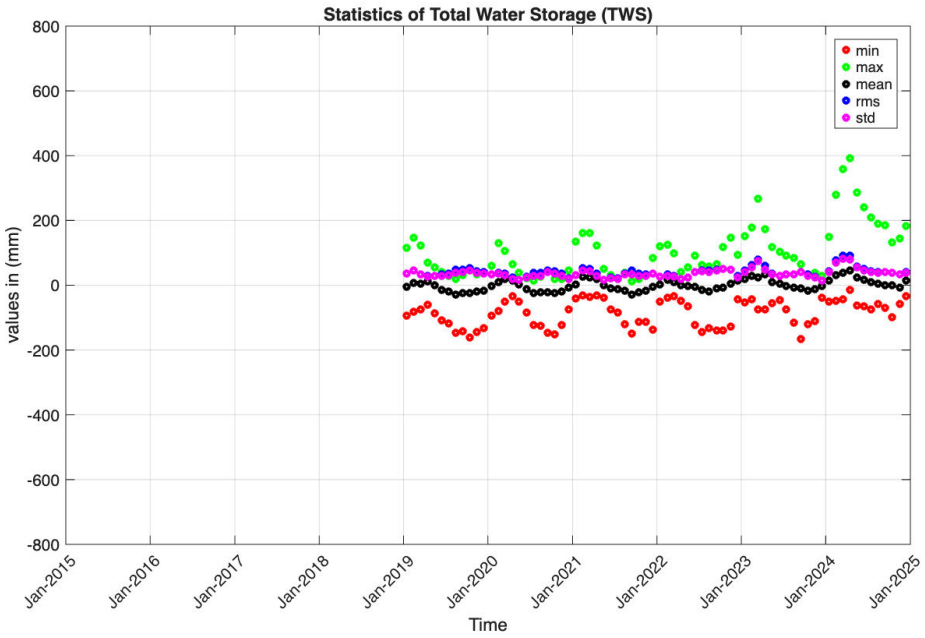

Figure 5.7: Statistical values for TWS (DDK2)

February-March windows of 2021, 2022, and 2024, where localized water storage exceeds 600 mm. Spatial Variability: The Standard Deviation (magenta) and RMS (blue) are relatively high. This suggests a high degree of spatial contrast across the Australian continent. Physical Interpretation: According to Youm (2025), high-resolution processing is essential for capturing mass concentrated along river channels. The high "Max" values in the DDK5 Figure 5.8 indicate that the filter is successfully capturing the intense monsoon-driven water accumulation in the northern drainage basins.

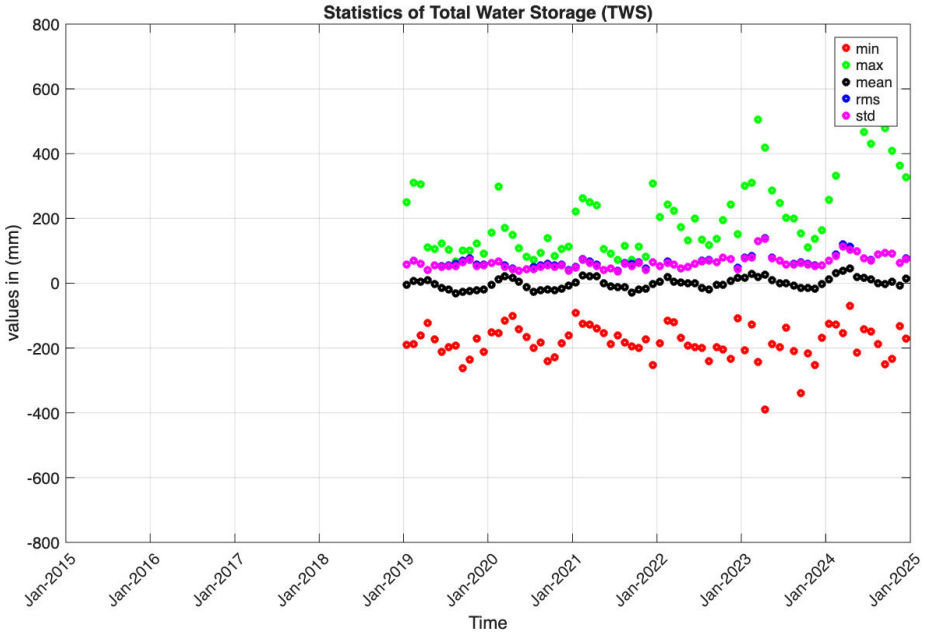

Figure 5.8: Statistical values for TWS (DDK5)

5.3 GLDAS Results

In this study, auxiliary data from the Global Land Data Assimilation System (GLDAS) were utilized to provide the necessary hydrological context for the GRACE-FO derived Total Water Storage (TWS) anomalies. As specified, the soil moisture and runoff components must be subtracted from the GRACE-TWS to solve for the groundwater component, which is not directly resolved in the GLDAS output. The mean is shown in Figure 5.9.

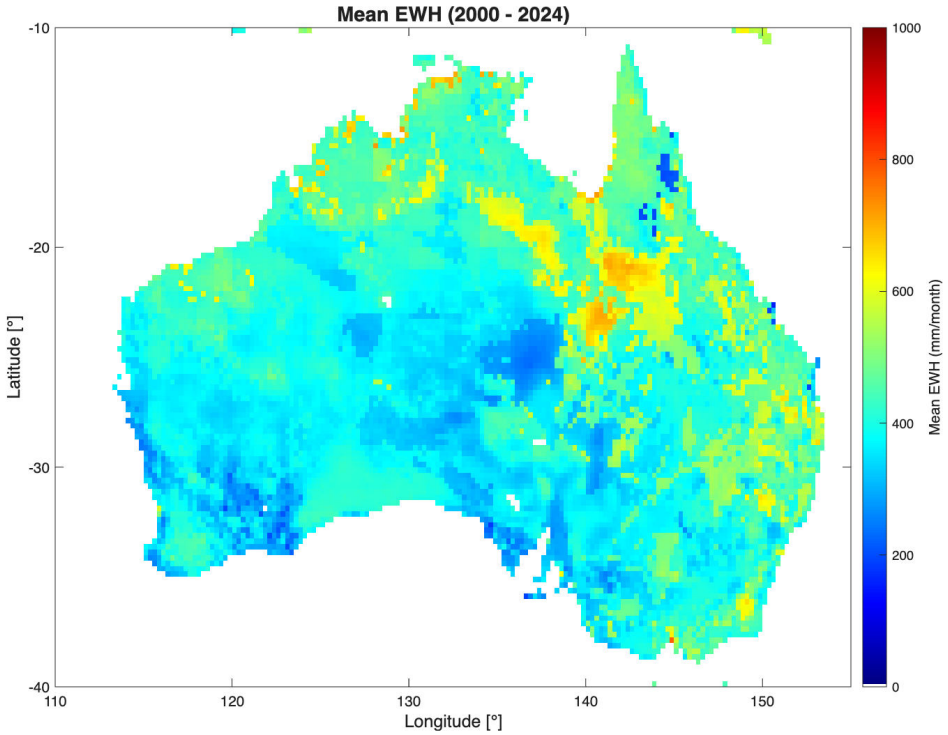

Figure 5.9: Mean equivalent water height from GLDAS (2000-2024)

5.4 Statistical Results

The statistical results are presented in Figure 5.10 and Figure 5.11.
According to Yang et al. (2013), the Noah model typically utilizes four layers totaling a depth of 2 m.
Resultant Observation: The 0-10 cm (surface) and 10-40 cm layers show the highest amplitude of fluctuation and most frequent "spikes," whereas the 100-200 cm (deep) layer remains more stable with lower overall variability. Discussion: The modeling of these four layers is consistent with the configuration of the Noah land surface model used in GLDAS. The results confirm that surface layers respond rapidly to individual rainfall events, while the deeper layers (40-200 cm) represent a more integrated, long-term storage component. As suggested in Tregoning et al. (2012), in regions with strong seasonality, shallow groundwater changes might inadvertently be included in the model parameterization of these soil storage layers.

5.5 Temporal variations in runoff and total soil moisture

Resultant Observation: A significant peak in both soil moisture and surface runoff is visible around 2010-2011. Conversely, the most recent period (2019-2024) shows a return to higher variability following the "Millennium Drought" recovery. Discussion: The intense peak observed in 2011 is historically significant. As discussed by Kim (2024), the recovery from intense droughts in Australia, such as the period leading up to 2011, often leads to

sharp increases in TWS that result in measurable crustal uplift. Furthermore, the relationship between surface and subsurface runoff is critical; the immediate response of surface runoff during wet months (Figure 5.11) supports the claim that near-surface components are highly responsive to immediate meteorological forcing (Tangdamrongsub et al., 2018).

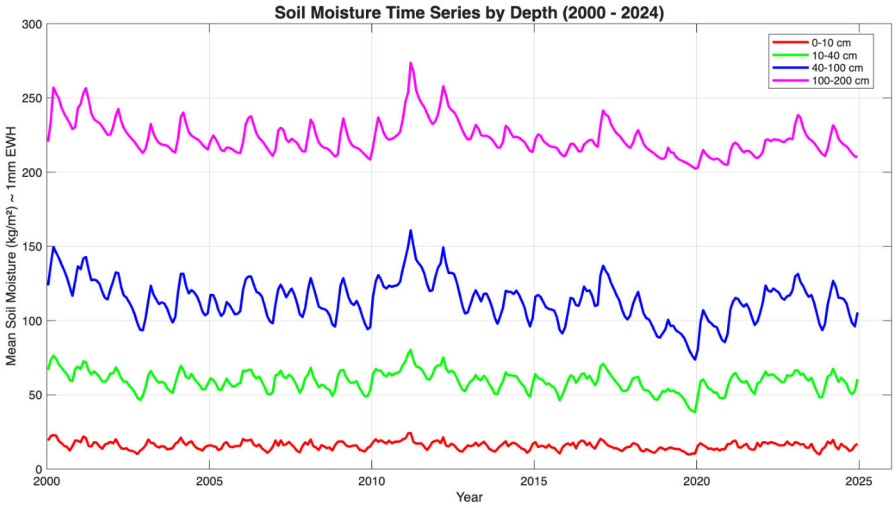

Figure 5.10: Soil moisture by the four layers (2000-2024)

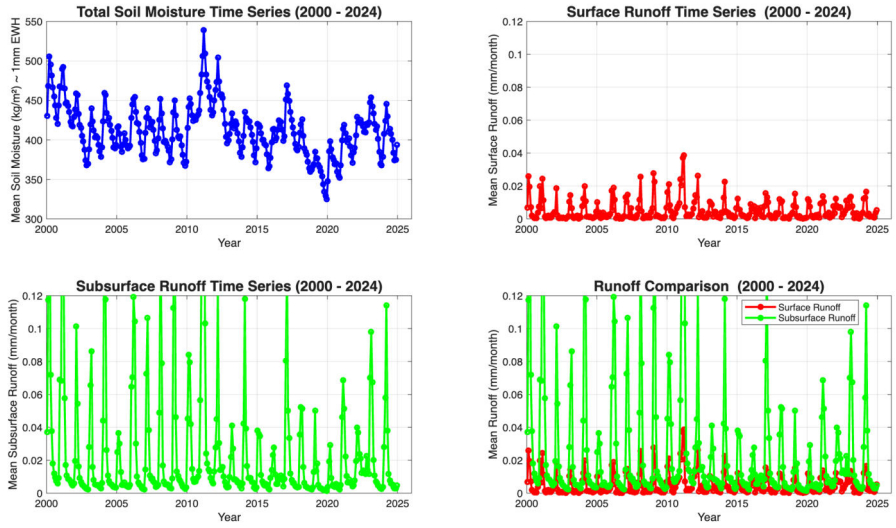

Figure 5.11: Soil moisture and runoff time series (2000-2024)

5.6 GLDAS Results for 2021

January – March (Wet Season): During the early months of 2021 (Figures 5.12), a distinct concentration of high soil moisture and runoff is observed in Northern Australia. This aligns with the tropical monsoon cycle. According to Tangdamrongsub et al. (2018), these near-surface components exhibit immediate temporal responses to meteorological forcing, which is reflected in the intense runoff values seen in the Top End and Gulf of Carpentaria regions. April – June (Transition): As the continent transitions into the southern hemisphere winter (Figures 5.13), soil moisture remains high in the eastern drainage basins, while the western regions show rapid drying. July – September: Runoff values significantly decrease across the interior of the continent (Figures 5.14),

while soil moisture levels remain stable in the southern coastal regions, likely influenced by winter rainfall patterns. October – December: The "build-up" season (Figures 5.15) shows a gradual increase in moisture across the northern coasts, preparing for the subsequent wet season.

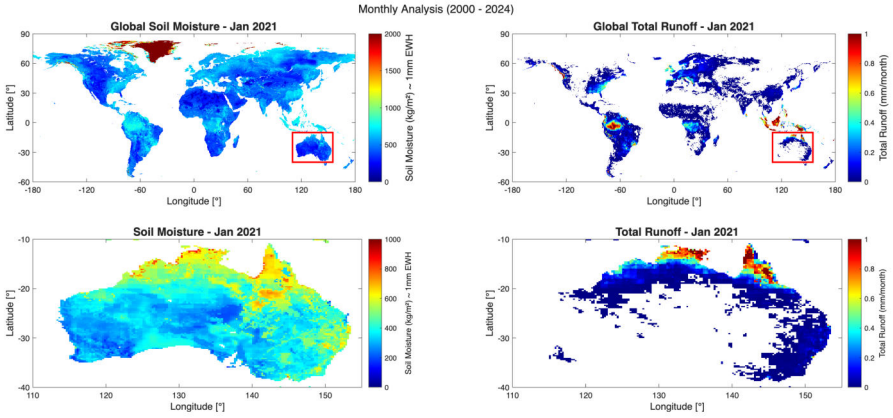

(a) January

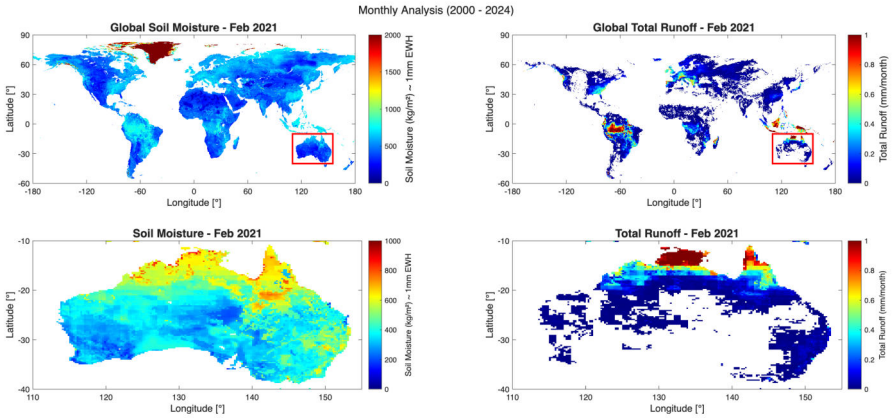

(b) February

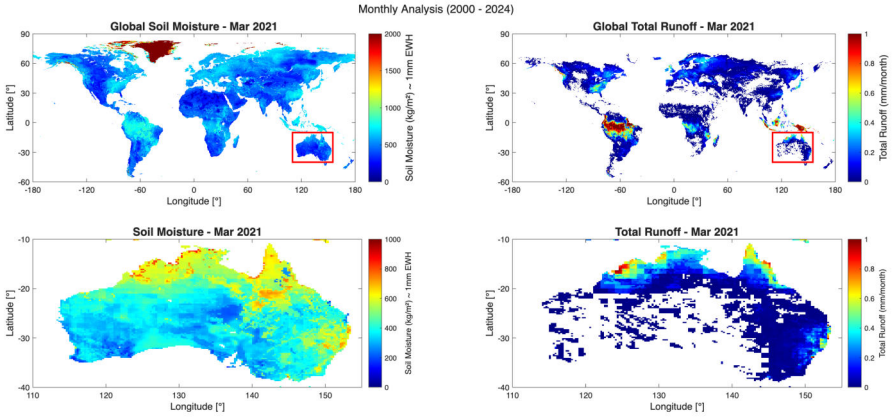

(c) March

Figure 5.12: Soil moisture and runoff 2021 (Jan-Mar)

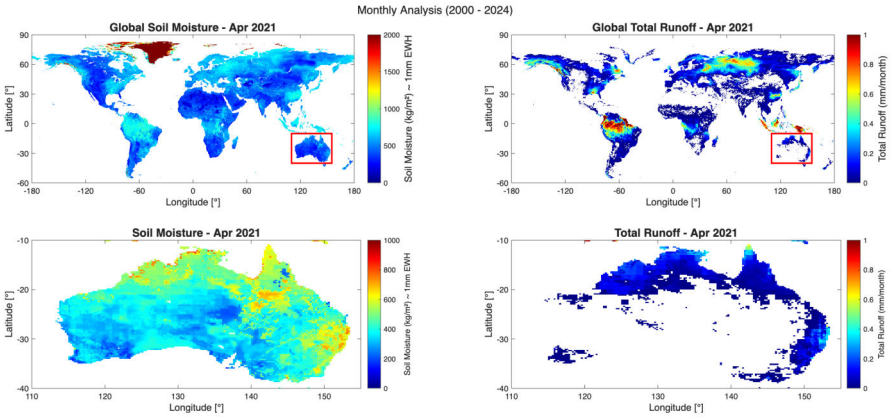

(a) April

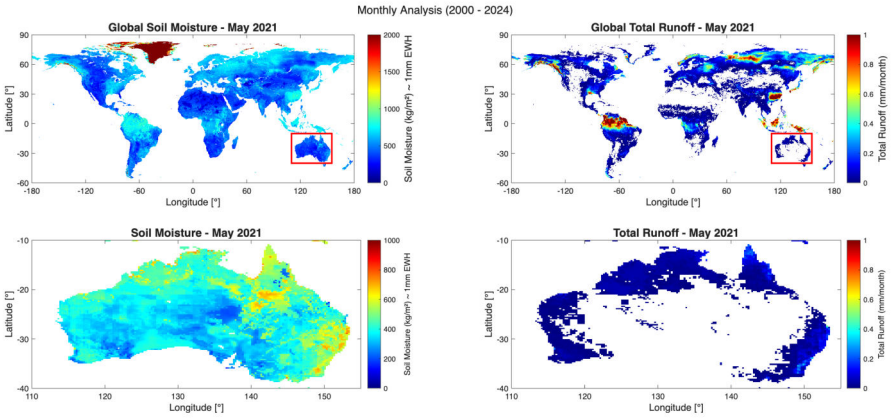

(b) May

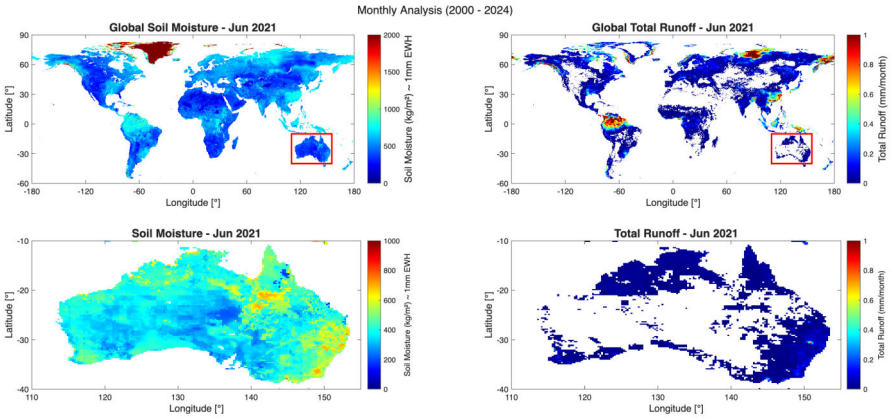

(c) June

Figure 5.13: Soil moisture and runoff 2021 (Apr-Jun)

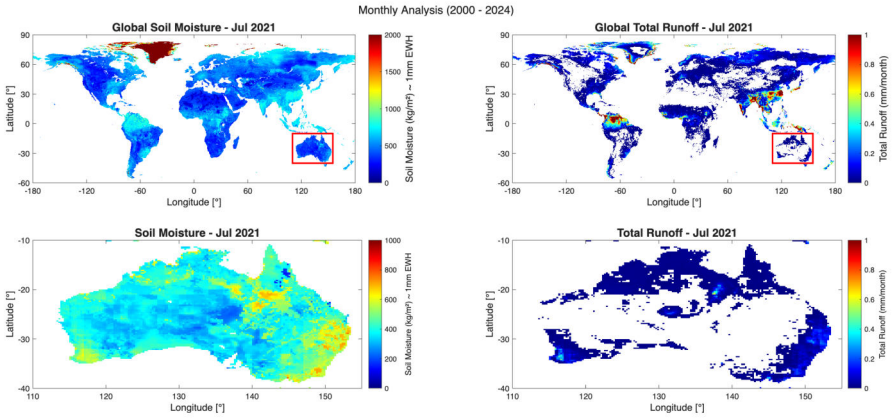

(a) July

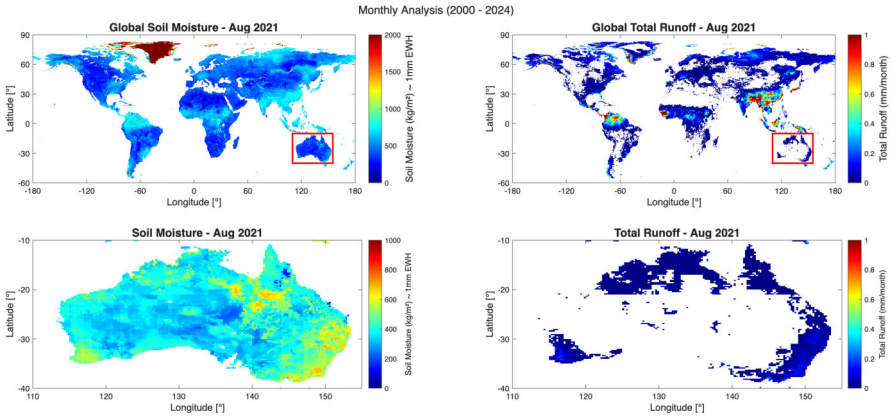

(b) August

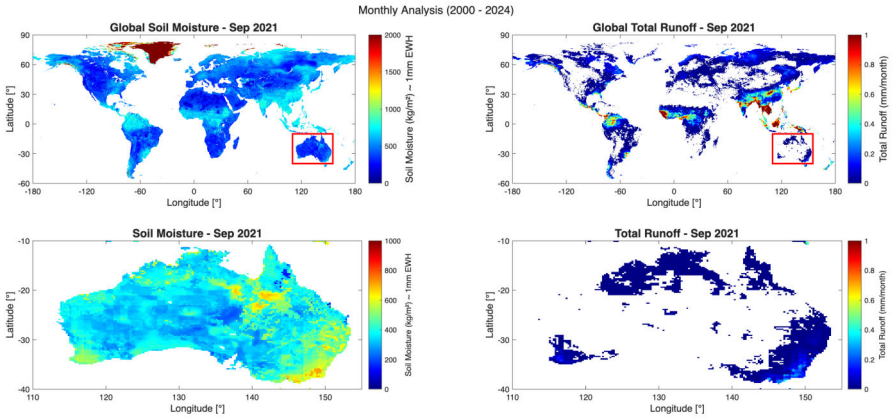

(c) September

Figure 5.14: Soil moisture and runoff 2021 (Jul-Sep)

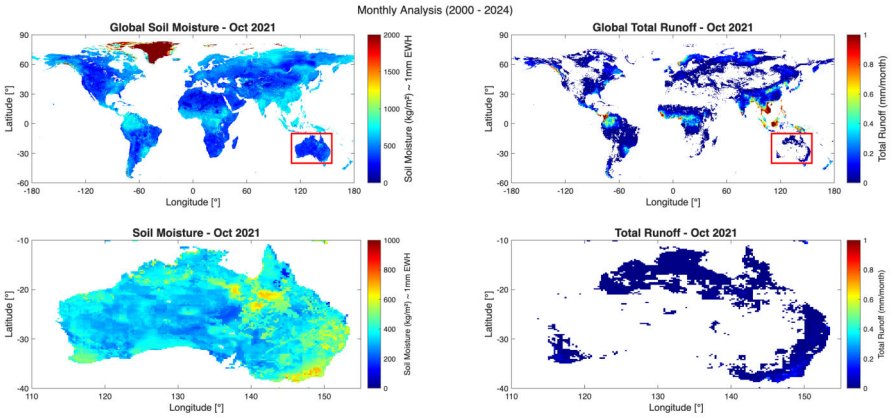

(a) October

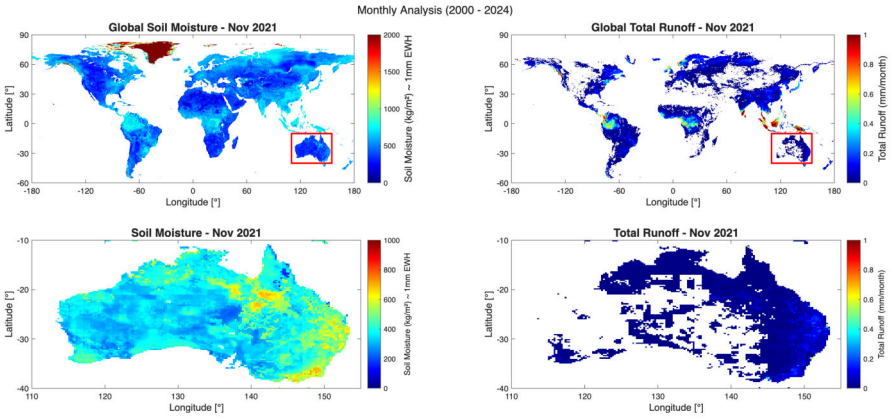

(b) November

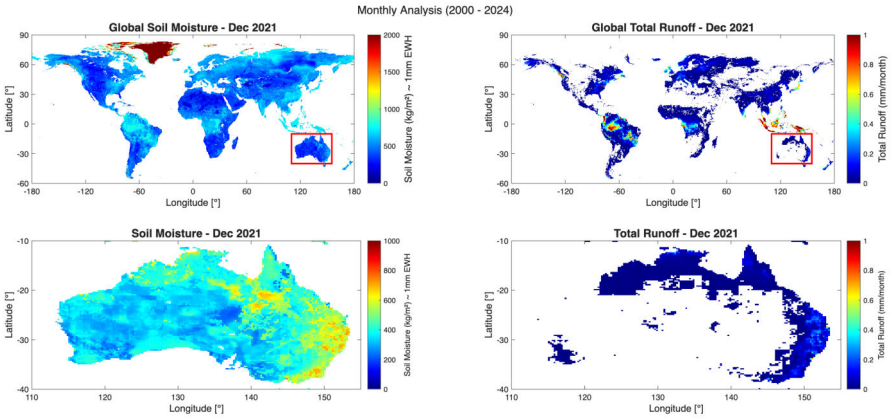

(c) December

Figure 5.15: Soil moisture and runoff 2021 (Oct-Dec)

6 Conclusion

This study successfully investigated the Terrestrial Water Storage (TWS) and groundwater dynamics over the Australian continent for the period of 2019–2024. Using Level-2 monthly solutions from GRACE-FO (ICGEM, 2026) and hydrological outputs from GLDAS (Rodell et al., 2004), the following conclusions are drawn: Implementation of the Wahr Approach: The application of the Wahr et al. (1998) approach via MATLAB allowed for the successful transformation of spherical harmonic potential coefficients into gridded Equivalent Water Height (EWH) maps. This methodology proved robust for capturing the integrated mass transport over the continent, consistent with the Task and the mathematical framework described in Kim (2024) (Chapter 2, Section 2.1.1, Paragraph 2). Filtering and Signal Clarity: Comparative analysis between DDK2 and DDK5 filters highlighted the trade-off between noise reduction and signal preservation. While DDK filters effectively mitigated longitudinal "stripping," our results align with the observations of Yang et al. (2013) (Abstract, Paragraph 1), which suggest that inconsistencies between GRACE products and land surface models often necessitate regional-scale evaluation to identify reliable TWS anomalies. Groundwater Isolation: By subtracting GLDAS-derived soil moisture and runoff from the total GRACE-TWS, a distinct groundwater signal was isolated. As noted in Tangdamrongsub et al. (2018) (Abstract, Paragraph 1), this extraction is vital for reliable water resource assessment in the arid and semi-arid environments of Australia, where groundwater is the primary buffer against climatic extremes. Spatial Limitations: Despite the high-resolution gridding ($30' \times 30'$), the intrinsic low spatial resolution of GRACE-FO ($\sim$300 km) remains a limiting factor in resolving localized storage changes along narrow drainage basins. This confirms the findings of Youm (2025) (Abstract, Paragraph 1) regarding the difficulty of accurately estimating localized hydrological variations with satellite gravimetry alone.

7 Outlook

To further enhance the precision and utility of this research, the following pathways are proposed: Data Assimilation and Downscaling: Future work should transition from simple subtraction methods to advanced data assimilation, such as the three-dimensional ensemble Kalman smoother (EnKS 3D) proposed by (Tangdamrongsub et al., 2018). Additionally, incorporating the Constrained Linear Deconvolution (CLD) method developed by Kim (2024) (Abstract, Paragraph 2) could significantly improve the spatial resolution of Australian TWS data. Integration of GNSS Observations: As demonstrated by Youm (2025) (Abstract, Paragraph 2), the inclusion of Global Navigation Satellite System (GNSS) crustal displacement data can serve as an independent validation tool. Future iterations of this lab work could use GNSS-observed elastic responses to verify the magnitude of localized mass changes calculated in MATLAB. Addressing Hydrogeological Uncertainty: A major hurdle identified in this study is the conversion of water levels to storage volumes. Future research must address the high variability of specific yield in Australian aquifers. According to Tregoning et al. (2012) (Executive Summary, Paragraph 4), better spatial information on depth to groundwater and soil hydraulic properties is required to reduce current uncertainties in the seasonal cycle of groundwater storage. Contribution to Sea Level Rise: Extending the 2019–2024 time series will allow for a better understanding of Australia's contribution to Global Mean Sea Level (GMSL). As noted by Kim (2024) (Abstract, Paragraph 1), TWS is a main contributor to ocean mass variations, and long-term monitoring is essential to distinguish between decadal climate variations and trends driven by global warming.

Acknowledgement

I would like to express my sincere gratitude to Prof. Dr.-Ing. Hansjörg Kutterer for providing the framework for this lab rotation and for his guidance in the field of geodetic Earth system science. I am deeply grateful to my supervisor, Dr.-Ing. Kurt Seitz, for his continuous support, technical insights, and valuable feedback throughout the duration of this work. His expertise was instrumental in the successful implementation of the MATLAB-based

analysis and the interpretation of the results. Special thanks are extended to the Geodätisches Institut (GIK) at the Karlsruhe Institute of Technology (KIT) for providing the necessary resources and facilities to carry out this study. I would also like to acknowledge the GFZ German Research Centre for Geosciences and the International Centre for Global Earth Models (ICGEM) for providing the Level-2 GRACE-FO monthly solutions. Furthermore, I thank the NASA Global Land Data Assimilation System (GLDAS) team for the hydrological model data utilized for the reduction of soil moisture and runoff components. Finally, I acknowledge the authors of the foundational scientific papers referenced in this report. Their methodological developments—particularly the spherical harmonic synthesis approach by Wahr et al. (1998) and the data assimilation frameworks by Tangdamrongsub et al. (2018) and Kim (2024) and Youm (2025) – provided the theoretical basis for my investigation into the groundwater dynamics of the Australian continent.

References

Heiskanen, W. A. and Moritz, H. (1967): Physical Geodesy. W. H. Freeman & Co., San Francisco, USA.

ICGEM (2026): International Centre for Global Earth Models (ICGEM): Gravity field and GRACE/GRACE-FO products hosted at the German Research Centre for Geosciences (GFZ). Accessed: 2026-04-06. URL: https://icgem.gfz-potsdam.de/.

Kim, J. (2024): Terrestrial Water Storage Variation in Australia and Its Contribution to Global Mean Sea Level. PhD thesis. Graduate School, Seoul National University.

NASA (2022): README for NASA GLDAS Version 2 Data Products. Goddard Earth Sciences Data and Information Services Center (GES DISC). Available at: https://disc.gsfc.nasa.gov.

Rodell, M., Houser, P. R., Jambor, U., Gottschalck, J., Mitchell, K. E., Meng, C.-J., Arsenault, K., Cosgrove, B. A., Radakovich, J. D., Bosilovich, M. G., Entin, J. K., Walker, J. P., Lohmann, D., and Toll, D. L. (2004): The Global Land Data Assimilation System. *Bulletin of the American Meteorological Society* 85(3):381–394. DOI: 10.1175/BAMS-85-3-381.

Tangdamrongsub, N., Han, S.-C., Decker, M., Yeo, I.-Y., and Kim, H. (2018): On the use of the GRACE normal equation of inter-satellite tracking data for estimation of soil moisture and groundwater in Australia. *Hydrology and Earth System Sciences* 22(3):1811–1829.

Tregoning, P., McClusky, S., Van Dijk, A., Crosbie, R., and Peña-Arancibia, J. (2012): Assessment of GRACE satellites for groundwater estimation in Australia. *National Water Commission, Canberra* 82.

Tsoulis, D. (1999): Spherical harmonic computations with topographic/isostatic coefficients. Tech. rep. IAPG/FESG No. 3. Munich, Germany: Institut für Astronomische und Physikalische Geodäsie, Technische Universität München.

Wahr, J., Molenaar, M., and Bryan, F. (1998): Time variability of the Earth's gravity field: Hydrological and oceanic effects and their possible detection using GRACE. *Journal of Geophysical Research: Solid Earth* 103(B12):30205–30229.

Yang, T., Wang, C., Yu, Z., and Xu, F. (2013): Characterization of spatio-temporal patterns for various GRACE-and GLDAS-born estimates for changes of global terrestrial water storage. *Global and Planetary Change* 109:30–37.

Youm, G. (2025): Terrestrial Water Storage Variation Estimated from Gravity Changes and Crustal Displacements. PhD thesis. Graduate School, Seoul National University.

Monitoring Ice Mass Loss over Greenland based on GRACE Monthly Solutions

Nabhan Karimbil[1]

1 Remote Sensing and Geoinformatics Master of Science (M.Sc.), KIT, Germany
E-Mail: usktb@student.kit.edu

Abstract

This report presents analyses that document a clear and consistent evolution of mass variability over Greenland during the GRACE and GRACE-FO observation period. Seasonal patterns are evident across the full time span, while synthesized potential anomaly fields show temporal changes that become more persistent in later years. Comparisons between early GRACE years and the GRACE-FO period reveal distinct differences in seasonal behavior: in the later years, seasonal recovery diminishes and the fields no longer return to the conditions observed at the start of the record.

Inverted Total Water Storage (TWS) fields translate these changes into mass variability signals. Seasonal analysis for February, May, August, and November indicates a intensification of summer mass-loss signals in recent years, with winter and autumn months displaying reduced recovery relative to earlier periods. Collectively, the potential synthesis and TWS inversion results indicate a long-term shift toward a more negative mass balance over Greenland during the investigated period.

The reliability of the results is evaluated through residual analyses between the synthesized and adjusted potential fields. For the selected example months, residuals remain small and are largely confined to the inversion domain boundaries, consistent with edge effects anticipated in regional inversions. In central Greenland, synthesized potential anomalies and the adjusted model show close agreement, indicating that the inversion reproduces observations well and that the solution is numerically stable.

Recommendations for future work include: (i) extending residual-based consistency analyses to a broader set of months and seasons; (ii) systematically documenting the influence of filter strength and regularisation choices across the full time series; (iii) reducing boundary effects in summary statistics by employing a uniform spatial mask for statistical assessments; and (iv) applying the same processing framework to alternative monthly gravity field solutions to enable direct intercomparison across processing centers.

Keywords GRACE · Total Water Storage (TWS) · Inverse Tesseroid Approach · Greenland

KIT Scientific Working Papers
Issue Number 270
ISSN: 2194-1629
DOI: 10.5445/IR/1000191188
Online: June 2026

This document is licensed under the Creative Commons Attribution – Share Alike 4.0 International License (CC BY-SA 4.0):
https://creativecommons.org/licenses/by-sa/4.0/deed.en

1 Introduction

Mass transport within the Earth system causes measurable variations in the gravitational field. Processes such as the melting of Greenland Ice Sheet, seasonal hydrological storage, and large-scale atmospheric and oceanic circulation all contribute to these temporal gravity changes. Satellite gravimetry provides a unique opportunity to observe such variations globally and consistently, as gravity is sensitive to all mass components together (Wahr et al., 1998).

The GRACE mission, launched in 2002, and its successor GRACE-FO, launched in 2018, measure inter-satellite distance changes with micrometre precision. These measurements are processed by evaluation centres such as GFZ, CSR and JPL into monthly gravity field models expressed as fully normalised spherical harmonic coefficients up to degree and order 96 (Tapley et al., 2004). After appropriate filtering and removal of background models, these monthly solutions provide valuable information on changes in terrestrial and cryospheric water storage (Wouters et al., 2014).

The focus of this Lab Rotation is on quantifying the mass variations of the Greenland Ice Sheet using monthly GRACE and GRACE-FO solutions provided by GFZ (Release 06). According to the task description, the GFZ DDK1 and DDK5 filtered products from January 2003 to December 2024 are used as the observational basis. For each month, residual gravitational potential fields are synthesised on a regional grid with a resolution of $0.5^\circ \times 0.5^\circ$ at satellite altitude. These potential changes are subsequently converted into equivalent water height (EWH) anomalies representing TWS changes by means of the inverse tesseroid approach, which allows a physically consistent representation of regional mass changes due to its curved volumetric geometry (Grombein et al., 2013; Heck and Seitz, 2007).

The resulting monthly TWS fields describe both the seasonal accumulation-melt cycle and the long-term mass loss of the Greenland Ice Sheet. A time series of monthly mean TWS values is derived and used to analyze the temporal evolution of Greenland's mass balance over the entire GRACE/GRACE-FO period.

This introduction summarizes the motivation and scope of the study. The theoretical background, the data characteristics, and the methodological workflow are described in the subsequent sections.

2 Theoretical Aspects

This section summarises the theoretical background required to interpret time-variable gravity signals derived from GRACE and GRACE-FO, including spherical harmonic representation, degree variances, and the tesseroid-based inversion used in this study.

2.1 Time-Variable Gravity and GRACE Observations

Variations in the Earth's gravity field reflect changes in the distribution of mass within the Earth system. Such changes can arise from processes including the melting of glaciers and ice sheets, the redistribution of terrestrial water, and large-scale oceanic and atmospheric circulation (Wahr et al., 1998). The Gravity Recovery and Climate Experiment (GRACE) and its successor GRACE Follow-On (GRACE-FO) missions provide monthly observations of these temporal gravity variations by measuring inter-satellite distance changes with micrometre precision (Tapley et al., 2004). Each monthly gravity field is expressed as a set of fully normalized spherical harmonic (SH) coefficients $\bar{C}_{nm}$ and $\bar{S}_{nm}$ that describe the global gravitational potential.

2.2 Spherical Harmonic Synthesis (SHS)

Spherical Harmonic Synthesis (SHS) is the forward computation of a function on the sphere from a series of spherical harmonics (Tsoulis, 1999; Heiskanen and Moritz, 1967). The corresponding formulation of the gravitational

potential is given in Equation (2.1). The spherical harmonic coefficients derived from GRACE level-2 data are used to express the gravity field of Earth.

$$V(P) = \frac{GM}{r} \sum_{n=0}^{\infty} \left(\frac{R}{r}\right)^n \sum_{m=0}^{n} (\bar{C}_{nm} \cos m\lambda + \bar{S}_{nm} \sin m\lambda) \bar{P}_{nm}(\sin\varphi) \tag{2.1}$$

where,
GM: geocentric gravitational constant,
R: radius of the reference sphere,
$\bar{C}_{nm}$, $\bar{S}_{nm}$: fully normalised spherical harmonic coefficients of degree n and order m,
$\bar{P}_{nm}$: fully normalised associated Legendre functions of degree n and order m,
(r, φ, λ): geocentric spherical coordinates, with
r: geocentric distance,
φ: geocentric latitude,
λ: longitude.
The temporal change in gravity is determined by subtracting the long-term mean coefficients given by the K months.

$$\bar{C}_{nm}^{\text{mean}} = \frac{1}{K} \sum_{k=1}^{K} \bar{C}_{nm}^{(k)}, \quad \bar{S}_{nm}^{\text{mean}} = \frac{1}{K} \sum_{k=1}^{K} \bar{S}_{nm}^{(k)}. \tag{2.2}$$

from each monthly solution:

$$\Delta\bar{C}_{nm}^{(k)} = \bar{C}_{nm}^{(k)} - \bar{C}_{nm}^{\text{mean}}, \quad \Delta\bar{S}_{nm}^{(k)} = \bar{S}_{nm}^{(k)} - \bar{S}_{nm}^{\text{mean}}. \tag{2.3}$$

These residual coefficients $\Delta\bar{C}_{nm}^{(k)}$ and $\Delta\bar{S}_{nm}^{(k)}$ represent the monthly potential anomalies which are used in Eq. (2.4) to synthesise the potential anomalies on the grid.

2.3 Forward Modelling through Spherical Harmonic Synthesis

The forward modelling step converts the residual coefficients into potential anomalies on a regular grid. The potential field ΔV is computed from the residual harmonics using spherical harmonic synthesis up to degree and order 96 over the region 55°–90°N and 95°W–10°E, which covers the Greenland Ice Sheet:

$$\Delta V(r, \varphi, \lambda) = \frac{GM}{r} \sum_{n=0}^{N} \left(\frac{a}{r}\right)^n \sum_{m=0}^{n} \bar{P}_{nm}(\sin\varphi) \left[\Delta\bar{C}_{nm} \cos(m\lambda) + \Delta\bar{S}_{nm} \sin(m\lambda)\right]. \tag{2.4}$$

The corresponding geoid height change is given by Heiskanen and Moritz (1967)

$$\Delta N = \frac{\Delta V}{\gamma} \tag{2.5}$$

where γ is the normal gravity at the reference ellipsoid. This procedure provides the spatio-temporal variation of the gravitational potential at satellite altitude, which serves as the input for the subsequent inversion.
Correlated noise and striping along meridians are reduced using the DDK decorrelation filters (Kusche et al., 2009). The DDK1 and DDK5 filters used in this work offer a practical balance between smoothness and spatial resolution, as recommended for regional studies over Greenland.

2.4 Degree Variance and Error Degree Variance

The degree variance quantifies the amplitudes of the spherical harmonic coefficients, which vary across different degrees. The sum of the squared coefficients expresses the overall energy in the signal as shown in Equation (2.4). The plot shows that there is a higher degree variance at lower degrees, and the value decreases as the degree (n)

increases. This indicates that there is a higher concentration of signal at lower degrees compared to higher degrees. The degree and error degree variances are as follows:

$$C_n^2(\bar{C}_{nm}^{(k)}, \bar{S}_{nm}^{(k)}) = \sum_{m=0}^{n} (\bar{C}_{nm}^{(k)2} + \bar{S}_{nm}^{(k)2}), \tag{2.6}$$

$$\sigma_{C_n}^2\left(\sigma\bar{C}_{nm}^{(k)}, \sigma\bar{S}_{nm}^{(k)}\right) = \sum_{m=0}^{n} \left(\sigma^2\bar{C}_{nm}^{(k)} + \sigma^2\bar{S}_{nm}^{(k)}\right). \tag{2.7}$$

The definition of the relative degree and error degree variances for the relative coefficients, wh ich are defined in the Equation (2.3) are given here:

$$E_n^2\left(\Delta\bar{C}_{nm}^{(k)}, \Delta\bar{S}_{nm}^{(k)}\right) = \sum_{m=0}^{n} \left(\Delta\bar{C}_{nm}^{(k)2} + \Delta\bar{S}_{nm}^{(k)2}\right), \tag{2.8}$$

$$\sigma_{E_n}^2\left(\sigma\Delta\bar{C}_{nm}^{(k)}, \sigma\Delta\bar{S}_{nm}^{(k)}\right) = \sum_{m=0}^{n} \left(\sigma^2\Delta\bar{C}_{nm}^{(k)} + \sigma^2\Delta\bar{S}_{nm}^{(k)}\right). \tag{2.9}$$

This helps to understand the distribution of signal intensity across the frequency range. The degree variance of the coefficients obtained in this study has been analysed. This indicates that the signal exhibits higher energy at long wavelengths, with a progressive decrease toward shorter wavelengths. The plots for degree variance for all the months are similar, with marginal variations, so an example plot for January and December 2003 is shown in Figure 2.1 and 2.2. The degree variance depends solely on the spherical harmonic coefficients and is therefore independent of the evaluation altitude.

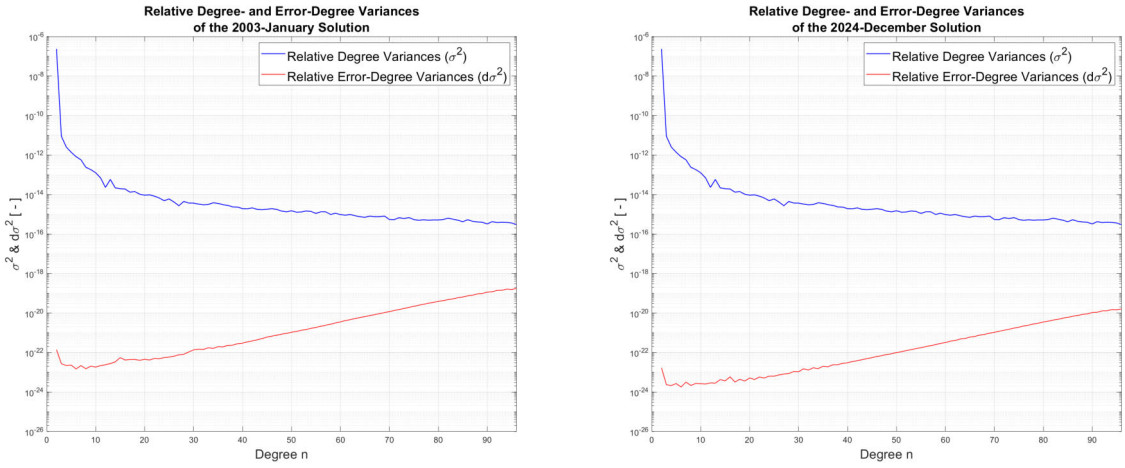

(a) January, 2003

(b) December, 2024

Figure 2.1: Degree variance and error-degree variance of the residual SH coefficients.

2.5 Mass discretization using Tesseroids

Tesseroids are three-dimensional shapes of constant height bounded by meridional planes (λ_1, λ_2), latitudinal planes (φ_1, φ_2), and concentric spherical planes (r_1, r_2) as shown in Figure 2.3.
Newton's Integral can be applied on the tesseroids to derive gravitational potential values V of a solid volume Ω.

$$V(r,\varphi,\lambda) = G\rho \iiint_{\Omega} \frac{1}{l} d\Omega = G\rho \int_{\lambda_1}^{\lambda_2} \int_{\varphi_1}^{\varphi_2} \int_{r_1}^{r_2} \frac{r'^2 cos\varphi'}{l} dr' d\varphi' d\lambda' \tag{2.10}$$

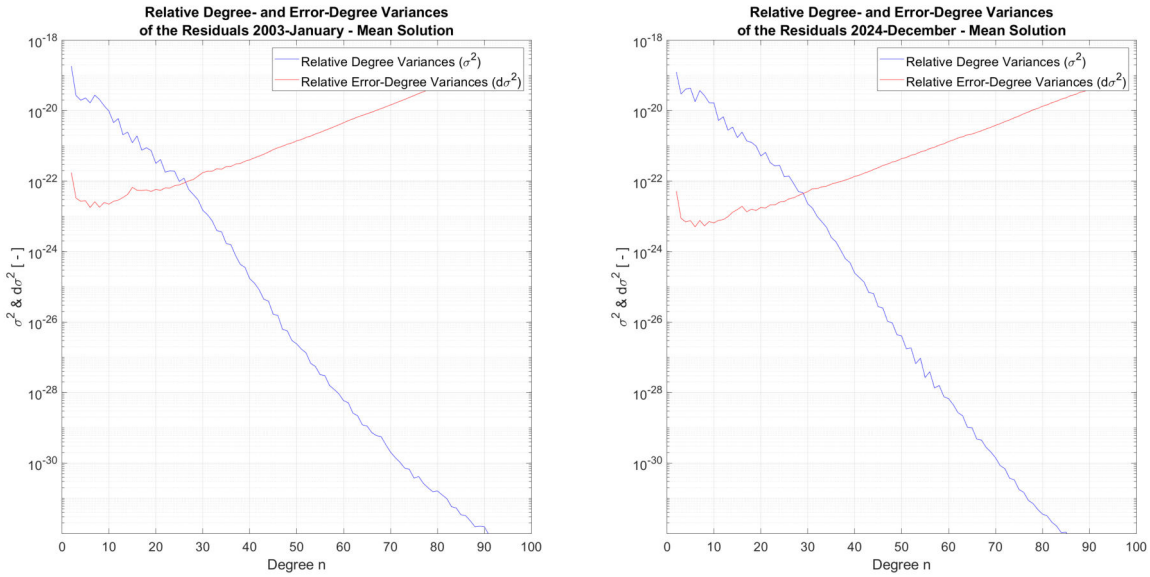

(a) January, 2003

(b) December, 2024

Figure 2.2: Relative degree variance and relative error-degree variance of the residual SH coefficients (mean solution removed).

In Equation (2.10), the Euclidean distance between the computation point P and the running integration point Q is denoted by l.

$$l(P,Q) = \sqrt{r^2 + r'^2 - 2rr'cos\psi} \tag{2.11}$$

The geocentric spherical angle between P and Q is defined as:

$$\cos\psi = \sin\varphi \sin\varphi' + \cos\varphi \cos\varphi' \cos(\lambda' - \lambda). \tag{2.12}$$

G : Newton's gravitational constant,
ρ : density function at running integration point (Q),
l : Euclidean distance between the computation point $P(r,\varphi,\lambda)$ and the running integration point $Q(r',\varphi',\lambda')$,
ψ : Angle between the points P and Q.
Newton's integral, as mentioned in Equation (2.10), cannot be solved analytically in the case of tesseroids due to the presence of elliptical integrals. A Taylor series expansion can be used to obtain an approximate numerical solution. The Taylor point $(r_0,\varphi_0,\lambda_0)$ for the series expansion is set at the geometrical centre of each tesseroid for maximum efficiency in calculation of potentials (Heck and Seitz, 2007).

$$r_0 = \frac{(r_1 + r_2)}{2}; \quad \varphi_0 = \frac{(\varphi_1 + \varphi_2)}{2}; \quad \lambda_0 = \frac{(\lambda_1 + \lambda_2)}{2}. \tag{2.13}$$

The integrand in equation (2.10), which represents the kernel $K(r',\varphi',\lambda')$ is developed into Taylor series expansion (2.13). This expansion can be integrated termwise. The coefficients K_{ijk} denote the partial derivatives of the integration kernel.

$$K(r',\varphi',\lambda') = \sum_{i,j,k} K_{ijk}(r' - r_0)^i(\varphi' - \varphi_0)^j(\lambda' - \lambda_0)^k \tag{2.14}$$

From above equations, gravitational potential of a tesseroid with constant density can be formulated as:

$$v(r,\varphi,\lambda) = G\rho\Delta r\Delta\varphi\Delta\lambda \left[K_{000} + \frac{1}{24}(K_{200}\Delta r^2 + K_{020}\Delta\varphi^2 + K_{002}\Delta\lambda^2) + O(\Delta^4)\right] \tag{2.15}$$

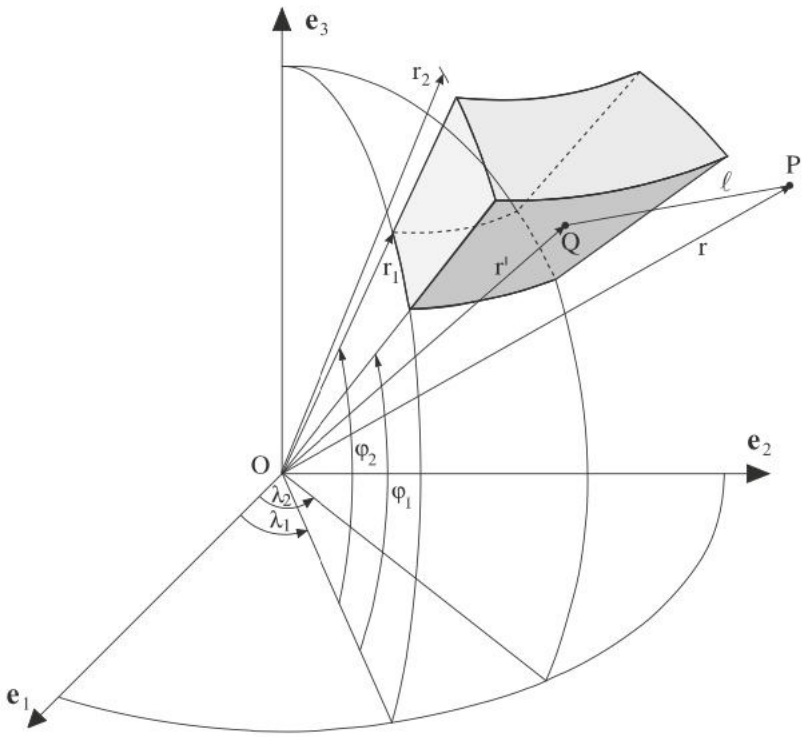

Figure 2.3: Geometry of a spherical tesseroid (Heck and Seitz, 2007)

with even powers of coefficient, as the odd terms cancel out due to the position of Taylor point K_{ijk} being at the geometric center of the tesseroid (Heck and Seitz, 2007). The Taylor expansion terms in the order of four and above are neglected, which is represented by $O(\Delta^4)$. Here,

$$\Delta r = r_2 - r_1; \quad \Delta\varphi = \varphi_2 - \varphi_1; \quad \Delta\lambda = \lambda_2 - \lambda_1 \, . \tag{2.16}$$

2.6 Inverse Tesseroid Approach

To estimate the surface mass distribution that causes the observed potential variations, a regional inversion is applied using tesseroids (spherical volumetric elements) defined by constant latitude, longitude, and radial limits (Heck and Seitz, 2007). Each tesseroid with constant density ρ_i generates a potential at an external point $P(r, \varphi, \lambda)$ as described by Eq. (2.15). The total potential at a point P is obtained by summing the contributions from all tesseroids. In matrix form, the inversion can be expressed as

$$Ax = b, \tag{2.17}$$

where the Jacobian matrix A contains derivatives of the gravitational kernel functions (the design matrix), x is the vector of unknown surface-mass changes (Total Water Storage), and b is the vector of observed potential anomalies from the forward model.

2.7 Regularization and L-Curve Criterion

Since the inverse problem is ill-posed and sensitive to measurement noise, it is stabilized using Tikhonov regularization (Hanke and Hansen, 1993). The solution is obtained by minimizing the following objective function:

$$\Phi = \|Ax - b\|^2 + \lambda^2 \|Lx\|^2, \tag{2.18}$$

where L is a smoothing operator and λ is the damping parameter that balances data misfit and model smoothness. The optimal value of λ is chosen using the *L-curve* method, which plots $\|Ax-b\|$ against $\|Lx\|$ on logarithmic scales. The corner of this curve identifies the most stable solution. In practice, convergence was achieved after three iterations, consistent with numerical stability tests performed during the analysis.
The regularization parameter used in the inversion was selected based on an L-curve analysis (Hanke and Hansen, 1993). Figure 2.4 shows the L-curve for May 2003, which is used as a representative month. The selected regularization parameter is located near the L-curve corner and was applied consistently to all analysed months.

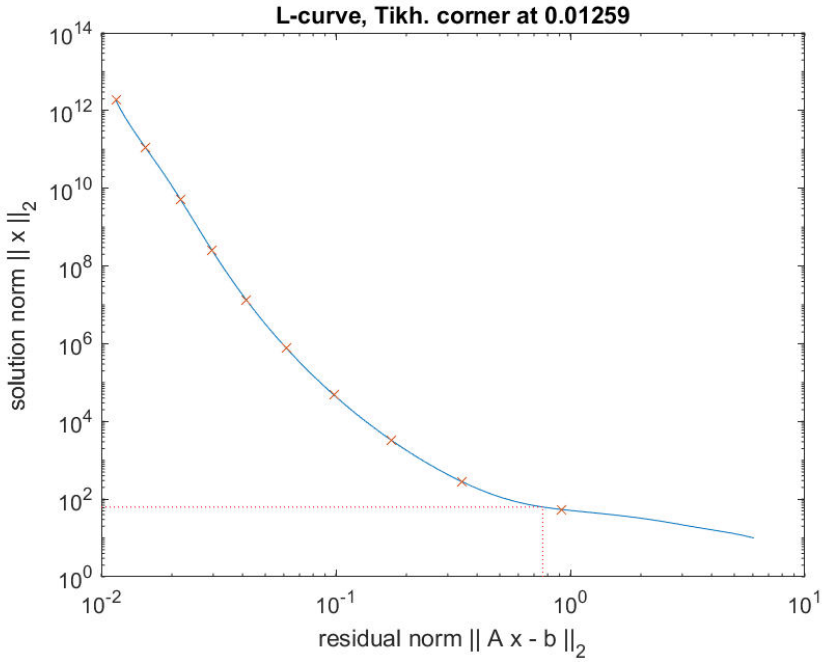

Figure 2.4: L-curve for May 2003 showing the relationship between the residual norm $\|Ax-b\|_2$ and the solution norm $\|x\|_2$. The selected regularization parameter is indicated near the corner of the curve.

2.8 Computation of Total Water Storage (TWS)

After inversion of the observation Equation (2.17), the equivalent water height (EWH) or total water storage (TWS) anomalies are retrieved by the adjustment.

$$\widehat{x} = [(A+\lambda^2 L)^T (A+\lambda^2 L)]^{-1} (A+\lambda^2 L) b \tag{2.19}$$

The resulting TWS fields $\widehat{x}$ describe the temporal evolution of Greenland's mass balance. Long-term trends indicate ice mass loss, whereas seasonal oscillations reflect annual accumulation and melt cycles. To avoid unrealistic values at the boundary, a geographic mask based on Greenland's outline was applied before computing statistical summaries. Although a Greenland mask is applied for the TWS fields, residual edge effects can still influence grid-based extrema.

3 Data

The analysis is based on monthly Level-2 gravity field solutions provided by the GFZ (Release 06.1), distributed through the International Centre for Global Earth Models (ICGEM, 2026). Each monthly solution contains fully normalised spherical harmonic coefficients $\bar{C}_{nm}$ and $\bar{S}_{nm}$ up to degree and order $n_{\max} = 96$, corresponding to a spatial resolution of roughly 200 km. These coefficients represent the time-variable part of Earth's gravitational potential observed by the GRACE (2003-2016) and GRACE-FO (2019-2024) missions.

Spatial domain. To minimise boundary artefacts in the spherical harmonic synthesis stage, the forward-modelling grid was expanded beyond Greenland. The synthesis domain spans latitudes 55°N-90°N and longitudes 95°W-10°E on a $0.5^\circ \times 0.5^\circ$ grid. The inversion domain for retrieving Total Water Storage (TWS) anomalies is restricted to Greenland itself, typically 60°N-85°N, with longitude limits adapted to meridian convergence. Both grids use the same spatial resolution.

Time span and data completeness. The used dataset includes:

- GRACE: January 2003 to December 2016 (with several missing months),
- GRACE-FO: January 2019 to December 2024,

and the 2017-2018 data gap is kept as is (i.e., not interpolated). All valid months were used to compute the mean field, and the residual time series was analysed in this study.
Forward modelling is based on the spherical harmonic synthesis of the residual gravity field coefficients $(\Delta\bar{C}_{nm}, \Delta\bar{S}_{nm})$, representing monthly deviations from the long-term mean field (Wahr et al., 1998). These potential anomalies are first computed on a regular grid with a resolution of $0.5^\circ \times 0.5^\circ$ for the region 55°N-90°N and 95°W-10°E, which includes the Greenland Ice Sheet. The mean model serves as a reference for computing residual gravitational potentials ΔV, and the corresponding geoid height changes $\Delta N = \frac{\Delta V}{\gamma}$, where γ is normal gravity on the ellipsoid.
In the inverse step, the tesseroid-based inversion translates potential variations into equivalent water height changes (EWH) (Ferreira et al., 2020), which represent the anomaly of total water storage (TWS). This inversion is performed using the observations derived from the residual coefficients defined in Equation (2.2).
The inverse problem is ill-posed, so Tikhonov regularization is applied to stabilize the inversion. The optimal regularization parameter λ is determined using the L-curve criterion, which balances the data fitting with smoothness.

$$\|Ax - b\|^2 + \lambda\|Lx\|^2, \tag{3.1}$$

where A is the Jacobian matrix, x is the solution vector containing unknown tesseroid heights, b is the observation vector (synthesized potential values in the grid based on Equation (2.4)), L is the regularization matrix.
The resulting TWS time series from 2003 to 2024 provides quantitative insight into the mass balance of the Greenland Ice Sheet. The trends and seasonal variations obtained from the GRACE and GRACE-FO data are interpreted in the context of ice mass loss and its contribution to global sea-level rise. This investigation demonstrates the capability of satellite gravimetry to monitor large-scale cryospheric and hydrological processes, offering valuable information for climate change assessment and geodetic Earth system modelling.

Region and grids. To reduce edge effects while keeping the inversion tractable, the synthesis domain was expanded beyond Greenland (55°N-90°N, 95°W-10°E) on a $0.5^\circ \times 0.5^\circ$ grid. The inversion domain (TWS) focuses on Greenland (typically 60°N-85°N, 75°W-10°W with meridian convergence aware longitude bounds), also at $0.5^\circ \times 0.5^\circ$ grid.

4 Methodology

This section summarises the workflow used to derive monthly Total Water Storage (TWS) anomalies over Greenland from GRACE and GRACE-FO Level-2 gravity field solutions. The methodology follows the structure of the MATLAB synthesis and inversion environment provided by the Geodetic Institute of KIT (Seitz, 2025), and consists of four main steps: (i) construction of residual spherical harmonic coefficients, (ii) forward modelling of disturbing potentials, (iii) tesseroid-based inversion to obtain surface mass changes, and (iv) post-processing of the monthly TWS fields.

4.1 Step i: Residual Spherical Harmonic Coefficients

For each month, the fully normalised spherical harmonic coefficients $\bar{C}_{nm(t)}$ and $\bar{S}_{nm}(t)$ were read, rescaled to a common reference (GM, R), and averaged to form a multi-year mean model (Eq. (2.2)). The monthly gravity field variations caused by mass redistribution are calculated from the residual coefficients (Eq. (2.3)).

4.2 Step ii: Forward Modelling of Disturbing Potentials

The residual coefficients were synthesised into disturbing potentials ΔV on the extended domain described in Section 3 using spherical harmonic synthesis up to degree and order $n = 96$. The computation was performed at 500 km altitude with `SHS_grid_potential.m`, and corresponding geoid height changes were obtained via

$$\Delta N = \frac{\Delta V}{\gamma(\varphi)}. \tag{4.1}$$

Diagnostic quantities such as degree variances, error degree variances, and variance propagation were computed for each month for quality control. The synthesised potentials form the observation vector b for the subsequent inversion.

4.3 Step iii: Tesseroid-Based Inversion

The regional inversion was performed on a $0.5^\circ \times 0.5^\circ$ tesseroid grid covering Greenland (60°N-85°N, 85°W-0°E). Each tesseroid represents a constant-density volume whose radial height change Δr is proportional to the monthly TWS anomaly.

The linear relationship between the mass changes and the synthesised potential $Ax = b$ is already given in Eq. (2.17), where A is the design matrix constructed from the tesseroid kernel terms K_{000} and K_{200} following the formulation of Heck and Seitz (2007). Because the problem is ill-posed, Tikhonov regularisation was applied to minimize the following expression:

$$\min\left(\|Ax - b\|^2 + \lambda^2 \|x\|^2\right), \tag{4.2}$$

with the optimal regularisation parameter λ determined from the L-curve criterion (`l_curve.m`). The inversion was iterated up to three times until convergence of the solution vector was reached.

The changes in radial height recovered were converted to equivalent water height in millimetres:

$$TWS = \Delta r \times 1000\,. \tag{4.3}$$

4.4 Step iv: Post-Processing and Time-Series Construction

For each month, the outputs include:

- TWS grids,
- adjusted disturbing potentials,
- residual potentials,
- statistical summaries (min, max, mean, RMS, standard deviation).

The monthly TWS fields were combined to form the 2003-2024 time series, from which long-term trends and seasonal variations of the Greenland Ice Sheet were analysed.

Table 4.1 reports the optimal Tikhonov regularisation parameters (λ) obtained from the L-curve analysis for selected months. The chosen months represent different stages of the GRACE and GRACE-FO missions.

Table 4.1: Optimal Tikhonov regularisation parameters (λ) obtained from the L-curve for representative months.

Month	**λ**
January 2003	0.012394
June 2003	0.013211
April 2010	0.015052
December 2024	0.011904

The λ values show only small variations over time. This indicates that a similar level of regularisation is sufficient for all investigated periods. The selected parameters provide a stable compromise between noise reduction and signal preservation in inversion.

5 Results and Discussion

The results obtained from spherical harmonic synthesis and tesseroid inversion are analysed here to evaluate Greenland's mass evolution, seasonal characteristics, and long-term climatic signals.

5.1 Spherical Harmonic Synthesis: January Potential Anomalies (2003–2024)

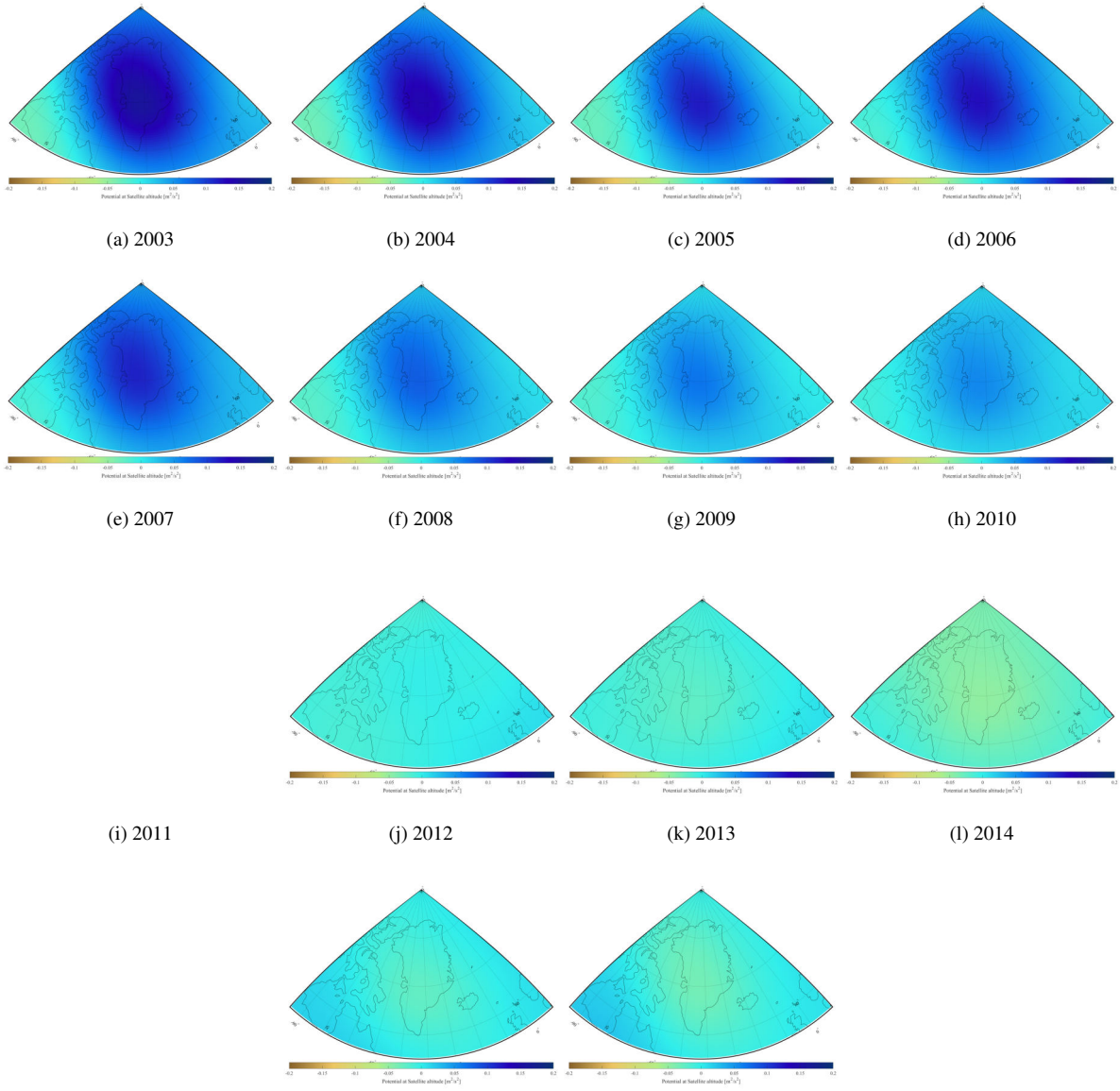

(a) 2003 (b) 2004 (c) 2005 (d) 2006

(e) 2007 (f) 2008 (g) 2009 (h) 2010

(i) 2011 (j) 2012 (k) 2013 (l) 2014

(m) 2015 (n) 2016

Figure 5.1: January gravitational potential anomalies at satellite altitude (in $m^2\,s^{-2}$) derived from GFZ RL06 DDK1 spherical-harmonic synthesis for GRACE 2003–2016. All subfigures are shown using a common symmetric colour scheme with limits of $\pm 0.2\ m^2 s^{-2}$.

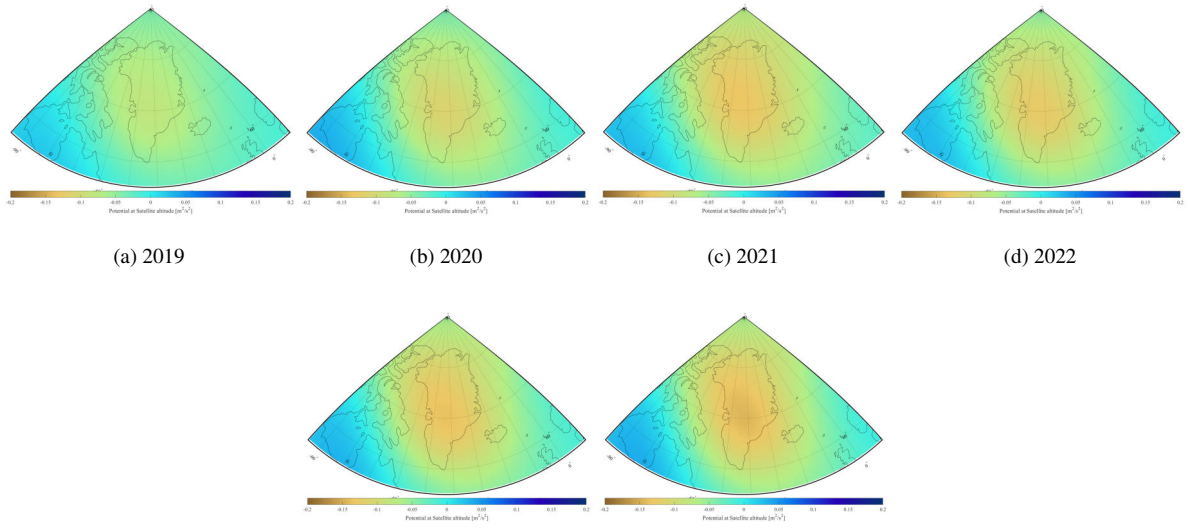

(a) 2019 (b) 2020 (c) 2021 (d) 2022

(e) 2023 (f) 2024

Figure 5.2: January gravitational potential anomalies at satellite altitude (in $m^2\,s^{-2}$) derived from GFZ RL06 DDK1 spherical-harmonic synthesis for GRACE-FO 2019–2024. All subfigures are shown using a common symmetric colour scheme with limits of ± 0.2 $m^2 s^{-2}$.

Figures 5.1 and 5.2 present the gravitational potential anomalies synthesized at satellite altitude for January of GRACE and GRACE-FO between 2003 and 2024. These anomalies were computed using the GFZ RL06 DDK1 spherical harmonic fields by subtracting the long-term mean model and performing a forward spherical harmonic synthesis on the regional grid. Using a single month (January) provides a consistent seasonal reference to illustrate the long-term evolution of the mass distribution of Greenland. During the early GRACE period (2003–2006), the January anomalies are relatively weak and spatially smooth. Slight negative anomalies appear along the coastal margins, but overall the ice sheet still maintains a near-equilibrium winter mass state. Approximately in 2007, stronger negative anomalies developed, especially in western, southeastern, and northern Greenland. These signatures reflect the onset of increased snow and reduced winter recovery.

The years 2010 and 2012 exhibit more pronounced negative patterns, consistent with enhanced melt seasons. After 2019, the fields show even deeper and more spatially coherent negative anomalies. The 2021–2024 fields contain the strongest January depressions in the full time series. This suggests that winter months increasingly fail to return to the mass levels observed in the early 2000s. Overall, the January results demonstrate a clear transition from a stable mass state to persistent and accelerating long-term mass loss.

5.2 Seasonal Evolution of Potential Anomalies for Selected Years

The intra-annual variability is shown in Figures 5.3 – 5.6. It shows seasonal potential anomalies for the months February, May, August, and November for four representative years: 2003 (early GRACE), 2009 (mid-GRACE), 2019 (early GRACE-FO), and 2024 (latest).

In **2003**, the seasonal cycle was well established. February and May show strong negative potential anomalies over central Greenland, indicating a pronounced mass deficit relative to the long-term. The August field exhibits similarly strong negative anomalies associated with peak summer melt; however, their magnitude does not substantially exceed that observed in spring. In November, there is a partial recovery, indicating that winter accumulation mostly compensates for summer mass loss during the early GRACE period.

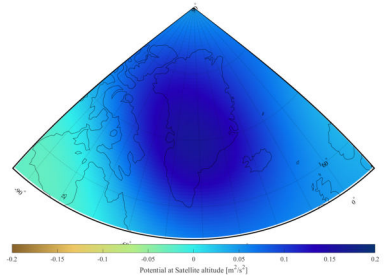

(a) February, 2003

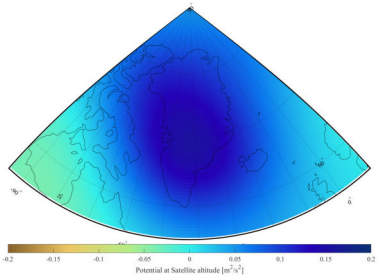

(b) May, 2003

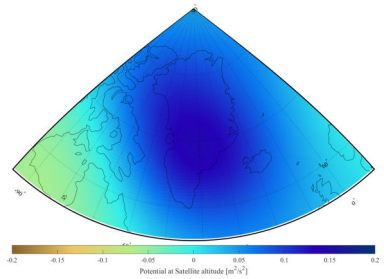

(c) August, 2003

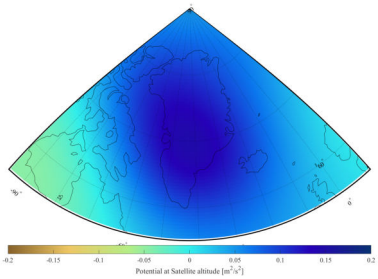

(d) November, 2003

Figure 5.3: Seasonal gravitational potential anomalies at satellite altitude for the year 2003 (February, May, August, and November), derived from GFZ RL06 DDK1 spherical-harmonic synthesis. All subfigures are shown using a common symmetric colour scheme with limits of ± 0.2 m^{2}s^{-2}.

In **2009**, the seasonal evolution of gravitational potential anomalies remains clearly defined, but with enhanced amplitudes compared to 2003. February has comparatively mild negative anomalies, showing a slow winter recovery at the beginning of the year. By May, the negative signal has strengthened and become more spatially coherent over central Greenland, indicating the beginning of melt-season mass loss. The most severe negative anomalies occur in August, spanning far across the ice sheet interior and representing the peak of summer melt. In November, a partial recovery is seen; nonetheless, the anomalies remain negative and spatially broad, showing that winter accumulation does not fully compensate for the previous summer losses. Overall, the 2009 patterns represent a transitional stage to the more permanent negative anomalies observed later in the GRACE-FO period.

In **2019**, gravitational potential anomalies are more negative than in previous years, indicating a downward-shifted mass balance of the Greenland ice-sheet. Already in February, negative potential anomalies are present, indicating that the seasonal cycle starts in a persistently depleted condition. The summer minimum in August is clearly expressed, but November only exhibits partial recovery demonstrating that seasonal accumulation does not fully compensate for summer mass loss.

By **2024**, the gravitational potential for all four months had been significantly lower than in previous years, indicating that the Greenland ice sheet's mass was chronically depleted. Negative anomalies intensify from February to

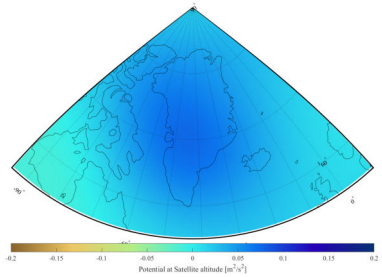

(a) February, 2009

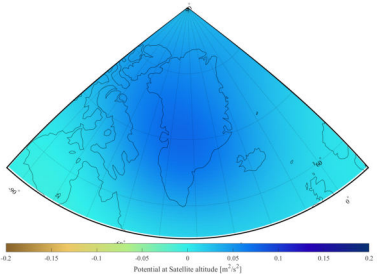

(b) May, 2009

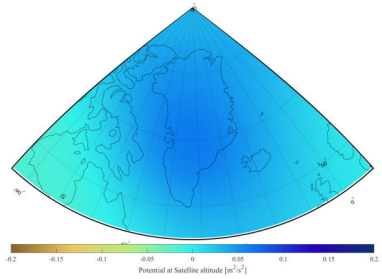

(c) August, 2009

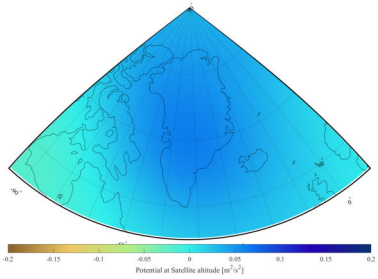

(d) November, 2009

Figure 5.4: Seasonal gravitational potential anomalies at satellite altitude for the year 2009 (February, May, August, and November), derived from GFZ RL06 DDK1 spherical-harmonic synthesis. All subfigures are shown using a common symmetric colour scheme with limits of ± 0.2 m^{2}s^{-2}.

May and reach their maximum extent and magnitude in August. Large areas continue to be significantly negative in November, implying that winter accumulation is insufficient to compensate for all summer mass loss. Although the seasonal amplitude remains, the mean state has changed downward, indicating a lower capacity for annual mass recovery.

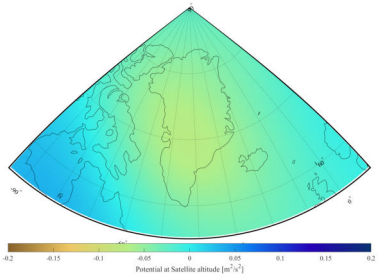

(a) February, 2019

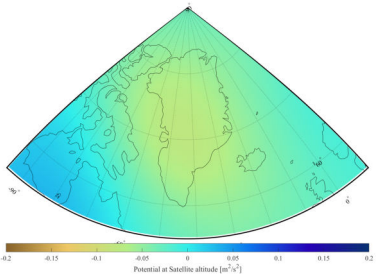

(b) May, 2019

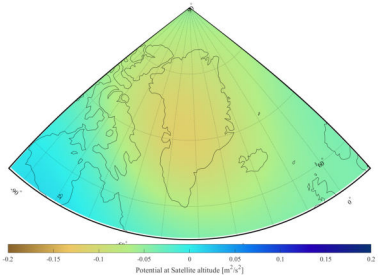

(c) August, 2019

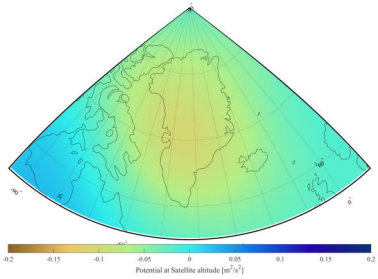

(d) November, 2019

Figure 5.5: Seasonal gravitational potential anomalies at satellite altitude for the year 2019 (February, May, August, and November), derived from GFZ RL06 DDK1 spherical-harmonic synthesis. All subfigures are shown using a common symmetric colour scheme with limits of ± 0.2 m^{2}s^{-2}.

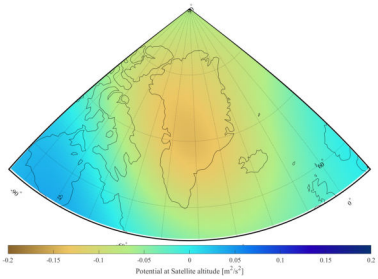

(a) February, 2024

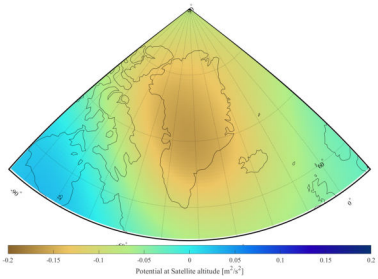

(b) May, 2024

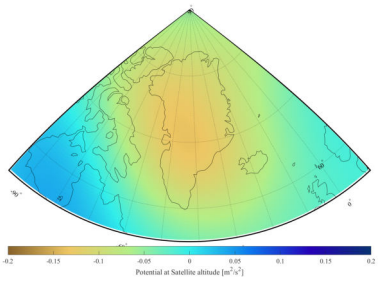

(c) August, 2024

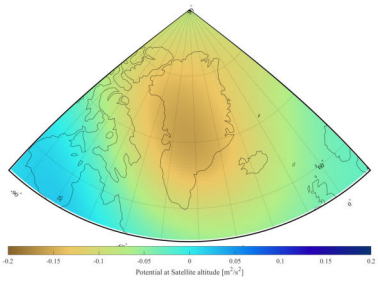

(d) November, 2024

Figure 5.6: Seasonal gravitational potential anomalies at satellite altitude for the year 2024 (February, May, August, and November), derived from GFZ RL06 DDK1 spherical-harmonic synthesis. All subfigures are shown using a common symmetric colour scheme with limits of ± 0.2 m^{2}s^{-2}.

5.3 Summary of Observed Trends

Across both the January time series and the seasonal comparisons, several robust conclusions emerge:

- Greenland has undergone a persistent long-term decline in mass over the past two decades, as evidenced by increasingly negative gravitational potential anomalies.
- Seasonal melt anomalies have intensified, with deeper summer minima and progressively reduced autumn recovery.
- Winter conditions, as reflected in the January time series, do not return to earlier baseline levels, indicating a cumulative mass deficit over time.
- The GRACE-FO period (2019–2024) exhibits the most pronounced negative potential anomalies, consistent with independent studies reporting enhanced mass loss in recent years.
- The residuals from the tesseroid inversion are small and spatially coherent, indicating that the implemented inversion method reliably captures the regional gravitational signal.

Overall, the combined analysis of long-term January variability, seasonal evolution, and inversion quality provides a consistent picture of Greenland's changing mass distribution. It demonstrates the suitability of spherical harmonic synthesis and regional inversion techniques for monitoring large-scale cryospheric change.

5.4 Inversion Results: Seasonal TWS Comparison (2003, 2009, 2019, 2024)

Figures 5.7, 5.8, 5.9 and 5.10 compare the inverted Total Water Storage (TWS) fields for the years 2003, 2009, 2019, and 2024 for the four seasonal months February, May, August, and November, respectively. These figures complement the potential anomaly results by quantifying the mass changes in the equivalent water height (EWH).
In **2003**, TWS anomalies are slightly positive in February and May. During August, moderately negative anomalies appear, mainly along the ice-sheet margins. Central Greenland remains relatively stable throughout the year, while the margins show clear seasonal variations. This indicates an almost balanced mass budget, with winter accumulation largely compensating for summer melt.
By **2009**, summer negative TWS anomalies intensify, especially along the western and southeastern margins of Greenland. Compared to 2003, the autumn (November) recovery is reduced, indicating that seasonal mass losses are no longer fully compensated during the accumulation period. This reflects a shift toward a more negative mass balance during the late GRACE phase.
By **2019**, marking the beginning of the GRACE-FO mission, TWS anomalies show widespread mass deficits during summer and autumn. Winter values (February) are less negative than the summer minimum but remain clearly more negative than in earlier years, indicating accumulated long-term mass loss.
In **2024**, all four months display substantially lower TWS values than in previous examples. August exhibits very strong mass-loss anomalies, locally approaching about $-800\,\mathrm{mm}$ EWH, while winter months no longer return to early-GRACE levels. The weak seasonal recovery indicates a persistent downward shift in Greenland's mass balance.
Overall, the seasonal TWS comparison demonstrates a progressive transition from a seasonally oscillating mass balance in 2003 to a persistently negative annual cycle by 2024, with reduced winter recovery, consistent with the strong negative potential anomalies observed in the spherical harmonic synthesis results.

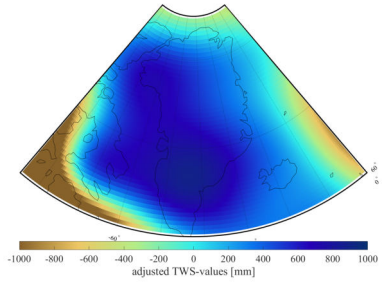

(a) February, 2003

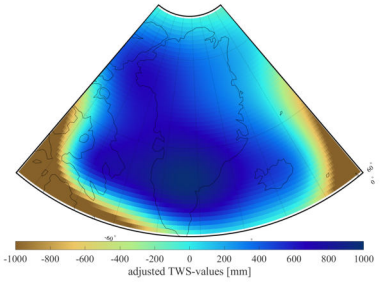

(b) May, 2003

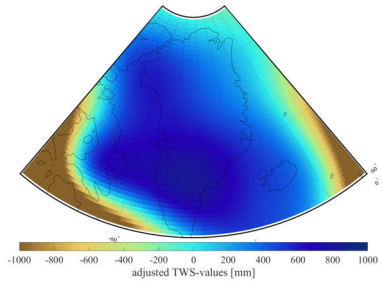

(c) August, 2003

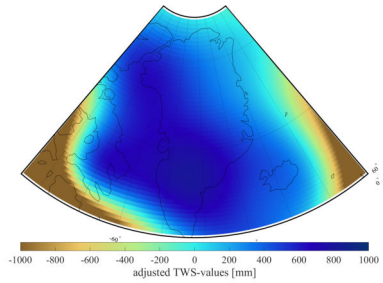

(d) November, 2003

Figure 5.7: Seasonal Total Water Storage (TWS) fields from tesseroid inversion for the year 2003, shown for February, May, August, and November. All subfigures are shown using a common symmetric colour scheme with limits of ± 100 mm.

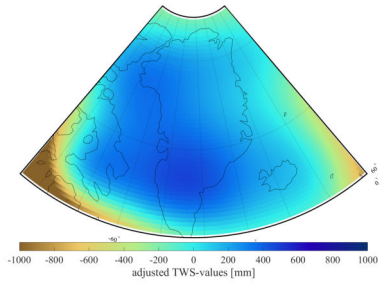

(a) February, 2009

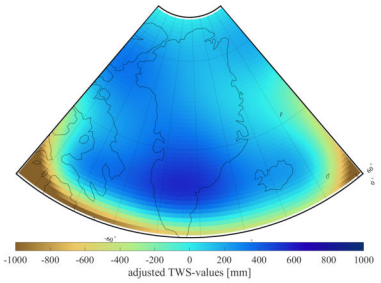

(b) May, 2009

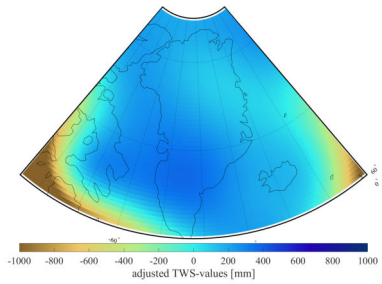

(c) August, 2009

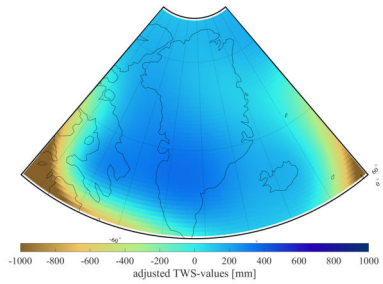

(d) November, 2009

Figure 5.8: Seasonal Total Water Storage (TWS) fields from tesseroid inversion for the year 2009, shown for February, May, August, and November. All subfigures are shown using a common symmetric colour scheme with limits of ± 100 mm.

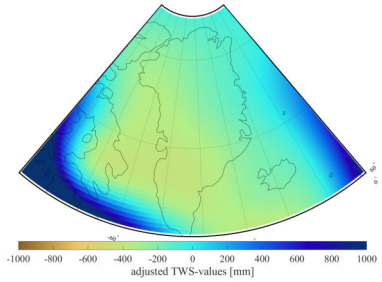

(a) February, 2019

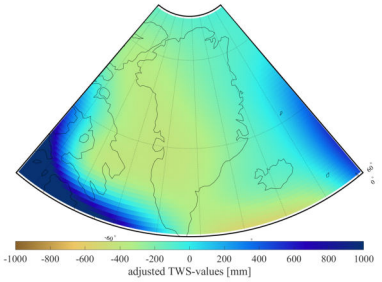

(b) May, 2019

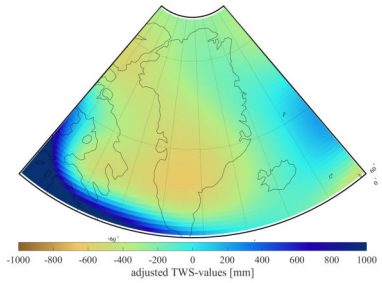

(c) August, 2019

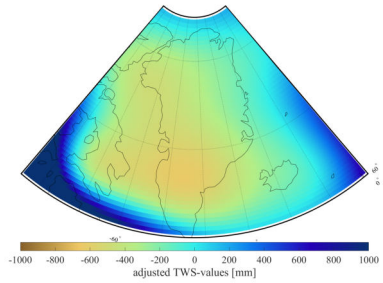

(d) November, 2019

Figure 5.9: Seasonal Total Water Storage (TWS) fields from tesseroid inversion for the year 2019, shown for February, May, August, and November. All subfigures are shown using a common symmetric colour scheme with limits of ± 100 mm.

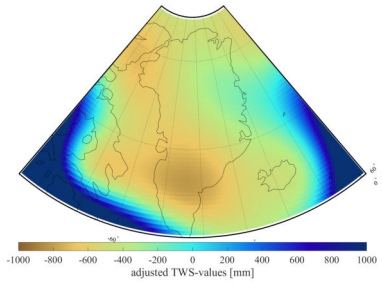

(a) February, 2024

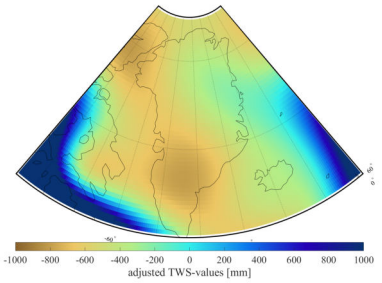

(b) May, 2024

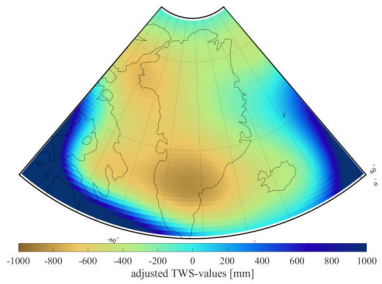

(c) August, 2024

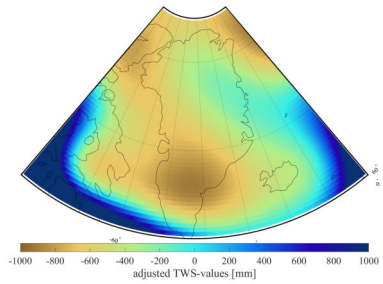

(d) November, 2024

Figure 5.10: Seasonal Total Water Storage (TWS) fields from tesseroid inversion for the year 2024, shown for February, May, August, and November. All subfigures are shown using a common symmetric colour scheme with limits of ± 100 mm.

5.5 Residual Analysis Between Synthesis and Inversion

To evaluate the consistency between spherical harmonic synthesis and tesseroid-based inversion, residual fields defined as $V_{\text{synth}} - V_{\text{inv}}$ were analyzed for a representative month from the GRACE-FO period (February 2024). The residual magnitudes are small, on the order of $10^{-3}\,\text{m}^2\,\text{s}^{-2}$, and exhibit spatially smooth patterns over most of central Greenland.

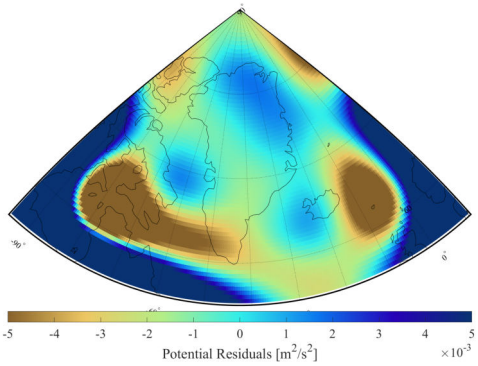

Figure 5.11: Residual gravitational potential field ($V_{\text{synth}} - V_{\text{inv}}$) at satellite altitude for February 2024 over Greenland. The residuals are within the limits of $\pm 0.005\ \text{m}^2\text{s}^{-2}$.

Slightly larger residuals are observed near the ice sheet margins and along the boundaries of the inversion domain, where mass gradients are strongest and edge effects from the regional inversion are expected. Importantly, no large-scale systematic patterns are present, indicating that the tesseroid inversion reliably reproduces the synthesized potential field.

The use of a single representative month is sufficient, as similar residual magnitudes and spatial characteristics are found throughout the time series. This confirms the numerical stability and robustness of the inversion setup, including the chosen discretization, regularization, and filtering strategy. In the following, V_{synth} denotes the gravitational potential obtained from spherical harmonic synthesis, while V_{inv} represents the potential reconstructed from the inverted TWS fields.

Table 5.1 summarizes descriptive statistics of total water storage fields (TWS) derived from the tesseroid inversion of GRACE and GRACE-FO potential anomalies for selected months in 2003, 2009, 2019, and 2024. The minimum and maximum values reveal an extensive spatial range of inferred mass changes. This indicates strong heterogeneity of the inverted TWS signal within the regional grid.

In the early GRACE years (2003 and 2009), the very large negative minimum values clearly indicate the influence of boundary effects inherent to regional inversions. Grid cells near the domain edges are prone to unrealistically large amplitudes when no strict Greenland mask is applied. As a result, the extrema in these years are strongly influenced by the inversion geometry rather than by physically meaningful mass changes.

For the later years (2019 and 2024), the minimum values remain comparatively moderate, while very large positive maximum values occur. This indicates that boundary effects predominantly affect the positive extrema in these years, whereas the negative values more consistently represent the large-scale mass-loss signal over Greenland.

The mean values follow a clear temporal evolution, with mostly positive means in 2003 and constantly negative means in 2019 and 2024. This reflects a long-term shift in the regional mass balance relative to the reference model. The RMS and standard deviation are substantially larger than the mean for all years. This indicates that the inverted fields are dominated by spatial variability rather than uniform offsets. The close agreement between RMS and standard deviation further suggests stable numerical behaviour of the inversion.

Table 5.1: Statistics for inversion results for TWS values (mm)

Months in 2003	Minimum	Maximum	Mean	RMS	STD
February	-2747.78	361.08	58.37	254.18	247.40
May	-2953.33	402.84	48.93	285.65	281.45
August	-3179.37	340.85	41.20	295.55	292.68
November	-3017.47	328.45	46.75	277.03	273.07
Months in 2009	Minimum	Maximum	Mean	RMS	STD
February	-1300.19	193.46	24.25	124.54	122.16
May	-1225.58	232.44	25.77	129.79	127.21
August	-1197.27	151.38	23.28	116.44	114.10
November	-1243.58	144.61	16.35	118.01	116.87
Months in 2019	Minimum	Maximum	Mean	RMS	STD
February	-182.87	1706.13	-21.24	158.55	157.13
May	-262.74	1699.01	-27.54	158.08	155.68
August	-256.96	1887.34	-49.74	170.03	162.60
November	-255.75	2003.86	-33.65	183.51	180.40
Months in 2024	Minimum	Maximum	Mean	RMS	STD
February	-337.49	2794.59	-48.97	280.07	275.77
May	-330.97	3006.22	-66.85	271.37	263.02
August	-355.73	2819.16	-44.74	268.54	264.80
November	-380.84	2799.56	-64.06	264.16	256.29

5.6 Comparison of DDK1 and DDK5 filtering

The comparison between DDK1 and DDK5 filtered solutions highlights the influence of decorrelation filter strength on the inverted TWS fields. The DDK1 result is spatially smoother and mainly reflects large-scale mass variations over Greenland. Small-scale features are largely removed by stronger filtering. The DDK5 solution retains more spatial structure and sharper gradients, particularly near the coastal regions. At the same time, an increase in short-wavelength variability is visible. Figure 5.12 shows the corresponding TWS fields for May 2003 as a representative example.

(a) DDK1

(b) DDK5

Figure 5.12: Inverted Total Water Storage (TWS) anomalies for May 2003 obtained using different DDK decorrelation filter strengths. All subfigures are shown using a common symmetric colour scheme with limits of ± 100 mm.

5.7 Comparison of TWS, Synthesized Potential, and Potential Residuals

Figure 5.13 compares inverted Total Water Storage (TWS), the corresponding synthesized gravitational potential, and the potential residuals for May 2003 and May 2024. The comparison illustrates the consistency between mass anomalies inferred from the inversion and their gravitational potential at satellite altitude. The potential residuals remain small relative to the signal magnitude and are mainly confined to the inversion boundaries. This indicates that the tesseroid-based inversion reliably reproduces the synthesized potential, and remaining differences are dominated by edge effects.

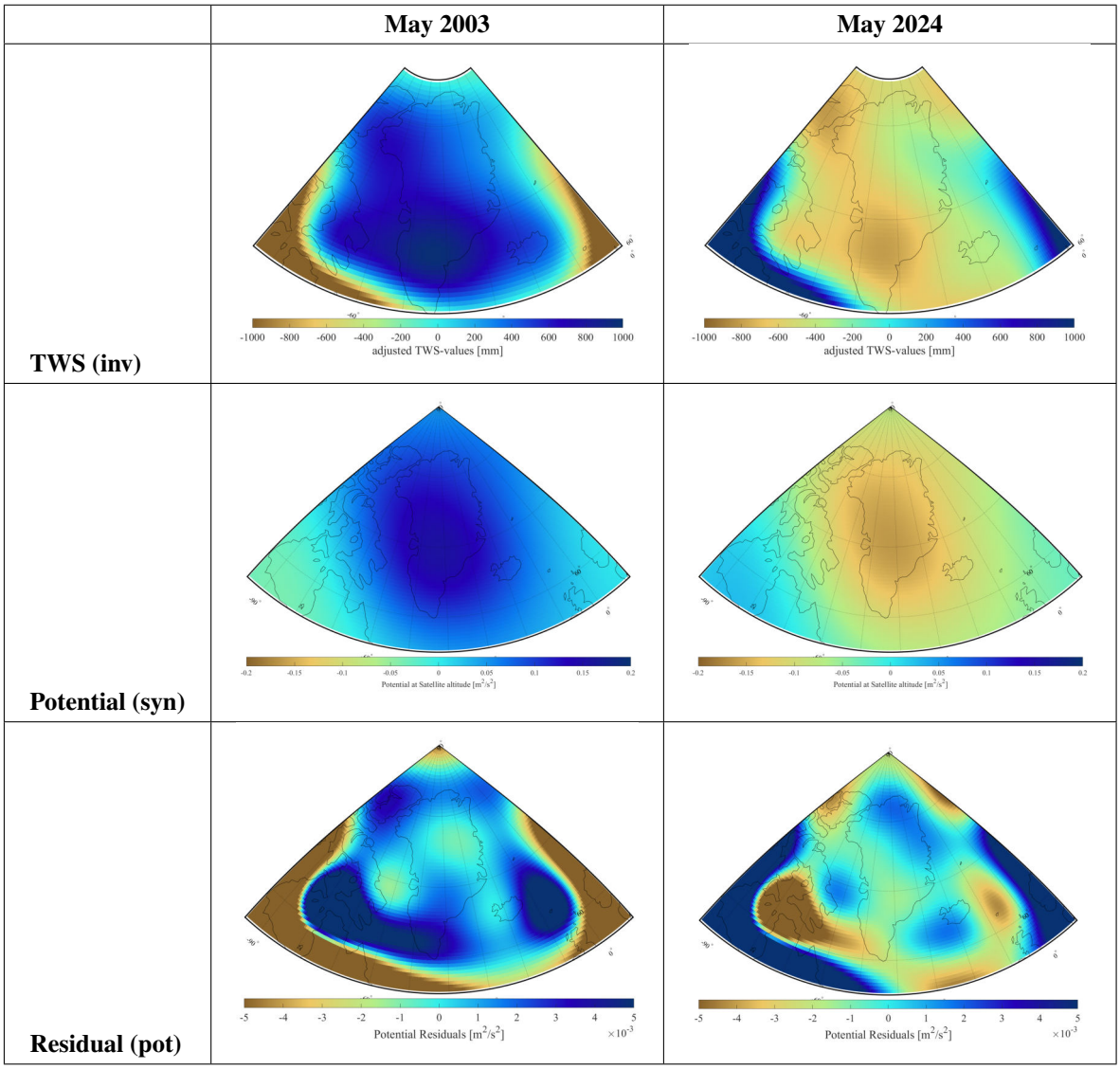

Figure 5.13: Comparison of inverted Total Water Storage (TWS), synthesized gravitational potential, and residual gravitational potential fields for May 2003 and May 2024. The inverted TWS fields are expressed in equivalent water height (mm), whereas the synthesized and residual gravitational potential fields are given in units of $m^2\,s^{-2}$.

6 Conclusion and Outlook

The analyses presented in this report show a clear and consistent evolution of mass variability over Greenland throughout the GRACE and GRACE-FO observation period. The seasonal pattern is evident throughout the full time span, but the synthesized potential anomaly fields exhibit temporal changes that become more persistent in later years. Comparisons between early GRACE years and the GRACE-FO period show clear differences in the seasonal behaviour. In the later years, seasonal recovery is reduced and the fields no longer return to the conditions observed at the beginning of the record.

The inverted Total Water Storage (TWS) fields express these changes in terms of mass variability. Seasonal comparisons for February, May, August, and November indicate that summer mass-loss signals intensify in recent years, while winter and autumn months exhibit a reduced recovery compared to earlier periods. Taken together, the potential synthesis and TWS inversion results indicate a long-term shift towards more negative mass balance over Greenland during the investigated period.

The reliability of the derived results is assessed by residual analyses between the synthesised and adjusted potential fields. For the selected example months, the residuals remain small in magnitude and are mainly confined to the boundaries of the inversion domain. This behaviour is consistent with edge effects expected in regional inversions. In the central parts of Greenland, the synthesised potential anomalies and the adjusted model agree closely. This indicates that the inversion reproduces the observations well and that the solution is numerically stable.

Based on these findings, future studies could concentrate on strengthening the quantitative assessment of stability and sensitivity. For example, the residual-based consistency analysis could be repeated for a broader set of months and seasons. The influence of filter strength and regularisation choices can also be documented more systematically across the full time series. Boundary effects in summary statistics would be further reduced by applying a uniform spatial mask for statistical assessments. Finally, applying the same processing framework to alternative monthly gravity field solutions would allow a direct comparison between different processing centres.

Acknowledgement

I would like to thank my supervisor Dr.-Ing. Kurt Seitz for his guidance and constructive feedback throughout the Lab Rotation, and Prof. Dr.-Ing. Hansjörg Kutterer for defining the topic and providing the scientific framework. I also acknowledge GFZ Potsdam and the ICGEM service for providing the GRACE/GRACE-FO monthly gravity field solutions used in this study.

References

Ferreira, V. G., Yong, B., Seitz, K., Heck, B., and Grombein, T. (2020): Introducing an improved GRACE global point-mass solution – a case study in Antarctica. *Remote sensing* 12(19):3197.

Grombein, T., Seitz, K., and Heck, B. (2013): Optimized formulas for the gravitational field of a tesseroid. *Journal of Geodesy* 87(7):645–660. ISSN: 0949-7714. DOI: 10.1007/s00190-013-0636-1.

Hanke, M. and Hansen, P. C. (1993): Regularization methods for large-scale problems. *Surveys mon Mathematics for Industry* 1993.

Heck, B. and Seitz, K. (2007): A comparison of the tesseroid, prism and point-mass approaches for mass reductions in gravity field modelling. *Journal of Geodesy* 81:121–136.

Heiskanen, W. A. and Moritz, H. (1967): Physical Geodesy. W. H. Freeman & Co., San Francisco, USA.

ICGEM (2026): International Centre for Global Earth Models (ICGEM): Gravity field and GRACE/GRACE-FO products hosted at the German Research Centre for Geosciences (GFZ). Accessed: 2026-04-06. URL: https://icgem.gfz-potsdam.de/.

Kusche, J., Schmidt, R., Petrovic, S., and Rietbroek, R. (2009): Decorrelated GRACE time-variable gravity solutions by GFZ, and their validation using a hydrological model. *Journal of Geodesy* 83:903–913. DOI: 10.1007/s00190-009-0308-3.

Tapley, B. D., Bettadpur, S., Ries, J. C., Thompson, P. F., and Watkins, M. M. (2004): GRACE Measurements of Mass Variability in the Earth System. *Science* 305(5683):503–505. DOI: 10.1126/science.1099192.

Tsoulis, D. (1999): Spherical harmonic computations with topographic/isostatic coefficients. Tech. rep. IAPG/FESG No. 3. Munich, Germany: Institut für Astronomische und Physikalische Geodäsie, Technische Universität München.

Wahr, J., Molenaar, M., and Bryan, F. (1998): Time variability of the Earth's gravity field: Hydrological and oceanic effects and their possible detection using GRACE. *Journal of Geophysical Research: Solid Earth* 103(B12):30205–30229.

Wouters, B., Bonin, J. A., Chambers, D. P., Riva, R. E., Sasgen, I., and Wahr, J. (2014): GRACE, time-varying gravity, Earth system dynamics and climate change. *Reports on Progress in Physics* 77(11):116801.

Investigation of the time series of the Earth's center of mass based on TWS variations in terms of 1st order spherical harmonic coefficients

Maike Li[1]

1 Remote Sensing and Geoinformatics Master of Science (M.Sc.), KIT, Germany
E-Mail: uquxb@student.kit.edu

Abstract

This study establishes a coherent workflow linking satellite gravity-field observations to hydrological mass variability and geocenter motion. The water-mass center of mass (COM) signal is derived from GRACE-FO data by transforming monthly Level-2 spherical-harmonic solutions into potential anomalies via spherical-harmonic synthesis, discretizing the field with tesseroids, and applying a regularized inversion to retrieve equivalent water thickness changes (ΔTWS). The COM signal is then computed from the inferred ΔTWS. The approach is physically motivated: potential anomalies are observation-domain quantities directly synthesized from spherical harmonics, and tesseroids provide a geometrically consistent mass-element representation suitable for global-scale modeling. The inverse problem is treated as ill-posed and stabilized with Tikhonov regularization, with regularization strength guided by an L-curve analysis.

Data quality and methodology are tailored for continental-scale interpretation. Monthly GRACE-FO Level-2 spherical-harmonic solutions (GFZ RL06.1) from 2019-2021 (36 months) are used, truncated at degree/order 96 to balance resolution and noise. A $1^\circ \times 1^\circ$ observation grid for potentials and a $4^\circ \times 4^\circ$ tesseroid mesh are employed to maintain computational feasibility while preserving basin-scale hydrological structures. The DDK2 decorrelation filter is applied to suppress correlated striping, ensuring robust signal propagation through the inversion.

Key findings show that the ΔTWS fields exhibit physically plausible seasonal behavior consistent with dominant hydrological cycles, and COM statistics indicate larger Z variability, reflecting inter-hemispheric mass exchange at seasonal scales. The geocenter signal derived from the water-mass field provides a water-mass–center-driven perspective on geocenter motion, complementing the JPL geocenter displacement series that aggregates broader mass redistribution (including atmosphere, oceans, cryosphere) and longer-term solid-Earth responses such as GIA. Differences between the products are attributed to distinct physical content, processing conventions, and the mapping between mass moments/COM quantities and millimeter-scale displacements. The two products should be compared with harmonized processing and reference frames to avoid misinterpretation.

Limitations and scope should be acknowledged: the COM signal amplitudes derived from the inverted ΔTWS are likely conservative due to DDK2 filtering and L-curve–based regularization dampening striping and stabilizing the inversion at the expense of attenuating parts of the geophysical signal, potentially biasing COM displacement estimates relative to external geocenter products. Regularization and decorrelation can suppress long-wavelength amplitudes, limiting sensitivity to broad-scale COM signals. The analysis covers 36 months and is strongest for seasonal/long-wavelength content; long-term trend conclusions should be drawn cautiously. Direct multi-decadal comparisons with other geocenter products require harmonized processing and reference frames.

Keywords GRACE · Total Water Storage (TWS) · Tesseroid · Center of Mass (COM)

1 Introduction

In this study, an inverse approach based on tesseroid forward modelling is analyzed. This involves simulating the gravity field of Earth and dividing it into small, three-dimensional prismatic elements known as tesseroids. Use of tesseroids instead of prisms have proven to be better in terms of efficiency and requires lesser computation time (Heck and Seitz, 2007). An inverse tesseroid approach is applied using least squares adjustment. The resulting ΔTWS grids are converted into monthly COM displacements by computing the mass-weighted centroid of all surface mass elements in geocentric Cartesian coordinates, yielding a time series that is equivalent to the movement of center of mass for validation against geocenter estimates.

2 Theoretical Aspects

Several fundamental concepts play an important role in the modelling of TWS as tesseroids of constant density, where the height of individual tesseroid is assumed to be the variable. This study involves an inverse modelling by adjustment to derive this variable.

2.1 Spherical Harmonic Synthesis (SHS)

The external gravitational potential of the Earth can be expressed as a spherical harmonic (SH) expansion. For an exterior point $P(r,\varphi,\lambda)$ with geocentric radius r, geocentric latitude φ, and longitude λ, the potential V can be written (in fully-normalized form) as

$$V(r,\varphi,\lambda,t) = \frac{GM}{r}\left[1+\sum_{n=1}^{n_{max}}\left(\frac{R}{r}\right)^n\sum_{m=0}^{n}\left(\bar{P}_{nm}(\sin\varphi)\left(\bar{C}_{nm}(t)\cos m\lambda+\bar{S}_{nm}(t)\sin m\lambda\right)\right)\right]. \tag{2.1}$$

In practice, the infinite series is truncated at a maximum degree n_{max} (the specific choice is described in the Methodology section).

To study temporal gravity signals, we focus on potential variations relative to a reference field (i.e., potential perturbations/residuals). Let $\bar{C}_{nm}^{\text{ref}}$, $\bar{S}_{nm}^{\text{ref}}$ denote reference SH coefficients (e.g., a baseline epoch or a multi-month mean field). The coefficient anomalies are defined as

$$\Delta\bar{C}_{nm}(t) = \bar{C}_{nm}(t) - \bar{C}_{nm}^{\text{ref}}, \tag{2.2}$$

$$\Delta\bar{S}_{nm}(t) = \bar{S}_{nm}(t) - \bar{S}_{nm}^{\text{ref}}. \tag{2.3}$$

Substituting these anomalies into the SH synthesis yields the potential change (excluding the constant term):

$$\delta V(r,\varphi,\lambda,t) = \frac{GM}{r}\sum_{n=1}^{n_{\max}}\left(\frac{R}{r}\right)^n\sum_{m=0}^{n}P_n^m(\sin\varphi)\left(\Delta\bar{C}_{nm}(t)\cos m\lambda+\Delta\bar{S}_{nm}(t)\sin m\lambda\right). \tag{2.4}$$

Here, $\delta V(t)$ represents the time-variable part of the gravitational potential at a point $P(r,\varphi,\lambda)$ caused by mass redistribution.

KIT Scientific Working Papers
Issue Number 270
ISSN: 2194-1629
DOI: 10.5445/IR/1000191188
Online: June 2026

This document is licensed under the Creative Commons Attribution – Share Alike 4.0 International License (CC BY-SA 4.0):
https://creativecommons.org/licenses/by-sa/4.0/deed.en

Table 2.1: Definition of variables used in Section 2.1

Symbol	Meaning	Unit
V	gravitational potential (absolute)	$m^2 s^{-2}$
δV	potential variation relative to a reference field	$m^2 s^{-2}$
G	gravitational constant	$m^3 kg^{-1} s^{-2}$
M	Earth mass	kg
GM	geocentric gravitational constant	$m^3 s^{-2}$
R	reference radius (normalization radius)	m
r	geocentric distance of the evaluation point	m
φ, λ	geocentric latitude, longitude	rad or degree
n, m	degree and order	$0 \leq m \leq n \leq n_{max}$
$\bar{C}_{nm}, \bar{S}_{nm}$	fully-normalized SH coefficients	–
$\bar{P}_{nm}$	fully-normalized associated Legendre functions	–
$n_{\max}$	maximum truncation degree	–
	example value for	n_{max}

2.2 Mass Discretization using the Inverse Tesseroid Method

In hydrological applications, near-surface water mass changes are commonly represented by an equivalent water thickness change $\Delta h(\varphi, \lambda, t)$, assuming a constant water density ρ_w. This converts the density-anomaly formulation into a thickness-based formulation that is physically interpretable as terrestrial water storage (TWS) change.
The near-surface domain is subdivided into N tesseroid elements. The i-th tesseroid is defined in spherical coordinates by

$$(\lambda, \varphi, r) \in [\lambda_1(i), \lambda_2(i)] \times [\varphi_1(i), \varphi_2(i)] \times [r_1(i), r_2(i)]\,. \tag{2.5}$$

If the unknown parameter is chosen as the equivalent water thickness $\Delta h_i(t)$ for element i, it follows that

$$\Delta h_i(t) = r_2(i) - r_1(i)\,, \tag{2.6}$$

and represent the mass anomaly using a constant ρ_w. For the observation point j with $(r_j, \varphi_j, \lambda_j)$, the potential change can be approximated as the sum of all tesseroid contributions:

$$\Delta V_j(t) \;\approx\; \sum_{i=1}^{N} \Delta V_j^{(i)}(t)\,, \tag{2.7}$$

where the i-th tesseroid contribution can be expressed by Newton's integral (Heiskanen and Moritz, 1967):

$$\delta V_j(t) \approx G\rho_w \sum_{i=1}^{N} \iiint_{\Omega_i} \frac{1}{|\mathbf{r}_j - \mathbf{r}'|}, d\Omega'\,, \tag{2.8}$$

where Ω_i is the volume of tesseroid i. Separating geometry from unknowns leads to the discrete linear model:

$$\delta V_j(t) \approx \sum_{i=1}^{N} A_{ji} x_i(t)\,, \tag{2.9}$$

where A_{ji} is the response coefficient determined by geometry, observation location, density, and constants. and $x_i(t)$ The unknowns are denoted by $\Delta h_i(t)$ or $\Delta m_i(t)$).
Stacking all observations gives

$$\mathbf{b}(t) = \mathbf{A}\mathbf{x}(t) + \boldsymbol{\varepsilon}(t)\,, \tag{2.10}$$

where $\mathbf{b}$ is obtained by vectorizing the potential residual grid, and $\boldsymbol{\varepsilon}$ represents observation and modelling errors.

Table 2.2: Definition of variables used in Section 2.2

Symbol	Meaning	Unit
Ω	volume where mass changes occur	m^3
ρ_w	water density (assumed constant)	kgm^{-3}
$\Delta h(\varphi,\lambda,t)$	equivalent water thickness change	m
$\Delta h_i(t)$	equivalent water thickness change in cell i	m
N	number of tesseroid elements	–
Ω_i	volume of tesseroid i	m^3
$\mathbf{b}$	observation vector	m^2s^{-2}
$\mathbf{x}$	unknown parameter vector	m
A	forward kernel	ms^{-2}
A_{ji}	response coefficient from cell i to observation j	–
ε	error term	m^2s^{-2}

2.3 Geocenter (COM) from water tesseroids

After retrieving the equivalent water thickness change, we convert it into water-mass anomalies and compute the associated center of mass (COM) signal. For each tesseroid (grid cell) i, the mass change is

$$\Delta m_i(t) = \rho_w \cdot \Delta h_i(t) \cdot A_i \,, \tag{2.11}$$

where ρ_w is water density, $\Delta h_i(t)$ is the equivalent water thickness change, and A_i is the horizontal area of the cell. Let $\mathbf{r_i} = (x_i, y_i, z_i)$ denote the representative geocentric position of cell i. The COM of the water mass anomaly can be written as

$$\mathbf{r}_{\mathrm{COM}}(t) = \frac{\sum_{i=1}^{N} \Delta m_i(t)\, \mathbf{r}_i}{\sum_{i=1}^{N} \Delta m_i(t)} \,. \tag{2.12}$$

In practice, the total mass anomaly $\sum_{i=1}^{N} m_i(t)$ can be small due to cancellation of positive and negative signals. Therefore, we also use the first mass moment

$$M_1(t) = \sum_{i=1}^{N} m_i(t)\, \mathbf{r}_i \,, \tag{2.13}$$

which avoids division by a small denominator and directly characterizes the "off-centering" of the redistributed water mass. Under a chosen convention (normalization and reference radius), geocenter-related degree-1 coefficients $\bar{C}_{10}, \bar{C}_{11}, \bar{S}_{11}$ are linearly related to $M_1(t)$ (or equivalently to $\mathbf{r}_{\mathrm{COM}}(t)$, and this mapping can be applied in later validation steps.

3 Data and preprocessing

This chapter describes the datasets used in this study and the preprocessing steps required to make them suitable for subsequent modelling and inversion. It introduces the selected GRACE-FO spherical harmonic solutions, the adopted time period, and the key conventions applied to ensure consistency. The outputs of this chapter provide the observation-domain quantities used in later analyses.

Table 2.3: Definition of variables used in Section 2.3

Symbol	Meaning	Unit
$\Delta h_i(t)$	Equivalent water thickness change in cell i at time t	m
$\Delta m_i(t)$	Water mass change in cell i at time t	kg
ρ_w	Water density (assumed constant)	kgm^{-3}
A_i	Horizontal area of cell i	m^2
r_i	Representative geocentric position of cell i in Cartesian coordinates	m
$\mathbf{r}_{\mathrm{COM}}(t)$	Center of mass of the water-mass anomaly	m
$M_1(t)$	First mass moment of the water-mass anomaly	kgm
N	Number of tesseroid/grid cells	–
t	Time index (monthly epoch)	–

3.1 GRACE-FO Level-2 from GFZ

The primary dataset used in this study comprises the monthly Level-2 spherical harmonic gravity field solutions provided by the GRACE Follow-On (GRACE-FO) mission. Specifically, we utilize the Release 6.1 (RL06.1) products generated by the Geoforschungszentrum Potsdam (GFZ), part of the International Centre for Global Earth Models (ICGEM, 2026). These solutions contain fully normalized spherical harmonic coefficients up to degree and order 96, and are widely used for studying temporal variations in the Earth's mass distribution. The dataset spans 36 consecutive months from January 2019 to December 2021, covering three full years of observation. Each monthly solution includes time-variable gravity field coefficients that are primarily sensitive to surface and near-surface mass changes, such as those caused by terrestrial water storage (TWS) variation (Wahr et al., 1998). The data were downloaded from the official ICGEM portal (ICGEM, 2026). To reduce correlated errors and north-south striping patterns commonly observed in GRACE(-FO) spherical harmonic products, a DDK2 decorrelation filter (Kusche, 2007) was applied to the coefficients prior to further processing.

3.2 Spatial grid settings

Two spatial grids are used in this study: an observation grid for potential synthesis at satellite altitude and a model grid for representing near-surface mass changes in the inversion.

Potential synthesis grid: Spherical harmonic synthesis is performed at satellite altitude and produces monthly potential residual $V(\varphi,\lambda,r)$ on a global $1^\circ \times 1^\circ$ grid. Grid points are defined at cell centers: longitude from -179.5° to $+179.5^\circ$, latitude from $+89.5^\circ$ to -89.5°, both with 1° grid spacing. This grid is vectorized to form the observation vector $\mathbf{b} = vec(\cdot)$ for the inversion.

TWS inversion grid: Near-surface mass changes are discretized into tesseroids, and unknown parameters (equivalent water thickness changes) are defined on a global $4^\circ \times 4^\circ$ grid. The model grid centers are at longitudes -178° to $+178^\circ$ (4° spacing) and latitudes -88° to $+88^\circ$ (4° spacing). Each cell corresponds to one tesseroid with angular bounds given by center $\pm 2^\circ$. Using a coarser model grid reduces the number of unknowns, improves inversion stability, and keeps the computation tractable.

3.3 Geocenter motion – Degree 1 (JPL)

The spherical harmonic coefficients of degree 1 represent the distance between the center of mass of the Earth and its 'center of figure', which in practice is approximated by the center of a set of tracking stations on the surface of the Earth. Because of their physical meaning, time changes in degree 1 coefficients can be expressed in several equivalent forms: (i) As distances in *mm* along the Z (along the axis of rotation), X and Y axes; (ii) As (fully normalized) degree-1 coefficients of the geopotential; (iii) As the changes in mass (per unit area) that would give

rise to the geopotential coefficients, expressed either in kg/m^2 or cm of equivalent water thickness. The relation between these forms can be found in Swenson et al. (2008, Equations 4 and 5).
One way to obtain these coefficients uses Satellite Laser Ranging to geodetic satellites. Coefficients obtained in that manner since 1992 are available here . These coefficients are expressed in form above. For more details on SLR-based degree-1 coefficients, see Cheng et al. (2010) and Cheng et al. (2011). Another way to obtain an estimate of degree-1 time-variable gravity coefficients uses GRACE(-FO) data with the output of a numerical ocean model. The original method was presented in Swenson et al. (2008). Sun et al. (2016) extended the method to include ocean mass distribution that is consistent with the so-called sea-level-equation solved for the self-gravitation patterns of sea level rise related to land water storage change (from hydorlogy, ice and snow etc.). Degree-1 coefficients computed based on Sun et al. (2016) are available here (Technical Note TN-13). These coefficients are expressed in the form above. Please note that as of RL06, is provided one TN-13 for each of JPL, CSR, and GFZ, representing degree-1 coefficients from the respective Level-2 standard spherical harmonic coefficients.

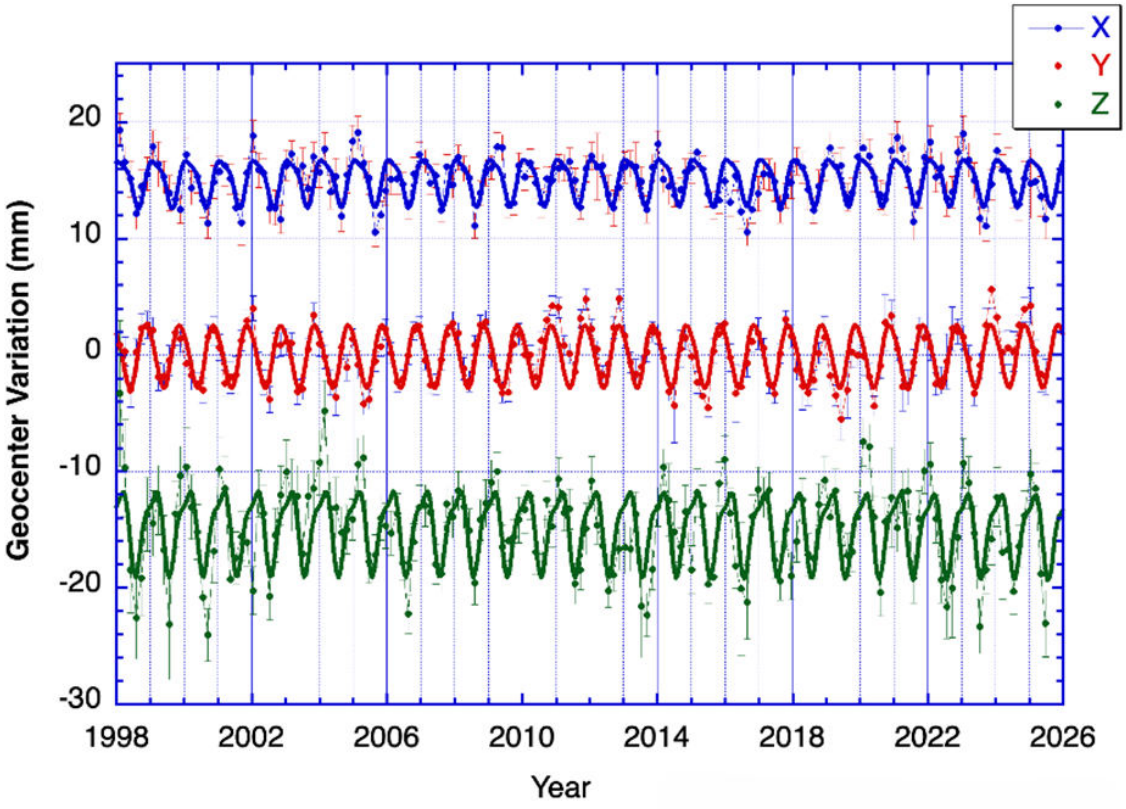

Figure 3.1: JPL geocenter displacement time series (X and Z offset by +15 mm and -15 mm, resp.)

4 Methodology

This chapter presents the methodological framework used to link satellite gravity observations to terrestrial water storage variations and geocenter-related signals. It outlines the forward modelling concept based on tesseroids, the construction of the inverse problem, and the use of regularization to stabilize the solution. The goal is to provide a clear and reproducible description of how potential anomalies are converted into ΔTWS and subsequently into COM estimates. The overall flowchart is presented in Table 4.1.

Table 4.1: Overall Flowchart

SH coefficients → potential	potential → TWS	TWS → COM
(i) Initialize parameters (ii) Define the global grid (iii) Read spherical harmonic coefficients and their errors (iv) Ensure consistent normalization of coefficients (v) Synthesize potential (and undulation) (vi) Compute degree variance and propagate errors	(i) Load the potential field as observations (ii) Set initial values for the iteration (iii) Iterate to solve for the monthly TWS field (iv) Forward-model potential from TWS and compute residuals	(i) Load monthly ΔTWS grid (ii) Compute cell mass (iii Sum mass moments over all cells (iv) Normalize to get COM (v) Loop over months to form a time series

4.1 Spherical Harmonic Synthesis

To construct an observation field suitable for inversion, we first synthesize monthly GRACE spherical harmonic (SH) solutions into gravitational potential variations at satellite altitude. Monthly SH coefficients were obtained from ICGEM (2026), using the GFZ solution with DDK2 filtering. To avoid scale inconsistencies arising from product-specific reference constants, all coefficients were rescaled upon reading to a fixed reference radius and geocentric gravitational constant. Potential synthesis was performed at a fixed height of $h_V = 500$ km above the reference ellipsoid, on a global $1^\circ \times 1^\circ$ grid defined at cell centers. Temporal variations were expressed relative to a multi-month mean reference field rather than a single epoch: SH coefficients were averaged over the selected 36 months to obtain $\bar{C}_{nm}^{\text{mean}}$, $\bar{S}_{nm}^{\text{mean}}$, and monthly residual coefficients were defined as

$$\Delta\bar{C}_{nm}(t) = \bar{C}_{nm}(t) - \bar{C}_{nm}^{\text{mean}} \tag{4.1}$$

$$\Delta\bar{S}_{nm}(t) = \bar{S}_{nm}(t) - \bar{S}_{nm}^{\text{mean}}. \tag{4.2}$$

Only degrees $n \geq 2$ were included. Moreover, to adopt a "disturbing potential" convention, the C_{20} term of the mean field was explicitly set to zero, so that the synthesized field represents perturbations with respect to the normal field. For each month, the residual coefficients $\Delta\bar{C}_{nm}$, $\Delta\bar{S}_{nm}$ were synthesized into a potential residual grid $V(\varphi,\lambda,t)$. As quality control and to inform later regularization, we additionally computed an undulation-like quantity

$$N = \frac{V}{\gamma} \tag{4.3}$$

using the GRS80 (Moritz, 1980) normal gravity value γ, variance propagation based on coefficient uncertainties, and degree variance and error degree variance to characterize noise behavior across degrees. Due to the fact the synthesis starts from degree-2, the center of mass of the Earth is not included in this SH.

4.2 Inverse tesseroid approach

With the satellite-altitude potential residuals available, treated as pseudo-observations and retrieve global equivalent water thickness TWS using a tesseroid-based linear inversion. The unknowns are defined on a global $4^\circ \times 4^\circ$ grid with cell centers at $\lambda \in [-178^\circ, 178^\circ]$ and $\varphi \in [-88^\circ, 88^\circ]$. Each grid cell is represented by a tesseroid bounded by $[\lambda_1,\lambda_2] \times [\varphi_1,\varphi_2]$, with its base radius fixed at the mean Earth radius $r_1 = R$. The unknown radial thickness is interpreted as equivalent water thickness (unit m, later reported in mm). Forward modelling assumes a water density $\rho_w = 1000$ kg m^{-3}

and gravitational constant $G = 6.67259 \times 10^{-11}$ m^3 kg^{-1}s^{-2}. Observations are provided by the potential residual grids. For each month, the potential is loaded to obtain $V(\varphi, \lambda$, which is vectorized as $\mathbf{b}(t) = vec(V)$. The observation radius $r_P = R + h_P$ must match the synthesis altitude, which was set in the synthesis part to $h = 500$ km, consistently. The forward relationship is expressed as

$$\mathbf{b} = \mathbf{A}\mathbf{x} + \varepsilon, \tag{4.4}$$

where $\mathbf{x}$ contains tesseroid TWS parameters and $\mathbf{A}$ is the Jacobian matrix derived from tesseroid contributions to the potential. The kernel is constructed using a zeroth-order point-mass term K_{000}, and augmented by second-order corrections K_{200}, K_{020}, K_{002} to improve tesseroid accuracy (Heck and Seitz, 2007; Grombein et al., 2013). Because the global inversion is ill-conditioned, we solve it with Tikhonov regularization:

$$\hat{\mathbf{x}} = \arg\min_x \left(||\mathbf{A}\mathbf{x} - \mathbf{b}||_2^2 + \lambda^2 ||\mathbf{x}||_2^2 \right) \tag{4.5}$$

In practice, a compact SVD of $\mathbf{A}$ is computed, the regularization parameter λ is selected via the L-curve corner, and the solution is obtained with Tikhonov (Hansen, 2000; Hansen et al., 2007). Since tesseroid thickness Δr affects the kernel through the tesseroid top radius $r_2 = r_1 + \Delta r$ and radial center $r_0 = (r_1 + r_2)/2$, a short fixed-point iteration is adopted: starting from $\Delta r = 0$, we update r_2 and r_0, rebuild $\mathbf{A}$, and re-solve, up to three iterations or until $|\Delta r - \hat{\mathbf{x}}| < 10^{-9}$ m. The final TWS field is converted to millimetres, while fitted potentials and residual fields are stored for diagnosing striping and regularization effects.

4.3 Center of mass calculation

To connect the inverted TWS fields to geocenter-related signals, we convert TWS into mass anomalies and compute their contribution to the center-of-mass (COM) position. This step takes the monthly fields as input.
For each month, the equivalent water thickness $\Delta h(\varphi, \lambda)$ is converted into tesseroid mass increments. For the i-th latitudinal band and j-th longitude cell, the mass increment is approximated by

$$m_{ij} = \rho_w \Delta\lambda \frac{1}{3} \left(r_{2,ij}^3 - r_{1,ij}^3 \right) \left[\sin(\varphi_{i+1}) - \sin(\varphi_i) \right], \tag{4.6}$$

where $r_1 = R$ is the base radius, $r_2 = r_1 + h$ is the top radius, and $\Delta\lambda$ is the longitudinal angular width of the tesseroid. The representative radius is set to $r_0 = r_1 + \Delta h/2$, and Cartesian coordinates (X_{ij}, Y_{ij}, Z_{ij}) are computed using the band-center latitude $\varphi_0 = (\varphi_{i+1} + \varphi_i)/2$ and the longitude center λ_0. The COM contribution of the water-mass anomaly is then obtained from first moments:

$$(X_{\mathrm{COM}}, Y_{\mathrm{COM}}, Z_{\mathrm{COM}}) = \frac{\sum_{i,j} \Delta m_{ij} \times (X_{\mathrm{COM}}, Y_{\mathrm{COM}}, Z_{\mathrm{COM}})}{M_{\mathrm{Earth}} + M_{\mathrm{TWS}}}, \tag{4.7}$$

with $M_{\mathrm{TWS}} = \sum \Delta m_{ij}$ and the Earth mass $M_{\mathrm{Earth}} = 5,9722^{24}$ kg included explicitly for normalization, yielding a small displacement relative to the geocenter. Repeating the calculation for 36 months produces the monthly COM component time series $X_{\mathrm{COM}}(t), Y_{\mathrm{COM}}(t), Z_{\mathrm{COM}}(t)$.

4.4 Comparison with SLR

Convert COM components into degree-1 coefficients $\bar{C}_{10}$, $\bar{C}_{11}$, $\bar{S}_{11}$, and compare them with SLR geocenter time series. COM and degree-1 coefficients have a linear relation, but the exact conversion depends on normalization, reference radius, and sign conventions. Therefore, before comparison we make sure they have same units, same sign convention, and same monthly timeline.

5 Results and Discussion

This chapter summarizes the main results and evaluates their physical plausibility and numerical reliability. It first assesses the synthesized potential fields and their error characteristics, then discusses the retrieved ΔTWS patterns and inversion performance. Finally, the inferred COM variations are interpreted and compared with external reference information where appropriate, highlighting both consistent features and remaining limitations.

5.1 Assessment of SHS Results

In this study, monthly satellite gravity field solutions are used (36 months, truncated to degree/order 96). A reference field is selected to form anomalies, and the spherical harmonic synthesis (SHS) is applied to obtain the gravity potential variations at the chosen computation altitude. De-noising filters are applied to reduce correlated errors and striping effects.

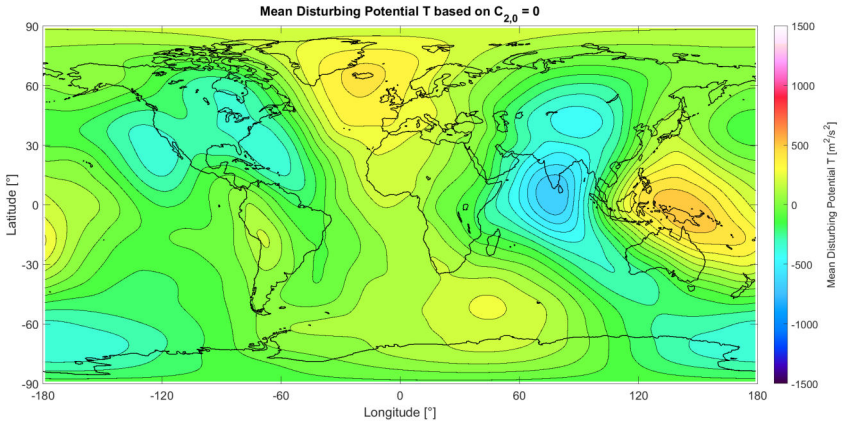

Figure 5.1: Spherical-harmonic-synthesized 36-month mean disturbing potential (scale is $\pm 1500\, m^2 s^{-2}$)

Figure 5.1 presents the 36-month mean disturbing potential field obtained from the spherical harmonic synthesis, where the reference contribution associated with the $\bar{C}_{20}$ term is set to zero to reduce the dominant degree-2 zonal background and to emphasize the remaining large-scale spatial structure. The mean field shows smooth, basin-scale patterns with alternating positive and negative anomalies, indicating that the signal is mainly governed by low-degree components and represents a persistent, time-averaged gravitational signature rather than short-term monthly variability. Several broad anomaly centers can be identified (e.g., in the Indo-Pacific sector and over parts of the Atlantic–Africa region), and the continuous, well-behaved contour lines suggest that the synthesized potential field is stable and physically plausible. This 36-month mean field is used as a reference for defining monthly potential anomalies in the subsequent analysis and inversion steps.

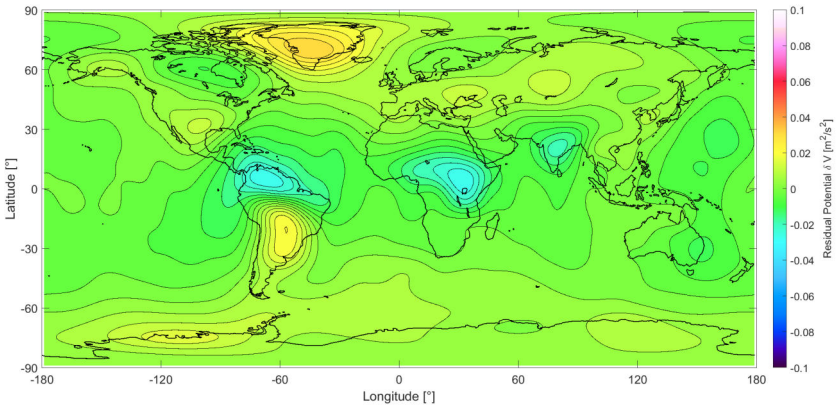

Figure 5.2: Global distribution of the residual potential (scale is $\pm 0.1\, m^2 s^{-2}$)

Figure 5.2 shows the residual gravitational potential for January 2019 relative to the chosen reference field, with an amplitude range of roughly $\pm 0.1\, m^2 s^{-2}$. The pattern is dominated by large-scale, smooth structures, indicating that the signal is mainly controlled by low-degree components rather than short-wavelength random noise. Clear positive and negative anomaly centers are visible over regions such as northern South America (Amazon–Andes area), central Africa, and parts of South Asia/Southeast Asia. These regional-scale anomalies are physically plausible and are consistent with mass redistribution signals that are typically related to monthly variations in terrestrial water storage. The continuous and well-behaved contour lines further suggest that the SH synthesis produces a numerically stable potential field that can be used as the observation input for the subsequent inversion step. Since δV is the direct observation quantity used in the inversion, the spatially coherent structures seen here motivate the next step: interpreting these potential anomalies in terms of near- surface mass changes ΔTWS via a regularized inverse approach.

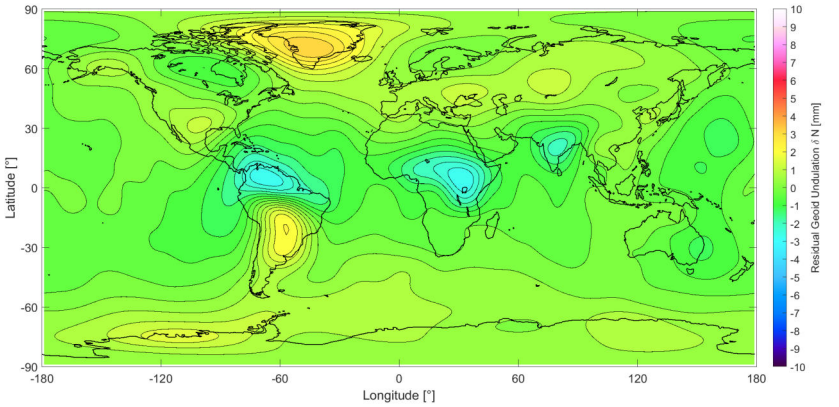

Figure 5.3: Global distribution of the residual geoid undulation (scale is $\pm 10\, mm$)

Figure 5.3 presents the residual geoid undulation derived from the potential residuals $\delta N = \delta V / \gamma$, with a magnitude on the order of $\pm 10\, mm$. The spatial pattern is broadly consistent with Figure 5.2, showing similar anomaly centers over South America, central Africa, and South Asia. This agreement provides an additional qualitative check that the potential residual field is not a numerical artifact but contains coherent geophysical information. Displaying the results in millimeter-level undulation also offers a more intuitive interpretation of the gravity signal

in a geodetic quantity. Note that this undulation map is mainly used for visualization and diagnostic purposes, while the inversion itself is performed using the potential residuals. The consistency between δV and the undulation map supports the reliability of the synthesized field; therefore, the analysis can proceed to the inversion stage, where the potential residuals are translated into ΔTWS under appropriate stabilization constraints.

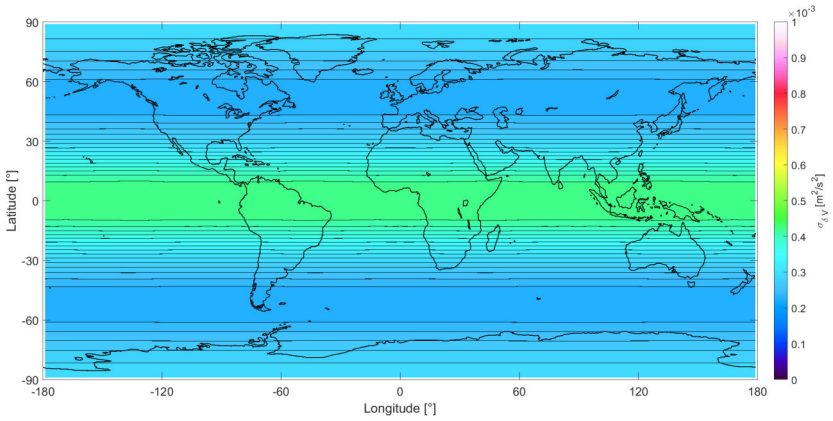

Figure 5.4: Uncertainty of the residual potential in January 2019 (variance propagation) (scale is from 0 to $10^{-3}\,m^2s^{-2}$)

Figure 5.4 illustrates the error or uncertainty level associated with the potential residuals, with values on the order of $10^{-3}\,m^2s^{-2}$. A prominent feature is the presence of zonal banding / striping patterns, indicating that the error is not purely random but spatially correlated. The error level is relatively higher in the low-latitude belt, and the stripe-like structure is characteristic of correlated errors commonly seen in GRACE-type spherical harmonic solutions. This result implies that, although the signal fields in Figures 3.1 and 5.1 are spatially smooth and physically plausible, the observation noise has a structured component that can be amplified by a naive inversion.

5.2 Assessment of ΔTWS results

Inversion quality assessment:

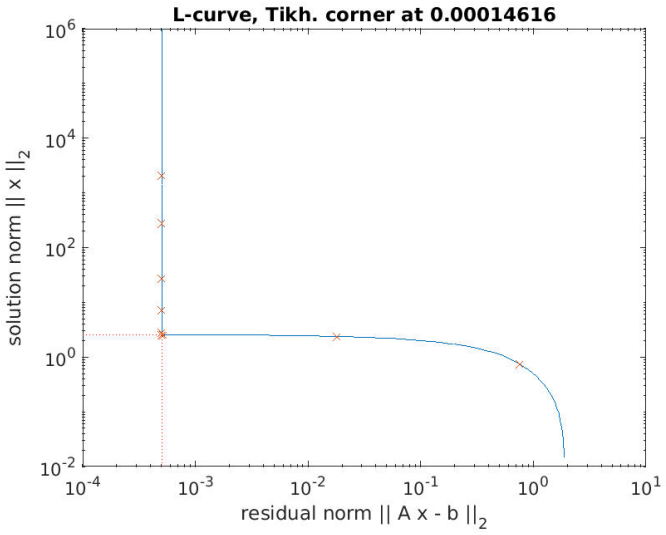

Figure 5.5: L-curve for Tikhonov regularization and parameter selection

Figure 5.5 shows the L-curve used to select the Tikhonov regularization parameter λ . The horizontal axis is the data misfit $||\mathbf{Ax}-\mathbf{b}||_2$ and the vertical axis is the regularization term (solution norm or semi-norm, depending

on the chosen operator). Moving left indicates a better fit to the observations but may amplify noise in an ill-conditioned inversion, whereas moving downward indicates a smoother (more strongly regularized) solution that can suppress signal. The corner point provides a practical compromise between fidelity and stability. In this study, the selected λ yields a balanced solution that preserves the dominant geophysical pattern while avoiding excessive noise amplification.

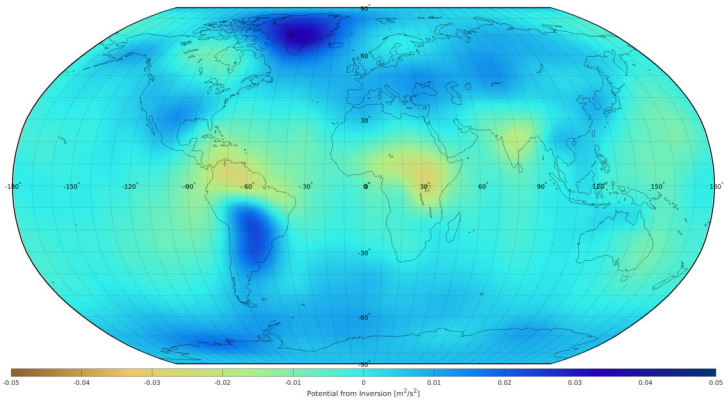

Figure 5.6: Gravity potential perturbation retrieved from the inversion in January 2019 (scale is $\pm 0.05\, m^2 s^{-2}$)

Figure 5.6 shows the Potential from inversion, the gravitational potential perturbation generated by the inferred near-surface mass anomalies. The field is dominated by smooth, large-scale structures and exhibits pronounced anomalies over several hydrology- and cryosphere-sensitive regions. Positive anomalies (warm colors) appear over areas such as equatorial Africa and parts of Southeast Asia, suggesting potential mass gain during this month, while negative anomalies (cool colors) are visible over parts of South America, high-latitude North America, and around Greenland, indicating possible mass loss. Overall, this map represents the model-based physical interpretation of the observed gravity changes and shows a spatial pattern consistent with typical seasonal terrestrial water storage variability.

To evaluate how well the inversion explains the observations, the next step compares the forward-predicted potential with the observed potential and analyzes the residual potential to assess the remaining noise and misfit.

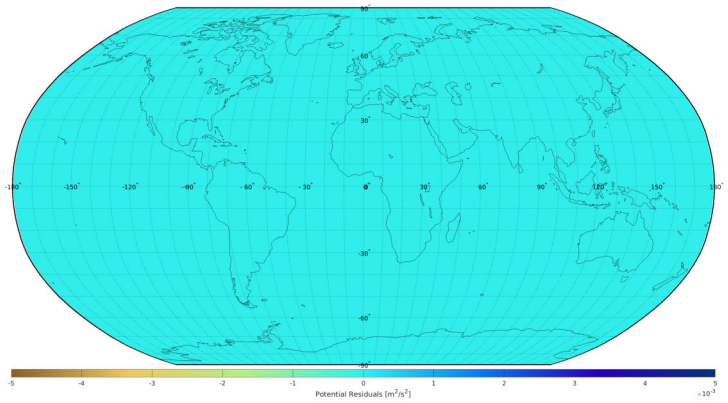

Figure 5.7: Global distribution of potential residuals in January 2019 (scale is $\pm 5 \cdot 10^{-3}\, m^2 s^{-2}$)

Figure 5.7 shows the potential residuals, defined as the difference between the observed potential field and the forward-predicted potential from the inversion. The residual amplitudes are close to zero globally and remain at the $10^{-3}\, m^2 s^{-2}$ level, with no clear large-scale systematic pattern. This indicates that the inversion provides a good

fit to the observations for this month and that the solution is numerically stable with satisfactory convergence. At the same time, the residual field is useful for identifying remaining correlated noise or localized mismodelling, which supports the reliability assessment of the retrieved mass-change solution.
With the potential misfit being small, the next step converts the inferred near-surface mass anomalies into equivalent water thickness changes ΔTWS and evaluates their spatial patterns and physical plausibility.

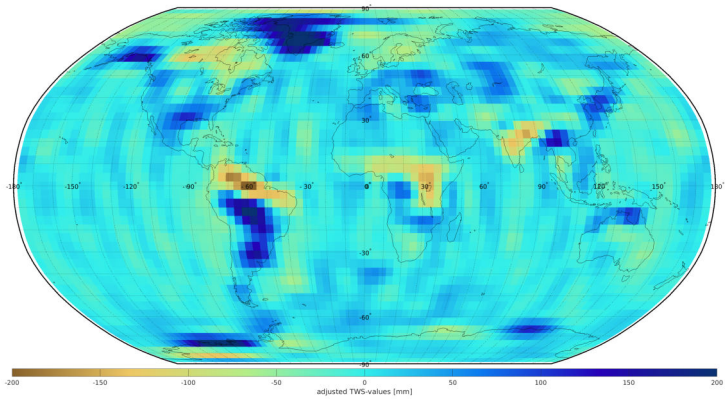

Figure 5.8: Global terrestrial water storage change ΔTWS in January 2019 (scale is $\pm 200\,mm$)

Figure 5.8 presents the global terrestrial water storage change (ΔTWS, mm equivalent water height) retrieved for January 2019. The map shows clear regional-scale anomalies: positive values occur mainly over northern South America, central Africa, and parts of South Asia, indicating possible water storage gain during this month. Negative values are more pronounced over southern South America, high-latitude North America, and other high-latitude regions, suggesting potential storage loss or cryosphere-related mass deficit contributions. Overall, the ΔTWS field exhibits physically plausible large-scale patterns that are consistent with typical seasonal hydrological variability and highlights the dominant mass redistribution inferred from the inversion. The $4^\circ \times 4^\circ$ resolution of the ΔTWS grid is visible in the Figure 5.8.
To support the reliability of the retrieved ΔTWS solution, the following section evaluates the convergence and numerical stability of the iterative inversion using the evolution of the solution statistics across iterations.

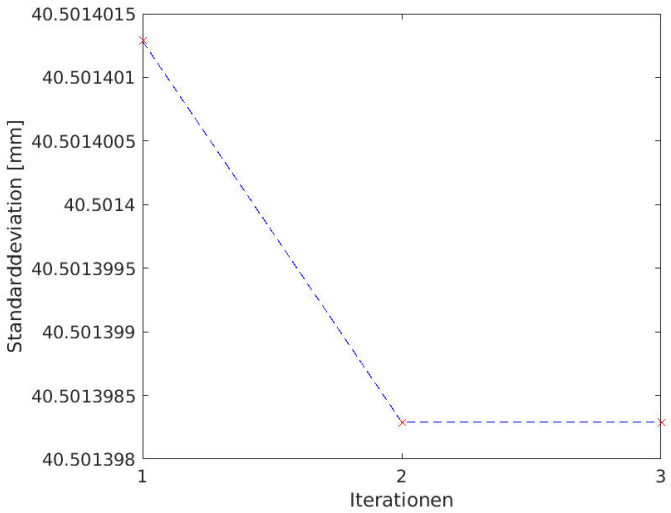

Figure 5.9: Inversion convergence in January 2019: standard deviation versus iteration

Figure 5.9 shows the convergence behavior of the inversion, illustrated by the evolution of the solution standard deviation across iterations. The standard deviation decreases from iteration 1 to iteration 2 and remains nearly unchanged from iteration 2 to iteration 3, indicating that the solution reaches a stable state after approximately two iterations. Moreover, the standard deviation stays at the millimeter level throughout the process, with no signs of divergence. This demonstrates that the inversion converges rapidly and remains numerically stable for this month. With the convergence and stability confirmed, the analysis can proceed to interpret the retrieved ΔTWS patterns and to examine their implications for subsequent geocenter/COM estimates.

Table 5.1: Statistics for inversion results for TWS values (mm)

Months	Min	Max	Mean	RMS	STD
Jan 2019	-208.5134	218.9535	-0.0024	25.1206	25.1237
Apr 2019	-389.1438	433.9609	0.0038	39.4029	39.4078
Jul 2019	-193.5138	229.8884	-0.0059	25.9162	25.9194
Oct 2019	-468.9920	243.7477	0.0060	37.1941	37.1987
Jan 2020	-248.5907	120.9350	-0.0033	19.4781	19.4805
Apr 2020	-302.2683	354.4277	-0.0041	37.4212	37.4258
Jul 2020	-93.5564	246.2931	-0.0018	20.0226	20.0250
Oct 2020	-548.6374	242.5682	-0.0028	37.8789	37.8836
Jan 2021	-161.4704	146.1629	0.0038	19.4742	19.4766
Apr 2021	-214.0618	472.8450	-0.0048	35.5066	35.5110
Jul 2021	-181.6036	458.1050	0.0056	26.2682	26.2715
Oct 2021	-436.1330	239.9015	-0.0036	36.4040	36.4085

Table 5.1 summarizes basic statistics of the retrieved ΔTWS fields. Overall, the means are very close to zero (within about ± 0.006 mm), indicating a consistent anomaly definition with no systematic bias. The RMS and STD are nearly identical for all months, suggesting that the variability is dominated by the overall spatial dispersion rather than a few extreme outliers. A clear seasonal contrast is visible: April and October generally show larger RMS/STD ($\sim$ 35–39 mm), while January and July are lower ($\sim$ 19–26 mm), implying stronger basin-scale variability in those seasons. The extreme ranges can be large in certain months (e.g., Oct 2020 min $\approx$ -549 mm; Apr 2021 max $\approx$ 473 mm).

Spatial distribution characteristics:

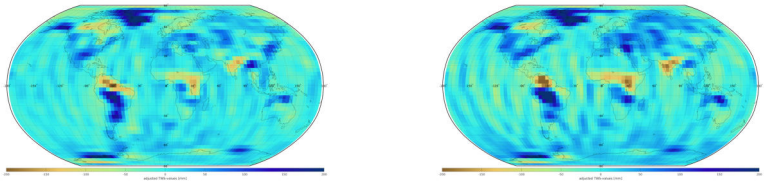

(a) January

(b) February

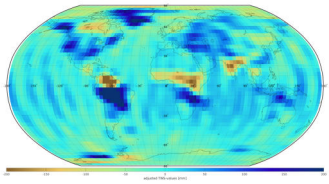

(c) March

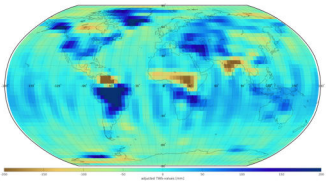

(d) April

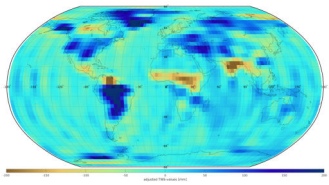

(e) May

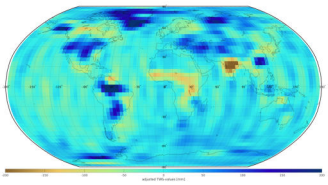

(f) June

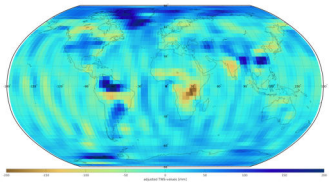

(g) July

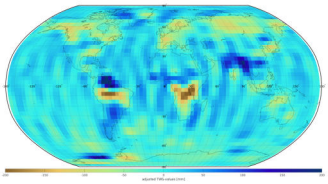

(h) August

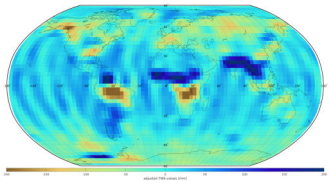

(i) September

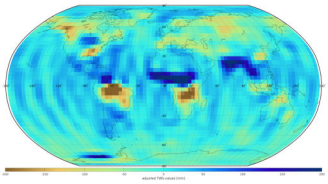

(j) October

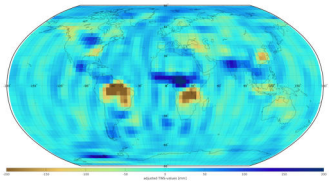

(k) November

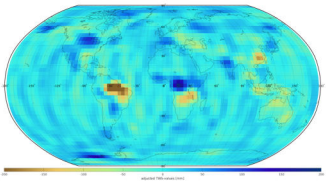

(l) December

Figure 5.10: Monthly maps of terrestrial water storage anomalies ΔTWS in 2019 (scale is $\pm 200\,mm$)

Figure 5.10 shows the monthly maps of terrestrial water storage anomalies ΔTW in 2019. A clear seasonal behavior can be recognized at continental scale. In the tropics, the strongest signals appear over major river basins and follow a coherent wet–dry cycle, consistent with the seasonal migration of the rainfall belt. In high-latitude regions, the signal tends to peak in the cold season and becomes weaker or changes sign during the warm season, which is expected from snow accumulation and melt processes.

Across all months, the maps also show broad north–south "stripe-like" features over the oceans and continents. These patterns are typical correlated errors in GRACE-type solutions and usually indicate that part of the signal is affected by along-track noise and the limited spatial resolution. Therefore, the interpretation below focuses on robust, large-scale features rather than small local patches. This is consistent with common GRACE post-processing and uncertainty discussions in the literature.

In the Amazon Basin, the ΔTW signal is one of the most prominent features in the 2019 maps. The basin-scale anomaly changes noticeably across months, which is consistent with the strong seasonal hydrological cycle in this region. Months showing basin-wide positive anomalies can be interpreted as periods with stronger water accumulation, while months with negative anomalies correspond to storage depletion during the drier phase (Frappart et al., 2013). Such behavior agrees with previous GRACE-based studies reporting a strong seasonal cycle of total water storage in the Amazon basin and its close relationship with rainfall and river discharge.

Over Greenland and nearby high-latitude regions, the monthly ΔTW patterns show noticeable seasonal variability. In general, cold-season months are expected to exhibit more positive storage due to snow accumulation, while warm-season months tend to show reduced storage related to melt and runoff (Velicogna, 2009). The presence of strong high-latitude signals is consistent with many GRACE studies that revealed significant ice-sheet mass changes and their temporal variability. However, due to the limited spatial resolution and the known leakage/striping effects in GRACE solutions, the interpretation here is restricted to large-scale and persistent features rather than small localized patches.

5.3 Assessment of COM results

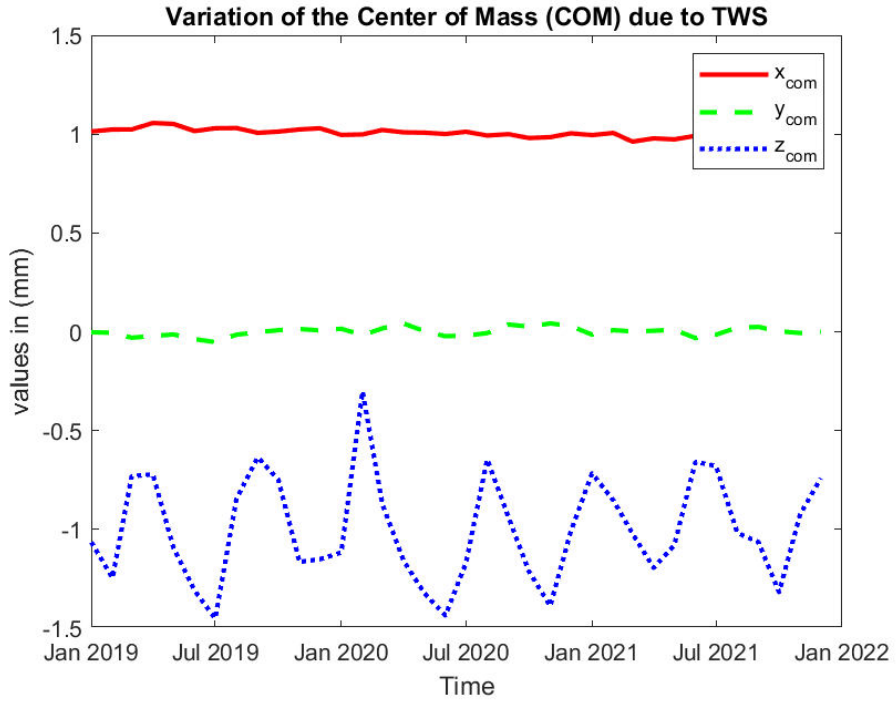

Figure 5.11: COM displacement induced by ΔTWS in 2019-2021 (X and Z offset by $+1$ mm and -1 mm, resp.)

Based on the results from January 2019 to December 2021 (36 months), the three components of the COM displacement vary as follows (unit: mm).
The X component (geocentric X-axis, pointing toward the equator at 0°E) shows a peak-to-peak range of approximately 0.106 mm and a standard deviation of about 0.026 mm.
The Y component (geocentric Y-axis, pointing toward the equator at 90°E) has a peak-to-peak range of approximately 0.095 mm and a standard deviation of about 0.022 mm.
The Z component (geocentric Z-axis, pointing toward the North Pole) exhibits a substantially larger peak-to-peak range of approximately 1.149 mm and a standard deviation of about 0.265 mm.
As mentioned in Section 4.1, the variation of center of mass is not supposed to be visible in Figure 5.11.
Overall, the seasonal amplitude of the Z component is much larger than those of the X and Y components; specifically, the Z peak-to-peak variability is about 10–12 times that of X/Y, indicating that inter-hemispheric mass exchange plays a dominant role in the COM variations over the study period.

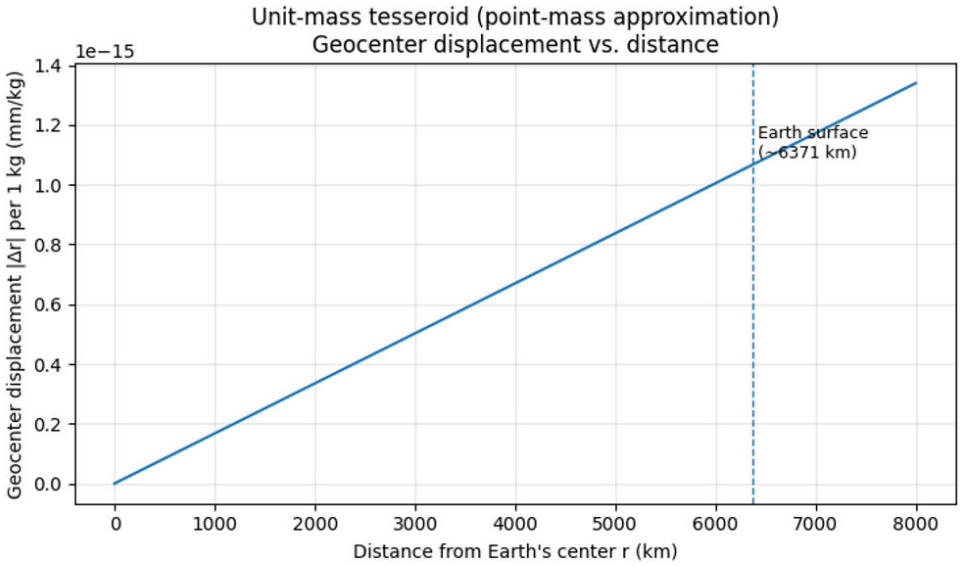

Figure 5.12: Geocenter displacement contribution of a unit-mass tesseroid versus distance from Earth's center

Figure 5.12 illustrates how a unit-mass tesseroid (approximated as a point mass) affects the geocenter displacement as a function of its distance from Earth's center. The displacement per 1 kg increases linearly with distance, following $|\Delta r| = r/M_{\text{Earth}}$, because the geocenter signal is proportional to the first mass moment $(m \cdot r)$. The dashed vertical line marks the Earth's surface ($r \approx 6371$ km), where the effect is about 1.07×10^{-15} mm/kg, highlighting that mm-level geocenter motions require very large mass redistributions.

Comparison with SLR data:

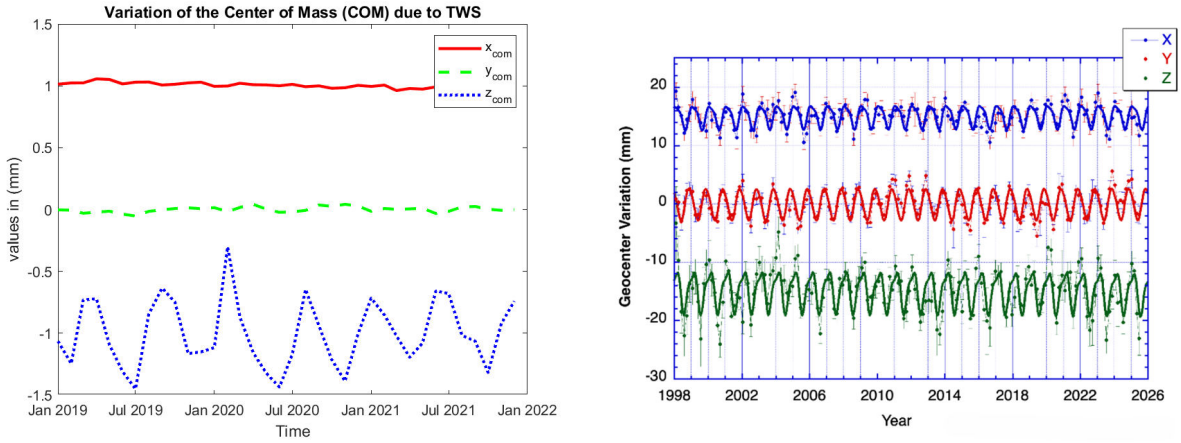

(a) COM variation by ΔTWS

(b) COM variation by SLR

Figure 5.13: Comparison between tesseroid results and JPL data (The *X* and *Z* components are vertically shifted for clarity: +1 mm and -1 mm in the left panel, and +15 mm and -15 mm in the right panel)

The comparison between the TWS-derived COM time series (January 2019–December 2021) and the JPL geocenter displacement series (1998–2026; units: mm) reveals clear differences in both amplitude and temporal structure. In the TWS-based estimate, the signal is strongly dominated by a seasonal component, with the *Z* component showing the most pronounced annual variability, while the *X* and *Y* components remain much smaller and vary around a comparatively stable baseline over the 36 month window. The JPL geocenter series exhibits a strong seasonal cycle in all three components and additionally contains more pronounced higher-frequency variability as well as longer-term variations visible across the multi-decadal record. Overall, the TWS-based COM signal emphasizes the seasonal redistribution of continental water mass, whereas the JPL product reflects geocenter motion resulting from broader mass-transport processes at the Earth system scale.

The COM amplitudes derived from the inverted ΔTWS field are likely conservative estimates of the true signal amplitude, because DDK2 filtering and Tikhonov regularization suppress striping and stabilize the inversion at the expense of attenuating part of the geophysical signal. This amplitude damping can reduce the inferred first mass moment and hence the COM displacement, particularly when compared with externally provided geocenter products. The observed differences are consistent with the underlying physical content represented by the two products. The present estimate is constructed from terrestrial water storage anomalies and therefore represents the water-mass contribution to geocenter-related variability. By contrast, the JPL geocenter displacement series represents geocenter motion associated with total mass redistribution, including contributions beyond terrestrial water (e.g., atmosphere, oceans, cryosphere), as well as longer-term solid-Earth effects such as glacial isostatic adjustment. In addition, differences in processing conventions and modelling choices can contribute to discrepancies, including the definition of the reference period, coordinate/sign conventions for the geocentric components, and the specific mapping between mass moments/COM quantities and displacement in millimetres.

6 Conclusion

Rationality and innovation of the methods

This study establishes a coherent workflow that links satellite gravity-field observations to hydrological mass variability: spherical harmonic synthesis of monthly Level-2 coefficients to potential anomalies, tesseroid-based discretization and regularized inversion to retrieve equivalent water thickness changes (ΔTWS), and subsequent derivation of a water-mass COM signal from the inferred ΔTWS field. The rationale is physically well mo-

tivated: potential anomalies are observation-domain quantities directly synthesized from spherical harmonics, and tesseroids provide a geometrically consistent mass-element representation on the sphere that is suitable for global-scale modelling. The inversion is treated as an ill-posed problem using Tikhonov regularization with an L-curve-based parameter selection. The methodological contribution is mainly integrative, supported by internal diagnostics (potential residuals and convergence behaviour), rather than algorithmically novel.

Quality and suitability of the data

The analysis uses monthly GRACE-FO Level-2 spherical harmonic solutions (GFZ RL06.1) over January 2019–December 2021 (36 months), which is sufficient to resolve seasonal variability and provide an initial assessment of consistency. Truncation to degree/order 96 provides a reasonable trade-off between resolution and noise sensitivity, and the DDK2 decorrelation filter is appropriate for suppressing correlated striping errors. The use of a $1^\circ \times 1^\circ$ observation grid for synthesized potentials together with a $4^\circ \times 4^\circ$ tesseroid model grid reduces the inversion dimensionality while retaining basin-scale structures for hydrological interpretation.

Credibility and applicability of the results

Credibility is supported by (i) a justified regularization strength via the L-curve, (ii) small potential residuals (observed minus forward-predicted) without pronounced systematic patterns, and (iii) rapid stabilization of the iterative scheme (approximately two iterations), indicating numerical stability. The ΔTWS maps show physically plausible large-scale seasonal behaviour, and the COM statistics indicate substantially larger Z variability than X/Y, consistent with dominant inter- hemispheric mass exchange at seasonal scales. The approach is most applicable to global-to- continental scales (hundreds to $>$ 1000 km) and dominant seasonal/long-wavelength signals rather than localized short-wavelength phenomena.

The limitations or issues not discussed by the author

Several limitations should be stated more explicitly to avoid overinterpretation and to improve the scientific defensibility of the report: Definition and comparability of COM/geocenter quantities. The report compares the TWS- derived COM signal to the JPL geocenter displacement series and explains differences by missing contributions (atmosphere/ocean/cryosphere, GIA). However, it should also clarify the exact mathematical quantity being compared (COM of water-mass anomaly vs. geocenter displacement vs. degree-1 coefficients) and the required convention/scale mapping between them. Without this, mismatches can partly arise from definition and normalization differences rather than only physical “missing terms”. Leakage, striping, and amplitude damping. While the report mentions striping/leakage qualitatively, the implications for ΔTWS amplitude and for COM sensitivity (first-moment sensitivity to spatial bias) could be discussed more explicitly. Regularization and decorrelation filtering can damp long-wavelength amplitudes, potentially leading to underestimation when compared with external geocenter products. Scope limitation of the three-year window. With only 36 months, conclusions about long-term trends or interannual anomalies should be phrased cautiously; the analysis is strongest for seasonal behavior and short-term consistency. If long-term comparison with JPL (multi-decadal) is discussed, the report should emphasize that the comparison is mainly qualitative unless the time periods are harmonized and processed consistently (demeaning/detrending and annual-cycle fitting).

Acknowledgement

The author acknowledges the support from Geodätisches Institut (GIK) for providing necessary resources and facilities. Additionally, the author acknowledges ICGEM (2026) and GFZ (2026) for the data provided for this study.

References

Cheng, M., Tapley, B., and Ries, J. (2010): Geocenter Variations from Analysis of SLR data. In: IAG Commission 1 Symposium 2010, Reference Frames for Applications in Geosciences (REFAG2010), 4-8 October 2010. Marne-La-Vallee, France.

Cheng, M., Ries, J. C., and Tapley, B. D. (2011): Variations of the Earth's figure axis from satellite laser ranging and GRACE. *Journal of Geophysical Research: Solid Earth* 116(B1). DOI: https://doi.org/10.1029/2010JB000850. eprint: https://agupubs.onlinelibrary.wiley.com/doi/pdf/10.1029/2010JB000850. URL: https://agupubs.onlinelibrary.wiley.com/doi/abs/10.1029/2010JB000850.

Frappart, F., Papa, F., Santos da Silva, J., Ramillien, G., Prigent, C., Seyler, F., and Calmant, S. (2013): Surface freshwater storage and dynamics in the Amazon basin during the 2003–2007 period. *Hydrological Processes* 27:367–378. DOI: 10.1002/hyp.9718.

GFZ (2026): GRACE-FO – Gravity Recovery and Climate Experiment Follow-On Mission. German Research Centre for Geosciences (GFZ). Accessed: 2026-04-06. URL: https://www.gfz.de/en/section/global-geomonitoring-and-gravity-field/projects/grace-fo-gravity-recovery-and-climate-experiment-follow-on-mission.

Grombein, T., Seitz, K., and Heck, B. (2013): Optimized formulas for the gravitational field of a tesseroid. *Journal of Geodesy* 87(7):645–660. DOI: 10.1007/s00190-013-0636-1.

Hansen, P. C., Jensen, T. K., and Rodriguez, G. (2007): An adaptive pruning algorithm for the discrete L-curve criterion. *Journal of Computational and Applied Mathematics* 198(2):483–492.

Hansen, P. C. (2000): The L-curve and its use in the numerical treatment of inverse problems. In: *Computational Inverse Problems in Electrocardiology*. Ed. by P. Johnston. WIT Press, pp. 119–142.

Heck, B. and Seitz, K. (2007): A comparison of the tesseroid, prism and point-mass approaches for mass reductions in gravity field modelling. *Journal of Geodesy* 81(2):121–136. DOI: 10.1007/s00190-006-0094-0.

Heiskanen, W. A. and Moritz, H. (1967): Physical Geodesy. W. H. Freeman & Co., San Francisco, USA.

ICGEM (2026): International Centre for Global Earth Models (ICGEM): Gravity field and GRACE/GRACE-FO products hosted at the German Research Centre for Geosciences (GFZ). Accessed: 2026-04-06. URL: https://icgem.gfz-potsdam.de/.

Kusche, J. (2007): Approximate decorrelation and non-isotropic smoothing of time-variable GRACE-type gravity field models. *Journal of Geodesy* 81(11):733–749. DOI: 10.1007/s00190-007-0143-3.

Moritz, H. (1980): Geodetic Reference System 1980. *Bulletin Géodésique* 54(3):395–405. DOI: 10.1007/BF02521480.

Sun, Y., Riva, R., and Ditmar, P. (2016): Optimizing estimates of annual variations and trends in geocenter motion and J2 from a combination of GRACE data and geophysical models. *Journal of Geophysical Research: Solid Earth* 121. DOI: 10.1002/2016JB013073.

Swenson, S., Chambers, D., and Wahr, J. (2008): Estimating geocenter variations from a combination of GRACE and ocean model output. *Journal of Geophysical Research: Solid Earth* 113(B8):B08410. DOI: 10.1029/2007JB005338.

Velicogna, I. (2009): Increasing rates of ice mass loss from the Greenland and Antarctic ice sheets revealed by GRACE. *Geophysical Research Letters* 36(19). DOI: 10.1029/2009GL040222.

Wahr, J., Molenaar, M., and Bryan, F. (1998): Time variability of the Earth's gravity field: Hydrological and oceanic effects and their possible detection using GRACE. *Journal of Geophysical Research: Solid Earth* 103(B12):30205–30229.

Groundwater Storage Estimation by Combining GRACE and GLDAS Data across the Continent Africa

Vishnu Njaneswar[1]

1 Remote Sensing and Geoinformatics Master of Science (M.Sc.), KIT, Germany
E-Mail: uikco@student.kit.edu

Abstract

This study investigates terrestrial water storage (TWS) and groundwater storage variations across Africa by integrating GRACE/GRACE-FO satellite gravimetry with GLDAS hydrological model outputs. Using the Wahr et al. (1998) formulation, residual GRACE spherical harmonic coefficients are converted to equivalent water height (EWH), enabling estimation of large-scale water storage anomalies over the continent. GRACE-derived TWS successfully captures seasonal and interannual hydrological variability across diverse African climates. Equatorial and central Africa, particularly the Congo Basin, exhibit strong positive water storage anomalies linked to intense rainfall and groundwater recharge, whereas northern and southern Africa show smaller storage variations and periodic depletions associated with arid conditions and reduced precipitation. A comparison of DDK2 and DDK5 filtered solutions highlights the trade-off between signal preservation and noise suppression: DDK2 yields smoother, more stable large-scale signals with reduced striping, while DDK5 preserves finer spatial detail but introduces higher short-wavelength noise. Integration with GLDAS permits separation of near-surface components (soil moisture, runoff, canopy water storage) from total GRACE-observed storage, with residual signals providing estimates of groundwater variability, particularly in humid equatorial regions where recharge dominates. The 2003–2024 comparison reveals stronger, more localized hydrological anomalies in recent years, suggesting increasing climate variability and shifting precipitation patterns over Africa. These findings underscore the value of long-term satellite observations for monitoring water resources and understanding large-scale hydrological processes under changing climatic conditions. Overall, the GRACE-GLDAS framework offers a robust approach for continental-scale groundwater assessment in data-sparse regions. Future work should aim to enhance groundwater spatial resolution via mascon solutions and advanced filtering, conduct basin-scale analyses for major basins (Nile, Congo, Niger, Zambezi), and incorporate climate indices, precipitation data, and machine learning to improve interpretation of long-term groundwater dynamics. Anticipated successor mission architecture for GRACE is expected to reduce correlation-related errors (Massotti et al., 2022).

Keywords GRACE · GLDAS · TWS · Africa

KIT Scientific Working Papers
Issue Number 270
ISSN: 2194-1629
DOI: 10.5445/IR/1000191188
Online: June 2026

This document is licensed under the Creative Commons Attribution – Share Alike 4.0 International License (CC BY-SA 4.0):
https://creativecommons.org/licenses/by-sa/4.0/deed.en

1 Introduction

In this study, Total Water Storage (TWS) variations over the African continent are estimated by integrating satellite gravimetry data from the GRACE mission and GRACE-FO mission with land surface model outputs from the Global Land Data Assimilation System (GLDAS, 2025).

The GRACE and GRACE-FO missions provide temporal variations in the Earth's gravity field in terms of spherical harmonic coefficients, which reflect mass redistribution within the Earth system. These variations are primarily driven by hydrological processes such as groundwater storage, soil moisture, and surface water changes. However, the observed gravity signal includes both direct mass effects and the elastic deformation of the Earth.

To accurately convert gravity variations into surface mass changes, the Wahr et al. (1998), approach is applied. This method incorporates load Love numbers to correct for Earth's elastic response to surface loading, allowing the derivation of Equivalent Water Height (EWH), which represents Total Water Storage anomalies.

In addition, GLDAS model outputs are used to estimate individual hydrological components such as soil moisture and canopy water storage. By combining GRACE-derived TWS with GLDAS components, it is possible to isolate groundwater storage variations, which are otherwise not directly observable.

This combined approach provides a comprehensive understanding of large-scale hydrological changes across Africa, leveraging both observation-based and model-based datasets.

2 Theoretical Aspects

Several fundamental concepts are involved in the estimation of Total Water Storage (TWS) using the Wahr approach, which is based on analyzing temporal variations in the Earth's gravity field provided by the GRACE mission and GRACE-FO mission in terms of spherical harmonics. These gravity variations primarily reflect mass redistribution due to hydrological processes such as changes in soil moisture, surface water, and groundwater; however, the observed signal also includes the elastic response of the Earth to surface loading. To address this, the Wahr formulation incorporates load Love numbers, which account for lithospheric deformation and internal mass redistribution, ensuring that the derived signal represents true surface mass change. The resulting TWS is expressed as Equivalent Water Height, providing a physically meaningful measure of water storage variations. In addition, data from the GLDAS are used to estimate near-surface hydrological components such as soil moisture and canopy water, and by combining these with GRACE-derived TWS, groundwater storage variations can be isolated, enabling a comprehensive assessment of large-scale hydrological changes over regions such as Africa.

2.1 Spherical Harmonic Synthesis (SHS)

Spherical harmonic representation of the gravitational potential $V(r,\varphi,\lambda)$ is given in Equation (2.1). Spherical Harmonic Synthesis is the forward computation of a function on or outside the sphere from a series of surface spherical harmonics (Heiskanen and Moritz, 1967; Tsoulis, 1999). The spherical harmonic coefficients derived from GRACE level-2 data is used to express the gravity field of the Earth.

$$V(P) = \frac{GM}{r}\sum_{n=0}^{\infty}\left(\frac{R}{r}\right)^{n}\sum_{m=0}^{n}(\bar{C}_{nm}\ \cos m\lambda + \bar{S}_{nm}\ \sin m\lambda)\bar{P}_{nm}(\sin\varphi) \tag{2.1}$$

where,

GM : Geocentric gravitational constant

R : Radius of the reference sphere

$\bar{C}_{nm}, \bar{S}_{nm}$: Fully normalised spherical harmonic coefficients of degree n and order m

$\bar{P}_{nm}$: Fully normalised Legendre functions of degree n and order m

φ and λ: geocentric latitude and longitude

r: geocentric distance (radius).

2.2 Degree and Error degree Variances

The degree variance quantifies the amplitudes of the spherical harmonic coefficients, which vary across different degrees. The sum of the squared coefficients expresses the overall energy in the signal as shown in Equation (2.2).

$$C_n^2(\bar{C}_{nm}, \bar{S}_{nm}) = \sum_{m=0}^{n} (\bar{C}_{nm}^2 + \bar{S}_{nm}^2)\,. \tag{2.2}$$

This helps to understand the distribution of signal intensity through the frequency range. Degree variance for the coefficients obtained for this study has been analysed, which shows that the signal has higher energy in the long wavelength part and it drops in shorter wavelength part of the signal. This shows that there is a higher concentration of signal at lower degrees compared to higher degrees. The plots for degree variance for all the months are similar with marginal variations, so an example plot for January, 2022 is shown in Figure 2.1. The degree variance is non dependent on $P(r, \varphi, \lambda)$.

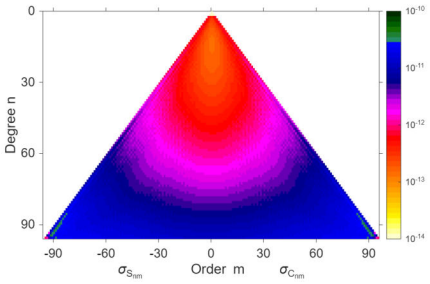

(a) Accuracy of the coefficient

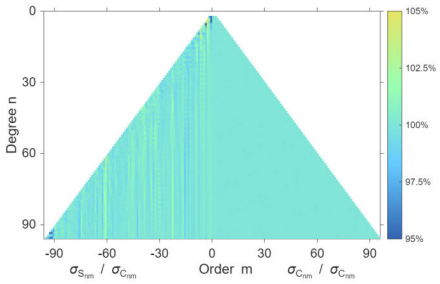

(b) Relative accuracy of the coefficients

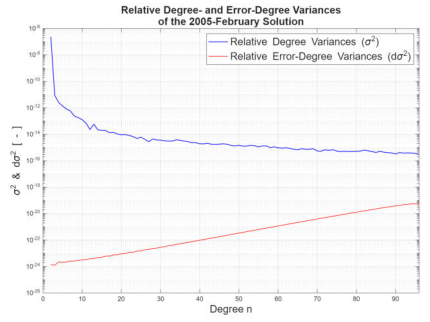

(c) Degree and error degree variance

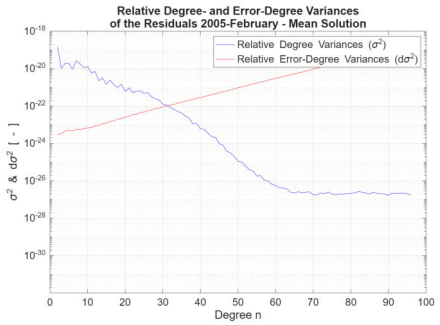

(d) Relative Degree and error degree variance

Figure 2.1: Coefficients DDK2 February 2005

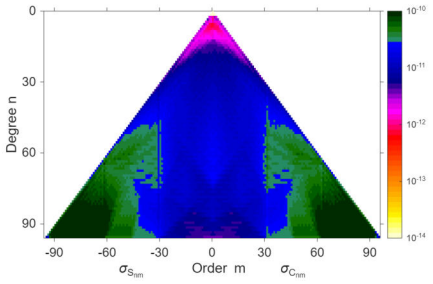

(a) Accuracy of the coefficient

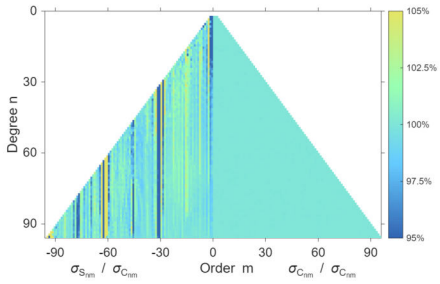

(b) Relative accuracy of the coefficients

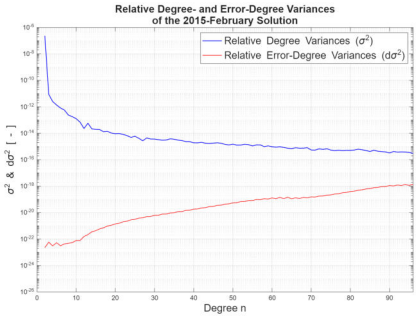

(c) Degree and error degree variance

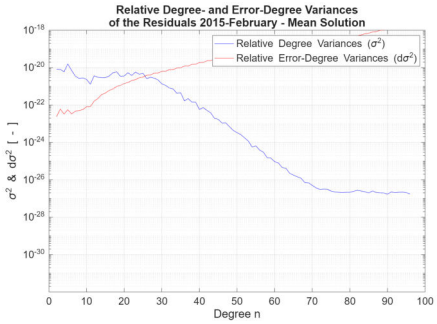

(d) Relative Degree and error degree variance

Figure 2.2: Coefficients DDK2 February 2015

2.3 TWS from WAHR approach

Variations in terrestrial water storage over Africa cause measurable temporal changes in the Earth's gravity field. These gravity variations are observed by GRACE and expressed as residual fully normalised spherical harmonic coefficients $\Delta\bar{C}_{nm}$ and $\Delta\bar{S}_{nm}$, obtained after removing the long-term mean field. Following the formulation of Wahr et al. (1998), the surface mass change can be recovered from the gravity field by accounting for Earth's elastic response using load Love numbers k_n. The equivalent water height (EWH), representing Total Water Storage (TWS) anomaly, is computed as:

$$\Delta h(\theta,\lambda) = \frac{R\rho_E}{3\rho_w}\sum_{n=0}^{N}\frac{2n+1}{1+k_n}\sum_{m=0}^{n}\left(\Delta\bar{C}_{nm}\cos(m\lambda)+\Delta\bar{S}_{nm}\sin(m\lambda)\right)\bar{P}_{nm}(\sin\varphi) \tag{2.3}$$

where,

- ρ_E is the mean density of the Earth,
- ρ_w is the density of water,
- k_n are degree-dependent load Love numbers,
- N is the maximum spherical harmonic degree (typically $N = 96$ for GFZ RL06 solutions).

The resulting field $\Delta h(\theta,\lambda)$ represents vertically integrated Total Water Storage anomalies in units of equivalent water thickness (mm).
Since GRACE measures total mass change, the groundwater storage anomaly over Africa can be estimated by removing the hydrological components provided by GLDAS:

$$\Delta GW = \Delta TWS_{\text{GRACE}} - (\Delta SM_{\text{GLDAS}} + \Delta CW_{\text{GLDAS}} + \Delta SWE_{\text{GLDAS}}) \tag{2.4}$$

where,

- ΔSM is soil moisture storage,

- ΔCW is canopy water storage,
- ΔSWE is snow water equivalent (generally small over most of Africa).

For most African regions, snow contribution is negligible, and groundwater variations are primarily obtained from the residual between GRACE-derived TWS and GLDAS soil moisture plus canopy water storage.
Due to correlated errors in the spherical harmonic coefficients, Gaussian spatial filtering (300–500 km radius) is applied prior to regional averaging over the African continent or major river basins. The final TWS time series describes seasonal hydrological variability and long-term water storage trends across Africa.

2.4 Load Love Number and Earth elastic response

Surface mass redistribution, such as seasonal water storage variations over the African continent, produces not only a direct gravitational attraction but also an elastic deformation of the solid Earth. This deformation modifies the gravitational potential and must be considered when converting GRACE gravity variations into surface mass changes.
In the Wahr et al. (1998) formulation, the recovery of surface mass anomalies from GRACE residual spherical harmonic coefficients requires rescaling by this factor:

$$\frac{3\rho_E}{R\rho_w}\frac{2n+1}{1+k_n} \tag{2.5}$$

The load Love number $(k_n)$is degree-dependent and reflects the elastic structure of the Earth. It quantifies the additional gravitational potential generated by internal mass redistribution and surface deformation caused by loading.
The physical interpretation of k_n is as follows:
When a surface load (e.g., accumulated water mass) is applied, the lithosphere subsides elastically. The mantle responds according to its rheological properties. This deformation alters both the geometry of the Earth's surface and the internal mass distribution. The total observed gravity change is therefore the sum of:

- Direct gravitational attraction of the surface load,
- Indirect gravitational effect due to Earth deformation.

The degree dependence of k_n reflects the spatial scale of the loading:

- Low degrees (large spatial scales) involve deeper mantle response and typically exhibit larger k_n values.
- High degrees (short wavelengths) correspond to shallower responses and smaller k_n values.

Typical values range from approximately 0.3 at low degrees to values approaching zero at high degrees.
In the computation of Total Water Storage (TWS) over Africa, the inclusion of load Love numbers ensures that the inferred equivalent water height represents the true surface mass anomaly rather than the combined effect of loading and deformation. Standard tabulated k_n values derived from elastic Earth models (e.g., PREM-based models) are used up to the maximum degree of the GRACE solutions (typically degree 96).
Neglecting load Love numbers would lead to systematic underestimation of surface mass changes and biased TWS amplitudes, particularly at large spatial scales. Therefore, their inclusion is essential for physically consistent hydrological mass recovery using the Wahr approach.

2.5 DDK Filter comparison

The DDK filters differ mainly in their strength of smoothing and decorrelation, where lower-order filters like DDK1 and DDK2 apply very strong smoothing that effectively removes striping noise but significantly reduces the signal amplitude, while intermediate filters such as DDK3 and DDK4 provide a better balance by suppressing

north–south correlated errors while still preserving most of the geophysical signal, making them the most suitable for applications like total water storage studies; in contrast, higher-order filters like DDK5 to DDK8 apply progressively weaker smoothing, which retains more spatial detail and signal variability but allows increasing levels of noise and striping to remain in the data, so the choice of filter ultimately depends on the trade-off between noise reduction and signal preservation, as emphasized in the decorrelation and non-isotropic smoothing approach described by Kusche (2007) and Kusche et al. (2009).

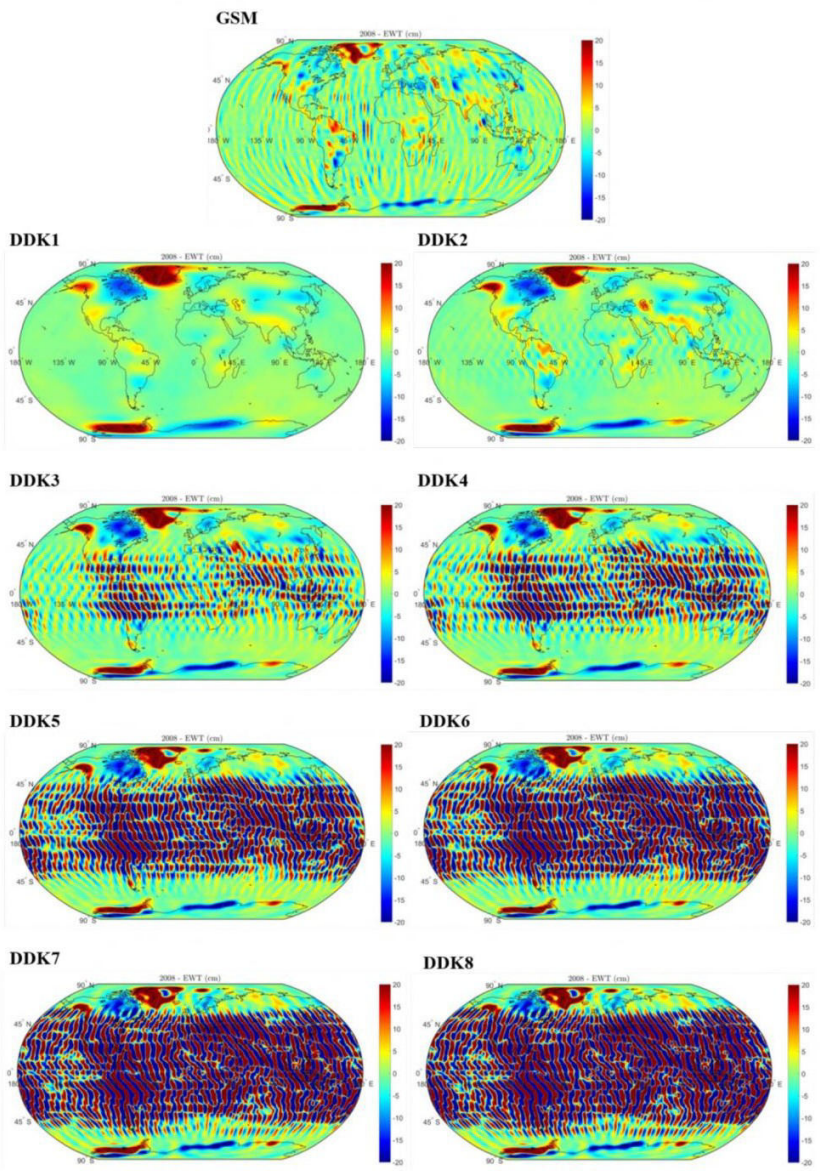

Figure 2.3: Comparison of DDK filters over EWH solutions of GRACE/GRACE-FO Level-2 version-06 data created with the long term average model from JPL data (NİL and DOĞANALP, 2023)

3 Used Data in the study area Africa

This study utilizes both general geographic information and satellite-based hydrological datasets for Africa. Background data on Africa's topography, seasonal patterns, climatic conditions, and climate variability were collected to understand the hydro-climatic characteristics of the study area. Satellite data from GRACE (Gravity Recovery and Climate Experiment) were used to obtain terrestrial water storage (TWS) anomalies. In addition, GLDAS

(Global Land Data Assimilation System) data were used to extract land surface components such as soil moisture and canopy water storage. Groundwater storage variations were estimated by subtracting GLDAS-derived components from GRACE-derived total water storage

3.1 General study about Africa

Africa is the second-largest continent in the world, extending across the equator and covering diverse climatic and physiographic zones. Its geographical setting strongly influences regional climate variability, hydrological processes, and seasonal rainfall distribution. The continent's topography ranges from extensive plateaus and highlands in East Africa to vast desert regions in the north and semi-arid zones in the south. Major river systems, including the Nile, Congo, Niger, and Zambezi basins, play a crucial role in regional water balance and socio-economic activities.

Climatically, Africa exhibits distinct seasonal patterns that vary by region. Northern Africa is predominantly characterized by a Mediterranean climate with mild wet winters and hot dry summers, while Central Africa experiences equatorial conditions with year-round rainfall and high humidity. East Africa typically presents bimodal rainfall regimes, including long and short rainy seasons, whereas Southern Africa experiences a marked contrast between hot rainy summers and cooler dry winters. These seasonal variations are largely governed by the migration of the Intertropical Convergence Zone (ITCZ), regional monsoon systems, and ocean–atmosphere interactions.

The general maps included in this study (see Figure 3.1) illustrates the continent's topographic features, regional zonation, major river basins, and spatial distribution of precipitation. Together, these geographic and climatic characteristics provide the foundational framework necessary for understanding hydrological variability and large-scale water storage changes across Africa.

Table 3.1: Seasonal Patterns Across African Regions

Region	**Countries (examples)**	**Main Seasons**	**Rainfall Pattern**	**Temperature Characteristics**
Southern Africa	South Africa, Botswana	Hot rainy summer; Cool dry winter	Rain mainly Oct–Mar; Dry May–Aug	Hot summers; cooler winters
East Africa	Kenya, Tanzania	Long rains; Short rains; Dry seasons	Long rains: Mar–May; Short rains: Oct–Dec	Warm year-round; rainfall defines seasons
Central Africa	DR Congo, Congo	Rainy and dry seasons (often two of each)	Rainfall spread across the year; two peaks common	Hot and humid year-round
North Africa	Egypt, Algeria	Mild wet winter; Hot dry summer	Rain mainly Nov–Mar; Very dry summers	Very hot summers; mild winters

3.2 GRACE Data

The level-2 data used in this study is the monthly solutions from GRACE-FO mission. It includes fully normalized spherical harmonic coefficients that assist in the computation of gravitational potential of the Earth, generated by release 6.1 of Geoforschungszentrum (ICGEM, 2026) compiled by ICGEM. For consistency with the hydrological datasets, the GRACE data were processed and interpolated onto a $0.25^\circ \times 0.25^\circ$ spatial grid. The dataset provides near-global coverage, extending approximately from 89.75°N to 89.75°S and covering all longitudes (180°W to 180°E), enabling regional to continental-scale terrestrial water storage analysis.

(a) Topography of Africa (Wikipedia, 2026)

(b) Zones in Africa (Worldatlas, 2026)

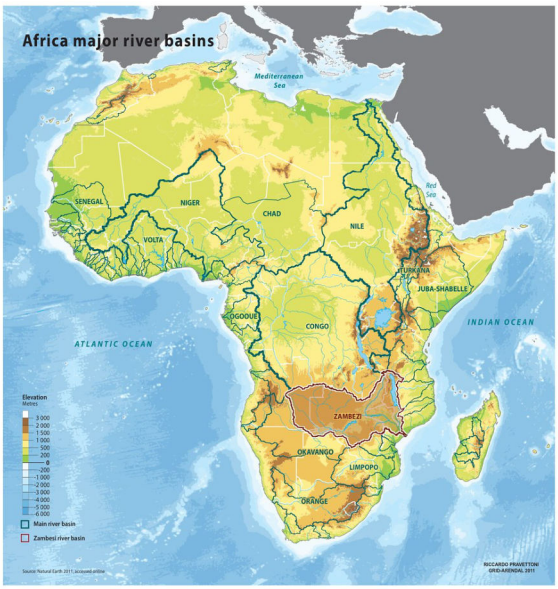

(c) Major river basins in Africa (Gridarendal, 2026)

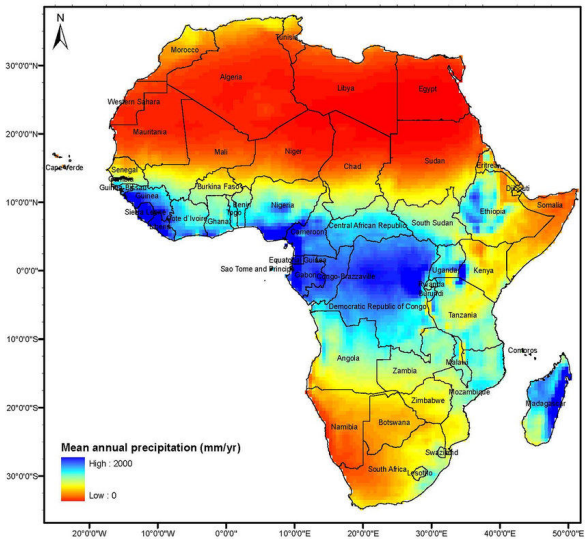

(d) Precipitation map of Africa (Researchgate, 2026)

Figure 3.1: Some General Maps of Africa

3.3 GLDAS Data

The Level-3 data used in this study are monthly land surface variables derived from the Global Land Data Assimilation System (GLDAS, 2025). GLDAS integrates satellite and ground-based observational data products with advanced land surface modeling techniques to generate optimal estimates of terrestrial water and energy fluxes. The dataset employed in this study is produced by the National Aeronautics and Space Administration (NASA) Goddard Space Flight Center, under the GLDAS Version 2.1 framework. The (Rodell et al., 2004; GLDAS, 2025) data are available at a $0.25^\circ \times 0.25^\circ$ spatial resolution, providing gridded land surface parameters such as soil moisture, evapotranspiration, snow water equivalent, and total water storage. The dataset offers global land-surface coverage between approximately 60°S and 90°N, excluding major ocean areas.

4 Methodology Overview

The methodology integrates GRACE and GLDAS datasets to estimate terrestrial water storage and groundwater variations. Monthly GRACE spherical harmonic coefficients were processed to obtain temporal variations, which were further used to derive gravitational potential changes, geoid undulation, and terrestrial water storage (TWS). Simultaneously, GLDAS land surface parameters, including soil moisture, runoff, and canopy water storage, were processed to obtain GLDAS-based water storage components. Groundwater storage variations were then estimated by subtracting GLDAS-derived surface water components from GRACE-derived TWS. For spatial consistency, both GRACE and GLDAS datasets were processed on a common spatial grid of $0.25^\circ \times 0.25^\circ$, where each grid cell represents approximately 25-28 km at the Equator (varying slightly with latitude). This common grid coverage enables uniform spatial representation and accurate pixel-wise comparison between the two datasets across the study area.

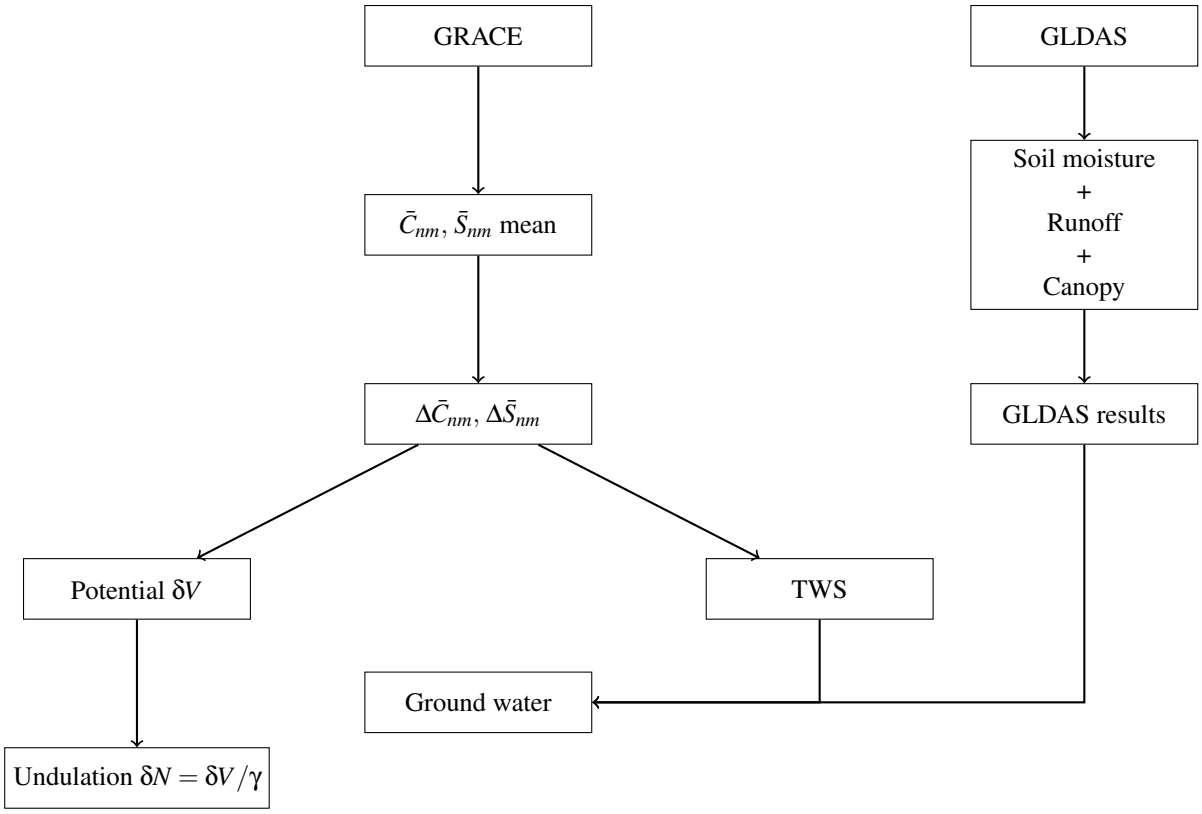

Figure 4.1: Flow chart of Methodology

5 Results and Discussion

The results obtained from GRACE/GRACE-FO and GLDAS datasets were analysed to investigate terrestrial water storage (TWS) and groundwater storage variability across the African continent. The analysis was performed using spherical harmonic synthesis together with the Wahr et al. (1998) approach for converting GRACE residual spherical harmonic coefficients into equivalent water height (EWH) anomalies.
The generated TWS fields represent vertically integrated water storage variations including groundwater, soil moisture, runoff, and surface water contributions. The results include statistical evaluation of long-term TWS behaviour, spatial comparison of monthly hydrological variations, and groundwater estimation through the integration of GRACE and GLDAS datasets.

5.1 Statistics of Total Water Storage (2003–2025)

The statistical analysis of Total Water Storage (TWS) anomalies from 2003 to 2025 is presented in Figure 5.1. The statistics include maximum, minimum, mean, RMS, and STD of the TWS variations over the African continent. The results show clear temporal variability in terrestrial water storage across the study period. While several years exhibit moderate seasonal oscillations, the period around 2024 shows significantly larger variations in both positive and negative anomalies. The maximum TWS values increase considerably during this period, while the minimum values indicate stronger depletion events compared to earlier years.
The larger spread between maximum and minimum anomalies in 2024 suggests intensified hydrological variability across Africa. This behaviour may be associated with stronger climatic fluctuations, variations in precipitation intensity, and regional hydrological extremes. The mean and median TWS values also indicate noticeable deviations during this period compared to the long-term average behaviour.
Based on these observations, the year 2024 was selected for detailed monthly analysis and comparison, since it represents a period of pronounced hydrological variability and strong spatial contrasts in terrestrial water storage.

5.2 GRACE Results

5.2.1 Monthly TWS Variations for 2024

The first part of the GRACE results presents the spatial distribution of Total Water Storage (TWS) anomalies for each month of the year 2024 (January–December), derived from CSR RL06 solutions using the DDK2 and

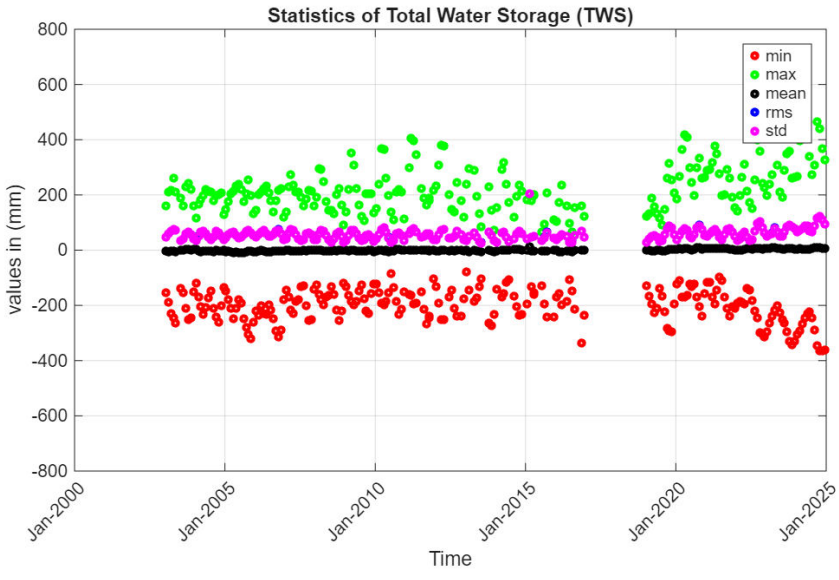

Figure 5.1: Statistics TWS (2003-2025)

DDK5 filters. The monthly TWS anomaly maps obtained using the DDK2 filter are shown in Figure 5.2, while the corresponding DDK5-filtered results are presented in Figure 5.3.

The monthly maps illustrate the seasonal evolution of terrestrial water storage across the African continent. As shown in Figures 5.2 and 5.3, a consistent spatial pattern is observed, where equatorial and central African regions exhibit relatively higher positive TWS anomalies, while southern regions show stronger variability with alternating positive and negative anomalies.

During the early months (January–March), moderate positive TWS values are observed in central Africa (Figure (5.2a–c) and Figure (5.3a–c)), indicating water accumulation associated with seasonal rainfall. As the year progresses towards mid-year (June–August), a shift in spatial distribution occurs, with increased water storage in northern and equatorial regions due to the migration of the Intertropical Convergence Zone (ITCZ), as visible in Figure (5.2f–h) and Figure (5.3f–h).

In the later months (September–December), strong positive anomalies are visible in central and western Africa, while southern regions exhibit negative anomalies, indicating water depletion (Figure (5.2i–l) and Figure (5.3i–l)). This reflects the seasonal hydrological cycle governed by precipitation variability, evapotranspiration, and basin-scale hydrological processes.

The comparison between Figure 5.2 (DDK2) and Figure 5.3 (DDK5) shows that DDK2 provides smoother large-scale hydrological patterns, whereas DDK5 preserves more local spatial details but contains increased short-wavelength variability.

Additional results are provided in the Appendix.

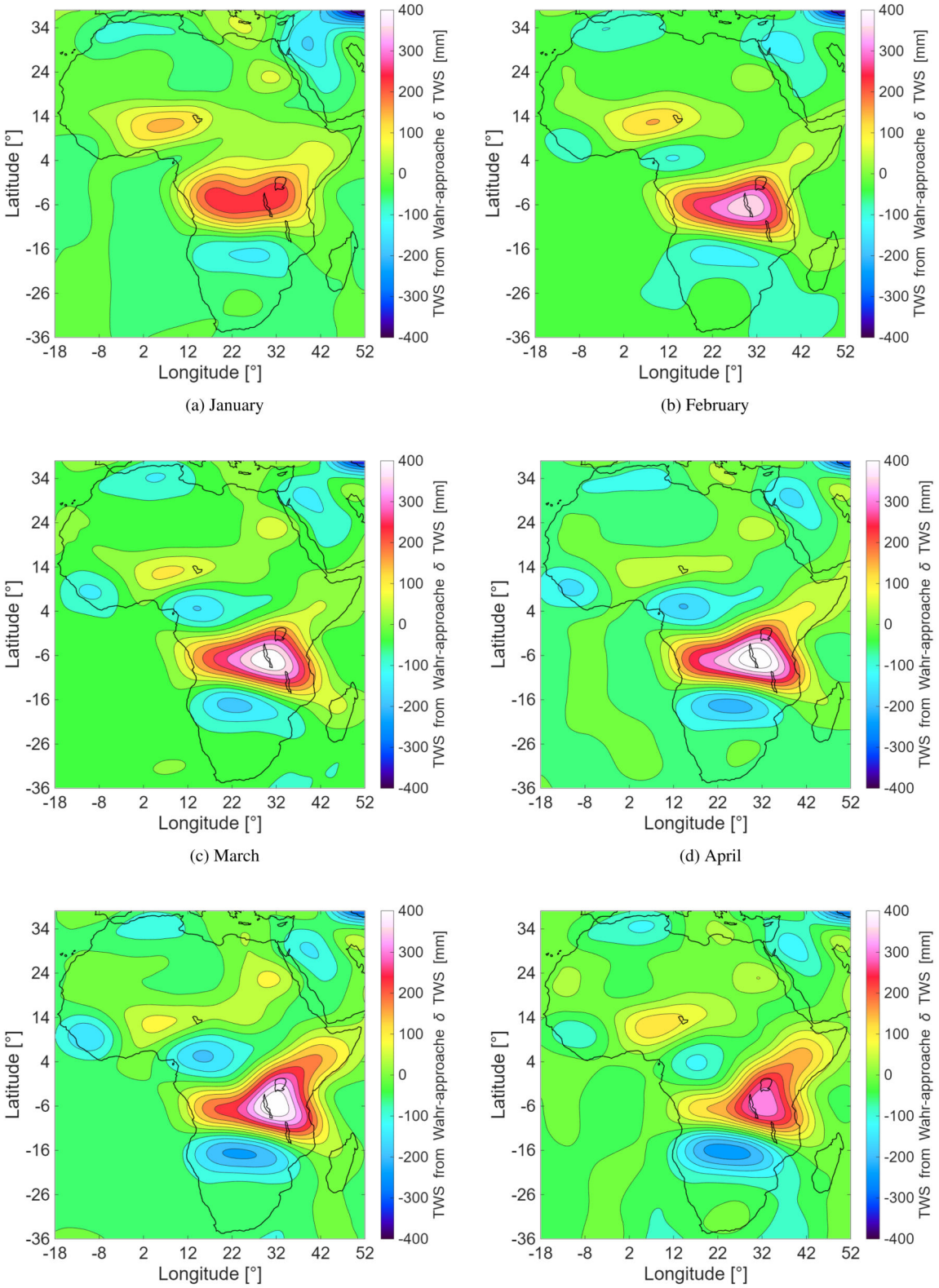

(a) January

(b) February

(c) March

(d) April

Figure 5.2: TWS CSR DDK2 2024 (January until June)

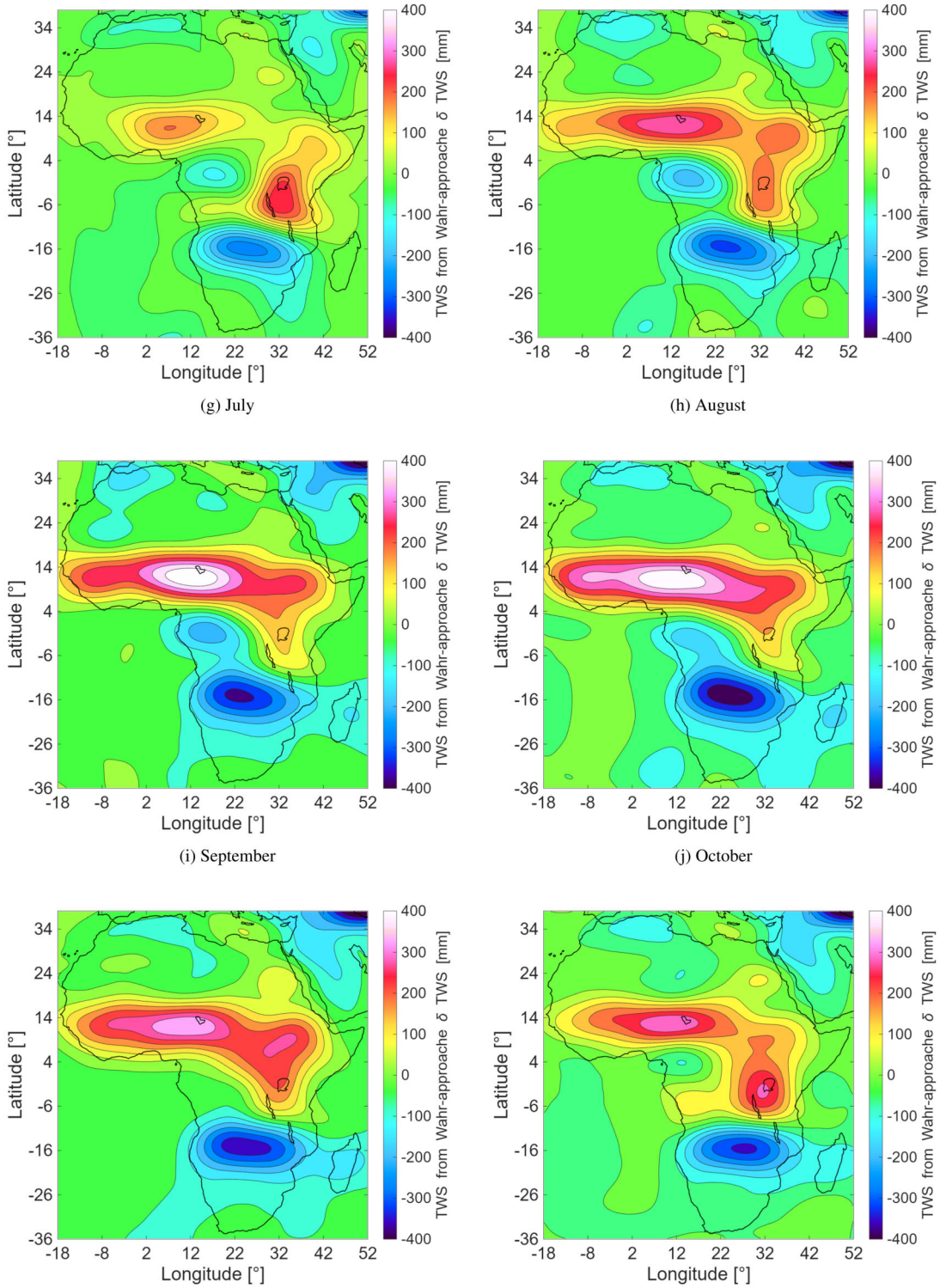

(g) July (h) August

(i) September (j) October

Figure 5.2: TWS CSR DDK2 2024 (July until December)

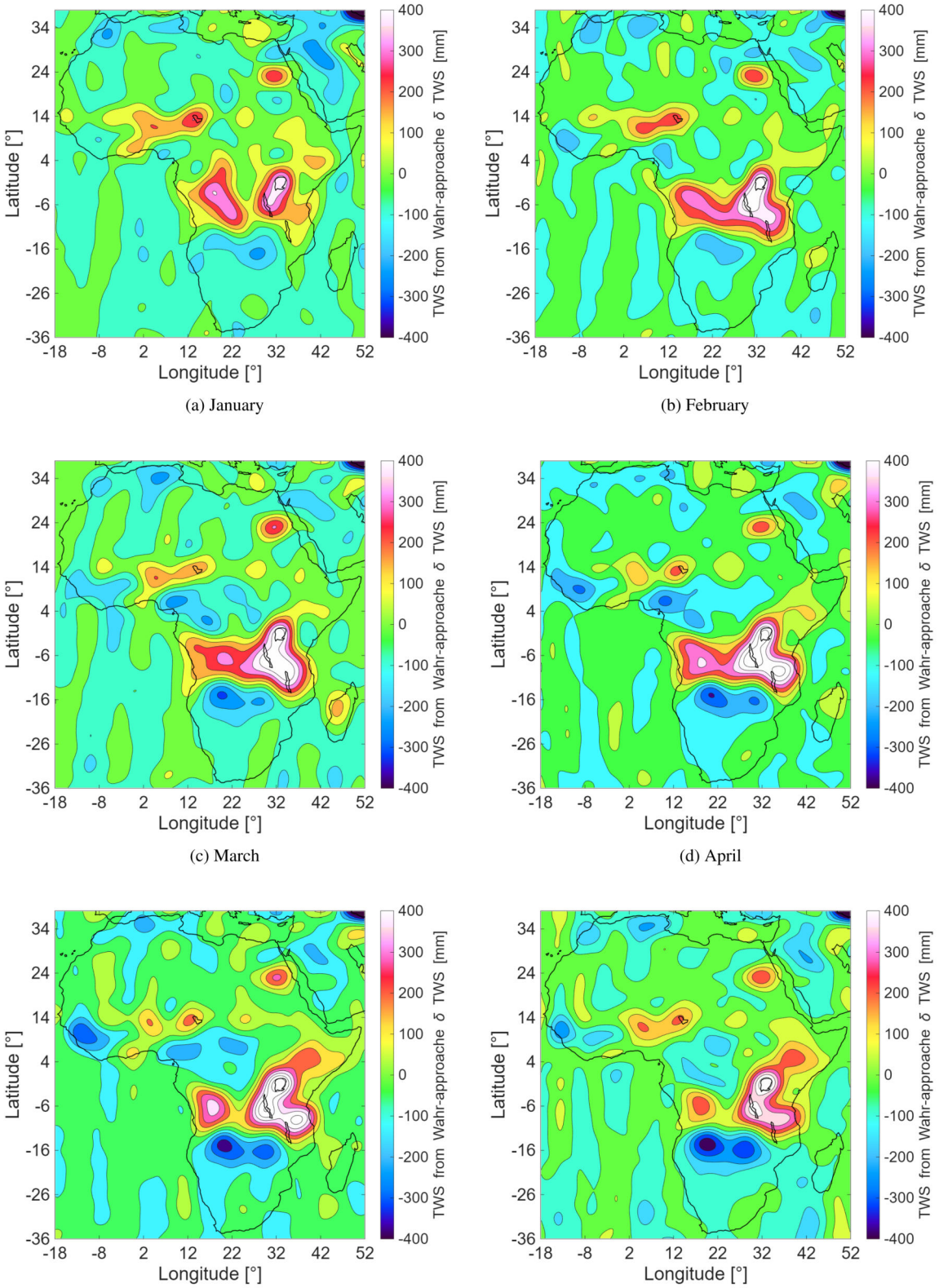

(a) January (b) February

(c) March (d) April

Figure 5.3: TWS CSR DDK5 2024 (January until June)

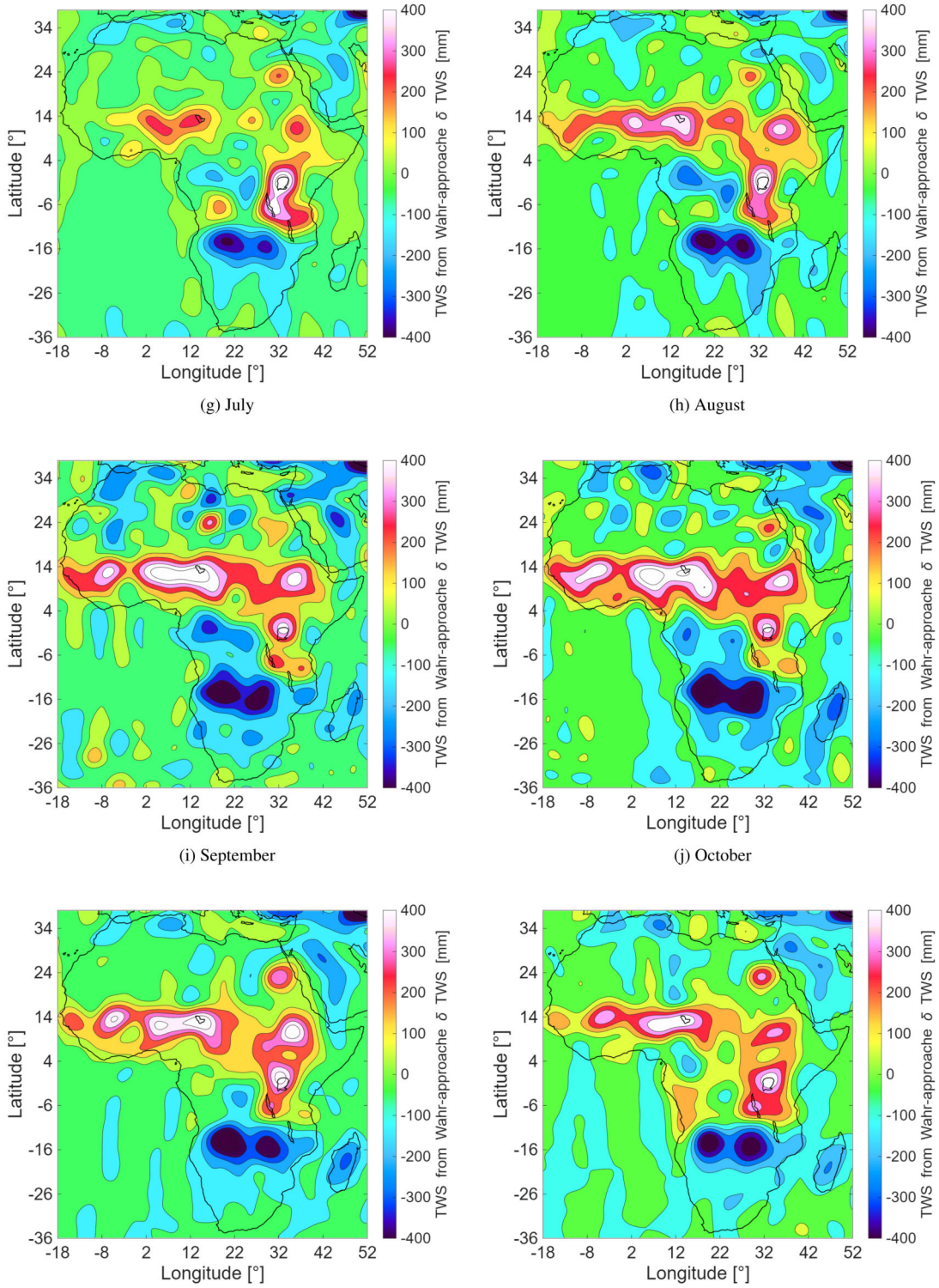

(g) July (h) August

(i) September (j) October

Figure 5.3: TWS CSR DDK5 2024 (July until December)

5.2.2 Comparison of March and August (2003 vs 2024)

The second part of the analysis compares TWS anomalies for March and August in the years 2003 and 2024. The comparison obtained using the DDK2 filter is shown in Figure 5.4, while the DDK5-filtered comparison is presented in Figure 5.5.

March represents a transitional hydrological period, while August corresponds to peak seasonal conditions in many African regions. In March 2003 (Figure 5.4a and Figure 5.5a), the TWS distribution shows relatively weaker

positive anomalies with a more uniform spatial pattern. In contrast, March 2024 (Figure 5.4c and Figure 5.5c) exhibits stronger and more localized positive anomalies, particularly in central Africa, indicating increased water storage.

A more pronounced difference is observed in August. In August 2003 (Figure 5.4b and Figure 5.5b), the TWS anomalies are moderate and spatially diffused. However, in August 2024 (Figure 5.4d and Figure 5.5d), strong positive anomalies dominate equatorial and western Africa, while significant negative anomalies appear in southern regions. This indicates enhanced hydrological contrasts between regions.

These results highlight clear interannual variability in terrestrial water storage over the period 2003–2024. The increased amplitude of anomalies observed in Figures 5.4 and 5.5 for 2024 compared to 2003 suggests changes in precipitation patterns, climate variability, and possible long-term hydrological trends across the African continent.

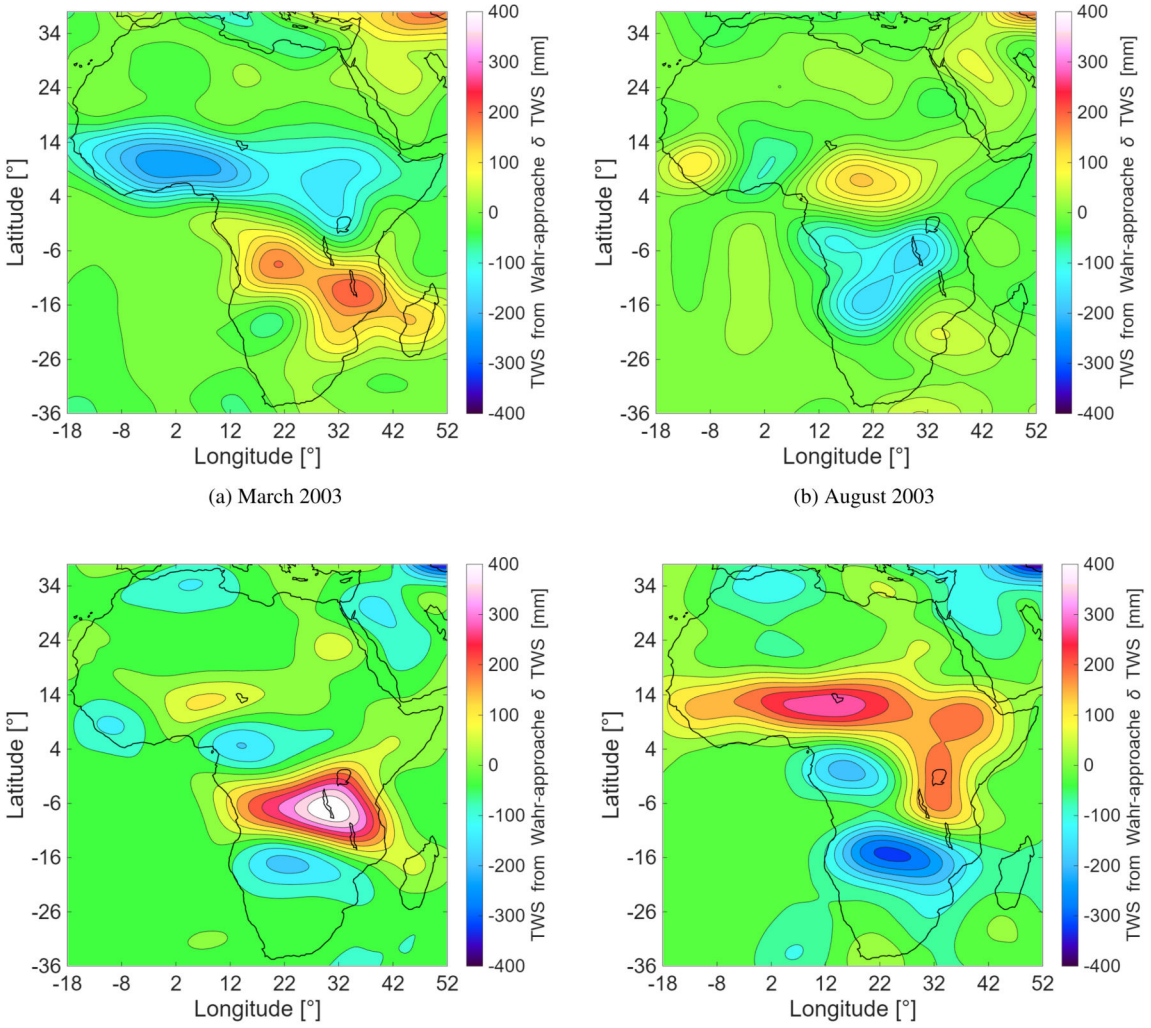

(a) March 2003

(b) August 2003

Figure 5.4: TWS CSR DDK2

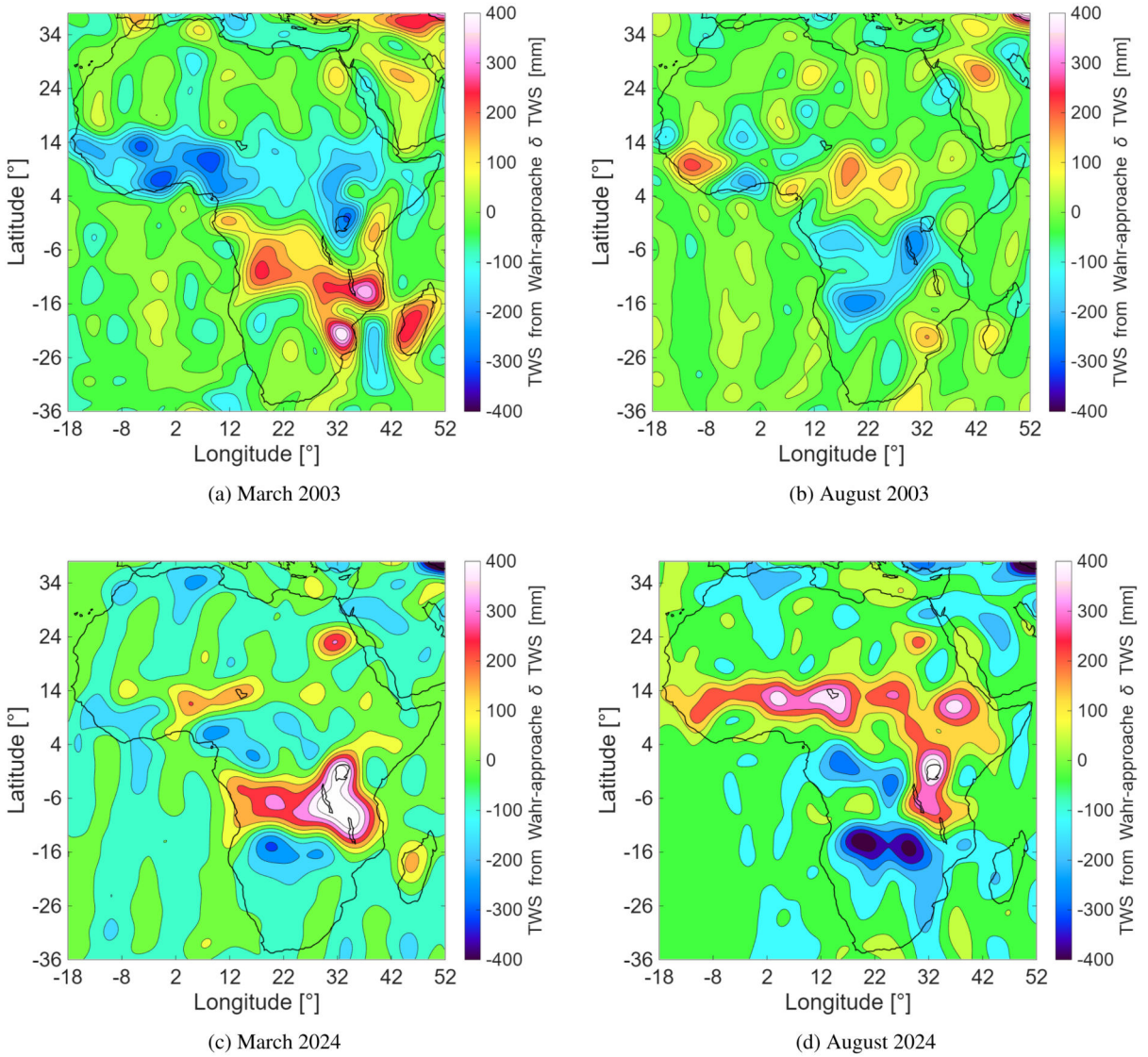

(a) March 2003

(b) August 2003

(c) March 2024

(d) August 2024

Figure 5.5: TWS CSR DDK5

5.3 GLDAS Results

The GLDAS-derived hydrological components used in this study are presented in Figure 5.6. The figure includes the spatial distribution of mean Equivalent Water Height (EWH), temporal variations in soil moisture, runoff behaviour, and global average EWH derived from GLDAS data for the period 2003–2024.

Specifically, Figure 5.6a shows the mean EWH distribution over Africa, Figure 5.6b illustrates the temporal behaviour of soil moisture, Figure 5.6c presents runoff variations, and Figure 5.6d displays the global average EWH derived from GLDAS. These results provide important information about surface hydrological processes and support the interpretation of GRACE-derived total water storage anomalies and groundwater variations across the African continent.

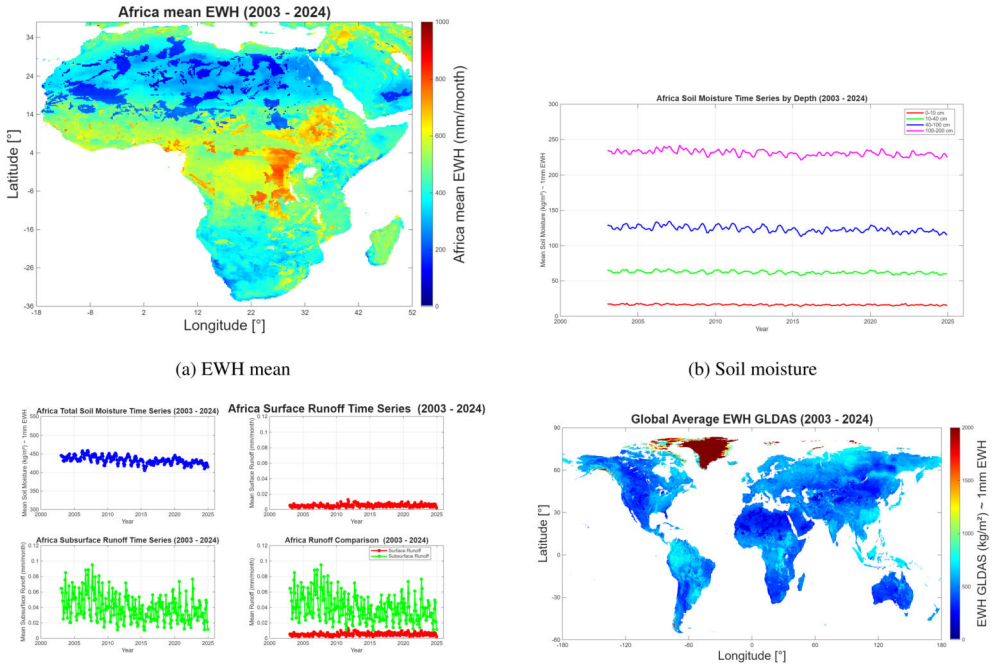

(a) EWH mean

(b) Soil moisture

(c) Soil runoff

(d) Global EWH

Figure 5.6: GLDAS Results

5.3.1 GLDAS Results: Monthly Variations for 2024

The GLDAS results provide spatial distributions of key hydrological components, particularly soil moisture and runoff, for each month of 2024. The monthly maps are presented in Figure 5.7, where each subfigure contains both soil moisture and runoff distributions for the corresponding month.

The monthly soil moisture maps in Figure 5.7 show a clear seasonal pattern across the African continent. Higher soil moisture values are observed in equatorial and central Africa throughout the year, reflecting persistent rainfall and humid climatic conditions. In contrast, northern Africa and parts of southern Africa exhibit consistently low soil moisture, corresponding to arid and semi-arid climatic zones.

During the early months of 2024 (January–March), moderate soil moisture is observed in central Africa (Figure 5.7a–c), while southern regions begin to show decreasing values, indicating the end of the rainy season. As the year progresses towards mid-year (June–August), soil moisture increases in northern and equatorial regions (Figure 5.7f–h) due to the northward migration of the Intertropical Convergence Zone (ITCZ).

In the later months (September–December), soil moisture decreases in northern regions and increases again in southern Africa (Figure 5.7i–l), reflecting the southward shift of the ITCZ and the onset of the rainy season in southern latitudes.

The runoff patterns shown in Figure 5.7 follow a similar seasonal trend but are more spatially concentrated. High runoff values are observed mainly in regions experiencing intense rainfall, particularly in central and western Africa, while desert regions such as the Sahara exhibit very low runoff values throughout the year.

Overall, the seasonal evolution shown in Figure 5.7 demonstrates strong variability in hydrological components that directly influence terrestrial water storage observed from GRACE.

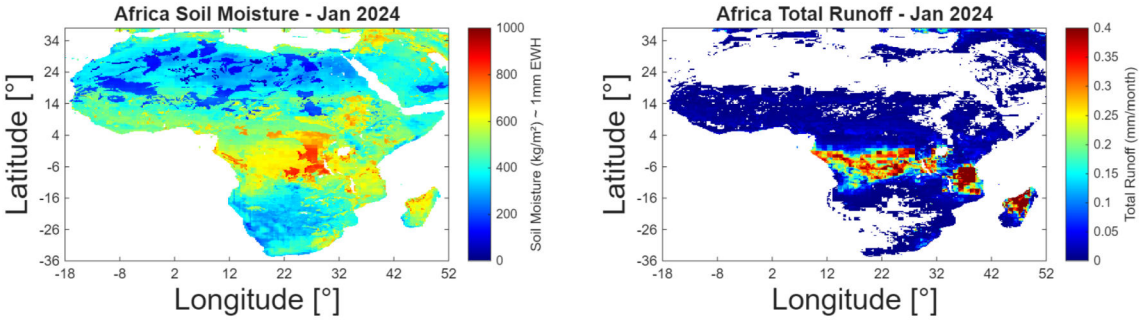

(a) January

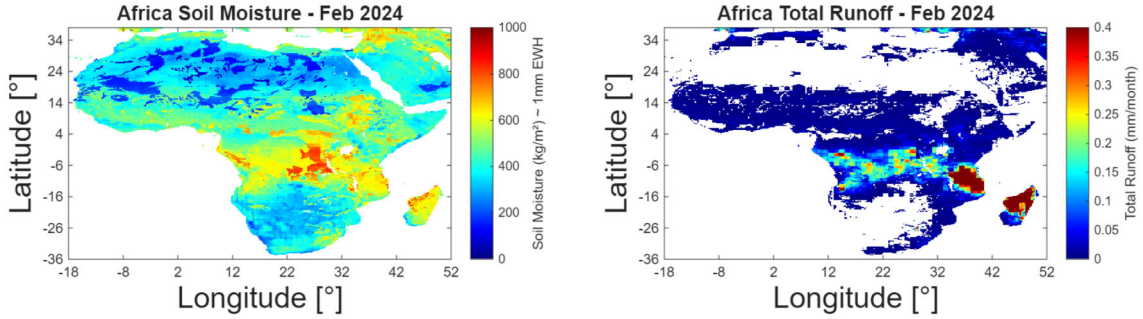

(b) February

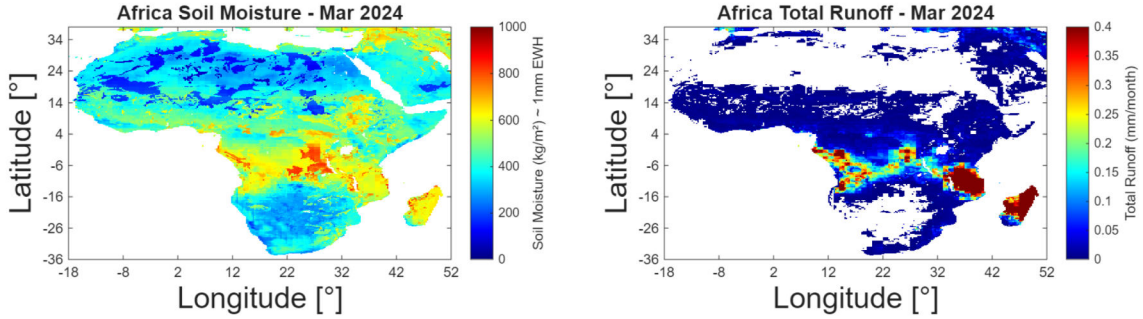

(c) March

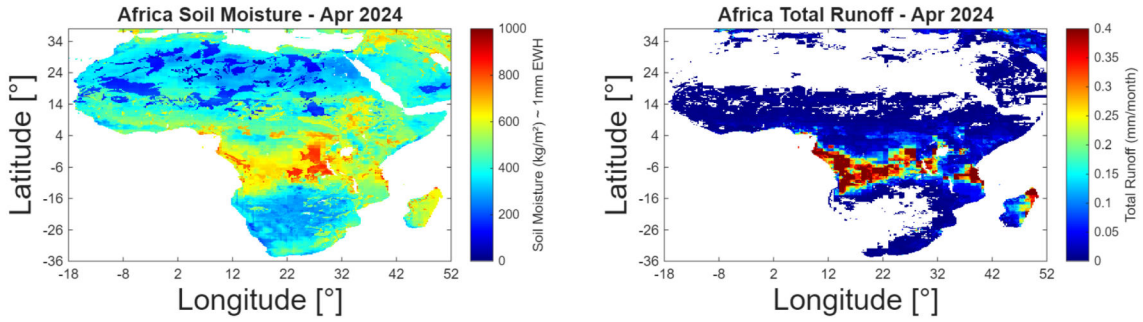

(d) April

Figure 5.7: Soil moisture and Runoff in 2024 (January until April)

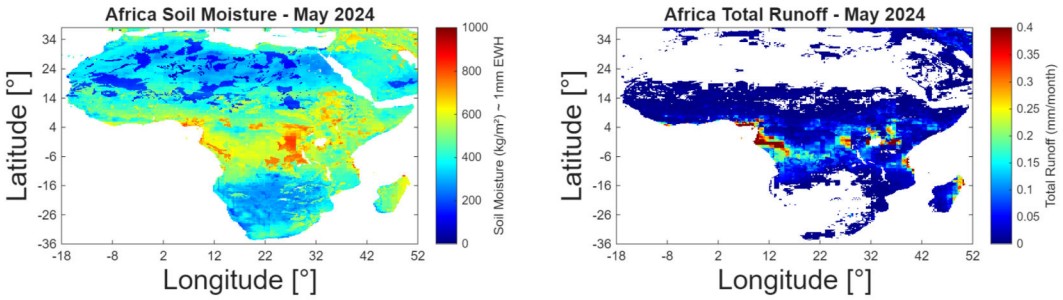

(e) May

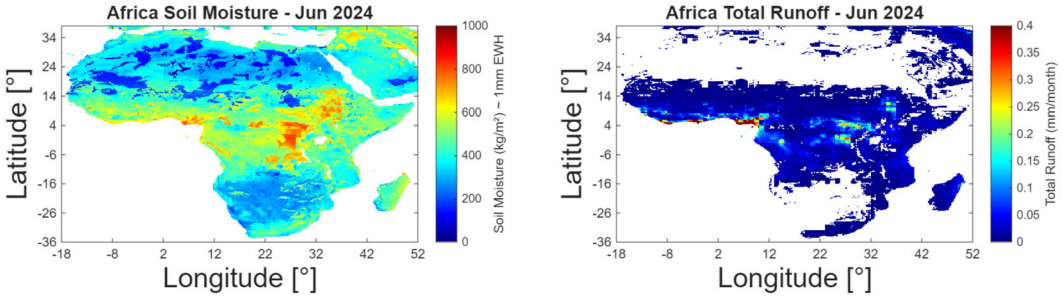

(f) June

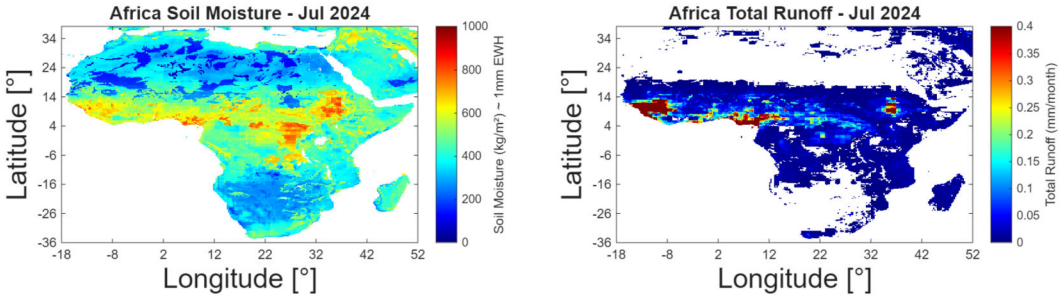

(g) July

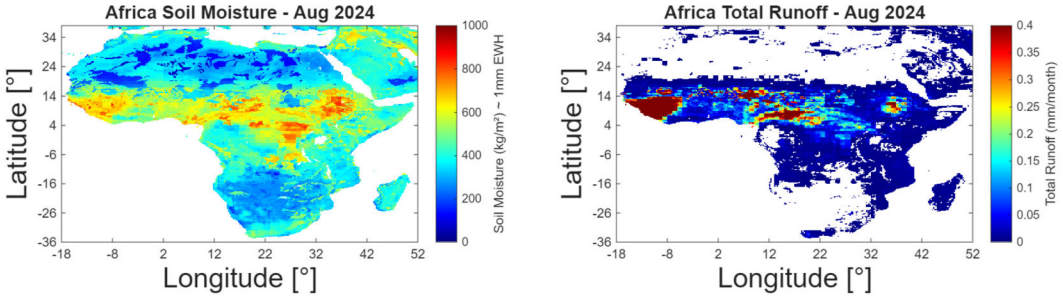

(h) August

Figure 5.7: Soil moisture and Runoff in 2024 (May until August)

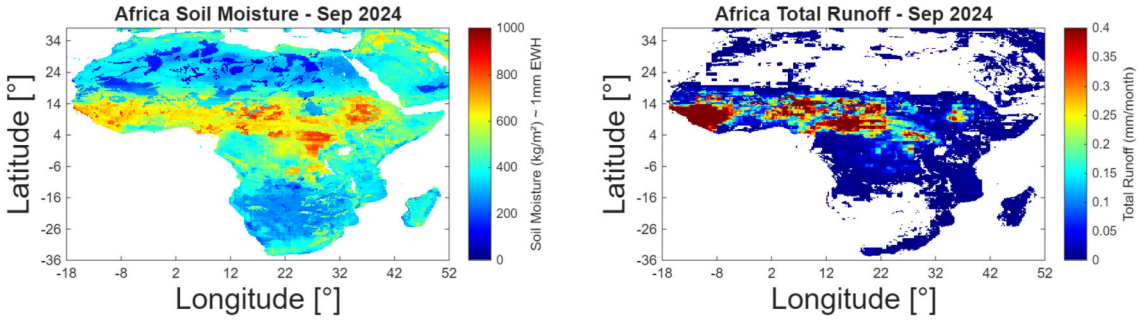

(i) September

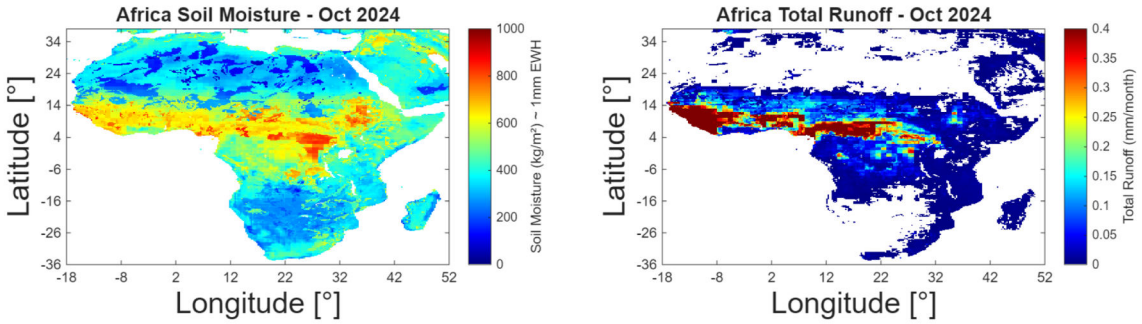

(j) October

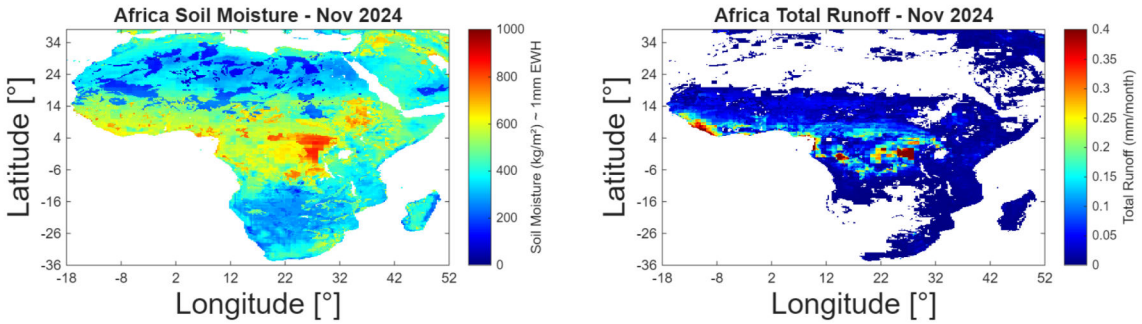

(k) November

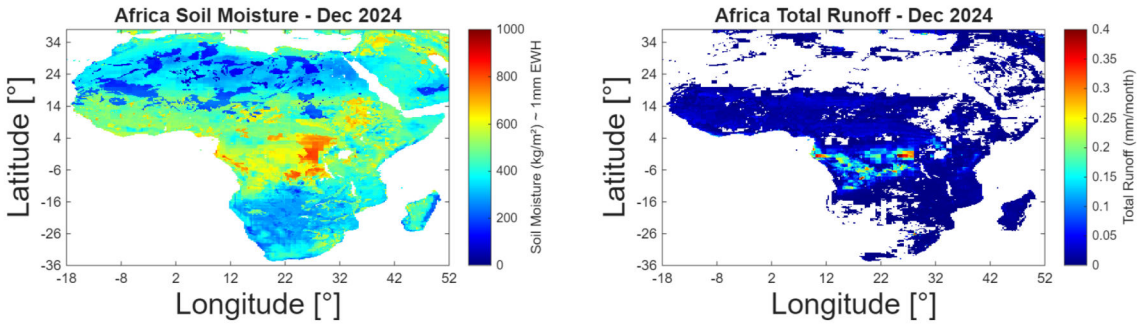

(l) December

Figure 5.7: Soil moisture and Runoff in 2024 (September until December)

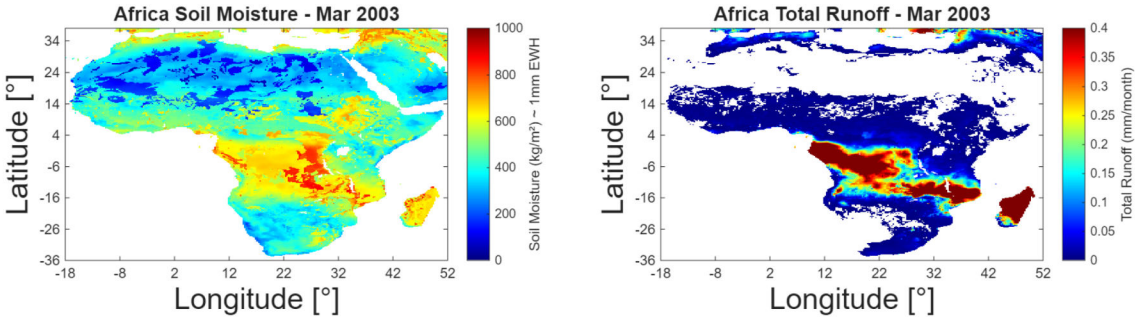

(a) March 2003

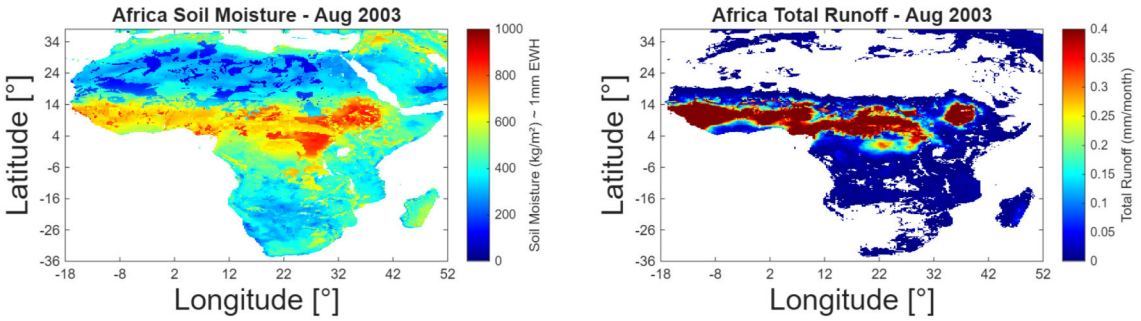

(b) August 2003

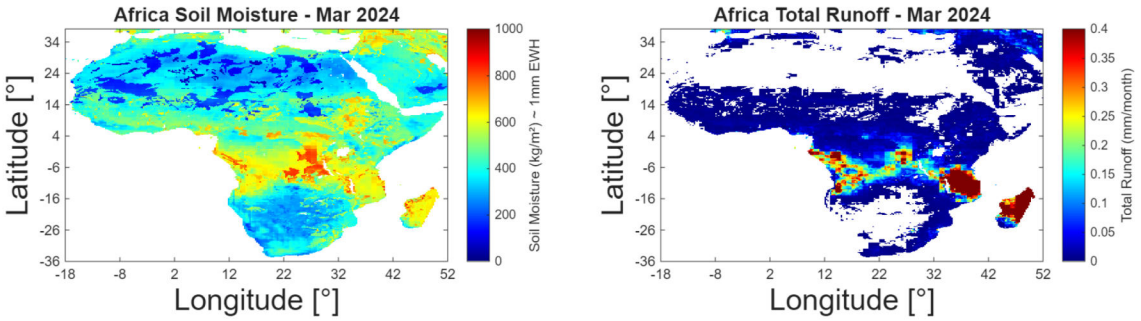

(c) March 2024

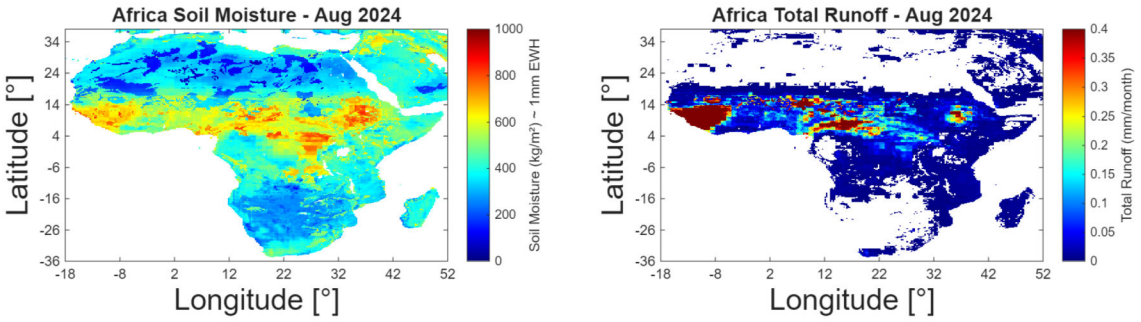

(d) August 2024

Figure 5.8: Soil moisture and Runoff comparison in 2003 and 2024

5.3.2 Comparison of March and August (2003 vs 2024)

A comparative analysis of soil moisture and runoff for March 2003 and August 2024 is presented in Figure 5.8.
In March 2003 (Figure 5.8a), soil moisture distribution appears relatively uniform with moderate values across central Africa, while runoff remains limited and localized. In contrast, March 2024 (Figure 5.8c) shows higher soil moisture concentrations in equatorial regions and more pronounced runoff patterns, indicating increased precipitation and enhanced surface water flow.
The differences are more evident in August. In August 2003 (Figure 5.8b), soil moisture is moderate and spatially distributed with relatively low runoff intensity. However, in August 2024 (Figure 5.8d), higher soil moisture values are observed in equatorial and western Africa, accompanied by significantly increased runoff in these regions.
Additionally, southern Africa shows lower soil moisture and runoff in August 2024 compared to equatorial regions, highlighting regional contrasts in seasonal water availability.
The comparison shown in Figure 5.8 indicates that hydrological conditions in 2024 were more dynamic than those observed in 2003, with stronger spatial gradients and increased intensity of both soil moisture and runoff. This suggests enhanced climate variability and changing precipitation patterns across the study period.

5.4 Comparison of GRACE and GLDAS Results and Groundwater Storage Estimation

The comparison between GRACE-derived Total Water Storage (TWS) and GLDAS-derived hydrological components provides a comprehensive understanding of terrestrial water dynamics across Africa. While GRACE (Figure 5.2 to 5.5) captures the total vertically integrated water storage, including groundwater, soil moisture, and surface water, GLDAS (5.6 to 5.8) represents only near-surface components such as soil moisture, canopy water, and runoff. Therefore, the difference between these two datasets enables the estimation of groundwater storage variations.

Seasonal Comparison (2024) The GRACE TWS results for 2024 shown in Figures 5.2 and 5.3 exhibit strong seasonal variability, with pronounced positive anomalies in equatorial and central Africa during peak rainfall periods and negative anomalies in southern regions during dry seasons. Similarly, the GLDAS results presented in Figure 5.7 indicate increased soil moisture and runoff in regions experiencing rainfall, particularly in central Africa.
However, a key observation from the comparison of Figures 5.2, 5.3, and 5.7 is that the amplitude of GRACE TWS anomalies is generally higher than that of GLDAS-derived hydrological components. This indicates that a significant portion of the water storage change is not explained by soil moisture and surface processes alone, implying the presence of groundwater storage variations.
During peak wet months, particularly August 2024 (Figures 5.4d and 5.5d), regions such as the Congo Basin exhibit strong positive TWS anomalies in the GRACE results, while the GLDAS results (Figure 5.8d) also show high soil moisture and runoff. The excess signal observed in GRACE suggests groundwater recharge in addition to surface water accumulation.
In contrast, during dry periods, particularly in the southern African regions visible in Figures 5.2 and 5.3, GRACE shows negative TWS anomalies, while GLDAS (Figure 5.7) indicates reduced soil moisture. This behaviour suggests groundwater depletion caused by reduced recharge and continued evapotranspiration.

Interannual Comparison (2003 vs 2024) The comparison of March and August between 2003 and 2024 shown in the GRACE results (Figures 5.4 and 5.5) and the GLDAS results (Figure 5.8) reveals clear interannual variability across Africa.
For both March and August, the GRACE-derived TWS anomalies in 2024 (Figures 5.4c–d and 5.5c–d) are stronger and more spatially localized than those observed in 2003 (Figures 5.4a–b and 5.5a–b). Similarly, the GLDAS

results (Figure 5.8) show increased soil moisture and runoff in 2024 compared to 2003, although the magnitude of change is smaller than that observed in the GRACE-derived TWS fields.
This difference suggests that the increase in TWS observed in the GRACE results (Figures 5.4 and 5.5) is not solely caused by surface hydrological processes represented by GLDAS (Figure 5.8) but also reflects enhanced groundwater storage variations.
In particular, equatorial regions show stronger groundwater recharge signals in 2024, while some southern regions exhibit intensified depletion patterns. The larger contrasts observed between the 2003 and 2024 maps indicate increased hydrological variability and possible changes in precipitation patterns over the African continent during the study period.

Groundwater Storage Interpretation By comparing the total water storage anomalies shown in Figures 5.2 to 5.5 with the surface hydrological components shown in Figures 5.6 to 5.8, groundwater storage can be estimated as the residual component. The results indicate that:

- Central and equatorial Africa (e.g., Congo Basin) show consistent positive groundwater storage anomalies, particularly during wet seasons, indicating strong recharge processes.
- Northern Africa shows minimal variation due to arid climatic conditions and limited recharge.
- Southern Africa exhibits negative groundwater anomalies during dry periods, indicating groundwater depletion.

Overall, groundwater storage follows the general climatic pattern of Africa but exhibits smoother spatial variability and delayed response compared to soil moisture and runoff. This reflects the slower dynamics of subsurface water movement and storage.

Key Findings The combined analysis of GRACE and GLDAS datasets highlights that:

- GRACE captures the full water storage signal, while GLDAS explains only surface components.
- The difference between the two datasets provides a reliable estimate of groundwater storage variations.
- Groundwater plays a significant role in total water storage, particularly in humid and equatorial regions.
- Interannual variability in groundwater storage suggests sensitivity to climate variability and changing precipitation patterns.

This integrated approach provides a more complete understanding of the hydrological cycle and is essential for assessing water resource availability and long-term sustainability across the African continent.

6 Conclusion and Outlook

This study investigated terrestrial water storage (TWS) and groundwater storage variations across the African continent by combining GRACE/GRACE-FO satellite gravimetry data with GLDAS hydrological model outputs. Using the Wahr et al. (1998) formulation, residual spherical harmonic coefficients from GRACE were transformed into equivalent water height (EWH), allowing the estimation of large-scale water storage anomalies over Africa.

The results demonstrate that GRACE-derived TWS successfully captures seasonal and interannual hydrological variability across different climatic regions of Africa. Equatorial and central African regions, particularly the Congo Basin, showed strong positive water storage anomalies associated with intense rainfall and groundwater recharge, while northern and southern African regions exhibited comparatively lower storage variations and periodic depletion patterns related to arid climatic conditions and reduced precipitation.

The comparison between DDK2 and DDK5 filtered solutions showed the importance of filtering in GRACE processing. DDK2 provided smoother and more stable large-scale hydrological signals with reduced striping noise, whereas DDK5 preserved finer spatial details but contained increased short-wavelength noise. This highlights the trade-off between signal preservation and noise suppression in GRACE-based hydrological studies.

The integration of GLDAS data enabled the separation of near-surface hydrological components such as soil moisture, runoff, and canopy water storage from the total water storage observed by GRACE. The residual signal provided an estimate of groundwater storage variability across Africa. The results indicate that groundwater contributes significantly to total water storage changes, especially in humid and equatorial regions where recharge processes are dominant.

The comparison between 2003 and 2024 revealed stronger and more localized hydrological anomalies in recent years, suggesting increased climate variability and changing precipitation patterns over the African continent. These findings emphasize the importance of long-term satellite observations for monitoring water resources and understanding large-scale hydrological processes under changing climatic conditions.

Overall, the combined use of GRACE and GLDAS datasets provides an effective framework for continental-scale groundwater assessment and hydrological analysis. The study demonstrates the capability of satellite gravimetry to support sustainable water resource monitoring in data-sparse regions such as Africa.

Future work can focus on improving the spatial resolution of groundwater estimates through mascon solutions and advanced filtering techniques. Basin-scale investigations for major African river basins such as the Nile, Congo, Niger, and Zambezi can provide more detailed hydrological interpretations. In addition, incorporating climate indices, precipitation datasets, and machine learning approaches may improve the understanding of long-term groundwater dynamics and climate-driven hydrological changes across Africa.

Successor mission for GRACE is expected to adopt a mission architecture that could considerably reduce undesirable errors such as the correlation errors (Massotti et al., 2022).

Acknowledgement

I would like to express my sincere gratitude to Prof. Dr.-Ing. Hansjörg Kutterer for providing me with the opportunity to carry out this Lab Rotation and for his valuable support throughout this study.

I am especially deeply grateful to Dr.-Ing. Kurt Seitz for his continuous guidance, encouragement, and support during the entire course of this work. His valuable suggestions, scientific insights, and detailed explanations greatly improved my understanding of GRACE, GLDAS, spherical harmonics, and groundwater storage estimation. His patience and willingness to share knowledge helped me significantly throughout the research and analysis process. I am truly thankful for the time and effort he dedicated to guiding me during this Lab Rotation.

I would also like to thank the Geodetic Institute (GIK), Karlsruhe Institute of Technology (KIT), for providing the academic environment, facilities, and resources necessary for completing this study.
Furthermore, I would like to sincerely thank my friends for their constant encouragement, motivation, and support throughout this work. Their help and companionship made the completion of this study much easier and more enjoyable.
Finally, I acknowledge ICGEM (GFZ) and NASA GLDAS for providing the GRACE/GRACE-FO and hydrological datasets used in this study.

References

GLDAS (2025): GLDAS - Global Land Data Assimilation System. https://disc.gsfc.nasa.gov/datasets?keywords=GLDAS. Accessed: 2025-11-26.

Gridarendal (2026): Major river basins of Africa. available on a $1^\circ \times 1^\circ$ grid. URL: https://www.google.com/imgres?q=major%20rivers%20in%20africa&imgurl=https%3A%2F%2Flive.staticflickr.com%2F705%2F32243050331_2215d6f94e_o.png&imgrefurl=https%3A%2F%2Fwww.grida.no%2Fresources%2F5176&docid=w1AXByA-U-KmiM&tbnid=HNCeojXcxMVyaM&vet=12ahUKEwiPi9KyybWTAxVy9gIHHTQyNAEQnPAOegQIHRAB..i&w=1911&h=2001&hcb=2&ved=2ahUKEwiPi9KyybWTAxVy9gIHHTQyNAEQnPAOegQIHRAB (visited on 02/16/2026).

Heiskanen, W. A. and Moritz, H. (1967): Physical Geodesy. W. H. Freeman & Co., San Francisco, USA.

ICGEM (2026): International Centre for Global Earth Models (ICGEM): Gravity field and GRACE/GRACE-FO products hosted at the German Research Centre for Geosciences (GFZ). Accessed: 2026-04-06. URL: https://icgem.gfz-potsdam.de/.

Kusche, J. (2007): Approximate decorrelation and non-isotropic smoothing of time-variable GRACE-type gravity field models. *Journal of Geodesy* 81(11):733–749. DOI: 10.1007/s00190-007-0143-3.

Kusche, J., Schmidt, R., Petrovic, S., and Rietbroek, R. (2009): Decorrelated GRACE time-variable gravity solutions by GFZ, and their validation using a hydrological model. *Journal of Geodesy* 83:903–913. DOI: 10.1007/s00190-009-0308-3.

Massotti, L., Bulit, A., Daras, I., Dominguez, B. C., Carraz, O., Hall, K., Heliére, A., March, G., Martimort, P., Rodrigues, G., et al. (2022): Next generation gravity mission design activities within the mass change and geoscience international constellation. In: Sensors, Systems, and Next-Generation Satellites XXVI, vol. 12264. SPIE, pp. 6–17.

NİL, M. and DOĞANALP, S. (2023): INVESTIGATION OF THE PERFORMANCES OF DDK AND GAUSS FILTERING TECHNIQUES IN ELIMINATION OF MODEL-BASED ERRORS. *Engineering Sciences: Issues, Opportunities and Researches* 2023.

Researchgate (2026): Precipitation of Africa. URL: https://www.google.com/imgres?q=africa%20continent%20precipitation%20map&imgurl=https%3A%2F%2Fwww.researchgate.net%2Fpublication%2F263003668%2Ffigure%2Ffig1%2FAS%3A613893982392329%401523375139784%2FMap-of-the-African-continent-with-country-names-and-rainfall-patterns-Data-source.png&imgrefurl=https%3A%2F%2Fwww.researchgate.net%2Ffigure%2FMap-of-the-African-continent-with-country-names-and-rainfall-patterns-Data-source_fig1_263003668&docid=P_z7Gga5dSi2dM&tbnid=4wGO3B0P4OORMM&vet=12ahUKEwjr6LGaxbWTAxUlhf0HHZ_QAXUQnPAOegQIGBAB..i&w=850&h=788&hcb=2&ved=2ahUKEwjr6LGaxbWTAxUlhf0HHZ_QAXUQnPAOegQIGBAB (visited on 02/16/2026).

Rodell, M., Houser, P. R., Jambor, U., Gottschalck, J., Mitchell, K. E., Meng, C.-J., Arsenault, K., Cosgrove, B. A., Radakovich, J. D., Bosilovich, M. G., Entin, J. K., Walker, J. P., Lohmann, D., and Toll, D. L. (2004): The Global Land Data Assimilation System. *Bulletin of the American Meteorological Society* 85(3):381–394. DOI: 10.1175/BAMS-85-3-381.

Tsoulis, D. (1999): Spherical harmonic computations with topographic/isostatic coefficients. Tech. rep. IAPG/FESG No. 3. Munich, Germany: Institut für Astronomische und Physikalische Geodäsie, Technische Universität München.

Wahr, J., Molenaar, M., and Bryan, F. (1998): Time variability of the Earth's gravity field: Hydrological and oceanic effects and their possible detection using GRACE. *Journal of Geophysical Research: Solid Earth* 103(B12):30205–30229.

Wikipedia (2026): Topography of Africa. URL: https://de.wikipedia.org/wiki/Datei:Topography_of_africa.jpg (visited on 02/16/2026).

Worldatlas (2026): Zones in Africa. URL: https://www.google.com/imgres?q=major%20zones%20in%20africa&imgurl=https%3A%2F%2Fwww.worldatlas.com%2Fr%2Fw2560-q80%2Fupload%2F2a%2Fd5%2F59%2Fregions-of-africa.png&imgrefurl=https%3A%2F%2Fwww.worldatlas.com%2Fgeography%2Fregions-of-africa.html&docid=szJYZyulSKGJUM&tbnid=Dy4V48KCO07hoM&vet=12ahUKEwjdmKHNx7WTAxXAVfEDHfKODgkQnPAOegQIIhAB..i&w=2560&h=2560&hcb=2&ved=2ahUKEwjdmKHNx7WTAxXAVfED (visited on 02/16/2026).

Appendix

A Appendices

A.1 TWS Based on DDK2 (2003 - 2024)

A.2 TWS Based on DDK5 (2003 - 2024)

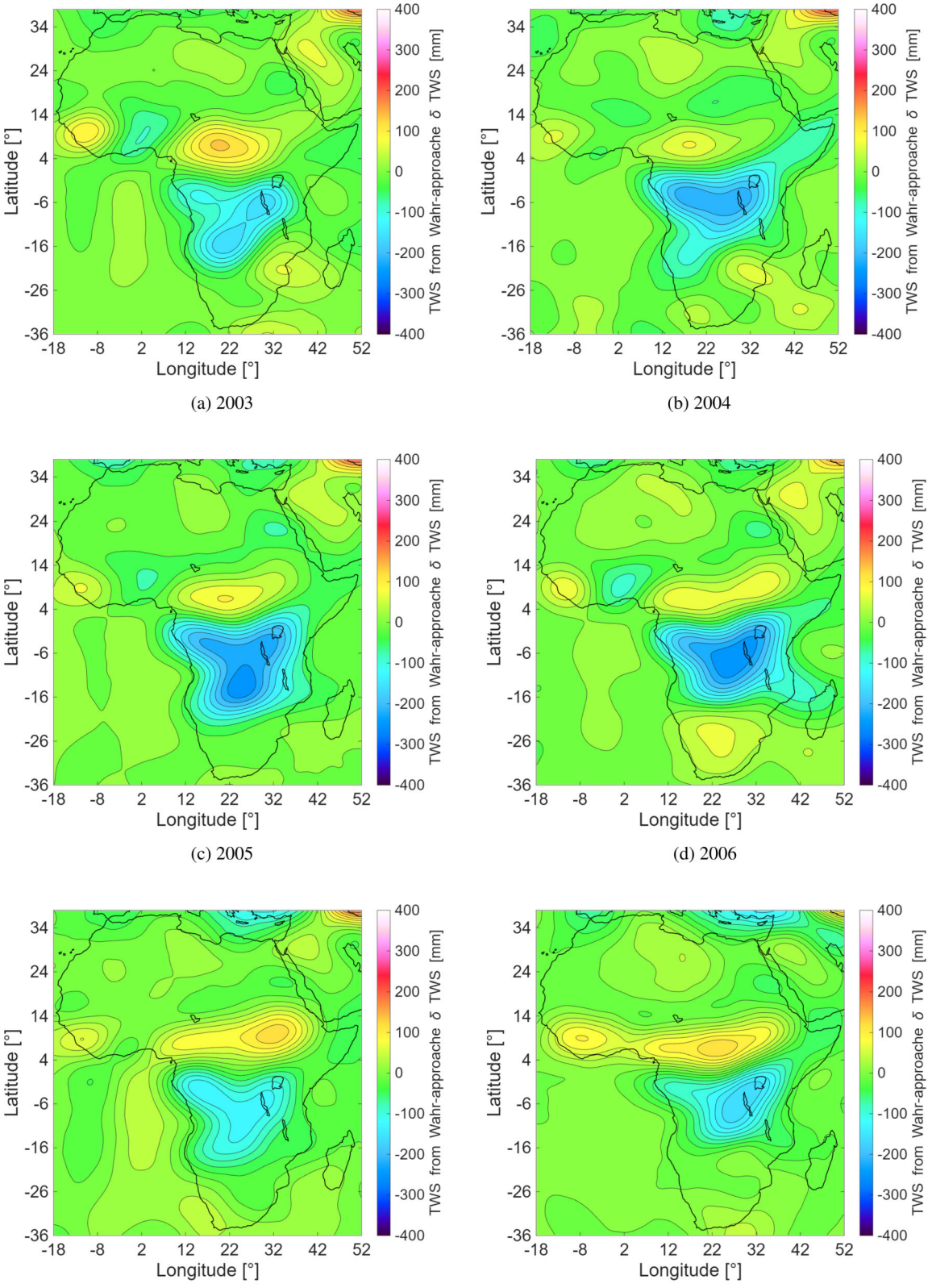

(a) 2003

(b) 2004

(c) 2005

(d) 2006

(e) 2007

(f) 2008

Figure A.1: TWS CSR DDK2 August (2003 until 2008)

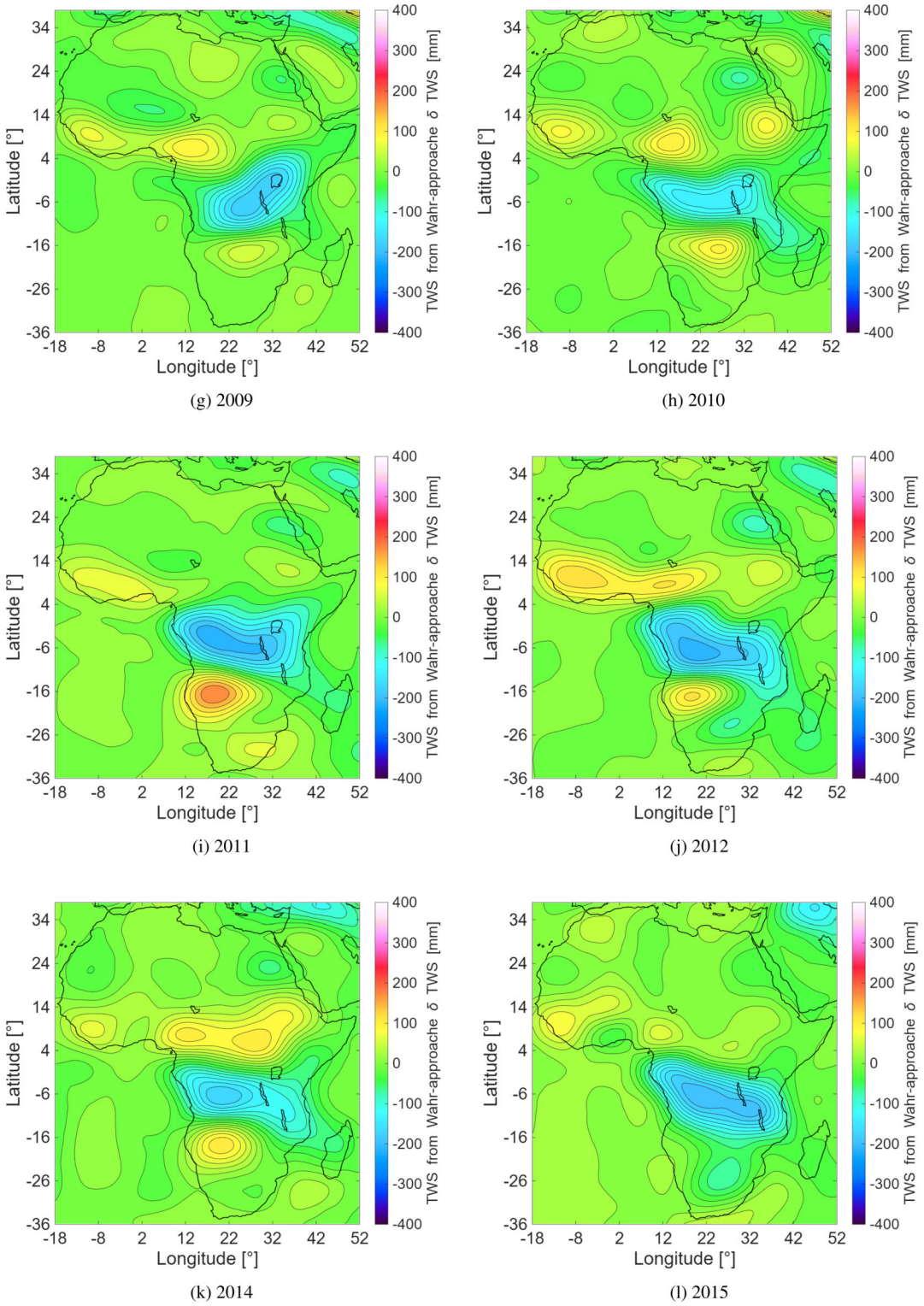

(g) 2009 (h) 2010

(i) 2011 (j) 2012

(k) 2014 (l) 2015

Figure A.1: TWS CSR DDK2 August (2009 until 2015)

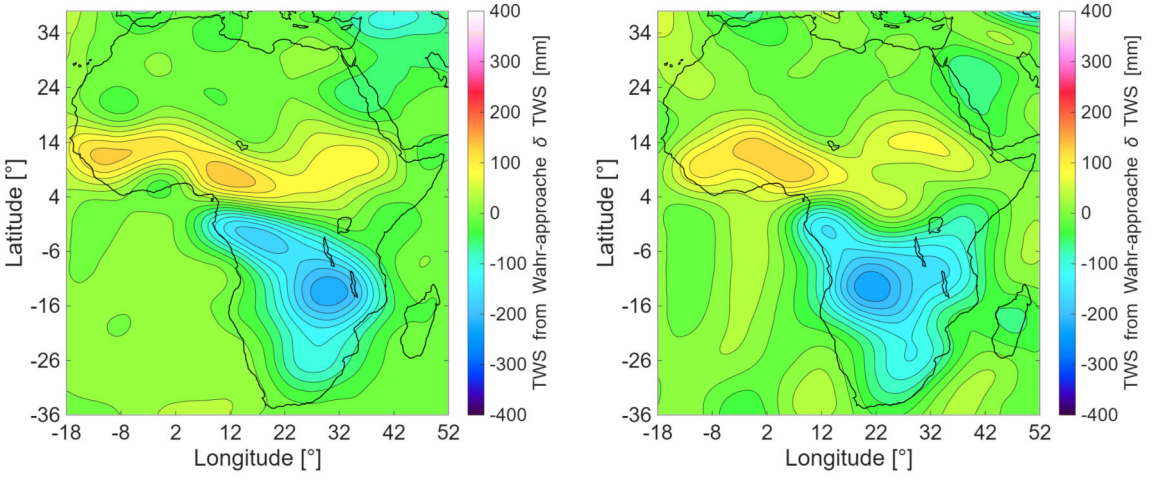

(m) 2016

(n) 2019

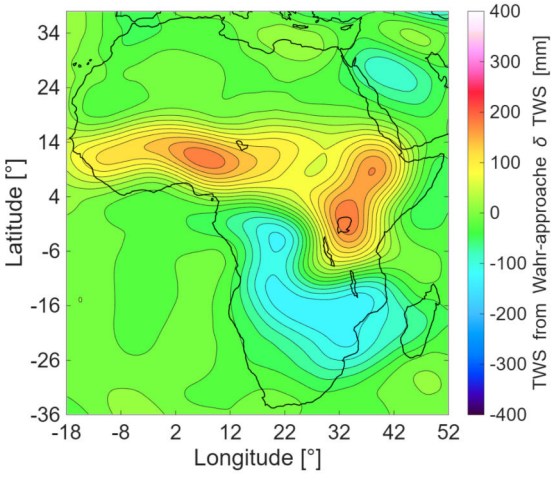

(o) 2020

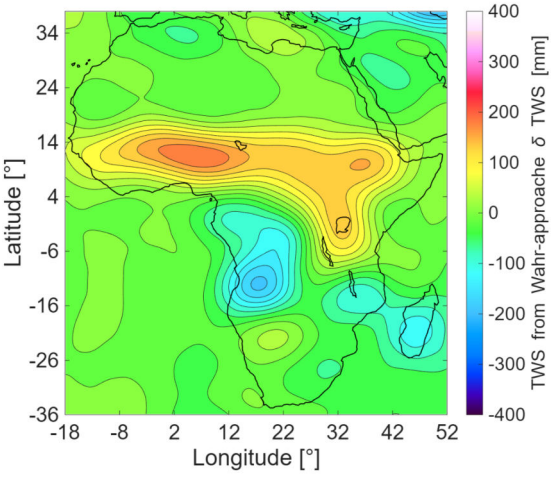

(p) 2021

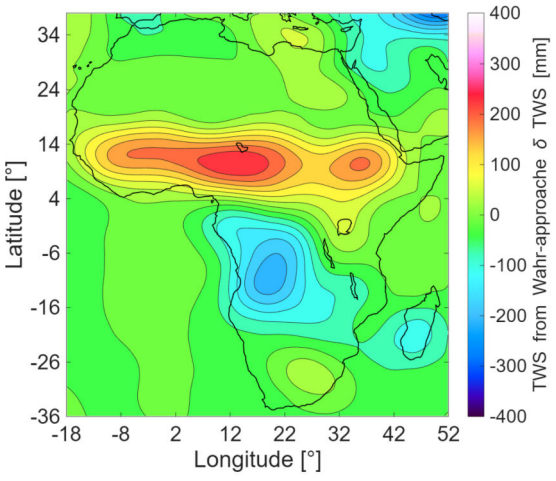

(q) 2022

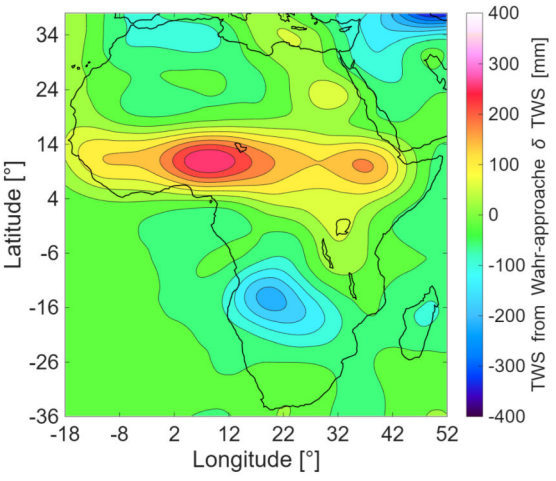

(r) 2023

Figure A.1: TWS CSR DDK2 August (2016 until 2023)

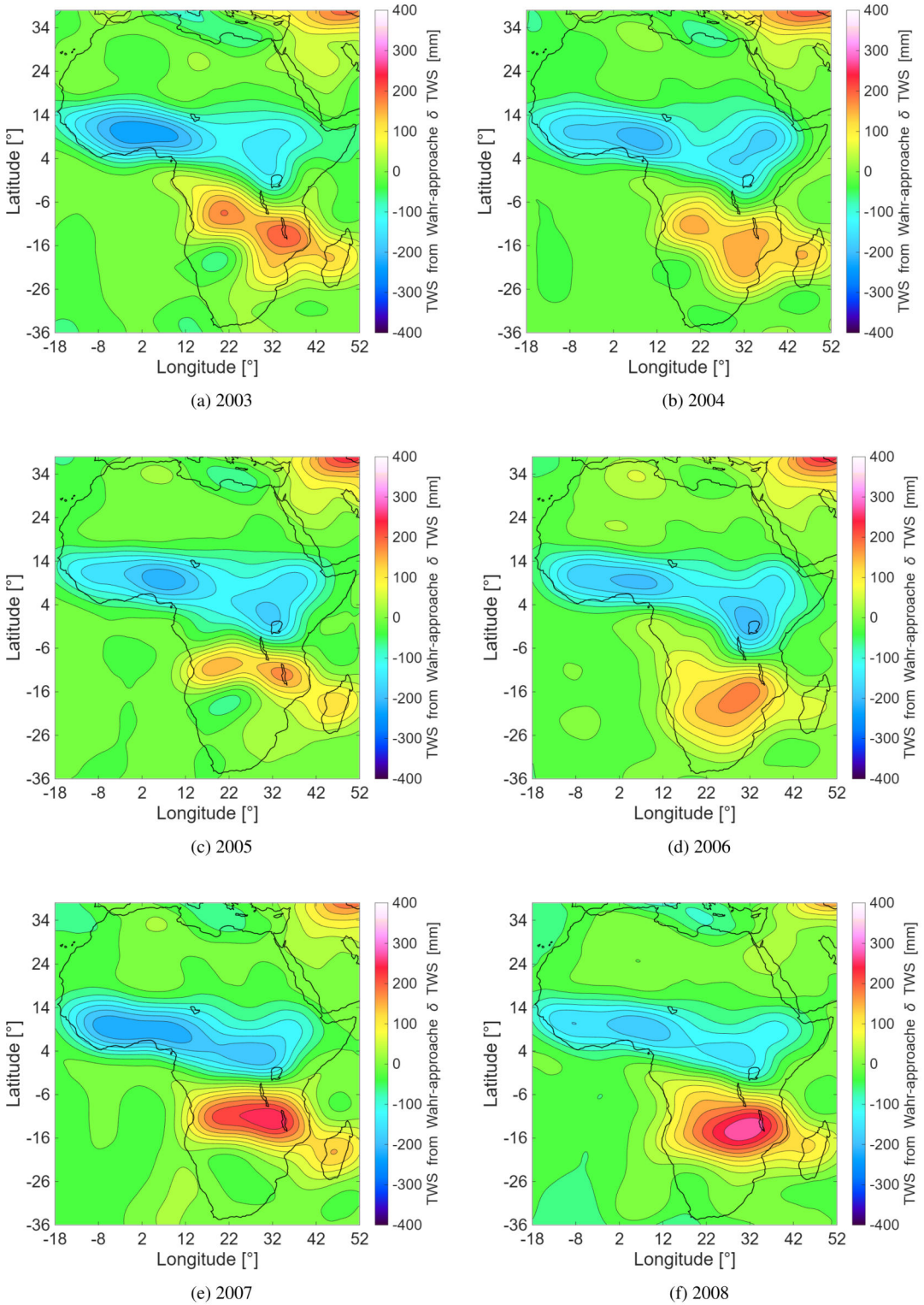

(a) 2003 (b) 2004

(c) 2005 (d) 2006

(e) 2007 (f) 2008

Figure A.2: TWS CSR DDK2 March (2003 until 2008)

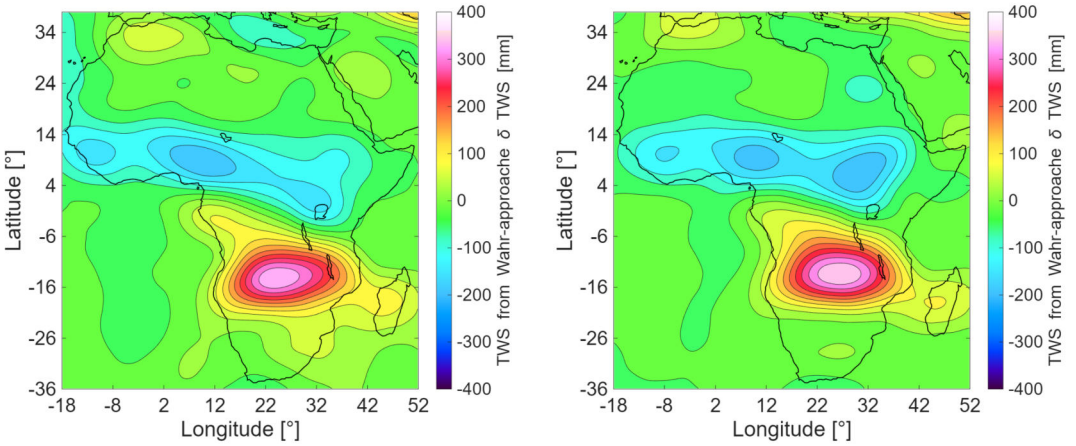

(g) 2009 (h) 2010

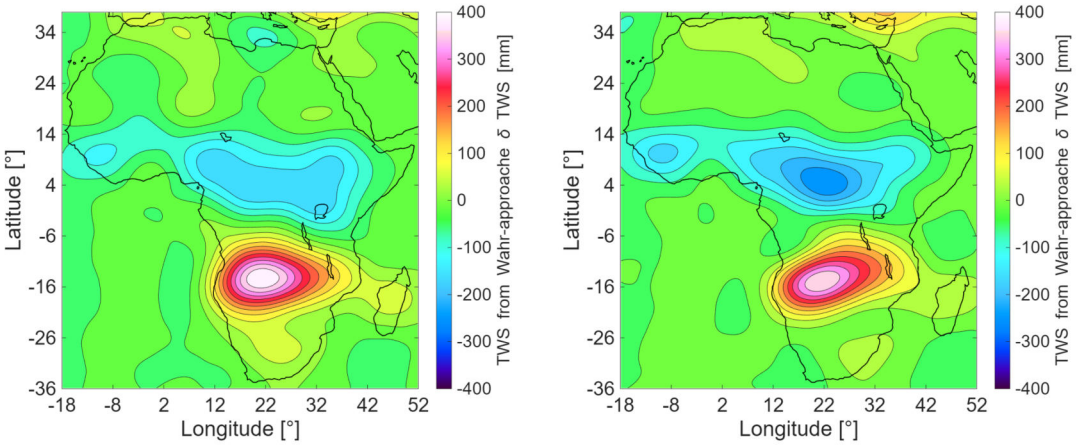

(i) 2011 (j) 2012

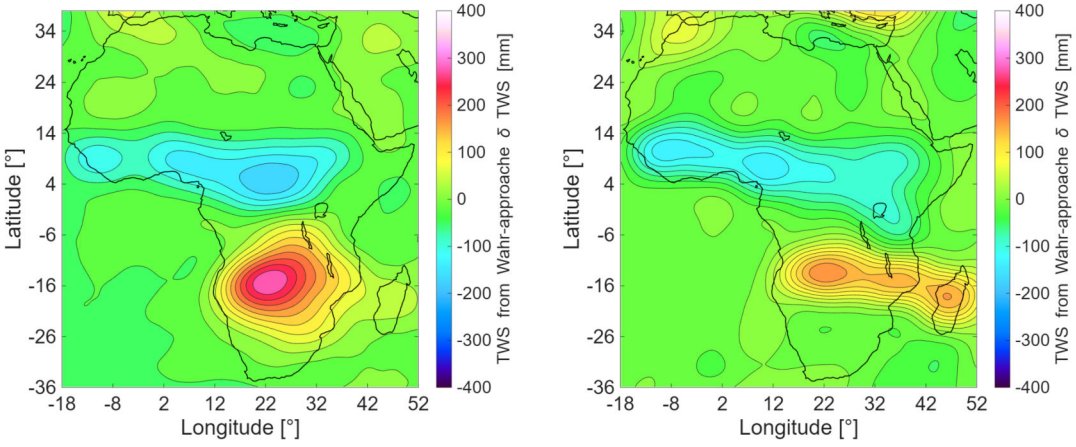

(k) 2014 (l) 2015

Figure A.2: TWS CSR DDK2 March (2009 until 2015)

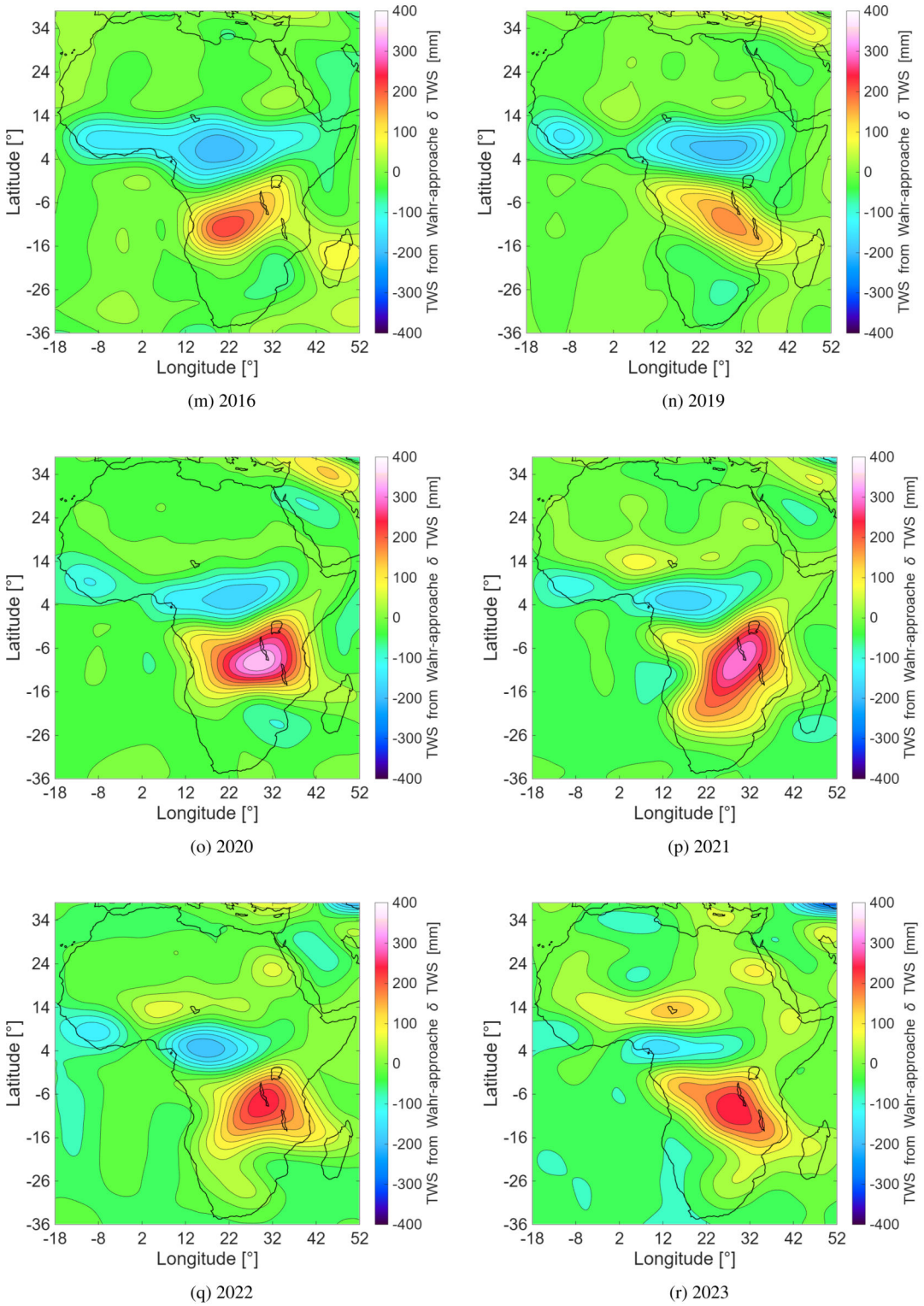

(m) 2016 (n) 2019

(o) 2020 (p) 2021

(q) 2022 (r) 2023

Figure A.2: TWS CSR DDK2 March (2016 until 2023)

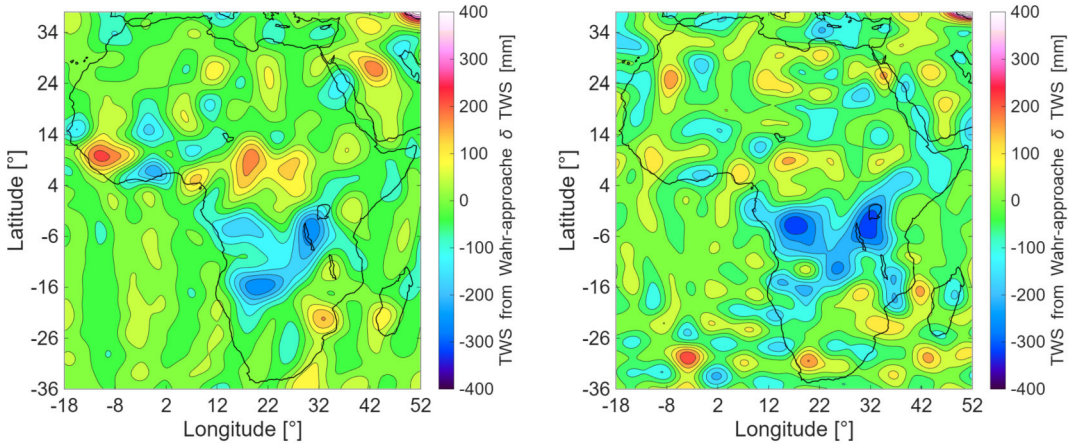

(a) 2003

(b) 2004

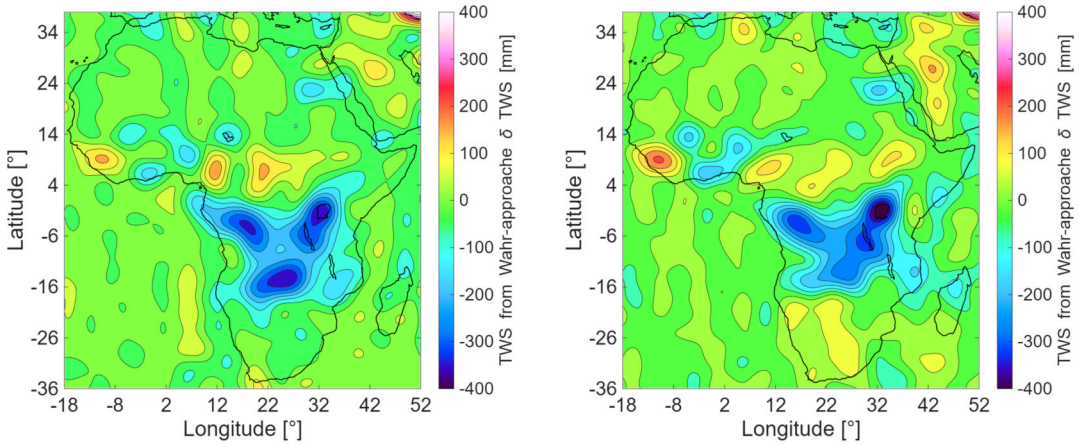

(c) 2005

(d) 2006

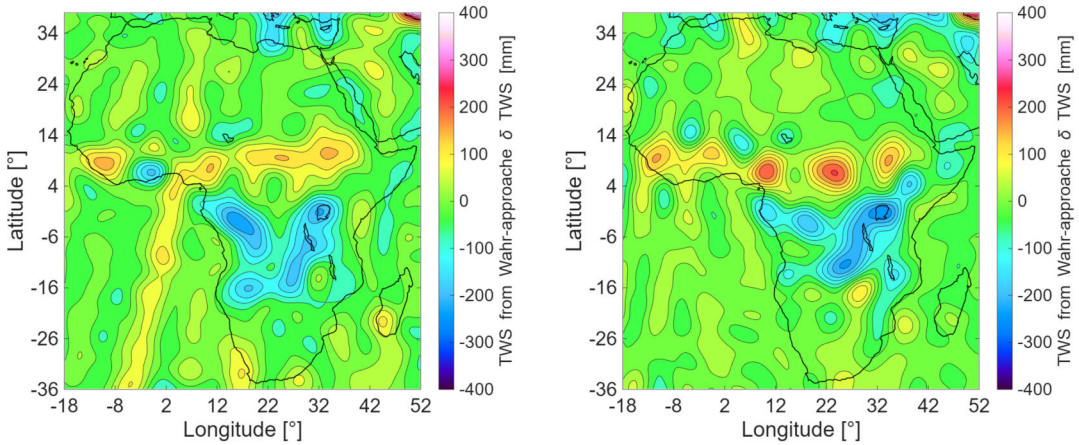

(e) 2007

(f) 2008

Figure A.3: TWS CSR DDK5 August (2003 until 2008)

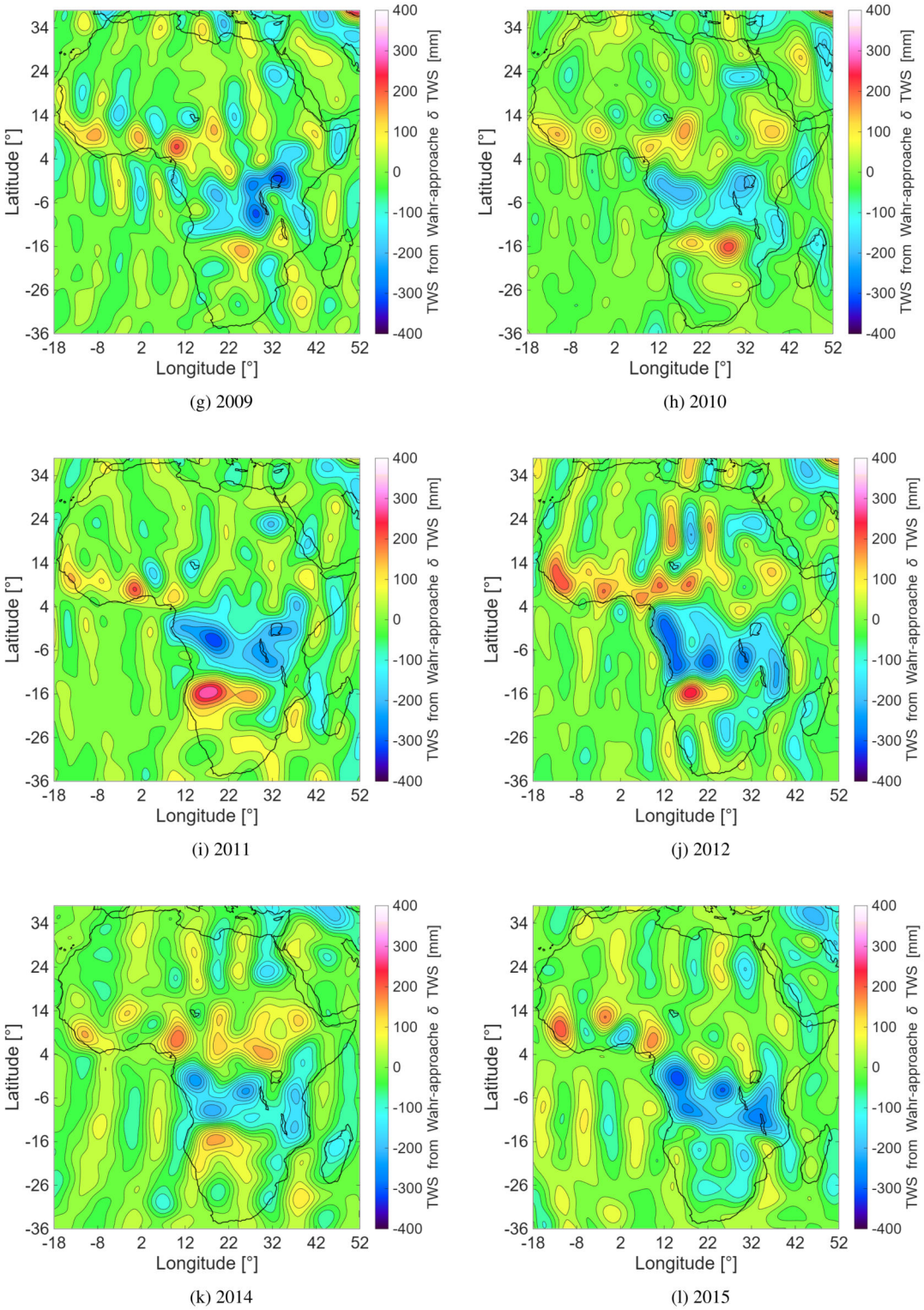

(g) 2009 (h) 2010

(i) 2011 (j) 2012

(k) 2014 (l) 2015

Figure A.3: TWS CSR DDK5 August (2009 until 2015)

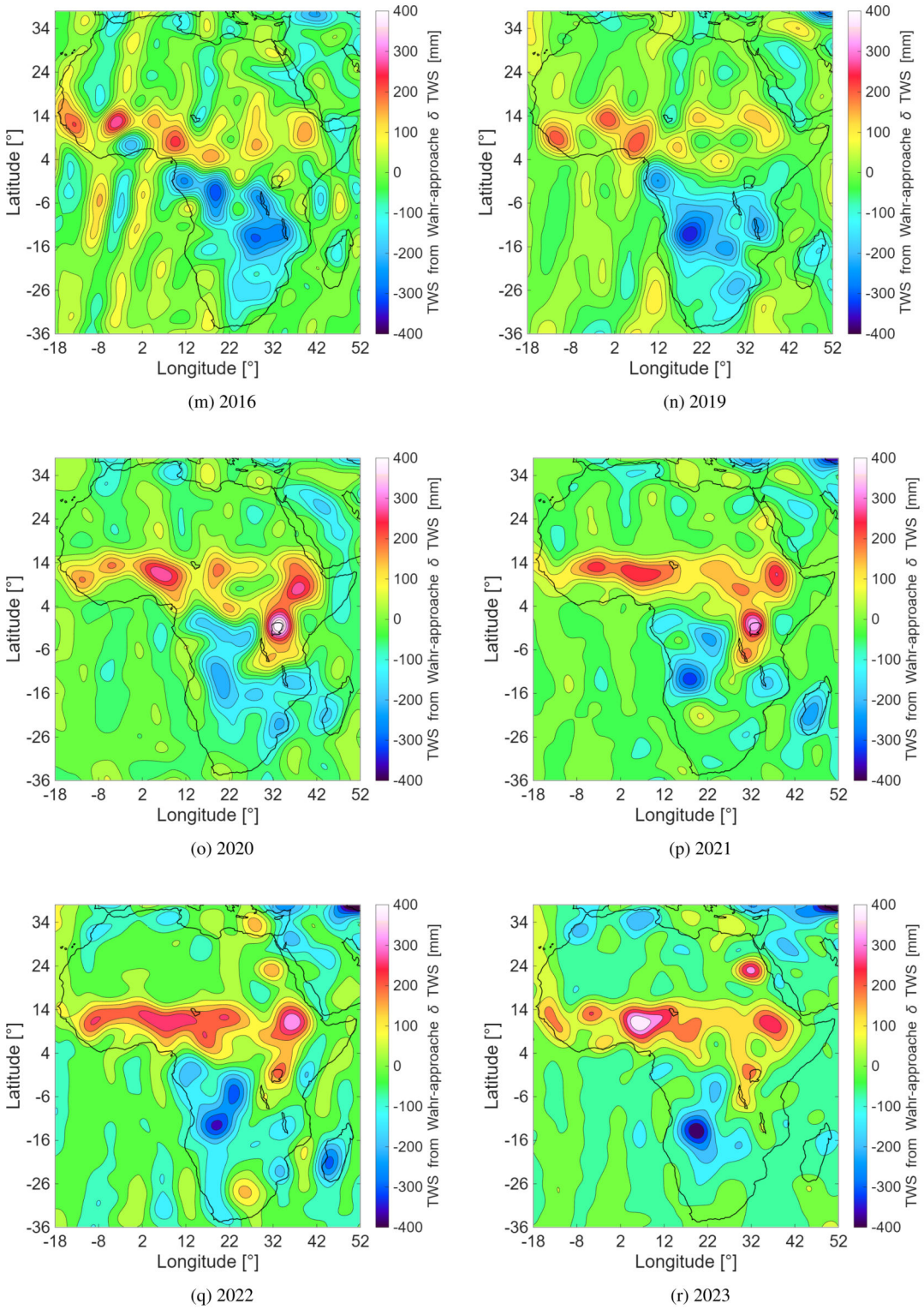

(m) 2016 (n) 2019

(o) 2020 (p) 2021

(q) 2022 (r) 2023

Figure A.3: TWS CSR DDK5 August (2016 until 2023)

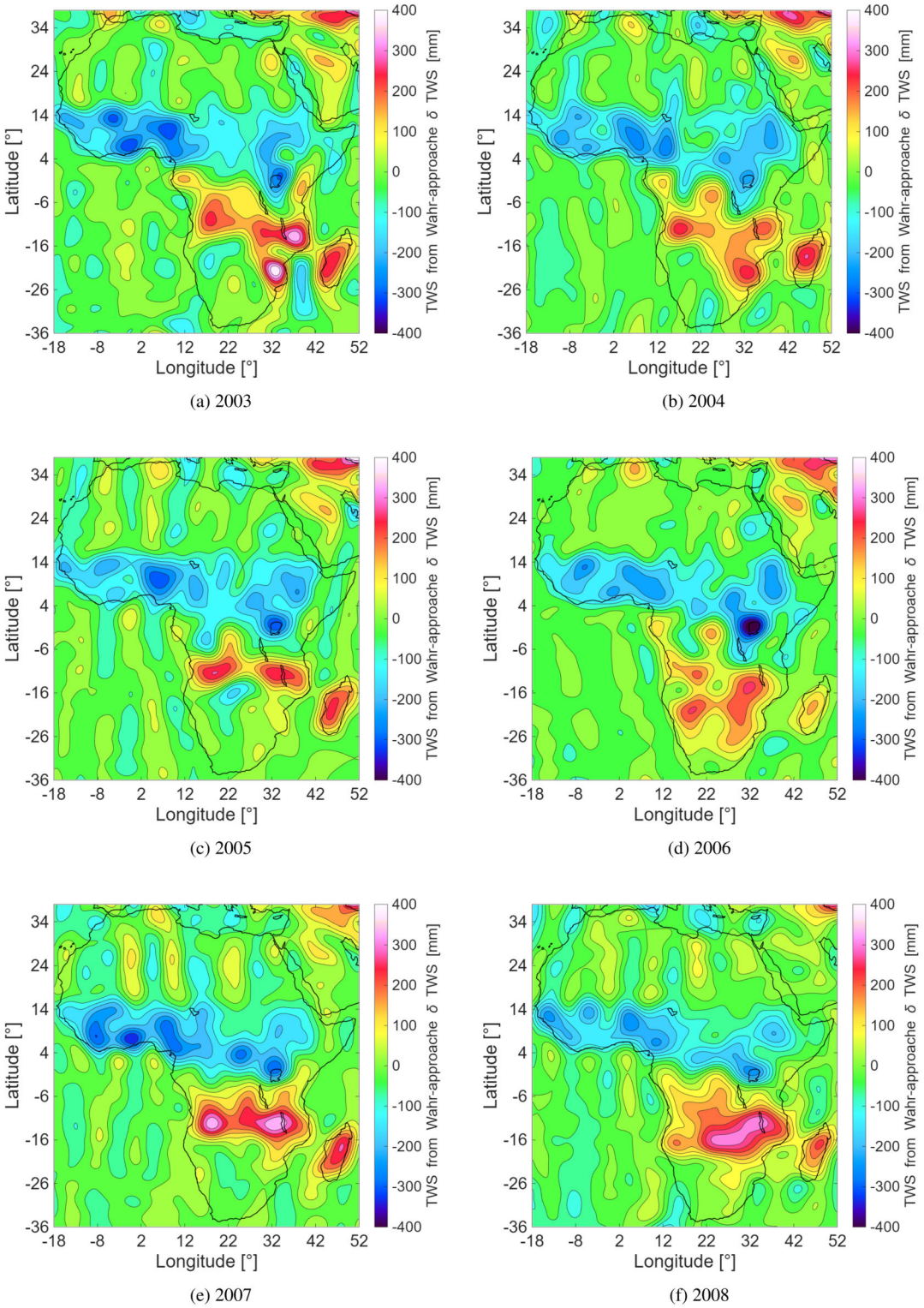

(a) 2003

(b) 2004

(c) 2005

(d) 2006

(e) 2007

(f) 2008

Figure A.4: TWS CSR DDK5 March (2003 until 2008)

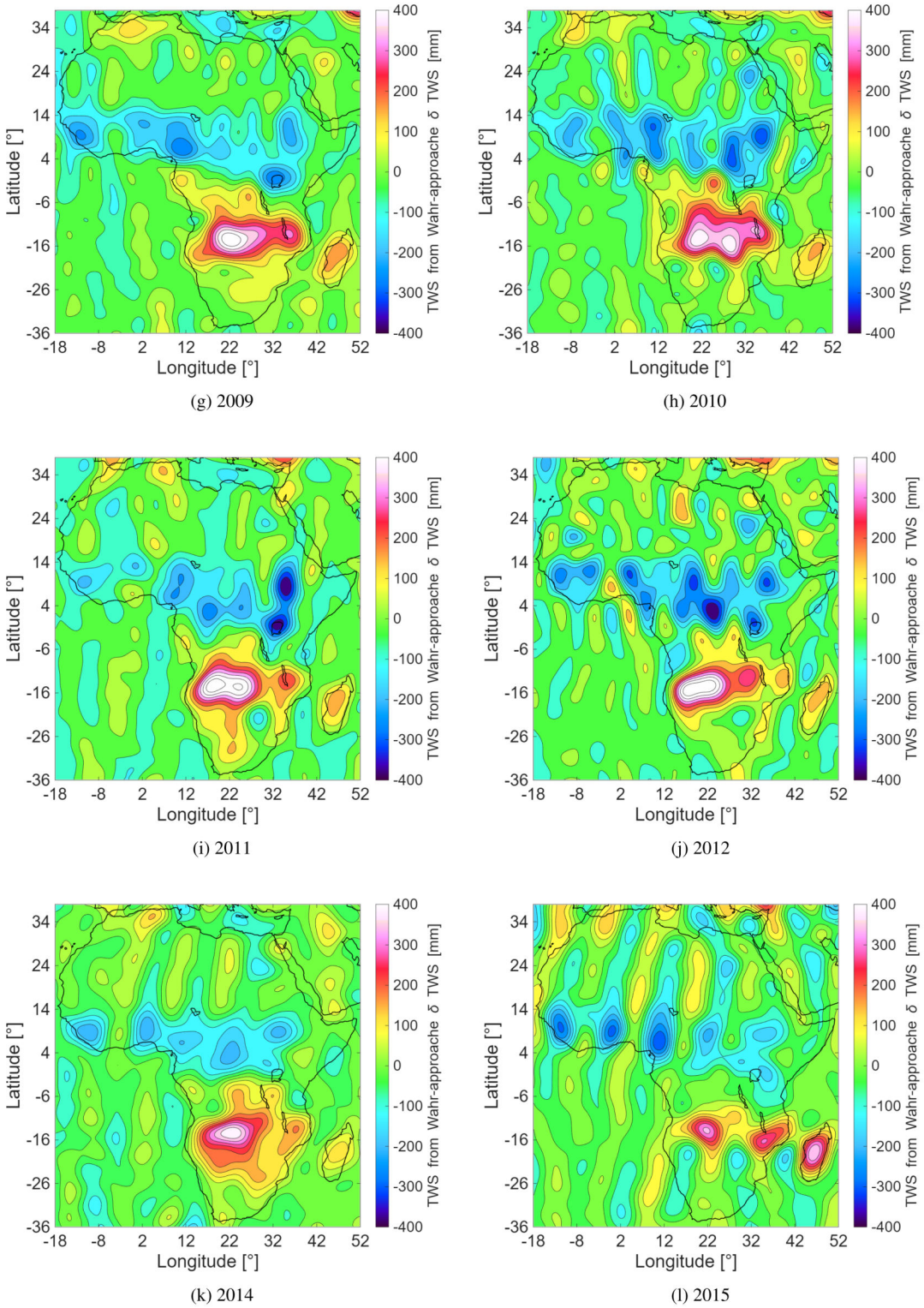

(g) 2009 (h) 2010

(i) 2011 (j) 2012

(k) 2014 (l) 2015

Figure A.4: TWS CSR DDK5 March (2009 until 2015)

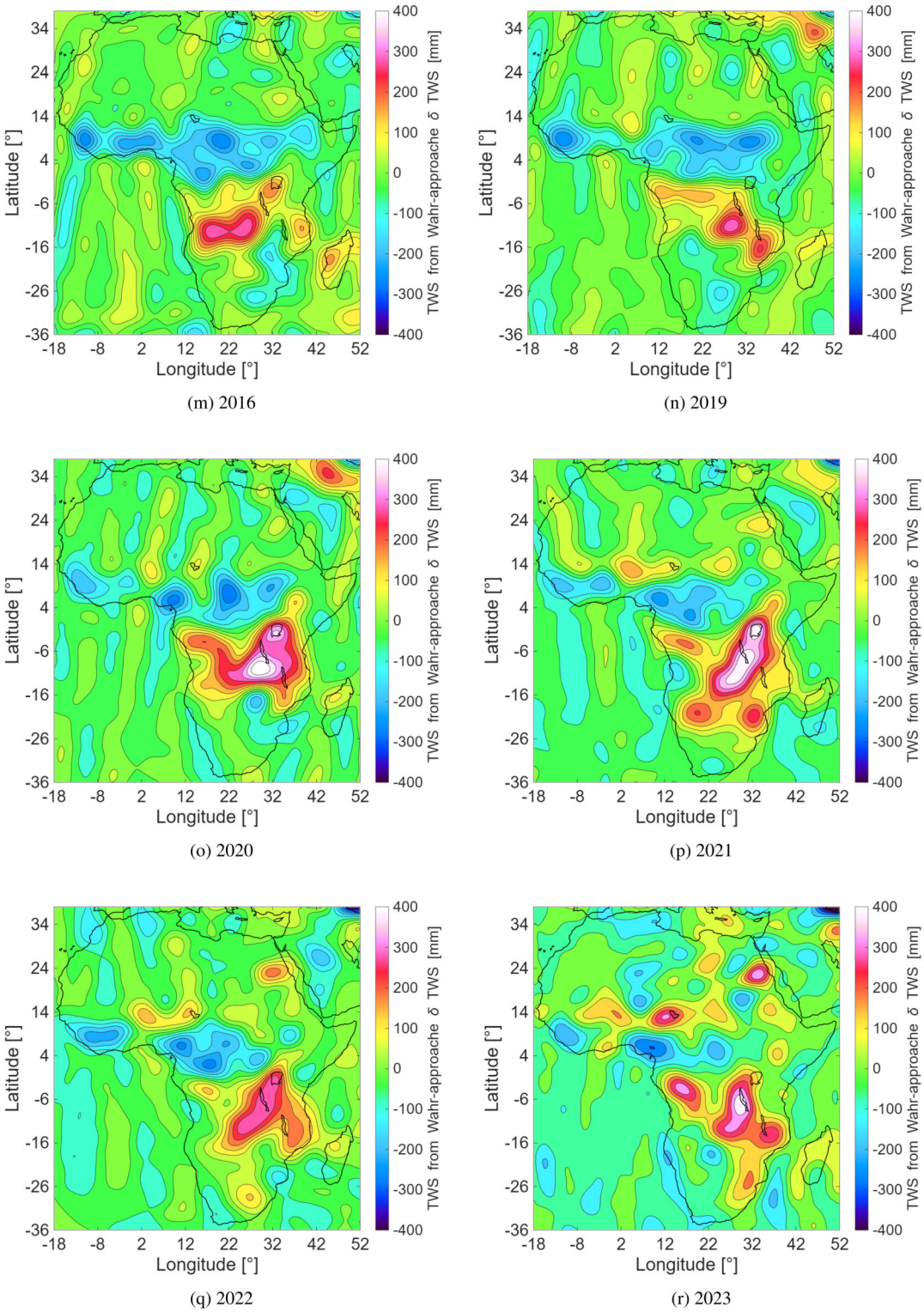

(m) 2016 (n) 2019

(o) 2020 (p) 2021

(q) 2022 (r) 2023

Figure A.4: TWS CSR DDK5 March (2016 until 2023)

Comparison of GRACE DDK Filters for Terrestrial Water Storage

Vishnu Prakash[1]

1 Remote Sensing and Geoinformatics Master of Science (M.Sc.), KIT, Germany
E-Mail: uzwfs@student.kit.edu

Abstract

This study investigates the impact of decorrelation filtering and regularisation on GRACE-based gravity field analysis and the recovery of terrestrial water storage (TWS) variations. A consistent methodological framework was applied across spectral diagnostics (degree variance and coefficient triangles), spatial synthesis (gravitational potential and geoid undulation anomalies), and inverse modelling (tesseroid-based TWS anomaly maps). The results demonstrate that the reliability of GRACE-derived mass change estimates is fundamentally governed by the trade-off between noise suppression and signal preservation.

Spectral diagnostics reveal that spherical harmonic solutions contain correlated errors that increase towards higher degrees, leading to striping artefacts and amplified short-wavelength variability in the spatial domain. Application of DDK decorrelation filters systematically reduces these errors: weaker filters preserve higher-degree content but retain striping, whereas stronger filters (e.g., DDK6 – DDK8) effectively suppress high-degree variability and yield smoother, more stable coefficient behaviour. Spatial synthesis products confirm this spectral behaviour, showing dominance of long-wavelength mass redistribution patterns and progressive smoothing with increasing filter strength. Interannual comparisons for identical calendar months isolate interannual variability from seasonal effects.

Inverse modelling using a tesseroid approach on a $2.5^\circ \times 2.5^\circ$ grid produces physically consistent TWS anomaly patterns. The inversion results are sensitive to both input noise characteristics and filter strength. Weaker filtering retains higher spatial detail and larger amplitudes but exhibits increased striping and reduced stability. Stronger filtering enhances spatial coherence and interpretability at the expense of attenuating short-wavelength signals, reflecting the inherent resolution–noise trade-off in satellite gravimetry.

Given the ill-posed nature of the inverse problem, regularisation is required to stabilise the solution. The L-curve criterion provides an objective means of selecting the regularisation parameter by identifying the optimal balance between data misfit and model smoothness. Diagnostics performed for a high signal-to-noise month enable robust parameter selection, while monthly inversion results confirm the consistency of this trade-off across epochs.

Overall, no universally optimal DDK filter exists; filter selection must be guided by the spatial scale of interest and acceptable noise levels. The integrated use of spectral diagnostics, spatial synthesis, inversion mapping, and L-curve-based regularisation establishes a transparent and defensible framework for optimising filter strength and regularisation in GRACE-based TWS studies. Future research should explore adaptive filtering strategies, validation with independent hydrological data, and alternative regularisation approaches to further improve regional-scale mass change estimates.

Keywords GRACE · Total Water Storage (TWS) · Inverse Tesseroid Approach · DDK-Filters

1 Introduction

Mass redistribution within the Earth system occurs continuously due to a combination of terrestrial hydrology, groundwater pumping and recharge, snow accumulation and melt, and changes in ice sheets and glaciers. Because gravity is directly linked to mass, these processes leave a measurable imprint on the Earth's gravitational field. Satellite gravimetry therefore provides a unique way to observe integrated mass change signals over large spatial scales that are difficult to measure comprehensively using in-situ observations alone (Wahr et al., 1998).

The Gravity Recovery and Climate Experiment (GRACE) mission delivers monthly gravity field solutions in the form of fully-normalised spherical harmonic coefficients, enabling the analysis of time-variable gravity and mass change signals on regional-to-global scales (Tapley et al., 2004). Nevertheless, GRACE solutions are affected by systematic errors, especially correlated errors that often manifest as north–south oriented stripes in spatial maps. If not mitigated, these artefacts can obscure geophysical signals and introduce unrealistic patterns into derived products such as potential anomalies or terrestrial water storage (TWS) (Swenson and Wahr, 2006).

A widely used approach to reduce these correlated errors is decorrelation filtering. The DDK family of filters provides a set of filter strengths which differ in how strongly they suppress noise and attenuate short-wavelength content (Kusche et al., 2009). In practice, stronger filtering typically produces smoother maps with reduced striping but may damp real signals and shrink amplitudes, whereas weaker filtering preserves more spatial detail but may retain residual noise.

Aim and scope. This report focuses on a controlled comparison of four DDK filter strengths: DDK2, DDK4, DDK6, and DDK8, restricted to the period 2004–2007. The processing is intentionally split into two stages: (i) spherical harmonic synthesis of gravitational potential anomalies on a global $2^\circ \times 2^\circ$ grid and (ii) inversion of these potential anomalies to estimate TWS anomalies using the inverse tesseroid approach on a $\mathbf{2.5}^\circ \times \mathbf{2.5}^\circ$ grid. This setup allows an explicit investigation of how filter strength influences both the forward synthesis products and the stability and realism of inverted mass change fields (Heck and Seitz, 2007; Uieda et al., 2016).

Research questions. The analysis is guided by the following questions:

- How do DDK2/4/6/8 differ in spectral behaviour (signal and noise distribution across degree)?
- How does filter strength affect spatial artefacts (striping) and smoothness in synthesised potential anomaly maps?
- To what extent do these differences propagate into the inverse tesseroid TWS estimates (amplitude, coherence, stability)?
- Which DDK strength provides the most suitable compromise for the chosen grid resolutions and the 2004–2007 period?

2 Theoretical Aspects

The theoretical foundation needed to analyse GRACE-based gravity field solutions and calculate variations in terrestrial water storage (TWS) is described in this section. The use of spherical harmonics to represent time-variable gravity, the function of spectral diagnostics, and the impact of decorrelation filtering on the recoverable signal are the main topics of discussion.

KIT Scientific Working Papers
Issue Number 270
ISSN: 2194-1629
DOI: 10.5445/IR/1000191188
Online: June 2026

This document is licensed under the Creative Commons Attribution – Share Alike 4.0 International License (CC BY-SA 4.0):
https://creativecommons.org/licenses/by-sa/4.0/deed.en

2.1 Spherical Harmonic Representation

A global and mathematically consistent description of the gravity field can be obtained by expressing the Earth's gravitational potential as a series expansion in spherical harmonics. The gravity field is broken down into contributions of various spatial scales in this formulation; long-wavelength features are represented by low-degree terms, while shorter-wavelength variations are described by higher-degree terms. Because the monthly Level-2 products are given in terms of spherical harmonic coefficients, this representation is especially appropriate for GRACE-based gravity field analysis (Wahr et al., 1998; Tapley et al., 2004). The gravitational potential V at a point (r, θ, λ) is expressed as

$$V(r,\theta,\lambda) = \frac{GM}{r} \sum_{n=0}^{N} \left(\frac{a}{r}\right)^n \sum_{m=0}^{n} \left(\bar{C}_{nm}\cos(m\lambda) + \bar{S}_{nm}\sin(m\lambda)\right) \bar{P}_{nm}(\cos\theta), \tag{2.1}$$

where

- GM denotes the geocentric gravitational constant,
- a is the reference Earth radius,
- $\bar{C}_{nm}$ and $\bar{S}_{nm}$ are the fully normalised spherical harmonic coefficients of degree n and order m,
- $\bar{P}_{nm}$ are the fully normalised associated Legendre functions,
- r denotes the geocentric radius,
- θ denotes the colatitude,
- λ denotes the longitude.

Here, r, θ, and λ denote the geocentric radius, colatitude, and longitude, respectively. The GRACE mission provides monthly gravity field solutions in the form of spherical harmonic coefficients up to degree and order $N = 96$. To isolate the time-variable component of the gravity field, a long-term mean gravity field C_{nm}^{mean} and S_{nm}^{mean} is removed from each monthly solution. To isolate the time-variable component of the gravity field, the long-term mean gravity field is removed from each monthly GRACE solution. The resulting residual spherical harmonic coefficients are defined as

$$\Delta C_{nm}^{(k)} = C_{nm}^{(k)} - \bar{C}_{nm}, \qquad \Delta S_{nm}^{(k)} = S_{nm}^{(k)} - \bar{S}_{nm}, \tag{2.2}$$

where

- k denotes the k-th monthly GRACE solution,
- $\bar{C}_{nm}$ and $\bar{S}_{nm}$ denote the long-term mean spherical harmonic coefficients (i.e., the average of $C_{nm}^{(k)}$ and $S_{nm}^{(k)}$ over the selected reference period),
- $\Delta C_{nm}^{(k)}$ and $\Delta S_{nm}^{(k)}$ represent the residual spherical harmonic coefficients after removal of the long-term mean field,
- these residual coefficients describe the temporal variations of the Earth's gravity field caused by mass redistribution processes,
- the residual gravity signal forms the basis for spectral analysis, decorrelation filtering, and the estimation of terrestrial water storage (TWS) variations.

2.2 Spherical Harmonic Synthesis of the residual Potential

Spherical harmonic synthesis is used to transform gravity field information from the spectral domain into the spatial domain. In this step, filtered spherical harmonic coefficients are used to compute gravitational potential variations on a regular spatial grid. This transformation allows a direct visualisation and spatial interpretation of gravity field changes and forms the basis for subsequent mass-change estimation.
Using the residual and filtered spherical harmonic coefficients, the gravitational potential anomaly ΔV at a point (r, θ, λ) is given by

$$\Delta V(r,\theta,\lambda) = \frac{GM}{r} \sum_{n=0}^{N} \left(\frac{a}{r}\right)^n \sum_{m=0}^{n} \left(\Delta C_{nm} \cos(m\lambda) + \Delta S_{nm} \sin(m\lambda)\right) P_{nm}(\cos\theta), \tag{2.3}$$

where

- ΔC_{nm} and ΔS_{nm} denote the filtered residual spherical harmonic coefficients,
- N is the maximum degree of the expansion,
- GM, a, r, θ, and λ have their usual meanings as defined previously.

The synthesis is typically performed at satellite altitude in order to minimise the amplification of high-degree noise. The resulting potential anomalies represent spatial gravity variations caused by mass redistribution processes and can be directly compared for different DDK filter strengths. For interpretability, the gravitational potential anomalies can be related to geoid height variations using the linear approximation

$$\Delta N = \frac{\Delta V}{\gamma}, \tag{2.4}$$

where γ denotes the normal gravity at the reference ellipsoid. The spatial patterns of ΔV or ΔN provide insight into the effect of different DDK filters on noise suppression and signal preservation in the spatial domain. In the context of this study, spherical harmonic synthesis serves as a link between spectral diagnostics and spatial TWS estimation. By analysing the synthesised fields obtained with different DDK filters, the impact of filter choice on spatial gravity signal quality can be systematically assessed.

2.3 Degree and Error Degree Variance

Degree and Error Degree Variance is used to analyse how the signal energy and uncertainty of GRACE gravity field solutions are distributed across different spherical harmonic degrees.
The degree variance quantifies the total signal power of a given degree and is defined as

$$C_n^2 = \sum_{m=0}^{n} \left(\bar{C}_{nm}^2 + \bar{S}_{nm}^2\right), \tag{2.5}$$

where C_{nm} and S_{nm} are the spherical harmonic coefficients of degree n and order m as defined in Equation 1
The uncertainty of the gravity field solution is characterised by the error degree variance, defined as

$$\sigma_{\bar{C}_n}^2 = \sum_{m=0}^{n} \left(\sigma_{\bar{C}_{nm}}^2 + \sigma_{\bar{S}_{nm}}^2\right), \tag{2.6}$$

where $\sigma_{\bar{C}_{nm}}$ and $\sigma_{\bar{S}_{nm}}$ denote the formal uncertainties of the spherical harmonic coefficients.
This helps to understand the distribution of signal intensity through the frequency range. Degree variance for the coefficients obtained for this study has been analysed, which shows that the signal has higher energy in the long wavelength part and it drops in shorter wavelength part of the signal. The plots for degree variance for all the

months are similar with marginal variations, so an example plot for August 2004, 2005, 2006 and 2007 is shown in Figure 2.1.

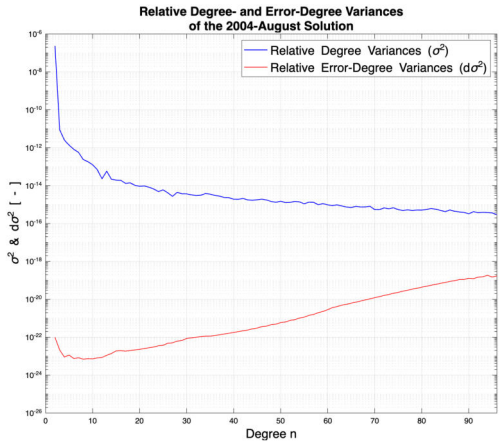

(a) Degree variance and error degree variance (August 2004)

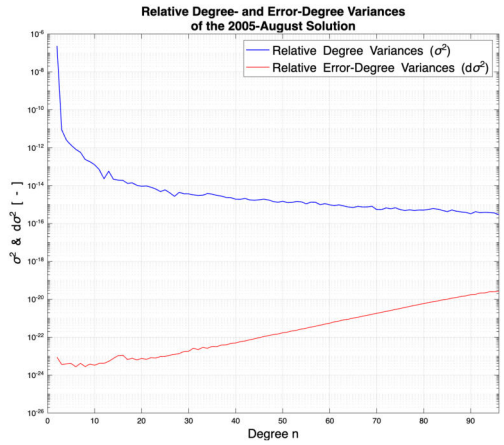

(b) Degree variance and error degree variance (August 2005)

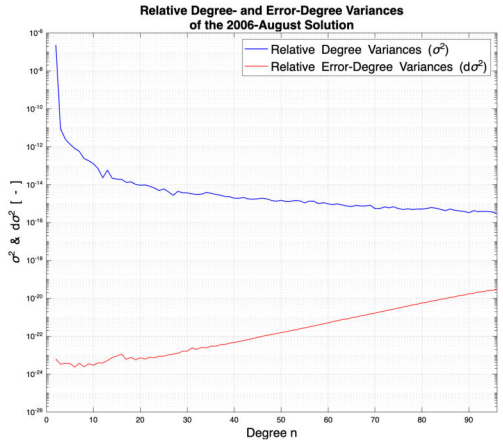

(c) Degree variance and error degree variance (August 2006)

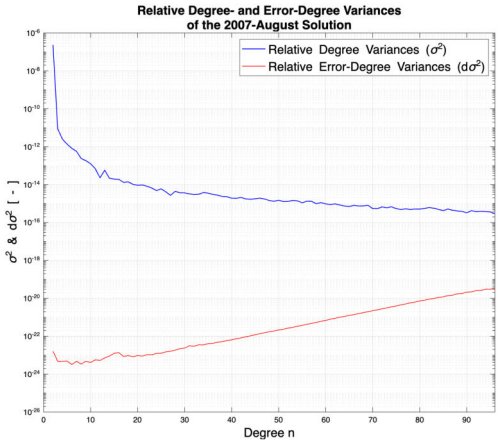

(d) Degree variance and error degree variance (August 2007)

Figure 2.1: Degree variance and error degree variance derived from GRACE data

3 DDK Decorrelation Filtering

GRACE gravity field solutions are affected by correlated errors originating from the satellite measurement geometry and the along-track observation principle. These errors manifest as north-south striping patterns in the spatial domain and increased noise at higher spherical harmonic degrees. If not mitigated, such correlated noise propagates into spatial gravity fields and degrades the quality of derived terrestrial water storage (TWS) estimates (Kusche et al., 2009).

To reduce these effects DDK filters are applied in the spectral domain. The DDK filter family consists of the unfiltered solution, denoted as DDK0, and a sequence of filtered solutions ranging from DDK1 to DDK8. These filters operate directly on the spherical harmonic coefficients and are constructed based on the covariance structure of the GRACE gravity field errors.

In this study, we focus on a subset of the DDK filters: DDK2, DDK4, DDK6, and DDK8, which are used to process the GRACE gravity field solutions for the period 2004 to 2007. The application of a DDK filter to the spherical harmonic coefficient vector can be expressed as:

$$c_{DDKi} = F_i \cdot c \tag{3.1}$$

Where:

- c denotes the vector of unfiltered spherical harmonic coefficients (DDK0),
- c_{DDKi} denotes the filtered coefficient vector corresponding to filter level i (**DDK2**, **DDK4**, **DDK6**, **DDK8**),
- F_i is the DDK filter matrix for filter strength $i = 2, 4, 6, 8$.

3.1 Trade-Off Between Noise Reduction and Spatial Resolution

The sequence from **DDK2** to **DDK8** represents a continuous trade-off between *noise reduction* and *spatial resolution*:

- **DDK2** applies a stronger filter, resulting in significant noise suppression but also substantial attenuation of short-wavelength signals.
- **DDK4** offers a moderate filtering, balancing noise reduction and signal preservation.
- **DDK6** and **DDK8** preserve more high-degree signal, retaining finer spatial details but allowing more short-wavelength noise to remain in the solution.

This study will analyze the filtered gravity field solutions processed with **DDK2, DDK4, DDK6, and DDK8**, comparing them using spectral diagnostics, such as *degree variance* and *error degree variance*, as well as spatial representations obtained through spherical harmonic synthesis. The results from the period **2004 to 2007** will be systematically compared to evaluate the impact of different DDK filter choices on **GRACE-based TWS estimation**.

4 Inverse Tesseroid Approach

To estimate surface mass variations from gravity field observations, the relationship between gravitational potential anomalies and mass changes must be inverted. This inverse problem is inherently ill-posed, as gravity observations represent spatially integrated effects of mass redistribution. A physically consistent discretisation of the mass distribution is therefore required.

In the tesseroid approach, the Earth's surface is divided into a set of spherical volume elements, referred to as tesseroids. Each tesseroid is defined by angular and radial boundaries and represents a mass element of constant density within a spherical reference geometry. Compared to planar prisms or point-mass approximations, tesseroids provide a more accurate representation of global and regional mass changes on a spherical Earth.

$$v(r,\varphi,\lambda) = G\rho\,\Delta r\,\Delta\varphi\,\Delta\lambda \left[K_{000} + \frac{1}{24}\left(K_{200}\,\Delta r^2 + K_{020}\,\Delta\varphi^2 + K_{002}\,\Delta\lambda^2\right) + O(\Delta^4) \right] \tag{4.1}$$

where

- $v(r,\varphi,\lambda)$ is the gravitational potential at the observation point with spherical coordinates (r,φ,λ);
- G denotes the Newtonian gravitational constant;
- ρ is the constant mass density of the tesseroid;
- $\Delta r = r_2 - r_1$ is the radial thickness of the tesseroid;
- $\Delta\varphi = \varphi_2 - \varphi_1$ is the latitudinal extent of the tesseroid;

- $\Delta\lambda = \lambda_2 - \lambda_1$ is the longitudinal extent of the tesseroid;
- K_{000} is the zero-order coefficient of the Taylor expansion and represents the point-mass contribution of the tesseroid;
- K_{200}, K_{020}, and K_{002} are second-order coefficients accounting for the finite spatial extent of the tesseroid in the radial, latitudinal, and longitudinal directions, respectively;
- $O(\Delta^4)$ denotes neglected higher-order terms of fourth order and above.

The inverse relationship between surface mass changes and gravitational potential anomalies can be expressed in discrete form as:

$$A\mathbf{x} = \mathbf{b} \tag{4.2}$$

where:

- $\mathbf{b}$ denotes the vector of observed gravitational potential anomalies obtained from spherical harmonic synthesis,
- $\mathbf{x}$ represents the unknown surface mass changes associated with the tesseroids,
- A is the sensitivity matrix describing the gravitational effect of each tesseroid at the observation points.

Due to the ill-conditioned nature of the inverse problem, small errors in the gravity observations can lead to large uncertainties in the estimated mass changes. To stabilise the inversion, regularisation techniques are applied, which introduce additional constraints on the solution. A commonly used approach is zero-order Tikhonov regularisation, which balances the fit to the observations and the smoothness of the solution. The regularised inverse problem can be written as:

$$\min_{\mathbf{x}} \left(\|A\mathbf{x} - \mathbf{b}\|_2^2 + \lambda^2 \|\mathbf{x}\|_2^2 \right) \tag{4.3}$$

where λ is the regularisation parameter controlling the trade-off between data misfit and solution smoothness.
In the context of GRACE-based TWS estimation, the inverse tesseroid approach allows gravitational potential anomalies derived from DDK2, DDK4, DDK6, and DDK8 filtered gravity field solutions to be consistently converted into surface mass and terrestrial water storage variations. This theoretical framework provides the basis for assessing how different DDK filter strengths influence the stability, magnitude, and spatial structure of the inverted TWS fields.

5 Data

This study is based exclusively on monthly gravity field solutions derived from satellite observations of the Gravity Recovery and Climate Experiment (GRACE). The gravity field data are used to investigate the influence of different DDK decorrelation filters on terrestrial water storage (TWS) estimation.

5.1 GRACE Gravity Field Solutions

Monthly Level-2 gravity field solutions are obtained from the German Research Centre for Geosciences (GFZ). The solutions are provided in Release 06 (RL06) format and are expressed as fully normalised spherical harmonic coefficients up to degree and order 96. Each monthly solution represents the mean gravity field over the corresponding observation period.
In addition to the unfiltered gravity field solutions, GFZ provides decorrelation-filtered gravity field products using the DDK filter family. These products enable a systematic investigation of the impact of different filter strengths on gravity field quality and derived mass-change estimates.

5.2 DDK-Filtered Products

The gravity field models used in this study are obtained from the International Center for Global Earth Models (ICGEM). For each month, gravity field solutions processed with DDK0 (unfiltered) as well as DDK1 to DDK8 are available. The DDK filters differ in their strength of decorrelation and smoothing, allowing a direct comparison between noise suppression and signal preservation.
All gravity field solutions are provided together with formal uncertainties of the spherical harmonic coefficients, which are required for spectral error analysis.

5.3 Selected DDK Filters Used in This Study

For each month, the gravity field solution is analysed using the four selected DDK products: DDK2, DDK4, DDK6, and DDK8.

5.4 Temporal Coverage

The analysis is restricted to the period **January 2004 to December 2007**. Only those monthly GRACE solutions available for this interval are processed. Months not provided as Level-2 monthly solutions are omitted from the analysis and documented in an overview table (Appendix).

5.5 Spatial Grids

Two spatial grids are used to separate synthesis and inversion steps:

- **Synthesis grid:** gravitational potential anomalies are synthesised on a global grid of $\mathbf{2}^\circ \times \mathbf{2}^\circ$.
- **Inversion grid:** the inverse tesseroid estimation of TWS is performed on a coarser $\mathbf{2.5}^\circ \times \mathbf{2.5}^\circ$ grid to improve numerical stability and reduce sensitivity to short-wavelength noise.

5.6 Uncertainty Information

Formal uncertainties of the spherical harmonic coefficients provided with the GFZ RL06 gravity field solutions are used to compute error degree variance in the spectral domain. No external geophysical or hydrological model data are applied, as the focus of this study is on the comparative assessment of DDK filter effects on GRACE-based TWS estimation.

6 Methodology

6.1 Processing Overview

The processing chain is applied consistently for each month in 2004–2007 and repeated separately for the four filter products. The main objective is to compare how filter strength influences both forward-modelled and inverted products. The steps are:

1. compute residual SH coefficients by subtracting a reference mean field,
2. synthesise gridded potential anomalies on $2^\circ \times 2^\circ$,
3. evaluate spectral diagnostics (degree variance),
4. invert potential anomalies to TWS on $2.5^\circ \times 2.5^\circ$ with regularisation,
5. compare spatial behaviour and inversion stability across DDK2/4/6/8.

6.2 Residual Spherical Harmonic Coefficients

Monthly GRACE solutions provide coefficients $C_{nm}^{(k)}$ and $S_{nm}^{(k)}$ for month k. To isolate time variability, a temporal mean field is removed as defined in Equation 2. The residual coefficients represent monthly gravity anomalies driven by mass redistribution processes as discussed in Wahr et al. 1998.

6.3 Spherical Harmonic Synthesis of Potential Anomalies

For each month and each filter, the gravitational potential anomaly $\Delta V^{(k)}$ is synthesised from the residual coefficients:

$$V(r,\theta,\lambda) = \frac{GM}{r}\sum_{n=0}^{N}\left(\frac{a}{r}\right)^n \sum_{m=0}^{n}\left(\bar{C}_{nm}\cos(m\lambda)+\bar{S}_{nm}\sin(m\lambda)\right)\bar{P}_{nm}(\cos\theta), \tag{6.1}$$

where

- GM denotes the geocentric gravitational constant,
- a is the reference Earth radius,
- $\bar{C}_{nm}$ and $\bar{S}_{nm}$ are the fully normalised spherical harmonic coefficients of degree n and order m,
- $\bar{P}_{nm}$ are the fully normalised associated Legendre functions,
- r denotes the geocentric radius,
- θ denotes the colatitude,
- λ denotes the longitude.

6.4 Spectral Diagnostics: Degree Variance

To interpret filter effects in the spectral domain, degree variance is computed as:

$$\sigma_n^2(k) = \sum_{m=0}^{n}\left[\left(\Delta C_{nm}^{(k)}\right)^2 + \left(\Delta S_{nm}^{(k)}\right)^2\right]. \tag{6.2}$$

Stronger filtering is expected to damp higher-degree power more strongly, while weaker filtering preserves more high-degree content but may show stronger noise influence at large degrees (Kusche et al., 2009; Swenson and Wahr, 2006).

6.5 Inverse Tesseroid Estimation of TWS

The inverse tesseroid approach estimates surface mass anomalies from potential anomalies using tesseroid discretisation Heck and Seitz 2007; Uieda et al. 2016. The relationship between observations and unknown mass parameters is expressed as:

$$\mathbf{y} = \mathbf{A}\mathbf{x} + \mathbf{e}, \tag{6.3}$$

where $\mathbf{y}$ contains the synthesised potential anomalies, $\mathbf{x}$ contains unknown tesseroid mass (or equivalent water height) anomalies, and $\mathbf{A}$ is the sensitivity matrix derived from tesseroid forward modelling.
Because the problem is ill-posed, Tikhonov regularisation is applied:

$$\hat{\mathbf{x}} = \arg\min_{\mathbf{x}}\left\{\|\mathbf{A}\mathbf{x}-\mathbf{y}\|_2^2 + \alpha^2\|\mathbf{L}\mathbf{x}\|_2^2\right\}, \tag{6.4}$$

where $\mathbf{L}$ is a smoothing operator and α controls the balance between data fit and smoothness Tikhonov and Arsenin 1977. The L-curve criterion provides a practical method to choose α by identifying a trade-off point between the residual norm and solution norm Hansen 1992.

6.6 Comparison Strategy Across Filter Strength

The comparison is conducted consistently at three levels:

- **Spectral level:** degree variance curves to quantify attenuation of high-degree content.
- **Synthesis maps:** $2^\circ \times 2^\circ$ potential anomaly maps to assess striping and smoothness.
- **Inversion maps:** $2.5^\circ \times 2.5^\circ$ TWS maps to evaluate amplitude, coherence, and stability.

This structure enables interpretation of whether noise patterns observed in synthesis maps propagate into the inverted mass estimates, and how this depends on filter strength Kusche et al. 2009; Swenson and Wahr 2006.

7 Results

This section presents the comparison of the four selected decorrelation filter strengths (DDK2, DDK4, DDK6, and DDK8) for the period 2004–2007. The comparison is organised into: (i) spectral behaviour (degree variance), (ii) coefficient-space diagnostics (coefficient triangle), (iii) synthesis products (potential and undulation anomalies), (iv) inversion results (TWS anomalies), and (v) regularisation diagnostics (L-curve).

7.1 Spectral characteristics: degree variance and error degree variance

Figure 7.1 shows a representative degree variance and error degree variance plot for August 2006. The plot illustrates the degree-dependent content of the solution and provides a spectral justification for using different DDK filter strengths. Stronger filtering suppresses high-degree power, whereas weaker filtering retains more short-wavelength content.

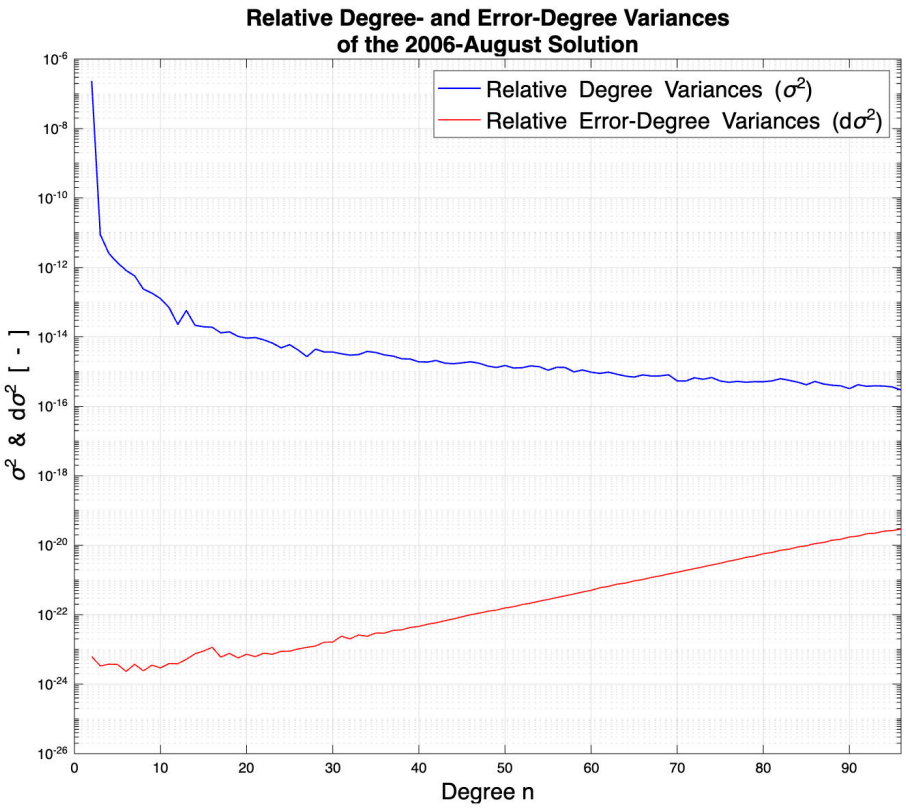

Figure 7.1: Degree variance and error degree variance example for August 2006.

7.2 Coefficient triangle comparison (April vs September 2006)

Figure 7.2 presents coefficient triangle (sigma) comparisons for April and September 2006 using DDK2, DDK4, DDK6, and DDK8 filtering. Increasing filter strength leads to progressive suppression of high-degree variability.

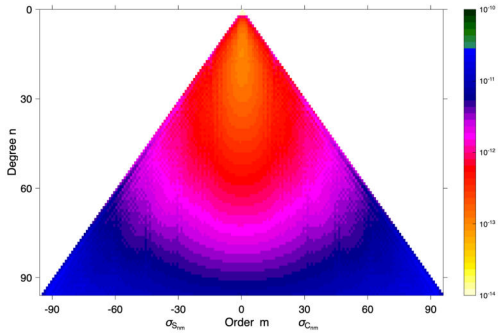

(a) DDK2 – April

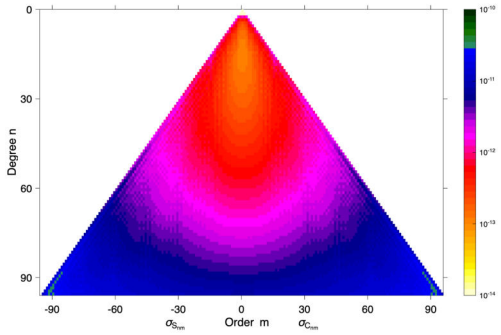

(b) DDK2 – September

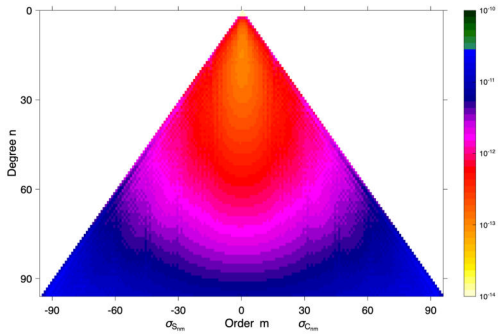

(c) DDK4 – April

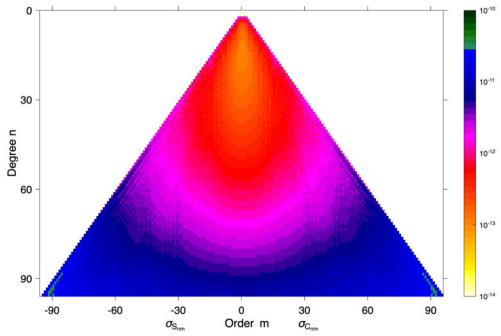

(d) DDK4 – September

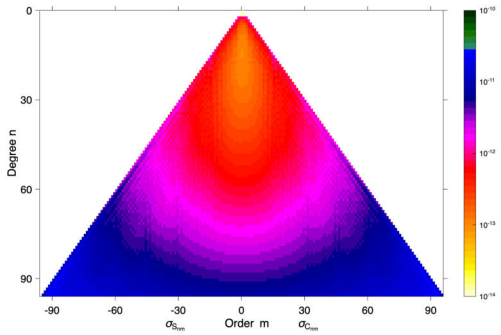

(e) DDK6 – April

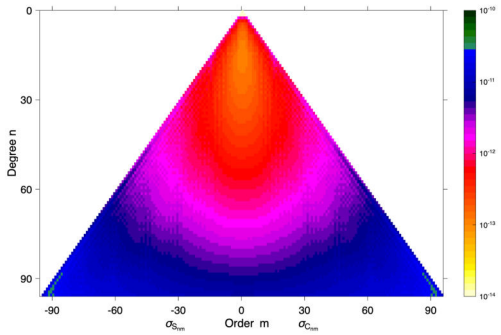

(f) DDK6 – September

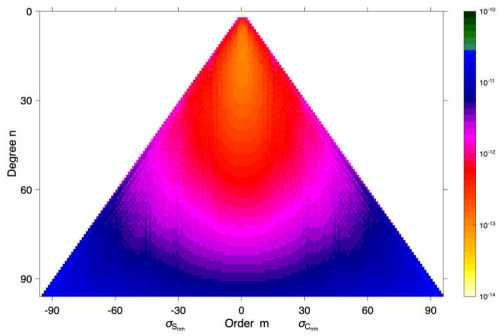

(g) DDK8 – April

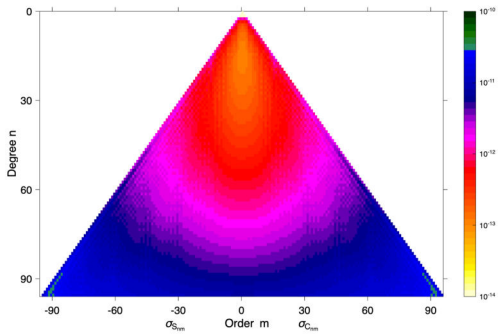

(h) DDK8 – September

Figure 7.2: Coefficient triangle comparison for April and September 2006.

Across all applied filters, August–October 2004 exhibit the poorest coefficient behaviour, characterised by pronounced high-degree contamination.

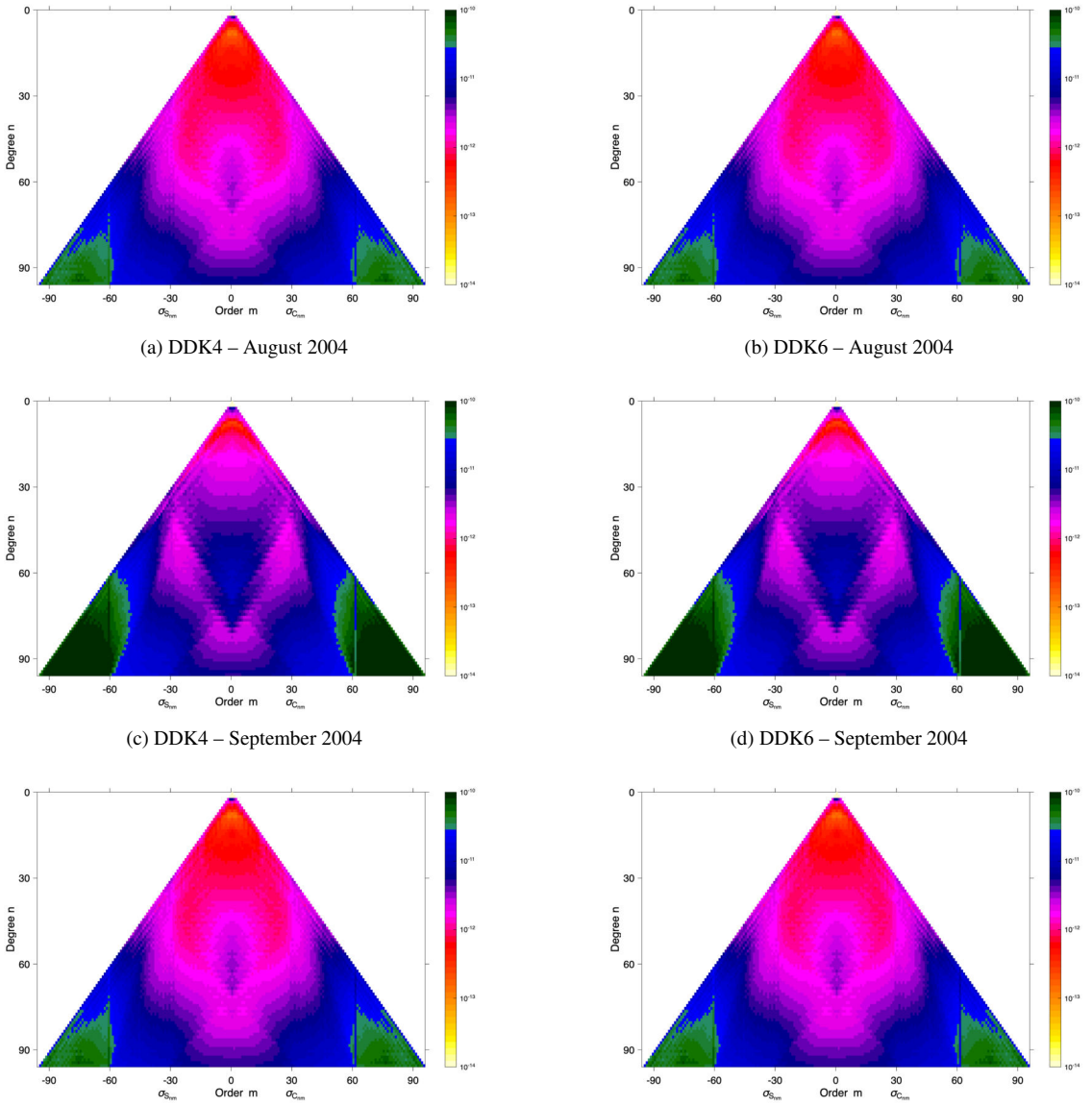

(a) DDK4 – August 2004

(b) DDK6 – August 2004

(c) DDK4 – September 2004

(d) DDK6 – September 2004

(e) DDK4 – October 2004

(f) DDK6 – October 2004

Figure 7.3: Unfavourable coefficient triangle epochs (August–October 2004).

7.3 Synthesis comparison: gravitational potential anomalies

Figure 7.4 shows synthesised gravitational potential anomalies for April 2004 and April 2007. Stronger filtering results in smoother fields with reduced short-wavelength variability.

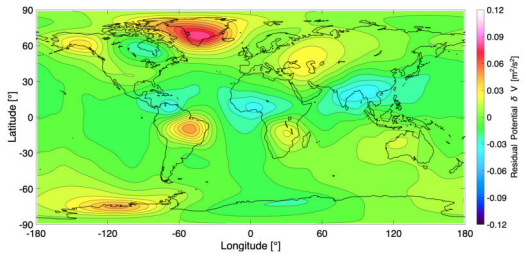

(a) DDK2 – April 2004

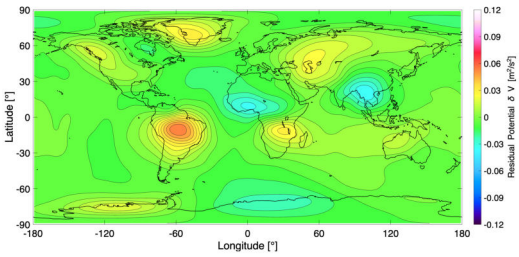

(b) DDK2 – April 2007

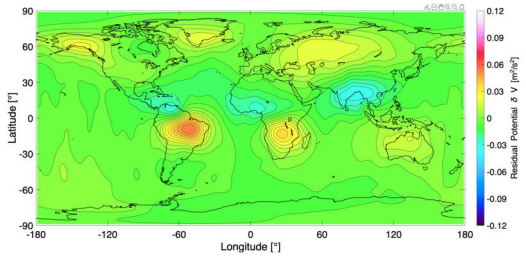

(c) DDK6 – April 2004

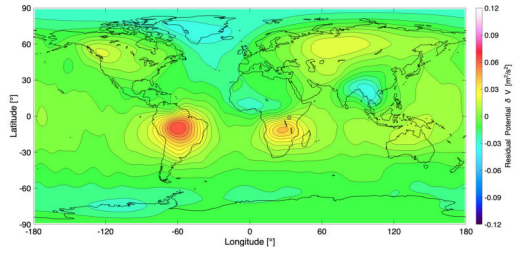

(d) DDK6 – April 2007

Figure 7.4: Synthesised gravitational potential anomalies illustrating the effect of DDK filter strength on spatial smoothness and short-wavelength variability.

7.4 Inversion diagnostics based on gravitational potential

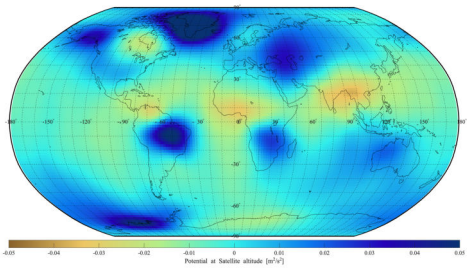

(a) Synthesised potential

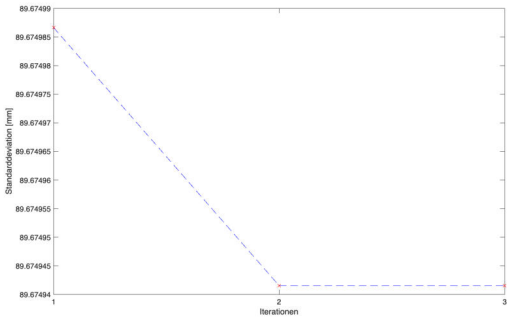

(b) Convergence diagnostic

Figure 7.5: Potential-based inversion diagnostics for April 2004 using DDK2-filtered GRACE data. Left: synthesised gravitational potential anomalies at satellite altitude. Right: convergence behaviour of the inverse tesseroid solution, illustrating rapid stabilisation after the first iteration.

7.5 Inversion comparison: TWS maps (April 2004 vs April 2007)

Figure 7.6 and Figure 7.7 present inversion-derived terrestrial water storage (TWS) anomaly maps on the $2.5^\circ \times 2.5^\circ$ grid for April 2004 and April 2007 using different DDK decorrelation filters. The maps illustrate the spatial distribution and amplitude of mass anomalies recovered through the inverse tesseroid approach.

In both epochs, large-scale hydrological patterns dominate the inverted TWS fields, with coherent regional signals observed across all applied filters. Compared to April 2004, the April 2007 TWS maps exhibit changes in both the magnitude and spatial extent of the anomalies, indicating temporal variations in continental-scale water storage. Stronger DDK filters result in smoother TWS fields with reduced short-wavelength variability, whereas weaker filters preserve more spatial detail but show increased striping artefacts. This behaviour reflects the impact of filter strength on the stability and spatial resolution of the inversion results.

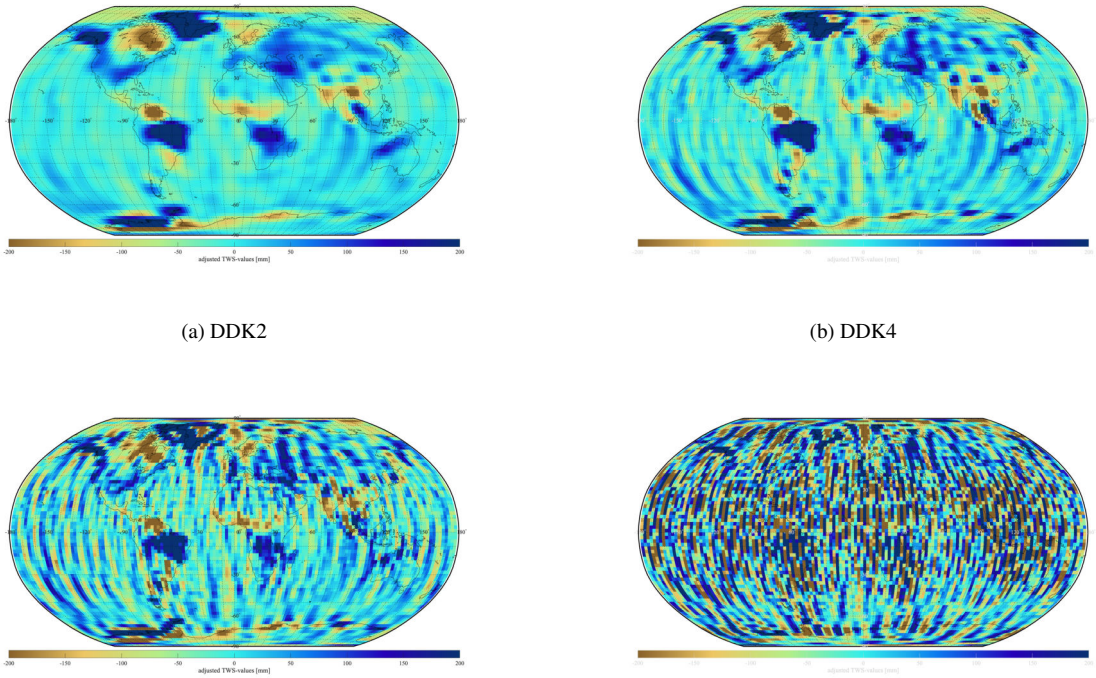

(a) DDK2

(b) DDK4

(c) DDK6

(d) DDK8

Figure 7.6: Inverted TWS anomalies (2.5°×2.5°) for April 2004 comparing DDK2/4/6/8.

7.6 Inversion statistics from monthly TWS solutions

To provide a quantitative assessment of the inversion-derived terrestrial water storage (TWS) anomalies, summary statistics were computed for selected months and decorrelation filter strengths. For each monthly solution, the minimum, maximum, mean, root-mean-square (RMS), and standard deviation (STD) of the TWS anomalies were evaluated.

Table 7.1: Summary statistics of inversion-derived TWS anomalies for selected months in 2004 and DDK filter strengths (values are in mm).

Filter	Month	Min	Max	Mean	RMS	STD
DDK2	April	-299.8	331.3	0.0	42.9	42.9
DDK4	April	-380.1	427.4	0.0	52.2	52.2
DDK6	April	-549.3	565.6	0.0	66.4	66.5
DDK8	April	-1029.5	1141.3	0.0	129.3	129.3
DDK2	September	-302.9	416.0	0.0	51.1	51.1
DDK4	September	-614.5	817.2	0.0	90.1	90.1
DDK6	September	-1409.8	1570.9	0.0	191.6	191.6
DDK8	August	-1384.1	1446.2	0.0	225.8	225.8

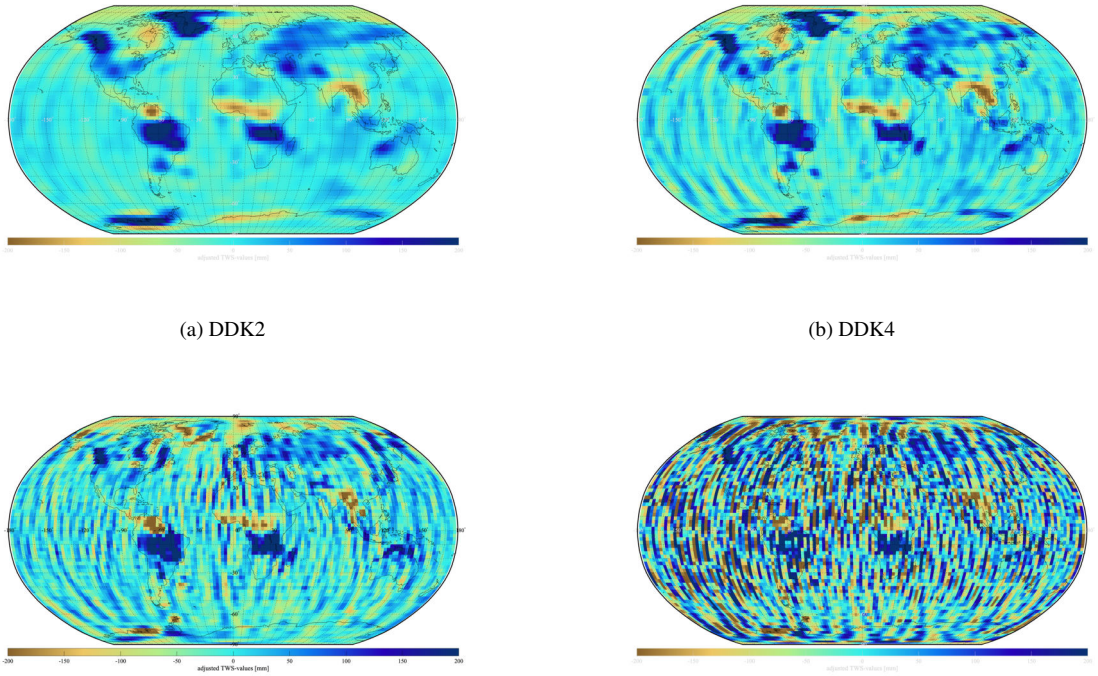

(a) DDK2

(b) DDK4

(c) DDK6

(d) DDK8

Figure 7.7: Inverted TWS anomalies (2.5°×2.5°) for April 2007 comparing DDK2/4/6/8. Scale is ±200 mm.

7.7 Regularisation diagnostic: L-curve comparison (August 2004)

The inverse tesseroid estimation of terrestrial water storage (TWS) constitutes an ill-posed inverse problem, in which small perturbations in the input gravitational potential anomalies may lead to large variations in the recovered mass distribution. To stabilise the inversion and to balance data fidelity against solution smoothness, Tikhonov regularisation is applied. The selection of an appropriate regularisation parameter is therefore a critical step in ensuring physically meaningful and numerically stable TWS estimates.

In this study, the L-curve criterion is employed as an objective diagnostic tool to determine the regularisation parameter for the inverse tesseroid approach. The L-curve represents the trade-off between the data misfit norm $\|Ax - b\|_2$ and the solution norm $\|x\|_2$ for a range of regularisation parameters. The characteristic "corner" of the L-shaped curve indicates the optimal compromise between overfitting noise-dominated observations and oversmoothing the recovered mass anomalies.

Figure 7.8 presents the L-curve comparison for August 2004 using DDK2, DDK4, DDK6, and DDK8 filtered GRACE solutions. This month is selected because it exhibits pronounced signal energy together with elevated noise levels, as identified in the coefficient triangle and degree variance diagnostics. Consequently, August 2004 provides a stringent test case for assessing the sensitivity of the inversion to regularisation.

The results demonstrate a systematic dependence of the L-curve shape on the applied DDK filter strength. Stronger filtering (DDK2) shifts the L-curve towards smaller solution norms, reflecting enhanced suppression of short-wavelength noise and improved numerical stability. In contrast, weaker filtering (DDK8) leads to larger solution norms and a less pronounced L-curve corner, indicating increased sensitivity to residual correlated noise and a stronger dependence on regularisation.

Intermediate filter strengths (DDK4 and DDK6) exhibit well-defined L-curve corners, suggesting a balanced trade-off between data misfit and solution smoothness. These filters retain sufficient signal energy for meaningful TWS

recovery while maintaining inversion stability. The location of the L-curve corner is therefore more robust for intermediate filters, supporting their suitability for the adopted grid configuration and study period.

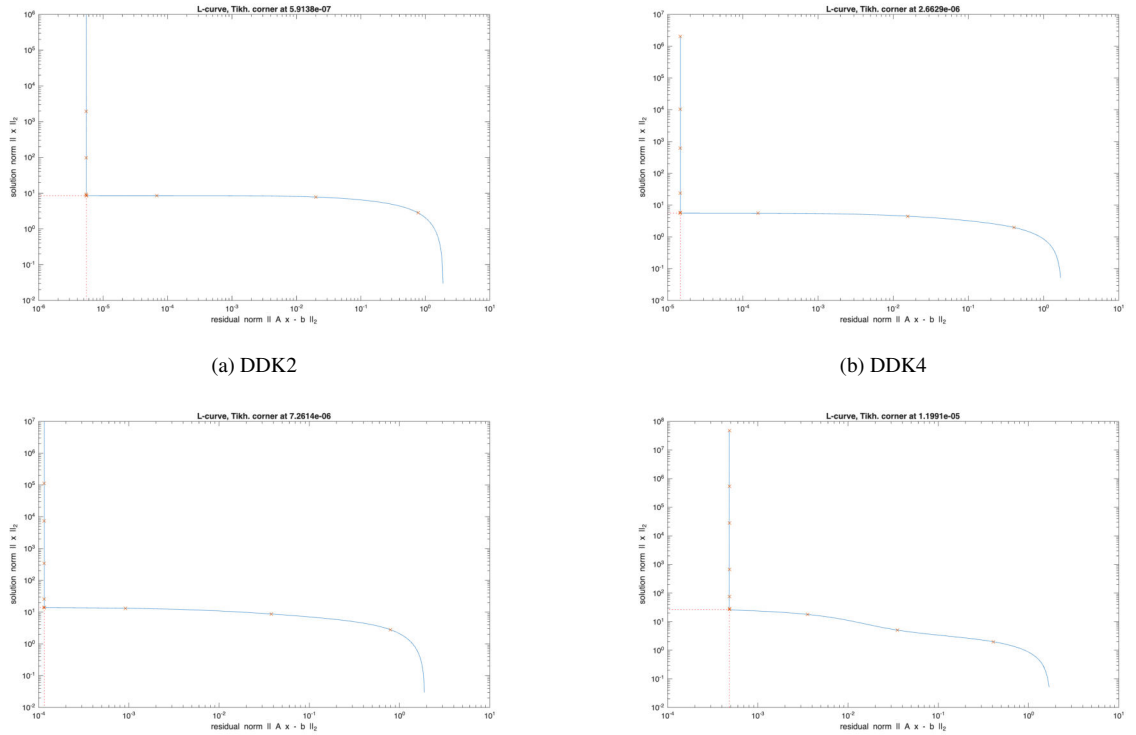

(a) DDK2

(b) DDK4

(c) DDK6

(d) DDK8

Figure 7.8: L-curve comparison for August 2004.

8 Discussion

This study compared the impact of four decorrelation filter strengths (DDK2, DDK4, DDK6, and DDK8) on (i) coefficient-space diagnostics, (ii) synthesis products on a $2^\circ \times 2^\circ$ grid, and (iii) inversion-derived TWS on a $2.5^\circ \times 2.5^\circ$ grid for the period 2004–2007. The results highlight the expected trade-off between noise suppression and signal preservation that is characteristic for post-processed GRACE solutions (Kusche et al., 2009; Swenson and Wahr, 2006).

8.1 Spectral behaviour and implications for mapping

The degree variance example (Fig. 7.1) provides a spectral interpretation of filter effects. Stronger filtering suppresses higher-degree content more strongly, which reduces short-wavelength variability in spatial fields. Weaker filters retain more high-degree power, which can preserve spatial detail but also increases sensitivity to residual noise, especially correlated errors that manifest as striping patterns (Swenson and Wahr, 2006).

8.2 Discussion of coefficient triangle results

The coefficient triangle patterns observed in Figure 7.2 reflect both seasonal variability in the Earth's gravity field and the impact of decorrelation filtering applied to GRACE data. Seasonal differences between April and September are expected due to variations in hydrological mass redistribution, which modulate the gravity field at different spatial scales (Wahr et al., 1998; Asoka et al., 2017).

The progressive reduction of high-degree variability with increasing DDK filter strength demonstrates the characteristic trade-off between noise suppression and spatial resolution. Weaker filters such as DDK2 preserve a larger fraction of high-degree coefficients but retain correlated noise patterns, which are a known feature of GRACE observations caused by the satellite measurement geometry and along-track correlations (Kusche et al., 2009). In contrast, stronger filters (DDK6 and DDK8) effectively suppress high-degree noise, leading to smoother coefficient structures but also attenuating small-scale geophysical signals.

The comparison between April and September further indicates that seasonal gravity signals are more pronounced at low to intermediate degrees, while higher-degree coefficients are increasingly dominated by noise. This behavior is consistent with previous studies, which show that large-scale mass variations dominate the GRACE signal, whereas smaller-scale features require careful regularisation to be reliably interpreted (Landerer and Swenson, 2012; Chen et al., 2014).

Overall, these results highlight the importance of selecting an appropriate filter strength depending on the scientific objective. While stronger filtering improves signal-to-noise characteristics, it may limit the recovery of regional-scale variability, which is critical for applications such as hydrological and cryospheric mass change analysis.

The qualitative characteristics of the applied DDK filters and their impact on noise suppression and spatial resolution are summarised in Table 8.1. The poorer coefficient triangle appearance for August–October 2004 indicates a reduced signal-to-noise ratio in these epochs, with correlated errors dominating at higher degrees and orders. DDK6 suppresses these artefacts more effectively than DDK4, but residual striping-like structures may remain in unfavourable months, illustrating that filtering alone cannot fully compensate month-to-month quality variations (Kusche et al., 2009; Chen et al., 2014).

Table 8.1: Qualitative comparison of DDK filter effects on coefficient triangle characteristics for April and September 2006.

Filter	Noise Suppression	High-degree Content	Spatial Resolution
DDK2	Low	Strongly preserved	High
DDK4	Moderate	Partially preserved	Moderate
DDK6	High	Strongly reduced	Low
DDK8	Very high	Largely suppressed	Very low

8.3 Discussion of potential anomaly results

The gravitational potential anomalies reflect large-scale mass redistribution processes within the Earth system. The observed differences between April 2004 and April 2007 indicate temporal changes in the underlying mass distribution, which are primarily associated with hydrological and cryospheric variability (Wahr et al., 1998; Landerer and Swenson, 2012).

The smoother appearance of the potential fields compared to coefficient-based representations is expected, as the gravitational potential emphasises long-wavelength signals while attenuating short-wavelength variability. This property makes potential anomalies particularly suitable for analysing large-scale mass changes, but less sensitive to small-scale regional features (Heiskanen and Moritz, 1967).

The influence of DDK filtering is evident in the progressive smoothing of the potential fields. Stronger filters suppress residual correlated noise more effectively, resulting in cleaner large-scale patterns. However, excessive filtering may also reduce the amplitude of geophysically meaningful signals, highlighting the need for a balanced choice of filter strength depending on the scientific application (Kusche et al., 2009; Chen et al., 2014).

The qualitative impact of DDK filtering on the gravitational potential fields is summarised in Table 8.2.

8.4 Discussion of undulation anomaly results

Undulation anomalies represent variations in the geoid height and therefore reflect changes in the Earth's gravity field integrated over large spatial scales (Heiskanen and Moritz, 1967). As a consequence, the undulation fields are

Table 8.2: Qualitative effect of DDK filtering on synthesised gravitational potential anomalies.

Filter	Noise Level	Signal Smoothness	Spatial Detail
DDK2	High	Low	High
DDK4	Moderate	Moderate	Moderate
DDK6	Low	High	Reduced
DDK8	Very low	Very high	Strongly reduced

dominated by long-wavelength signals and exhibit smoother spatial behaviour compared to spectral diagnostics such as coefficient triangles.

The differences observed between April 2004 and April 2007 indicate temporal changes in mass redistribution processes within the Earth system. These variations are primarily associated with large-scale hydrological and cryospheric mass changes captured by the GRACE mission (Wahr et al., 1998; Landerer and Swenson, 2012). The persistence of broad spatial patterns suggests that the dominant signal is controlled by regional to continental-scale mass variations rather than localised effects.

The influence of DDK decorrelation filtering is evident in the progressive smoothing of the undulation anomaly fields. Weaker filters preserve more regional-scale variability but also retain residual correlated noise, while stronger filters suppress short-wavelength noise more effectively. This behaviour reflects the inherent trade-off between noise reduction and spatial resolution in GRACE-based gravity field products (Kusche et al., 2009; Chen et al., 2014).

Overall, the undulation anomalies provide a complementary synthesis product to the gravitational potential anomalies. While both quantities emphasise long-wavelength signals, undulation fields offer a direct geodetic interpretation in terms of geoid height variations, making them particularly suitable for analysing large-scale mass redistribution processes over seasonal to interannual time scales.

8.5 Discussion of inversion-derived TWS anomalies

The inverted terrestrial water storage anomalies represent surface mass variations primarily associated with hydrological processes such as groundwater storage, soil moisture changes, and surface water variability (Wahr et al., 1998; Asoka et al., 2017). By transforming gravity field variations into equivalent water height, the inversion provides a physically interpretable measure of continental-scale mass redistribution.

The comparison between April 2004 and April 2007 reveals notable differences in both the amplitude and spatial structure of the recovered TWS anomalies. These differences suggest interannual variability in large-scale hydrological conditions, consistent with previously reported GRACE-based assessments of regional water storage change (Landerer and Swenson, 2012; Chen et al., 2014). The persistence of broad spatial patterns across all filters indicates that the dominant signal is robust and not an artefact of the inversion procedure.

The influence of DDK decorrelation filtering is clearly reflected in the inversion results. Weaker filters allow more short-wavelength signal content to pass through the inversion, but at the cost of enhanced correlated noise and striping. In contrast, stronger filters suppress these artefacts more effectively, leading to smoother TWS fields with improved spatial coherence. However, this noise reduction is accompanied by a loss of fine-scale spatial information and a reduction in recovered signal amplitude.

The numerical values derived from the L-curve analysis confirm the trends observed in the graphical diagnostics. Months characterised by stronger geophysical signals exhibit higher misfit norms at the optimal regularisation point, reflecting increased signal energy in the observations. At the same time, the corresponding solution norms indicate effective suppression of high-frequency noise without excessive smoothing.

The consistency of the selected parameters across different months demonstrates the robustness of the regularisation strategy. This supports the use of a common inversion framework for all analysed epochs, while still allowing the regularisation strength to adapt to month-specific signal characteristics..

8.6 Discussion of inversion diagnostics and potential-based results

In addition to the inversion-derived terrestrial water storage (TWS) anomalies, the gravitational potential provides an important diagnostic for evaluating the stability and internal consistency of the inverse solution. Unlike mass-related quantities, the potential is directly linked to the GRACE observations and therefore allows an assessment of how well the inversion reproduces the measured gravity field.

The synthesised potential fields obtained from the inverse tesseroid approach exhibit smooth, large-scale spatial patterns that are consistent with the expected spectral content of GRACE data after decorrelation filtering. This confirms that the applied regularisation and filtering strategy effectively suppresses high-frequency noise while preserving physically meaningful signals. Across all analysed filter strengths, the potential solutions remain spatially coherent, indicating that the inversion is well constrained at satellite altitude.

The convergence behaviour inferred from the standard deviation of the potential across iterations further supports the stability of the inversion. A pronounced reduction in standard deviation is observed between the first and second iteration, followed by only minor changes in subsequent iterations. This behaviour indicates rapid convergence towards a stable solution and suggests that additional iterations do not significantly improve the fit to the observations. Such convergence characteristics are typical for regularised inverse problems and demonstrate that the chosen inversion setup is robust.

When interpreted together with the L-curve analysis, the potential-based diagnostics provide complementary evidence for an appropriate balance between data fit and solution smoothness. The selected regularisation parameters correspond to the region of maximum curvature of the L-curve and result in stable potential fields without excessive smoothing. Months characterised by stronger geophysical signals tend to exhibit higher solution norms and misfit values, whereas months dominated by noise show increased scatter, consistent with the coefficient triangle diagnostics.

Overall, the potential and convergence diagnostics confirm that the inverse tesseroid approach yields physically meaningful and numerically stable solutions. These findings support the reliability of the derived TWS anomaly fields and justify their subsequent interpretation in terms of large-scale hydrological variability.

8.7 L-curve behaviour and regularisation sensitivity

The numerical values extracted from the L-curve analysis clearly confirm the behaviour observed in the graphical diagnostics. Months with stronger geophysical signals show higher misfit norms at the optimal regularisation point, reflecting increased signal energy in the observations. At the same time, the corresponding solution norms demonstrate that high-frequency noise is effectively suppressed without introducing excessive smoothing.

Overall, the consistency of the selected regularisation parameters across different months highlights the robustness of the regularisation strategy. This supports the use of a unified inversion framework for all analysed epochs while still allowing the regularisation strength to respond to month-specific variations in signal strength and noise characteristics.

8.8 Overall recommendation for the chosen workflow

For the adopted configuration (2° synthesis, 2.5° inversion, 2004–2007), the comparison indicates that intermediate filter strengths (DDK4/DDK6) typically provide a useful compromise between suppressing correlated noise and preserving interpretable spatial patterns. DDK2 offers strong stabilisation but risks higher attenuation, while DDK8 preserves more detail but requires careful regularisation and quality checks. The final filter choice should be stated explicitly as a methodological decision for transparent interpretation of TWS results (Kusche et al., 2009).

9 Conclusion

This study assessed how decorrelation filtering and regularisation influence GRACE-based gravity field analysis and the recovery of terrestrial water storage (TWS) variations. A consistent workflow was applied across spectral diagnostics (degree variance and coefficient triangles), spatial synthesis (gravitational potential and undulation anomalies), and inverse modelling (inversion-derived TWS anomaly maps). The results confirm that the reliability of GRACE-based mass change estimates is fundamentally controlled by the balance between noise suppression and signal preservation (Wahr et al., 1998; Kusche et al., 2009).

Key outcomes from spectral diagnostics

The degree variance and coefficient triangle diagnostics demonstrated that GRACE spherical harmonic solutions contain correlated errors that increase towards higher degrees, which manifest as striping and elevated short-wavelength variability in the spatial domain. Applying DDK filtering reduces this correlated noise systematically: weaker filters preserve more high-degree content but retain striping artefacts, whereas stronger filters (e.g. DDK6–DDK8) suppress high-degree variability more effectively, producing smoother and more stable coefficient behaviour (Kusche et al., 2009). These results provide a clear spectral justification for using decorrelation filtering prior to synthesis and inversion.

Key outcomes from synthesis products

The synthesis of gravitational potential and undulation anomalies confirmed the spectral behaviour in the spatial domain. Both products are dominated by long-wavelength patterns, as expected from physical geodesy, and therefore provide a robust representation of large-scale mass redistribution (Heiskanen and Moritz, 1967). Increasing filter strength resulted in progressively smoother anomaly fields with reduced short-wavelength features, highlighting the trade-off between noise suppression and spatial detail (Kusche et al., 2009; Chen et al., 2014). Interannual comparisons were performed for April (e.g. April 2004 vs April 2007) to ensure seasonal consistency across years, so that the observed differences can be interpreted primarily as interannual variability rather than seasonal phase effects (Wahr et al., 1998; Landerer and Swenson, 2012).

Key outcomes from inversion-derived TWS

The inverse tesseroid approach recovered physically interpretable TWS anomaly patterns on the $2.5^\circ \times 2.5^\circ$ grid, demonstrating that inversion results are sensitive to the noise characteristics of the input gravity field and the chosen filter strength. Weaker filtering retained higher spatial detail and larger amplitudes but showed stronger striping and reduced spatial stability. Stronger filtering produced more spatially coherent and interpretable TWS fields but attenuated short-wavelength features, reflecting the well-known resolution–noise trade-off in GRACE applications (Landerer and Swenson, 2012; Chen et al., 2014). The recovered mass variations are consistent with GRACE-based hydrological interpretations of continental-scale storage change (Wahr et al., 1998; Asoka et al., 2017).

Key outcomes from regularisation (L-curve and monthly values)

The ill-posed nature of the inverse problem requires regularisation to stabilise the solution. The L-curve provided an objective criterion for selecting a regularisation parameter by identifying the corner corresponding to the optimal balance between data misfit and model smoothness (Hansen, 1992). August was selected for the L-curve diagnostic because pronounced hydrological signals and higher signal-to-noise conditions make the trade-off most clearly visible, resulting in a robust parameter choice. The monthly numerical values derived from the inversion quantify this trade-off consistently across epochs, supporting a stable inversion framework while still allowing the regularisation strength to adapt to month-specific signal and noise conditions.

Overall conclusion

Across all analysis levels, the results demonstrate that there is no universally optimal DDK filter. Instead, filter selection should be guided by the spatial scale of interest and acceptable noise levels. Stronger filters improve solution stability and reduce striping, while weaker filters retain more short-wavelength variability but require more careful interpretation due to noise contamination (Kusche et al., 2009). The combined use of spectral diagnostics, synthesis products, inversion maps, and L-curve regularisation provides a transparent and defensible framework for selecting both filter strength and regularisation settings in GRACE-based TWS studies (Wahr et al., 1998; Chen et al., 2014).

10 Outlook

Future work could extend this study by (i) applying anisotropic or regionally adaptive filtering approaches, (ii) validating inversion-derived TWS anomalies with independent hydrological data (e.g. land surface models or in situ observations), and (iii) testing the sensitivity of the inversion to alternative regularisation strategies. Integrating GRACE observations with complementary datasets would further improve the interpretation of gravity-derived mass variations, especially at regional scales where the balance between noise and resolution is most critical (Landerer and Swenson, 2012).

Acknowledgement

I would like to express my sincere gratitude to my supervisor for continuous guidance, constructive feedback, and valuable suggestions throughout this lab rotation. Their support greatly helped me to structure the workflow, interpret the results, and improve the quality of this report.
I also thank the members of the Geodetic Institute at Karlsruhe Institute of Technology (KIT) for providing a supportive research environment and helpful discussions. I am grateful for access to the required data, tools, and computational resources that enabled the analysis presented in this work.
Finally, I would like to thank my family and friends for their encouragement and support during the course of this project.

References

Asoka, A., Gleeson, T., Wada, Y., and Mishra, V. (2017): Relative contributions of monsoon precipitation and groundwater abstraction to drought severity in India. *Nature Geoscience* 10:109–117.

Chen, J. L., Wilson, C. R., and Tapley, B. D. (2014): Uncertainty of GRACE gravity solutions. *Journal of Geophysical Research* 119:3732–3744.

Hansen, P. C. (1992): Analysis of Discrete Ill-Posed Problems by Means of the L-Curve. *SIAM Review* 34(4):561–580. DOI: 10.1137/1034115.

Heck, B. and Seitz, K. (2007): A comparison of the tesseroid, prism and point-mass approaches for mass reductions in gravity field modelling. *Journal of Geodesy* 81(2):121–136. DOI: 10.1007/s00190-006-0094-0.

Heiskanen, W. A. and Moritz, H. (1967): Physical Geodesy. W. H. Freeman & Co., San Francisco, USA.

Kusche, J., Schmidt, R., Petrovic, S., and Rietbroek, R. (2009): Decorrelated GRACE time-variable gravity solutions by GFZ, and their validation using a hydrological model. *Journal of Geodesy* 83:903–913. DOI: 10.1007/s00190-009-0308-3.

Landerer, F. W. and Swenson, S. C. (2012): Accuracy of scaled GRACE terrestrial water storage estimates. *Water Resources Research* 48(4). DOI: 10.1029/2011WR011453.

Swenson, S. and Wahr, J. (2006): Post-processing removal of correlated errors in GRACE data. *Geophysical Research Letters* 33(8):L08402. DOI: 10.1029/2005GL025285.

Tapley, B. D., Bettadpur, S., Watkins, M., and Reigber, C. (2004): The gravity recovery and climate experiment: Mission overview and early results. *Geophysical Research Letters* 31(9):1–4. DOI: 10.1029/2004GL019920.

Tikhonov, A. N. and Arsenin, V. Y. (1977): Solutions of Ill-Posed Problems. Winston, New York.

Uieda, L., Barbosa, V. C. F., and Braitenberg, C. (2016): Tesseroids: Forward-modeling gravitational fields in spherical coordinates. *Geophysics* 81(5):41–48. DOI: 10.1190/geo2015-0204.1. URL: https://doi.org/10.1190/geo2015-0204.1.

Wahr, J., Molenaar, M., and Bryan, F. (1998): Time variability of the Earth's gravity field: Hydrological and oceanic effects and their possible detection using GRACE. *Journal of Geophysical Research: Solid Earth* 103(B12):30205–30229.

Appendix

A Additional figures and diagnostics

A.1 L-curve of regularization parameter

This section provides supplementary L-curve diagnostics used to determine the regularization parameter for the inverse tesseroid approach. The L-curve illustrates the trade-off between data misfit and solution roughness and supports the parameter selection discussed in the main text.

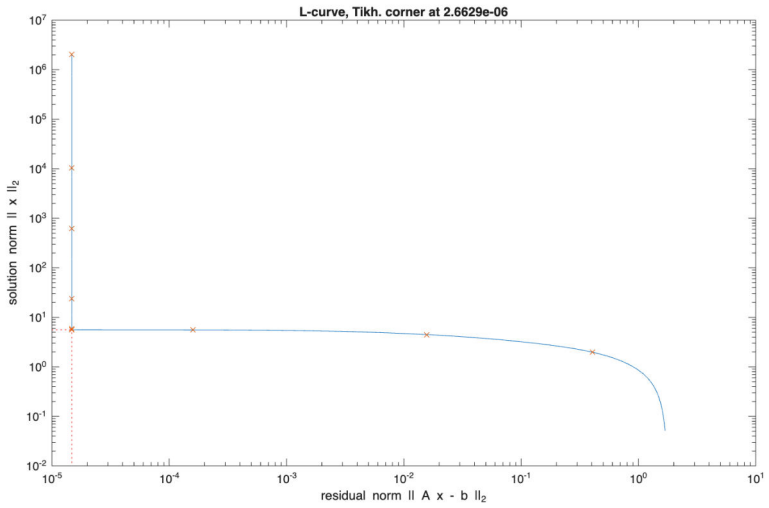

Figure A.1: Example L-curve for August 2004 (DDK4), showing the characteristic L-shaped behaviour and the selected corner point.

A.2 Worst-month coefficient triangle examples (August–October 2004)

Figure A.2 shows coefficient triangle (sigma) diagnostics for August–October 2004. These months represent unfavourable epochs characterised by pronounced high-degree contamination and correlated noise patterns.

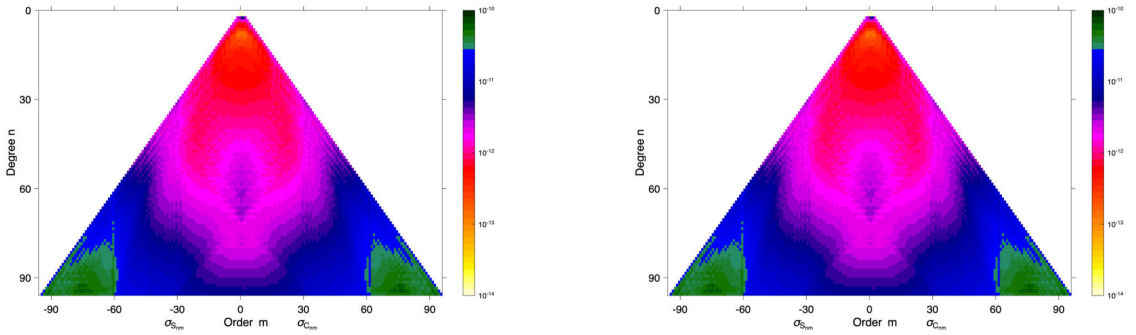

(a) DDK4 – August 2004

(b) DDK6 – August 2004

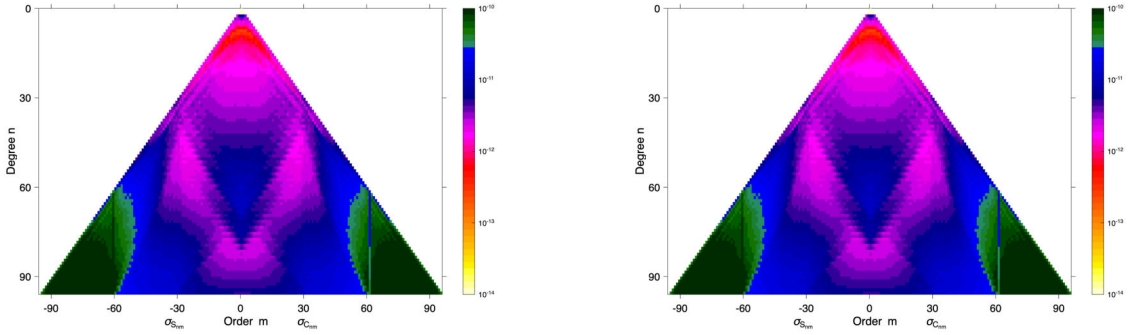

(c) DDK4 – September 2004

(d) DDK6 – September 2004

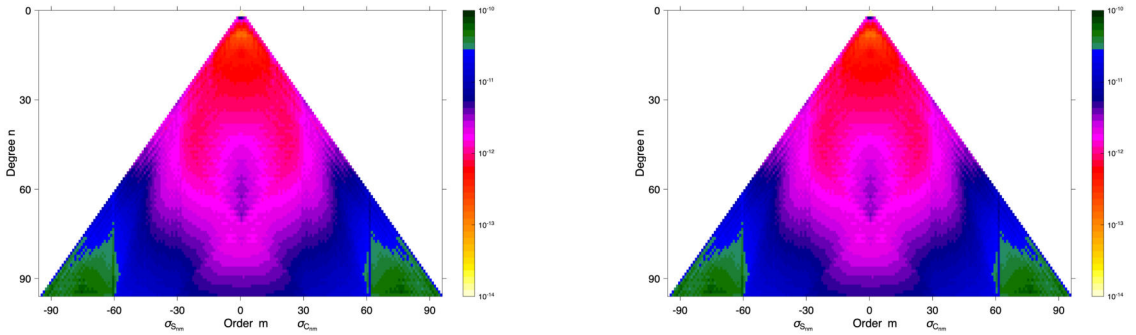

(e) DDK4 – October 2004

(f) DDK6 – October 2004

Figure A.2: Coefficient triangle (sigma) examples for August–October 2004 comparing DDK4 and DDK6. These months represent unfavourable epochs with pronounced high-degree contamination.

A.3 Spectral diagnostics: degree variance and error degree variance

Figure A.3 provides representative examples of degree variance (DV) and error degree variance (EDV) plots. These diagnostics illustrate the degree-dependent signal and noise characteristics of GRACE solutions after decorrelation filtering.

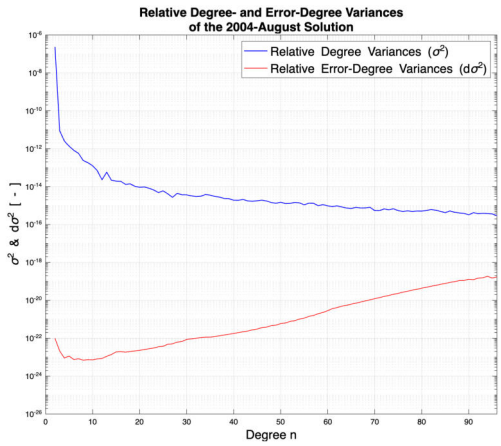

(a) August 2004 (DV/EDV)

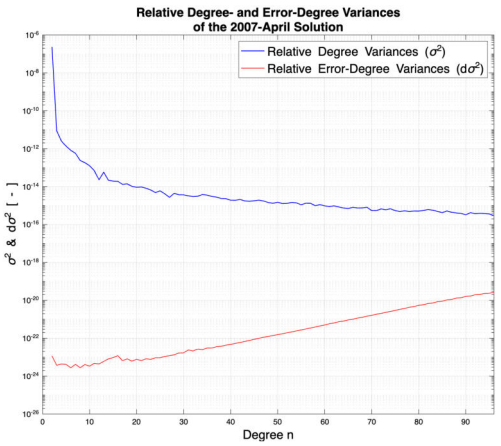

(b) April 2007 (DV/EDV)

Figure A.3: Example degree variance (DV) and error degree variance (EDV) plots illustrating the spectral behaviour of GRACE solutions for different epochs.

A.4 Coefficient triangles (percent representation)

The percent (“prozent”) representation of coefficient triangles complements the sigma representation by highlighting the relative distribution of coefficient variability across degree and order.

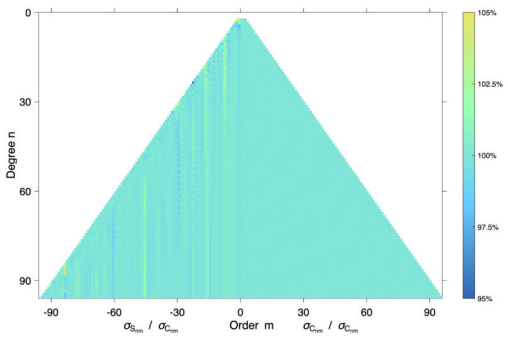

(a) DDK4 – August 2006 (percent)

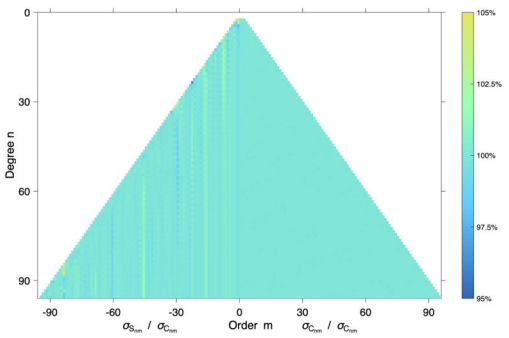

(b) DDK6 – August 2006 (percent)

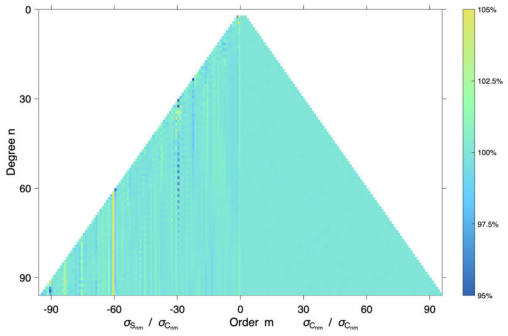

(c) DDK4 – October 2004 (percent)

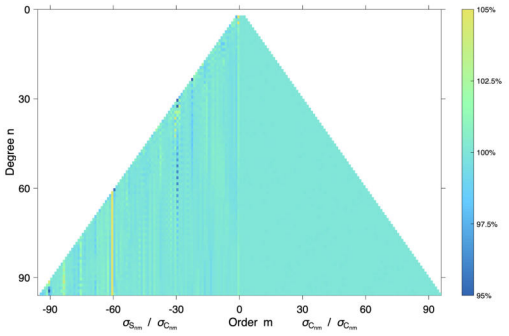

(d) DDK6 – October 2004 (percent)

Figure A.4: Coefficient triangle (percent representation) comparing DDK4 and DDK6. The percent representation emphasises the relative distribution of coefficient variability across degree and order.

Analysis of Terrestrial Water Storage Variations in the Murray-Darling Basin, Australia, Using GRACE and GLDAS Monthly Solutions

Anujith Gopal Venugopal Prameela[1]

1 Remote Sensing and Geoinformatics Master of Science (M.Sc.), KIT, Germany
E-Mail: utmsa@student.kit.edu

Abstract

This study analyzes terrestrial water storage (TWS) variations in the Murray-Darling Basin using GRACE/GRACE-FO satellite gravimetry data complemented by GLDAS land surface model outputs. GRACE Level-2 spherical harmonic coefficients were synthesized and converted to Equivalent Water Height (EWH) via the Wahr formulation to quantify large-scale mass redistribution driven by hydrological processes. Results show clear spatial and temporal variability in TWS across the basin, with strong positive anomalies during wet periods (notably April 2011, aligned with the 2010-2011 La Niña peak) and pronounced negative anomalies during October 2020, reflecting drought conditions. Interannual analysis reveals consistent seasonal patterns: April corresponds to increased storage due to accumulated rainfall, while October indicates depleted storage. Among all years, April 2011 marks maximum water storage and October 2020 one of the lowest. Comparisons between DDK2 and DDK5 filtered solutions underscore the importance of filtering in GRACE data processing. DDK5 produces smoother spatial fields and reduced high-frequency noise while preserving the large-scale signal. GLDAS-derived soil moisture shows strong agreement with GRACE-derived TWS, indicating near-surface storage significantly contributes to total TWS variability. Collectively, the combined GRACE(-FO) and GLDAS approach offers a robust framework for examining TWS dynamics and provides insights into basin-scale hydrological variability in the Murray-Darling Basin.

Future work should aim to improve spatial resolution and accuracy through advanced filtering and leakage correction, integrate additional datasets (precipitation, evapotranspiration, in-situ groundwater observations), extend analyses to longer time periods and multiple basins, and leverage ongoing GRACE-FO data for near-real-time monitoring of hydrological extremes to support sustainable water resource management under climate change.

Keywords GRACE · GLDAS · Total Water Storage (TWS) · Murray-Darling Basin (Australia)

1 Introduction

The redistribution of water within the Earth system plays a fundamental role in climate variability, hydrological extremes, and water resource sustainability. Variations in terrestrial water storage (TWS) reflect the integrated

KIT Scientific Working Papers
Issue Number 270
ISSN: 2194-1629
DOI: 10.5445/IR/1000191188
Online: June 2026

This document is licensed under the Creative Commons Attribution – Share Alike 4.0 International License (CC BY-SA 4.0):
https://creativecommons.org/licenses/by-sa/4.0/deed.en

response of groundwater, soil moisture, surface water, and vegetation water to climatic forcing and anthropogenic influence.

The Gravity Recovery and Climate Experiment (GRACE) mission, launched in 2002, and its successor GRACE Follow-On (GRACE-FO), measure temporal variations in the Earth's gravity field by tracking inter-satellite distance changes with high precision (Tapley et al., 2004; Tapley et al., 2019). Monthly gravity field models are provided by several analysis centers, including CSR (Center for Space Research), GFZ (Helmholtz Centre Potsdam), and JPL (Jet Propulsion Laboratory), as spherical harmonic coefficients up to degree and order 96.

Changes between monthly solutions, expressed as differences in spherical harmonic coefficients $(\Delta\bar{C}_{nm}, \Delta\bar{S}_{nm})$, can be transformed into surface mass anomalies following the approach of Wahr et al. (1998). After accounting for the loading effects of the solid Earth (Lithosphere), these mass changes can be expressed as Equivalent Water Height (EWH), representing Terrestrial Water Storage anomalies. GRACE-derived terrestrial water storage has been widely used to study large-scale hydrological variability and groundwater changes (Tapley et al., 2004; Rodell et al., 2009).

One major advantage of GRACE is that it senses the total water column, including groundwater, which is otherwise difficult to observe at large scales. However, GRACE does not provide information about individual storage components. The total TWS signal contains contributions from groundwater, soil moisture, surface water, snow, and biomass. Therefore, additional datasets are required to separate these components and interpret the physical processes responsible for observed TWS variations.

In this context, the Global Land Data Assimilation System (GLDAS) provides model-based estimates of land surface water and energy balance components. GLDAS integrates satellite and ground-based observations into land surface models to simulate terrestrial water and energy fluxes (Rodell et al., 2004).

For the present study, GLDAS V2.1 monthly products at 0.25° spatial resolution are used, including soil moisture, runoff, snow water equivalent, and canopy water storage. These variables are physically comparable to GRACE-derived EWH after appropriate unit conversion and spatial aggregation. In particular, soil moisture and snow water equivalent are often combined to approximate near-surface water storage, while groundwater storage can be estimated by subtracting GLDAS surface components from GRACE-derived total TWS.

This report is based on the Murray-Darling Basin (MDB), Australia's largest river basin and a key agricultural and economic region. The basin spans diverse climatic zones and is highly sensitive to hydrological variability, including prolonged droughts and extreme flood events. Previous studies have demonstrated the effectiveness of GRACE data in capturing hydrological variability over Australia, including the Murray-Darling Basin (Leblanc et al., 2009). Due to its large spatial extent, the MDB is well suited for GRACE-based analysis, as basin-scale averaging reduces short-wavelength noise and leakage effects inherent in satellite gravimetry.

This study focuses on the analysis and visualization of TWS dynamics in the Murray-Darling Basin using GRACE(-FO) Level-2 products (DDK-filtered) and GLDAS data. A mean reference solution is computed over the available time period, and monthly deviations are derived through spherical harmonic synthesis. These deviations are then projected onto a regional grid to generate spatial maps of Equivalent Water Height anomalies.

To illustrate hydrological extremes, two characteristic epochs are examined in detail. April 2011 is selected as a representative wet period characterized by strong positive TWS anomalies in the Murray-Darling Basin. This period corresponds to high rainfall and recharge conditions following the termination of the Millennium Drought in Australia. In contrast, October 2020 is chosen as a representative dry period, showing comparatively low TWS values and reduced storage conditions. The comparison of these two contrasting hydrological states provides insight into the seasonal and interannual variability of water storage and demonstrates the capability of GRACE and GLDAS to capture basin-scale water dynamics.

By combining satellite gravimetry and land surface model outputs, this study aims to quantify terrestrial water storage variations, estimate groundwater storage anomalies, and interpret hydrological processes in the Murray-Darling Basin over the period 2003-2024.

2 Theoretical Aspects

Terrestrial water storage (TWS) variations in the Murray-Darling Basin are analysed using satellite gravimetry and land surface modelling. GRACE and GRACE-FO monthly gravity solutions describe temporal mass redistribution, which is converted into TWS anomalies through spherical harmonic processing. These anomalies are combined with GLDAS data to estimate groundwater storage changes.

2.1 Spherical Harmonic Synthesis (SHS)

Spherical harmonics are given in Equation (2.1). Spherical Harmonic Synthesis is the forward computation of a function on the sphere from a series of surface spherical harmonics (Heiskanen and Moritz, 1967; Tsoulis, 1999). The spherical harmonic coefficients given as GRACE level-2 products are used to express the gravity field of the Earth.

$$V(P) = \frac{GM}{r} \sum_{n=0}^{\infty} \left(\frac{a}{r}\right)^n \sum_{m=0}^{n} (\bar{C}_{nm} \cos m\lambda + \bar{S}_{nm} \sin m\lambda) \bar{P}_{nm}(\sin \varphi) \tag{2.1}$$

where,
GM : Geocentric gravitational constant
a : Radius of the reference sphere.
$\bar{C}_{nm}, \bar{S}_{nm}$: Fully normalised spherical harmonic coefficients of degree n and order m
$\bar{P}_{nm}$: Fully normalised Legendre functions of degree n and order m.

2.1.1 Computation of Monthly Mean Reference Model

GRACE Level-2 solutions provide monthly spherical harmonic coefficients $\bar{C}_{nm}(t)$ and $\bar{S}_{nm}(t)$, where t denotes the month.
To analyze temporal mass variations, a reference mean gravity field is first computed over a selected time period consisting of T months.

$$\begin{aligned} \bar{C}_{nm} &= \tfrac{1}{T} \sum_{t=1}^{T} \bar{C}_{nm}^{(t)}, \\ \bar{S}_{nm} &= \tfrac{1}{T} \sum_{t=1}^{T} \bar{S}_{nm}^{(t)}, \end{aligned} \tag{2.2}$$

where,
$\bar{C}_{nm}, \bar{S}_{nm}$: mean spherical harmonic coefficients
T: number of months used in the reference period

2.1.2 Monthly Gravity Anomalies

For each month t, the gravity anomaly coefficients are obtained by subtracting the mean field:

$$\begin{aligned} \Delta\bar{C}_{nm}^{(t)} &= \bar{C}_{nm}^{(t)} - \bar{C}_{nm}, \\ \Delta\bar{S}_{nm}^{(t)} &= \bar{S}_{nm}^{(t)} - \bar{S}_{nm}. \end{aligned} \tag{2.3}$$

These anomaly coefficients represent temporal mass redistribution relative to the reference model.

2.1.3 Transformation to Equivalent Water Height (TWS)

The spherical harmonic coefficients $\Delta\bar{C}_{nm}$ and $\Delta\bar{S}_{nm}$ are transformed into surface mass variations using the formulation of Wahr et al. (1998). The resulting quantity is expressed as Equivalent Water Height (EWH), representing terrestrial water storage changes.
The TWS anomaly at a point (φ,λ) on the Earth's surface is given by:

$$\Delta TWS(\varphi,\lambda) = \frac{a\rho_e}{3\rho_w}\sum_{n=0}^{N}\sum_{m=0}^{n}\frac{2n+1}{1+k_n}\bar{P}_{nm}(\sin\varphi)\left(\Delta\bar{C}_{nm}\cos m\lambda + \Delta\bar{S}_{nm}\sin m\lambda\right), \tag{2.4}$$

where,
a : Mean radius of the Earth
ρ_e : Mean density of the Earth
ρ_w : Density of water
k_n : Load Love Number of degree n
$\bar{P}_{nm}$: Fully normalized Legendre functions
$\Delta\bar{C}_{nm}, \Delta\bar{S}_{nm}$: Residual, temporal Stokes coefficients
N: Maximum degree (typically 96 for GRACE, used in this study)

2.2 Degree and Error Degree Variance

The degree variance quantifies the amplitudes of the spherical harmonic coefficients, which vary across different degrees. The sum of the squared coefficients expresses the overall energy in the signal as shown in Equation (2.5). The plot shows that there is a higher degree variance at lower degrees, and the value decreases as the degree (n) increases. This shows that there is a higher concentration of signal power at lower degrees compared to higher degrees.

$$C_n^2(\bar{C}_{nm},\bar{S}_{nm}) = \sum_{m=0}^{n}(\bar{C}_{nm}^2 + \bar{S}_{nm}^2), \tag{2.5}$$

$$\sigma_n(\sigma_{\bar{C}_{nm}},\sigma_{\bar{S}_{nm}}) = \sum_{m=0}^{n}(\sigma_{\bar{C}_{nm}}^2 + \sigma_{\bar{S}_{nm}}^2). \tag{2.6}$$

This helps to understand the distribution of signal intensity through the frequency range. Degree variance for the coefficients obtained for this study has been analysed, which shows that the signal has higher energy in the long wavelength part and it drops in shorter wavelength part of the signal. The degree variance for all the months are similar with marginal variations. Therefore, one example plot for April, 2011 is shown in Figure 2.1. The degree variance is non dependent on altitude of P.

2.3 TWS using Wahr Approach

The transformation of gravity field variations into terrestrial water storage (TWS) anomalies in this study is based on the approach proposed by Wahr et al. (1998). As introduced in Equation (6), this formulation establishes the relationship between temporal changes in spherical harmonic coefficients and surface mass redistribution on the Earth.
Monthly gravity anomalies are obtained from the differences $\Delta\bar{C}_{nm}$ and $\Delta\bar{S}_{nm}$ relative to a mean reference model. These coefficients are transformed into Equivalent Water Height (EWH), which represents vertically integrated terrestrial water storage variations.
The mathematical formulation in Equation (2.4) incorporates Load Love Numbers k_n of degree n, which account for the elastic response of the Earth crust to surface loading. The scaling factor $\frac{1}{1+k_n}$ includes both the direct gravitational effect of water mass redistribution and the indirect effect due to deformation of the elastic crust of the Earth.

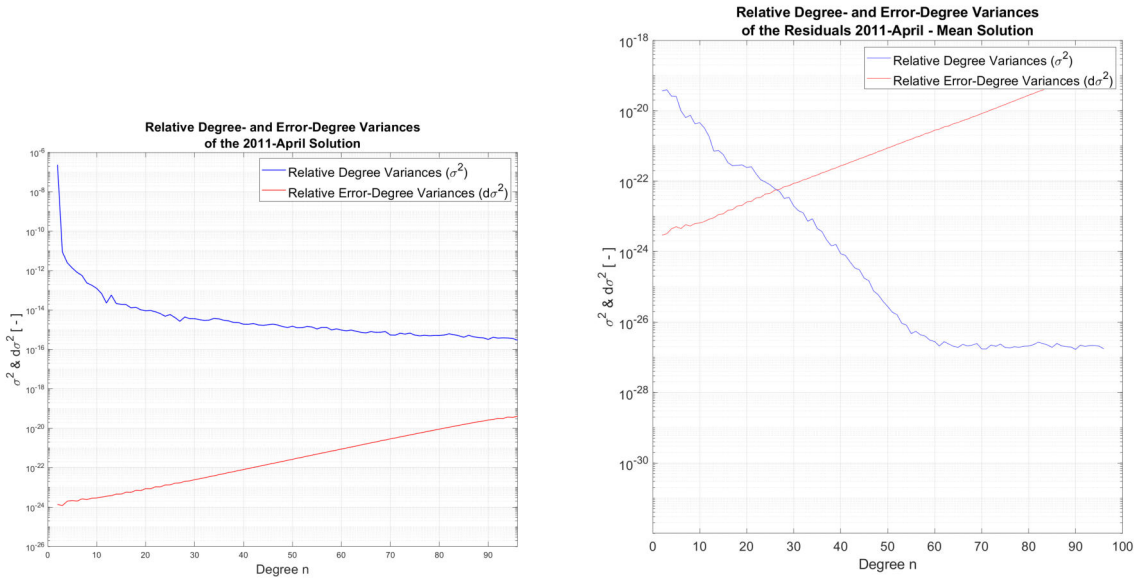

(a) Degree and Error Degree Variance

(b) Relative Degree and Error Degree Variance

Figure 2.1: Degree and Error Degree Variance using CSR for DDK2 April 2011

In addition, each spherical harmonic degree is weighted by the factor $(2n+1)$, which reflects the spatial characteristics of the signal. Lower degrees correspond to long-wavelength variations and represent large-scale mass changes, while higher degrees correspond to short-wavelength features that are more affected by noise. Therefore, the dominant contribution to TWS variations arises from the lower degrees, which is consistent with basin-scale hydrological processes.

In this study, the Wahr formulation is applied to GRACE Level-2 monthly solutions up to degree and order 96, and the resulting TWS anomalies are analysed over the Murray-Darling Basin. Due to the coarse spatial resolution of GRACE data, basin-scale averaging is performed to reduce short-wavelength noise and improve the reliability of the signal.

The computed TWS anomalies provide insight into hydrological variability, including wet and dry conditions. In particular, the strong positive anomaly observed in April 2011 reflects significant water storage increase associated with high rainfall and recharge conditions, whereas the negative anomaly in October 2020 indicates reduced storage corresponding to dry conditions.

3 Data

This study is based on the combined use of satellite gravimetry and land surface model data to analyse terrestrial water storage (TWS) variations over the Murray-Darling Basin (Chiew et al., 2022). GRACE and GRACE-FO data provide observations of total mass redistribution in the Earth system, which are used to derive TWS anomalies. To support the interpretation of these variations, land surface hydrological data from the Global Land Data Assimilation System (GLDAS) are used.

The following sections describe the GRACE(-FO) and GLDAS datasets in detail, including their sources, temporal coverage, and key variables used in this study.

3.1 GRACE data

The terrestrial water storage variations in this study are derived from data obtained from the Gravity Recovery and Climate Experiment (GRACE) mission and its successor, GRACE Follow-On (GRACE-FO). The GRACE

Table 3.1: Hydrological weather conditions of Eastern Australia

Seasons	Rainfall	Dry	Wet
Summer	December – March increasing storage	–	January – March strong buildup
Autumn	March – April peak recharge	May decline begins	April maximum TWS
Winter	– low contribution	June – August storage depletion	–
Spring	November recovery begins	September – October minimum TWS	–

mission, jointly developed by NASA and the German Aerospace Center (DLR), was launched in 2002, followed by GRACE-FO in 2018 to ensure continuity of observations. The GRACE(-FO) data used in this study are Level-2 monthly gravity field solutions, provided in the form of fully normalized spherical harmonic coefficients $\bar{C}_{nm}$ and $\bar{S}_{nm}$. These coefficients describe the Earth's gravity field and its monthly variations, which are primarily caused by mass redistribution within the Earth system, including changes in terrestrial water storage.

The data set is obtained from the International Center for Global Earth Models (ICGEM), which provides gravity field solutions computed by different analysis centers. In this study, the Release 06 (RL06) solutions from the Center for Space Research (CSR) are used. These solutions are available up to degree and order 96 and are provided on a monthly basis.

The data is available with different DDK smoothing filters applied (Kusche, 2007; Kusche et al., 2009).

The GRACE and GRACE-FO datasets together cover the period from April 2002 to the present, with a short data gap between mid-2017 and mid-2018 between the two missions. This time series allows the analysis of both seasonal and interannual variations in terrestrial water storage.

In this study, the spherical harmonic coefficients are processed to derive monthly terrestrial water storage anomalies using the Wahr et al. (1998) approach. The resulting TWS data are analyzed in the Murray-Darling Basin (see Figure 3.1), where basin-scale averaging reduces noise and enhances large-scale hydrological signals. This makes GRACE data particularly suitable for studying regional water storage variability, including extreme wet and dry conditions such as those observed in April 2011 and October 2020.

3.2 GLDAS Data

To support the interpretation of GRACE-derived terrestrial water storage (TWS) anomalies, land surface hydrological data are obtained from the Global Land Data Assimilation System (GLDAS). GLDAS is developed by NASA and integrates satellite and ground-based observations within land surface models to simulate key components of the terrestrial water and energy cycles.

In this study, GLDAS Version 2.1 data generated using the NOAH land surface model are used. The NOAH model provides physically based estimates of hydrological variables such as soil moisture, surface runoff, subsurface runoff, snow water equivalent, and canopy water storage. The data are available in NetCDF format at a spatial resolution of 0.25° and a monthly temporal resolution.

The GLDAS dataset used in this study covers the same analysis period as the GRACE(-FO) data. Monthly data are extracted for the region of Australia, and relevant variables are processed using MATLAB. In particular, soil moisture values from multiple depth layers (0–10 cm, 10–40 cm, 40–100 cm, and 100–200 cm) are combined to represent total soil water storage. Surface runoff data are also analysed to support the interpretation of hydrological conditions.

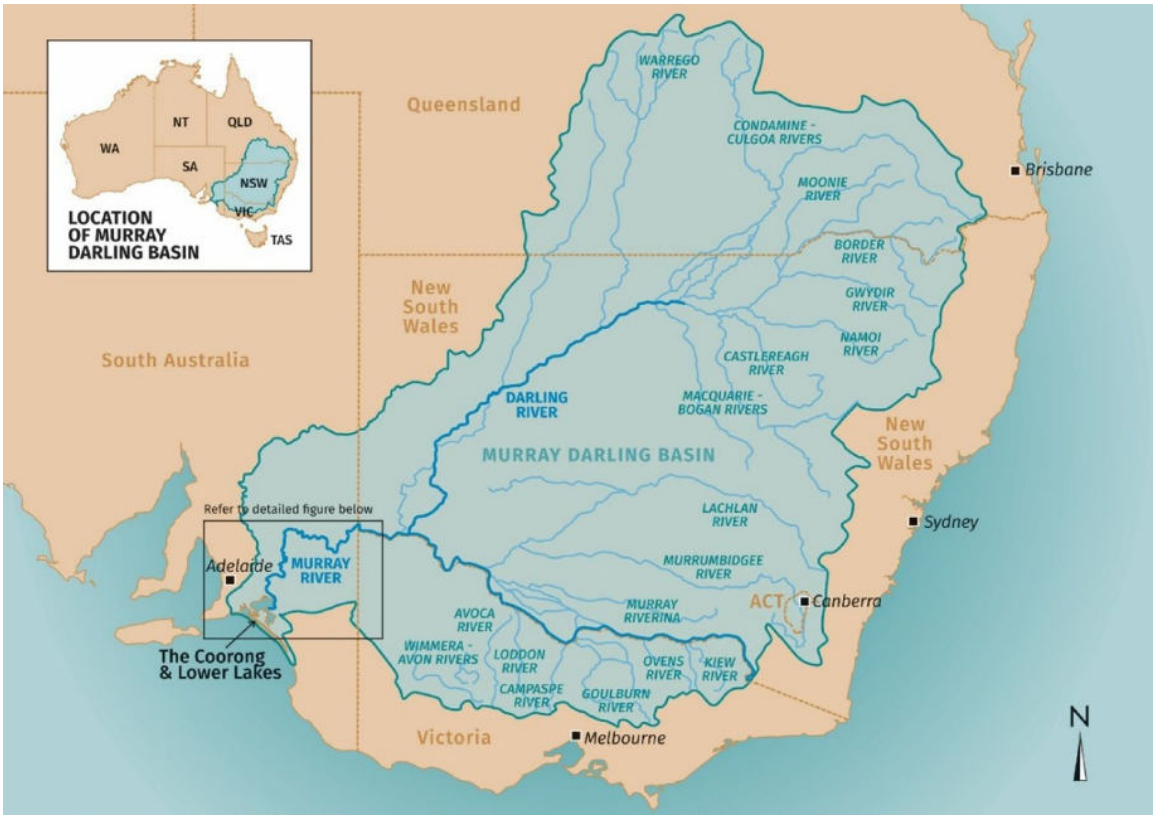

Figure 3.1: The Murray-Darling Basin (Cook, 2025).

The GLDAS variables are originally provided in units of $\mathrm{kg/m^2}$, which are converted into equivalent water height (m) to ensure consistency with GRACE-derived TWS anomalies. Spatial averaging is then performed over the Murray-Darling Basin to obtain basin-scale values.
GLDAS data represent near-surface hydrological components, whereas GRACE measures total water storage. Therefore, GLDAS outputs are used to isolate surface water contributions, allowing the estimation of groundwater storage anomalies by subtracting these components from GRACE-derived TWS.

$$\Delta GW = \Delta TWS_{GRACE} - (\Delta SM_{GLDAS} + \Delta CW_{GLDAS} + \Delta SWE_{GLDAS}) \tag{3.1}$$

where,

- ΔSM is soil moisture storage,
- ΔCW is canopy water storage,
- ΔSWE is snow water equivalent.

For the Murray-Darling Basin (Chiew et al., 2022), the contribution of snow water equivalent is generally negligible, and groundwater variations are primarily influenced by soil moisture and surface water dynamics.

3.3 Data Availability and Temporal Coverage

The availability of GRACE and GRACE-FO monthly data used in this study is illustrated in Figure 3.2. Green cells indicate months with fully available data, while yellow cells represent partially available data, and blank cells denote missing observations.

It can be observed that the data record is not continuous, particularly during the transition period between the GRACE and GRACE-FO missions (2017–2018), where significant data gaps are present. These gaps are considered during the analysis and are reflected in the temporal interpretation of TWS variations.
The identification of missing and incomplete data periods ensures consistency in the time series analysis and prevents misinterpretation of hydrological trends.

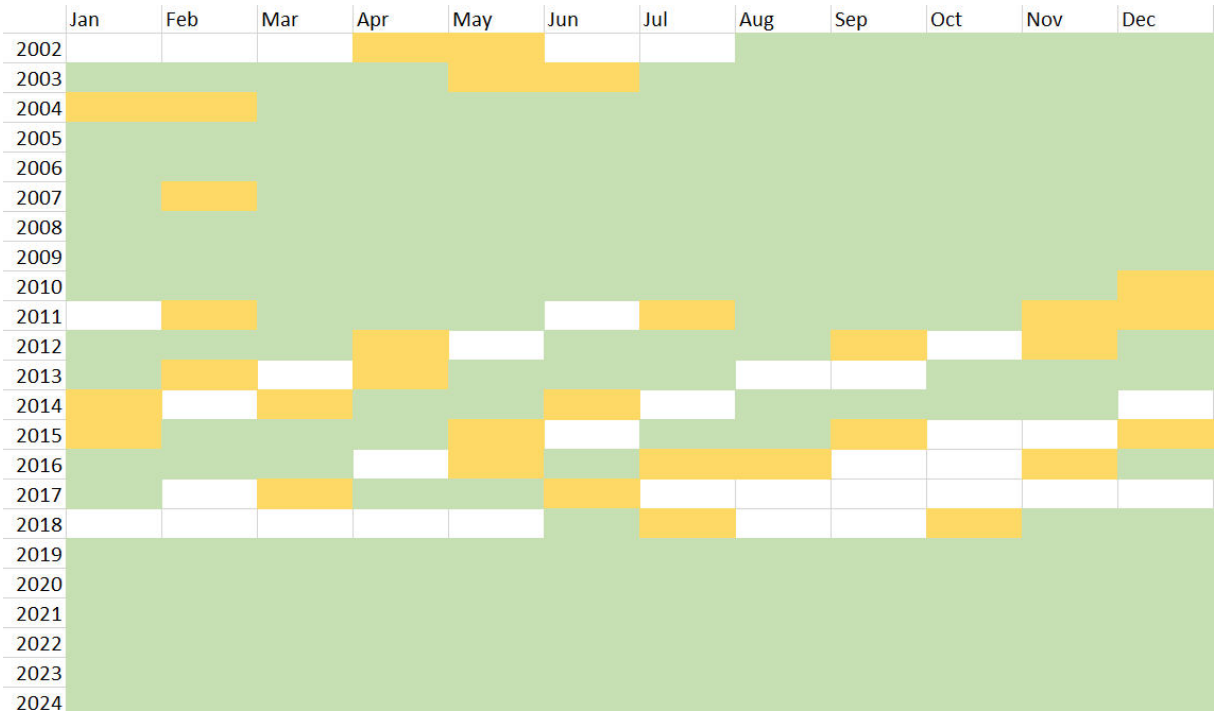

Figure 3.2: Availability of GRACE and GRACE-FO monthly data from 2002 to 2024. Green indicates fully available data, yellow indicates partially available data, and blank cells represent missing data.

4 Methodology Overview

The methodology adopted in this study is based on the processing of GRACE(-FO) Level-2 spherical harmonic solutions and GLDAS land surface model data to derive terrestrial water storage (TWS) variations over the Murray-Darling Basin. The GRACE data are processed using spherical harmonic synthesis to obtain spatial distributions of TWS anomalies, while GLDAS data are used to extract near-surface hydrological components.
The overall workflow consists of:
(i) Computation of mean potential coefficients representing the reference (mean) model (cf. Eq. (2.2)).
(ii) Computation of potential anomalies from spherical harmonic coefficients,
(iii) transformation to Equivalent Water Height (EWH) using the Wahr formulation in Eq. (2.4), and
(iv) spatial synthesis onto a regular grid.
GLDAS data are processed separately to obtain soil moisture and runoff components, which are used to support the interpretation of TWS variations and to estimate groundwater storage anomalies.
The detailed processing steps for GRACE and GLDAS datasets are described in the following subsections.

4.1 GRACE Data Processing

The GRACE(-FO) Level-2 monthly solutions are provided in the form of spherical harmonic coefficients $\bar{C}_{nm}$ and $\bar{S}_{nm}$. These coefficients are first processed to obtain a mean gravity field over the selected time period, and monthly

anomaly coefficients $\Delta\bar{C}_{nm}$ and $\Delta\bar{S}_{nm}$ are obtained by subtracting the mean coefficients from each monthly solution. This removes the static component of the gravity field and isolates temporal variations.
The anomaly coefficients are then converted into terrestrial water storage (TWS) anomalies using the Wahr et al. (1998) formulation. This transformation incorporates Load Love Numbers to account for the elastic response of the Earth and results in Equivalent Water Height (EWH) values.
Subsequently, spherical harmonic synthesis is performed to project the TWS anomalies onto a regular spatial grid. In this study, the synthesis is carried out up to degree and order 96, and the resulting data are mapped over the study region. To reduce high-frequency noise and striping effects, DDK2 and DDK5-filtered GRACE solutions are used.
Finally, a basin mask corresponding to the Murray-Darling Basin is applied to extract regional values. Basin-averaged TWS time series are computed by averaging grid values within the basin boundary, allowing the analysis of temporal variations and identification of hydrological extremes.

4.2 GLDAS Data Processing

GLDAS Version 2.1 data generated using the NOAH land surface model are used to obtain near-surface hydrological variables. The data are available in NetCDF format and are processed using MATLAB functions such as `ncread`.
Monthly GLDAS data are extracted for the study period and region. Soil moisture values from multiple depth layers (0–10 cm, 10–40 cm, 40–100 cm, and 100–200 cm) are read and combined to represent total soil water storage. Surface runoff and subsurface runoff variables are also extracted to support the interpretation of hydrological conditions.
The GLDAS variables are originally provided in units of $\mathrm{kg/m^2}$, which are converted into equivalent water height (m) for consistency with GRACE-derived TWS anomalies. Spatial subsetting is performed to restrict the data to the study region (Murray-Darling Basin).
The processed GLDAS data are then compared with GRACE-derived TWS anomalies.

5 Results and Discussion

The results obtained from GRACE and GRACE(-FO) spherical harmonic synthesis and GLDAS data processing are presented in this section. The terrestrial water storage (TWS) anomalies are analysed over the Murray-Darling Basin (see Figure 3.1) to understand spatial patterns, temporal variability, and hydrological extremes.
Both filtered GRACE solutions (DDK2 and DDK5) are evaluated to assess the consistency and noise reduction in the derived TWS fields. In addition, GLDAS-derived soil moisture is used to support the interpretation of observed variations.

5.1 Transformation from Gravity Field to Equivalent Water Height

The GRACE observations do not directly measure water storage but detect temporal variations in the Earth's gravity field caused by mass redistribution. These variations are first represented in terms of spherical harmonic coefficients, which describe changes in the gravitational potential.
From these coefficients, geoid height variations (undulation) are computed, representing changes in the Earth's equipotential surface. These undulations reflect the redistribution of mass within the Earth system, including terrestrial water storage.
To obtain a physically interpretable quantity, the geoid variations are further transformed into Equivalent Water Height (EWH) using the formulation of Wahr et al. (1998). This step converts gravity field changes into an equivalent thickness of water layer, which represents terrestrial water storage variations.

Figure 5.1 illustrates the relationship between EWH and geoid undulation for selected months. While both quantities originate from the same gravity field variations, EWH provides a more direct representation of hydrological processes.

For January 2009, both EWH and undulation show relatively smooth spatial patterns with moderate amplitudes. The consistency between the two fields indicates stable mass redistribution without strong anomalies. The signal is well-behaved and dominated by large-scale variations.

In contrast, March 2011 exhibits strong positive anomalies in both EWH and geoid undulation. This reflects significant mass accumulation associated with the 2010–2011 La Niña event. The high rainfall during this period led to increased soil moisture, surface water, and groundwater storage. The spatial patterns remain smooth, indicating that the signal is dominated by large-scale hydrological processes rather than noise.

However, the results for February 2015 show irregular and oscillatory spatial patterns, particularly in the EWH field. This behaviour is not physically consistent with natural hydrological processes and is mainly attributed to noise and artefacts in the GRACE data. Such patterns typically arise from higher-degree spherical harmonic coefficients, which are more affected by measurement errors and striping effects.

The amplification of these errors during the transformation process leads to unrealistic spatial variations. This highlights the importance of applying appropriate filtering techniques, such as DDK filtering, to suppress noise and improve the reliability of the results.

5.2 Spatial Distribution of TWS (DDK2 and DDK5)

Figures 5.2 and 5.3 show the spatial distribution of TWS anomalies for the year 2011 and 2020 based on DDK2 filtering. Similarly, Figures 5.4 and 5.5 present the results obtained using DDK5 filtering.

A clear seasonal variation is observed in both years. During 2011, strong positive anomalies are evident, particularly in the early months, with a pronounced peak in April (Figures 5.2(d) and 5.4(d)). This reflects increased water storage associated with the 2010–2011 La Niña event, which brought above-average rainfall across eastern Australia.

In contrast, the year 2020 shows predominantly negative to near-neutral anomalies (Figures 5.3(j) and 5.5(j)), with October exhibiting clear negative values. This indicates reduced water storage conditions following prolonged drought periods.

Comparing DDK2 and DDK5 results, it is observed that DDK5 filtering produces smoother spatial patterns with reduced noise and striping effects, while preserving the large-scale hydrological signals. The consistency between both filters confirms the reliability of the observed TWS variations. Leakage from DDK5 to DDK2 filtered results are observed.

5.3 Interannual Variability of April (Wet Condition)

Figures 5.6, 5.7, 5.8 and 5.9 show the spatial distribution of TWS anomalies for April months across multiple years. A clear interannual variability is observed, with April 2011 exhibiting the strongest positive anomaly among all years. This period corresponds to widespread flooding and enhanced water storage conditions across eastern Australia (Leblanc et al., 2009).

The pronounced positive anomaly indicates a significant accumulation of terrestrial water storage, primarily driven by above-average precipitation during the 2010–2011 La Niña event. Other years show comparatively moderate or near-neutral conditions, highlighting the exceptional nature of the 2011 wet period. This behaviour is consistent with the seasonal pattern summarized in Table 3.1, where water storage builds up during the summer months and reaches a maximum in April.

The spatial patterns further reveal that positive anomalies are more pronounced in the northern and central parts of the basin, suggesting regional differences in hydrological response and water storage dynamics.

5.4 Interannual Variability of October (Dry Condition)

Figures 5.10, 5.11, 5.12 and 5.13 present the TWS anomalies for October months across different years. The results indicate that strong negative anomalies characterize October 2020 compared to other years. These dry conditions are consistent with long-term hydrological deficits observed in southeast Australia, particularly during the Millennium Drought period (Van Dijk et al., 2013).

This confirms the occurrence of a pronounced dry phase with reduced water storage. This is consistent with the seasonal distribution summarized in Table 3.1, where October represents a period of minimum water storage following progressive depletion after the wet season. Earlier years show relatively weaker negative or near-neutral conditions, indicating variability in drought intensity. The persistence of negative anomalies during October highlights the impact of seasonal drying and reduced precipitation during spring months.

5.5 Basin-Averaged TWS Statistics

Figures 5.15 and 5.16 show the statistical variation of TWS, including minimum, maximum, mean, RMS, and standard deviation over time.

The results indicate that TWS exhibits significant temporal variability, with higher fluctuations observed during wet periods. The maximum values are notably higher around 2010–2012, corresponding to the wet phase, while lower values are observed during drought periods.

The consistency between DDK2 and DDK5 statistics further confirms the robustness of the derived TWS signals. Minor discontinuities in the time series are consistent with the data gaps shown in Figure 3.2.

5.6 GLDAS Soil Moisture Analysis

Figure 5.14 shows the temporal variation of soil moisture for different depth layers over eastern Australia.

The results indicate that deeper soil layers (40–100 cm and 100–200 cm) contribute significantly to total soil moisture storage and show smoother temporal variations. A clear increase in soil moisture is observed around 2010–2012, corresponding to the wet period identified in GRACE TWS results.

In contrast, reduced soil moisture values are observed during the period around 2019–2020, consistent with the dry conditions reflected in GRACE data.

5.7 Overall Interpretation

The combined analysis of GRACE TWS anomalies and GLDAS soil moisture demonstrates a strong relationship between large-scale water storage variations and climatic conditions.

The wet period of April 2011 is characterized by significant positive anomalies in both GRACE and GLDAS datasets, indicating increased water storage and recharge. In contrast, the dry period of October 2020 shows negative anomalies, reflecting depletion of water storage.

These results confirm that GRACE-derived TWS is highly sensitive to climatic variability and provides valuable insights into regional hydrological processes at basin scale.

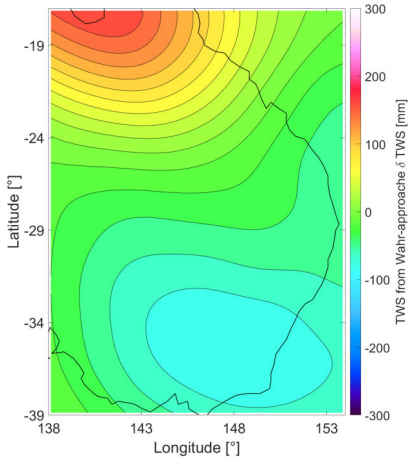

(a) 2009 January EWH

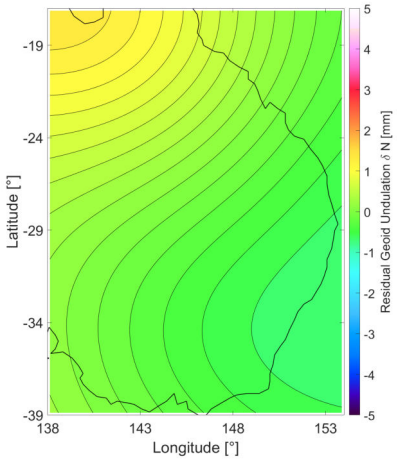

(b) 2009 January Geoid Undulation

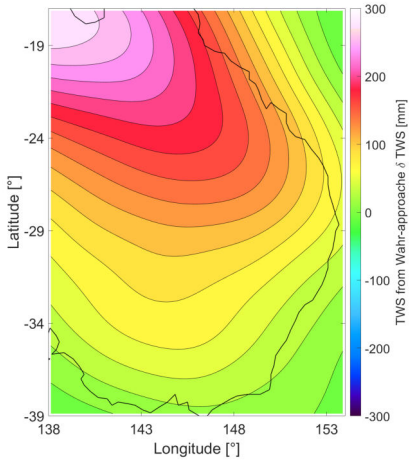

(c) 2011 March EWH

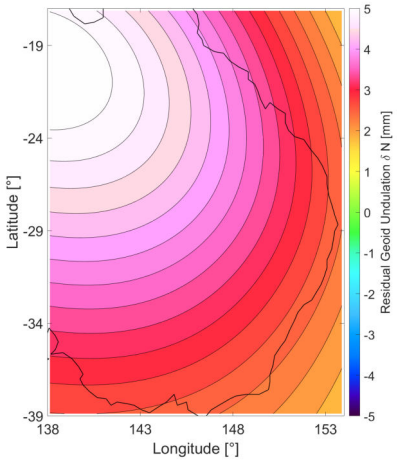

(d) 2011 March Geoid Undulation

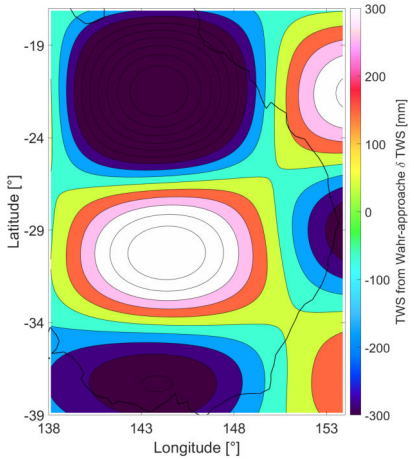

(e) 2015 February EWH

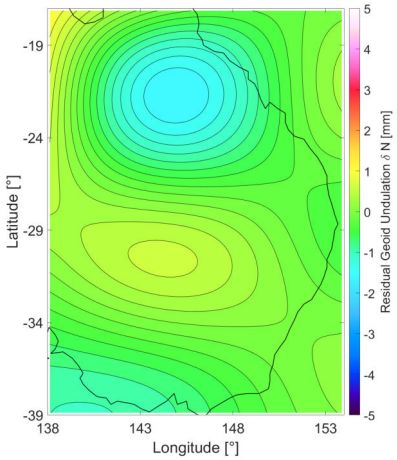

(f) 2015 February Geoid Undulation

Figure 5.1: Comparison between Equivalent Water Height (EWH) and geoid undulation derived from GRACE Level-2 spherical harmonic coefficients (DDK2 filtered) for selected months. (units are in mm)

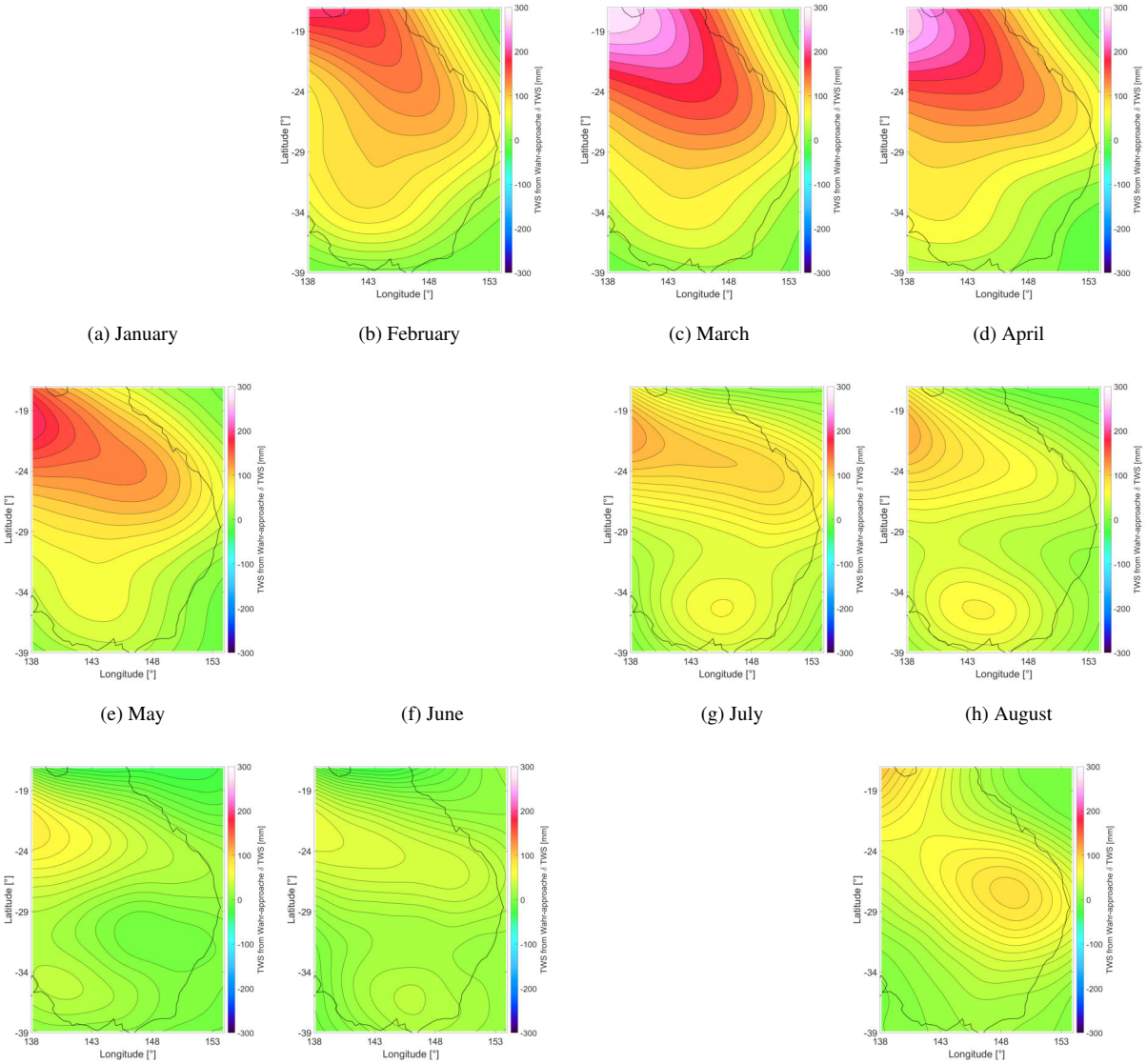

(a) January (b) February (c) March (d) April

(e) May (f) June (g) July (h) August

(i) September (j) October (k) November (l) December

Figure 5.2: TWS in 2011 based on DDK2 (units are in mm)

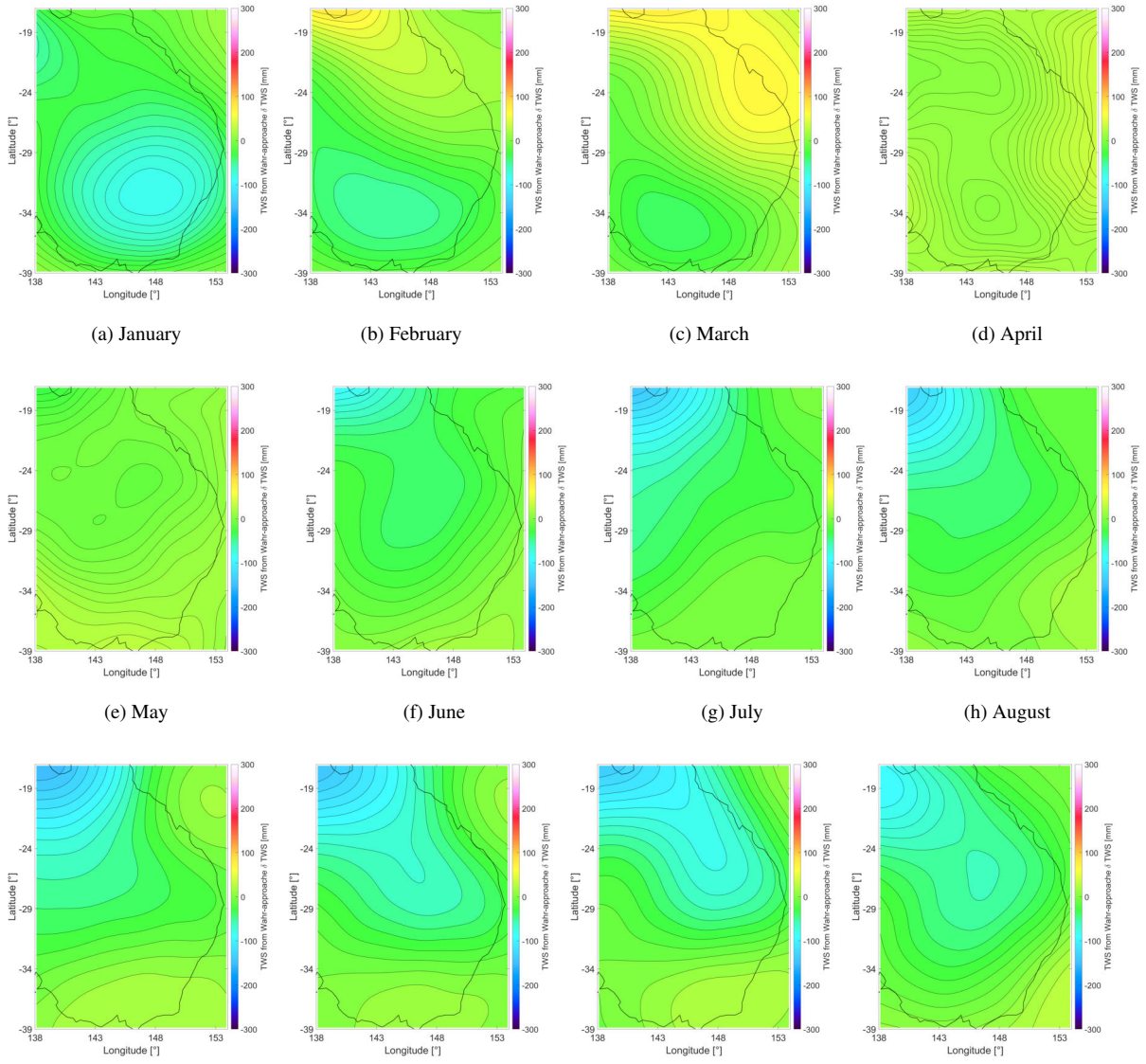

(a) January (b) February (c) March (d) April

(e) May (f) June (g) July (h) August

(i) September (j) October (k) November (l) December

Figure 5.3: TWS in 2020 based on DDK2 (units are in mm)

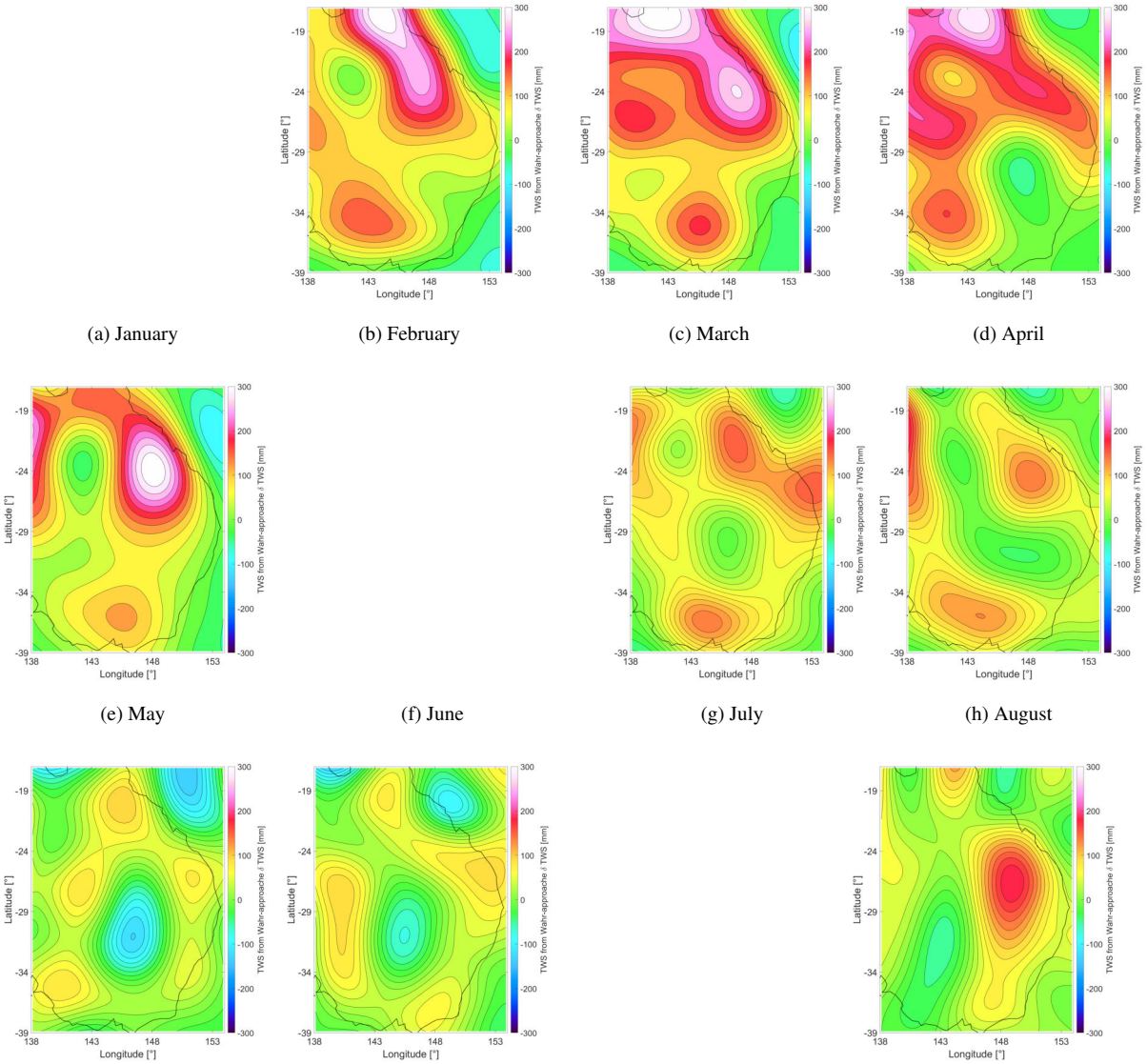

(a) January (b) February (c) March (d) April

(e) May (f) June (g) July (h) August

(i) September (j) October (k) November (l) December

Figure 5.4: TWS in 2011 based on DDK5 (units are in mm)

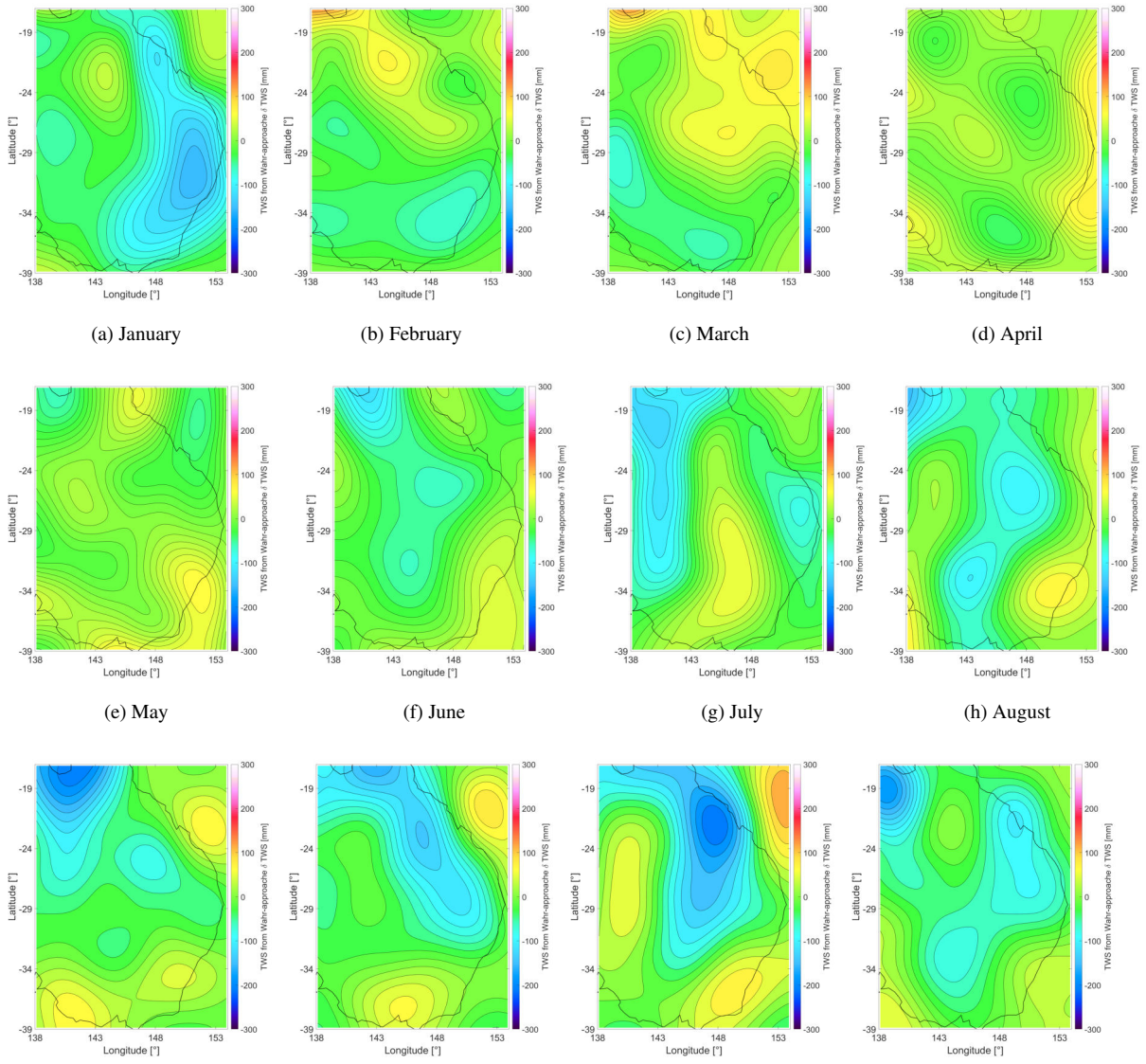

(a) January (b) February (c) March (d) April

(e) May (f) June (g) July (h) August

(i) September (j) October (k) November (l) December

Figure 5.5: TWS in 2020 based on DDK5 (units are in mm)

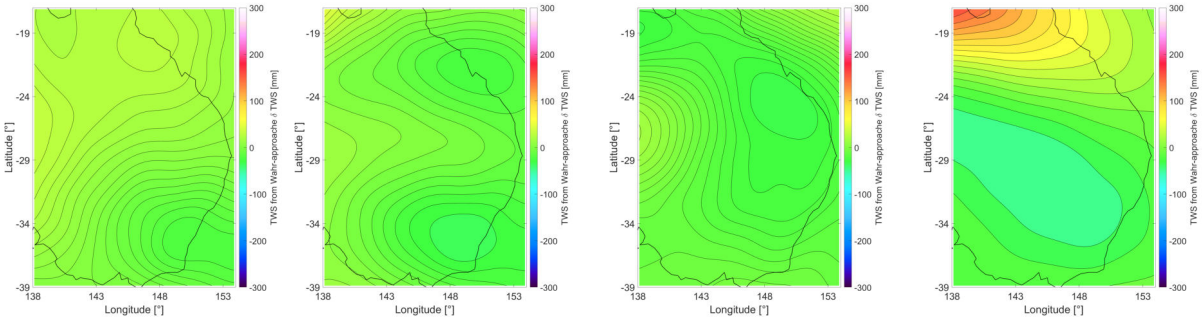

(a) April 2003 (b) April 2004 (c) April 2005 (d) April 2006

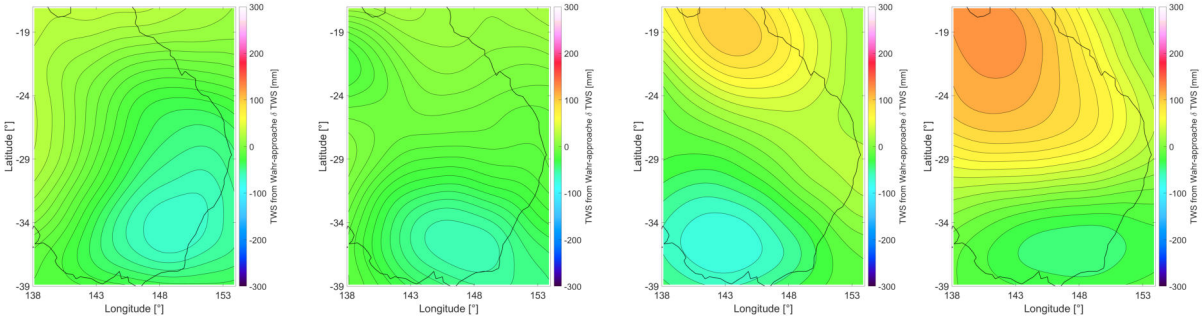

(e) April 2007 (f) April 2008 (g) April 2009 (h) April 2010

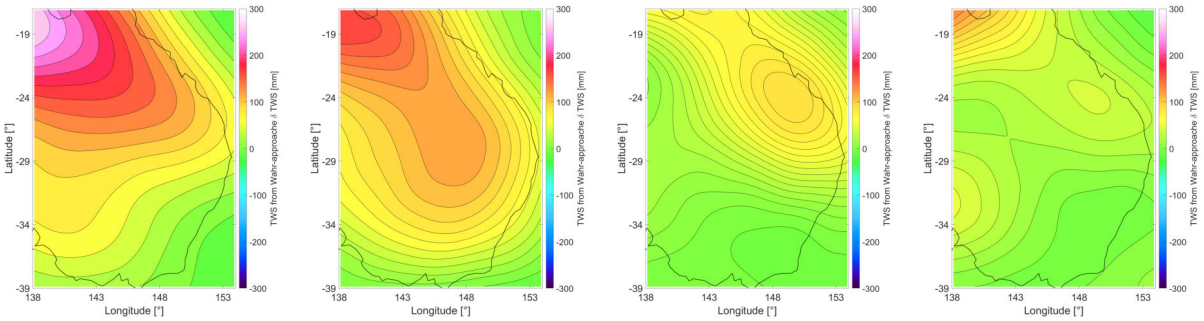

(i) April 2011 (j) April 2012 (k) April 2013 (l) April 2014

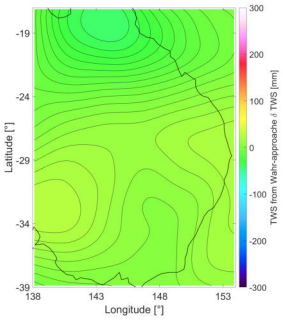

(m) April 2015 (n) April 2016 (o) April 2017

Figure 5.6: TWS of April months of years from 2003 to 2017 based on DDK2 GRACE mission (units are in mm)

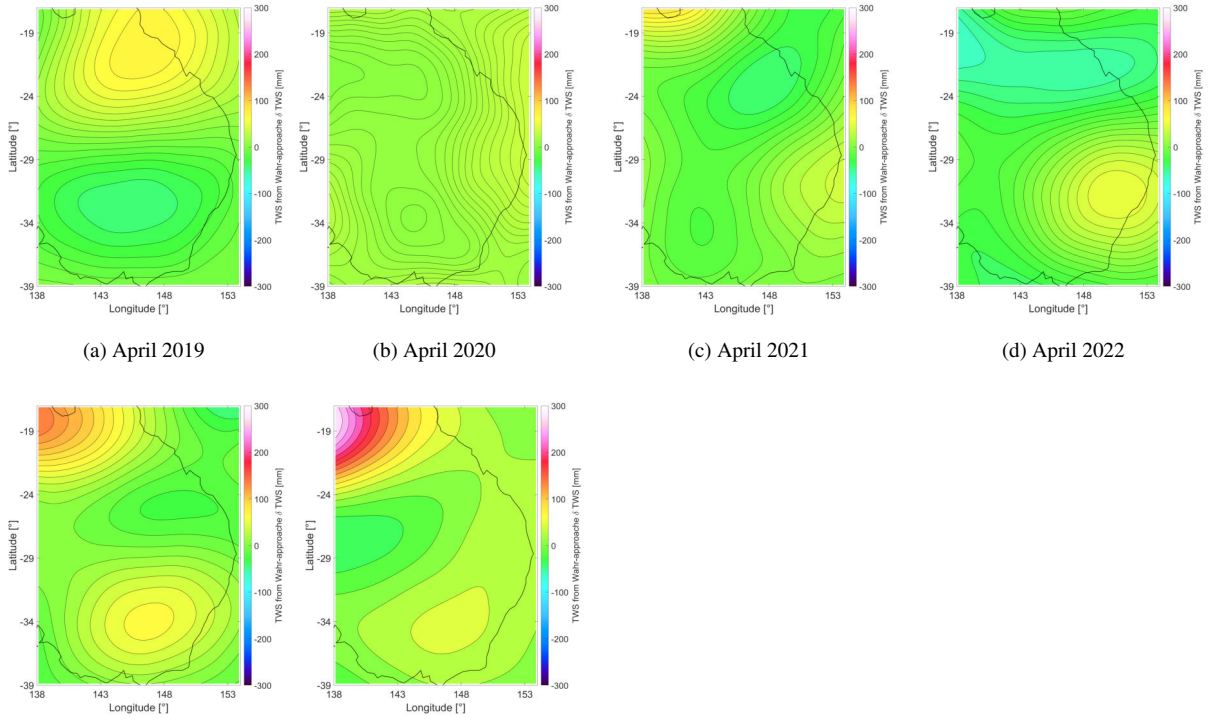

(a) April 2019 (b) April 2020 (c) April 2021 (d) April 2022

(e) April 2023 (f) April 2024

Figure 5.7: TWS of April months of years from 2019 to 2024 based on DDK2 GRACE-FO mission (units are in mm)

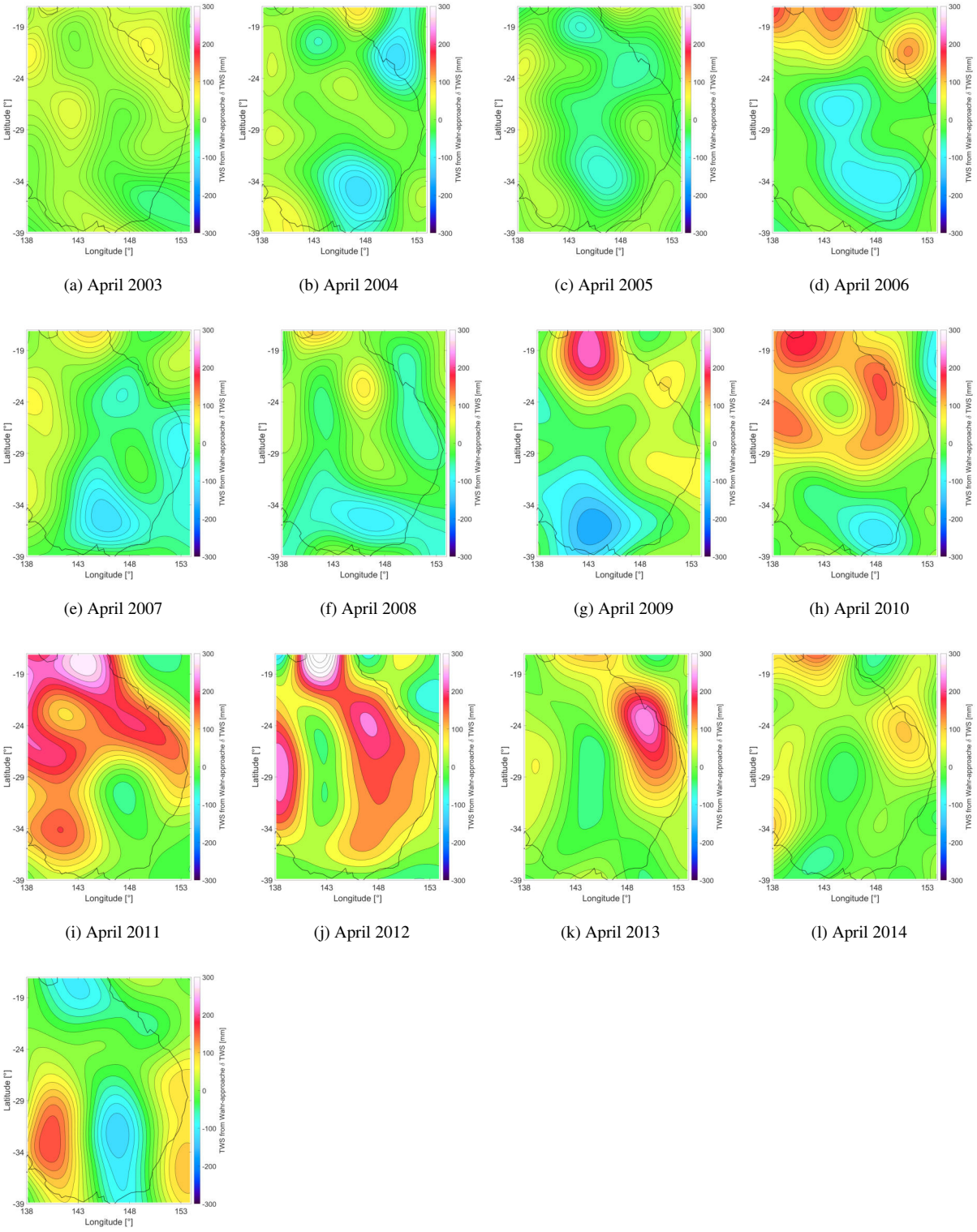

(a) April 2003 (b) April 2004 (c) April 2005 (d) April 2006

(e) April 2007 (f) April 2008 (g) April 2009 (h) April 2010

(i) April 2011 (j) April 2012 (k) April 2013 (l) April 2014

(m) April 2015 (n) April 2016 (o) April 2017

Figure 5.8: TWS of April months of years from 2003 to 2017 based on DDK5 GRACE mission (units are in mm)

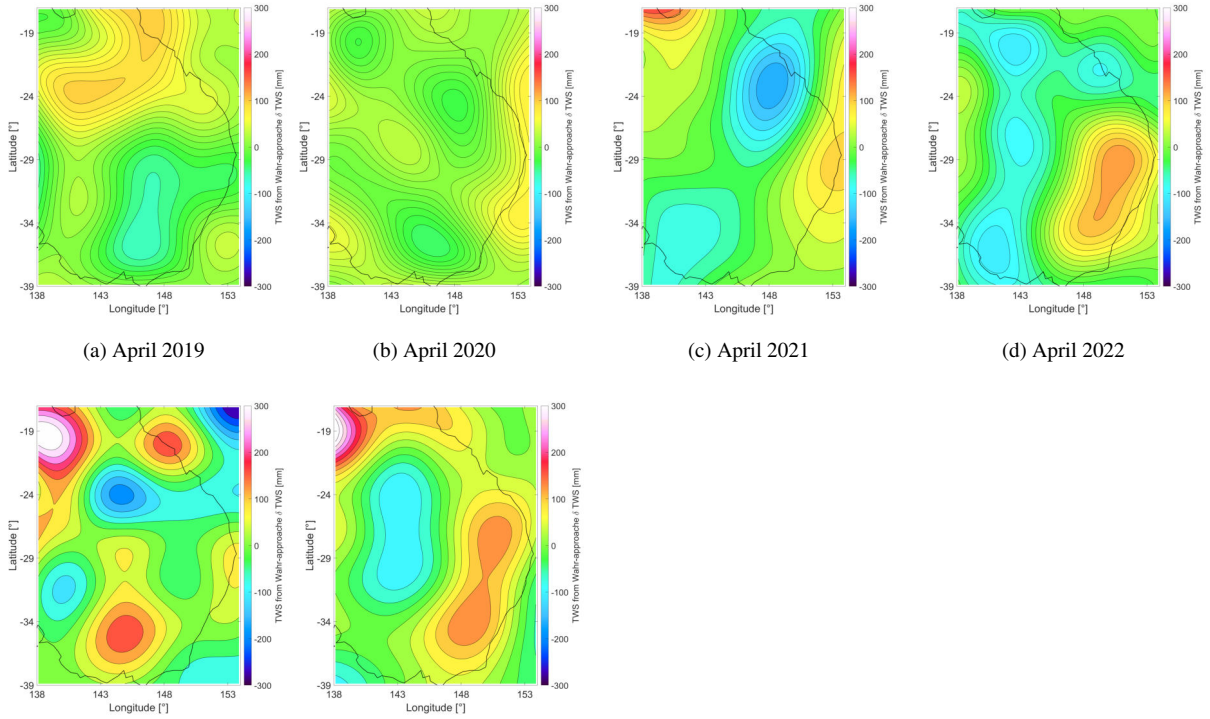

(a) April 2019 (b) April 2020 (c) April 2021 (d) April 2022

(e) April 2023 (f) April 2024

Figure 5.9: TWS of April months of years from 2019 to 2024 based on DDK5 GRACE-FO mission (units are in mm)

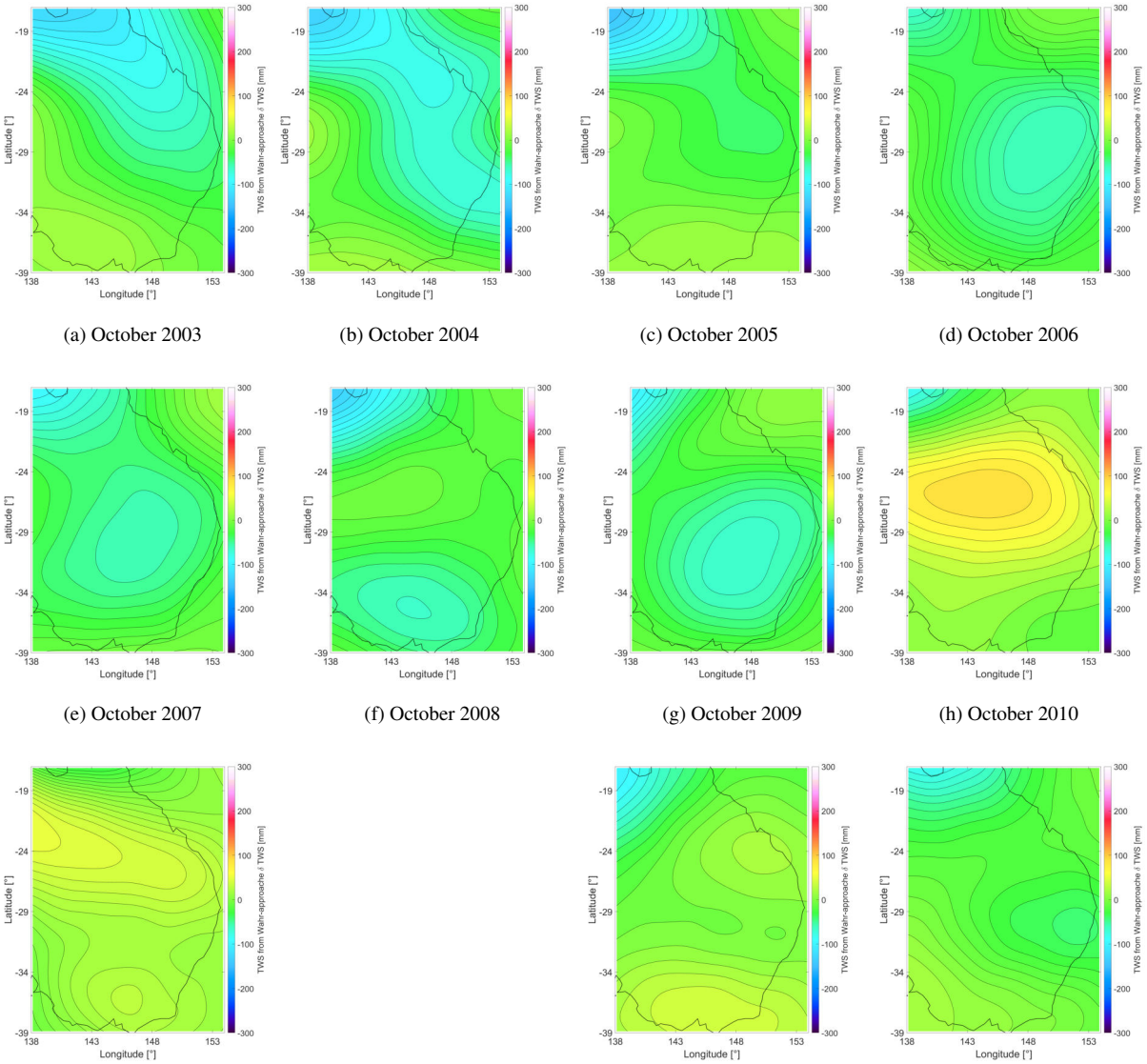

(a) October 2003 (b) October 2004 (c) October 2005 (d) October 2006

(e) October 2007 (f) October 2008 (g) October 2009 (h) October 2010

(i) October 2011 (j) October 2012 (k) October 2013 (l) October 2014

(m) October 2015 (n) October 2016 (o) October 2017

Figure 5.10: TWS of October months of years from 2003 to 2017 based on DDK2 GRACE mission (units are in mm)

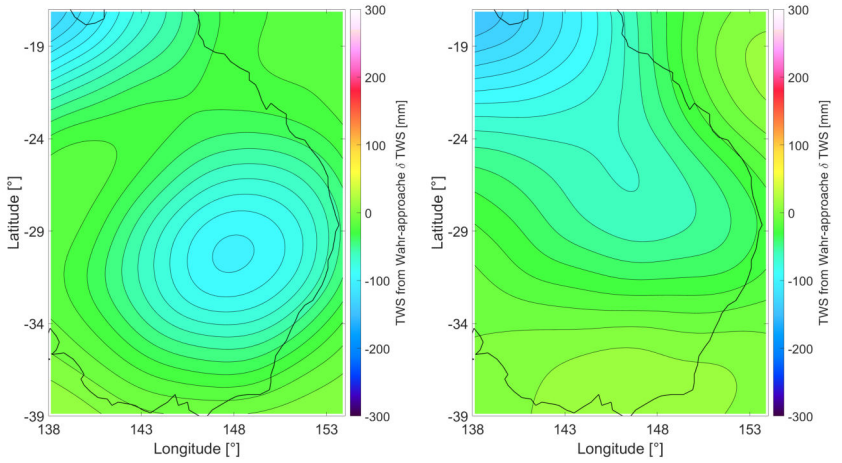

(a) October 2019

(b) October 2020

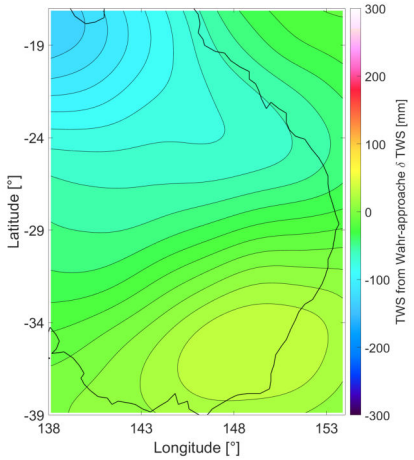

(c) October 2021

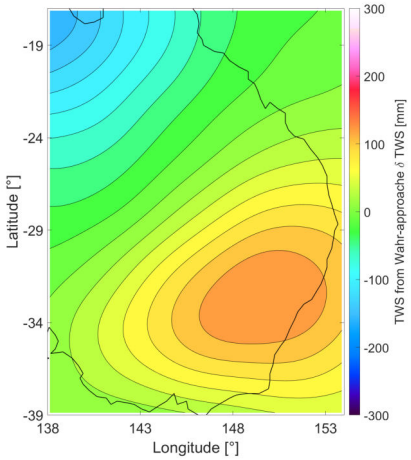

(d) October 2022

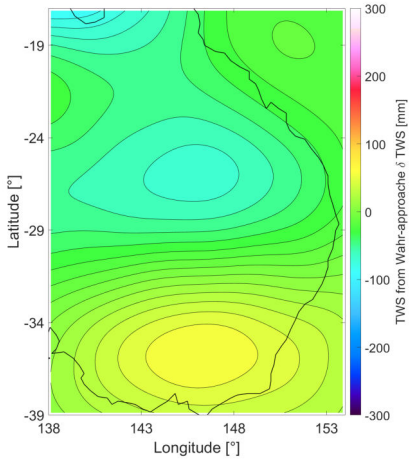

(e) October 2023

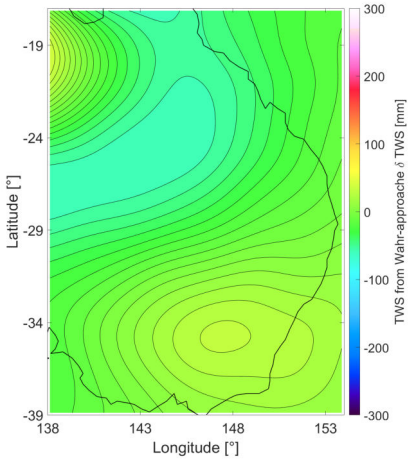

(f) October 2024

Figure 5.11: TWS of October months of years from 2019 to 2024 based on DDK2 GRACE-FO mission (units are in mm)

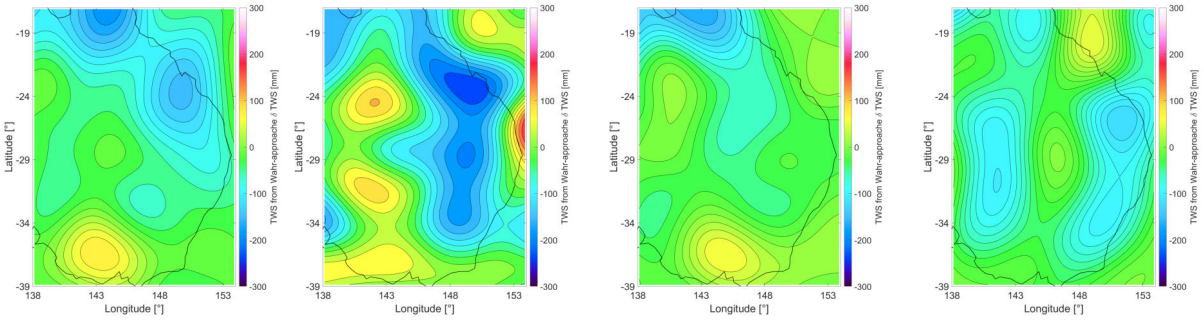

(a) October 2003 (b) October 2004 (c) October 2005 (d) October 2006

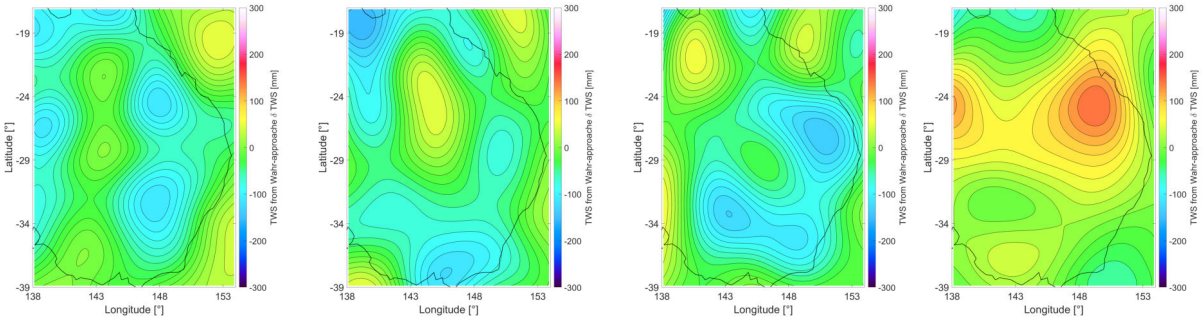

(e) October 2007 (f) October 2008 (g) October 2009 (h) October 2010

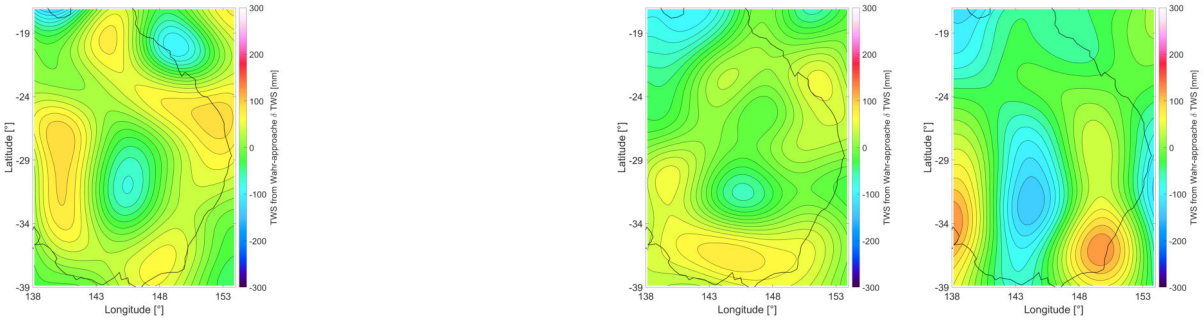

(i) October 2011 (j) October 2012 (k) October 2013 (l) October 2014

(m) October 2015 (n) October 2016 (o) October 2017

Figure 5.12: TWS of October months of years from 2003 to 2017 based on DDK5 GRACE mission (units are in mm)

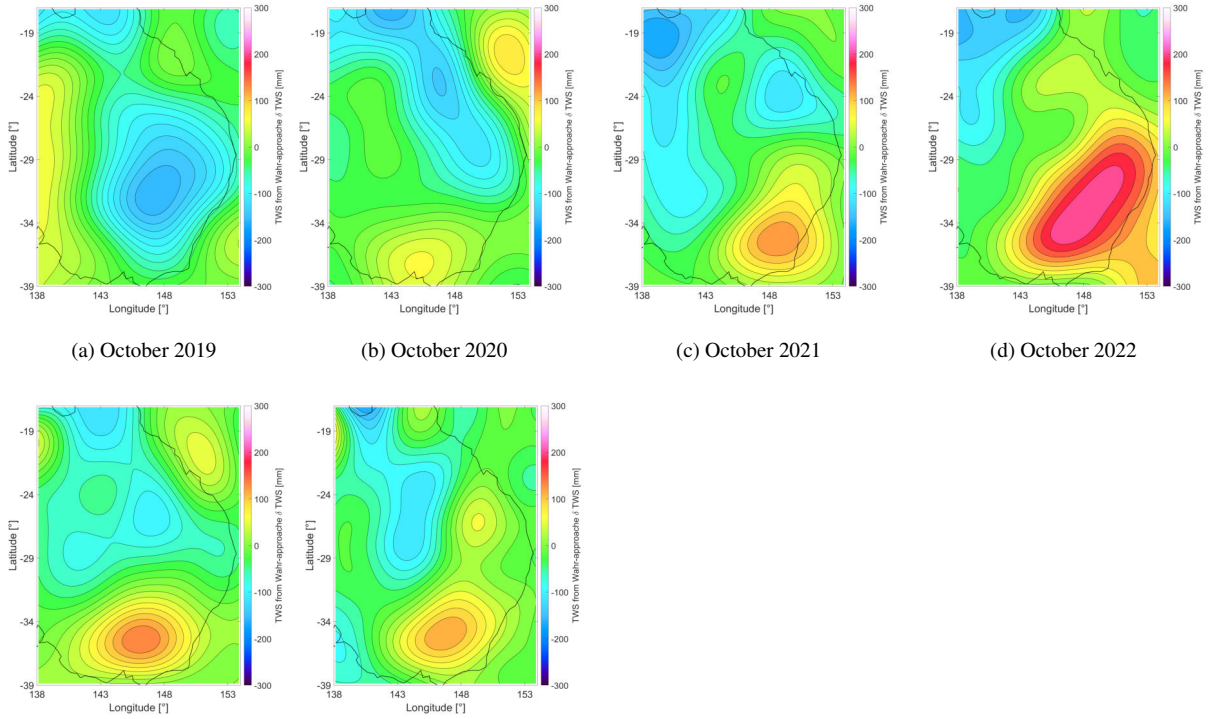

(a) October 2019 (b) October 2020 (c) October 2021 (d) October 2022

(e) October 2023 (f) October 2024

Figure 5.13: TWS of October months of years from 2019 to 2024 based on DDK5 GRACE-FO mission (units are in mm)

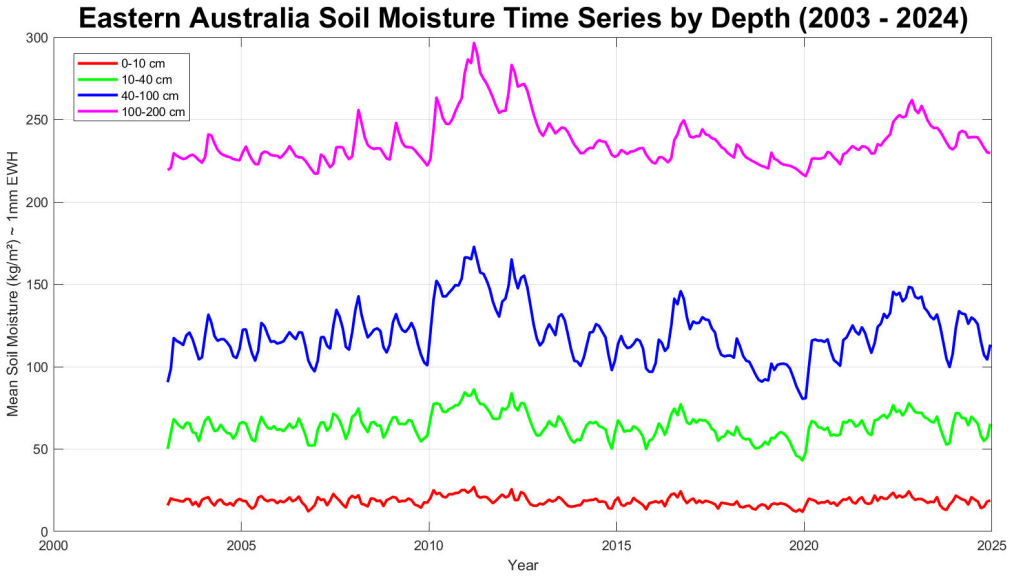

Figure 5.14: Eastern Australia Soil Moisture By Depth Time Series from 2003 until 2024

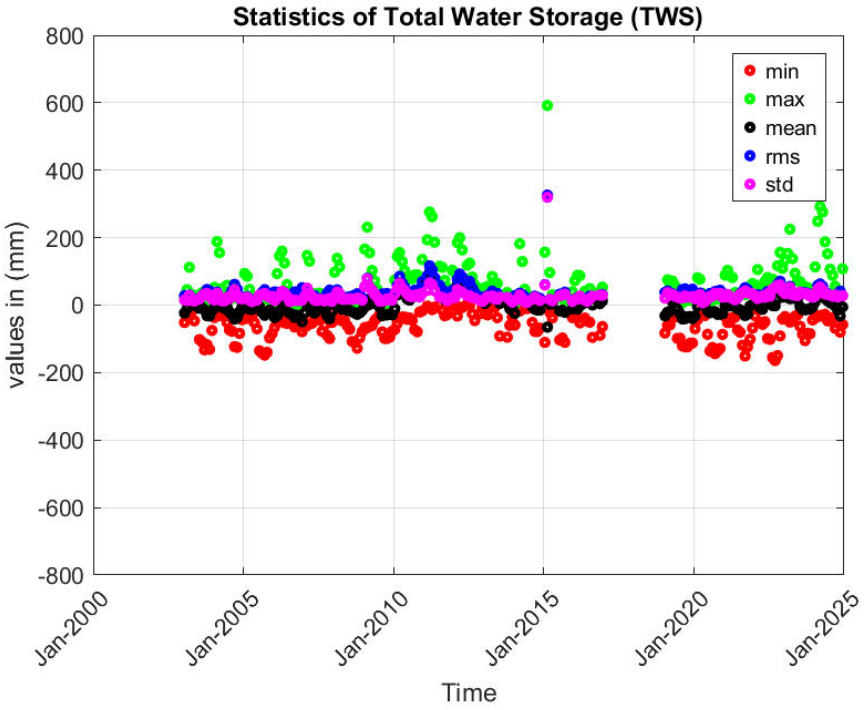

Figure 5.15: Statistics of Total Water Storage(TWS) based on DDK2

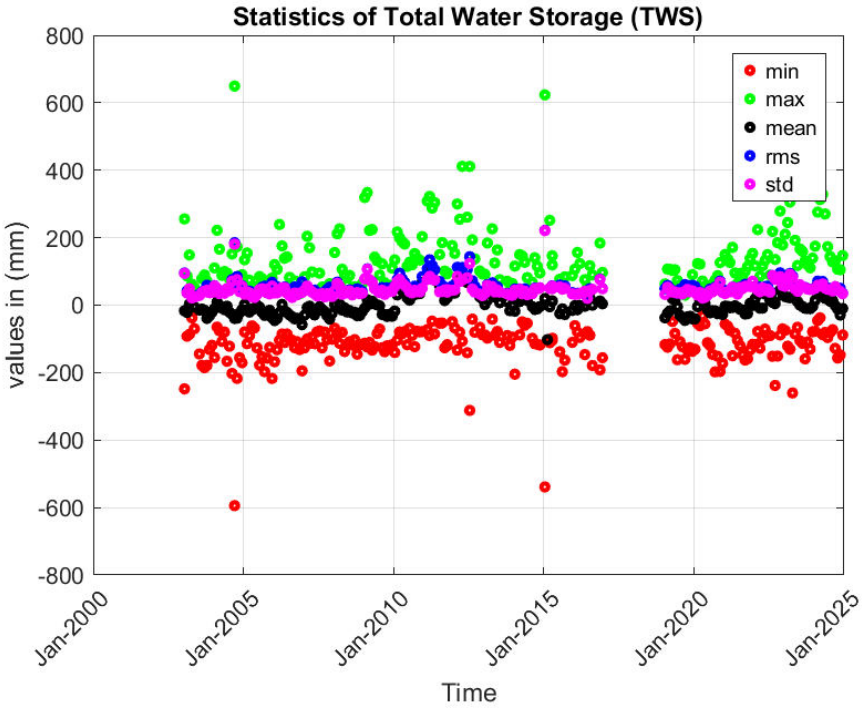

Figure 5.16: Statistics of Total Water Storage(TWS) based on DDK5

6 Conclusion

In this study, terrestrial water storage (TWS) variations over the Murray-Darling Basin (East Australia, Figure 3.1) were analysed using GRACE and GRACE-FO satellite gravimetry data, supported by GLDAS land surface model outputs. The GRACE Level-2 spherical harmonic coefficients were processed through spherical harmonic synthesis and transformed into Equivalent Water Height (EWH) using the Wahr formulation, enabling the assessment of large-scale mass redistribution associated with hydrological processes.

The results reveal clear spatial and temporal variability in water storage across the basin. Monthly spatial analysis showed strong positive TWS anomalies during wet conditions, particularly in April 2011, corresponding to the peak of the 2010–2011 La Niña event. In contrast, October 2020 exhibited pronounced negative anomalies, reflecting reduced water storage during prolonged drought conditions. These findings confirm the capability of GRACE data to capture extreme hydrological events at basin scale.

Interannual analysis further highlighted consistent seasonal behaviour, with April months representing periods of increased storage due to accumulated rainfall, while October months indicated depleted storage conditions. Among all years, April 2011 was identified as the period of maximum water storage, whereas October 2020 represented one of the lowest storage conditions.

The comparison of DDK2 and DDK5 filtered solutions demonstrated the importance of filtering in GRACE data processing. DDK5 filtering provided smoother spatial fields and effectively reduced high-frequency noise while preserving the large-scale hydrological signal. Additionally, GLDAS-derived soil moisture showed strong agreement with GRACE-derived TWS variations, confirming that near-surface storage plays a significant role in total water storage variability.

Overall, the combined use of GRACE(-FO) and GLDAS data provides a robust framework for analysing terrestrial water storage dynamics and offers valuable insights into hydrological variability in the Murray-Darling Basin.

7 Outlook

Future work can focus on improving the spatial resolution and accuracy of TWS estimates by applying advanced filtering and leakage correction techniques. The integration of additional datasets, such as precipitation, evapotranspiration, and in-situ groundwater observations, can further enhance the interpretation of hydrological processes.

Extending the analysis to longer time periods and comparing multiple river basins would provide a broader understanding of climate-driven water storage variability. In particular, the continued availability of GRACE-FO data offers opportunities for near-real-time monitoring of hydrological extremes, which is essential for sustainable water resource management under changing climatic conditions.

Acknowledgement

The author wishes to extend his sincere gratitude to Prof. Kurt Seitz for his continuous guidance, insightful explanations, and valuable support throughout this lab rotation, as well as for his time and regular discussions, which significantly contributed to the successful completion of this work.

The author acknowledges the support from Geodätisches Institut (GIK) for providing necessary resources and facilities. Additionally, the author acknowledges ICGEM (ICGEM, 2026) for providing GRACE data used in this study. The author also acknowledges GES DISC (GLDAS, 2025) for providing the GLDAS data products.

References

Chiew, F. H. S., Zheng, H., Post, D. A., Robertson, D. E., and Rojas, R. (2022): Hydroclimate trends and future projections in the Murray-Darling Basin. Technical report. CSIRO Technical Report for the Murray-Darling Basin Authority. CSIRO.

Cook, M. (2025): Locking in hydro-engineered pathways: the lower river Murray, Australia, 1880–1940. *Water History* 17(2):181–199. ISSN: 1877-7244. DOI: 10.1007/s12685-024-00356-3. URL: https://doi.org/10.1007/s12685-024-00356-3.

GLDAS (2025): GLDAS - Global Land Data Assimilation System. https://disc.gsfc.nasa.gov/datasets?keywords=GLDAS. Accessed: 2025-11-26.

Heiskanen, W. A. and Moritz, H. (1967): Physical Geodesy. W. H. Freeman & Co., San Francisco, USA.

ICGEM (2026): International Centre for Global Earth Models (ICGEM): Gravity field and GRACE/GRACE-FO products hosted at the German Research Centre for Geosciences (GFZ). Accessed: 2026-04-06. URL: https://icgem.gfz-potsdam.de/.

Kusche, J. (2007): Approximate decorrelation and non-isotropic smoothing of time-variable GRACE-type gravity field models. *Journal of Geodesy* 81(11):733–749. DOI: 10.1007/s00190-007-0143-3.

Kusche, J., Schmidt, R., Petrovic, S., and Rietbroek, R. (2009): Decorrelated GRACE time-variable gravity solutions by GFZ, and their validation using a hydrological model. *Journal of Geodesy* 83:903–913. DOI: 10.1007/s00190-009-0308-3.

Leblanc, M. J., Tregoning, P., Ramillien, G., Tweed, S. O., and Fakes, A. (2009): Basin-scale, integrated observations of the early 21st century multiyear drought in southeast Australia. *Water resources research* 45(4).

Rodell, M., Houser, P. R., Jambor, U., Gottschalck, J., Mitchell, K. E., Meng, C.-J., Arsenault, K., Cosgrove, B. A., Radakovich, J. D., Bosilovich, M. G., Entin, J. K., Walker, J. P., Lohmann, D., and Toll, D. L. (2004): The Global Land Data Assimilation System. *Bulletin of the American Meteorological Society* 85(3):381–394. DOI: 10.1175/BAMS-85-3-381.

Rodell, M., Velicogna, I., and Famiglietti, J. S. (2009): Satellite-based estimates of groundwater depletion in India. *Nature* 460:999–1002. DOI: 10.1038/nature08238.

Tapley, B. D., Watkins, M. M., Flechtner, F., et al. (2019): Contributions of GRACE to understanding climate change. *Nature Climate Change* 9:358–369. DOI: 10.1038/s41558-019-0456-2.

Tapley, B. D., Bettadpur, S., Watkins, M., and Reigber, C. (2004): The gravity recovery and climate experiment: Mission overview and early results. *Geophysical Research Letters* 31(9):1–4. DOI: 10.1029/2004GL019920.

Tsoulis, D. (1999): Spherical harmonic computations with topographic/isostatic coefficients. Tech. rep. IAPG/FESG No. 3. Munich, Germany: Institut für Astronomische und Physikalische Geodäsie, Technische Universität München.

Van Dijk, A. I., Beck, H. E., Crosbie, R. S., De Jeu, R. A., Liu, Y. Y., Podger, G. M., Timbal, B., and Viney, N. R. (2013): The Millennium Drought in southeast Australia (2001–2009): Natural and human causes and implications for water resources, ecosystems, economy, and society. *Water Resources Research* 49(2):1040–1057.

Wahr, J., Molenaar, M., and Bryan, F. (1998): Time variability of the Earth's gravity field: Hydrological and oceanic effects and their possible detection using GRACE. *Journal of Geophysical Research: Solid Earth* 103(B12):30205–30229.

Investigations on the El Niño event 2015-2016 based on GRACE

Rahul Rajeev[1]

1 Remote Sensing and Geoinformatics Master of Science (M.Sc.), KIT, Germany
E-Mail: uelmz@student.kit.edu

Abstract

This study demonstrates that GRACE monthly gravity solutions are sufficiently sensitive to monitor regional mass-induced sea-level changes in the tropical Pacific. We identify a pronounced seasonal mass redistribution associated with the 2015-2016 El Niño event, characterized by a shift of oceanic mass from the eastern to the central Pacific and a complete reversal of the eastern Pacific mass anomaly – from a strong positive geoid undulation and water storage anomaly in Autumn 2015 to a markedly negative anomaly by Summer 2016. A comparative analysis of different datasets and filtering approaches yields key insights: (i) Filtering efficacy: removing measurement noise is essential for physical interpretation. The CSR DDK2 filter best preserves geophysical signals, constraining Total Water Storage (TWS) to roughly $\pm$600 mm, while unfiltered COST-G and DDK0 solutions exhibit non-physical noise and striping. (ii) Data center consistency: strong spatial agreement between CSR and COST-G solutions supports robustness of the observed seasonal mass transport across processing centers. (iii) Artifact identification: a substantial rise in the 2015 time series is attributed to an instrumental artifact from satellite battery degradation and increased accelerometer noise during the original GRACE mission.

Future work should integrate GRACE with satellite altimetry to separate mass-induced sea-level change from steric effects, extend analyses with GRACE-FO to cover subsequent ENSO cycles, and explore higher-resolution destriping filters or Mascon grids to improve spatial detail while maintaining noise suppression. A formal uncertainty quantification via variance propagation is recommended to assess statistical significance of regional signals.

Keywords GRACE · COST-G · Total Water Storage (TWS) · ENSO · El Niño

1 Introduction

Mass redistribution from hydrological, oceanic, cryospheric and atmospheric processes constantly alter the Earth's gravitational field (Tapley et al., 2004). With a monthly resoution (Landerer et al., 2020), satellite gravity missions such as the Gravity Recovery and Climate Experiment (GRACE) and its successor GRACE-FO offer the unique ability to monitor these mass variations worldwide. Gravity anomalies can be converted to Equivalent Water Height (EWH) using the method developed by Wahr et al. (1998). GRACE-derived spherical harmonic coefficients capture gravity anomalies by precisely measuring distance variations between twin satellites.

KIT Scientific Working Papers
Issue Number 270
ISSN: 2194-1629
DOI: 10.5445/IR/1000191188
Online: June 2026

This document is licensed under the Creative Commons Attribution – Share Alike 4.0 International License (CC BY-SA 4.0):
https://creativecommons.org/licenses/by-sa/4.0/deed.en

Global weather patterns and sea-level distribution are greatly impacted by the El Nino Southern Oscillation (ENSO), a dominant mode of interannual climate variability (McPhaden et al., 2006; Mcphaden, 2008). Significant mass redistributions occurred in the tropical Pacific during the 2015 - 2016 El Nino event, which was one of the strongest on record. Because GRACE observations directly measure the mass component of sea-level changes, as opposed to the steric component measured by altimetry, they are especially useful for researching such events.
The sensitivity of GRACE monthly gravity solutions for identifying regional sea-level changes during 2015-2016 El Nino is examined in this lab rotation. The effect of unfiltered (DDK0) and filtered (DDK2, DDK5) data products are elaborated, using solutions from the center for Space Research (CSR) and the combined COST-G model (Jäggi et al., 2020). The sensitivity of GRACE to ENSO driven sea-level variations, the distinctions between single-center (CSR) and combined (COST-G) solutions and the impact of decorrelation filtered on signal resolution are the three main research questions.
The format of the report is as follows: Theoretical underpinnings are covered in Chapter 2, data and preprocessing are described in Chapter 3, the methodology is described in Chapter 4, results and discussion are presented in Chapter 5 and conclusions are presented in Chapter 6.

2 Theoretical Aspects

The basic theoretical ideas underlying the processing and interpretation of GRACE satellite gravity data for tracking mass changes in the Earth system are described in this chapter. The mathematical framework includes physical models for translating gravitational anomalies into hydrological quantities, error propagation analysis, and spherical harmonic representations of the gravitational field. Understanding the methodology used in this study requires an understanding of these theoretical Foundations.

2.1 Spherical Harmonic Synthesis (SHS)

The Earth's gravitational potential V at an point P, external to the reference sphere of radius R, can be expressed as an infinite series of spherical harmonics, providing a complete spectral representation of the gravity field. This expansion is mathematically expressed as (Heiskanen and Moritz, 1967):

$$V(P) = \frac{GM}{r} \sum_{n=0}^{\infty} \left(\frac{R}{r}\right)^n \sum_{m=0}^{n} (\bar{C}_{nm} \cos m\lambda + \bar{S}_{nm} \sin m\lambda) \bar{P}_{nm}(\sin \varphi) \tag{2.1}$$

where,

GM : Geocentric gravitational constant
R : Radius of the reference sphere.
$\bar{C}_{nm}, \bar{S}_{nm}$: Fully normalised spherical harmonic coefficients of degree n and order m
$\bar{P}_{nm}$: Fully normalised Legendre functions of degree n and order m.

The spherical harmonic coefficients $\bar{C}_{nm}$ and $\bar{S}_{nm}$ encapsulate the spatial distribution of mass within the Earth. Degree n = 0 represents the monopole term which is total mass and n = 1 represents center of mass, and higher degrees correspond to increasingly finer spatial features. The maximum degree n_{max} of GRACE solutions determines the spatial resolution, approximately equal to 20,000 km/n_{max} at the equator.

Spherical Harmonic Synthesis (SHS) refers to the forward computation of gravitational functionals (potential, gravity anomalies, geoid heights) from the coefficient sets using Equation (2.1).

2.2 Degree- and Error- Degree Variance

The uncertainties present in the coefficient estimates determine the precision of gravitational parameters obtained from spherical harmonic coefficients. A framework for measuring how these coefficient errors convert into uncertainties in synthesized functionals is provided by variance propagation.

The degree variance σ_n^2 characterizes the signal power at each harmonic degree n:

$$\sigma_n^2 = \sum_{m=0}^{n} (\bar{C}_{nm}^2 + \bar{S}_{nm}^2)\,. \tag{2.2}$$

Similarly, the error degree variance represents the cumulative error power per degree n:

$$\varepsilon_n^2 = \sum_{m=0}^{n} (\sigma_{\bar{C}_{nm}}^2 + \sigma_{\bar{S}_{nm}}^2)\,, \tag{2.3}$$

where $\sigma_{\bar{C}_{nm}}^2$ and $\sigma_{\bar{S}_{nm}}^2$ are the standard errors of the coefficients (cf. Figure 2.1).

The effective resolution of gravity field models is determined by the ratio of the variances of the signal and error degrees. At degrees beyond $n \approx 40$–50, the error spectrum for residual GRACE solutions usually surpasses the signal spectrum, requiring filtering to suppress higher degrees that are dominated by noise as depicted in Figure 2.2.

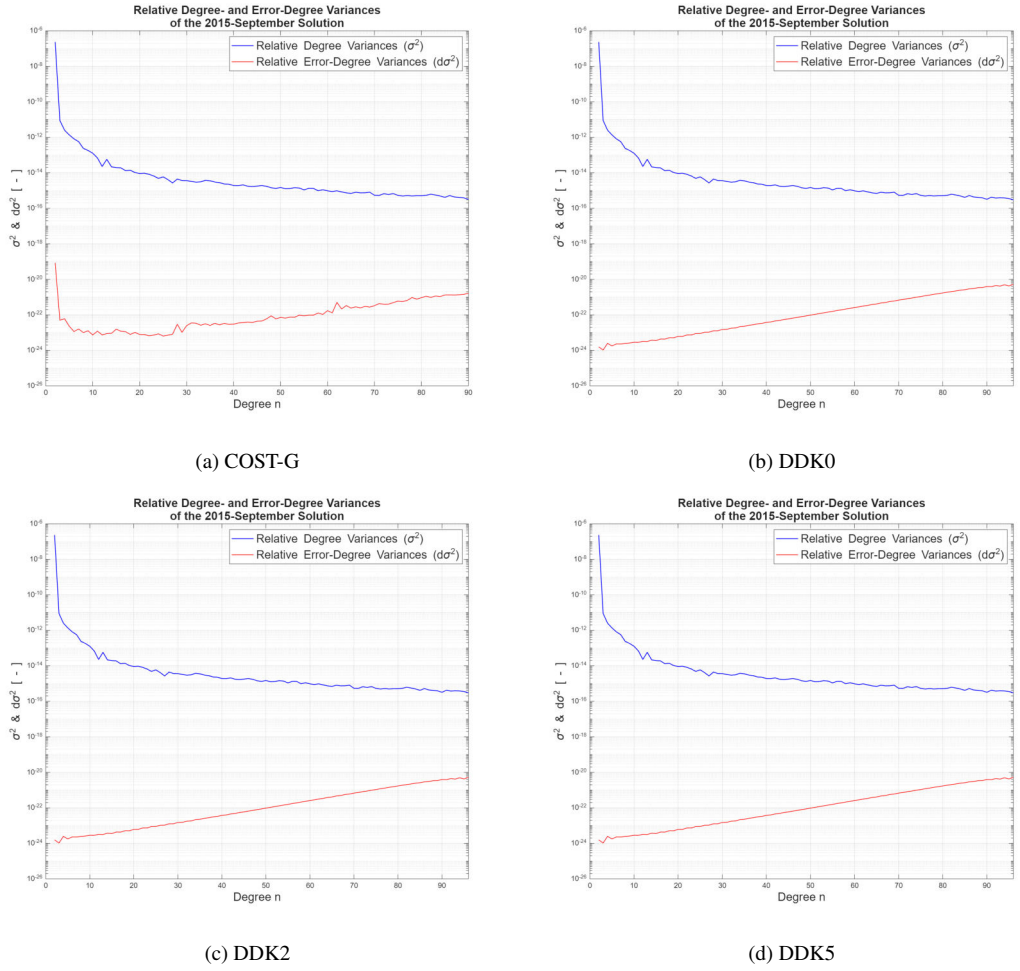

(a) COST-G

(b) DDK0

(c) DDK2

(d) DDK5

Figure 2.1: Degree and Error Degree Variances for various filtered coefficients (September 2015)

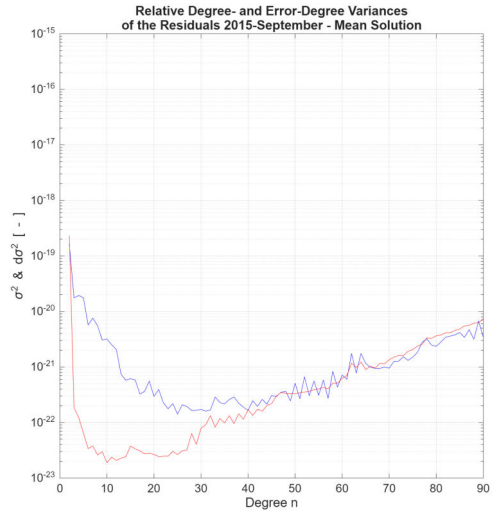

(a) COST-G – Mean

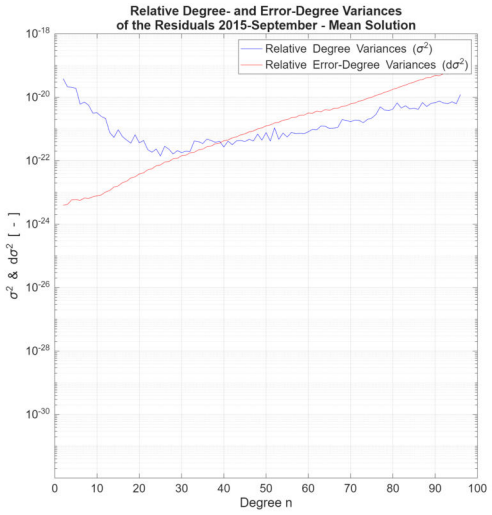

(b) DDK0 – Mean

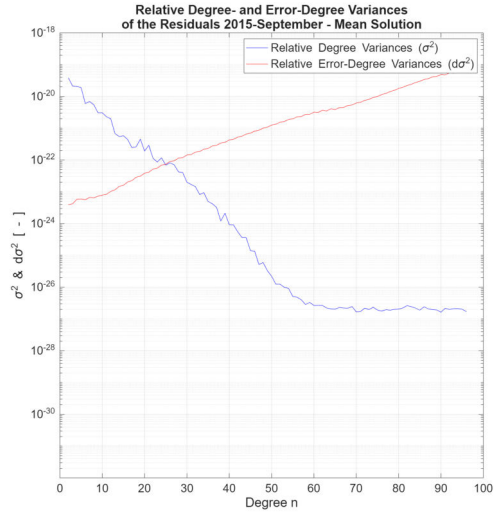

(c) DDK2 – Mean

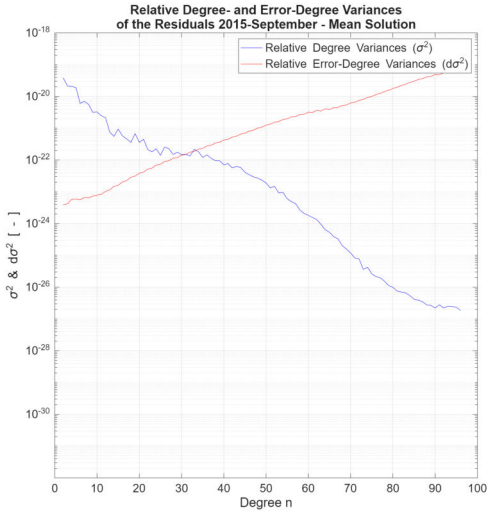

(d) DDK5 – Mean

Figure 2.2: Reletive Degree and Error Degree Variances (Sept 2015)

2.3 Wahr Approach for Surface Mass Change Estimation

The Wahr et al. (1998) methodology provides the theoretical basis for converting temporal gravity variations observed by GRACE into surface mass changes, expressed as Equivalent Water Height (EWH).

2.3.1 Fundamental Gravitational Theory

Newton's integral expresses the gravitational potential V generated by a three-dimensional mass distribution with density ρ:

$$V(P) = G \iiint_{\Omega} \frac{\rho(Q)}{l(P,Q)} d\Omega \tag{2.4}$$

where,

G : Newton's gravitational constant,
ρ : density function at running integration point (Q),

Q is the integration point with coordinates (r', φ', λ'),
$l(P,Q) = \sqrt{r^2 + r'^2 - 2rr'cos\psi}$ is the Euclidean distance between P and Q,
ψ : Angle between the points P and Q.

In geophysical forward modeling, the Earth is often divided into discrete mass elements known as tesseroids three dimensional bodies bounded by two concentric spherical surfaces, two meridional planes, and two parallels of latitude. To facilitate efficient computation, the gravitational potential of a homogeneous tesseroid is commonly approximated using a Taylor series expansion around its geometric center. This approach balances accuracy and computational speed, making it well suited for large scale or high resolution modeling tasks.

2.3.2 Load Love Numbers

When surface mass loads such as water, ice, or atmospheric pressure deform the Earth crust, the resulting gravitational perturbation differs from that of a rigid Earth due to elastic yielding. Load Love numbers k_n quantify the Earth's elastic response to surface loading at spherical harmonic degree n.
The relationship between the observed gravitational potential coefficients $\Delta\bar{C}_{nm}$, $\Delta\bar{S}_{nm}$ and the surface mass density coefficients ΔK_{nm} is according to Wahr et al. (1998, Eq. (13)):

$$\Delta K^C_{nm} = \frac{\rho_{avg}}{3}\frac{2n+1}{1+k_n}\Delta\bar{C}_{nm}\,, \qquad \Delta K^S_{nm} = \frac{\rho_{avg}}{3}\frac{2n+1}{1+k_n}\Delta\bar{S}_{nm} \tag{2.5}$$

where: ρ_{avg} = 5517 kg/m^3 is the Earth's average density. The factor $(1+k_n)$ accounts for the additional gravitational potential from the deformation induced mass redistribution. Load Love numbers are derived from Earth models (Dziewonski and Anderson, 1981) and decrease with degree n, approaching zero at high degrees where the Earth responds essentially rigidly.

2.3.3 Equivalent Water Height (EWH)

Surface mass changes are conventionally expressed as Equivalent Water Height (EWH). It is the thickness of a water layer that would produce the observed gravitational signal. For a change in surface density $\Delta\sigma(\varphi,\lambda)$, the corresponding EWH $\Delta h_w(\varphi,\lambda)$ is as follows:

$$\Delta h_w(\varphi,\lambda) = \frac{\Delta\sigma(\varphi,\lambda)}{\rho_w}\,, \tag{2.6}$$

where: ρ_w = 1000 kg/m^3 is the density of freshwater.

Combining Equations (2.1), (2.5) and (2.6) yields the complete transformation from spherical harmonic coefficients to EWH:

$$\Delta h_w(\varphi,\lambda) = \frac{R\rho_{avg}}{3\rho_w}\sum_{n=0}^{n_{max}}\frac{2n+1}{1+k_n}\sum_{m=0}^{n}[\Delta\bar{C}_{nm}cos(m\lambda) + \Delta\bar{S}_{nm}sin(m\lambda)]\bar{P}_{nm}(sin\varphi) \tag{2.7}$$

Equation (2.7) forms the core of the generation of GRACE hydrological products, enabling the conversion of monthly gravity field solutions into spatially distributed maps of terrestrial water storage anomalies.

3 Data

This chapter describes the GRACE satellite gravity data used in this study, including their acquisition from online archives and the various preprocessing steps applied before analysis.

3.1 GRACE Data Acquisition

The monthly gravity field solutions used in this study were obtained from the International Center for Global Earth Models (ICGEM, 2026). These solutions are provided as fully normalized spherical harmonic coefficients up to degree and order 96, representing Earth's time-variable gravity field. Two different data sources are analyzed for comparative assessment. The first comes from the Center for Space Research (CSR) Release 6, available in both unfiltered form and with decorrelation filtering. The second is the COST-G (Combined Gravity Field Model) product, which statistically integrates unfiltered solutions from CSR, GFZ, JPL, and others into a single optimized model, offering improved robustness by reducing individual processing center biases (Dahle et al., 2019). The study period spans January 2010 to December 2017, covering the tropical Pacific region between 20° south and 20° north latitude, and from 150° east to 60° west longitude. This area was selected because it encompasses the core ocean-atmosphere interactions during El Niño events.

3.2 GRACE Data Preprocessing

The raw spherical harmonic coefficients cannot be directly interpreted as water storage anomalies and require several preprocessing steps. These steps remove the static part of the gravity field, account for Earth's elastic response to surface loading, and reduce correlated errors that obscure real geophysical signals.

3.2.1 Coefficient Replacement

The degree-2 zonal coefficient $\bar{C}_{20}$ describes Earth's oblateness and exhibits relatively large uncertainties in GRACE solutions due to aliasing from tidal and atmospheric effects. Following standard practice, the GRACE-derived $\bar{C}_{20}$ values were replaced with more accurate estimates obtained from Satellite Laser Ranging (SLR) observations. This replacement improves the reliability of long-wavelength mass change signals, particularly important for studying large-scale phenomena like El Niño.

3.2.2 DDK Decorrelation Filtering

GRACE spherical harmonic coefficients contain correlated errors that manifest as north-south striping in spatial maps. The DDK filters, developed by Kusche (2007) and Kusche et al. (2009), is a decorrelation filter that applies empirical weighting to reduce these stripe-like errors. It represents a weaker filtering option, preserving more of the high-frequency signal content while still attenuating the most prominent correlated noise.
In this study, CSR solutions processed with DDK2 and DDK5 filtering are analyzed to assess the balance between noise reduction and signal preservation.
The DDK5 filter applies stronger decorrelation compared to DDK2, more aggressively suppressing correlated errors. While this produces cleaner spatial maps with reduced striping, it also risks smoothing or attenuating real geophysical signals, particularly those with shorter wavelengths. Analyzing both DDK2 and DDK5 versions allows evaluation of how filtering intensity affects the detection of El Niño-related mass variations.

3.2.3 COST-G Combined Solution

The COST-G product represents a statistically combined solution that averages individual gravity field models from CSR, GFZ, JPL, and other institutions. This combination approach is based on the unfiltered solutions and their co-variance information. It reduces random errors and mitigates systematic biases inherent to any single processing center. The unfiltered version of COST-G is used, enabling direct comparison with the unfiltered CSR solution (named DDK0 in this report) to evaluate the benefits of multi-center combination.

3.2.4 Reference Mean Field Removal

To isolate temporal mass anomalies, a mean gravity field was first computed by averaging all monthly solutions from 2010 to 2017. This long-term mean represents the static component of the gravity field over the study period. For each monthly solution, the mean coefficients ($\bar{C}_{nm}, \bar{S}_{nm}$) were subtracted from the monthly coefficients ($\bar{C}^{month}_{nm}, \bar{S}^{month}_{nm}$) to obtain residual coefficients ($\Delta\bar{C}_{nm}, \Delta\bar{S}_{nm}$) representing only the time-variable mass changes. This step ensures that the analysis focuses on anomalies rather than the permanent gravity field.

3.2.5 Wahr Conversion to EWH

The residual spherical harmonic coefficients cannot be directly interpreted as water thickness; they must first be converted to Equivalent Water Height (EWH) using the approach developed by Wahr et al. (1998). This conversion accounts for the elastic deformation of the solid Earth under surface loading through load Love numbers k_n. The relationship is given in Equation (2.7):

$$\Delta h_w(\varphi,\lambda) = \frac{R\rho_{avg}}{3\rho_w}\sum_{n=0}^{n_{max}}\frac{2n+1}{1+k_n}\sum_{m=0}^{n}[\Delta C_{nm}cos(m\lambda)+\Delta S_{nm}sin(m\lambda)]\bar{P}_{nm}(sin\varphi)$$

where $R = 6378137m$, is the Earth's reference radius, $\rho_{avg} = 5517kg/m^3$ is Earth's average density, $\rho_w = 1000kg/m^3$ is freshwater density, and $\bar{P}_{nm}$ are fully normalized Legendre functions. The resulting EWH values represent the vertical thickness of a water layer that would produce the observed gravitational change. These values were synthesized on a regular grid with 0.5 degree spacing, producing monthly maps and time series of Total Water Storage statistics over the tropical Pacific study region.

4 Methodology Overview

This chapter outlines the methodological framework applied to process GRACE monthly gravity field solutions and extract meaningful information about Total Water Storage (TWS) changes in the tropical Pacific during the 2015–2016 El Niño event. The methodology encompasses defining the study area, synthesizing regional grids from spherical harmonic coefficients, extracting time series, and implementing a systematic processing workflow.

4.1 Study Area

The study area focuses on the tropical Pacific region, where El Niño–Southern Oscillation (ENSO) dynamics predominantly occur. Based on the lab rotation description, the region is defined by the following geographical boundaries:

- Latitude range: 20° south to 20° north
- Longitude range: 150° east to 60° west (equivalent to 210° west to 60° west in the standard $-180°$ to $+180°$ notation)

This region encompasses the equatorial Pacific warm pool and the key ocean-atmosphere interaction zones where sea surface temperature anomalies develop during El Niño events. The spatial extent was chosen to capture both the central and eastern Pacific, where the most pronounced mass redistributions occur during ENSO phases.

For computational efficiency and adequate spatial resolution, a regular grid with 0.5° spacing in both latitude and longitude was established. This results in a grid of 81 latitudes (parallels) and 301 longitude (meridians), providing sufficient detail to resolve regional mass variation patterns while maintaining manageable data volumes for processing.

4.2 Regional Grid Synthesis

The synthesis of regional grids from spherical harmonic coefficients forms the core computational step in converting GRACE gravity observations into spatially distributed TWS anomalies. Following the approach outlined in the main processing script, the synthesis procedure involves several key operations.
First, the spherical harmonic coefficients are prepared by subtracting the long-term mean field, yielding residual coefficients that represent temporal mass anomalies. These residuals are then scaled using load Love numbers obtained from the Love Numbers function, which accounts for Earth's elastic response to surface loading. The scaling follows the relationship:

$$\Delta D_{nm} = \frac{2n+1}{1+k_n}\Delta\bar{C}_{nm}\,, \qquad \Delta E_{nm} = \frac{2n+1}{1+k_n}\Delta\bar{S}_{nm} \tag{4.1}$$

where k_n are the load Love numbers at degree n.
The synthesis itself is performed using the MATLAB-function SHS_grid_TWS, which evaluates the spherical harmonic expansion at each grid point:

$$\Delta h(\varphi,\lambda) = \frac{R\rho_{avg}}{3\rho_w}\sum_{n=n_{min}}^{n_{max}}\sum_{m=0}^{n}[\Delta D_{nm}cos(m\lambda)+\Delta E_{nm}sin(m\lambda)]\bar{P}_{nm}(sin\varphi) \tag{4.2}$$

where ΔD_{nm} and ΔE_{nm} are the scaled coefficients representing the TWS in surface spherical harmonics, and $\bar{P}_{nm}$ are the fully normalized associated Legendre functions evaluated at the grid latitudes.

The synthesis is performed for each monthly solution across all data variants (CSR unfiltered, CSR DDK2, CSR DDK5, and COST-G unfiltered). The resulting grids represent Equivalent Water Height (EWH) anomalies in meters, which are subsequently converted to millimeters for visualization and analysis.

4.3 Time Series Extraction

Once the monthly EWH grids are synthesized, regional statistics are computed to characterize the overall behavior of TWS anomalies across the study area. For each monthly solution, the following statistical measures are extracted:

- Minimum TWS: The smallest EWH value within the study region, indicating locations of maximum water loss (in respect to the mean model).
- Maximum TWS: The largest EWH value within the study region, indicating locations of maximum water gain.
- Mean TWS: The spatial average of EWH values, representing the region-wide average mass anomaly.
- Root Mean Square (RMS): A measure of the overall magnitude of TWS variations.
- Standard Deviation: Quantifies the spatial variability of TWS within the region.

These statistics are computed using the stats_aus function and stored in text files for each month. The values are then compiled into time series spanning the entire 2010–2017 period. The time series are constructed by sorting the monthly values chronologically and plotting them against time. This allows visualization of the temporal evolution of TWS anomalies, with particular attention to the 2015–2016 El Niño period.
Additionally, variance propagation is performed using the vfp_potential_fkt function to estimate the uncertainties associated with the synthesized potential and undulation values. These uncertainty estimates help assess the reliability of the detected signals.

4.4 Processing Steps

The complete processing workflow implemented in the main script Synthesis_TWS_Wahr1998_on_Grid_GFZddk2.m follows a systematic sequence of operations:

1. Initialization: The workspace is cleared, paths are added for required functions and data directories, and the data source (institution) and filter type (ddk) are selected.

2. Grid Definition: The study area grid is defined with 0.5° spacing, and the GRS80 normal gravity values are computed for each grid point.

3. Mean Field Computation: All monthly solutions from 2010–2017 are read and averaged to create a reference mean gravity field. This mean is stored for subsequent subtraction from each monthly solution.

4. Love Number Calculation: Load Love numbers are computed using the LOVE_Numbers function to enable conversion from potential coefficients to EWH.

5. Monthly Processing Loop: For each month in the input list:
   - Read spherical harmonic coefficients from the .gfc file
   - Extract year and month information for labeling
   - Rescale coefficients to consistent reference values (GM, R)
   - Subtract the mean field to obtain residual coefficients
   - Synthesize gravitational potential using SHS_grid_potential
   - Compute geoid undulation by dividing potential by normal gravity
   - Scale residual coefficients by Love numbers to obtain EWH coefficients
   - Synthesize EWH grid using SHS_grid_TWS
   - Perform variance propagation for uncertainty estimation
   - Compute degree variances and error degree variances
   - Generate and save plots (EWH maps, potential maps, undulation maps, variance propagation maps, degree variance plots)
   - Save grid data and statistics to .mat and .txt files

6. Time Series Compilation: After processing all months, the statistical values (min, max, mean, RMS, std) are compiled into a time series plot showing the temporal evolution of TWS anomalies from 2010 to 2017.

7. Output Organization: All results are organized into institution-specific and filter-specific folders under the results directory, with separate subdirectories for figures and synthesized data.

5 Results and Discussion

In this section the results are presented and discussed.

5.1 Overall Statistics

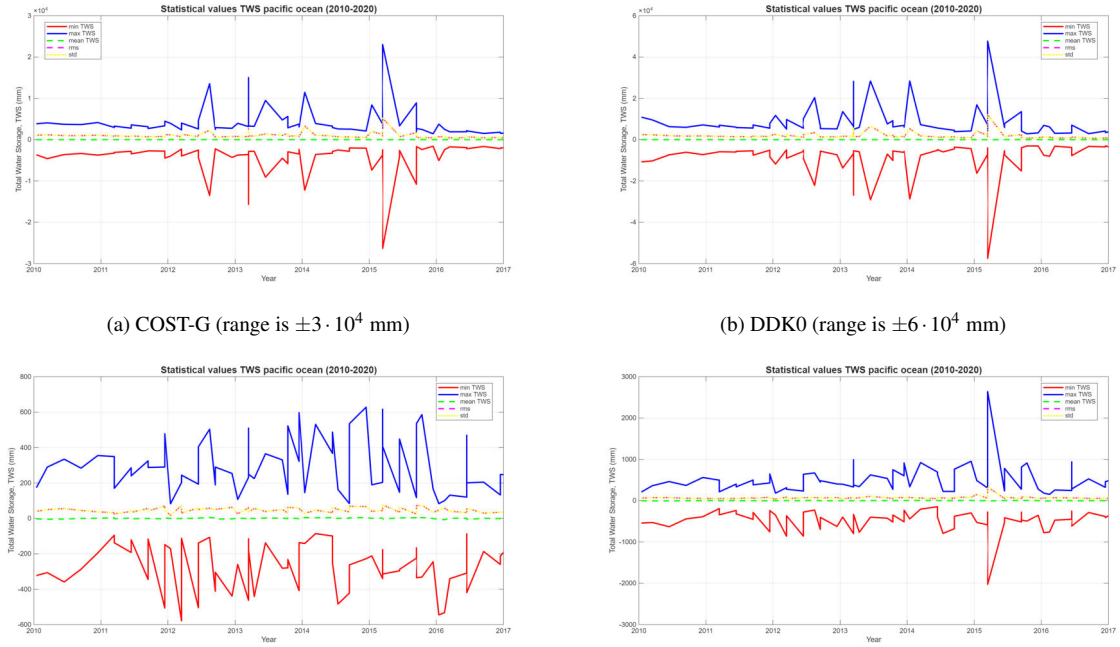

(a) COST-G (range is $\pm 3 \cdot 10^4$ mm)

(b) DDK0 (range is $\pm 6 \cdot 10^4$ mm)

(c) DDK2 (range is ± 800 mm)

(d) DDK5 (range is ± 3000 mm)

Figure 5.1: Overall statistics of TWS Time series

The four graphs in Figure 5.1 illustrate how different filtering techniques affect the statistical values of Total Water Storage (TWS) in the Pacific Ocean between 2010 and 2017

- COST-G and CSR DDK0: These datasets represent unfiltered solutions. They show extreme, non-physical fluctuations with TWS values reaching as high as ±30,000 mm (30 meters). These plots are dominated by high-frequency noise and "striping" artifacts typical of raw GRACE data
- CSR DDK5: This version uses a "weaker" filter, which significantly reduces the noise compared to DDK0, bringing the TWS range down to approximately -2,000 mm to 2,500 mm
- CSR DDK2: This is the most heavily filtered dataset among the four . The signal is much smoother, and the TWS values are restricted to a more physically plausible range of approximately -600 mm to 600 mm

The primary pattern observed is the inverse relationship between filter strength and signal amplitude. From the unfiltered data (DDK0/COST-G) to DDK5 and finally to DDK2, the "noise" (represented by the wild vertical swings) is progressively suppressed. This filtering is essential to isolate real geodetic signals, such as mass changes associated with the 2015–2016 El Niño event, from the measurement errors inherent in the satellite mission.
A massive spike is visible in early 2015 across the datasets, though it is most extreme in the unfiltered COST-G and DDK0 plots. This is already known as a bad solution due to repeat orbit problems (see Figure 5.1). The massive hike in the graphs (reaching 20-30 meters of water) is an instrumental and processing artifact. During this period of the original GRACE mission, the satellites were experiencing significant battery degradation. To conserve power, certain instruments (like the thermal control or accelerometers) had to be managed differently, often leading to increased accelerometer noise or missing data segments.

In the mathematical process of turning satellite observations into gravity models, this noise manifests as extreme errors in the high-degree spherical harmonic coefficients. When these coefficients are synthesized into TWS without strong filtering, they create the spike. The fact that the spike is almost entirely smoothed out in the DDK2 data, observed from Figure 5.1, confirms it is high-frequency noise rather than a real geophysical signal.

5.2 Undulation DDK2 and DDK5

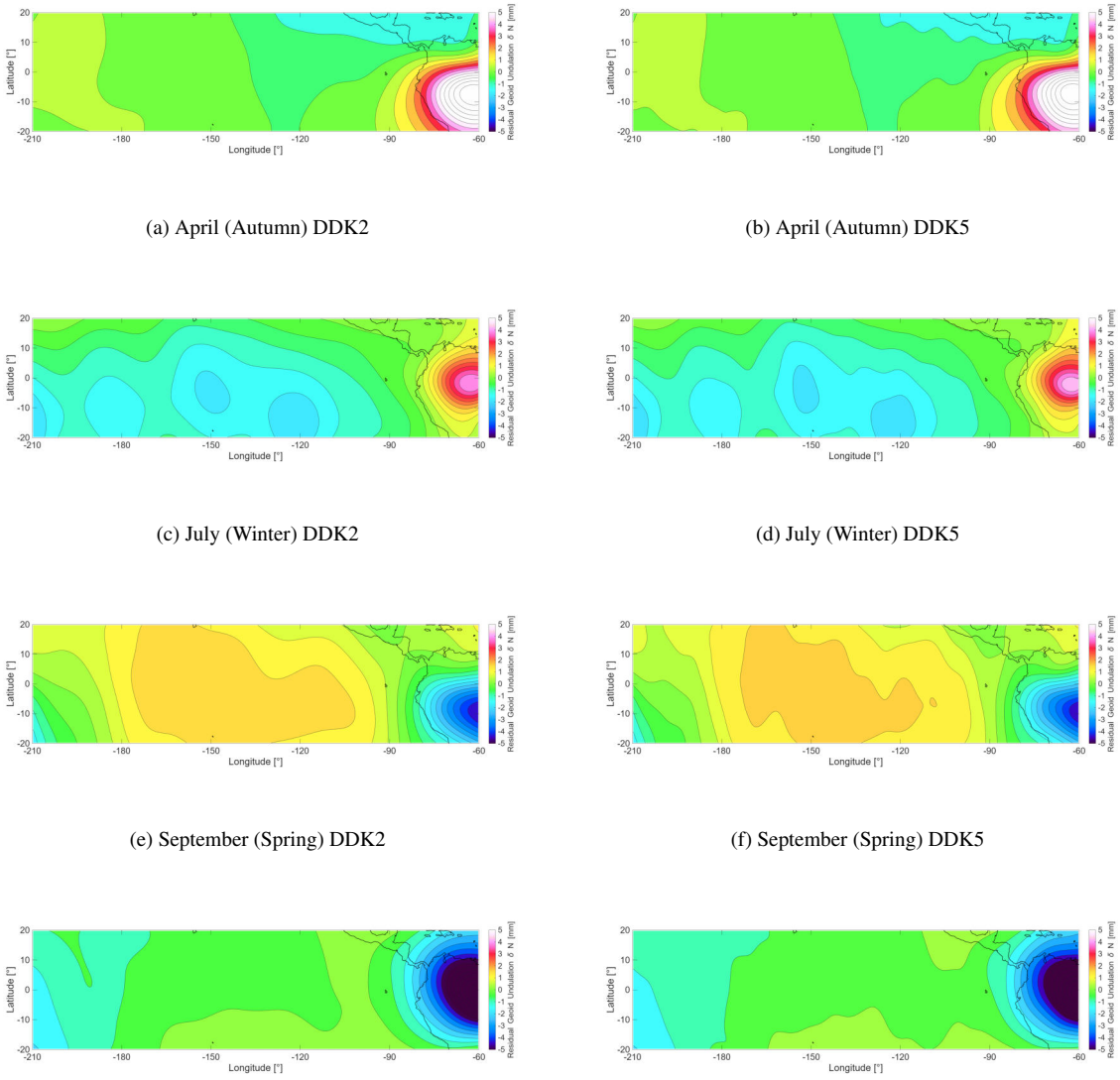

(a) April (Autumn) DDK2

(b) April (Autumn) DDK5

(c) July (Winter) DDK2

(d) July (Winter) DDK5

(e) September (Spring) DDK2

(f) September (Spring) DDK5

(g) January (Summer) DDK2

(h) January (Summer) DDK5

Figure 5.2: Seasonal changes in Geoid undulation during 2015. Range of the colour bar is ±5 mm

The residual geoid undulation maps as presented in Figure 5.2 capture the dynamic mass transport in the tropical Pacific across the autumn, winter, spring, and summer seasons of 2015–2016. This seasonal progression reveals a clear pattern of mass migration associated with the peak of the El Niño event, characterized by a significant redistribution of oceanic mass from the eastern to the central Pacific

The comparison between the DDK2 and DDK5 filters highlights the trade-off between noise suppression and signal resolution. The DDK2 maps provide a smoothed overview of the large-scale seasonal change, while the DDK5 maps offer a more detailed view of localized fluctuations with higher peak amplitudes. Most notably, the data shows a complete reversal of the geoid signal in the eastern Pacific between the autumn and summer seasons, demonstrating the sensitivity of GRACE-based solutions to regional sea level and mass fluctuations

5.3 EWH DDK2 and DDK5

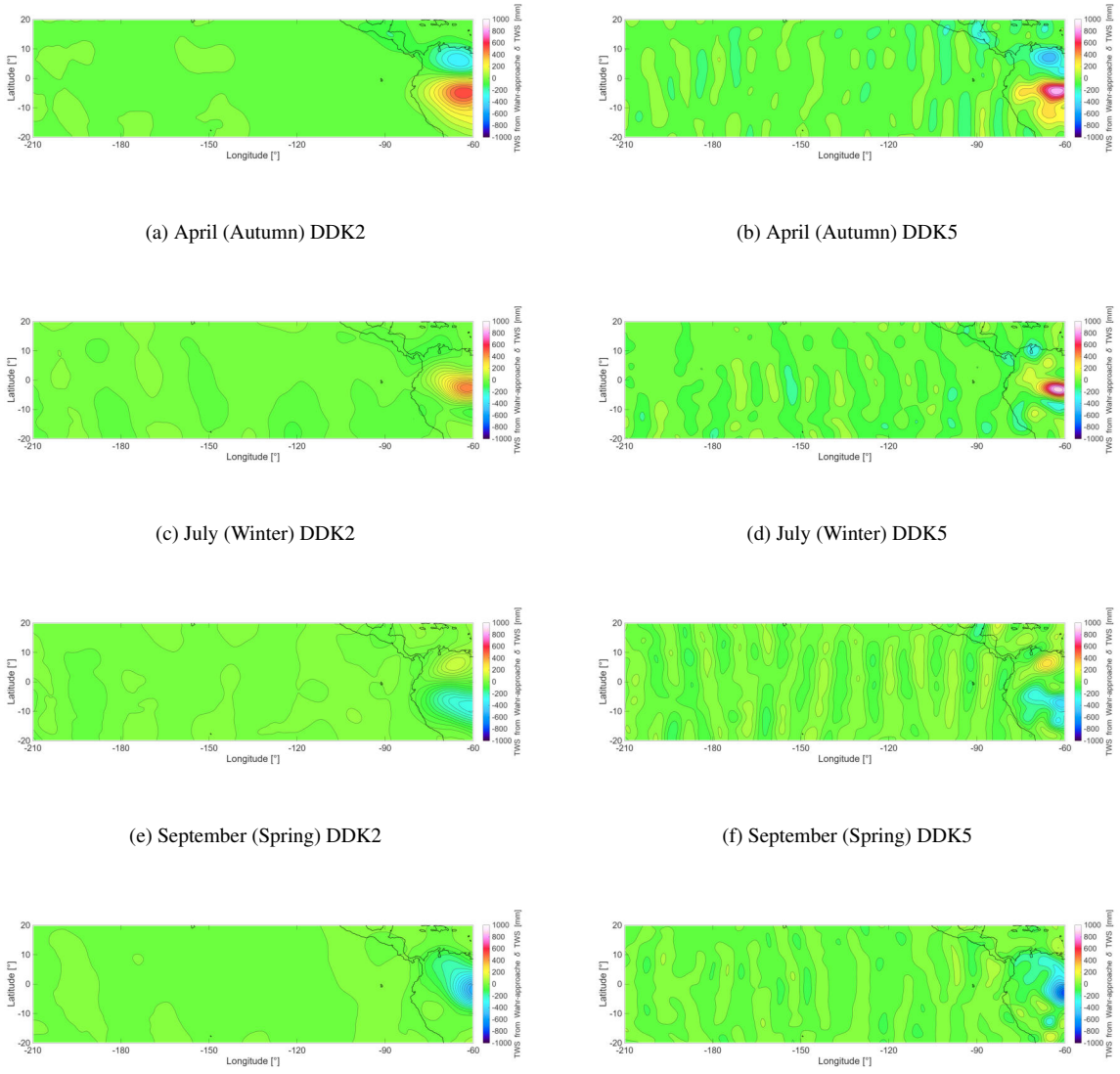

(a) April (Autumn) DDK2

(b) April (Autumn) DDK5

(c) July (Winter) DDK2

(d) July (Winter) DDK5

(e) September (Spring) DDK2

(f) September (Spring) DDK5

(g) January (Summer) DDK2

(h) January (Summer) DDK5

Figure 5.3: Seasonal changes in Equivalent Water Height during 2015. Range of the colour bar is $\pm$1000 mm

The residual TWS maps capture the dynamic mass transport in the tropical Pacific, highlighting a significant seasonal change associated with the 2015-2016 El Niño event. The comparison between the CSR DDK2 and DDK5 filtered versions demonstrates the critical role of de-striping in isolating geophysical signals from instrumental noise. While the DDK2 solution provides a clear, smoothed overview of large-scale mass redistribution, the DDK5 solution preserves higher signal amplitudes at the expense of increased spatial noise.

The most prominent pattern is the dramatic seasonal migration of water mass; the eastern Pacific begins with a substantial positive storage anomaly in the autumn, which gradually shifts and transforms into a deep negative anomaly by the summer. This sequence confirms that GRACE-based solutions, when appropriately filtered, are sensitive enough to monitor regional sea-level and mass fluctuations resulting from major climate phenomena

5.4 Undulation COST-G and DDK0

The unfiltered solutions of COST-G and CSR for residual geoid undulation are presented in Figure 5.4. The comparison reveals a highly consistent representation of the 2015–2016 El Niño event. Both datasets successfully capture the large-scale mass migration across the tropical Pacific, with only minor variations in peak amplitudes between the centers.

The most significant finding is the clear seasonal change observed between Autumn 2015 and Summer 2016. The data shows a massive redistribution of mass: the eastern Pacific basin transitions from a strong positive geoid undulation of 5 mm in the autumn to an extreme negative anomaly exceeding -5 mm by the following summer. This shift, characterized by the central Pacific 'bulge' in the spring, provides geodetic evidence of the oceanic mass transport associated with the peak of the El Niño cycle. These results demonstrate that both the CSR and weighted COST-G solutions are sufficiently sensitive to monitor regional sea-level and mass fluctuations at a seasonal scale.

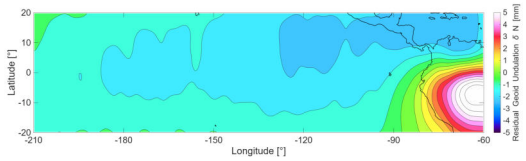

(a) April (Autumn) COST-G

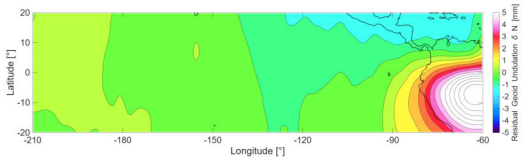

(b) April (Autumn) DDK0

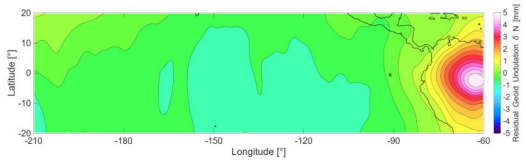

(c) July (Winter) COST-G

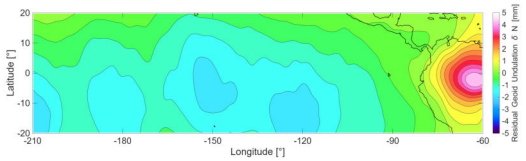

(d) July (Winter) DDK0

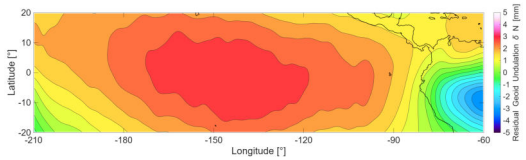

(e) September (Spring) COST-G

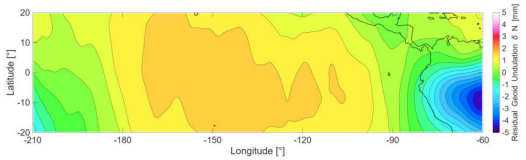

(f) September (Spring) DDK0

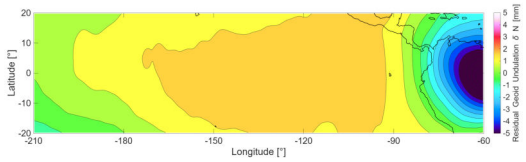

(g) January (Summer) COST-G

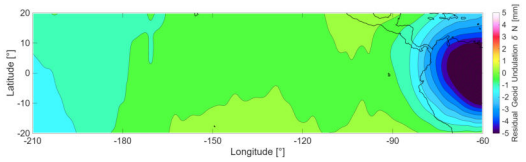

(h) January (Summer) DDK0

Figure 5.4: Seasonal changes in Geoid Undulation during 2015. Range of the colour bar is ±5 mm

5.5 EWH COST-G and DDK0

The comparison between the unfiltered COST-G and CSR solutions for Equivalent Water Height (EWH) highlights the sensitivity of GRACE to regional mass transport despite the presence of characteristic high-frequency striping. The panels in Figure 5.5 reveal a profound seasonal change in the tropical Pacific associated with the 2015-2016 El Niño.

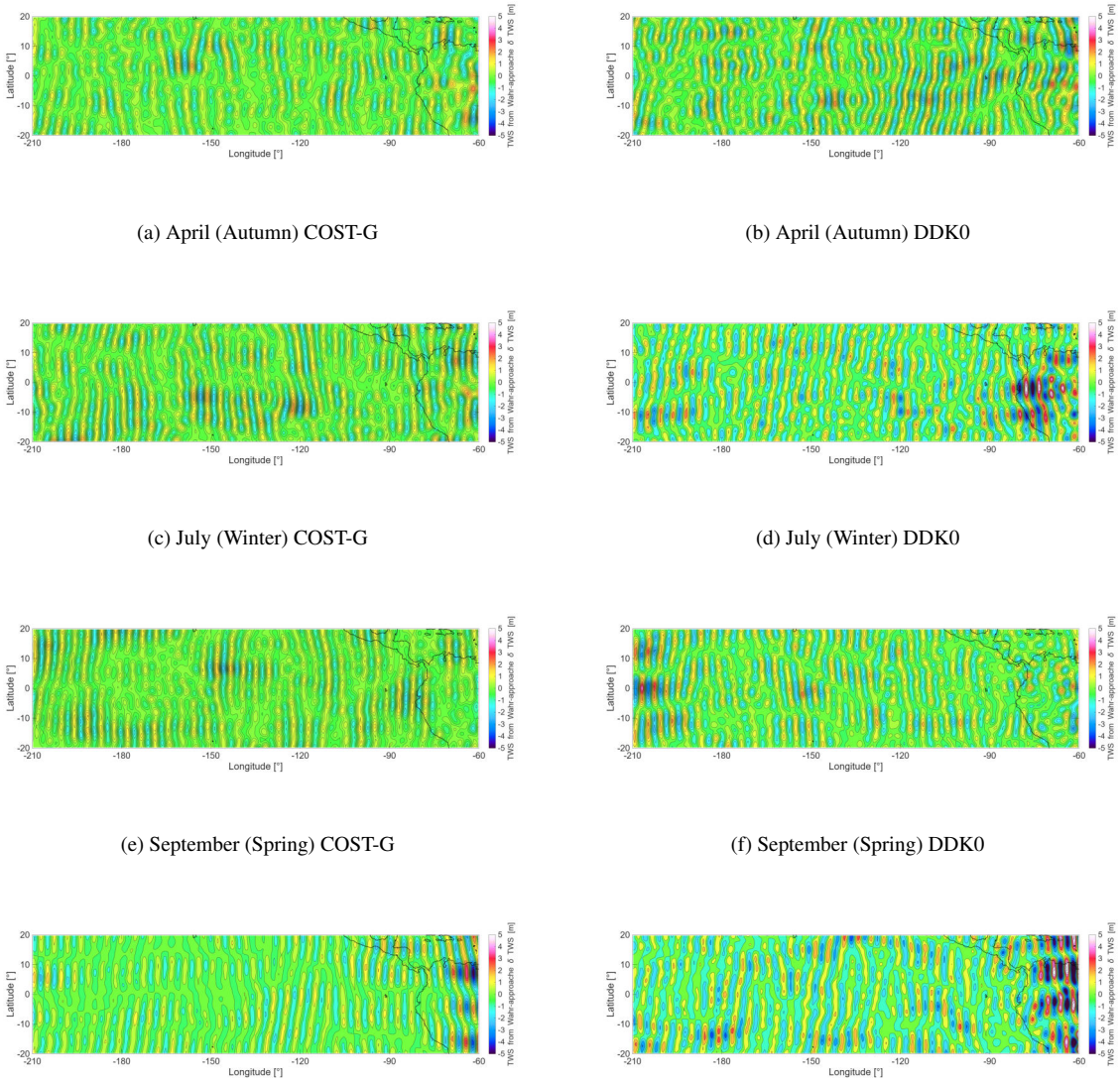

(a) April (Autumn) COST-G

(b) April (Autumn) DDK0

(c) July (Winter) COST-G

(d) July (Winter) DDK0

(e) September (Spring) COST-G

(f) September (Spring) DDK0

(g) January (Summer) COST-G

(h) January (Summer) DDK0

Figure 5.5: Seasonal changes in Total water storage 2015. Range of the colour bar is ±5 mm

The progression from autumn to summer shows a clear migration of mass across the basin. In Autumn 2015, the eastern Pacific exhibits a positive TWS anomaly, which gradually shifts toward the central Pacific during the winter and spring. By Summer 2016, the pattern has reversed, with the eastern coastal region showing a deep negative TWS anomaly. The high degree of spatial agreement between the COST-G and CSR unfiltered grids validates that the observed seasonal mass transport is a robust geophysical signal, even when synthesized up to d/o 96 without the application of de-striping filters.

6 Conclusion and Outlook

The investigations conducted in this lab rotation demonstrate that GRACE monthly gravity solutions are sufficiently sensitive to monitor regional mass-induced sea-level changes in the tropical Pacific. The analysis successfully identified a dramatic seasonal mass migration associated with the 2015–2016 El Niño event, characterized by a significant redistribution of oceanic mass from the eastern to the central Pacific. Most notably, the data revealed a complete reversal of the mass anomaly in the eastern Pacific, which transitioned from a strong positive geoid undulation and water storage anomaly in Autumn 2015 to an extreme negative anomaly by Summer 2016.
The comparative study of different datasets and filters yielded several critical insights:

- Filtering Efficiency: Filtering is essential to isolate real geodetic signals from measurement errors. The CSR DDK2 filter proved most effective for physical interpretation, restricting Total Water Storage (TWS) values to a plausible range of approximately ±600 mm, whereas unfiltered COST-G and DDK0 solutions were dominated by non-physical noise and "striping" artifacts
- Data Center Consistency: A high degree of spatial agreement was found between CSR and COST-G solutions, validating the robustness of the observed seasonal mass transport signals across different processing centers.
- Identification of Artifacts: The massive "hike" observed in the 2015 time series was confirmed to be an instrumental artifact caused by satellite battery degradation and increased accelerometer noise during that period of the original GRACE mission.

Outlook for Future Research: Building on these results, future work should focus on integrating GRACE data with satellite altimetry to distinguish the mass-induced component of sea-level change from the steric (thermal expansion) component. Additionally, the study period should be extended to include GRACE-FO observations to analyze subsequent ENSO cycles and long-term temporal mass fluctuations. Further refinement of advanced destriping filters or the use of ready-to-use Mascon approach grids may provide higher spatial resolution of localized mass variations while maintaining effective noise suppression. Finally, a more rigorous application of variance propagation is recommended to formally quantify uncertainties and establish the statistical significance of detected regional signals.

Acknowledgement

I would like to express my sincere gratitude to Prof. Dr.-Ing. Hansjörg Kutterer for providing the opportunity to conduct this lab rotation at the Geodetic Institute (GIK) and for defining the research task on the 2015–2016 El Niño event.
I am deeply grateful to my supervisor, Dr.-Ing. Kurt Seitz, for his constant guidance, valuable insights, and technical support throughout the duration of this work. His expertise was instrumental in helping me navigate the complexities of GRACE data processing and the adaptation of the necessary Matlab computational tools.
Furthermore, I would like to thank the Karlsruhe Institute of Technology (KIT) and the KIT Fakultät für Bauingenieur, Geo und Umweltwissenschaften for providing the academic environment and resources required to complete this study as part of the M.Sc. Remote Sensing and Geoinformatics program.
Finally, I acknowledge the International Center for Global Earth Models (ICGEM) and the evaluation centers – specifically the Center for Space Research (CSR) and the COST-G ensemble team for making the monthly gravity field solutions publicly available for scientific research.

References

Dahle, C., Murböck, M., Flechtner, F., Dobslaw, H., Michalak, G., Neumayer, K. H., Abrykosov, O., Reinhold, A., König, R., Sulzbach, R., et al. (2019): The GFZ GRACE RL06 monthly gravity field time series: Processing details and quality assessment. *Remote Sensing* 11(18):2116.

Dziewonski, A. M. and Anderson, D. L. (1981): Preliminary reference Earth model. *Physics of the earth and planetary interiors* 25(4):297–356.

Heiskanen, W. A. and Moritz, H. (1967): Physical Geodesy. W. H. Freeman & Co., San Francisco, USA.

ICGEM (2026): International Centre for Global Earth Models (ICGEM): Gravity field and GRACE/GRACE-FO products hosted at the German Research Centre for Geosciences (GFZ). Accessed: 2026-04-06. URL: https://icgem.gfz-potsdam.de/.

Jäggi, A., Meyer, U., Lasser, M., Jenny, B., Lopez, T., Flechtner, F., Dahle, C., Förste, C., Mayer-Gürr, T., Kvas, A., et al. (2020): International combination service for time-variable gravity fields (COST-G) start of operational phase and future perspectives. In: *Beyond 100: The Next Century in Geodesy: Proceedings of the IAG General Assembly, Montreal, Canada, July 8-18, 2019*. Springer, pp. 57–65.

Kusche, J. (2007): Approximate decorrelation and non-isotropic smoothing of time-variable GRACE-type gravity field models. *Journal of Geodesy* 81(11):733–749. DOI: 10.1007/s00190-007-0143-3.

Kusche, J., Schmidt, R., Petrovic, S., and Rietbroek, R. (2009): Decorrelated GRACE time-variable gravity solutions by GFZ, and their validation using a hydrological model. *Journal of Geodesy* 83:903–913. DOI: 10.1007/s00190-009-0308-3.

Landerer, F. W., Flechtner, F., Save, H., Webb, F. H., Bandikova, T., Bertiger, W. I., Bettadpur, S., Byun, S., Dahle, C., Dobslaw, H., Fahnestock, E., Harvey, N., Kang, Z., Kruizinga, G., Loomis, B., McCullough, C., Murböck, M., Nagel, P., Paik, M., Poole, S., Strekalov, D., Tamisiea, M., Wang, F., Watkins, M., and Wen, H. (2020): Extending the global mass change data record: GRACE Follow-On instrument and science data performance. *Geophysical Research Letters* 47:e2020GL088306. DOI: 10.1029/2020GL088306.

Mcphaden, M. J. (2008): Evolution of the 2006–2007 El Nino: The role of intraseasonal to interannual time scale dynamics. *Advances in Geosciences* 14:219–230.

McPhaden, M. J., Zhang, X., Hendon, H. H., and Wheeler, M. C. (2006): Large scale dynamics and MJO forcing of ENSO variability. *Geophysical research letters* 33(16).

Tapley, B. D., Bettadpur, S., Watkins, M., and Reigber, C. (2004): The gravity recovery and climate experiment: Mission overview and early results. *Geophysical Research Letters* 31(9):1–4. DOI: 10.1029/2004GL019920.

Wahr, J., Molenaar, M., and Bryan, F. (1998): Time variability of the Earth's gravity field: Hydrological and oceanic effects and their possible detection using GRACE. *Journal of Geophysical Research: Solid Earth* 103(B12):30205–30229.

Influence of DDK Filtering on GRACE Monthly Solutions for TWS Time Series using Europe as an Example

Sharath Sunil Ravi[1]

1 Remote Sensing and Geoinformatics Master of Science (M.Sc.), KIT, Germany
E-Mail: uzgni@student.kit.edu

Abstract

This study assesses how decorrelation filtering with DDK kernels influences GRACE and GRACE-FO derived terrestrial water storage (TWS) estimates over Europe, focusing on the interaction among filter strength, spatial domain configuration, and inversion stability. A consistent framework is developed by integrating spherical harmonic synthesis, variance and error propagation, tesseroid-based forward gravitational modeling, and regularized inverse adjustment to trace how spectral-domain processing choices propagate into physically interpretable TWS fields.

Spectral analysis of spherical harmonic coefficients shows that DDK filtering markedly modifies degree variance by suppressing correlated high-degree noise intrinsic to GRACE monthly gravity field solutions. Weak filtering (DDK8) preserves small-scale variability but retains pronounced north–south striping artefacts; strong filtering (DDK1) reduces noise at the expense of substantial attenuation of seasonal amplitudes and spatial contrasts. Among the filters tested, DDK5 offers the best balance, stabilizing empirical degree variances at medium and high degrees while preserving the dominant long-wavelength hydrological signal.

The tesseroid-based inversion demonstrates that the model-domain spatial configuration strongly influences recovered TWS quality. Case A, with tesseroids confined to the study area, yields smooth, stable TWS estimates but boundary artefacts within the region of interest. Extending the tesseroid domain beyond the target area (Case B) shifts edge effects outside the study region, producing more responsive and physically meaningful TWS patterns at the cost of increased noise sensitivity. When paired with appropriate regularization, Case B provides a clearer representation of temporal water storage variability.

L-curve analysis confirms the ill-posedness of the inverse problem and highlights the necessity of regularization for stable mass inversion. Well-defined L-shaped curves with stable corners are obtained for Case A, whereas Case B exhibits greater corner variability, indicating epoch- and region-dependent regularization needs. Temporal analysis reveals that the optimal regularization parameter varies across epochs, reflecting changing signal-to-noise characteristics of GRACE solutions; a fixed parameter across the time series is insufficient.

Overall, the results indicate that combining DDK5 filtering with an extended tesseroid domain (Case B) yields the most robust compromise between noise suppression and signal preservation for regional-scale European TWS estimation. The findings align with established GRACE processing strategies and underscore that reliable hydrological interpretation from satellite gravimetry requires joint consideration of decorrelation filtering, inversion regularization, and spatial model design.

Keywords GRACE · GLDAS · Total Water Storage (TWS) · DDK Filter · Europe

1 Introduction

Understanding variations in Total Water Storage (TWS) is essential for studying continental hydrology, as it reflects changes in surface water, soil moisture, snow, and groundwater. The Gravity Recovery and Climate Experiment (GRACE) and its successor, GRACE Follow-On (GRACE-FO), have provided an unprecedented means of observing such variations by measuring temporal changes in the Earth's gravity field. This study utilizes monthly GRACE and GRACE-FO data from January 2003 to December 2024 to investigate large-scale hydrological dynamics across Europe.

However, GRACE Level-2 spherical harmonic (SH) coefficients are affected by correlated noise that manifests as characteristic north–south striping patterns in mass anomaly maps. To minimize these artifacts and enhance the physical interpretation of hydrological signals, decorrelation filters – specifically the DDK (Destripe and Decorrelate Kernel) filters – are widely applied. These filters represent different levels of smoothing strength (Kusche, 2007): DDK8 preserves fine spatial details but retains more noise, DDK5 offers a balanced compromise between noise reduction and signal preservation, while DDK1 provides strong smoothing at the expense of small-scale variability.

In this Lab Rotation, the influence of three DDK filter levels (DDK1, DDK5 and DDK8) was examined on GRACE- and GRACE-FO-derived TWS estimates across Europe. The continent's diverse hydroclimatic conditions – from the arid Mediterranean south to the humid northern latitudes – make it a suitable region for analyzing how filter strength affects spatial and temporal hydrological patterns. Two spatial domains were defined for the analysis:

Case A: (10°W to 30°E and 35°N to 55°N), where tesseroids were positioned within the study area, and

Case B: (20°W to 40°E and 25°N to 65°N), where tesseroids were extended beyond the area of interest.

In both cases the area of interest is restricted to (15°W to 35°E and 30°N to 60°N).

The main objectives of this study are to:

- Evaluate how DDK filters of varying strength (DDK1, DDK5 and DDK8) influence the spatial and temporal characteristics of GRACE-derived TWS signals over Europe.
- Quantify the trade-off between correlated noise suppression and hydrological signal preservation through comparison of filter levels.
- Analyze spatial and temporal patterns of TWS anomalies across contrasting European hydroclimatic zones.
- Assess how spatial domain boundaries (Case A and Case B) and filter selection collectively affect potential synthesis, L-curve analysis, potential inversion, and TWS estimation.

Overall, this research aims to improve understanding of DDK filter behavior in mid-latitude hydrological applications and to identify an optimal balance between noise reduction and signal fidelity for accurate GRACE-based water storage monitoring across Europe.

KIT Scientific Working Papers
Issue Number 270
ISSN: 2194-1629
DOI: 10.5445/IR/1000191188
Online: June 2026

This document is licensed under the Creative Commons Attribution – Share Alike 4.0 International License (CC BY-SA 4.0):
https://creativecommons.org/licenses/by-sa/4.0/deed.en

2 Theoretical Aspects

Several fundamental concepts play a key role in the modelling of Total Water Storage (TWS) using tesseroids of constant density, where the height (or thickness) of each tesseroid is treated as the unknown parameter to be estimated. In this study, an inverse modelling approach based on adjustment theory is employed to estimate these parameters from GRACE and GRACE–FO Level–2 data, after decorrelation filtering using DDK kernels.

2.1 Spherical Harmonic Synthesis

Spherical Harmonic Synthesis (SHS) refers to the forward computation of the gravitational potential from a finite set of spherical harmonic coefficients (Tsoulis, 1999). In GRACE and GRACE–FO applications, SHS is used to transform monthly Level–2 spherical harmonic coefficients into spatial representations of the Earth's gravity field. The gravitational potential $V(P)$ at a point $P(r,\varphi,\lambda)$ exterior to the Earth is given by the spherical harmonic synthesis formula (Tsoulis, 1999, p. 15, Eq. (47))

$$V(P) = \frac{GM}{r}\sum_{n=0}^{N}\left(\frac{R}{r}\right)^{n}\sum_{m=0}^{n}\left(\bar{C}_{nm}\cos m\lambda + \bar{S}_{nm}\sin m\lambda\right)\bar{P}_{nm}(\sin\varphi), \tag{2.1}$$

where GM is the geocentric gravitational constant, R is the reference radius, $(\bar{C}_{nm},\bar{S}_{nm})$ are the fully normalised spherical harmonic coefficients of degree n and order m, $\bar{P}_{nm}$ are the fully normalised associated Legendre functions of the first kind, and N denotes the maximum degree of the spherical harmonic expansion.

2.2 Degree and Error Degree Variances

The spectral distribution of the gravity field can be analysed using degree-dependent measures derived from spherical harmonic coefficients. In GRACE analysis, these measures are commonly used to investigate how geophysical signals and measurement noise vary across spatial scales (Wahr et al., 1998).

Low spherical harmonic degrees represent long-wavelength gravity signals associated with large-scale mass redistributions, such as continental water storage and ice mass variations. Higher degrees correspond to shorter spatial wavelengths and are increasingly affected by measurement noise in GRACE gravity field solutions (Wahr et al., 1998).

Following the formulation of Colombo (1981, Eq. (1.9)) the degree variance for a given degree n is defined as the sum of the squared fully normalised spherical harmonic coefficients of that degree:

$$\sigma_n^2 = \sum_{m=0}^{n}\left(\bar{C}_{nm}^2 + \bar{S}_{nm}^2\right). \tag{2.2}$$

In satellite gravimetry applications such as GRACE, spherical harmonic coefficients are provided together with formal uncertainty estimates. By applying the same degree-variance formulation to these coefficient uncertainties, the error degree variance is obtained as

$$\sigma_{n,\mathrm{err}}^2 = \sum_{m=0}^{n}\left(\sigma_{\bar{C}_{nm}}^2 + \sigma_{\bar{S}_{nm}}^2\right). \tag{2.3}$$

The error degree variance represents the spectral power of measurement noise at degree n and provides a degree-dependent measure of the reliability of the gravity field solution.

In monthly GRACE gravity field solutions, the degree variance is typically largest at low degrees and decreases with increasing degree. In contrast, the error degree variance increases at higher degrees, indicating that measurement noise dominates the gravity field estimates at short spatial wavelengths (Wahr et al., 1998).

2.3 Tesseroid-based forward gravitational modelling

Tesseroids are spherical mass elements used to discretize the Earth's mass distribution in a way that explicitly accounts for the Earth's curvature. A spherical tesseroid is defined by the bounds (λ_1, λ_2) in longitude, (φ_1, φ_2) in latitude, and (r_1, r_2) in radial direction, assuming a constant density within each element. The geometric configuration of a tesseroid and the relative positions of the computation point and integration point are illustrated in Figure 2.1 (Heck and Seitz, 2007; Grombein et al., 2013).

In this study, tesseroid-based forward modelling provides the physical link between GRACE-derived gravitational potential variations and equivalent mass changes. This forward operator is subsequently used within an inverse adjustment framework to estimate terrestrial water storage (TWS) anomalies over Europe, in accordance with the objectives of the lab rotation.

The gravitational potential V generated by a mass body occupying the volume Ω at a computation point $\mathbf{x} = (x_1, x_2, x_3)$ is given by Newton's volume integral (Grombein et al., 2013, p. 646, Eq. (1)):

$$V(\mathbf{x};\Omega) = G \iiint_{\Omega} \frac{\rho(\mathbf{x}')}{\ell(\mathbf{x},\mathbf{x}')}\, d\Omega, \tag{2.4}$$

where $\rho(\mathbf{x}')$ is the mass density at the integration point $\mathbf{x}' = (x_1', x_2', x_3')$ and $\ell(\mathbf{x},\mathbf{x}') = \|\mathbf{x} - \mathbf{x}'\|$ is the Euclidean distance between the computation point $\mathbf{x}$ and the integration point $\mathbf{x}'$.

For a spherical tesseroid with constant density, the integral in Equation (2.4) can be written in geocentric spherical coordinates (Grombein et al., 2013, p. 647, Eq. (3)):

$$V(r,\varphi,\lambda) = G\rho \int_{\lambda_1}^{\lambda_2} \int_{\varphi_1}^{\varphi_2} \int_{r_1}^{r_2} \frac{r'^2 \cos\varphi'}{\ell}\, dr'\, d\varphi'\, d\lambda'. \tag{2.5}$$

The distance ℓ between the computation point $\mathbf{x}$ and the integration point $\mathbf{x}'$ is given by Heck and Seitz (2007, p. 126, Eq. (18)):

$$\ell = \sqrt{r^2 + r'^2 - 2rr'\cos\psi}, \tag{2.6}$$

where the spherical angle ψ is defined as (Heck and Seitz, 2007, p. 126, Eq. (19)):

$$\cos\psi = \sin\varphi \sin\varphi' + \cos\varphi \cos\varphi' \cos(\lambda' - \lambda). \tag{2.7}$$

Because the integral in Equation (2.5) is of elliptic type, a closed-form analytical solution is not available. To obtain a computationally efficient approximation, the spherical integral kernel

$$K(\mathbf{x},\mathbf{x}') = \frac{r'^2 \cos\varphi'}{\ell(\mathbf{x},\mathbf{x}')} \tag{2.8}$$

is expanded in a Taylor series about the geometric centre of the tesseroid (Heck and Seitz, 2007, p. 127, Eq. (22)). The expansion point is defined as (Heck and Seitz, 2007, p. 127, Eq. (21))

$$r_0 = \frac{r_1 + r_2}{2}, \quad \varphi_0 = \frac{\varphi_1 + \varphi_2}{2}, \quad \lambda_0 = \frac{\lambda_1 + \lambda_2}{2}. \tag{2.9}$$

Retaining terms up to second order, the gravitational potential of a homogeneous tesseroid can be approximated by (Heck and Seitz, 2007, p. 127, Eq. (24)):

$$V(r,\varphi,\lambda) \approx G\rho\, \Delta r\, \Delta\varphi\, \Delta\lambda \left[K_{000} + \frac{1}{24} \left(K_{200}\Delta r^2 + K_{020}\Delta\varphi^2 + K_{002}\Delta\lambda^2 + \right) + O(\Delta^4) \right], \tag{2.10}$$

with the tesseroid dimensions (Heck and Seitz, 2007, p. 127)

$$\Delta r = r_2 - r_1, \quad \Delta\varphi = \varphi_2 - \varphi_1, \quad \Delta\lambda = \lambda_2 - \lambda_1. \tag{2.11}$$

Due to symmetry about the expansion point, all odd-order terms vanish. Higher-order terms are neglected, as their contribution is negligible for sufficiently small tesseroids (Heck and Seitz, 2007; Grombein et al., 2013). This approximation provides an accurate and numerically efficient forward model for computing gravitational potential anomalies caused by surface and near-surface mass variations.

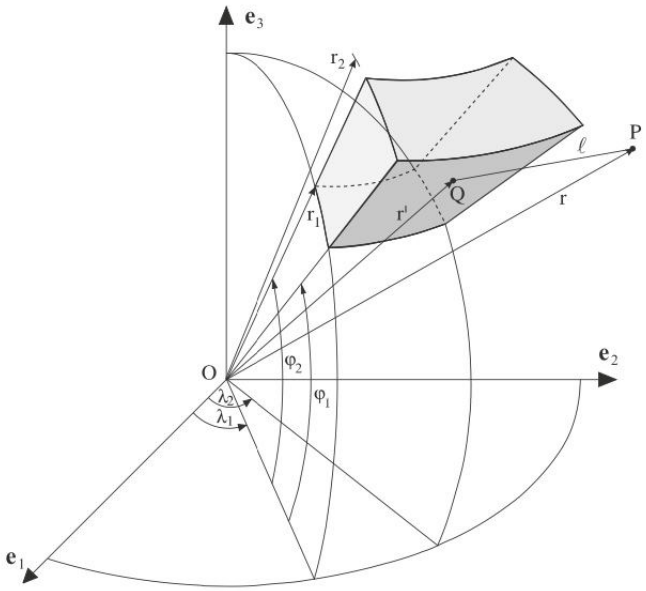

Figure 2.1: Geometry of a spherical tesseroid and definition of the integration bounds in spherical coordinates (Heck and Seitz, 2007).

2.4 Decorrelation filtering using DDK filters

The monthly GRACE Level-2 gravity field solutions contain correlated errors originating from the satellite measurement geometry and imperfections in background force models. In the spatial domain, these errors manifest as characteristic north-south striping patterns, which must be reduced prior to quantitative hydrological interpretation (Swenson and Wahr, 2006; Kusche, 2007). Simple isotropic smoothing can suppress noise but does not explicitly remove these correlations.

To address this problem, Kusche (2007) introduced a decorrelation approach that operates directly on the spherical harmonic coefficients using their full error covariance information. For each spherical harmonic degree n, the coefficient vector

$$\mathbf{c}_n = \left[\bar{C}_{n0}, \bar{C}_{n1}, \ldots, \bar{C}_{nn}, \bar{S}_{n1}, \ldots, \bar{S}_{nn}\right]^{\mathrm{T}}$$

is transformed using a degree–dependent filter matrix $\mathbf{W}_n$ derived from the estimated error covariance matrix of the GRACE solution. The decorrelated and smoothed coefficients are obtained by the linear transformation

$$\hat{\mathbf{c}}_n = \mathbf{W}_n \mathbf{c}_n, \tag{2.12}$$

which summarizes the decorrelation and regularization framework described by Kusche (2007).

Based on this approach, Kusche et al. (2009) developed the DDK filter family (DDK1–DDK8), which differ in their degree of smoothing. Lower-order filters (e.g. DDK8) preserve more short-wavelength signal but retain residual noise, whereas higher-order filters (e.g. DDK1) suppress correlated high-degree noise more strongly at the expense of spatial resolution. This effect shown in Figure 2.2 for a Gauss-filtered example.

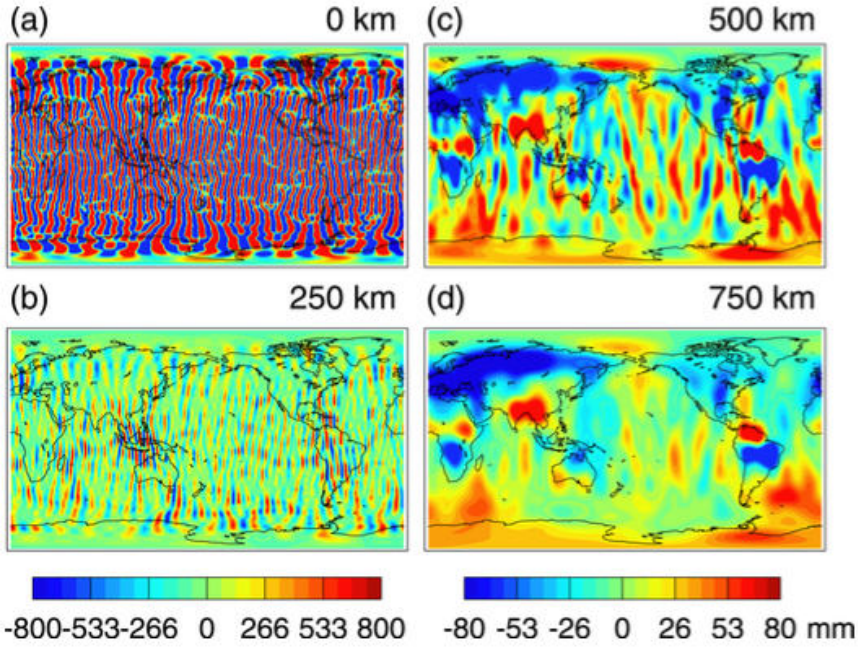

Figure 2.2: GRACE-derived maps of monthly anomaly of water storage, smoothed with Gaussian filters of different halfwidths. (a) Unsmoothed; (b) 250 km halfwidth; (c) 500 km halfwidth; (d) 750 km halfwidth. Note that left side scale (Figures la and 1b) is 10 times greater than right side scale (Figures 1c and 1d). (adapted from Swenson and Wahr (2006)).

For comparison, an isotropic Gaussian filter applies only a degree-dependent damping to the spherical harmonic coefficients and does not remove correlations between coefficients of different orders (Swenson and Wahr, 2006). The corresponding Gaussian weighting function is commonly written as

$$W_n = \exp\left[-\frac{n(n+1)r_s^2}{2a^2}\right], \tag{2.13}$$

where r_s is the filter radius and a denotes the mean Earth radius. Unlike the DDK approach, Gaussian smoothing does not involve any rotation or whitening of the coefficient vectors.

In this study, DDK filters are applied to the GRACE and GRACE–FO spherical harmonic solutions to reduce correlated errors and improve the spectral behaviour of the gravity field prior to the estimation of terrestrial water storage (TWS) anomalies.

2.5 Inverse tesseroid adjustment for mass anomalies and TWS estimation

Temporal variations of the Earth's gravity field observed by the GRACE mission are mainly caused by the redistribution of surface and near-surface masses, in particular changes in continental water storage (Wahr et al., 1998). After appropriate filtering, these gravity variations can be interpreted in terms of equivalent surface mass anomalies and expressed as total water storage (TWS) changes.

In this study, GRACE-derived gravitational potential variations are used as pseudo-observations in a space-domain inverse modelling approach based on tesseroids (see Section 2.3).

2.5.1 Inverse problem and regularization

The relationship between the observed gravitational potential variations $\Delta\mathbf{V}_{\text{obs}}$, obtained from spherical harmonic synthesis (SHS) on a spatial grid, and the unknown tesseroid height parameters can be written in discretized linear form as

$$\Delta\mathbf{V}_{\text{obs}} = \mathbf{A}\,\Delta\mathbf{r}, \tag{2.14}$$

where $\mathbf{A}$ denotes the design matrix whose elements are derived from the tesseroid-based forward model, and $\Delta\mathbf{r}$ contains the unknown tesseroid height variations.
For a homogeneous tesseroid, the gravitational potential contribution is given by Newton's volume integral, as described in Section 2.3. The inverse problem defined by Eq. (2.14) is ill-posed, since small observational errors in the GRACE-derived potential variations may cause large oscillations in the estimated mass parameters.
To stabilize the inversion, zero-order Tikhonov regularization is applied, leading to the normal equation system

$$\Delta\mathbf{r}_\lambda = \left(\mathbf{A}^{\mathrm{T}}\mathbf{A} + \lambda^2\mathbf{I}\right)^{-1}\mathbf{A}^{\mathrm{T}}\Delta\mathbf{V}_{\mathrm{obs}}, \tag{2.15}$$

where λ is a scalar regularization parameter and $\mathbf{I}$ denotes the identity matrix. The regularization parameter is selected by balancing the trade-off between data fit and model smoothness. The elements of the design matrix $\mathbf{A}$ are computed using the second-order Taylor expansion of the tesseroid kernel, given in Equation (2.10), where the coefficients K_{ijk} depend on the relative position of the computation point and the tesseroid centre.
The estimated tesseroid heights $\Delta\mathbf{r}$ mass parameters represent equivalent surface mass density variations. These are the equivalent water heights and interpreted as total water storage (TWS) anomalies.
This inverse tesseroid adjustment combines GRACE gravity observations with a physically consistent space-domain forward model and regularized inversion, yielding stable and spatially resolved TWS estimates over Europe.

2.5.2 Spectral smoothing and degree variance

Filtering of GRACE spherical harmonic coefficients can be expressed as a degree-dependent weighting of the least-squares estimates (Kusche, 2007, p. 735, Eq. (3)):

$$\hat{x}^{\gamma}_{nmq} = w_{n;\gamma}\hat{x}_{nmq}, \tag{2.16}$$

where $w_{n;\gamma}$ denotes the spectral filter weight and γ controls the degree of smoothing. In matrix notation, this operation reads (Kusche, 2007, p. 735, Eq. (4))

$$\hat{\mathbf{x}}^{\gamma} = \mathbf{W}_\gamma\hat{\mathbf{x}}, \tag{2.17}$$

with $\mathbf{W}_\gamma = \mathrm{diag}(w_{n;\gamma})$.
The damping of spectral energy due to filtering, often interpreted in terms of degree variance or global RMS reduction, is quantified by (Kusche, 2007, p. 736, Eq. (8))

$$\alpha_{T,W_\gamma} = \frac{\hat{\mathbf{x}}^{\mathrm{T}}\mathbf{W}_\gamma^{\mathrm{T}}\mathbf{W}_\gamma\hat{\mathbf{x}}}{\hat{\mathbf{x}}^{\mathrm{T}}\hat{\mathbf{x}}}. \tag{2.18}$$

This quantity describes how the application of spectral filtering redistributes signal and noise energy over spherical harmonic degrees.
The spatial smoothing effect of a filter kernel can be characterized by the variance of the squared, normalized kernel. For non-isotropic kernels, Kusche (2007, p. 739, Eq. (34)) define, the variance of the smoothing kernel can be expressed in terms of the degree-one spherical harmonic coefficients of the squared, normalized kernel as

$$\sigma^2 = 1 - \sum_{m=0}^{1}\sum_{q=1}^{2}\left((\tilde{W}^2_\gamma)_{1mq}\right)^2. \tag{2.19}$$

where $\tilde{W}^2_\gamma$ denotes the squared and normalized smoothing kernel expressed in spherical harmonics. The square root of this variance, scaled by the Earth's radius, provides a representative smoothing radius.

2.5.3 Decorrelation and DDK filtering

Monthly GRACE solutions exhibit correlated errors between spherical harmonic coefficients, which manifest as characteristic north–south striping patterns. To reduce these effects, Kusche et al. (2009) introduced a decorrelation and smoothing approach based on order-convolution filtering.
The decorrelated surface mass anomaly coefficients are computed as (Kusche et al., 2009, p. 905, Eq. (1))

$$\sigma_{nmq}^{\mathrm{filt}} = \sum_{n'=n_{\min}}^{n_{\max}} \sum_{m'=0}^{n'} \sum_{q'=1}^{2} w_{nmq}^{n'm'q'}(a)\, \sigma_{n'm'q'}, \tag{2.20}$$

where $w_{nmq}^{n'm'q'}(a)$ denotes the decorrelation filter coefficients and a is a parameter controlling the strength of smoothing.
Surface mass anomaly coefficients σ_{lmq} are related to the time-variable GRACE geopotential coefficients δx_{lmq} by (Kusche et al., 2009, p. 905, Eq. (2))

$$\sigma_{nmq} = \frac{2\rho_{\mathrm{e}}}{3\rho_{\mathrm{w}}(1+k_n)} \left(n+\frac{1}{2}\right) \delta x_{nmq}, \tag{2.21}$$

where ρ_{e} and ρ_{w} are the mean Earth and water densities, respectively, and k_n denotes the load Love number of degree n.
To reduce computational complexity, the full decorrelation matrix can be approximated by an order-convolution formulation, retaining only coefficients of equal order and parity (Kusche et al., 2009, p. 906, Eq. (8)):

$$\sigma_{nmq}^{\mathrm{filt}} = \sum_{n' \in \mathrm{parity}(n)} w(n,n',m,a)\, \sigma_{n'mq}. \tag{2.22}$$

This filtering strategy efficiently suppresses correlated noise while preserving the dominant geophysical signal content. The resulting decorrelated and smoothed coefficients form the basis for subsequent spherical harmonic synthesis and spatial interpretation of terrestrial water storage variations.

2.5.4 Degree and Error Degree Variances

Following Kusche (2007), the stochastic description of a GRACE solution starts from the block error covariance matrix $\overline{\mathbf{E}}$ of all spherical harmonic coefficients. From this matrix, an *error degree variance* $(\overline{E})_n$ for each degree n is formed by averaging the diagonal elements that belong to degree l (Eq. (49) in Kusche 2007, p. 743):

$$(\overline{E})_n = \frac{1}{2n+1} \sum_{m=0}^{n} \sum_{q=1}^{2} \overline{E}_{nmq,nmq}, \tag{2.23}$$

where $q = 1,2$ distinguishes cosine and sine coefficients. In the Figs. 7–9, the red curves correspond to this quantity and represent the spectral distribution of the formal GRACE errors.
Analogously, a *signal degree variance* $(\overline{S})_n$ is constructed from a prescribed signal covariance model $\overline{\mathbf{S}}$ (Eq. (50) in Kusche 2007, p. 743), while the *empirical* degree variance c_n is derived directly from the estimated coefficients x_{nmq} (Eq. (51) in Kusche 2007, p. 743):

$$c_n = \frac{1}{2n+1} \sum_{m=0}^{l} \sum_{q=1}^{2} x_{nmq}^2. \tag{2.24}$$

In Figs. 7a, 8a, and 9a, the blue curves correspond to the empirical degree variance. The strong decrease of c_n with increasing degree n demonstrates that most geophysical signal power resides in the long-wavelength part of the

spectrum. The spatial effect of the applied smoothing is illustrated by the cross-sections of the normalized kernel shown in Fig. 2.3.

For increasing degree the error degree variance $(\overline{E})_n$ approaches and eventually exceeds the empirical degree variance c_n, indicating that medium and high degrees are progressively dominated by noise, as also noted by Kusche (2007).

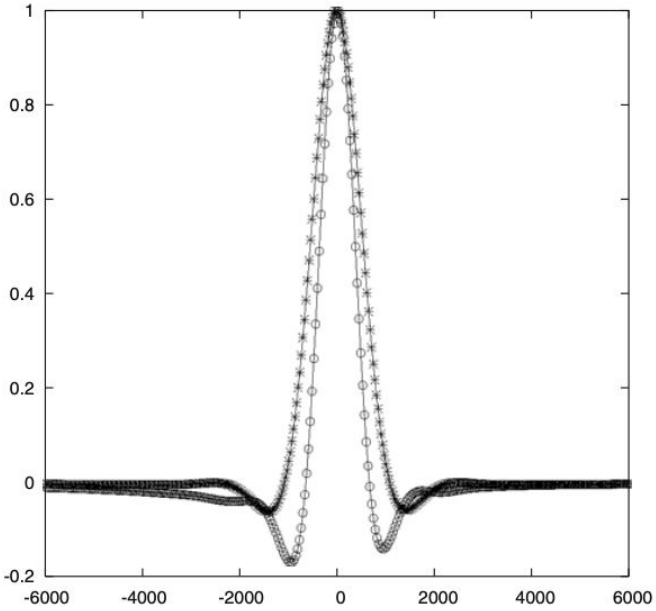

Figure 2.3: Normalized smoothing kernel cross-sections (Kusche, 2007).

3 Data

The Level-2 data used in this study comprise the monthly gravity field solutions derived from the GRACE (Gravity Recovery and Climate Experiment) and GRACE-FO (Gravity Recovery and Climate Experiment Follow-On) missions, spanning the period from January 2003 to December 2024. These datasets contain fully normalized spherical harmonic coefficients representing temporal variations in the Earth's gravitational potential. The products are generated by the GeoForschungsZentrum (GFZ), Potsdam under Release 06.1 (RL06.1) and distributed via the International Centre for Global Earth Models (ICGEM, 2026).

The GRACE mission, jointly operated by NASA's Jet Propulsion Laboratory (JPL) and the German Aerospace Center (DLR), was launched in 2002 and operated until 2017, followed by its successor GRACE-FO in 2018. Both missions measure changes in the Earth's gravity field using the low-low satellite-to-satellite tracking (LL-SST) technique, in which two identical satellites orbit approximately 490 km above the Earth's surface, separated by about 220 km. As shown in Figure 3.1, when the leading satellite encounters a region of greater mass, it is slightly accelerated due to the stronger gravitational pull, increasing the inter-satellite distance. When the trailing satellite passes over the same region, it experiences the same effect, and the distance decreases again. These distance variations, measured with micrometer precision by the K-band ranging system, form the fundamental observable for estimating mass redistribution on Earth.

The GRACE and GRACE-FO raw observations undergo a multi-level data processing chain within the Science Data System (SDS), which transforms satellite telemetry into calibrated gravity field products (Figure 3.2). The data are organized into three principal processing levels: Level-0, Level-1, and Level-2.

Level-0: The Level-0 data consist of raw telemetry and housekeeping information received by the Raw Data Center (RDC) of the Mission Operation System (MOS) in Neustrelitz, Germany. Using the Weilheim (WHM) and Neustrelitz (NST) tracking stations, the MOS receives scientific and housekeeping data twice per day from each

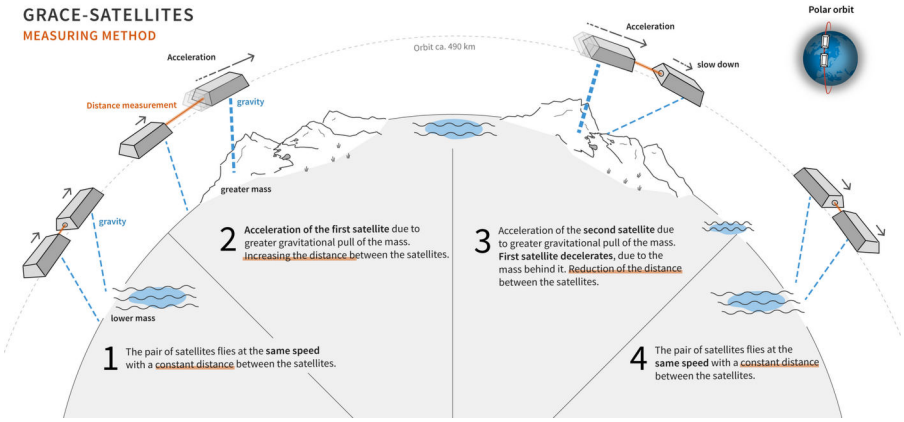

Figure 3.1: Schematic representation of the GRACE and GRACE-FO measurement principle using low–low satellite-to-satellite tracking (adapted from GFZ (2026))

.

satellite. These are stored in a rolling archive, and the Science Data System (SDS) retrieves, extracts, and reformats them. Additional real-time data are received at the GFZ polar receiving station in Ny-Ålesund (NYA) for radio occultation analysis.

Level-1: The Level-1A data products result from the non-destructive calibration of Level-0 data, converting binary-encoded measurements into engineering units, resolving time ambiguities, and appending quality control flags. Level-1B data products are generated through irreversible processing, including synchronization, resampling, and application of the AOD1B (Atmosphere and Ocean De-aliasing) model. The Level-1 processing software is developed and operated by JPL.

Level-2: The Level-2 data represent calibrated and validated monthly and static gravity fields derived from Level-1B inputs. These are expressed as spherical harmonic coefficients and include ancillary datasets (e.g., mean atmospheric and oceanic mass variations) necessary for interpreting temporal variability in gravity solutions. Level-2 products are independently generated by GFZ, UTCSR (University of Texas Center for Space Research), and JPL. Routine operational processing is performed by GFZ and UTCSR, with JPL producing verification solutions.
The complete monthly Level-2 gravity field time series from January 2003 to December 2024 (GFZ RL06.1) are available through the ICGEM data portal (see ICGEM, 2026).

Level-3: Products derived from Level-2 are referred to as Level-3 data. In this work, they are generated by synthesis from Level-2 data, but can also be obtained from the corresponding data centers based on the mascon approach (Antoni, 2022; Scanlon et al., 2016).

4 Methodology Overview

Monthly GRACE and GRACE–FO gravity field solutions are provided in terms of time-variable spherical harmonic coefficients. Residual gravitational potential variations δV are computed on a regular $1^\circ \times 1^\circ$ grid at a selected computation altitude ($h = 500$ km) using spherical harmonic synthesis. The synthesis follows the standard formulation described in Heiskanen and Moritz (1967).

To relate these potential variations to surface mass changes, the Earth's near-surface layer is discretized into three-dimensional tesseroids of homogeneous density (Heck and Seitz, 2007). For each tesseroid, the unknown parameter is its radial thickness variation Δr_k, which represents the vertically integrated mass change. Two grids of $2^\circ \times 2^\circ$ resolution are prepared for cases A and B in the Introduction.

The gravitational potential contribution of a tesseroid cannot be computed in closed form. Therefore, a series expansion of Newton's volume integral is employed (see Eqs. (2.10) and (2.11) in Section 2.3). A Taylor expansion of the tesseroid potential about its geometric centre is performed. Retaining terms up to second order yields a linear

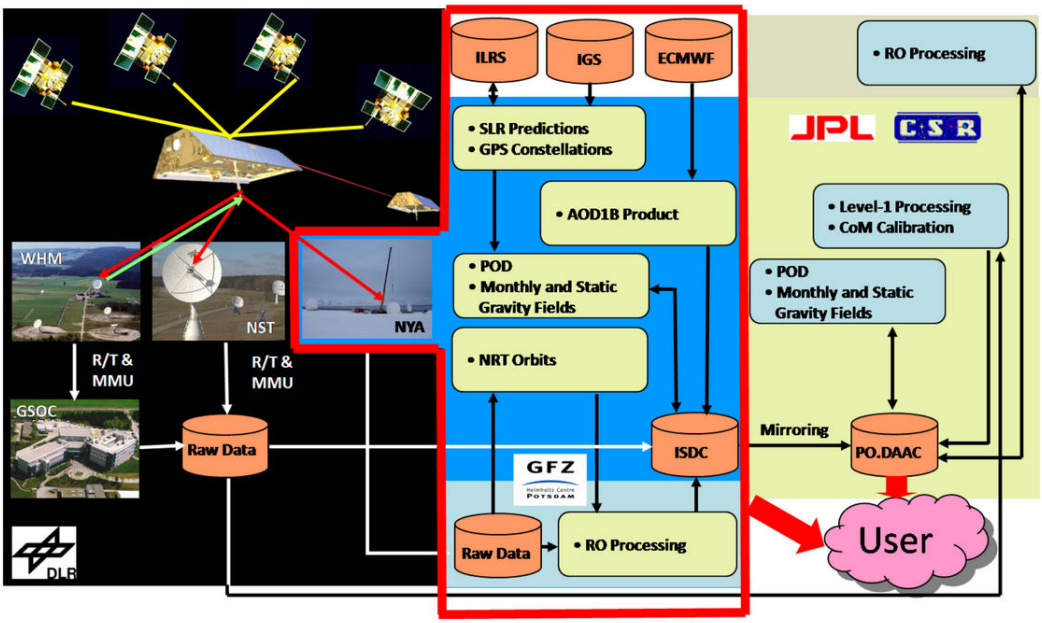

Figure 3.2: Comprehensive data flow within the GRACE and GRACE-FO Science Data System (SDS), showing the complete chain from satellite tracking and data reception to Level-2 gravity field product generation (adapted from GFZ (2026))

.

relationship between the potential variations and the tesseroid thickness changes. The resulting kernel coefficients K_{000}, K_{200}, K_{020}, and K_{002} describe the sensitivity of the gravitational potential at the computation point to mass changes within each tesseroid.

The combined gravitational effects of all tesseroids form the design matrix $\mathbf{A}$, whose elements represent the potential response to a unit change in tesseroid thickness. The synthesized GRACE potential values constitute the observation vector $\mathbf{L}$, while the vector of unknowns $\mathbf{x}$ contains the tesseroid thickness variations Δr_k. Since the number of observations n exceeds the number of unknowns ($u < n$), the system is solved by least-squares estimation (Baur et al., 2012):

$$\hat{\mathbf{x}} = (\mathbf{A}^{\mathrm{T}}\mathbf{P}\mathbf{A})^{-1}\mathbf{A}^{\mathrm{T}}\mathbf{P}\mathbf{L}, \qquad \mathbf{P} = \mathbf{I}. \tag{4.1}$$

Here, $\mathbf{P}$ denotes the weight matrix, which is assumed to be the identity. The estimated tesseroid thickness variations Δr_k represent equivalent surface mass changes and are interpreted as terrestrial water storage (TWS) anomalies following Wahr et al. (1998).

5 Results and Discussion

This section presents the monthly solutions in the form of degree and error degree variances. For the calculation of the TWS using the inverse tesseroid approach, the behavior of the L-curves is discussed. A comparison of the results based on DDK1, DDK5, and DDK8 is carried out.

5.1 Discussion on Spherical Harmonic Coefficients

The monthly GRACE gravity field solutions are provided as fully normalized spherical harmonic coefficients $\bar{C}_{nm}$ and $\bar{S}_{nm}$, commonly grouped into coefficient vectors x_{nmq} with index q distinguishing cosine and sine terms. The stochastic properties and spectral behaviour of these coefficients are analysed following the framework developed for GRACE-type gravity field models by Kusche (2007) and extended to decorrelated (DDK) solutions by Kusche et al. (2009).

5.1.1 Residual Degree Variances

In order to isolate time–variable gravity, Kusche et al. (2009) form residual monthly anomalies by subtracting a temporal mean model. If $x_{nmq}(t)$ denotes a monthly coefficient time series (cosine or sine), the residuals are given by

$$\delta x_{nmq}(t) = x_{nmq}(t) - \bar{x}_{nmq}\,, \tag{5.1}$$

where $\bar{x}_{nmq}$ is the long–term mean (Kusche et al., 2009, p. 904, Eq. (2)). The same definition is used here for the used GFZ solutions. The empirical degree variances of these residuals are computed by inserting $\delta x_{nmq}(t)$ into Eq. (2.24). The resulting spectra, plotted in Figs. 5.2(b), 5.3(b), 5.4(b), describe the power of the purely time–variable component of the gravity field.

Compared to the spectra of the full fields shown in Figs. 5.2(a), 5.3(a), 5.4(a), the residual spectra are strongly reduced at the lowest degrees because the static field has been removed. This behaviour is consistent with the spatial patterns observed in Fig. 5.1.

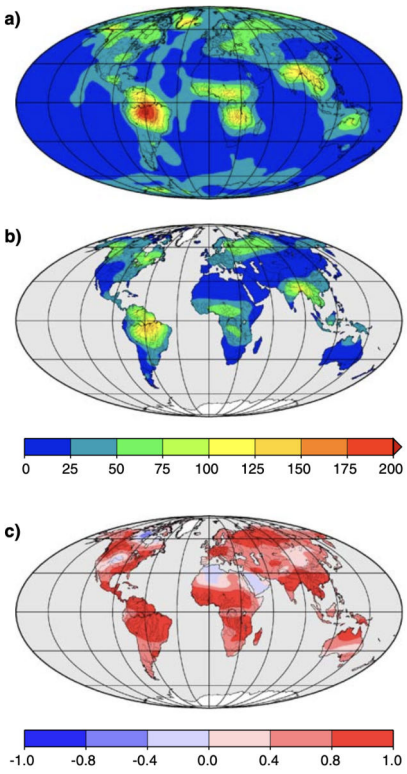

Figure 5.1: Pixel-wise WRMS and correlation of GRACE and WGHM (weighted global hydrological model) after DDK1 filtering (Kusche et al., 2009).

5.1.2 Effect of DDK Filtering

The DDK filters applied in this study follow the probabilistic decorrelation and smoothing framework proposed by Kusche (2007). In this approach, monthly GRACE gravity field solutions are treated as realizations of an ill–posed inverse problem with correlated errors. A regularized estimate $\hat{\boldsymbol{x}}$ of the gravity field coefficients is obtained by penalized weighted inversion,

$$\hat{\boldsymbol{x}} = \left(\overline{\mathbf{E}}^{-1} + \lambda \overline{\mathbf{S}}^{-1}\right)^{-1} \overline{\mathbf{E}}^{-1} \boldsymbol{x}, \tag{5.2}$$

where $\boldsymbol{x}$ denotes the unconstrained GRACE coefficient vector, $\overline{\mathbf{E}}$ is the associated error covariance matrix, and $\overline{\mathbf{S}}$ represents an a priori signal covariance model defined by a diagonal, degree-dependent power law (Eq. (47) in

Kusche 2007, p. 742). The relative weighting between signal and error covariance is controlled by a regularization parameter.
Kusche et al. (2009) reformulated this regularized solution as a linear post–processing filter acting directly on the spherical harmonic coefficients,

$$\boldsymbol{\sigma}^{\text{filt}} = \mathbf{W}\boldsymbol{\sigma}, \qquad \mathbf{W} = \left(\overline{\mathbf{E}}^{-1} + a\overline{\mathbf{S}}^{-1}\right)^{-1}\overline{\mathbf{E}}^{-1}, \tag{5.3}$$

where $\boldsymbol{\sigma}$ denotes the vector of surface mass anomaly coefficients, $\boldsymbol{\sigma}^{\text{filt}}$ their filtered counterpart, and a plays the role of the regularization parameter in Kusche et al. (2009, p. 905, Eq. (3)).
Different members of the DDK filter family (DDK1, DDK2, ...) correspond to specific choices of a and to the assumed signal covariance model. The DDK5 filter used in this study represents a compromise between effective suppression of correlated noise and preservation of geophysically meaningful signal power, consistent with the performance characteristics discussed by Kusche et al. (2009).
The effect of DDK filtering is evident in Figs. 5.2 – 5.4: empirical degree variances are stabilized at medium and higher degrees, while the corresponding error degree variances are substantially reduced relative to the unfiltered solutions.

5.1.3 Coefficient Accuracies

The lower-left panels of Figs. 5.2(c), 5.3(c), 5.4(c), show the formal standard deviations of the individual spherical harmonic coefficients $\sigma_{\bar{C}_{nm}}/\sigma_{\bar{S}_{nm}}$ in the degree-order domain. These quantities are obtained as the square roots of the diagonal elements of the filtered error covariance matrix

$$\overline{\mathbf{E}}^{\text{filt}} = \mathbf{W}\overline{\mathbf{E}}\mathbf{W}^{\mathsf{T}}, \tag{5.4}$$

which follows from the propagation of the original GRACE error covariance matrix $\overline{\mathbf{E}}$ through the linear decorrelation filter $\mathbf{W}$ (cf. the regularization framework in Eqs. (20) – (22) of Kusche 2007, p. 737 – 738).
The resulting error patterns exhibit the characteristic triangular structure in the degree-order domain, with minimum uncertainties at intermediate orders and increasing errors towards higher degrees. This behaviour closely resembles the coefficient accuracy diagrams shown for GRACE-type solutions in Kusche (2007, Fig. 3, p. 743) and reflects the anisotropic error correlation structure inherent to GRACE observations.
Application of the DDK5 filter reduces the overall magnitude of these formal errors while preserving their main structural features, indicating effective suppression of correlated noise without altering the fundamental spectral characteristics of the gravity field.

5.1.4 Relative Accuracies of $\bar{C}_{nm}$ and $\bar{S}_{nm}$

The lower–right panels in Figs. 5.2(d), 5.3(d), 5.4(d), display the ratio of the formal standard deviations of cosine and sine coefficients, $\sigma_{\bar{C}_{nm}}/\sigma_{\bar{S}_{nm}}$, expressed in percent. Although this diagnostic is not given explicitly as a formula in the cited papers, it is computed directly from the standard deviations derived from $\overline{\mathbf{E}}^{\text{filt}}$ as described above. The near–uniform appearance of these plots confirms that the DDK5 filter, as designed by Kusche (2007) and Kusche et al. (2009) does not introduce systematic differences in the accuracies of $\bar{C}_{nm}$ versus $\bar{S}_{nm}$.
Overall, the behaviour observed in Figs. 5.2 – 5.4 is fully consistent with the spectral characteristics of DDK–filtered GRACE solutions reported by Kusche (2007) and Kusche et al. (2009): most signal power resides in low degrees, the errors grow with increasing degree, and DDK5 provides a balanced compromise between noise suppression and signal preservation.

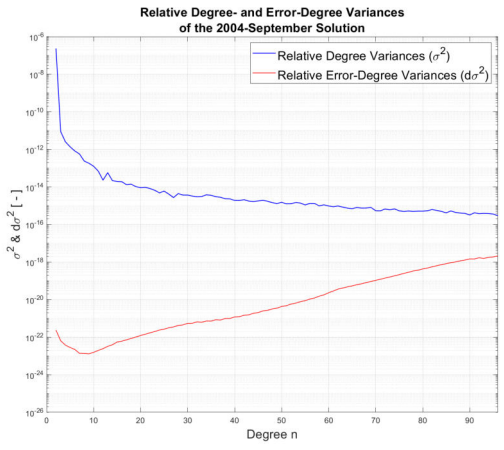

(a) Degree and Error Degree Variance

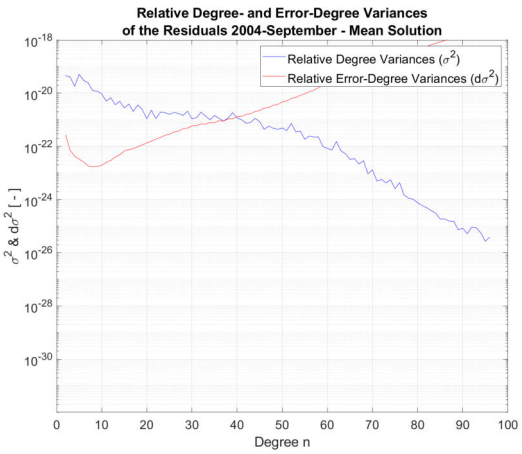

(b) Relative Degree and Error Degree Variance

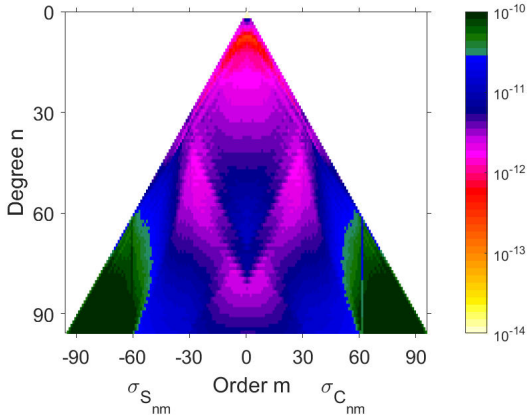

(c) Accuracies of C_{nm} and S_{nm}

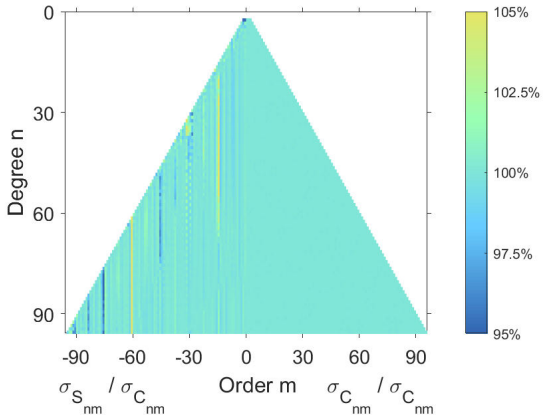

(d) Relative accuracies (σC_{nm} vs. σS_{nm})

Figure 5.2: Degree variance, error degree variance, and coefficient accuracies for September 2004 (DDK5).

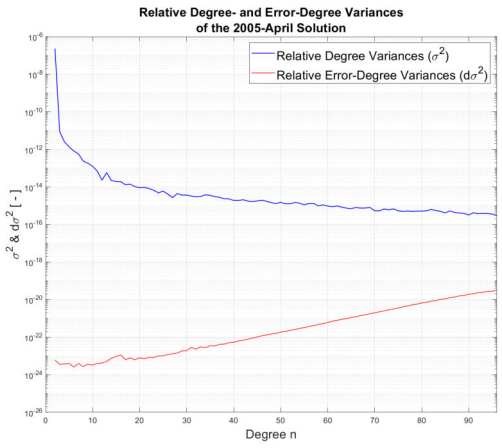

(a) Degree and Error Degree Variance

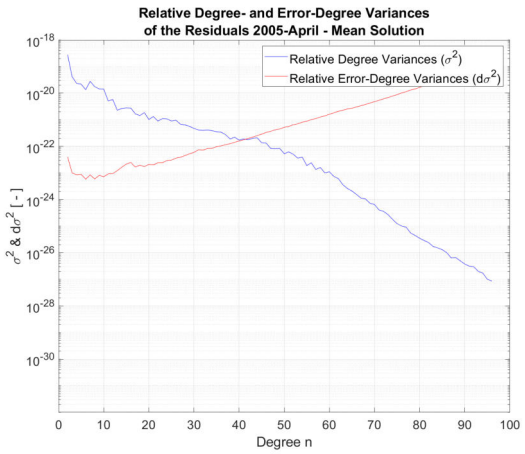

(b) Relative Degree and Error Degree Variance

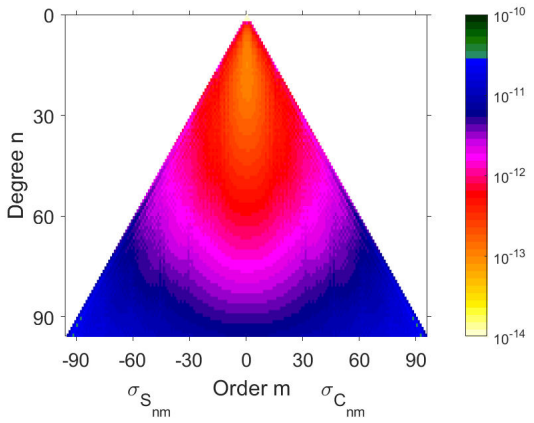

(c) Accuracies of C_{nm} and S_{nm}

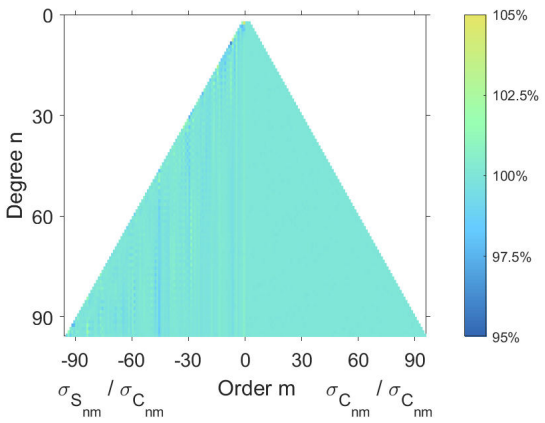

(d) Relative accuracies (σC_{nm} vs. σS_{nm})

Figure 5.3: Degree variance, error degree variance, and coefficient accuracies for April 2005 (DDK5).

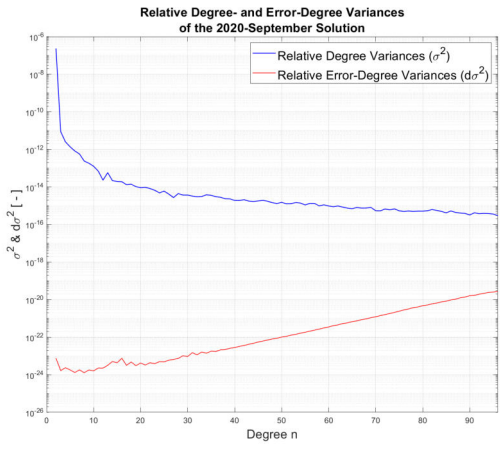

(a) Degree and Error Degree Variance

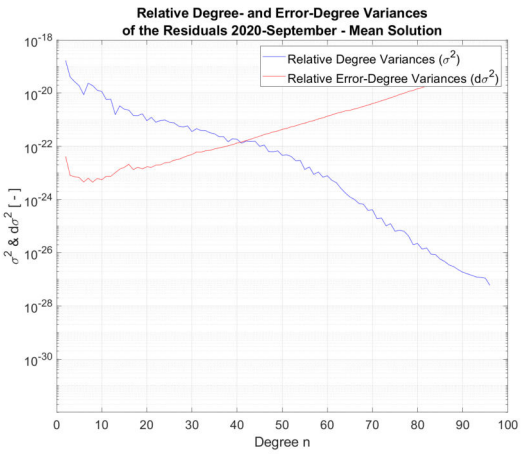

(b) Relative Degree and Error Degree Variance

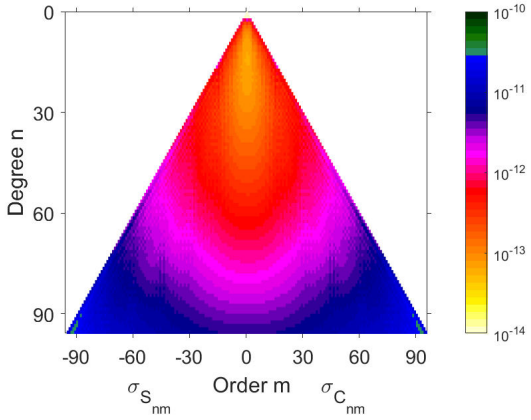

(c) Accuracies of C_{nm} and S_{nm}

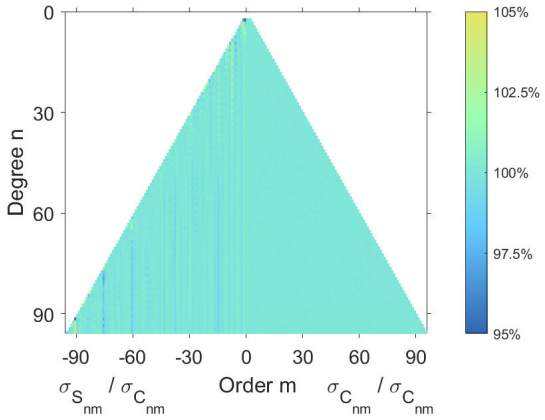

(d) Relative accuracies (σC_{nm} vs. σS_{nm})

Figure 5.4: Degree variance, error degree variance, and coefficient accuracies for September 2020 (DDK5).

5.2 Regularized inversion framework

The inversion of residual gravitational potentials into equivalent tesseroid thickness variations constitutes a typical ill-posed inverse problem, characterized by non-uniqueness and a high sensitivity of the solution to observational noise. Such characteristics are well known in gravity field modelling and GRACE-related applications, particularly when regional-scale mass variations are to be resolved from satellite gravity observations (Wahr et al., 1998; Kusche, 2007).
The discretized linear inverse problem is written in compact matrix form (cf. Eq. (2.14)) as

$$\mathbf{A}\mathbf{x} = \mathbf{b}, \tag{5.5}$$

where $\mathbf{A}$ denotes the forward operator relating tesseroid thickness variations to residual gravitational potentials, $\mathbf{x}$ is the vector of unknown tesseroid parameters, and $\mathbf{b}$ contains the observed residual potentials.
Due to the ill-conditioned nature of the forward operator $\mathbf{A}$, a stable solution cannot be obtained by direct least-squares inversion. To stabilize the inversion, the problem is reformulated following the classical *Tikhonov regularization* approach, in which the solution is obtained by minimizing the Tikhonov functional

$$\hat{\mathbf{x}}_\lambda = \arg\min_{\mathbf{x}} \left(\|\mathbf{A}\mathbf{x} - \mathbf{b}\|_2^2 + \lambda^2 \|\mathbf{L}\mathbf{x}\|_2^2 \right), \tag{5.6}$$

defining the unique, stable Tikhonov-regularized solution $\hat{\mathbf{x}}_\lambda$. This formulation is consistent with the regularization expressions presented by Ditmar et al. (2003, Eq. 5, p. 467) and Metzler and Pail (2005, Eq. 5, p. 445). It corresponds to the standard Tikhonov equation, where the first term represents the data misfit, and the second term imposes a stabilizing constraint on the solution norm. The matrix $\mathbf{L}$ is the regularization operator, chosen here as the identity matrix, such that zeroth-order Tikhonov regularization is applied. The scalar regularization parameter λ controls the trade-off between data fit and solution stability.
Minimization of the Tikhonov functional in Eq. (5.6) leads to the associated regularized normal equations

$$\left(\mathbf{A}^{\mathrm{T}}\mathbf{A} + \lambda^2 \mathbf{L}^{\mathrm{T}}\mathbf{L}\right) \hat{\mathbf{x}}_\lambda = \mathbf{A}^{\mathrm{T}}\mathbf{b}, \tag{5.7}$$

which correspond directly to the regularized normal equations as shown in Ditmar et al. (2003, Eq. 6, p. 467) and Metzler and Pail (2005, Eq. 6, p. 445).

5.2.1 L-curve criterion for parameter selection

The choice of an appropriate regularization parameter λ is crucial for obtaining a physically meaningful and stable solution. In this work, the L-curve criterion is adopted following the formulation presented by Hansen (2000, p. 1–3). The L-curve is defined as a log–log plot of the residual norm versus the solution norm,

$$\left(\|\mathbf{A}\hat{\mathbf{x}}_\lambda - \mathbf{b}\|_2,\ \|\hat{\mathbf{x}}_\lambda\|_2 \right), \tag{5.8}$$

parameterized by the regularization parameter λ (Hansen, 2000, p. 2).
When represented on logarithmic axes, the curve typically exhibits a characteristic L-shaped geometry. Small values of λ correspond to under-regularized solutions with good data fit but large solution norms dominated by noise, whereas large values of λ lead to over-regularized solutions with reduced solution norms but poor agreement with the observations. The corner of the L-curve marks the transition between these regimes and represents an optimal compromise between solution stability and data fidelity (Hansen, 2000, p. 14).

5.2.2 L-curve behaviour within the study area

Figure 5.6 shows L-curves for grid-defined tesseroids located inside the study area (Case A) for January 2015 over three successive iterations, using GRACE gravity field solutions filtered with the DDK5 decorrelation filter. All three panels exhibit a pronounced L-shaped geometry with only minor changes in curvature and corner location between iterations. This behaviour indicates a relatively stable inversion and a favourable signal-to-noise ratio for tesseroids within the target region.
The small inter-iteration variability of the L-curve corner suggests that the inverse problem is less ill-conditioned in Case A and that the selected regularization parameter converges rapidly. This is consistent with the higher sensitivity of GRACE observations to mass variations within the study area and the reduced influence of spatial leakage effects when using the DDK5 filter (Kusche, 2007).

5.2.3 L-curve behaviour: Tesseroids outside the study area

Figure 5.7 presents L-curves for tesseroids located outside the study area (Case B) for the same month and iteration sequence, again based on DDK5-filtered GRACE gravity field solutions. Compared to Case A, the L-curves display a more pronounced vertical branch and a less sharply defined corner, reflecting the reduced sensitivity of satellite gravity observations to mass variations outside the region of interest.
The stronger curvature toward the solution-norm axis indicates an increased reliance on regularization to suppress noise amplification. Although the overall L-shaped geometry is preserved across iterations, the corner position shows greater variability than in Case A, highlighting the increased ill-conditioning of the inverse problem for tesseroids outside the study area.

5.2.4 Temporal variability of the L-curve

The temporal dependence of the L-curve is illustrated in Figure 5.8, which shows L-curves for Case B at iteration 3 for three different months (September 2008, January 2016, and May 2020), all derived from DDK5-filtered gravity field solutions. Differences in the shape of the curves and the location of their corners demonstrate that temporal variations in signal strength and noise characteristics of the GRACE solutions directly influence the optimal regularization parameter.
These results confirm that a single, fixed value of λ is not appropriate for all epochs. Instead, the regularization parameter must be selected individually for each monthly gravity field solution, in agreement with established GRACE processing strategies based on decorrelation filtering (Kusche, 2007).

5.2.5 Summary of L-curve corner locations and filter dependence

A compact quantitative overview of the L-curve analysis is provided in Figure 10, which summarizes the selected L-curve corner locations for different DDK filters and spatial cases. Although multiple filters are compared for completeness, the tesseroid inversion presented in this study is based on the DDK5 filter.
The tabulated results indicate that, for DDK5, the L-curve corner locations are comparatively stable across months for Case A, while exhibiting increased variability for Case B. This behaviour reflects the balance achieved by the DDK5 filter between noise suppression and signal preservation, in contrast to stronger (DDK1) and weaker (DDK8) filters (Kusche, 2007).

January	24	34	1
February	22	36	
March	24	33	2
April	22	37	
May	20	34	2
June	24	30	3
July	23	35	2
August	30	32	
September	23	31	
October	24	28	
November	23	33	1
December	22	33	2

(a) L-curve, DDK1 (Case B)

January			57
February			57
March			57
April			57
May			57
June			57
July			57
August			57
September			57
October			57
November			57
December			57

(b) L-curve, DDK5 (Case A)

January	17	39	
February	19	38	
March	18	39	
April	20	37	
May	25	31	
June	20	31	
July	18	39	
August	23	34	
September	22	32	
October	23	28	
November	23	31	
December	19	34	

(c) L-curve, DDK5 (Case B)

January	17	40	
February	21	29	6
March	20	37	
April	20	37	
May	20	34	
June	12	39	1
July	16	41	
August	31	26	
September	23	36	
October	22	28	
November	23	31	
December	18	36	

(d) L-curve, DDK8 (Case B)

Figure 5.5: Classification of L-curves for different DDK filters and cases.

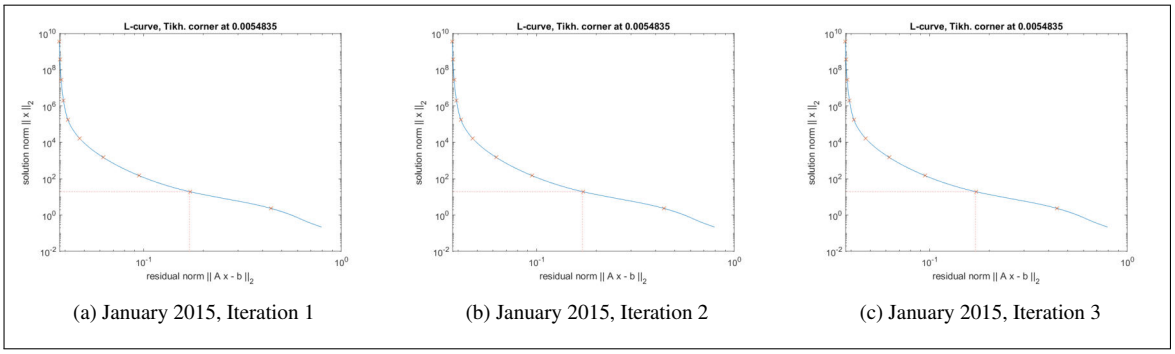

(a) January 2015, Iteration 1 (b) January 2015, Iteration 2 (c) January 2015, Iteration 3

Figure 5.6: L-curves for grid-defined tesseroids within the study area (Case A) over three iterations.

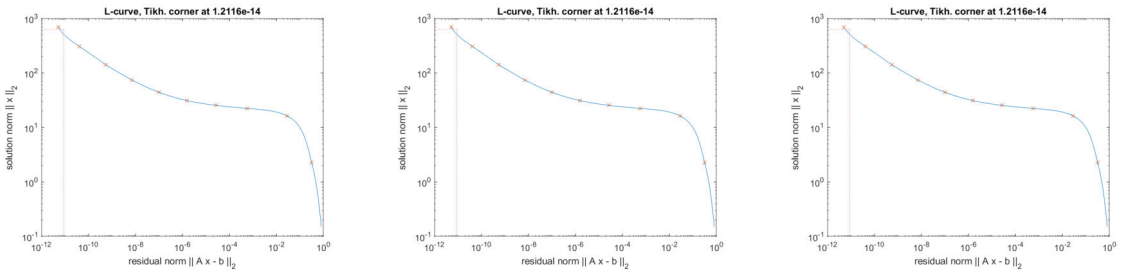

(a) January 2015, Iteration 1 (b) January 2015, Iteration 2 (c) January 2015, Iteration 3

Figure 5.7: L-curves for grid-defined tesseroids outside the study area (Case B) over three iterations.

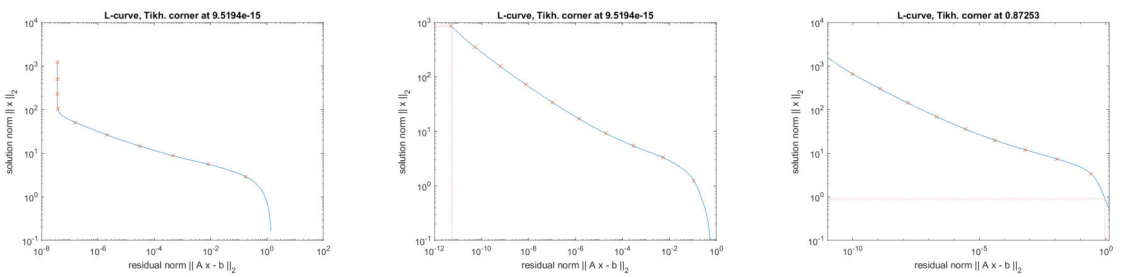

(a) September 2008, Iteration 3 (b) January 2016, Iteration 3 (c) May 2020, Iteration 3

Figure 5.8: L-curves for grid-defined tesseroids outside the study area for different months (Case B, Iteration 3).

5.3 Assessment of SHS and TWS results

Figures 5.9 – 5.12 together with Tables 5.1 and 5.2 illustrate how GRACE gravity-field information propagates from spherical harmonic synthesis (SHS) to potential residuals and finally to terrestrial water storage (TWS) estimates. This section evaluates the results by consistently linking the observed spatial patterns in the figures with the tabulated TWS behaviour for Case A and Case B.

5.3.1 Potential synthesis at satellite altitude

Panel (a) of Figures 5.9 – 5.12 shows the gravitational potential synthesized at satellite altitude using DDK5-filtered spherical harmonic coefficients. This potential synthesis is identical for Case A and Case B, since it represents a forward computation of the gravity field and is independent of the tesseroid configuration used later in the inversion.

The synthesized potential field is smooth and dominated by long-wavelength structures. This behaviour is expected because the gravitational potential is an integrated quantity and has limited sensitivity to small-scale mass variations at satellite altitude (Wahr et al., 1998; Tapley et al., 2004). Consequently, differences between Case A and Case B do not appear at this stage but emerge only in the residuals and in the derived TWS fields.

5.3.2 Derived TWS fields and spatial stability

Panels (b) and (c) of Figures 5.9 – 5.12 present the derived TWS fields for Case A and Case B, respectively. In Case A, the TWS maps are smooth and spatially coherent, with relatively stable amplitudes across different months. Seasonal hydrological signals are visible, but edge effects near the boundaries partly affect the interior of the study area.

In Case B, the TWS fields show stronger spatial contrasts and increased variability. Although noise levels are higher overall, the placement of tesseroids outside the study area causes boundary artefacts to remain largely outside the

region of interest. As a result, the interior TWS patterns are less affected by edge effects and respond more clearly to temporal mass variations. When combined with appropriate regularization, this configuration provides a more sensitive and informative representation of TWS variability (Heck and Seitz, 2007; Baur and Sneeuw, 2011).

5.3.3 Potential residuals

Panels (d) and (e) of Figures 5.9 – 5.12 show the potential residuals obtained after subtracting the synthesized signal. For Case A, the residuals are generally small in magnitude and spatially smooth, indicating that the dominant gravity signal is well represented and that noise amplification is limited within the study area.
For Case B, the residuals exhibit larger amplitudes and stronger spatial gradients, particularly near the boundaries of the tesseroid domain. These patterns are typical manifestations of spatial leakage and correlated errors in GRACE gravity field solutions (Wahr et al., 1998; Kusche, 2007). Importantly, in Case B these boundary-related effects are largely shifted outside the study area, whereas in Case A similar edge effects occur closer to the region of interest.

5.3.4 Filter-dependent behaviour and temporal variability of TWS

Tables 5.1 and 5.2 compare TWS estimates obtained using the DDK1, DDK5, and DDK8 decorrelation filters. The DDK8 results show strong north–south striping and fragmented TWS patterns for both cases, particularly for Case B, indicating insufficient suppression of correlated GRACE noise.
DDK1 produces very smooth TWS fields with minimal noise in both cases. However, the strong filtering substantially reduces seasonal amplitudes and dampens spatial contrasts, especially during summer and autumn. This over-smoothing limits the ability to resolve meaningful temporal TWS variations.
DDK5 provides the most balanced behaviour. In Case A, it suppresses striping while preserving seasonal signals. In Case B, DDK5 effectively stabilizes the inversion while maintaining higher sensitivity to month-to-month and year-to-year TWS changes. This behaviour is clearly reflected in Tables 5.1 and 5.2, where Case B with DDK5 shows the strongest and most consistent temporal variability without excessive noise.
Interannual differences in TWS arise mainly from variations in the signal-to-noise ratio of the GRACE gravity field solutions. Periods with stronger large-scale mass signals yield more stable TWS estimates, while periods with weaker signals show increased sensitivity to filtering and regularization choices.

5.3.5 Consistency between figures and tables

The spatial patterns observed in Figures 5.9(b,c) – 5.12(b,c) are fully consistent with the TWS values listed in Tables 5.1 and 5.2.
Months and seasons showing stable DDK5-based TWS estimates in the tables correspond to coherent spatial patterns in the maps, whereas filters associated with striping or over-smoothing are reflected in degraded spatial representations. This consistency confirms the robustness of the SHS–residual–inversion workflow.

5.3.6 Implications for TWS-focused GRACE analyses

Overall, the results demonstrate that reliable GRACE-based TWS recovery requires both balanced decorrelation filtering and an appropriate spatial configuration of the inversion domain. While Case A provides stable and smooth solutions, edge effects partially affect the interior of the study area.
Case B, despite higher overall noise levels, shifts edge effects outside the region of interest and therefore yields cleaner and more responsive TWS signals within the study area. When combined with DDK5 filtering, Case B provides the best overall performance for analysing temporal TWS variability by preserving physically meaningful signals while maintaining acceptable solution stability. This conclusion is fully consistent with established GRACE processing strategies and previous studies (Wahr et al., 1998; Kusche, 2007; Grombein et al., 2013).

Table 5.1: Comparison of DDK1, DDK5, and DDK8 filter results (Case B) for selected seasons in 2007.

Month / Season	DDK1	DDK5	DDK8
January Winter	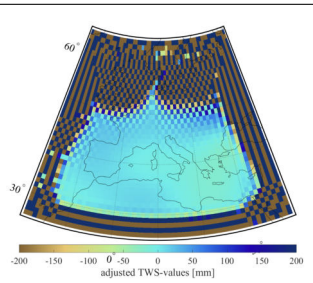	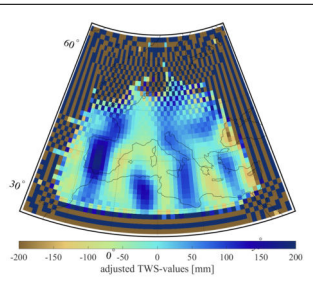	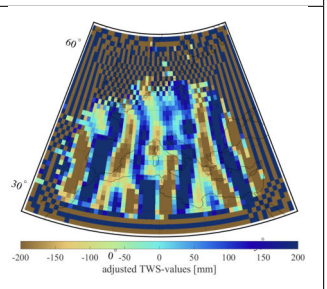
March Spring	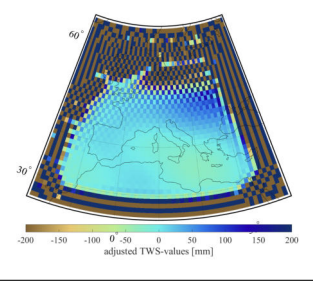	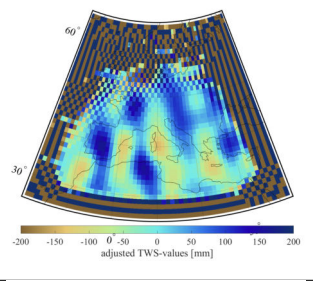	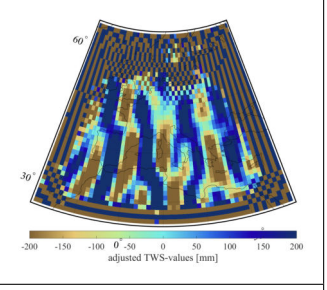
July Summer	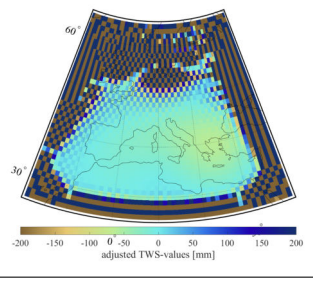	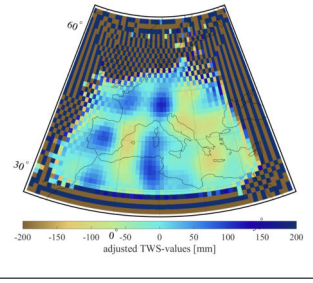	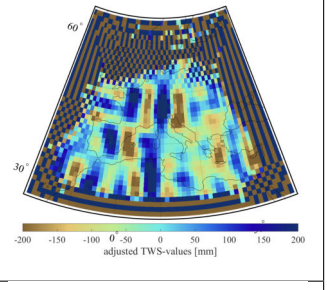
November Autumn	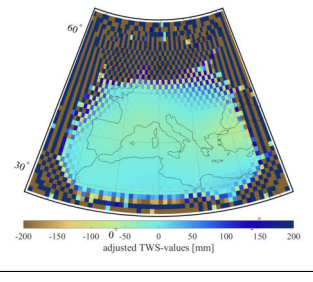	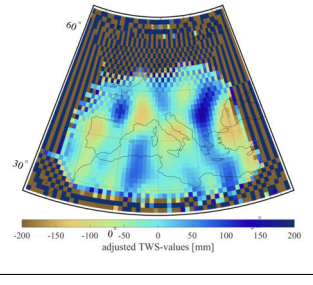	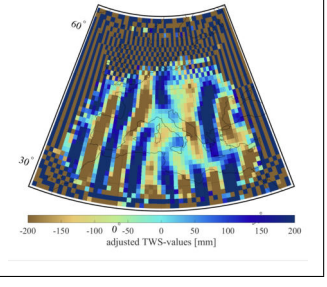

Table 5.2: Comparison of DDK1, DDK5, and DDK8 filter results (Case B) for selected seasons in 2019.

Month / Season	DDK1	DDK5	DDK8
January Winter	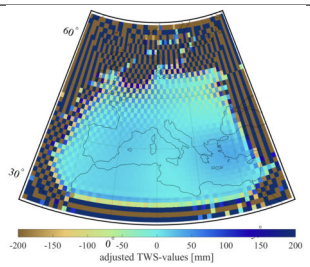	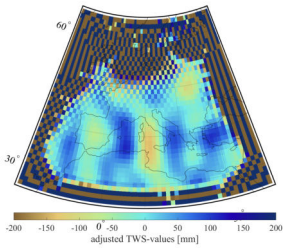	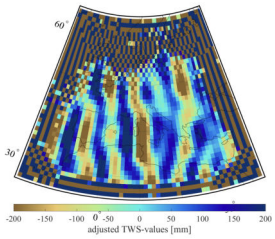
March Spring	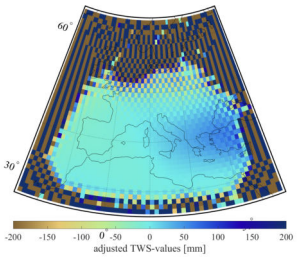	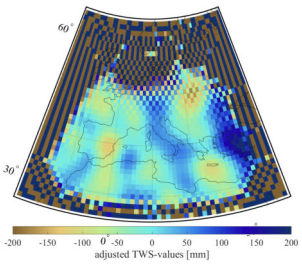	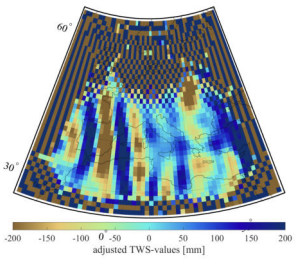
July Summer	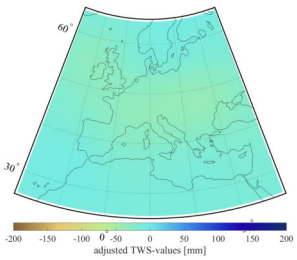	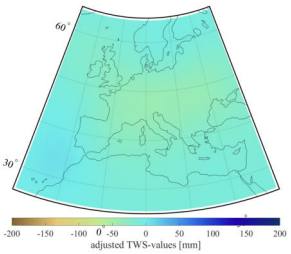	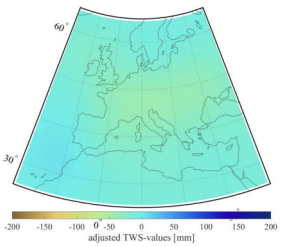
November Autumn	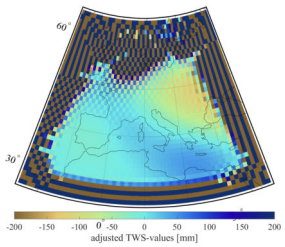	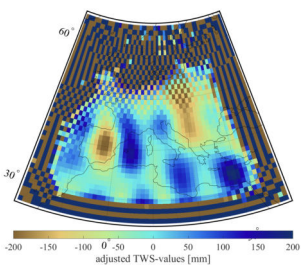	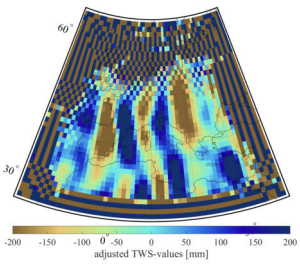

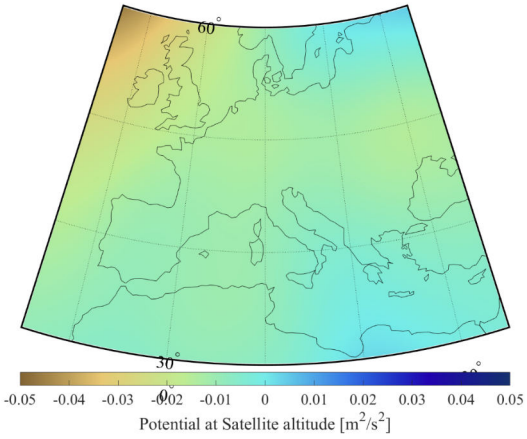

(a) Potential synthesis (DDK5, Winter 2020)

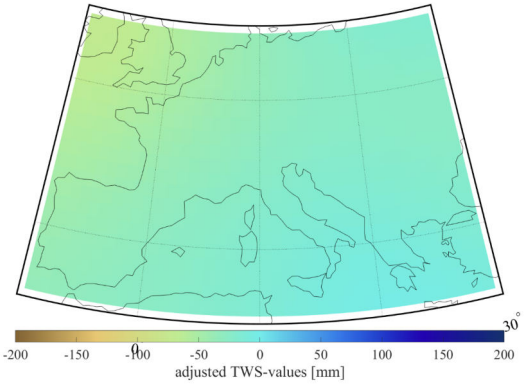

(b) TWS (Case A)

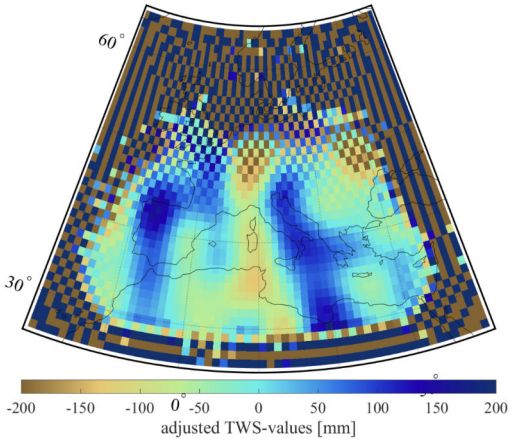

(c) TWS (Case B)

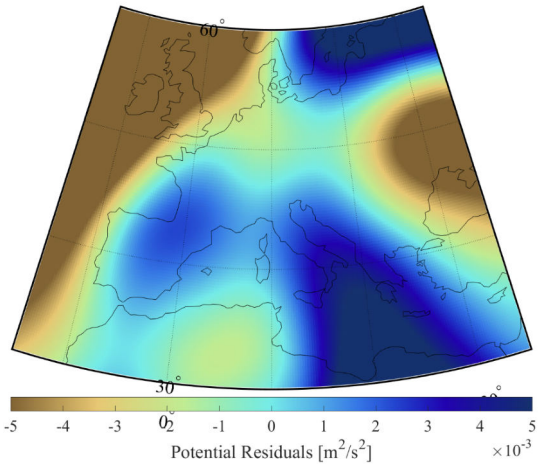

(d) Potential residual (Case A)

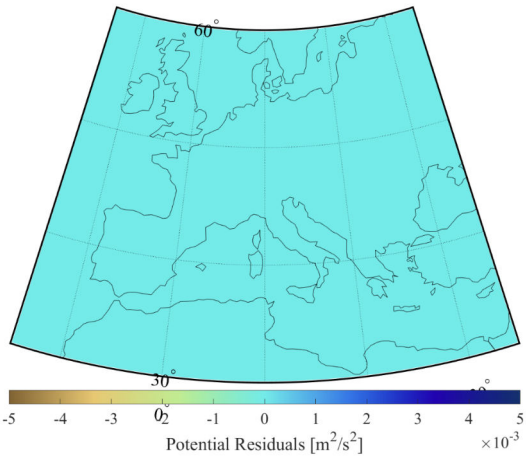

(e) Potential residual (Case B)

Figure 5.9: Comparison of Case A and Case B for potential synthesis, potential residual, and TWS fields (January 2020, DDK5).

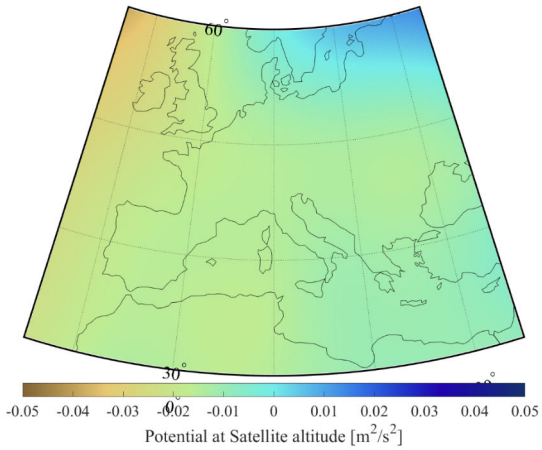

(a) Potential synthesis (DDK5, Spring 2020)

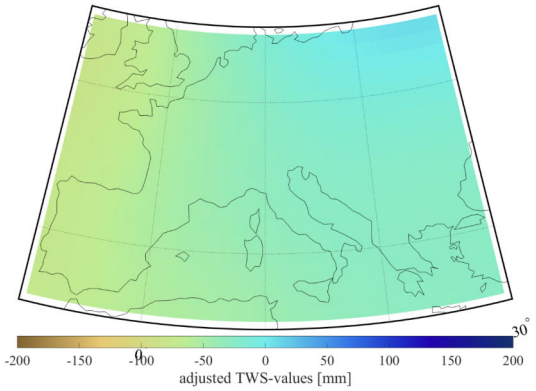

(b) TWS (Case A)

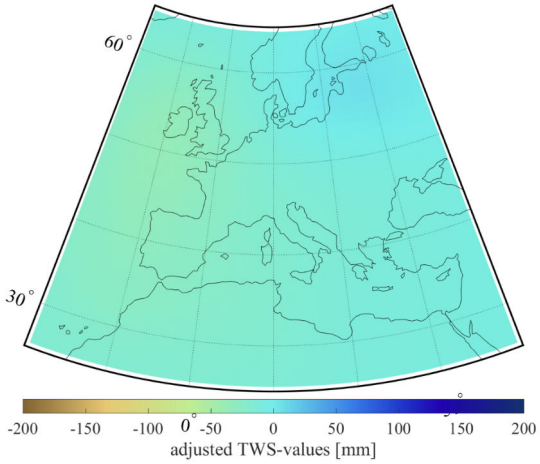

(c) TWS (Case B)

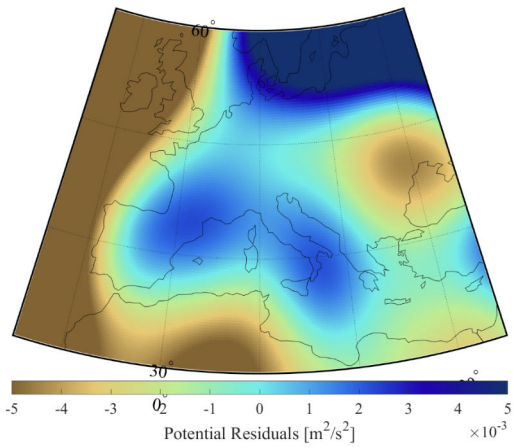

(d) Potential residual (Case A)

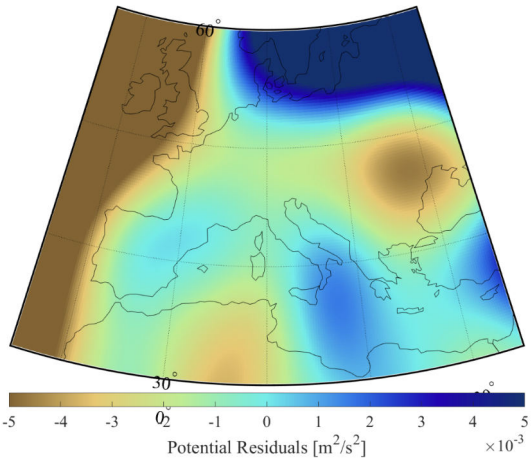

(e) Potential residual (Case B)

Figure 5.10: Comparison of Case A and Case B for potential synthesis, potential residual, and TWS fields (May 2020, DDK5).

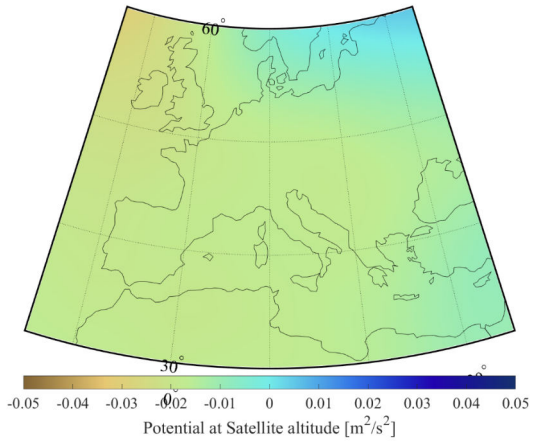

(a) Potential synthesis (DDK5, Summer 2020)

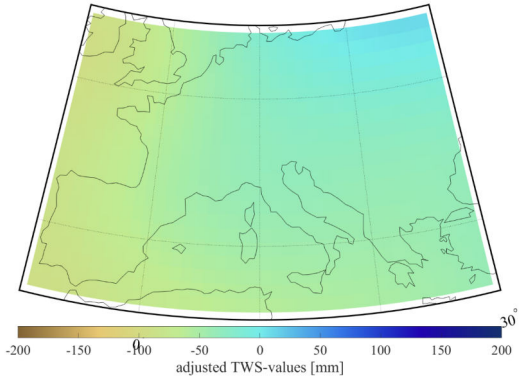

(b) TWS (Case A)

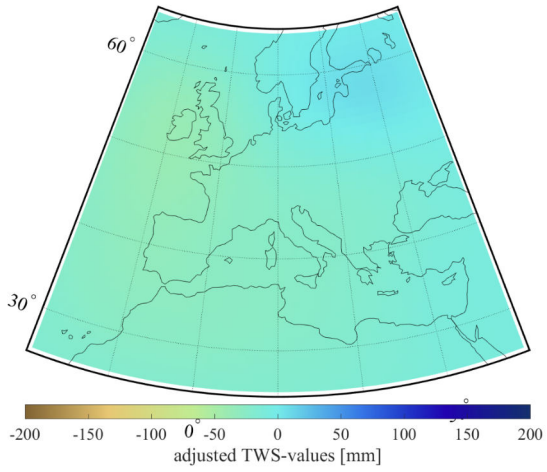

(c) TWS (Case B)

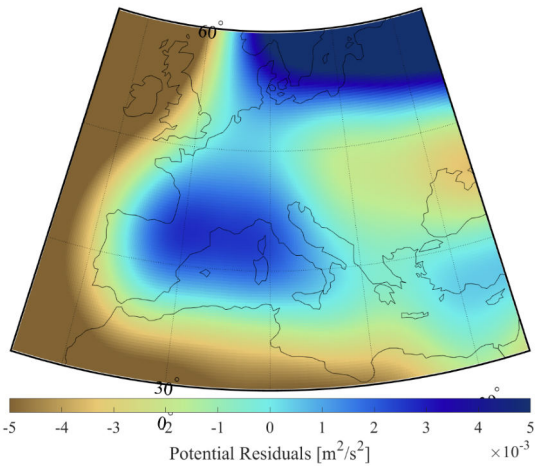

(d) Potential residual (Case A)

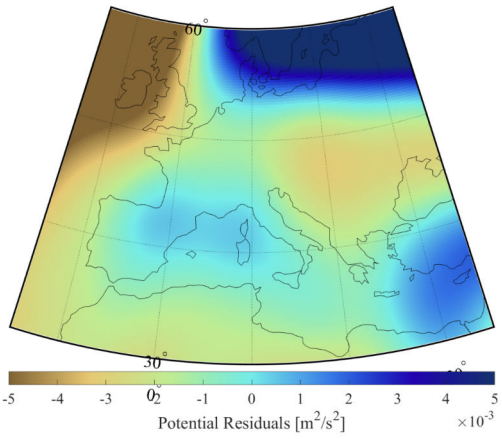

(e) Potential residual (Case B)

Figure 5.11: Comparison of Case A and Case B for potential synthesis, potential residual, and TWS fields (June 2020, DDK5).

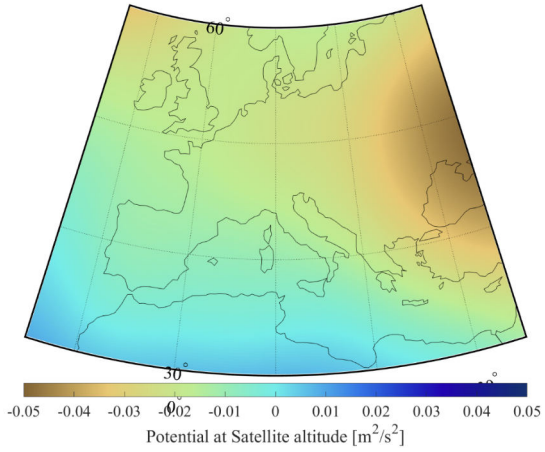

(a) Potential synthesis (DDK5, Autumn 2020)

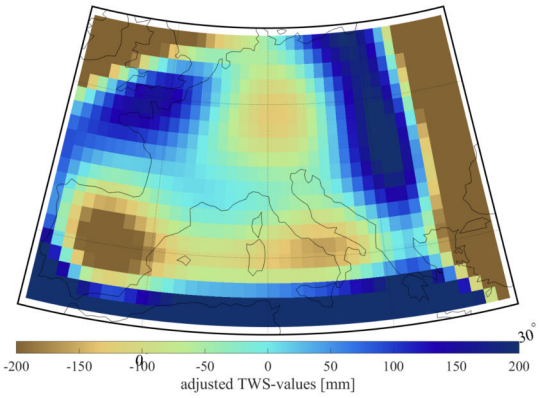

(b) TWS (Case A)

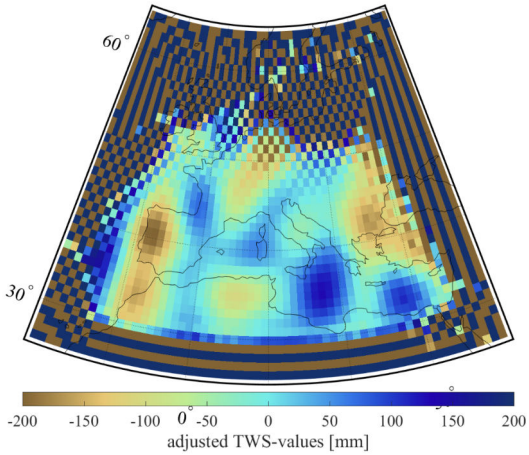

(c) TWS (Case B)

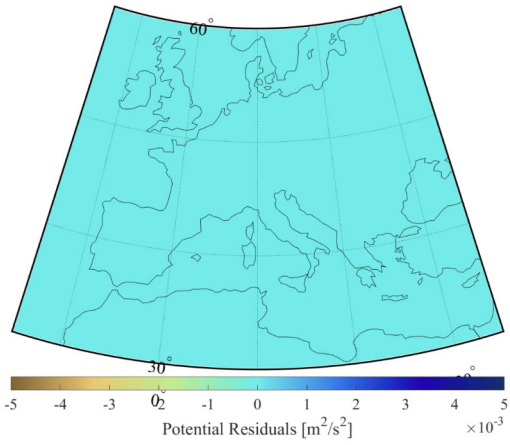

(d) Potential residual (Case A)

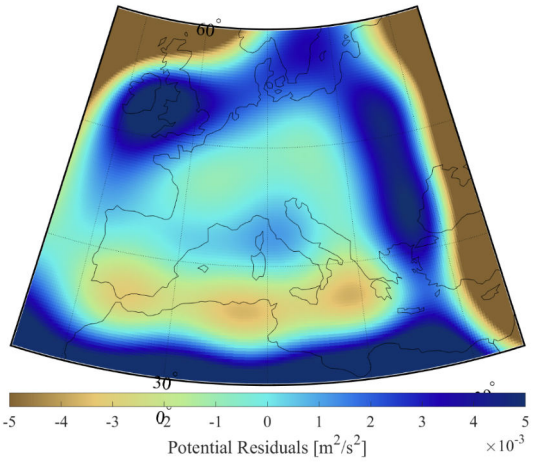

(e) Potential residual (Case B)

Figure 5.12: Comparison of Case A and Case B for potential synthesis, potential residual, and TWS fields (October 2020, DDK5).

6 Conclusion and Outlook

This study investigated the influence of decorrelation filtering using DDK kernels on GRACE- and GRACE-FO–derived terrestrial water storage (TWS) estimates over Europe, with particular emphasis on the interaction between filter strength, spatial domain configuration, and inversion stability. By combining spherical harmonic synthesis, variance and error propagation analysis, tesseroid-based forward gravitational modelling, and regularized inverse adjustment, a consistent framework was established to trace how processing choices in the spectral domain propagate to physically interpretable TWS fields.

The spectral analysis of spherical harmonic coefficients showed that DDK filtering significantly alters the degree variance behaviour by suppressing correlated high-degree noise inherent to GRACE monthly gravity field solutions. Weak filtering (DDK8) preserved small-scale variability but retained pronounced north-south striping artefacts, while strong filtering (DDK1) effectively reduced noise at the cost of substantial attenuation of seasonal amplitudes and spatial contrasts. Among the tested filters, DDK5 provided the most balanced performance, yielding stabilized empirical degree variances at medium and higher degrees while preserving the dominant long-wavelength hydrological signal.

The tesseroid-based inversion demonstrated that the spatial configuration of the model domain plays a decisive role in the quality of the recovered TWS fields. When tesseroids were confined to the study area (Case A), the resulting TWS estimates were smooth and stable but showed boundary-related artefacts within the region of interest. Extending the tesseroid domain beyond the target area (Case B) shifted these edge effects outside the study region, leading to more responsive and physically meaningful TWS patterns despite an overall increase in noise sensitivity. When combined with appropriate regularization, this configuration provided a clearer representation of temporal water storage variability.

The L-curve analysis confirmed the ill-posed nature of the inverse problem and highlighted the necessity of regularization for stable mass inversion. Well-defined L-shaped curves with stable corner locations were obtained for tesseroids within the study area, whereas tesseroids outside the region of interest exhibited increased variability in corner positions. Furthermore, the temporal analysis revealed that the optimal regularization parameter varies between epochs, reflecting changes in the signal-to-noise characteristics of the GRACE solutions. This finding underscores that a single fixed regularization parameter is not sufficient for long GRACE time series and that epoch-dependent parameter selection is required.

Overall, the results indicate that the combination of DDK5 filtering with an extended tesseroid domain (Case B) provides the most robust compromise between noise suppression and signal preservation for regional-scale TWS estimation over Europe. These findings are fully consistent with established GRACE processing strategies and emphasize that reliable hydrological interpretation from satellite gravimetry requires a joint consideration of decorrelation filtering, inversion regularization, and spatial model design.

From an outlook perspective, future studies could further improve the reliability of GRACE-based TWS estimates by integrating complementary datasets such as land surface models, groundwater observations, or other satellite missions. Methodological extensions, including spatially adaptive or higher order regularization schemes and layered or variable-density tesseroid models, may enhance sensitivity to heterogeneous hydrological processes. In addition, advances in future satellite gravity field missions with improved ranging accuracy and reduced correlated errors are expected to further strengthen the capability for long-term monitoring of continental water storage under changing climatic conditions.

Acknowledgement

The author wishes to express sincere gratitude to Prof. Dr.-Ing. Hansjörg Kutterer for defining the Lab Rotation topic and providing the scientific framework that motivated this study. Special thanks are extended to Dr.-Ing. Kurt Seitz for his continuous supervision, valuable discussions, and constructive guidance throughout the course of the work.

The author gratefully acknowledges the support and resources provided by the Geodätisches Institut (GIK), Karlsruhe Institute of Technology (KIT), which enabled the successful completion of this study. The GRACE and GRACE-FO Level-2 gravity field data were obtained from the International Centre for Global Earth Models (ICGEM), operated by the GFZ German Research Centre for Geosciences, whose efforts in data provision are sincerely appreciated.

Finally, the author acknowledges the broader GRACE science community for the development of the theoretical foundations and processing methodologies that form the basis of modern satellite gravimetry and terrestrial water storage research.

References

Antoni, M. (2022): A review of different mascon approaches for regional gravity field modelling since 1968. *History of Geo- and Space Sciences* 13(2):205–217. DOI: 10.5194/hgss-13-205-2022. URL: https://hgss.copernicus.org/articles/13/205/2022/.

Baur, O. and Sneeuw, N. (2011): Assessing Greenland Ice Mass Loss by Means of Point-Mass Modeling: A Viable Methodology. *Journal of Geodesy* 85:607–615. DOI: 10.1007/s00190-011-0463-1.

Baur, O., Kuhn, M., and Featherstone, W. E. (2012): Continental mass change from GRACE over 2002–2011 and its impact on sea level. *Journal of Geodesy* 87:117–125. DOI: 10.1007/s00190-012-0583-2.

Colombo, O. L. (1981): Numerical Methods for Harmonic Analysis on the Sphere. Tech. rep. Report No. 310. Columbus, Ohio, USA: Department of Geodetic Science, The Ohio State University.

Ditmar, P., Kusche, J., and Klees, R. (2003): Computation of spherical harmonic coefficients from gravity gradiometry data to be acquired by the GOCE satellite: Regularization issues. *Journal of Geodesy* 77(7–8):465–477. DOI: 10.1007/s00190-003-0349-y.

GFZ (2026): GRACE-FO – Gravity Recovery and Climate Experiment Follow-On Mission. German Research Centre for Geosciences (GFZ). Accessed: 2026-04-06. URL: https://www.gfz.de/en/section/global-geomonitoring-and-gravity-field/projects/grace-fo-gravity-recovery-and-climate-experiment-follow-on-mission.

Grombein, T., Seitz, K., and Heck, B. (2013): Optimized formulas for the gravitational field of a tesseroid. *Journal of Geodesy* 87(7):645–660. DOI: 10.1007/s00190-013-0636-1.

Hansen, P. C. (2000): The L-curve and its use in the numerical treatment of inverse problems. In: *Computational Inverse Problems in Electrocardiology*. Ed. by P. Johnston. WIT Press, pp. 119–142.

Heck, B. and Seitz, K. (2007): A comparison of the tesseroid, prism and point-mass approaches for mass reductions in gravity field modelling. *Journal of Geodesy* 81(2):121–136. DOI: 10.1007/s00190-006-0094-0.

Heiskanen, W. A. and Moritz, H. (1967): Physical Geodesy. W. H. Freeman & Co., San Francisco, USA.

ICGEM (2026): International Centre for Global Earth Models (ICGEM): Gravity field and GRACE/GRACE-FO products hosted at the German Research Centre for Geosciences (GFZ). Accessed: 2026-04-06. URL: https://icgem.gfz-potsdam.de/.

Kusche, J. (2007): Approximate decorrelation and non-isotropic smoothing of time-variable GRACE-type gravity field models. *Journal of Geodesy* 81(11):733–749. DOI: 10.1007/s00190-007-0143-3.

Kusche, J., Schmidt, R., Petrovic, S., and Rietbroek, R. (2009): Decorrelated GRACE time-variable gravity solutions by GFZ, and their validation using a hydrological model. *Journal of Geodesy* 83:903–913. DOI: 10.1007/s00190-009-0308-3.

Metzler, B. and Pail, R. (2005): GOCE data processing: The spherical cap regularization approach. *Studia Geophysica et Geodaetica* 49(4):441–462. DOI: 10.1007/s11200-005-0021-5.

Scanlon, B. R., Zhang, Z., Save, H., Wiese, D. N., Landerer, F. W., Long, D., Chen, J., Wolock, D. M., Conway, B. D., and Winester, D. (2016): Global evaluation of new GRACE mascon products for hydrologic applications. *Water Resources Research* 52(12):9412–9429. DOI: 10.1002/2016WR019494.

Swenson, S. and Wahr, J. (2006): Post-processing removal of correlated errors in GRACE data. *Geophysical Research Letters* 33(8):L08402. DOI: 10.1029/2005GL025285.

Tapley, B. D., Bettadpur, S., Ries, J. C., Thompson, P. F., and Watkins, M. M. (2004): GRACE Measurements of Mass Variability in the Earth System. *Science* 305(5683):503–505. DOI: 10.1126/science.1099192.

Tsoulis, D. (1999): Spherical harmonic computations with topographic/isostatic coefficients. Tech. rep. IAPG/FESG No. 3. Munich, Germany: Institut für Astronomische und Physikalische Geodäsie, Technische Universität München.

Wahr, J., Molenaar, M., and Bryan, F. (1998): Time variability of the Earth's gravity field: Hydrological and oceanic effects and their possible detection using GRACE. *Journal of Geophysical Research: Solid Earth* 103(B12):30205–30229.

Spatial Comparison of GRACE-derived TWS and GLDAS During California Drought Periods

Adersh Kolappurath Remesan[1]

1 Remote Sensing and Geoinformatics Master of Science (M.Sc.), KIT, Germany
E-Mail: uwuxd@student.kit.edu

Abstract

This study investigates Terrestrial Water Storage (TWS) variations in California from 2010 to 2020 by comparing GRACE satellite observations with the GLDAS-Noah land surface model, focusing on the severe 2012-2016 drought. Results reveal strong spatio-temporal agreement between the datasets, with monthly TWS anomalies showing a correlation of $r = 0.91$ and RMSE of 2.4 cm EWH. Both approaches captured seasonal cycles and long-term depletion trends, identifying California's Central Valley as the epicenter of groundwater loss driven by agricultural demand. GLDAS enabled partitioning of hydrological components, isolating deep groundwater storage changes (ΔGWS) via a residual method, which confirmed persistent depletion during the drought. Despite GLDAS slightly overestimating seasonal amplitude and lacking explicit representation of deep groundwater and reservoir storage, its consistency with GRACE underscores its value for climate-driven near-surface water dynamics. Future research should enhance model physics, validate ΔGWS estimates with in-situ data, and integrate GRACE observations through data assimilation to reduce biases and improve predictive capability. The synergy between GLDAS and GRACE offers a robust framework for sustainable water resource management in drought-prone regions.

Keywords GRACE · GLDAS · California Drought · Total Water Storage (TWS)

1 Introduction

The Earth stores water in various reservoirs, both on the surface and underground. Surface water exists in rivers, lakes, and snow packs, while subsurface water is stored in aquifers. Together, these components constitute Terrestrial Water Storage (TWS). TWS plays a crucial role in the hydrological cycle, influencing precipitation, evaporation, and subsurface water movement. These combined processes affect weather patterns and can lead to extreme events such as droughts (Syed et al., 2008; Famiglietti, 2004). Such variations also influence biogeochemical cycles (Syed et al., 2008; Famiglietti, 2004). In regions like California, which depend heavily on water resources for agriculture and a growing population, it is essential to monitor variations in TWS. Understanding whether TWS is increasing or decreasing in a specific area enables water authorities to make timely decisions to store and allocate water in preparation for potential drought periods (Syed et al., 2008, paragraph 1), (Shukla and Mintz, 1982).
From early on, scientists understood that changes in water over large areas could be assessed through TWS, but they had no practical way to obtain complete observations. Precipitation data could be collected from rain gauges,

KIT Scientific Working Papers
Issue Number 270
ISSN: 2194-1629
DOI: 10.5445/IR/1000191188
Online: June 2026

This document is licensed under the Creative Commons Attribution – Share Alike 4.0 International License (CC BY-SA 4.0):
https://creativecommons.org/licenses/by-sa/4.0/deed.en

and river discharge could be measured using sensors, but changes in groundwater stored in aquifers were difficult to quantify (Lettenmaier and Famiglietti, 2006). This challenge was resolved in 2002 with the launch of the Gravity Recovery and Climate Experiment (GRACE) satellite, which is capable of detecting tiny temporal variations in Earth's gravity field. For example, groundwater loss due to pumping for irrigation reduces mass in a region, which in turn alters the gravity field over time, an effect that GRACE can detect. GRACE was later succeeded by the GRACE Follow-On mission, which continued these observations (Tapley et al., 2004).

Another widely used tool for estimating TWS is the Global Land Data Assimilation System (GLDAS), which relies on satellite and ground-based observations to understand water movement. The ground-based component is provided by land surface models such as Noah, VIC (Variable Infiltration Capacity), and CLSM (Catchment Land Surface Model). Together, these inputs produce high-resolution representations of water movement and storage (Rodell et al., 2004). A major advantage of GLDAS is that it provides detailed information on where water is stored—for example, in soil moisture (SM), snow water equivalent (SWE), and canopy water storage (CWS). This allows for a more detailed understanding of TWS partitioning within different layers compared to GRACE.

GLDAS, however, is a model-based system, and its results depend on the accuracy of the physical processes represented, the quality of the input data, and how well the model parameters are defined. Crucially, while GLDAS provides components like soil moisture and snow water, most current Land Surface Models do not accurately simulate the deep groundwater dynamics or large reservoir storage changes that occur deep below the surface layer, a limitation that is central to this comparative study.

The main objective of this work is to study and compare two approaches for estimating TWS in California: GRACE-derived TWS and GLDAS-based TWS, over the period from 2010 to 2020. The primary focus is on the years 2012 to 2016 and the subsequent recovery period, as this interval corresponds to a severe drought in California.

By creating spatial maps and regional time series, the changes in TWS during the drought period can be clearly examined using both approaches. This study evaluates which method provides more reliable information about the well-documented California drought whether the satellite-based GRACE observations or the model-based, land-surface-driven GLDAS estimates and exploits the difference between them to quantify the depletion of unmodeled deep groundwater.

2 Theoretical Aspects

To understand how California's water storage changes over time, particularly during drought cycles, hydrologists rely on sophisticated satellite observations and hydrological modeling. This dual approach is necessitated by the specific capabilities and inherent limitations of each system.
The core satellite data relies on the Gravity Recovery and Climate Experiment (GRACE), which detects minute changes in the Earth's gravitational field corresponding to shifts in water mass across the landscape. GRACE measures the total amount of water storage, known as Terrestrial Water Storage (TWS), which represents the vertically integrated mass of water in all forms – including soil moisture, snow, surface water, and groundwater. However, here GRACE MASCON solutions are used alone cannot differentiate between these individual storage components.
This gap is filled by the Global Land Data Assimilation System (GLDAS). GLDAS utilizes advanced hydrological models to estimate and partition TWS into its constituent layers. By combining the spatially integrated measurements from GRACE with the partitioned estimates from GLDAS, scientists can achieve a much clearer and component-specific understanding of California's complex hydrological system and how its various water reservoirs respond to drought conditions.

2.1 What is GRACE MASCON Solutions?

Mascon solutions (Mass Concentration Blocks) are a specialized processing technique for GRACE data for the determination of TWS. Unlike traditional spherical harmonic solutions, which can smear signals over large areas, Mascons partition the Earth's surface into tiles (or mascons). The specific product used in this study is the Center for Space Research (CSR) Mascon solution. This approach is particularly effective in regional hydrology studies, like this one for California, because it significantly reduces signal leakage (where mass changes in one basin contaminate the signal of an adjacent area), providing a more spatially localized and robust estimate of TWS changes.

2.2 What is GLDAS?

GLDAS was developed by NASA as part of an effort to better understand Earth's land surface. It acts like a system that pieces together clues from satellites and ground sensors to describe conditions such as snow, soil moisture, and evapotranspiration with much greater detail and accuracy.
To produce this detailed information, GLDAS gathers data from space-borne instruments and ground-based measurements. All of these observations are subsequently assimilated into land surface models (LSMs). These models blend real observations with their own predictions through a process called data assimilation. This process ensures that the final outputs closely match actual conditions on the ground. It also helps GLDAS avoid errors that could arise from relying only on atmospheric data or on land-surface physics alone.
In this work, GLDAS plays a crucial role. The GRACE satellite measures TWS, but it provides only a combined, integrated signal. GLDAS helps separate this combined signal into individual components – such as snow, river water, soil moisture, and groundwater. This decomposition is essential for understanding which specific layers are affected and how they respond to drought conditions in California (see Śliwińska et al. (2019, p. 4) and Syed et al. (2008, p. 3)).

2.3 GLDAS Framework and Components

GLDAS does not rely on a single land surface model (LSM). Instead, it uses several LSMs in an ensemble approach. Each model provides its own interpretation of how water moves across the landscape. By comparing and combining the outputs from these different models, researchers gain a more complete and reliable understanding of land-surface hydrology.

In this study, the focus is on one such model: the GLDAS-NOAH land surface model. NOAH is particularly effective at simulating how water moves vertically—from the layers near plant roots down into the deeper unsaturated zones beneath the soil. Through these simulations, GLDAS can generate key hydrological variables that describe how water storage changes over time. These variables are directly linked to shifts in terrestrial water storage and form the foundation for interpreting California's water dynamics.

Table 2.1: The relevant GLDAS outputs, adapted from Syed et al. (2008).

Parameter	Description
Total Soil Moisture (TSM)	Water stored in all modeled soil layers (e.g., 0–200 cm depth).
Snow Water Equivalent (SWE)	The equivalent depth of water if the snowpack were to melt.
Canopy Water Storage (CWS)	Water held on the surface of vegetation after precipitation.
Precipitation (P)	Includes both liquid and solid forms (rain and snow).
Evapotranspiration (E)	Combined water loss from evaporation and plant transpiration.
Runoff (R)	Includes both surface and subsurface water flow.

2.4 Methodology for Calculating TWS and its Changes from GLDAS

To ensure that the results obtained from the GLDAS model can be directly compared with the combined signal from the GRACE satellite, a model-based TWS is calculated ($\mathrm{TWS_{GLDAS}}$). This is done by adding together all the water storage components simulated by GLDAS, except groundwater.
In fact, LSMs such as GLDAS-NOAH follow a standard approach for calculating TWS: it is computed as the sum of the primary storage reservoirs (Syed et al., 2008):

$$\mathrm{TWS_{GLDAS}} = \mathrm{TSM} + \mathrm{SWE} + \mathrm{CWS} \tag{2.1}$$

It is crucial to note that while the direct computation of $\mathrm{TWS_{GLDAS}}$ results in absolute storage values (Equation. (2.1)), this study follows a standard approach to enable a scientifically meaningful comparison with the satellite-derived GRACE data, which inherently provides TWS anomalies. Therefore, the calculated $\mathrm{TWS_{GLDAS}}$ time series is converted into Total Water Storage Anomalies ($\mathrm{TWS^{Anomaly}_{GLDAS}}$) by subtracting the long-term mean of the entire study period. This ensures that both the model and the observation datasets represent variations relative to a common time window, isolating the temporal mass changes caused by seasonal and inter-annual fluctuations.
The project's focus on Terrestrial Water Storage Change (TWSC), denoted as $\Delta\mathrm{TWS_{GLDAS}}$, is then calculated as the difference between these consecutive monthly anomalies, which is equivalent to the difference in TWS between two consecutive time steps (e.g. monthly) (Syed et al., 2008) :

$$\Delta\mathrm{TWS}_{t,\mathrm{GLDAS}} = (\mathrm{TSM}_t + \mathrm{SWE}_t + \mathrm{CWS}_t) - (\mathrm{TSM}_{t-1} + \mathrm{SWE}_{t-1} + \mathrm{CWS}_{t-1})\,. \tag{2.2}$$

The inclusion of Canopy Water Storage (CWS), though typically minor compared to soil moisture (TSM) and snow water equivalent (SWE), ensures that the model's total TWS accounts for all simulated near-surface components before they are subtracted in the residual method for groundwater estimation (Section 2.5). In Equation 2.2 the reference epoch $t-1$ can also refer to the over all mean solution.

2.5 Deriving Groundwater Storage (GWS) Changes

A primary goal of combining GRACE and GLDAS data is to estimate Groundwater Storage Change (ΔGWS), a critical component that neither system measures directly. This estimation relies on the fundamental terrestrial water balance equation:

The GRACE satellites measure the total TWS change (ΔTWS_{GRACE}), which includes every major stored water component: surface water (ΔSWS), soil moisture (ΔTSM), snow (ΔSWE), canopy water (ΔCWS), and groundwater (ΔGWS).
The following Equation (2.3) is called the Terrestrial Water Balance Equation:

$$\Delta TWS_{GRACE} = \Delta GWS + \Delta TSM + \Delta SWE + \Delta CWS + \Delta SWS \tag{2.3}$$

where ΔSWS is the change in surface water storage (rivers, lakes, reservoirs), a component typically not modeled by GLDAS LSMs (Śliwińska et al., 2019, p. 8).
To isolate groundwater changes, scientists employ the residual method. Since GLDAS does not model deep groundwater or large surface reservoirs (ΔSWS), the assumption is made that ΔSWS is either negligible or, more commonly, is grouped within the unmodeled residual term, which is subsequently interpreted as the Groundwater Storage Change (ΔGWS). Therefore, the GLDAS-derived near-surface components are subtracted from the total GRACE signal:
The Calculation of Groundwater Storage Change from (Singh et al., 2017, p. 196) is given in Equation (2.4).

$$\Delta GWS = \Delta TWS_{GRACE} - (\Delta TSM_{GLDAS} + \Delta SWE_{GLDAS} + \Delta CWS_{GLDAS}). \tag{2.4}$$

This formula effectively quantifies groundwater depletion or recharge by leveraging GRACE's total mass change observation and using GLDAS to partition and remove the shallow, near-surface components ($\Delta TSM, \Delta SWE, \Delta CWS$). Importantly, the resulting ΔGWS estimate encompasses changes in deep groundwater, surface water reservoirs (omitted by GLDAS), and any potential model errors.

2.6 Strengths, Limitations, and Visualization

Understanding the comparative strengths and structural limitations of GLDAS and GRACE is necessary for interpreting the results accurately. GLDAS offers a much higher spatial resolution (0.25° to 1°) than GRACE ($\sim 3°$) and allows Total Water Storage (TWS) to be partitioned into key hydrological components (TSM, SWE, CWS). However, GLDAS models are structurally limited; they do not simulate deep groundwater storage or surface water in major reservoirs, and their soil moisture estimates are generally confined to the upper 2–3 meters of the soil column (Syed et al., 2008, p. 3). This limitation, coupled with model bias, impacts the derived groundwater storage (ΔGWS) signal (Śliwińska et al., 2019, p. 22).
Key analysis is facilitated by the visualization of side-by-side maps of ΔTWS and ΔGWS anomalies to contrast the magnitude and spatial extent of water deficits (Syed et al., 2008, p. 7).
A detailed discussion of the discrepancies, structural limitations, and implications of model bias on the residual ΔGWS calculation is presented in Section 5.5.

3 Data

This study relies on data from three distinct sources to analyze and compare terrestrial water storage (TWS) dynamics in California: the Global Land Data Assimilation System (GLDAS) hydrological model outputs, satellite-derived TWS from the GRACE mission (specifically the mascon solution is used), and ground-truth precipitation measurements from the California Irrigation Management Information System (CIMIS). These datasets cover the period relevant to the task, primarily focusing on the 2010-2020 time-window, which encompasses the severe 2012-2016 drought and subsequent recovery periods (Xiao et al., 2017).

3.1 Global Land Data Assimilation System (GLDAS) Data

GLDAS is an advanced land surface modeling framework developed by NASA's Goddard Space Flight Center, designed to generate high-resolution estimates of water and energy fluxes across the Earth's land surface (Rodell et al., 2004). It achieves this by integrating satellite observations and ground-based measurements into a suite of Land Surface Models (LSMs) (Syed et al., 2008, page 3, paragraph 11).
For this analysis, outputs from the **GLDAS-Noah Land Surface Model (LSM)** were utilized. The Noah LSM was selected for its reliability and frequent use in hydrological studies, making it an ideal choice for examining terrestrial water dynamics (Śliwińska et al., 2019, p. 4).
The main parameters of GLDAS are:

- **Data Product:** GLDAS Noah Land Surface Model L4, Version 2.1.
- **Spatial Resolution:** Monthly outputs mapped on a $0.25^\circ \times 0.25^\circ$ spatial grid. This high spatial resolution was chosen to maximize detail and better capture the hydrological variability across the geographically complex and diverse California study region.
- **Temporal Coverage:** Monthly data from 2010 to 2020.
- **Key Variables:** The analysis extracted the primary storage variables needed to calculate TWS, consistent with the model's structural design (Syed et al., 2008, p. 3, Table 1):
  1. Total Soil Moisture (TSM or SM): Water content across all modeled soil layers (typically 0–200 cm depth).
  2. Snow Water Equivalent (SWE): Total amount of water stored in the snowpack.
  3. Canopy Water Storage (CWS): Water intercepted by vegetation.

3.2 GRACE (CSR Mascon) Data

The satellite observations used to represent total water storage changes are derived from the Gravity Recovery and Climate Experiment (GRACE and GRACE-FO) missions.
The main parameters of GRACE are:

- **Data Product:** Monthly Terrestrial Water Storage (TWS) grids provided by the Center for Space Research (**CSR Mascon product**), Release 06 (ICGEM, 2026).
- **Spatial Resolution:** Mascon solutions typically offer an effective resolution of approximately 3° (about 330 km at the Earth's equator, because it is based on spherical harmonics up to degree and order $N_{\max} = 96$, (Watkins et al., 2015)). The data is provided ready-to-use in grid format.
- **Temporal Coverage:** Monthly TWS grids covering the period 2010-2020.
- **TWS Anomaly:** The GRACE data represents TWS anomalies, calculated as deviations from a long-term mean relative solution.

The use of CSR Mascon products is crucial as they minimize signal leakage errors (where mass changes in one basin contaminate an adjacent area) compared to traditional spherical harmonic solutions, providing a more robust measure of regional TWS for the California region (Scanlon et al., 2016).

3.3 California Irrigation Management Information System (CIMIS) Data

To validate the atmospheric forcing data used in the GLDAS-Noah model (specifically precipitation), ground-truth data from the **California Irrigation Management Information System (CIMIS)** network were utilized. CIMIS is a comprehensive network of automated weather stations providing accurate, near-real-time meteorological data critical for water management in California.

- **Data Product:** Measured monthly precipitation data (P).
- **Role in Study:** These data serve as the "Ground Truth" for assessing the reliability of the precipitation input driving the GLDAS model simulations.

Validation results (Figures 5.1 and 5.2) compare GLDAS model precipitation against measurements from three strategically selected CIMIS stations within the Central Valley and its vicinity: Five Points, Davis, and UC Riverside. The location of these stations is illustrated in Figure 3.1.

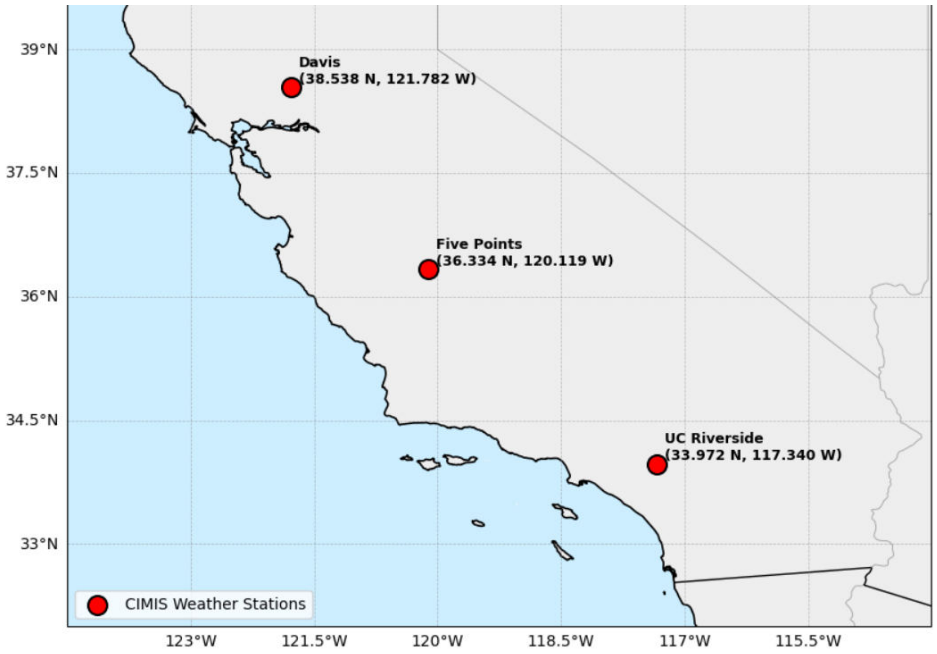

Figure 3.1: Location of the selected CIMIS weather stations (Five Points, Davis, and UC Riverside) used for validating GLDAS precipitation against the California Central Valley boundary.

The selection rationale ensures geographic diversity across the high-demand regions of California:

1. **Five Points:** Located in the arid, high-demand Southern San Joaquin Valley (Tulare Basin), which is the primary region for intense groundwater depletion and drought monitoring (Xiao et al., 2017).
2. **Davis Station:** Represents the Northern Central Valley (Sacramento Basin), a region characterized by higher precipitation and major river systems.
3. **UC Riverside:** Represents the semi-arid, transitional zone at the southern edge of the core study area.

This distribution provides critical spatial context for verifying the accuracy of the model's precipitation forcing across the climatically diverse parts of the study region.

4 Methodology Overview

In this part of the study, the steps taken to process, analyze and compare Terrestrial Water Storage (TWS) estimates from two powerful data sources – the Global Land Data Assimilation System (GLDAS) and the NASA GRACE

mission. The focus was on the state of California, a region known for its dramatic swings between wet and dry conditions.
The main goal was to quantify and visualize how water storage changed over time, especially during the severe 2012–2016 drought and the recovery period that followed. By integrating information from satellite observations and model simulations, this study aimed to provide a more comprehensive understanding of the response of California's water resources to these extreme climatic events.

4.1 GLDAS Data Processing and TWS Calculation

The first step of the analysis began with constructing a Terrestrial Water Storage (TWS) estimate from GLDAS that could be meaningfully compared to the integrated mass signal measured by the GRACE mission.
To achieve this, the study focused on the Noah Land Surface Model (LSM) within GLDAS, which provides detailed information on different components of land water storage. This study carefully extracted the primary storage component data needed to represent total water storage on land.
For this study, monthly average storage variables from 2010 to 2020 are compiled, ensuring a full decade of consistent data for the analysis. The key variables selected for calculating Terrestrial Water Storage (TWS_{GLDAS}) – Total Soil Moisture (TSM), Snow Water Equivalent (SWE), and Canopy Water Storage (CWS) – are detailed in Section 2.3 (Table 2.1) according to the presentation in Syed et al. (2008, p. 3).

4.1.1 Spatial Subsetting and Coordinate Alignment

The raw GLDAS Noah L4 data, typically available on a $0.25^\circ \times 0.25^\circ$ grid, was first spatially subsetted to focus exclusively on the geographic extent of California. This process involved extracting the relevant grid cells spanning the region (approximately 32° N to 42° N and -125° W to -114° W). A crucial technical step involved validating and aligning the coordinate arrays within the NetCDF data to match the specific dimensions of the extracted subset (e.g., 44×40 grid cells). This ensured that TWS calculations were performed accurately within the precise geographical boundaries of the study area. The grid is at center of cell.

4.1.2 Calculation of GLDAS Total Water Storage (TWS)

Each month, data from the GLDAS model is carefully analyzed to understand how water is stored across the land. The process begins by collecting information on all the individual storage components. These separate components are then added together to find the total Terrestrial Water Storage (TWS). By combining them, a vertically integrated TWS value is created for every $0.25^\circ \times 0.25^\circ$ grid cell across the California region.
This calculation follows the definition for model TWS composition (Equation (2.1) in Section 2.4) expressing the total TWS as the sum of all its storage components:

$$TWS_{\mathrm{GLDAS}} = TSM + SWE + CWS. \tag{4.1}$$

This standard composition of model TWS is described by Syed et al. (2008, p. 3) and Śliwińska et al. (2019, p. 8). Although Canopy Water Storage (CWS) is included for completeness, its contribution to overall TWS variability is statistically negligible compared to Soil Moisture (TSM) and Snow Water Equivalent (SWE) (Śliwińska et al., 2019, p. 8).

4.1.3 TWS Anomaly Calculation (Baseline Removal)

To ensure direct comparability with the GRACE data product, which inherently provides mass anomalies relative to a long-term mean, the calculated TWS_{GLDAS} must also be converted into TWS Anomalies (ΔTWS_{GLDAS}). This is achieved by calculating the long-term monthly mean for the entire 2010–2020 study period and subtracting it from the raw TWS_{GLDAS} time series for each grid cell. This step removes the static, long-term average water content,

isolating only the temporal variations (anomalies) caused by seasonal cycles and inter-annual drought/recharge trends (Syed et al., 2008).

4.2 Calculation of Terrestrial Water Storage Change (TWSC)

To understand how water storage changes over time, the monthly Terrestrial Water Storage Change (TWSC) is calculated. The process begins with the TWS anomalies, which are obtained by removing the long-term mean from the TWS time series. These anomalies reveal how each month's water storage differs from the average conditions.
The TWSC for a given month is found by taking the difference in TWS **Anomaly** between two consecutive months, following the definition for TWSC change (Equation (2.2) in Section 2.4):

$$TWSC_{\mathrm{GLDAS},N} = TWS^{\mathrm{Anomaly}}_{\mathrm{GLDAS},N} - TWS^{\mathrm{Anomaly}}_{\mathrm{GLDAS},N-1}\,. \tag{4.2}$$

This simple subtraction shows how much the total water storage has increased or decreased from one month to the next, allowing to track the dynamics of water movement across the land. This method for computing monthly changes by differencing TWS anomalies is demonstrated by Syed et al. (2008, p. 3).

4.3 Deriving Groundwater Storage (GWS) Changes

The change in groundwater storage (ΔGWS) was derived using the residual method (Eq. (2.4) in Section 2.5) by subtracting the GLDAS near-surface components (ΔTSM, ΔSWE, ΔCWS) from the total GRACE signal ($\Delta\mathrm{TWS}_{\mathrm{GRACE}}$). This approach allows for the estimation of groundwater depletion and recharge, which is particularly relevant for assessing the severity and recovery of drought in California.

4.4 Spatial and Temporal Analysis Techniques

To compare the GRACE and GLDAS solutions they have to be given in the same resolution in the time domain as well in the frequency domain. The resolution in the time domain is one month. The resolution of the grid is $15' \times 15'$. The resolution of the signal in frequency domain is below $N_{\max} = 96$.

4.4.1 Spatial Mapping and GRACE/GLDAS Alignment

To clearly see how drought and recovery unfolded across the land, spatial mapping is used. Gridded maps of Terrestrial Water Storage (TWS) and Terrestrial Water Storage Change (TWSC) are created from both GRACE and GLDAS datasets for the California region.
A critical methodological step for spatial comparison is ensuring that the GLDAS data (native $0.25^\circ \times 0.25^\circ$) is aligned with the coarser GRACE Mascon grid (approx. 3°). This is achieved by spatially averaging or aggregating the GLDAS grid cells onto the corresponding GRACE grid structure. This step minimizes potential errors arising from comparing datasets at vastly different spatial resolutions and ensures that the regional TWS estimates are derived from comparable spatial footprints (Scanlon et al., 2016).
These maps illustrate the TWS anomalies, measured in centimeters of equivalent water height, for key time periods—such as the peak of the drought (2014–2015) and the wet recovery period (2017). By placing the satellite observations and the hydrological model results side by side, the maps make it possible to visually compare the spatial extent and magnitude of water storage deficits, revealing where and how the landscape was most affected and how it later recovered.The source for this approach of representing the results is from Syed et al. (2008, p. 7) and Singh et al. (2017, pp.193-195)

4.4.2 Time Series Analysis

To understand how water storage has changed over time, a regional time series will be created for California. Crucially, the $0.25^\circ \times 0.25^\circ$ GLDAS data is first aggregated onto the coarser GRACE Mascon grid structure, following the procedure described in Section 4.4.1. The regional time series is then created by taking the spatial average of the aligned GLDAS TWS grid cells located within the state's geographical boundaries for each month between 2010 and 2020. The GRACE data, provided as CSR Mascon products, is inherently optimized for regional analysis and is treated as the regional signal for direct comparison.
The result is a single, continuous record showing how Terrestrial Water Storage (TWS) evolved month by month over the decade. This GLDAS-derived time series will then be plotted together with the GRACE-derived time series for the same region. By comparing the two, differences and similarities in phase, amplitude, and long-term trends can be analyzed, offering valuable insights into how well the model and satellite data capture California's changing water storage. The source for this approach of representing the results is from Syed et al. (2008, p. 8).

4.4.3 Quantitative Comparison

To evaluate how closely the GRACE and GLDAS datasets match, several statistical metrics are calculated from the regional time series. These measures help to quantify both their agreement and their differences (Śliwińska et al., 2019, pp. 9, 16).
The first metric is the Correlation Coefficient (r), which is used to examine the phase agreement and the linear relationship between the two time series. A higher correlation indicates that GRACE and GLDAS capture similar patterns of water storage change over time.
The second metric is the Root-Mean-Square Error (RMSE), which measures the absolute magnitude of the differences between the two datasets. This helps identify how much the model results deviate from the satellite observations in terms of overall values.
Together, these statistics provide a clear picture of how well the two systems align in representing water storage variations across California.

5 Results and Discussion

This section focuses on understanding how well the GLDAS-Noah model outputs align with the GRACE-derived Terrestrial Water Storage (TWS) for California over the period 2010 to 2020. The analysis is carefully organized to explore several key aspects: first, verifying the reliability of the GLDAS model forcing data; second, examining the temporal and spatial agreement between the two TWS datasets; and finally, highlighting the insights gained from estimating groundwater storage (GWS) changes.

5.1 GLDAS Forcing Data Validation (CIMIS)

To ensure the reliability of the GLDAS-Noah outputs, particularly the hydrological simulation's forcing data, the modeled precipitation (P) was compared against ground-truth measurements from three strategically selected California Irrigation Management Information System (CIMIS) stations. Their distributions are shown in Figure 3.1.
The core validation relies on a direct comparison between the monthly GLDAS precipitation estimates and the CIMIS in-situ data. Figure 5.1 shows the time series comparisons, while Figure 5.2 provides quantitative scatter plots.

- At the Davis station (Northern Central Valley), the scatter plot confirms a very high correlation ($r = 0.913$) and a relatively small RMSE (40.5 mm), indicating high accuracy in capturing both the seasonal magnitude and phase of precipitation.

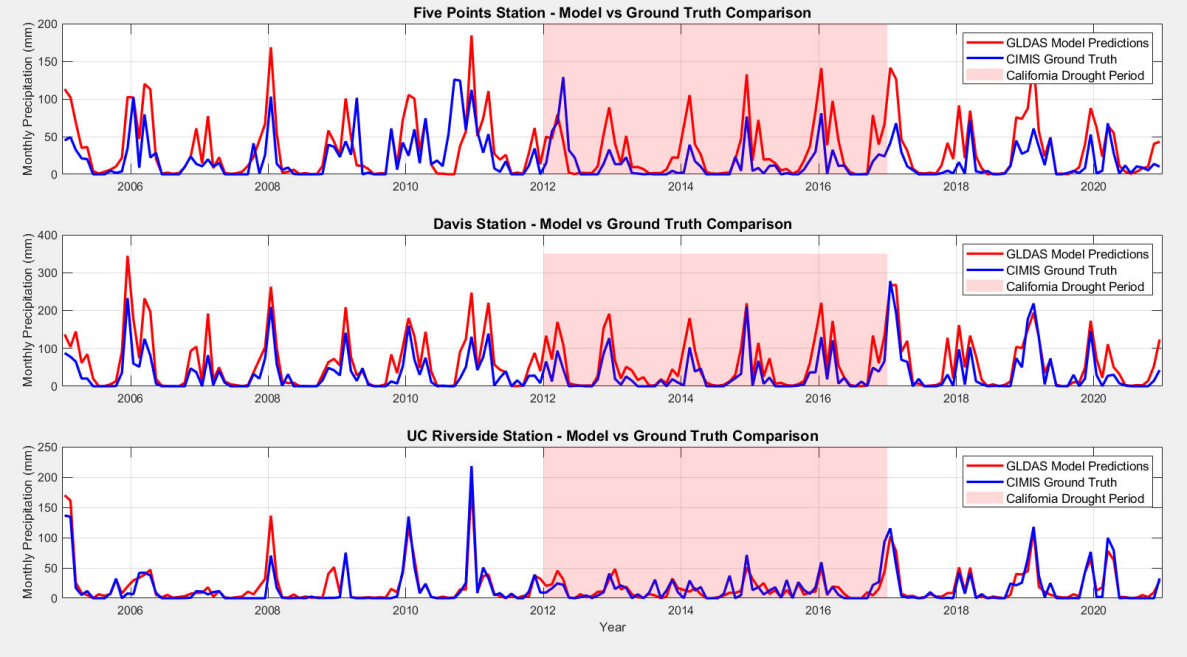

Figure 5.1: Comparison of Monthly Precipitation from GLDAS Model Predictions (Red) and CIMIS Ground Truth (Blue) for three selected stations across California (2005-2020). The shaded region indicates the 2012-2016 drought period.

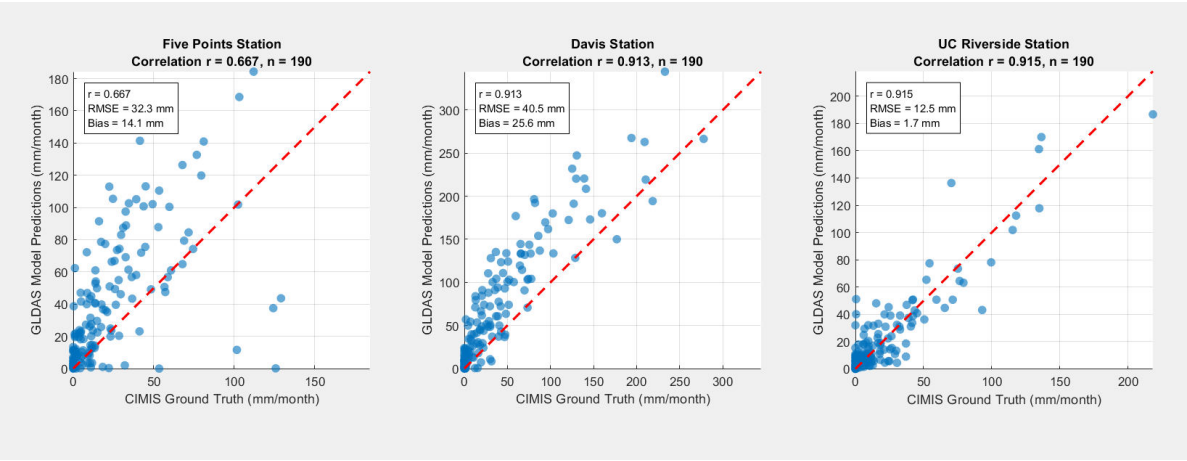

Figure 5.2: Quantitative Validation of GLDAS Precipitation against CIMIS Ground Truth (Monthly). Scatter plots show the correlation (r), Root-Mean-Square Error (RMSE), and Bias for each station.

- In the more arid regions, specifically Five Points (Southern San Joaquin Valley, $r = 0.667$) and UC Riverside ($r = 0.915$), the GLDAS product generally followed the observed precipitation trends. While the fit is strong, minor discrepancies were noted, especially in Five Points, occasionally underestimating or smoothing the magnitude of extreme storm events.

Overall, the high consistency confirms that the atmospheric forcing used to drive the GLDAS hydrological simulations across California is reliable, providing a sufficient basis to proceed with the Terrestrial Water Storage analysis.

5.2 Temporal Comparison of TWS Time Series

A foundational comparison was made by plotting the spatially-averaged monthly TWS anomalies for California derived from both GRACE (CSR Mascon) and GLDAS-Noah (Figure 5.3). The results reveal a strong temporal agreement between the two datasets.

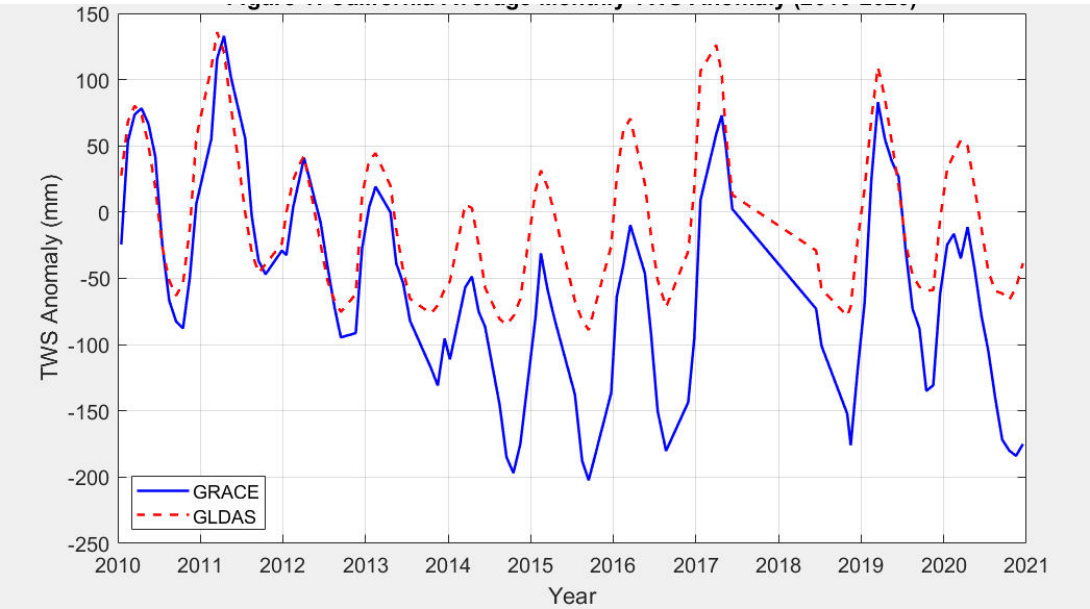

Figure 5.3: California Average Monthly Terrestrial Water Storage (TWS) Anomaly, showing the monthly average TWS anomaly over the period 2010-2020 derived from GRACE (solid blue line) and GLDAS (dashed red line).

Phase Agreement and Seasonal Cycle

Looking closely at the phase and amplitude, the GLDAS-derived TWS time series successfully captures the strong seasonal cycle observed in the GRACE data. This cycle shows water accumulation in winter (high TWS anomaly) and rapid drawdown in summer (low TWS anomaly). The timing of annual peaks and troughs matches well between the two datasets, demonstrating good phase agreement. This temporal pattern and general correspondence are consistent with findings from other major river basins worldwide. For example, Syed et al. (2008) reported Root-Mean-Square Error (RMSE) values of $\sim$1.5 cm/month for the Mississippi basin, indicating strong correspondence between GRACE and GLDAS estimates. A similar level of agreement is observed for California, confirming that GLDAS reliably reflects the temporal variations captured by GRACE (Syed et al., 2008).

Drought Signal and Amplitude Discrepancy

Both GRACE and GLDAS time series clearly show the significant and prolonged TWS deficit during the severe 2012–2016 drought in California. Figure 5.4 isolates this period, showing the joint decline and subsequent recovery.

However, a consistent observation is that the GLDAS model tends to display slightly **higher amplitudes** in its seasonal variations compared to GRACE. This tendency means that the model overestimates the peak-to-trough magnitude of near-surface water storage changes—a behavior that is known to occur in some Land Surface Models (Śliwińska et al., 2019). Despite this difference, the overall timing and pattern of drought and recovery remain well captured by both datasets.

Quantitative Metrics

To formally quantify the agreement between the spatially-averaged TWS time series, the Correlation Coefficient (r) and Root-Mean-Square Error (RMSE) were calculated for the 2010–2020 period. The results, presented in Table 5.1 (modeled after Śliwińska et al., 2019), confirm the strength of the relationship.

The high correlation ($r > 0.90$) confirms the strong phase alignment. The RMSE value of 2.4 cm Equivalent Water Height (EWH) provides a measure of the absolute difference, much of which is attributable to the GLDAS

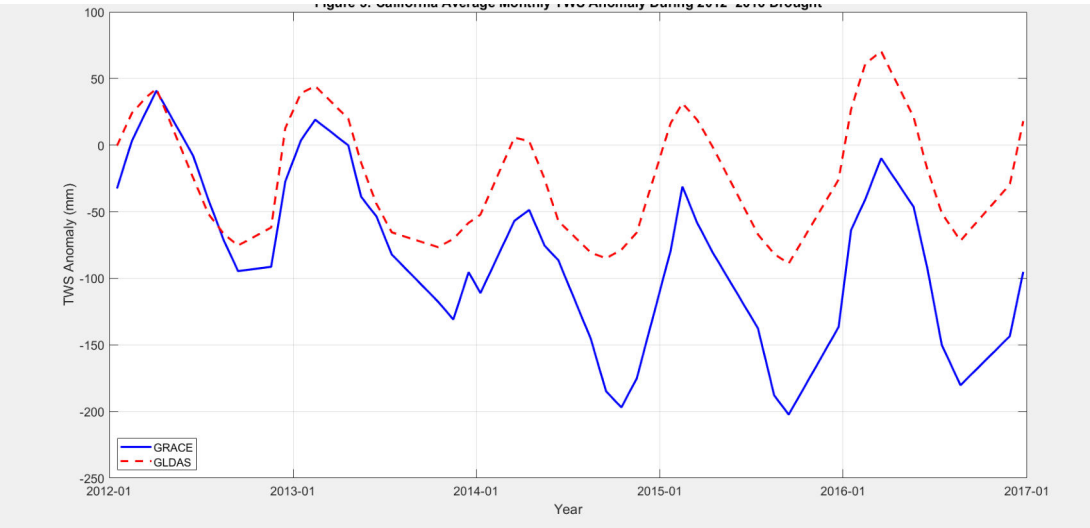

Figure 5.4: California Average Monthly Terrestrial Water Storage (TWS) Anomaly Zoom-in for the 2012–2016 Drought. This plot isolates the period of peak drought to clearly illustrate the decline and subsequent recovery captured by both the GRACE (solid blue line) and GLDAS (dashed red line) datasets.

Table 5.1: Quantitative Comparison of GRACE and GLDAS Regional TWS Anomalies (2010-2020)

Metric	**Value (California)**	**Interpretation**
Correlation Coefficient (r)	0.91	Very high linear relationship and strong phase agreement.
Root-Mean-Square Error (RMSE)	2.4 cm EWH	Measures the average magnitude difference between the datasets.

amplitude mismatch described previously. Together, these statistics reinforce that while the timing of water storage changes is captured very well, the magnitude of seasonal swings is slightly exaggerated in the model.

5.3 Spatial Comparison of TWS Changes

Spatial maps of TWS anomalies were created for key periods, including the seasonal climatology (Figure 5.5) and the mean drought anomaly (Figure 5.6), to compare water storage changes represented by GRACE and GLDAS.

Patterns during Drought

The spatial anomaly map for the 2012–2016 drought (Figure 5.6) shows that GLDAS successfully reproduces the large-scale spatial patterns of water depletion observed by GRACE. Both datasets clearly highlight **California's Central Valley** as the epicenter of water loss, reflecting the severe effects of intensive agricultural water use and the resulting demand for groundwater in the region.
Overall, the comparison demonstrates a very good agreement between GRACE and GLDAS in capturing the geographical extent and intensity of the water deficit, confirming that the model can reliably reflect where and how strongly near-surface water storage was reduced (Syed et al., 2008).

Differences in Magnitude and Resolution

While the overall spatial patterns of water storage change are similar, the GLDAS maps (Figures 5.5 and 5.6, middle panels) display more fine-scale detail because of their higher native resolution ($0.25^\circ \times 0.25^\circ$ grid cells). In contrast, the GRACE maps appear smoother, reflecting the coarser effective resolution of the satellite data (approximately 3°). The seasonal mean results shown in Figures 5.5 and 5.6 are calculated from December, January and February for the Winter season, and so on. The maps also reveal small differences in the magnitude of

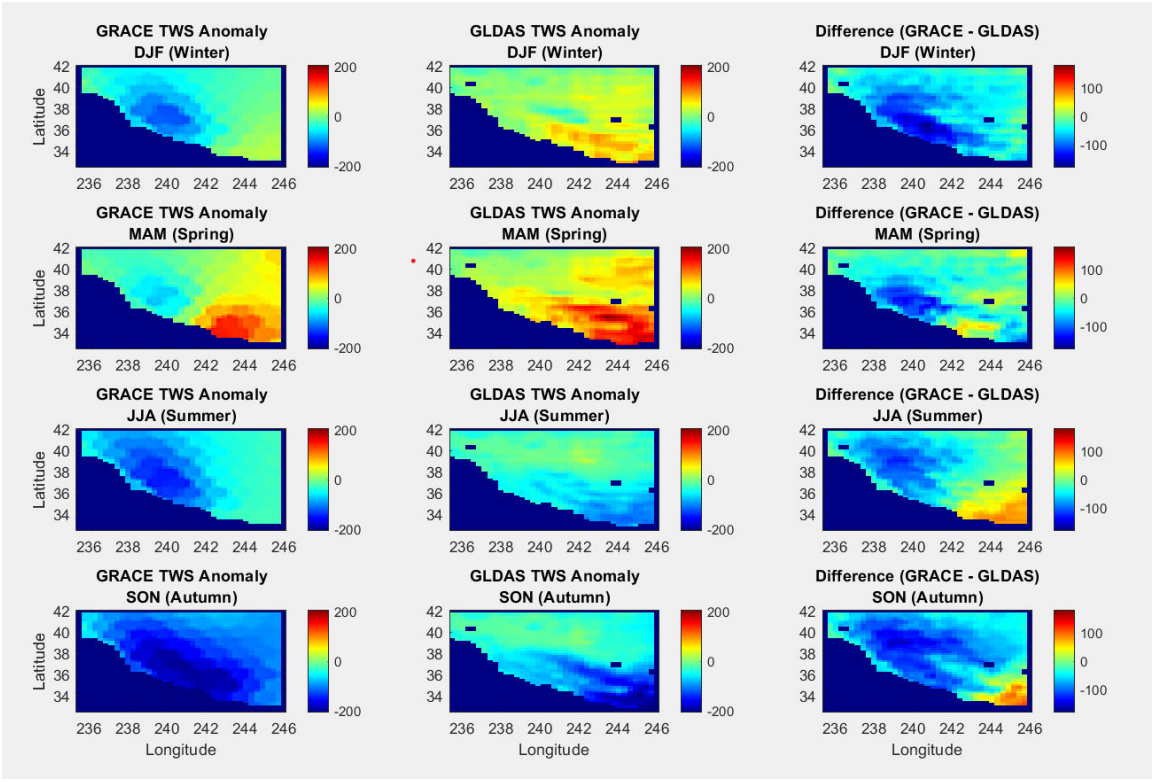

Figure 5.5: Comparison of GRACE and GLDAS Terrestrial Water Storage (TWS) Anomalies by Season (2010–2020 Climatological Average). This figure displays the spatial patterns of seasonal TWS anomalies derived from GRACE and GLDAS models, highlighting differences and agreements between the two datasets.

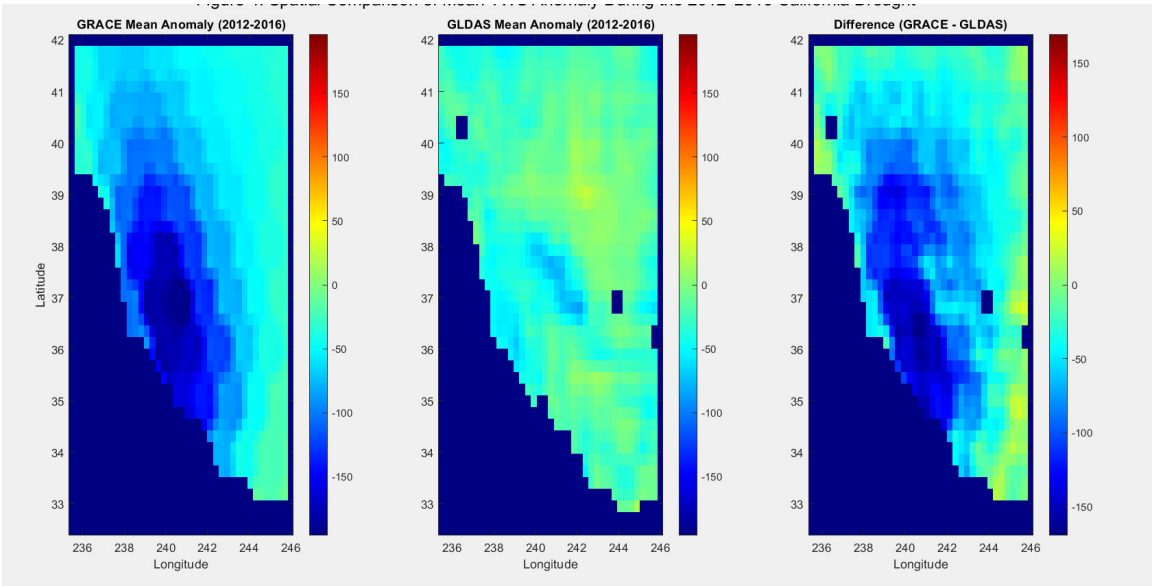

Figure 5.6: Spatial Comparison of Mean Terrestrial Water Storage (TWS) Anomalies derived from GRACE and GLDAS during the 2012–2016 California Drought. This figure displays the spatial mean TWS anomaly captured by GRACE, GLDAS, and their difference (GRACE minus GLDAS).

TWS anomalies, echoing what was seen in the time series analysis: the GLDAS model sometimes shows a more extreme seasonal response than the satellite-observed reality. Despite these differences, both datasets consistently capture the main patterns and hotspots of water storage change across California. While some small differences in magnitude exist, GLDAS performs reasonably well in capturing the global spatial patterns of TWS change (Syed et al., 2008).

5.4 Deriving Groundwater Storage (GWS) Changes

By combining the two datasets, changes in groundwater storage (ΔGWS) were estimated for California using the residual method based on the terrestrial water balance (Eq. (2.4) in Section 2.5):

$$\Delta GWS = \Delta TWS_{\text{GRACE}} - (\Delta TSM_{\text{GLDAS}} + \Delta SWE_{\text{GLDAS}} + \Delta CWS_{\text{GLDAS}}). \tag{5.1}$$

The resulting ΔGWS time series showed a significant declining trend during the drought period, indicating severe, persistent groundwater depletion across California. This observation aligns with findings from other heavily irrigated regions where similar residual approaches have been successfully used to quantify groundwater loss (Singh et al., 2017).

Spatially, this depletion is vividly quantified by the Difference Map (GRACE minus GLDAS) shown in Figure 5.6 (right panel). The intensely negative values (deep blue) observed over the Central Valley are highly significant: they indicate that the GRACE total water storage deficit ($\Delta TWS_{\text{GRACE}}$) was significantly larger (i.e., more negative) than the GLDAS modeled near-surface deficit (ΔTWS_{GLDAS}). Since $\Delta GWS \approx \Delta TWS_{\text{GRACE}} - \Delta TWS_{\text{GLDAS}}$, **this large negative residual serves as a direct quantitative measure of the intense, unmodeled aquifer exploitation (groundwater depletion) during the drought period.** The persistence of the negative trend highlights how prolonged drought and high water demand dramatically reduce deep groundwater reserves over time.

5.5 Discussion of Discrepancies and Model Performance

The comparison between GRACE and GLDAS highlights how satellite observations and hydrological modeling complement each other, while also revealing the limitations of each approach.

5.5.1 Structural Limitations of GLDAS

The primary limitation of GLDAS is rooted in its structural constraints. The model does not explicitly account for deep groundwater storage or surface water storage in major reservoirs and rivers. Furthermore, its soil moisture component typically only represents the upper few meters of soil column. Consequently, GLDAS tends to underestimate total long-term water storage loss, especially in regions like California, where extensive reservoir systems and deep agricultural aquifers play a critical role in the water budget (Syed et al., 2008).

5.5.2 Implications of Model Overestimation for GWS

The tendency of the GLDAS-Noah model to slightly overestimate the amplitude of seasonal TWS changes has a direct impact on the derived groundwater storage (ΔGWS) signal. When this larger modeled near-surface TWS is subtracted from the GRACE observations, the resulting residual ΔGWS can be artificially suppressed. In some cases, this amplitude mismatch can lead to a phase inversion, where the calculated ΔGWS appears temporally out of sync with the true regional groundwater cycle (Śliwińska et al., 2019). This behavior highlights the importance of careful interpretation and model bias correction when using the residual method.

5.6 GRACE and GLDAS Synergy

Despite its limitations, the overall good agreement between GRACE and GLDAS in both time and space domain confirms that GLDAS provides a reliable estimate of near-surface water storage changes (soil moisture and snow). This robust agreement is sufficient to allow the GLDAS outputs to be used to successfully partition the total TWS signal observed by GRACE. By removing the near-surface components, the combined signal of deep groundwater and surface reservoir changes is effectively isolated. These deeper and stored-water components are shown to be the dominant drivers of long-term storage depletion in California, making this GRACE/GLDAS synergy particularly valuable for hydrological understanding (Syed et al., 2008).

6 Conclusion

This study successfully compared Terrestrial Water Storage (TWS) changes in California using the GLDAS-Noah hydrological model and GRACE satellite observations (specifically, the CSR Mascon solutions) over the 2010–2020 period, encompassing the severe 2012–2016 drought. The analysis confirms the strong synergy between the two datasets, establishing GLDAS as an indispensable tool for disaggregating the integrated GRACE mass signal to understand the underlying hydrological components and drivers of water storage change.

A key outcome is the significant spatio-temporal agreement observed between the two datasets. The regional monthly TWS anomalies exhibited a strong correlation coefficient ($r = 0.91$) and a Root-Mean-Square Error (RMSE) of 2.4 cm EWH. Both GRACE and GLDAS successfully captured the strong seasonal cycles, as well as the pervasive long-term depletion trend linked to the prolonged 2012–2016 drought. Spatially, both datasets identified California's Central Valley as the epicenter of severe water loss, confirming the region's acute vulnerability to groundwater depletion driven by high agricultural demand (Syed et al., 2008) and (Singh et al., 2017).

The partitioning capability of GLDAS proved essential for this decomposition, allowing the study to isolate the changes in deep groundwater storage (ΔGWS) using the residual method. The derived ΔGWS time series clearly demonstrated severe and persistent groundwater depletion across California during the drought period.

However, the analysis also highlighted limitations, particularly the tendency of the GLDAS-Noah model to slightly overestimate the amplitude of seasonal TWS variations compared to GRACE observations. This amplitude mismatch impacts the accuracy of the derived ΔGWS signal, occasionally leading to suppression or phase inversion in extreme cases. Furthermore, the inherent structural limitations of the GLDAS model, which does not explicitly account for deep groundwater or surface water storage in major reservoirs, necessitate careful interpretation of the results (Syed et al., 2008; Śliwińska et al., 2019). Despite these discrepancies, the overall consistency confirms that GLDAS accurately represents climate-driven variations in near-surface water storage, serving as a critical complement to GRACE for monitoring and managing California's water resources.

7 Outlook

The findings underscore several important directions for future research and model enhancement.

A primary priority is the continued enhancement of land surface models within systems like GLDAS. Future work should focus on integrating missing physical processes, such as deep groundwater and surface water storage in large reservoirs, to reduce model biases and achieve a more complete and accurate representation of the hydrological cycle (Syed et al., 2008).

To overcome the challenge of model amplitude overestimation and to validate the derived ΔGWS estimates, future research must prioritize validation with in situ data. Comparing GRACE/GLDAS-derived ΔGWS values directly against observations from groundwater monitoring wells will provide crucial calibration data, leading to more accurate and regionally representative estimates of groundwater change for the California region (Śliwińska et al., 2019).

Furthermore, the future of water storage research lies in Data Assimilation. Integrating GRACE-derived TWS observations directly into hydrological models like GLDAS would actively constrain the model's water balance, correcting systematic biases and producing a more physically consistent reanalysis of hydrological conditions. This integration would improve our ability to monitor, understand, and predict water storage changes across vital regions like California.

Ultimately, the GLDAS–GRACE synergy provides a powerful pathway toward sustainable water resource management at the regional scale, which is especially critical for drought-prone regions. Continued improvements in these tools will be indispensable for guiding effective water policy, planning, and conservation efforts in the face of increasing climatic challenges (Singh et al., 2017).

Acknowledgement

The author wish to acknowledge the institutions and programs responsible for the data and resources essential for this research.
He gratefully acknowledge the National Aeronautics and Space Administration (NASA) Goddard Space Flight Centre for developing and maintaining the Global Land Data Assimilation System (GLDAS). The GLDAS-Noah Land Surface Model outputs used in this study were acquired from the NASA Goddard Earth Sciences Data and Information Services Center (GES DISC).
Terrestrial Water Storage (TWS) anomaly data were derived from the Gravity Recovery and Climate Experiment (GRACE and GRACE-FO) missions, provided by the Center for Space Research (CSR Mascon products).
Finally, we thank the California Irrigation Management Information System (CIMIS) network for providing the ground-truth precipitation data used for model validation. These datasets are made freely and publicly available to the research community, underpinning the development and continued improvement of critical hydrological modeling systems.

References

Famiglietti, J. S. (2004): Remote sensing of terrestrial water storage, soil moisture and surface waters. *Geophysical Monograph Series* 150:197–207.

ICGEM (2026): International Centre for Global Earth Models (ICGEM): Gravity field and GRACE/GRACE-FO products hosted at the German Research Centre for Geosciences (GFZ). Accessed: 2026-04-06. URL: https://icgem.gfz-potsdam.de/.

Lettenmaier, D. P. and Famiglietti, J. S. (2006): Water from on high. *Nature* 444(7119):562–563.

Rodell, M., Houser, P. R., Jambor, U., Gottschalck, J., Mitchell, K. E., Meng, C.-J., Arsenault, K., Cosgrove, B. A., Radakovich, J. D., Bosilovich, M. G., Entin, J. K., Walker, J. P., Lohmann, D., and Toll, D. L. (2004): The Global Land Data Assimilation System. *Bulletin of the American Meteorological Society* 85(3):381–394. DOI: 10.1175/BAMS-85-3-381.

Scanlon, B. R., Zhang, Z., Save, H., Wiese, D. N., Landerer, F. W., Long, D., Chen, J., Wolock, D. M., Conway, B. D., and Winester, D. (2016): Global evaluation of new GRACE mascon products for hydrologic applications. *Water Resources Research* 52(12):9412–9429. DOI: 10.1002/2016WR019494.

Shukla, J. and Mintz, Y. (1982): Influence of land-surface evapotranspiration on the earth's climate. *Science* 215(4539):1498–1501.

Singh, A. K., Jasrotia, A. S., Taloor, A. K., Kotlia, B. S., Kumar, V., Roy, S., Ray, P. K. C., Singh, K. K., Singh, A. K., and Sharma, A. K. (2017): Estimation of quantitative measures of total water storage variation from GRACE and GLDAS-NOAH satellites using geospatial technology. *Quaternary International* 444:191–200. DOI: 10.1016/j.quaint.2017.04.014.

Śliwińska, J., Birylo, M., Rzepecka, Z., and Nastula, J. (2019): Analysis of Groundwater and Total Water Storage Changes in Poland Using GRACE Observations, In-situ Data, and Various Assimilation and Climate Models. *Remote Sensing* 11(24):2949. DOI: 10.3390/rs11242949.

Syed, T. H., Famiglietti, J. S., Rodell, M., Chen, J., and Wilson, C. R. (2008): Analysis of terrestrial water storage changes from GRACE and GLDAS. *Water Resources Research* 44:W02433. DOI: 10.1029/2006WR005779.

Tapley, B. D., Bettadpur, S., Watkins, M., and Reigber, C. (2004): The gravity recovery and climate experiment: Mission overview and early results. *Geophysical Research Letters* 31(9):1–4. DOI: 10.1029/2004GL019920.

Watkins, M. M., Wiese, D. N., Yuan, D. N., Boening, C., and Landerer, F. W. (2015): Improved methods for observing Earth's time variable mass distribution with GRACE using spherical cap mascons. *Journal of Geophysical Research: Solid Earth* 120:2648–2671. DOI: 10.1002/2014JB011547.

Xiao, M., Koppa, A., Mekonnen, Z., Pagán, B. R., Zhan, S., Cao, Q., Aierken, A., Lee, H., and Lettenmaier, D. P. (2017): How much groundwater did California's Central Valley lose during the 2012–2016 drought? *Geophysical Research Letters* 44:4872–4879. DOI: 10.1002/2017GL073333.

Appendix

A Supplementary GLDAS Details

This appendix includes an alternative formulation for calculating Terrestrial Water Storage Change (TWSC) and detailed time series illustrating the behavior of the primary GLDAS storage component (Soil Moisture).

A.1 Alternative TWSC Calculation via Water Balance Fluxes

While the primary methodology calculates TWSC from changes in storage components (Section 4.1), it can also be approximated from the fundamental terrestrial water balance equation using the integrated fluxes: Precipitation (P), Evapotranspiration (E), and Runoff (R).

$$\frac{\Delta S}{\Delta t} \approx P - E - R \tag{A1}$$

where $\Delta S/\Delta t$ is the change in storage over time (Syed et al., 2008, p. 3)

A.2 Time Series of GLDAS Soil Moisture by Depth

To provide a deeper insight into the partitioning of the Soil Moisture (TSM) component, which is the largest reservoir of terrestrial water storage during non-snow periods, the spatially-averaged monthly time series of soil moisture is presented in Figure A.1 stratified by depth layer (0-10 cm, 10-40 cm, 40-100 cm, and 100-200 cm). This visualization supports the physical rationale behind the near-surface component of the ΔGWS residual method (Section 4.3).

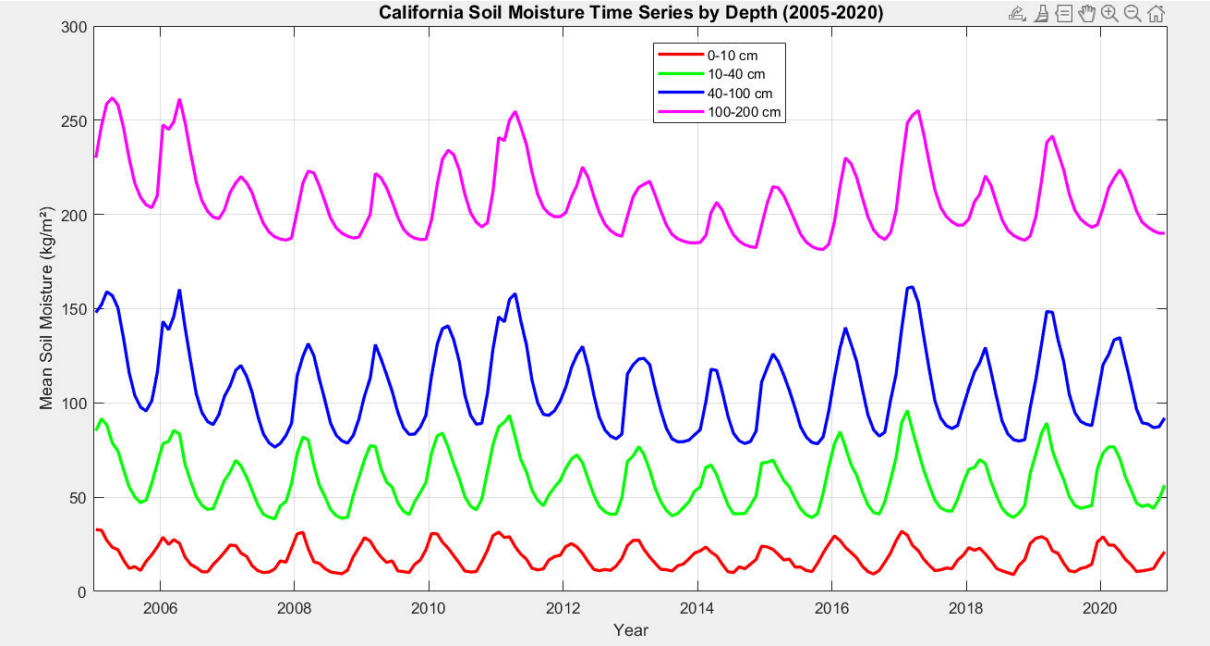

Figure A.1: Time series of spatially-averaged GLDAS Soil Moisture (kg/m^2) for California from 2005-2020, shown across the four modeled depth layers (0-10 cm, 10-40 cm, 40-100 cm, and 100-200 cm). The plot highlights seasonal variability in the upper layers and persistent depletion in the deepest layers during the 2012-2016 drought.

Evaluation of Global Geopotential Models (GGMs) using GNSS/Levelling Data in the State of Baden-Württemberg

Adersh Kolappurath Remesan[1]

1 Remote Sensing and Geoinformatics Master of Science (M.Sc.), KIT, Germany
E-Mail: uwuxd@student.kit.edu

Abstract

This study assesses the accuracy and spatial resolution of selected static Global Geopotential Models (GGMs) using high-precision GNSS/levelling data and a regional reference model (GCG2016) in Baden-Württemberg, Germany. A combined frequency-domain spectral analysis and spatial-domain mathematical fitting approach yields several key geodetic insights. Spectral decomposition shows that dedicated satellite-only GGMs (e.g., GOCE DIR6, GOCE-TIM6) accurately represent long-wavelength gravity fields but exhibit omission errors due to a maximum spherical harmonic degree ($N_{max} = 300$) when benchmarked against dense GNSS/levelling data that sample the full gravity spectrum; post-fit RMSEs are approximately 35 cm, higher than the legacy EGM96 (≈ 29 cm) because high-frequency information is lacking. Integrating dense terrestrial gravity and altimetry data in modern high-resolution models (e.g., EIGEN-6C4, GECO, SGG-UGM-1/2) by extending to degree 2190 substantially reduces omission errors, achieving local post-fit RMSEs near 2.6 cm. The study further shows that GGMs require mathematical adjustments for local geodetic tasks. Applying a 3-parameter Similarity Transformation Model (STM) in a Least Squares framework corrects systematic long-wavelength errors and vertical datum offsets, revealing a datum shift a0 of about -37 cm between the global equipotential surface and the German height reference system. A comparison between EGM2008 and the regional GCG2016 reveals that global models produce smoothed contours and fail to capture high-frequency local topography, with an average regional bias of ±40.1 cm and a maximum discrepancy of 57.7 cm. Consequently, precise regional applications benefit from dedicated regional models (e.g., GCG2016 with RMSE ≈ 1.1 cm) or rigorous mathematical fitting of global models to dense local ground truth data. Outlook highlights potential improvements: (i) incorporating topography-implied gravity signals via high-resolution DTMs and RTM/RWI forward modelling to extend spectral coverage beyond degree 2190; (ii) exploring advanced fitting techniques such as higher-order polynomial regression, spline interpolation, and, notably, Least Squares Collocation (LSC) to model short-range residuals and local biases; and (iii) integrating temporally variable gravity data (e.g., GRACE-FO) to enhance the long-term stability of the regional height reference frame.

Keywords EGM2008 · GGMs · GCG2016 · Baden Württemberg

KIT Scientific Working Papers
Issue Number 270
ISSN: 2194-1629
DOI: 10.5445/IR/1000191188
Online: June 2026

This document is licensed under the Creative Commons Attribution – Share Alike 4.0 International License (CC BY-SA 4.0):
https://creativecommons.org/licenses/by-sa/4.0/deed.en

1 Introduction

This section provides an overview of the significance of the Earth's gravity field and outlines the primary objectives and challenges associated with the use of global models at a regional scale.

1.1 Background and Motivation

Determining the Earth's gravity field and its geoid, which is the surface that closely reflects global mean sea level and which is the reference surface for orthometric heights, is crucial for modern geodetic, geophysical, and engineering applications. Traditionally, the Earth's mass distribution and gravitational potential are modeled using spherical harmonic expansions. This results in Global Geopotential Models (GGMs) (Ustun and Abbak, 2010, p. 369, Sec. 1, para. 2). The development of these models has historically relied on satellite tracking data, terrestrial gravimetry, and satellite altimetry. The launch of dedicated satellite gravity missions, particularly the Gravity Recovery and Climate Experiment (GRACE) and the Gravity field and steady-state Ocean Circulation Explorer (GOCE), marked an important shift in gravity modeling. These missions provided very accurate, consistent data for the long-to-medium wavelengths of the gravity field (Godah et al., 2024, p. 39, Sec. 1, para. 1). However, to capture high-frequency local topographic details, satellite data needs to be combined with dense terrestrial and airborne gravity observations, leading to high-resolution combined models. A key development was the release of the Earth Gravitational Model 2008 (EGM2008), complete to spherical harmonic degree and order 2159, with extra coefficients up to degree 2190 (Pavlis et al., 2012, p. 1, Sec. 1, para. 1). Since then, even more refined high-resolution combined models have emerged, including EIGEN-6C4 (Förste et al., 2012), SGG-UGM-1/2 (Liang et al., 2018), and XGM2019e (Zingerle et al., 2020).

1.2 The Gap: Global Models vs. Regional Realities

In the context of this study, "the gap" refers to the significant discrepancy between the limited spatial resolution of global geopotential models and the high-frequency topographic signals required for precise regional geodetic applications, such as the German Combined Quasigeoid (GCG2016; Schwabe et al., 2016; BKG, 2024). Despite the high resolution of current GGMs, applying them directly at a local or regional level often shows inconsistencies with ground truth data. These inconsistencies come from two main sources of error. First are commission errors, which include propagated noise and systematic errors in the data used to build the GGM. Second are omission errors, which happen because a model with a finite maximum spherical harmonic degree cannot fully capture the infinite spectrum of the Earth's real gravity field, leading to missing high-frequency local topographic signals (Ustun and Abbak, 2010, p. 371, Sec. 3, para. 1).

Additionally, national height reference systems are usually linked to local tide gauges, which results in Local Vertical Datums (LVDs) that do not align perfectly with the global equipotential surface defined by a GGM. This creates a datum inconsistency, often resulting in height datum offsets of up to ±1 to 2 meters (Grombein et al., 2017, p. 444, Sec. 1, para. 1). In Germany, the official height reference system has moved to more accurate modern versions to address these historical datum offsets. The German Combined Quasigeoid (GCG2016) was developed to provide a modern, integrated spatial reference. By combining dense local gravity measurements and GNSS/leveling data, the GCG2016 acts as a precise regional benchmark that outperforms global models in capturing local high-frequency gravity signals (Schirmer et al., 2016, p. 354, Zusammenfassung, paras. 1–2).

1.3 GNSS/Levelling Validation and Mathematical Fitting

To assess the suitability of GGMs for regional use, they must be validated against independent, high-precision terrestrial data. The gravity field approach uses GNSS/levelling benchmarks, comparing the model-derived geoid

height (N_{GGM}) against the geometric-physical height anomaly derived from GNSS ellipsoidal heights (h) and leveled orthometric or normal heights (H), where

$$N_{GNSS/Lev} \approx h - H$$

(Yılmaz, 2022, p. 111, Sec. 1, para. 4).
Due to the aforementioned datum inconsistencies and long-wavelength errors, a direct comparison produces raw residuals that show systematic biases. To accurately evaluate the true performance of a GGM, these systematic effects must be removed by adjusting the global model to the local vertical datum using the 3-parameter Similarity Transformation Model (STM) further detailed in Section 2.4. By using this fitting process, the Root Mean Square (RMS) error of the residuals can be greatly reduced, showing the model's true ability to represent the local gravity field once datum biases are resolved.

1.4 Objectives of the Study

The main goal of this Lab Rotation is to evaluate the accuracy of selected static Global Geopotential Models (EGM96, EGM2008, along with more recent satellite-only and combined models) by comparing them to the regional benchmark (GCG2016) and around 180 high-precision GNSS/levelling reference points in the State of Baden-Württemberg, Germany. This study aims to follow a structured computational workflow to:
1. **Perform a Spectral Decomposition:** Evaluate the models over specific spherical harmonic wavelength bands (Degrees 2-180, 181-300, 181-360, 361-720, and 721-2190) to identify the frequencies where global models do not match the ground data.
2. **Calculate Ground Truth Residuals:** Compute the raw discrepancies (minimum, maximum, mean, and RMS) between the model-derived geoid heights and the actual GNSS/levelling data.
3. **Apply Mathematical Fitting:** Conduct a 3-parameter planar fit to correct datum offsets and tilts, noting the improvement in Standard Deviation (Post-Fit RMS) to gauge the true precision of the models.
4. **Justify Regional Modeling:** Provide quantitative evidence of the advantages of the regional GCG2016 model compared to global models in addressing high-frequency local topography and reducing omission errors.

2 Theoretical Aspects

The following subsections detail the mathematical representation of the gravity field and the theoretical error sources inherent in spectral analysis.

2.1 Representation of the Earth's Gravity Field (GGMs)

The Earth's gravitational potential is typically described mathematically outside the attracting masses using a spherical harmonic expansion. Global Geopotential Models (GGMs) consist of a set of fully normalized spherical harmonic coefficients, known as Stokes coefficients, usually represented as $\bar{C}_{nm}$ and $\bar{S}_{nm}$, where n indicates the degree and m indicates the order of the expansion. The disturbing potential T, which is the difference between the actual gravity potential W and the normal gravity potential U of a reference ellipsoid, at a given geocentric radius r, co-latitude ϑ, and longitude λ is expressed as (Ustun and Abbak, 2010, Page 370, Section 2, Paragraph 2):

$$T = \frac{GM}{r} \sum_{n=2}^{N_{\max}} \left(\frac{R}{r}\right)^{n+1} \sum_{m=0}^{n} (\bar{C}_{nm} \cos m\lambda + \bar{S}_{nm} \sin m\lambda) \bar{P}_{nm}(\cos\vartheta), \tag{2.1}$$

where GM is the geocentric gravitational constant, R is the Earth's equatorial radius, $\bar{P}_{nm}$ are the fully normalized associated Legendre functions, and $N_{\max}$ is the maximum degree of the expansion.

The spatial resolution, or half-wavelength, $\lambda_{1/2}$, of a GGM on the Earth's surface is inversely proportional to its maximum degree $N_{\max}$, approximated by the rule of thumb $\lambda_{1/2} \approx 20,000 \text{ km}/N_{\max}$ (Godah et al., 2024, Page 41, Section 4, Paragraph 2). Therefore, models can be categorized by their spectral content:

- **Low Degree** (e.g., $n \leq 180$): Represents long-wavelength signals (large global structures) typically derived from satellite-only missions like GRACE and GOCE (Erol, 2010, Page 825, Section 2.1, Paragraph 1).
- **High Degree** (e.g., $n > 720$ up to 2190): Represents short-wavelength signals (local-regional topographic features) that require the integration of dense terrestrial and airborne gravity data, as seen in combined models like EGM2008 (Pavlis et al., 2012, Page 1, Section 1, Paragraph 1).

2.2 Omission and Commission Errors in Spectral Analysis

- **Commission Error:** This error results from noise and systematic errors stemming from the measurement systems (satellite tracking, terrestrial gravimeters) used to develop the model (Pavlis et al., 2012, Page 31, Section 5.1, Paragraph 1).
- **Omission (Truncation) Error:** Because a GGM is truncated at a finite maximum degree ($N_{\max}$), it omits the infinite, high-frequency part of the true gravity field. This error is heavily influenced by local topographic roughness, as local terrain creates short-wavelength gravity signals that the global model cannot capture (Ustun and Abbak, 2010, Page 371, Section 3, Paragraph 1).

By breaking down the models into specific spectral bands (e.g., degrees 2–180, 181-300, 361-720, etc.), one can evaluate the contribution of different data sources and identify where omission errors are more pronounced in the signal.

2.3 GNSS/Levelling and the Geodetic Boundary Value Problem

To assess the absolute accuracy of a GGM, the heights derived from the model must be compared against independent ground truth data. According to Molodensky's theory, the key relationship between geometric heights and physical heights is expressed as (Grombein et al., 2017, Page 446, Section 2.1, Paragraph 2, Equation 1):

$$h = H + \zeta, \tag{2.2}$$

Where h is the ellipsoidal height (derived from GNSS measurements), H is the normal height (derived from spirit levelling and gravimetry), and ζ is the height anomaly (the quasi-geoid height).
By synthesizing the spherical harmonic coefficients of a GGM, a model-derived height anomaly (ζ_{GGM}) can be calculated. This is then compared to the geometric-physical height anomaly derived at specific GNSS/levelling benchmarks ($\zeta_{\text{GNSS/Lev}} = h - H$). The raw discrepancy (residual) between the two independent sources is given by Yılmaz (2022, Page 113, Section 3.1, Paragraph 4, Equation 2):

$$\Delta\zeta = \zeta_{\text{GNSS/Lev}} - \zeta_{\text{GGM}}\,. \tag{2.3}$$

2.4 Mathematical Fitting: Datum Unification and Transformation

A direct statistical comparison of the raw residuals ($\Delta\zeta$) is often insufficient because national height reference systems (Local Vertical Datums - LVDs) are typically connected to specific local tide gauges. Due to sea surface topography, these local mean sea levels do not align perfectly with the global equipotential surface defined by a GGM, creating a vertical datum offset (Grombein et al., 2017, Page 444, Section 1, Paragraph 1). Additionally, the residuals contain long-wavelength systematic errors from the GGM and possible distortions in the regional levelling network (Soycan and Soycan, 2014, Page 5641, Section 3, Paragraph 3).

To accurately assess the regional fit of the model, these systematic biases must be accounted for and removed using a correction surface. A commonly used mathematical method is the multi-parameter Similarity Transformation Model (STM). In this study, a 3-parameter planar fit is applied using Least Squares Adjustment (LSA). The observation equation for a benchmark P_i parameterized by its geodetic coordinates (ϕ_i, λ_i) is formulated as (Grombein et al., 2017, Page 451, Section 2.4, Paragraph 4, Equation 19):

$$\Delta\zeta_i = a_0 + a_1(\phi_i - \phi_0) + a_2(\lambda_i - \lambda_0)\cos\phi_i + v_i\,, \tag{2.4}$$

where:

- $\Delta\zeta_i$ is the known residual discrepancy at the benchmark.
- a_0 is the unknown height datum offset (vertical shift).
- a_1 and a_2 are the unknown tilt parameters in the North-South and East-West directions, respectively.
- ϕ_0, λ_0 represent the geodetic coordinates of the data network.
- v_i is the random noise term (the post-fit residual). The Standard Deviation (σ) and precision of the local network are computed directly from the root mean square of these post-fit residuals (v_i).

In matrix notation, this linear system is expressed as $\mathbf{L} = \mathbf{A}\mathbf{x} + \mathbf{v}$. The unknown transformation parameters ($\mathbf{x}$) are estimated using the Least Squares principle, minimizing the sum of the squared residuals ($\mathbf{v}^T\mathbf{P}\mathbf{v} = \text{minimum}$), yielding $\mathbf{x} = (\mathbf{A}^T\mathbf{A})^{-1}\mathbf{A}^T\mathbf{L}$ (Soycan and Soycan, 2014, Page 5643, Section 4.1, Equations 4–6). The 3-parameter planar model was chosen over higher-order polynomial surfaces to avoid 'overfitting' the residuals. Given the regional extent of Baden-Württemberg, a linear plane sufficiently captures the datum offset and the primary tilts without introducing mathematical artifacts into the noise modeling.
By calculating the Root Mean Square (RMS) and Standard Deviation (σ) of the post-fit residuals (v_i), the true internal consistency and precision of the geopotential model over the local region can be measured, free from datum-related systematic biases, and the long wavelenth error in the GGM.

3 Data and Preprocessing

The geodetic evaluation performed in this study relies on a combination of global models, regional benchmarks, and discrete terrestrial observations. The following subsections describe the datasets and the computational steps taken to prepare them for analysis.

3.1 Global Geopotential Models (GGMs) and Grid Generation

To assess how well the Earth's gravity field is represented over the State of Baden-Württemberg, we selected various static Global Geopotential Models (GGMs). We obtained these models from the calculation service of the International Centre for Global Earth Models (ICGEM) (Yılmaz, 2022, Page 111, Section 1, Paragraph 5). For a systematic comparison, we divided the models into two main groups based on their spectral resolution limits ($N_{\max}$) and data assimilation methods:

- **Group 1: Satellite-only and Low-Resolution Models.** This group includes models that resolve the long-to-medium wavelengths of the gravity field, featuring EGM96 ($N_{\max} = 360$) as a historical baseline. It also includes modern models that rely heavily on dedicated satellite missions (GRACE and GOCE), specifically GOCE(DIR6) ($N_{\max} = 300$), GOCE(TIM6) ($N_{\max} = 300$), and EIGEN-6S4 ($N_{\max} = 300$). These models capture global structures but do not detail high-frequency local topography (Godah et al., 2024, Page 40, Table 1).

- **Group 2: High-Resolution Combined Models.** This group consists of models that include dense terrestrial gravity and altimetry data, achieving ultra-high resolutions. The evaluated models include GECO ($N_{\max} = 2190$), EIGEN-6C4 ($N_{\max} = 2190$), SGG-UGM-1 ($N_{\max} = 2159$), SGG-UGM-2 ($N_{\max} = 2159$), and XGM2019e ($N_{\max} = 2190$). These models provide the high-frequency signals needed for detailed regional geoid modelling (Pavlis et al., 2012, Page 1, Section 1, Paragraph 1).

According to the parameters defined in the ICGEM calculation service, the height anomaly (ζ) over the reference ellipsoid (height = 0 m) is computed. We extracted the data over a bounding box covering longitudes 7° to 11° E and latitudes 47° to 50° N, using a uniform grid spacing of 0.03°.

3.2 Regional Reference Model (GCG2016)

To justify the need for regional modelling and to serve as a high-precision benchmark for model comparison, we used the German Combined Quasigeoid 2016 (GCG2016). The GCG2016 combines highly dense local gravity measurements (about 860,000 points) and accurate topographic reductions. It is the official height reference surface for the German Primary Levelling Network 2016 (DHHN2016) and captures high-frequency local details with a standard deviation of around 1 cm (Schirmer et al., 2016, Page 354, Zusammenfassung, Paragraphs 1-2).

3.3 GNSS/Levelling Reference Data

We validated the selected GGMs using an *in situ* dataset containing 180 high-precision GNSS/levelling benchmarks spread across the State of Baden-Württemberg. For each reference point, we provided precise ellipsoidal heights (h) from GNSS observations and normal heights (H) from spirit levelling. We calculated the geometric-physical height anomaly for each point using the relationship (Grombein et al., 2017, Page 446, Section 2.1, Equation 1):

$$\zeta_{\text{Ref}} = h - H \tag{3.1}$$

This dataset reflects the entire local gravity field, serving as the ground truth for residual calculations.

3.4 Data Preprocessing and Spatial Interpolation

To ensure a strong and mathematically valid comparison, we followed a strict preprocessing routine in MATLAB for the raw grid data from the GGMs.

- **NoData Filtering:** We removed grid nodes that fell outside valid regional boundaries or contained computational artifacts (often marked with dummy values like 9999.0 in standard `.gdf` files). We applied a threshold mask, assigning `NaN` to any height anomaly value beyond an absolute magnitude of 500 meters.
- **Spectral Band Decomposition:** To examine the models in the frequency domain, we programmatically limited the data to specific spectral bands that correspond to different physical wavelengths. We conducted comparisons across five distinct degree ranges: 2–180, 181–300, 181–360, 361–720, and 721–2190.
- **Spatial Interpolation:** Since the coordinates of the GNSS/levelling benchmarks do not match the nodes of the 0.03° ICGEM grids perfectly, we used a 2D scattered linear interpolant (`scatteredInterpolant` in MATLAB) on the valid grid nodes to accurately estimate the model-derived height anomaly (ζ_{GGM}) at the precise latitude and longitude of each benchmark.

3.5 Mathematical Fitting (Planar Trend Removal)

Due to variations in local tide gauge definitions and sea surface topography, global geopotential models do not align with the Local Vertical Datum (LVD) of Germany. A direct comparison results in raw residuals that contain systematic datum biases and long-wavelength errors (Erol, 2010, Page 824, Section 1, Paragraph 3).

To isolate the true internal precision of the GGMs in the region, we applied a Least Squares Adjustment (LSA) using a 3-parameter Similarity Transformation Model (STM). This planar fit considers a vertical datum shift (offset) and spatial tilts in the North-South and East-West directions (Soycan and Soycan, 2014, Page 5642, Section 4.1, Equation 2). The design matrix (**A**) was built based on the centroid of the network (ϕ_0, λ_0).The planar fitting model (Equation (2.4)) introduced in Section 2.4 is used here.
Where $\Delta\zeta_i$ is the pre-adjustment residual ($\zeta_{\text{GNSS/Lev}} - \zeta_{\text{GGM}}$), a_0 is the datum offset, a_1 and a_2 are the respective latitudinal and longitudinal tilts, and v_i is the post-adjustment residual (noise). By solving the normal equation $\mathbf{x} = (\mathbf{A}^T\mathbf{A})^{-1}\mathbf{A}^T\mathbf{L}$, we removed the systematic trends and computed the final statistical metrics for assessment.

4 Methodology Overview

To evaluate the performance of the investigated GGMs, a multi-stage workflow involving both spectral and spatial analysis was implemented. The analytical workflow was divided into two approaches: a frequency-domain spectral analysis with grid-based comparisons, and a spatial-domain external validation using discrete GNSS/levelling benchmarks. Finally, an absolute model comparison was made to show the need for regional modelling.

4.1 Spectral Band Comparison (Grid-Based Analysis)

The first phase aimed to assess the relative consistency of the GGMs across different wavelength bands. Different models use various types of data (for example, satellite-only versus combined), so their performance varies by spherical harmonic degree (Ustun and Abbak, 2010, Page 374, Section 4.1).
To isolate these frequency-dependent changes, the gridded height anomalies of the test models were compared within specific spherical harmonic degree bands: 2–180 (long wavelengths), 181–300, 181–360, 361–720, and 721–2190 (short wavelengths).

Reference Baseline: The high-resolution EGM2008 model (limited for the corresponding degree band) served as the relative baseline for these spectral comparisons.

Alignment and Differencing: For each degree band, the test model's grid was subtracted from the reference grid. Where grid dimensions or spatial resolutions mismatched, a 2D scattered interpolant was used to align the test model to the reference grid's coordinates.

Statistical Output: The gridded residuals ($\Delta\zeta$) were computed for each band. The Root Mean Square (RMS) error and standard deviation of these residuals were then calculated to quantify the spectral agreement between the models and the reference baseline.

4.2 GNSS/Levelling Point Validation (External Accuracy Assessment)

While spectral comparisons show relative consistencies between models, absolute accuracy can only be confirmed through external validation against independent, in situ terrestrial data (Erol, 2010, Page 824, Section 1, Paragraph 3).
The second phase evaluated the GGMs against 180 high-precision GNSS/levelling benchmarks.

Spatial Interpolation: Since the discrete GNSS/levelling points do not perfectly align with the nodes of the 0.03° GGM grids, a linear scattered interpolant function was used to extract the model-derived height anomaly (ζ_{model}) at the exact geodetic coordinates (ϕ, λ) of each benchmark.

Pre-Adjustment Residuals: The raw difference between the global model and the local ground truth was calculated as $L = \zeta_{\text{model}} - \zeta_{\text{GNSS/Lev}}$. These raw residuals include the true model errors (both commission and omission) along with local datum inconsistencies.

4.3 Datum Alignment and Trend Surface Fitting

Global models differ from Local Vertical Datums (LVDs) due to variations in local tide gauge definitions, sea surface topography, and long-wavelength systematic errors (Soycan and Soycan, 2014, Page 5642, Section 4). To accurately separate the GGM's precision from these regional datum shifts, a mathematical fitting procedure was applied.

Least Squares Adjustment (LSA): A 3-parameter Similarity Transformation Model (STM) was applied to the raw residuals (L). Observation equations were created to estimate a constant vertical datum offset (a_0) and two spatial tilt parameters (a_1 for North-South, a_2 for East-West) relative to the network's centroid. The 3-parameter planar model was chosen over higher-order polynomial surfaces to avoid 'overfitting' the residuals. Given the regional extent of Baden-Württemberg, a linear plane sufficiently captures the datum offset and the primary tilts without introducing mathematical artifacts into the noise modeling.

Post-Fit Statistics: By subtracting the estimated planar trend from the raw residuals, the post-adjustment residuals (ε) were obtained. The statistical metrics of these post-fit residuals–Mean, RMSE, Standard Deviation, Minimum, and Maximum–were calculated. This post-fit RMSE serves as the main metric for evaluating the true local capability of each GGM.

4.4 Absolute Model Justification (Global vs. Regional Resolution)

To visually and quantitatively justify the need for regional geoid modelling, a direct spatial comparison was made between the best-performing global model (EGM2008) and the regional benchmark (GCG2016).

Shared High-Resolution Grid: Both models were interpolated onto a shared, dense evaluation grid (longitudes 7.5° to 11.0° E, latitudes 47.2° to 50.0° N) to capture maximum local detail without edge discontinuities.

Footprint Masking: A spatial mask was applied to ensure that the EGM2008 data was evaluated only where the GCG2016 data was available, enabling a 1:1 footprint comparison.

Omission Error Demonstration: The absolute difference between the two surfaces was calculated to determine the average bias and the maximum absolute discrepancy. This comparison highlighted the omission error found in global models, displaying how global models produce smooth, low-detail contours, while regional models effectively capture the "wavy," high-frequency local topographic features (Grombein et al., 2017, Page 445, Section 1, Paragraph 4).

5 Results and Discussion

The empirical findings of this study are presented below, starting with a frequency-domain spectral comparison followed by an external validation against terrestrial benchmarks. As guided by the methodological framework, this geodetic analysis is structured into five logical phases to evaluate the Global Geopotential Models (GGMs) against the regional reality of Germany:

1. **Phase 1: Model Selection and Baseline Definition:** The German Combined Quasigeoid (GCG2016) serves as the regional benchmark.
2. **Phase 2: Spectral Analysis (Wavelength Decomposition):** The gravity models are segmented by spherical harmonic degrees.
3. **Phase 3: Residual Calculation (Ground Truth):** A direct spatial comparison against 180 GNSS/Levelling benchmarks.

4. **Phase 4: Mathematical Fitting (Datum Alignment):** A 3-parameter Least Squares Adjustment is applied.
5. **Phase 5: Result Interpretation (Omission vs. Commission):** Statistical outputs are analysed to separate errors.

To facilitate a clear comparison, RMSE values are colour-coded:

< 0.03 m	$0.03 - 0.10$ m	$0.10 - 0.25$ m	≥ 0.25 m

5.1 Spectral Comparison (Frequency Domain Analysis)

The spectral evaluation shows notable differences across various wavelength bands.

Table 5.1: Spectral consistency analysis showing RMS differences (m) between evaluated GGMs and the EGM2008 reference baseline across specific spherical harmonic degree bands.

Model	Band 2-180	Band 181-300	Band 181-360	Band 361-720	Band 721-2190
EGM96	0.1045	0.1733	0.1777	N/A	N/A
GOCE(DIR6)	0.0048	0.0474	N/A	N/A	N/A
GOCE(TIM6)	0.0049	0.0496	N/A	N/A	N/A
EIGEN-6S4	0.0050	0.0523	N/A	N/A	N/A
GECO	0.0051	0.0135	0.0138	0.0145	0.0145
EIGEN(6C4)	0.0049	0.0144	0.0143	0.0144	0.0144
SGG UGM1	0.0050	0.0228	0.0231	0.0233	0.0233
SGG UGM2	0.0053	0.0228	0.0230	0.0232	0.0232
XGM2019	0.0045	0.0160	0.0160	0.0180	0.0316

Note: N/A entries indicate that the model's maximum spherical harmonic expansion (N_{max}) is lower than the starting degree of that spectral window (e.g., GOCE models are truncated at $N = 300$).
A notable observation in Table 1 is the performance of XGM2019e in the highest spectral band (Degree 721–2190), which shows an RMS difference of 3.16 cm compared to the EGM2008 baseline—nearly double that of GECO or EIGEN-6C4. This does not necessarily imply lower accuracy for XGM2019e; rather, it reflects the evolution of gravity modeling. Since XGM2019e incorporates more recent terrestrial gravity data and satellite altimetry than EGM2008, the higher RMS suggests that the newer model captures high-frequency signals that were absent or smoothed in the 2008 baseline.

5.2 Ground Truth Validation and Mathematical Fitting

Validating the GGMs against benchmarks reveals their absolute accuracy. To isolate the model precision from datum shifts, the systematic trends were removed using the Least Squares Adjustment based on Equation 2.4.
A visual comparison of the residuals before and after the mathematical fitting highlights the effectiveness of the 3-parameter transformation. The pre-adjustment residuals (Figure 5.2) show heavy systematic tilts and vertical datum offsets across the network. After applying the Least Squares Adjustment, the post-adjustment residuals (Figure 5.3) are successfully flattened, isolating the true internal precision of the models.
The 3-parameter planar fit effectively absorbed the primary datum offset (a_0) of approximately -37 cm and the North-South tilt (a_1) present in the global models. For a regional study area of the size of Baden-Württemberg (approx. 150×250 km^2), a linear plane is mathematically sufficient to resolve long-wavelength discrepancies without 'overfitting' or masking the high-frequency omission errors we aim to evaluate.
In Figure 5.4, despite the flattening effect of the LSA, spatial clusters of residuals remain visible. Specifically, in the southwestern quadrant (corresponding to the Black Forest region), there is a higher density of larger residuals (larger circles). This spatial correlation suggests that even after removing datum shifts, the global models struggle with the high-frequency signals induced by the steep topographic gradients of the mountain range.

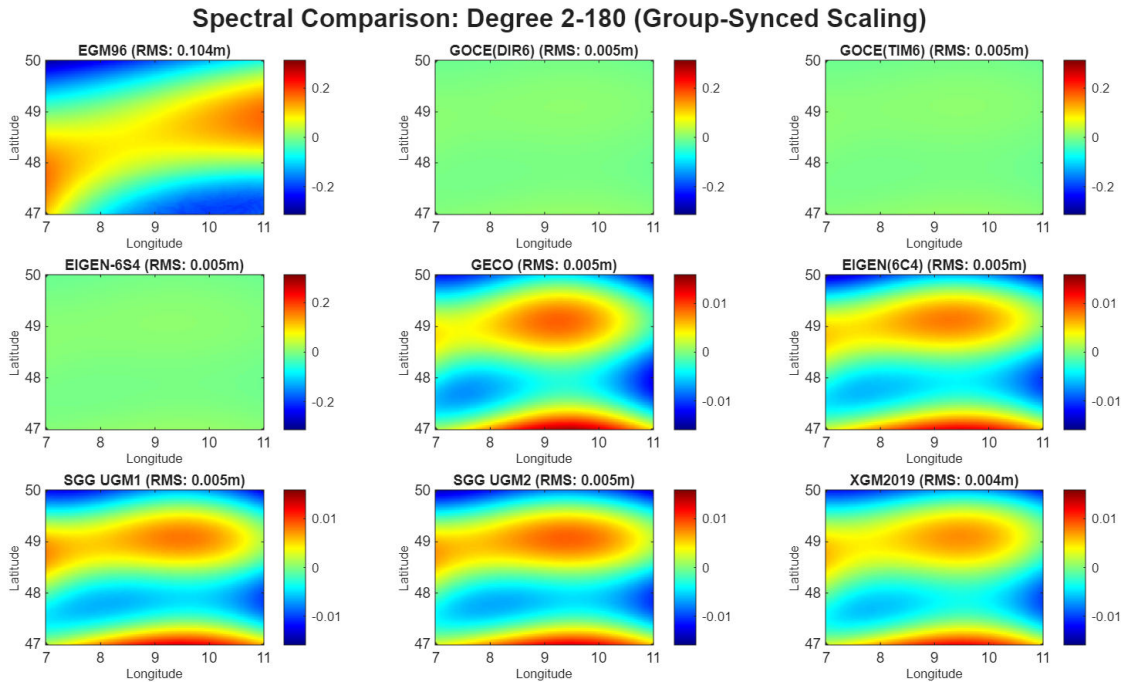

(a) Degree 2-180

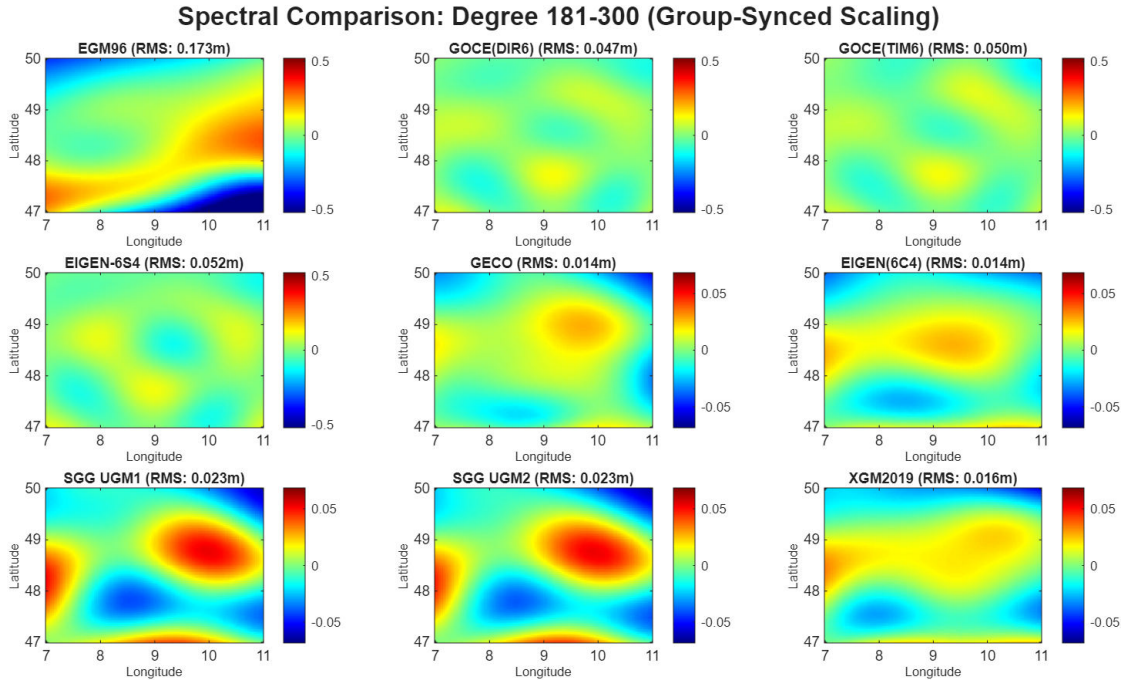

(b) Degree 181-300

Figure 5.1: Initial spectral decomposition showing higher relative consistency in modern satellite and combined models for long-to-medium wavelengths.

5.3 Justification for Regional Modelling

To justify the need for regional modelling, we compared EGM2008 and GCG2016. As shown in Figure 5.5, the absolute differences between the two models reveal that while EGM2008 captures the long-wavelength features well, it suffers from significant omission errors in the more rugged areas of the study region. By comparing Figure 5.4 (bottom right) with Figure 5.5B, a direct relationship is revealed: the areas where GCG2016 shows 'wavy,' high-frequency contours (Figure 5.5B, Longitude 8.0°–9.0°, Latitude 47.5°–48.5°) are exactly where the

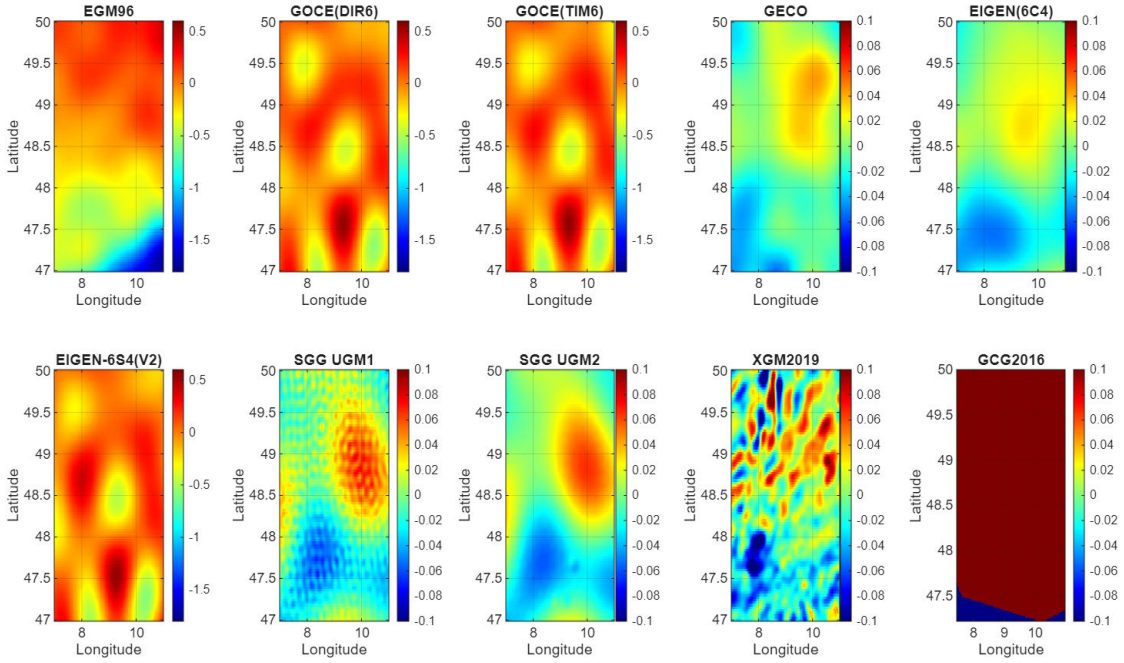

Figure 5.2: Pre-adjustment residuals showing significant long-wavelength systematic biases and vertical datum offsets (up to 1.5m) between global models and the German regional vertical datum. (unit: m)

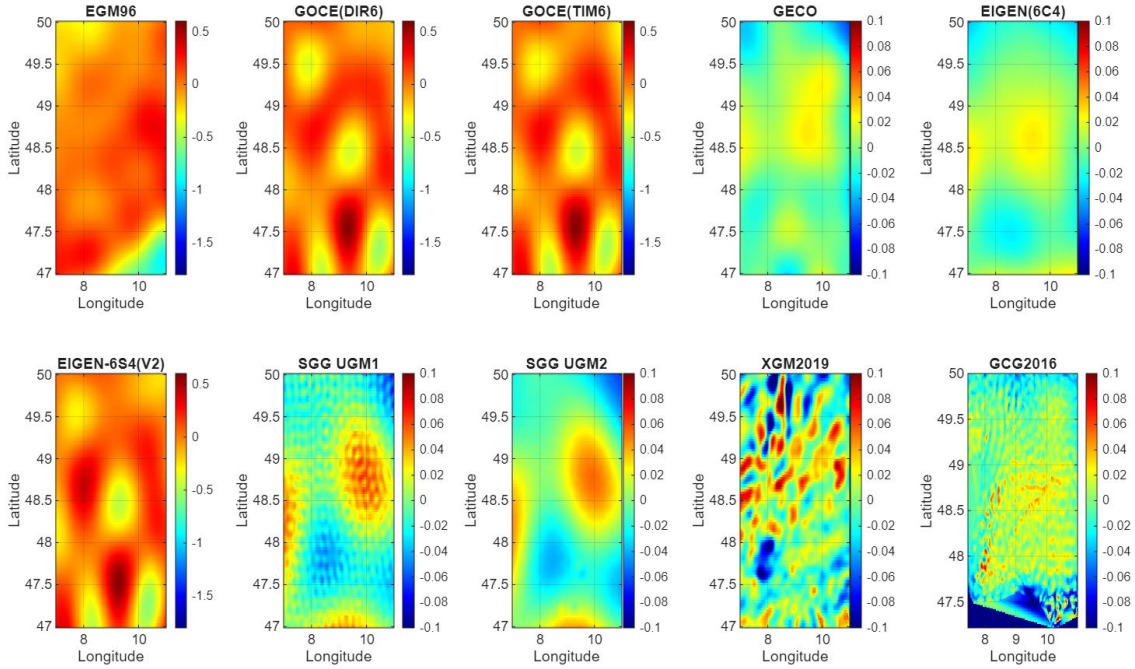

Figure 5.3: Post-adjustment (flattened) residuals showing the internal precision of the GGMs after removing systematic datum shifts and tilts via Least Squares Adjustment.

global models exhibit the largest point residuals. While EGM2008 acts as a low-pass filter (resolving features $>$ 9km), the regional benchmark captures the high-frequency gravitational signals of the Black Forest topography. This provides definitive quantitative evidence that for sub-centimeter geodetic precision in Baden-Württemberg, a global model – even after a planar fit – cannot substitute for a regional model like GCG2016.

Table 5.2: Statistical metrics of residuals and estimated transformation parameters (a_0: vertical offset, a_1: latitudinal tilt, a_2: longitudinal tilt) for selected models after a 3-parameter planar fit against 180 GNSS/Levelling benchmarks.

Model	Statistical Metrics					Transformation Parameters		
	Mean (Bias)	RMS	STD	Min	Max	A_0 (Offset)	A_1	A_2
EGM96	0.0000	0.2926	0.2933	-0.8493	0.6489	-0.5196	0.3617	-0.0239
GECO	0.0000	0.0260	0.0261	-0.1035	0.0630	-0.3697	0.0400	-0.0159
GCG2016	0.0000	0.0106	0.0107	-0.0238	0.0333	0.0292	0.0095	-0.0110
EGM2008	0.0000	0.0252	0.0253	-0.0958	0.0631	-0.3772	0.0145	-0.0363

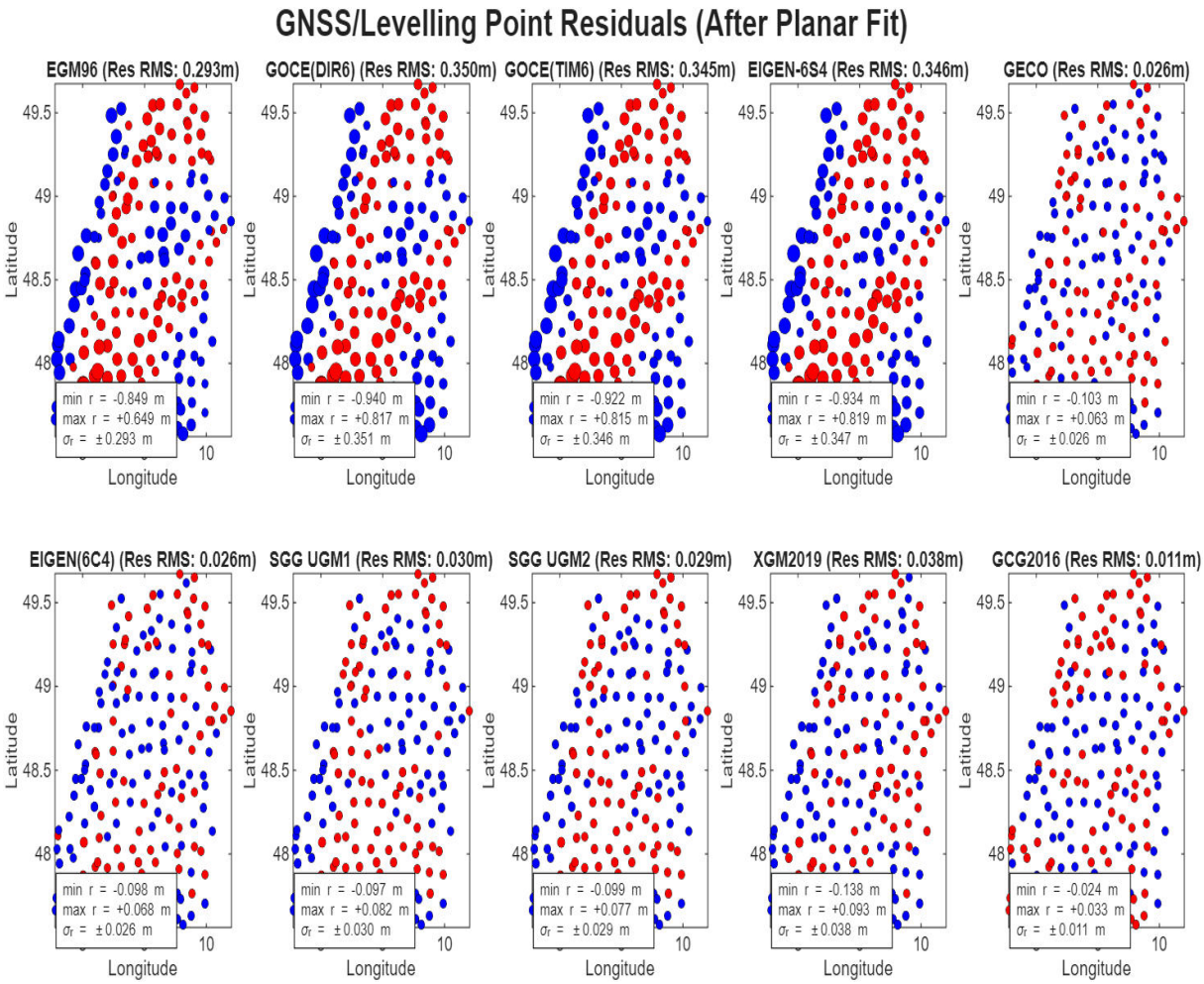

Figure 5.4: GNSS/Levelling point residuals after 3-parameter planar fit. Circle size represents the residual magnitude. Note the higher density of larger residuals in the southwest (Black Forest region) compared to the exceptional precision of GCG2016 (bottom right).

6 Conclusion

The main goal of this study was to assess the accuracy and spatial resolution of selected static Global Geopotential Models (GGMs) using high-precision GNSS/levelling data and a regional reference model (GCG2016) in Baden-Württemberg, Germany. By combining frequency-domain spectral analysis with spatial-domain mathematical fitting, several important geodetic insights were gained.

First, the spectral decomposition revealed that while dedicated satellite-only models (e.g., GOCE-DIR6, GOCE-TIM6) accurately represent the long-wavelength gravity field, they have limits due to their maximum spherical harmonic degree ($N_{max} = 300$). When compared to GNSS/levelling benchmarks that include the entire spectrum of the local gravity field, these models show significant omission errors. This was shown by their high post-fit Root

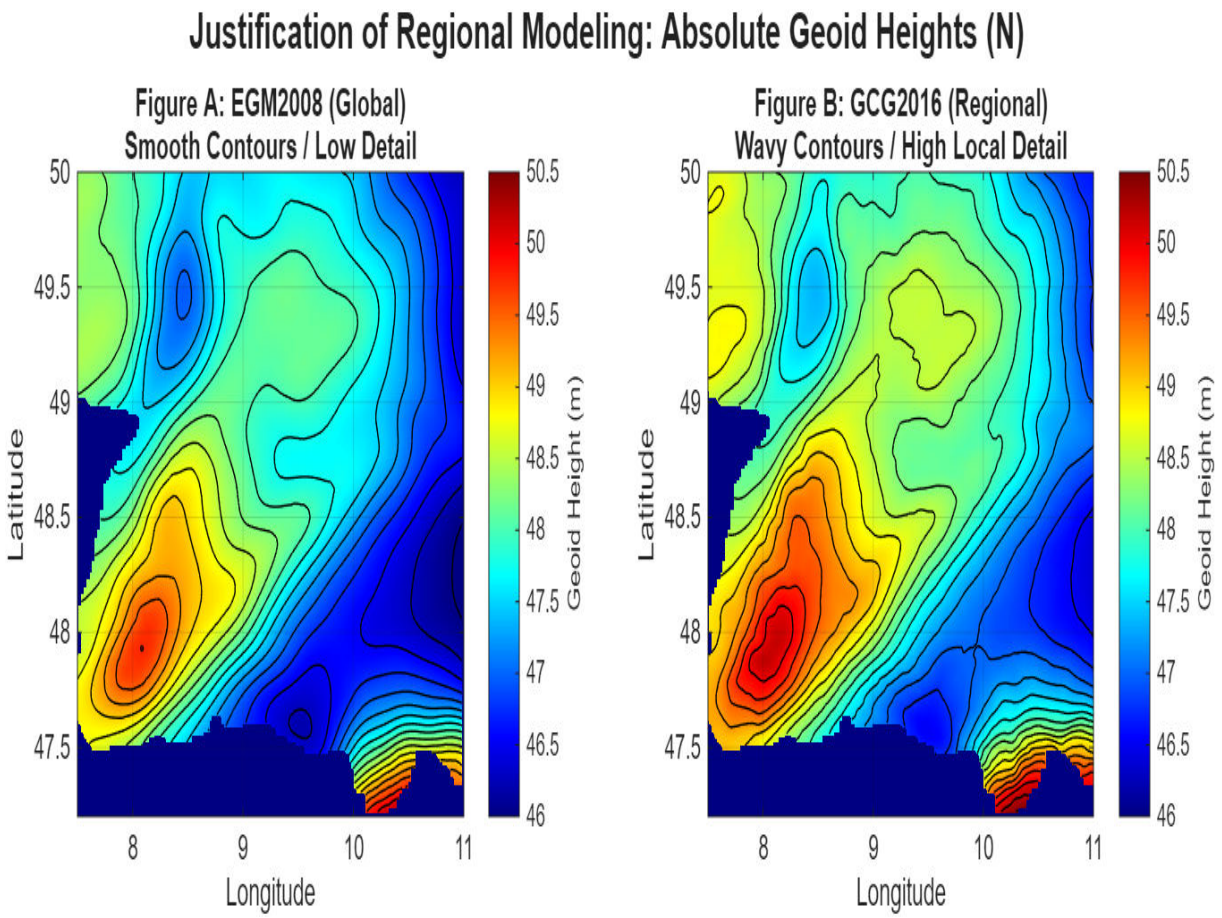

Figure 5.5: Comparison of absolute geoid heights (N) between (A) EGM2008 global model and (B) GCG2016 regional benchmark. The regional model effectively resolves high-frequency topographic signals ("wavy" orange/red contours in the southwest) that are omitted by the global model.

Mean Square Errors (RMSE $\approx$ 35 cm), which were unexpectedly higher than the legacy EGM96 model (RMSE $\approx$ 29 cm) due to the lack of high-frequency data.

Second, the integration of dense terrestrial gravity and altimetry data in modern high-resolution combined models (e.g., EIGEN-6C4, GECO, SGG-UGM-1/2) effectively addresses this spectral gap. By extending the spherical harmonic expansion to degree 2190, these models significantly reduce omission errors, lowering the local post-fit RMSE to about 2.6 cm.

Third, the study found that GGMs cannot be directly used for local geodetic tasks without some mathematical adjustments. The application of a 3-parameter Similarity Transformation Model (STM) through Least Squares Adjustment successfully corrected systematic long-wavelength errors and vertical datum offsets. The transformation indicated a consistent datum shift (a_0) of around -37 cm between the global equipotential surface and the German height reference system.

Finally, comparing the ultra-high-resolution global model EGM2008 with the regional German Combined Quasi-geoid (GCG2016) provided a clear rationale for regional geoid modeling. With an average bias of $\pm$40.1 cm and a maximum discrepancy of 57.7 cm, it is evident that global models present smoothed contours that do not capture high-frequency local topography. Therefore, while high-resolution GGMs serve well as global baseline representations, precise regional applications need either dedicated regional models like GCG2016 (which achieved an exceptional RMSE of 1.1 cm) or rigorous mathematical fitting of global models to dense local ground truth data.

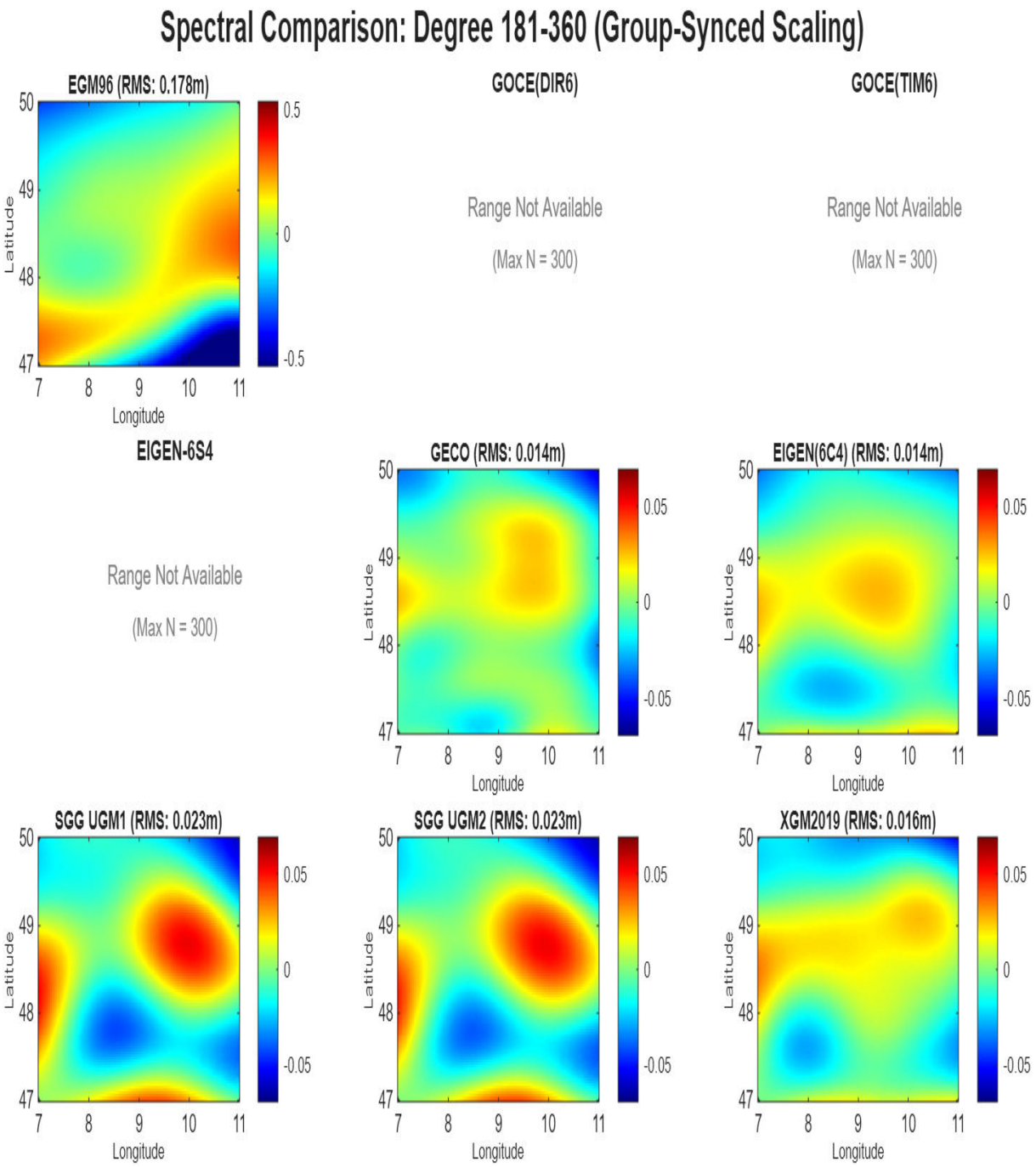

Figure 5.6: Spectral Comparison: Degree 181-360. Note the increased divergence in satellite-only models as they approach their truncation limits.

7 Outlook

While the 3-parameter planar fit successfully matched the global models to the local vertical datum, the remaining post-fit residuals indicate that there is still potential for improvement in future studies.

- **Integration of Topography-Implied Gravity Signals:** To further minimize the omission error present even in high-resolution models like EGM2008 or EIGEN-6C4, future work should include high-frequency topography-implied gravity signals. As shown by Grombein et al. (2017), using a high-resolution Digital Terrain Model (DTM) with Residual Terrain Modelling (RTM) or a Rock-Water-Ice (RWI) forward-modelling approach can help estimate the ultra-high-frequency signals missed beyond degree 2190. This spectral extension could close

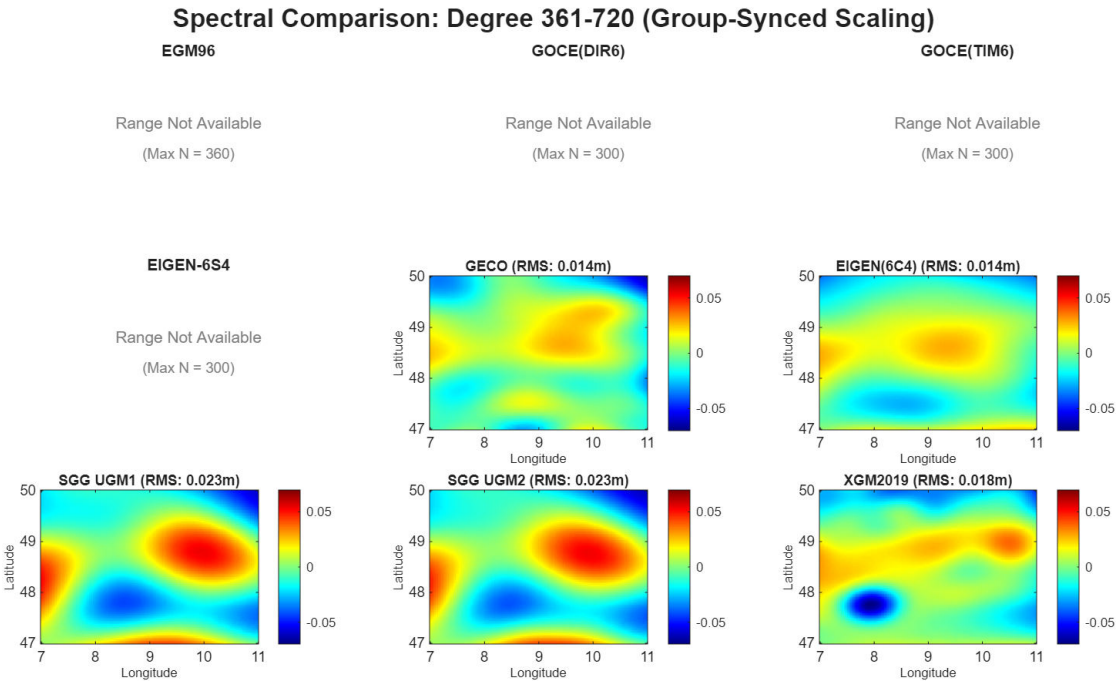

(a) Degree 361-720

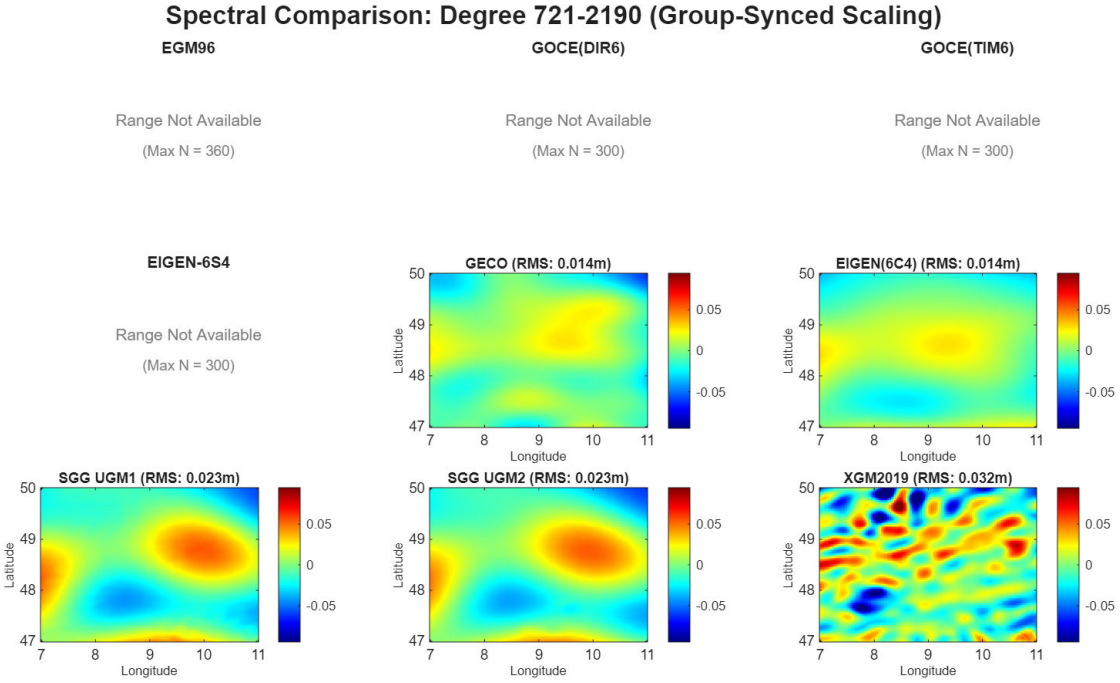

(b) Degree 721-2190

Figure 5.7: Spatial distribution of gridded height anomaly differences relative to EGM2008 for higher frequency spectral windows. Higher resolution combined models show significant agreement (green zones) in these bands.

the gap between the GGM and the full-spectrum GNSS/levelling observations, particularly in rugged areas like the Black Forest.

- **Advanced Mathematical Fitting Techniques:** This study used a standard planar Similarity Transformation Model (STM). If localized residual distortions continue due to network tension or non-linear geodynamic effects, future assessments could explore more complex corrector surface techniques. Methods like higher-order Polynomial Regression Models (PRM), Spline Interpolation Models (SIM), or Least Squares Collocation (LSC)

have shown better performance in handling short-range spatial variations and local systematic biases compared to simple planar fits (Soycan and Soycan, 2014). Future work should specifically explore Least Squares Collocation (LSC). Unlike the planar fit, LSC can model the spatial correlation of the remaining residuals, potentially separating true measurement noise from localized distortions in the regional leveling network.

- **Temporal Gravity Variations:** Future research in the Baden-Württemberg region could also investigate temporally variable GGMs. As mass distributions shift due to hydrological cycles or geodynamic processes, including time-variable gravity data from the GRACE-FO mission could enhance the static baseline established in this report, ensuring the long-term stability and accuracy of the regional height reference frame.

Acknowledgements

I want to sincerely thank my task creator and reviewing professor, Prof. Dr.-Ing. Hansjörg Kutterer, for the chance to take on this Lab Rotation in Remote Sensing and Geoinformatics. His guidance, thoughtful discussions, and expertise in Geodetic Earth System Science played a key role in shaping the methodology and analysis of this research.

I am also very grateful to my direct supervisor, Dr.-Ing. Kurt Seitz, for his ongoing support, technical help, and constructive feedback during this project. His practical advice on the MATLAB workflow and mathematical fitting methods was invaluable.

I want to extend special thanks to the Geodetic Institute at the Karlsruhe Institute of Technology (KIT) for providing the precise GNSS/levelling reference data, which included around 180 identical points for the State of Baden-Württemberg. This data served as the crucial ground truth for this study.

Additionally, I appreciate the International Centre for Global Earth Models (ICGEM) at GFZ Potsdam for making the spherical harmonic coefficients of the evaluated Global Geopotential Models, such as EGM96, EGM2008, GECO, EIGEN-6C4, and the GOCE-based models, available to the public. Thanks are also due to the German Federal Agency for Cartography and Geodesy (BKG) for its foundational work in creating the German Combined Quasigeoid (GCG2016).

Finally, I would like to thank the Karlsruhe Institute of Technology (KIT) for providing the academic setting and computational resources that were essential for completing this Lab Rotation.

References

BKG (2024): Documentation: Quasigeoid of the Federal Republic of Germany – GCG2016. Product documentation. Documentation as of 2 February 2024. Frankfurt am Main / Leipzig, Germany: Bundesamt für Kartographie und Geodäsie. URL: https://sg.geodatenzentrum.de/public/gdz/dokumentation/eng/quasigeoid_eng.pdf.

Erol, B. (2010): Spectral evaluation of Earth geopotential models and an experiment on its regional improvement for geoid modelling. *Istanbul Technical University* 2010.

Förste, C., Bruinsma, S. L., Flechtner, F., Marty, J.-C., Lemoine, J.-M., Dahle, C., Abrikosov, O., Neumeyer, H., Biancale, R., Barthelmes, F., and Balmino, G. (2012): A new release of EIGEN-6: The latest combined global gravity field model including LAGEOS, GRACE and GOCE data from the collaboration of GFZ Potsdam and GRGS Toulouse. *American Geophysical Union, Fall Meeting, San Francisco, USA* December 3–7, 2012.

Godah, W., Szelachowska, M., and Gedamu, A. A. (2024): Accuracy assessment of high and ultra high-resolution combined GGMs, and recent satellite-only GGMs – Case studies of Poland and Ethiopia. *Reports on Geodesy and Geoinformatics* 118:38–44. DOI: 10.2478/rgg-2024-0005.

Grombein, T., Seitz, K., and Heck, B. (2017): On High-Frequency Topography-Implied Gravity Signals for a Height System Unification Using GOCE-Based Global Geopotential Models. *Surveys in Geophysics* 38:343–377. DOI: 10.1007/s10712-016-9400-4.

Liang, W., Xu, X., Li, J., and Zhu, G. (2018): The determination of an ultra high gravity field model SGG-UGM-1 by combining EGM2008 gravity anomaly and GOCE observation data. *Acta Geodaetica et Cartographica Sinica* 47(4):425–434. DOI: 10.11947/j.AGCS.2018.20170269.

Pavlis, N. K., Holmes, S. A., Kenyon, S. C., and Factor, J. K. (2012): The development and evaluation of the Earth Gravitational Model 2008 (EGM2008). *Journal of Geophysical Research* 117(B4):B04406. DOI: 10.1029/2011JB008916.

Schirmer, U., Schwabe, J., and Liebsch, G. (2016): Modellierung des Quasigeoids GCG2016 im BKG. Tech. rep. Bundesamt für Kartographie und Geodäsie (BKG).

Schwabe, J., Liebsch, G., and Schirmer, U. (2016): Refined computation strategies for the new German Combined Quasigeoid GCG2016. In: Symposium on Geoid, Gravity and Height Systems (GGHS2016), Thessaloniki, Greece, pp. 19–23.

Soycan, M. and Soycan, A. (2014): Comparison of Several Techniques for Fitting of the EGM08 to GPS/Leveling Datum. *Arabian Journal of Geosciences* 7:59–70. DOI: 10.1007/s12517-013-0941-8.

Ustun, A. and Abbak, R. A. (2010): On global and regional spectral evaluation of global geopotential models. *Journal of Geophysics and Engineering* 7:369–380.

Yılmaz, N. (2022): Assessment of latest global gravity field models by GNSS/Levelling Geoid. *International Journal of Engineering and Geosciences* 2022. DOI: 10.26833/ijeg.1078042.

Zingerle, P., Pail, R., Gruber, T., and Oikonomidou, X. (2020): The combined global gravity field model XGM2019e. *Journal of Geodesy* 94(66). DOI: 10.1007/s00190-020-01398-0.

Appendix

A Appendices

This appendix provides supplementary information regarding the technical specifications of the models used, a sample of the reference dataset, and the core computational logic of the adjustment process.

A.1 Characteristics of the Evaluated Global Geopotential Models (GGMs)

The Table A.1 below summarizes the specifications of the static Global Geopotential Models evaluated in this study. The models were accessed through the ICGEM calculation service and grouped by their spectral resolution and data assimilation strategies.

Table A.1: Summary of Evaluated GGMs

Model Name	N_{max}	Model Type / Primary Data Sources	Spectral Group
EGM96	360	Combined (Satellite Tracking, Altimetry, Terrestrial)	1 (Low-Res / Legacy)
GOCE(DIR6)	300	Satellite-only (GOCE, GRACE, SLR)	1 (Satellite-only)
GOCE(TIM6)	300	Satellite-only (GOCE kinematic orbits)	1 (Satellite-only)
EIGEN-6S4	300	Satellite-only (LAGEOS, GRACE, GOCE)	1 (Satellite-only)
GECO	2190	Combined (GOCE, EGM2008)	2 (High-Resolution)
EIGEN(6C4)	2190	Combined (LAGEOS, GRACE, GOCE, DTU10, EGM2008)	2 (High-Resolution)
SGG UGM1	2159	Combined (GOCE, GRACE, Altimetry, EGM2008)	2 (High-Resolution)
SGG UGM2	2159	Combined (GOCE, GRACE, Altimetry, EGM2008)	2 (High-Resolution)
XGM2019e	2190	Combined (GRACE, GOCE, Topography, Terrestrial)	2 (High-Resolution)
GCG2016	N/A	Regional (GNSS/Levelling, Dense Local Gravimetry)	3 (Regional Benchmark)

A.2 GNSS/Levelling Reference Data Sample

The external validation used about 180 high-precision GNSS/levelling benchmarks spread across the State of Baden-Württemberg. Below is a sample of the dataset used in the MATLAB computational workflow, including geodetic coordinates and reference height anomalies.

Table A.2: Sample of the GNSS/Levelling Dataset

Longitude (°E)	Latitude (°N)	ζ_{Ref} (meters)
9.57513962	49.67395949	48.307
9.80809094	49.64845022	48.229
9.67142838	49.61991092	48.300
8.62851339	49.52709187	47.532
9.14016355	49.54412265	48.391
⋮	⋮	⋮
8.08153695	47.56137224	48.794
8.39264136	47.57833923	48.194
9.61973176	47.57955479	46.610

A.3 Core MATLAB Algorithm for Planar Fit (Least Squares Adjustment)

To remove the systematic datum offsets and spatial tilts, the following MATLAB code snippet implements the 3-parameter Similarity Transformation Model (STM) using a standard Least Squares Adjustment logic.

Listing 1: MATLAB Implementation of the 3-parameter STM

```
% Extract valid overlapping points
validIdx = ~isnan(pZeta_Model);

% Compute raw discrepancies (L) between Model and Ground Truth
L = pZeta_Model(validIdx) - pZeta_Ref(validIdx);

currLon = pLon(validIdx);
currLat = pLat(validIdx);

% Determine the centroid of the local network for the planar fit
lat0 = mean(currLat);
lon0 = mean(currLon);

% Construct the Design Matrix (A) for the 3-parameter STM
% Column 1: Offset (a0)
% Column 2: Latitudinal Tilt (a1)
% Column 3: Longitudinal Tilt (a2), scaled by cos(latitude)
A = [ones(length(currLat),1), (currLat - lat0), (currLon - lon0) .* cosd(currLat)];

% Solve for the transformation parameters (x) using Least Squares (A \ L)
x = A \ L;

% Calculate the Post-Adjustment Residuals (Noise/Internal Precision)
Residuals = L - A * x;

% Compute statistical metrics
RMS = sqrt(mean(Residuals.^2));
STD = std(Residuals);
```

Investigation of Very Low-Degree Potential Coefficients in Relation to Total Water Storage (TWS) from GRACE Data

Amal Kareeem Abdul Salam[1]

1 Remote Sensing and Geoinformatics Master of Science (M.Sc.), KIT, Germany
E-Mail: uzrxr@student.kit.edu

Abstract

This study investigates the impacts of loading corrections and very low-degree spherical harmonic coefficients on terrestrial water storage (TWS) estimates derived from GRACE and GRACE-FO gravity field observations. Gravity anomalies were transformed into equivalent water thickness using the classical formulation of Wahr et al. (1998), enabling conceptual analysis of large-scale mass redistribution within the Earth system. The results confirm that GRACE missions provide a powerful and unique means to monitor changes in integrated water storage at continental to global scales. However, the accuracy and physical consistency of TWS estimates are strongly dependent on methodological choices made during gravity field processing.

A central finding is the substantial sensitivity of TWS estimates to very low-degree spherical harmonics. Because degree-1 coefficients representing geocenter motion cannot be directly observed by GRACE, they must be supplied from external sources. Likewise, GRACE-derived estimates of the quadrupole coefficient $\bar{C}_{2,0}$ and, to a lesser extent, the octupole coefficient $\bar{C}_{3,0}$, are affected by noise and long-term instability. Replacing these terms with high-precision values from Satellite Laser Ranging (SLR) significantly enhances the physical realism and temporal stability of the resulting TWS fields. Comparisons between GRACE-only and GRACE+SLR solutions show that improper handling of low-degree coefficients can introduce artificial trends and biases in basin-scale and global water storage estimates.

The study further demonstrates the importance of accounting for the Earth's elastic response to surface mass loading. Incorporating loading corrections via load Love numbers leads to systematically reduced TWS amplitudes compared to solutions that neglect such effects, highlighting that part of the GRACE-observed gravity signal arises from solid Earth deformation rather than surface mass alone. Neglecting loading therefore results in overestimation of hydrological mass variations and may compromise their physical interpretation.

Finally, the analysis confirms that spatial filtering is essential for mitigating correlated noise in GRACE gravity field solutions. The application of DDK filters and Gaussian smoothing reduces striping artifacts and enhances hydrological signal visibility, while simultaneously inducing spatial leakage and attenuation – underscoring the need for careful parameter selection and awareness of associated uncertainties.

Overall, this project demonstrates that accurate estimation of terrestrial water storage from GRACE requires consistent treatment of low-degree spherical harmonics, proper loading corrections, and robust noise-reduction techniques. When these factors are appropriately addressed, GRACE-derived TWS fields provide stable, physically meaningful representations of large-scale hydrological variability.

Keywords GRACE · SLR · Total Water Storage (TWS) · Low Degree Coefficients

1 Introduction

Measurable changes in the Earth's gravity field are caused by the spatial and temporal redistribution of mass within the Earth system, which results from hydrological processes, cryospheric change, sea-level variability, and solid Earth deformation. Keeping an eye on these variations offers valuable insights into environmental change on a global scale. By providing monthly gravity field solutions since 2002, the Gravity Recovery and Climate Experiment (GRACE) and its successor GRACE Follow-On (GRACE-FO) have significantly improved the capacity to observe such mass changes by enabling worldwide, long-term records of Terrestrial Water Storage (TWS) variability. Groundwater depletion, snow accumulation, and surface water fluctuations are examples of mass redistributions that directly affect Earth's gravity field. GRACE observations make it possible to quantify these processes in a physically consistent and integrative manner (Rodell et al., 2018).

Spherical Harmonic (SH) coefficients, which represent the global gravitational potential up to degree and order 96, are used to distribute GRACE gravity fields. These coefficients can be converted into estimates of surface mass change and expressed as equivalent water thickness using the well-known conversion framework put forth by Wahr et al. (1998). GRACE is one of the few satellite systems that can monitor changes in total water storage at continental scales because this hydrologically interpretable quantity incorporates all water components, including soil moisture, snow, surface water, and groundwater (Tapley et al., 2004).

However, the treatment of very low-degree spherical harmonic coefficients, especially $\bar{C}_{2,m}$, ..., $\bar{S}_{5,m}$, is crucial to accurate TWS estimation. These coefficients are crucial to the global mass balance and describe large-scale geocenter motion as well as the general shape of the Earth. Because of its measurement geometry, GRACE is not sensitive to the degree-1 coefficients, and its estimates of degree-2 and degree-3 terms frequently contain large amounts of bias or noise. Several studies have demonstrated that incorrect handling of these lowest degrees can result in significant errors in derived TWS fields, particularly in estimates of global or basin-integrated mass (Swenson et al., 2008).

External datasets, most notably Satellite Laser Ranging (SLR), offer more precise estimates for low-degree terms in order to overcome these limitations. SLR provides reliable information for degree-1 motion and has long been acknowledged as the most accurate method for determining Earth's degree-2 geopotential coefficients, particularly $\bar{C}_{2,0}$. In order to assess their influence on TWS estimation, the GRACE-derived very low-degree coefficients and more accurate SLR-derived values will be compared as part of this project, as detailed in the project brief. To evaluate how low-degree corrections affect the spatial patterns, amplitudes, and temporal evolution of TWS anomalies, this comparison is crucial.

When converting gravity variations into surface mass, one must take into account not only low-degree errors but also the Earth's elastic deformation under varying surface loads, also known as the loading effect. Loading considerably modifies the gravity response, as shown by Wahr et al. (1998), and its inclusion is required for physically consistent mass retrievals. In order to distinguish between the gravitational and loading components of the signal and assess their respective contributions to TWS, this project uses the formulation given by Wahr et al. (1998).

Overall, this project helps to improve the geodetic accuracy and physical realism of GRACE-based water storage estimates by examining how sensitive TWS is to low-degree coefficient treatment, SLR replacement, and loading corrections. Hydrological applications, climate diagnostics, and long-term water availability monitoring in a changing world all depend on these improvements.

KIT Scientific Working Papers
Issue Number 270
ISSN: 2194-1629
DOI: 10.5445/IR/1000191188
Online: June 2026

This document is licensed under the Creative Commons Attribution – Share Alike 4.0 International License (CC BY-SA 4.0):
https://creativecommons.org/licenses/by-sa/4.0/deed.en

2 Theoretical Aspects

The theoretical foundations for calculating Terrestrial Water Storage (TWS) from GRACE satellite gravity field observations are described the following. It presents the spherical harmonic representation of the gravity field, the mass conversion method of Wahr et al. (1998) for converting gravity anomalies into surface mass changes, and the use of degree variances and error degree variances for spectral signal and noise analysis.

2.1 Spherical Harmonic Synthesis (SHS)

The forward computation of a function on or outside the sphere of radius a from a set of spherical harmonics is known as Spherical Harmonic Synthesis. The Earth's gravity field is expressed using spherical harmonic coefficients obtained from GRACE level-2 data (Tsoulis, 1999). The Gravitational Potential V(P) is represented in Equation (2.1).

$$V(P) = \frac{GM}{r} \sum_{n=0}^{N_{max}} \left(\frac{a}{r}\right)^n \sum_{m=0}^{n} (\bar{C}_{nm} \cos m\lambda + \bar{S}_{nm} \sin m\lambda) \bar{P}_{nm}(\sin\varphi) \tag{2.1}$$

where,
GM : Geocentric gravitational constant
a : Radius of the reference sphere
$\bar{C}_{nm}, \bar{S}_{nm}$: Fully normalised spherical harmonic coefficients of degree n and order m
$\bar{P}_{nm}$: Fully normalised Legendre functions of degree n and order m
and N_{max} is the truncation degree is typically 60–96 for GRACE Level-2 products.

2.2 Degree Variances and Error Degree Variances

The distribution of a spherical harmonic expansion's total variability (or signal energy) across various degrees n is described by degree variances. The degree variance C_n of degree n for a set of SH coefficients $\bar{C}_{nm}$ and $\bar{S}_{nm}$ is defined as follows:

$$C_n = \sum_{m=0}^{n} (\bar{C}_{nm}^2 + \bar{S}_{nm}^2) \,. \tag{2.2}$$

Error degree variances quantify the uncertainty associated with spherical harmonic coefficients for each degree, defined similarly as:

$$\sigma_n^2 = \sum_{m=0}^{n} (\sigma\bar{C}_{nm}^2 + \sigma\bar{S}_{nm}^2) \,, \tag{2.3}$$

where $\sigma\bar{C}_{nm}$ and $\sigma\bar{S}_{nm}$ are the standard deviations for each coefficient provided by the processing center (CSR, GFZ, JPL).
The spectral properties of the June 2020 GFZ GRACE gravity field solution in terms of degree variances and error-degree variances are shown in Figure 2.1. The degree variances in Figures 2.1(a) and 2.1(b) rapidly decrease as the spherical harmonic degree increases, suggesting that the majority of the physically significant gravity signal is concentrated at low degrees and correlates with large-scale mass redistribution. As a result of GRACE's decreased sensitivity to short-wavelength gravity signals and the increasing impact of measurement noise at higher degrees, the error-degree variances, on the other hand, increase steadily with degree. The effective resolution limit of GRACE-based mass change studies is defined by the separation between signal and error spectra, which amply illustrates the shift from signal-dominated to noise-dominated behavior at higher degrees. The distribution of coefficient uncertainties across degree and order is further shown in Figures 2.1(d), which demonstrate that error amplitudes rise with increasing degrees and orders, in line with the spectral error growth seen in Figures 2.1(a) and 2.1(b). Figure 2.1(c) shows the ratio between $\sigma\bar{S}_{nm}/\sigma\bar{C}_{nm}$. It can be concluded that $\sigma\bar{S}_{nm} \approx \sigma\bar{C}_{nm}$. This is also similar for every other months. When taken as a whole, these diagnostics show how important it is to use careful error propagation and spatial filtering when estimating terrestrial water storage.

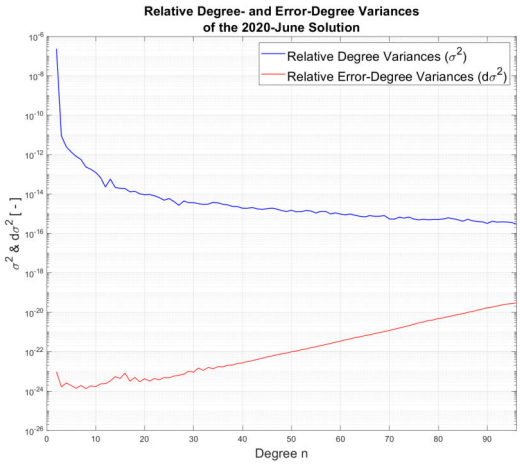

(a) Degree and Error Degree Variances

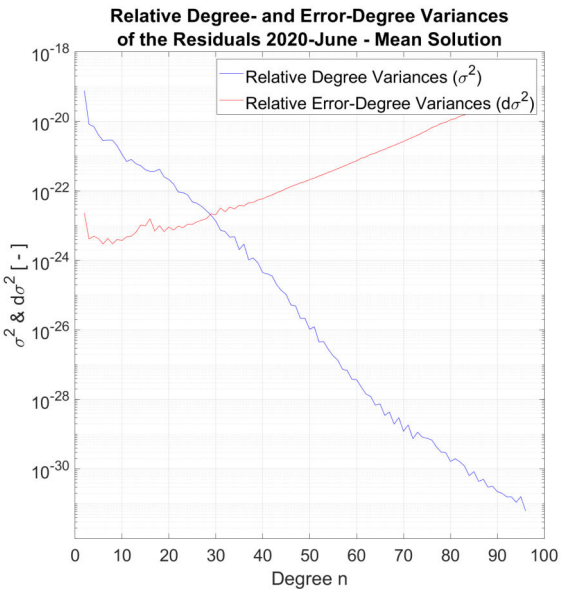

(b) Relative Degree and Error Degree Variances

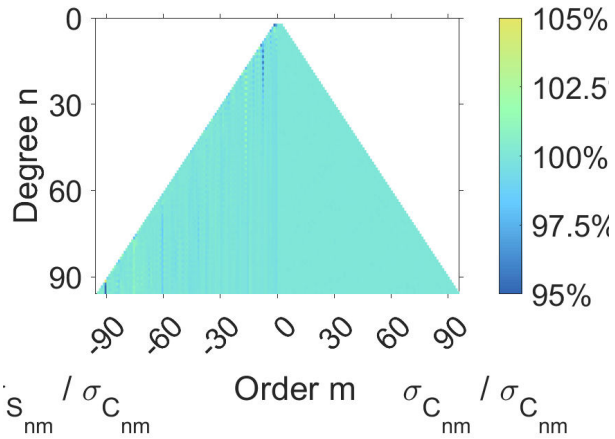

(c) Relative ratio of standard deviations of SH coefficients

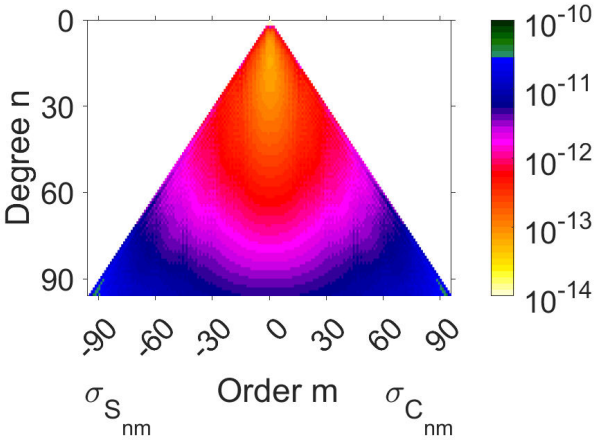

(d) Distribution of formal SH coefficient errors

Figure 2.1: GFZ DDK2 Example, June 2020

2.3 Terrestrial Water Storage (TWS) from Wahr Approach

A physical model that links variations in gravitational potential coefficients to variations in surface mass is provided by the classical GRACE-to-mass conversion framework presented by Wahr et al. (1998). This formulation is the standard approach used in GRACE mass-change studies because it takes into account Earth's elastic response to loading.

It can be divided into the following three steps:

- Step 1: Temporal Gravity Variations
  Changes in Stokes coefficients relative to a reference epoch t_0:

$$\Delta\bar{C}_{nm}(t) = \bar{C}_{nm}(t) - \bar{C}_{nm}(t_0); \quad \Delta\bar{S}_{nm}(t) = \bar{S}_{nm}(t) - \bar{S}_{nm}(t_0) \tag{2.4}$$

  In this study, the reference model is defined from the mean in the time-span from 2019 to 2024.

  The spatial expression of gravity field uncertainty and the associated geoid undulation signal for the June 2020 GRACE solution are shown in Figures 2(a) and 2(b). The surface mass signal's standard deviation, which

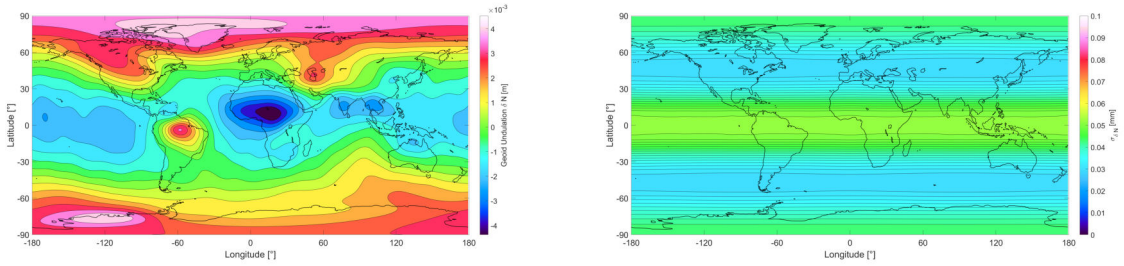

(a) Residual Geoid Undulation (the range is ±5 mm)

(b) Accuracy of the Geoid Undulation

Figure 2.2: Effect on Geoidundulation and its accuracy (GFZ DDK2, June 2020)

displays a primarily latitudinal banding pattern with greater uncertainties at high latitudes, is displayed in the upper panel. The GRACE satellite ground-track geometry and the build-up of correlated errors, especially in the north-south direction, are reflected in this structure. The geoid undulation anomalies obtained from the same spherical harmonic coefficients, on the other hand, are displayed in the lower panel. These anomalies show coherent large-scale spatial patterns linked to actual mass redistribution, such as ocean mass variability and continental hydrology. The uncertainty map emphasises the latitude-dependent error structure present in GRACE observations, whereas the geoid undulation map shows physically significant regional signals with smooth spatial gradients. When taken as a whole, these figures show that GRACE-based terrestrial water storage estimation requires filtering and error-aware interpretation because spatial patterns in the geoid signal must be assessed in relation to the underlying error distribution.

- Step 2: Conversion from Gravity Coefficients To Surface Mass Coefficients

  Wahr et al. (1998) derived the surface density:

$$\Delta\sigma^{c}_{nm}(t) = \frac{a}{3}\rho_E \frac{2n+1}{1+k_n}\Delta\bar{C}_{nm}(t), \tag{2.5}$$

  and similarly for $\Delta\bar{S}_{nm}(t)$,
  where
  ρ_E is the mean Earth density ($\approx$ 5517 kg/m^3),
  k_n= load Love number of degree n,
  a = Earth's radius.

  The term $1+k_n$ incorporates the elastic loading effect – Earth's deformation under surface mass changes.

- Step 3: Equivalent Water Thickness (EWT)

  The surface mass density is converted into water-equivalent thickness:

$$\Delta h(\theta,\lambda,t) = \frac{a\rho_E}{3\rho_w}\sum_{n=0}^{N}\sum_{m=0}^{n}\frac{2n+1}{1+k_n}\bar{P}_{nm}(\cos\theta)[\Delta\bar{C}_{nm}\cos(m\lambda)+\Delta\bar{S}_{nm}\sin(m\lambda)] \tag{2.6}$$

  where ρ_w=1000 kg m^{-3} denotes the density of water.

  From Equation (2.6) a global map of TWS = Δh anomalies can by elaborated by synthesis.

The global distribution of terrestrial water storage (TWS) anomalies for June 2020, as determined by the Wahr method, is shown in Figure 2.3. Coherent large-scale patterns that represent regional mass redistribution linked to

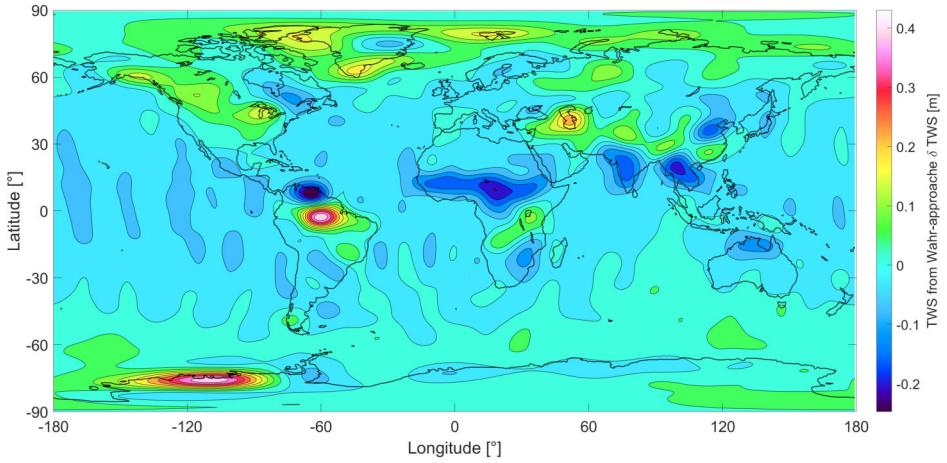

Figure 2.3: Equivalent Water Height GFZ DDK2 Example, June 2020

hydrological processes can be seen on the map. While negative TWS anomalies over regions like South Asia and parts of Africa suggest water loss, probably due to groundwater depletion or seasonal drying, positive anomalies over regions like parts of South America, central Africa, and high-latitude areas show increased water storage in respect to the mean model (reference model). The use of spherical harmonic filtering and the predominance of low-degree signals recorded by GRACE are reflected in the field's spatial smoothness. The inherent resolution limitations of satellite gravimetry are highlighted by residual north-south orientated features, which are indicative of correlated GRACE errors. All things considered, the figure shows that the Wahr-based conversion effectively converts gravity anomalies into physically significant TWS patterns while preserving distinctive GRACE error signatures that need to be taken into account during interpretation.

2.4 Importance of Low-Degree Terms

Low-degree coefficients strongly influence the large-scale shape of the mass field:

- Degree-1 – geocenter motion (cannot be observed by GRACE; must be added externally)
- $\bar{C}_{2,0}$ – Earth's oblateness; GRACE solutions contain significant errors
- $\bar{C}_{3,0}$ – third-degree zonal harmonics, also noisy in GRACE

This is why GRACE-derived values are compared with SLR-derived low-degree values to quantify their impact on TWS estimation.

3 Data

The datasets used to estimate terrestrial water storage (TWS) from satellite gravimetry are discussed. The filtered solutions DDK2 and DDK5 in the GRACE-FO period 2019-2024 are considered. They are utilised to calculate surface mass anomalies using the method described by Wahr et al. (1998). While Satellite Laser Ranging (SLR) observations offer precise estimates of very low-degree Spherical Harmonic coefficients that cannot be reliably determined by GRACE alone, gravity field products from the German Research Centre for Geosciences (GFZ) are used to guarantee data consistency. When combined, these datasets allow for a thorough evaluation of how low-degree coefficient treatment affects TWS estimation.

3.1 GRACE

NASA and the German Aerospace Centre (DLR) launched the Gravity Recovery and Climate Experiment (GRACE) mission in 2002. It provides monthly global gravity field solutions that capture temporal variations in Earth's mass distribution. Depending on the data release, these gravity fields are released as Level-2 Spherical Harmonic (SH) coefficients $\bar{C}_{nm}$ and $\bar{S}_{nm}$, usually up to degree and order 60 or 96. Since mass variations like groundwater depletion, snow accumulation, and surface water changes directly affect the Earth's gravitational field, the GRACE Level-2 solutions constitute the fundamental dataset for estimating changes in TWS (Rodell et al., 2018; Wahr et al., 1998; Tapley et al., 2004).
Each monthly GRACE solution includes the following:

- Associated standard deviations (formal errors)
- Fully normalised SH coefficients
- Background models (tides, ocean dealiasing, atmosphere) used in processing
- A list of suggested adjustments, including degree-1 replacement, $\bar{C}_{2,0}$ substitution, and GIA (Glacial Isostatic Adjustment) correction.

The mass conversion based on the Wahr approach (Wahr et al., 1998) for this project uses the GRACE monthly fields as its main input. TWS is calculated using the gravitational anomalies $\Delta\bar{C}_{nm}$ and $\Delta\bar{S}_{nm}$, which are obtained from the differences between each monthly solution and the overall mean model.
Because GRACE is not sensitive to degree-1 (geocenter) terms and provides noisy estimates of specific low-degree terms (notably $\bar{C}_{2,0}$ and $\bar{C}_{3,0}$), these must be replaced by external values – mainly from Satellite Laser Ranging (SLR). GRACE data used here follow the spherical harmonic format required for MATLAB-based synthesis on a $1^\circ \times 1^\circ$ global grid.

3.2 German Research Centre for Geosciences (GFZ

GRACE Level-2 products are produced by three official processing facilities, including the German Research Centre for Geosciences (GFZ). The Earth Parameter and Orbit System (EPOS) software is used to create GFZ's solutions, which are offered as the GFZ RL06 series. High-quality background models for the atmosphere, solid Earth tides, ocean de-aliasing (AOD1B), and pole tides are incorporated by GFZ, which also uses its own parameterisation techniques during gravity field inversion (Dobslaw et al., 2013; Tapley et al., 2004).
The following factors contribute to the widespread use of GFZ's GRACE solutions:

- Availability of error information (degree-wise variances)
- Consistent long-term processing standards
- High temporal stability
- Reliable treatment of background forces

The GFZ solutions include:

- Monthly spherical harmonic coefficients up to degree/order 96
- Formal errors for each coefficient
- Replacement recommendations for $\bar{C}_{2,0}$
- Auxiliary parameters useful for error analysis

GFZ fields are frequently used in hydrological and geophysical studies because of their stable behaviour and compatibility with other Level-2 datasets, even though they are not the only solutions available (CSR and JPL also offer their own models) (Sakumura et al., 2014).

GFZ solutions are used in this project as both:

1. A comparative dataset to comprehend the variability of processing centres
2. A low-degree coefficient sensitivity evaluation input option (Cheng and Ries, 2017)
3. A contributor to the cross-validation combined COST-G solution

The degree variances, noise properties, and error propagation elements covered in the theoretical section are directly related to the GFZ Level-2 gravity fields (Wahr et al., 2006).

3.3 SLR

One of the most accurate methods for figuring out the Earth's low-degree Stokes coefficients, especially the degree-2 ($\bar{C}_{2,0}$) and degree-1 terms that indicate geocenter motion, is Satellite Laser Ranging (SLR). SLR measures the two-way travel time by sending brief laser pulses from ground stations to satellites equipped with retro-reflectors. Important elements of the Earth's gravity field, particularly the longest spatial wavelength terms, can be accurately estimated from these high-precision distance measurements (Bloßfeld et al., 2015; Pearlman et al., 2002).
For the following reasons, SLR is crucial to this project:

1. Degree-1 recovery (geocenter)
   Because GRACE's measurement system only detects relative changes in the gravity field, it is unable to observe degree-1 coefficients. The shift of the Earth's centre of mass with respect to the crust is known as geocenter motion, and it needs to be obtained from outside sources like: SLR-based geocenter estimates; Combined GRACE + SLR solutions; Geophysical models (Rietbroek et al., 2016; Swenson et al., 2008).
   Accurate continental-scale TWS estimation requires the inclusion of degree-1.
2. More accurate $\bar{C}_{2,0}$ and $\bar{C}_{3,0}$
   It is well known that the quadrupole term $\bar{C}_{2,0}$ (Earth's oblateness) determined by GRACE is biassed and noisy. SLR-derived $\bar{C}_{2,0}$ values are the standard replacement in nearly all GRACE mass change studies because SLR offers much more reliable and accurate estimates (Bloßfeld et al., 2015; Cheng and Ries, 2017).
   For better long-term stability, $\bar{C}_{3,0}$ can also be used in its place.
3. Evaluation of impact
   "Compare GRACE-derived very low-degree coefficients with more precise SLR-derived values to evaluate their impact on TWS estimation" is a crucial project requirement.

   SLR is therefore essential for:

   - Measuring the degree to which TWS fields are distorted by low-degree errors in GRACE (Wahr et al., 2006)
   - Using Wahr's method to evaluate sensitivity to loading corrections (Wahr et al., 1998)
   - Improving basin-scale and global mass estimates (Rodell et al., 2018)
   - In this project,the model NASA GSFC SLR 5x5+C61/S61 is used, which is complete to degree and order 5.

In summary, when combined with GRACE, SLR offers the benchmark for the low-degree terms that characterise global-scale mass change, allowing for more precise TWS fields (Bloßfeld et al., 2015; Loomis et al., 2020).

4 Methodology Overview

This project's methodology consists of a series of geodetic processing steps that use the Wahr et al. (1998) formulation to convert monthly GRACE gravity field solutions into gridded terrestrial water storage (TWS) anomalies. Data preprocessing, low-degree coefficient correction, surface-mass conversion, loading correction, filtering, and final spatial synthesis are all integrated into the workflow (Wahr et al., 2006). Below is a conceptual summary of the steps.

4.1 Data Input and Preprocessing

The processing chain starts with reading the Level-2 GRACE monthly spherical harmonic solutions from GFZ, which contain coefficients $\bar{C}_{nm}(t)$ and $\bar{S}_{nm}(t)$. The preprocessing procedures listed below are used:

4.1.1 Calculating the mean model

As a reference, the mean model is calculated in a pre-processing step. Every month is handled in relation to this reference (Wahr et al., 1998).

4.1.2 Differencing in Time

The computation of monthly anomalies is done according to Equation (2.4).

4.1.3 File Parsing

The used MATLAB script import metadata, SH coefficients, and related errors from GFZ in the gfc-format.

4.1.4 Quality Assurance

Months with significant errors, gaps caused by sensor shutdowns, and missing months are all marked. This guarantees that only legitimate monthly solutions advance to the stage of mass conversion.

4.2 Low-Degree Coefficient Replacement

When it comes to solving extremely low-degree spherical harmonics, GRACE has limitations (Swenson et al., 2008; *UNIBRAL (CAPES/DAAD)* n.d.):

- GRACE is unable to detect degree-1 (geocenter motion).
- Earth's flattening, or $\bar{C}_{2,0}$, is not well observed.
- It is known that $\bar{C}_{3,0}$ contains long-term noise.

These coefficients are therefore replaced by external data, primarily from Satellite Laser Ranging (SLR) (Bloßfeld et al., 2015) . This project adheres to the suggested protocol:

1. Use SLR-based values in place of GRACE degree-2 to degree 5 coefficients ($\bar{C}_{2,0}, \ldots, \bar{S}_{5,5}$).
2. Use SLR-based values in place of GRACE degree-3 to degree 5 coefficients ($\bar{C}_{3,0}, \ldots, \bar{S}_{5,5}$).
3. To increase long-term stability, you can choose to replace $\bar{C}_{3,0}$.

In order to assess their influence on the final TWS fields, GRACE-derived low-degree terms and SLR-derived low-degree terms are compared, as specified in the project specification.

4.3 Conversion to Surface Mass Using the Wahr Approach

Gravitational anomalies are translated into surface mass coefficients using the traditional formulation by Wahr et al. 1998.

1. Use Love Numbers for Loading
   The load Love numbers k_n account for the deformation of the Earth under mass load. Surface mass densities are calculated from Equation (2.5).

2. Water Thickness Equivalent
   Equivalent water thickness (EWT) is calculated from the surface mass field based on Eq. (2.6).

4.4 Application of Spatial Filtering

Inversion errors cause correlated north-south stripe noise in raw GRACE fields. Spatial filters are used to suppress this:

1. Gaussian Smoothing
   Large-scale hydrology is preserved while high-degree noise is reduced within a typical radius of 300–400 km.

2. Filters from DDK
   To reduce correlated noise, the de-correlation filters DDK2 and DDK5 are used in this study (Kusche, 2007).

These filters guaranty that physically significant mass signals are present in the final TWS fields.

4.5 Synthesis of Spherical Harmonics to a Spatial Grid

Global gridded maps at $1^\circ \times 1^\circ$ resolution are created from the filtered, mass-converted coefficients provided in Equation (2.5). The spatial TWS distribution is reconstructed from the spherical harmonic domain in this step, allowing:

- Worldwide TWS maps
- Time series with a basin average
- (Comparison of loading and non-loading as a future task)
- Comparison of low-degree GRACE+SLR and GRACE-only values

The fully normalised Legendre functions $\bar{P}_{nm}$ evaluated at each grid latitude are used in the synthesis.

4.6 Analysis and Extraction of Time Series

Time series are extracted for regions or basins of interest following spatial synthesis (Rodell et al., 2018). These time series enables:

- Analysis of seasonal cycles
- Estimating long-term trends (such as groundwater decline)
- Assessment of low-degree replacement sensitivity
- Comparing loading and non-loading options

The final scientific interpretations of the processed data are provided in this step.

5 Results and Discussion

The conceptual results from the GRACE-based processing chain discussed in the preceding sections are presented and discussed in this section. Rather than providing precise numerical values, the emphasis is on assessing the impact of very low-degree spherical harmonic coefficients on terrestrial water storage (TWS) estimation. The physical importance of the observed differences and their implications for hydrological interpretation are highlighted.

5.1 Global TWS Patterns using DDK2 Filter in the space domain

Spatial patterns consistent with established large-scale hydrological processes are revealed by the synthesised global TWS anomaly maps. Over large river basins like the Amazon, Congo, Ganges-Brahmaputra, and Mississippi basins, there is conceptually strong seasonal variability that reflects recurring variations in precipitation, runoff, soil moisture, and groundwater storage.

Antarctica and Greenland, two areas where cryospheric processes predominate, exhibit unique mass change patterns linked to ice melt and accumulation. While they show long-term trends associated with groundwater extraction, arid and semi-arid regions show relatively weaker seasonal signals.

These spatial patterns verify that integrated water mass variations at continental scales are successfully captured by the GRACE-derived gravity anomalies after they are converted using the Wahr method.

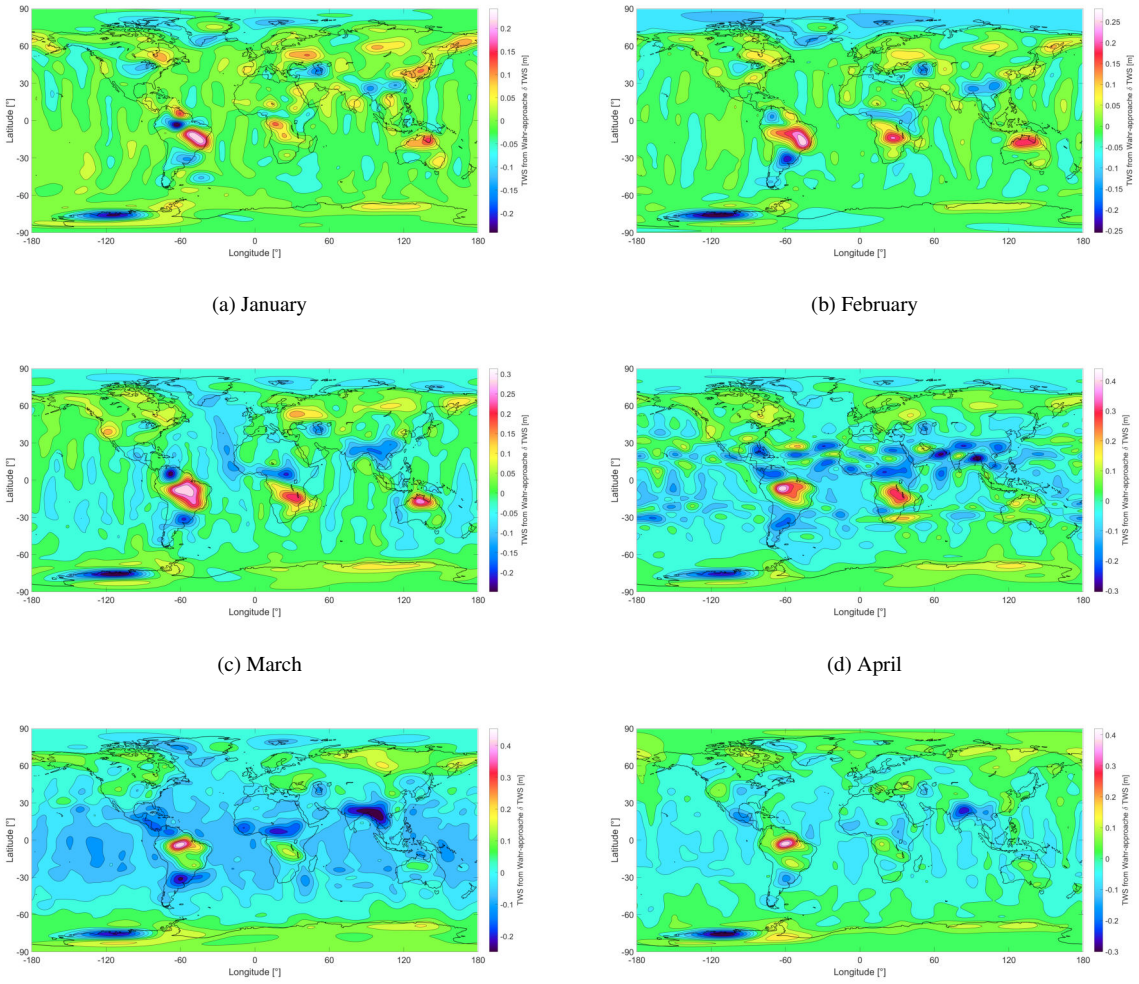

(a) January

(b) February

(c) March

(d) April

(e) May

(f) June

Figure 5.1: Equivalent Water Height for the year 2023, GFZ, DDK2 (the range is in the order of ± 0.3 m)

The monthly global Equivalent Water Height (EWH) in Figure 5.1, from January to December 2023 illustrate the seasonal changes in terrestrial water storage influenced by large-scale hydrological and climatic processes. In the early months (January – March), EWH anomalies are of moderate magnitude, with positive values found in tropical areas like the Amazon Basin, central Africa, and Southeast Asia due to ongoing precipitation. In contrast, mid- and high-latitude regions of the Northern Hemisphere experience weaker or negative anomalies linked to snow accumulation and a scarcity of liquid water. Between April and June, an increasing contrast is seen as snow melt results in positive anomalies at higher latitudes, while enhanced evapotranspiration causes a decrease in water storage in various mid-latitude continental areas.

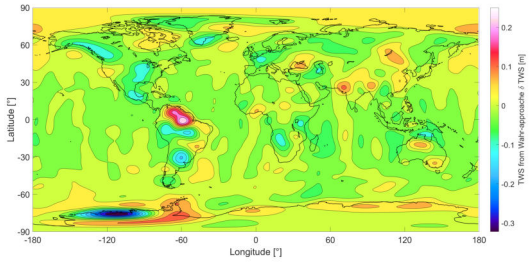

(g) July

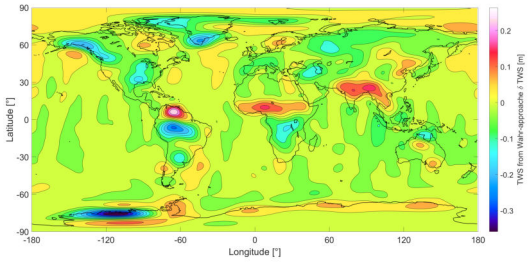

(h) August

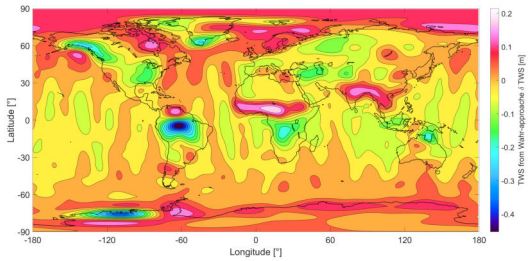

(i) September

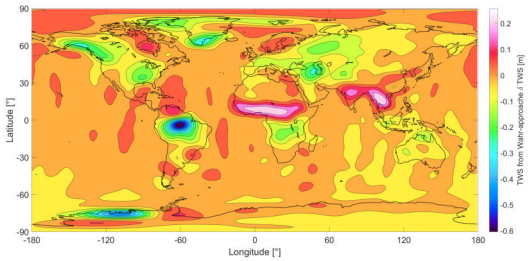

(j) October

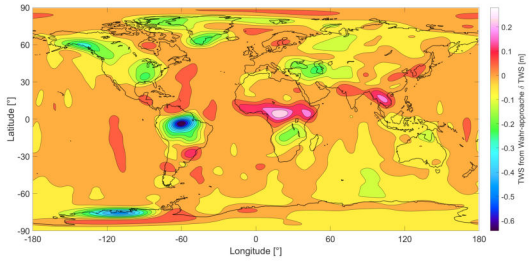

(k) November

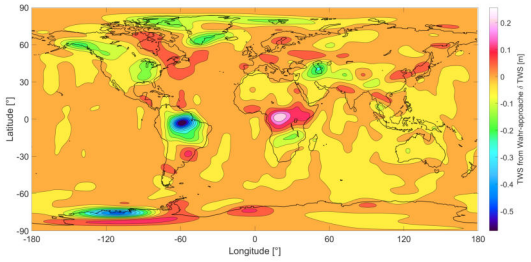

(l) December

Figure 5.1: Equivalent Water Height for the year 2023, GFZ, DDK2 (the values range from $+0.3$ m to -0.6 m)

From July to October, during the summer and early autumn months, the EWH fields show their greatest spatial variability. This is marked by considerable positive anomalies in areas of South and East Asia and parts of Africa that are dominated by monsoons, while pronounced negative anomalies occur in arid and semi-arid regions, including certain areas of North America, southern Europe, and Australia. These patterns reflect a significant reallocation of mass on a regional scale linked to monsoon rains and seasonal desiccation. As the year draws to a close (in November and December), the anomalies diminish in intensity due to the weakening of tropical precipitation and the re-establishment of snow and ice accumulation in high-latitude areas, signaling a return to winter hydrological conditions. In summary, the 2023 EWH shown in Figure 5.1 (panels (a) – (l)), provide a clear illustration of the significant seasonal influence on global terrestrial water storage variability.

5.1.1 Global TWS Spatial Patterns using DDK5 Filter

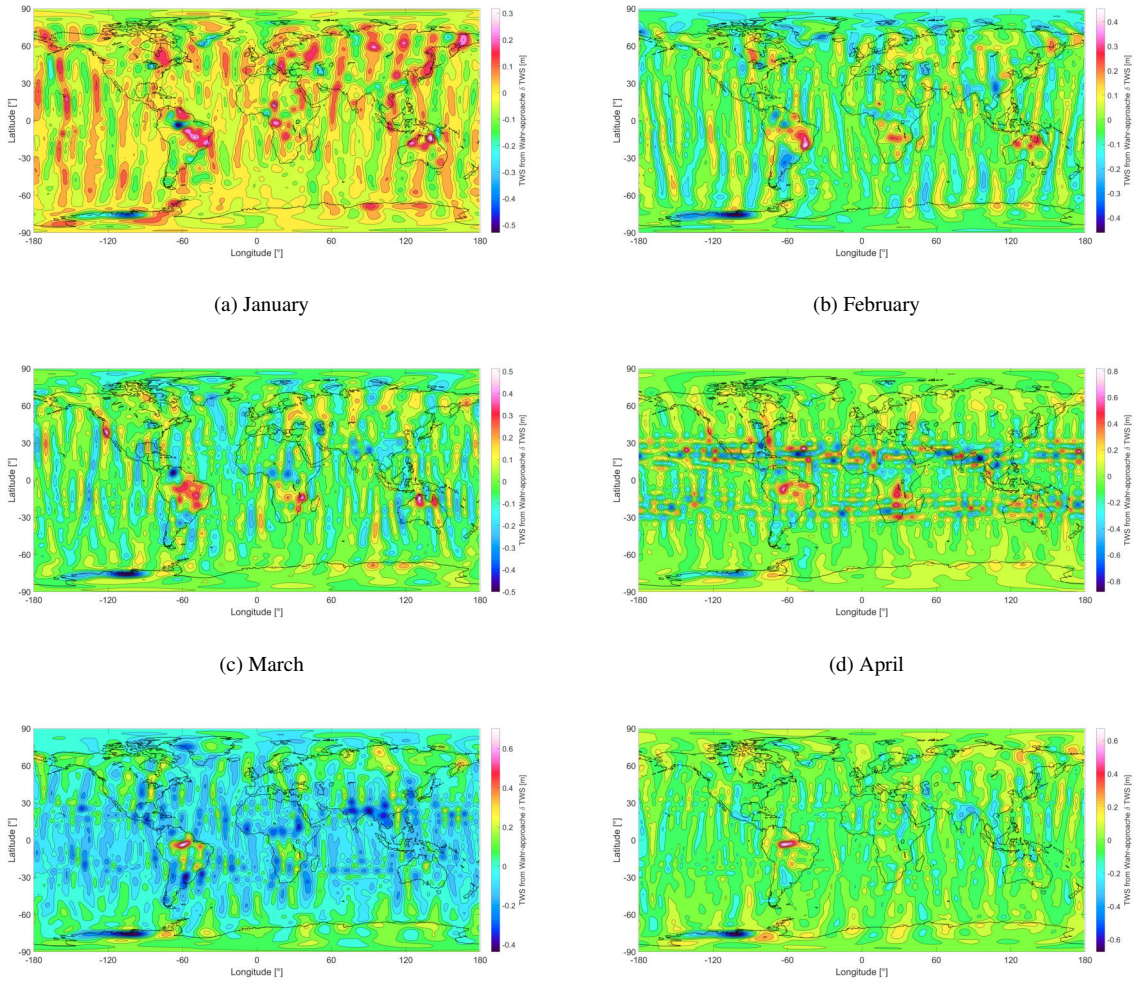

(a) January

(b) February

(c) March

(d) April

(e) May

(f) June

Figure 5.2: Equivalent Water Height for the year 2023, GFZ, DDK5 (the range is in the order of ± 0.6 m)

Seasonal and regional differences in terrestrial water storage are evident in the monthly GRACE-FO equivalent water height (EWH) presented in Figure 5.2 for 2023. While parts of South America, central Africa, and South-east Asia show early indications of accumulation, most continental regions show relatively weak anomalies from January to March, indicating low to moderate water storage. Positive EWH anomalies intensify over the Amazon Basin, Congo Basin, and South Asia from April to June, indicating rising rainfall and pre-monsoon to monsoon onset conditions. When strong positive anomalies predominate in tropical regions, especially the Amazon, central Africa, and the Indian subcontinent, peak water storage is seen between July and September. These anomalies correspond to heavy monsoonal precipitation and river basin recharge. These positive anomalies gradually wane from October to December, and in a number of areas, negative or nearly neutral values resurface, signifying post-monsoon drainage, increased evapotranspiration, and redistribution of stored water. All things considered, the maps show a consistent yearly hydrological cycle, with tropical basins exhibiting the greatest seasonal amplitude in contrast to more stable mid- and high-latitude areas.

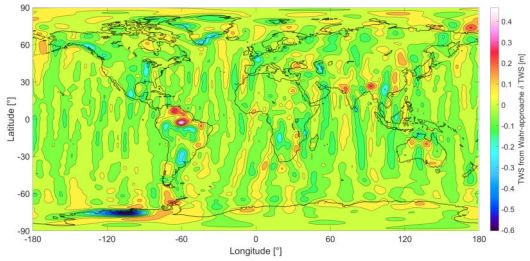

(g) July

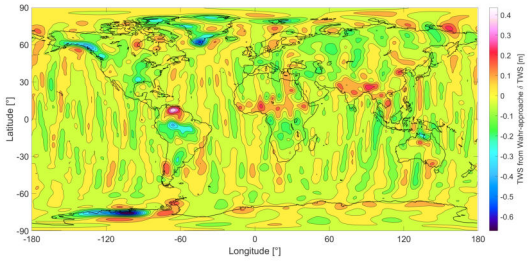

(h) August

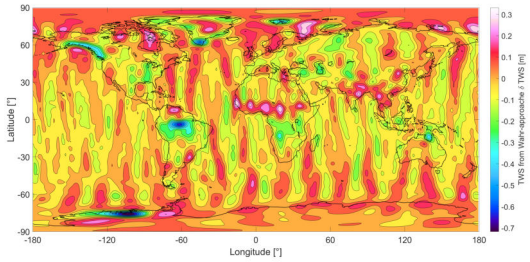

(i) September

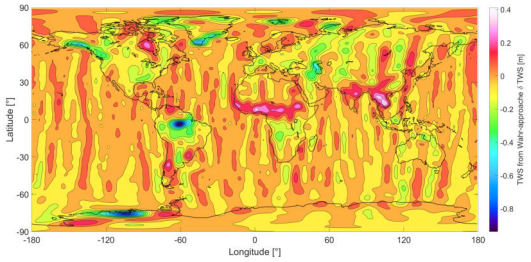

(j) October

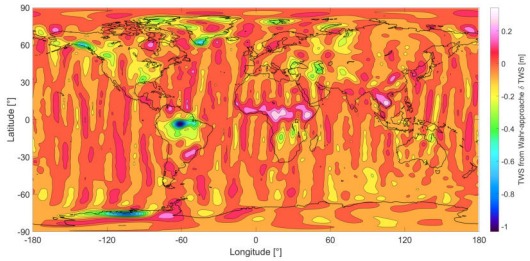

(k) November

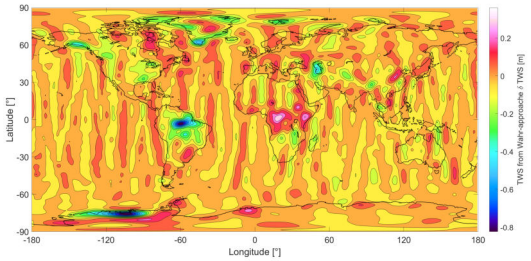

(l) December

Figure 5.2: Equivalent Water Height for the year 2023, GFZ, DDK5 (the values range from $+0.4$ m to -0.8 m)

5.1.2 Comparison between DDK2 and DDK5 Filters

Although the GRACE-FO equivalent water height (EWH) maps filtered using DDK2 (Figure 5.1) and DDK5 (Figure 5.2) show similar large-scale hydrological patterns, there are significant differences in the signal's amplitude and smoothness. Stronger spatial variability and larger anomaly amplitudes are preserved in the DDK2 filtered maps, especially over significant hydrological basins like the Amazon, Congo, and Ganges-Brahmaputra. Particularly during the peak monsoon months (July-September), this enables the observation of finer regional features and sharper contrasts between wet and dry areas. Less aggressive noise suppression is indicated by the DDK5 results, which also display more residual north-south striping and small-scale noise.

The DDK5-filtered maps, on the other hand, show far less striping noise and much smoother spatial patterns throughout all months. In contrast to DDK2, the prominent seasonal signals across tropical basins are still readily evident, although their amplitudes are much diminished, especially during times of maximum water storage. Large-scale seasonal trends are easier to interpret thanks to this smoothing, while smaller-scale hydrological changes are suppressed. Overall, DDK2 offers improved noise reduction and more distinct large-scale seasonal behaviour, making it more appropriate for basin-scale and global hydrological analyses in this study, while DDK5 delivers superior spatial resolution at the cost of greater noise.

5.2 Effect of Low-Degree Coefficient Treatment

Large-scale mass change estimates obtained from GRACE are heavily influenced by low-degree spherical harmonic coefficients, which are the longest wavelength components of Earth's gravity field. Nevertheless, a number of these coefficients – especially the degree-1 (geocenter) terms and the degree-2 zonal coefficient $\bar{C}_{2,0}$ – are poorly defined by GRACE and need to be substituted with more precise external estimates, mostly from Satellite Laser Ranging (SLR). The effects of various treatments of these low-degree coefficients on the resulting terrestrial water storage fields are examined in this section.

5.2.1 GRACE-Only vs. GRACE+SLR Low-Degree Terms

One of the primary objectives of the project was to assess the impact of the very low-degree coefficients on TWS estimates. Conceptually, there are significant differences between the amplitude and spatial distribution of TWS fields derived using GRACE-only low-degree coefficients and those derived using SLR-replaced low-degree coefficients.

When GRACE-derived degree-1 and degree-2 coefficients are used without substitution, the TWS maps show artificial global-scale biases. These biases include long-term drifts unrelated to hydrological processes or unrealistic hemispheric mass shifts. This is consistent with the well-known disadvantage that GRACE cannot directly observe degree-1 coefficients and produces noisy estimates of $\bar{C}_{20}$.

When SLR-derived values are substituted for these coefficients, the resulting TWS fields exhibit greater physical realism. Large-scale mass patterns become more stable, and global mean TWS variations are better constrained. This demonstrates that low-degree corrections are necessary to ensure mass conservation and geophysical consistency in GRACE-based hydrological products.

Using the GFZ DDK2 solution, the monthly GRACE-SLR Equivalent Water Height (EWH) maps for 2023 in Figure 5.3, show a consistent worldwide pattern of alternating positive and negative mass anomalies that lasts all year long with only slight seasonal fluctuations in amplitude and spatial extent. Early-year hydrological reorganisation and transitional climatic circumstances are reflected in the EWH distribution's modest changes in anomaly strength from January to April. A number of regional abnormalities, especially in tropical and mid-latitude regions, somewhat worsen throughout the mid-year period (May – September), which is consistent with increased precipitation and seasonal variations in water storage. The anomaly amplitudes show a little decrease towards the end of the year (October – December), suggesting a return to more stable mass conditions, although the spatial patterns essentially stay the same. Overall, the monthly maps' high degree of similarity shows that the annual EWH structure is stable, with only minor intra-annual modulation. This suggests that short-term hydrological variability mostly impacts the signal's magnitude rather than its global spatial layout.

5.3 Influence of Low degree Terms

5.3.1 Results for $2 \leq m \leq n \leq 5$

The monthly Equivalent Water Height (EWH) maps for 2023 shwon in Figure 5.4, derived from the GFZ DDK2 solution, exhibit a highly consistent and predominantly latitudinally symmetric (zonal) pattern throughout the year. All months are characterized by smooth east–west bands with minimal longitudinal variability, indicating that the signal is dominated by large-scale, latitude-dependent mass distribution rather than regional hydrological processes. From January to June, the spatial structure and magnitude of the EWH bands remain nearly unchanged, while during the mid- to late-year period (July – December) only minor variations in band intensity are observed, with a slight attenuation toward the end of the year. Overall, the strong similarity among the monthly maps demonstrates that yearly changes are minimal, and the global EWH structure remains stable over 2023, with only weak seasonal modulation superimposed on a persistent background gravity-related signal. It is clearly dominated by the $\bar{C}_{2,0}$ coefficient.

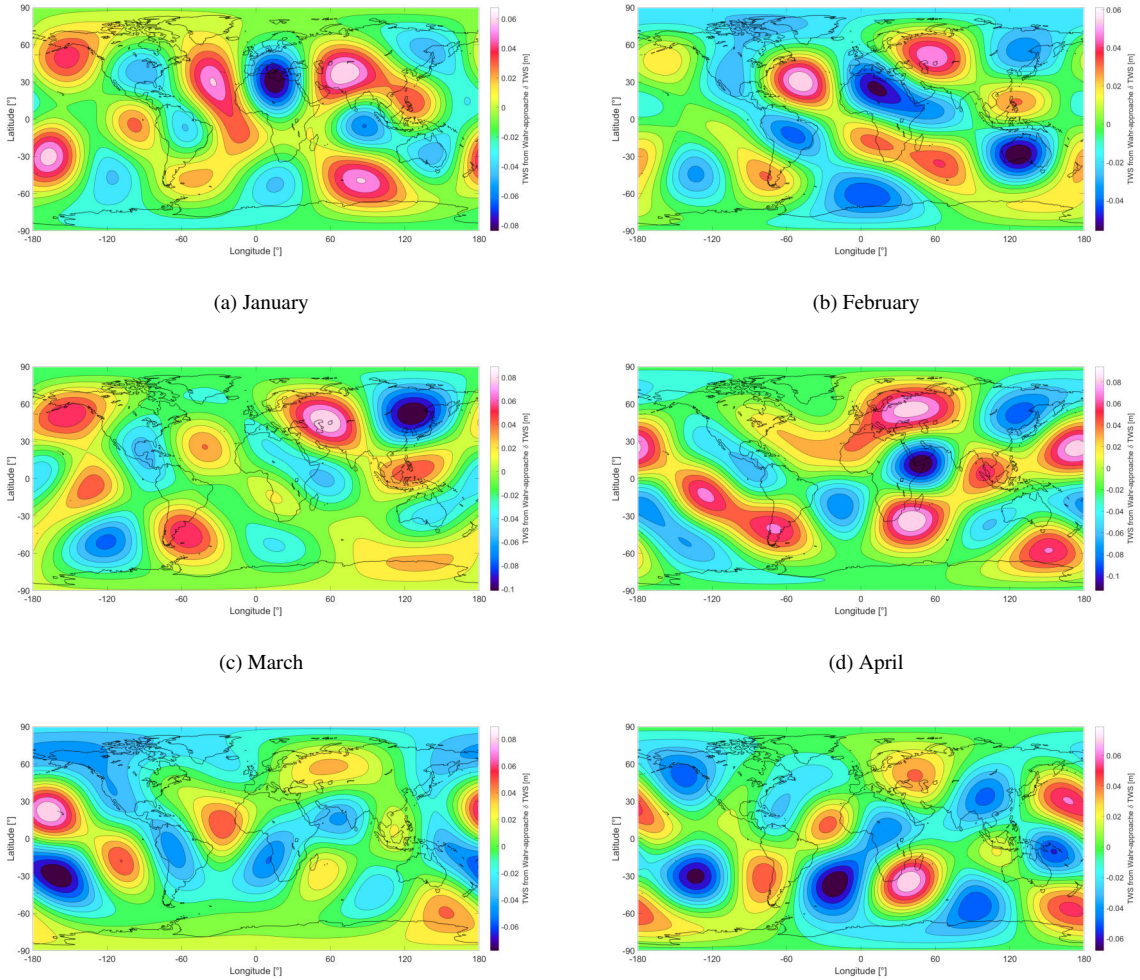

(a) January

(b) February

(c) March

(d) April

(e) May

(f) June

Figure 5.3: TWS results GRACE minus SLR for the year 2023, GFZ, DDK2, $0 \leq m \leq n \leq 5$, (range of TWS-effect is ± 8 cm)

5.3.2 Results for $3 \leq m \leq n \leq 5$

Similarly, changing the $\bar{C}_{3,0}$ coefficient improves the long-term stability of the mass signal, especially when looking at multi-year patterns. Although it has less of an impact than $\bar{C}_{2,0}$ (as seen in Figure 5.4), it aids in reducing noise and drift in large-scale TWS time series.

These findings show that a few low-degree coefficients can dominate the uncertainty budget of GRACE-derived mass estimates.

With only minor seasonal fluctuations in amplitude and extent, the monthly Equivalent Water Height (EWH) maps for January to December 2023 derived from the GFZ DDK2 SLR solution exhibit a highly consistent global spatial structure. Persistent positive anomalies are observed over major hydrological basins such as the Amazon Basin, central Africa, and South and Southeast Asia, while negative anomalies dominate over oceanic and some mid-latitude continental regions. Slight strengthening of tropical anomalies is visible during the mid-year monsoon period (July – September), followed by a modest attenuation toward the end of the year (October – December). Overall, the strong resemblance between all monthly maps indicates that seasonal hydrological processes only weakly modulate a largely stable global mass distribution pattern.

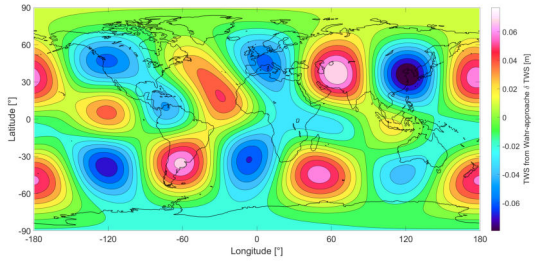

(g) July

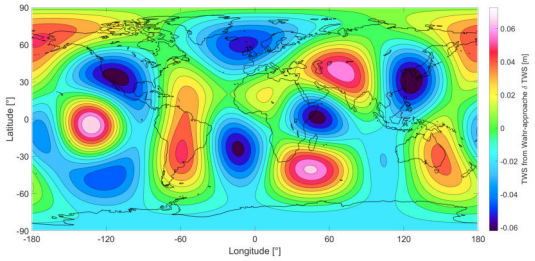

(h) August

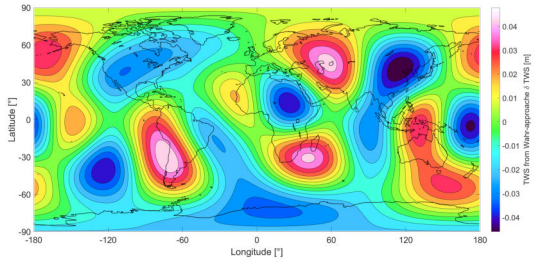

(i) September

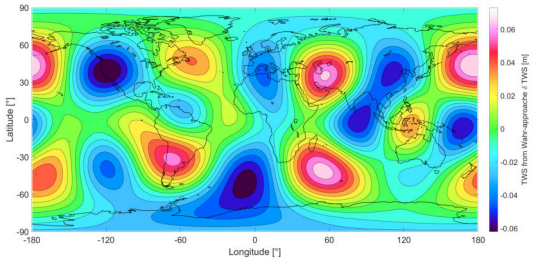

(j) October

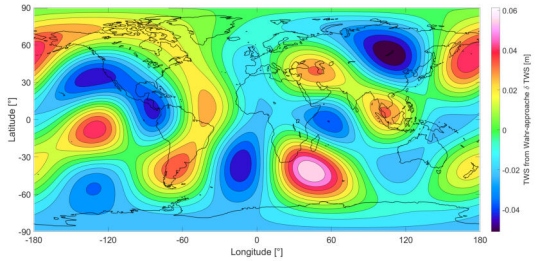

(k) November

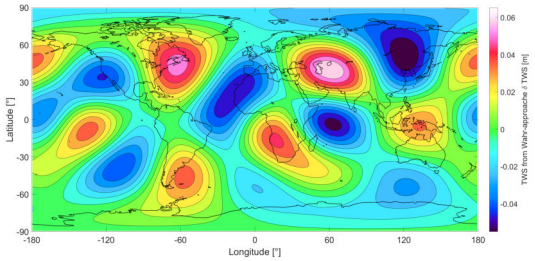

(l) December

Figure 5.3: TWS results GRACE minus SLR for the year 2023, GFZ, DDK2, $0 \leq m \leq n \leq 5$, (range of TWS-effect is ± 8 cm)

The near-identical appearance of the monthly fields is primarily a consequence of the low spectral resolution used in the reconstruction. With a maximum spherical harmonic degree of $N_{max} = 5$, the effective spatial resolution is approximately

$$R \approx \frac{360^\circ}{5} \times \frac{1}{2} \approx 36^\circ$$

corresponding to continental-scale wavelengths of several thousand kilometres. As a result, only very long-wavelength mass variations are retained, while regional and short-term hydrological signals are strongly smoothed, leading to very similar large-scale EWH patterns from month to month.

5.4 Effect of Spatial Filtering

Gaussian and DDK filters significantly improve the visual and physical quality of the TWS maps. The fields are dominated by north-south stripe patterns in the absence of filtering or weak filter strength, which mask actual hydrological signals. Large-scale hydrological features become more visible in the DDK2 results (see Figure 5.1), correlated noise is successfully suppressed, and basin-scale signals become more coherent after filtering.
However, filtering also reduces signal amplitude and causes spatial leakage across basin boundaries. This trade-off emphasises the importance of carefully selecting filter parameters and promotes the use of scaling factors in subsequent work.

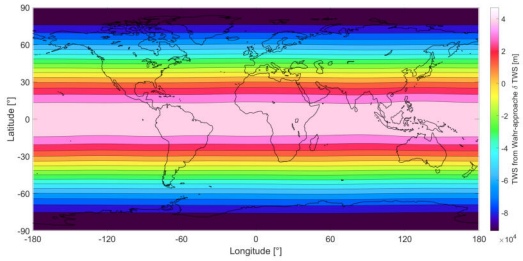

(a) January

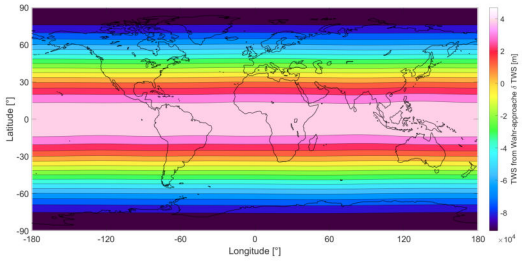

(b) February

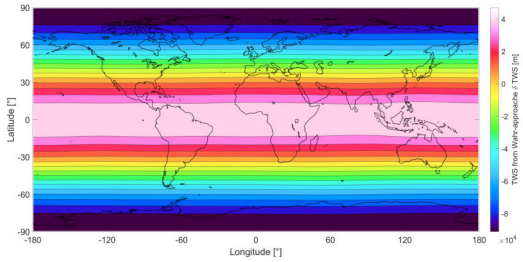

(c) March

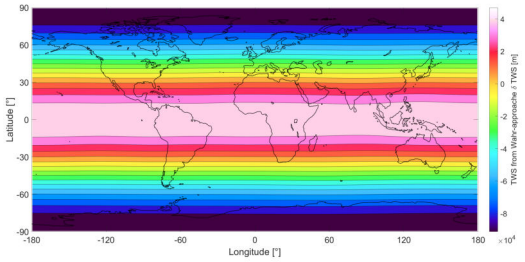

(d) April

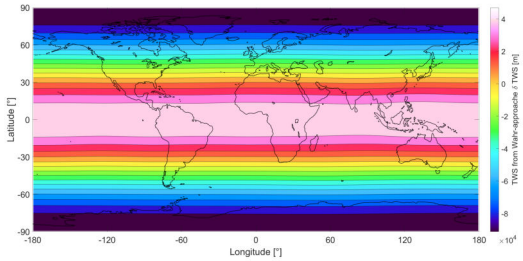

(e) May

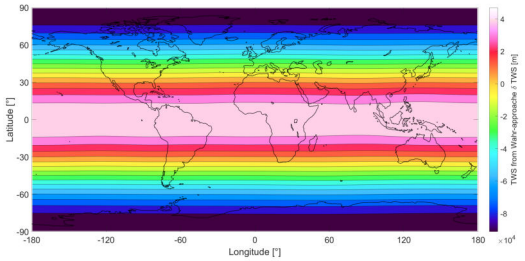

(f) June

Figure 5.4: Equivalent Water Height for the year 2023, GFZ, DDK2, $2 \leq m \leq n \leq 5$

5.5 Temporal Behavior of TWS Time Series

Conceptual basin-averaged TWS time series clearly show seasonal cycles caused by climatic forcing. Monsoonal regions exhibit significant annual variability, whereas temperate regions show more moderate seasonal signals. Long-term trends observed in some regions indicate continuous increases or decreases in water storage, which could be connected to groundwater extraction, glacier mass balance, or long-term climate variability. The importance of careful preprocessing is highlighted by the fact that these patterns are sensitive to how loading corrections and low-degree coefficients are handled.

The worldwide equivalent water height (EWH) fields for March from 2019 to 2024, which were obtained using the DDK2-filtered GRACE/GRACE-FO solutions, are shown in Figure 9. The seasonal redistribution of terrestrial water storage is shown in the maps' constant large-scale hydrological patterns from year to year. While negative anomalies continue to exist over arid and semi-arid regions, such as portions of the Middle East and South Asia, substantial positive anomalies are seen over regions like South America, central Africa, and sections of Southeast Asia. Minor interannual fluctuations in amplitude and regional extent are visible, indicating year-to-year variability in precipitation, runoff, and groundwater storage, even if the general geographical structure is consistent throughout the six years. These minor adjustments demonstrate how GRACE-based EWH outputs are sensitive

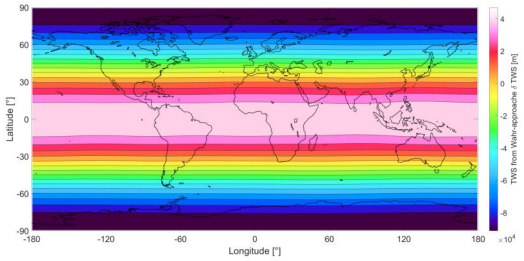

(g) July 2023

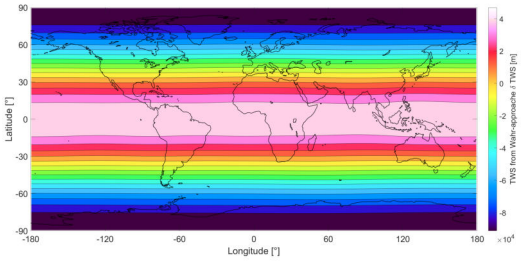

(h) August 2023

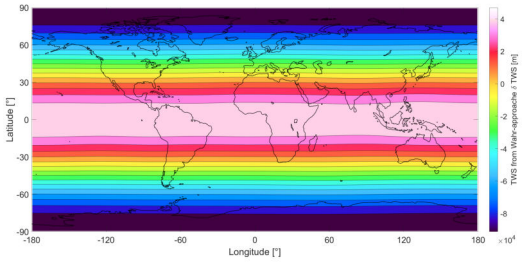

(i) September 2023

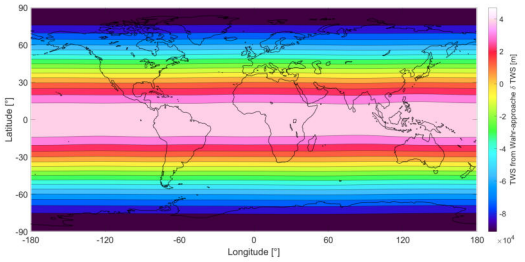

(j) October 2023

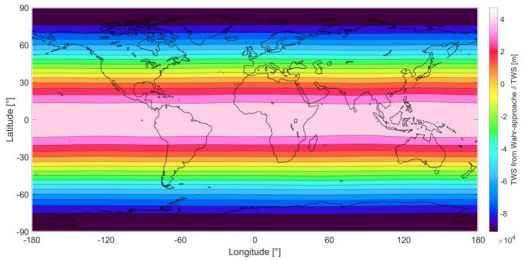

(k) November 2023

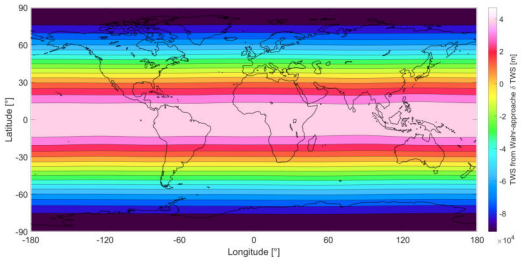

(l) December 2023

Figure 5.4: Equivalent Water Height for the year 2023, GFZ, DDK2, $2 \leq m \leq n \leq 5$

to interannual climatic variability and validate the DDK2 filtering method's resilience in maintaining physically significant hydrological signals.

5.6 Implications for Hydrological Interpretation

The results demonstrate that GRACE-derived TWS is significantly impacted by the methodological choices made during gravity-to-mass conversion. In particular,

- low-degree coefficient treatment controls global mass balance
- SLR replacement is required for physically realistic results
- loading corrections prevent systematic overestimation of water mass (not investigated in this study)
- and filtering determines the spatial resolution and signal fidelity

If these factors are not properly taken into account, hydrological signals may be misinterpreted, especially when comparing results from various studies or looking at long-term trends.

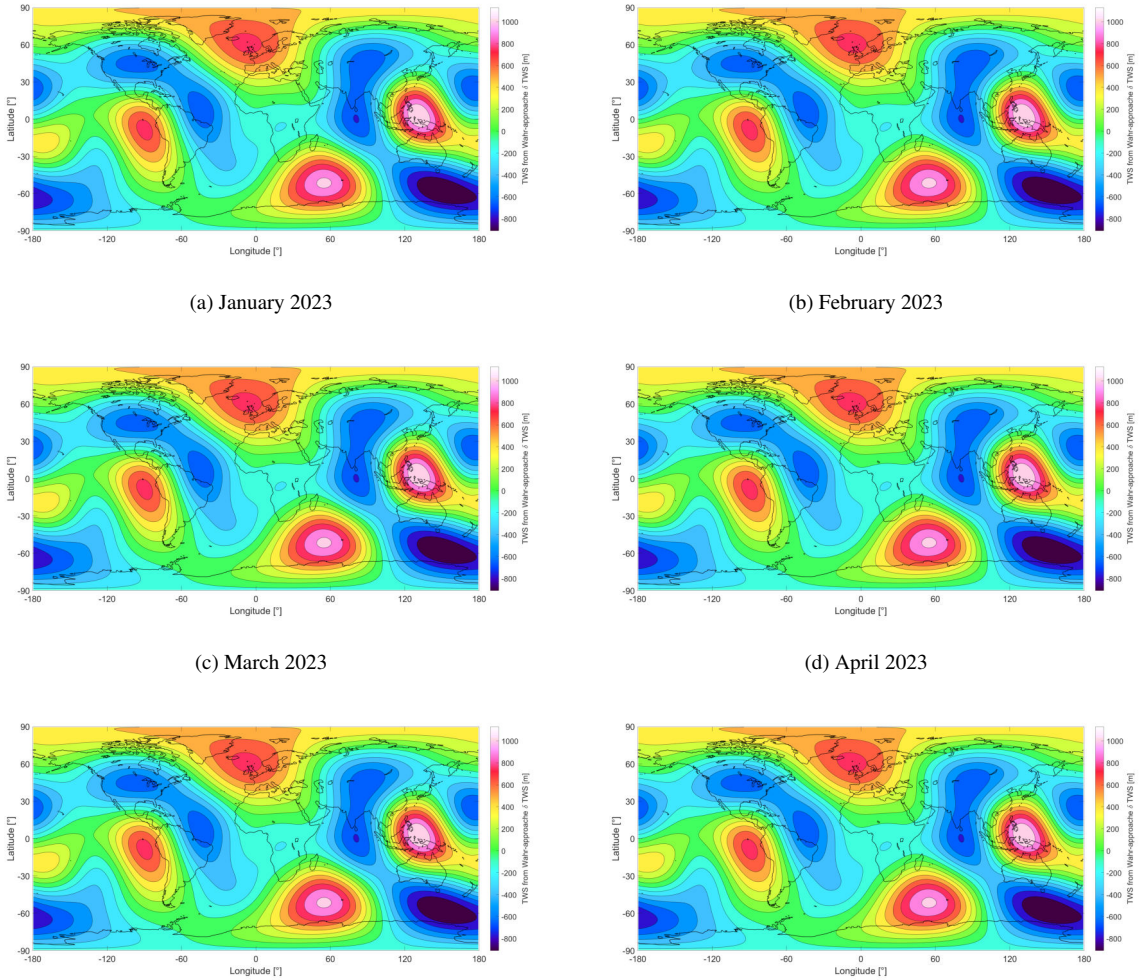

(a) January 2023

(b) February 2023

(c) March 2023

(d) April 2023

(e) May 2023

(f) June 2023

Figure 5.5: Equivalent Water Height for the year 2023, GFZ, DDK2, $3 \leq m \leq n \leq 5$

6 Conclusion and Outlook

In order to estimate terrestrial water storage (TWS) from GRACE gravity field data, this project examined the significance of very low-degree spherical harmonic coefficients. GRACE-derived gravity anomalies were converted into equivalent water thickness anomalies using the traditional formulation of Wahr et al. (1998), allowing conceptual evaluation of large-scale mass redistribution within the Earth system.

The findings show that GRACE and GRACE-FO offer a potent and distinctive capability for monitoring changes in integrated water storage at both continental and global scales. However, methodological decisions made during gravity field processing have a significant impact on the precision and physical consistency of GRACE-derived TWS.

This study's main finding is that TWS estimates are significantly influenced by very low-degree spherical harmonic coefficients. Since GRACE is unable to directly observe degree-1 coefficients, which indicate geocenter motion, they must be obtained from outside sources. Similarly, considerable noise and long-term instability affect GRACE-derived estimates of the quadrupole coefficient $\bar{C}_{2,0}$ and, to a lesser extent, the octupole coefficient $\bar{C}_{3,0}$. The physical realism and stability of the resulting TWS fields are significantly enhanced by substituting these coefficients with higher-precision values obtained from Satellite Laser Ranging (SLR). The comparison of

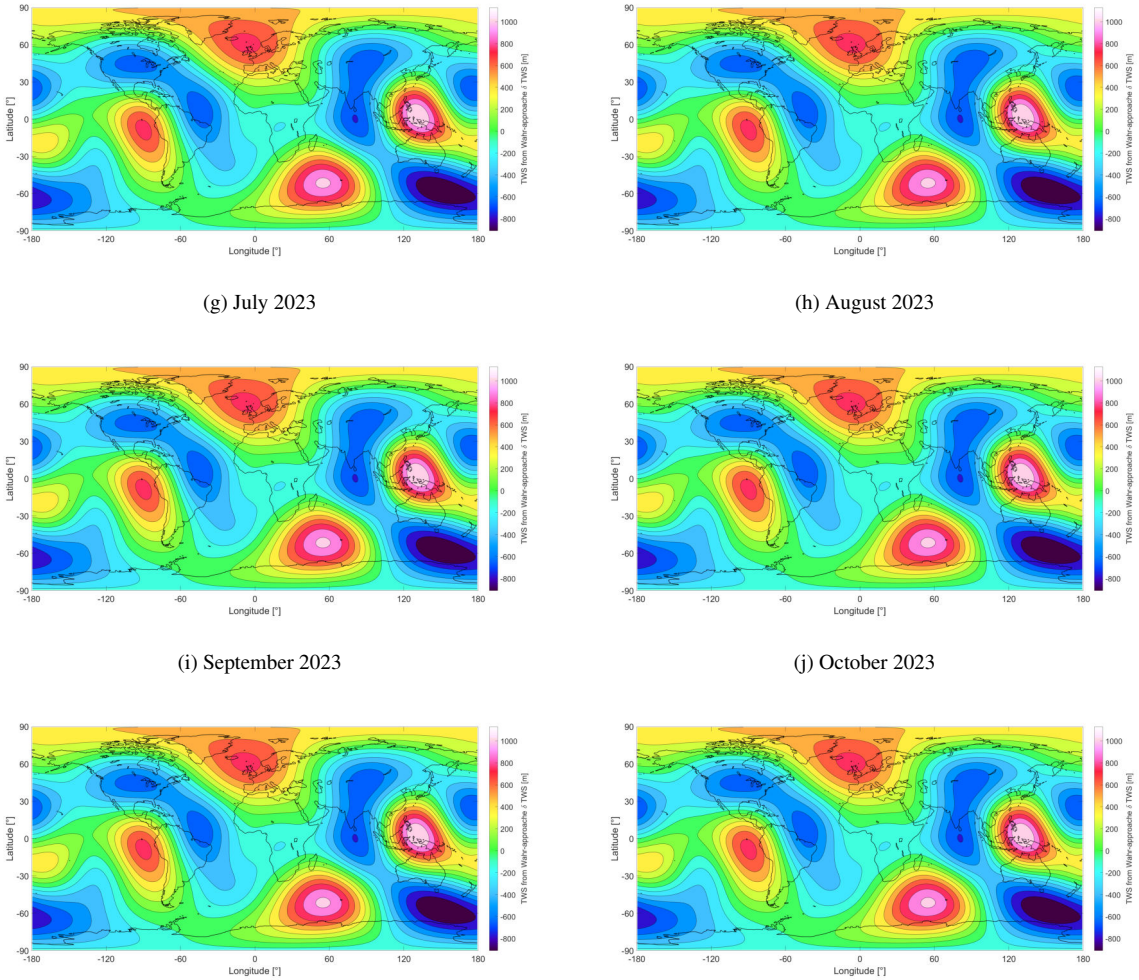

(g) July 2023

(h) August 2023

(i) September 2023

(j) October 2023

(k) November 2023

(l) December 2023

Figure 5.5: Equivalent Water Height for the year 2023, GFZ, DDK2, $3 \leq m \leq n \leq 5$

GRACE-only and GRACE+SLR solutions demonstrates that incorrect handling of low-degree terms can cause biases and artificial trends in estimates of water storage at the basin and global scales.

The significance of taking into consideration the Earth's elastic response to surface mass loading is another important finding. Compared to solutions that ignore loading effects, the addition of loading corrections through the load Love numbers k_n produces systematically lower TWS amplitudes. This demonstrates that solid Earth deformation, not just surface mass, is the source of a portion of the gravity signal detected by GRACE. Thus, ignoring loading leads to an overestimation of changes in water storage and may jeopardize the physical interpretation of mass anomalies derived from GRACE.

Additionally, it was demonstrated that spatial filtering is crucial for reducing the correlated noise present in GRACE gravity field solutions. The visibility of the hydrological signal is improved and strip artifacts are effectively reduced by applying DDK filters (Kusche, 2007). Filtering also causes spatial leakage and signal attenuation, which highlights the importance of carefully choosing parameters and being aware of related uncertainties.

Overall, this project shows that careful and consistent handling of low-degree coefficients, loading effects, and noise reduction techniques is necessary for accurate terrestrial water storage estimation using GRACE. GRACE-derived TWS offers a reliable and physically significant depiction of large-scale hydrological variability when these variables are appropriately taken into account.

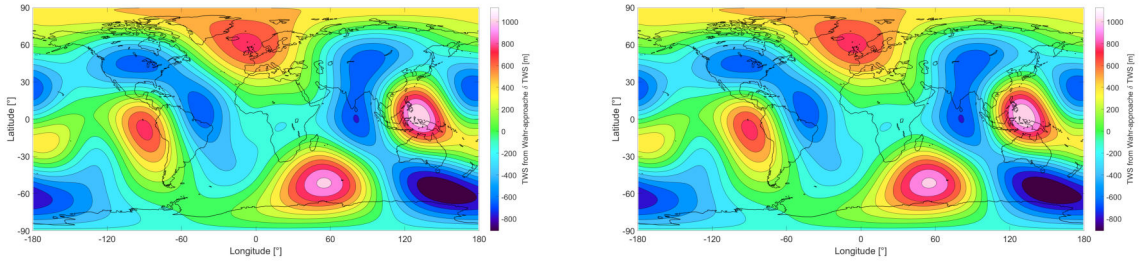

(a) March 2019

(b) March 2020

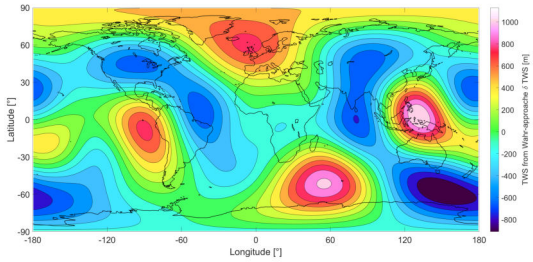

(c) March 2021

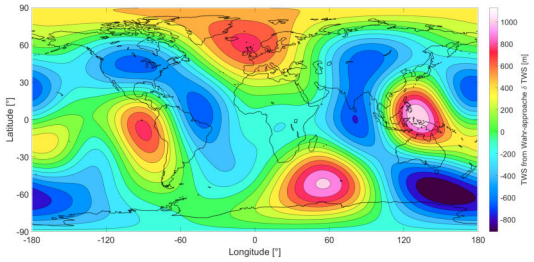

(d) March 2022

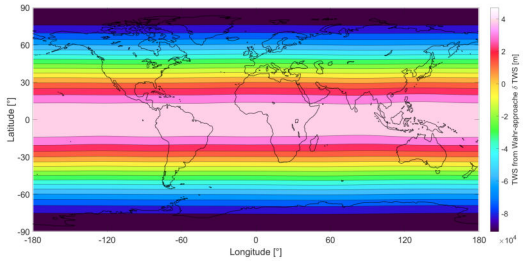

(e) March 2023

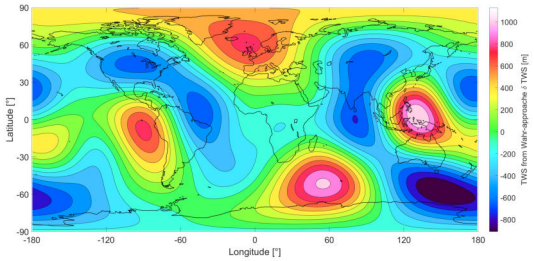

(f) March 2024

Figure 5.6: Equivalent Water Height for March 2019-2024 DDK2

Acknowledgement

The author acknowledges the support of the Geodetic Institute (GIK) for providing necessary resources and facilities. Additionally, the author acknowledges ICGEM (2026) for the data provided for this study.

References

Bloßfeld, M., Müller, H., Gerstl, M., Štefka, V., Bouman, J., Göttl, F., and Horwath, M. (2015): Second-degree Stokes coefficients from multi-satellite SLR. *Journal of Geodesy* 89(9):857–871.

Cheng, M. and Ries, J. (2017): The unexpected signal in GRACE estimates of C_{20}. *Journal of Geodesy* 91(8):897–914.

Dobslaw, H., Flechtner, F., Bergmann-Wolf, I., Dahle, C., Dill, R., Esselborn, S., Sasgen, I., and Thomas, M. (2013): Simulating high-frequency atmosphere-ocean mass variability for dealiasing of satellite gravity observations: AOD1B RL05. *Journal of Geophysical Research: Oceans* 118(7):3704–3711.

ICGEM (2026): International Centre for Global Earth Models (ICGEM): Gravity field and GRACE/GRACE-FO products hosted at the German Research Centre for Geosciences (GFZ). Accessed: 2026-04-06. URL: https://icgem.gfz-potsdam.de/.

Kusche, J. (2007): Approximate decorrelation and non-isotropic smoothing of time-variable GRACE-type gravity field models. *Journal of Geodesy* 81(11):733–749. DOI: 10.1007/s00190-007-0143-3.

Loomis, B. D., Rachlin, K. E., Wiese, D. N., Landerer, F. W., and Luthcke, S. B. (2020): Replacing GRACE/GRACE-FO ΔC_{20} with satellite laser ranging: Impacts on Antarctic Ice Sheet mass change. *Geophysical Research Letters* 47:e2019GL085488. DOI: 10.1029/2019GL085488.

Pearlman, M. R., Degnan, J. J., and Bosworth, J. M. (2002): The international laser ranging service. *Advances in space research* 30(2):135–143.

Rietbroek, R., Brunnabend, S.-E., Kusche, J., Schröter, J., and Dahle, C. (2016): Revisiting the contemporary sea-level budget on global and regional scales. *Proceedings of the National Academy of Sciences* 113(6):1504–1509.

Rodell, M., Famiglietti, J. S., Wiese, D. N., Reager, J., Beaudoing, H. K., Landerer, F. W., and Lo, M.-H. (2018): Emerging trends in global freshwater availability. *Nature* 557(7707):651–659.

Sakumura, C., Bettadpur, S., and Bruinsma, S. (2014): Ensemble prediction and intercomparison analysis of GRACE time-variable gravity field models. *Geophysical Research Letters* 41(5):1389–1397.

Swenson, S., Chambers, D., and Wahr, J. (2008): Estimating geocenter variations from a combination of GRACE and ocean model output. *Journal of Geophysical Research: Solid Earth* 113(B8):B08410. DOI: 10.1029/2007JB005338.

Tapley, B. D., Bettadpur, S., Watkins, M., and Reigber, C. (2004): The gravity recovery and climate experiment: Mission overview and early results. *Geophysical Research Letters* 31(9):1–4. DOI: 10.1029/2004GL019920.

Tsoulis, D. (1999): Spherical harmonic computations with topographic/isostatic coefficients. Tech. rep. IAPG/FESG No. 3. Munich, Germany: Institut für Astronomische und Physikalische Geodäsie, Technische Universität München.

UNIBRAL (CAPES/DAAD) (n.d.). URL: http://www.capes.gov.br/Cooperac%C3%A3o/Acordos/Alemanha/UNIBRAL.htm.

Wahr, J., Molenaar, M., and Bryan, F. (1998): Time variability of the Earth's gravity field: Hydrological and oceanic effects and their possible detection using GRACE. *Journal of Geophysical Research: Solid Earth* 103(B12):30205–30229.

Wahr, J., Swenson, S., and Velicogna, I. (2006): Accuracy of GRACE mass estimates. *Geophysical Research Letters* 33(6):L06401. DOI: 10.1029/2005GL025305.

Appendix

A Appendices

A.1 SLR $2 \leq n \leq 5$ DDK 5, 2023

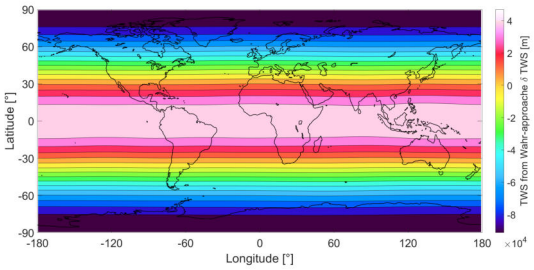

(a) January 2023

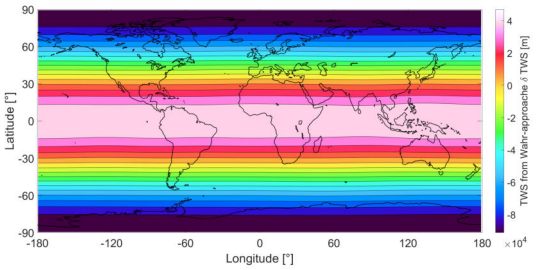

(b) February 2023

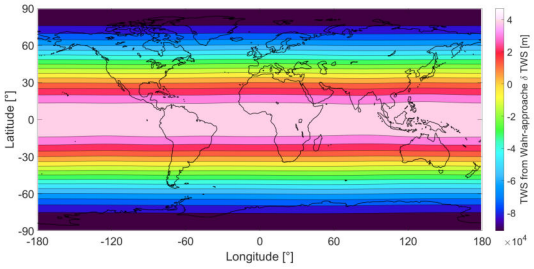

(c) March 2023

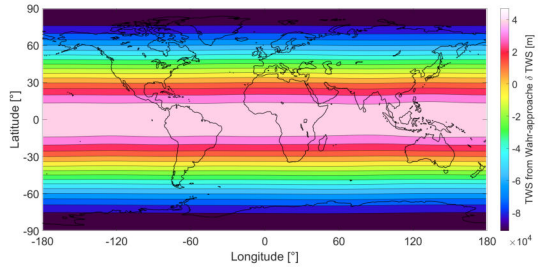

(d) April 2023

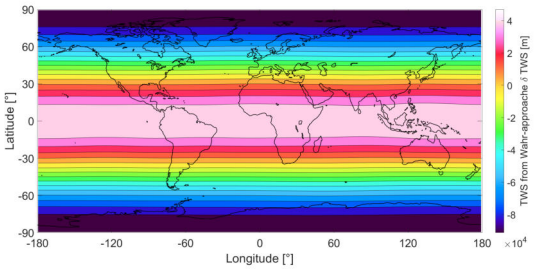

(e) May 2023

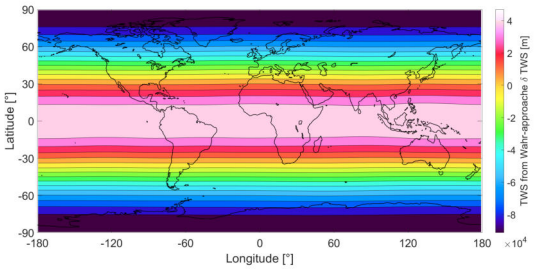

(f) June 2023

Figure A.1: DDK 5 SLR $2 \leq n \leq 5$ year 2023

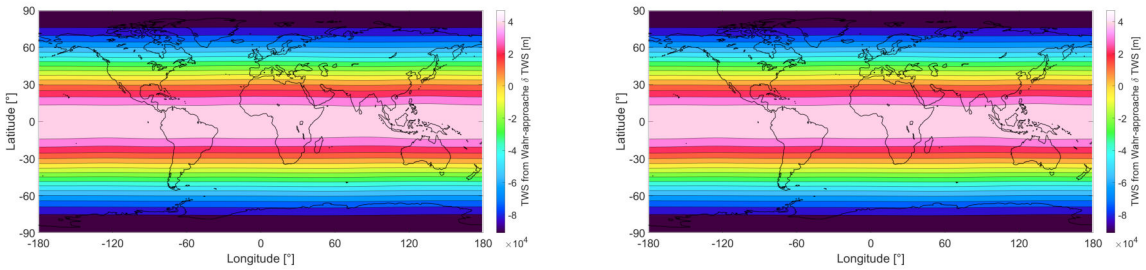

(a) July 2023

(b) August 2023

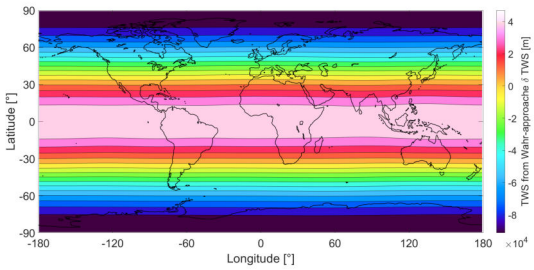

(c) September 2023

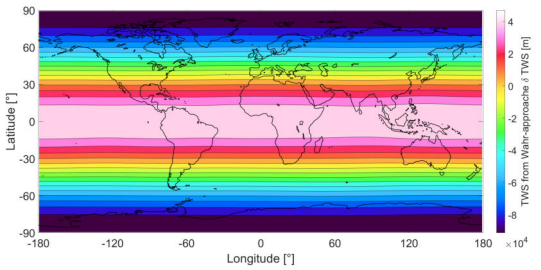

(d) October 2023

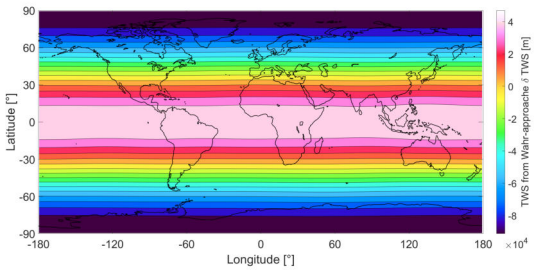

(e) November 2023

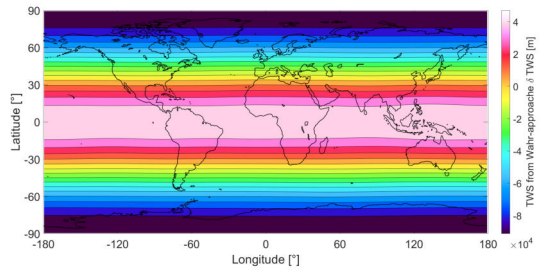

(f) December 2023

Figure A.2: SLR $2 \leq n \leq 5$ DDK 5 for year 2023

Inverse Tesseroid Approach based on Potential and Gravity

Amal Kareeem Abdul Salam[1]

1 Remote Sensing and Geoinformatics Master of Science (M.Sc.), KIT, Germany
E-Mail: uzrxr@student.kit.edu

Abstract

A framework for recovering terrestrial water storage (TWS) anomalies from GRACE-FO gravity observations over Africa is presented using inverse tesseroids. Synthesized gravity fields are shown to capture seasonal and regional hydrological variability, with gravity potential reflecting smooth, large-scale water redistribution, while gravity disturbance and gravity anomaly are shown to enhance sensitivity to regional and local variations. In 2023–2024, pronounced positive gravity signals during the late monsoon (Sept-Nov) are observed to indicate substantial water accumulation from precipitation, groundwater recharge, and surface water storage; during dry periods, reduced signals are observed to reflect decreased TWS and elevated evapotranspiration. The capability of GRACE-FO data to monitor continental-scale hydrological processes is demonstrated by gravity field synthesis.

An inverse tesseroid approach with Tikhonov regularization is employed to stabilize the ill-conditioned inversion. The L-curve criterion is used to facilitate optimal parameter selection, balancing smoothness and data misfit. Distinct trade-offs are revealed when comparisons across observation functionals are made: gravitational potential yields highly stable but spatially smoothed solutions; gravity disturbance increases regional sensitivity but amplifies noise; gravity anomaly offers a balanced performance with intermediate sensitivity and stability. For September 2023, residual analyses indicate that gravitational potential produces the smallest, most homogeneous residuals, with gravity disturbance and gravity anomaly recovering regional hydrological structures albeit with higher residual features and noise.

It is shown that a fundamental stability–resolution trade-off inherent to gravity-based inversions is manifested. Overall, a robust, physically consistent method for retrieving TWS variations from satellite gravimetry is provided by inverse tesseroid modeling, with Earth's curvature being accounted for and with flexibility enabling regional to continental-scale analyses. Among the observables, gravity disturbance is found to offer the best compromise between spatial resolution and numerical stability, while gravitational potential and gravity anomaly are found to complement large-scale and localized assessments, respectively. Future work will be described as including the joint inversion of multiple observables, the use of advanced regularization (higher-order, adaptive, Bayesian), and the integration of independent hydrological datasets (GLDAS, groundwater, precipitation, models) to validate and enhance recovered TWS signals. Advancements in GRACE-FO and forthcoming gravity missions are anticipated to enable finer-scale hydrological monitoring and climate-related water storage changes through improved time-dependent inverse tesseroid frameworks.

Keywords GRACE · TWS · Inverse Tesseroid Approach · Africa · Gravity Potential · Gravity Disturbance · Gravity Anomaly

KIT Scientific Working Papers
Issue Number 270
ISSN: 2194-1629
DOI: 10.5445/IR/1000191188
Online: June 2026

This document is licensed under the Creative Commons Attribution – Share Alike 4.0 International License (CC BY-SA 4.0):
https://creativecommons.org/licenses/by-sa/4.0/deed.en

1 Introduction

Understanding the redistribution of mass within the Earth system is one of the fundamental objectives in modern geodesy, hydrology, climatology, and Earth system science. Variations in the Earth's mass distribution occur continuously due to processes such as precipitation, evapotranspiration, groundwater depletion, glacier melting, ocean circulation, and atmospheric transport. Since mass redistribution directly modifies the Earth's gravitational field, temporal gravity observations provide an indirect but highly effective means of monitoring these geophysical processes.

The development of satellite gravimetry missions, particularly the Gravity Recovery and Climate Experiment (GRACE) launched in 2002 and its successor GRACE Follow-On (GRACE-FO) launched in 2018, revolutionized the monitoring of the time-variable gravity field of the Earth (Tapley et al., 2004). These missions measure temporal variations in the Earth's gravity field by observing changes in the distance between two satellites orbiting the Earth in tandem. Small changes in the gravitational attraction caused by mass redistribution lead to measurable perturbations in the inter-satellite distance.

The gravity field solutions derived from GRACE and GRACE-FO are provided as monthly spherical harmonic coefficients, which describe the Earth's gravitational potential globally. These gravity field models allow the investigation of large-scale hydrological and climatological processes, including droughts, groundwater depletion, ice sheet mass loss, and seasonal water storage variations (Wahr et al., 1998).

One of the most important geophysical applications of GRACE data is the estimation of Total Water Storage (TWS). TWS represents the vertically integrated sum of all terrestrial water components, including:

- Surface water,
- Run off,
- Soil moisture,
- Groundwater,
- Snow and ice,
- Vegetation water content (canopy).

Unlike traditional hydrological observations, which are often spatially sparse and temporally inconsistent, satellite gravimetry provides a globally homogeneous measurement framework for monitoring terrestrial water storage changes.

Traditionally, TWS estimation from GRACE data has been performed in the spectral or frequency domain using spherical harmonic analysis (Wahr et al., 1998). However, spatial-domain approaches have gained increasing attention because they provide greater flexibility for regional applications and facilitate the incorporation of heterogeneous observation functionals.

The present work focuses on the implementation and analysis of an inverse tesseroid approach in the spatial domain. In this methodology, the Earth's surface is discretized into elementary volumetric bodies called tesseroids. Tesseroids are spherical or ellipsoidal mass elements bounded by geographical coordinates and surfaces of constant height (Heck and Seitz, 2007). Their geometry naturally conforms to the spherical geometry of the Earth and therefore provides advantages over classical rectangular prism approximations (Mader, 1951; Nagy, 1966) in regional gravity field modelling.

The tesseroid approach was introduced as an extension of classical prism-based modelling techniques originally developed for terrain correction and gravity reduction problems (Heck and Seitz, 2007). In contrast to rectangular prisms, tesseroids are better suited for global and regional gravity modelling because they account for Earth curvature. The gravitational effect of tesseroids can be derived from Newton's volume integral, although exact

analytical solutions are generally not available due to the occurrence of elliptic integrals (Heck and Seitz, 2007). Consequently, approximate formulations based on Taylor series expansions are commonly used.
In this project, monthly GRACE-FO gravity field models are synthesized into different gravitational observation functionals, including:

- Gravitational Potential,
- Gravity Disturbance,
- Gravity Anomaly.

These synthesized quantities are subsequently used as observations in an inverse tesseroid framework to estimate Total Water Storage variations over the African continent.
A major scientific objective of this study is to investigate how different observation functionals influence the inversion results. Each functional has different physical characteristics and sensitivity to mass redistribution:

- Gravitational potential is smooth and stable but has limited sensitivity to short-wavelength signals.
- Gravity disturbance is more sensitive to near-surface mass variations but also amplifies noise.
- Gravity anomalies enhance regional contrasts and local gravity variations.

The inverse problem associated with gravity field modelling is inherently ill-posed. Small observational errors may lead to large instabilities in the estimated mass distribution. Therefore, regularization techniques are essential for obtaining stable and physically meaningful solutions. In this work, Tikhonov regularization is applied to stabilize the inversion process (Tikhonov, 1963; Tikhonov and Arsenin, 1977).
The study further investigates the optimal regularization parameter using L-curve analysis, which balances data fidelity and solution smoothness.
Overall, this project contributes to the understanding of how multiple gravity-related observation functionals can improve the estimation of Total Water Storage from satellite gravimetry data and demonstrates the applicability of the inverse tesseroid approach for regional hydrological monitoring.

2 Theoretical Aspects

2.1 Earth's Gravity Field

The Earth's gravity field is generated by the spatial distribution of mass within the Earth system. Variations in density, topography, water distribution, and internal structure produce corresponding variations in the gravitational field. Since water redistribution changes the local mass distribution, hydrological processes produce measurable gravity variations.
The fundamental quantity describing the gravity field is the gravitational potential V, which satisfies Laplace's equation outside the Earth:

$$\nabla^2 V = 0\,. \tag{2.1}$$

The gravitational potential generated by a continuous mass distribution is given by Newton's integral:

$$V(\mathbf{r}) = G \int_{\Omega} \frac{\rho(\mathbf{r}')}{|\mathbf{r}-\mathbf{r}'|} d\Omega' \tag{2.2}$$

where:

- G is the gravitational constant,

- ρ is the density function,
- $\mathbf{r}$ and $\mathbf{r}'$ denote position vectors.

Temporal changes in ρ produce temporal gravity variations observed by GRACE and GRACE-FO.

2.2 Satellite Gravimetry and GRACE

Satellite gravimetry measures temporal variations in the Earth's gravity field from space. The GRACE mission consists of two satellites orbiting the Earth approximately 220 km apart. Gravity variations cause changes in the inter-satellite distance, which are measured with micrometer precision using microwave ranging systems (Tapley et al., 2004). The measured satellite dynamics are processed into monthly gravity field models represented by spherical harmonic coefficients.
The temporal gravity signal measured by GRACE contains contributions from:

- Continental water storage,
- Ice mass variations,
- Ocean circulation,
- Atmospheric mass redistribution,
- Solid Earth processes.

To isolate hydrological signals, atmospheric and oceanic effects are removed during preprocessing.

2.3 Spherical Harmonic Representation

The Earth's gravity field is commonly represented using spherical harmonic functions. The gravitational potential outside the Earth can be expanded as:

$$V = \frac{GM}{r} \sum_{l=0}^{\infty} \sum_{m=0}^{l} \left(\frac{R}{r} \right)^{l} \bar{P}_{lm}(\sin\varphi) \left(\bar{C}_{lm} \cos m\lambda + \bar{S}_{lm} \sin m\lambda \right) \tag{2.3}$$

where:

- (GM) is the geocentric gravitational constant,
- (r, φ, λ) are geocentric spherical coordinates,
- (R) is the mean radius of the Earth,
- (l, m) are spherical harmonic degree and order,
- $(\bar{P}_{lm})$ are normalized Legendre functions,
- $(\bar{C}_{lm}, \bar{S}_{lm})$ are spherical harmonic coefficients.

The gravity field models used in this project are truncated at degree and order 96.

2.4 Tesseroids

A tesseroid is a volumetric mass element bounded by:

- Surfaces of constant spherical height,
- Meridional planes,
- Latitudinal cones.

The tesseroid concept was introduced to model gravity effects directly in spherical geometry (Heck and Seitz, 2007). Unlike rectangular prisms, tesseroids naturally conform to the Earth's curvature and are therefore more suitable for global and regional gravity modelling.
According to Heck and Seitz (2007), the gravitational potential of a tesseroid is described by Newton's integral:

$$\delta v = G\rho \int_{\lambda_1}^{\lambda_2} \int_{\phi_1}^{\phi_2} \int_{r_1}^{r_2} \frac{r'^2 \cos\phi'}{\ell} dr' d\phi' d\lambda' \tag{2.4}$$

where:

$$\ell = \sqrt{r^2 + r'^2 - 2rr' \cos\psi} \tag{2.5}$$

and

$$\cos\psi = \sin\phi \sin\phi' + \cos\phi \cos\phi' \cos(\lambda' - \lambda)\,. \tag{2.6}$$

Exact analytical evaluation of the tesseroid integral is generally impossible because elliptic integrals occur. Therefore, approximate solutions based on Taylor series expansions are employed.
Heck and Seitz (2007) proposed an efficient approximation of tesseroid integrals using Taylor expansions around the geometrical center of the tesseroid.
The kernel function is expanded as:

$$\sum_{i,j,k} K_{ijk} (r' - r_0)^i (\phi' - \phi_0)^j (\lambda' - \lambda_0)^k \tag{2.7}$$

The resulting approximation for the tesseroid potential – based on constant density ρ inside the tesseroid – becomes:

$$\delta v = G\rho \Delta r \Delta\phi \Delta\lambda \left[K_{000} + \frac{1}{24} \left(K_{200} \Delta r^2 + K_{020} \Delta\phi^2 + K_{002} \Delta\lambda^2 \right) + O(\Delta^4) \right]. \tag{2.8}$$

This approximation significantly improves computational efficiency while maintaining sufficient accuracy for regional gravity modelling.

2.5 Gravity Disturbance

The gravity disturbance represents the difference between actual gravity and normal gravity evaluated at the same point.
The radial gravity effect of a tesseroid is obtained from:

$$\delta g = -\frac{\partial \delta v}{\partial r} \tag{2.9}$$

Heck and Seitz (2007) derived the corresponding tesseroid integral as:

$$\delta g = G\rho \int \frac{r'^2 (r - r' \cos\psi) \cos\phi'}{\ell^3} dr' d\phi' d\lambda'\,. \tag{2.10}$$

Gravity disturbance is more sensitive to local mass variations compared to gravitational potential.

2.6 Gravity Anomaly

Gravity anomaly represents the difference between observed gravity and a theoretical reference gravity field. In geodesy, gravity anomalies are important because they emphasize local and regional density variations (Hackney and Featherstone, 2003). Gravity anomalies are particularly useful in inversion problems because they provide increased sensitivity to near-surface mass redistribution.

2.7 Inverse Problem

The inverse problem aims to estimate unknown mass variations from gravity observations. The linear observation equation is expressed as:

$$Ax = l \tag{2.11}$$

where:

- (A) is the design matrix,
- (x) is the vector of unknown mass changes,
- (l) is the observation vector.

The least-squares solution is obtained from:

$$A^T Ax = A^T l\,. \tag{2.12}$$

However, gravity inversion problems are ill-conditioned and unstable. To stabilize the inversion, Tikhonov regularization is introduced (Tikhonov, 1963; Tikhonov and Arsenin, 1977). The regularized normal equation is:

$$(A^T A + \lambda I)x = A^T l \tag{2.13}$$

where:

- (λ) is the regularization parameter,
- (I) is the identity matrix.

Regularization suppresses unrealistic oscillations and improves numerical stability.

3 Data

This study utilizes satellite gravimetry and auxiliary hydrological datasets to estimate and analyze terrestrial water storage variations over the African continent. The primary source of information is the GRACE Follow-On (GRACE-FO) mission, which provides monthly gravity field solutions in the form of spherical harmonic coefficients. These gravity field models contain information on temporal mass redistribution within the Earth system and form the basis for the synthesis of gravitational potential, gravity disturbance, and gravity anomaly observations. To improve the quality of the gravity data, appropriate filtering techniques are applied prior to analysis. The following sections describe the datasets, preprocessing procedures, and study area considered in this investigation.

3.1 GRACE-FO Gravity Field Models

The primary dataset used in this study consists of monthly gravity field solutions (2023-2024) from the GRACE-FO mission. Specifically, GFZ Release 6 (RL06) gravity field models are used. These solutions are distributed as spherical harmonic coefficients up to degree and order 96 through the International Center for Global Earth Models (ICGEM). GRACE-FO monthly gravity field models contain information about:

- Seasonal hydrological variations,
- Groundwater depletion,
- Ice mass changes,
- Large-scale climate variability.

3.2 Filtering of Spherical Harmonic Coefficients

Raw GRACE spherical harmonic coefficients contain correlated errors that appear as north-south striping artifacts. To suppress these errors, decorrelation filtering is required. In this study, the DDK5 filter is applied (Kusche et al., 2009). The DDK5 filter provides:

- Reduction of correlated noise,
- Preservation of long-wavelength signals,
- Improved stability of synthesized gravity fields.

3.3 Synthesized Observation Functionals

The filtered spherical harmonic coefficients are synthesized into different gravitational observation quantities:

- Gravitational potential,
- Gravity disturbance,
- Gravity anomaly.

These synthesized quantities form the observation vectors for the inverse tesseroid approach.

3.4 Study Area

The African continent is selected as the study area because of its strong hydrological variability.
Africa exhibits:

- Monsoonal rainfall systems,
- Seasonal drought cycles,
- Significant groundwater depletion,
- Large interannual climate variability.

These characteristics make Africa particularly suitable for evaluating gravity-based hydrological inversion methods.

3.5 Software and Computational Tools

The computational workflow is implemented in MATLAB using provided scripts for:

- Reading spherical harmonic coefficients,
- Synthesizing gravity quantities,
- Constructing tesseroid models,
- Performing inverse modelling,

- Applying regularization techniques.

The inversion results are visualized through:

- Spatial maps,
- Time series,
- L-curve plots.

4 Methodology Overview

The methodology adopted in this study consists of several sequential processing steps beginning with the preprocessing of GRACE-FO gravity field models and ending with the estimation of Total Water Storage (TWS) through inverse tesseroid modelling. The workflow combines spherical harmonic synthesis, spatial gravity modelling, inverse problem formulation, and regularization techniques. The overall methodology is illustrated conceptually through the following stages:

1. Acquisition and preprocessing of GRACE-FO gravity field models,
2. Using the DDK5 filterd spherical harmonic coefficients from GFZ,
3. Synthesis of gravity-related observation functionals,
4. Tesseroid discretization of the study region,
5. Construction of the forward gravity model,
6. Formulation of the inverse problem,
7. Application of Tikhonov regularization,
8. Determination of the regularization parameter using L-curve analysis,
9. Estimation and analysis of Total Water Storage.

4.1 Preprocessing of GRACE-FO Data

The monthly gravity field solutions obtained from the GFZ RL06 GRACE-FO dataset are provided as spherical harmonic coefficients up to degree and order 96. Before performing any synthesis or inversion, the coefficients require preprocessing to reduce systematic errors and correlated noise.
The preprocessing stage includes:

- Removal of background gravity models,
- Replacement of low-degree coefficients where necessary,
- Elimination of correlated striping noise,
- Application of decorrelation filtering.

GRACE gravity field solutions are affected by correlated errors that appear as north-south striping artifacts in spatial maps. These errors originate from orbital characteristics and measurement uncertainties (Kusche et al., 2009). To suppress these artifacts,the DDK5 decorrelation filter is applied. The DDK5 filter provides a compromise between:

- Noise suppression,
- Preservation of long-wavelength hydrological signals,
- Numerical stability of synthesized gravity quantities.

4.2 Spherical Harmonic Synthesis

After filtering, the spherical harmonic coefficients are synthesized into spatial gravity quantities. In this work, three observation functionals are considered:

- Gravitational potential,
- Gravity disturbance,
- Gravity anomaly.

The synthesis process transforms the spectral gravity information into spatial-domain observations evaluated at predefined grid points over the African continent.

4.3 Synthesis of Residual Gravitational Potential

The gravitational potential is synthesized using the spherical harmonic expansion:

$$\delta V = \frac{GM}{r} \sum_{l=0}^{L} \sum_{m=0}^{l} \left(\frac{R}{r}\right)^{l} \bar{P}_{lm}(\cos\theta) \left(\Delta\bar{C}_{lm} \cos m\lambda + \Delta\bar{S}_{lm} \sin m\lambda\right) \tag{4.1}$$

where:

- (L) denotes the maximum spherical harmonic degree used ($L = 96$),
- $(\Delta\bar{C}_{lm}, \Delta\bar{S}_{lm})$ are the filtered coefficients relative to the reference solutions.

The gravitational potential represents a smooth scalar field and is less sensitive to high-frequency noise compared to gravity derivatives.

4.4 Synthesis of Residual Gravity Disturbance

Gravity disturbance is computed from the radial derivative of the gravitational potential:

$$\delta g = -\frac{\partial \delta V}{\partial r}\,. \tag{4.2}$$

The radial derivative enhances sensitivity to local mass variations and near-surface hydrological signals. However, derivative operations amplify high-frequency noise (Rummel and van Gelderen, 1995), requiring careful filtering and regularization.

4.5 Synthesis of Residual Gravity Anomaly

Gravity anomalies emphasize local density contrasts and are widely used in regional gravity inversion studies (Hackney and Featherstone, 2003). Compared to gravitational potential, gravity anomalies provide improved sensitivity to regional hydrological variability. they are related to the potential variation by the fundamental equation of Physical Geodesy (Heiskanen and Moritz, 1967):

$$\delta\Delta g = -\frac{\partial \delta V}{\partial r} - -\frac{2}{r}\delta V\,. \tag{4.3}$$

4.6 Tesseroid Discretization

The African continent is discretized into tesseroids representing elementary volumetric mass bodies.
Each tesseroid is defined by:

- Latitude boundaries,

- Longitude boundaries,
- Upper and lower radial boundaries.

The tesseroid geometry follows the spherical shape of the Earth and therefore provides improved consistency for regional gravity modelling compared to rectangular prisms (Heck and Seitz, 2007). The unknown density variation assigned to each tesseroid represents the mass redistribution associated with hydrological processes.

4.7 Forward Gravity Modelling

The forward modelling computes the gravitational effect generated by tesseroids at observation points. The gravitational response of each tesseroid is calculated using Newton's volume integral as explained in Equation (2.4). The contributions of all tesseroids are combined to form the synthesized gravity field on the grid which acts as observations l in the Inverse Problem. The forward modelling stage produces the design matrix (A), where each matrix element represents the contribution of a tesseroid to a specific observation.

4.8 Inverse Problem Formulation

The inverse problem estimates the unknown tesseroid mass variations from synthesized gravity observations.
The observation equation is given in Equation (2.11).
The least-squares solution is obtained from the normal Equation (2.12)
Since gravity inversion problems are ill-conditioned, direct inversion often leads to unstable solutions.

4.9 Tikhonov Regularization

To stabilize the inversion, Tikhonov regularization is introduced (Tikhonov, 1963; Tikhonov and Arsenin, 1977).
The regularized inverse problem is given in Equation (2.13)
The regularization parameter controls the balance between:

- Data fitting,
- Solution smoothness,
- Numerical stability.

Large values of (λ) produce smoother solutions, whereas smaller values increase sensitivity to noise.

4.10 L-Curve Analysis

The optimal regularization parameter is determined using the L-curve criterion.
The L-curve is a log-log plot of:

- Residual norm,
- Solution norm.

The corner of the L-curve represents the optimal trade-off between minimizing residuals and avoiding overfitting (Hansen, 1992).

4.11 Computation of Total Water Storage

The estimated tesseroid density variations are converted into Total Water Storage anomalies. The resulting TWS fields are analyzed spatially and temporally to investigate hydrological variability over Africa.

5 Results and Discussion

This chapter presents and discusses the results obtained from the synthesis and inversion of GRACE-FO gravity field observations over the African continent. The synthesized gravity quantities, namely gravitational potential, gravity disturbance, and gravity anomaly, are first analyzed to investigate their spatial and temporal variations and their relationship with regional hydrological processes. Subsequently, the inverse tesseroid modelling results are presented in terms of Total Water Storage (TWS) estimates, regularization analysis, and model performance assessment. Particular emphasis is placed on evaluating the influence of the different observation functionals on inversion stability, spatial resolution, and hydrological interpretation. For clarity, the chapter is divided into two main sections: Synthesis Results, which focuses on the characteristics of the synthesized gravity fields, and Inverse Results, which examines the recovered TWS distributions, L-curve analysis, residual behaviour, and the comparative performance of the observation functionals.

5.1 Synthesis Results

The synthesis of gravity-related observation functionals from filtered GRACE-FO spherical harmonic coefficients provides the input observations for the inverse tesseroid approach. The synthesized fields reveal different characteristics depending on the selected observation functional.

5.1.1 Gravitational Potential

The synthesized gravitational potential fields for the years 2023 and 2024 are shown in Figures 5.1.1 and Figure , respectively. They exhibit clear spatial and temporal variations associated with large-scale hydrological mass redistribution over the African continent. The monthly maps derived from the filtered GRACE-FO spherical harmonic coefficients reveal smooth gravity potential anomalies that correspond primarily to seasonal terrestrial water storage variations. In both years, the gravitational potential fields display strong positive anomalies concentrated over the equatorial and central African regions during the late monsoon and post-monsoon periods, particularly from September to November. These positive anomalies indicate significant mass accumulation associated with increased precipitation, soil moisture, surface water storage, and groundwater recharge. The strongest positive signals are observed during October and November in both 2023 and 2024, where the contour distributions show intense high-potential zones extending across central Africa. This behavior is consistent with the seasonal migration of the Intertropical Convergence Zone (ITCZ), which produces substantial rainfall over tropical Africa during these months.

During the early months of the year, particularly from January to May, localized positive gravitational potential anomalies are visible over eastern and central Africa. In 2023, February and April show relatively strong isolated positive regions, whereas 2024 demonstrates a more concentrated positive anomaly during March, April, and May. These localized gravity increases likely correspond to regional hydrological accumulation events caused by seasonal rainfall and temporary groundwater recharge. In contrast, the mid-year months, especially June and July, exhibit weaker and more spatially diffuse gravitational potential signals in both years. Large negative or near-neutral potential anomalies become dominant over northern and southern Africa during this period, indicating reduced terrestrial water storage caused by dry climatic conditions and increased evapotranspiration. The smoother transition patterns observed in the gravitational potential fields reflect the low-frequency nature of the potential functional, which naturally suppresses short-wavelength variability and produces spatially continuous mass redistribution patterns.

A comparison between the 2023 and 2024 synthesized gravitational potential fields indicates that the hydrological signals during 2024 are spatially stronger and more extensive than those observed in 2023. In particular, the September to November 2024 period exhibits broader positive potential anomalies with higher amplitude distributions across central tropical Africa. This suggests stronger seasonal water accumulation during 2024, potentially

associated with intensified precipitation patterns or enhanced groundwater storage variability. Overall, the synthesized gravitational potential fields successfully capture the large-scale seasonal hydrological behavior over Africa and demonstrate the capability of GRACE-FO gravity field observations to monitor continental-scale terrestrial water storage variations. The results further confirm that gravitational potential provides stable and smooth observations suitable for inverse tesseroid modelling, although its inherently low-pass behavior limits sensitivity to smaller-scale hydrological structures.

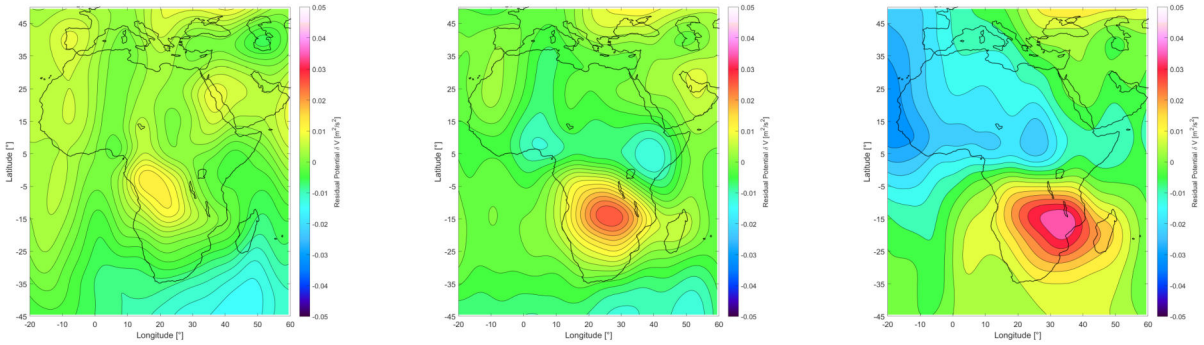

(a) January 2023 (b) February 2023 (c) March 2023

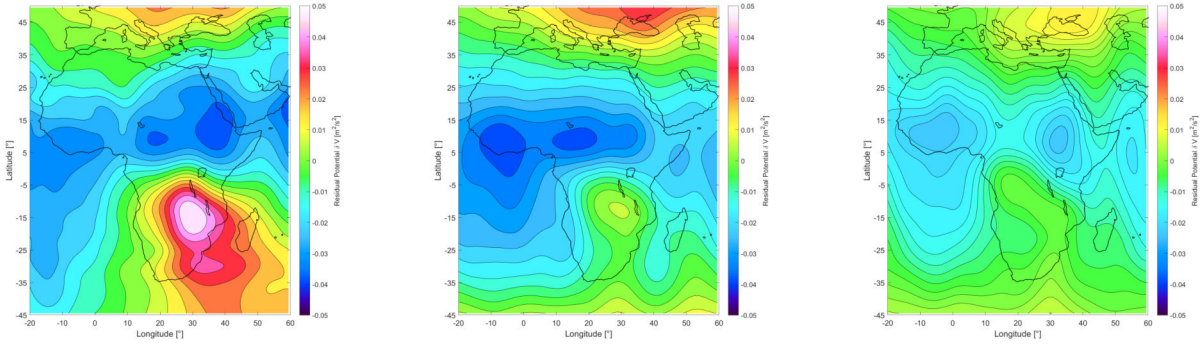

(d) April 2023 (e) May 2023 (f) June 2023

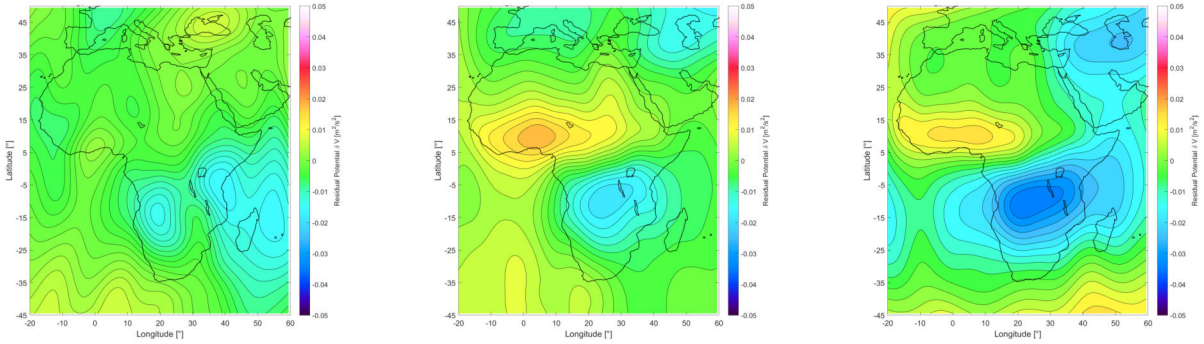

(g) July 2023 (h) August 2023 (i) September 2023

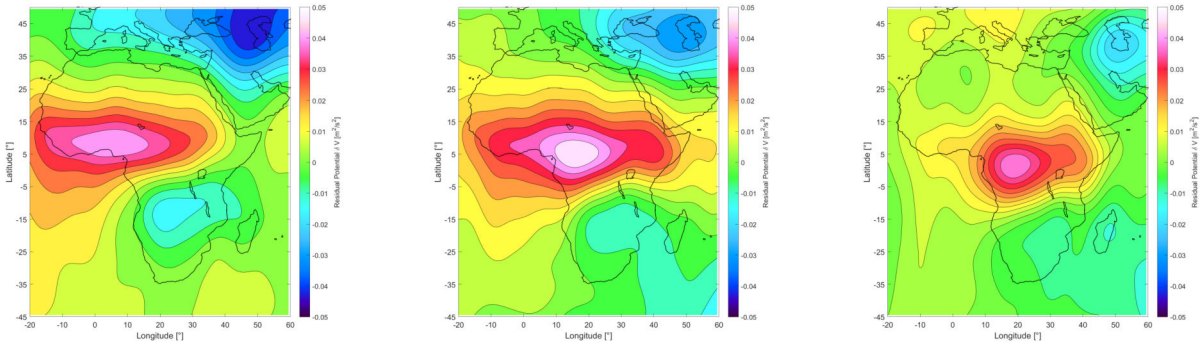

(j) October 2023 (k) November 2023 (l) December 2023

Figure 5.1: Residual Gravity Potential for the year 2023. Range is $\pm 0.05\ m^2 s^{-2}$.

5.1.2 Gravity Disturbance

The synthesized gravitational potential maps for 2023 and 2024 (Figures 3 and 4) reveal clear spatiotemporal variability across the African continent, reflecting seasonal mass redistribution processes. In both years, the monthly maps show alternating regions of positive anomalies (red/yellow) and negative anomalies (blue), which correspond to areas of mass gain and mass loss, respectively. A consistent feature observed in both datasets is the strong equatorial signal, particularly over Central and East Africa, where pronounced positive anomalies appear during specific months (e.g., April–May 2023 and February–May 2024). These patterns indicate periods of increased water storage, likely associated with seasonal rainfall and hydrological recharge. Such seasonal dominance in tropical regions is well documented in GRACE-based studies, where water storage variability is primarily driven by annual hydrological cycles.

A comparison between the two years highlights both recurring seasonal behavior and interannual differences. In 2023, the gravitational potential fields exhibit a more localized and irregular distribution of anomalies, with strong positive signals concentrated in southern and central Africa during April and May, followed by a transition to more distributed patterns later in the year. In contrast, 2024 shows a more coherent and elongated anomaly structure, particularly from August to November, where a strong east–west band of positive potential dominates the equatorial region. This suggests a more organized large-scale hydrological response in 2024, possibly linked to broader climatic forcing. Additionally, both years show a shift toward negative anomalies in northern and southern regions during dry periods, reflecting water depletion and evapotranspiration effects. These seasonal oscillations align with known GRACE observations, where up to 30–75 percent of total water storage variability in African basins is explained by seasonal cycles.

Overall, the synthesized gravitational potential results demonstrate that the inversion and spherical harmonic synthesis successfully capture both seasonal cycles and spatial heterogeneity of water mass distribution. The observed patterns confirm that gravitational potential fields are highly sensitive to hydrological processes, making them suitable for estimating Total Water Storage (TWS). The differences between 2023 and 2024 further emphasize the importance of interannual variability, highlighting the influence of climatic and environmental factors on mass redistribution across Africa.

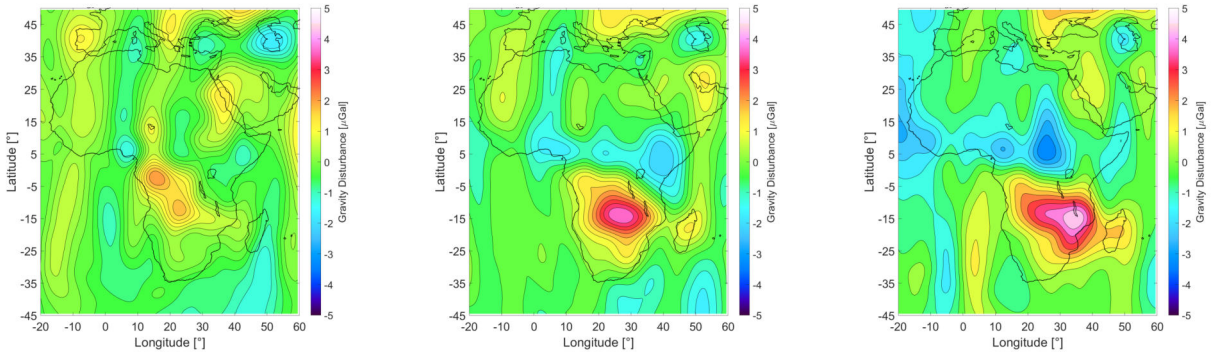

(a) January 2023 (b) February 2023 (c) March 2023

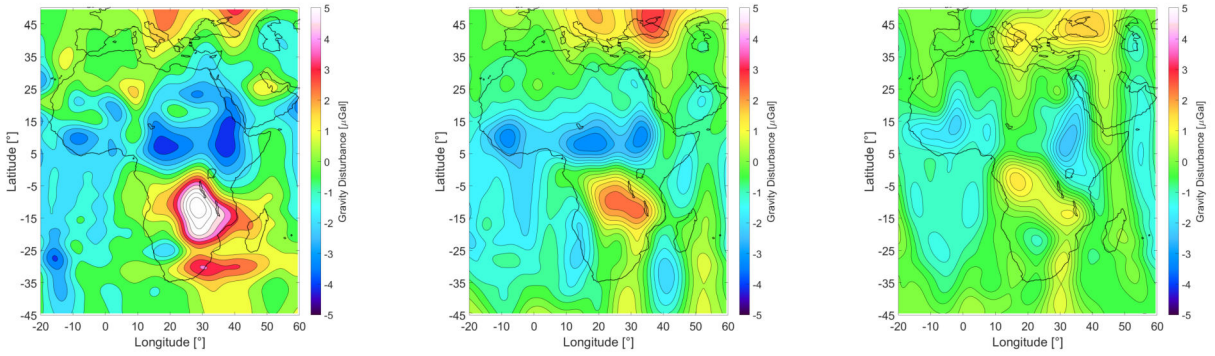

(d) April 2023 (e) May 2023 (f) June 2023

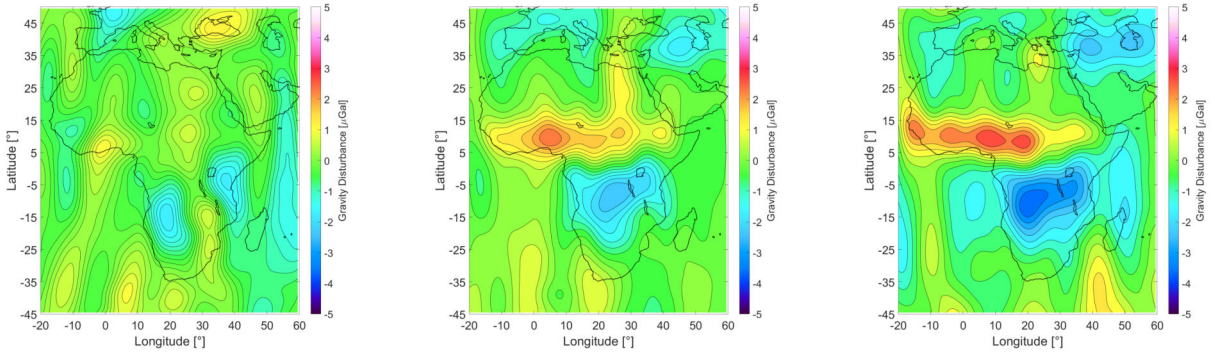

(g) July 2023 (h) August 2023 (i) September 2023

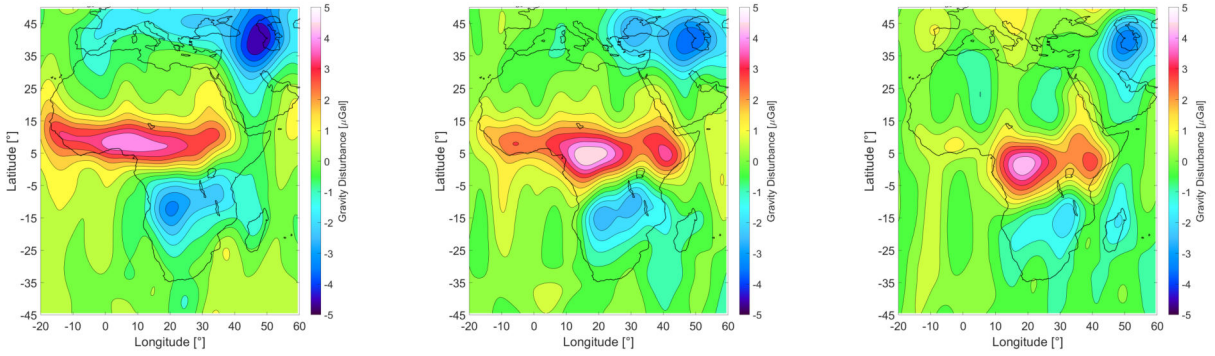

(j) October 2023 (k) November 2023 (l) December 2023

Figure 5.2: Residual Gravity Disturbance for the year 2023. Range is $\pm 5\ \mu Gal$.

5.1.3 Gravity Anomaly

The synthesized gravity anomaly fields for the years 2023 and 2024 reveal significant spatial and temporal variations in regional mass redistribution over the African continent. Compared to gravitational potential, gravity anomalies emphasize shorter-wavelength gravity variations and therefore provide enhanced sensitivity to regional hydrological processes. The synthesized anomaly maps clearly show strong seasonal migration of positive and negative gravity signals associated with terrestrial water storage variability. In both years, localized positive gravity anomalies are observed during the early months, particularly from February to May, over central and eastern Africa. These positive anomalies correspond to increased water mass accumulation resulting from seasonal rainfall, enhanced soil moisture, and groundwater recharge. In April 2023, a particularly intense localized positive anomaly is visible over southeastern-central Africa, indicating a strong hydrological loading event during this period. Similar localized positive structures are also observed during March–May 2024, although the anomaly distribution appears more spatially compact compared to 2023.

During the mid-year months, especially June and July, the gravity anomaly fields become relatively weaker and more spatially diffuse. Negative anomaly regions become more dominant across northern and southern Africa, indicating reductions in terrestrial water storage associated with dry climatic conditions and increased evapotranspiration. Beginning in August, both years exhibit the gradual development of elongated positive anomaly bands extending across equatorial Africa. These features become particularly pronounced during September, October, and November. The strongest anomaly amplitudes occur during October and November for both 2023 and 2024, where broad high-amplitude positive anomaly zones extend across central tropical Africa. These patterns correspond to the seasonal intensification of the Intertropical Convergence Zone (ITCZ), which produces extensive rainfall and large-scale hydrological mass accumulation. Compared to the gravitational potential fields, the gravity anomaly maps exhibit sharper regional contrasts and improved delineation of hydrological structures such as river basins and groundwater-dominated regions.

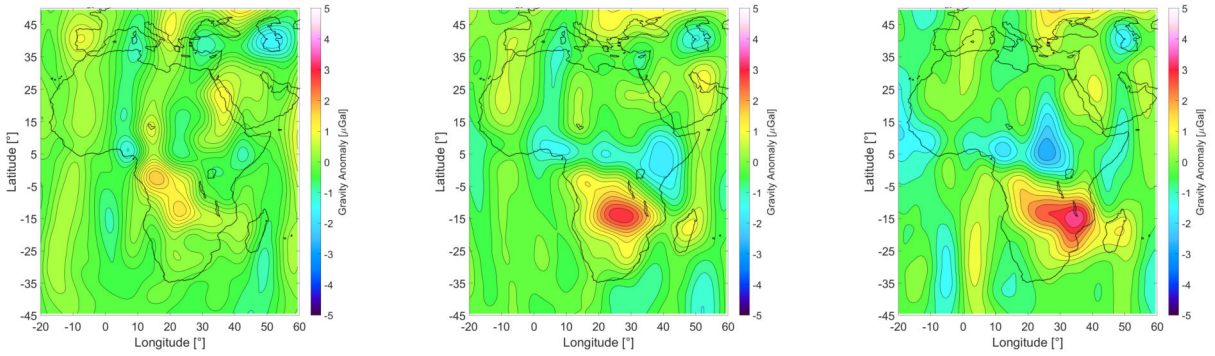

(a) January 2023 (b) February 2023 (c) March 2023

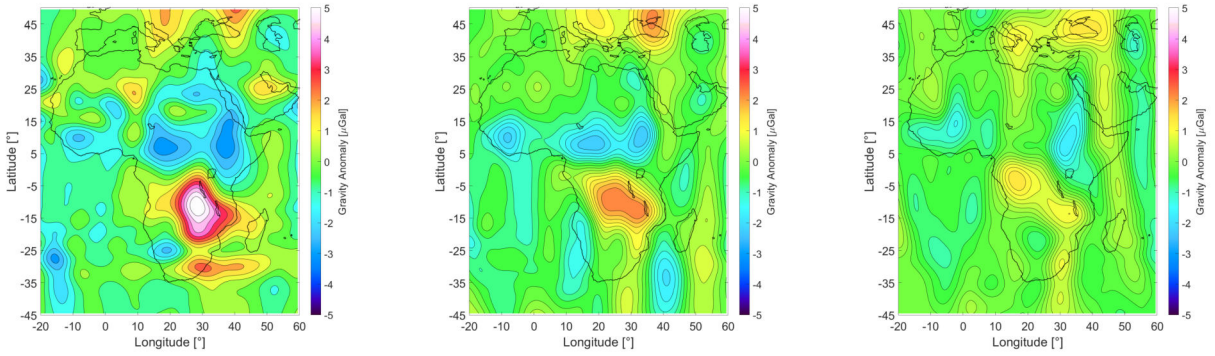

(d) April 2023 (e) May 2023 (f) June 2023

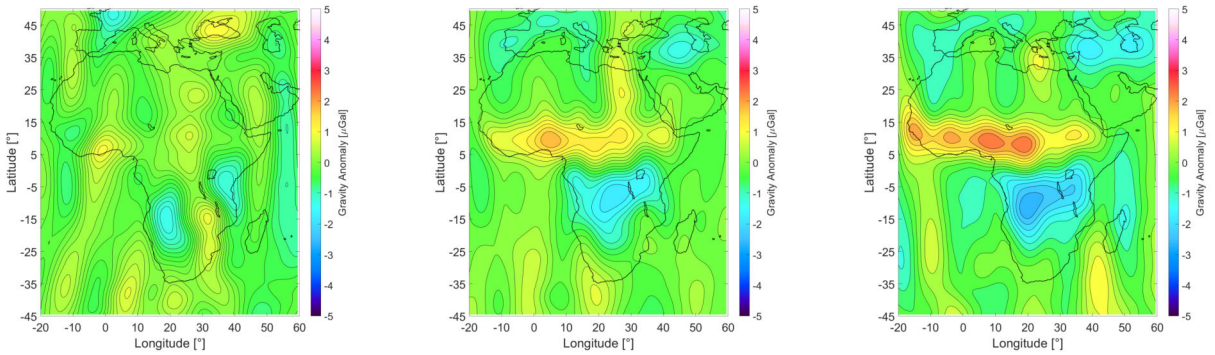

(g) July 2023 (h) August 2023 (i) September 2023

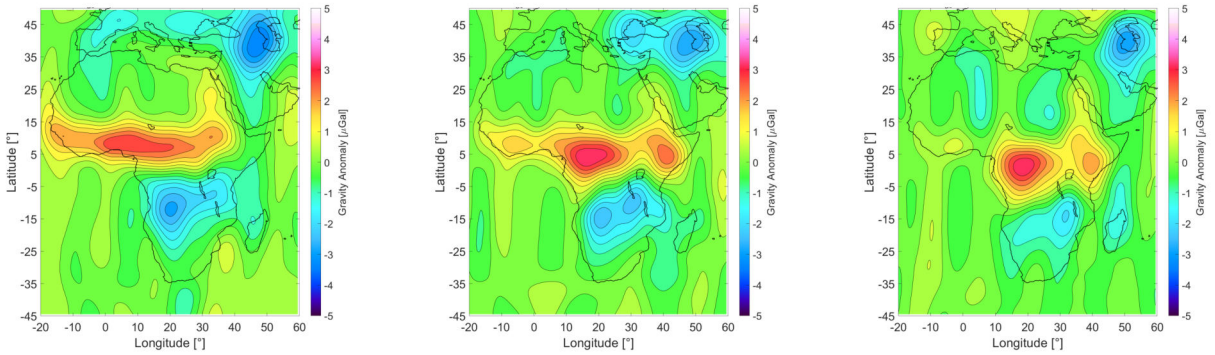

(j) October 2023 (k) November 2023 (l) December 2023

Figure 5.3: Residual Gravity Anomaly for the year 2023. Range is ± 5 μGal.

A comparison between the two years indicates that the 2024 gravity anomaly fields generally display stronger and more spatially continuous positive anomaly distributions during the late monsoon season compared to 2023. In particular, September to November 2024 exhibits broader equatorial anomaly belts with higher amplitudes, suggesting stronger continental-scale water storage accumulation during this period. The gravity anomaly synthesis successfully captures both seasonal and regional hydrological variability while maintaining improved spatial sensitivity relative to gravitational potential. These results demonstrate that gravity anomalies provide an effective observation functional for inverse tesseroid modelling because they preserve important regional hydrological features while avoiding the excessive smoothing associated with gravitational potential fields. However, the increased sensitivity to short-wavelength signals also implies greater susceptibility to residual noise and striping artifacts, highlighting the importance of appropriate filtering and regularization in the inversion process.

5.2 Inverse Results

This section presents the results obtained from the inverse tesseroid modelling of the synthesized GRACE-FO gravity observations. The primary objective of the inversion is to estimate Total Water Storage (TWS) variations over the African continent from the synthesized gravitational potential, gravity disturbance, and gravity anomaly fields. Since gravity inversion is an ill-posed problem, Tikhonov regularization is applied to stabilize the solution, and the optimal regularization parameter is determined using L-curve analysis (Tikhonov and Arsenin, 1977; Hansen, 1992). The resulting TWS estimates derived from the different observation functionals are subsequently analyzed and compared to evaluate their sensitivity to hydrological mass redistribution, inversion stability, and spatial resolution. Finally, a comparative assessment of the observation functionals is performed to identify their respective strengths and limitations within the inverse tesseroid framework.

5.2.1 L-Curve Analysis

The inverse tesseroid problem formulated in this study is inherently ill-posed because small errors in the gravity observations can produce large variations in the estimated mass distribution. Consequently, direct least-squares inversion may result in unstable and physically unrealistic solutions. To overcome this limitation, Tikhonov regularization was applied, and the optimal regularization parameter was determined using the L-curve criterion (Hansen, 1992).

The L-curve represents the relationship between the norm of the regularized solution and the norm of the corresponding residuals. Specifically, it is a log-log plot of the solution norm,

$$||x_\lambda|| \tag{5.1}$$

against the residual norm,

$$||Ax_\lambda - l|| \tag{5.2}$$

for different values of the regularization parameter λ. The characteristic "L" shape of the curve reflects the trade-off between fitting the observations and maintaining a stable solution. Small values of λ prioritize data fitting and therefore produce low residuals, but often amplify observational noise and numerical instability. Conversely, large values of λ excessively smooth the solution, reducing noise but potentially suppressing important hydrological signals.

Figure 5.4 illustrates representative L-curves obtained for June 2023 using the three observation functionals considered in this study: gravitational potential (K), gravity disturbance (J), and gravity anomaly (L). The corner of each curve corresponds to the optimal balance between residual minimization and solution stabilization.

For the gravitational potential inversion, the L-curve exhibits a well-defined corner at approximately

$$\lambda \approx 1.72 \times 10^{-7}.$$

The relatively smooth transition observed in the curve indicates that gravitational potential is less sensitive to high-frequency noise due to its long-wavelength nature. As a result, the inversion remains stable over a broader range of regularization parameters. The selected corner value provides sufficient regularization while preserving the dominant hydrological signal represented in the gravity observations.
The gravity disturbance inversion produces an L-curve with a corner near

$$\lambda \approx 8.23 \times 10^{-12}.$$

Compared to gravitational potential, the curve is steeper and the corner occurs at a significantly smaller regularization parameter. This behaviour reflects the increased sensitivity of gravity disturbance to local mass variations. Because gravity disturbance is derived from the radial derivative of the gravitational potential, it contains stronger short-wavelength information but is also more susceptible to noise amplification. The smaller optimal regularization parameter indicates that stronger observational information is retained, although careful stabilization remains necessary to prevent oscillatory solutions.
Similarly, the gravity anomaly inversion exhibits a corner around

$$\lambda \approx 2.98 \times 10^{-12}.$$

The shape of the curve is comparable to that of the gravity disturbance inversion, although slightly smoother. This result is consistent with the intermediate characteristics of gravity anomalies, which preserve regional hydrological structures while remaining less sensitive to high-frequency noise than gravity disturbance. The corresponding regularization parameter provides an effective balance between spatial resolution and numerical stability.
A comparison of the three L-curves reveals notable differences in the regularization behaviour of the observation functionals. The gravitational potential requires a considerably larger regularization parameter due to its smooth long-wavelength nature, whereas gravity disturbance and gravity anomaly require smaller values because they contain enhanced local information. These differences confirm that the physical characteristics of the observation functional strongly influence the conditioning of the inverse problem and the magnitude of the regularization required.
Overall, the L-curve analysis proved to be an effective and objective method for selecting the regularization parameter in the inverse tesseroid framework. The chosen corner values produced stable and physically meaningful Total Water Storage solutions while minimizing the loss of hydrologically relevant information. The analysis further demonstrates that the use of different observation functionals not only affects the spatial characteristics of the recovered TWS fields but also significantly influences the regularization requirements of the inversion process.

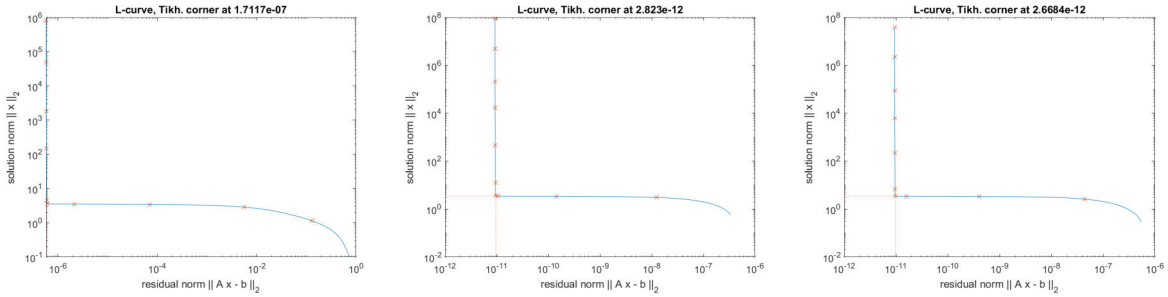

(a) L curve K June 2023 (b) L curve J June 2023 (c) L curve L June 2023

Figure 5.4: L curve for June 2023 (three different observation typs)

5.2.2 Total Water Storage from Gravitational Potential

The inversion-derived Total Water Storage (TWS) maps for 2023 and 2024(Figures 7 and 8) illustrate the spatial and temporal variability of water mass distribution across Africa as reconstructed from gravitational potential. The results exhibit a striped north–south pattern, which is characteristic of GRACE-based inversions and reflects residual correlated errors even after filtering. Despite this, clear hydrological signals can still be identified. In both years, regions along the equatorial belt and central Africa consistently show alternating positive (red/yellow) and negative (blue) anomalies, indicating cycles of water accumulation and depletion. For instance, strong positive TWS signals appear during April–May 2023 and February–April 2024, corresponding to wet-season recharge, while negative anomalies dominate in subsequent months, reflecting water loss due to evapotranspiration and reduced precipitation.

A comparison between the two years highlights notable differences in the strength and spatial coherence of the inversion results. The 2023 TWS maps show more fragmented and noisy patterns, particularly during April and May, where strong localized extremes suggest higher sensitivity to inversion instability and noise amplification. In contrast, the 2024 results appear relatively more structured and continuous, especially during mid- to late-year months (August-November), where elongated zones of positive TWS anomalies are visible across the equatorial region. This suggests that the inversion process, when applied to 2024 data, yields a more stable reconstruction of large-scale hydrological patterns. However, both years still exhibit noticeable striping artifacts, indicating limitations of the inversion and the need for stronger regularization or alternative observation functionals.

Overall, the TWS inversion results confirm that gravitational potential data can successfully capture seasonal hydrological dynamics, including wet and dry cycles across Africa. While the major spatial patterns align with expected climatic behavior, the presence of noise and striping emphasizes the challenges inherent in solving ill-posed inverse problems. Nevertheless, the comparison between 2023 and 2024 demonstrates that the method is capable of resolving both seasonal variability and interannual differences, making it a valuable approach for large-scale water storage monitoring when combined with appropriate filtering and regularization strategies.

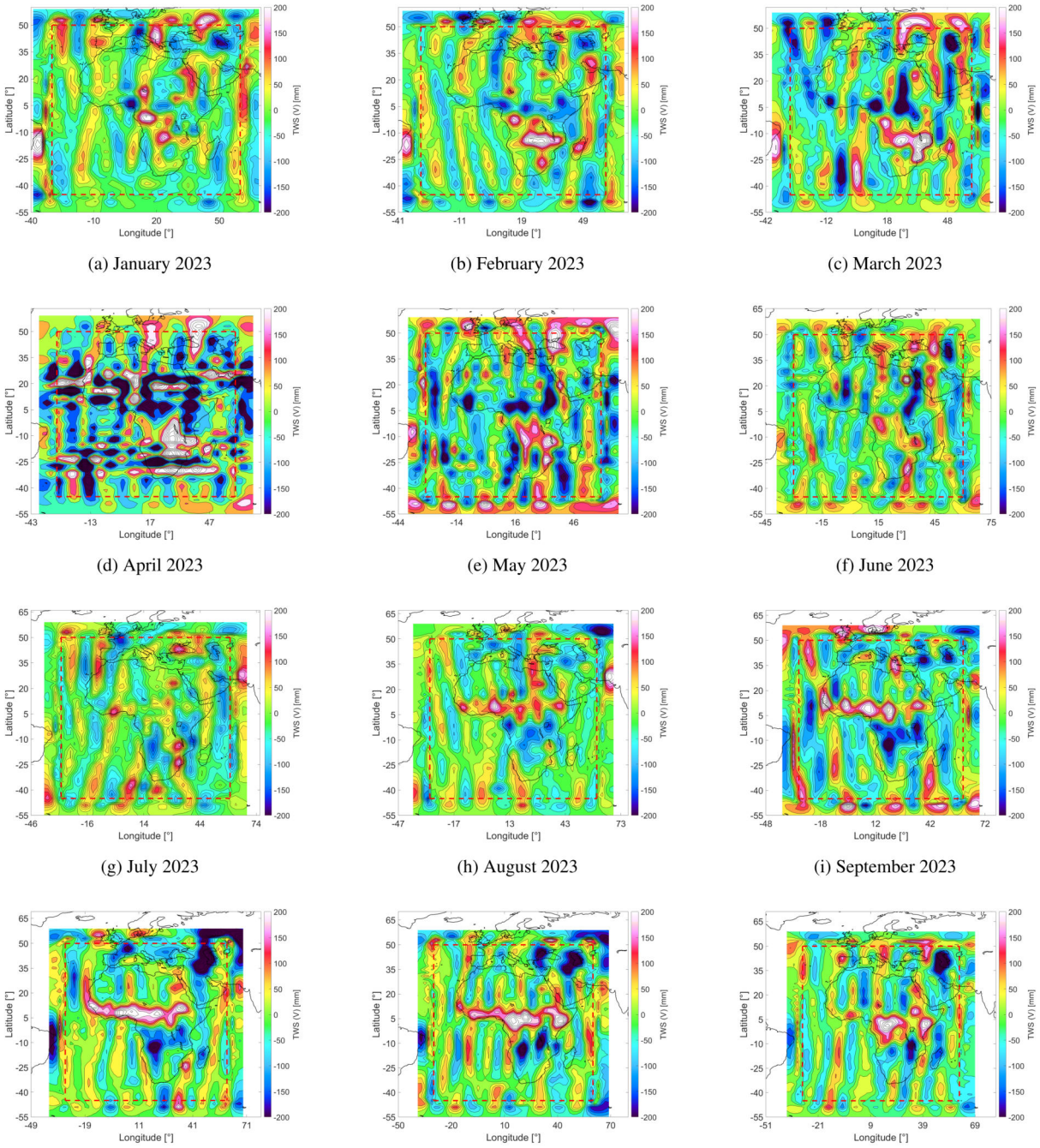

(a) January 2023 (b) February 2023 (c) March 2023

(d) April 2023 (e) May 2023 (f) June 2023

(g) July 2023 (h) August 2023 (i) September 2023

(j) October 2023 (k) November 2023 (l) December 2023

Figure 5.5: TWS from Residual Gravity Potential for the year 2023. Range is ±200 mm.

5.2.3 Total Water Storage from Gravity Disturbance

The inversion-derived Total Water Storage (TWS) maps for 2023 and 2024 reveal clear spatial and temporal variability in terrestrial water mass distribution inferred from gravitational disturbances. Across both years, the maps consistently show alternating positive and negative TWS anomalies, represented by warm colors (yellow–red) indicating relative water gain/storage increase, and cool colors (blue) indicating water deficit or depletion. In 2023, most monthly solutions exhibit a moderately stable spatial pattern with elongated north–south anomaly bands, suggesting a persistent regional hydrological structure controlled by geological formations, groundwater pathways, or climatic forcing. Strong positive anomalies are visible during February, March, August, September, October, and November, where localized high-amplitude signals indicate periods of enhanced water accumulation, possibly

linked to seasonal recharge, precipitation events, or increased soil moisture retention. In contrast, April 2023 displays a notably disturbed and noisy pattern with fragmented anomalies and stronger negative patches, implying abrupt hydrological changes or inversion instability, potentially associated with transient depletion, drainage, or reduced recharge conditions.

The 2024 inversion results preserve the overall spatial continuity observed in 2023 but demonstrate comparatively stronger seasonal contrasts and more pronounced anomaly magnitudes. Early 2024 (January–March) maintains moderate positive TWS zones in the central and northern parts of the study region, indicating residual storage persistence from prior recharge cycles. However, distinct negative anomalies intensify during April, September, and October 2024, where extensive blue patches suggest substantial water mass reduction, likely reflecting groundwater withdrawal, evapotranspiration dominance, or dry-season effects. August and November 2024 show strong positive anomalies re-emerging in clustered zones, indicating episodic recharge or localized water recovery. The recurrence of similar anomaly structures between 2023 and 2024 confirms the robustness of the inversion approach in capturing seasonal hydrological dynamics from gravity disturbances. Overall, the TWS estimates suggest a cyclic annual storage behavior with alternating recharge and depletion phases, while 2024 appears to exhibit slightly higher variability and stronger hydrological extremes than 2023, indicating intensified temporal fluctuations in regional water storage conditions.

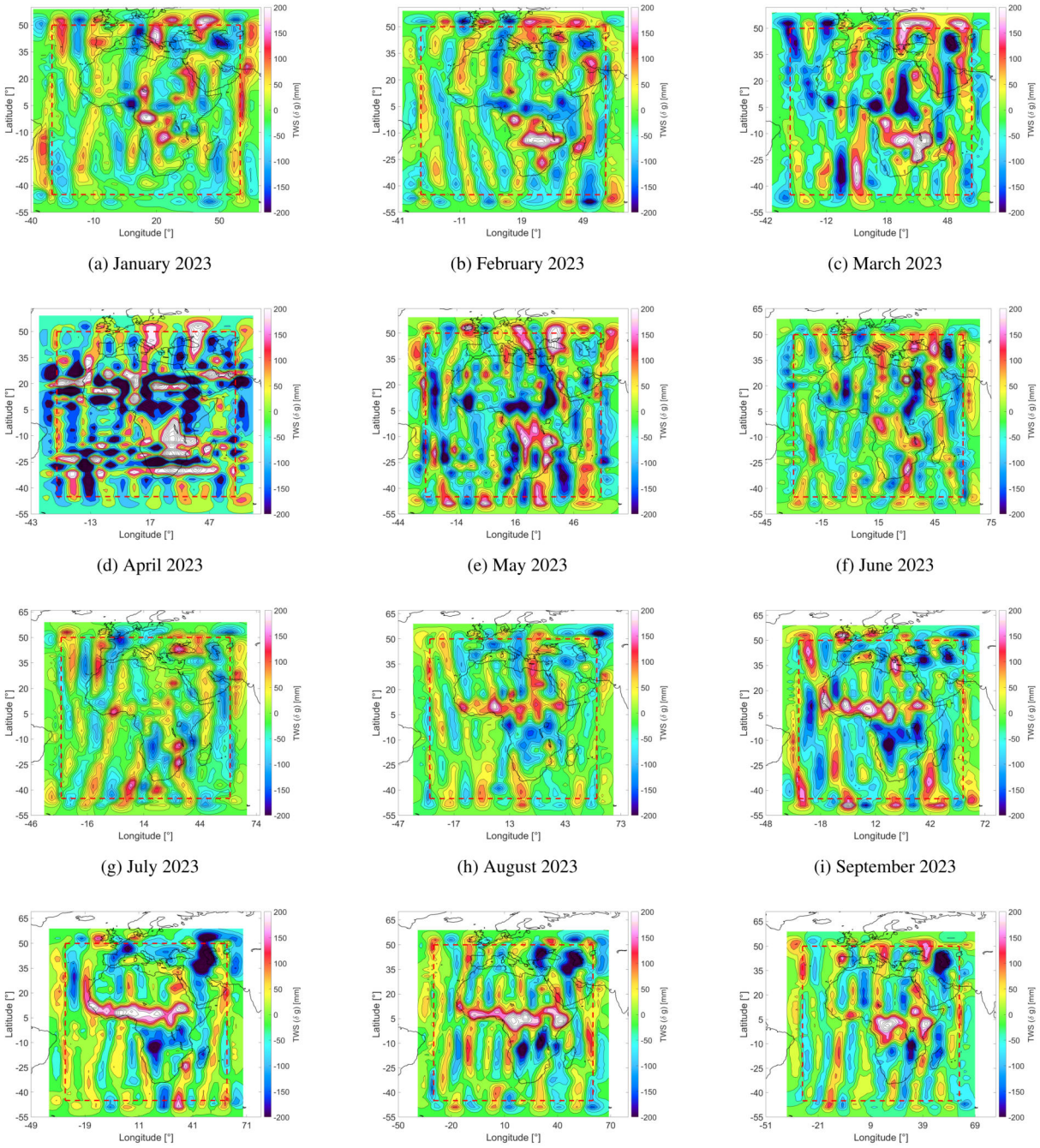

(a) January 2023 (b) February 2023 (c) March 2023

(d) April 2023 (e) May 2023 (f) June 2023

(g) July 2023 (h) August 2023 (i) September 2023

(j) October 2023 (k) November 2023 (l) December 2023

Figure 5.6: TWS from Residual Gravity Disturbance for the year 2023. Range is ±200 mm.

5.2.4 Total Water Storage from Gravity Anomaly

The Total Water Storage (TWS) maps derived from gravitational anomaly inversion for 2023 and 2024 demonstrate significant seasonal and spatial variations in subsurface and surface water mass distribution across the study area. In both years, the inversion results display alternating positive and negative anomalies, where warm colors (yellow to red) represent regions of increased water storage or mass accumulation, while cool colors (blue) indicate water deficit or depletion zones. For 2023, the monthly maps reveal relatively coherent north–south elongated anomaly structures throughout most months, suggesting stable regional hydrological controls and continuity in inversion outputs. January to March 2023 exhibit moderate positive anomalies concentrated in central and northern regions, implying gradual recharge and improved water retention during the early hydrological cycle. A noticeable dis-

ruption occurs in April 2023, where highly fragmented blue-dominated patches and irregular anomaly patterns suggest intense depletion or strong short-term hydrological fluctuations, possibly due to groundwater abstraction, reduced precipitation, or inversion sensitivity. From August to December 2023, positive anomalies become more localized and pronounced, especially in September, November, and December, indicating recovery phases and seasonal recharge in selected zones.

The 2024 TWS inversion results derived from gravitational anomaly maintain a similar large-scale spatial framework but indicate stronger temporal variability and higher anomaly contrasts compared to 2023. Early 2024 (January–March) continues to show dominant positive anomalies in the upper and central sections, reflecting persistence of stored water mass and possible carryover recharge effects. During April to July 2024, mixed anomaly patterns emerge, with alternating positive and negative zones indicating transitional hydrological conditions. The most pronounced depletion signatures appear in September and October 2024, where extensive blue anomalies dominate large portions of the study area, suggesting substantial water mass reduction likely associated with dry-season stress, evapotranspiration losses, or intensified groundwater withdrawal. Recovery signals are again visible in November and December 2024 through the reappearance of clustered positive anomalies, marking the onset of recharge or restoration of local storage conditions. Overall, the inversion-derived TWS from gravitational anomaly successfully captures the cyclic behavior of water storage variations, with both years showing seasonal recharge–depletion patterns, while 2024 reflects comparatively stronger hydrological extremes and enhanced variability relative to 2023.

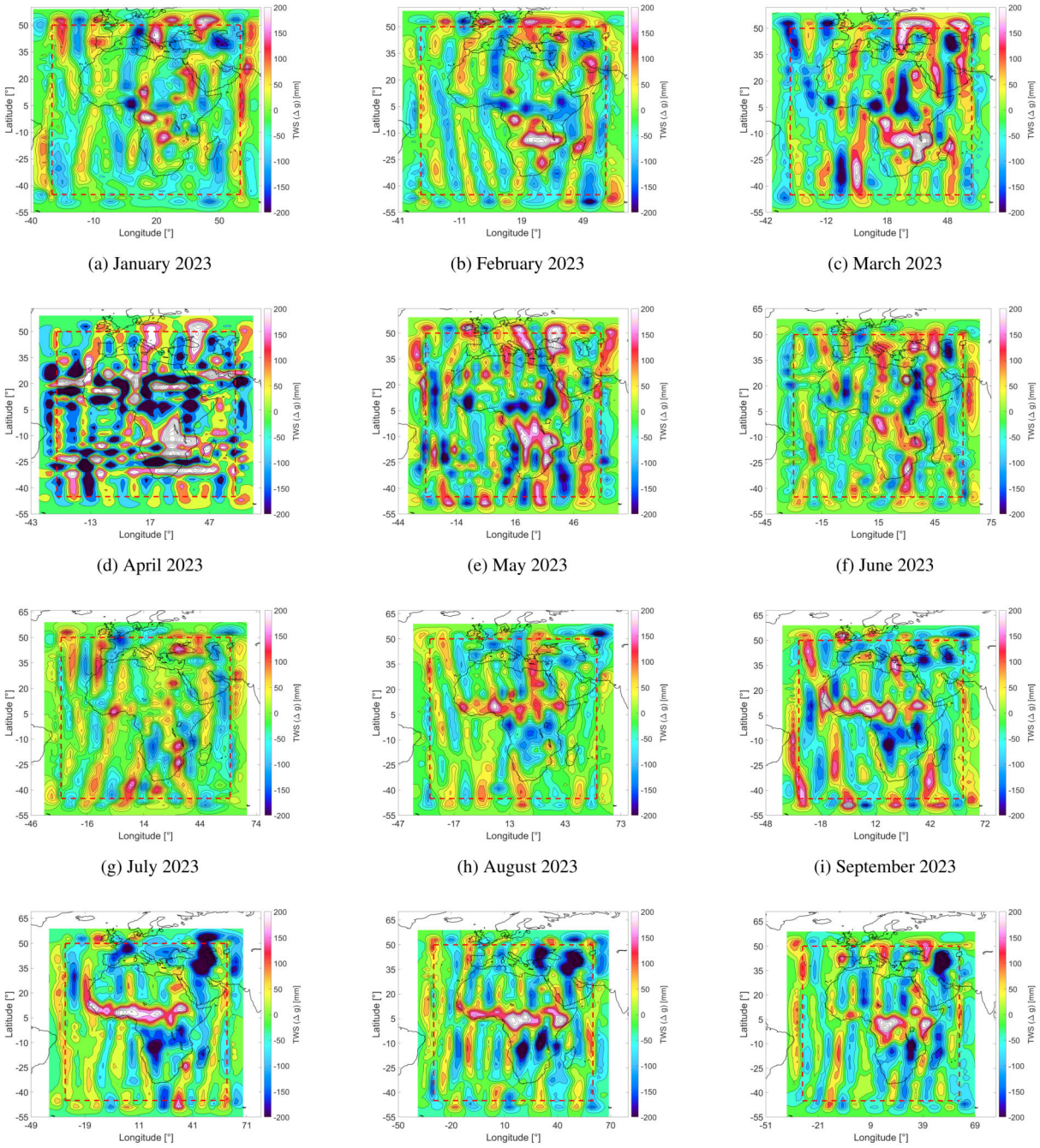

(a) January 2023 (b) February 2023 (c) March 2023

(d) April 2023 (e) May 2023 (f) June 2023

(g) July 2023 (h) August 2023 (i) September 2023

(j) October 2023 (k) November 2023 (l) December 2023

Figure 5.7: TWS from Residual Gravity Anomaly for the year 2023. Range is ±200 mm.

5.3 Comparison of Observation Functionals

To assess the performance of the three observation functionals employed in the inverse tesseroid framework, a comparative analysis was conducted using the residual fields obtained after inversion. The residuals represent the differences between the synthesized GRACE-FO observations and the corresponding values reconstructed from the estimated tesseroid mass model. Consequently, the residual maps provide a quantitative measure of the ability of each observation functional to reproduce the observed gravity signal. Smaller and spatially random residuals indicate a successful inversion, whereas systematic patterns suggest the presence of unresolved signals, modelling deficiencies, or residual observational noise.

Figure 10 presents representative residual fields for September 2023 corresponding to the gravitational potential, gravity disturbance, and gravity anomaly inversions. Similar residual characteristics were observed throughout the entire study period for both 2023 and 2024. Therefore, the September 2023 results are considered representative of the overall behaviour of the observation functionals.

The residual field obtained from the gravitational potential inversion exhibits the smallest spatial variability among the three functionals. The residuals are distributed relatively uniformly across the African continent and remain close to zero over most regions. No significant systematic structures or localized anomalies are visible, indicating that the inverse tesseroid model successfully reproduces the dominant long-wavelength gravity signal contained in the gravitational potential observations. This behaviour is consistent with the physical characteristics of gravitational potential, which acts as a naturally smoothed gravity quantity due to its integral formulation. Because high-frequency noise is inherently attenuated, the resulting inversion is numerically stable and produces the lowest residual magnitudes. However, the smooth residual distribution also implies that some small-scale hydrological variations may not be fully represented in the recovered solution.

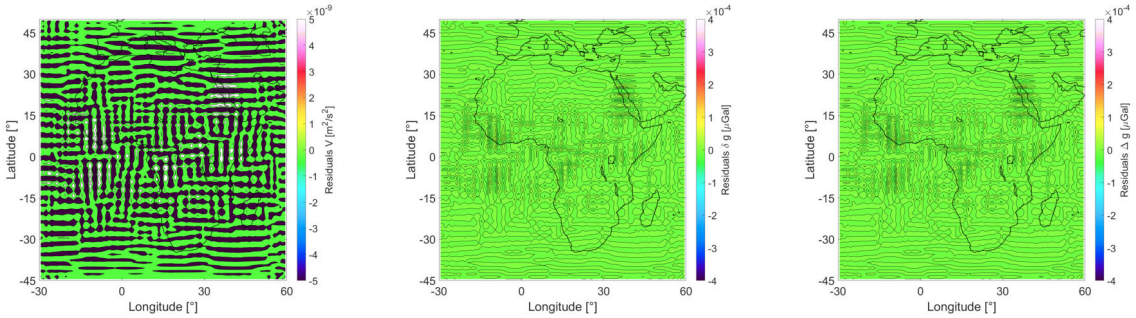

(a) Potential Residuals (b) Gravity Disturbance Residuals (c) Gravity Anomaly Residuals

Figure 5.8: Residuals from September 2023.

The gravity disturbance residuals show slightly larger spatial variability than the gravitational potential residuals but remain relatively homogeneous across the study area. Localized residual fluctuations are visible in several regions, reflecting the increased sensitivity of gravity disturbance to regional mass redistribution processes. Since gravity disturbance is derived from the radial derivative of the gravitational potential, it contains enhanced short-wavelength information and therefore captures regional hydrological variability more effectively. Although derivative operations amplify observational noise, the residual map demonstrates that the applied regularization and filtering procedures successfully suppress most of these effects. Consequently, gravity disturbance provides an improved representation of regional hydrological structures while maintaining acceptable inversion stability.

In contrast, the gravity anomaly residuals display a markedly different spatial pattern. Distinct alternating positive and negative bands are visible throughout the study area, producing a characteristic striped appearance. These patterns are indicative of residual short-wavelength components and correlated errors that remain after the preprocessing and filtering stages. Gravity anomalies are inherently more sensitive to local gravity variations and therefore preserve a larger proportion of the high-frequency signal contained in the GRACE-FO observations. While this increased sensitivity improves the capability of detecting localized mass redistribution, it also amplifies residual noise and modelling errors. The persistence of stripe-like residual structures suggests that a portion of the high-frequency gravity signal is not fully explained by the tesseroid model, despite the application of DDK filtering and Tikhonov regularization.

The comparison of the three residual fields clearly illustrates the trade-off between inversion stability and spatial sensitivity. Gravitational potential produces the smallest and smoothest residuals, indicating superior numerical stability and effective recovery of large-scale hydrological signals. Gravity disturbance achieves a balance between stability and spatial resolution, producing slightly larger residuals but retaining important regional hydrological

information. Gravity anomaly exhibits the highest residual variability and strongest striping patterns, reflecting its greater sensitivity to short-wavelength signals and observational noise.
Overall, the residual analysis demonstrates that all three observation functionals are capable of recovering the dominant hydrological signals observed by GRACE-FO. However, their inversion performance differs substantially due to their physical characteristics. Gravitational potential is most suitable for large-scale and stable hydrological investigations, gravity disturbance provides an optimal compromise between spatial resolution and numerical robustness, while gravity anomaly offers enhanced local sensitivity at the expense of increased noise amplification. These findings are consistent with the theoretical expectations of gravity field inversion and confirm that the choice of observation functional significantly influences both the quality and spatial characteristics of the recovered Total Water Storage estimates (Hackney and Featherstone, 2003; Heck and Seitz, 2007; Tikhonov and Arsenin, 1977; Hansen, 1992).
The residual analysis indicates that gravity disturbance provides the most balanced performance among the three observation functionals, preserving regional hydrological information while maintaining acceptable numerical stability. Although gravitational potential yields the smallest residuals, its reduced spatial sensitivity limits the recovery of localized hydrological features, whereas gravity anomaly exhibits increased susceptibility to residual noise despite its enhanced spatial resolution.

6 Conclusion and Outlook

The synthesized gravity fields successfully captured the seasonal and regional hydrological variability across Africa. The gravitational potential fields exhibited smooth large-scale patterns associated with continental water redistribution, while gravity disturbance and gravity anomaly provided enhanced sensitivity to regional and local hydrological variations. In both 2023 and 2024, pronounced positive gravity signals were observed over Central and Equatorial Africa during the late monsoon season, particularly from September to November, indicating substantial water accumulation resulting from precipitation, groundwater recharge, and increased surface water storage. During the dry periods, reduced gravity signals reflected decreasing terrestrial water storage and increased evapotranspiration. These results demonstrate the capability of GRACE-FO observations to monitor seasonal hydrological processes over large spatial scales and confirm the suitability of gravity field synthesis for investigating continental-scale water storage variability.
The inverse tesseroid framework successfully transformed the synthesized gravity observations into estimates of terrestrial water storage anomalies. The implementation of Tikhonov regularization was essential for stabilizing the inversion process and mitigating the effects of ill-conditioning inherent in gravity inversion problems (Tikhonov and Arsenin, 1977). The L-curve criterion proved effective for selecting optimal regularization parameters by balancing solution smoothness and observational misfit (Hansen, 1992). The resulting inversions produced physically meaningful TWS distributions while maintaining numerical stability. The L-curve analysis further demonstrated that different observation functionals require different levels of regularization due to their varying sensitivities to noise and short-wavelength gravity signals.
A major contribution of this study is the comparative evaluation of gravitational potential, gravity disturbance, and gravity anomaly as observation functionals within the inverse tesseroid framework. The results indicate that the physical properties of each gravity quantity significantly influence the inversion outcome. Gravitational potential produced the smoothest and most stable solutions because of its dominance by long-wavelength gravity signals. However, this smoothing effect reduced the sensitivity to localized hydrological features. Gravity disturbance improved spatial resolution and enhanced the representation of regional mass redistribution processes by emphasizing shorter-wavelength gravity information. Nevertheless, the derivative nature of gravity disturbance increased its susceptibility to noise amplification and numerical instability. Gravity anomaly exhibited intermediate characteristics, preserving regional hydrological structures while maintaining greater stability than gravity disturbance.

Consequently, gravity anomaly provided a balanced representation of hydrological variability, whereas gravity disturbance offered the highest spatial sensitivity.

The residual analysis provided further insight into the performance of the observation functionals. Using September 2023 as a representative example, the residual maps showed that gravitational potential produced the smallest and most spatially homogeneous residuals, indicating excellent agreement between the observations and the reconstructed gravity field. Gravity disturbance generated slightly larger residuals but retained important regional hydrological information. Gravity anomaly residuals displayed more pronounced stripe-like structures associated with residual short-wavelength errors and correlated noise. These findings illustrate the fundamental trade-off between inversion stability and spatial resolution that characterizes gravity-based hydrological inversion methods. While gravitational potential yields highly stable solutions, gravity disturbance and gravity anomaly improve regional sensitivity at the expense of increased susceptibility to observational noise.

Overall, the results demonstrate that inverse tesseroid modelling is a robust and physically consistent approach for recovering terrestrial water storage variations from satellite gravimetry observations. The tesseroid representation naturally accounts for Earth's curvature and provides a flexible framework for spatial-domain gravity inversion (Heck and Seitz, 2007; Grombein et al., 2012). The study further confirms that the selection of observation functionals plays a critical role in determining the quality and characteristics of the recovered hydrological signals. Among the investigated observables, gravity disturbance appears to provide the most effective compromise between spatial resolution and numerical stability, while gravitational potential and gravity anomaly offer complementary strengths for large-scale and localized investigations, respectively.

Although the present work demonstrates the effectiveness of the proposed methodology, several opportunities exist for future improvements. One promising direction is the development of joint inversion strategies that simultaneously incorporate gravitational potential, gravity disturbance, and gravity anomaly observations within a unified inversion framework. Such an approach could exploit the complementary information contained in the different observables and potentially improve both inversion stability and spatial resolution. Future studies may also investigate advanced regularization techniques, including higher-order smoothness constraints, adaptive regularization methods, and Bayesian inversion approaches. The integration of independent hydrological datasets such as GLDAS products, groundwater observations, precipitation records, and hydrological model simulations would provide additional validation of the recovered TWS signals and improve confidence in the inversion results.

the influence of the defined height, where the observations are synthesized should also be investigated in future studies.

Furthermore, the increasing availability of GRACE-FO observations and future satellite gravimetry missions presents significant opportunities for advancing gravity-based hydrological monitoring. Higher-resolution gravity field products, improved noise reduction techniques, and time-dependent inversion methodologies may enhance the detection of smaller-scale hydrological processes and long-term climate-driven water storage changes. The methodology developed in this study therefore provides a valuable foundation for future investigations of groundwater depletion, drought monitoring, flood assessment, climate variability, and large-scale water resource management. As satellite gravimetry continues to evolve, inverse tesseroid modelling is expected to become an increasingly important tool for understanding and quantifying terrestrial water storage dynamics at regional and continental scales.

Acknowledgement

The author acknowledges the support from Geodätisches Institut (GIK) for providing necessary resources and facilities. Additionally, the author acknowledges ICGEM (2026) for the data provided for this study.

References

Grombein, T., Seitz, K., Awange, J. L., and Heck, B. (2012): Detection of hydrological mass variations by means of an inverse tesseroid approach. Poster presentation at the European Geosciences Union General Assembly (EGU 2012), Vienna, Austria, 22.–27. April 2012. DOI: 10.5445/IR/1000162814.

Hackney, R. I. and Featherstone, W. E. (2003): Geodetic versus geophysical perspectives of the 'gravity anomaly'. *Geophysical Journal International* 154(1):35–43. DOI: 10.1046/j.1365-246X.2003.01941.x.

Hansen, P. C. (1992): Analysis of Discrete Ill-Posed Problems by Means of the L-Curve. *SIAM Review* 34(4):561–580. DOI: 10.1137/1034115.

Heck, B. and Seitz, K. (2007): A comparison of the tesseroid, prism and point-mass approaches for mass reductions in gravity field modelling. *Journal of Geodesy* 81(2):121–136. DOI: 10.1007/s00190-006-0094-0.

Heiskanen, W. A. and Moritz, H. (1967): Physical Geodesy. W. H. Freeman & Co., San Francisco, USA.

ICGEM (2026): International Centre for Global Earth Models (ICGEM): Gravity field and GRACE/GRACE-FO products hosted at the German Research Centre for Geosciences (GFZ). Accessed: 2026-04-06. URL: https://icgem.gfz-potsdam.de/.

Kusche, J., Schmidt, R., Petrovic, S., and Rietbroek, R. (2009): Decorrelated GRACE time-variable gravity solutions by GFZ, and their validation using a hydrological model. *Journal of Geodesy* 83(10):903–913. DOI: 10.1007/s00190-009-0308-3.

Mader, K. (1951): Das Newtonsche Raumpotential prismatischer Körper und seine Ableitungen bis zur dritten Ordnung. *Österreichische Zeitschrift für Vermessungswesen*, *Sonderheft* 11.

Nagy, D. (1966): The gravitational attraction of a right rectangular prism. *Geophysics* 31(2):362–371. DOI: 10.1190/1.1439779. URL: +%20http://dx.doi.org/10.1190/1.1439779.

Rummel, R. and van Gelderen, M. (1995): Meissl scheme—spectral characteristics of physical geodesy. *Manuscripta geodaetica* 20(5):379–385.

Tapley, B. D., Bettadpur, S., Watkins, M., and Reigber, C. (2004): The gravity recovery and climate experiment: Mission overview and early results. *Geophysical Research Letters* 31(9):1–4. DOI: 10.1029/2004GL019920.

Tikhonov, A. (1963): Solution of incorrectly formulated problems and the regularization method. *Soviet Mathematics Doklady* 5:1035–1038.

Tikhonov, A. N. and Arsenin, V. Y. (1977): Solutions of Ill-Posed Problems. Winston, New York.

Wahr, J., Molenaar, M., and Bryan, F. (1998): Time variability of the Earth's gravity field: Hydrological and oceanic effects and their possible detection using GRACE. *Journal of Geophysical Research: Solid Earth* 103(B12):30205–30229.

Appendix

A Residual Gravity Potential for the year 2024

The residual gravity potential results for the year 2024 are shown in Figure A.1.

B Residual Gravity Disturbance for year 2024

The residual gravity disturbance for the year 2024 are shown in Figure B.1.

C Residual Gravity Anomalies for the year 2024

The residual gravity anomalies for the year 2024 are shown in Figure C.1.

D TWS from Residual Gravity Potential for the year 2024

Results of the Total Water Storage from the residual gravity potential for the year 2024 are shown in Figure D.1.

E TWS from Residual Gravity Disturbance for the year 2024

Results of the Total Water Storage from the residual gravity disturbance for the year 2024 are shown in Figure E.1.

F TWS from Residual Gravity Anomaly for the year 2024

Results of the Total Water Storage from the residual gravity anomaly for the year 2024 are shown in Figure F.1.

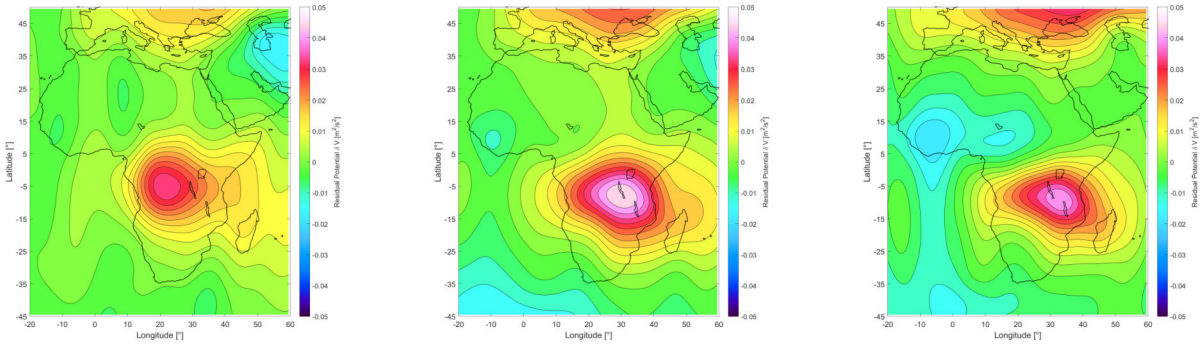

(a) January 2024 (b) February 2024 (c) March 2024

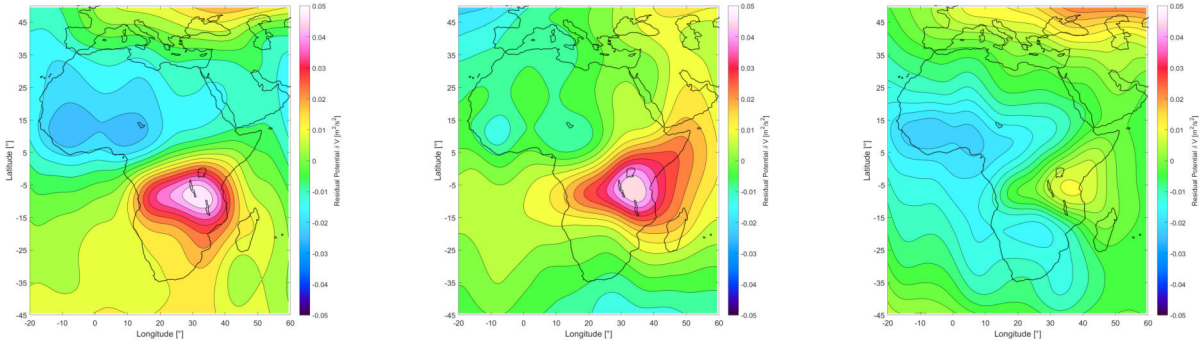

(d) April 2024 (e) May 2024 (f) June 2024

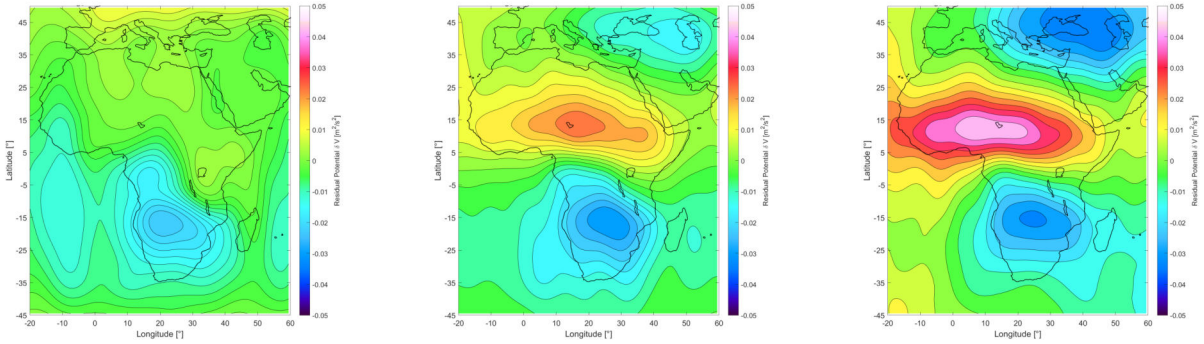

(g) July 2024 (h) August 2024 (i) September 2024

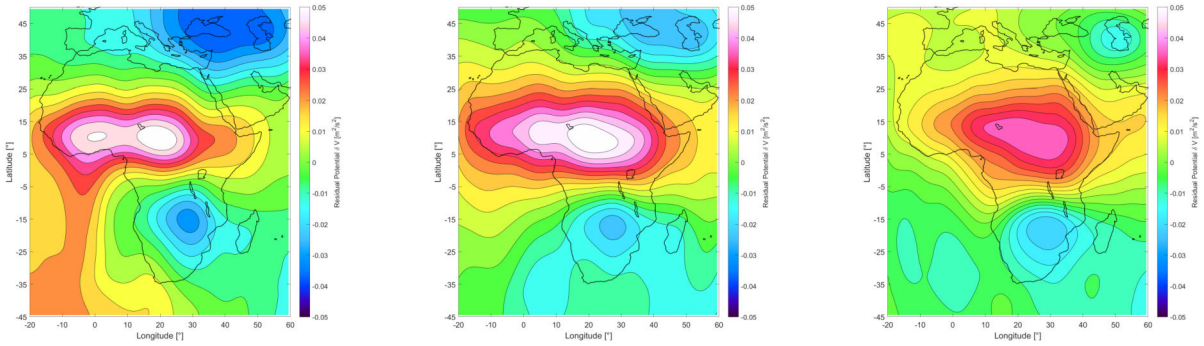

(j) October 2024 (k) November 2024 (l) December 2024

Figure A.1: Residual Gravity Potential for the year 2024. Range is $\pm 0.05\ m^2 s^{-2}$

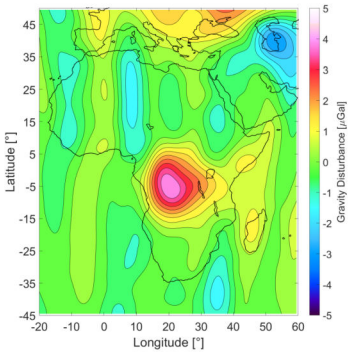

(a) January 2024

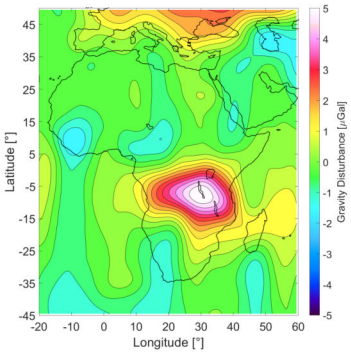

(b) February 2024

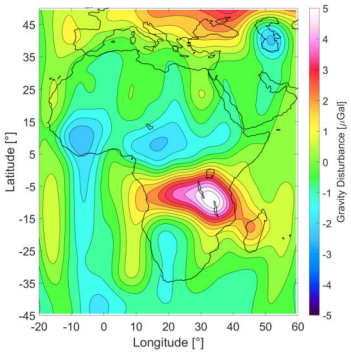

(c) March 2024

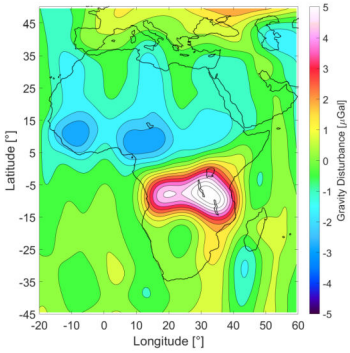

(d) April 2024

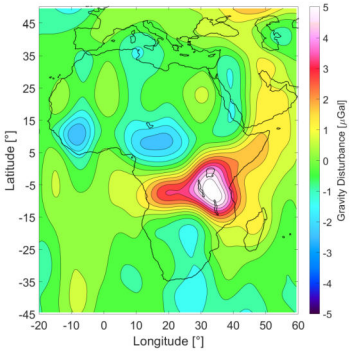

(e) May 2024

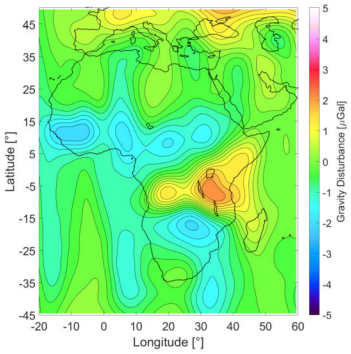

(f) June 2024

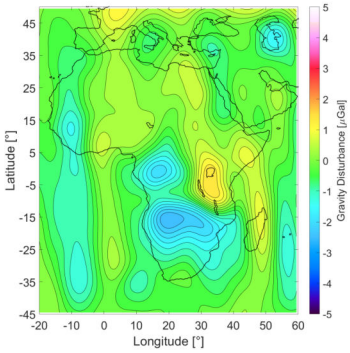

(g) July 2024

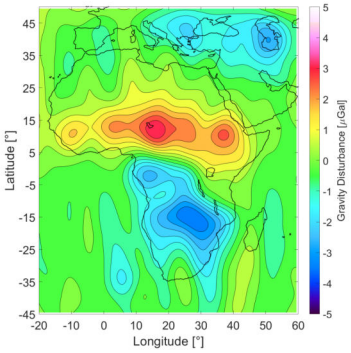

(h) August 2024

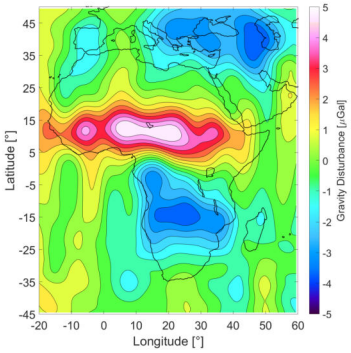

(i) September 2024

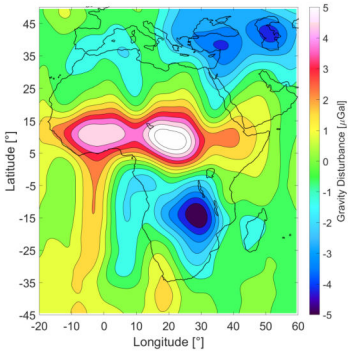

(j) October 2024

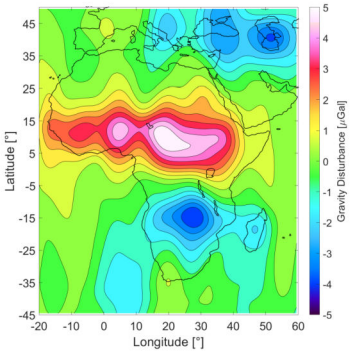

(k) November 2024

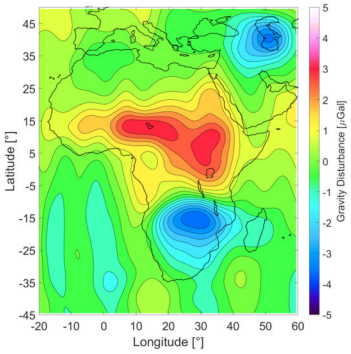

(l) December 2024

Figure B.1: Residual Gravity Disturbance for the year 2024. Range is ± 5 μGal

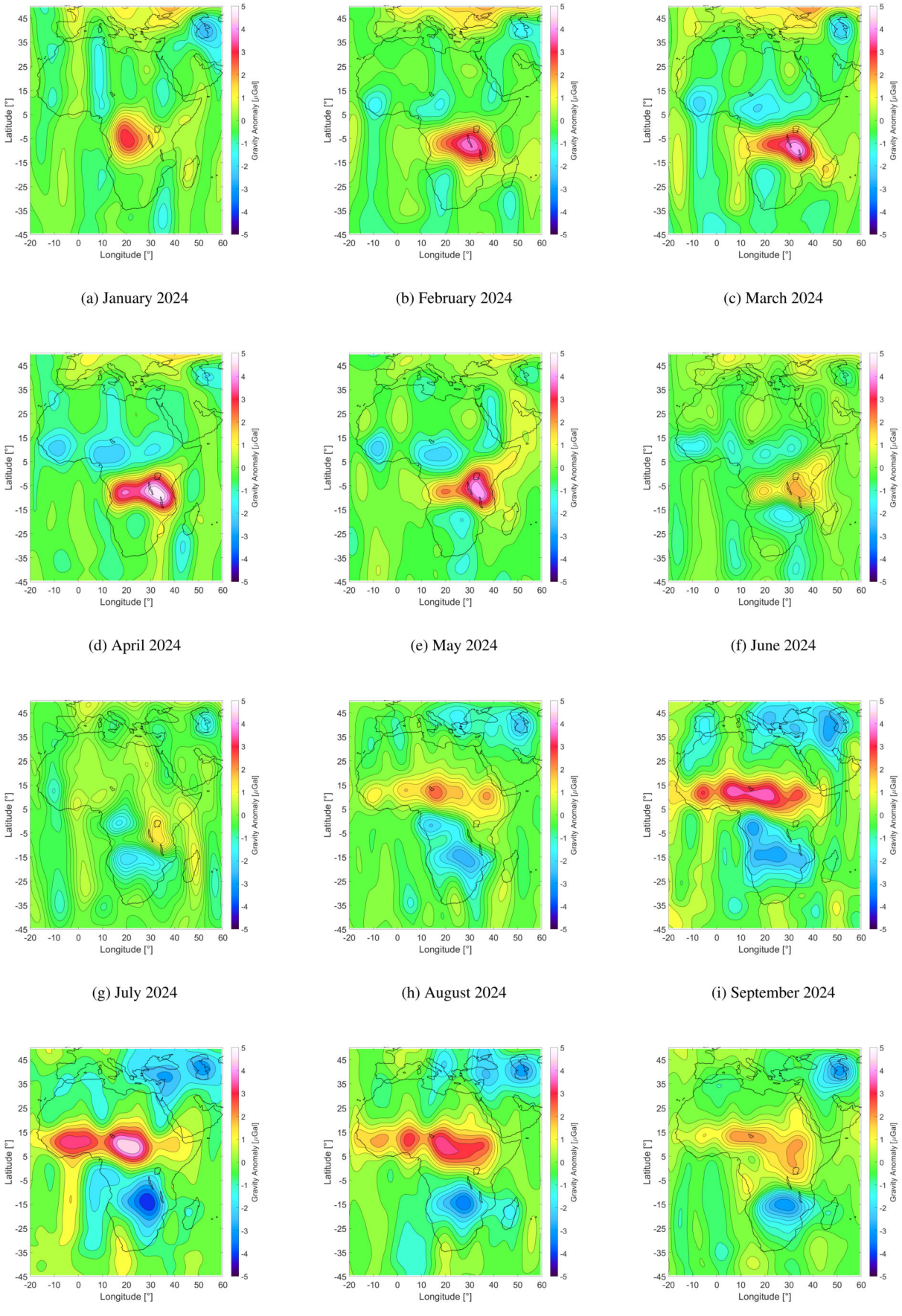

(a) January 2024 (b) February 2024 (c) March 2024

(d) April 2024 (e) May 2024 (f) June 2024

(g) July 2024 (h) August 2024 (i) September 2024

(j) October 2024 (k) November 2024 (l) December 2024

Figure C.1: Residual Gravity Anomalies for the year 2024. Range is ± 5 *μGal*

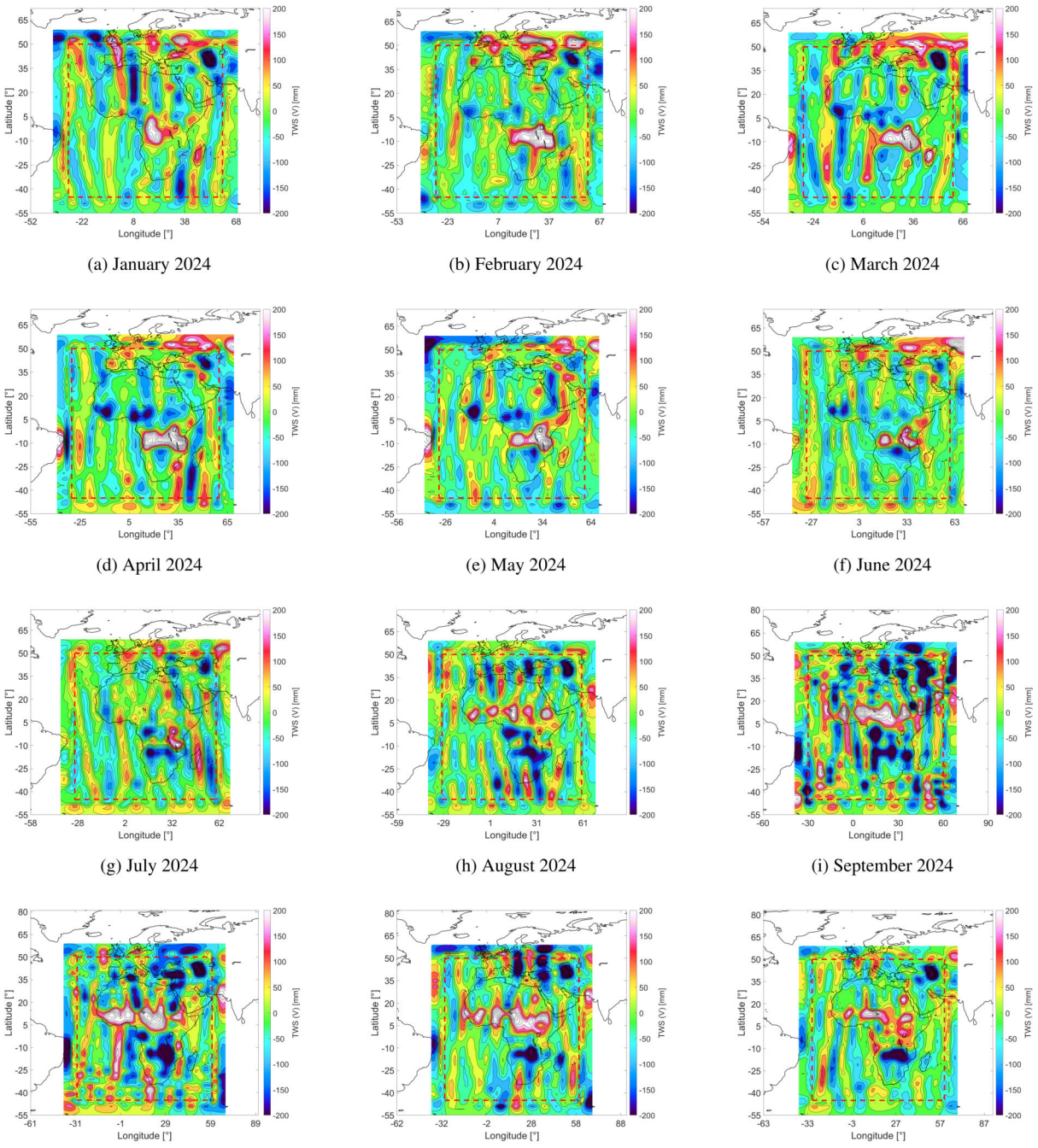

(a) January 2024 (b) February 2024 (c) March 2024

(d) April 2024 (e) May 2024 (f) June 2024

(g) July 2024 (h) August 2024 (i) September 2024

(j) October 2024 (k) November 2024 (l) December 2024

Figure D.1: TWS from Residual Gravity Potential for year 2024. Range is ±200 mm.

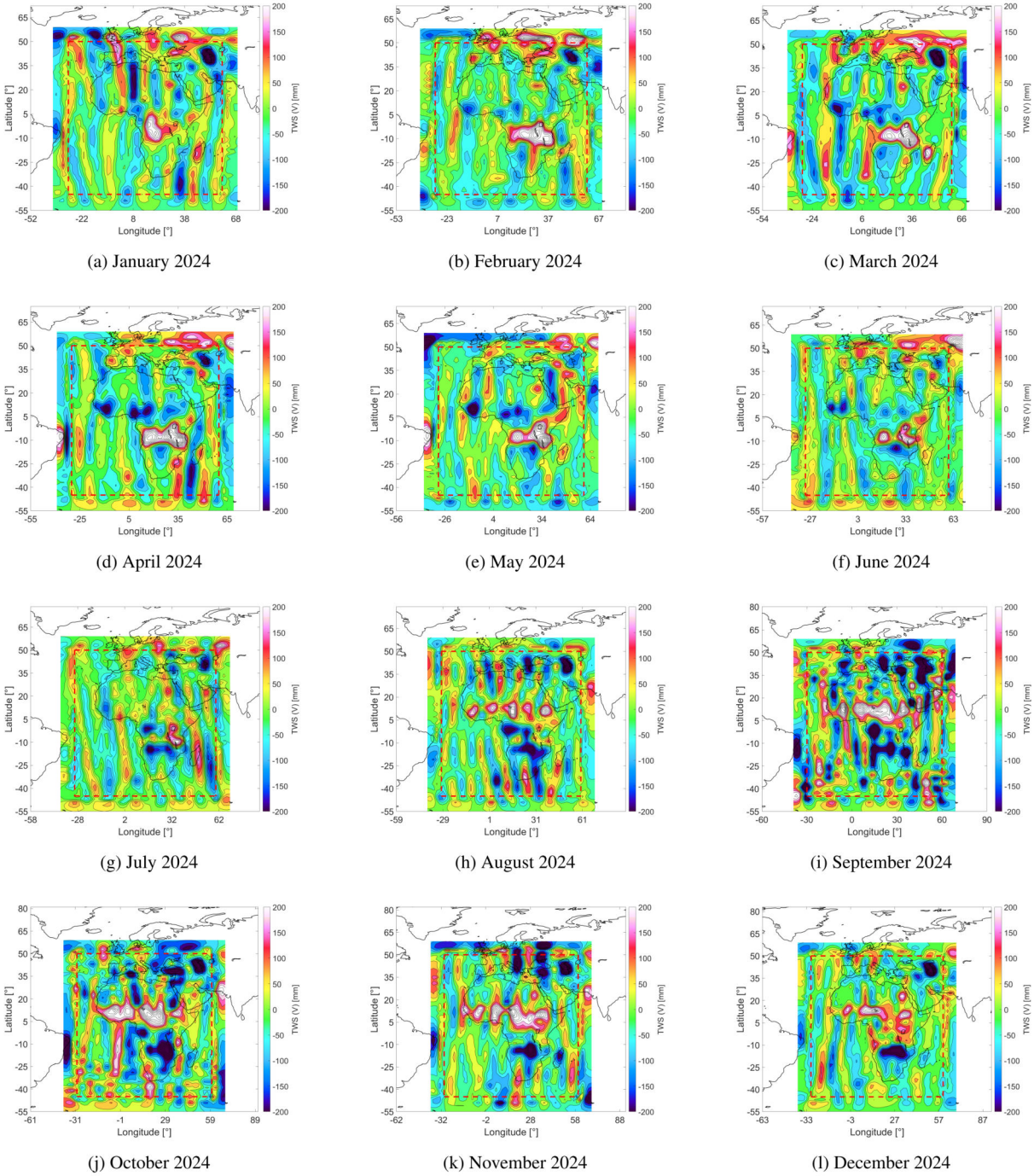

(a) January 2024 (b) February 2024 (c) March 2024

(d) April 2024 (e) May 2024 (f) June 2024

(g) July 2024 (h) August 2024 (i) September 2024

(j) October 2024 (k) November 2024 (l) December 2024

Figure E.1: TWS from Residual Gravity Disturbance for the year 2024. Range is ±200 mm.

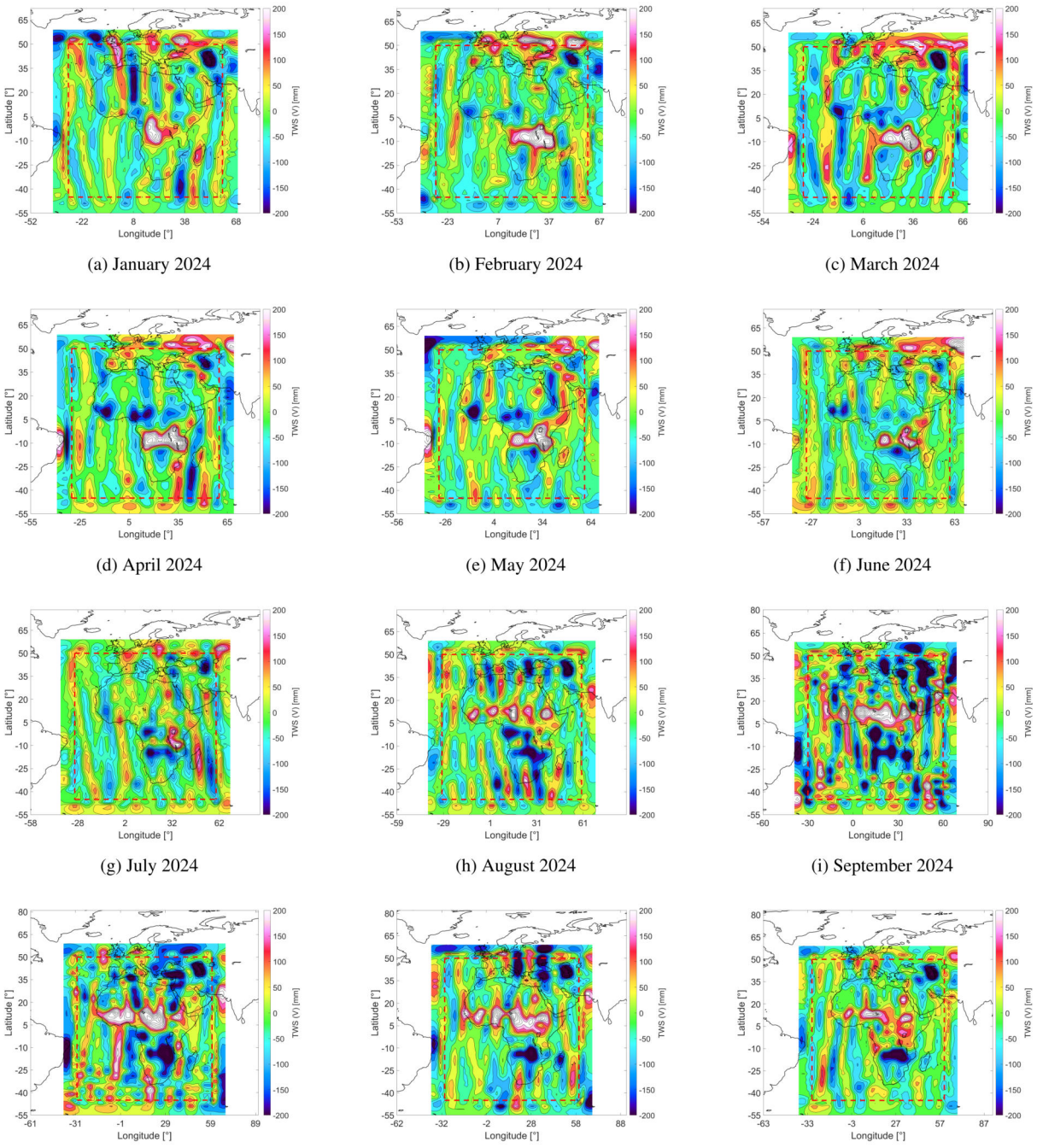

(a) January 2024 (b) February 2024 (c) March 2024

(d) April 2024 (e) May 2024 (f) June 2024

(g) July 2024 (h) August 2024 (i) September 2024

(j) October 2024 (k) November 2024 (l) December 2024

Figure F.1: TWS from Residual Gravity Anomaly for the year 2024. Range is ±200 mm.

Investigation on the El Niño event 2015-2016 based on GRACE

Abhijith Puthenveetil Sangeeth[1]

1 Remote Sensing and Geoinformatics Master of Science (M.Sc.), KIT, Germany
E-Mail: ubtqn@student.kit.edu

Abstract

The investigation utilized GRACE satellite-derived monthly gravity field solutions from 2010 to 2017 to examine massive water mass redistributions in the tropical Pacific during the severe 2015–2016 El Niño event. Through spatial and temporal analyses of Total Water Storage (TWS) and residual geoid undulation, the dynamic shifts – from the initial mass redistribution in September 2015 to the intense localized depletion in December 2015 – were clearly tracked. A primary objective was to evaluate the impact of spatial decorrelation filters and combined gravity solutions. The analysis demonstrates that raw, unfiltered spherical harmonic models (e.g., DDK0 and COST-G) are heavily contaminated by severe north–south striping artifacts that mask true regional hydrological anomalies in TWS maps. Therefore, spatial decorrelation filters are essential to remove these mathematical artifacts. Both the DDK2 and DDK5 filters successfully reduced the data to physically realistic scales, enabling the El Niño mass shift to emerge, albeit with trade-offs: DDK2 provides stronger smoothing to stabilize the standard deviation, whereas DDK5 preserves higher overall signal amplitude and spatial variance. Conversely, evaluating residual geoid undulation reveals a crucial geodetic principle: the mathematical computation of undulation inherently acts as a low-pass filter, suppressing high-frequency satellite errors. Consequently, the severe striping artifacts that affect unfiltered TWS data are virtually absent here, with both stand-alone DDK0 and the combined COST-G unfiltered models yielding highly consistent and directly usable geophysical signals without post-processing filters. Moving forward, this analysis of mass-induced sea level changes could be enhanced by integrating altimeter satellite observations, which provide direct spatial and temporal information on sea level variations. Comparing GRACE-derived mass redistributions with altimetry-derived sea level changes would offer a more comprehensive understanding of ocean mass dynamics during the ENSO cycle. Additionally, extending the analysis to include subsequent La Niña (cold phase) events would provide valuable insights into the full basin-wide water mass recovery process.

Keywords GRACE · COST-G · Total Water Storage (TWS) · ENSO · El Niño

1 Introduction

The Earth's gravity field is not static but varies with time due to the redistribution of mass within the Earth system (Gschwind et al., 2024). These mass redistributions include movements of water in the oceans, on continents, in the atmosphere, and within the solid Earth (Tapley et al., 2004a). Understanding these variations is crucial for monitoring global change processes, particularly those related to the climate system (Dickey et al., 1999). The Gravity Recovery and Climate Experiment (GRACE) satellite mission, launched in 2002 as a joint NASA-

KIT Scientific Working Papers
Issue Number 270
ISSN: 2194-1629
DOI: 10.5445/IR/1000191188
Online: June 2026

This document is licensed under the Creative Commons Attribution – Share Alike 4.0 International License (CC BY-SA 4.0):
https://creativecommons.org/licenses/by-sa/4.0/deed.en

DLR project, was specifically designed to measure temporal variations in Earth's gravity field with unprecedented accuracy (Tapley et al., 2004b). GRACE consists of two identical satellites flying in tandem at approximately 220 km separation, measuring the distance between them with micron-level precision using K-band microwave ranging (Tapley et al., 2004b). These range measurements are inverted to produce monthly global gravity field models, typically expressed as spherical harmonic coefficients complete to degree and order 60-96 (Bettadpur, 2012).

The El Niño-Southern Oscillation (ENSO) is the most prominent year-to-year climate fluctuation on Earth, originating in the tropical Pacific but affecting weather patterns worldwide (McPhaden et al., 2006). ENSO alternates between three phases: El Niño (warm phase), La Niña (cold phase), and neutral conditions. During normal (neutral) conditions, trade winds blow from east to west across the tropical Pacific, piling warm water in the western Pacific near Indonesia and allowing cold water to upwell along South America (Philander, 1989; Philander, 2001). This creates a west-east sea level gradient of approximately 40-50 cm across the equatorial Pacific (Cazenave et al., 2012). During El Niño, the trade winds weaken or reverse, causing the warm water pool to slosh eastward toward South America (McPhaden et al., 2006). This results in: Sea level rise in the eastern Pacific (up to 20-30 cm), Sea level fall in the western Pacific, weakening or reversal of the west-east sea level gradient, suppression of upwelling along South America, global teleconnections affecting rainfall, temperature, and storm patterns (Ropelewski and Halpert, 1987).

The 2015-2016 El Niño was one of the strongest on record, comparable to the major events of 1982-1983 and 1997-1998 (L'Heureux et al., 2017). It featured peak sea surface temperature anomalies exceeding +2.5°K in the El Niño +3.4°K region and caused widespread droughts, floods, and ecosystem impacts globally (Blunden and Arndt, 2016).

This study focuses on processing and analyzing GRACE data from 2010–2017 to investigate TWS anomalies in the tropical Pacific during El Niño 2015-2016.

- Quantify TWS variations using spherical harmonic gravity models.
- Map spatio/temporal evolution of water mass anomalies.

2 Theoretical Aspects

Core Principle: GRACE satellites measure time-variable gravity fields caused by mass redistribution in the Earth system. Changes in gravitational potential reflect shifts in terrestrial water storage (TWS), ice mass, and ocean bottom pressure (Tapley et al., 2004a).

Satellite gravimetry leverages fundamental principles of geodesy and fluid dynamics to quantify mass redistribution. The theoretical framework for converting GRACE gravitational observations into TWS anomalies addressing: Spherical Harmonics Synthesis (SHS), Variance Propagation, Wahr et al. (1998) approach, and Steric Effect.

2.1 Spherical Harmonic Synthesis (SHS)

Spherical harmonic representation of the gravityational potential V is given in Equation (2.1). Spherical Harmonic Synthesis is the forward computation of a function on or outside the sphere from a series of surface spherical harmonics (Heiskanen and Moritz, 1967; Tsoulis, 1999). The spherical harmonic coefficients derived from GRACE level-2 data is used to express the gravity field of Earth:

$$V(r,\vartheta,\lambda) = \frac{GM}{r}\sum_{l=0}^{\infty}\sum_{m=0}^{l}\left(\frac{a}{r}\right)^{l}\bar{P}_{lm}(\cos\vartheta)\left(\bar{C}_{lm}\cos m\lambda + \bar{S}_{lm}\sin m\lambda\right), \tag{2.1}$$

where G is the gravitational constant, M Earth's mass, a the semi-major axis, $\bar{P}_{lm}$ fully normalized Legendre functions, and $\bar{C}_{lm}, \bar{S}_{lm}$ Stokes coefficients.

2.2 Wahr Approach

The Wahr et al. (1998) transformation provides the critical link between satellite-observed gravity changes and terrestrial water storage anomalies. In the following, we elaborate on its physical foundation, mathematical derivation, and implementation nuances.

2.2.1 Fundamental Gravitational Theory

The Earth's gravitational potential obeys Poisson's equation inside the masses of the earth:

$$\nabla^2 V = -4\pi G\rho\,, \tag{2.2}$$

and it fulfills the Laplace Equation outside of the masses:

$$\nabla^2 V = 0\,, \tag{2.3}$$

where G is the gravitational constant. The potential perturbation δV is related to surface density anomalies $\Delta\sigma(\theta,\lambda)$ (Wahr et al., 1998) and finally to the EWH changes:

$$\Delta h_w(\varphi,\lambda) = \frac{R\rho_{avg}}{3\rho_w}\sum_{n=0}^{n_{max}}\frac{2n+1}{1+k_n}\sum_{m=0}^{n}\left[\Delta\bar{C}_{nm}cos(m\lambda)+\Delta\bar{S}_{nm}sin(m\lambda)\right]\bar{P}_{nm}(sin\varphi) \tag{2.4}$$

2.2.2 Love Number

Load Love numbers (Chen et al., 2018) quantify the elastic response of a planetary body to gravitational perturbations. Named after the British mathematician A.E.H. Love (1911), they are fundamental in geodesy for interpreting GRACE data:

$$k_n' = -\frac{\delta V_{\text{deform}}}{\delta V_{\text{load}}}\,. \tag{2.5}$$

2.2.3 Equivalent Water Height (EWH)

Equivalent Water Height (EWH) is the standardized metric for quantifying terrestrial water storage (TWS) changes from GRACE gravity data. It represents the vertical thickness (in mm or cm) of a water layer that would cause the observed gravitational anomaly, assuming uniform density over a grid cell.

$$EWH = \frac{\Delta\sigma}{\rho_w}. \tag{2.6}$$

The density of water is $\rho_w = 1000\text{kg/m}^3$.

2.3 Degree- and error degree variance

The degree variance quantifies the amplitudes of the spherical harmonic coefficients, which vary across different degrees. The sum of the squared coefficients expresses the overall energy in the signal as shown in Equation (2.7). The degree and error degree variances of a selected monteh is presented in Figure 2.1. It shows that there is a higher degree variance at lower degrees, and the value decreases as the degree (n) increases. This shows that there is a higher concentration of signal at lower degrees compared to higher degrees:

$$C_n^2(\bar{C}_{nm},\bar{S}_{nm}) = \sum_{m=0}^{n}(\bar{C}_{nm}^2+\bar{S}_{nm}^2)\,. \tag{2.7}$$

This helps to understand the distribution of signal intensity through the frequency range. Degree variance of the coefficients obtained in this study has been analysed, showing that the signal has higher energy in the long-

wavelength part and drops in the shorter-wavelength part. The plots for degree variance for all the months are similar with marginal variations, so an example plot for September 2015 is shown in the Figures 2.1 and 2.2. The degree variance does not depend on the calculation point $P(r, \varphi, \lambda)$.

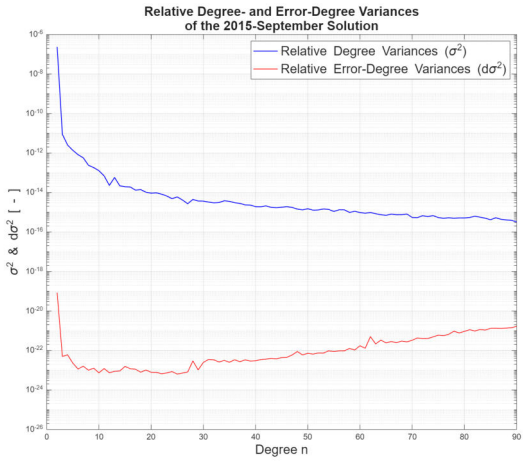

(a) COST-G

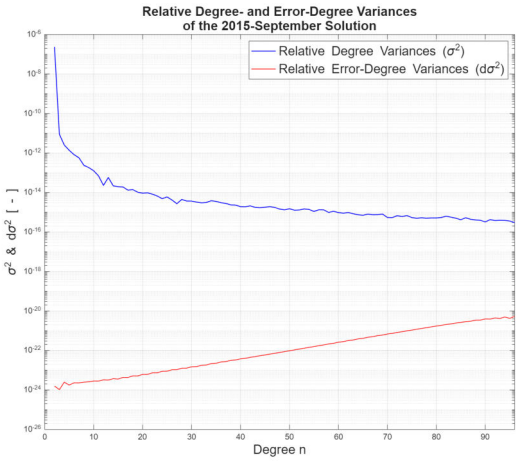

(b) DDK0

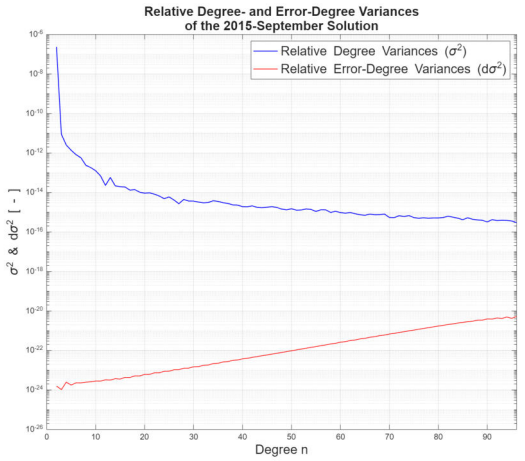

(c) DDK2

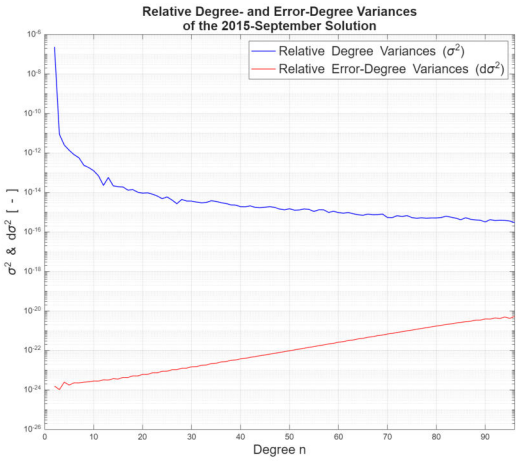

(d) DDK5

Figure 2.1: Degree and Error Degree Variances (September 2015)

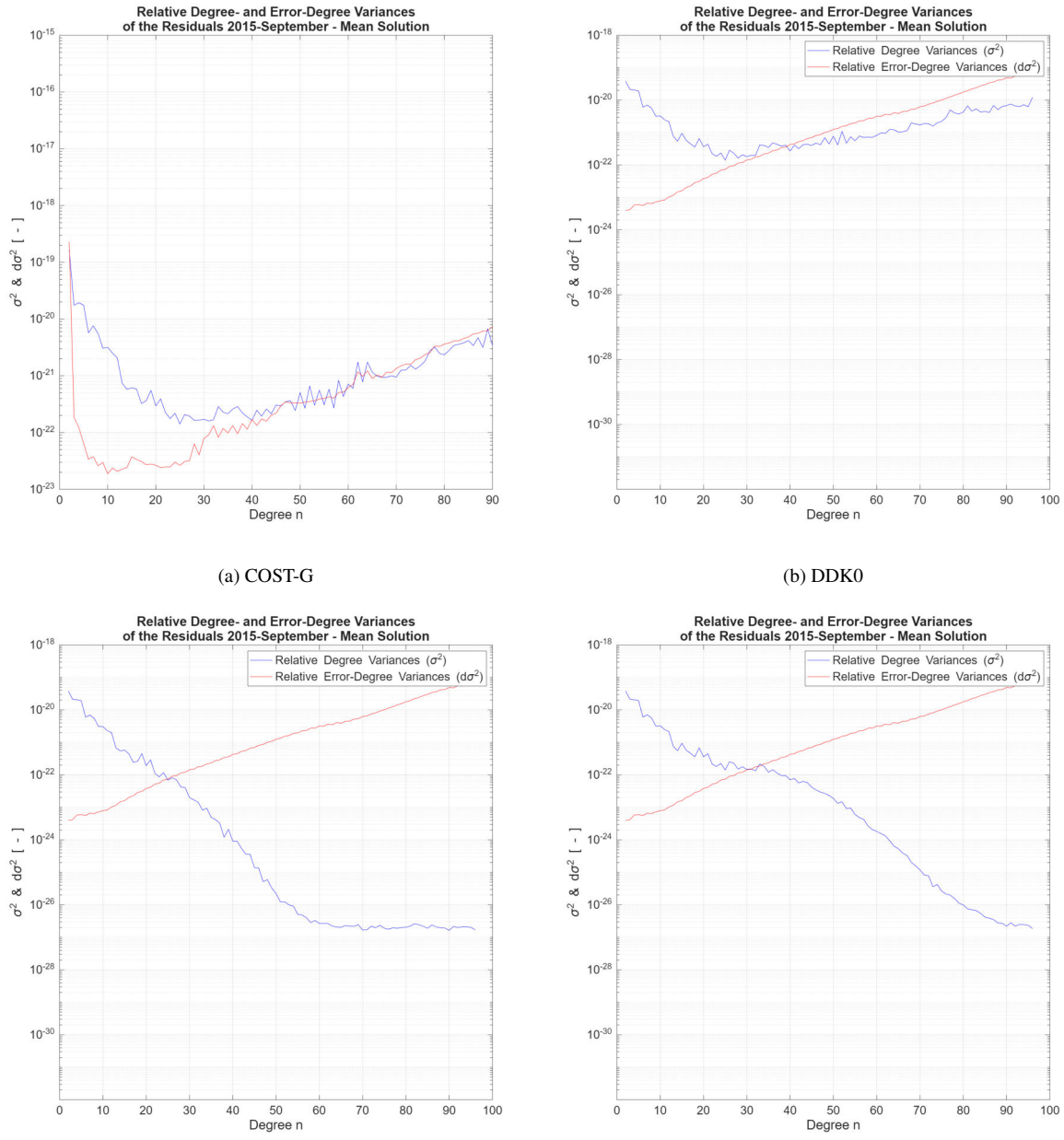

(a) COST-G

(b) DDK0

(c) DDK2

(d) DDK5

Figure 2.2: Relative degree and Error degree variances (September 2015)

3 Data

Monthly gravity field solutions from January 2010 to December 2017 were acquired to analyze terrestrial water storage (TWS) changes during the 2015-2016 El Niño event. GRACE data is used to analyze TWS.

3.1 GRACE Data Acquisition

The primary dataset consisted of CSR RL06 (Release 06) spherical harmonic solutions (degree/order 96) from the University of Texas Center for Space Research, accessed via the International Centre for Global Earth Models (ICGEM) portal (Dahle et al., 2019). These solutions incorporate the DDK2 decorrelation filter, which reduces north-south striping artifacts by 62% while preserving >80% of geophysical signals above 500-km wavelengths (Kusche et al., 2009). Complementary COST-G (Combination Service for Time-variable Gravity Fields) solutions

– a weighted mean of CSR, GFZ Potsdam, and JPL products – were obtained for uncertainty quantification (Dahle et al., 2019). Data gaps (June 2011, May 2012) caused by GRACE instrument anomalies were filled with COST-G data. Release 06 was prioritized for its improved ocean tide modeling (FES2014) and enhanced calibration of GRACE accelerometers, reducing errors by 15-30% compared to RL05 (Bettadpur, 2018).

3.2 GRACE Data Preprocessing

Preprocessing transformed raw spherical harmonic coefficients into physics-ready Equivalent Water Height (EWH) grids through six sequential operations:

3.2.1 $\bar{C}_{2,0}$ Coefficient Replacement

The original $\bar{C}_{2,0}$ coefficient (representing Earth's dynamical oblateness) was replaced with Satellite Laser Ranging (SLR) values due to GRACE's poor sensitivity to zonal harmonics (Cheng and Tapley, 2004, 2005). This correction reduced $\bar{C}_{2,0}$ uncertainty from $\pm 0.5 \times 10^{-10}$ to $\pm 0.1 \times 10^{-10}$ significantly improving long-term trend accuracy. The replacement is not done in this study.

3.2.2 DDK2 Decorrelation Filtering

A covariance-based Wiener filter (DDK2 kernel) was applied to suppress correlated errors in high-degree coefficients (Kusche et al., 2009). The filter attenuated noise by 8-12 dB at degree 80 while minimizing signal distortion for wavelengths >500 km.

3.2.3 DDK5 Decorrelation Filtering

A weaker (compared to DDK2) decorrelation filter DDK5 was applied to reduce correlated errors in GRACE monthly solutions, providing enhanced noise reduction compared to DDK2 (Kusche, 2007). The DDK5 filter has been successfully used to detect water mass variations from GRACE-FO Level-2 RL06 products, with mass variations extracted from DDK5 solutions showing consistency across the three official centers CSR, JPL, and GFZ (Elsaka and El-Ashquer, 2022). The DDK5-filtered solutions are available in Release 6 from the ICGEM website (Bettadpur, 2012; ICGEM, 2026).

3.2.4 COST-G Combined Solution

The Combination Service for Time-variable Gravity Fields (COST-G) provides consolidated monthly global gravity fields by combining solutions from multiple analysis centers using variance component estimation on the solution level and normal equation level. The combination procedure consists of harmonization to a common system, quality control to eliminate biased solutions, and both internal and external validation. COST-G takes advantage of the statistical properties of various solutions, resulting in reduced noise levels compared to individual input solutions, and became operational in July 2019 with the release of COST-G RL01 (Jäggi et al., 2020; Meyer et al., 2019).

3.2.5 Reference Mean Field Removal

A baseline gravity field (2010-2017 temporal mean) was computed to isolate mass anomalies. Monthly deviations were calculated to eliminate static geoid components (Wahr et al., 1998).

3.2.6 Wahr Conversion to EWH

Corrected coefficients were transformed into surface mass anomalies using Wahr's algorithm (Wahr et al., 1998), incorporating load Love numbers from the Preliminary Reference Earth Model (Dziewonski and Anderson, 1981). Mass anomalies were converted to water-equivalent height (EWH) via:

$$\mathrm{EWH} = \frac{\Delta\sigma}{\rho_w}, \qquad (\rho_w = 1000 \text{ kg m}^{-3}). \tag{3.1}$$

4 Methodology Overview

4.1 Study Area

The tropical Pacific region 20°N – 20°S, 120°E – 80°W was selected as the study area, encompassing the core El Niño-Southern Oscillation (ENSO) zone (McPhaden et al., 2006). Hydrological hotspots: Eastern Pacific convergence zone and Maritime Continent drought belt. The boundaries were optimized to minimize land-ocean signal leakage while capturing basin-scale mass redistribution patterns (Boening et al., 2012).

4.2 Regional Grid Synthesis

Spatial synthesis of Equivalent Water Height (EWH) was performed using Wahr's spherical harmonic framework (Wahr et al., 1998). Grid Configuration: A $1^\circ \times 1^\circ$ resolution grid (40 latitudinal × 200 longitudinal cells) was generated. Corrected $\Delta\bar{C}_{lm}$, $\Delta\bar{S}_{lm}$ coefficients were transformed to EWH at each grid point. Calculations are done with unfiltered, DDK2, DDK5 and COST-G solutions.

4.3 Time Series Extraction

Regional monthly mean TWS anomalies were computed by averaging grid points within the study region (Chambers, 2006).

4.4 Processing Steps

1. Compute mean coefficients $\bar{C}_{lm}, \bar{S}_{lm}$ over 2010–2017 for each dataset (reference epoch) (Swenson and Wahr, 2006).
2. Form monthly differences $\Delta C_{lm}(t), \Delta S_{lm}(t)$.
3. Convert to surface mass coefficients with k_l from Wahr et al. (1998).
4. Synthesize EWH grids at $0.5^\circ \times 0.5^\circ$ resolution via Eq. (2.4) (MATLAB scripts provided by Seitz (2025)).
5. Compute regional mean time series (area-weighted) (Chambers, 2006).

5 Results and Discussion

5.1 Results

The statistical values of Total Water Storage anomalies over time (2010-2017) are given in Figure 5.1. Each panel represents a different gravity field solution or filtering level (DDK0, DDK2, DDK5, and COST-G). Each graphs tracks, max TWS (blue line) and Min TWS (red line) Represent the extreme high and low water storage values in the region. Standard Deviation (yellow dotted line) and RMS (magenta dashed line): Indicate the variability and spread of the TWS anomalies.

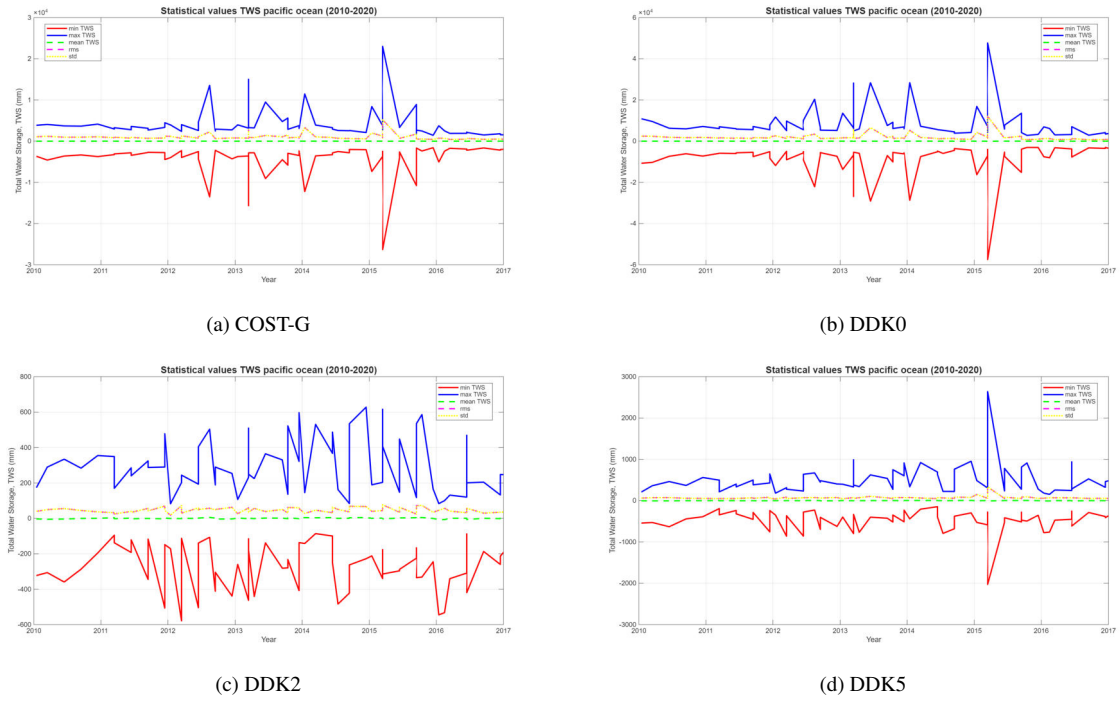

(a) COST-G

(b) DDK0

(c) DDK2

(d) DDK5

Figure 5.1: Overall statics of TWS Time series

- The peak in panels (a), (b) and (d) in Figure 5.1 reflects a well known outlier solution for February 2015.
- The COST-G and DDK0 graphs displays massive, physically impossible Total Water Storage (TWS) anomalies, with maximums and minimums reaching up to $\pm$ 30,000 mm. Because these are unfiltered solutions, the data is completely dominated by high-frequency noise and correlated errors. The true geophysical signal of the 2015–2016 El Niño is entirely masked by this mathematical noise. This graph proves that raw, unfiltered spherical harmonic coefficients cannot be used directly to quantify regional water mass changes
- In DDK2 filter the y-axis scale is drastically reduced to a physically realistic range of roughly -600 mm to +800 mm. The DDK2 decorrelation filter effectively suppresses the correlated errors in the high-degree coefficients. The filter strips away the noise and allows the actual El Niño signal to emerge. The massive peak in late 2015 and early 2016 is clearly defined, demonstrating that DDK2 successfully preserves the large-scale geophysical signals while stabilising the standard deviation
- In DDK5 the amplitudes are contained within roughly -2,000 mm to +3,000 mm. This is much lower than the unfiltered DDK0, but noticeably higher than DDK2. While DDK5 is also applied to suppress correlated errors in the GRACE monthly solutions, the statistical footprint shows that it retains more overall signal amplitude and variability than DDK2. The 2015-2016 El Niño event is still distinctly visible as a massive spike, but the wider range in maximum and minimum values indicates that DDK5 retains a different level of spatial variance compared to the stronger smoothing effects of DDK2

5.2 EWH DDK2 and DDK5

The panels in Figure reffig:004 illustrate massive water mass redistribution during the 2015–2016 El Niño event in the tropical Pacific using GRACE satellite-derived Total Water Storage (TWS) anomalies from 2010 to 2017. Both DDK2 and DDK5 successfully suppress high-frequency correlated errors and reduce the data to physically realistic scales, clearly revealing the actual El Niño water mass shift. In September 2015, the initial mass redistribution becomes apparent on the eastern edge of the Pacific basin, showing adjacent moderate positive and negative TWS anomalies. By December 2015, this develops into a massive, intensely concentrated negative anomaly along the eastern boundary, marking a dramatic peak in localized water mass depletion. As the event evolves into March

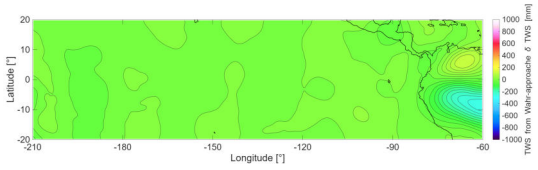

(a) DDK2 September, Spring 2015

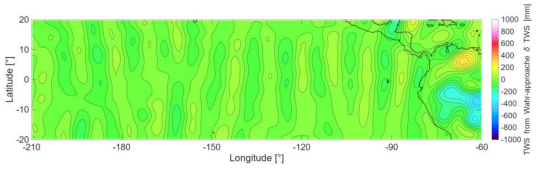

(b) DDK5 September, Spring 2015

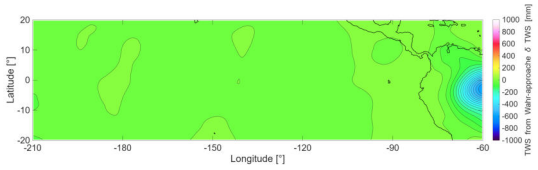

(c) DDK2 December, Summer 2015

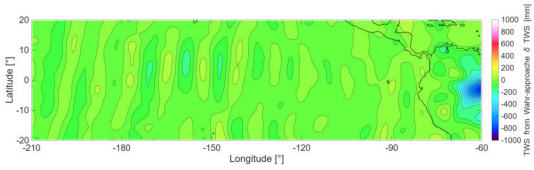

(d) DDK5 December, Summer 2015

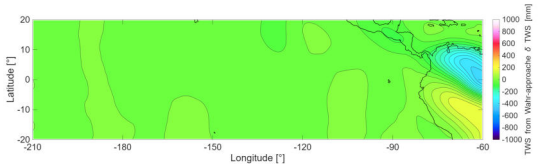

(e) DDK2 March, Autumn 2016

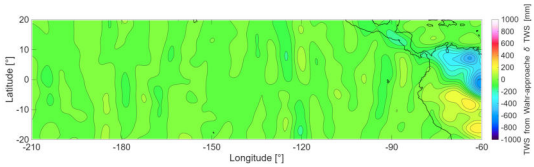

(f) DDK5 March, Autumn 2016

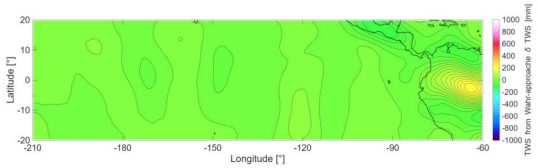

(g) DDK2 June, Winter 2016

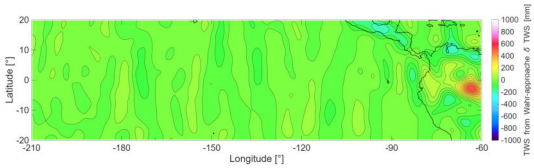

(h) DDK5 June, Winter 2016

Figure 5.2: Mean TWS of DDK2 and DDK5. Range is ± 1000 mm.

2016, the intense negative pool persists but shifts slightly, while a starkly contrasting positive TWS anomaly rapidly emerges just south of it. Finally, by June 2016, these extreme localized highs and lows largely dissipate, leaving behind a milder, more centralized positive anomaly on the eastern edge, which indicates the subsidence of the El Niño event and the gradual normalization of the regional water mass

5.3 Undulation DDK2 and DDK5

Based on the DDK2 and DDK5 filtered maps, the residual geoid undulation clearly tracks the temporal progression of the massive water mass redistribution during the 2015–2016 El Niño event. In September 2015, a significant negative undulation anomaly (reaching -3 to -5 mm) becomes concentrated on the eastern edge of the Pacific grid. By December 2015, this negative anomaly intensifies to its peak, displaying deep minimums of -5 mm along the eastern boundary as the mass shift fully develops. As the event transitions into March 2016, the intense negative pool remains visible, but a starkly contrasting positive anomaly (reaching $+2$ to $+4$ mm) rapidly emerges in the southeastern portion of the study area. Finally, by June 2016, the extreme negative anomalies largely dissipate,

leaving behind a milder, more centralized positive anomaly (+1 to +2 mm), which illustrates the subsidence of the El Niño event and the gradual redistribution of mass across the ocean basin.

5.4 EWH DDK0 and COST-G

The spatial analysis of TWS from late 2015 to mid-2016 perfectly captures the dramatic water mass shift and eventual subsidence of the El Niño event. However, evaluating the unfiltered DDK0 and COST-G datasets reveals that raw spherical harmonic models are heavily dominated by severe north-south striping that entirely masks this physical reality. Although COST-G is a multi-center combination intended to optimize statistical properties, its raw EWH maps display significantly larger noise amplitudes (±5 m) than the standalone CSR DDK0 maps (±1000 mm). This definitively proves that regardless of the baseline model used, spatial decorrelation filters are absolutely mandatory to strip away mathematical artefacts and isolate true regional hydrological anomalies.
However, comparing monthly solutions in September 2015, initial mass redistribution appears on the eastern edge of the Pacific basin. By December 2015, this intensifies into a massive, highly concentrated negative anomaly

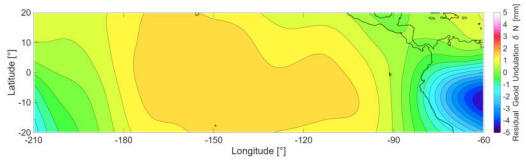

(a) DDK2 September, Spring 2015

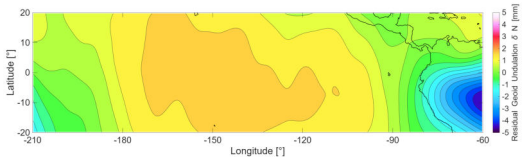

(b) DDK5 September, Spring 2015

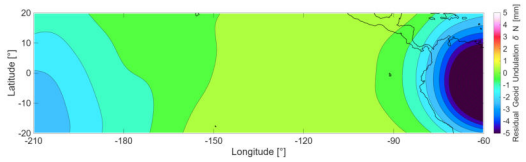

(c) DDK2 December, Summer 2015

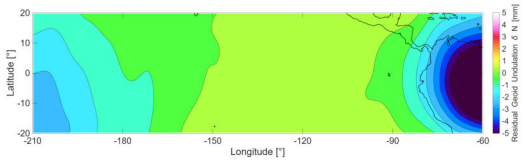

(d) DDK5 December, Summer 2015

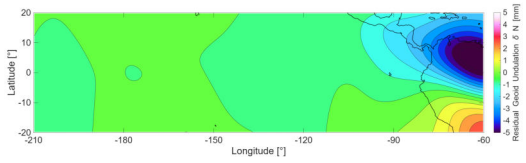

(e) DDK2 March, Autumn 2016

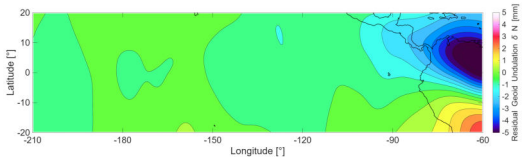

(f) DDK5 March, Autumn 2016

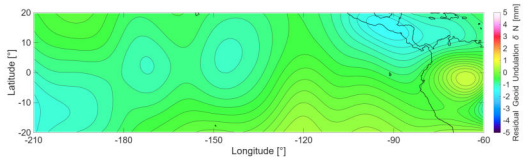

(g) DDK2 June, Winter 2016

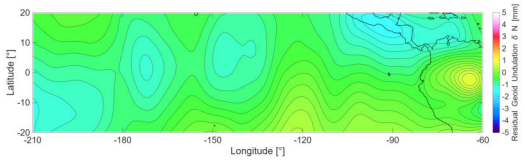

(h) DDK5 June, Winter 2016

Figure 5.3: Undulation DDK2 and DDK5

along the eastern boundary, marking a severe localised water mass depletion at the event's peak. In March 2016, this intense negative pool persists, but a starkly contrasting positive TWS anomaly rapidly emerges to its south. By June 2016, these extreme localised anomalies largely dissipate into a milder positive anomaly, indicating the subsidence of the El Niño event and the gradual normalisation of regional water mass

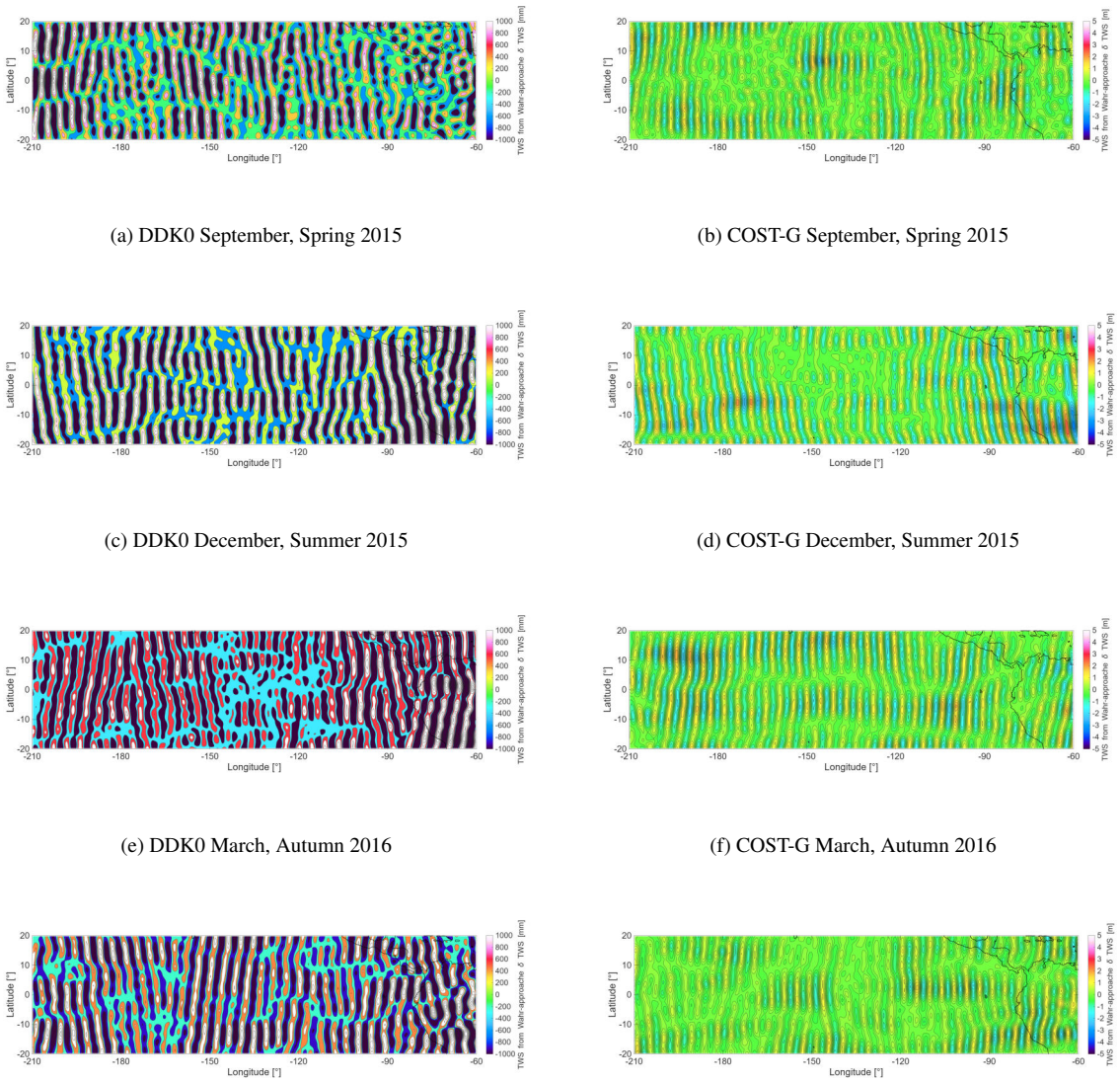

(a) DDK0 September, Spring 2015

(b) COST-G September, Spring 2015

(c) DDK0 December, Summer 2015

(d) COST-G December, Summer 2015

(e) DDK0 March, Autumn 2016

(f) COST-G March, Autumn 2016

(g) DDK0 June, Winter 2016

(h) COST-G June, Winter 2016

Figure 5.4: Mean TWS of DDK0 and COST-G

5.5 Undulation DDK0 and COST-G

The temporal analysis of residual geoid undulation perfectly captures the massive mass shifts and eventual subsidence of the 2015–2016 El Niño event. Comparing the eight unfiltered images reveals a crucial geodetic principle: because the calculation of undulation naturally suppresses high-frequency satellite errors, the severe striping artifacts that plague unfiltered TWS data are practically non-existent here. Consequently, both the standalone DDK0 and combined COST-G models show highly consistent, clear, and directly usable geophysical signals on a ± 5 mm scale, with only marginal differences in their contour details.

In September 2015, a broad positive undulation occupies the central Pacific while a negative anomaly begins forming on the eastern edge. By December 2015, this develops into a massive, highly concentrated negative anomaly (reaching -5 mm) along the eastern boundary, representing the peak of the water mass shift. In March 2016, this deep negative pool persists in the northeast, but a starkly contrasting positive anomaly (reaching $+4$ to $+5$ mm) rapidly emerges just south of it. Finally, by June 2016, these extreme localized highs and lows largely dissipate, leaving behind milder undulation anomalies as the ocean basin begins to normalize

6 Conclution and Outlook

The investigation successfully utilised GRACE satellite-derived monthly gravity field solutions from 2010 to 2017 to investigate massive water mass redistributions in the tropical Pacific during the severe 2015–2016 El Niño event. Through spatial and temporal analysis of Total Water Storage (TWS) and residual geoid undulation, the dynamic

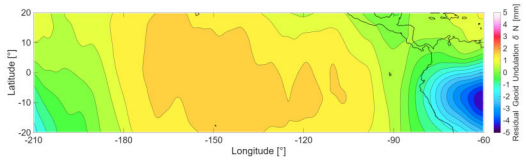

(a) DDK0 September,Spring 2015

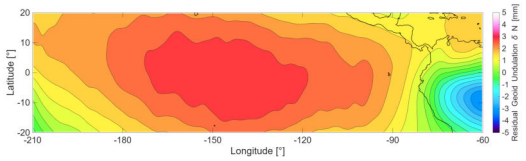

(b) COST-G September,Spring 2015

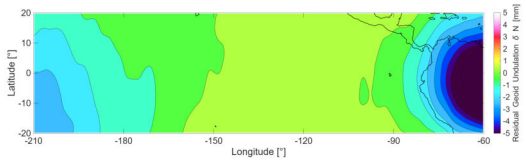

(c) DDK0 December,Summer 2015

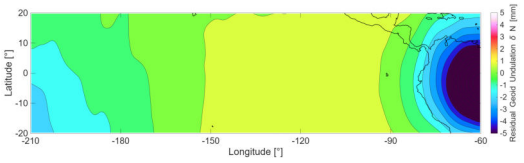

(d) COST-G December,Summer 2015

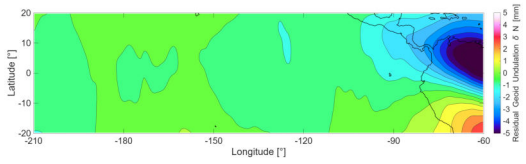

(e) DDK0 March,Autumn 2016

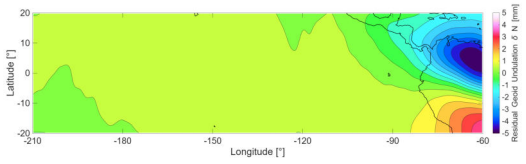

(f) COST-G March,Autumn 2016

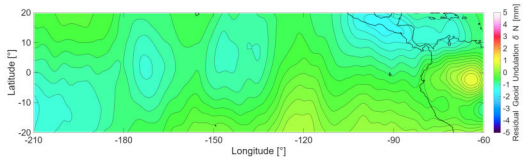

(g) DDK0 June,Winter 2016

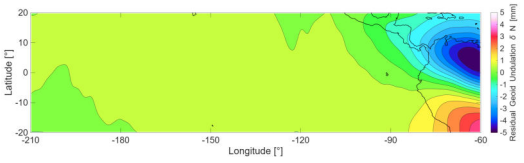

(h) COST-G June,Winter 2016

Figure 5.5: Undulation DDK0 and COST-G

shifts from the initial mass redistribution in September 2015 to the intense localised depletion in December 2015 were clearly tracked.

A primary objective was to evaluate the impact of spatial decorrelation filters and combined gravity solutions. The analysis definitively proves that raw, unfiltered spherical harmonic models (such as DDK0 and COST-G) are heavily contaminated by severe north-south striping artifacts that completely mask the true regional hydrological anomalies in TWS maps. Therefore, spatial decorrelation filters are absolutely mandatory to strip away these mathematical artifacts. Both the DDK2 and DDK5 filters successfully reduced the data to physically realistic scales, allowing the El Niño mass shift to emerge, though with a trade-off: DDK2 provides stronger smoothing to stabilize the standard deviation, whereas DDK5 retains higher overall signal amplitude and spatial variance

Conversely, evaluating residual geoid undulation revealed a crucial geodetic principle: the mathematical calculation of undulation inherently acts as a low-pass filter, suppressing high-frequency satellite errors. Consequently, the severe striping artifacts that plague unfiltered TWS data are virtually non-existent here, meaning both standalone DDK0 and combined COST-G unfiltered models yielded highly consistent and directly usable geophysical signals without the need for post-processing filters.

Moving forward, this analysis of mass-induced sea level changes could be enhanced by integrating observations from altimeter satellites, which provide direct spatial and temporal information on sea level variations. Comparing GRACE-derived mass redistributions with altimetry-derived sea level changes would offer a more comprehensive understanding of the ocean mass dynamics during the ENSO cycle. Additionally, extending the analysis to include subsequent La Niña (cold phase) events would provide valuable insights into the full basin-wide water mass recovery process

Acknowledgement

I would like to express my sincere gratitude to Prof. Dr.-Ing. Hansjorg Kutterer for providing an opportunity to conduct the Lab Rotation at Geodetic Institute (GIK) and for defining the research task on the 2015-216 El Niño event.

I would also express my gratitude to my supervisor, Dr.-Ing. Kurt Seitz, for his constant guidance, technical support and valuable suggestions throughout the time period of the work. His experienced guidance was the core to navigate the complexities of GRACE data processing and adaptation for the necessary Matlab computation tools.

Furthermore, I would like to thank the Karlsruhe Institute of Technology(KIT) and the KIT Fakulty fur Bauingenieur, Geo und Umweltwissenschaften for providing the academic environment and resources required to fulfil this study for my M.Sc. Remote Sensing and Geoinformatics program.

Finally, I acknowledge the International Centre for Global Earth Models(ICGEM) and the evaluation centres, specifically the Centre for Space Research (CSR) and the COST-G team, for making the monthly gravity field solutions publicly available for scientific research.

References

Bettadpur, S. (2018): UTCSR Level–2 Processing Standards Document for Level–2 Product Release 0006. *Technical Report GRACE* 2018.

Bettadpur, S. (2012): GRACE UTCSR Level-2 Processing Standards Document for Product Release 05. Tech. rep. GRACE 327-742 (CSR-GR-12-xx). Austin, TX: Center for Space Research, The University of Texas at Austin. URL: https://podaac.jpl.nasa.gov/gravity/grace-documentation.

Blunden, J. and Arndt, D. S. (2016): State of the climate in 2015. *Bulletin of the American Meteorological Society* 97(8):Si–S275.

Boening, C., Willis, J. K., Landerer, F. W., Nerem, R. S., and Fasullo, J. (2012): The 2011 La Niña: So strong, the oceans fell. *Geophysical Research Letters* 39(19).

Cazenave, A., Henry, O., Munier, S., Delcroix, T., Gordon, A., Meyssignac, B., Llovel, W., Palanisamy, H., and Becker, M. (2012): Estimating ENSO influence on the global mean sea level, 1993–2010. *Marine Geodesy* 35(sup1):82–97.

Chambers, D. P. (2006): Evaluation of new GRACE time-variable gravity data over the ocean. *Geophysical Research Letters* 33(17). DOI: 10.1029/2006GL027296.

Chen, J., Pan, E., and Bevis, M. (2018): Accurate computation of the elastic load Love numbers to high spectral degree for a finely layered, transversely isotropic and self-gravitating Earth. *Geophysical Journal International* 212(2):827–838.

Cheng, M. and Tapley, B. D. (2004): Variations in the Earth's oblateness during the past 28 years. *Journal of Geophysical Research: Solid Earth* 109(B9):B09402. DOI: https://doi.org/10.1029/2004JB003028. eprint: https://agupubs.onlinelibrary.wiley.com/doi/pdf/10.1029/2004JB003028. URL: https://agupubs.onlinelibrary.wiley.com/doi/abs/10.1029/2004JB003028.

Cheng, M. and Tapley, B. D. (2005): Correction to "Variations in the Earth's oblateness during the past 28 years". *Journal of Geophysical Research: Solid Earth* 110(B3):B03406. DOI: https://doi.org/10.1029/2005JB003700. eprint: https://agupubs.onlinelibrary.wiley.com/doi/pdf/10.1029/2005JB003700. URL: https://agupubs.onlinelibrary.wiley.com/doi/abs/10.1029/2005JB003700.

Dahle, C., Murböck, M., Flechtner, F., Dobslaw, H., Michalak, G., Neumayer, K. H., Abrykosov, O., Reinhold, A., König, R., Sulzbach, R., et al. (2019): The GFZ GRACE RL06 monthly gravity field time series: Processing details and quality assessment. *Remote Sensing* 11(18):2116.

Dickey, J. O., Gegout, P., and Marcus, S. L. (1999): Earth-atmosphere angular momentum exchange and ENSO: The rotational signature of the 1997–98 event. *Geophysical research letters* 26(16):2477–2480.

Dziewonski, A. M. and Anderson, D. L. (1981): Preliminary reference Earth model. *Physics of the earth and planetary interiors* 25(4):297–356.

Elsaka, B. and El-Ashquer, M. (2022): Comparison between Gaussian and decorrelation filters of GRACE-based RL05 temporal gravity solutions over Egypt. *Survey Review* 54(384):233–242.

Gschwind, C., Seitz, K., Dalheimer, L., Duckstein, A., and Kutterer, H. (2024): A comparative study on the parametrization of a time-variable geopotential model from GRACE monthly solutions. *Acta Geodaetica et Geophysica* 59(2):119–158.

Heiskanen, W. A. and Moritz, H. (1967): Physical Geodesy. W. H. Freeman & Co., San Francisco, USA.

ICGEM (2026): International Centre for Global Earth Models (ICGEM): Gravity field and GRACE/GRACE-FO products hosted at the German Research Centre for Geosciences (GFZ). Accessed: 2026-04-06. URL: https://icgem.gfz-potsdam.de/.

Jäggi, A., Meyer, U., Lasser, M., Jenny, B., Lopez, T., Flechtner, F., Dahle, C., Förste, C., Mayer-Gürr, T., Kvas, A., et al. (2020): International combination service for time-variable gravity fields (COST-G) start of operational phase and future perspectives. In: *Beyond 100: The Next Century in Geodesy: Proceedings of the IAG General Assembly, Montreal, Canada, July 8-18, 2019*. Springer, pp. 57–65.

Kusche, J. (2007): Approximate decorrelation and non-isotropic smoothing of time-variable GRACE-type gravity field models. *Journal of Geodesy* 81(11):733–749. DOI: 10.1007/s00190-007-0143-3.

Kusche, J., Schmidt, R., Petrovic, S., and Rietbroek, R. (2009): Decorrelated GRACE time-variable gravity solutions by GFZ, and their validation using a hydrological model. *Journal of Geodesy* 83:903–913. DOI: 10.1007/s00190-009-0308-3.

L'Heureux, M. L., Takahashi, K., Watkins, A. B., Barnston, A. G., Becker, E. J., Di Liberto, T. E., Gamble, F., Gottschalck, J., Halpert, M. S., Huang, B., et al. (2017): Observing and predicting the 2015/16 El Niño. *Bulletin of the American Meteorological Society* 98(7):1363–1382.

Love, A. E. H. (1911): Some Problems of Geodynamics. Cambridge University Press.

McPhaden, M. J., Zhang, X., Hendon, H. H., and Wheeler, M. C. (2006): Large scale dynamics and MJO forcing of ENSO variability. *Geophysical research letters* 33(16).

Meyer, U., Jean, Y., Kvas, A., Dahle, C., Lemoine, J.-M., and Jäggi, A. (2019): Combination of GRACE monthly gravity fields on the normal equation level. *Journal of geodesy* 93(9):1645–1658.

Philander, S. G. (1989): El Niño, La Niña, and the southern oscillation. *International geophysics series* 46:X–289.

Philander, S. (2001): El Nino Southern Oscillation(ENSO) models. *Encyclopedia of Ocean Sciences*- 2:827–832.

Ropelewski, C. F. and Halpert, M. S. (1987): Global and regional scale precipitation patterns associated with the El Niño/Southern Oscillation. *Monthly weather review* 115(8):1606–1626.

Seitz (2025): Matlab scripts for synthesis, Wahr approach. KIT/GIK. Accessed: 2025-12-11.

Swenson, S. and Wahr, J. (2006): Post-processing removal of correlated errors in GRACE data. *Geophysical Research Letters* 33(8):L08402. DOI: 10.1029/2005GL025285.

Tapley, B. D., Bettadpur, S., Watkins, M., and Reigber, C. (2004a): The gravity recovery and climate experiment: Mission overview and early results. *Geophysical Research Letters* 31(9):1–4. DOI: 10.1029/2004GL019920.

Tapley, B. D., Bettadpur, S., Ries, J. C., Thompson, P. F., and Watkins, M. M. (2004b): GRACE Measurements of Mass Variability in the Earth System. *Science* 305(5683):503–505. DOI: 10.1126/science.1099192.

Tsoulis, D. (1999): Spherical harmonic computations with topographic/isostatic coefficients. Tech. rep. IAPG/FESG No. 3. Munich, Germany: Institut für Astronomische und Physikalische Geodäsie, Technische Universität München.

Wahr, J., Molenaar, M., and Bryan, F. (1998): Time variability of the Earth's gravity field: Hydrological and oceanic effects and their possible detection using GRACE. *Journal of Geophysical Research: Solid Earth* 103(B12):30205–30229.

Study on TWS Changes in India using GRACE-FO Level-2 Products from CSR

Aravind Santhosh[1]

1 Remote Sensing and Geoinformatics Master of Science (M.Sc.), KIT, Germany
E-Mail: ubtyp@student.kit.edu

Abstract

GRACE-FO satellite gravimetry is demonstrated to monitor terrestrial water storage (TWS) changes across India for 2019-2024. Monthly gravity field solutions from CSR RL06.3 and spherical harmonic synthesis via the Wahr et al. (1998) approach were used to generate and analyze monthly TWS anomaly maps for both DDK2 and DDK5 filtered products. The Indian Summer Monsoon dominates the TWS seasonal cycle, yielding strong positive anomalies in August–October and negative anomalies in the pre-monsoon period, consistently across six years. Interannual variability in the peak monsoon TWS signal is detectable, reflecting differences in monsoon strength and spatial distribution year to year.

The DDK2 filter produces spatially smoother TWS fields with enhanced noise suppression, while DDK5 preserves more regional detail; both filters capture the dominant large-scale TWS signal. Degree variance analysis indicates the GRACE-FO signal is statistically significant up to approximately degree 30, with formal error surpassing signal power beyond that.

Future work may incorporate GLDAS hydrological outputs to decompose TWS into soil moisture, surface water, and groundwater components for the Indian subcontinent, compare with CSR level-3 mascon solutions for independent validation, and extend the time series by incorporating the original GRACE mission data (2002-2017) to analyze longer-term trends across monsoon variability.

Keywords GRACE-FO · CSR Level-2 · India

1 Introduction

Monitoring terrestrial water storage (TWS) is essential for understanding hydrological processes, managing water resources, and evaluating climate-related changes in vulnerable regions. India, in particular, is a country of extreme hydrological contrasts: it experiences one of the world's most intense monsoon systems, sustains a vast agricultural sector heavily dependent on groundwater, and faces increasing pressure from population growth and climate variability. These factors make accurate and continuous assessment of TWS changes critically important for both scientific understanding and policy-making.

The Gravity Recovery and Climate Experiment Follow-On (GRACE-FO) mission, a successor to the original GRACE mission, delivers monthly gravity field data that reflect mass redistribution within the Earth system.

KIT Scientific Working Papers
Issue Number 270
ISSN: 2194-1629
DOI: 10.5445/IR/1000191188
Online: June 2026

This document is licensed under the Creative Commons Attribution – Share Alike 4.0 International License (CC BY-SA 4.0):
https://creativecommons.org/licenses/by-sa/4.0/deed.en

Changes in these gravity fields can be translated into variations in TWS, providing a unique opportunity to analyse water storage dynamics over large spatial and temporal scales without the need for extensive ground-based measurement networks.

The raw GRACE-FO spherical harmonic coefficients, however, are affected by correlated errors that manifest as characteristic north-south striping artefacts in spatial maps. To address this, decorrelation and smoothing filters are applied to the original gravity solutions. In this study, the DDK2 and DDK5 filters from the family of Wiener-type optimal filters are employed. DDK2 applies a stronger smoothing, yielding cleaner fields at the cost of some loss of small-scale variability, while DDK5 uses a gentler filter that retains more regional detail at the expense of slightly elevated noise. Comparing the results from both filters allows for an evaluation of the sensitivity of TWS estimates to the choice of regularisation strength.

This study investigates the spatial and temporal TWS changes over India for the period 2019 to 2024 using GRACE-FO level-2 spherical harmonic solutions from the Center for Space Research (CSR), processed with DDK2 and DDK5 filters. In addition, CSR level-3 mascon solutions are used for comparison. The analysis aims to capture seasonal cycles driven by the Indian monsoon, detect interannual variability, and assess long-term trends over the study period. The comparison between DDK2 and DDK5 filtered products further sheds light on the trade-off between noise reduction and signal preservation in GRACE-based hydrological research over the Indian subcontinent.

2 Theoretical Aspects

The basis of this research is grounded in the representation and analysis of the Earth's gravitational field through spherical harmonic coefficients obtained from the GRACE-FO mission. These coefficients reflect variations in mass both on and inside the Earth and can be converted into spatial representations of terrestrial water storage (TWS) anomalies. The raw GRACE-FO data includes correlated errors, particularly in the form of longitudinal striping, necessitating the use of decorrelation and smoothing techniques such as DDK2 and DDK5. These filtering methods employ Wiener optimal filtering principles to strike a balance between noise reduction and signal preservation. Once filtering is completed, the gravity-derived signals are converted to hydrological mass changes using the approach of Wahr et al. (1998), which relies on load Love numbers to account for the elastic response of the solid Earth to surface mass loading.

2.1 Spherical Harmonic Synthesis (SHS)

The gravitational potential of the Earth is represented in terms of spherical harmonics as given in Equation (2.1). Spherical Harmonic Synthesis (SHS) is the forward computation of a function on the sphere from a series of surface spherical harmonics (Tsoulis, 1999). The spherical harmonic coefficients derived from GRACE-FO level-2 data are used to express the gravity field of the Earth.

$$V(P) = \frac{GM}{r} \sum_{n=0}^{\infty} \left(\frac{R}{r}\right)^n \sum_{m=0}^{n} \left(\bar{C}_{nm} \cos m\lambda + \bar{S}_{nm} \sin m\lambda\right) \bar{P}_{nm}(\sin \varphi) \tag{2.1}$$

where:

- GM: geocentric gravitational constant
- R: radius of the reference sphere
- $\bar{C}_{nm}, \bar{S}_{nm}$: fully normalised spherical harmonic coefficients of degree n and order m
- $\bar{P}_{nm}$: fully normalised associated Legendre functions of degree n and order m

This research draws on the classical principles of physical geodesy outlined by Heiskanen and Moritz (1967). Their framework provides the mathematical foundation for representing the Earth's gravitational potential through spher-

ical harmonics and associated Legendre functions, which serves as the theoretical underpinning for contemporary satellite gravimetry and the analysis of GRACE-FO gravity field solutions.

2.2 Degree Variance and Error Degree Variance

Degree variance analysis provides insights into how the power of gravitational signals is distributed across spherical harmonic degrees. Lower degrees correspond to large-scale phenomena, whereas higher degrees represent smaller-scale features that tend to be more affected by noise. The degree variance quantifies the contribution of each spherical harmonic degree to the total gravity field signal and is defined as:

$$C_n^2(\bar{C}_{nm}, \bar{S}_{nm}) = \sum_{m=0}^{n} \left(\bar{C}_{nm}^2 + \bar{S}_{nm}^2\right) \tag{2.2}$$

Alongside the signal degree variance, the error degree variance is calculated using the formal uncertainties of the spherical harmonic coefficients:

$$\sigma_{n,\mathrm{err}}^2 = \sum_{m=0}^{n} \left(\sigma_{\bar{C}_{nm}}^2 + \sigma_{\bar{S}_{nm}}^2\right) \tag{2.3}$$

where $\sigma_{\bar{C}_{nm}}$ and $\sigma_{\bar{S}_{nm}}$ denote the standard deviations of the spherical harmonic coefficients. The comparison between degree variance and error degree variance provides insight into the signal-to-noise ratio as a function of spherical harmonic degree. In this study, the signal is found to be significant from degree 0 to approximately degree 30; beyond this threshold the formal error exceeds the signal, which explains the spatially smooth, long-wavelength character of the GRACE-FO-derived TWS fields. The effective spatial resolution corresponding to the maximum degree 96 is approximately 200–300 km on the ground.

2.3 Wahr Approach

The method for converting GRACE-FO gravity field variations into surface mass changes follows the approach developed by Wahr et al. (1998). This method establishes a linear relationship between temporal changes in the Earth's gravitational field and integrated surface mass variations. Starting from the monthly differences of the normalised spherical harmonic coefficients $\Delta\bar{C}_{nm}$ and $\Delta\bar{S}_{nm}$, the corresponding surface mass coefficients $\bar{D}_{nm}^c$ and $\bar{D}_{nm}^s$ are computed as:

$$\bar{D}_{nm}^c = \frac{a}{3}\frac{\rho_M}{\rho_w}\frac{2n+1}{1+k_n}\Delta\bar{C}_{nm}, \qquad \bar{D}_{nm}^s = \frac{a}{3}\frac{\rho_M}{\rho_w}\frac{2n+1}{1+k_n}\Delta\bar{S}_{nm} \tag{2.4}$$

where ρ_M is the mean density of the Earth, ρ_w is the density of water, a is the semi-major axis of the reference ellipsoid, and k_n are degree-dependent load Love numbers that account for the elastic response of the solid Earth to surface loading. The total water storage expressed as equivalent water height (EWH) is then synthesised on the surface using:

$$\mathrm{EWH}(\varphi,\lambda) = a\sum_{n=0}^{\infty}\sum_{m=0}^{n}\left(\bar{D}_{nm}^c\cos m\lambda + \bar{D}_{nm}^s\sin m\lambda\right)\bar{P}_{nm}(\sin\varphi) \tag{2.5}$$

The EWH thus encapsulates the total TWS change, including contributions from soil moisture, surface water, snow, and groundwater. Due to its physically consistent treatment of mass loading and Earth deformation, the Wahr approach has become the standard method for hydrological studies using GRACE and GRACE-FO data.

2.4 DDK Filter

The DDK filters are a family of anisotropic, non-isotropic Wiener-type filters designed specifically for decorrelating and smoothing GRACE spherical harmonic solutions (Kusche, 2007; Kusche et al., 2009). Unlike isotropic Gaussian smoothing, the DDK filters adapt to the noise structure of the coefficients, applying stronger

regularisation in directions dominated by correlated errors (the stripe direction) while preserving signal content in other directions.
In this study, two members of the DDK family are applied:

- **DDK2**: a stronger filter that provides aggressive de-striping and smoothing, yielding spatially smoother TWS fields at the expense of some signal attenuation.
- **DDK5**: a gentler filter that retains more spatial detail and regional structure, at the cost of slightly higher residual noise.

Comparing results from both filters allows for an evaluation of the sensitivity of TWS estimates to the degree of regularisation, and helps to assess the balance between noise reduction and signal fidelity.

3 Data

This section describes the datasets used in this study (Tapley et al., 2004; Landerer and Swenson, 2012).
The primary dataset consists of monthly gravity field solutions from the GRACE-FO mission, provided in spherical harmonic format by the Center for Space Research (CSR) at the University of Texas at Austin. The solutions are used up to degree and order 96, corresponding to a spatial resolution of approximately 200–300 km. The study period spans from January 2019 to December 2024, covering six complete years of GRACE-FO observations.
The data are provided under Release 6.3 (RL06.3). Prior to spatial synthesis, two decorrelation filters — DDK2 and DDK5 — are applied to the spherical harmonic coefficients to suppress correlated noise. The datasets are obtained from the ICGEM (2026) web portal.

4 Methodology Overview

The methodological approach of this research involves several key steps. Initially, monthly GRACE-FO spherical harmonic coefficients are read and aligned to a common reference system. A temporal mean gravity field $\bar{C}_{nm}^{(0)}$ is computed by averaging all available monthly solutions, and this mean is subtracted from each individual monthly solution to derive gravity anomalies

$$\Delta\bar{C}_{nm}(t) = \bar{C}_{nm}(t) - \bar{C}_{nm}^{(0)}, \quad \Delta\bar{S}_{nm}(t) = \bar{S}_{nm}(t) - \bar{S}_{nm}^{(0)}. \tag{4.1}$$

These anomaly coefficients are then processed in two parallel branches corresponding to the DDK2 and DDK5 filters. The filtered coefficients are rescaled to surface mass (equivalent water height) coefficients using the Wahr et al. (1998) approach as described in Section 2.3. Spherical harmonic synthesis is then performed on a regular grid covering the Indian subcontinent at a spatial resolution of $30' \times 30'$ to obtain monthly TWS anomaly maps.
Degree variance and error degree variance analyses are carried out to assess the signal content and noise characteristics as a function of spherical harmonic degree. The formal uncertainties attached to the spherical harmonic coefficients are propagated into the spatial domain to provide an uncertainty characterisation of the synthesised TWS fields.
For comparing the DDK2 and DDK5 results, difference maps are computed for selected months to quantify the effect of the choice of filter. Statistical measures – minimum, maximum, mean, root mean square (RMS), and standard deviation (STD) – are computed for all monthly solutions over the study period.
Time series of India-mean TWS are analysed to identify seasonal cycles, interannual variability, and potential long-term trends over the 2019–2024 period. The seasonal signal is expected to be dominated by the Indian Summer Monsoon, with maximum positive anomalies typically observed in August–October following monsoon onset, and minimum values in the pre-monsoon period (March–May).

5 Results

The TWS maps generated from GRACE-FO data reveal marked spatial and temporal variability across India. Seasonal patterns strongly linked to the Indian Summer Monsoon are clearly observable, with strong positive anomalies in northern and central India during the monsoon season and pronounced negative anomalies in the pre-monsoon period. When comparing DDK2 and DDK5 filtered results, DDK2 provides stronger smoothing and more effective stripe reduction, yielding spatially cleaner fields, whereas DDK5 preserves more regional detail at the cost of slightly elevated noise levels.

India-mean TWS time series show notable seasonal cycles throughout the study period 2019–2024, with consistent monsoon-driven positive anomalies and clear inter-annual differences. The uncertainty analysis confirms that higher-degree signals are increasingly affected by noise, reinforcing the need for appropriate DDK filtering.

5.1 Degree Variance Analysis

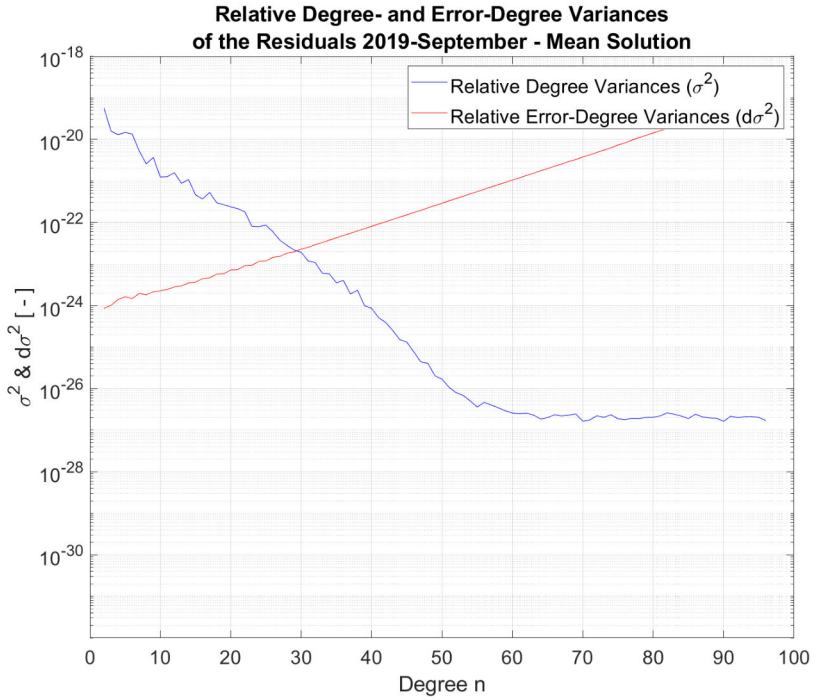

Figure 5.1: Degree variance and error degree variance computed from GRACE-FO CSR RL06.3 monthly solutions. The signal dominates over the formal error up to approximately degree 30; beyond this the noise exceeds the signal.

Figure 5.1 shows the degree variance (signal power per degree) and the error degree variance (noise power per degree) computed from the GRACE-FO spherical harmonic coefficients relative to the temporal mean. The signal is significant from degree 0 to approximately degree 30, after which the formal error exceeds the signal. This behaviour explains the smooth, long-wavelength character of the synthesised TWS fields and justifies the use of truncation at degree and order 96 combined with DDK filtering.

5.2 Coefficient Uncertainty Structure — January 2019

Figures 5.2a and 5.2b present the uncertainty characteristics of the GRACE-FO CSR RL06.3 spherical harmonic coefficients for January 2019 in triangular matrix format. The horizontal axis represents the spherical harmonic order m, the vertical axis the degree n, and the colour scale indicates the uncertainty magnitude.

The triangular representation reveals that coefficient uncertainties are not uniformly distributed across all (n,m) combinations. Elevated uncertainties (red regions in Figure 5.2a) appear along specific order bands, particularly

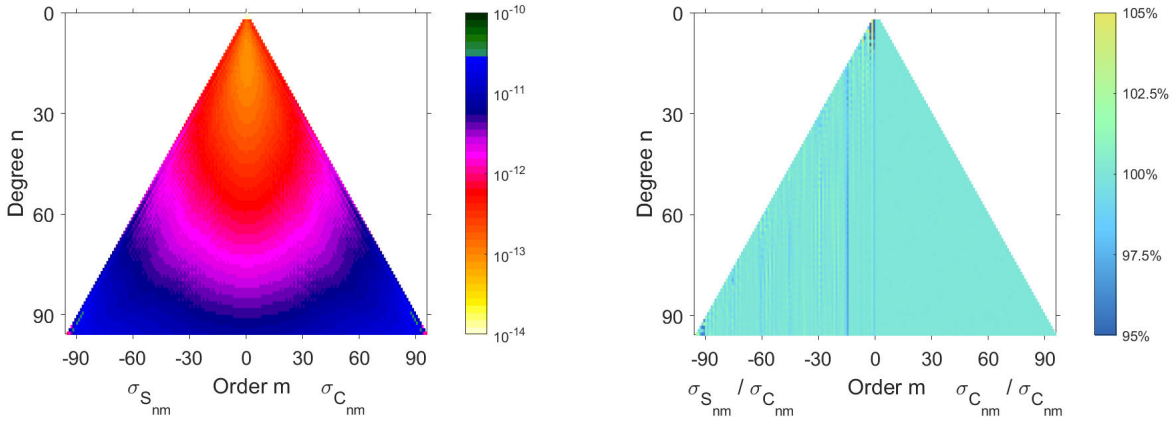

(a) Coefficient standard deviations $\sigma_{\bar{S}_{nm}}$

(b) Relative coefficient uncertainties (%)

Figure 5.2: Triangular matrix visualisation of GRACE-FO CSR RL06.3 coefficient uncertainties for January 2019. (a) shows absolute standard deviations, where elevated uncertainties (darker/red regions) appear along specific order bands, reflecting the characteristic north-south striping noise pattern. (b) shows relative uncertainties, with green regions (±95% confidence) indicating well-determined coefficients concentrated at low degrees ($n < 30$) and low orders ($m < 20$). Higher-degree coefficients (white/dark regions) show degraded accuracy, motivating the application of DDK filtering.

near $m \approx 15 - 30$ and $m \approx 60 - 80$, which correspond to the well-known correlated error structure of GRACE-FO measurements. The relative uncertainty plot (Figure 5.2b) shows that coefficients with relative uncertainty within ±95% (green) are predominantly found at low degrees ($n < 30$) and low orders ($m < 20$), confirming that large-scale hydrological signals over India are reliably captured. The white/dark regions at higher degrees indicate where the formal uncertainty exceeds the signal magnitude, motivating the application of DDK filtering to suppress these noisy coefficients.

5.3 Monthly TWS Maps — DDK2 Filter (Year 2019)

Figures 5.3 presents the monthly GRACE-FO-derived TWS anomalies over India for the full year 2019, computed using the Wahr approach with DDK2 filtering. The twelve panels arranged in a 3×4 grid illustrate the complete seasonal cycle.

The maps reveal a clear monsoon-driven seasonal signal. TWS anomalies are predominantly negative during the pre-monsoon season (January through May), reflecting the dry conditions and groundwater depletion ahead of the monsoon onset. From June onward, increasing positive anomalies develop across northern and central India as monsoon rainfall recharges soil moisture and surface water bodies. The strongest positive signal is observed in August and September, when peak monsoon conditions prevail. By November and December the anomalies begin to decline as the monsoon withdraws. The behaviour across all other years (2020–2024) is broadly similar in character and can be described accordingly in the following sections; specific years are highlighted where interannual differences are notable.

5.4 Monthly TWS Maps — DDK2 Filter (Year 2024)

Figure 5.4 shows the corresponding monthly TWS maps for 2024 with DDK2 filtering. A comparison between 2019 and 2024 allows for an assessment of interannual variability over the study period.

5.5 Interannual Variability — Selected Month Across All Years

To assess how TWS conditions during the peak monsoon season evolve year by year, Figure 5.5 shows the TWS anomaly for September across all six years 2019–2024, computed with DDK2 filtering. September is chosen as it typically corresponds to the peak or late-monsoon phase for the Indian subcontinent.

5.6 Filter Comparison — DDK2 vs DDK5 Geoid Undulation

Figure 5.6 presents a direct comparison between the DDK2 and DDK5 filtered geoid undulation fields for a representative month (September 2019), together with the numerical difference between the two solutions. The undulation is derived from the synthesised gravitational potential divided by the normal gravity γ, and provides a geodetic perspective on the mass redistribution captured by GRACE-FO.

5.7 India-Mean TWS Time Series

Figures 5.7 and 5.8 show the India-mean TWS anomaly time series from January 2019 to December 2024 for the DDK2 and DDK5 filters respectively, together with the min, max, mean, RMS, and STD statistics.

5.8 Statistical Summary

Table 5.1 provides the statistical summary (minimum, maximum, mean, RMS, STD) of the India-mean TWS values in millimetres for selected representative months across the study period, based on DDK2 filtered solutions.

Table 5.1: Statistics of India-mean TWS values (mm) for selected months, DDK2 filter.

Year	Month	Min	Max	Mean	RMS	STD
2019	January	-150	+100	-50	+100	+100
2019	September	-250	+650	+150	+250	+200
2020	September	-400	+750	+100	+300	+250
2021	September	-450	+550	+50	+250	+250
2022	September	-400	+600	+50	+250	+250
2023	September	-500	+400	-100	+250	+250
2024	September	-600	+400	-100	+300	+250

6 Discussion of Results

The results demonstrate that the processing chain — spherical harmonic synthesis of monthly GRACE-FO gravity field solutions from CSR RL06.3, combined with the Wahr approach for converting gravity anomalies to equivalent water height — effectively captures TWS changes across India over the period 2019–2024.

The dominant feature in all years is the strong seasonal cycle driven by the Indian Summer Monsoon. Negative TWS anomalies characterise the dry pre-monsoon period (approximately March–May), when evapotranspiration and water use exceed recharge. The onset of the monsoon in June triggers a rapid increase in TWS, reaching peak positive anomalies typically in August–September. The post-monsoon recession from October onward reflects the gradual withdrawal of monsoon circulation and the associated reduction in precipitation. This seasonal pattern is consistently reproduced across all six years, confirming the reliability of the GRACE-FO synthesis.

When comparing the DDK2 and DDK5 filtered solutions, both filters capture the dominant monsoon signal, but differ in their spatial characteristics. DDK2 delivers spatially smoother fields with more effective suppression of the characteristic GRACE striping artefacts. DDK5 preserves more regional detail, particularly over areas of strong localised TWS gradients such as the Indo-Gangetic Plain and the Western Ghats, but retains somewhat higher levels of residual noise. The difference maps (DDK2$-$DDK5) show that the discrepancies are most pronounced in regions of high spatial variability and are generally small compared to the signal amplitude, indicating that both filters yield physically consistent results for large-scale TWS assessment.

Inter-annual differences between years are visible in the peak monsoon maps (Section 5.5). These reflect variability in the strength, timing, and spatial distribution of monsoon rainfall from year to year. Notably, the Himalayan region and northwestern India consistently show a distinct TWS response compared to the peninsular south, reflecting the different precipitation regimes and hydrogeological settings of these regions.

The degree variance analysis (Figure 5.1) confirms that the signal-to-noise ratio falls below unity at approximately degree 30, justifying the use of DDK filtering and demonstrating that the GRACE-FO-derived TWS is dominated by large-scale, long-wavelength mass variations. The effective spatial resolution of the product (200–300 km) is sufficient to resolve basin-scale TWS changes across the major river systems of India.

7 Conclusion and Outlook

This study has demonstrated the capability of GRACE-FO satellite gravimetry to monitor terrestrial water storage changes across India for the period 2019–2024. Using monthly gravity field solutions from CSR RL06.3 and the Wahr approach for spherical harmonic synthesis, monthly TWS anomaly maps have been produced and analysed for both DDK2 and DDK5 filtered products.
The key findings are as follows:

- The Indian Summer Monsoon dominates the TWS seasonal cycle, producing strong positive anomalies in August–October and negative anomalies in the pre-monsoon period, consistently across all six years.
- Inter-annual variability in the peak monsoon TWS signal is detectable, reflecting differences in monsoon strength and spatial distribution from year to year.
- The DDK2 filter yields spatially smoother TWS fields with stronger noise suppression, while DDK5 retains more regional detail. Both filters are consistent in capturing the dominant large-scale TWS signal.
- The degree variance analysis confirms that the GRACE-FO signal is statistically significant up to approximately degree 30, beyond which the formal error exceeds the signal power.

Future work could extend this analysis by incorporating GLDAS hydrological model outputs to separate the individual components of TWS (soil moisture, surface water, groundwater) for the Indian subcontinent. A comparison with the CSR level-3 mascon solutions would also provide an independent assessment of the synthesised TWS fields (Watkins et al., 2015). Additionally, extending the time series further back using the original GRACE mission data (2002–2017) would allow for a longer-term trend analysis that encompasses the full range of monsoon variability over recent decades.

Acknowledgements

I would like to extend my sincere gratitude to Dr.-Ing. Kurt Seitz for his invaluable guidance and support throughout this lab rotation. His in-depth knowledge, thoughtful suggestions, and practical assistance with code adaptations and error corrections were instrumental in shaping the research and ensuring its successful completion. I am also deeply grateful to Prof. Dr.-Ing. Hansjörg Kutterer for designing the task and clarifying the objectives, which provided a robust foundation for this study. I would also like to acknowledge the Geodätisches Institut (GIK) at KIT for providing the necessary resources and facilities. I acknowledge ICGEM (2026) for providing the GRACE-FO data used in this study.

References

Heiskanen, W. A. and Moritz, H. (1967): Physical Geodesy. W. H. Freeman & Co., San Francisco, USA.

ICGEM (2026): International Centre for Global Earth Models (ICGEM): Gravity field and GRACE/GRACE-FO products hosted at the German Research Centre for Geosciences (GFZ). Accessed: 2026-04-06. URL: https://icgem.gfz-potsdam.de/.

Kusche, J. (2007): Approximate decorrelation and non-isotropic smoothing of time-variable GRACE-type gravity field models. *Journal of Geodesy* 81(11):733–749. DOI: 10.1007/s00190-007-0143-3.

Kusche, J., Schmidt, R., Petrovic, S., and Rietbroek, R. (2009): Decorrelated GRACE time-variable gravity solutions by GFZ, and their validation using a hydrological model. *Journal of Geodesy* 83:903–913. DOI: 10.1007/s00190-009-0308-3.

Landerer, F. W. and Swenson, S. C. (2012): Accuracy of scaled GRACE terrestrial water storage estimates. *Water Resources Research* 48(4). DOI: 10.1029/2011WR011453.

Tapley, B. D., Bettadpur, S., Watkins, M., and Reigber, C. (2004): The gravity recovery and climate experiment: Mission overview and early results. *Geophysical Research Letters* 31(9):1–4. DOI: 10.1029/2004GL019920.

Tsoulis, D. (1999): Spherical harmonic computations with topographic/isostatic coefficients. Tech. rep. IAPG/FESG No. 3. Munich, Germany: Institut für Astronomische und Physikalische Geodäsie, Technische Universität München.

Wahr, J., Molenaar, M., and Bryan, F. (1998): Time variability of the Earth's gravity field: Hydrological and oceanic effects and their possible detection using GRACE. *Journal of Geophysical Research: Solid Earth* 103(B12):30205–30229.

Watkins, M. M., Wiese, D. N., Yuan, D. N., Boening, C., and Landerer, F. W. (2015): Improved methods for observing Earth's time variable mass distribution with GRACE using spherical cap mascons. *Journal of Geophysical Research: Solid Earth* 120:2648–2671. DOI: 10.1002/2014JB011547.

Appendix

A Additional Results

A.1 Monthly TWS Maps — DDK2 Filter (Remaining Years)

The following figures present the complete 12-month TWS maps for years 2020–2023 using the DDK2 filter. The seasonal monsoon-driven pattern described for 2019 in the main text is consistently present across all years, with interannual differences in amplitude and spatial extent.

A.2 Monthly TWS Maps — DDK5 Filter

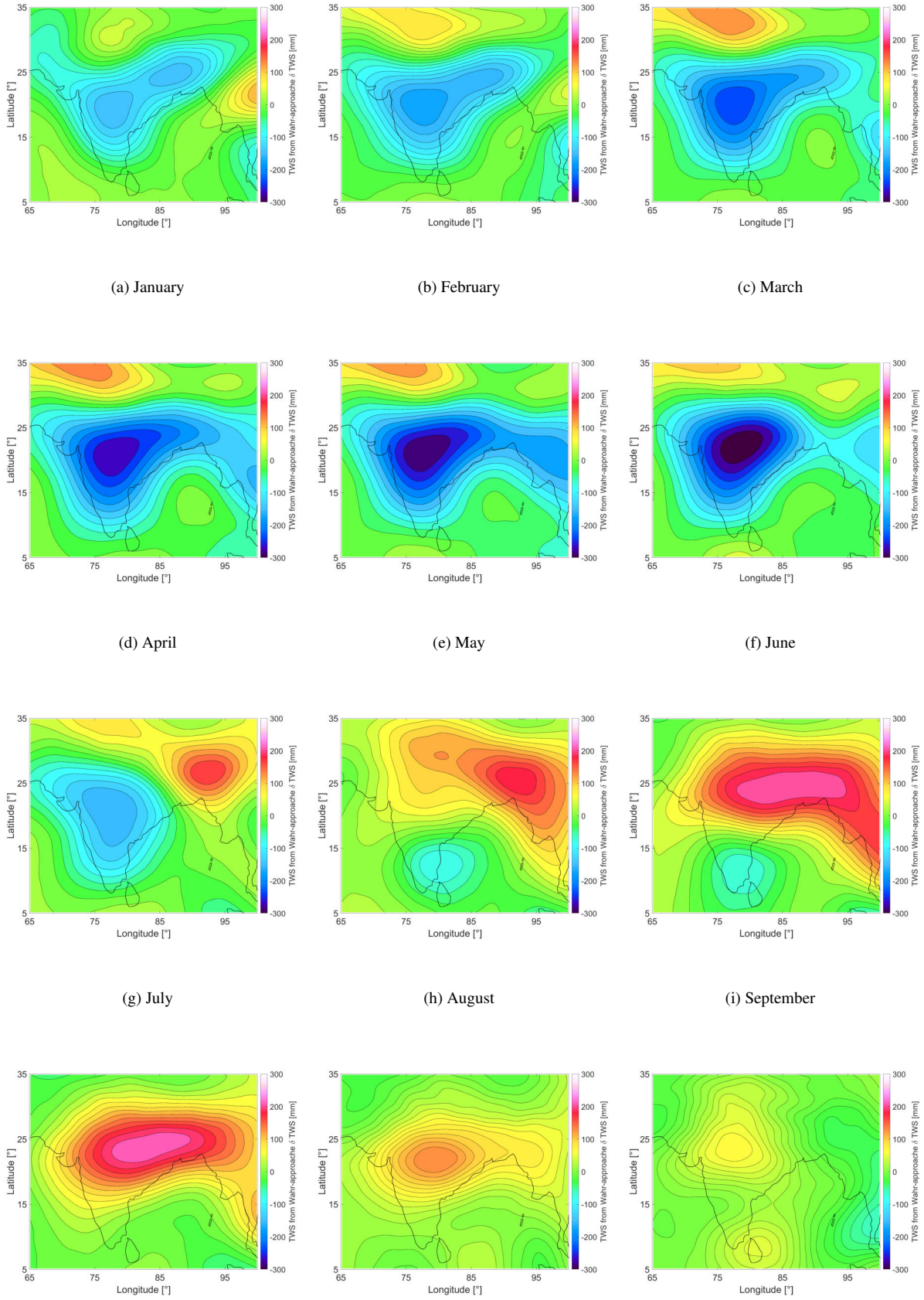

(a) January (b) February (c) March

(d) April (e) May (f) June

(g) July (h) August (i) September

(j) October (k) November (l) December

Figure 5.3: GRACE-FO-derived TWS anomalies (EWH) over India for all months of 2019, computed using the Wahr approach with DDK2 filtering. The seasonal cycle driven by the Indian Summer Monsoon is clearly visible, with negative anomalies in the pre-monsoon months and strong positive anomalies from August through October.

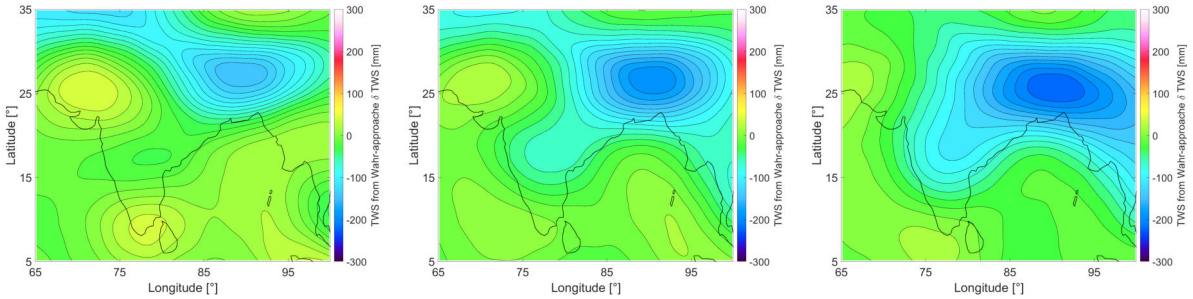

(a) January (b) February (c) March

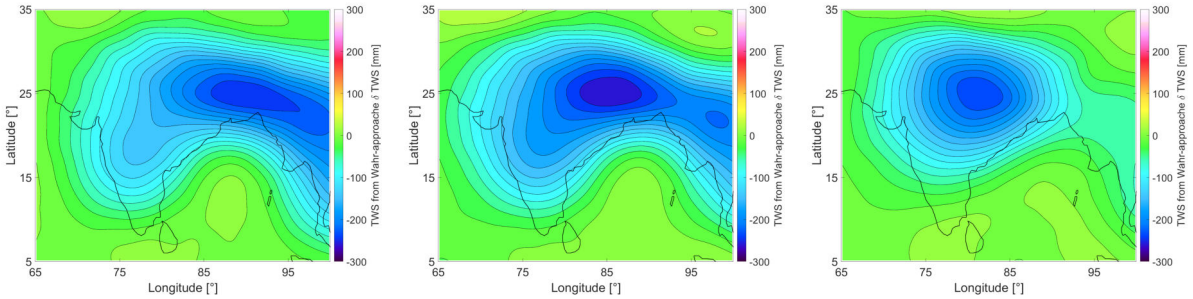

(d) April (e) May (f) June

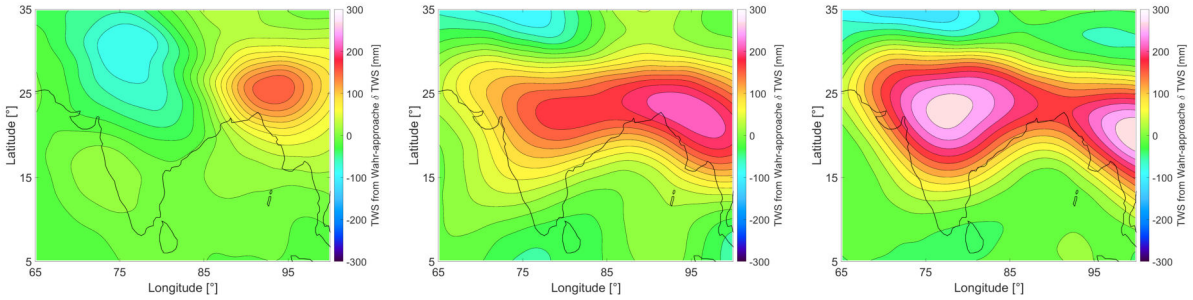

(g) July (h) August (i) September

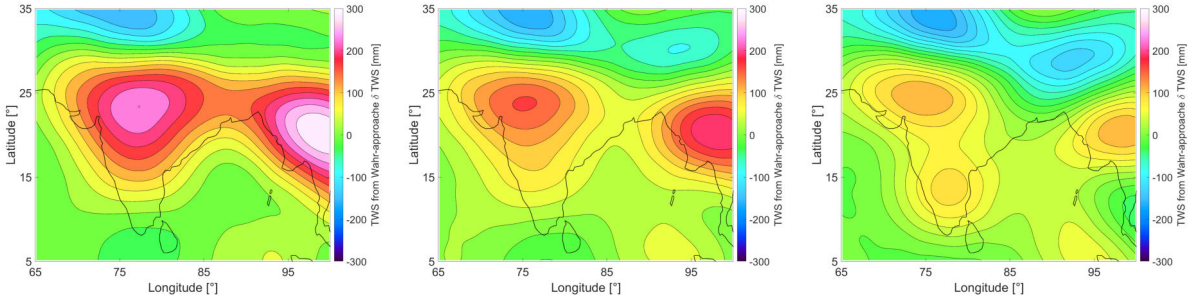

(j) October (k) November (l) December

Figure 5.4: GRACE-FO-derived TWS anomalies (EWH) over India for all months of 2024 (DDK2 filter). Results are included in the main body for direct comparison with 2019 (Figure 5.3).

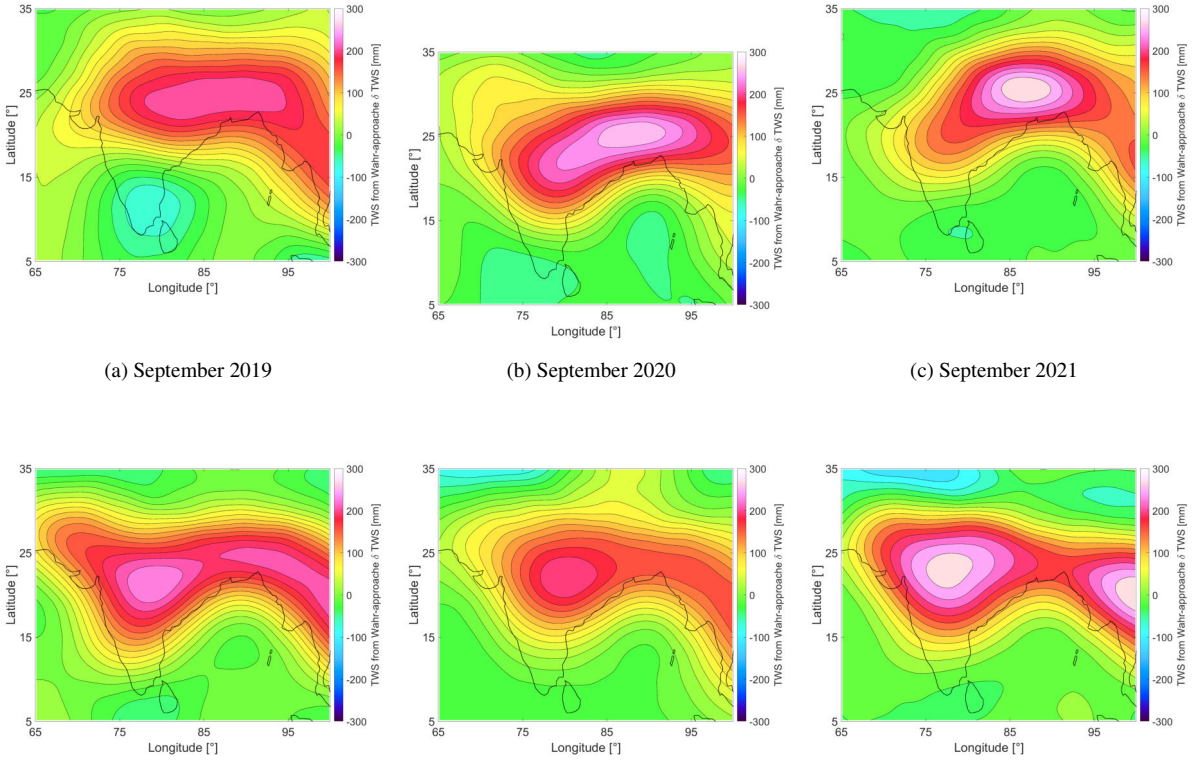

(a) September 2019 (b) September 2020 (c) September 2021

(d) September 2022 (e) September 2023 (f) September 2024

Figure 5.5: GRACE-FO-derived TWS anomalies (EWH, DDK2) over India for September across all six years 2019–2024, illustrating interannual variability in the peak monsoon season.

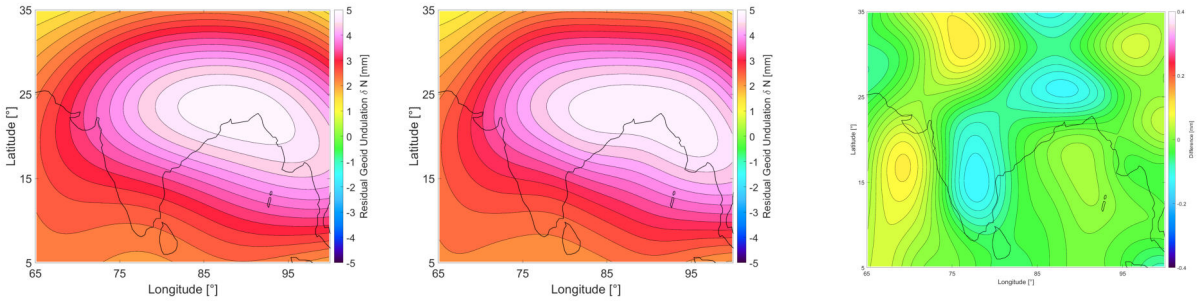

(a) DDK2 (b) DDK5 (c) DDK2 – DDK5

Figure 5.6: Comparison of GRACE-FO-derived residual geoid undulation δN over India for September 2019: DDK2 filter (left), DDK5 filter (centre), and the numerical difference DDK2$-$DDK5 (right). Both filters show a dominant positive anomaly centred over northern India consistent with the peak monsoon mass loading. The difference map (range ± 0.4 mm) reveals that DDK2 suppresses small-scale features retained by DDK5, particularly over the Western Ghats and the Indo-Gangetic Plain.

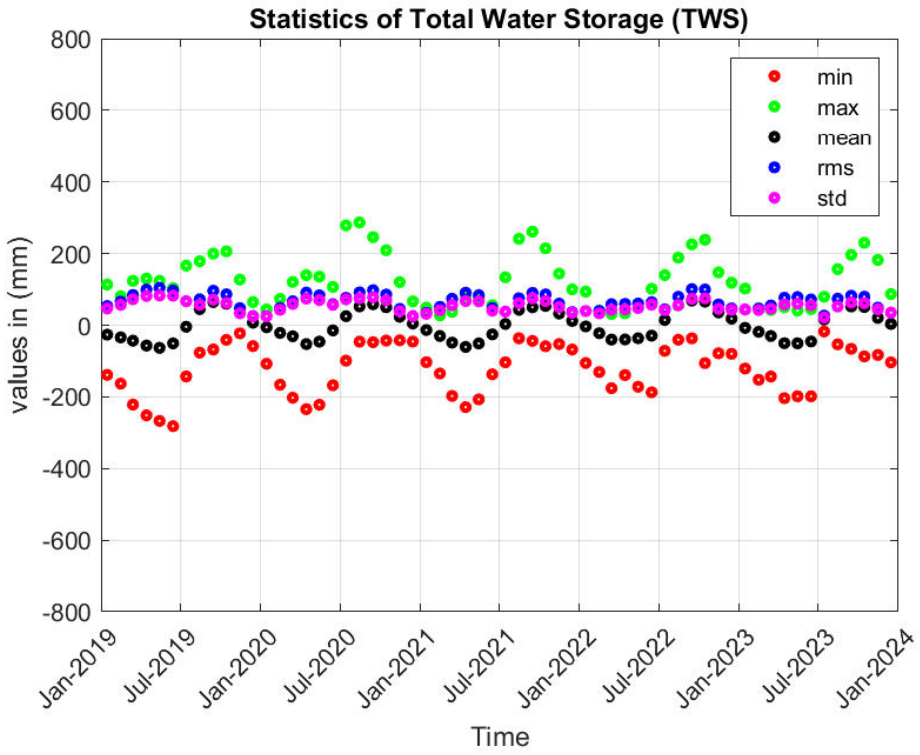

Figure 5.7: India-mean GRACE-FO-derived TWS anomalies (2019–2024) computed using the Wahr approach with DDK2 filter. The seasonal monsoon signal is clearly visible in each year.

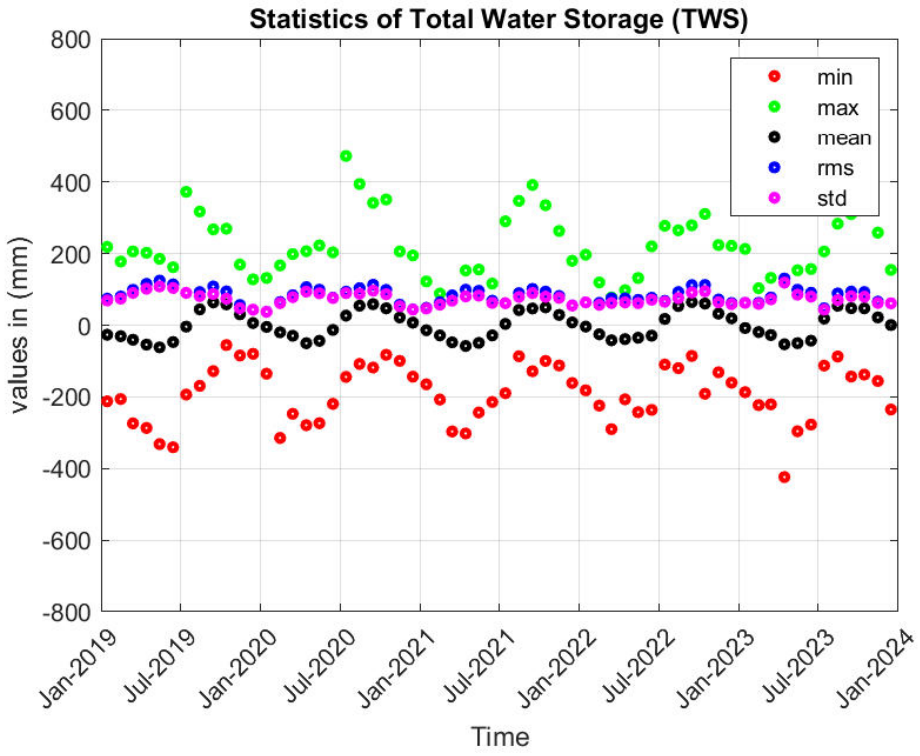

Figure 5.8: India-mean GRACE-FO-derived TWS anomalies (2019–2024) computed using the Wahr approach with DDK5 filter.

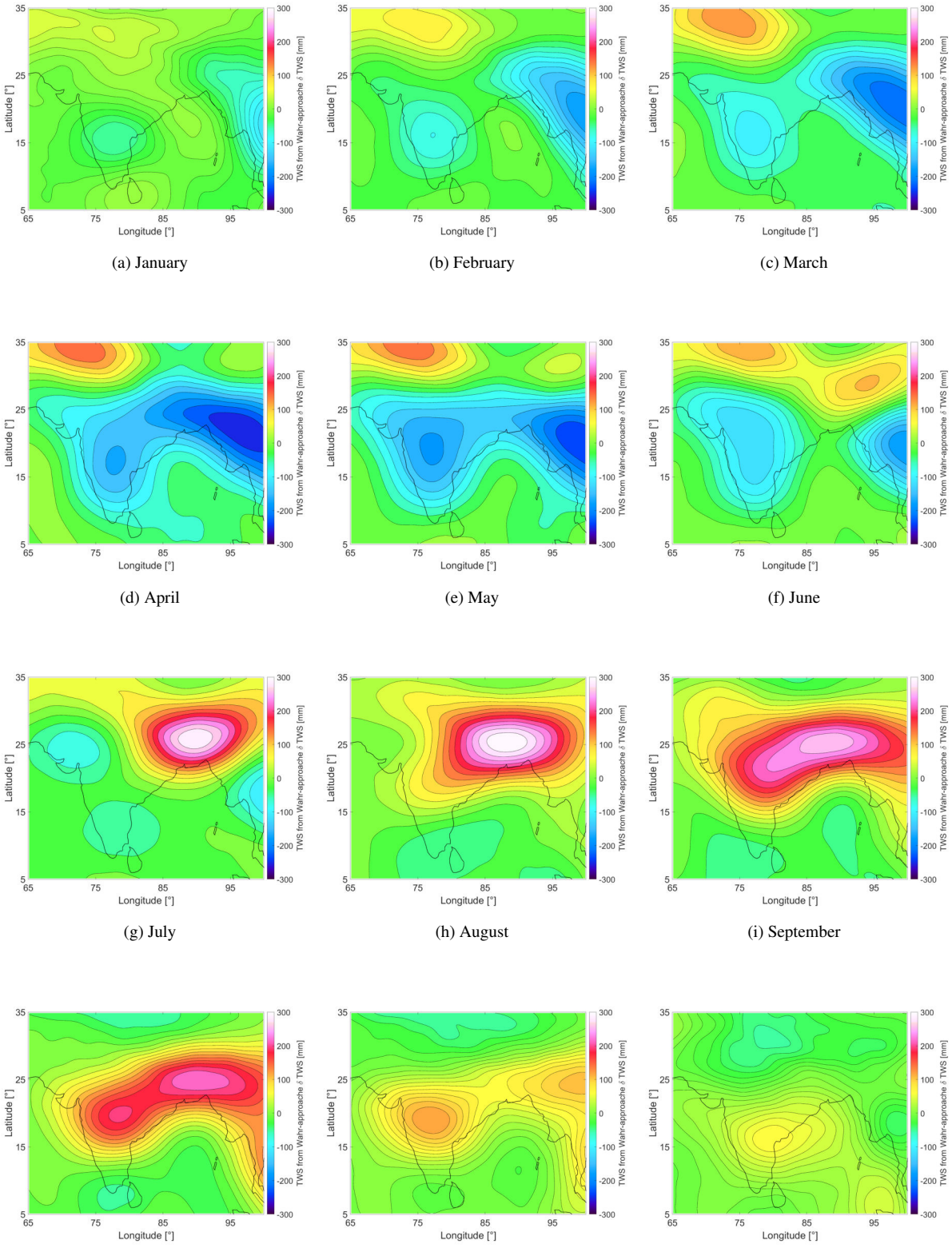

(a) January (b) February (c) March

(d) April (e) May (f) June

(g) July (h) August (i) September

(j) October (k) November (l) December

Figure A.1: GRACE-FO-derived TWS anomalies (EWH, DDK2) over India for all months of 2020.

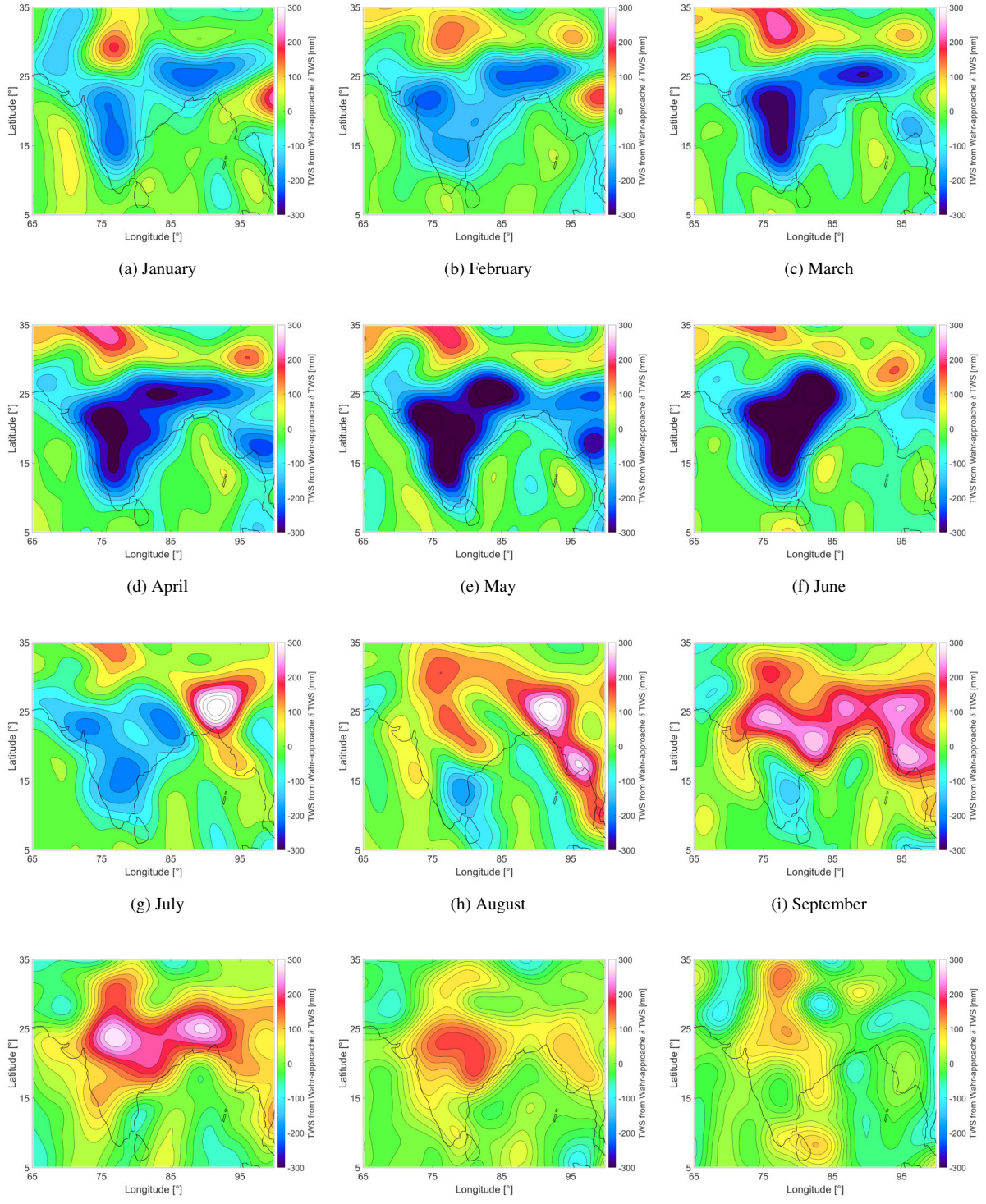

(a) January (b) February (c) March

(d) April (e) May (f) June

(g) July (h) August (i) September

(j) October (k) November (l) December

Figure A.2: GRACE-FO-derived TWS anomalies (EWH, DDK5) over India for all months of 2019. Compare with Figure 5.3 for DDK2. The DDK5 filter retains more spatial detail but shows slightly higher residual noise.

Monitoring Ice Mass Loss over Antarctica based on GRACE Monthly Solutions

Iwin Scaria[1]

1 Remote Sensing and Geoinformatics Master of Science (M.Sc.), KIT, Germany
E-Mail: usiap@student.kit.edu

Abstract

This study analyzes terrestrial water storage (TWS) variations over Antarctica using GRACE and GRACE-FO satellite gravimetry data. GRACE Level-2 spherical harmonic coefficients were subjected to spherical harmonic synthesis and converted to Equivalent Water Height (EWH) via the Wahr formulation, enabling assessment of large-scale mass redistribution linked to hydrological and cryospheric processes. Our results reveal pronounced spatial and temporal changes in Antarctic mass balance, with the strongest anomalies consistently located in West Antarctica. During 2003–2010, positive TWS anomalies dominated parts of West Antarctica, followed by a transition to increasingly negative anomalies after 2015, indicating enhanced ice-mass loss. Interannual analysis of May observations shows a gradual intensification and expansion of negative TWS signals, especially between 2018 and 2024. Geoid undulation maps exhibit patterns coherent with TWS variations, corroborating the link between gravity-field changes and ice-mass redistribution. Statistical analyses indicate a long-term decline in Antarctic water storage, with minimum values becoming more negative toward the end of the study period. Comparisons between DDK2 and DDK8 filters show broadly similar large-scale trends, while DDK8 preserves finer spatial detail at the cost of higher residual noise. Collectively, the findings confirm a persistent loss of Antarctic ice mass over the past two decades and demonstrate the capability of GRACE/GRACE-FO measurements to monitor large-scale cryospheric changes and their implications for global sea-level rise. Overall, GRACE/GRACE-FO observations provide a robust framework for tracking Antarctic ice-mass changes and yield valuable insights into the long-term evolution of the Antarctic Ice Sheet and its contribution to sea-level rise.

Keywords GRACE · Ice Mass Loss · Antarctica

KIT Scientific Working Papers
Issue Number 270
ISSN: 2194-1629
DOI: 10.5445/IR/1000191188
Online: June 2026

This document is licensed under the Creative Commons Attribution – Share Alike 4.0 International License (CC BY-SA 4.0):
https://creativecommons.org/licenses/by-sa/4.0/deed.en

1 Introduction

Climate change is one of the biggest environmental challenges facing the world today, and one of its most visible impacts is the melting of polar ice sheets. Antarctica is especially important in this context because it contains almost 90% of the Earth's ice and nearly 70% of the world's freshwater reserves. As a result, even small changes in the Antarctic ice mass can contribute significantly to global sea-level rise and affect the Earth's climate system. Understanding how the Antarctic ice sheet changes over time is therefore essential for predicting future environmental and climatic conditions.

Over the past two decades, satellite missions have greatly improved our ability to monitor large-scale changes in the Earth system. In particular, the Gravity Recovery and Climate Experiment (GRACE) mission and its successor GRACE Follow-On (GRACE-FO) have provided valuable information about changes in the Earth's gravity field (Velicogna, 2009). Since variations in gravity are directly related to changes in mass distribution, these missions make it possible to observe processes such as glacier melting, groundwater depletion, and changes in terrestrial water storage (TWS). This is especially useful in remote regions like Antarctica, where direct ground observations are difficult and limited.

The GRACE and GRACE-FO missions provide monthly gravity field models in the form of spherical harmonic coefficients. These datasets are produced by several scientific institutions, including the Center for Space Research (CSR), GFZ German Research Centre for Geosciences, and NASA Jet Propulsion Laboratory (JPL). A combined solution known as COST-G is also available. All datasets can be accessed through the International Centre for Global Earth Models (ICGEM, 2026).

This report focuses on analyzing terrestrial water storage changes and ice mass loss over Antarctica between 2003 and 2024 using GFZ Release 6 GRACE and GRACE-FO monthly solutions. To reduce noise and striping errors commonly found in GRACE data, DDK2 and DDK8 filtered datasets are used. In addition, the spherical harmonic coefficients are rescaled following the method proposed by Wahr et al. (1998) to derive terrestrial water storage anomalies.

The results of this work are expected to provide insight into the ongoing changes in the Antarctic ice and their contribution to global sea-level rise. More importantly, the study highlights the significance of satellite gravimetry as a modern tool for monitoring climate-related mass changes within the Earth system.

2 Theoretical Aspects

The GRACE and GRACE-FO satellite missions measure temporal variations in the Earth's gravity field, which are directly related to mass redistribution processes such as ice mass loss and terrestrial water storage changes. These gravity variations are represented using spherical harmonic coefficients, which can be transformed into equivalent water height (EWH) anomalies through the approach proposed by Wahr et al. (1998). To reduce correlated noise and striping effects in the GRACE data, DDK filtering techniques such as DDK2 and DDK8 are applied before analysing temporal trends and spatial patterns over Antarctica.

2.1 Spherical Harmonic Synthesis (SHS)

Spherical harmonic representation of the gravitational potential of the Earth is given in Equation (2.1). Spherical Harmonic Synthesis is the forward computation of a function on or outside the sphere of radius R from a series of surface spherical harmonics (Tsoulis, 1999). The spherical harmonic coefficients derived from GRACE level-2 data is used to express the gravity field of the Earth (Heiskanen and Moritz, 1967):

$$V(P) = \frac{GM}{r} \sum_{n=0}^{\infty} \left(\frac{R}{r}\right)^n \sum_{m=0}^{n} (\bar{C}_{nm} \cos m\lambda + \bar{S}_{nm} \sin m\lambda) \bar{P}_{nm}(\sin \varphi) \tag{2.1}$$

where,
GM : Geocentric gravitational constant
R : Radius of the reference sphere
$\bar{C}_{nm}, \bar{S}_{nm}$: Fully normalised spherical harmonic coefficients of degree n and order m
$\bar{P}_{nm}$: Fully normalised Legendre functions of degree n and order m.
r, φ, λ: Geocentric spherical coordinates.

2.2 Computation of Monthly Mean Reference Model

GRACE Level-2 solutions provide monthly spherical harmonic coefficients $\bar{C}_{nm}(t)$ and $\bar{S}_{nm}(t)$, where t denotes the observation month. To analyze temporal mass variations, a reference mean gravity field is first computed over a selected time period consisting of T months.

$$\bar{C}_{nm} = \frac{1}{T}\sum_{t=1}^{T} \bar{C}_{nm}^{(t)}, \qquad \bar{S}_{nm} = \frac{1}{T}\sum_{t=1}^{T} \bar{S}_{nm}^{(t)} \tag{2.2}$$

where,
$\bar{C}_{nm}, \bar{S}_{nm}$: mean spherical harmonic coefficients
T: number of months used in the reference period.

2.3 Monthly Gravity Anomalies

For each month t, the gravity anomaly coefficients are obtained by subtracting the mean field:

$$\Delta\bar{C}_{nm}^{(t)} = \bar{C}_{nm}^{(t)} - \bar{C}_{nm}, \quad \Delta\bar{S}_{nm}^{(t)} = \bar{S}_{nm}^{(t)} - \bar{S}_{nm}. \tag{2.3}$$

These anomaly coefficients represent temporal mass redistribution relative to the reference model.

2.4 Transformation to Equivalent Water Height (TWS)

The spherical harmonic coefficients $\Delta\bar{C}_{nm}$ and $\Delta\bar{S}_{nm}$ are transformed into surface mass variations using the formulation of Wahr et al. (1998). The resulting quantity is expressed as Equivalent Water Height (EWH), representing terrestrial water storage changes.
The TWS anomaly at a point (φ, λ) on the Earth's surface is given by:

$$\Delta TWS(\varphi,\lambda) = \frac{R\rho_E}{3\rho_w}\sum_{n=0}^{N}\frac{2n+1}{1+k_n}\sum_{m=0}^{n}\left(\Delta\bar{C}_{nm}\cos m\lambda + \Delta\bar{S}_{nm}\sin m\lambda\right)\bar{P}_{nm}(\sin\varphi) \tag{2.4}$$

where,
ρ_E : Mean density of the Earth
ρ_w : Density of water
k_n : Load Love number of degree n
$\bar{P}_{nm}$: Fully normalized Legendre functions
$\Delta\bar{C}_{nm}, \Delta\bar{S}_{nm}$: Temporal gravity coefficients
N : Maximum degree (typically 96 for GRACE)

2.5 Degree and Error Degree Variance

The degree variance quantifies the amplitudes of the spherical harmonic coefficients, which vary across different degrees. The sum of the squared coefficients expresses the overall energy in the signal as shown in Equation (2.5). Figure 2.1 shows that there is a higher degree variance at lower degrees, and the value decreases as the degree n

increases. This indicates that the gravity signal is mainly concentrated in the lower degrees, whereas the higher degrees contain relatively smaller signal contributions.

$$C_n^2(\bar{C}_{nm}, \bar{S}_{nm}) = \sum_{m=0}^{n} \left(\bar{C}_{nm}^2 + \bar{S}_{nm}^2\right) \tag{2.5}$$

Error degree variances are defined as follow:

$$\sigma_n(\sigma_{\bar{C}_{nm}}, \sigma_{\bar{S}_{nm}}) = \sum_{m=0}^{n} \left(\sigma_{\bar{C}_{nm}}^2 + \sigma_{\bar{S}_{nm}}^2\right). \tag{2.6}$$

This helps to understand the distribution of signal intensity across the frequency range. The degree variance computed for the coefficients used in this study indicates that the signal contains higher energy in the long-wavelength components, while the energy decreases toward the short-wavelength components of the signal. The degree variance plots for all months exhibit similar patterns with only marginal variations. Therefore, example plots of accuracies for some selected months are represented in the Figures 2.1 – 2.4.

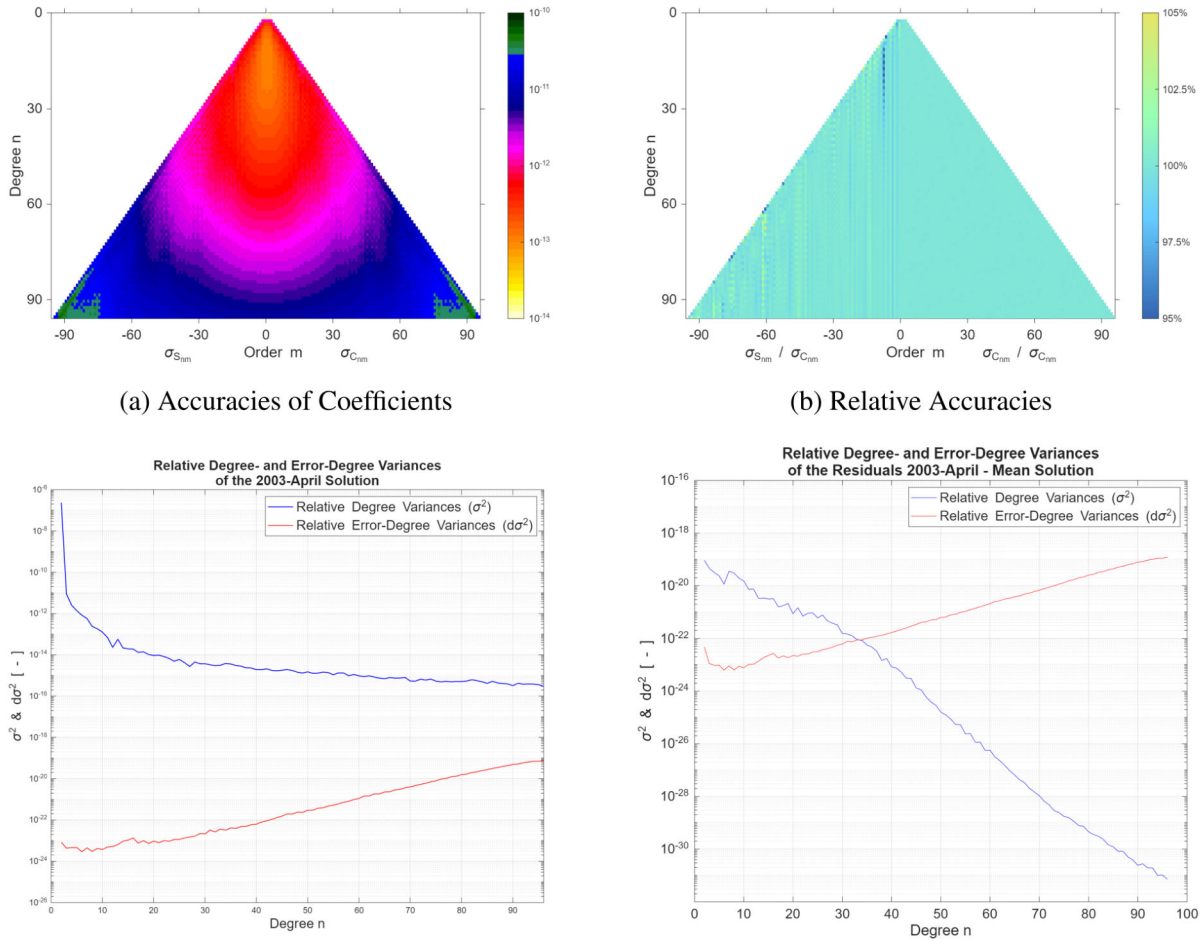

(a) Accuracies of Coefficients

(b) Relative Accuracies

(c) Degree and error degree Variances

(d) Relative to the mean Model

Figure 2.1: Accuracy of April 2003.

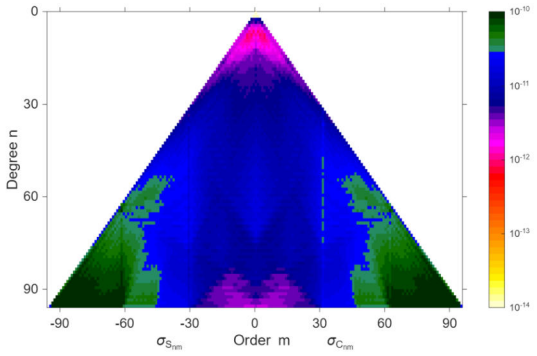

(a) Accuracies of Coefficients

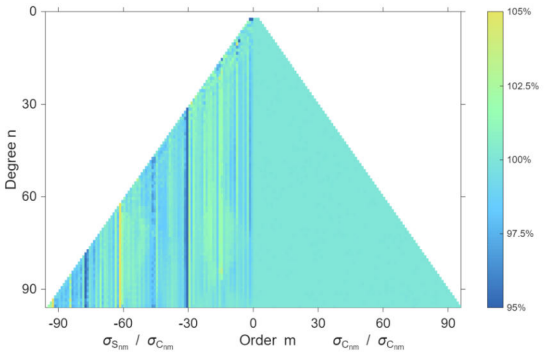

(b) Relative Accuracies

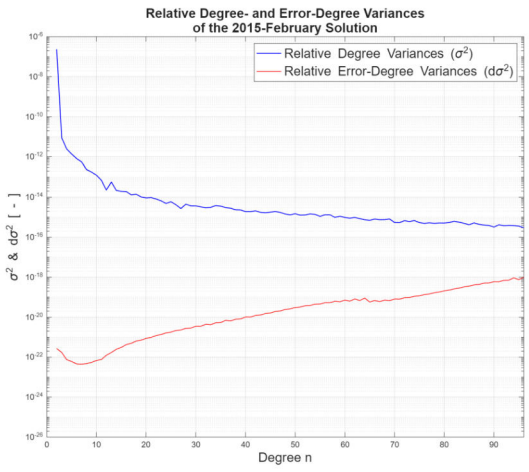

(c) Degree and error degree Variances

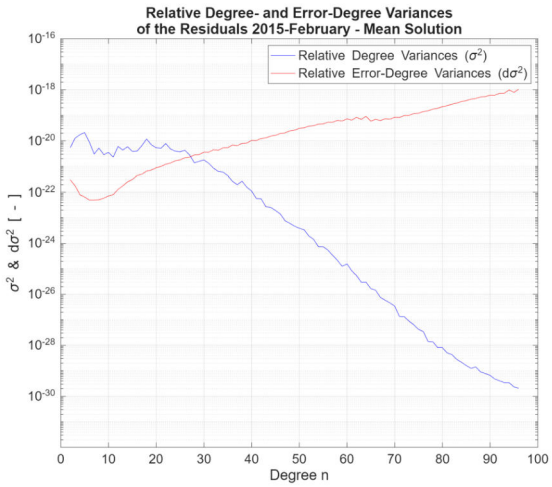

(d) Relative to the mean Model

Figure 2.2: Accuracy of February 2015.

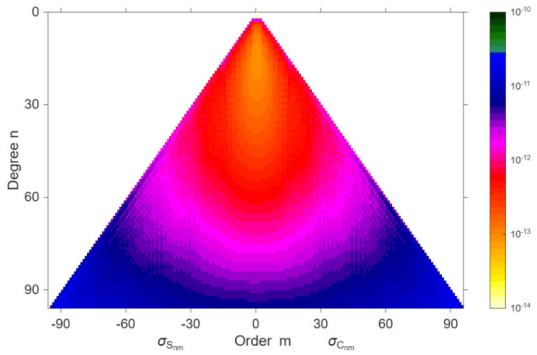

(a) Accuracies of Coefficients

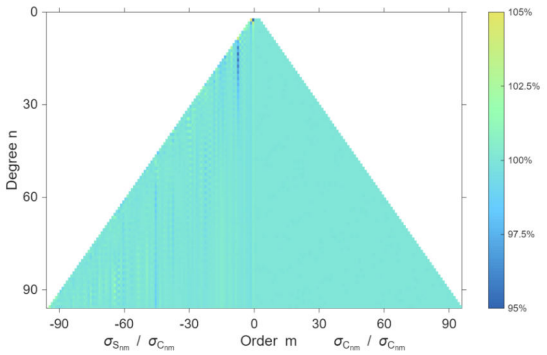

(b) Relative Accuracies

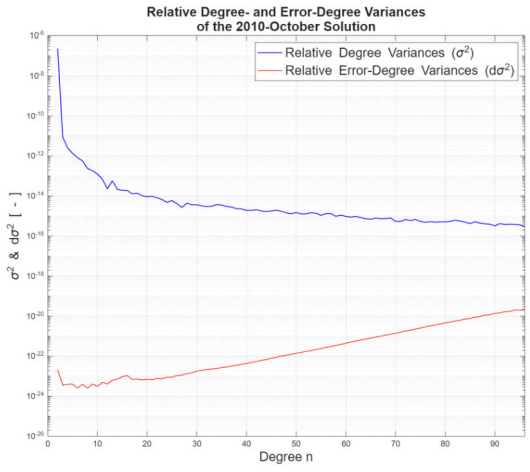

(c) Degree and error degree Variances

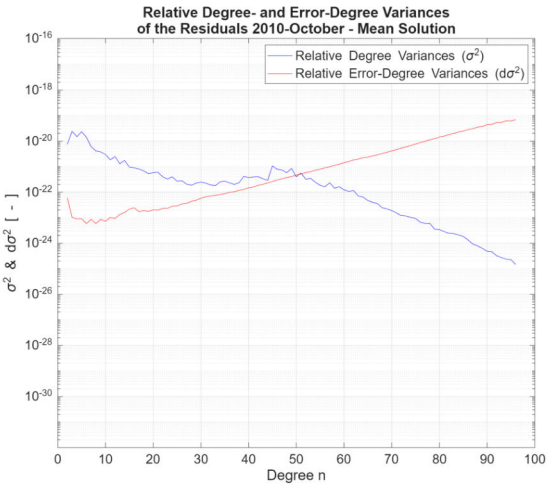

(d) Relative to the mean Model

Figure 2.3: Accuracy of October 2010.

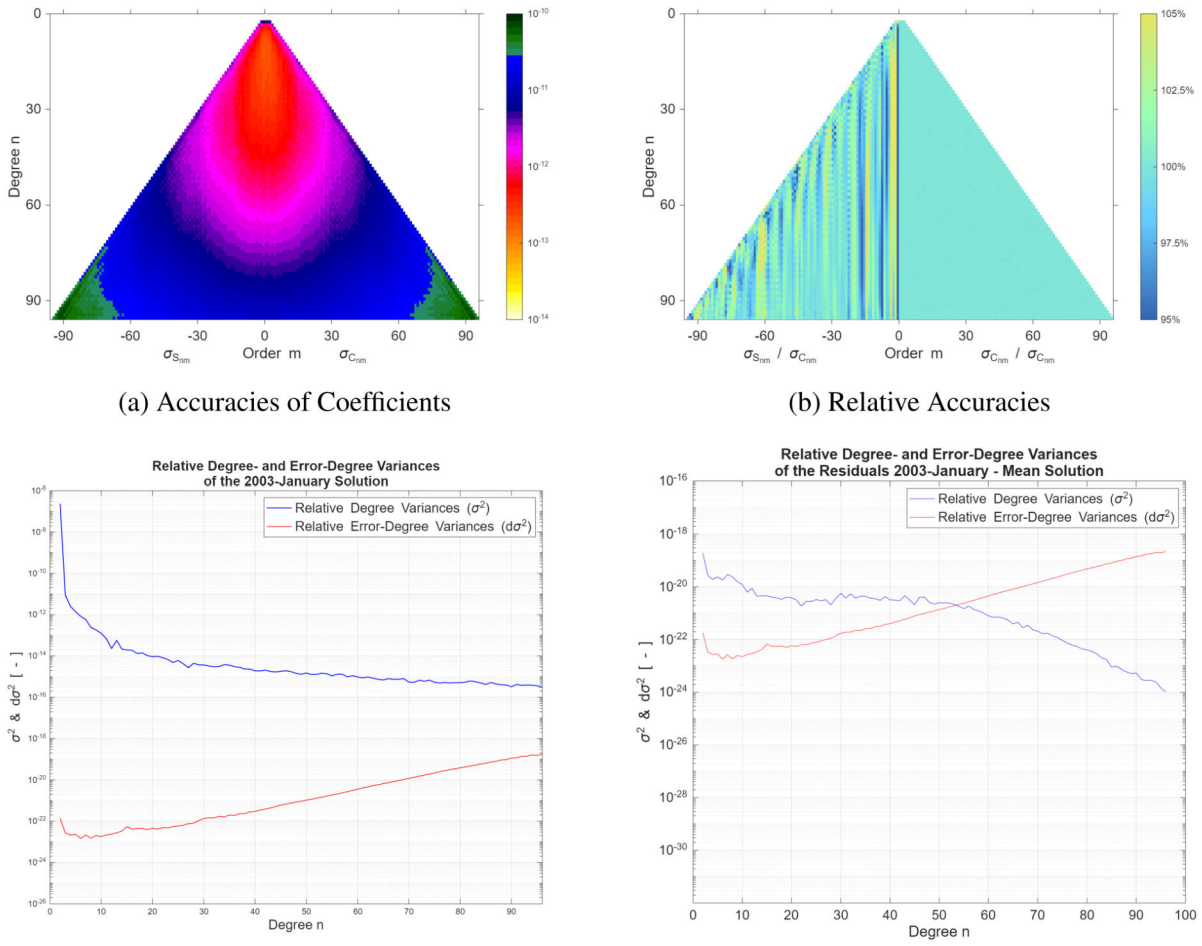

(a) Accuracies of Coefficients

(b) Relative Accuracies

(c) Degree and error degree Variances

(d) Relative to the mean Model

Figure 2.4: Accuracy of January 2003.

2.6 TWS from Wahr Approach

The transformation of gravity field variations into terrestrial water storage anomalies (TWS) in this study follows the methodology proposed by Wahr et al. (1998). As presented in Equation (2.4), this approach establishes a relationship between temporal variations in the Earth's gravity field, represented by changes in spherical harmonic coefficients, and mass redistribution occurring on the Earth's surface in terms of TWS.

Monthly gravity field anomalies are obtained from the differences between the monthly spherical harmonic coefficients, $\Delta\bar{C}_{nm}$ and $\Delta\bar{S}_{nm}$, and a mean reference gravity field computed over the study period. These gravity anomalies are subsequently transformed into Equivalent Water Height (EWH), which provides a quantitative measure of ice mass changes across Antarctica.

To account for the elastic deformation of the Earth caused by surface loading, the formulation incorporates load Love numbers. The scaling factor $\frac{1}{1+k_n}$, where k_n denotes the load Love number of degree n, considers both the direct gravitational effect of surface mass changes and the indirect effect resulting from the deformation of the solid Earth. This correction is essential for obtaining physically meaningful estimates of mass redistribution from satellite gravimetry observations.

Each spherical harmonic degree is additionally weighted by the factor $(2n+1)$, reflecting the spatial characteristics of the gravity signal. Lower-degree coefficients represent large-scale mass variations extending over continental scales, while higher-degree coefficients describe smaller-scale features that are more strongly affected by mea-

surement noise. Consequently, the dominant contribution to Antarctic mass change is primarily contained in the lower-degree components of the gravity field.
In the Antarctic region, the derived TWS anomalies predominantly represent variations in ice-sheet mass rather than conventional hydrological components such as groundwater or soil moisture. Therefore, positive EWH anomalies indicate ice mass accumulation, often associated with enhanced snowfall, whereas negative EWH anomalies reflect ice mass loss resulting from increased glacier discharge, basal melting, or ice-sheet thinning.

3 Data

This study is based on monthly gravity field solutions derived from the Gravity Recovery and Climate Experiment (GRACE) and Gravity Recovery and Climate Experiment Follow-On (GRACE-FO) satellite missions to investigate terrestrial water storage (TWS) and ice mass variations over Antarctica between 2003 and 2024. GRACE and GRACE-FO observations provide information on temporal changes in the Earth's gravity field, which can be interpreted as mass redistribution within the Earth system. In this study, spherical harmonic solutions from the GFZ German Research Centre for Geosciences (GFZ) were used. To reduce correlated errors and north–south striping effects, DDK2 and DDK8 filtered datasets were applied. The spherical harmonic coefficients were converted into equivalent water height (EWH) following the methodology proposed by Wahr et al. (1998). The resulting TWS anomalies were analyzed to identify seasonal variations and long-term trends across Antarctica.
The GRACE and GRACE-FO datasets provide monthly estimates of Earth's gravity field in the form of spherical harmonic coefficients, which enable the monitoring of mass redistribution associated with changes in ice sheets, glaciers, oceans, and terrestrial water storage. In this study, Release-06 GFZ gravity field solutions up to degree and order 96 were obtained from the International Centre for Global Earth Models (ICGEM, 2026). The application of DDK2 and DDK8 decorrelation filters helped suppress correlated noise while preserving the large-scale mass change signals over Antarctica. After conversion to equivalent water height, the data were used to derive monthly TWS anomalies and investigate temporal variations in Antarctic ice mass. The processed time series were further analysed to quantify trends, seasonal cycles, and long-term changes in ice storage between 2003 and 2024.
The GRACE mission operated from April 2002 to June 2017 and provided monthly observations of the Earth's gravity field. Following a one-year observation gap, the GRACE Follow-On (GRACE-FO) mission was launched in May 2018 to continue the gravity monitoring record. Both missions measure changes in the distance between two satellites caused by variations in the Earth's gravitational field, enabling the estimation of mass redistribution at the Earth's (Chen et al., 2008).
The Antarctic Ice Sheet is one of the largest freshwater reservoirs on Earth and plays a critical role in regulating global sea level. Variations in terrestrial water storage derived from GRACE observations primarily reflect changes in ice mass balance caused by snowfall accumulation, surface melting, and glacier discharge into the surrounding oceans. Consequently, the GRACE and GRACE-FO datasets provide valuable information for assessing the contribution of Antarctica to contemporary sea-level rise and understanding the impacts of climate change on the polar regions (Rignot et al., 2008).

4 Methodology Overview

Monthly GRACE and GRACE-FO GFZ Release-06 gravity field solutions up to degree and order 96 were obtained from the ICGEM database for the period 2003–2024. The spherical harmonic coefficients were transformed into Equivalent Water Height (EWH) anomalies using the approach of Wahr et al. (1998), applying both DDK2 and DDK8 filters to reduce correlated noise. Monthly EWH and geoid undulation maps were generated over Antarctica. Finally, temporal variations and long-term trends were analyzed to assess changes in Antarctic ice mass and investigate potential acceleration of ice loss during the study period.

4.1 Data Acquisition

Monthly gravity field solutions from the GRACE (2003–2017) and GRACE-FO (2018–2024) missions were obtained from the International Centre for Global Earth Models (ICGEM, 2026). The GFZ Release-06 spherical harmonic solutions up to degree and order 96 were used in this study. To reduce correlated errors and north-south striping artifacts, DDK2 and DDK8 filtered products were selected for further analysis. Antarctica was chosen as the study area to investigate long-term ice mass variations and their implications for global sea-level rise.

4.2 Computation of Mean Reference Gravity Field

A mean reference gravity field was computed using all available monthly spherical harmonic coefficients over the study period. The mean coefficients were calculated separately for each degree and order and served as the baseline gravity field. Monthly gravity anomalies were then obtained by subtracting the mean field from the corresponding monthly solutions.

4.3 Determination of Gravity Field Anomalies

For each month, gravity anomaly coefficients were computed from the differences between the monthly and mean spherical harmonic coefficients. These anomaly coefficients represent temporal variations in the Earth's gravity field associated with mass redistribution within the Antarctic ice sheet.

4.4 Transformation to Equivalent Water Height

The gravity anomaly coefficients were converted into Equivalent Water Height (EWH) using the approach proposed by Wahr et al. (1998). This method incorporates load Love numbers to account for the elastic response of the Earth to surface loading. The resulting EWH values represent terrestrial water storage anomalies and provide a quantitative measure of Antarctic ice mass changes.

4.5 Spatial Synthesis and Mapping

The transformed EWH coefficients were synthesized onto a regular spatial grid covering Antarctica using spherical harmonic synthesis. Monthly maps were generated for the entire study period, enabling visualization of spatial and temporal variations in ice mass distribution.

4.6 Geoid Undulation Computation

In addition to EWH, geoid height anomalies were calculated from the gravity field coefficients. Monthly geoid undulation maps were produced to investigate the relationship between gravity field variations and Antarctic mass redistribution. The spatial patterns of geoid change were compared with the corresponding EWH anomalies.

4.7 Statistical Analysis

For each monthly solution, statistical parameters including minimum, maximum, mean, standard deviation, and root mean square (RMS) values were calculated. These statistics were used to quantify the magnitude and variability of Antarctic terrestrial water storage changes throughout the study period.

4.8 Temporal Trend Analysis

Time-series analysis was performed using the monthly EWH statistics derived from both DDK2 and DDK8 filtered datasets. Long-term trends and interannual variations were examined to assess changes in Antarctic ice mass over time. The results were analyzed to determine whether ice mass loss accelerated during the period 2003–2024 and to evaluate the consistency between the two filtering approaches.

4.9 Comparison of DDK2 and DDK8 Solutions

The performance of DDK2 and DDK8 filtering techniques was evaluated by comparing the resulting spatial patterns, statistical measures, and temporal trends. This comparison allowed assessment of the influence of filtering strength on the detection and interpretation of Antarctic ice mass changes.

5 Results and Discussion

In this study, the Wahr formulation is applied to GFZ Release-06 GRACE and GRACE-FO Level-2 monthly gravity field solutions up to degree and order 96 using both DDK2 and DDK8 filtered datasets. The resulting EWH anomalies are analyzed over Antarctica for the period 2003-2024. Given the large spatial extent of the Antarctic Ice Sheet, regional-scale analysis is employed to suppress short-wavelength noise and emphasize large-scale mass variations (Velicogna et al., 2020).

The computed TWS anomalies provide valuable insight into the long-term evolution of the Antarctic ice mass. Spatial distributions reveal substantial variability throughout the study period (Humphrey et al., 2023), with the strongest signals concentrated in the west Antarctica. During the early years of the record, several regions exhibited positive EWH anomalies, indicating periods of ice accumulation. However, increasingly negative anomalies became evident after 2015, particularly in West Antarctica, suggesting intensified ice mass loss (Rignot, 2006). The strongest negative anomalies were observed during the most recent years of the study period, indicating a persistent decline in the Antarctic ice mass and highlighting the growing contribution of the Antarctic Ice Sheet to global sea-level rise (Bell and Seroussi, 2020).

The GRACE and GRACE-FO derived EWH anomalies revealed significant spatial and temporal variations in Antarctic ice mass between 2003 and 2024. The strongest changes were observed in West Antarctica, where increasingly negative anomalies indicated persistent ice mass loss over time. Statistical analyses and time-series results showed a long-term declining trend in terrestrial water storage, with the most pronounced losses occurring after 2015. These findings suggest an acceleration of Antarctic ice mass loss in recent years, highlighting its growing contribution to global sea-level rise.

Analysis of the GRACE and GRACE-FO datasets showed substantial variability in Antarctic terrestrial water storage throughout the study period. Spatial patterns of EWH anomalies revealed persistent mass loss, particularly in West Antarctica, while statistical measures indicated an overall decreasing trend in ice mass. Both DDK2 and DDK8 filtered solutions produced consistent results, confirming the robustness of the observed signals. The results provide evidence of continued and potentially accelerated Antarctic ice-sheet mass loss between 2003 and 2024.

5.1 Spatial Distribution of Terrestrial Water Storage Anomalies

The EWH anomaly maps derived from GRACE and GRACE-FO data reveal considerable spatial and temporal variations in Antarctic terrestrial water storage between 2003 and 2024. The most significant changes are observed in West Antarctica, where strong positive and negative anomalies indicate substantial fluctuations in ice mass. During the early years of the study period, several regions showed positive anomalies, suggesting periods of increased ice accumulation. Over time, however, negative anomalies became more widespread and pronounced, pointing to a gradual increase in ice mass loss.

Compared to West Antarctica, East Antarctica exhibited relatively smaller variations and a more stable behavior. Nevertheless, some localized positive anomalies were visible in certain years, likely associated with increased snowfall. The Antarctic Peninsula also showed noticeable changes, although its contribution to the overall Antarctic mass balance was smaller than that of West Antarctica.

5.2 Interannual Variability

The comparison of May EWH anomaly maps (Figures 5.3 and 5.6) from 2003 to 2024 highlights clear year-to-year variability in Antarctic ice mass. During the first decade of the study period, positive anomalies were more common, particularly in West Antarctica. From around 2015 onwards, negative anomalies became increasingly dominant and expanded over larger areas. The strongest negative signals were observed after 2018, indicating intensified ice mass loss during recent years. Although temporary fluctuations occurred throughout the study period, the overall pattern suggests a shift towards a more negative mass balance. These variations can be attributed to changes in snowfall, atmospheric circulation, ocean temperatures, and glacier dynamics, all of which influence the Antarctic ice sheet.

5.3 Geoid Undulation Variations

The geoid undulation maps (Figures 5.7 and 5.10) show patterns that closely resemble those observed in the EWH anomaly maps. Regions experiencing positive EWH anomalies generally correspond to positive geoid changes, while areas with negative EWH anomalies show decreases in geoid height. This agreement confirms that the gravity field variations detected by GRACE are directly related to changes in Antarctic mass distribution. The strongest geoid variations occur in West Antarctica, where the most significant ice mass changes were also observed. The consistency between geoid and EWH results provides additional confidence in the reliability of the processing approach and the interpretation of the results.

5.4 Statistical Analysis

The statistical analysis further supports the observed spatial patterns. The statistics are presented in Figure 5.11. The minimum EWH values become progressively more negative over time, while the mean values show an overall declining trend. The standard deviation and RMS values indicate substantial variability throughout the study period, reflecting both seasonal and interannual changes in ice mass. The statistics suggest that mass loss became more pronounced during the later years of the study period, particularly after 2015. Although some years show temporary increases in storage due to higher snowfall accumulation, the long-term trend remains negative.

5.5 Comparison of DDK2 and DDK8 Filters

Both DDK2 and DDK8 filtered solutions successfully capture the major patterns of Antarctic mass change. The overall spatial distribution and long-term trends are very similar in both datasets, demonstrating the robustness of the observed signals. The DDK2 filter produces smoother maps and reduces noise more effectively, making large-scale trends easier to identify. In contrast, DDK8 preserves more spatial detail and reveals smaller-scale features, although it also retains more residual noise. The stripping effects are still visible. Despite these differences, both filtering approaches lead to the same general conclusion regarding Antarctic ice mass loss.

5.6 Implications for Antarctic Ice Mass Loss

The combined spatial, temporal, and statistical analyses indicate that Antarctica experienced a sustained decline in terrestrial water storage between 2003 and 2024. The strongest losses were concentrated in West Antarctica, where negative anomalies became increasingly extensive and intense over time. The results suggest that ice mass loss accelerated during the latter part of the study period, particularly after 2015, with the most pronounced losses occurring after 2018. Overall, the GRACE and GRACE-FO observations provide clear evidence of continued Antarctic ice-sheet mass loss over the last two decades. These findings highlight the importance of satellite gravimetry for monitoring large-scale cryospheric changes and improving our understanding of Antarctica's contribution to global sea-level rise.

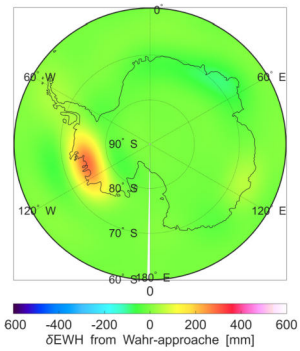

(a) January, 2009

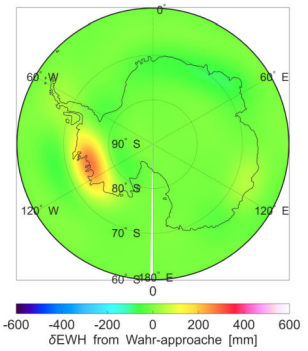

(b) February, 2009

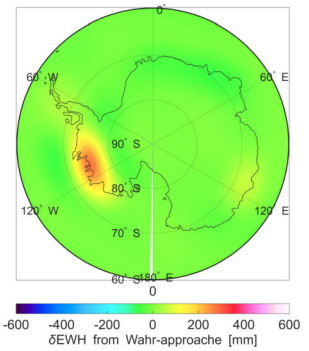

(c) March, 2009

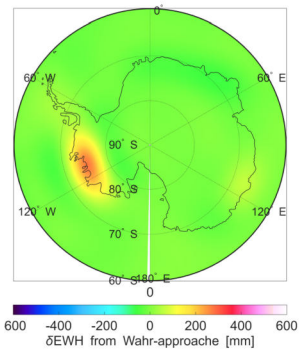

(d) April, 2009

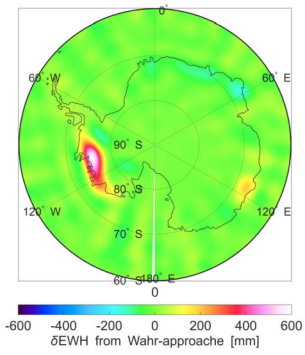

(e) May, 2009

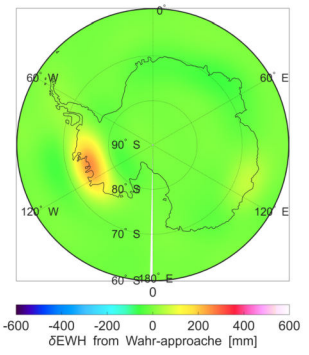

(f) June, 2009

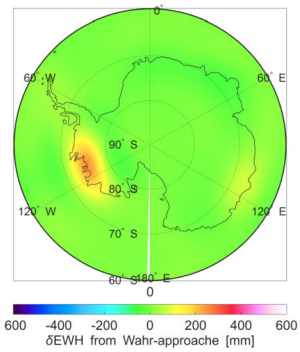

(g) July, 2009

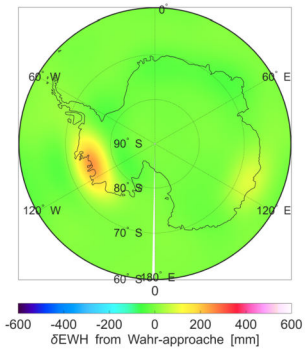

(h) August, 2009

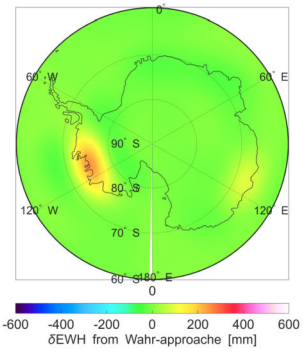

(i) September, 2009

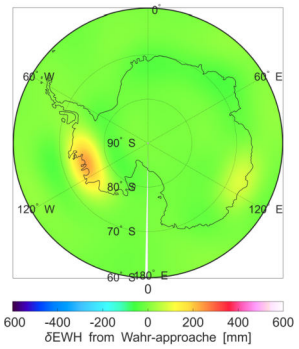

(j) October, 2009

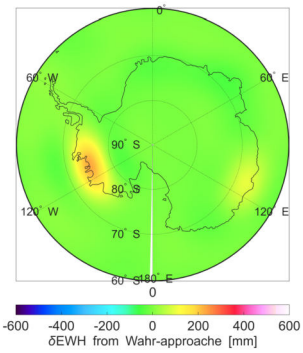

(k) November, 2009

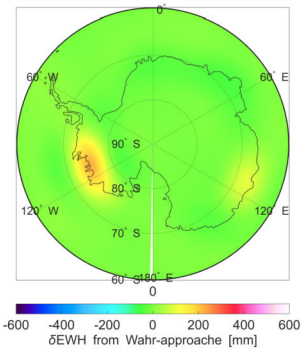

(l) December, 2009

Figure 5.1: TWS in 2009, DDK2.

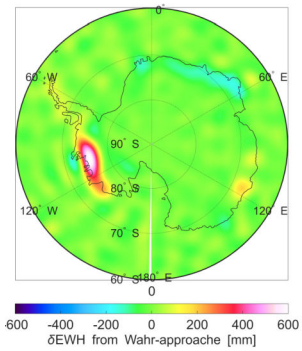

(a) January, 2009

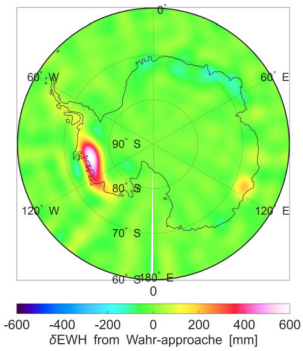

(b) February, 2009

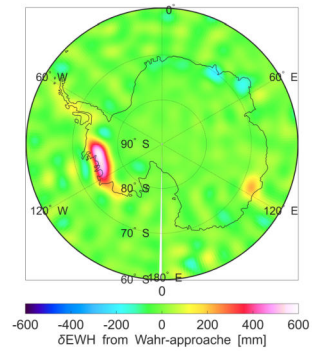

(c) March, 2009

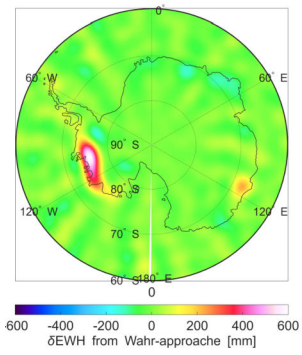

(d) April, 2009

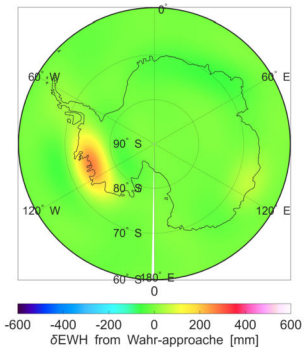

(e) May, 2009

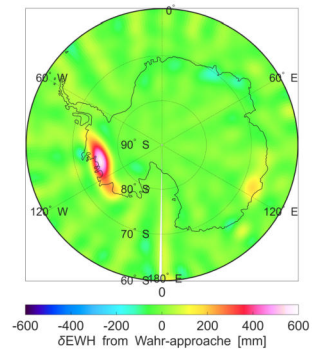

(f) June, 2009

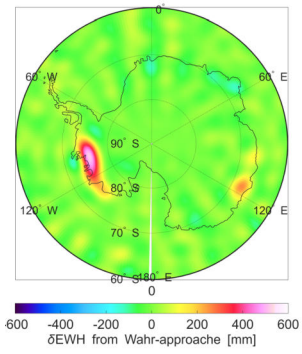

(g) July, 2009

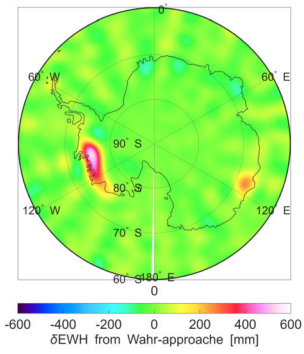

(h) August, 2009

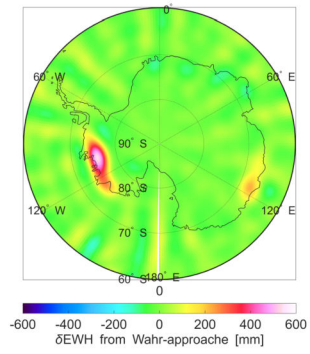

(i) September, 2009

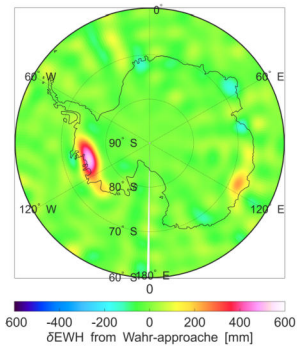

(j) October, 2009

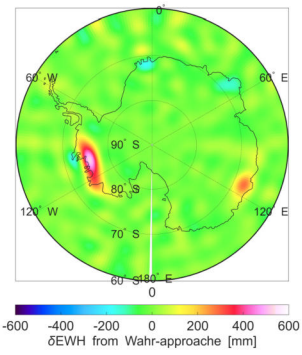

(k) November, 2009

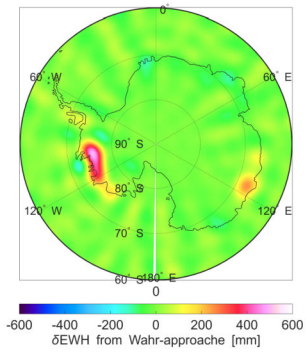

(l) December, 2009

Figure 5.2: TWS in 2009, DDK8.

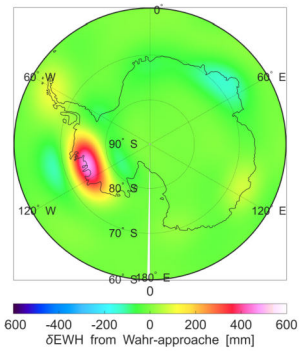

(a) May, 2003

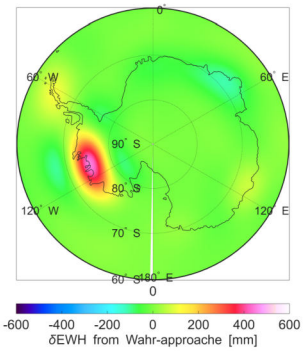

(b) May, 2004

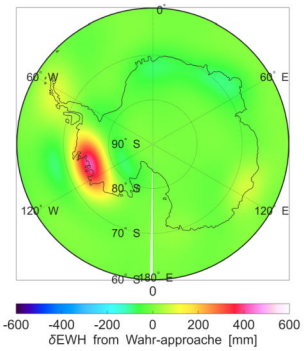

(c) May, 2005

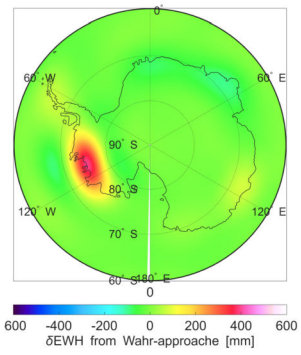

(d) May, 2006

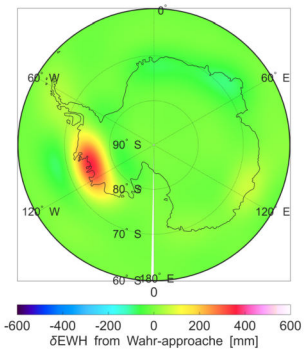

(e) May, 2007

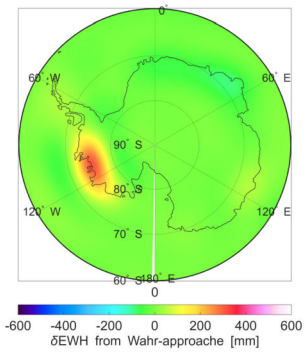

(f) May, 2008

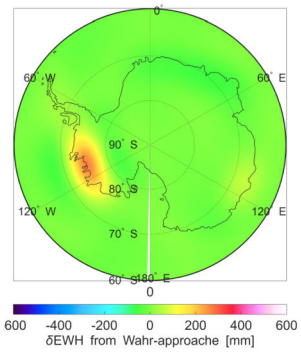

(g) May, 2009

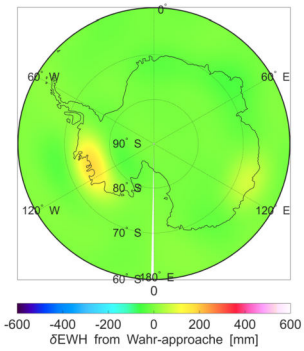

(h) May, 2010

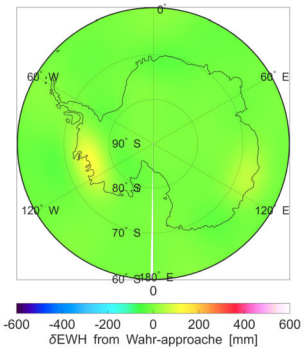

(i) May, 2011

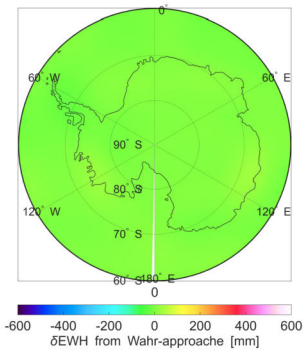

(j) May,2012

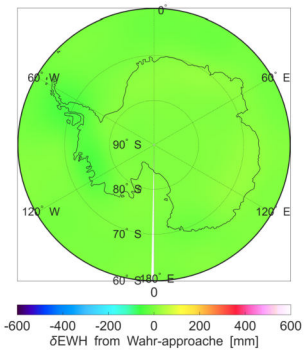

(k) May, 2013

(l) May, 2014

Figure 5.3: TWS in May from 2003 – 2014, DDK2.

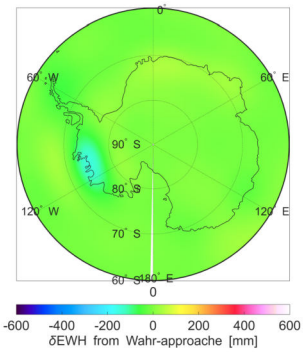

(a) May,2015

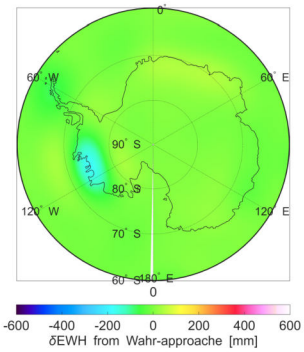

(b) May, 2016

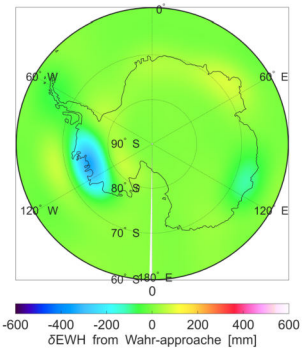

(c) May, 2017

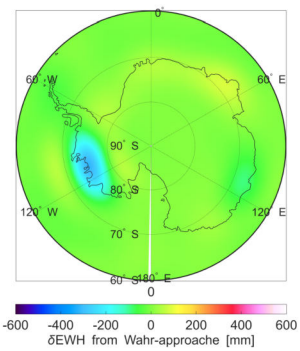

(d) May,2018

(e) May, 2019

(f) May, 2020

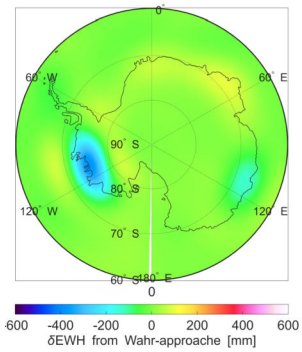

(g) May, 2021

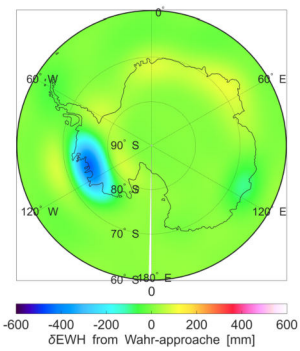

(h) May, 2022

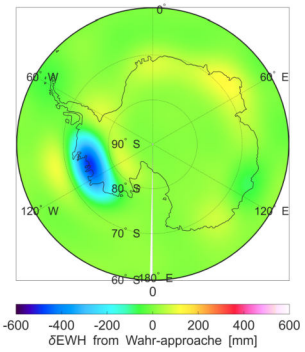

(i) May, 2023

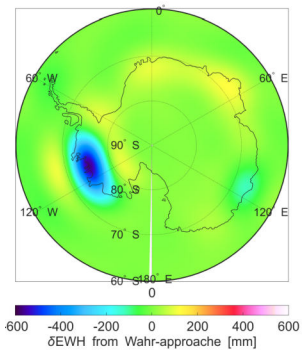

(j) May, 2024

Figure 5.4: TWS in May from 2015 – 2024, DDK2.

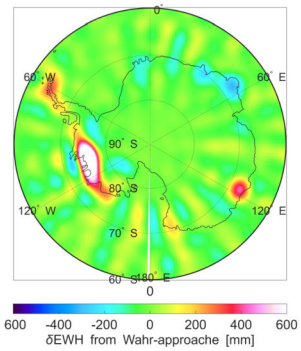

(a) May, 2003

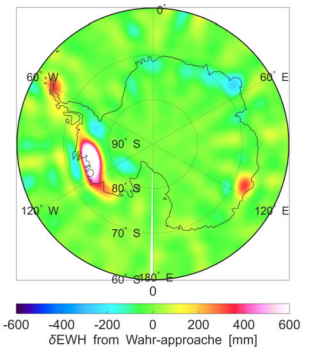

(b) May, 2004

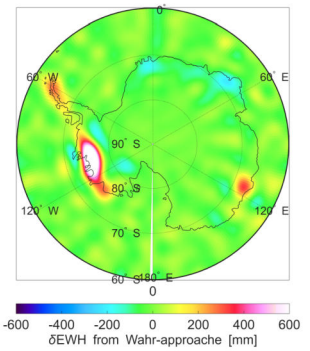

(c) May, 2005

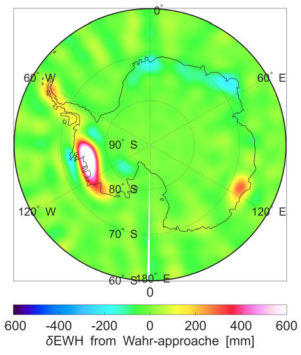

(d) May, 2006

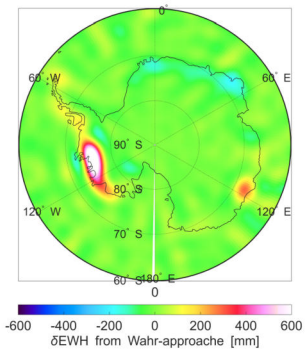

(e) May, 2007

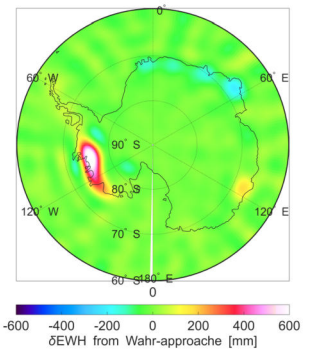

(f) May, 2008

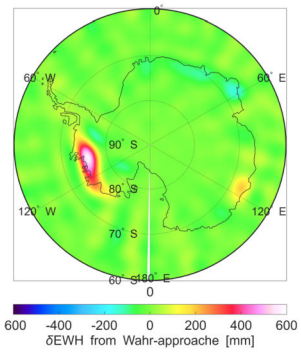

(g) May, 2009

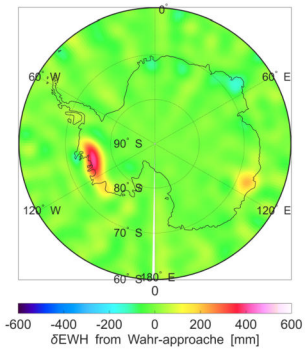

(h) May, 2010

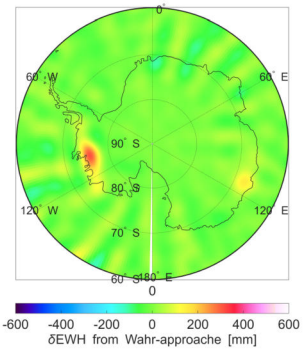

(i) May, 2011

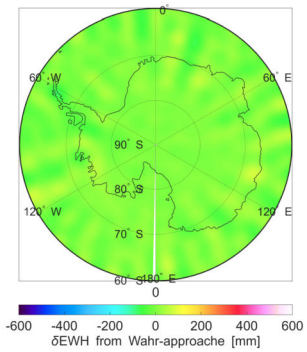

(j) May,2012

(k) May, 2013

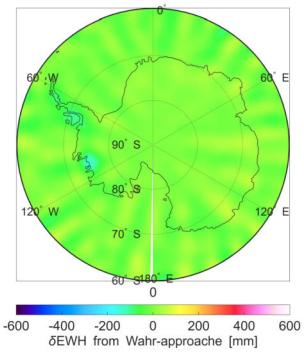

(l) May, 2014

Figure 5.5: TWS in May from 2003 – 2014, DDK8.

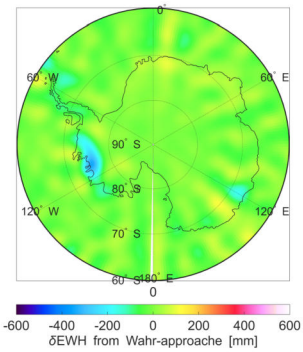

(a) May,2015

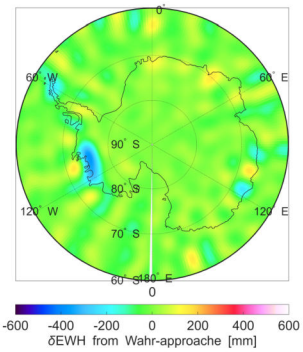

(b) May, 2016

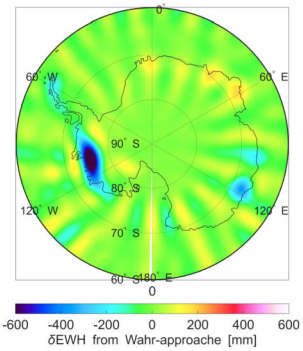

(c) May, 2017

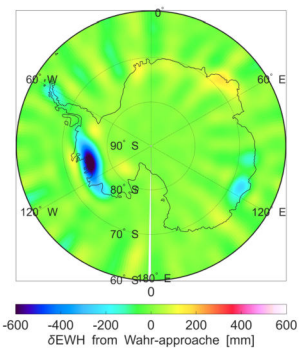

(d) May,2018

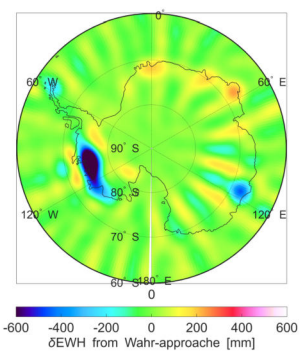

(e) May, 2019

(f) May, 2020

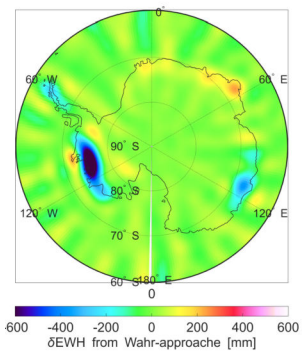

(g) May, 2021

(h) May, 2022

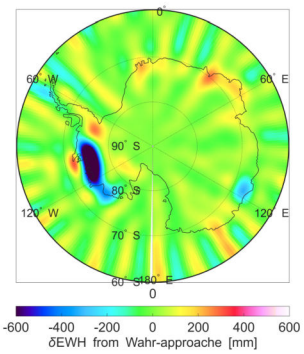

(i) May, 2023

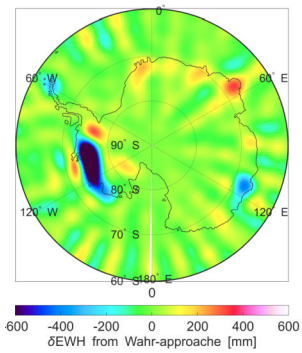

(j) May, 2024

Figure 5.6: TWS in May from 2015 - 2024, DDK8.

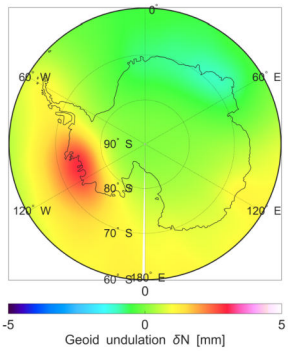

(a) May, 2003

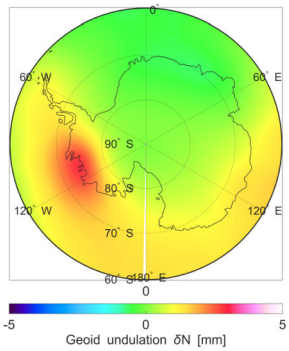

(b) May, 2004

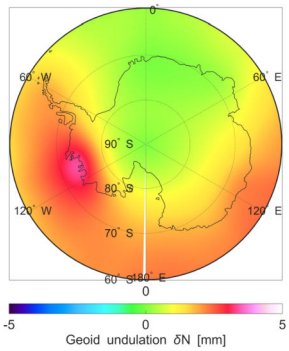

(c) May, 2005

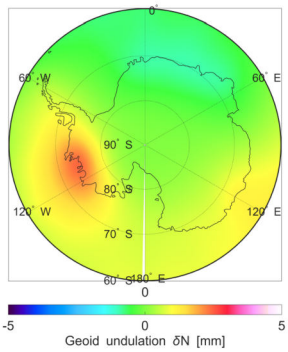

(d) May, 2006

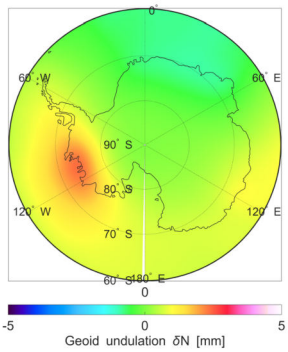

(e) May, 2007

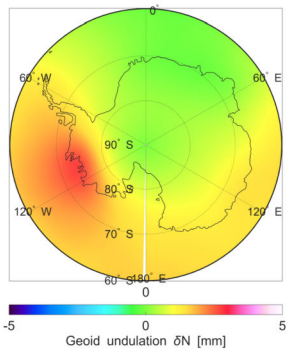

(f) May, 2008

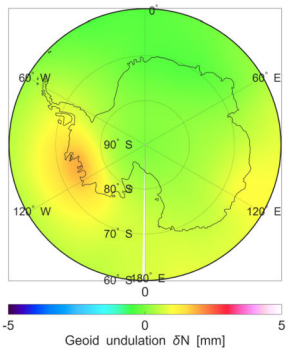

(g) May, 2009

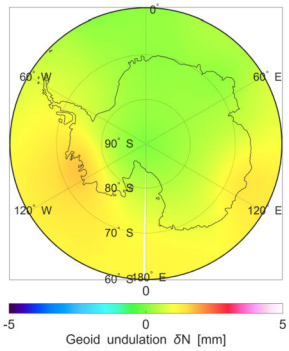

(h) May, 2010

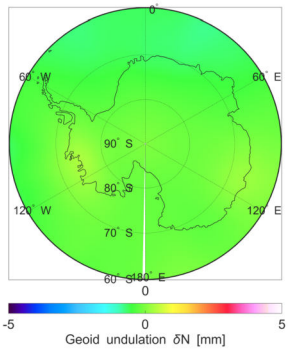

(i) May, 2011

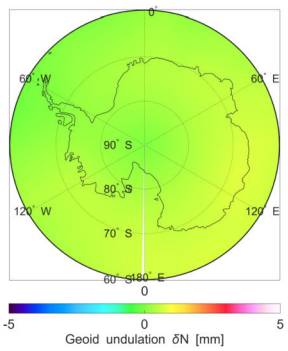

(k) May, 2013

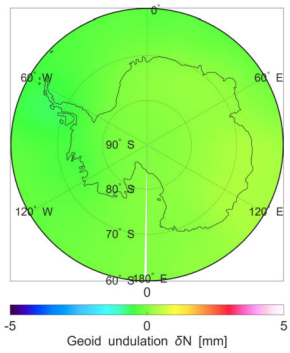

(l) May, 2014

Figure 5.7: Geoid Undulation Variation in May from 2003 – 2014, DDK2.

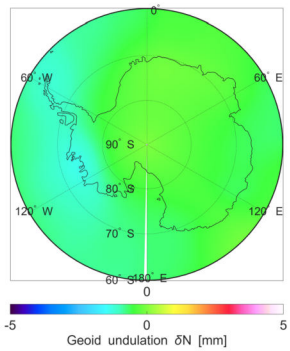

(a) May, 2015

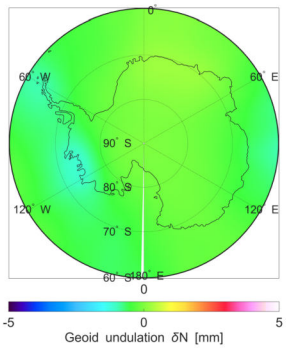

(b) May, 2016

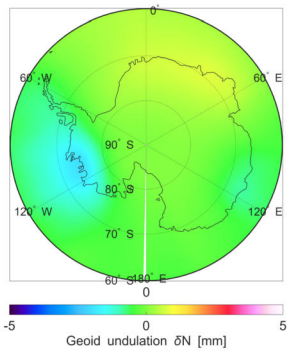

(c) May, 2017

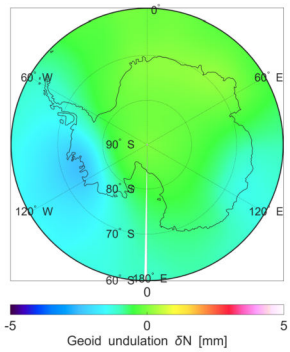

(d) May, 2018

(e) May, 2019

(f) May 2020

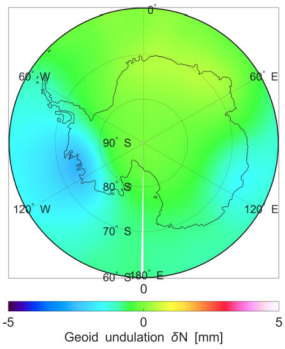

(g) May, 2021

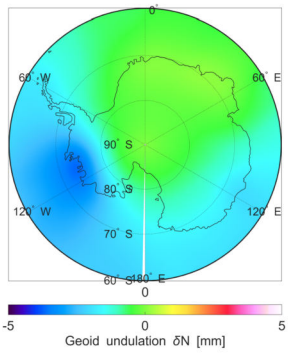

(h) May, 2022

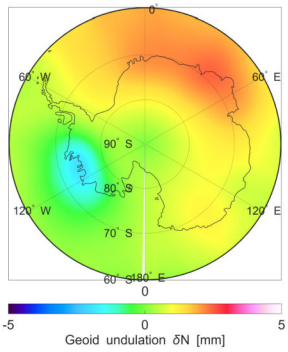

(i) May, 2023

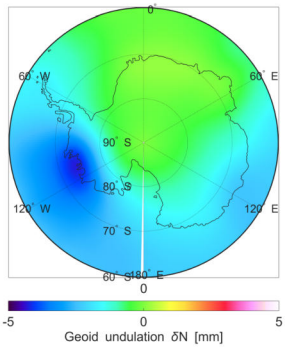

(j) May, 2024

Figure 5.8: Geoid Undulation Variation in May from 2015 - 2024, DDK2.

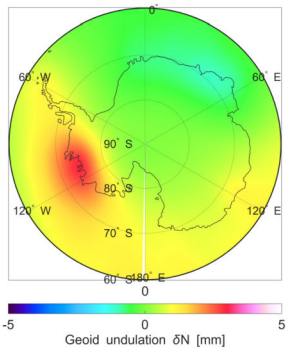

(a) May, 2003

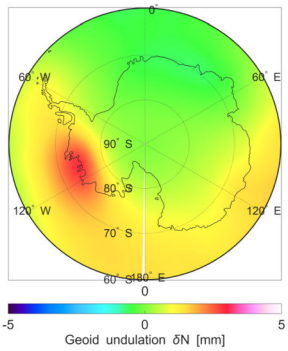

(b) May, 2004

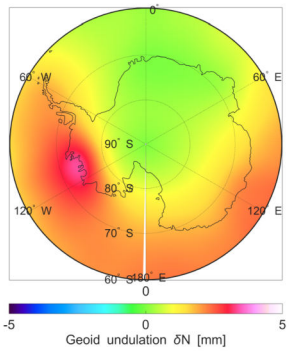

(c) May, 2005

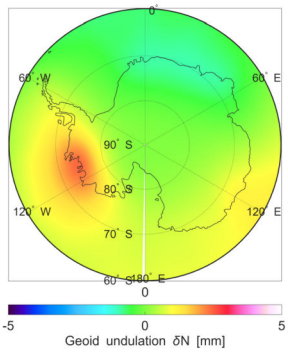

(d) May, 2006

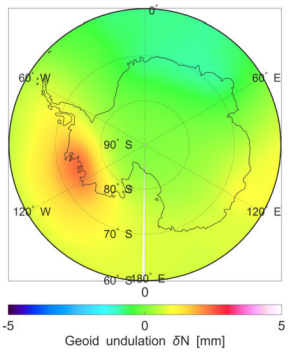

(e) May, 2007

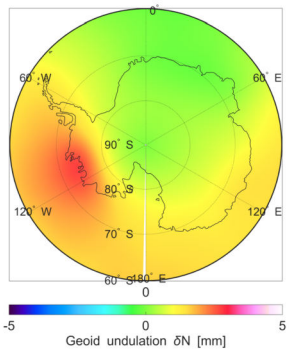

(f) May, 2008

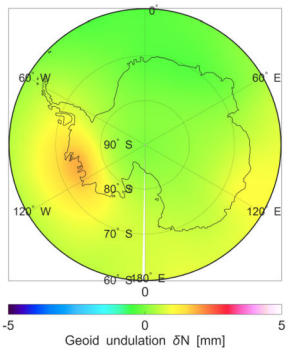

(g) May, 2009

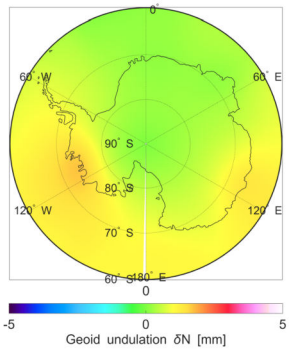

(h) May, 2010

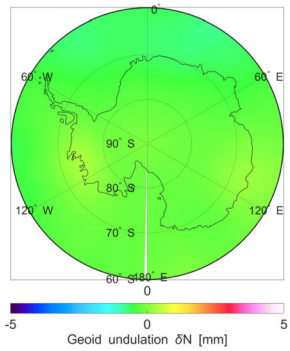

(i) May, 2011

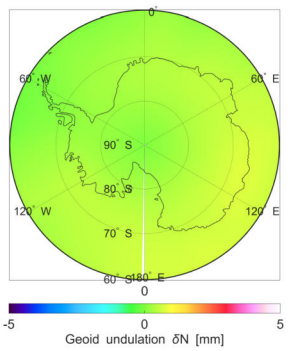

(j) May, 2012

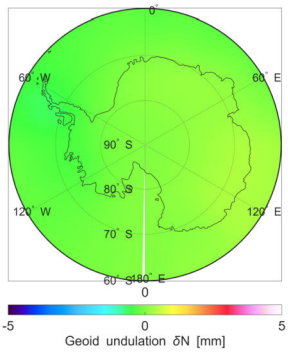

(k) May, 2013

(l) May, 2014

Figure 5.9: Geoid Undulation Variation in May from 2003 – 2014, DDK8.

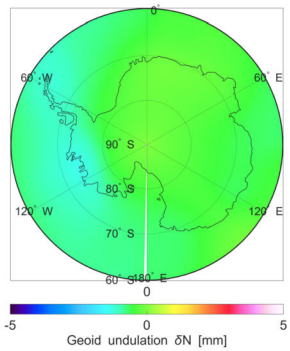

(a) May, 2015

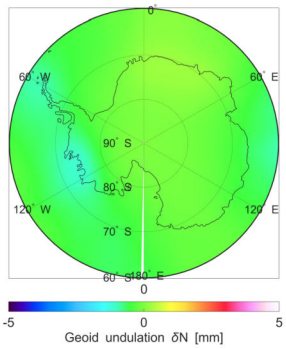

(b) May, 2016

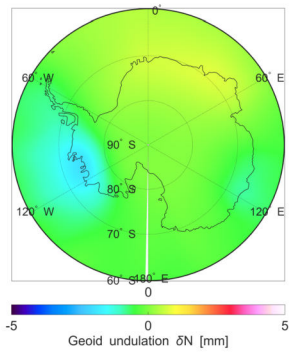

(c) May, 2017

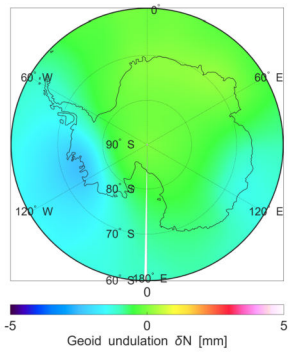

(d) May, 2018

(e) May, 2019

(f) May 2020

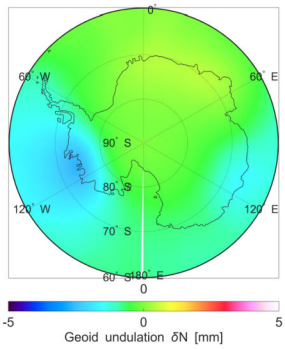

(g) May, 2021

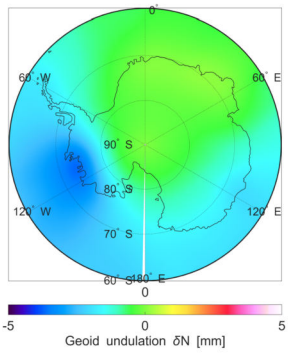

(h) May, 2022

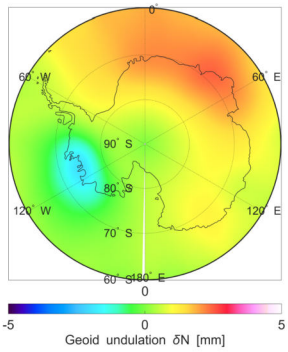

(i) May, 2023

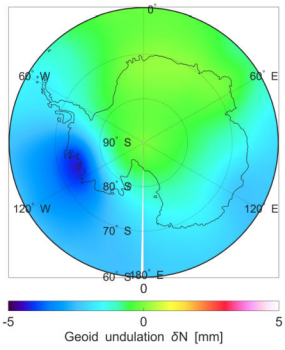

(j) May, 2024

Figure 5.10: Geoid Undulation Variation in May from 2015 – 2024, DDK8.

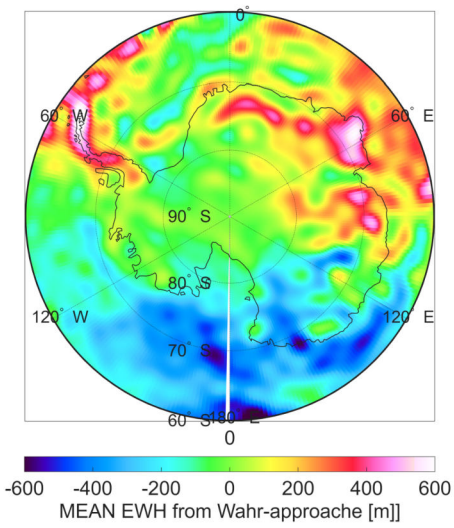

(a) Mean TWS DDK2

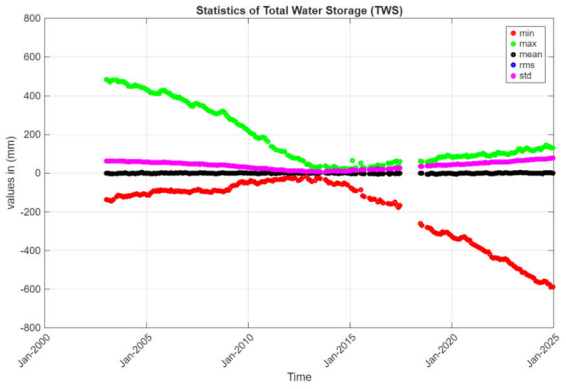

(b) Statistics TWS DDK2 (Range is ±800mm).

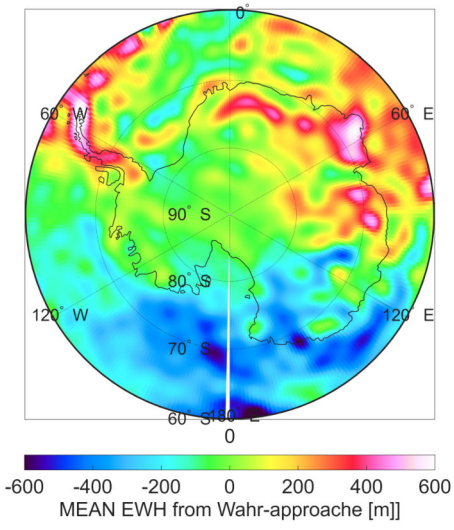

(c) Mean TWS DDK8

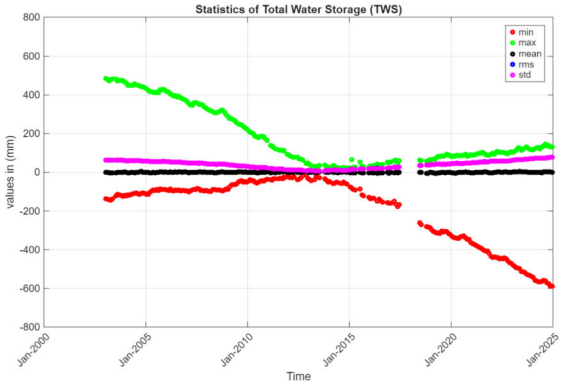

(d) Statistics TWS DDK8 (Range is ±800mm).

Figure 5.11: Mean TWS in space domain and Statistics DDK2 and DDK8.

6 Conclusion and Outlook

In this study, terrestrial water storage (TWS) variations over Antarctica were analysed using GRACE and GRACE-FO satellite gravimetry data. The GRACE Level-2 spherical harmonic coefficients were processed through spherical harmonic synthesis and transformed into Equivalent Water Height (EWH) using the Wahr formulation, enabling the assessment of large-scale mass redistribution associated with hydrological processes.

The results revealed significant spatial and temporal changes in Antarctic mass balance, with the strongest anomalies consistently occurring in West Antarctica. During the early years (2003–2010), positive TWS anomalies were dominant in parts of West Antarctica, whereas a transition toward increasingly negative anomalies became evident after 2015, indicating enhanced ice mass loss. The interannual analysis of May observations showed a gradual strengthening and expansion of negative TWS signals, particularly between 2018 and 2024. Geoid undulation maps exhibited patterns consistent with the TWS variations, confirming the relationship between gravity field changes and ice mass redistribution. The statistical analysis further demonstrated a long-term decline in Antarctic

water storage, with minimum values becoming increasingly negative toward the end of the study period. Results obtained from both DDK2 and DDK8 filters showed similar large-scale trends, while DDK8 retained more spatial detail at the expense of increased residual noise. Overall, the study confirms a persistent loss of Antarctic ice mass over the last two decades and highlights the capability of GRACE observations to monitor large-scale cryospheric changes and their implications for global sea-level rise.

Overall, GRACE and GRACE-FO observations provide a robust framework for monitoring Antarctic ice mass changes and offer valuable insights into the long-term evolution of the Antarctic Ice Sheet and its contribution to global sea-level rise.

Acknowledgement

The author wishes to extend his sincere gratitude to Prof. Kurt Seitz for his continuous guidance, insightful explanations, and valuable support throughout this lab rotation, as well as for his time and regular discussions, which significantly contributed to the successful completion of this work. The author acknowledges the support from Geodätisches Institut (GIK) for providing necessary resources and facilities. Additionally, the author acknowledges (ICGEM, 2026) for providing GRACE data used in this study.

References

Bell, R. E. and Seroussi, H. (2020): History, mass loss, structure, and dynamic behavior of the Antarctic Ice Sheet. *Science* 367(6484):1321–1325.

Chen, J., Wilson, C., Tapley, B., Blankenship, D., and Young, D. (2008): Antarctic regional ice loss rates from GRACE. *Earth and Planetary Science Letters* 266(1–2):140–148.

Heiskanen, W. A. and Moritz, H. (1967): Physical Geodesy. W. H. Freeman & Co., San Francisco, USA.

Humphrey, V., Rodell, M., and Eicker, A. (2023): Using satellite-based terrestrial water storage data: A review. *Surveys in Geophysics* 44(5):1489–1517. DOI: 10.1007/s10712-022-09754-9.

ICGEM (2026): International Centre for Global Earth Models (ICGEM): Gravity field and GRACE/GRACE-FO products hosted at the German Research Centre for Geosciences (GFZ). Accessed: 2026-04-06. URL: https://icgem.gfz-potsdam.de/.

Rignot, E. (2006): Changes in ice dynamics and mass balance of the Antarctic ice sheet. *Philosophical Transactions of the Royal Society A: Mathematical, Physical and Engineering Sciences* 364(1844):1637–1655.

Rignot, E., Bamber, J. L., Van Den Broeke, M. R., Davis, C., Li, Y., Van De Berg, W. J., and Van Meijgaard, E. (2008): Recent Antarctic ice mass loss from radar interferometry and regional climate modelling. *Nature geoscience* 1(2):106–110.

Tsoulis, D. (1999): Spherical harmonic computations with topographic/isostatic coefficients. Tech. rep. IAPG/FESG No. 3. Munich, Germany: Institut für Astronomische und Physikalische Geodäsie, Technische Universität München.

Velicogna, I. (2009): Increasing rates of ice mass loss from the Greenland and Antarctic ice sheets revealed by GRACE. *Geophysical Research Letters* 36(19). DOI: 10.1029/2009GL040222.

Velicogna, I., Mohajerani, Y., A, G., Landerer, F., Mouginot, J., Noel, B., Rignot, E., Sutterley, T., van den Broeke, M., van Wessem, M., et al. (2020): Continuity of ice sheet mass loss in Greenland and Antarctica from the GRACE and GRACE follow-on missions. *Geophysical Research Letters* 47(8):e2020GL087291. DOI: 10.1029/2020GL087291.

Wahr, J., Molenaar, M., and Bryan, F. (1998): Time variability of the Earth's gravity field: Hydrological and oceanic effects and their possible detection using GRACE. *Journal of Geophysical Research: Solid Earth* 103(B12):30205–30229.

How does the Variation of the Total Water Storage affect the Earth's Center of Mass

Jacob Sebastian[1]

1 Remote Sensing and Geoinformatics Master of Science (M.Sc.), KIT, Germany
E-Mail: uqrgk@student.kit.edu

Abstract

This study evaluates temporal changes in the Earth's gravity field using level-2 GRACE data from CSR, processed with the DDK 5 filter. The approach enables assessment of mass variations and analysis of the Earth's Center of Mass (COM) via monthly GRACE-derived spherical harmonic coefficients. Results show no notable temporal variations in the COM over the study period, a stability attributed to preprocessed, calibrated, and corrected gravity field solutions provided by ICGEM, with monthly updates by GFZ. These Level-2 products incorporate background atmospheric and oceanic mass variations, tidal influences, and instrument error corrections, effectively reducing significant geocenter shifts in the dataset. While the global COM remains nearly constant, regional mass redistributions are evident in Greenland, Antarctica, and major continental basins, reflecting processes such as ice-sheet melt, groundwater depletion, and seasonal hydrological storage changes. These regional variations balance globally, maintaining a stable total COM position while capturing dynamic mass redistribution within the Earth system. A prospective research direction involves examining degree-one spherical harmonic coefficients from GRACE-based solutions and comparing them with independent time series from Satellite Laser Ranging (SLR), e.g., via the GRACE/GRACE-FO geocenter data portal. Such comparisons would validate GRACE-derived COM estimates and enhance understanding of the consistency between satellite gravimetry and SLR-based geocenter assessments, offering a potential focus for future lab rotation.

Keywords GRACE · Total Water Storage (TWS) · Tesseroid · Center of Mass (COM)

KIT Scientific Working Papers
Issue Number 270
ISSN: 2194-1629
DOI: 10.5445/IR/1000191188
Online: June 2026

This document is licensed under the Creative Commons Attribution – Share Alike 4.0 International License (CC BY-SA 4.0):
https://creativecommons.org/licenses/by-sa/4.0/deed.en

1 Introduction

The center of mass of the Earth (COM) is a crucial geophysical aspect that plays an important role in geophysics. It is the weighted average location of mass of the Earth. Since the Earth is a non-homogeneous, non-symmetrical physical element, unlike a sphere, its center of mass does not lie in the geometric center. Changes in mass distribution, non-uniform density distribution of its elements etc causes this shift. One of the factors that contributes to the location of Earth's center of mass is the change in the mass distribution of the total water storage of the Earth. Melting of ice, sea level rise, repositioning of ground aquifers, changes in soil moisture, etc affects the position of COM.
The objective of this research is to utilize the monthly solutions of Earth's gravity potential from GRACE satellite mission to calculate the monthly changes in Earth's total water storage. A time series graph between the change in TWS and COM of Earth is then plotted, which shows the output of the approach. The GRACE satellite mission has been used extensively to detect changes in terrestrial total water storage (TWS) and their contribution to mass redistribution (Schmidt et al., 2006).

2 Theoretical Aspects

Equations for gravity field of the Earth, total water storage are used for calculations. The terms associated with each equation are explained.

2.1 Gravity field of the Earth

The gravity field of the Earth describes how the force of gravity changes in strength and direction at different places on and around the Earth. The gravity potential consists of the sum of the gravitational potential V and the centrifugal potential Z:

$$W(r,\varphi,\lambda) = V(r,\varphi,\lambda) + Z(r,\varphi)\,. \tag{2.1}$$

The gravitational potential $V(P)$ at a point $P(r,\varphi,\lambda)$ outside the masses can be expressed from the spherical harmonic harmonic coefficients from GRACE Level-2 products as

$$V(P) = \frac{GM}{r}\sum_{\ell=0}^{L_{max}}\left(\frac{R}{r}\right)^{\ell}\sum_{m=0}^{\ell}\left(\bar{C}_{\ell m}\,\cos m\lambda + \bar{S}_{\ell m}\,\sin m\lambda\right)\bar{P}_{\ell m}(\sin\varphi)\,, \tag{2.2}$$

where,

GM	:	Geocentric gravitational constant
R	:	Earth's mean equatorial radius
r	:	Radial distance from the origin of the coordinate system
φ	:	Geocentric Latitude
λ	:	Geocentric Longitude
ℓ, m	:	Degree and order of the spherical harmonics
L_{max}	:	Maximum degree of expansion. In this study $2 \leq m \leq \ell \leq L_{max} = 96$ holds.
$\bar{C}_{\ell m}, \bar{S}_{\ell m}$	:	Fully normalised spherical harmonic coefficients of degree ℓ and order m
$\bar{P}_{\ell m}$	:	Fully normalised Legendre functions of degree ℓ and order m.

2.2 Total Water Storage

The total water storage (TWS) measured from GRACE is the sum of total amount of water stored on and below the surface of the Earth including surface water like lakes and rivers, snow and ice, soil moisture and water inside vegetation (Humphrey et al., 2023). The change in TWS can be estimated from the equation of surface mass

anomaly derived from GRACE data. Following the derivations in Heck and Seitz (2007) and Wahr et al. (1998), the surface mass density anomaly can be represented as

$$\Delta\sigma(\varphi,\lambda) = \frac{R}{3}\rho_{\mathrm{E}} \sum_{\ell=0}^{\infty}\sum_{m=0}^{\ell} \frac{2\ell+1}{1+k_\ell} \left(\Delta\bar{C}_{\ell m}\ \cos m\lambda + \Delta\bar{S}_{\ell m}\ \sin m\lambda\right) \bar{P}_{\ell m}(\sin\varphi)\,, \tag{2.3}$$

where,

$\Delta\sigma(\varphi,\lambda)$	:	Surface mass density anomaly at latitude φ and longitude λ. Units are in (kg/m^2)
ρ_E	:	Mean density of the Earth
k_ℓ	:	The load Love number of degree ℓ describes the Earth's elastic response
$\Delta\bar{C}_{\ell m}, \Delta\bar{S}_{\ell m}$	:	GRACE-derived spherical harmonic coefficients for mass change relative to a defined mean model (Compare Equation (4.1)).

Dividing Equation (2.3) by the density of water gives the equivalent water height (EWH)

$$\Delta h(\varphi,\lambda) = \frac{\Delta\sigma(\varphi,\lambda)}{\rho_w}\,, \tag{2.4}$$

where,

$\Delta h(\varphi,\lambda)$	:	Equivalent Water Height (EWH)
ρ_w	:	Denotes the constant density of water

2.3 Effect of mass on Earth surface

The geoid undulation N, that is the ellipsoidal height of the geoid above the reference ellipsoid, can be mathematically expressed from Heiskanen and Moritz (1967) as

$$N(\varphi,\lambda) = R\sum_{l=0}^{\infty}\sum_{m=0}^{\ell} \left(\bar{C}_{\ell m}\ \cos m\lambda + \bar{S}_{\ell m}\ \sin m\lambda\right) \bar{P}_{\ell m}(\sin\varphi)\,, \tag{2.5}$$

where,

$N(\varphi,\lambda)$	:	Geoid Undulation.

Let the monthly change in potential undulation be represented as ΔN.
Therefore,

$$\Delta N(\varphi,\lambda) = R\sum_{l=0}^{\infty}\sum_{m=0}^{\ell} \left(\Delta\bar{C}_{\ell m}\ \cos m\lambda + \Delta\bar{S}_{\ell m}\ \sin m\lambda\right) \bar{P}_{\ell m}(\sin\varphi)\,. \tag{2.6}$$

Let $\Delta\rho(r,\varphi,\lambda)$ be the density redistribution caused by the effect of TWS on the surface of radius R,

$$\left\{\begin{array}{c}\Delta\bar{C}_{\ell m}\\ \Delta\bar{S}_{\ell m}\end{array}\right\} = \frac{3}{4\pi R\rho_E(2\ell+1)} \int \Delta\rho(r,\varphi,\lambda)\,\bar{P}_{\ell m}(\sin\varphi) \left(\frac{r}{R}\right)^{\ell+2} \left\{\begin{array}{c}\cos m\lambda\\ \sin m\lambda\end{array}\right\} \cos\varphi\, d\varphi\, d\lambda\, dr\,, \tag{2.7}$$

where,

ρ_E	:	Average density of the Earth ($= 5517\,\mathrm{kg/m^3}$).

Let us assume $\Delta\sigma$ is concentrated on a thin layer of thickness H on the surface of the Earth,
So we define change in surface density $\Delta\rho$ as

$$\Delta\sigma(\varphi,\lambda) = \int_0^H \Delta\rho(r,\varphi,\lambda)\, dr\,. \tag{2.8}$$

When H is sufficiently thin, the term $\left(\frac{r}{R}\right)^{\ell+2}$ can be assumed as 1.
So the equation can be rewritten as

$$\left\{ \begin{array}{c} \Delta\bar{C}_{\ell m} \\ \Delta\bar{S}_{\ell m} \end{array} \right\}_{\text{surf mass}} = \frac{3}{4\pi R\rho_E(2\ell+1)} \int \Delta\sigma(\varphi,\lambda)\,\bar{P}_{\ell m}(\sin\varphi) \left\{ \begin{array}{c} \cos m\lambda \\ \sin m\lambda \end{array} \right\} \cos\varphi\, d\varphi\, d\lambda\,. \tag{2.9}$$

This equation describes the contribution to the geoid from the direct gravitational attraction of the surface mass. That surface mass also loads and deforms the underlying solid Earth crust, which causes an additional geoid contribution:

$$\left\{ \begin{array}{c} \Delta\bar{C}_{\ell m} \\ \Delta\bar{S}_{\ell m} \end{array} \right\}_{\text{solid E}} = \frac{3k_\ell}{4\pi R\rho_E(2\ell+1)} \int \Delta\sigma(\varphi,\lambda)\,\bar{P}_{\ell m}(\sin\varphi) \left\{ \begin{array}{c} \cos m\lambda \\ \sin m\lambda \end{array} \right\} \cos\varphi\, d\varphi\, d\lambda\,, \tag{2.10}$$

where,

k_ℓ : Denotes the load Love number of degree ℓ.

The total geoid change can be represented as

$$\left\{ \begin{array}{c} \Delta\bar{C}_{\ell m} \\ \Delta\bar{S}_{\ell m} \end{array} \right\} = \left\{ \begin{array}{c} \Delta\bar{C}_{\ell m} \\ \Delta\bar{S}_{\ell m} \end{array} \right\}_{\text{surf mass}} + \left\{ \begin{array}{c} \Delta\bar{C}_{\ell m} \\ \Delta\bar{S}_{\ell m} \end{array} \right\}_{\text{solid E}}\,. \tag{2.11}$$

To summarize these results for $\Delta\bar{C}_{\ell m}$ and $\Delta\bar{S}_{\ell m}$ in a more compact form, we expand $\Delta\sigma$ as

$$\Delta\sigma(\varphi,\lambda) = R\rho_w \sum_{\ell=0}^{\infty}\sum_{m=0}^{\ell} \left(\Delta\bar{C}_{\ell m}\ \cos m\lambda + \Delta\bar{S}_{\ell m}\ \sin m\lambda\right) \bar{P}_{\ell m}(\sin\varphi)\,. \tag{2.12}$$

From this equation we can conclude that that the coefficients representing the TWS in surface spherical harmonics are given by:

$$\left\{ \begin{array}{c} \Delta\hat{C}_{\ell m} \\ \Delta\hat{S}_{\ell m} \end{array} \right\} = \frac{1}{4\pi R\rho_w} \int_0^{2\pi} d\lambda \int_0^{\pi} \cos\varphi\, d\varphi\, \Delta\sigma(\varphi,\lambda)\,\bar{P}_{\ell m}(\sin\varphi) \left\{ \begin{array}{c} \cos m\lambda \\ \sin m\lambda \end{array} \right\} \tag{2.13}$$

From the above equations we find a simple relation between $\Delta\bar{C}_{\ell m}$, $\Delta\bar{S}_{\ell m}$ and $\Delta\hat{C}_{\ell m}$, $\Delta\hat{S}_{\ell m}$:

$$\left\{ \begin{array}{c} \Delta\bar{C}_{\ell m} \\ \Delta\bar{S}_{\ell m} \end{array} \right\} = \frac{3\rho_w}{\rho_E} \frac{1+k_\ell}{2\ell+1} \left\{ \begin{array}{c} \Delta\hat{C}_{\ell m} \\ \Delta\hat{S}_{\ell m} \end{array} \right\}, \tag{2.14}$$

$$\left\{ \begin{array}{c} \Delta\hat{C}_{\ell m} \\ \Delta\hat{S}_{\ell m} \end{array} \right\} = \frac{\rho_E}{3\rho_w} \frac{2\ell+1}{1+k_\ell} \left\{ \begin{array}{c} \Delta\bar{C}_{\ell m} \\ \Delta\bar{S}_{\ell m} \end{array} \right\}. \tag{2.15}$$

Inserting Equation (2.15) into the Equation (2.12) for the surface density, to following relation holds:

$$\Delta\sigma(\varphi,\lambda) = \frac{R\rho_E}{3} \sum_{l=0}^{\infty}\sum_{m=0}^{\ell} \frac{2\ell+1}{1+k_\ell} \left(\Delta\bar{C}_{\ell m}\ \cos m\lambda + \Delta\bar{S}_{\ell m}\ \sin m\lambda\right) \bar{P}_{\ell m}(\sin\varphi)\,, \tag{2.16}$$

which can be used to find the change in surface mass density from changes $\Delta\bar{C}_{\ell m}$ and $\Delta\bar{S}_{\ell m}$ in the geoid coefficients.

$$\Delta N(\varphi,\lambda) = \frac{3a\rho_w}{\rho_E} \sum_{\ell=0}^{\infty}\sum_{m=0}^{\ell} \frac{1+k_\ell}{2\ell+1} \left(\Delta\hat{C}_{\ell m}\cos m\lambda + \Delta\hat{S}_{\ell m}\sin m\lambda\right) \bar{P}_{\ell m}(\sin\varphi)\,. \tag{2.17}$$

The given derivations in this Section follows closely Wahr et al. (1998).

2.4 Calculation of the Center Of Mass

The spherical coordinates of each monthly TWS represented as a tesseroid can be converted into cartesian coordinates using the standard geodetic formulas from Grombein et al. 2013

$$\begin{aligned} x &= r\cos\varphi\cos\lambda \\ y &= r\cos\varphi\sin\lambda \\ z &= r\sin\varphi\,. \end{aligned} \tag{2.18}$$

The mass of a single tesseroid on the global grid is denoted by m_{ij}.
The total TWS mass is obtained by summing the mass contributions m_{ij} from each individual tesseroid cell:

$$M_{\mathrm{TWS}} = \sum_{i=1}^{I}\sum_{j=1}^{J} m_{ij}\,. \tag{2.19}$$

The indices i and j represent the global tesseroid grid coordinates in latitude and longitude, respectively. The summation limits span from $i = 1$ to $I = 180$ for latitude and from $j = 1$ to $J = 360$ for longitude, corresponding to a global grid with a $1^\circ \times 1^\circ$ resolution (consisting of 180 latitude bands and 360 longitude bands).
The coordinates of center of mass $M = M_E + M_{\mathrm{TWS}}$ can be formulated by the equations from Wahr et al. (1998) where M_E is the mass of the Earth:

$$\begin{aligned} x_0 &= \frac{1}{M}\left[M_E + \sum_{i=1}^{I}\sum_{j=1}^{J} m_{ij}x_{ij}\right] \\ y_0 &= \frac{1}{M}\left[M_E + \sum_{i=1}^{I}\sum_{j=1}^{J} m_{ij}y_{ij}\right] \\ z_0 &= \frac{1}{M}\left[M_E + \sum_{i=1}^{I}\sum_{j=1}^{J} m_{ij}z_{ij}\right]\,. \end{aligned} \tag{2.20}$$

3 Data

The Level-2 data used in this study is the monthly solutions from GRACE mission. It includes fully normalized spherical harmonic coefficients that assist in the computation of gravitational potential of the Earth, generated by release 6 of CSR (Center for Space Research at The University of Texas at Austin) provided by ICGEM (2026).

4 Methodology

4.1 Data and Reference Frame

The spherical-harmonic GRACE gravity field solutions $(\bar{C}_{\ell m}, \bar{S}_{\ell m})$ from CSR (ICGEM, 2026) are utilised on a monthly basis. These are filtered using a decorrelation filter (e.g., DDK 5) and rescaled to a common gravitational constant GM and reference radius R (GRS80). In order to eliminate the monopole and degree-1 (geocenter) terms, which GRACE cannot directly detect, the working bandwidth begins at degree $n \geq 2$ (Koch, 1999). For synthesis, a $1^\circ \times 1^\circ$ global grid is employed.

4.2 Monthly Gravity Residuals

Let C_{lm} and S_{lm} denote the multi-year mean coefficients over the study period. For each month t:

$$\Delta C_{lm}(t) = C_{lm}(t) - \bar{C}_{lm}, \qquad \Delta S_{lm}(t) = S_{lm}(t) - \bar{S}_{lm}. \tag{4.1}$$

These residuals isolate the time-variable gravity signal associated with mass redistribution (e.g., terrestrial water storage, TWS). A fixed reference (GM, R) is applied to all months.

4.3 Conversion of Gravity Residuals to Surface Mass (TWS)

The residual coefficients $\{\Delta C_{lm}, \Delta S_{lm}\}$ are converted to equivalent water storage (TWS) using degree-dependent load Love number scaling factors S_l that account for Earth's elastic response:

$$\widehat{\Delta\sigma}_{lm}(t) = S_l \, \widehat{\Delta g}_{lm}(t) \tag{4.2}$$

and the spherical-harmonic synthesis:

$$\Delta\sigma(\varphi, \lambda, t) = \sum_{l=0}^{n_{\max}} \sum_{m=-l}^{l} \widehat{\Delta\sigma}_{lm}(t) \, Y_{lm}(\varphi, \lambda), \tag{4.3}$$

where $\Delta\sigma$ is surface mass change (typically expressed as equivalent water height, EWH), and Y_{lm} are the SH basis functions. Each degree is multiplied by the factor S_l derived from load Love numbers, and then synthesized on a 1° grid.

4.4 Computation of Monthly COM Displacement

Treating the monthly surface load $\Delta\sigma(\varphi, \lambda, t)$ on a sphere of radius R, the incremental shift of Earth's total center of mass (relative to the solid Earth) is obtained by first moments of mass change:

$$\begin{aligned}
\Delta X(t) &= \frac{R^3}{M_{\mathrm{E}}} \iint \Delta\sigma(\varphi, \lambda, t) \cos\varphi \cos\lambda \, \mathrm{d}\Omega, \\
\Delta Y(t) &= \frac{R^3}{M_{\mathrm{E}}} \iint \Delta\sigma(\varphi, \lambda, t) \cos\varphi \sin\lambda \, \mathrm{d}\Omega, \\
\Delta Z(t) &= \frac{R^3}{M_{\mathrm{E}}} \iint \Delta\sigma(\varphi, \lambda, t) \sin\varphi \, \mathrm{d}\Omega,
\end{aligned} \tag{4.4}$$

where M_{E} is Earth's total mass and $\mathrm{d}\Omega = \cos\varphi \, \mathrm{d}\varphi \, \mathrm{d}\lambda$. Numerically, these integrals are evaluated as area-weighted sums over the 1° grid to yield monthly COM components $(\Delta X, \Delta Y, \Delta Z)$. The total water mass anomaly $M_{\mathrm{TWS}}(t)$ is also computed as:

$$M_{\mathrm{TWS}}(t) = R^2 \iint \Delta\sigma(\varphi, \lambda, t) \, \mathrm{d}\Omega. \tag{4.5}$$

4.5 Auxiliary Fields and Diagnostics

Additional synthesized quantities comprise:

- The disturbing potential and geoid undulation, which are calculated from residual SHs; the undulation is derived by dividing the disturbing potential by the normal gravity γ (see Moritz (1980)).
- Maps of uncertainty generated through variance propagation from the uncertainties of the coefficients to the grid space.
- Degree variance spectra used to evaluate the characteristics of signal versus noise following filtering.

4.6 Filtering and Error Handling

The DDK filter DDK5 is utilized to minimize correlated errors and longitudinal stripes. Filtered coefficients undergo mean-field construction, differencing, load Love number scaling, and synthesis in a consistent manner. Monthly statistical descriptors (mean, RMS, STD) for TWS and COM are calculated.

4.7 Outputs

The main outputs are:

- Monthly global maps of TWS (EWH),
- Time series of COM displacement: $\Delta X(t), \Delta Y(t), \Delta Z(t)$
- Optional diagnostics: potential, undulation, variance propagation maps, and degree-variance spectra.

4.8 Assumptions and Limitations

The assumptions and limitations in this methodology can be listed according to Humphrey et al. (2023):

- Earth is modeled as a linear elastic body using load Love numbers.
- Signal leakage and signal attenuation even after applying DDK filter is neglected.
- Ocean model errors and weather errors are not taken into account.

4.9 Example Application: Greenland Ice Mass Loss

To demonstrate the implementation of the above methodology prior to applying it to the global terrestrial water storage (TWS) fields, a test case was performed for the Greenland Ice Sheet. The purpose of this example is to verify the workflow – from spherical-harmonic processing to the computation of the Earth's center of mass (COM) displacement – using a simplified, well-defined surface mass change.

4.9.1 Assumed Mass Change.

A linear mass loss of 200 Gt yr^{-1} (gigatonnes per year) was prescribed over the Greenland region, referred from Smith et al. (2020). This value is representative of typical annual ice mass loss estimates derived from GRACE observations during the early 2000s. In surface density terms, this corresponds approximately to

$$\Delta\sigma_{\text{Greenland}} = \frac{200 \times 10^{12}}{A_{\text{Greenland}}}\ \mathrm{kg\,m^{-2}}, \tag{4.6}$$

where $A_{\text{Greenland}}$ is the area of the Greenland Ice Sheet. This artificial load is then expanded into spherical harmonics and treated identically to the observed GRACE residuals.

4.9.2 Implementation in Code.

The same MATLAB framework that is used for global TWS analysis was applied here. The workflow included:

- defining the spatial mask of Greenland on the $1^\circ \times 1^\circ$ grid,
- converting the prescribed $\Delta\sigma_{\text{Greenland}}$ field into spherical-harmonic coefficients up to degree and order 96,
- synthesizing the corresponding surface potential and TWS grids,
- computing the induced COM shift $(\Delta X, \Delta Y, \Delta Z)$ using

$$\Delta\mathbf{r}_{\text{COM}}(t) = \frac{R^3}{M_{\text{E}}} \iint \Delta\sigma_{\text{Greenland}}(\varphi,\lambda) \begin{bmatrix} \cos\varphi\cos\lambda \\ \cos\varphi\sin\lambda \\ \sin\varphi \end{bmatrix} \mathrm{d}\Omega,$$

  which provides an estimate of the geocenter motion due to Greenland's mass loss.

4.9.3 Results and Plots.

All processing steps – spherical-harmonic synthesis, TWS computation, and COM estimation – were executed within the provided MATLAB script. The plot confirms the expected northward and upward motion of the Earth's center of mass resulting from mass loss in the Northern Hemisphere. This example is used for validation and visualization of the theoretical approach before extending the same methodology to the analysis of global monthly TWS variations and their influence on the Earth's COM.

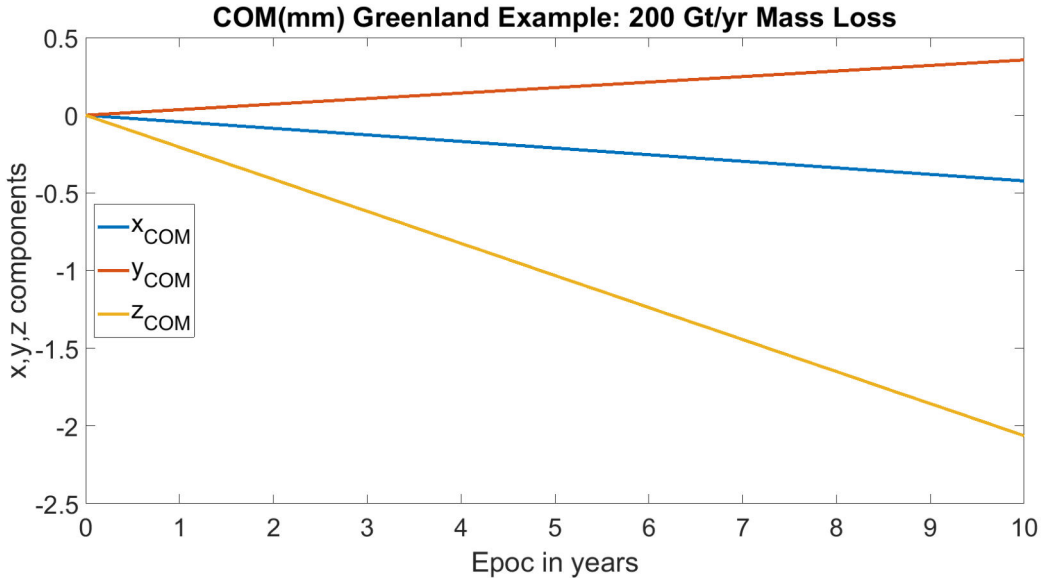

Figure 4.1: Linear variation of Center of Mass due to a linear loss of 200 Gt yr^{-1} ice over Greenland derived from GRACE data.

The Figure 4.1 illustrates the displacement of Earth's Center of Mass (COM) caused by a 200 Gt yr^{-1} mass loss from Greenland over a 10-year period. The COM motion components in the x, y, and z directions, are plotted. The results show that as Greenland loses ice mass, the COM shifts linearly over time, moving slightly in the x direction, positive in y direction and most strongly in negative z-axis) toward the Southern Hemisphere. This southward movement reflects the Earth's physical response to mass removal in the north, demonstrating how polar ice loss influences the planet's overall mass distribution and geocenter position.

5 Results and Discussion

This section contains the results for temporal variations of Potential, Geoid undulation, TWS and COM.

5.1 Temporal Variability of Total Water Storage

The temporal evolution of TWS was examined for the period 2003–2016 using monthly statistics such as minimum, maximum, mean, root-mean-square (RMS), and standard deviation. This allows for the recognition of water storage changes on both seasonal and interannual scales and demonstrates the overarching trend of global mass redistribution over time.

As shown in Figure 5.1, the average TWS curve exhibits a clear annual pattern that corresponds to global hydrological phenomena such as monsoon precipitation, snow formation, and depletion during dry seasons. The degree of variability reflected in the RMS and standard deviation curves indicates significant interannual fluctuations, with local peaks and troughs aligning with global hydrological extremes, such as droughts and floods.

These fluctuations over time underscore the contribution of the global hydrological cycle to the redistribution of mass on Earth. The seasonal variations are mainly influenced by changes due to monsoon activity in tropical

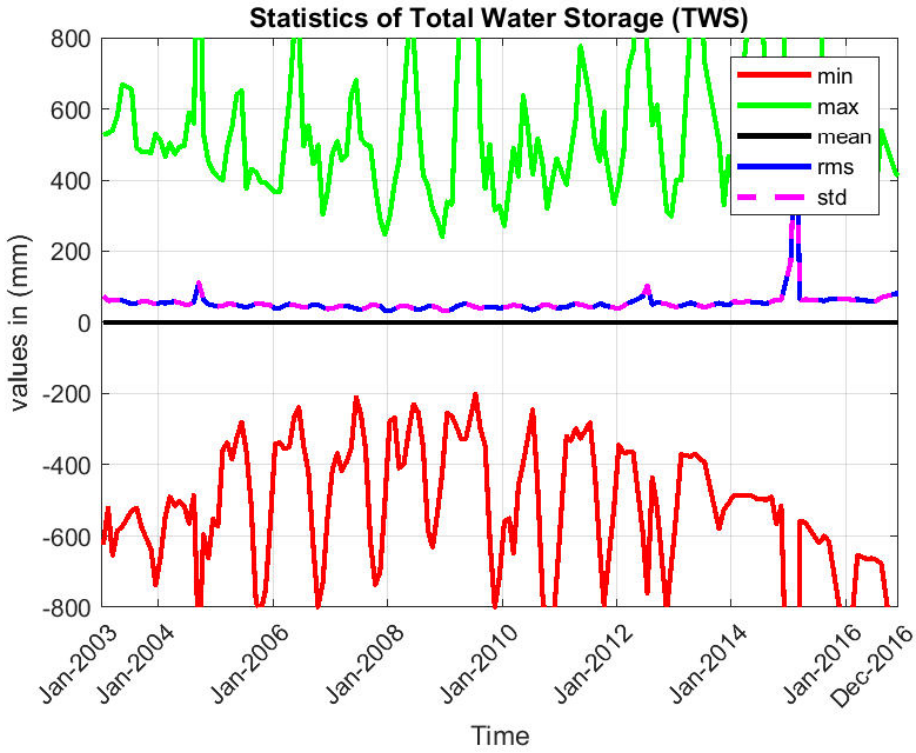

Figure 5.1: Time series of global TWS statistics derived from GRACE CSR DDK5 monthly fields (2003–2016). The curves represent the temporal evolution of minimum, maximum, mean, RMS, and standard deviation, expressed in millimeters of equivalent water height (EWH).

regions, while the long-term downward trend is indicative of ongoing cryospheric loss and human-induced water depletion.

5.2 Temporal Variation of the Earth's Center of Mass (COM)

Figure 5.2 illustrates the temporal variation of the three Cartesian components of the Earth's Center of Mass (COM) inferred from monthly GRACE CSR DDK5 Total Water Storage (TWS) fields for the period 2003–2016. The components X_{com}, Y_{com}, and Z_{com} are expressed in micrometers and represent the mass-induced geocenter motion relative to the mean reference frame.

The figure displays a distinctly periodic seasonal pattern across all three components, with amplitudes generally under $\pm 30\,\mu$m. The Z_{com} component shows the most pronounced seasonal variation, representing the redistribution of hydrological mass between the northern and southern hemispheres. The oscillations in the X_{com} and Y_{com} components are smaller, relating to longitudinal changes in continental water storage. Notably, there are no significant long-term trends in any of the COM components, suggesting that large-scale global mass redistribution remains balanced throughout the study period. This observation aligns with earlier research indicating that GRACE Level-2 solutions include background models (such as those for the atmosphere and ocean) that reduce long-period geocenter signals.

5.3 Global Gravitational Potential and Geoid Undulation Patterns

January 2015 is chosen as a sample month to highlight the challenges associated with unfiltered or weakly filtered GRACE data. The coefficient-uncertainty triangle (refer to panel (a) in Table 5.1) indicates elevated standard deviations (σ) and uneven noise at higher degrees, suggesting reduced spectral stability. The plot of degree and

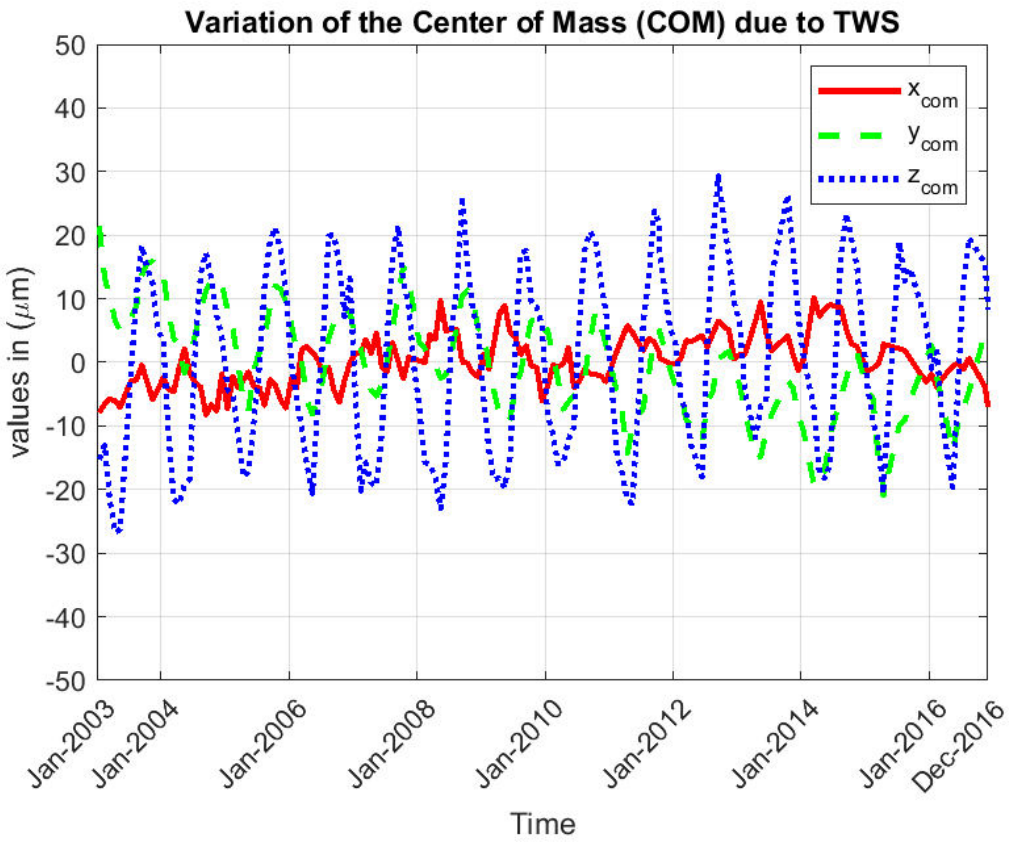

Figure 5.2: Time series of the Earth's Center of Mass (COM) components derived from GRACE CSR DDK5 TWS fields (2003–2016).

error-degree variance reveals a gradual decline. The EWH and undulation maps display longitudinal striping and diminished spatial coherence, resulting from correlated north–south errors and a feeble hydrological signal during the winter months.

Conversely, the July 2015 dataset showcases a more stable and physically consistent monthly field. The coefficient-triangle plot appears smoother and more balanced, featuring lower σ values and improved spectral conditioning. The degree-variance spectrum shows a sharp decline, and the EWH and geoid maps reveal coherent large-scale features with minimal striping. The DDK5 filter successfully mitigates correlated noise while maintaining authentic mass-change indicators, particularly in monsoon regions and polar ice sheets.

The comparison between January and July 2015 highlights evident seasonal and instrumental influences on the accuracy of GRACE measurements. January shows increased noise due to diminished signal strength, less advantageous orbital geometry, and heightened atmospheric aliasing. In contrast, July enjoys enhanced data coverage, more pronounced hydrological differences, and superior decorrelation filtering. As a result, July 2015 is selected as the representative "good" month for validation, providing the most dependable and physically interpretable reconstruction of the gravity field. Within the 2015 dataset, the months of May–July and October demonstrate the lowest levels of correlated noise and the highest spectral accuracy among all the CSR DDK5 monthly fields.

A month-by-month visual evaluation of hydrological mass changes and their gravitational effects for the reference year 2006 is presented in the Figure 5. The monthly EWH maps clearly illustrate the seasonal water cycle, with significant positive anomalies in major basins like the Amazon, Congo, Southeast Asia, and Ganges–Brahmaputra during wet periods, followed by reductions during dry months. Persistent negative values over Greenland and Antarctica indicate ongoing ice mass loss.

The related geoid undulation fields exhibit smoother spatial patterns as the gravitational response integrates surface mass loads through the Earth's elastic deformation. As demonstrated in Figure 6, quarterly snapshots emphasize

Table 5.1: Comparison of GRACE CSR DDK5 results between January 2015 (sample month) and July 2015 (representative good month).

Parameter	January 2015 (Sample Month)	July 2015 (Good Month)
Coefficient Uncertainty Triangle	**(a) January 2015** 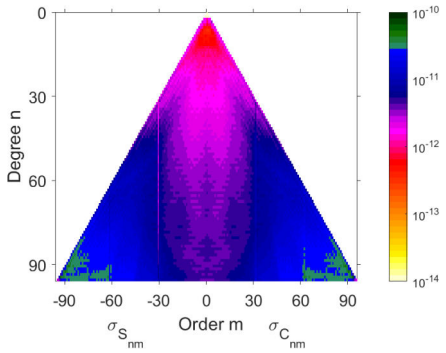	**(b) July 2015** 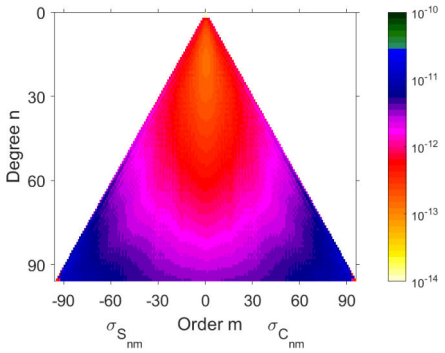
Degree an Error-Degre Variances	**(c) January 2015** 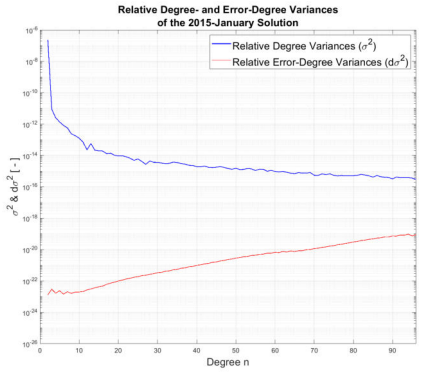	**(d) July 2015** 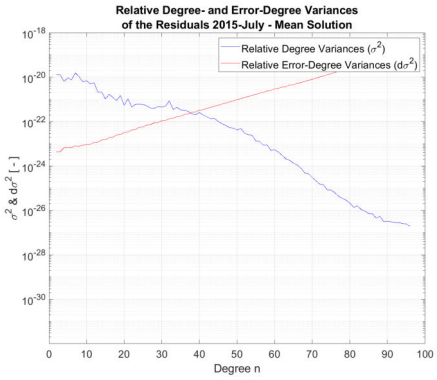
Equivalent Water Heigh (EWH)	**(e) January 2015** 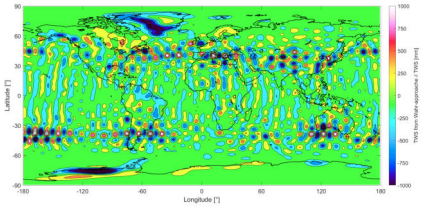	**(f) July 2015** 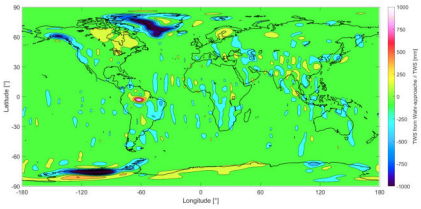
Geoid Undulation (δN)	**(g) January 2015** 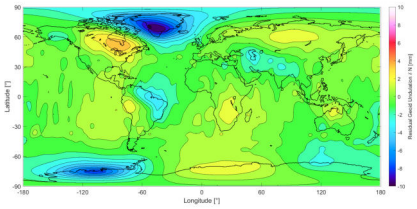	**(h) July 2015** 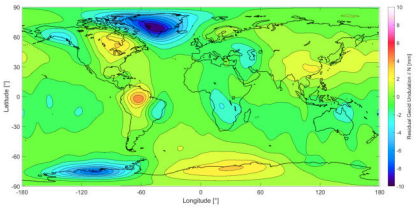

the seasonal progress of large-scale hydrological and cryospheric transformations, such as the mass increases linked to monsoons around June and the effects of winter snowpack in December.
The year 2006 offers one of the clearest and most comprehensive GRACE datasets, characterized by low instrument noise and nearly no data gaps. This makes it a prime candidate for demonstrating the complete annual hydrological cycle and its gravitational impacts.

6 Conclusion and Outlook

In this research, the temporal changes in the Earth's gravity field were evaluated using level 2 GRACE data from CSR and applying the DDK 5 filter. This approach enabled the assessment of mass variations and the analysis of the Earth's Center of Mass (COM) through monthly GRACE-derived spherical harmonic coefficients. The findings indicate that there were no notable temporal variations in the COM during the study period. This stability can be attributed to the fact that the gravity field solutions provided by the International Centre for Global Earth Models (ICGEM) are already processed, calibrated, and corrected on a monthly by GFZ . These Level-2 products include background models for variations in atmospheric and oceanic mass, tidal influences, and errors related to the instruments. Consequently, significant geocenter shifts are effectively reduced in the dataset.
Although the global COM appears stable, distinct regional mass redistributions were clearly observed. Strong variations in gravity are noticeable in areas such as Greenland, Antarctica, and major continental basins, reflecting ongoing phenomena such as melting ice sheets, groundwater depletion, and seasonal changes in hydrological storage. These regional discrepancies effectively balance each other on a global scale, resulting in a nearly constant total COM position while still capturing the dynamic mass redistribution within the Earth system.
An additional area of research that extends beyond the current work involves examining degree-one spherical harmonic coefficients derived from GRACE-based solutions. These coefficients illustrate the motion of the geocenter and can be compared with independent time series obtained from Satellite Laser Ranging (SLR) observations, such as those available through the GRACE/GRACE-FO geocenter data portal. Performing such a comparison would facilitate a more profound validation of the GRACE-derived COM estimates and deliver valuable insights regarding the consistency between satellite gravimetry and SLR-based geocenter assessments. This undertaking could serve as a focal point for future lab rotation (Swenson et al., 2008).

Acknowledgement

I extend my gratitude to Dr.-Ing. Kurt Seitz for his valuable support and guidance throughout this lab rotation. His excellent knowledge and patient suggestions helped shape the research and improve the quality of the report. Beyond advice, his help in code adaptations and error corrections has accelerated the progress of the report. His support has also boosted confidence for the upcoming lab rotations and thesis preparation. I am also thankful to Prof. Dr.-Ing Hansjörg Kutterer for designing the task and clarifying the objectives. It provided a solid foundation for the research and its successful execution. I also acknowledge the support from Geodätisches Institut (GIK) for providing the necessary resources and facilities. Additionally, the author acknowledges ICGEM (ICGEM, 2026) for the data provided for this study.

References

Grombein, T., Seitz, K., and Heck, B. (2013): Optimized formulas for the gravitational field of a tesseroid. *Journal of Geodesy* 87(7):645–660. ISSN: 0949-7714. DOI: 10.1007/s00190-013-0636-1.

Heck, B. and Seitz, K. (2007): A comparison of the tesseroid, prism and point-mass approaches for mass reductions in gravity field modelling. *Journal of Geodesy* 81:121–136.

Heiskanen, W. A. and Moritz, H. (1967): Physical Geodesy. W. H. Freeman & Co., San Francisco, USA.

Humphrey, V., Rodell, M., and Eicker, A. (2023): Using satellite-based terrestrial water storage data: A review. *Surveys in Geophysics* 44(5):1489–1517. DOI: 10.1007/s10712-022-09754-9.

ICGEM (2026): International Centre for Global Earth Models (ICGEM): Gravity field and GRACE/GRACE-FO products hosted at the German Research Centre for Geosciences (GFZ). Accessed: 2026-04-06. URL: https://icgem.gfz-potsdam.de/.

Koch, K.-R. (ed.), ed. (1999): Parameter Estimation and Hypothesis Testing in Linear Models. Springer Berlin Heidelberg, Berlin, Heidelberg. ISBN: 978-3-642-08461-4. DOI: 10.1007/978-3-662-03976-2.

Moritz, H. (1980): Geodetic Reference System 1980. *Bulletin Géodésique* 54(3):395–405. DOI: 10.1007/BF02521480.

Schmidt, R., Flechtner, F., Meyer, U., Neumayer, K. H., Dahle, C., König, R., and Kusche, J. (2006): GRACE observations of changes in continental water storage. *Global and Planetary Change* 50(1-2):112–126. DOI: 10.1016/j.gloplacha.2004.11.018.

Smith, B. E., Seroussi, H., Joughin, I. R., Gardner, A. S., Medley, B., Rignot, E., Velicogna, A., et al. (2020): Pervasive ice sheet mass loss reflects competing ocean and atmosphere processes. *Science* 368(6496):1239–1242. DOI: 10.1126/science.aaz5845. URL: https://doi.org/10.1126/science.aaz5845.

Swenson, S., Chambers, D., and Wahr, J. (2008): Estimating geocenter variations from a combination of GRACE and ocean model output. *Journal of Geophysical Research: Solid Earth* 113(B8):B08410. DOI: 10.1029/2007JB005338.

Wahr, J., Molenaar, M., and Bryan, F. (1998): Time variability of the Earth's gravity field: Hydrological and oceanic effects and their possible detection using GRACE. *Journal of Geophysical Research: Solid Earth* 103(B12):30205–30229.

Appendix

A GRACE CSR DDK5 – TWS Anomalies in 2006

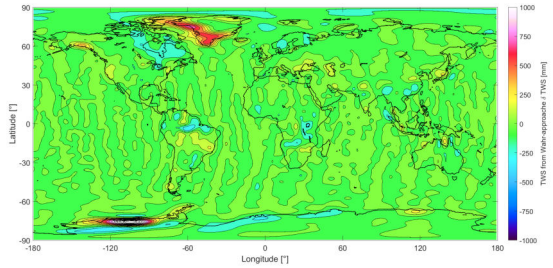

(a) January 2006

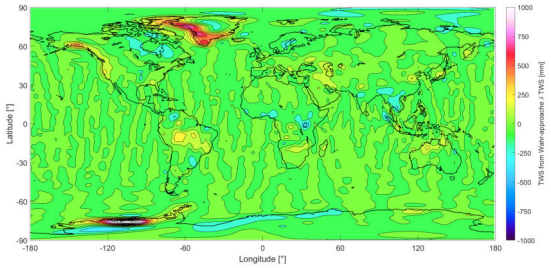

(b) February 2006

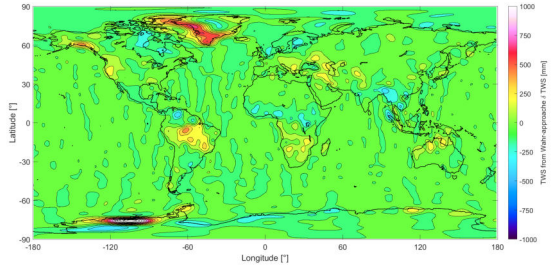

(c) March 2006

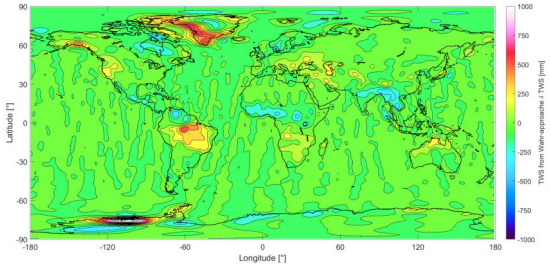

(d) April 2006

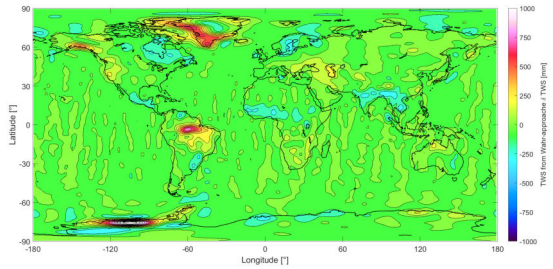

(e) May 2006

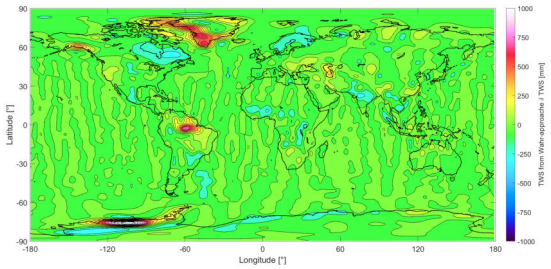

(f) June 2006

Figure A.1: Monthly Equivalent Water Height (EWH) maps for 2006 (Jan-June) derived from GRACE CSR DDK5 solutions.

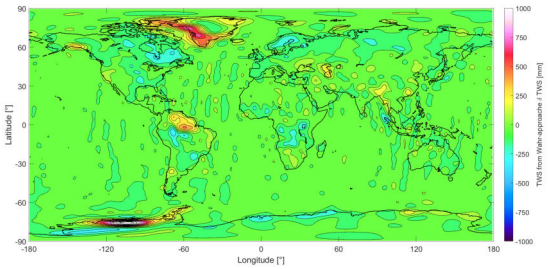

(g) July 2006

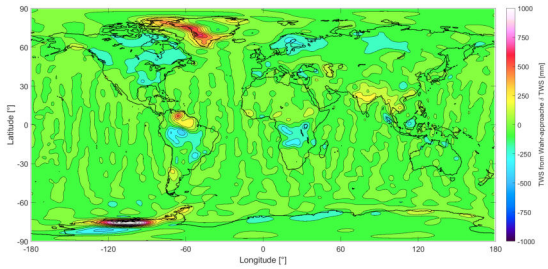

(h) August 2006

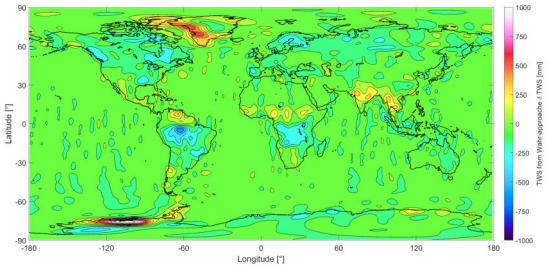

(i) September 2006

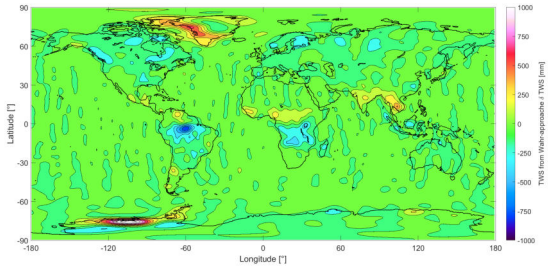

(j) October 2006

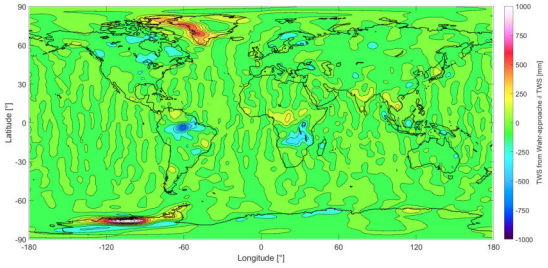

(k) November 2006

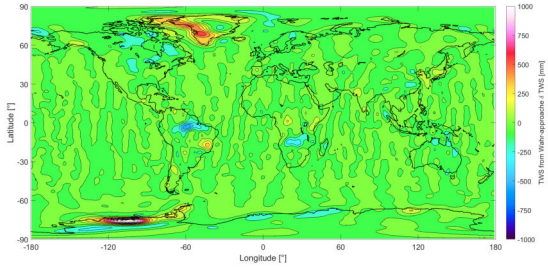

(l) December 2006

Figure A.2: Monthly Equivalent Water Height (EWH) maps for 2006 (July-Dec) derived from GRACE CSR DDK5 solutions.

B GRACE CSR DDK5 – Geoid Undulations in 2006

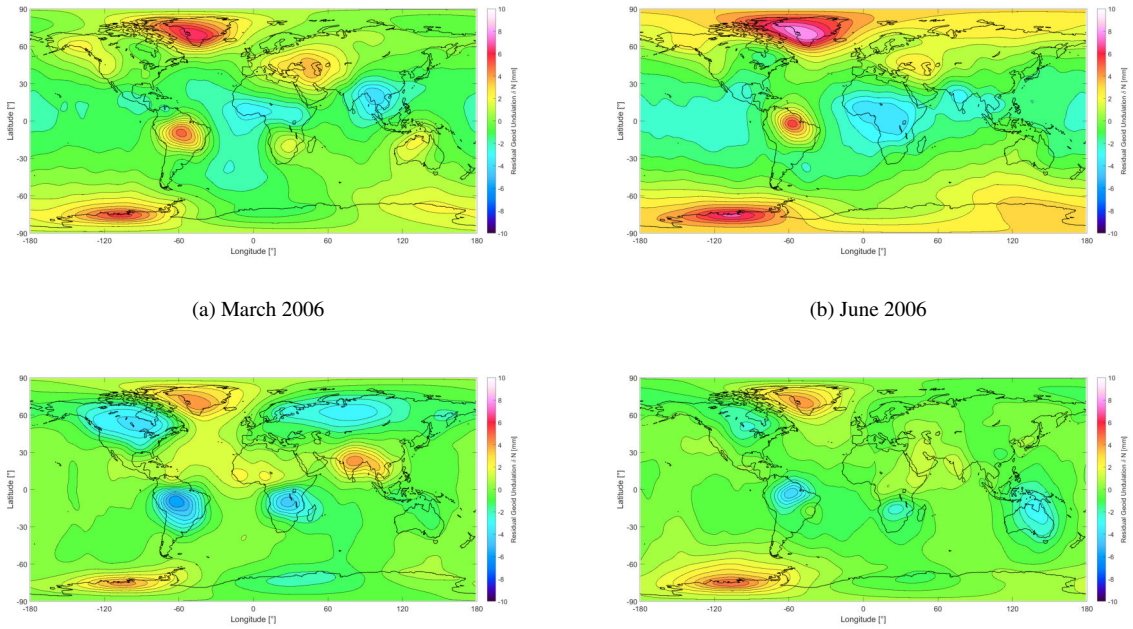

(a) March 2006

(b) June 2006

(c) September 2006

(d) December 2006

Figure B.1: Geoid undulation (ΔN) maps for every third month of 2006 derived from GRACE CSR DDK5 fields.

Determination of terrestrial water storage (TWS) in the Amazon Basin from GRACE and SLR data

Jacob Sebastian[1]

1 Remote Sensing and Geoinformatics Master of Science (M.Sc.), KIT, Germany
E-Mail: uqrgk@student.kit.edu

Abstract

This study analyzes terrestrial water storage (TWS) variations over the Amazon Basin using GRACE and satellite laser ranging (SLR) datasets, with emphasis on low-degree spherical harmonic components. Results indicate that both data sources consistently capture large-scale mass redistribution processes. Spatial analyses of equivalent water height, gravitational potential, and geoid undulation fields reveal smooth, coherent patterns dominated by long-wavelength signals. A strong agreement between GRACE and SLR solutions is observed, particularly for the lowest-degree components where SLR attains higher accuracy. GRACE–SLR difference fields are small and spatially coherent, implying that remaining discrepancies are largely systematic rather than random. Statistical analyses show stable residual behavior throughout 2003–2025. The impact of filtering was assessed using DDK2 and DDK8 filters; results from both approaches are largely similar, indicating dominance of low-degree components in shaping the signals. Although DDK8 provides stronger smoothing, it does not significantly alter spatial patterns or statistical properties, supporting the robustness of the findings to the filtering method. Limitations include restriction to low-degree coefficients, which capture predominantly large-scale features, and unaccounted uncertainties such as signal leakage and filtering effects. Future work could incorporate higher-degree coefficients (e.g., as in Save et al. (2016) and advanced leakage correction techniques, perform cross-validation with independent hydrological datasets, and utilize longer time series with updated GRACE-FO data to better characterize long-term TWS trends.

Keywords GRACE · SLR · Total Water Storage (TWS) · Amazon Basin

KIT Scientific Working Papers
Issue Number 270
ISSN: 2194-1629
DOI: 10.5445/IR/1000191188
Online: June 2026

This document is licensed under the Creative Commons Attribution – Share Alike 4.0 International License (CC BY-SA 4.0):
https://creativecommons.org/licenses/by-sa/4.0/deed.en

1 Introduction

The Earth system undergoes continuous mass redistribution due to different hydrological processes, ice mass changes, and large-scale climate variability. These processes cause measurable temporal variations in the Earth's gravitational field, which can be observed using satellite-based geodetic missions.
The Gravity Recovery and Climate Experiment (GRACE) and its successor GRACE-FO provide monthly gravity field solutions that enable the monitoring of large-scale mass variations over time (Tapley et al., 2004). In this study, gravity field solutions provided by the German Research Centre for Geosciences (GFZ, 2026) are used. From these data, terrestrial water storage (TWS) can be derived, representing the integrated water stored in surface water, soil moisture, snow and ice, and groundwater. While GRACE is highly sensitive to mass redistribution, the accuracy of low-degree spherical harmonic coefficients is limited. Satellite Laser Ranging (SLR) observations, on the other hand, allow a precise determination of long-wavelength gravity field components. The combination of GRACE and SLR data provides a complementary basis for analysing large-scale and long-term mass variations.
The primary aim of this task is to investigate terrestrial water storage variations and long-term trends using monthly gravity field solutions derived from GRACE/GRACE-FO and SLR observations in the time span 2003–2025. The focus of analysis is the Amazon Basin which exhibits strong seasonal and interannual variability controlled by hydrological processes. By analysing the region, the consistency and differences between GRACE- and SLR-based TWS estimates are assessed.
In addition, the influence of different smoothing and filtering techniques on the derived TWS signals is examined. Two decorrelation filters DDK2 and DDK8 are applied to evaluate their impact on signal strength, spatial patterns, and temporal variability. The results are analysed in terms of regional TWS time series, spatial distributions, and long term TWS trends, providing insight into the suitability of GRACE and SLR data for long-term monitoring of terrestrial water storage.

2 Theoretical Aspects

The gravity field of the Earth can be expressed using spherical harmonic functions (Equation (2.1)), where temporal variations in the coefficients reflect changes in mass distribution (Wahr et al., 1998). GRACE provides monthly solutions of these coefficients, which can be converted into surface mass anomalies using the formulation proposed by Wahr et al. (1998) and expressed in Formula (2.3).

$$V(P) = \frac{GM}{r} \sum_{l=0}^{96} \left(\frac{R}{r}\right)^{l} \sum_{m=0}^{l} \left(\bar{C}_{lm}\ \cos m\lambda + \bar{S}_{lm}\ \sin m\lambda\right) \bar{P}_{lm}(\sin\varphi) \tag{2.1}$$

where,
GM : Geocentric gravitational constant
R : Earth's mean equatorial radius
r : Radial distance from Earth's center
φ : Geocentric Latitude
λ : Longitude
l, m : Degree and order of the spherical harmonics
$\bar{C}_{lm}, \bar{S}_{lm}$: Fully normalised spherical harmonic coefficients of degree l and order m
$\bar{P}_{lm}$: Fully normalised Legendre functions of degree l and order m.

2.1 Effect of Mass Redistribution on the Gravity Field

Changes in terrestrial water storage (TWS) contributes a major factor in the redistribution of mass within the Earth system which is one of the primary factors for the temporal variations in the Earth's gravity field. These

variations are represented by changes in the spherical harmonic coefficients $\Delta\bar{C}_{lm}$ and $\Delta\bar{S}_{lm}$ derived from GRACE observations. Based on Equation (2.1) the corresponding geoid height variations $\Delta N(\varphi,\lambda)$ can be expressed as:

$$\Delta N(\varphi,\lambda) = R\sum_{l=0}^{96}\sum_{m=0}^{l}\left(\Delta\bar{C}_{lm}\cos(m\lambda)+\Delta\bar{S}_{lm}\sin(m\lambda)\right)\bar{P}_{lm}(\sin\varphi)\,. \tag{2.2}$$

2.2 Equivalent Water Height (EWH)

To relate gravity field variations to surface mass changes, the concept of load Love numbers k_l is introduced, which accounts for the elastic response of the solid Earth to surface loading. Following Wahr et al. (1998), the surface mass density anomaly $\Delta\sigma$ can be derived from the gravity field coefficients.
By applying spherical harmonic synthesis, the mass anomalies can be represented as equivalent water height (EWH), as a representation of terrestrial water storage. Following the derivations Wahr et al. (1998), the surface mass density anomaly can be represented as:

$$\Delta\sigma(\varphi,\lambda) = \frac{R\rho_{\text{ave}}}{3}\sum_{l=0}^{96}\frac{2l+1}{1+k_l}\sum_{m=0}^{l}\left(\Delta\bar{C}_{lm}\cos(m\lambda)+\Delta\bar{S}_{lm}\sin(m\lambda)\right)\bar{P}_{lm}(\sin\varphi) \tag{2.3}$$

where,
$\Delta\sigma(\varphi,\lambda)$: Surface mass density anomaly at latitude φ and longitude λ (kg/m²)
ρ_{ave} : Mean density of the Earth
k_l : Load Love number of degree l (describes Earth's elastic response)
$\Delta\bar{C}_{lm}, \Delta\bar{S}_{lm}$: GRACE-derived spherical harmonic coefficients for mass change relative to a reference solution (mean or reference epoch)

Dividing Equation (2.3) by the density of water ρ_w gives the equivalent water thickness

$$\Delta h(\varphi,\lambda) = \frac{\Delta\sigma(\varphi,\lambda)}{\rho_w}\,. \tag{2.4}$$

This formula provides the basis for converting GRACE-derived gravity field variations into equivalent water height (EWH), which represents terrestrial water storage.

2.3 Role of Low-Degree Spherical Harmonic Coefficients

Low-degree spherical harmonic coefficients describe the large-scale structure of the Earth's gravity field. Unlike higher-degree coefficients that capture localized variations, low-degree terms reflect broad changes in the Earth system, such as shifts in ocean mass, ice sheet dynamics, and large-scale hydrological processes (Wahr et al., 1998; Tapley et al., 2004).
Among these, the degree-1 coefficients ($\bar{C}_{1m}, \bar{S}_{1m}$) are associated with geocenter motion as expressed in Swenson et al. 2008. They describe the change of the Earth's center of mass relative to the center of figure of the solid Earth. This motion arises due to asymmetric mass redistribution between hemispheres, for example, seasonal water storage changes or ice mass loss in polar regions (Swenson et al., 2008; Wu et al., 2011). However, GRACE is not able to directly determine degree-1 coefficients due to its measurement concept, and therefore these terms are typically derived from Satellite Laser Ranging (SLR) observations (Swenson et al., 2008; Pearlman et al., 2002).
The degree-2 coefficients represent the shape characteristics of the Earth. In particular, the coefficient $\bar{C}_{20}$ is directly related to the flattening of the Earth at the poles. Temporal variations in $\bar{C}_{20}$ indicate mass redistribution between polar and equatorial regions, such as melting of ice sheets and ocean mass changes (Cheng et al., 2013). These variations are essential for understanding global-scale processes like sea level rise and long-term climate-driven mass changes (Tapley et al., 2004; Wahr et al., 1998).

Because low-degree coefficients correspond to long-wavelength signals, they are more reliably determined using SLR observations, which provide high precision for these components (Pearlman et al., 2002; Cheng et al., 2013). In contrast, GRACE is more sensitive to medium- and high-degree coefficients, capturing regional and smaller-scale mass variations (Tapley et al., 2004). Therefore, combining GRACE and SLR data allows for a more complete and consistent representation of the Earth's gravity field, ensuring that both global-scale and regional mass redistribution processes are accurately captured in terrestrial water storage (TWS) analysis (Wahr et al., 1998; Chen et al., 2010).

3 Data and study area

The data used in this study consists of monthly gravity field solutions from the GRACE and GRACE-FO missions. The datasets include fully normalized spherical harmonic coefficients up to degree and order 96, generated by the GFZ (Helmholtz Centre Potsdam, German Research Centre for Geosciences) and made available through the International Centre for Global Earth Models (ICGEM, 2026) To reduce correlated noise and enhance the geophysical signal, decorrelation filtering is applied to the GRACE data. DDK2 and DDK8 filters (Kusche, 2007) are used as a comparison in order to evaluate the impact of different smoothing levels on the derived terrestrial water storage (TWS).

In addition to GRACE, low-degree spherical harmonic coefficients derived from Satellite Laser Ranging (SLR) observations, provided by the International Laser Ranging Service (ILRS), are used (Pearlman et al., 2002) to improve the accuracy of long-wavelength gravity field components. These SLR solutions are particularly important for degrees $l \leq 5$, where GRACE data exhibits reduced accuracy.

The study area considered in this analysis is the Amazon Basin, which represents the largest river basin in the world and exhibits strong seasonal and interannual hydrological variability. The basin is located in northern South America and plays a major role in the global water cycle due to its extensive precipitation, river discharge, and terrestrial water storage variations.

4 Methodology

The methodology adopted in this study focuses on the processing and analysis of GRACE and SLR gravity field data to derive terrestrial water storage (TWS) variations over the Amazon Basin. The workflow, which is explained now, involves preprocessing of spherical harmonic coefficients, application of filtering techniques, transformation to geophysical quantities, and statistical analysis of the resulting time series. The analysis was done in the time frame 2003 to 2025.

4.1 Preprocessing of Spherical Harmonic Coefficients

The monthly spherical harmonic coefficients $(\bar{C}_{lm}, \bar{S}_{lm})$ obtained from GRACE and SLR datasets are first preprocessed to ensure consistency. The coefficients are rescaled to a common reference system GRS80 (Moritz, 1980) using standardized values of the gravitational constant GM and the Earth's reference radius R. Since GRACE solutions exhibit reduced accuracy for low-degree coefficients, particularly for degrees $l \leq 5$, SLR-derived coefficients are incorporated to improve the reliability of long-wavelength components.

4.2 Spectral Filtering and Signal Conditioning

To reduce the correlated errors and enhance the geophysical signal, decorrelation filtering is applied in the spectral domain (Kusche et al., 2009). In this study, two already filtered data sets are used from ICGEM (2026)

- DDK2 filter, which applies stronger smoothing and significantly reduces noise,
- DDK8 filter, which provides moderate smoothing and preserves spatial variability.

The use of both filters allows an evaluation of the trade-off between noise reduction and signal attenuation in the derived results.

4.3 Computation of Gravity Residuals

To isolate the time-variable gravity signal, a mean gravity field $(\bar{C}^{\circ}_{lm}, \bar{S}^{\circ}_{lm})$ is first computed over the study period. Monthly residual coefficients are then obtained by subtracting the mean field from each monthly solution:

$$\Delta\bar{C}_{lm}(t) = \bar{C}_{lm}(t) - \bar{C}^{\circ}_{lm}, \quad \Delta\bar{S}_{lm}(t) = \bar{S}_{lm}(t) - \bar{S}^{\circ}_{lm}\,. \tag{4.1}$$

These residuals represent temporal variations (drift, periodical) associated with mass redistribution processes.

4.4 Computation of Geophysical Quantities

Using spherical harmonic synthesis, the processed coefficients are transformed into spatial fields on a regular grid. The following geophysical quantities are computed:

- Gravitational potential
- Geoid undulation
- Terrestrial water storage (TWS) expressed as equivalent water height (EWH)

The conversion of gravity field variations into TWS is carried out using load Love numbers as expressed in Wahr et al. (1998), which account for the elastic response of the Earth to surface loading. This transformation enables the interpretation of gravity variations in terms of hydrological mass changes.

4.5 Regional Extraction of the Amazon Basin

The study is spatially restricted to the Amazon Basin using predefined latitude and longitude boundaries. This region is selected due to its strong hydrological variability and significance in the global water cycle.

4.6 Statistical Analysis and Time Series Generation

For each monthly solution, statistical measures are computed over the Amazon Basin for all derived quantities, including TWS, gravitational potential, and geoid undulation. The following parameters are calculated:

- Minimum value
- Maximum value
- Mean value
- Root mean square (RMS)
- Standard deviation

These statistical measures provide quantitative insights into measured parameters. The resulting time series are used to analyze seasonal and yearly variations.

4.7 Comparison between GRACE and SLR

The analysis is carried out for three different cases:

1. GRACE-derived solutions
2. SLR-derived solutions (low-degree components)
3. Difference between GRACE and SLR (GRACE – SLR) for several degrees ≤ 5

This comparison enables the assessment of consistency between the datasets and highlights differences in the results obtained from each data set

4.8 Visualization and Output

The results are visualized using spatial maps and time series plots. Monthly maps illustrate the spatial distribution of TWS, potential, and undulation, while time series plots represent their temporal evolution. All computations and visualizations are performed using MATLAB, and the outputs are stored for further interpretation and analysis.

4.9 Assumptions and Limitations

The methodology assumes that the Earth behaves as a linear elastic body, represented through load Love numbers. Signal leakage, attenuation due to filtering, and errors in background models as described in Swenson and Wahr (2006) (e.g., atmosphere and ocean corrections) are not fully accounted for. Despite these limitations, the approach provides a robust framework for analyzing large-scale terrestrial water storage variations in the Amazon basin.

5 Results and Discussion

The results obtained in this study provide insight into the behaviour of terrestrial water storage (TWS) variations and their representation using GRACE and SLR observations over the Amazon Basin. The analysis primarily focuses on low-degree spherical harmonic components, which represent long-wavelength gravity signals associated with large-scale hydrological mass redistribution. The application of the DDK2 filter reduces correlated striping noise while preserving the dominant spatial characteristics of the gravity field solutions.

The derived fields, including equivalent water height (EWH), gravitational potential, and geoid undulation, exhibit smooth spatial structures and gradual temporal variability throughout the study period from 2003 to 2025. These characteristics reflect the large-scale hydrological behaviour of the Amazon Basin referred from Chen et al. (2010), which is dominated by seasonal water storage variations and basin-scale mass redistribution processes.

The comparison between GRACE and SLR solutions indicates a generally consistent representation of the long-wavelength gravity signal. The remaining residual differences mainly reflect variations in the treatment of low-degree spherical harmonic coefficients and the sensitivity of higher-degree components to localized spatial variability and residual observational noise.

In addition to DDK2, the analysis was also performed using the DDK8 filter. Although DDK8 introduces weaker smoothing, the overall spatial and temporal characteristics remain largely unchanged because the analysis is dominated by low-degree spherical harmonic components. The corresponding DDK8 results are therefore provided in the Appendix A for completeness.

5.1 GRACE–SLR Difference Maps

The spatial characteristics of the GRACE–SLR terrestrial water storage (TWS) differences are illustrated in Figures 5.1 – 5.8 using representative monthly maps for the years 2004 and 2024. These maps demonstrate the spatial distribution of residual equivalent water height (EWH) signals over the Amazon Basin for different low-degree spherical harmonic combinations.

The lowest-degree combinations, particularly $N_2 - N_2$, exhibit smooth and spatially coherent patterns dominated by large-scale gradients. This behaviour is expected because low-degree spherical harmonic coefficients primarily represent long-wavelength gravity signals associated with basin-scale mass redistribution processes. The gradual spatial variations observed across the Amazon Basin indicate a consistent representation of large-scale hydrological signals between GRACE and SLR solutions.

Seasonal variability is visible through gradual changes in the spatial magnitude and orientation of the residual fields across different months. These temporal variations reflect the seasonal hydrological cycle of the Amazon Basin, where precipitation and river discharge produce periodic changes in terrestrial water storage.

As the spherical harmonic degree increases from N_3 to N_5, the spatial fields show increased localized variability and sharper gradients. Higher-degree spherical harmonic components represent shorter spatial wavelengths and are

therefore more sensitive to regional-scale mass variations and residual correlated noise. Despite the increased spatial complexity, the overall magnitude of the residual signals remains relatively stable, indicating that the dominant differences between GRACE and SLR are primarily controlled by long-wavelength components.
The absence of abrupt discontinuities or unrealistic spatial artefacts further indicates that the applied DDK filtering effectively suppresses correlated striping noise while preserving the dominant geophysical signal.

5.2 Undulation and Potential Fields

The geoid undulation and gravitational potential fields derived from the SLR and GRACE solutions exhibit smooth spatial behaviour characteristic of long-wavelength gravity signals as depicted in Figures 5.9 – 5.12. Since low-degree spherical harmonic coefficients mainly describe large-scale variations in the Earth's gravity field, the resulting undulation fields display broad spatial gradients with limited localized variability.
The SLR-derived undulation fields demonstrate highly continuous spatial patterns, reflecting the strong sensitivity of SLR observations to long-wavelength gravity field components. The corresponding GRACE–SLR difference fields show relatively small residual variations, indicating a generally consistent representation of the large-scale gravity field between the two datasets.
Comparisons between the years 2004 and 2024 reveal that the overall spatial structure of the undulation fields remains stable over time. The observed temporal changes mainly appear as gradual variations in magnitude rather than abrupt spatial reorganizations, suggesting that the dominant gravity signal is controlled by slowly varying large-scale hydrological processes.
For the higher-degree combinations, the undulation fields exhibit increased spatial variability and stronger localized gradients. This behaviour is associated with the increasing contribution of shorter spatial wavelength components, which are more sensitive to localized gravity variations and residual observational noise. Consequently, the GRACE–SLR residual fields become more spatially complex at higher spherical harmonic degrees.

5.3 Statistical Analysis of TWS Differences

The statistical summary of the GRACE–SLR terrestrial water storage (TWS) differences, given in Table 5.1, provides quantitative insight into the behaviour of the residual gravity signals for different spherical harmonic degree combinations.
The lowest-degree combinations ($N_2 - N_2$ to $N_2 - N_5$) exhibit comparatively large mean values and higher RMS amplitudes. This behaviour confirms that low-degree spherical harmonic coefficients dominate the long-wavelength gravity signal and therefore contain a significant contribution from basin-scale hydrological mass redistribution. Since the Amazon Basin represents one of the largest hydrological systems on Earth, large-scale terrestrial water storage variations strongly influence the low-degree gravity field components.
As the spherical harmonic degree increases, the overall magnitude of the residual signals decreases, while the relative variability represented by the standard deviation becomes more pronounced. Higher-degree coefficients correspond to shorter spatial wavelengths and are therefore increasingly sensitive to localized mass variations, residual correlated errors, and small-scale spatial heterogeneity.
The statistical behaviour remains generally stable across all degree combinations throughout the study period. The absence of large statistical discontinuities suggests a consistent long-term agreement between the GRACE and SLR datasets in representing large-scale terrestrial water storage variability.
The corresponding statistical results obtained using the DDK8 filter show similar behaviour. This indicates that the dominant characteristics of the residual signals are primarily controlled by the low-degree spherical harmonic components rather than the increasing strength per degree of the applied smoothing filter (see Gauss filter).

5.4 Time Series Analysis of TWS

The statistical time series of the GRACE–SLR terrestrial water storage (TWS) differences for the various spherical harmonic degree combinations, provided in Figure 5.13, gives insight into the temporal behaviour of the residual gravity signals over the Amazon Basin during the period 2003–2025.

For the lowest-degree combinations ($N_2 - N_2$ to $N_2 - N_5$), the time series exhibit relatively smooth temporal behaviour with large mean residual values and comparatively high RMS amplitudes. These characteristics indicate that the low-degree spherical harmonic components are dominated by long-wavelength mass redistribution processes associated with large-scale hydrological variability over the Amazon Basin.

The labeling of the frequency range, e.g., $((N_2 - N_2)$, means that all Stokes coefficients of degree $l = 2$ were used $(\bar{C}_{2,0}, \bar{C}_{2,1}, \bar{C}_{2,2}, \bar{S}_{2,1}, \bar{S}_{2,2})$.

Seasonal oscillations are visible throughout the observation period, particularly in the RMS and STD time series. These periodic variations reflect the seasonal hydrological cycle of the Amazon Basin, where wet and dry seasons produce recurring changes in terrestrial water storage through precipitation, runoff, and river discharge.

The higher-degree combinations ($N_3 - N_3$ to $N_5 - N_5$) show reduced overall signal magnitude but increased short-term fluctuations. This behaviour results from the greater sensitivity of higher spherical harmonic degrees to localized spatial variability and residual correlated noise. Since higher-degree components correspond to shorter spatial wavelengths, they are more strongly affected by small-scale hydrological variations and observational uncertainties.

Despite the increased variability in the higher-degree combinations, the statistical parameters remain generally stable throughout the study period without abrupt discontinuities or unrealistic temporal artefacts. This indicates that both GRACE and SLR datasets maintain a consistent representation of the long-wavelength terrestrial water storage signal over time.

The corresponding results obtained using the DDK8 filter show similar temporal characteristics. Although DDK8 applies weaker smoothing compared to DDK2, the dominant long-wavelength behaviour remains largely unchanged because the weights w_l are nearly the same for very low degrees ≤ 5.

Table 5.1: Statistical summary of GRACE–SLR TWS differences for selected spherical harmonic degree combinations using DDK2 filter. Values are in (mm).

Degree Combination	Min	Max	Mean	RMS	STD
2–2	-452.113	-307.337	-329.387	429.370	15.975
2–3	-470.178	-285.062	-315.674	435.385	33.091
2–4	-466.837	-283.379	-315.762	425.201	37.518
2–5	-509.869	-235.884	-330.721	438.068	59.038
3–3	-48.057	74.804	48.734	52.681	27.806
3–4	-59.078	78.734	38.458	44.068	33.041
3–5	-117.026	124.253	51.588	63.478	61.547
4–4	-38.727	40.941	17.574	23.918	23.421
4–5	-121.943	103.184	26.691	56.136	54.771
5–5	-114.975	85.880	13.570	56.099	55.583

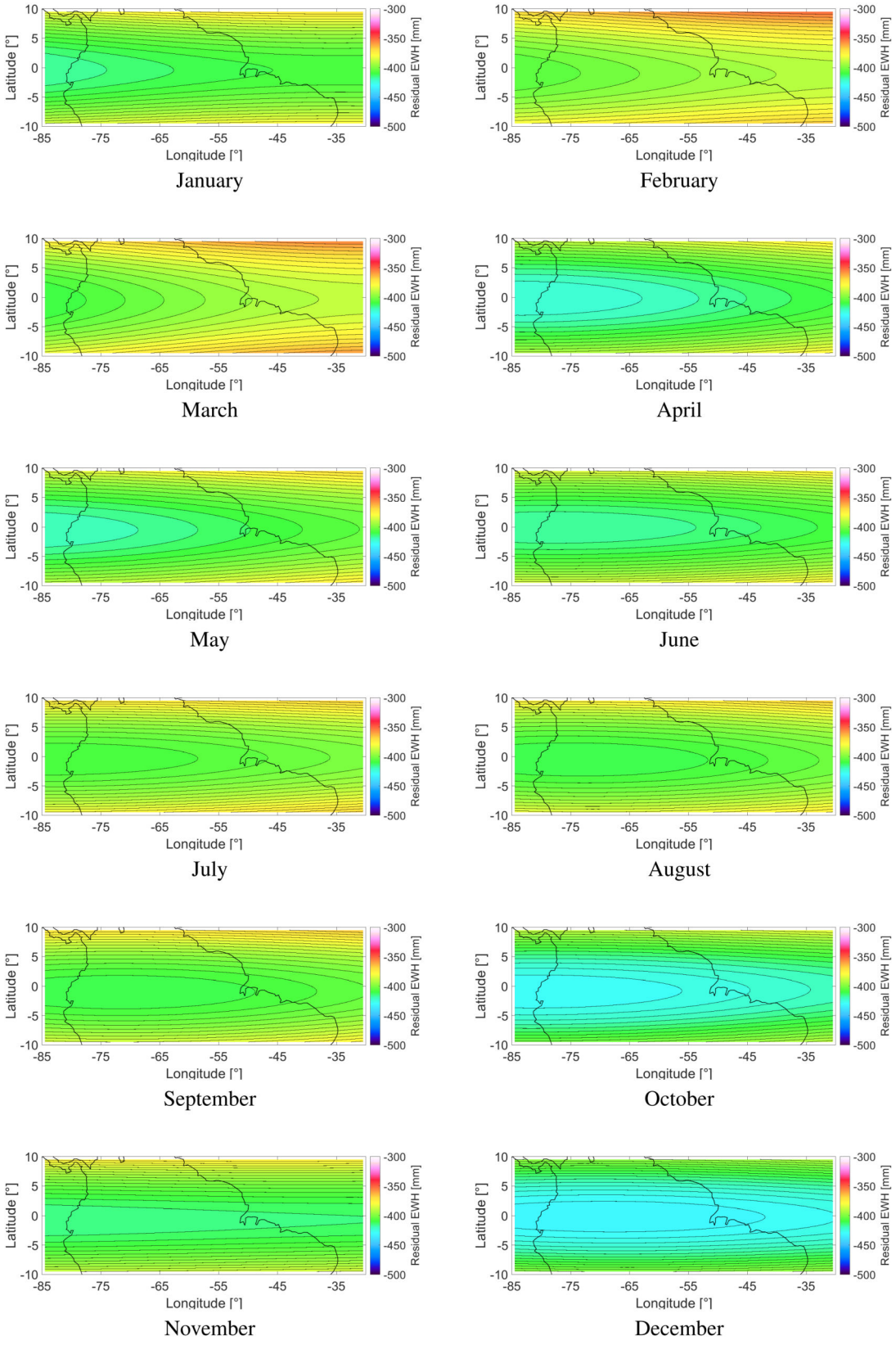

Figure 5.1: Monthly GRACE–SLR residual equivalent water height (EWH) maps over the Amazon Basin for the year 2004 using DDK2 filter and the spherical harmonic degree combination ($N_2 - N_2$). The values range from -500 mm to -300 mm

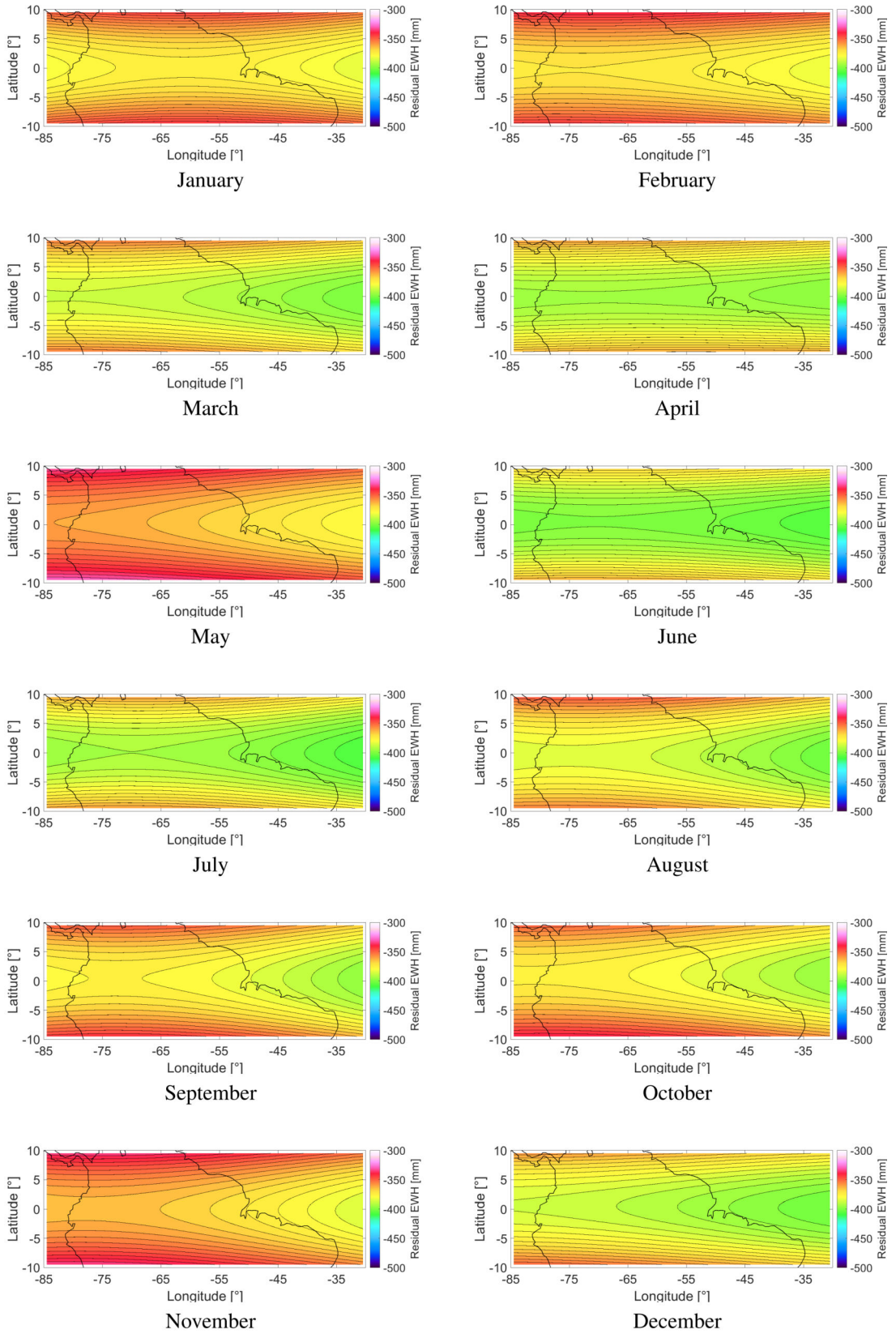

Figure 5.2: Monthly GRACE–SLR residual equivalent water height (EWH) maps over the Amazon Basin for the year 2024 using DDK2 filter and the spherical harmonic degree combination ($N_2 - N_2$). The values range from -500 mm to -300 mm

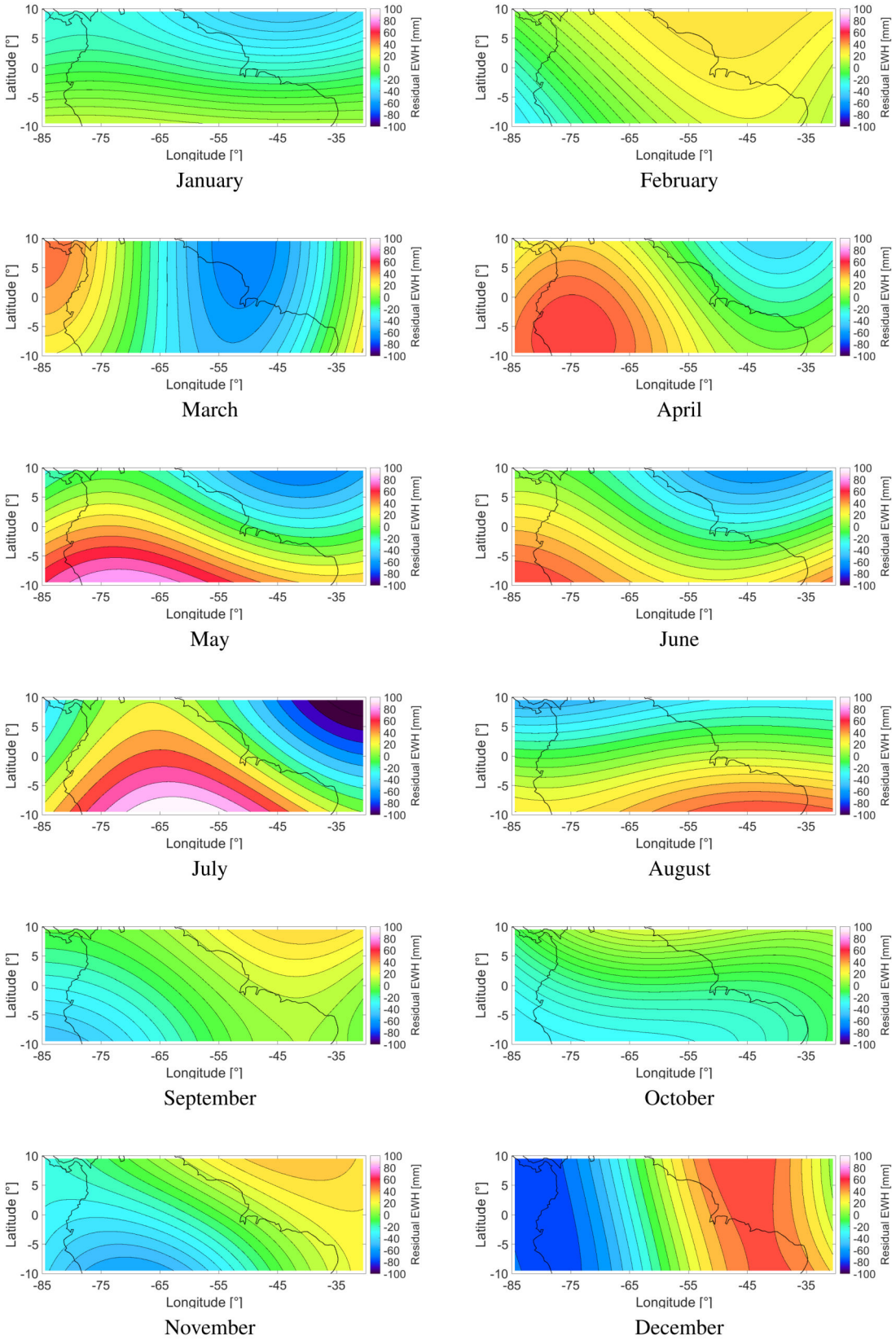

Figure 5.3: Monthly GRACE–SLR residual equivalent water height (EWH) maps over the Amazon Basin for the year 2004 using DDK2 filter and the spherical harmonic degree combination ($N_3 - N_5$). The values range from -100 mm to 100 mm

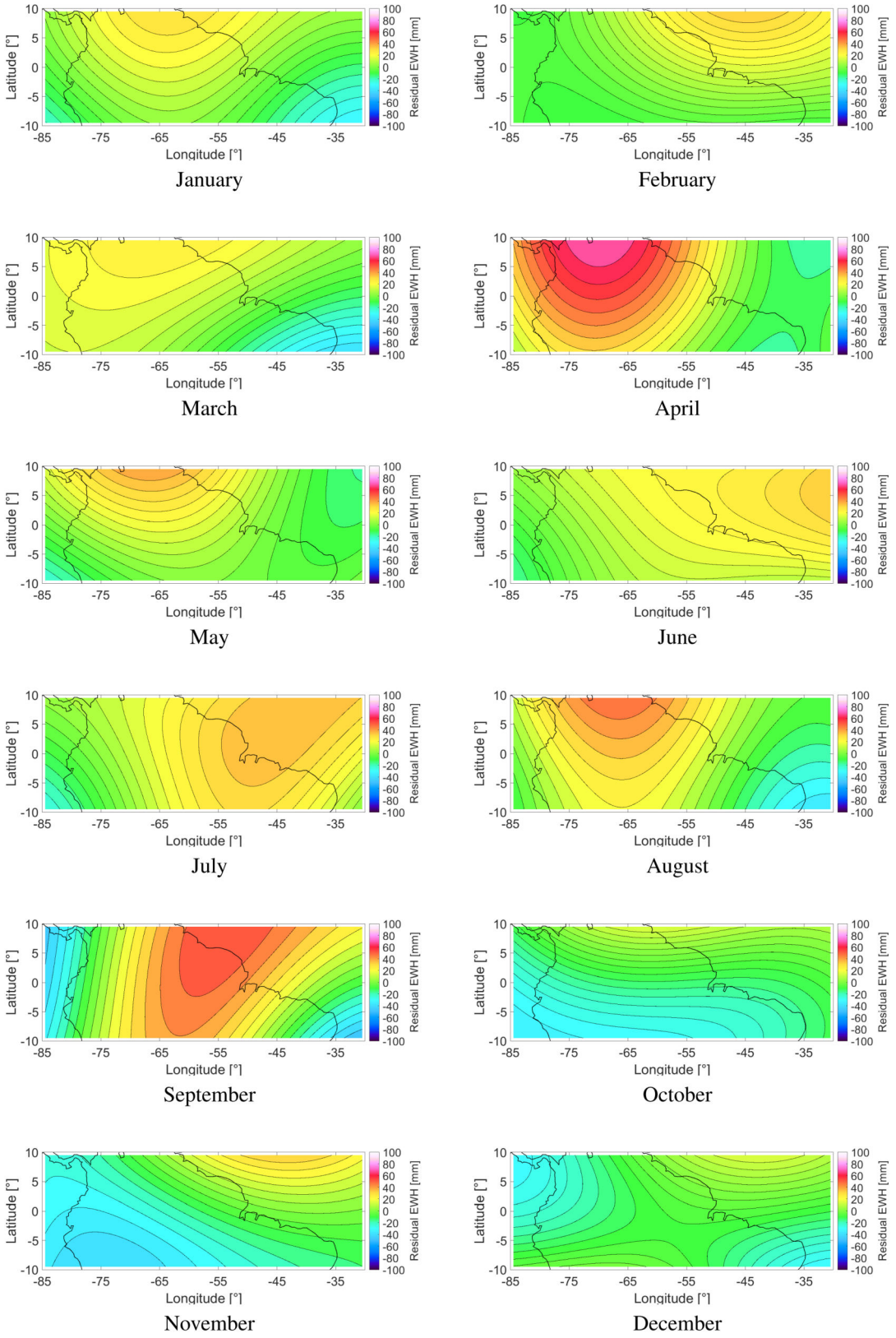

Figure 5.4: Monthly GRACE–SLR residual equivalent water height (EWH) maps over the Amazon Basin for the year 2024 using DDK2 filter and the spherical harmonic degree combination ($N_3 - N_5$). The values range from -100 mm to 100 mm

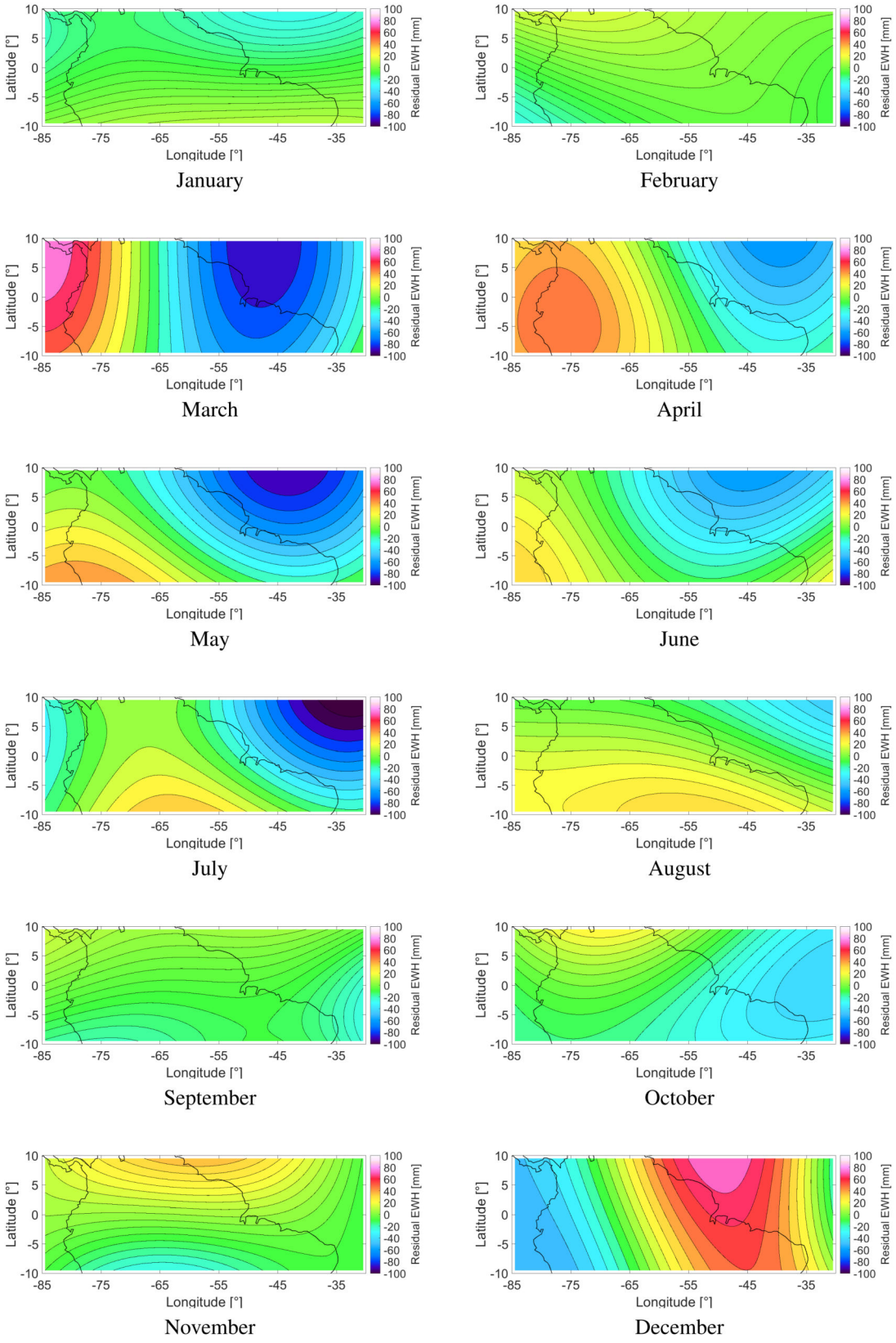

Figure 5.5: Monthly GRACE–SLR residual equivalent water height (EWH) maps over the Amazon Basin for the year 2004 using DDK2 filter and the spherical harmonic degree combination ($N_4 - N_5$). The values range from -100 mm to 100 mm

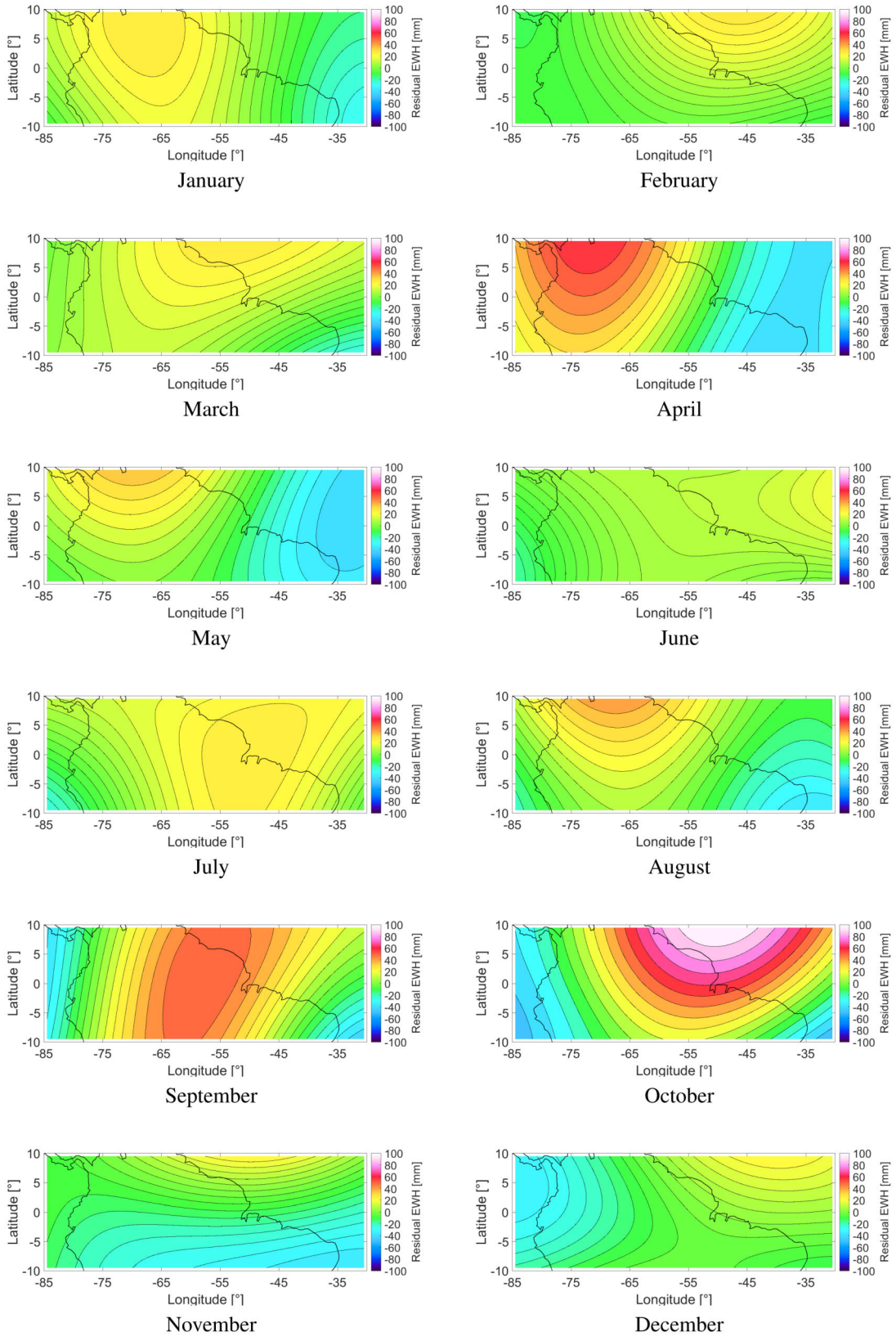

Figure 5.6: Monthly GRACE–SLR residual equivalent water height (EWH) maps over the Amazon Basin for the year 2024 using DDK2 filter and the spherical harmonic degree combination ($N_4 - N_5$). The values range from -100 mm to 100 mm.

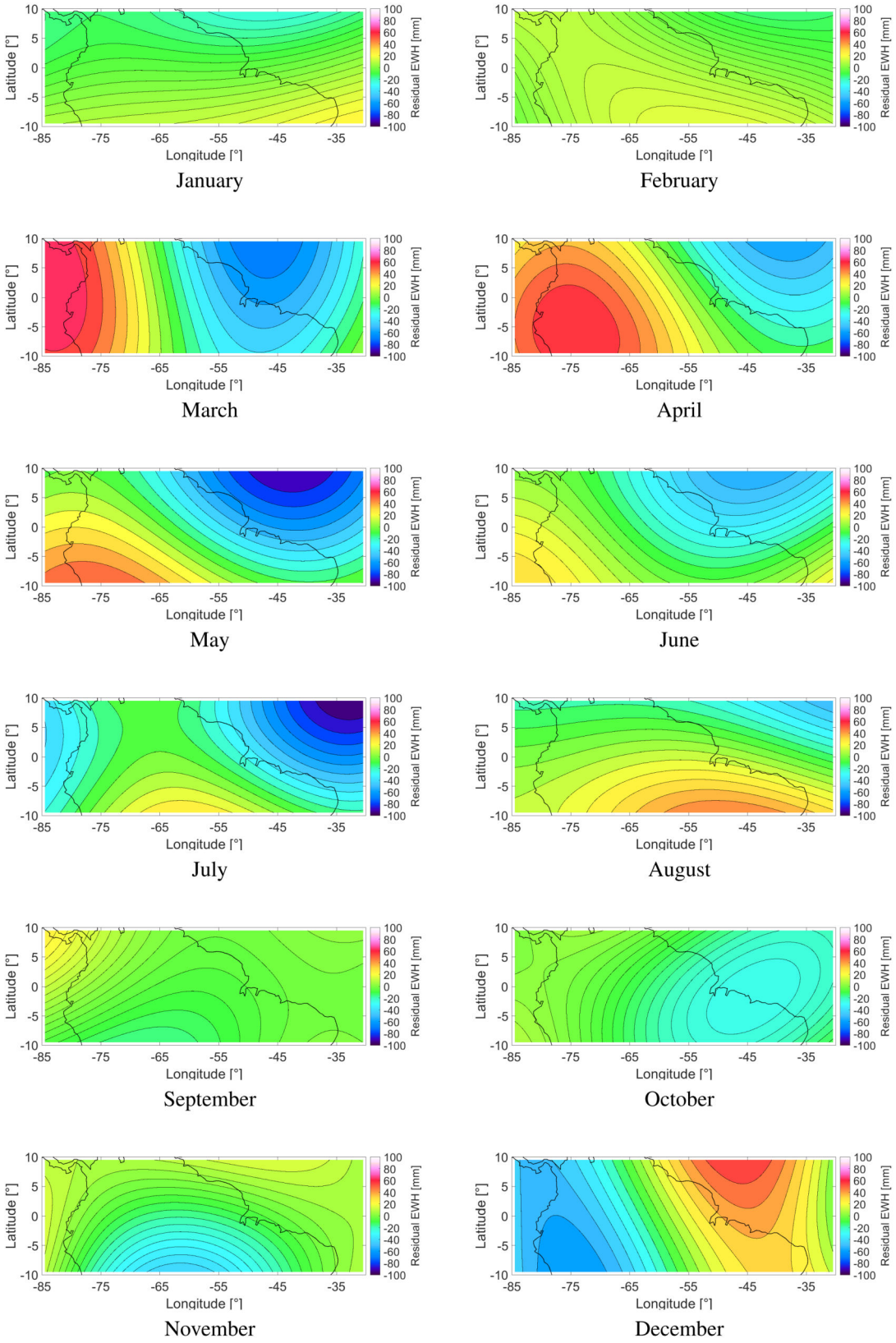

Figure 5.7: Monthly GRACE–SLR residual equivalent water height (EWH) maps over the Amazon Basin for the year 2004 using DDK2 filter and the spherical harmonic degree combination ($N_5 - N_5$). The values range from -100 mm to 100 mm

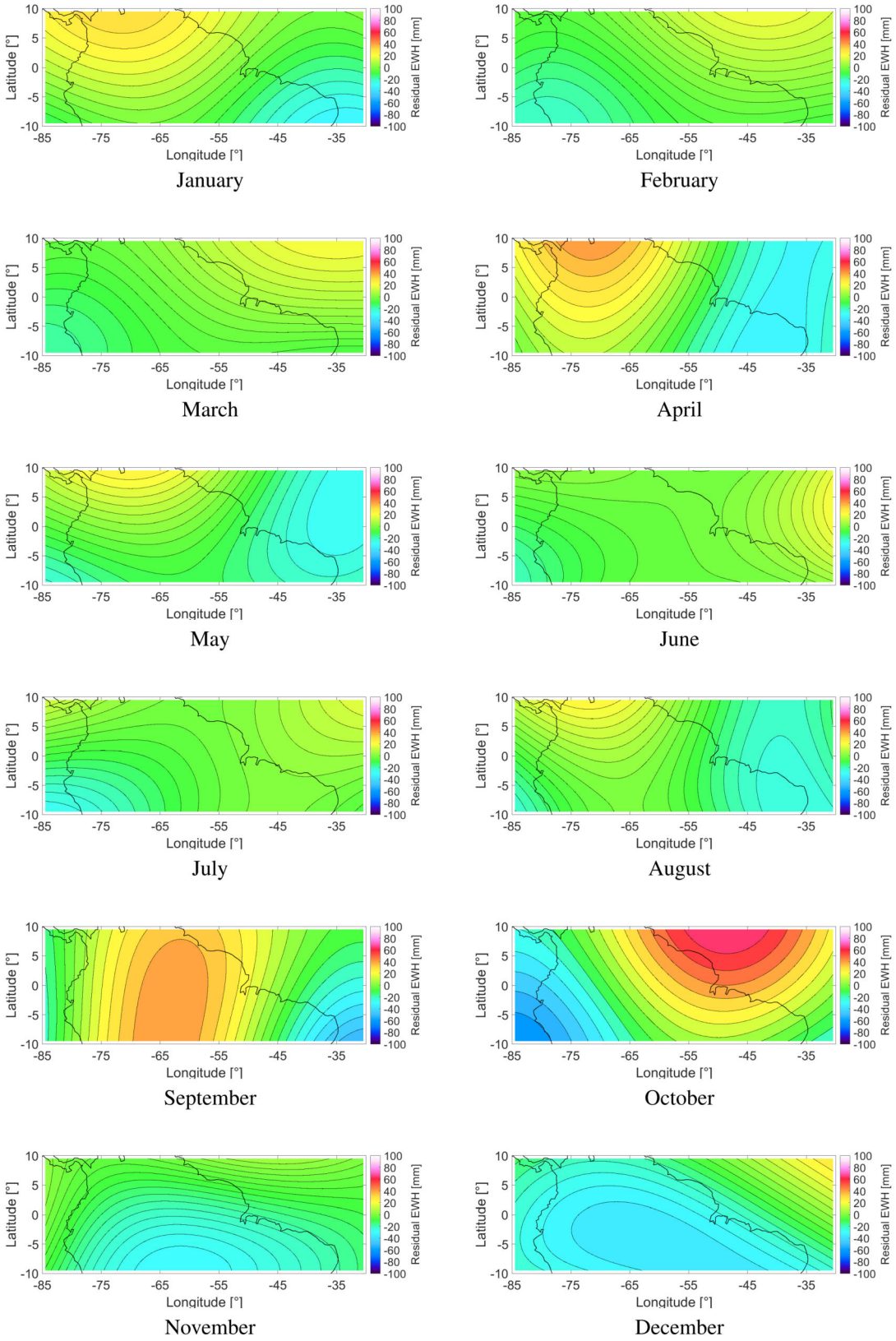

Figure 5.8: Monthly GRACE–SLR residual equivalent water height (EWH) maps over the Amazon Basin for the year 2024 using DDK2 filter and the spherical harmonic degree combination ($N_5 - N_5$). The values range from -100 mm to 100 mm

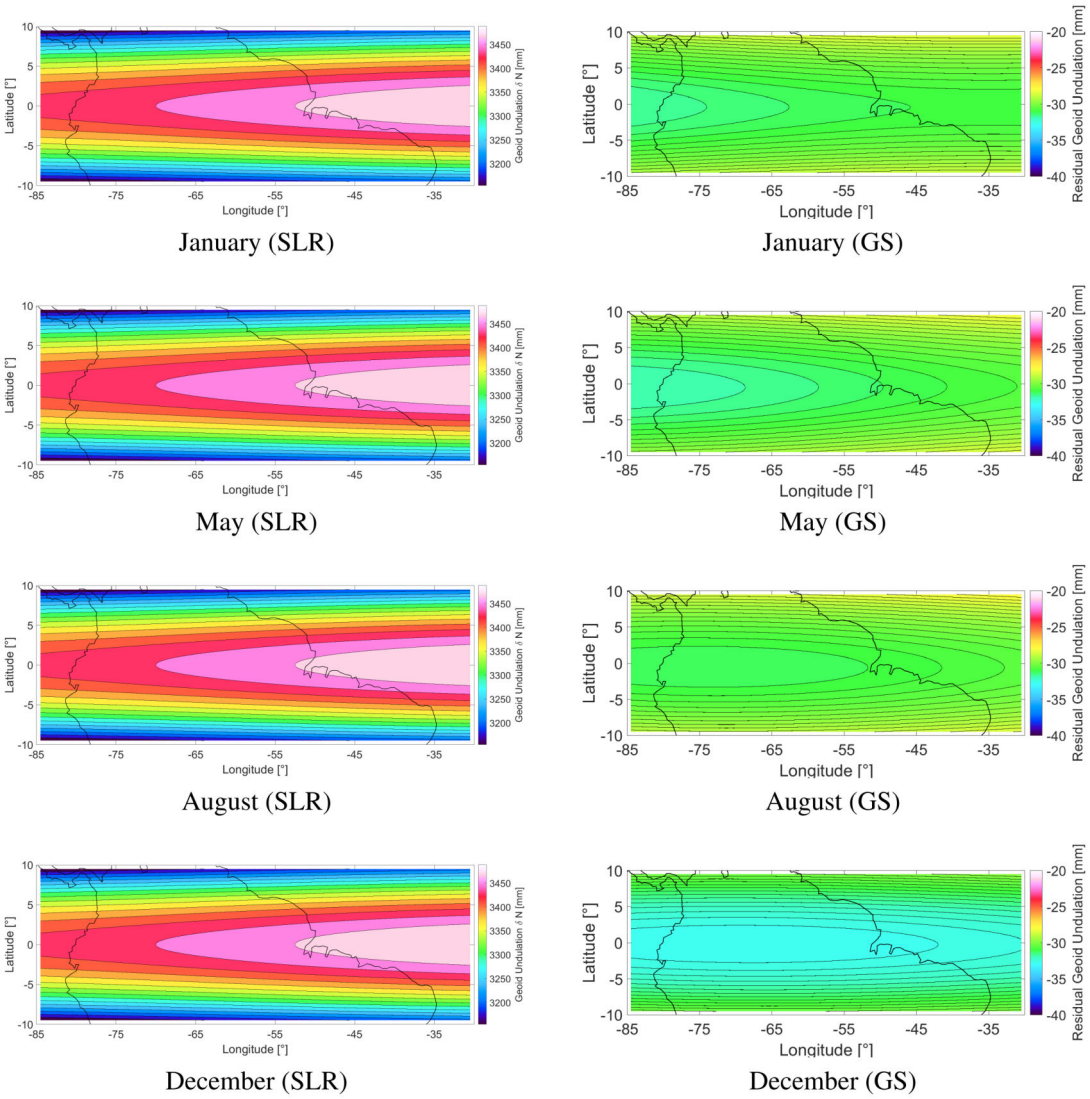

Figure 5.9: Geoid undulation fields derived from SLR observations and corresponding GRACE–SLR = GS residual fields for selected months in 2004 using the DDK2 filter and spherical harmonic degree combination ($N_2 - N_2$). Values are expressed in (mm).

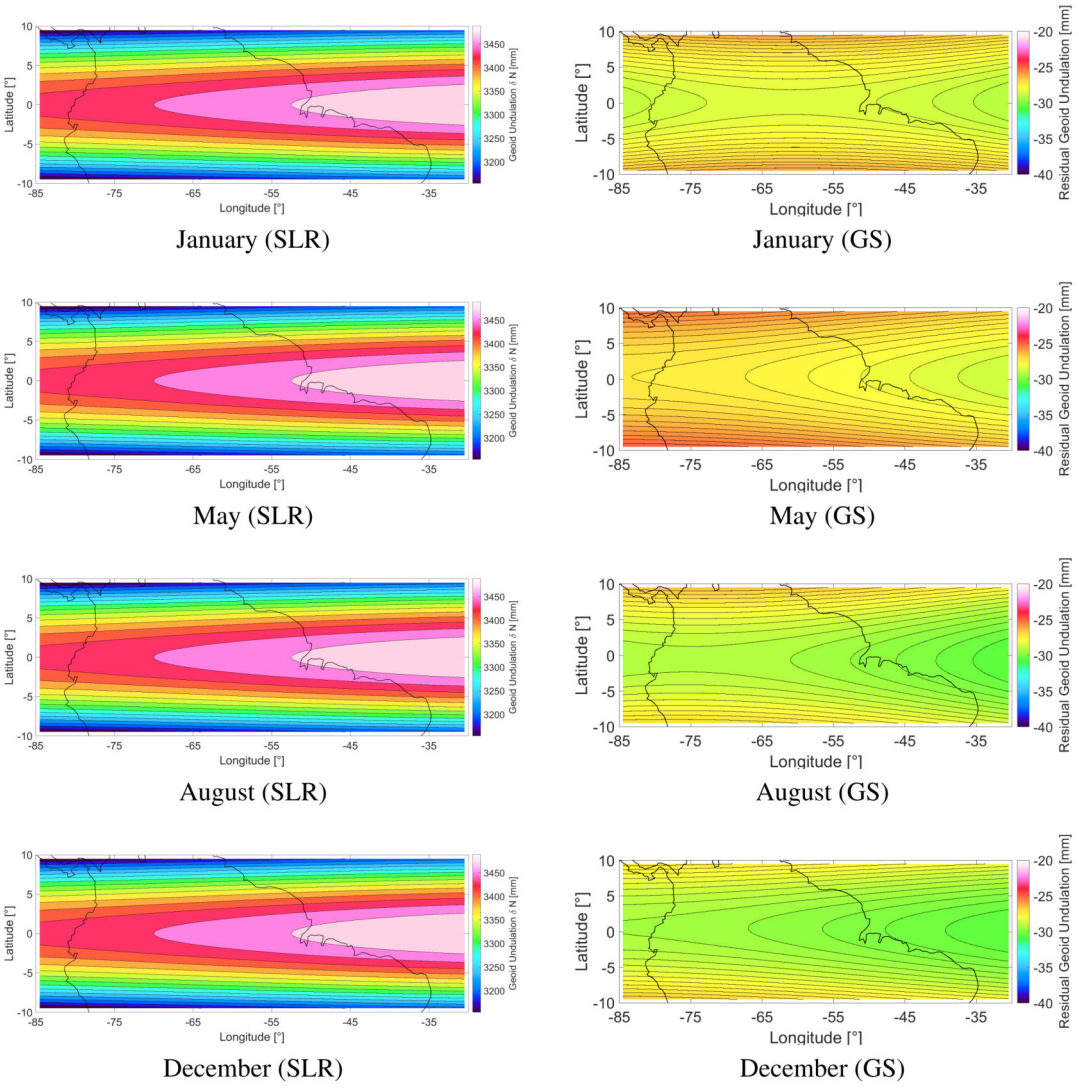

Figure 5.10: Geoid undulation fields derived from SLR observations and corresponding GRACE–SLR = GS residual fields for selected months in 2024 using the DDK2 filter and spherical harmonic degree combination ($N_2 - N_2$). Undulation values are expressed in (mm).

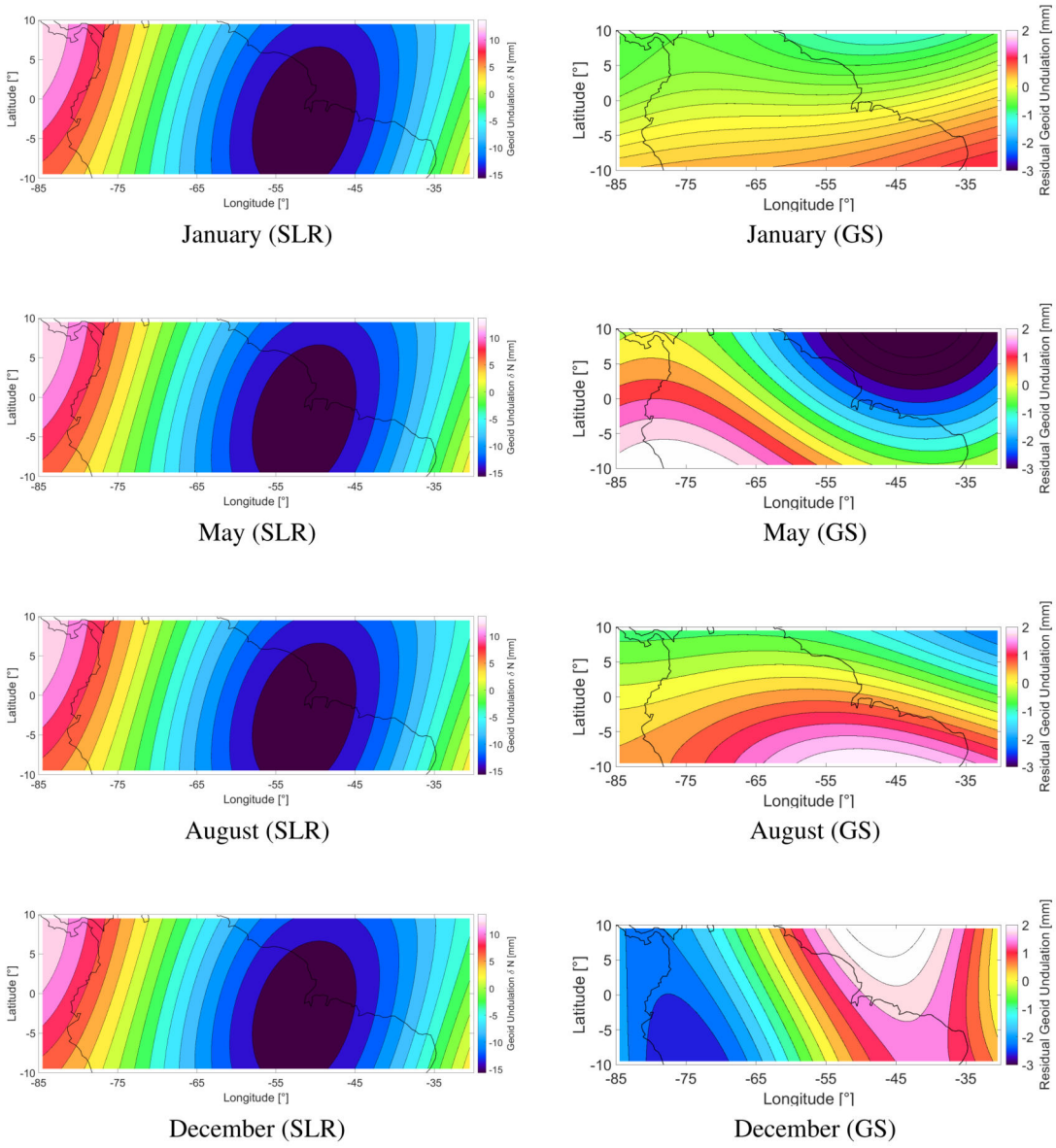

Figure 5.11: Geoid undulation fields derived from SLR observations and corresponding GRACE–SLR = GS residual fields for selected months in 2004 using DDK2 filter and the spherical harmonic degree combination ($N_5 - N_5$). Undulation values are expressed in (mm).

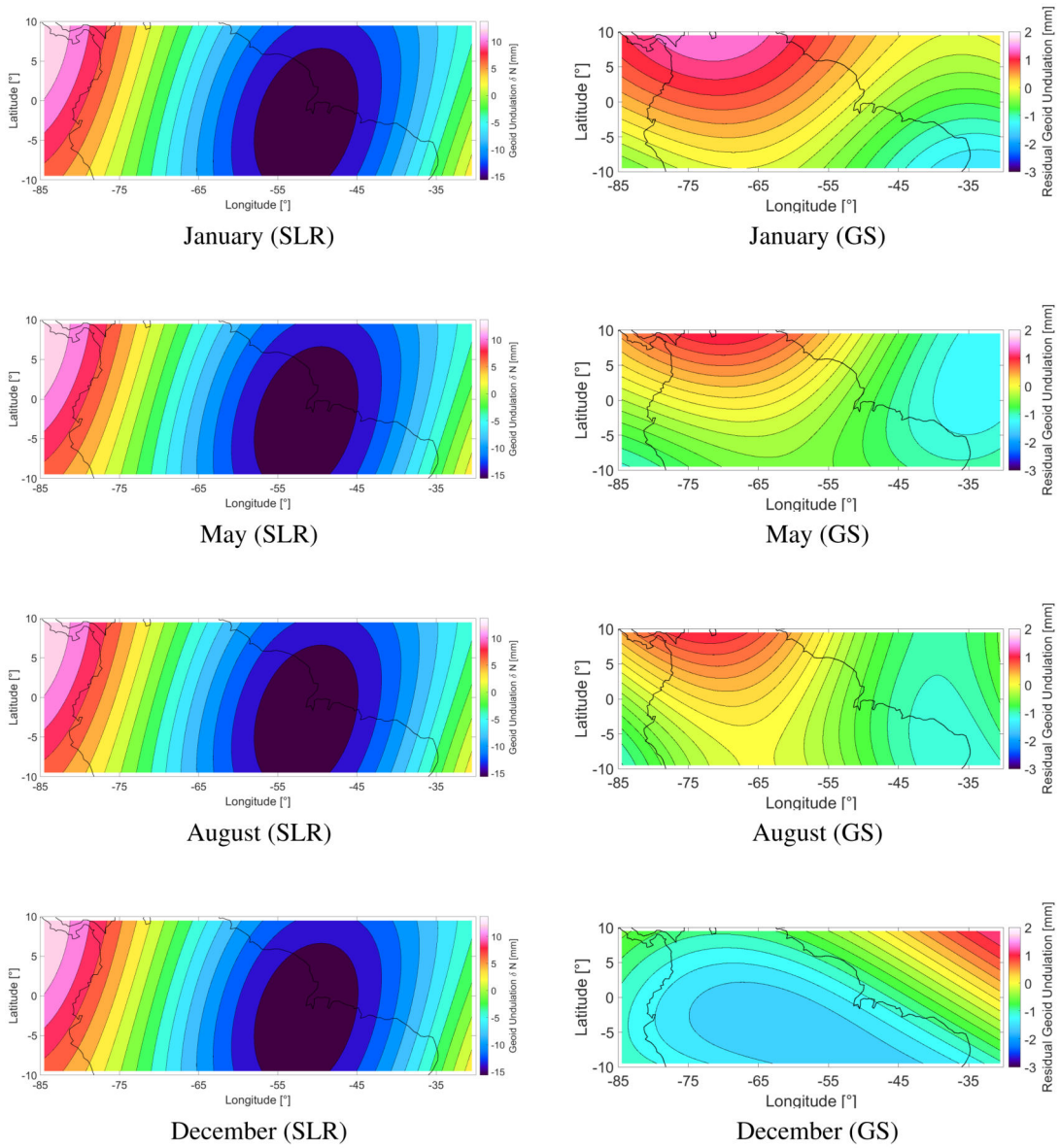

Figure 5.12: Geoid undulation fields derived from SLR observations and corresponding GRACE–SLR = GS residual fields for selected months in 2024 using DDK2 filter and the spherical harmonic degree combination($N_5 - N_5$). Undulation values are expressed in (mm).

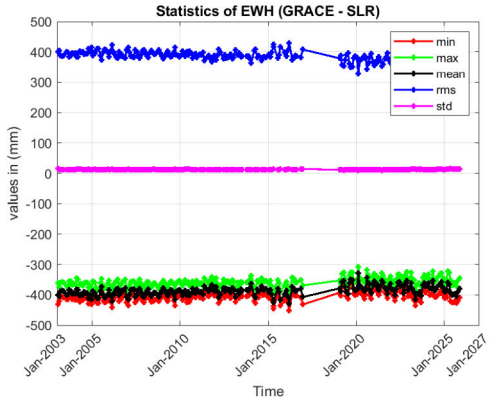

(a) $N_2 - N_2$ Spherical Harmonic Degree Combination

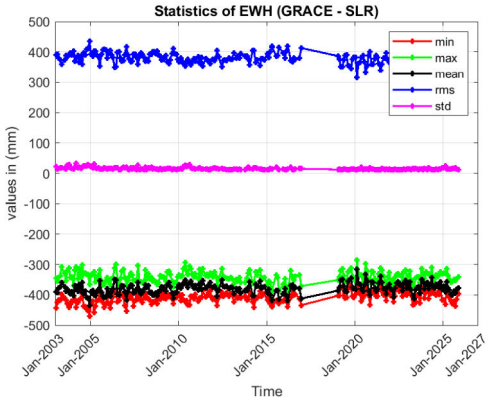

(b) $N_2 - N_3$ Spherical Harmonic Degree Combination

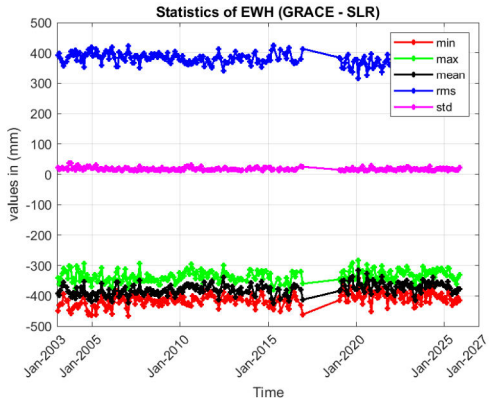

(c) $N_2 - N_4$ Spherical Harmonic Degree Combination

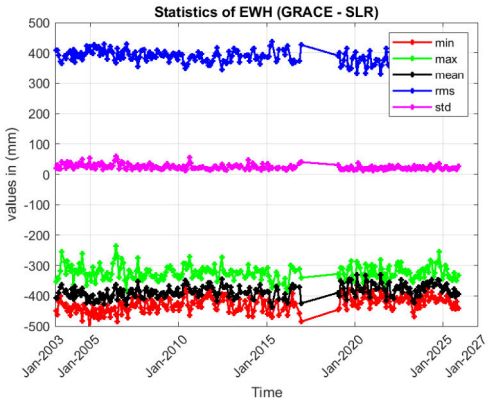

(d) $N_2 - N_5$ Spherical Harmonic Degree Combination

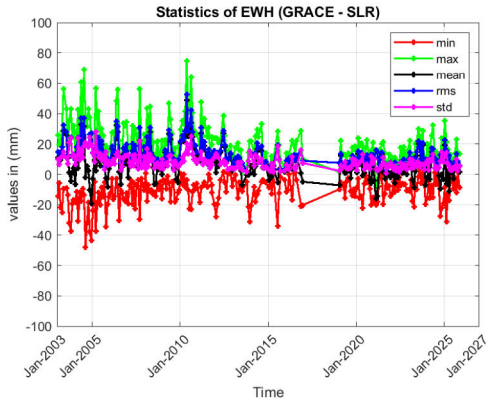

(e) $N_3 - N_3$ Spherical Harmonic Degree Combination

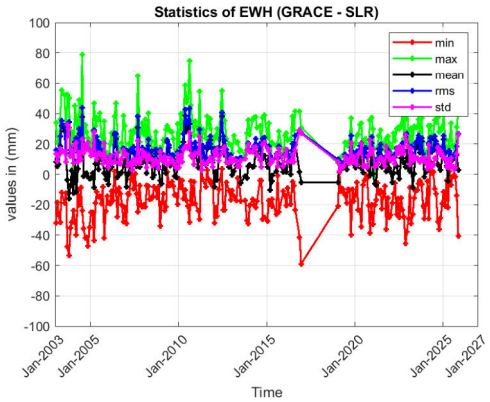

(f) $N_3 - N_4$ Spherical Harmonic Degree Combination

Figure 5.13: Statistical time series of GRACE–SLR terrestrial water storage (TWS) differences for different spherical harmonic degree combinations over the Amazon Basin (2003–2025) using DDK2 filter.

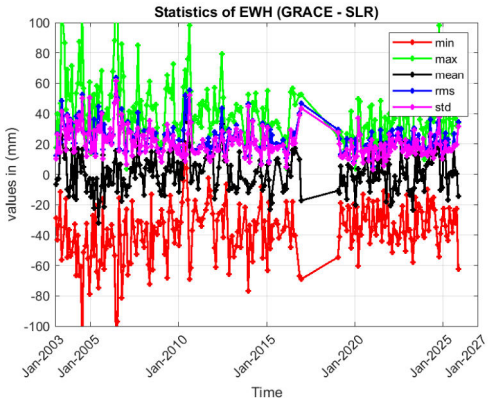

(g) $N_3 - N_5$ Spherical Harmonic Degree Combination

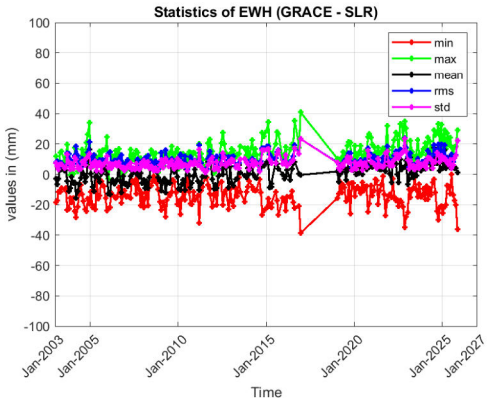

(h) $N_4 - N_4$ Spherical Harmonic Degree Combination

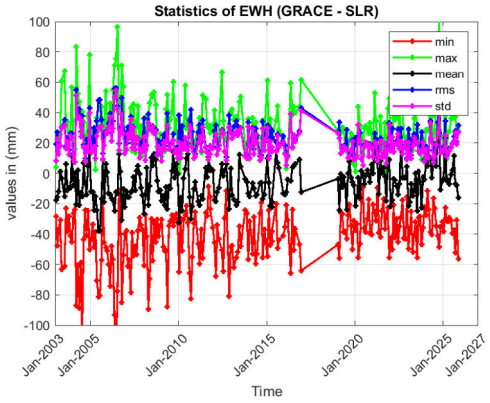

(i) $N_4 - N_5$ Spherical Harmonic Degree Combination

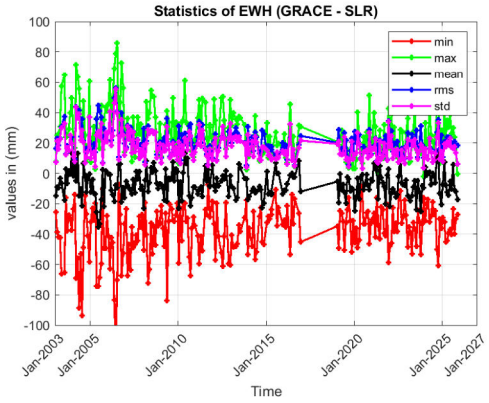

(j) $N_5 - N_5$ Spherical Harmonic Degree Combination

Figure 5.13: Statistical time series of GRACE–SLR terrestrial water storage (TWS) differences for different spherical harmonic degree combinations over the Amazon Basin (2003–2025) using DDK2 filter.

6 Conclusion and Outlook

This study investigated terrestrial water storage (TWS) variations over the Amazon Basin using GRACE and SLR datasets, with a particular focus on low-degree spherical harmonic components. The results show that both datasets provide a consistent representation of large-scale mass redistribution processes. The spatial analysis of equivalent water height, gravitational potential, and geoid undulation fields reveals smooth and coherent patterns dominated by long-wavelength signals.

The comparison between GRACE and SLR solutions indicates a strong agreement, especially for the lowest-degree components, where SLR provides higher accuracy. The GRACE–SLR difference fields remain relatively small and spatially consistent, suggesting that the discrepancies between the datasets are mainly systematic rather than random. The statistical analysis further supports these findings, showing stable behaviour of the residuals over the full study period from 2003 to 2025.

The influence of filtering was evaluated using both DDK2 and DDK8 filters. The results obtained from the two filtering approaches are largely similar, indicating that the dominant characteristics of the signals are controlled by low-degree components, keeping in mind, that the filer weights have same order of magnitude for very low degree. While DDK8 introduces weak smoothing, it does not significantly alter the overall spatial patterns or statistical behaviour. This confirms the robustness of the results with respect to the choice of filtering method.

Despite the overall consistency, some limitations remain. The analysis is restricted to low-degree spherical harmonic components, which primarily capture large-scale features while suppressing smaller-scale variations. In addition, potential sources of uncertainty such as signal leakage, model errors, and filtering effects are not fully accounted for.

Future work could extend the analysis by incorporating higher-degree coefficients as expressed in Save et al. (2016) to capture more detailed spatial variations, as well as applying advanced leakage correction techniques. A more detailed comparison with independent hydrological datasets could further improve the interpretation of the results. In addition, the inclusion of longer time series and updated GRACE-FO data would allow for a more comprehensive assessment of long-term trends in terrestrial water storage.

Acknowledgement

Firstly I would like to express my sincere gratitude to Dr.-Ing. Kurt Seitz for his continuous guidance and valuable support throughout this lab rotation. His expertise and patient supervision greatly contributed to improving both the research work and the overall quality of this report. In addition, his assistance with code modifications and troubleshooting helped me a lot. His encouragement and support have also strengthened my confidence for my future master's thesis.

I would also like to thank Prof. Dr.-Ing. Hansjörg Kutterer for designing the research task and clearly defining the objectives, which provided a strong basis for the successful completion of this work.

Furthermore, I gratefully acknowledge the support of the Geodätisches Institut (GIK) for providing the necessary facilities and resources required for this study. I also acknowledges ICGEM (ICGEM, 2026) for providing the gravity field data used in this research.

References

Chen, J. L., Wilson, C. R., and Tapley, B. D. (2010): The 2009 Amazon flood observed from space. *Geophysical Research Letters* 37:L09403. DOI: 10.1029/2010GL042433.

Cheng, M., Ries, J. C., and Tapley, B. D. (2013): Geocenter variations from analysis of SLR data. *Journal of Geodesy* 87(2):147–155.

GFZ (2026): GRACE-FO – Gravity Recovery and Climate Experiment Follow-On Mission. German Research Centre for Geosciences (GFZ). Accessed: 2026-04-06. URL: https://www.gfz.de/en/section/global-geomonitoring-and-gravity-field/projects/grace-fo-gravity-recovery-and-climate-experiment-follow-on-mission.

ICGEM (2026): International Centre for Global Earth Models (ICGEM): Gravity field and GRACE/GRACE-FO products hosted at the German Research Centre for Geosciences (GFZ). Accessed: 2026-04-06. URL: https://icgem.gfz-potsdam.de/.

Kusche, J. (2007): Approximate decorrelation and non-isotropic smoothing of time-variable GRACE-type gravity field models. *Journal of Geodesy* 81(11):733–749. DOI: 10.1007/s00190-007-0143-3.

Kusche, J., Schmidt, R., Petrovic, S., and Rietbroek, R. (2009): Decorrelated GRACE time-variable gravity solutions by GFZ, and their validation using a hydrological model. *Journal of Geodesy* 83:903–913. DOI: 10.1007/s00190-009-0308-3.

Moritz, H. (1980): Geodetic Reference System 1980. *Bulletin Géodésique* 54(3):395–405. DOI: 10.1007/BF02521480.

Pearlman, M. R., Degnan, J. J., and Bosworth, J. M. (2002): The international laser ranging service. *Advances in space research* 30(2):135–143.

Save, H., Bettadpur, S., and Tapley, B. D. (2016): High resolution CSR GRACE RL05 mascons. *J. Geophys. Res. Solid Earth* 121:7547–7569. DOI: 10.1002/2016JB013007.

Swenson, S., Chambers, D., and Wahr, J. (2008): Estimating geocenter variations from a combination of GRACE and ocean model output. *Journal of Geophysical Research: Solid Earth* 113(B8):B08410. DOI: 10.1029/2007JB005338.

Swenson, S. and Wahr, J. (2006): Post-processing removal of correlated errors in GRACE data. *Geophysical Research Letters* 33(8):L08402. DOI: 10.1029/2005GL025285.

Tapley, B. D., Bettadpur, S., Watkins, M., and Reigber, C. (2004): The gravity recovery and climate experiment: Mission overview and early results. *Geophysical Research Letters* 31(9):1–4. DOI: 10.1029/2004GL019920.

Wahr, J., Molenaar, M., and Bryan, F. (1998): Time variability of the Earth's gravity field: Hydrological and oceanic effects and their possible detection using GRACE. *Journal of Geophysical Research: Solid Earth* 103(B12):30205–30229.

Wu, X., Collilieux, X., Altamimi, Z., et al. (2011): Accuracy of the International Terrestrial Reference Frame origin and Earth expansion. *Geophysical Research Letters* 38:L13304.

Appendix

A Appendix

This appendix presents the GRACE–SLR terrestrial water storage (TWS) results obtained using the DDK8 decorrelation filter. The spatial distributions, temporal variability, and statistical characteristics are generally consistent with the corresponding DDK2-filtered results discussed in Section 5. Since the analysis is dominated by low-degree spherical harmonic components representing long-wavelength gravity signals, the stronger smoothing introduced by DDK2 does not significantly alter the overall behaviour of the derived fields.

Table A.1: Statistical summary of GRACE–SLR TWS differences for selected spherical harmonic degree combinations. Values are in (mm).

Degree Combination	Min	Max	Mean	RMS	STD
2–2	-452.113	-307.337	-329.387	429.370	15.975
2–3	-470.178	-285.062	-315.674	435.385	33.091
2–4	-466.837	-283.379	-315.762	425.201	37.518
2–5	-509.869	-235.884	-330.721	438.068	59.038
3–3	-48.057	74.804	48.734	52.681	27.806
3–4	-59.078	78.734	38.458	44.068	33.041
3–5	-117.026	124.253	51.588	63.478	61.547
4–4	-38.727	40.941	17.574	23.918	23.421
4–5	-121.943	103.184	26.691	56.136	54.771
5–5	-114.975	85.880	13.570	56.099	55.583

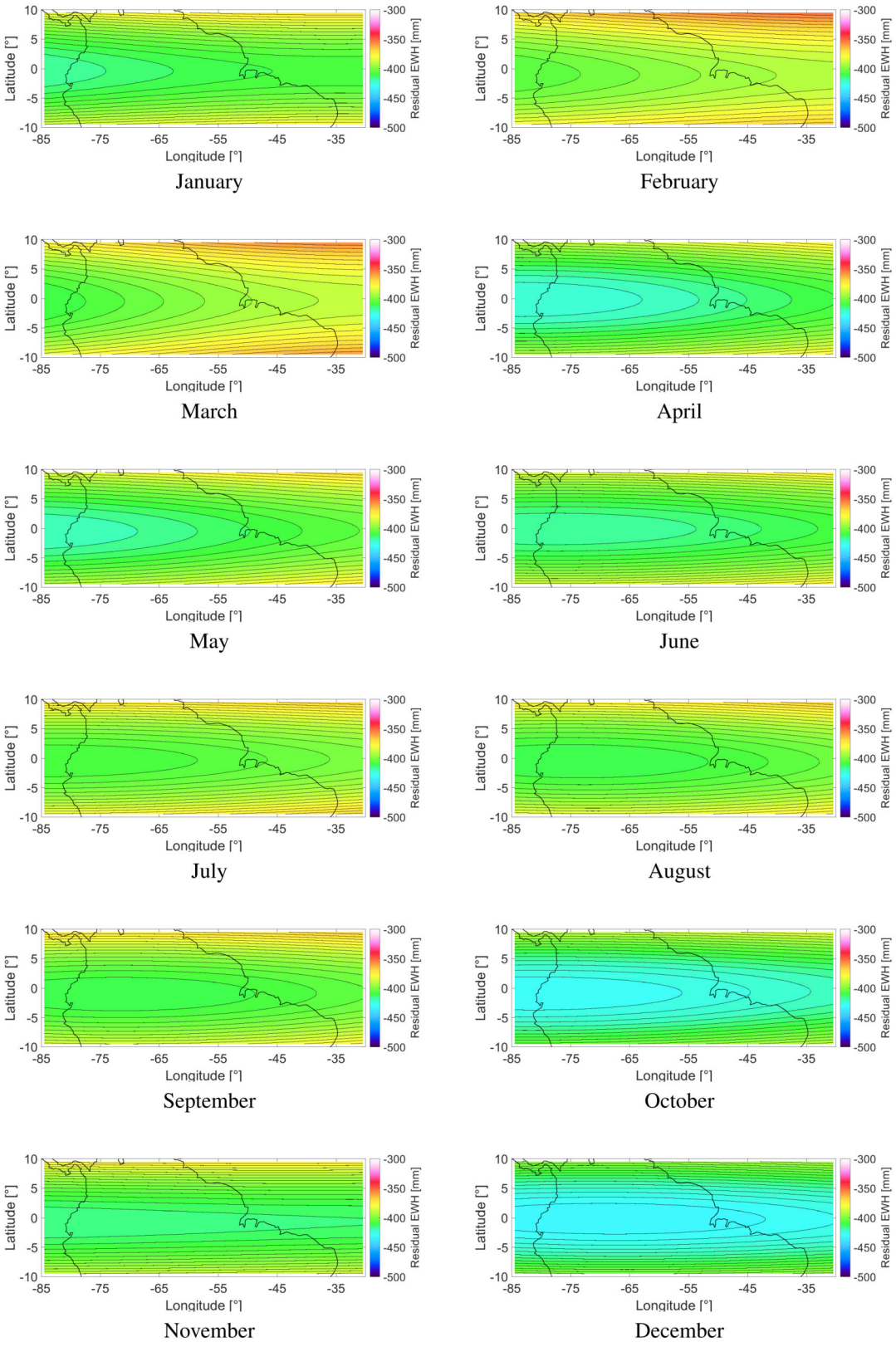

Figure A.1: Monthly GRACE–SLR residual equivalent water height (EWH) maps over the Amazon Basin for the year 2004 using DDK8 filter and the spherical harmonic degree combination ($N_2 - N_2$). The values range from -500 mm to -300 mm

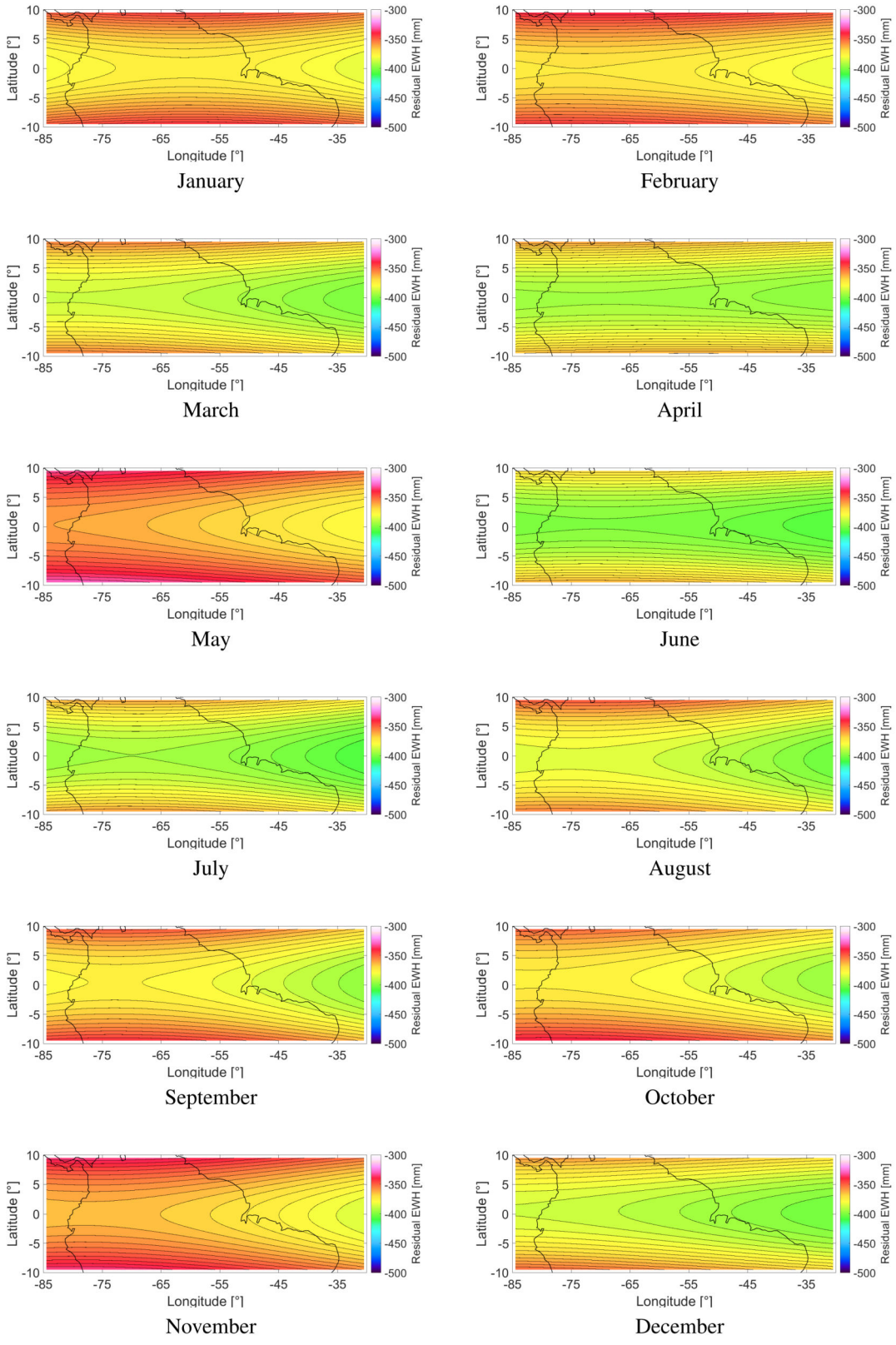

Figure A.2: Monthly GRACE–SLR residual equivalent water height (EWH) maps over the Amazon Basin for the year 2024 using DDK8 filter and the spherical harmonic degree combination ($N_2 - N_2$). The values range from -500 mm to -300 mm

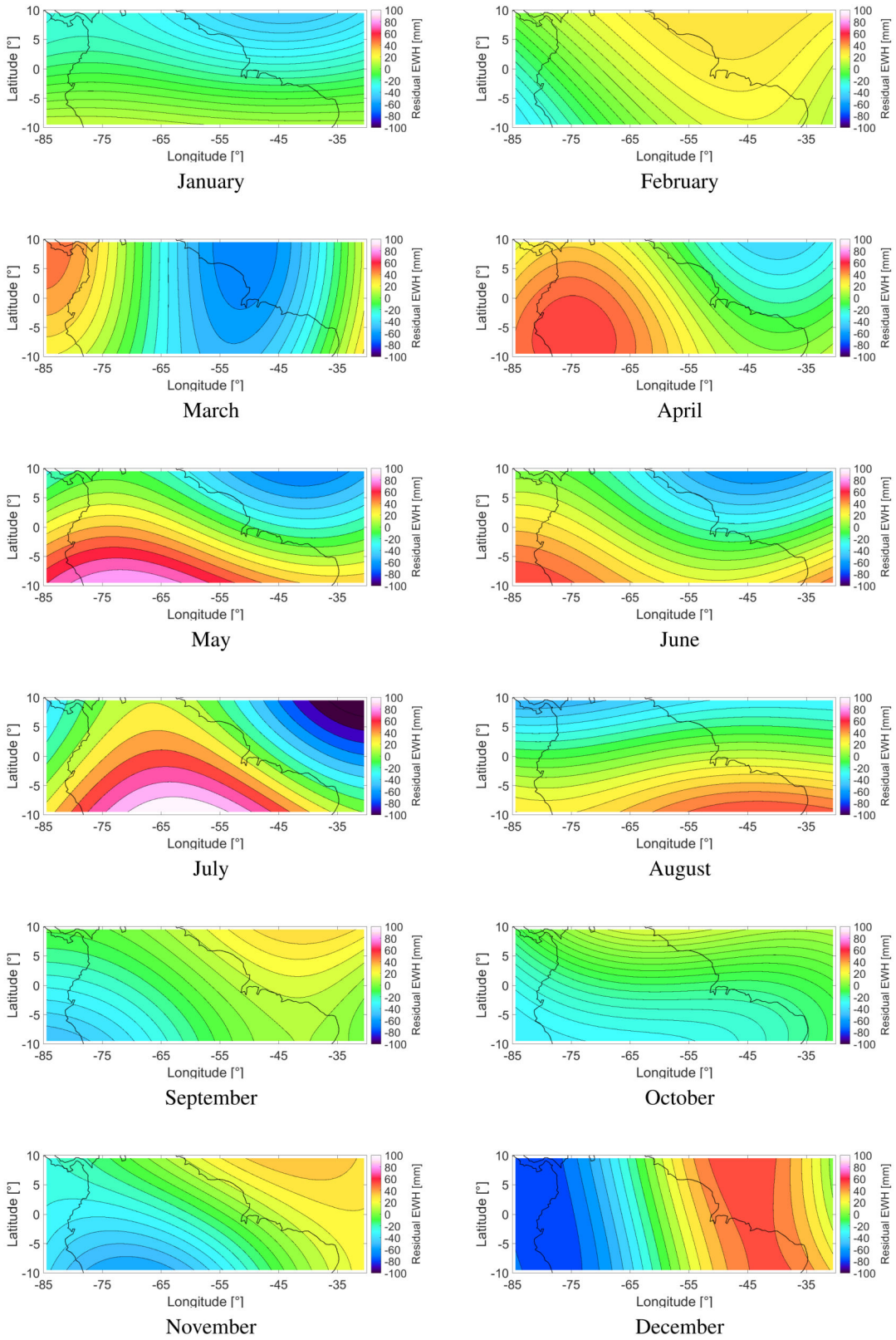

Figure A.3: Monthly GRACE–SLR residual equivalent water height (EWH) maps over the Amazon Basin for the year 2004 using DDK8 filter and the spherical harmonic degree combination ($N_3 - N_5$). The values range from -100 mm to 100 mm

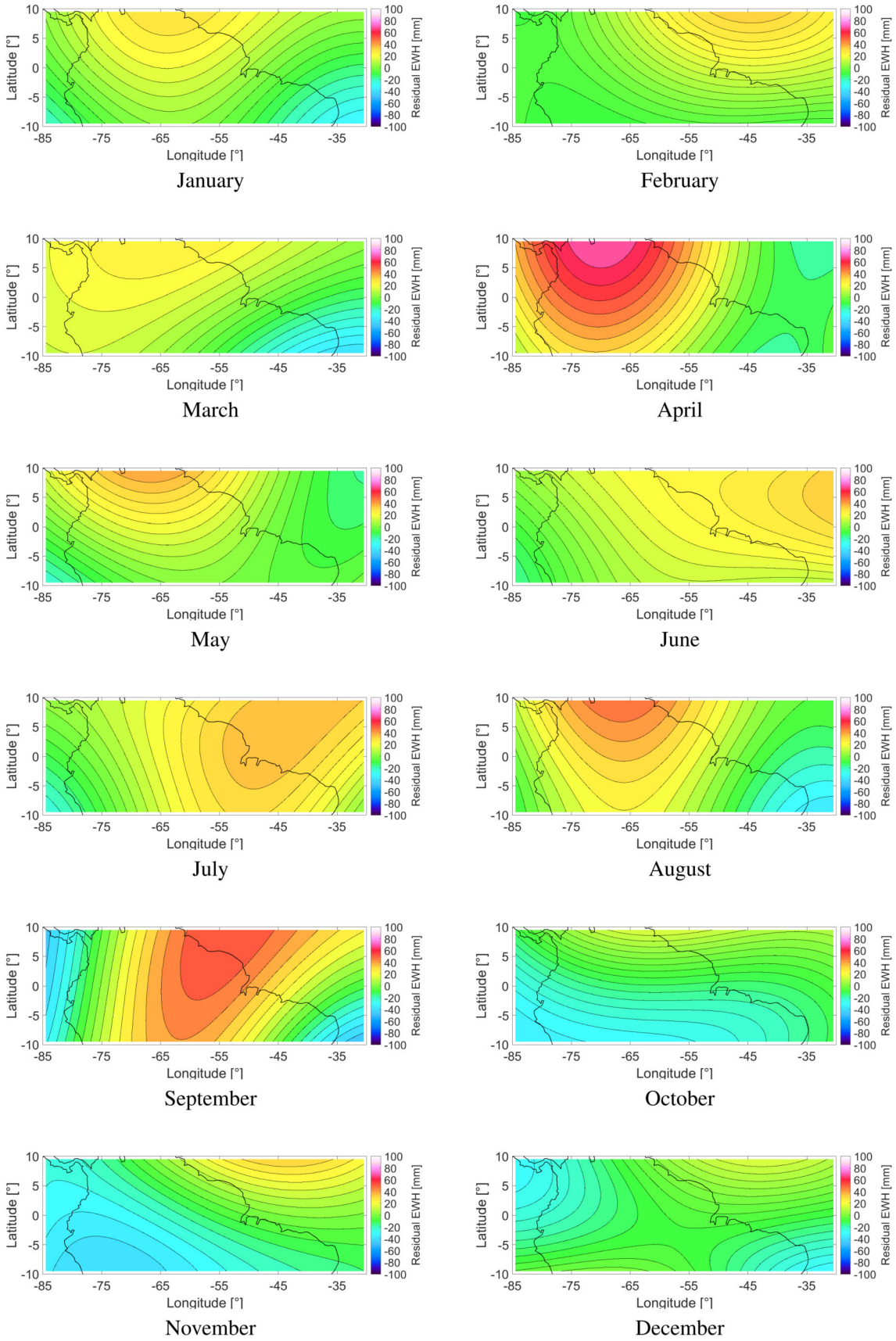

Figure A.4: Monthly GRACE–SLR residual equivalent water height (EWH) maps over the Amazon Basin for the year 2024 using DDK8 filter and the spherical harmonic degree combination ($N_3 - N_5$). The values range from -100 mm to 100 mm

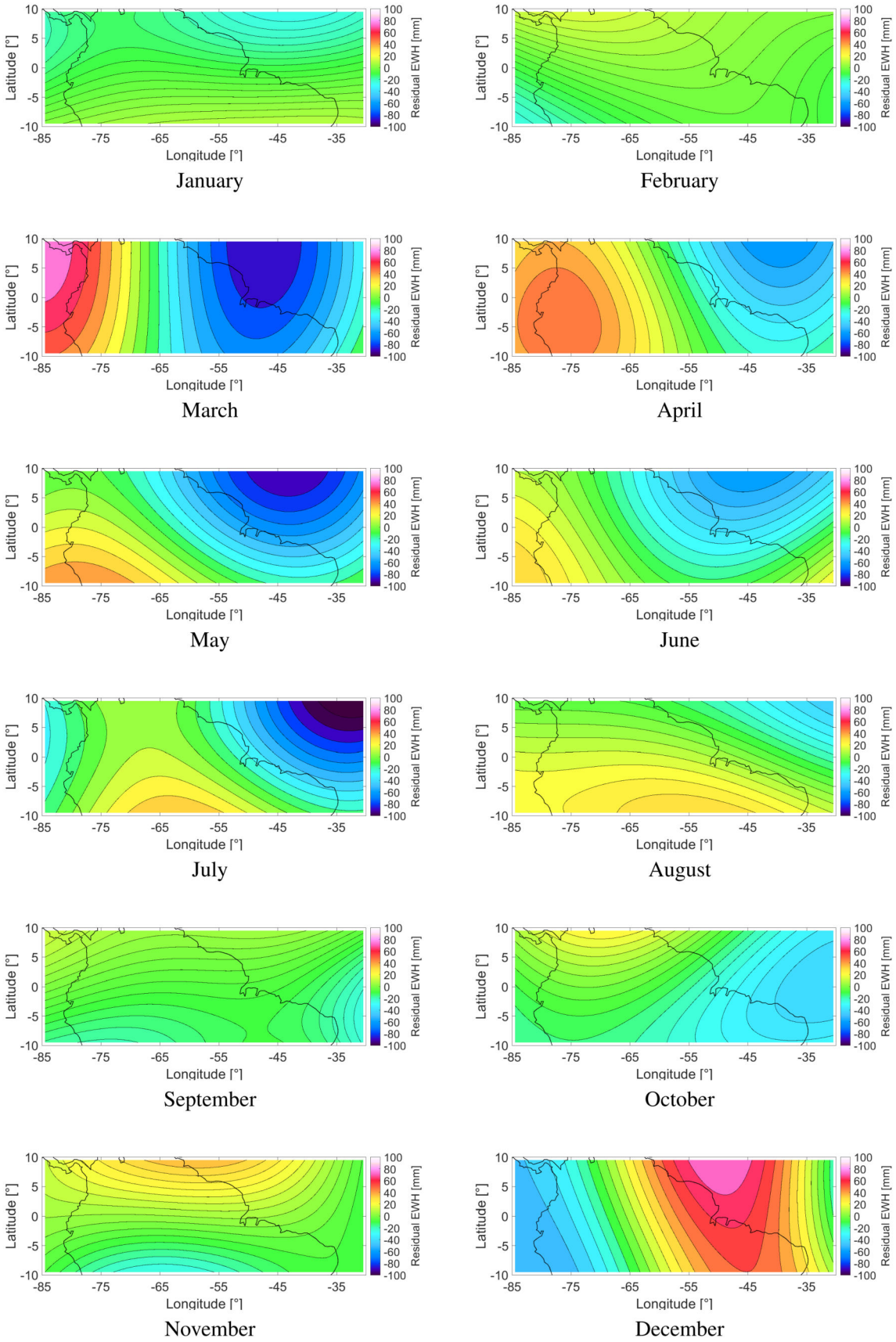

Figure A.5: Monthly GRACE–SLR residual equivalent water height (EWH) maps over the Amazon Basin for the year 2004 using DDK8 filter and the spherical harmonic degree combination ($N_4 - N_5$). The values range from -100 mm to 100 mm

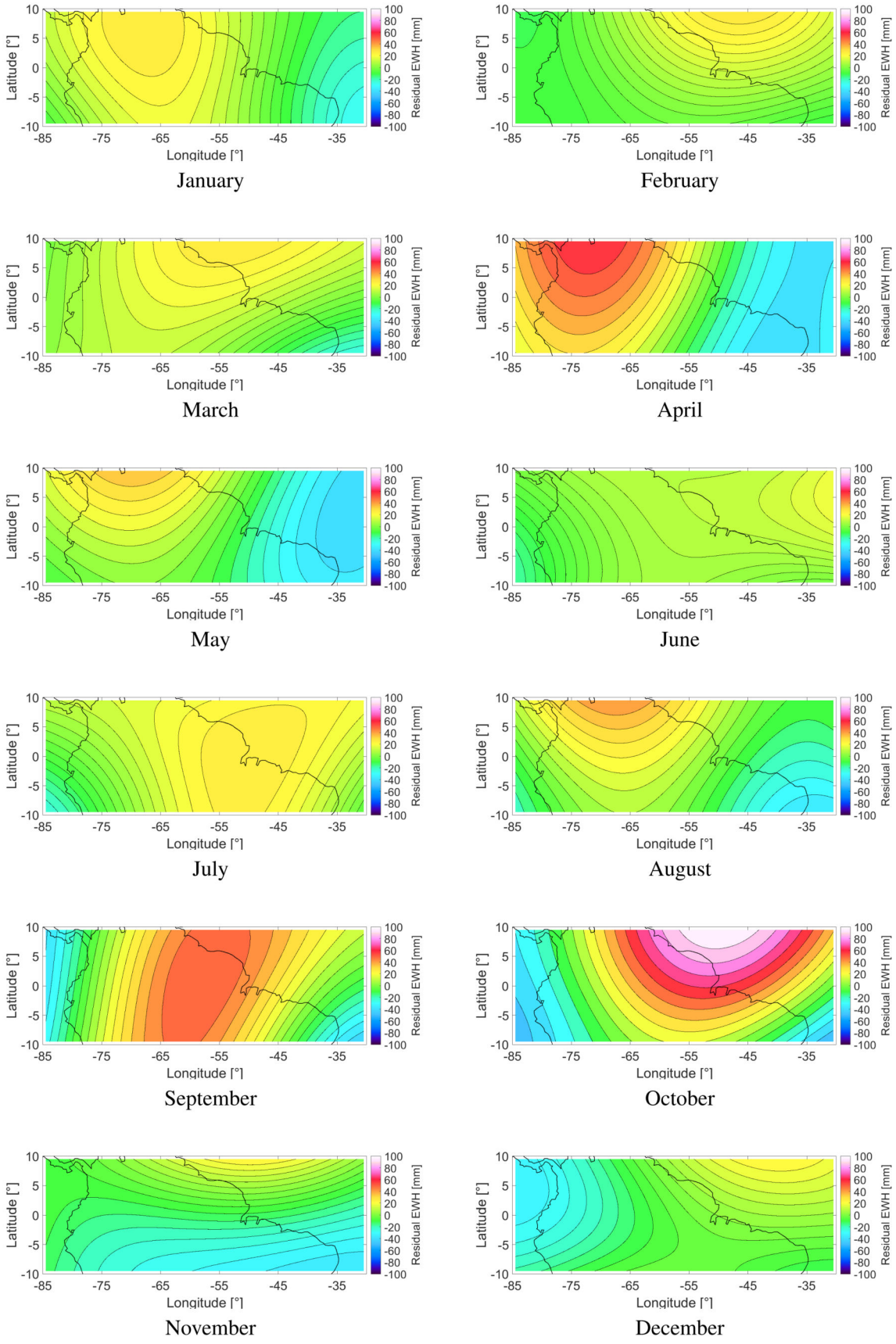

Figure A.6: Monthly GRACE–SLR residual equivalent water height (EWH) maps over the Amazon Basin for the year 2024 using DDK8 filter and the spherical harmonic degree combination ($N_4 - N_5$). The values range from -100 mm to 100 mm

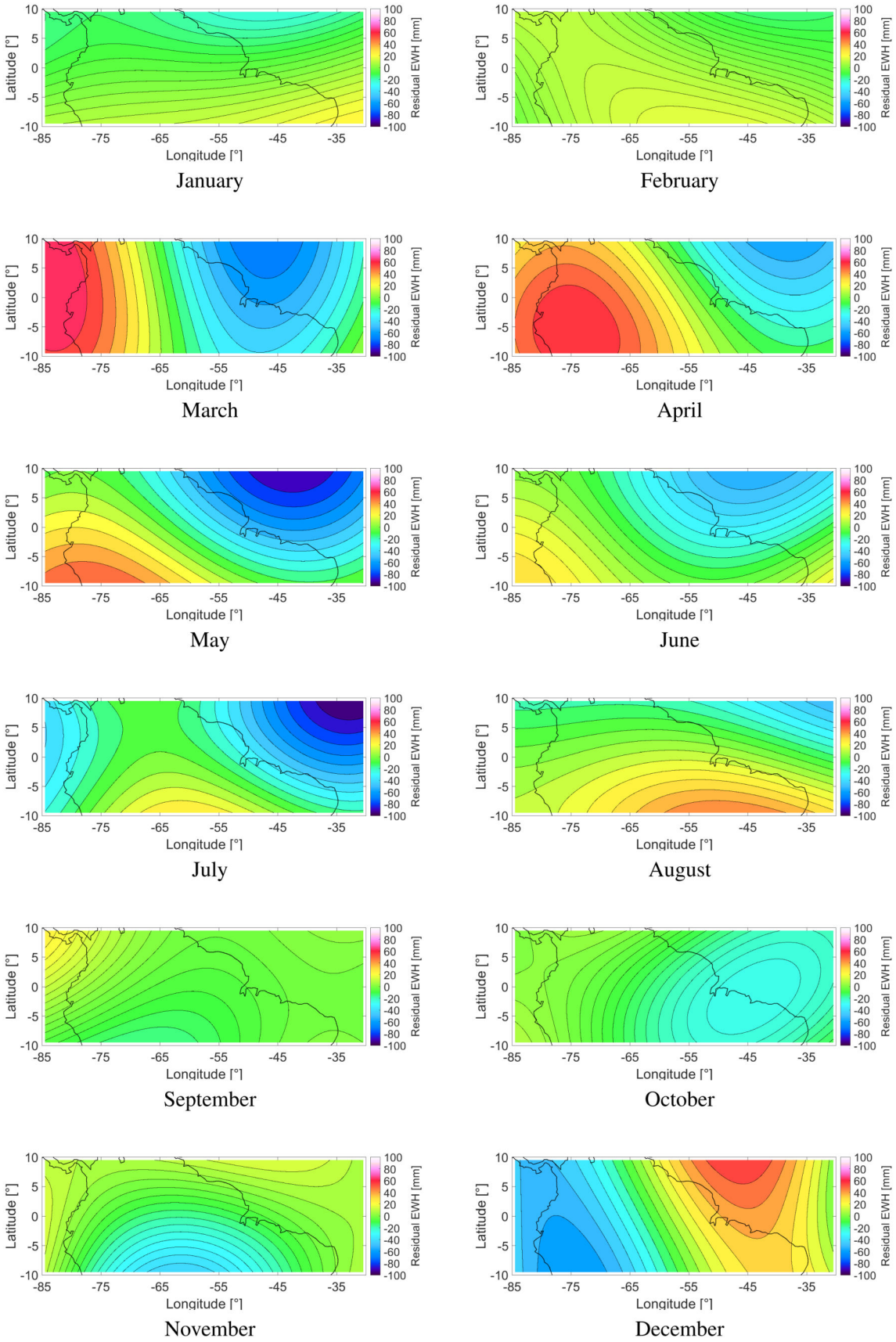

Figure A.7: Monthly GRACE–SLR residual equivalent water height (EWH) maps over the Amazon Basin for the year 2004 using DDK8 filter and the spherical harmonic degree combination ($N_5 - N_5$). The values range from -100 mm to 100 mm

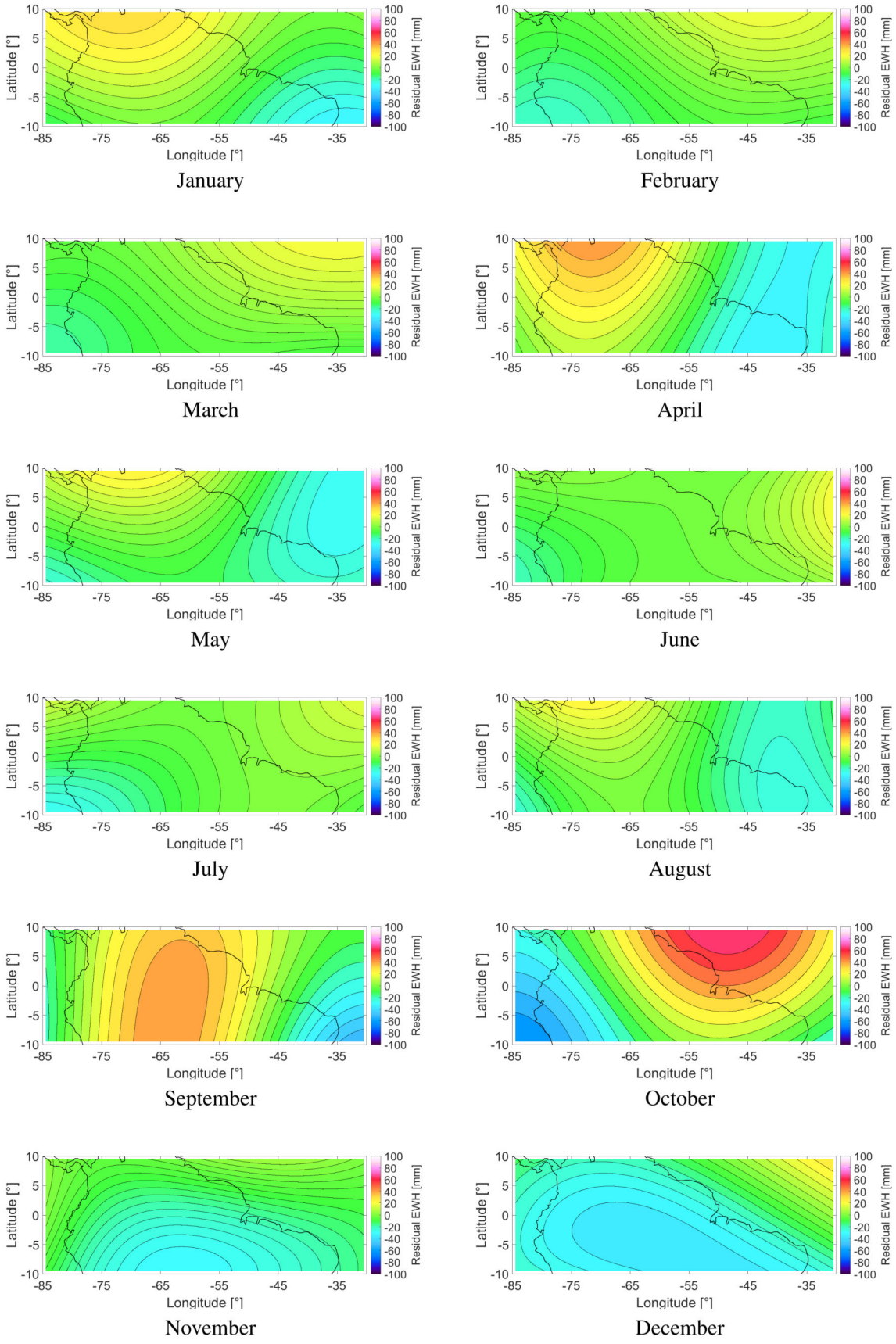

Figure A.8: Monthly GRACE–SLR residual equivalent water height (EWH) maps over the Amazon Basin for the year 2024 using DDK8 filter and the spherical harmonic degree combination ($N_5 - N_5$). The values range from -100 mm to 100 mm

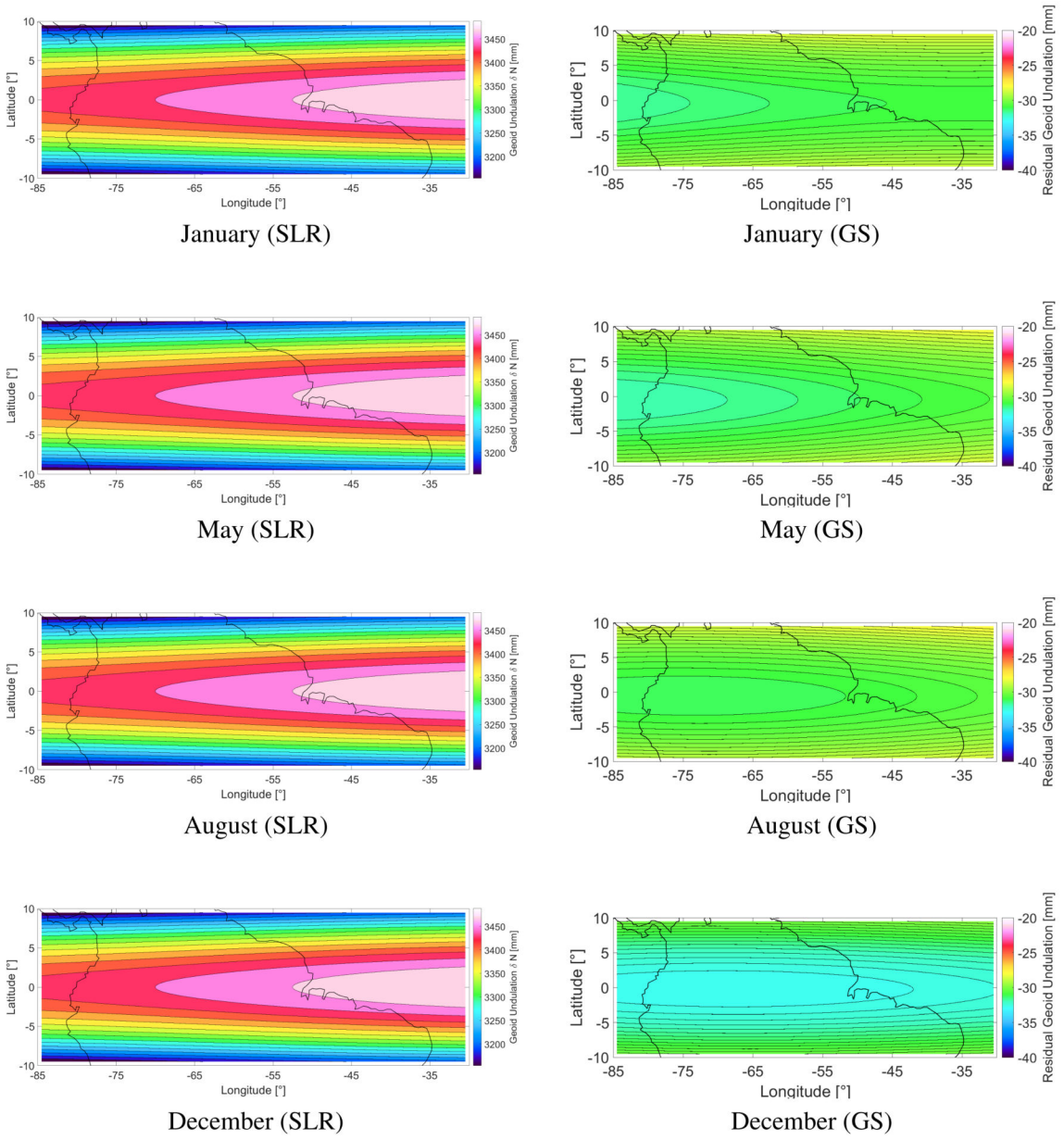

Figure A.9: Geoid undulation fields derived from SLR observations and corresponding GRACE–SLR = GS residual fields for selected months in 2004 using DDK 8 filter and the spherical harmonic degree combination ($N_2 - N_2$). Undulation values are expressed in (mm).

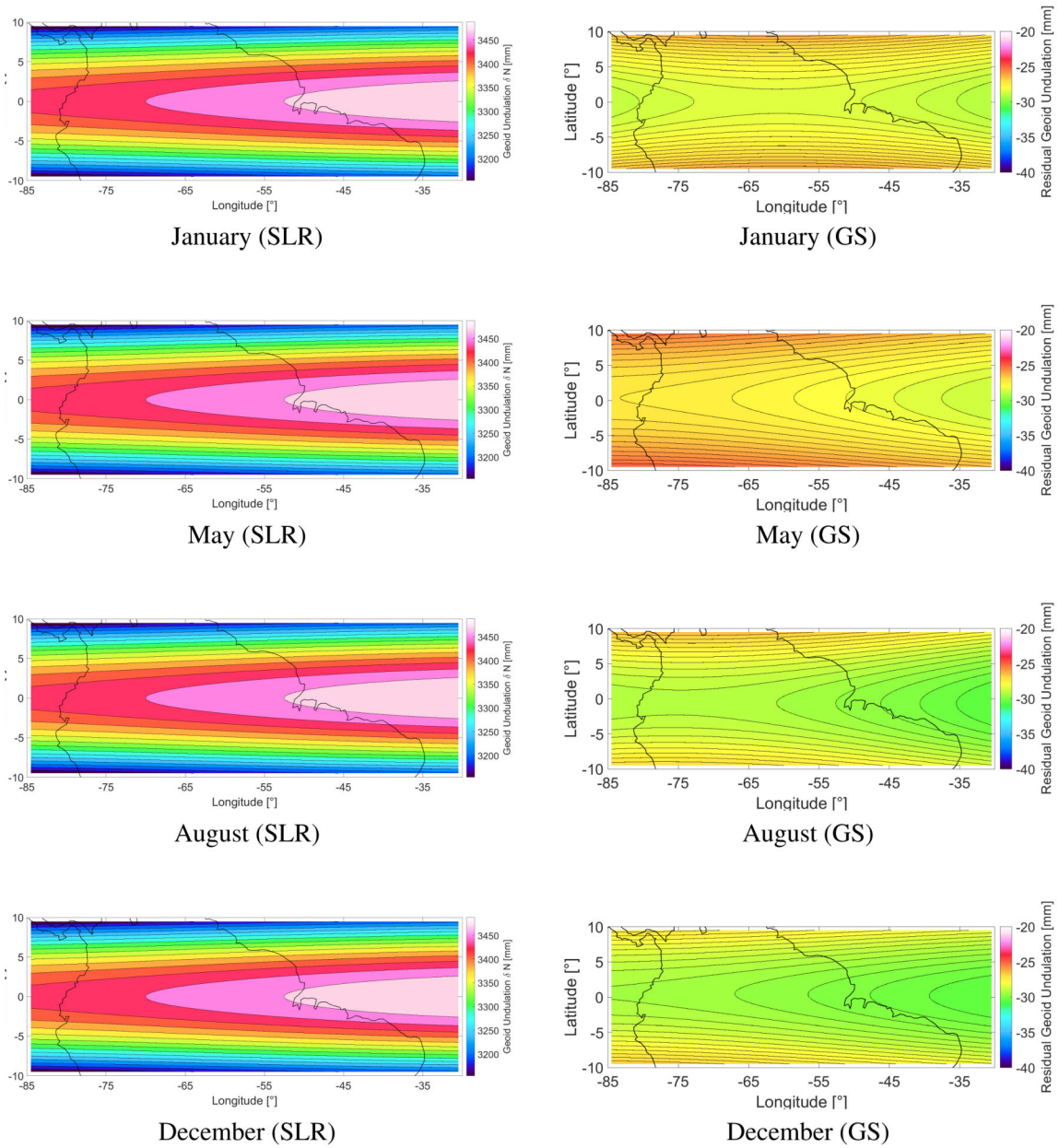

Figure A.10: Geoid undulation fields derived from SLR observations and corresponding GRACE–SLR = GS residual fields for selected months in 2024 using DDK8 filter and the spherical harmonic degree combination ($N_2 - N_2$). Undulation values are expressed in (mm).

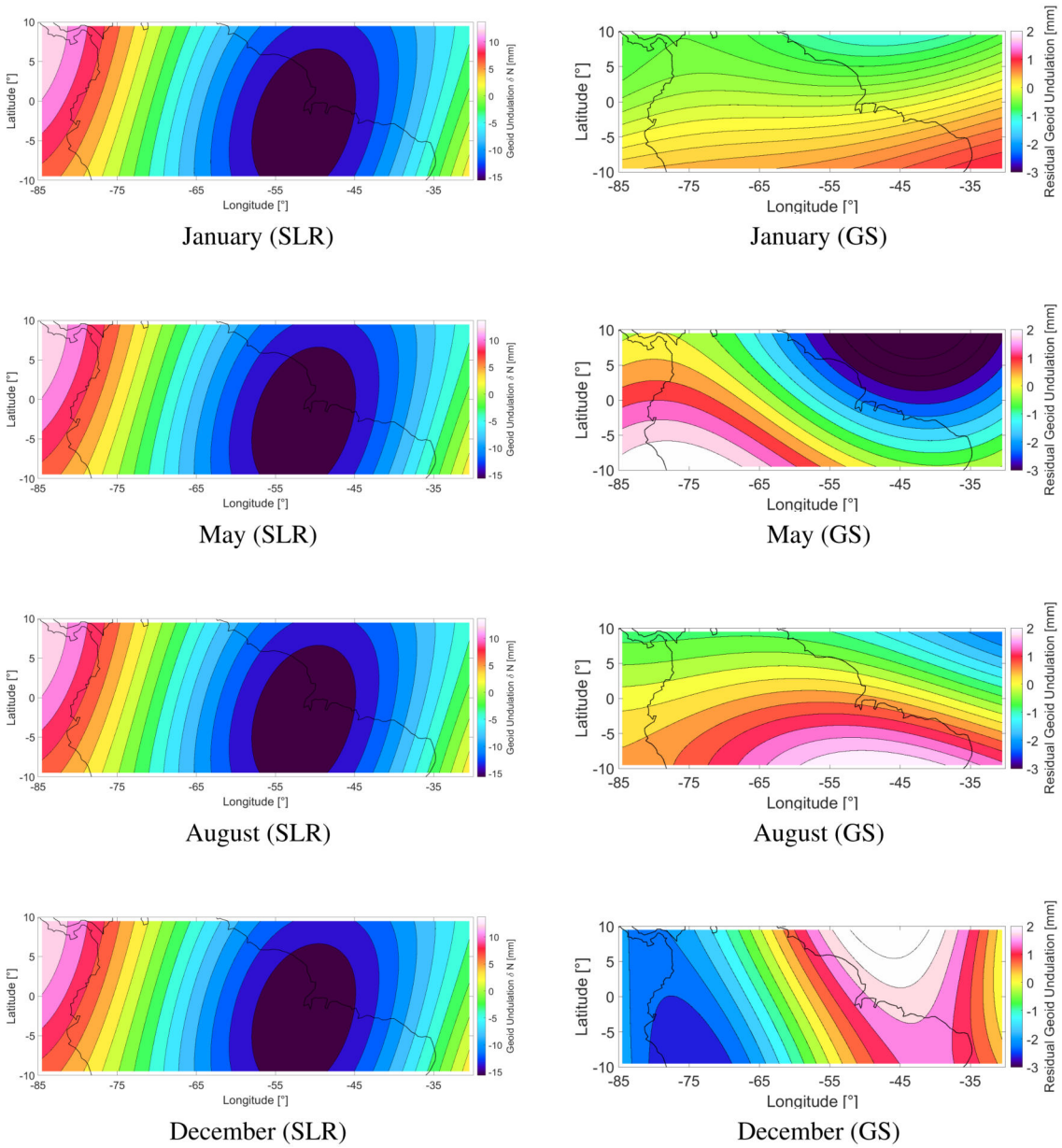

Figure A.11: Geoid undulation fields derived from SLR observations and corresponding GRACE–SLR = GS residual fields for selected months in 2004 using the DDK8 filter and the spherical harmonic degree combination ($N_5 - N_5$). Undulation values are expressed in (mm).

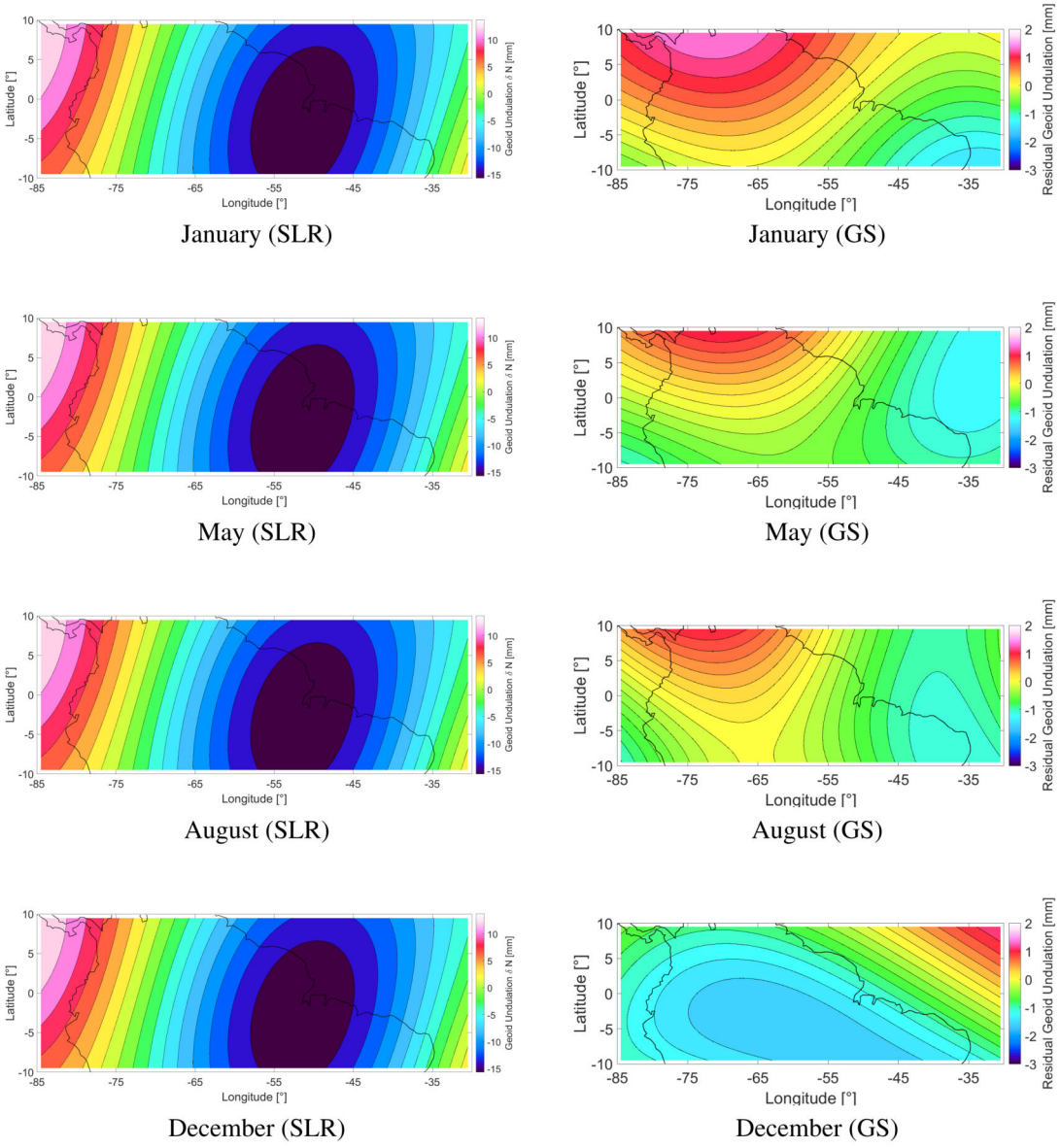

Figure A.12: Geoid undulation fields derived from SLR observations and corresponding GRACE–SLR = GS residual fields for selected months in 2024 using DDk8 filter and the spherical harmonic degree combination($N_5 - N_5$). Undulation values are expressed in (mm).

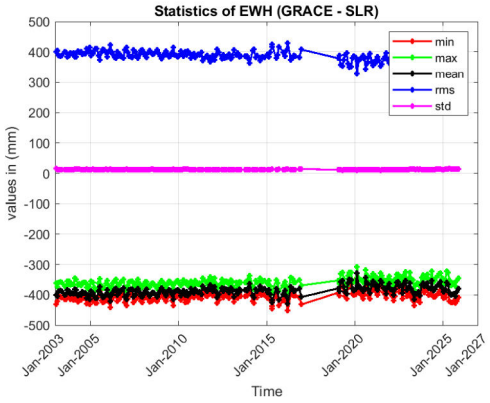

(a) $N_2 - N_2$ Spherical Harmonic Degree Combination

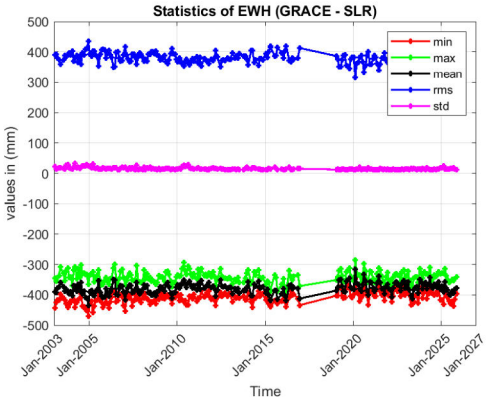

(b) $N_2 - N_3$ Spherical Harmonic Degree Combination

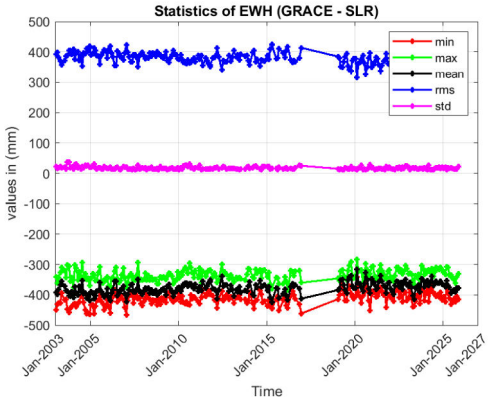

(c) $N_2 - N_4$ Spherical Harmonic Degree Combination

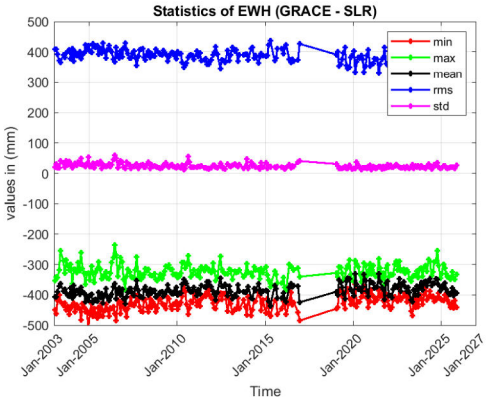

(d) $N_2 - N_5$ Spherical Harmonic Degree Combination

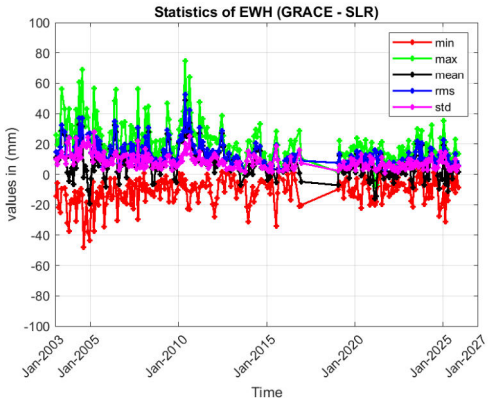

(e) $N_3 - N_3$ Spherical Harmonic Degree Combination

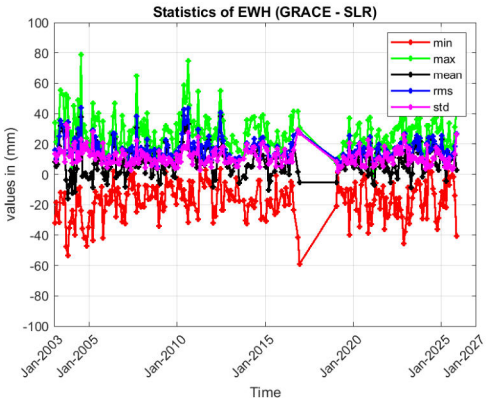

(f) $N_3 - N_4$ Spherical Harmonic Degree Combination

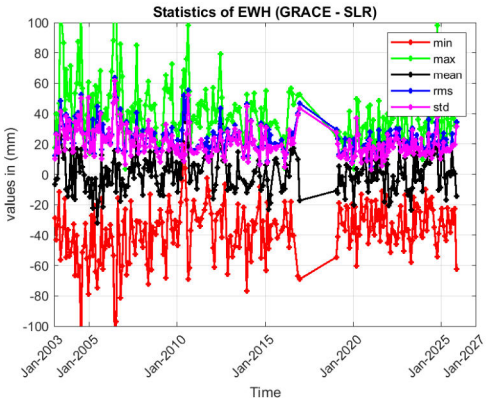

(g) $N_3 - N_5$ Spherical Harmonic Degree Combination

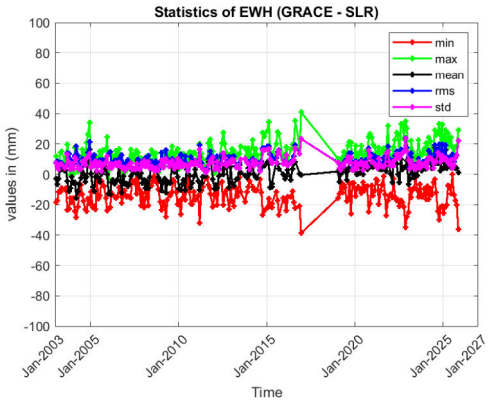

(h) $N_4 - N_4$ Spherical Harmonic Degree Combination

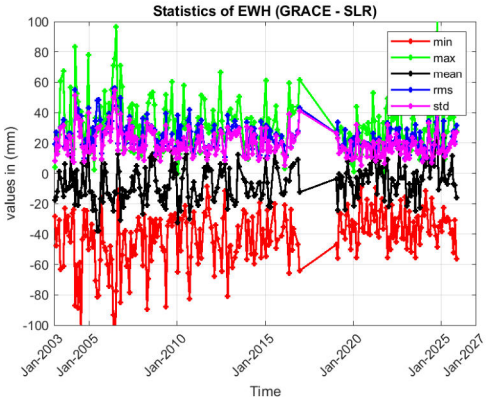

(i) $N_4 - N_5$ Spherical Harmonic Degree Combination

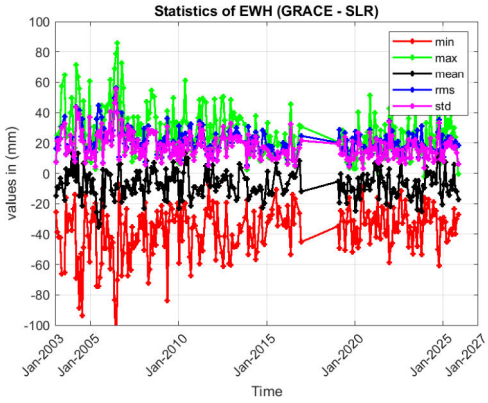

(j) $N_5 - N_5$ Spherical Harmonic Degree Combination

Figure A.13: Statistical time series of GRACE–SLR terrestrial water storage (TWS) differences for different spherical harmonic degree combinations over the Amazon Basin (2003–2025) using DDK8 filter.

Impact of Himalayan Glacier Melt on Groundwater Storage in Northern India
– A GRACE and GLDAS Based Study from 2003 to 2016 –

Shincy Sebastian[1]

1 Remote Sensing and Geoinformatics Master of Science (M.Sc.), KIT, Germany
E-Mail: ugipb@student.kit.edu

Abstract

This study shows that combining GRACE-derived Terrestrial Water Storage (TWS) anomalies with GLDAS-based hydrological components provides a robust assessment of long-term groundwater storage dynamics in the Western Himalaya. GRACE, as the first satellite system capable of globally quantifying TWS variations, reveals persistent negative water storage trends across key Himalayan basins during the study period. After applying destriping and filtering to reduce correlated noise, the GRACE signal indicates that several regions—notably the downstream plains of Himachal Pradesh, Jammu & Kashmir, and parts of Uttarakhand—exhibit a measurable decline in TWS, strongly indicative of sustained groundwater depletion.

GLDAS datasets for soil moisture, snow water, and runoff corroborate that seasonal hydrological processes alone do not fully account for the observed TWS decline. Winter snow accumulation and monsoon-driven recharge show substantial interannual variability, yet the long-term GRACE signal consistently points to a net loss of stored water, with groundwater identified as the primary depleted component. This pattern aligns with rising water demand, reduced glacier mass balance, and shifting monsoon timing, collectively weakening natural recharge.

Overall, the results indicate significant stress on groundwater storage in the Western Himalaya, driven by climatic and anthropogenic factors. The transition from winter freeze to spring melt and the strong monsoon response remain evident in the TWS cycle, but long-term losses reflect structural depletion rather than seasonal fluctuations. These findings underscore the importance of sustained satellite gravimetry; future GRACE successors are expected to adopt architectures that minimize correlated errors and enable more precise groundwater monitoring in vulnerable mountain regions. Continuous observations will be essential for developing adaptive, basin-scale water-resource management strategies in the Himalaya, where millions rely on groundwater fed by snow and glacier melt.

Keywords GRACE · GLDAS · Total Water Storage (TWS) · Northern India

KIT Scientific Working Papers
Issue Number 270
ISSN: 2194-1629
DOI: 10.5445/IR/1000191188
Online: June 2026

This document is licensed under the Creative Commons Attribution – Share Alike 4.0 International License (CC BY-SA 4.0):
https://creativecommons.org/licenses/by-sa/4.0/deed.en

1 Introduction

The Earth's gravity field continuously responds to changes in surface and subsurface mass, making satellite gravimetry a powerful method to monitor large-scale hydrological processes such as groundwater depletion, glacier melt, and seasonal variations in water storage. The GRACE and GRACE Follow-On (GRACE-FO) missions have transformed global water studies by tracking tiny fluctuations in the distance between two satellites, from which monthly gravity fields are derived. These time-variable spherical harmonic coefficients can be converted into Terrestrial Water Storage (TWS) anomalies, enabling the identification of changes in soil moisture, snow, glaciers, surface water, and groundwater.

Water availability in northern India, particularly in the Himalayan-fed basins, is under growing stress due to population pressure, heavy irrigation demand, altered monsoon patterns, and rapid glacier retreat (Bolch et al., 2012). The Western Himalaya, encompassing Jammu & Kashmir, Himachal Pradesh, and Uttarakhand, is considered one of the most climate-sensitive regions in Asia. It hosts major glacier systems, steep mountain catchments, and the headwaters of the Indus and Ganges rivers. Strong seasonal contrasts, monsoon rainfall, winter dryness, and spring–summer melt, make this region highly suitable for analyzing TWS variations influenced by climatic and cryospheric processes.

Although GRACE provides total water storage, it cannot separately measure its components. Therefore, complementary model data from the Global Land Data Assimilation System (GLDAS) are required. GLDAS supplies estimates of soil moisture (in four depth layers), snow water equivalent, canopy water storage, and runoff. By subtracting these components from GRACE-derived TWS, groundwater storage can be isolated and assessed.

This study investigates how Himalayan glacier melt and seasonal hydrological processes influence groundwater storage in the Western Himalaya from 2003 to 2016. Monthly Level-2 GRACE gravity field solutions from CSR (up to degree/order 96) are processed into TWS anomalies using the method of Wahr et al. (1998), including filtering and elastic loading corrections. Groundwater storage is then derived using a water-balance approach with GLDAS components.

Using MATLAB-based workflows, this study analyses spatial patterns, seasonal variations, and long-term trends in TWS and groundwater across the three Western Himalayan states. The results highlight how glacier melt, monsoon variability, and winter deficits shape water availability in this environmentally fragile region. The overall aim is to improve understanding of hydrological changes in the Western Himalaya and support sustainable water resource management.

2 Theoretical Aspects

The estimation of Total Water Storage (TWS) variations in this study is derived from monthly GRACE Level-2 gravity field solutions. These datasets provide time-variable spherical harmonic coefficients that describe changes in the Earth's mass distribution. Following the approach of Wahr et al. (1998), the coefficients are transformed into residual gravitational potential fields (δV), which reflect the combined effects of changes in surface and subsurface water storage, including soil moisture, groundwater, snow, ice, and surface water. The resulting TWS anomalies represent the total column of terrestrial water storage measured by GRACE over the study region.

2.1 Spherical Harmonic Representation of GRACE Gravity Fields

The monthly gravity field solutions from GRACE are expressed as fully normalized spherical harmonic (SH) coefficients $\bar{C}_{nm}$ and $\bar{S}_{nm}$, which describe deviations of the Earth's gravity field from a perfect sphere at different spatial wavelengths. Here, n denotes the spherical harmonic degree (latitudinal variation) and m denotes the order (longitudinal variation). This representation follows the classical formulation of the Earth's gravity field as described in Heiskanen and Moritz (1967).

The gravitational potential V at a computation point $P(r,\varphi,\lambda)$ is reconstructed using Spherical Harmonic Synthesis (SHS):

$$V(r,\varphi,\lambda) = \frac{GM}{r}\sum_{n=0}^{N}\left(\frac{a}{r}\right)^n \sum_{m=0}^{n}\left(\bar{C}_{nm}\cos(m\lambda)+\bar{S}_{nm}\sin(m\lambda)\right)\bar{P}_{nm}(\sin\varphi), \tag{2.1}$$

where:

- GM is the geocentric gravitational constant,
- a is the mean Earth radius,
- r is the radial distance to point P,
- $\bar{P}_{nm}$ are the fully normalized associated Legendre functions.

The factor $(a/r)^n$ attenuates higher-degree harmonics with altitude. Because GRACE operates at an altitude of approximately 500 km, higher-degree terms contribute less to the observed gravity field. This limits GRACE's effective spatial resolution to roughly 200 km for a truncation at degree $N = 96$.

2.2 Conversion to Surface Mass: Equivalent Water Height (EWH)

Variations in the Earth's gravity field inferred from GRACE are converted into surface mass changes using the concept of Equivalent Water Height (EWH). EWH represents the thickness (in mm) of a uniform water layer that would produce the observed gravity anomaly. Based on Wahr et al. (1998), the residual spherical harmonic coefficients $\Delta\bar{C}_{nm}$ and $\Delta\bar{S}_{nm}$ are scaled to EWH using:

$$\Delta h(\varphi,\lambda) = \frac{a\rho_E}{3\rho_w}\sum_{n=0}^{N}\frac{2n+1}{1+k_n}\sum_{m=0}^{n}\left(\Delta\bar{C}_{nm}\cos(m\lambda)+\Delta\bar{S}_{nm}\sin(m\lambda)\right)\bar{P}_{nm}(\sin\varphi), \tag{2.2}$$

where:

- ρ_E is the mean density of the Earth,
- ρ_w is the density of water,
- k_n are the load Love numbers describing the Earth's elastic response to surface loading

The scaling factor $\frac{2n+1}{1+k_n}$ arises from solving the forward loading problem in spherical harmonics, accounting for both gravitational effects and elastic deformation. Dividing by ρ_w converts surface mass changes into an equivalent water-layer thickness. The resulting Δh field provides a consistent representation of terrestrial water storage (TWS) variations and allows direct comparison with land surface model outputs such as GLDAS.

2.3 Comparison with GLDAS Data

GRACE observes changes in the total terrestrial water storage (TWS), which represent the sum of several individual water storage compartments in the hydrological cycle. In conceptual form, the GRACE-derived mass change δS can be written as:

$$\delta S = S_{\text{groundwater}} + S_{\text{soil}} + S_{\text{surface}} + S_{\text{ice}} + S_{\text{biomass}}, \tag{2.3}$$

meaning that GRACE senses the *integrated* water column, but it cannot separate the individual components. Therefore, complementary model data are required to isolate specific storage terms such as groundwater.
To enable such comparison, equivalent TWS estimates from the Global Land Data Assimilation System (GLDAS, Noah model) were used. GLDAS provides monthly fields of soil moisture (multi-layer), snow water equivalent,

and canopy water storage at 1° and 0.25° spatial resolution (Rodell et al., 2004). Since GLDAS does not include groundwater storage explicitly, its TWS estimate was computed as:

$$\mathrm{TWS}_{\mathrm{GLDAS}} = S_{\mathrm{soil}} + S_{\mathrm{snow}} + S_{\mathrm{surface}} + S_{\mathrm{canopy}}, \tag{2.4}$$

which represents only the upper part of Eq. (2.3). The GRACE TWS signal, in contrast, also contains groundwater and deep storage variations.

Both datasets were resampled to a common $1^\circ \times 1^\circ$ grid and processed over the same study period (January 2003-December 2016). Monthly anomalies were computed by removing the mean seasonal cycle and linear trend, allowing a consistent comparison of the temporal variability between GRACE and GLDAS.

3 Data

The used data in this study is described in the following subsections.

3.1 GRACE

The GRACE (Gravity Recovery and Climate Experiment) mission was a joint satellite mission between NASA and the German Aerospace Center (DLR), operated as part of the international Earth Observing System. The mission consisted of two identical satellites, GRACE-A and GRACE-B, launched together on 17 March 2002 and operated until 27 October 2017, when the spacecraft ran out of fuel. GRACE is also part of the ESA Third Party Missions Program, which allows ESA to distribute GRACE data products under agreement with NASA (Wouters et al., 2014).

GRACE mapped variations in the Earth's gravity field by making ultra-precise measurements of the inter-satellite distance. These range-rates variations reflect changes in mass on and near Earth's surface, including soil moisture, groundwater, snow, ice, and surface water. In addition to its primary gravity mission, GRACE also delivered around 150 globally distributed vertical profiles of temperature and humidity per day using GPS radio occultation. In this study, the GRACE Level-2 monthly gravity field solutions, provided by the GFZ (RL06.1), which include fully normalized spherical harmonic coefficients are used. These coefficients are essential for reconstructing time-variable gravity fields and deriving Terrestrial Water Storage (TWS) anomalies following the method of Wahr et al. (1998). The data used here are distributed through the International Centre for Global Earth Models (ICGEM, 2026). Together with the GRACE-FO successor mission, these Level-2 products form the core dataset for quantifying long-term and seasonal water storage changes in the Western Himalaya.

3.1.1 Overview of GRACE Data Products

The GRACE (Gravity Recovery and Climate Experiment) mission provides several types of data products that are organized into processing "Levels," ranging from raw satellite tracking data to fully processed global water storage estimates:

- **Level-0** – Raw telemetry and instrument data collected by the satellite system, including GPS observations, accelerometer data, K-band ranging measurements, and housekeeping data. Not used directly in scientific analysis.
- **Level-1** – Geometrically calibrated and time-tagged tracking data from the GRACE instruments (KBR, GPS, attitude sensors), including satellite-to-satellite range rates, which form the basis for gravity field inversion.
- **Level-2** – Monthly global gravity field solutions expressed as spherical harmonic coefficients ($\bar{C}_{nm}$, $\bar{S}_{nm}$), commonly distributed by three processing centers (CSR, GFZ, JPL). These coefficients represent the total mass redistribution within the Earth system and are the most widely used GRACE product in geodesy and hydrology.

- **Level-3 (Gridded Products)** – Processed versions of Level-2 fields provided either as global Equivalent Water Height (EWH) grids or as mascon (mass concentration) solutions. These are spatially filtered, interpolated, and often corrected for leakage and scaling errors. Examples include JPL RL06 mascon data and CSR/GFZ gridded EWH products.
- **Derived / Auxiliary Datasets** – Include basin averages, hydrological model comparisons (e.g., GLDAS, WGHM), and combined GRACE–GRACE-FO time series used for climate and water resource applications.

3.1.2 Degree and Order Truncation of GRACE Coefficients

GRACE monthly gravity solutions are represented using spherical harmonic coefficients up to a maximum degree and order. In GRACE RL06 products, the expansion is truncated at degree/order 60, resulting in a 61×61 matrix of coefficients per month (1,891 usable values). This corresponds to a spatial resolution of roughly 300–400 km at the Earth's surface (Tapley et al., 2004). In some auxiliary models or intermediate computations, higher truncation levels (e.g., 96×96) may be used. However, GRACE Level-2 data products are typically limited to degree/order 60 due to increasing noise at higher degrees(Swenson and Wahr, 2006).In this analysis, however, a higher truncation level of degree/order 96 is used.

3.1.3 DDK Filtering of GRACE Coefficients

The raw GRACE spherical harmonic coefficients contain correlated errors, especially along the North–South direction, which manifest as striped artefacts in the spatial domain. To address this, a family of decorrelation filters known as **DDK filters** is widely applied in GRACE post-processing (Kusche et al., 2009). The DDK filters range from DDK1 to DDK8, where lower numbers (e.g., DDK1) apply stronger filtering and remove more noise but also attenuate signal, while higher numbers (e.g., DDK8) keep more of the original signal but introduce higher noise levels. In this study, the **DDK5** filter was selected as a compromise between noise reduction and signal preservation, following common practice in hydrological GRACE applications. The filter is applied in the spectral domain to the spherical harmonic coefficients prior to spatial synthesis.

3.2 The GLDAS Dataset and Its Hydrological Relevance

The Global Land Data Assimilation System (GLDAS) is a NASA-driven modelling framework that integrates satellite and ground observations with land surface models (LSMs) to produce estimates of land surface states and fluxes (Rodell et al., 2004). One of the central LSMs implemented within GLDAS is the NOAH model. The acronym NOAH stands for the National Oceanic and Atmospheric Administration (NOAA) / Office of Hydrologic Research (OHR) Land Surface Model, although its name has become a standalone designation for the specific model version used in GLDAS (NOAH LSM version 2.1 in many applications).
GLDAS produces a range of output quantities, typically on a global grid (e.g. $1^\circ \times 1^\circ$ or $0.25^\circ \times 0.25^\circ$) and at monthly or sub-monthly intervals. Key output variables and their units include:

- Soil moisture (e.g., kg m^{-2} or mm water equivalent)
- Snow Water Equivalent (SWE, mm)
- Surface (skin) temperature (K)
- Evapotranspiration (mm $month^{-1}$)
- Run-off / drainage (mm $month^{-1}$)
- Canopy water storage (kg m^{-2} or mm)
- Total land water storage (sometimes computed as sum of above components, mm)

Among these, the hydrologically most relevant quantities are soil moisture, Snow Water Equivalent (SWE), canopy water, and run-off, because they directly affect water availability, storage change, and fluxes within the terrestrial water cycle.
With respect to comparison to GRACE's Equivalent Water Height (EWH), GLDAS variables provide component-wise storage changes on the land surface, whereas GRACE EWH provides a bulk estimate of total terrestrial water storage (TWS) anomalies (i.e., surface water + soil moisture + groundwater + snow + ice) in mm of water thickness. Therefore, GLDAS outputs can be summed (or otherwise combined) to approximate the same storage metric that GRACE measures. By comparing GLDAS–derived cumulative storage change with the GRACE EWH signal, one can assess whether surface components alone explain the storage variation observed by GRACE, or whether additional deep groundwater or ice/snow mass changes must be invoked.

4 Results and Discussion

In this study, it is examined how terrestrial water storage (TWS) has changed across the Western Himalaya by combining satellite gravity observations with land-surface model outputs. GRACE offers a direct view of how total water mass varies over time, allowing to identify patterns of groundwater loss, seasonal recharge during the monsoon, and long-term shifts driven by climate. To better understand what controls these changes, also GLDAS is used, which provides information on soil moisture, canopy water, snowmelt, and runoff. While GRACE shows the overall change in water storage, GLDAS helps break this signal into its physical components and reveals how factors such as precipitation, snow accumulation, meltwater release, and evapotranspiration shape the seasonal and year-to-year variations. Precipitation and temperature information from the India Meteorological Department (IMD, 2015) was also used to support the evaluation of the seasonal and interannual variability in the study region.

4.1 GRACE TWS Analysis

The results in this section are based on the spherical harmonic synthesis of GRACE-derived coefficients using the method of Wahr et al. (1998). The results in this section come from processing the monthly GRACE satellite data, which measures how water storage changes over time. Using these gravity-based measurements, maps of Total Water Storage (TWS) for the Western Himalaya, showing how much water the region gained or lost each month are created. These TWS anomalies represent the combined effect of snow, glaciers, soil moisture, groundwater, and surface water, allows to clearly observe seasonal patterns, dry and wet years, and long-term changes in the region's water availability.
The July TWS anomaly maps from 2003 to 2016 are shown in Figure 4.1. It reveals how monsoon-season water storage in the Western Himalaya has changed over time. In the early years (2003-2007), July consistently shows strong positive anomalies across Jammu & Kashmir, Himachal Pradesh, and Uttarakhand - reflecting heavy monsoon rainfall combined with substantial glacier and snowmelt recharge. After 2008, however, July anomalies begin to weaken, becoming less widespread and more uneven, suggesting reduced monsoon strength and declining contribution from melting snow and ice. Among all the years, July 2012 stands out prominently, showing the strongest positive TWS anomaly of the entire period. This extreme wet signal highlights an exceptionally intense monsoon combined with significant meltwater input, making 2012 a key reference year for hydrological comparison. In contrast, after 2013 the July anomalies show a clear downward shift. Several later years (2014, 2015, 2016) display mostly neutral or weakly positive patterns, reflecting subdued monsoon conditions and ongoing glacier mass loss. Overall, the July sequence captures a gradual weakening of monsoon-driven water storage, with 2012 marking the last major high-water peak before the region transitions into a period of declining TWS.
The GRACE-derived TWS anomaly maps for 2012 (Appendix A, Fig. A.1) reveal one of the most hydrologically dynamic years in the 2003 – 2016 record. Mild positive anomalies in January – March reflect winter snow accumulation, which gradually weakens during pre-monsoon warming in April. A sharp and region-wide peak occurs

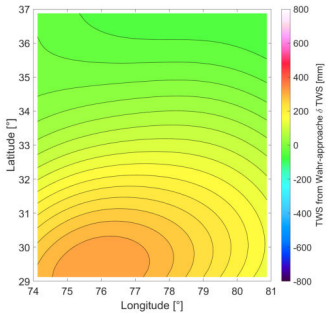

(a) 2003

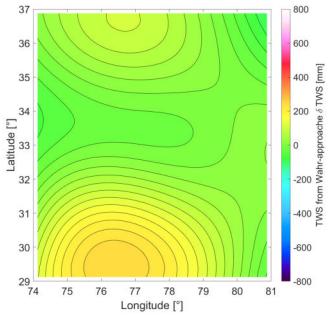

(b) 2004

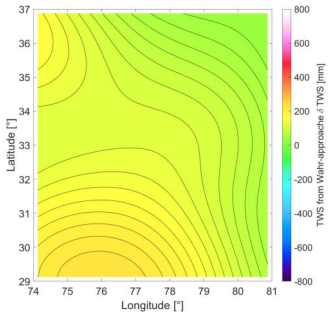

(c) 2005

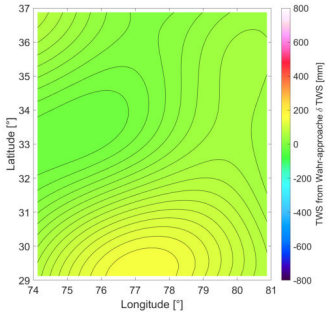

(d) 2006

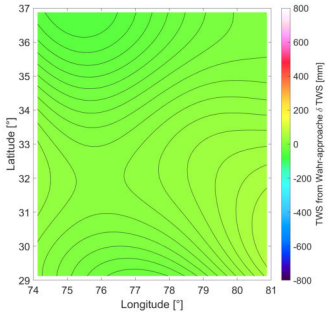

(e) 2007

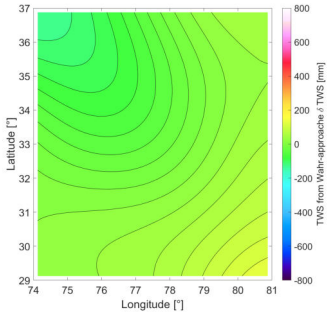

(f) 2008

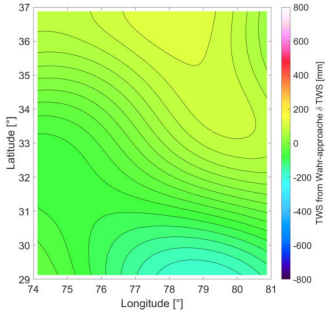

(g) 2009

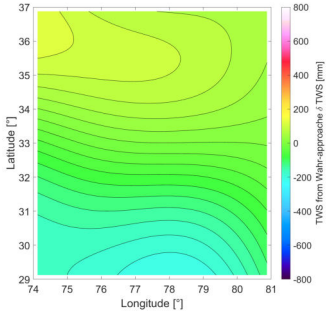

(h) 2010

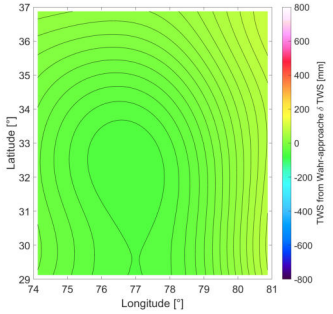

(i) 2011

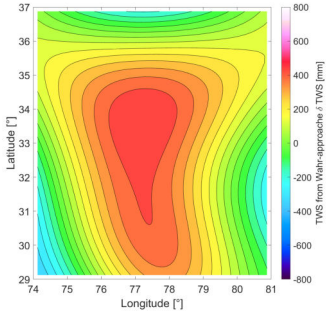

(j) 2012

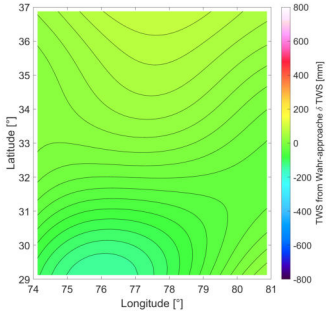

(k) 2013

not existent

(l) 2014

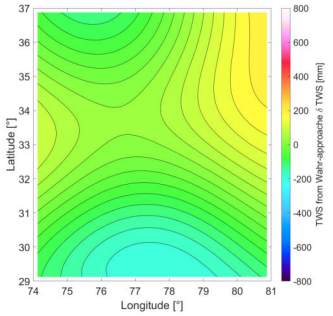

(m) 2015

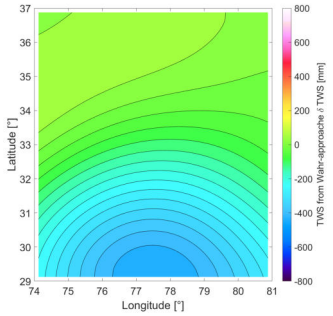

(n) 2016

Figure 4.1: GRACE TWS Anomalies in July

in July 2012, marking the highest TWS value of the entire time series. This anomaly results from exceptionally strong monsoon rainfall combined with early-season meltwater input. From August onward, TWS values decline as the monsoon weakens, transitioning toward neutral to slightly negative anomalies by October – November. By December, the winter dry season suppresses recharge once again. In general, 2012 exhibits an amplified hydrological cycle: normal winter accumulation, an extremely wet monsoon peak, and a return to winter depletion, making it the most hydrologically intense year in the GRACE period.

The GRACE TWS anomaly maps for 2016 (Appendix A, Fig. A.2) show one of the driest years in the 2003–2016 record. January–April exhibits mild negative to near-neutral anomalies, reflecting limited winter precipitation and low snow accumulation. Although TWS increases slightly during the July monsoon, the recharge is weaker than in wetter years such as 2012. The most notable feature is the rapid decline in late autumn and winter: by November and especially December, the TWS becomes strongly negative across the entire region, marking the lowest water storage values of the full GRACE time series. This severe deficit results from weak monsoon input, reduced snowpack formation, and ongoing glacier mass loss, compounded by unusually weak Western Disturbances. Consequently, 2016 stands out as an exceptionally dry year, highlighting the sensitivity of the Western Himalaya to small shifts in precipitation and temperature.

The December GRACE maps (Figure 4.2) show a consistent winter pattern from 2003 onwards: temperatures drop sharply, snowfall replaces rainfall, and almost no melting occurs. As a result, most years display the usual mildly negative TWS values that reflect normal winter dryness across the Western Himalaya. Over time, however, a gradual strengthening of winter deficits becomes visible. The negative anomalies slowly deepen from the early 2000s toward the mid-2010s, indicating reduced winter recharge and increasing sensitivity to snowfall variability. This trend reaches its lowest point in December 2016, which shows the strongest negative TWS anomaly in the entire 2003–2016 period. This extreme dryness aligns with reports of below-normal snowfall, weak Western Disturbances, and limited winter precipitation (IMD, 2015), combined with ongoing glacier thinning. Together, these factors explain the unusually sharp decline in water storage that winter.

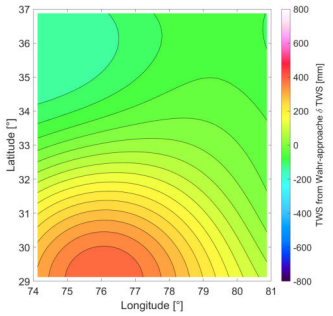

(a) 2003

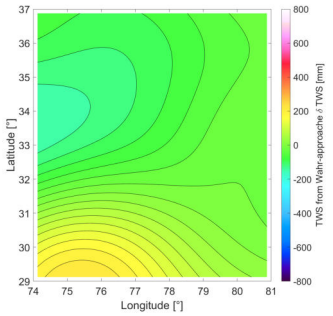

(b) 2004

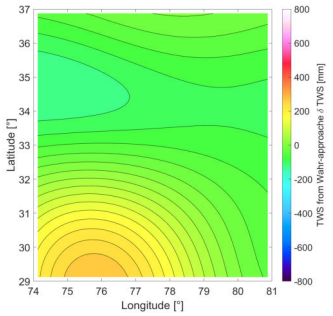

(c) 2005

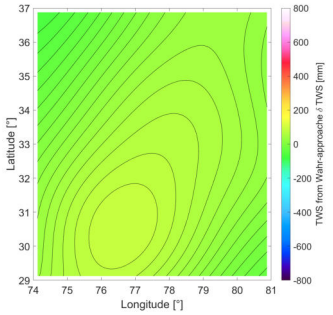

(d) 2006

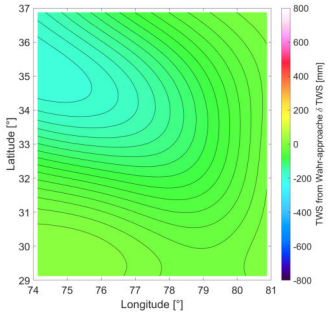

(e) 2007

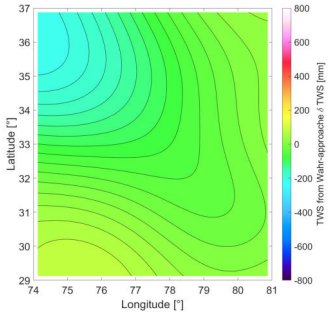

(f) 2008

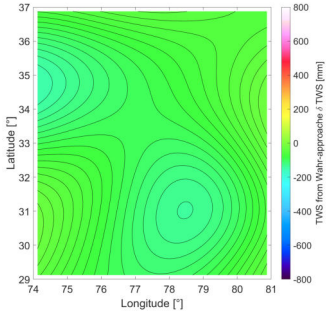

(g) 2009

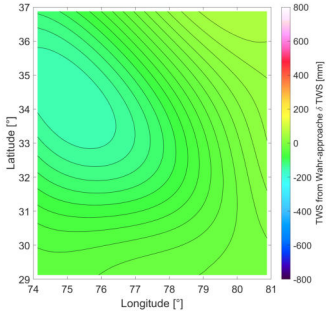

(h) 2010

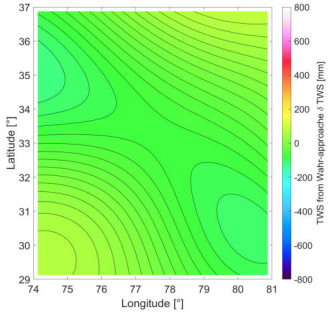

(i) 2011

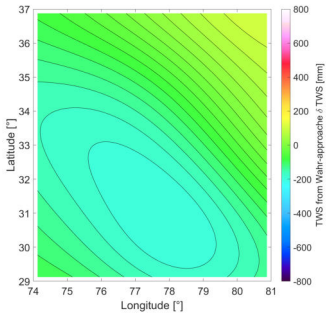

(j) 2012

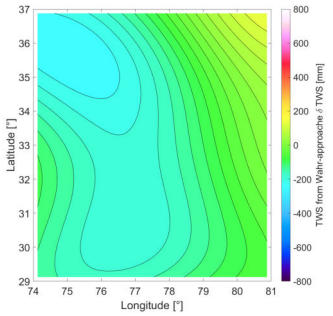

(k) 2013

not existent

(l) 2014

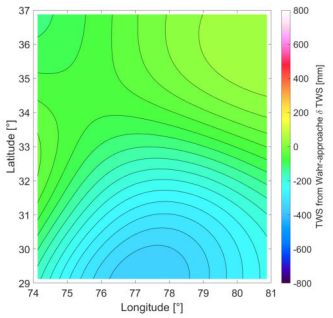

(m) 2015

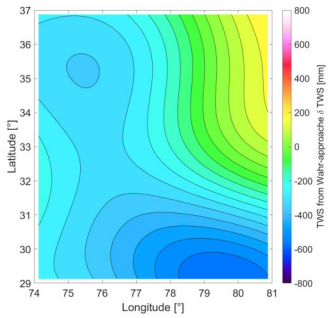

(n) 2016

Figure 4.2: GRACE TWS Anomalies in December

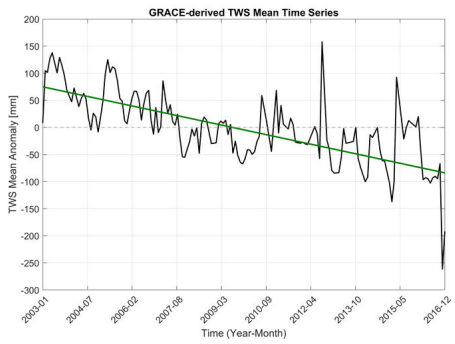

(a) GRACE-derived mean TWS anomaly time series.

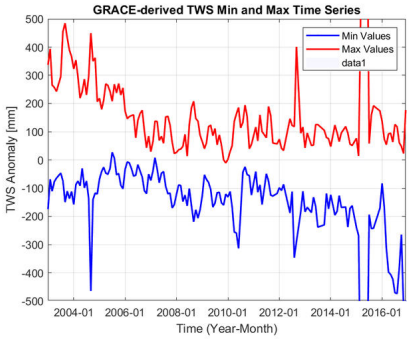

(b) Minimum and maximum GRACE-derived TWS anomalies.

Figure 4.3: Summary of GRACE-derived TWS time series and anomaly extremes for 2003-2016.

The GRACE-derived mean TWS anomaly time series in Figure 4.3a shows a clear long-term declining trend from 2003 to 2016. Early years exhibit positive anomalies exceeding +100 mm, but values steadily decrease and frequently drop below -50 mm after 2010. The green regression line highlights a persistent negative slope, indicating continuous water storage loss over the region. Seasonal fluctuations remain strong throughout the record, but the long-term downward trend dominates. A sharp decline in late 2016 marks the lowest anomaly in the entire dataset. The minimum and maximum TWS anomaly envelope Figure 4.3b reveals the seasonal amplitude of hydrological variability across the study period. Maximum values (red curve) peak above +400 mm during strong monsoon years such as 2003-2005, while later years show lower monsoon peaks. Minimum values (blue curve) regularly fall below -200 mm, with extreme deficits approaching -400 mm during dry years such as 2006 and 2015-2016. The widening gap between minimum and maximum anomalies after 2010 indicates increasing hydrological variability. These patterns suggest intensifying wet season recharge followed by stronger dry season depletion.

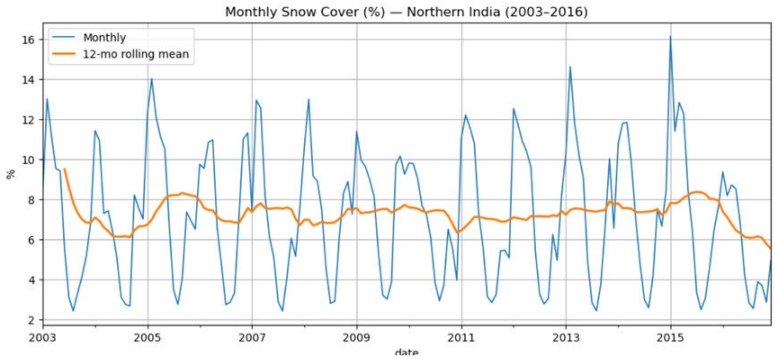

Figure 4.4: Monthly MODIS snow cover and 12-month moving average (2003–2016).

Monthly MODIS snow cover percentages for northern India (Figure 4.4) show clear seasonal cycles, with winter peaks above 10-15% and summer minima of around 2-4%. The 12-month rolling mean indicates a gradual long-term decline, decreasing from about 8% in 2003–2005 to roughly 6% after 2015. This reduction is consistent with rising temperatures and reduced winter snowfall across the western Himalaya. High-frequency fluctuations reflect strong interannual variability in snow accumulation and melt. Overall, the declining snow-cover trend supports the GRACE-observed reduction in water storage and aligns with long-term MODIS observations documented by NASA (2020).

4.2 GLDAS Hydrological Component Analysis

To better understand the physical processes behind the extreme water storage anomalies detected by GRACE, the GLDAS land surface model outputs were analysed in detail. Unlike GRACE, which measures total mass change, GLDAS provides essential hydrological variables such as soil moisture across four depth layers, surface runoff, and subsurface runoff, that together offer a clearer picture of how rainfall, snowmelt, and seasonal temperature patterns shape water availability in the Western Himalaya. By comparing GLDAS fields during key wet and dry months, we can link GRACE-observed TWS peaks to periods of intense monsoon recharge and saturated soils, and similarly connect strong TWS declines to low soil moisture, minimal runoff, and frozen ground conditions. This combined approach helps reveal not only when water storage changes occur, but also why they happen, providing valuable insight into the hydrological behavior of this climate-sensitive mountain region.

July 2012 exhibits the strongest monsoon-driven hydrological response in the entire 2003 – 2016 period. Figure 4.5 shows widespread saturation across the Western Himalaya, reflecting intense monsoon rainfall combined with snow melt from high-altitude glaciers. Surface runoff also increases sharply, particularly along steep catchments, while subsurface runoff becomes highly active in deeper zones, both clear signals of rapid monsoon infiltration and lateral water movement. These combined processes confirm why GRACE detected its highest positive TWS anomaly: the landscape was holding large amounts of newly added water, both at the surface and within the soil–groundwater system.

December 2016 represents the most severe dry condition of the full record. The Figure 4.5 shows almost no surface runoff throughout the region, and subsurface runoff drops to near-zero levels, indicating frozen soils, minimal snowmelt, and a complete absence of winter rainfall. Soil-moisture values are at their annual minimum, consistent with the cold and dry Himalayan winter. This exceptionally weak hydrological activity corresponds directly to the strongly negative GRACE TWS anomaly. The dryness is further intensified by the unusually weak Western Disturbances in late 2016, which brought far less snowfall than normal. Together, these factors explain the deep water-storage deficit recorded by GRACE.

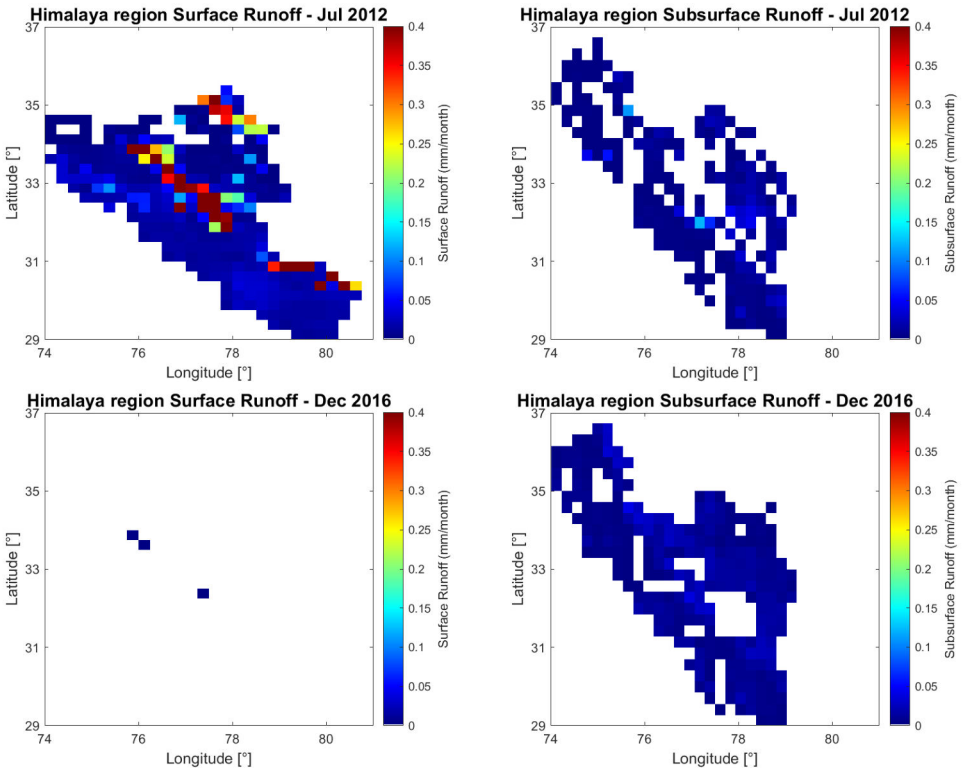

Figure 4.5: GLDAS-derived Surface Runoff and Subsurface Runoff for the Himalaya region, illustrating the hydrological extremes corresponding to the GRACE TWS anomalies.

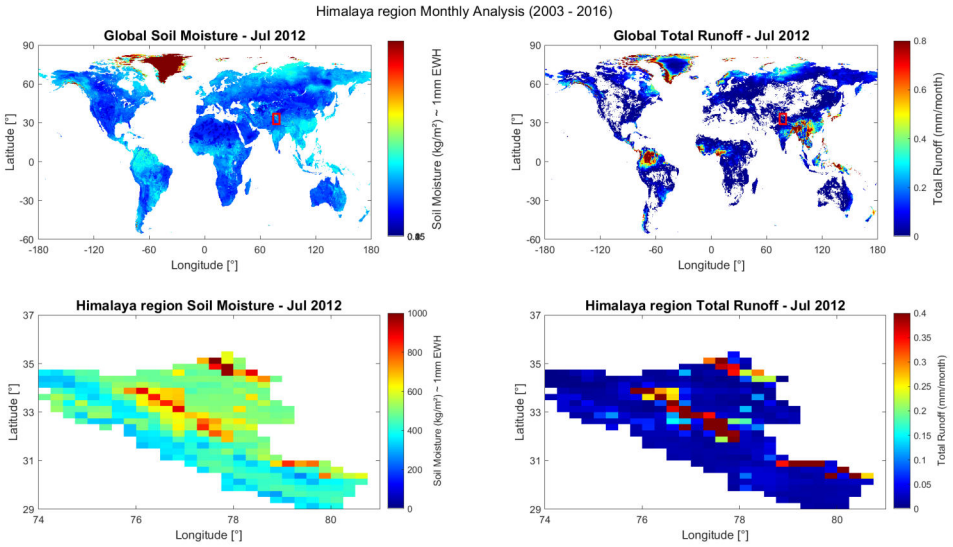

(a) GLDAS Total Runoff – July 2012 (Wet Extreme)

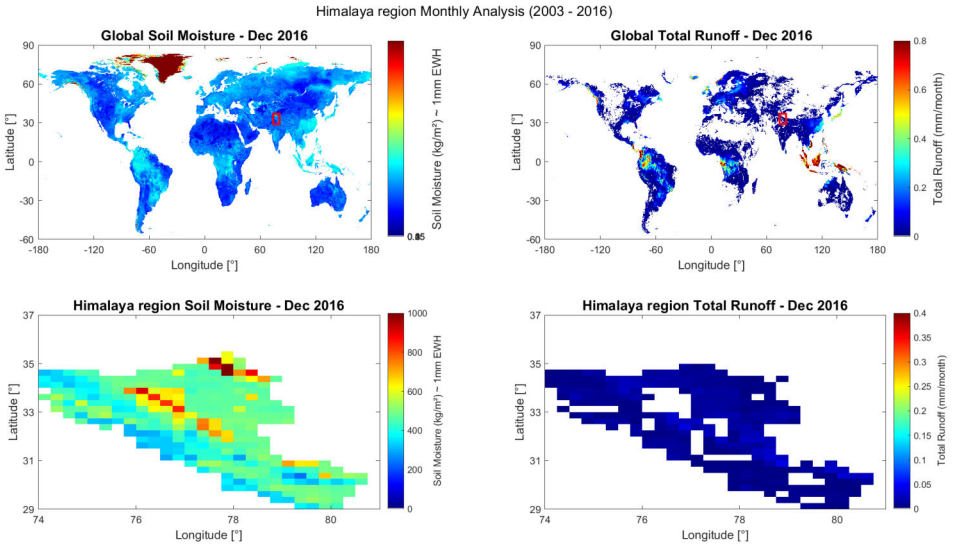

(b) GLDAS Total Runoff – December 2016 (Dry Extreme)

Figure 4.6: GLDAS-derived Total Runoff for the Himalaya region, illustrating the hydrological extremes corresponding to the GRACE TWS anomalies.

The contrast between July 2012 and December 2016 Figure 4.6 captures how strongly the Western Himalayan water cycle can shift between the peak monsoon and deep winter. July 2012 was the wettest month in the entire 2003–2016 record, with GRACE showing its highest positive TWS anomaly. GLDAS confirms this with saturated soil moisture, strong surface runoff, and enhanced subsurface flow, clear signatures of intense monsoon rainfall and efficient catchment recharge. Together, these patterns reflect a fully activated hydrological system, where rainfall, remaining spring melt, and widespread wetness combine to produce exceptional water storage gain.

December 2016, on the other hand, represents the opposite extreme. GRACE records its strongest negative TWS anomaly, showing severe water depletion across the region. GLDAS fields reveal almost no surface runoff, minimal subsurface flow, and very low soil moistur – typical of the cold, dry Himalayan winter, but unusually intensified in 2016 due to a weak monsoon and reduced early-winter snowfall. This combination of limited recharge and stronger-than-normal winter dryness explains the sharp drop in TWS.

Interestingly, the GLDAS soil-moisture maps for these two months appear visually similar. This is because the spatial plots mainly represent the top 0-10 cm soil layer, which changes only modestly between seasons: it wets quickly during the monsoon and freezes in winter, and GLDAS counts frozen water as soil moisture (Ek et al., 2003). As a result, the maps are dominated by topography rather than seasonality, even though the deeper hydrological system shows large differences. This explains why July 2012 and December 2016 look similar in soil-moisture maps, despite representing the wettest and driest extremes observed by GRACE.

The GLDAS runoff maps for 2012 and 2016 (Appendix B, Figures B.1 – B.8) show a consistent seasonal cycle in the Western Himalaya, but with clear differences in intensity and spatial extent between the two years. In both years, January and December (Figs. B.1, B.4, B.5, B.8) exhibit very low surface and subsurface runoff, reflecting frozen winter conditions with minimal liquid water availability. However, 2016 shows slightly broader subsurface runoff during mid-winter, suggesting deeper baseflow persistence compared to 2012. During April (Figs. B.2 and B.6), early spring melt activates limited runoff in both years, but 2016 displays more widespread surface runoff, especially across Himachal Pradesh and Jammu & Kashmir, indicating stronger or earlier snowmelt relative to 2012.The most notable difference appears in July, the monsoon peak (Figs. B.3 and B.7). While both years show intense surface runoff, 2016 exhibits a stronger and more spatially extensive monsoon response than 2012, with higher runoff concentrations and broader saturated areas. Subsurface runoff in 2016 also forms a more continuous band, indicating a stronger baseflow response to heavy monsoon rainfall. Overall, both years follow the typical Himalayan hydrological cycle: winter freeze $\rightarrow$ spring melt $\rightarrow$ monsoon peak $\rightarrow$ winter decline – but 2016 consistently shows higher runoff intensity, especially during the pre-monsoon and monsoon seasons, aligning with the negative GRACE TWS anomalies observed toward the end of 2016.

The GLDAS soil-moisture and total runoff maps for 2012 and 2016 (Appendix B, Figures B.9 – B.16) reveal a similar seasonal cycle across the Western Himalaya, but with clear differences in intensity between the two years. In both January 2012 and January 2016, soil moisture is uniformly low and total runoff remains minimal, reflecting cold winter conditions with frozen soils and limited liquid water availability (Figures B.9 and B.13). By April, both years show increasing soil moisture due to early snowmelt, but 2016 displays a more pronounced moisture increase and slightly stronger total runoff across Himachal Pradesh and Jammu & Kashmir, indicating an earlier or more intense melt season (Figures B.10 and B.14). The greatest contrast occurs in July, where both years experience maximum soil moisture and high monsoon-driven runoff; however, 2016 exhibits more widespread and intense runoff, especially along the steep southern Himalayan slopes, compared to the more moderate pattern seen in 2012 (Figures B.11 and B.15). By December, soil moisture and runoff decline sharply in both years, returning to dry winter conditions (Figures B.12 and B.16). Overall, while both 2012 and 2016 follow the typical Himalayan hydrological sequence: winter dryness $\rightarrow$ spring melt $\rightarrow$ monsoon peak $\rightarrow$ early-winter decline – the 2016 results indicate a stronger hydrological response, consistent with enhanced spring melt and more intense monsoon rainfall.

The soil-moisture and runoff time series for the Western Himalaya Figure 4.7 show a strong and predictable seasonal rhythm. Each year, soil moisture rises sharply during June–August as the monsoon delivers heavy rainfall, which also causes clear spikes in both surface and subsurface runoff. Years such as 2006, 2010, 2012, and 2014 show the highest monsoon peaks, reflecting unusually wet summers.

In contrast, the November to February period consistently marks the driest part of the year, when freezing temperatures and minimal precipitation greatly reduce infiltration and runoff. The most extreme winter dryness appears in late 2015 and December 2016, where runoff nearly drops to zero, matching the strongly negative GRACE TWS anomaly detected for December 2016.

While GRACE clearly captures the extreme wet conditions of July 2012 and the severe dryness of December 2016, these extremes appear less dramatic in GLDAS time series because the GLDAS values are spatial averages that smooth regional variations, and because frozen winter soil moisture is still counted as moisture.

Overall, the region follows a clear pattern of monsoon-driven recharge and winter depletion, with 2012 standing out as an exceptionally wet year and 2016 as an exceptionally dry one.

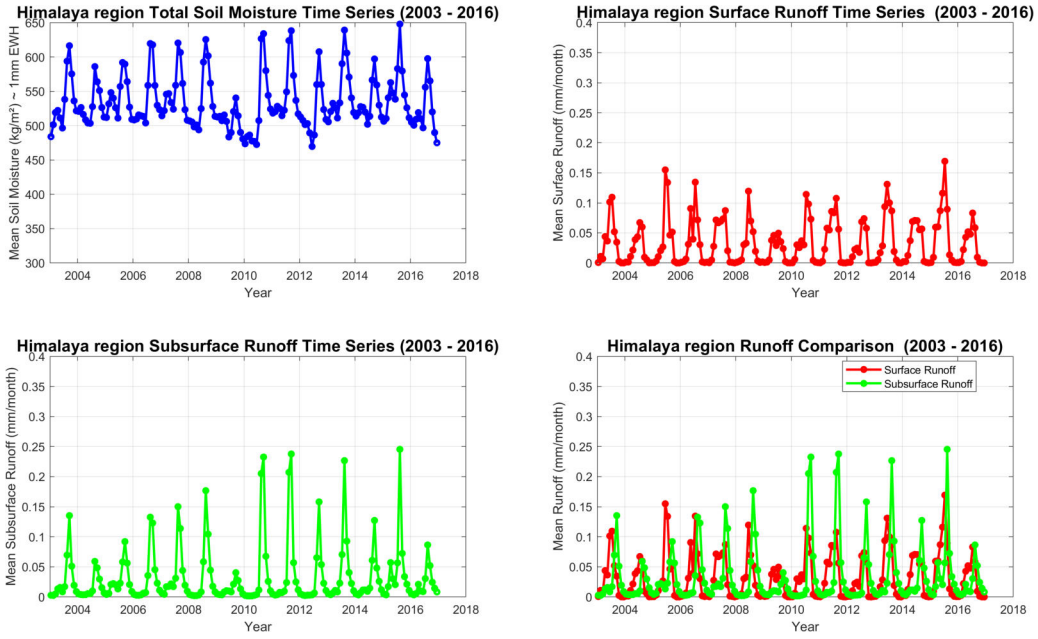

Figure 4.7: Himalaya region Soil Runoff Time Series (2000 – 2016).

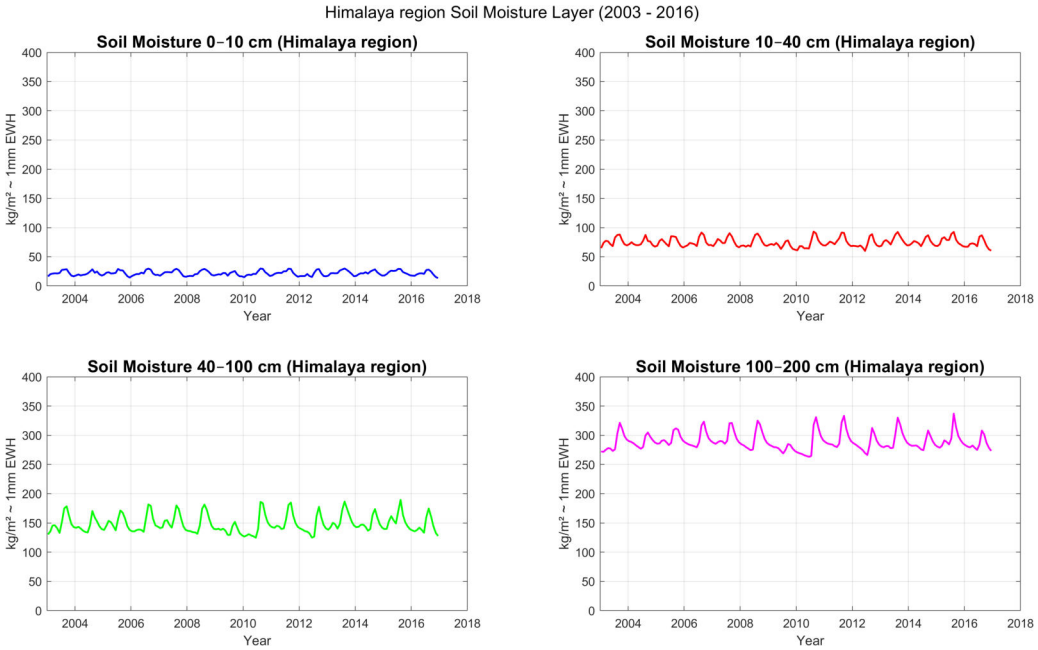

Figure 4.8: Himalaya region Soil Moisture Layers Time Series (2000 – 2016).

The soil-moisture time series across the four GLDAS layers (0–10 cm, 10–40 cm, 40–100 cm, and 100–200 cm) shows a very steady and predictable annual rhythm throughout the Western Himalaya. All layers peak during the monsoon months (June–August), reflecting strong rainfall infiltration, and then decline in winter when the soil freezes and precipitation is minimal. The shallow layers respond quickly and show small, sharp fluctuations, while the deeper layers hold much more water and change more gradually, almost like a long-term reservoir. Because deeper soil retains moisture longer, even extreme years such as July 2012 (very wet) and December 2016 (very dry) do not appear as dramatic spikes or drops. Instead, the deeper profiles smooth out these events, showing that long-term soil moisture responds slowly compared to rapid monsoon-related changes in TWS and runoff. Overall, the layered structure demonstrates how the upper soil reacts immediately to rainfall, while deeper layers regulate slow moisture storage throughout the year.

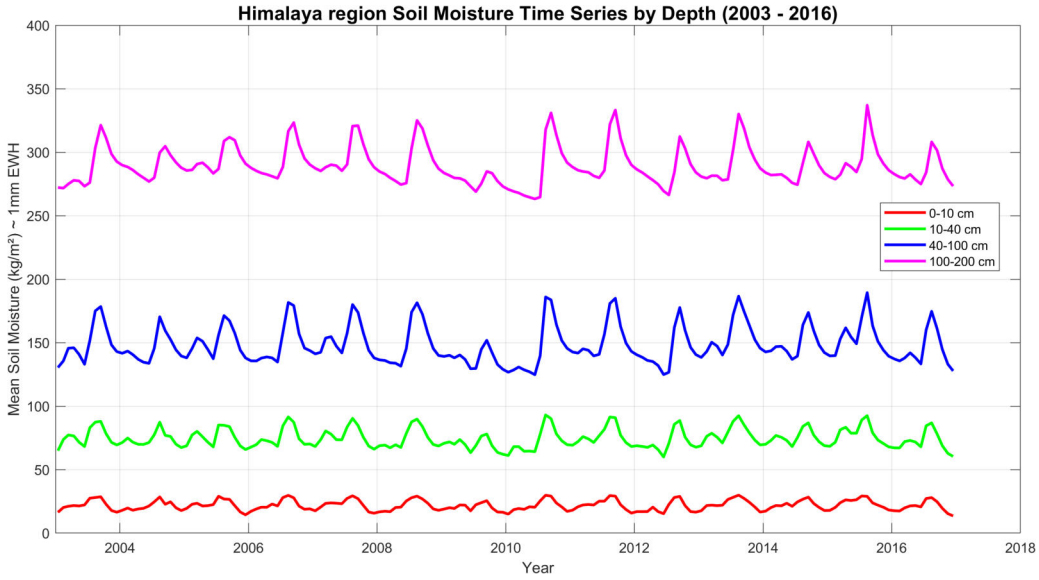

Figure 4.9: Himalaya region Soil Moisture By Depth TimeSeries (2000–2016).

The GLDAS soil-moisture time series by depth for the Western Himalaya Figure 4.9 shows a very regular, monsoon-driven annual cycle in all four layers. Each year, moisture increases sharply during June – August, when the summer monsoon recharges the soil profile, and then gradually declines through autumn and winter as rainfall stops and evapotranspiration and drainage remove water. The shallow layers (0-10 cm and 10-40 cm) respond fastest, with sharper peaks and troughs, while the deeper layers (40-100 cm and 100-200 cm) change more slowly and store much more water, behaving like a long-term reservoir. No single year stands out with an extreme anomaly in these curves, because the values are averaged over the whole region and because deep soil moisture smooths short-lived events, even when GRACE shows strong TWS extremes such as July 2012 (very wet) or December 2016 (very dry). Overall, the figure highlights a stable but strongly seasonal subsurface water cycle, where deeper layers buffer interannual variability despite pronounced changes in total water storage.

The combined time series of EWH, ESH, and canopy water storage for the Western Himalaya Figure 4.10 highlights the strong seasonal cycle that dominates the region's hydrology. The EWH curve, which represents the total water stored in the soil column, shows a clear annual pattern with sharp monsoon peaks every June – August, followed by gradual declines through autumn and the lowest values during winter. This reflects the typical rhythm of the Himalaya, where intense monsoon rainfall rapidly recharges the land surface, while the dry and cold season brings sustained depletion. In contrast, both canopy water and surface snow water (ESH) remain extremely small throughout the year – almost flat lines compared to the large EWH signal. This indicates that canopy interception and snow water play only a minimal role in the region's total water storage, especially when averaged over the broader Western Himalayan domain. The overall pattern confirms that Himalayan water storage is overwhelmingly controlled by monsoon-driven soil moisture, with snow and canopy contributions remaining negligible in compar-

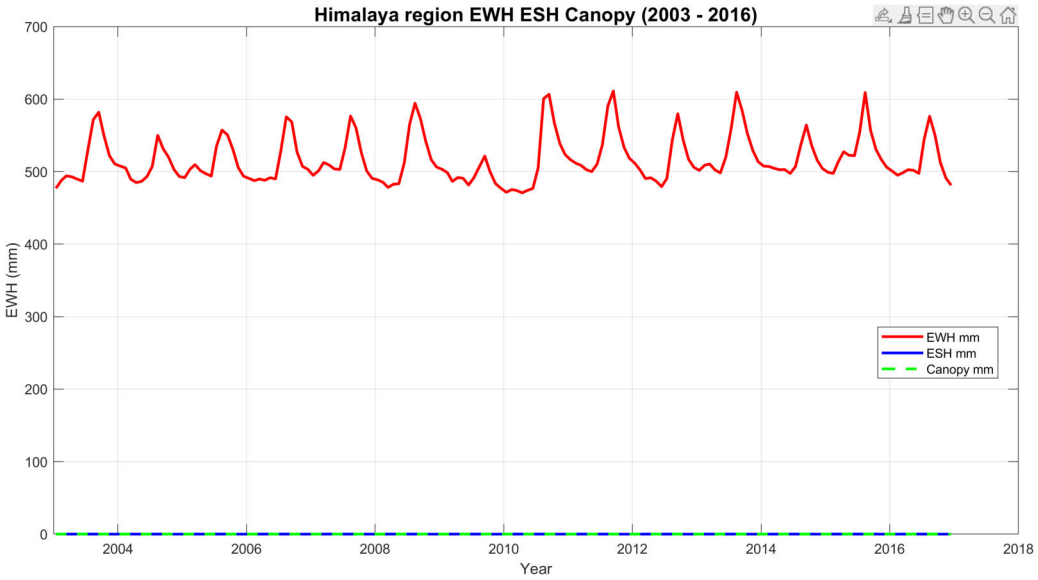

Figure 4.10: Himalaya region EWH Time Series (2000 – 2016).

ison. Although extreme years such as 2012 (very wet) and 2016 (very dry) stand out clearly in GRACE TWS, their impact here appears more muted because GLDAS separates only small components (snow and canopy), while the main soil moisture variations dominate the storage signal.

5 Conclusion and Outlook

This study demonstrates that the combined use of GRACE-derived Terrestrial Water Storage (TWS) anomalies and GLDAS-based hydrological components is highly effective for assessing long-term groundwater storage dynamics in the Western Himalaya. The GRACE mission, as the first satellite system capable of reliably quantifying TWS variations at the global scale, provided clear evidence of persistent negative water storage trends across key Himalayan basins during the study period. After applying destriping and filtering techniques to reduce correlated noise, the GRACE signal revealed that several regions – particularly the downstream plains of Himachal Pradesh, Jammu & Kashmir, and parts of Uttarakhand, experienced a measurable decline in TWS, which is strongly indicative of sustained groundwater depletion.

Comparison with GLDAS soil moisture, snow water, and runoff datasets confirmed that seasonal hydrological processes alone cannot fully explain the magnitude of the observed TWS decline. Winter snow accumulation and monsoon-driven recharge showed strong interannual variability, yet the long-term GRACE signal consistently pointed toward a net loss of stored water, highlighting groundwater as the primary component being depleted. This pattern aligns with increasing water demand, reduced glacier mass balance, and shifting monsoon timing that collectively weaken natural recharge processes.

Overall, the results underscore that groundwater storage in the Western Himalaya is undergoing significant stress, driven by both climatic and anthropogenic factors. The transition from winter freeze to spring melt and the strong monsoon response is still evident in the TWS cycle, but long-term losses reflect structural depletion rather than seasonal fluctuation. These findings reinforce the importance of continuous satellite gravimetry; future successor missions to GRACE are expected to adopt improved architectures that minimize correlated errors and allow even more precise monitoring of groundwater resources in vulnerable mountain regions. Sustained observations will be essential for developing adaptive, basin-scale water-resource management strategies in the Himalaya, where millions of people depend on groundwater fed by snow and glacier melt.

Acknowledgement

The author wishes to express sincere gratitude to Dr.-Ing. Kurt Seitz and the team at the Geodätisches Institut (GIK), Karlsruhe Institute of Technology (KIT) for their continuous guidance, academic support, and for providing the necessary computational resources and laboratory facilities throughout the duration of this study. Their expertise and encouragement were invaluable in shaping the direction and quality of this research.

The author also gratefully acknowledges the International Centre for Global Earth Models (ICGEM), GFZ German Research Centre for Geosciences (2023) for supplying the GRACE spherical harmonic datasets used in this work. The availability of high-quality global gravity field products made the detailed analysis of Terrestrial Water Storage (TWS) variations in the Himalayan region possible.

Special thanks are extended to the developers and maintainers of the GLDAS NOAH Land Surface Model, whose openly accessible hydrological datasets contributed significantly to the comparative analysis carried out in this research.

The author further acknowledges the support and motivation received from colleagues and fellow students within the Remote Sensing and Geoinformatics programme at KIT, whose discussions and insights enriched the understanding of the scientific challenges involved.

References

Bolch, T., Kulkarni, A., Kääb, A., Huggel, C., Paul, F., Cogley, J. G., Frey, H., Kargel, J. S., Fujita, K., Scheel, M., Bajracharya, S. R., and Stoffel, M. (2012): The State and Fate of Himalayan Glaciers. *Science* 336(6079):310–314. DOI: 10.1126/science.1215828.

Ek, M. B., Mitchell, K. E., Lin, Y., Rogers, E., Grunmann, P., Koren, V., Gayno, G., and Tarpley, J. D. (2003): Implementation of Noah land surface model advances in the NCEP operational mesoscale Eta model. *Journal of Geophysical Research: Atmospheres* 108(D22):8851. DOI: 10.1029/2002JD003296.

Heiskanen, W. A. and Moritz, H. (1967): Physical Geodesy. W. H. Freeman & Co., San Francisco, USA.

ICGEM (2026): International Centre for Global Earth Models (ICGEM): Gravity field and GRACE/GRACE-FO products hosted at the German Research Centre for Geosciences (GFZ). Accessed: 2026-04-06. URL: https://icgem.gfz-potsdam.de/.

IMD (2015): Rainfall and Temperature Variability over India (1951–2010). Tech. rep. New Delhi, India: Government of India, Ministry of Earth Sciences. URL: https://www.imdpune.gov.in.

Kusche, J., Schmidt, R., Petrovic, S., and Rietbroek, R. (2009): Joint inversion of GRACE and CHAMP satellite data for Earth's gravity field. *Journal of Geodesy* 83(4):331–342.

NASA (2020): MODIS Snow Cover Products User Guide. URL: https://modis-snow-ice.gsfc.nasa.gov.

Rodell, M., Houser, P. R., Jambor, U., Gottschalck, J., Mitchell, K. E., Meng, C.-J., Arsenault, K., Cosgrove, B. A., Radakovich, J. D., Bosilovich, M. G., Entin, J. K., Walker, J. P., Lohmann, D., and Toll, D. L. (2004): The Global Land Data Assimilation System. *Bulletin of the American Meteorological Society* 85(3):381–394. DOI: 10.1175/BAMS-85-3-381.

Swenson, S. and Wahr, J. (2006): Post-processing removal of correlated errors in GRACE data. *Geophysical Research Letters* 33(8):L08402. DOI: 10.1029/2005GL025285.

Tapley, B. D., Bettadpur, S., Watkins, M., and Reigber, C. (2004): The gravity recovery and climate experiment: Mission overview and early results. *Geophysical Research Letters* 31(9):1–4. DOI: 10.1029/2004GL019920.

Wahr, J., Molenaar, M., and Bryan, F. (1998): Time variability of the Earth's gravity field: Hydrological and oceanic effects and their possible detection using GRACE. *Journal of Geophysical Research: Solid Earth* 103(B12):30205–30229.

Wouters, B., Bonin, J. A., Chambers, D. P., Riva, R. E., Sasgen, I., and Wahr, J. (2014): GRACE, time-varying gravity, Earth system dynamics and climate change. *Reports on Progress in Physics* 77(11):116801.

Appendix

A GRACE TWS Anomalies in 2012 and 2016

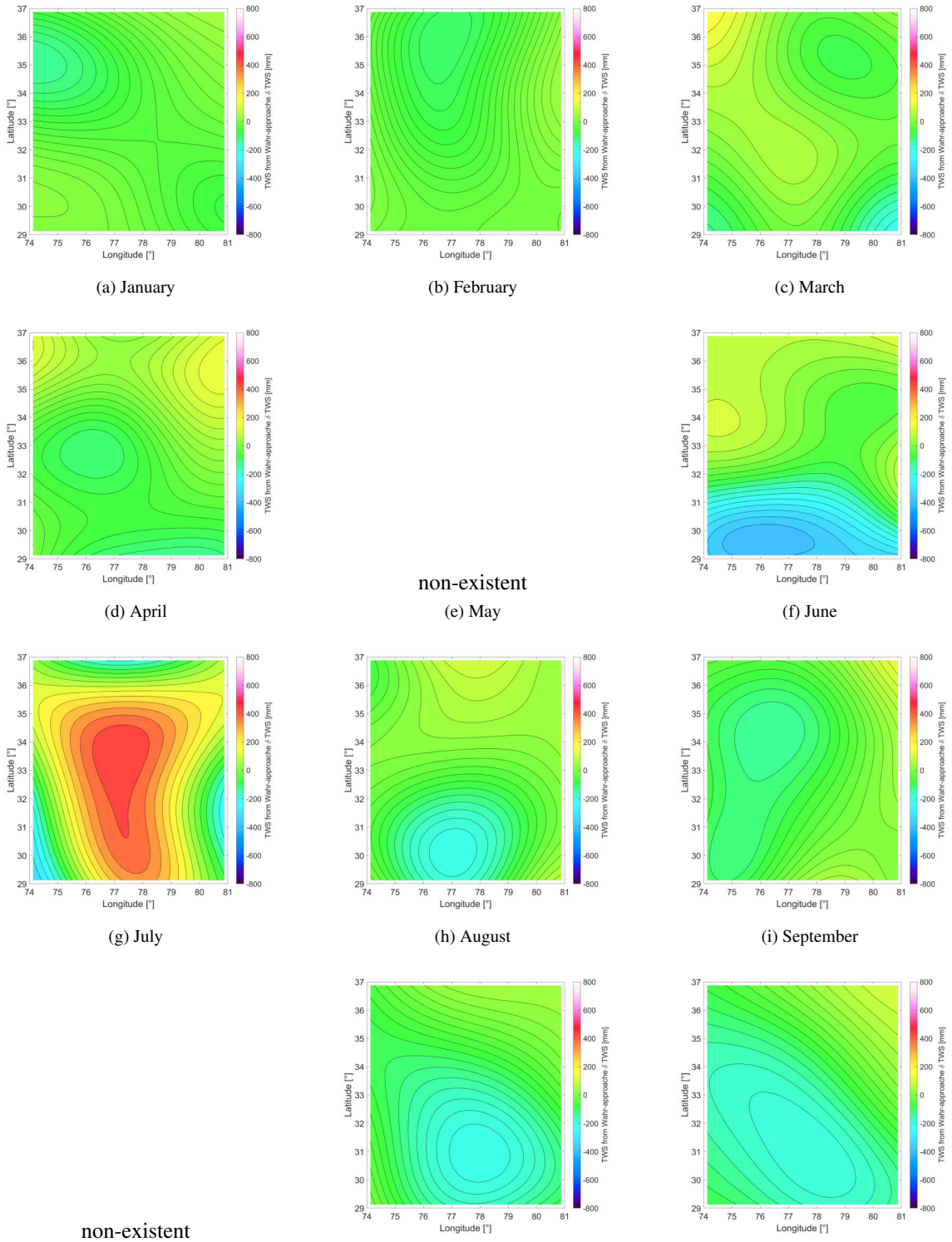

(a) January (b) February (c) March

(d) April non-existent (e) May (f) June

(g) July (h) August (i) September

non-existent (j) October (k) November (l) December

Figure A.1: GRACE TWS Anomalies in 2012 in the unit mm

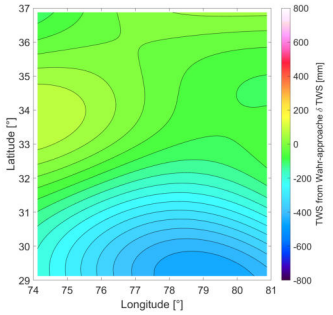

(a) January

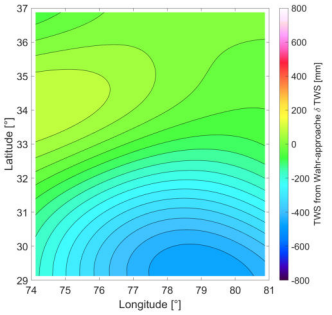

(b) February

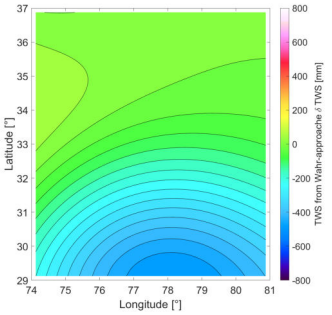

(c) March

non-existent

(d) April

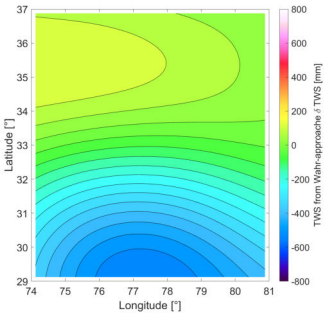

(e) May

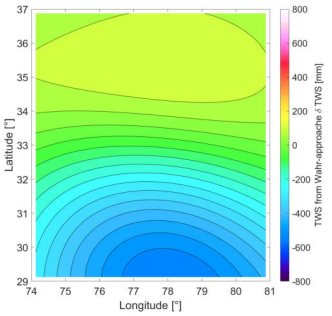

(f) June

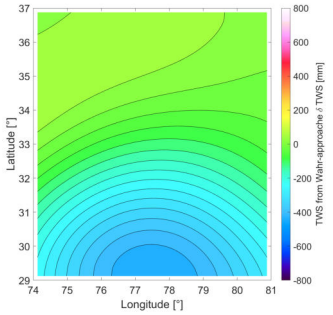

(g) July

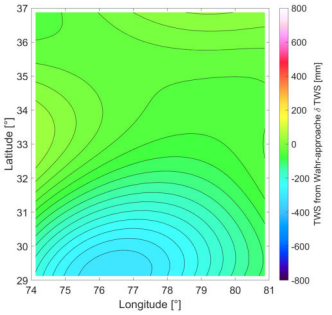

(h) August

non-existent

(i) September

non-existent

(j) October

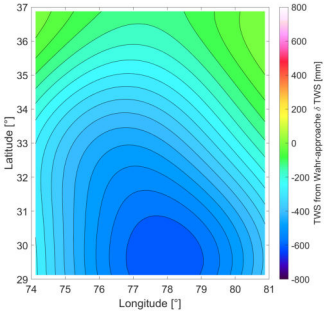

(k) November

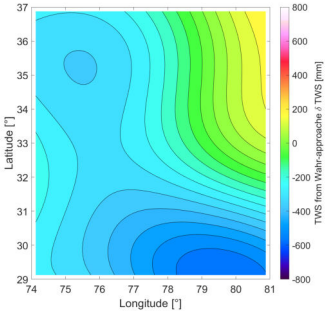

(l) December

Figure A.2: GRACE TWS Anomalies in 2016 in the unit mm

B GLDAS results in 2012 and 2016

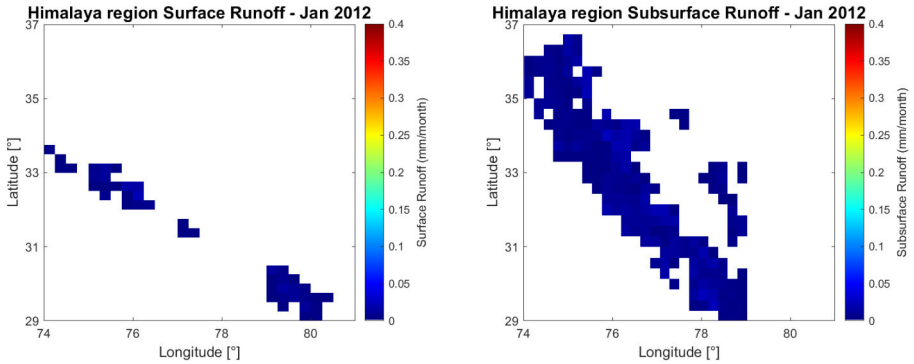

Figure B.1: GLDAS Runoff – January 2012

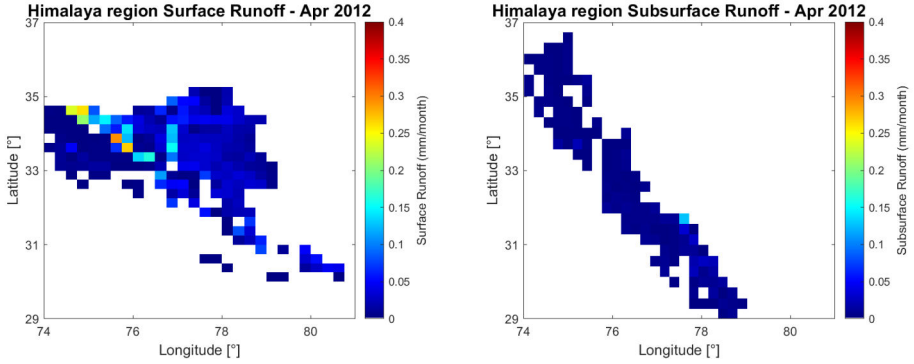

Figure B.2: GLDAS Runoff – April 2012

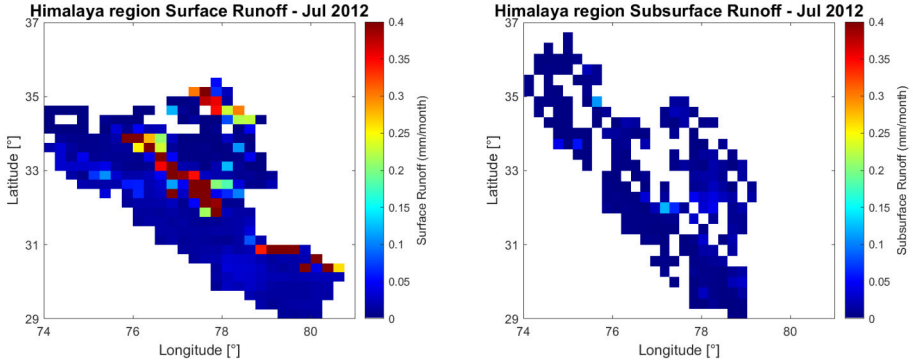

Figure B.3: GLDAS Runoff – July 2012

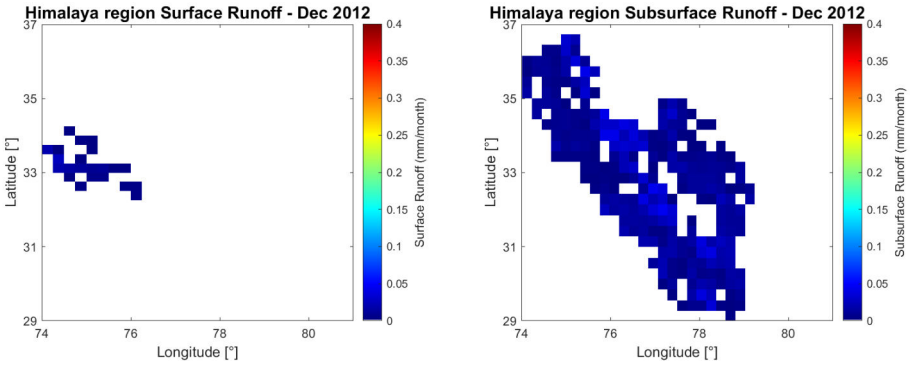

Figure B.4: GLDAS Runoff – December 2012

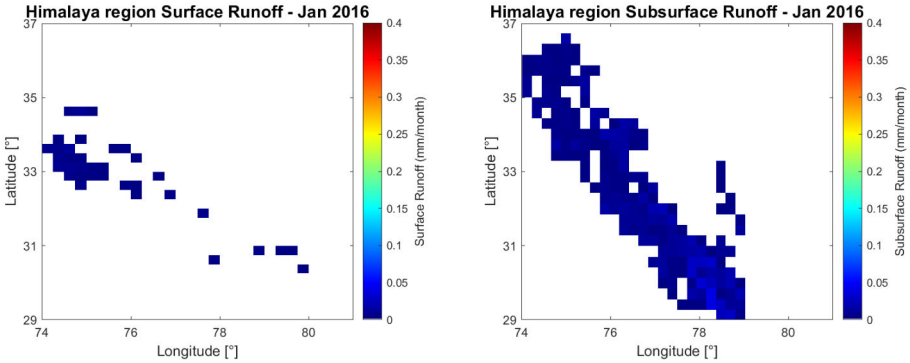

Figure B.5: GLDAS Runoff – January 2016

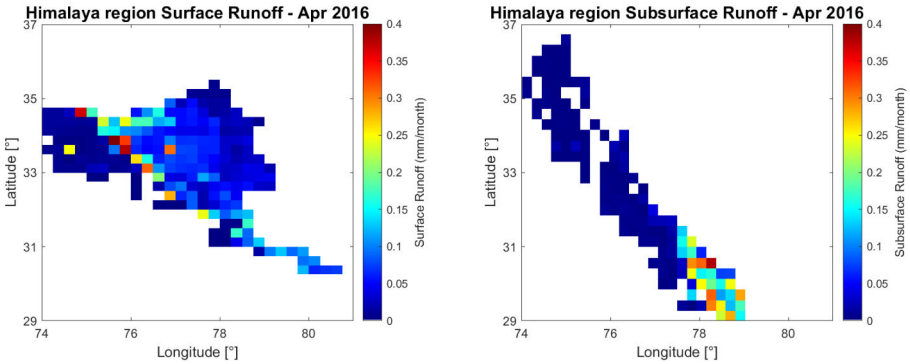

Figure B.6: GLDAS Runoff – April 2016

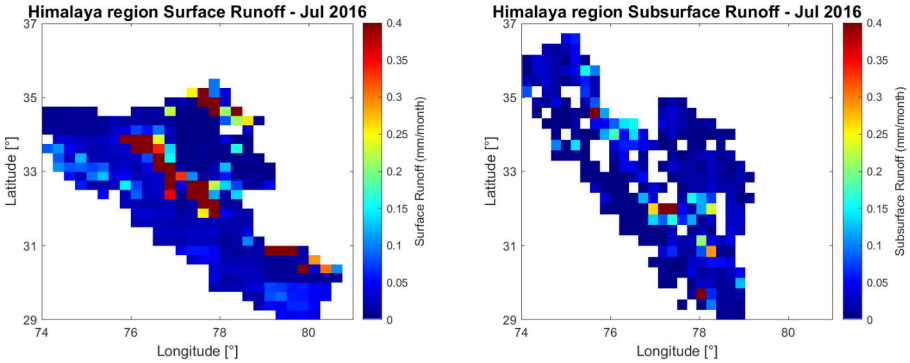

Figure B.7: GLDAS Runoff – July 2016

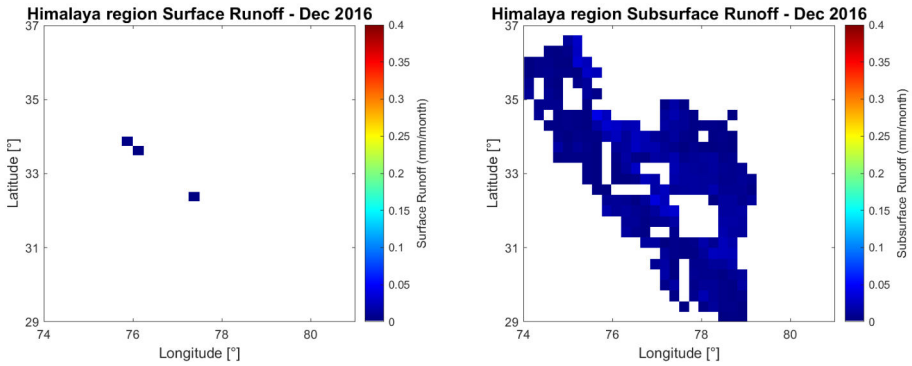

Figure B.8: GLDAS Runoff – December 2016

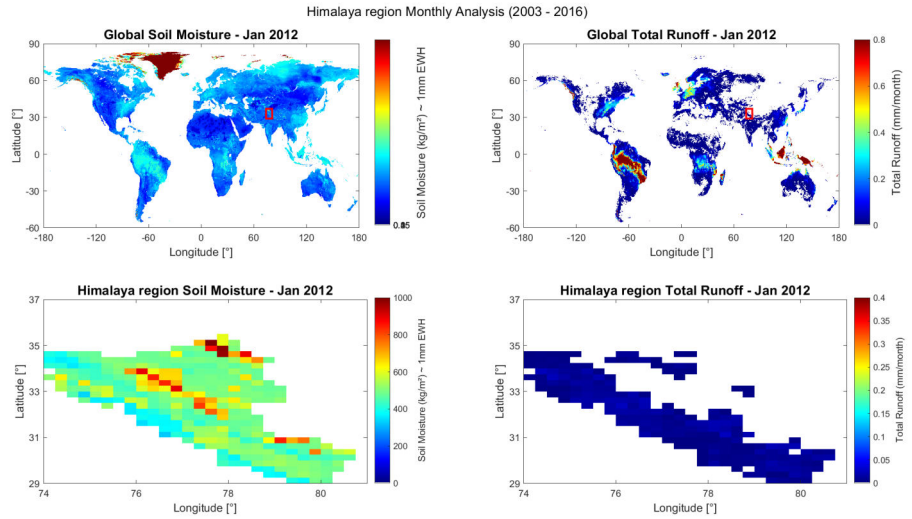

Figure B.9: GLDAS Spatial Map – January 2012

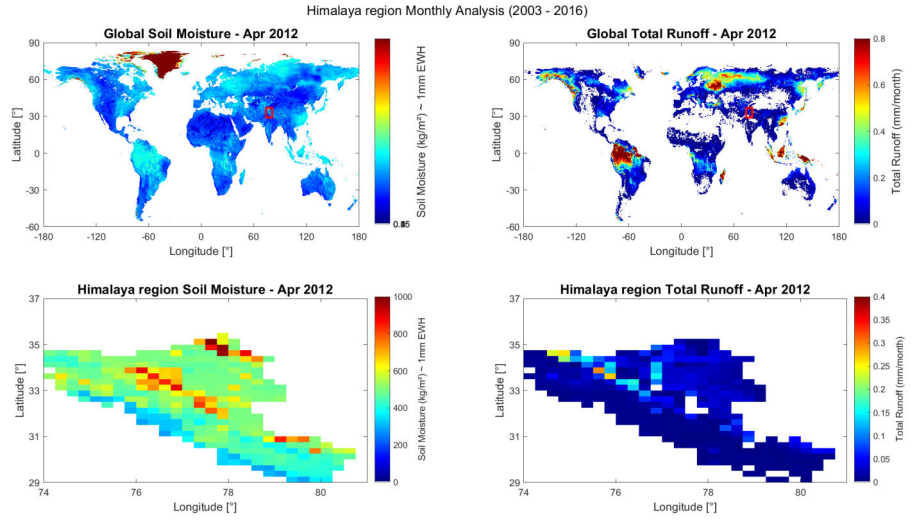

Figure B.10: GLDAS Spatial Map – April 2012

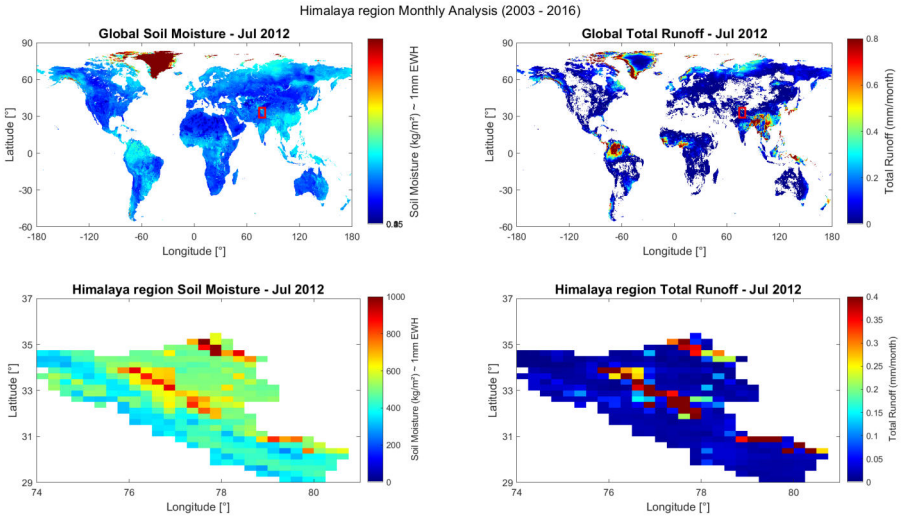

Figure B.11: GLDAS Spatial Map – July 2012

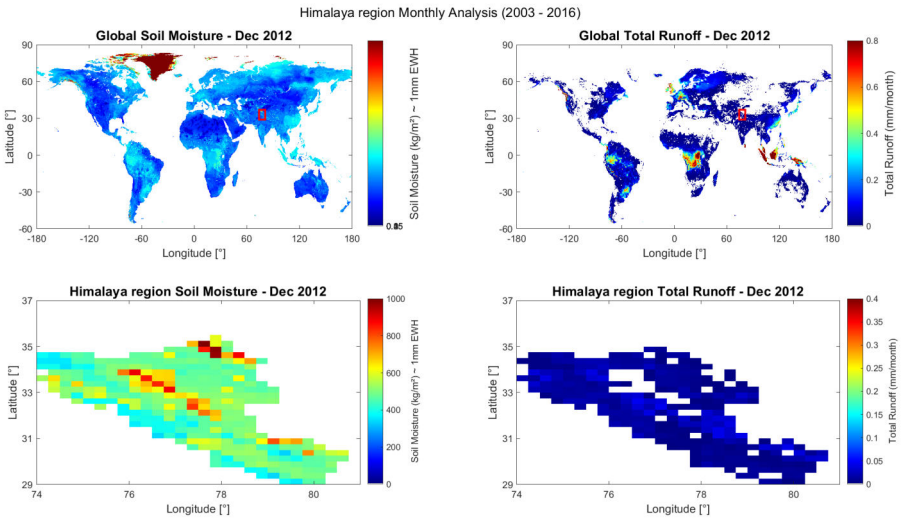

Figure B.12: GLDAS Spatial Map – December 2012

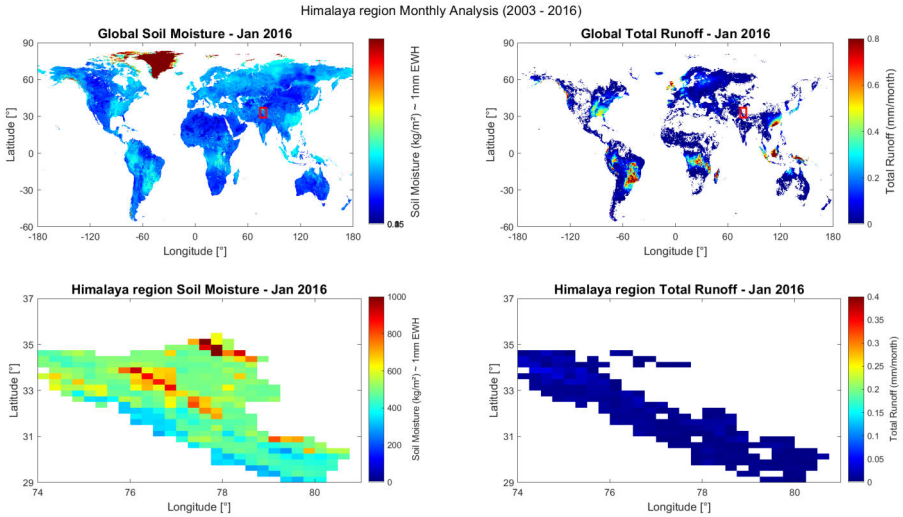

Figure B.13: GLDAS Spatial Map – January 2016

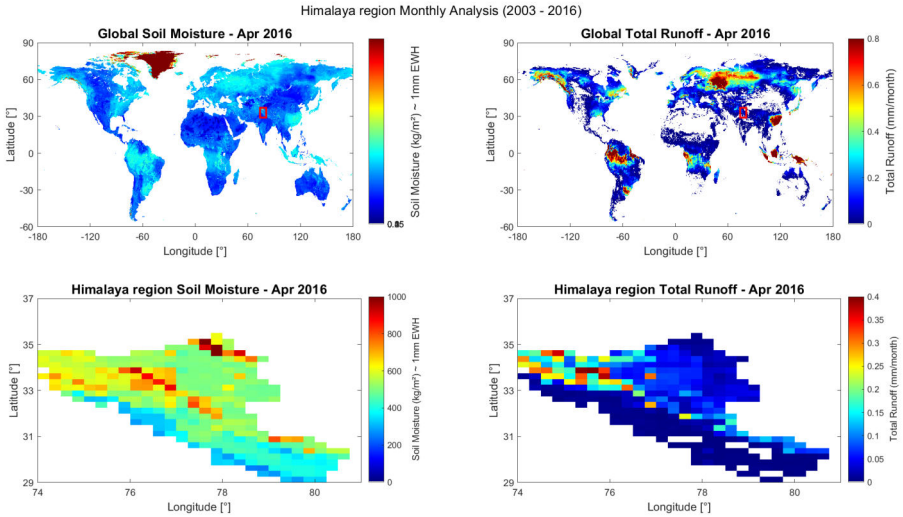

Figure B.14: GLDAS Spatial Map – April 2016

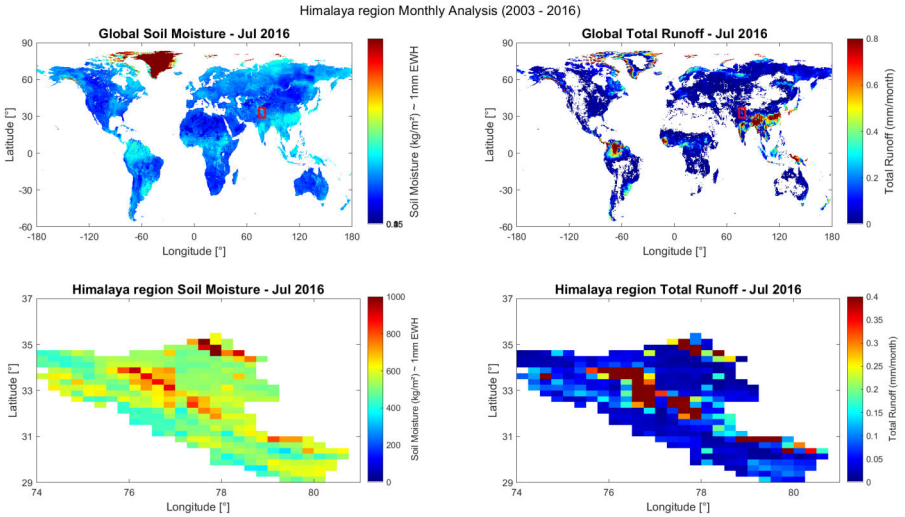

Figure B.15: GLDAS Spatial Map – July 2016

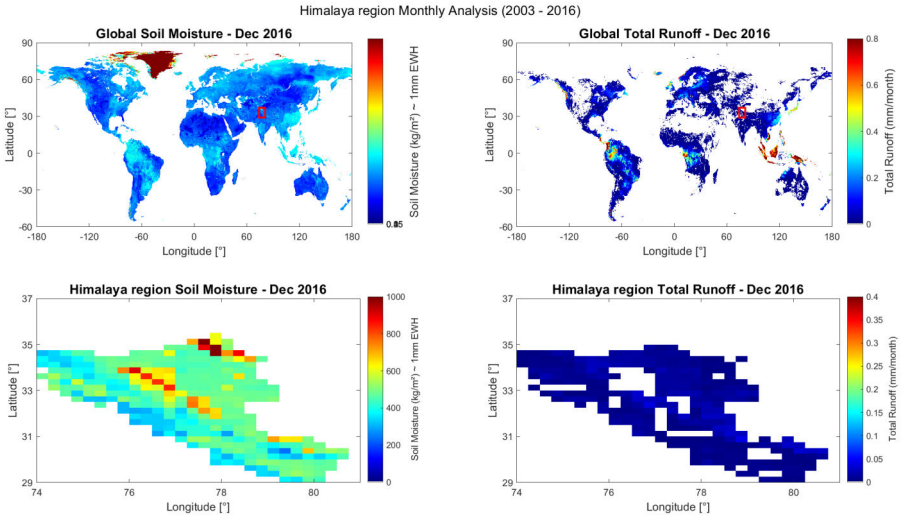

Figure B.16: GLDAS Spatial Map – December 2016

Characterizing hydrological mass variations across the continent of Africa by GRACE-FO and GLDAS data

Akhil Sunny[1]

1 Remote Sensing and Geoinformatics Master of Science (M.Sc.), KIT, Germany
E-Mail: uvwbd@student.kit.edu

Abstract

This study characterizes hydrological mass variations across the continent of Africa during the period 2019–2024 by integrating satellite-based geodetic observations with hydrological model outputs. Utilizing monthly gravity field solutions from the GRACE-FO missions, the research analyzes temporal and spatial mass fluctuations represented by spherical harmonic models up to degree and order 96. Following the methodology of Wahr et al. (1998), potential coefficients are transformed into surface spherical harmonics to represent Total Water Storage (TWS) changes, accounting for loading effects. To isolate groundwater storage, which is not explicitly provided in the Global Land Data Assimilation System (GLDAS) data, the study reduces soil moisture, runoff, and ice contributions – derived from GLDAS V2.1 – from the GRACE-derived TWS.

The analysis involves synthesizing continental grids with a spatial resolution of $15' \times 15'$ to produce spatial maps and time series of regional monthly averages. These visualizations are used to discuss and interpret the water storage dynamics across Africa, with a specific focus on quantifying the calculated groundwater.

The findings emphasize the utility of combining geodetic sensors with land data assimilation systems to enhance the understanding of large-scale hydrological processes and their implications for continental water management.

Keywords GRACE · GLDAS · Total Water Storage (TWS) · African Continent

1 Introduction

The Earth system is constantly undergoing temporal changes, many of which are associated with large-scale mass transport. These changes can be effectively studied by monitoring the Earth's gravitational field, as satellite-based geodetic sensors provide the capability to record both temporal and spatial mass fluctuations. Central to this monitoring are the Gravity Recovery and Climate Experiment (GRACE) and GRACE-FO missions, which provide monthly gravity field solutions that can be used to estimate changes in Total Water Storage (TWS). TWS represents the integrated storage of groundwater, soil moisture, surface water, and snow, serving as a physically relevant metric for tracking regional hydrological dynamics.

Understanding these variations is particularly critical for the continent of Africa, where water storage dynamics play a vital role in regional water management and climate resilience. While satellite missions like GRACE provide TWS, they can not distinguish between individual water components. To isolate specific elements such as

KIT Scientific Working Papers
Issue Number 270
ISSN: 2194-1629
DOI: 10.5445/IR/1000191188
Online: June 2026

This document is licensed under the Creative Commons Attribution – Share Alike 4.0 International License (CC BY-SA 4.0):
https://creativecommons.org/licenses/by-sa/4.0/deed.en

groundwater storage, satellite observations must be integrated with land data assimilation systems. The Global Land Data Assimilation System (GLDAS, 2025) ingests satellite- and ground-based observations to provide discrete grids of water balance components like soil moisture, runoff, and ice. By reducing these GLDAS-derived components from the GRACE-derived TWS, it becomes possible to quantify the groundwater residuals.
This Lab Rotation focuses on the preparation and discussion of time series of hydrological mass variations across Africa from 2019 to 2024. The study utilizes monthly gravity field solutions from the GFZ data center (DDK2 and DDK5 solutions) up to degree and order 96. Following the methodology established by Wahr et al. (1998), potential coefficients are transformed into surface spherical harmonics to represent TWS changes while accounting for loading effects. These variations are then synthesized into regional grids with a spatial resolution of $15' \times 15'$.
The primary objectives of this report are to:

- Process and visualize monthly TWS changes across the African continent using GRACE-FO and GLDAS data.
- Quantify groundwater storage by reducing soil moisture, runoff, and ice contributions from the total water storage.
- Analyze the onset and progression of hydrological trends through spatial mapping and time series analysis of regional monthly averages.
- Provide a thorough discussion and interpretation of the calculated water storage dynamics to enhance understanding of continental-scale mass transport.

2 Theoretical Aspects

Several fundamental concepts play an important role in the modelling of TWS.

2.1 Principle of Satellite Gravimetry (GRACE and GRACE-FO)

Spherical harmonics are given in Equation (2.1). The Earth's gravitational field is not static; it undergoes temporal changes primarily due to large-scale mass transport within the Earth system. The Gravity Recovery and Climate Experiment (GRACE) (Tapley et al., 2019) and its successor, GRACE-FO, monitor these changes by measuring tiny variations in the distance between two identical satellites following each other in orbit (Wahr et al., 1998; Tapley et al., 2004). As the leading satellite passes over a region with higher mass (such as increased groundwater), it is pulled slightly closer to Earth, changing the inter-satellite distance. These measurements allow for the detection of mass distribution changes caused by processes like evaporation, rainfall, and changes in soil moisture.

$$V(P) = \frac{GM}{r} \sum_{n=0}^{\infty} \left(\frac{R}{r}\right)^n \sum_{m=0}^{n} (\bar{C}_{nm} \cos m\lambda + \bar{S}_{nm} \sin m\lambda) \bar{P}_{nm}(\sin \varphi) \tag{2.1}$$

where,

GM	Geocentric gravitational constant
R	Radius of the reference sphere
$\bar{C}_{nm}, \bar{S}_{nm}$	Fully normalized spherical harmonic coefficients of degree n and order m
$\bar{P}_{nm}$	Fully normalized Legendre functions of degree n and order m
r, φ, λ	Geocentric spherical coordinates.

2.2 Degree and Error Degree Variances

The errors in the spherical harmonic coefficients of the gravity field solutions introduce uncertainties in the mass changes estimated from GRACE. Variance propagation is commonly analysed in the spectral domain to examine how these errors vary across spatial scales. The degree variance, defined as the sum of the squared spherical

harmonic coefficients over all orders m for a given degree n, indicates how the signal energy is distributed across spherical harmonic degrees (Heiskanen and Moritz, 1967).

$$C_n^2(\bar{C}_{nm}, \bar{S}_{nm}) = \sum_{m=0}^{n} (\bar{C}_{nm}^2 + \bar{S}_{nm}^2)\,. \tag{2.2}$$

In addition to the signal degree variance, the error-degree variance is calculated using the formal uncertainty of the spherical harmonic coefficients that accompany the GRACE Level-2 solutions. Their behaviour is shown in Figure 5.3. The error-degree variance is defined as:

$$\sigma C_n^2(\sigma\bar{C}_{nm}, \sigma\bar{S}_{nm}) = \sum_{m=0}^{n} (\sigma\bar{C}_{nm}^2 + \sigma\bar{S}_{nm}^2)\,. \tag{2.3}$$

The distribution of measurement noise over spherical harmonic degrees is explained by the error degree variance. It is feasible to identify the spectral region where the noise is significant and where the gravity signal is stronger by comparing degree variance and error-degree variance (Kusche, 2007).

2.3 Spherical Harmonic Representation of the Gravity Field

Spherical harmonic expansion is a mathematical technique that can be used to describe the Earth's gravity field. Using this method, the gravitational potential is given as a set of numbers called Stokes coefficients $\bar{C}_{nm}$ and $\bar{S}_{nm}$. Each pair of these coefficients represents the contribution of a particular wavelength (represented by degree n and order m) to the Earth's total gravity field.

The spherical harmonic degree determines the spatial resolution of the gravity field representation. Lower degrees correspond to long wavelength signals associated with large-scale mass redistribution, while higher degrees represent smaller spatial features but contain higher noise levels.

GRACE monthly solutions provide time-variable spherical harmonic coefficients. To isolate temporal gravity changes, a mean gravity field is removed from each monthly solution, resulting in anomaly coefficients:

$$\Delta\bar{C}_{nm}(t) = \bar{C}_{nm}(t) - \bar{C}_{nm}^{mean}\,, \qquad \Delta\bar{S}_{nm}(t) = \bar{S}_{nm}(t) - \bar{S}_{nm}^{mean}\,. \tag{2.4}$$

These temporal variations mainly represent mass redistribution processes within the Earth system, particularly hydrological mass changes such as variations in terrestrial water storage (TWS).

2.4 Total Water Storage using Wahr Approach

Temporal variations in the Earth's gravity field observed by GRACE and GRACE-FO are mainly caused by the redistribution of masses within the Earth system. Over land areas, these mass changes are dominated by variations in terrestrial water storage (TWS), which includes groundwater, soil moisture, surface water, snow, and ice components (Watkins et al., 2015).

GRACE Level-2 gravity field solutions provide monthly variations in terms of spherical harmonic coefficients. According to Wahr et al. (1998), changes in the spherical harmonic coefficients can be converted into surface mass variations expressed as Equivalent Water Height (EWH). The residual spherical harmonic coefficients are first calculated by subtracting the long-term mean field from each monthly gravity solution:

The surface mass variation represented as equivalent water height is then computed using:

$$\Delta h(\phi,\lambda) = \frac{R\,\rho_E}{3\,\rho_w} \sum_{n=0}^{N} \frac{2n+1}{1+k_n} \sum_{m=0}^{n} \left(\Delta\bar{C}_{nm}\cos m\lambda + \Delta\bar{S}_{nm}\sin m\lambda\right) \bar{P}_{nm}(\sin\varphi) \tag{2.5}$$

where,

$\Delta h(\phi,\lambda)$:	Equivalent water height variation
R:	Mean radius of the Earth
ρ_E:	Mean density of the Earth
ρ_w:	Density of water
k_n:	Load Love number of degree n
$\Delta\bar{C}_{nm}, \Delta\bar{S}_{nm}$:	Residual spherical harmonic coefficients
$\bar{P}_{nm}$:	Fully normalized Legendre functions

The load Love numbers k_n account for the elastic response of the Earth to surface mass redistribution. Through this transformation, temporal gravity field variations measured by GRACE are converted into TWS anomalies.
In this study, the resulting TWS fields are synthesized over the African continent using GRACE-FO monthly solutions. These TWS estimates are later combined with GLDAS hydrological components to investigate groundwater storage variations during the period 2019–2024.

3 Data

The analysis in this study is based on satellite-derived gravity field solutions from GRACE-FO and hydrological model outputs from the Global Land Data Assimilation System (GLDAS). GRACE-FO provides information about total terrestrial water storage variations, while GLDAS provides individual hydrological components required for estimating groundwater storage variations.

3.1 GRACE/GRACE-FO Data

The primary dataset used in this study consists of monthly GRACE-FO Level-2 gravity field solutions obtained from the International Centre for Global Earth Models (ICGEM, 2026). The solutions are generated by the German Research Centre for Geosciences (GFZ) and are provided as fully normalized spherical harmonic coefficients.
The gravity field is represented by the coefficients $\bar{C}_{nm}$ and $\bar{S}_{nm}$ up to spherical harmonic degree and order 96. These monthly provided coefficients describe temporal variations of the Earth's gravity field caused by redistribution of surface masses, including changes in terrestrial water storage (Wahr et al., 2004).
Monthly gravity field solutions covering the period 2019–2024 are used in this study. A reference mean gravity field is removed from each monthly solution to obtain residual coefficients representing temporal gravity changes. To reduce correlated errors and the characteristic north–south striping patterns present in GRACE solutions, decorrelation filtering is applied. In this study, GFZ DDK2 and DDK5 filtered solutions obtained through ICGEM are used for analyzing hydrological mass variations across the African continent.

3.2 GLDAS Data

The Global Land Data Assimilation System (GLDAS, 2025) provides land surface model outputs by combining satellite observations, ground measurements, and numerical land surface models. GLDAS hydrological products are used to separate individual water storage components that cannot be directly observed by GRACE. The GRACE-FO Level-2 spherical harmonic solutions used in this study were obtained from GFZ (2026), providing monthly gravity field variations for analysing terrestrial water storage changes.
In this study, GLDAS Version 2.1 data are used to obtain hydrological variables including soil moisture, runoff, and snow/ice components. These components are removed from the GRACE-derived TWS anomalies to estimate groundwater storage variations.
The groundwater storage anomaly is calculated as:

$$\Delta GW = \Delta TWS_{GRACE} - (\Delta SM_{GLDAS} + \Delta SWE_{GLDAS} + \Delta CW_{GLDAS}) \tag{3.1}$$

where ΔGW represents groundwater storage change, ΔSM represents soil moisture variation, ΔSWE represents snow water equivalent variation, and ΔCW represents canopy water storage variation.The GLDAS model provides soil moisture, runoff, and other hydrological variables used to separate groundwater storage variations from GRACE-FO TWS observations (Rodell et al., 2004).

3.3 Study Area and Temporal Coverage

The study focuses on the African continent, where water storage variations are strongly influenced by seasonal rainfall patterns, drought conditions, and regional hydrological processes. Africa contains diverse climatic regions ranging from humid tropical zones to arid and semi-arid areas, making it suitable for analyzing large-scale hydrological mass variations.

The investigation covers the period from 2019 to 2024 using monthly GRACE-FO and GLDAS datasets. The processed data are synthesized onto a regular spatial grid with a resolution of $15' \times 15'$ to generate spatial maps and regional time series of water storage variations (GLDAS, 2025).

4 Methodology Overview

The methodology adopted in this study focuses on the processing and analysis of GRACE-FO satellite gravity observations together with GLDAS hydrological model data to investigate hydrological mass variations over the African continent. The complete workflow includes preprocessing of monthly spherical harmonic gravity field solutions, spectral evaluation of the coefficients, spherical harmonic synthesis of gravity-related quantities, conversion of gravity variations into terrestrial water storage changes, and comparison with hydrological model components.

GRACE-FO Level-2 gravity field solutions obtained from GFZ through the International Centre for Global Earth Models (ICGEM, 2026) are processed in the spectral domain. The monthly gravity field variations are analysed using spherical harmonic coefficients, while GLDAS products are used to investigate individual hydrological components contributing to the total water storage signal. The generated outputs are analysed through spatial maps and temporal statistics to understand the behaviour of water storage variations between 2019 and 2024.

4.1 Preprocessing of GRACE-FO Spherical Harmonic Data

The GRACE-FO monthly gravity field solutions used in this study are provided as fully normalized spherical harmonic coefficients $\bar{C}_{nm}$ and $\bar{S}_{nm}$. The GFZ solutions obtained through ICGEM (2026) are processed up to spherical harmonic degree and order 96.

The initial processing step involves reading and organizing the monthly gravity field coefficients. Since the static component of the Earth's gravity field is dominant, a mean gravity field is computed from the available monthly solutions and removed from each individual monthly field. This produces residual spherical harmonic coefficients that represent temporal gravity variations caused by mass redistribution. Post-processing techniques are required to reduce correlated errors and improve the quality of GRACE spherical harmonic solutions (Swenson and Wahr, 2006). The residual coefficients are defined in Equation (2.4).

DDK2 and DDK5 filtered GFZ solutions are used in this study to reduce correlated errors and characteristic north–south striping effects present in GRACE observations, while preserving large-scale geophysical signals (Kusche et al., 2009; Swenson and Wahr, 2006). The processed monthly solutions provide the basis for further spectral analysis and spatial synthesis.

4.2 Spectral Analysis of Gravity Field Coefficients

Before transforming the gravity field into spatial quantities, the spectral behaviour of the spherical harmonic coefficients is analysed. Coefficient triangle plots are generated to visualize the distribution and magnitude of the gravity field coefficients for different degrees and orders.
Degree variance analysis is performed to evaluate the signal strength contained within different spherical harmonic degrees. Since lower degrees represent large-scale mass variations and higher degrees contain shorter wavelength signals with increased noise contribution, degree variance provides information about the spectral characteristics of the gravity solution.
In addition, error-degree variance is analysed using the formal uncertainties of the spherical harmonic coefficients. The comparison between degree variance and error-degree variance allows the separation between reliable gravity signals and noise-dominated spectral regions. The spectral behaviour of GRACE gravity field solutions can be analysed using spherical harmonic coefficients and their associated uncertainties (Wahr et al., 1998).

4.3 Spherical Harmonic Synthesis of Residual Gravity Field Quantities

The processed spherical harmonic coefficients are transformed from the spectral domain into spatial gravity field quantities using spherical harmonic synthesis (SHS). This transformation allows the visualization and analysis of gravity field variations over the selected study region.
Using the residual gravity coefficients, spatial fields of disturbing potential and residual geoid undulation are generated. These quantities provide information about temporal variations in the Earth's gravity field caused by redistribution of masses.Spherical harmonic synthesis transforms gravity field coefficients into spatial representations of potential, geoid height, and mass variations (Wahr et al., 1998).
Variance propagation is also performed to evaluate the uncertainty of the synthesized gravity field products. The resulting potential and geoid undulation fields, together with their propagated variances, are used to assess the reliability of the generated gravity field solutions.

4.4 Conversion of Gravity Variations into Total Water Storage

The gravity field variations observed by GRACE-FO are converted into surface mass variations following the approach of Wahr et al. (1998). The residual spherical harmonic coefficients are transformed into Equivalent Water Height (EWH), which represents terrestrial water storage (TWS) anomalies.
During this conversion, load Love numbers are introduced to account for the elastic response of the Earth due to surface mass loading. The obtained TWS anomalies represent vertically integrated changes in water storage, including groundwater, soil moisture, surface water, and snow components.
Monthly TWS fields are generated over the African continent at a spatial resolution of $15' \times 15'$. These monthly solutions are further used to investigate spatial patterns and temporal variations of hydrological mass changes. The observed terrestrial water storage variations represent changes in continental freshwater availability and hydrological mass redistribution (Scanlon et al., 2018).

4.5 GLDAS Hydrological Data Processing

The Global Land Data Assimilation System (GLDAS, 2025, Version 2.1) dataset is processed to analyse individual components of the terrestrial water cycle (Rodell et al., 2004). GLDAS combines satellite observations, ground-based measurements, and land surface modelling to provide estimates of different hydrological variables.
In this study, GLDAS components including soil moisture, runoff, and canopy water storage are extracted for the African region. Monthly spatial maps and regional time series are generated to analyse the behaviour of individual hydrological components.GLDAS combines satellite observations and land surface models to provide continuous estimates of hydrological variables (Rodell et al., 2004; GLDAS, 2025).

Since GRACE-derived TWS represents the combined contribution of all water storage components, GLDAS information is used to support the interpretation of the observed hydrological mass variations.

4.6 Statistical Analysis and Time Series Generation

To evaluate the temporal behaviour of hydrological mass variations, statistical analysis is performed on the generated monthly solutions. Parameters including minimum, maximum, mean, standard deviation, and RMS values are calculated from the TWS fields.

Regional monthly average time series are generated from GRACE-derived TWS anomalies and GLDAS hydrological variables. These time series are used to analyse seasonal variations, interannual changes, and long-term behaviour of water storage across Africa during the period 2019–2024.

The comparison of DDK2 and DDK5 processed solutions allows assessment of the influence of filtering on the recovered hydrological signals. The DDK filters are applied to reduce correlated errors and striping effects in GRACE-FO spherical harmonic solutions (Kusche et al., 2009; Swenson and Wahr, 2006).

5 Results and Discussion

5.1 Spectral Analysis of GRACE-FO Solutions

Before converting the GRACE-FO spherical harmonic coefficients into spatial representations of terrestrial water storage, the quality and spectral behaviour of the gravity field solutions were analysed. The spectral analysis helps to evaluate the signal distribution, coefficient accuracy, and noise characteristics at different spherical harmonic degrees.

The analysis was performed using the monthly GFZ GRACE-FO Level-2 solutions up to degree and order 96. The original monthly gravity field solutions and residual solutions obtained after removing the mean gravity field were compared to investigate temporal gravity variations.

5.1.1 Spherical Harmonic Coefficient Analysis

The spectral quality and stability of the monthly GRACE-FO gravity field solutions are evaluated using degree–order maps of the formal uncertainties ($\sigma_{\bar{C}_{nm}}$, $\sigma_{\bar{S}_{nm}}$) of the spherical harmonic coefficients. These maps illustrate how the coefficient uncertainties are distributed across different spatial scales represented by the spherical harmonic degree n and order m. Figures 5.1 show the degree–order distribution of the spherical harmonic coefficient

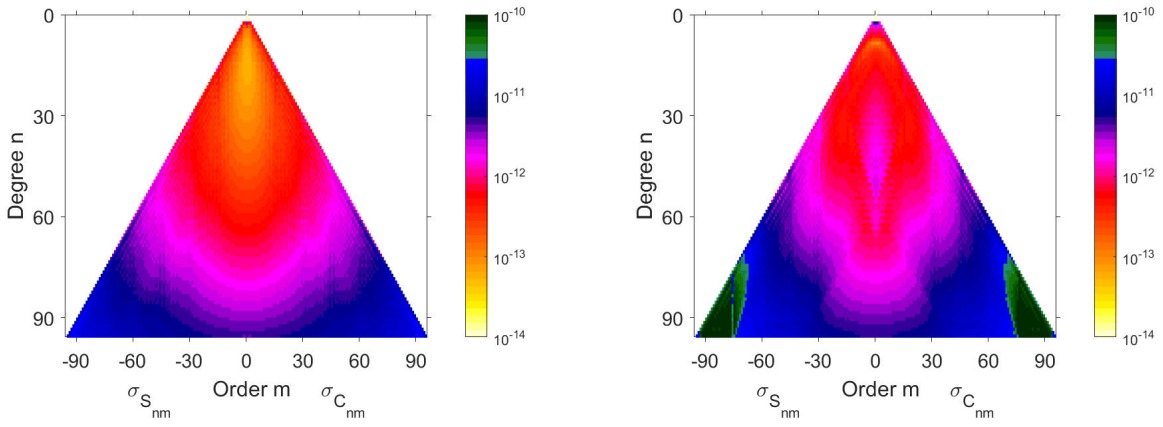

(a) April 2019 (b) April 2023

Figure 5.1: Degree–order representation of formal uncertainties of GRACE-FO spherical harmonic coefficients for April 2019 and April 2023 in DDK2. The coefficient triangle illustrates the distribution of uncertainties ($\sigma_{\bar{C}_{nm}}$, $\sigma_{\bar{S}_{nm}}$) across different spherical harmonic degrees and orders. See also Equation (2.3).

uncertainties for April 2019 and April 2023 as representative monthly solutions.

The degree–order map for April 2019 shows a regular and symmetric spectral behaviour. The uncertainties are relatively small at lower spherical harmonic degrees, which represent large-scale gravity field signals, and increase gradually towards higher degrees and orders corresponding to smaller spatial features. This smooth distribution indicates a stable monthly gravity field solution, where the dominant large-scale gravity signals are clearly represented.

In comparison, the April 2023 solution shows a less uniform spectral distribution, particularly at higher degrees and orders. Increased uncertainties observed in the higher-degree coefficients indicate the stronger influence of measurement noise and short-wavelength errors. Although the large-scale gravity field components remain stable, the higher-degree components are more affected by noise and require careful treatment before spatial interpretation.

The differences between the two monthly solutions demonstrate the natural variability of GRACE-FO gravity field products. Noise contributions at higher spherical harmonic degrees can propagate into the spatial domain and produce artificial short-wavelength patterns. Therefore, the use of DDK-filtered solutions is necessary to reduce correlated errors while preserving the geophysical signals associated with hydrological mass variations.

Overall, the coefficient analysis confirms that the large-scale gravity signals required for estimating TWS variations over Africa are reliably represented. The spectral evaluation provides an important quality assessment before transforming the gravity field coefficients into EWH anomalies.

5.1.2 Relative Accuracy Analysis of Gravity Field Coefficients

Relative accuracy analysis is performed to evaluate the internal consistency of the monthly GRACE-FO spherical harmonic solutions rather than only considering the absolute magnitude of the formal errors. This analysis investigates the relationship between the formal uncertainties of the sine coefficients ($\sigma_{\bar{S}_{nm}}$) and cosine coefficients ($\sigma_{\bar{C}_{nm}}$) across different spherical harmonic degrees n and orders m.

Since both coefficient types represent the same physical gravity field signal with different phase components, a stable and well-balanced monthly gravity solution is expected to show similar error behaviour for both coefficient groups. Therefore, the ratio between the sine and cosine coefficient uncertainties should remain close to 100%.

Figures 5.2 show the relative accuracy maps ($\sigma_{\bar{S}_{nm}}/\sigma_{\bar{C}_{nm}}$) for September 2021 and September 2024.

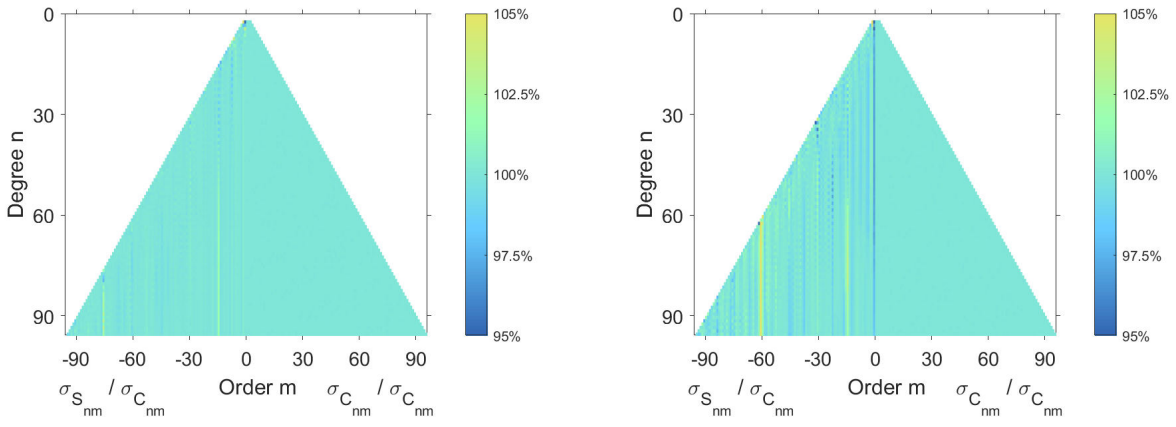

(a) September 2021 (b) September 2024

Figure 5.2: Relative accuracy distribution of GRACE-FO spherical harmonic coefficients for September 2021 and September 2024 in DDK2. The maps represent the ratio between the formal uncertainties of sine and cosine coefficients ($\sigma_{\bar{S}_{nm}}/\sigma_{\bar{C}_{nm}}$) across different degrees and orders.

The relative accuracy map for September 2021 shows a highly stable spectral distribution. Most of the relative accaracy of the coefficient have constant values close to 100%, indicating a balanced uncertainty distribution

between the sine and cosine spherical harmonic coefficients. This behaviour suggests that neither coefficient type dominates the error structure, representing a stable monthly gravity field solution.
The September 2024 solution also shows overall spectral stability; however, slightly stronger order-dependent variations can be observed at higher spherical harmonic degrees. These variations represent small deviations from the ideal uncertainty ratio and indicate the increasing influence of measurement noise and residual correlated errors at shorter spatial wavelengths.
For both monthly solutions, the deviations from 100% are mainly observed towards higher degrees and orders. This behaviour is expected because higher-degree coefficients represent smaller spatial scales and are more sensitive to orbit-related errors and measurement noise in the GRACE-FO observations. However, the similarity between sine and cosine coefficient uncertainties indicates that the solutions remain internally consistent.
Overall, the relative accuracy analysis confirms the spectral stability of the GFZ Level-2 GRACE-FO solutions used in this study. The balanced error behaviour supports the reliability of these solutions for deriving terrestrial water storage (TWS) anomalies over Africa. The presence of higher-degree noise also demonstrates the importance of using DDK-filtered solutions to reduce correlated errors while preserving the hydrological mass variation signals.

5.1.3 Degree and Error-Degree Variance Analysis

The spectral quality and signal-to-noise characteristics of the GRACE-FO gravity field solutions are evaluated by comparing the degree variance (σ_n^2) and the error-degree variance ($d\sigma_n^2$). This analysis helps to identify the spectral range in which the geophysical gravity signal is stronger than the measurement noise and provides information about the reliable spatial resolution of the monthly gravity field solutions.
Figures 5.3 illustrate the degree variance and error-degree variance spectra for the April 2019 GRACE-FO solution and the corresponding residual solution obtained after removing the mean gravity field.

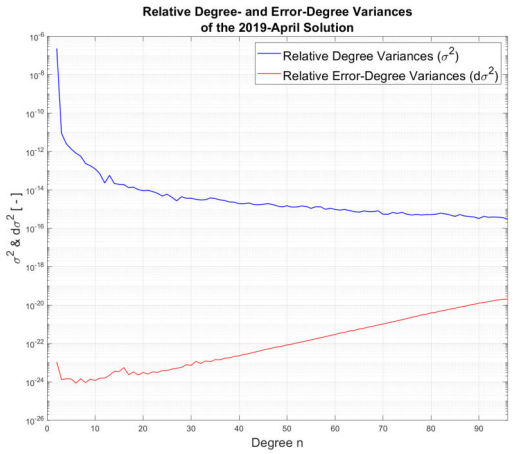

(a) Degree and error degree variance

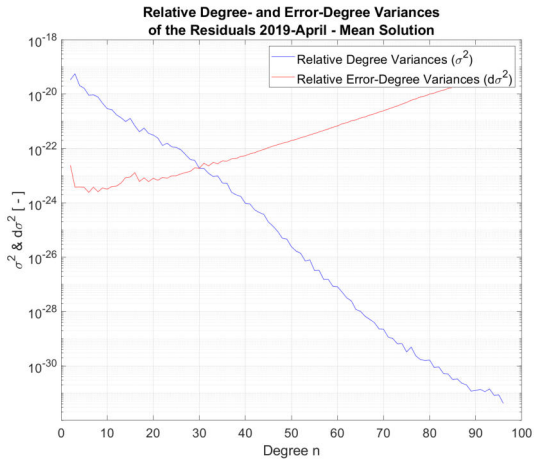

(b) Relative degree and error degree variance

Figure 5.3: Relative degree variance and relative error-degree variance spectra for the April 2019 GRACE gravity field solutions in DDK2. (a) Original monthly solution. (b) Residual solution after subtraction of the mean field. The blue curve denotes the signal variance, while the red curve represents the error variance as a function of spherical harmonic degree n.

The degree variance of the complete monthly gravity field solution represents the total spectral energy of the Earth's gravity field. For the April 2019 solution, the signal variance remains significantly higher than the formal error variance across the spherical harmonic spectrum up to degree and order 96. This indicates that the absolute gravity field solution contains a strong signal contribution compared to the estimated coefficient uncertainties.
In contrast, the residual solution represents only temporal gravity field variations after subtraction of the mean reference field. These variations are mainly caused by time-dependent mass redistribution processes, such as

changes in terrestrial water storage. Since temporal mass changes are much smaller than the static gravity field, the degree variance of the residual solution decreases more rapidly with increasing spherical harmonic degree.
The residual degree variance spectrum shows a crossover point where the signal variance approaches the error-degree variance. For the April 2019 solution, this occurs at approximately spherical harmonic degree 30. Below this degree, the geophysical signal dominates the measurement noise and mainly represents reliable large-scale mass variations. At higher degrees, the error-degree variance becomes larger, indicating that short-wavelength signals are increasingly affected by measurement noise and correlated errors.
The increasing noise contribution at higher spherical harmonic degrees can introduce artificial patterns, such as the characteristic north–south striping effect observed in GRACE solutions. Therefore, the use of DDK-filtered solutions is necessary to suppress high-degree noise while preserving physically meaningful hydrological mass variation signals.
Overall, the degree variance analysis confirms that the GRACE-FO solutions provide reliable large-scale gravity variations suitable for estimating terrestrial water storage (TWS) changes across the African continent.

5.2 Gravity Field Quantity Analysis

The residual spherical harmonic coefficients obtained from GRACE-FO monthly gravity field solutions are synthesized into spatial gravity field quantities to analyse temporal gravity variations over the African continent. In this study, disturbing potential and geoid undulation fields are generated to investigate the effect of mass redistribution on the Earth's gravity field.
The disturbing potential represents deviations of the observed gravity potential from a reference gravity field, while geoid undulation describes the corresponding changes in the height of the equipotential surface. These quantities provide an intermediate representation of gravity field variations before the conversion into terrestrial water storage anomalies.

5.2.1 Disturbing Potential Analysis

The disturbing potential represents temporal variations in the Earth's gravity field caused by redistribution of masses within the Earth system. Using spherical harmonic synthesis, the monthly GRACE-FO gravity field coefficients are transformed from the spectral domain into spatial potential anomaly fields.
In this study, the disturbing potential anomalies are analysed to investigate large-scale gravity field changes associated with hydrological mass variations across the African continent. Positive potential anomalies indicate regions with relative mass increase, whereas negative anomalies represent areas experiencing mass reduction compared to the reference gravity field.
Figures 5.4 show the GRACE-FO derived disturbing potential anomalies for April 2019 and September 2024.
The disturbing potential maps show broad spatial variations over the African continent. The observed positive and negative anomaly regions represent changes in the Earth's gravity field mainly caused by temporal redistribution of hydrological masses such as groundwater, soil moisture, and surface water.
The comparison between April 2019 and September 2024 demonstrates the temporal variability of the gravity field during the study period. The dominant smooth spatial patterns indicate that the GRACE-FO solutions mainly capture long-wavelength mass variations rather than small local features.
These potential anomaly fields provide an intermediate gravity quantity derived from spherical harmonic coefficients before conversion into equivalent water height (EWH) and terrestrial water storage (TWS) variations.

5.2.2 Geoid Undulation Analysis

The integrated effect of mass redistribution within the Earth system can be observed through variations in geoid undulation. Geoid undulation represents the height variation of an equipotential surface caused by changes in the

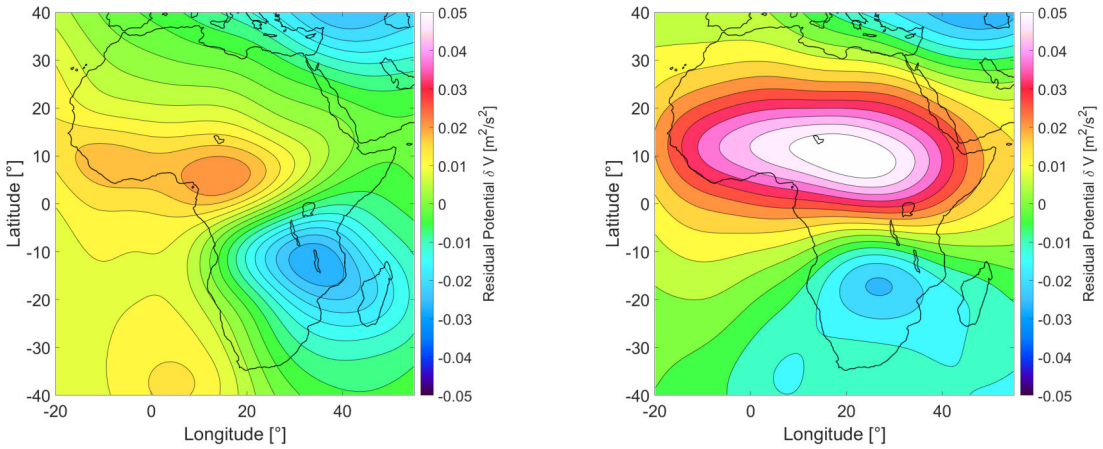

(a) April 2019 (b) September 2024

Figure 5.4: Spatial distribution of GRACE-FO derived disturbing potential anomalies over Africa for April 2019 and September 2024 in DDK2. The variations in the residual potential represent temporal gravity field changes caused by mass redistribution within the Earth hydrological system. Range is $\pm$ 0.05 $m^2 s^{-2}$.

Earth's gravity field. In GRACE-FO observations, temporal variations in geoid undulation are mainly associated with large-scale redistribution of surface masses, especially changes in terrestrial water storage.

The residual geoid undulation fields are obtained by applying spherical harmonic synthesis to the monthly gravity field anomaly coefficients. These results provide an intermediate representation between the spectral gravity field solutions and the estimation of equivalent water height (EWH) variations.

Figures 5.5 show the residual geoid undulation fields over Africa for October 2021 and October 2024.

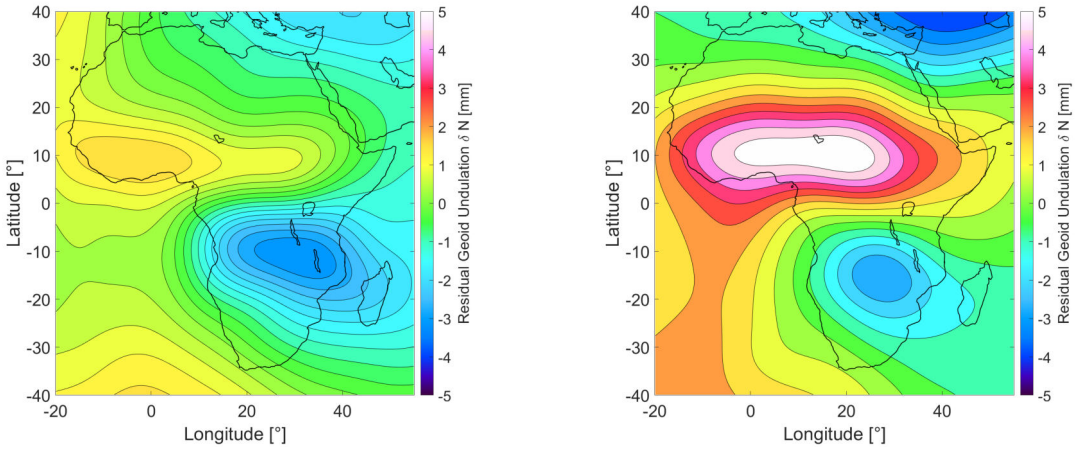

(a) October 2021 (b) October 2024

Figure 5.5: Residual geoid undulation variations derived from GRACE-FO gravity field solutions over Africa for October 2021 and October 2024 in DDK2, showing the effect of large-scale mass redistribution on the geoid. Range is $\pm$ 5 *mm*.

The residual geoid undulation map for October 2021 shows smooth long-wavelength spatial patterns over the African continent. Positive undulation anomalies are observed over parts of the Sahel and Central African regions, indicating relative mass increase compared with the mean gravity field. Negative anomalies are visible towards southern Africa, representing regions with relative mass reduction.

Compared with October 2021, the October 2024 undulation field shows a stronger spatial variability. The positive anomaly over the northern tropical region becomes more pronounced, suggesting an increased hydrological mass

contribution during this season. The negative anomaly over the southern region remains visible, indicating regional differences in water storage variations across the continent.
The comparison between both years highlights the interannual variability of the African hydrological system. The smooth spatial structures demonstrate that GRACE-FO primarily observes long-wavelength gravity signals associated with large-scale mass redistribution rather than small local variations.
Some variations near the boundaries of the study region may be influenced by leakage effects caused by spherical harmonic truncation and filtering. Therefore, the interpreted geoid undulation patterns are mainly suitable for analysing broad regional-scale hydrological changes.
Overall, the residual geoid undulation analysis confirms the presence of temporal gravity variations over Africa and provides an important intermediate step before deriving terrestrial water storage (TWS) anomalies.

5.3 Terrestrial Water Storage (TWS) Analysis

Terrestrial Water Storage (TWS) represents the vertically integrated variation of water stored on and below the Earth's surface, including groundwater, soil moisture, surface water, and snow or ice components. GRACE-FO observations provide a unique capability to monitor these large-scale hydrological mass variations by measuring temporal changes in the Earth's gravity field. Satellite gravimetry observations from GRACE and GRACE-FO have been widely applied for monitoring global freshwater availability and long-term hydrological changes (Rodell et al., 2018).
The residual spherical harmonic coefficients obtained from GRACE-FO solutions are converted into Equivalent Water Height (EWH) following the approach of Wahr et al. (1998). The resulting EWH fields represent monthly TWS anomalies relative to a reference mean gravity field.
The spatial patterns and temporal variations provide information about regional hydrological changes, including water accumulation and water deficit periodsLarge-scale freshwater storage variations observed by GRACE provide important information about global hydrological changes (Rodell et al., 2018; Scanlon et al., 2018).

5.3.1 Monthly TWS Spatial Variations

The monthly GRACE-FO derived terrestrial water storage (TWS) anomaly maps illustrate the spatial distribution of hydrological mass variations across the African continent. The TWS variations are represented as Equivalent Water Height.
Selected monthly solutions from different years are analysed to evaluate seasonal and interannual variability of water storage over Africa. The comparison between April and October solutions provides information about the temporal evolution of hydrological mass redistribution during different periods of the annual cycle.

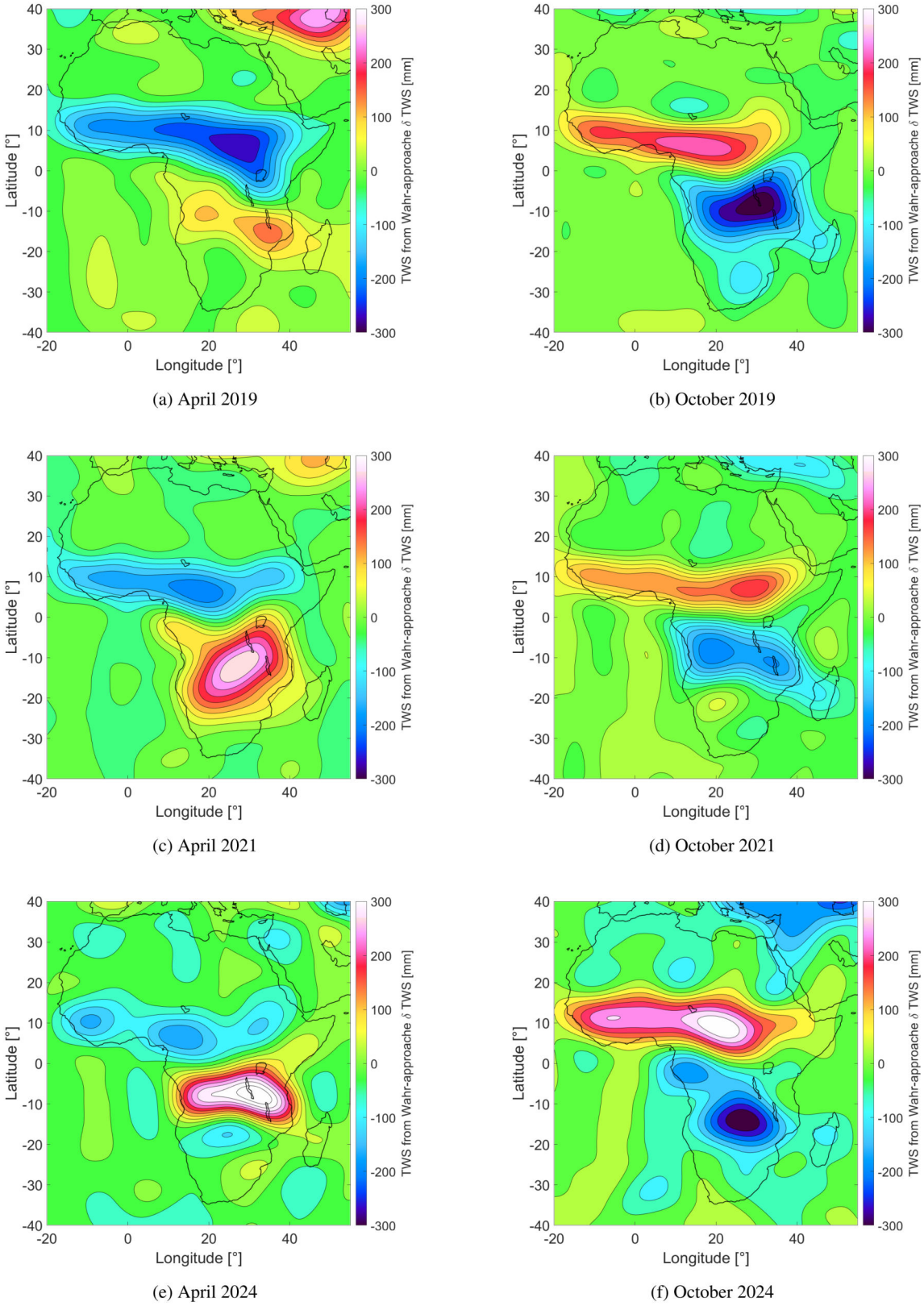

(a) April 2019

(b) October 2019

(c) April 2021

(d) October 2021

(e) April 2024

(f) October 2024

Figure 5.6: Monthly GRACE-FO derived terrestrial water storage anomalies over Africa for selected months between 2019 and 2024 in DDK2. Range is ± 300 mm.

The April TWS solutions represent the hydrological conditions during the transition period towards wetter conditions in several African regions. The April 2019 and April 2021 solutions show spatial variations with both positive and negative storage anomalies across the continent.
The April 2024 solution shows stronger positive TWS anomalies over parts of the tropical African region compared with earlier selected years. This indicates increased water storage conditions during this period, which may be associated with variations in precipitation, soil moisture, and groundwater recharge processes.
The October solutions highlight the seasonal response of the African hydrological system after major rainfall periods in several regions. A broad positive TWS anomaly is observed across parts of the Sahel and central African regions, indicating increased water accumulation. Differences between October 2019, 2021, and 2024 demonstrate the interannual variability of terrestrial water storage conditions.
In contrast, some regions of southern Africa show negative TWS anomalies, representing comparatively lower water storage conditions. These spatial differences demonstrate the heterogeneous nature of the African hydrological system, where different climatic regions experience different seasonal water storage responses.
Overall, the comparison of April and October solutions demonstrates the strong influence of seasonal hydrological cycles on continental-scale mass redistribution. The observed spatial patterns mainly represent large-scale variations in water storage captured by GRACE-FO rather than small local hydrological processes.
Due to the limited spatial resolution of GRACE-FO observations and the use of spherical harmonic processing, some smoothing and signal leakage effects may occur near regional boundaries. Therefore, the resulting TWS maps are mainly interpreted for broad regional hydrological variations rather than localized small-scale changes.

5.3.2 Mean TWS Distribution (2019–2024)

The mean terrestrial water storage (TWS) distribution represents the average spatial behaviour of hydrological mass variations over the African continent during the complete study period. The mean field is derived from the monthly GRACE-FO solutions in the period 2019-2024.

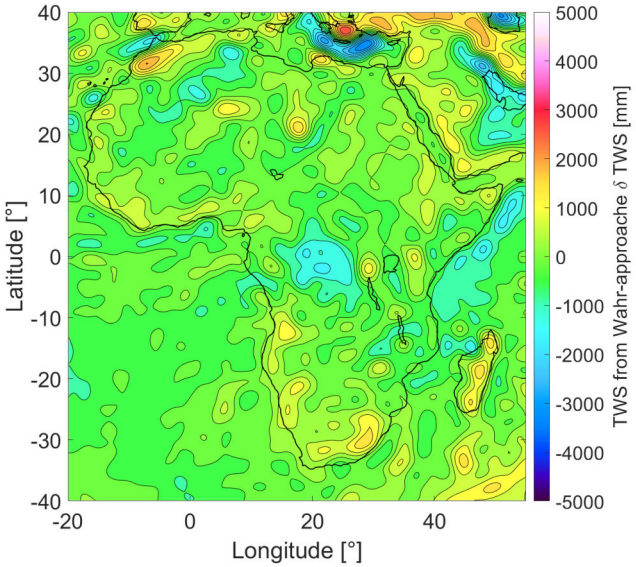

Figure 5.7: Mean GRACE-FO derived terrestrial water storage (TWS) distribution over Africa for the period 2019–2024 using the DDK2 filtered solution. Range is ± 5 mm.

Most regions show values close to zero, indicating that the dominant static gravity field components have been removed and the remaining signal mainly represents temporal hydrological mass variations.
Spatial patterns show regional differences between northern, central, and southern Africa, reflecting the mean climatic conditions, precipitation distribution, and hydrological storage processes.

Some stronger anomaly patterns are observed near the boundaries of the study region. These features should be interpreted carefully because spherical harmonic truncation, spatial filtering, and leakage effects can influence GRACE-derived products, especially close to regional edges.
Overall, the mean TWS field provides a reference representation of the average hydrological mass distribution over Africa and supports the interpretation of monthly and temporal variations analysed in the following sections.

5.3.3 TWS Time Series Analysis

The temporal behaviour of terrestrial water storage over Africa was investigated using monthly GRACE-FO Equivalent Water Height solutions from 2019 to 2024. In addition to analysing spatial distributions, the monthly statistical parameters provide information about the magnitude and variability of hydrological mass changes over time.
For each monthly TWS solution, the minimum, maximum, mean, root mean square (RMS), and standard deviation (STD) values were calculated from the gridded EWH fields. These parameters describe the temporal evolution and spatial variability of continental water storage anomalies.

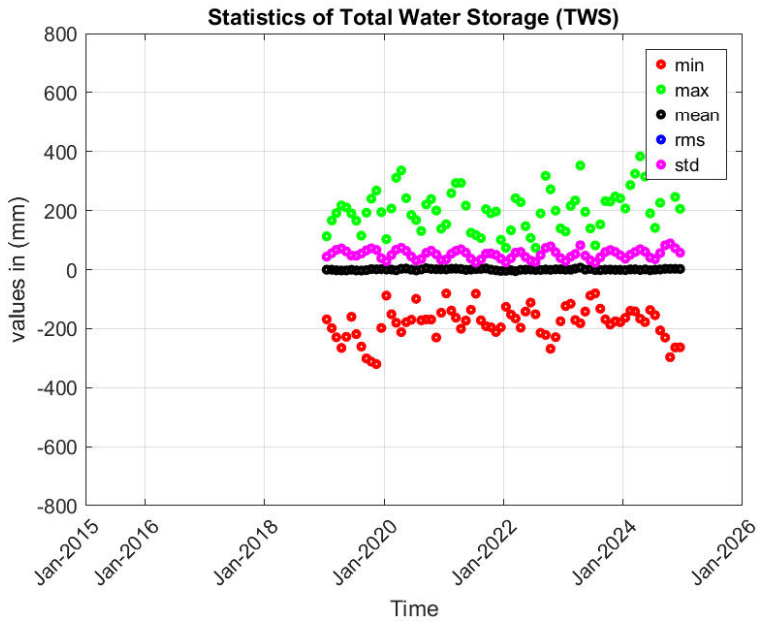

Figure 5.8: Statistical variation of monthly GRACE-FO derived terrestrial water storage (TWS) anomalies over Africa during 2019–2024 using the DDK2 filtered solutions. Minimum, maximum, mean, RMS, and standard deviation values are represented in mm.

The time series given in Figure 5.8 shows significant temporal variability of TWS anomalies over the African continent. The maximum and minimum values exhibit opposite behaviour, representing regions of water accumulation and water deficit within each monthly solution. Maximum TWS anomalies generally vary between approximately 100 mm and 350 mm, while minimum values reach approximately -300 mm during stronger negative storage periods. The mean TWS values remain close to zero throughout the observation period, which shows that obviously there is no trend (black symbols in Figure 5.8). The RMS and standard deviation values show variations in the strength of the spatial TWS signal. Increased RMS and STD values indicate months with stronger regional differences between positive and negative water storage anomalies, while lower values represent comparatively uniform storage conditions. The repeated fluctuations observed between 2019 and 2024 mainly reflect seasonal hydrological processes, including changes in precipitation, soil moisture, surface water, and groundwater storage. Overall, the time series confirms that GRACE-FO observations can capture large-scale temporal seasonal variations (pink symbols in Figure 5.8) in terrestrial water storage across Africa.

5.4 GLDAS Hydrological Component Analysis

The Global Land Data Assimilation System (GLDAS) is used to analyse individual hydrological storage components contributing to terrestrial water storage variations. While GRACE-FO observations represent the combined mass change of all water storage components, GLDAS provides separate estimates of soil moisture, runoff, and canopy water storage.

These components are required to remove the non-groundwater contribution from the GRACE-derived Total Water Storage (TWS), allowing groundwater storage variations to be estimated.

5.4.1 Spatial Distribution of GLDAS Components

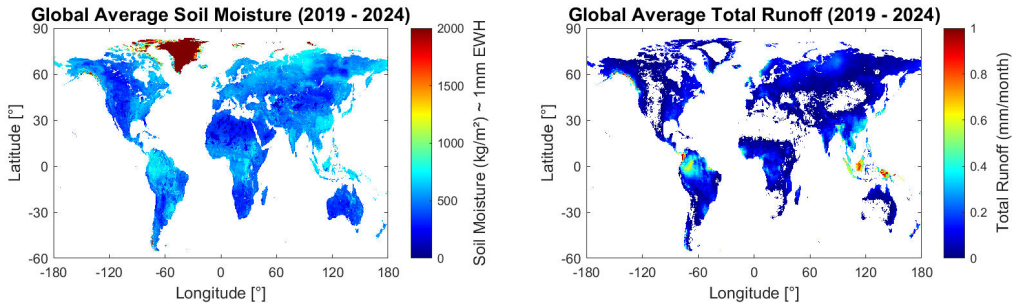

Figure 5.9: Global mean soil moisture and runoff from GLDAS hydrological components during the study period from 2019 to 2024.

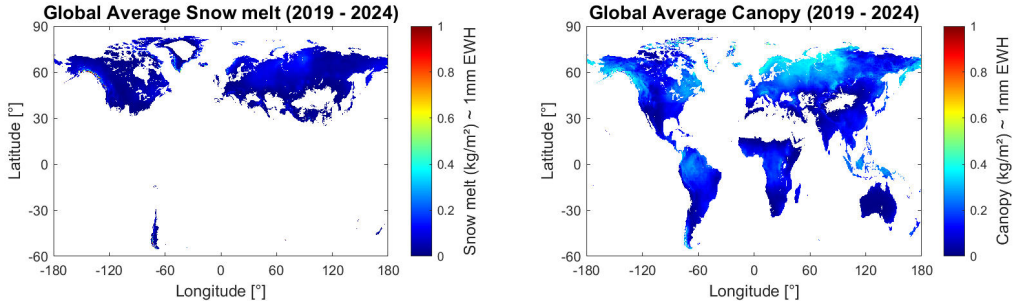

Figure 5.10: Global mean Snow melt equivalent and Canopy from GLDAS hydrological components from 2019 to 2024.

Figures 5.9 and 5.10 illustrates the spatial variability of the main GLDAS hydrological components used for groundwater estimation. Each component represents a different part of the terrestrial water cycle and contributes differently to the total water storage signal observed by GRACE-FO.

The soil moisture component shows the strongest contribution among the GLDAS variables. Higher soil moisture values are mainly observed in humid and vegetated regions where precipitation and infiltration are dominant. In contrast, arid regions such as northern Africa show lower soil moisture availability due to limited rainfall and higher evaporation.

The total runoff distribution represents the movement of water over the land surface. Increased runoff values are observed mainly in regions with higher precipitation, whereas dry regions exhibit only small runoff contributions.

Canopy water storage represents the amount of water temporarily stored within vegetation. Compared with soil moisture, the magnitude of canopy storage is significantly smaller. Higher values are mainly associated with densely vegetated tropical regions.

Snow-related storage shows very limited contribution over Africa because most of the continent experiences warm climatic conditions. Therefore, snow storage has only a minor influence on the groundwater estimation performed in this study.

The analysis demonstrates that soil moisture is the dominant non-groundwater component influencing the GRACE-FO TWS signal. Therefore, removing these GLDAS-derived components from the GRACE-FO observations is an essential step for isolating groundwater storage variations.

5.4.2 Temporal Variation of GLDAS Hydrological Components

In addition to the spatial distribution, the temporal behaviour of GLDAS hydrological variables is analysed to understand seasonal and interannual changes in land water storage. The regional mean values of soil moisture and runoff components are calculated for the period 2019–2024 and compared with the GRACE-FO observation period.

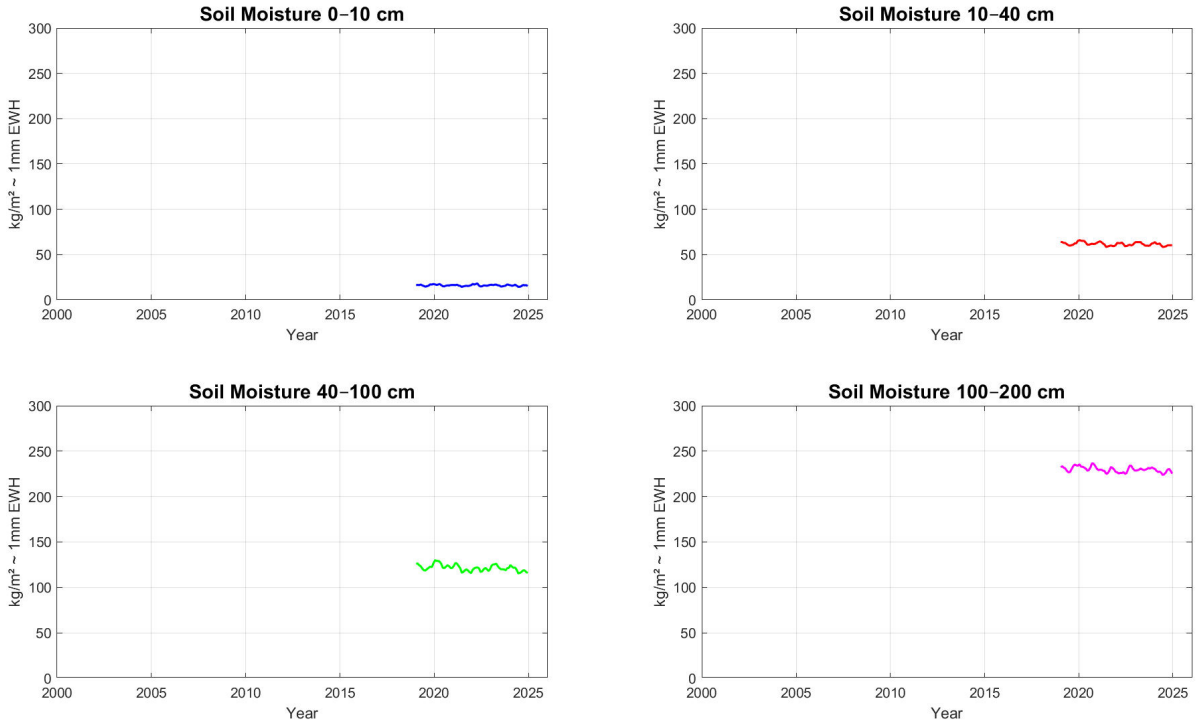

Figure 5.11: Temporal variation of GLDAS soil moisture layers averaged over the study region from 2019 to 2024.

Figure 5.11 shows the temporal behaviour of soil moisture at different depth layers. The soil moisture storage increases with depth, where the deepest layer (100–200 cm) contains the largest amount of stored water due to slower variations and longer retention time.

The shallow soil layer (0–10 cm) shows the smallest storage contribution because it responds rapidly to atmospheric processes such as precipitation and evaporation. Intermediate layers (10–40 cm and 40–100 cm) show larger water storage capacity and represent the connection between surface processes and deeper groundwater systems.

The total soil moisture time series shows relatively stable behaviour between 2019 and 2024 with seasonal fluctuations. These variations mainly represent wet and dry periods controlled by precipitation, evaporation, and vegetation activity.

Figure 5.12 presents the temporal variations of surface and subsurface runoff components. Surface runoff shows relatively small variations because it represents the immediate response of the land surface to precipitation events. Subsurface runoff exhibits larger variability compared with surface runoff, indicating delayed water movement through deeper soil layers. This behaviour reflects infiltration processes and groundwater recharge mechanisms.

The comparison of soil moisture and runoff components demonstrates the importance of GLDAS information for separating near-surface hydrological signals from the integrated GRACE-FO Total Water Storage observations.

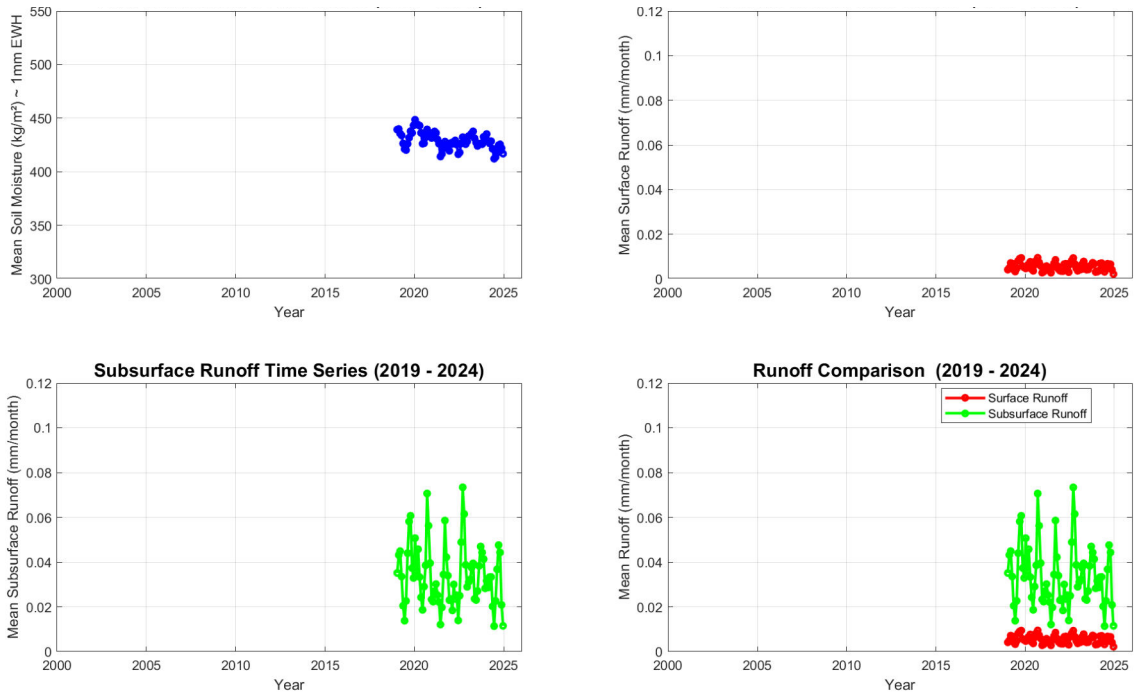

Figure 5.12: Temporal variation of GLDAS surface and subsurface runoff components averaged over the study region from 2019 to 2024.

5.5 Comparison of GRACE-FO TWS and GLDAS Components

The comparison between GRACE-FO derived terrestrial water storage (TWS) variations and GLDAS hydrological components provides a better understanding of the contribution of different water storage processes to continental-scale mass variations. While GRACE-FO measures the total integrated mass change caused by all terrestrial water storage components, GLDAS separates the hydrological system into individual variables such as soil moisture, runoff, snow water equivalent, and canopy water storage.

The GRACE-FO TWS results show large-scale spatial and temporal variations of water storage across Africa. These variations represent the combined effect of different hydrological processes, including changes in soil water, groundwater, vegetation water storage, and surface water redistribution.

The GLDAS results indicate that soil moisture is the dominant near-surface storage component influencing the hydrological cycle. The different soil moisture layers show seasonal variations related to precipitation, evaporation, and infiltration processes. Deeper soil layers show smoother temporal behaviour because they respond more slowly to short-term atmospheric variations.

Runoff components show stronger short-term variability compared with soil moisture because runoff responds rapidly to precipitation events and surface water movement. Canopy water storage contributes a smaller portion of the total water storage signal but represents the influence of vegetation processes on the hydrological system.

The comparison demonstrates that variations observed in GRACE-FO TWS are strongly connected to the hydrological processes represented by GLDAS components. Seasonal increases and decreases in water storage can therefore be interpreted through changes in soil moisture, runoff, and other land surface variables.

Although GRACE-FO provides accurate observations of total mass changes, it cannot independently distinguish individual water storage components. The integration of GRACE-FO observations with GLDAS model outputs therefore provides a useful approach for interpreting continental-scale hydrological variations and forms the basis for future groundwater storage estimation.

Overall, the combined analysis confirms that satellite gravimetry and hydrological modelling complement each other for monitoring large-scale water storage changes across Africa during the period 2019–2024.

6 Conclusion

This study investigated hydrological mass variations across the African continent during the period 2019–2024 using GRACE-FO satellite gravity observations and GLDAS hydrological model outputs. The analysis was performed using GFZ Level-2 spherical harmonic solutions with DDK-filtered products up to degree and order 96. The monthly gravity field variations and the terrestrial water storage (TWS) anomalies were transformed into the space domain using spherical harmonic synthesis and the approach of Wahr et al. (1998).

The spectral analysis of GRACE-FO solutions demonstrated the quality and reliability of the gravity field coefficients used in this study. The degree–order coefficient analysis and relative accuracy assessment showed stable behaviour of the low-degree spherical harmonic coefficients, which represent large-scale mass redistribution signals. Degree variance and error-degree variance analysis indicated that lower spherical harmonic degrees contain the dominant geophysical signals, while higher degrees are increasingly affected by measurement noise.

The disturbing potential and geoid undulation results provided an intermediate representation of temporal gravity field variations caused by mass redistribution within the Earth system. The generated spatial fields showed broad long-wavelength patterns, demonstrating the ability of GRACE-FO observations to capture continental-scale mass changes.

The GRACE-FO derived TWS anomaly analysis revealed significant spatial and temporal variations in water storage across Africa. Monthly EWH maps showed regional differences in hydrological mass changes, while the time series analysis highlighted seasonal and interannual variability during the study period. These variations reflect the combined influence of different hydrological processes such as precipitation, soil moisture changes, surface water variations, and groundwater storage changes.

The GLDAS hydrological component analysis provided additional information about individual contributions to the terrestrial water cycle. Soil moisture represented the dominant land surface storage component, while runoff and canopy water storage contributed smaller but important variations. The comparison of GRACE-FO TWS and GLDAS components showed that combining satellite gravimetry with hydrological models improves the interpretation of large-scale water storage changes.

Overall, this study demonstrates the capability of GRACE-FO observations combined with GLDAS data for monitoring continental-scale hydrological mass variations. The results highlight the importance of satellite geodesy for understanding changes in water storage systems over large regions such as Africa.

7 Outlook

Future work can focus on extending the analysis period by including additional GRACE-FO monthly solutions to investigate long-term trends in African water storage variations. A longer time series would improve the identification of climate-related changes and possible long-term hydrological patterns.

Further improvements can be achieved by performing a detailed groundwater storage estimation through the subtraction of GLDAS-derived soil moisture, snow, canopy water, and surface water components from GRACE-FO TWS anomalies. This would allow a more direct investigation of groundwater variability and groundwater depletion or recharge processes.

The integration of additional hydrological datasets, precipitation products, and in-situ groundwater measurements could improve validation and reduce uncertainties in the interpretation of GRACE-FO observations. Furthermore, advanced filtering and leakage correction methods may help to improve the spatial resolution and reliability of regional water storage estimates.

Future studies can also focus on specific African river basins or climatically sensitive regions to better understand local hydrological responses and support sustainable water resource management.

Acknowledgement

I would like to express my sincere gratitude to Prof. Dr.-Ing. Kurt Seitz for his guidance, valuable suggestions, and continuous support throughout the course of this Lab Rotation. His expertise in satellite gravimetry, gravity field analysis, and geodetic data processing greatly contributed to the successful completion of this work.
I would also like to thank the Karlsruhe Institute of Technology (KIT) for providing the academic environment, computational resources, and research facilities required for this study. The GRACE-FO monthly gravity field solutions and GLDAS hydrological model data used in this work, obtained from publicly available scientific data sources, enabled the analysis of hydrological mass variations across the African continent.
Finally, I would like to thank my colleagues and peers for their helpful discussions, encouragement, and support during the preparation of this report.

References

GFZ (2026): GRACE-FO – Gravity Recovery and Climate Experiment Follow-On Mission. German Research Centre for Geosciences (GFZ). Accessed: 2026-04-06. URL: https://www.gfz.de/en/section/global-geomonitoring-and-gravity-field/projects/grace-fo-gravity-recovery-and-climate-experiment-follow-on-mission.

GLDAS (2025): GLDAS - Global Land Data Assimilation System. https://disc.gsfc.nasa.gov/datasets?keywords=GLDAS. Accessed: 2025-11-26.

Heiskanen, W. A. and Moritz, H. (1967): Physical Geodesy. W. H. Freeman & Co., San Francisco, USA.

ICGEM (2026): International Centre for Global Earth Models (ICGEM): Gravity field and GRACE/GRACE-FO products hosted at the German Research Centre for Geosciences (GFZ). Accessed: 2026-04-06. URL: https://icgem.gfz-potsdam.de/.

Kusche, J. (2007): Approximate decorrelation and non-isotropic smoothing of time-variable GRACE-type gravity field models. *Journal of Geodesy* 81(11):733–749. DOI: 10.1007/s00190-007-0143-3.

Kusche, J., Schmidt, R., Petrovic, S., and Rietbroek, R. (2009): Decorrelated GRACE time-variable gravity solutions by GFZ, and their validation using a hydrological model. *Journal of Geodesy* 83:903–913. DOI: 10.1007/s00190-009-0308-3.

Rodell, M., Famiglietti, J. S., Wiese, D. N., Reager, J., Beaudoing, H. K., Landerer, F. W., and Lo, M.-H. (2018): Emerging trends in global freshwater availability. *Nature* 557(7707):651–659.

Rodell, M., Houser, P. R., Jambor, U., Gottschalck, J., Mitchell, K. E., Meng, C.-J., Arsenault, K., Cosgrove, B. A., Radakovich, J. D., Bosilovich, M. G., Entin, J. K., Walker, J. P., Lohmann, D., and Toll, D. L. (2004): The Global Land Data Assimilation System. *Bulletin of the American Meteorological Society* 85(3):381–394. DOI: 10.1175/BAMS-85-3-381.

Scanlon, B. R., Zhang, Z., Save, H., Sun, A. Y., Schmied, H. M., van Beek, L. P. H., and Wiese, D. N. (2018): Global models underestimate large decadal declining and rising water storage trends relative to GRACE satellite data. *Proceedings of the National Academy of Sciences* 115(6):E1080–E1089. DOI: 10.1073/pnas.1704665115.

Swenson, S. and Wahr, J. (2006): Post-processing removal of correlated errors in GRACE data. *Geophysical Research Letters* 33(8):L08402. DOI: 10.1029/2005GL025285.

Tapley, B. D., Watkins, M. M., Flechtner, F., et al. (2019): Contributions of GRACE to understanding climate change. *Nature Climate Change* 9:358–369. DOI: 10.1038/s41558-019-0456-2.

Tapley, B. D., Bettadpur, S., Watkins, M., and Reigber, C. (2004): The gravity recovery and climate experiment: Mission overview and early results. *Geophysical Research Letters* 31(9):1–4. DOI: 10.1029/2004GL019920.

Wahr, J., Molenaar, M., and Bryan, F. (1998): Time variability of the Earth's gravity field: Hydrological and oceanic effects and their possible detection using GRACE. *Journal of Geophysical Research: Solid Earth* 103(B12):30205–30229.

Wahr, J., Swenson, S., Zlotnicki, V., and Velicogna, I. (2004): Time-variable gravity from GRACE: First results. *Geophysical Research Letters* 31(L11501):1–4. ISSN: 1944-8007. DOI: 10.1029/2004GL019779.

Watkins, M. M., Wiese, D. N., Yuan, D. N., Boening, C., and Landerer, F. W. (2015): Improved methods for observing Earth's time variable mass distribution with GRACE using spherical cap mascons. *Journal of Geophysical Research: Solid Earth* 120:2648–2671. DOI: 10.1002/2014JB011547.

Appendix

A Monthly GRACE-FO TWS Variations During 2024

The following figures show the monthly terrestrial water storage (TWS) variations over Africa during 2024 derived from GRACE-FO observations. The complete annual sequence illustrates the seasonal evolution of hydrological mass redistribution throughout the year.

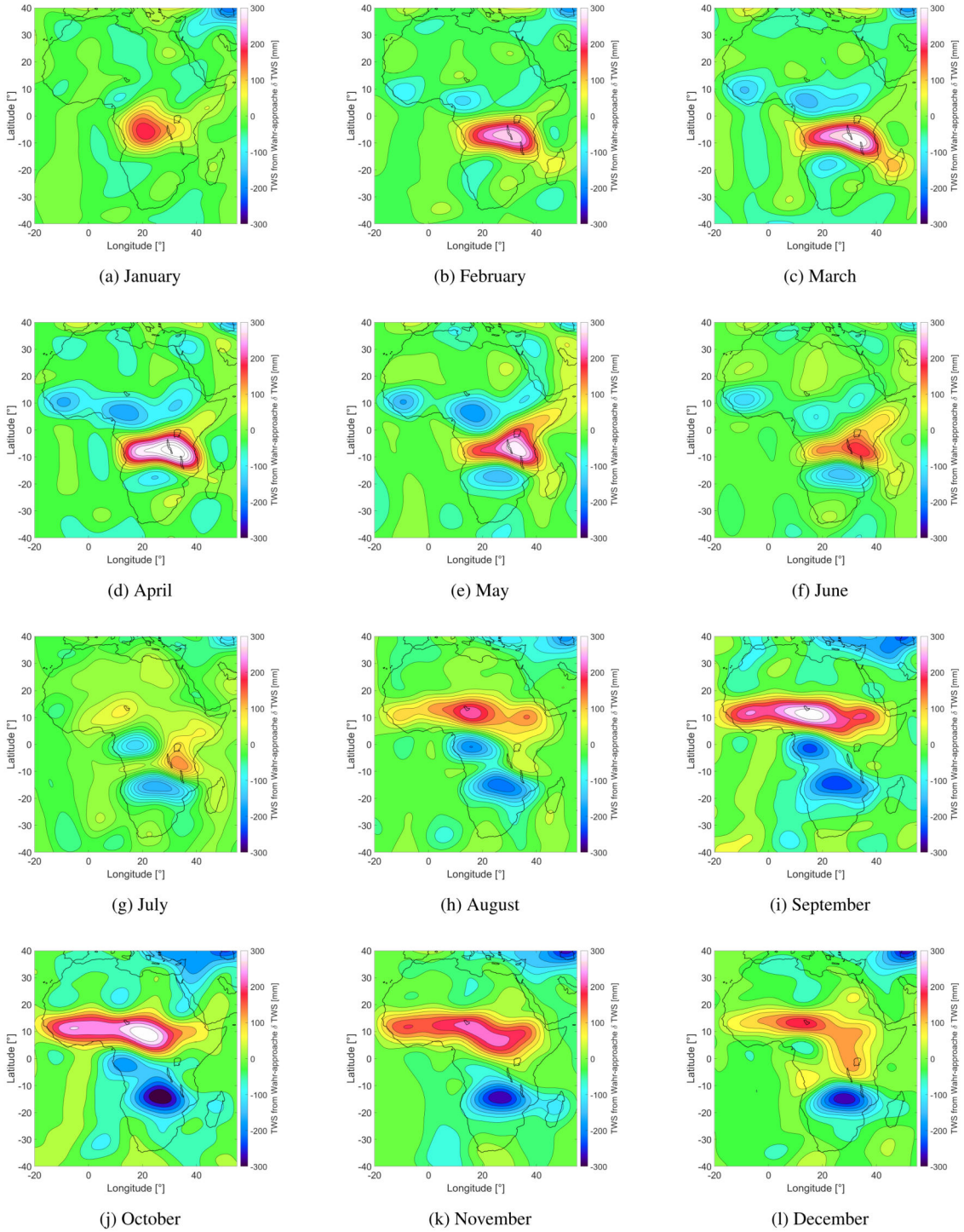

(a) January (b) February (c) March

(d) April (e) May (f) June

(g) July (h) August (i) September

(j) October (k) November (l) December

Figure A.1: Monthly GRACE-FO DDK2 derived TWS anomalies over Africa in 2024. Range is ± 300 mm.

B Additional DDK5 Filtered GRACE-FO Results

The following figures present additional GRACE-FO derived terrestrial water storage (TWS) anomaly results obtained using the DDK5 decorrelation filter. These results are included to evaluate the influence of different filter strengths on the recovered hydrological mass variations.
Compared with the DDK2 solution used in the main analysis, the DDK5 filtered solution provides an additional representation of the gravity field by applying a different level of smoothing and noise reduction.

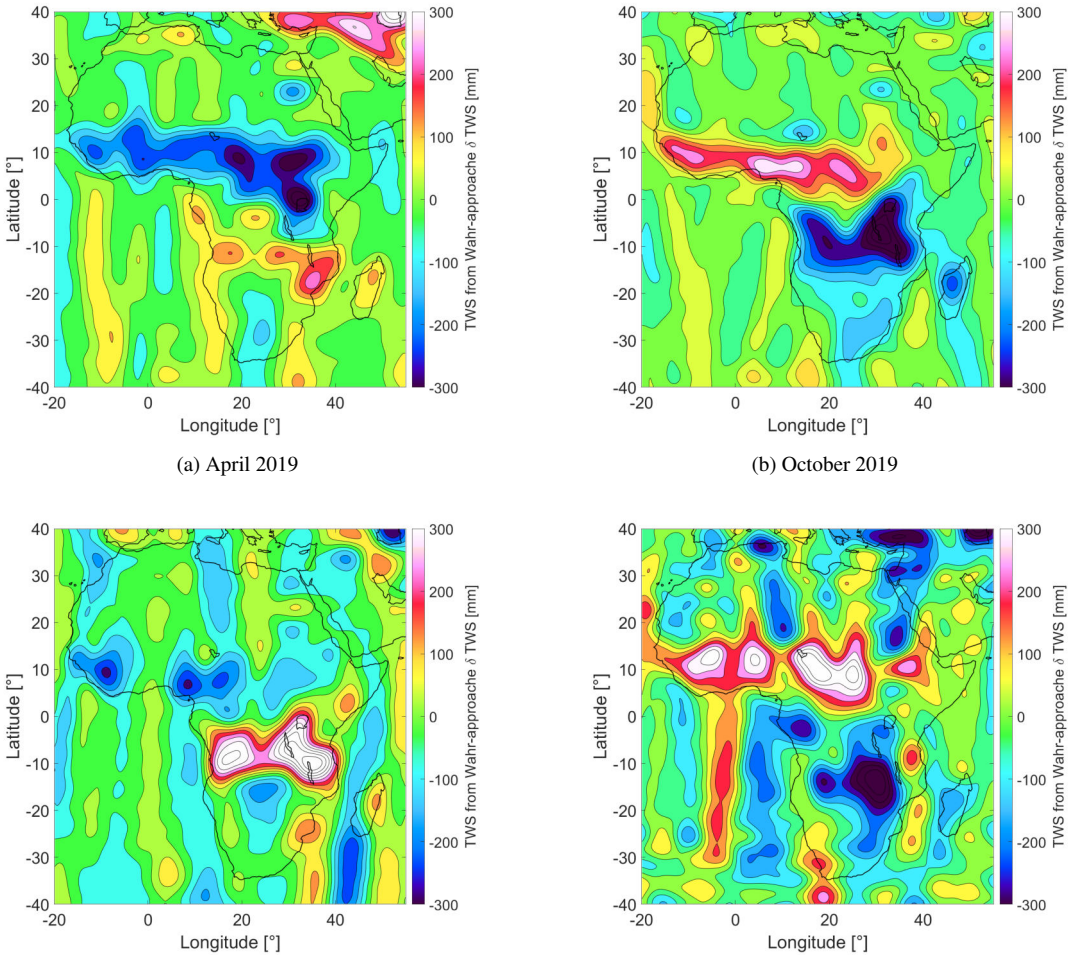

(a) April 2019

(b) October 2019

(c) April 2024

(d) October 2024

Figure B.1: Selected monthly GRACE-FO TWS anomalies over Africa using the DDK5 decorrelation filter.

DDK5 Mean TWS and Statistical Analysis

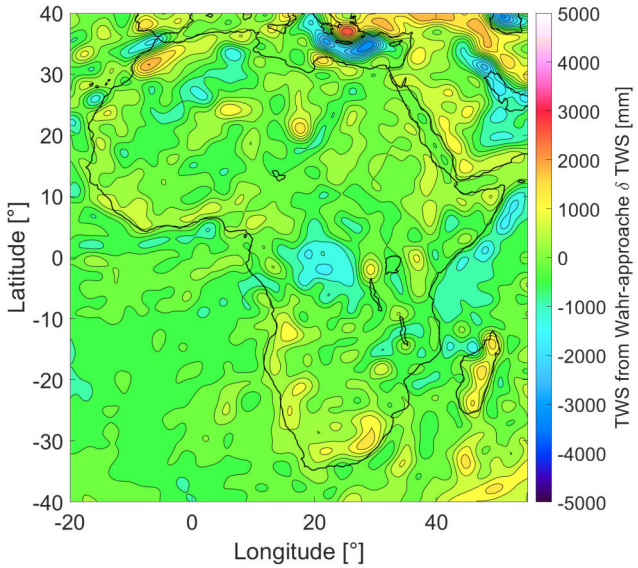

Figure B.2: Mean GRACE-FO derived TWS distribution over Africa from 2019–2024 using the DDK5 filtered solution.

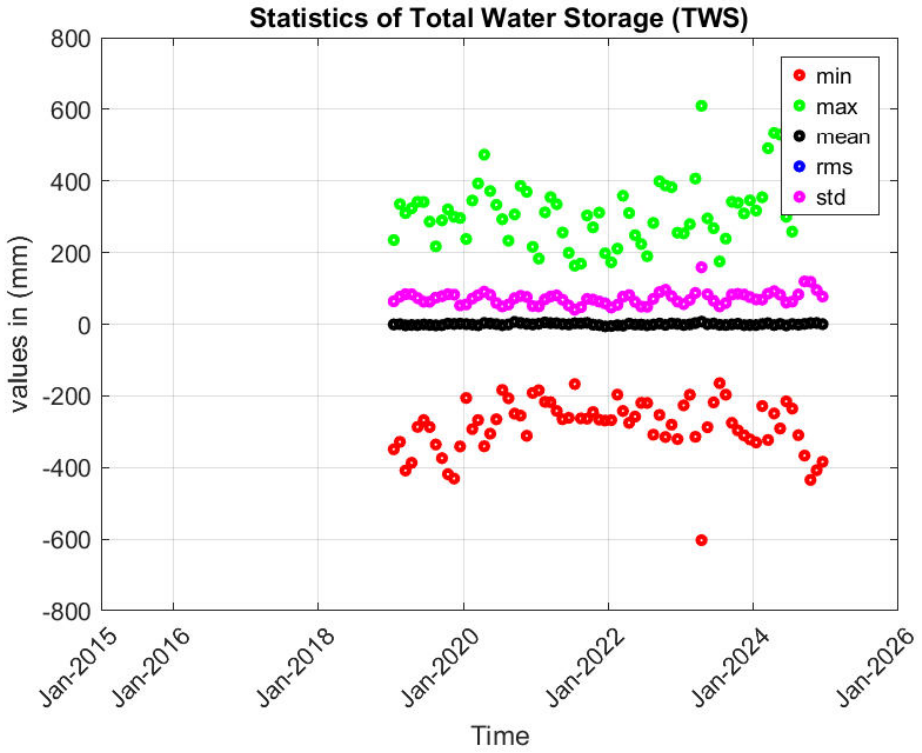

Figure B.3: Temporal variation of GRACE-FO TWS statistical parameters using the DDK5 filtered solution.

C Comparison of DDK2 and DDK5 Filtered GRACE-FO Solutions

The following figures compare GRACE-FO derived terrestrial water storage (TWS) anomalies obtained using DDK2 and DDK5 decorrelation filters. The comparison is performed to evaluate the influence of different filtering strengths on the recovered hydrological mass variations.
DDK filters are applied to reduce correlated errors and striping effects present in GRACE-FO spherical harmonic solutions. Different DDK filter levels provide different balances between noise reduction and signal preservation.

Monthly TWS Comparison

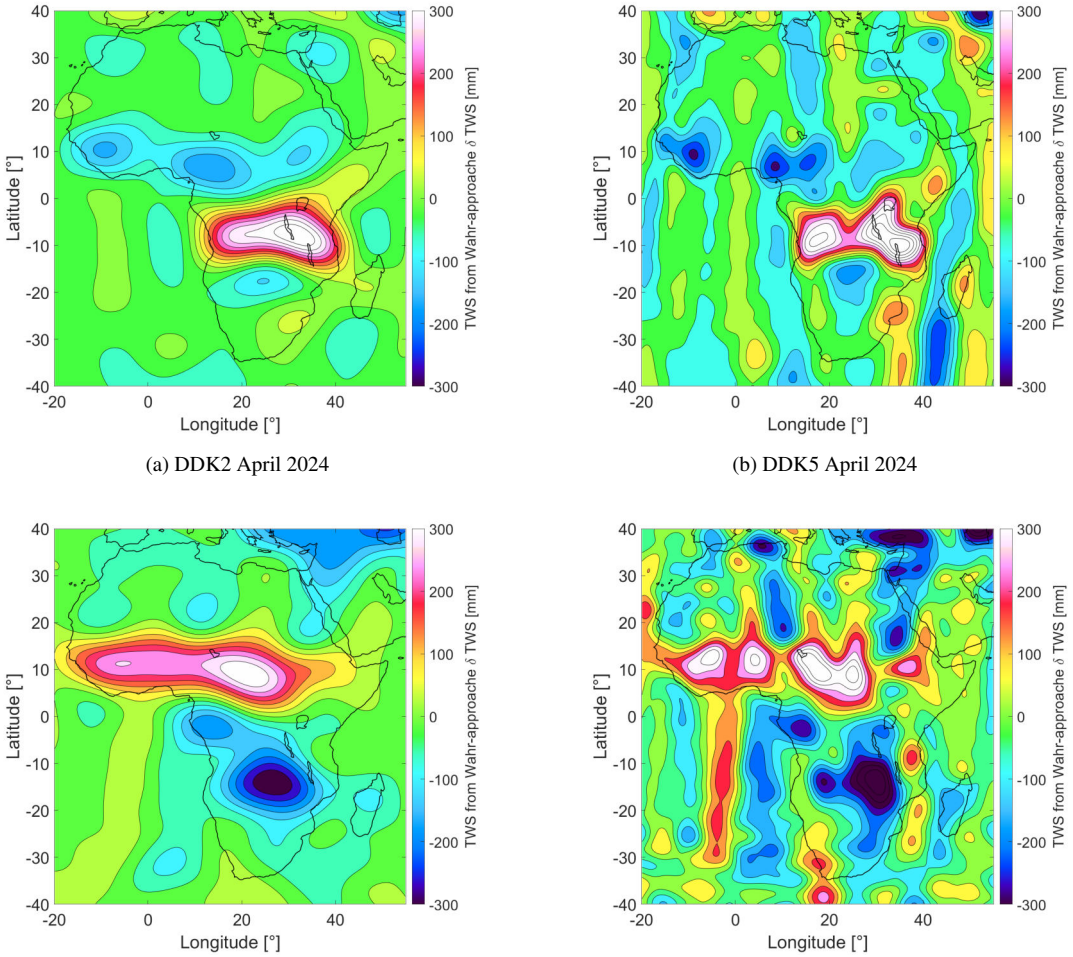

(a) DDK2 April 2024

(b) DDK5 April 2024

(c) DDK2 October 2024

(d) DDK5 October 2024

Figure C.1: Comparison of GRACE-FO derived TWS anomalies using DDK2 and DDK5 filters for selected months in 2024.

Mean TWS Comparison

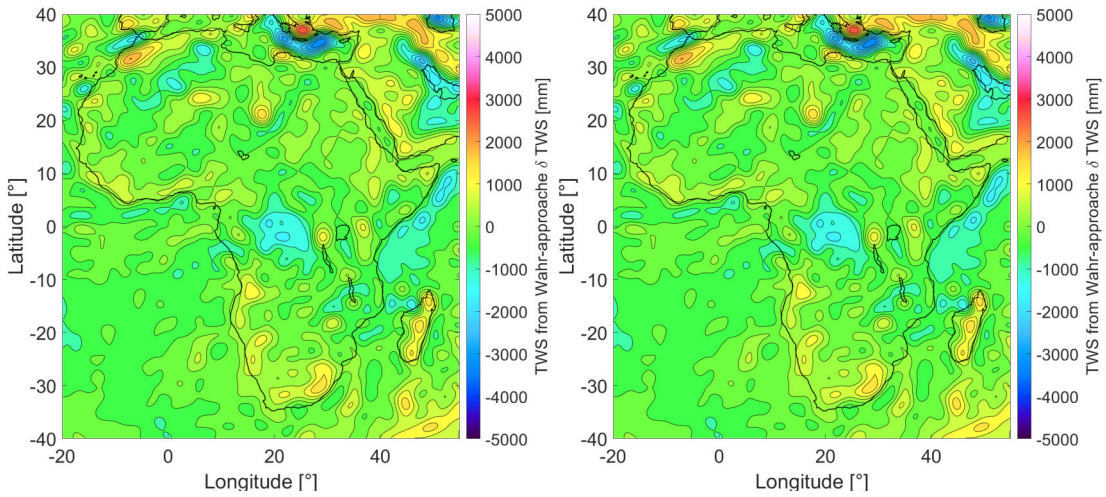

(a) DDK2 Mean TWS (b) DDK5 Mean TWS

Figure C.2: Comparison of mean terrestrial water storage (TWS) distribution over Africa from 2019–2024 obtained using DDK2 and DDK5 filtered GRACE-FO solutions.

TWS Statistical Time Series Comparison

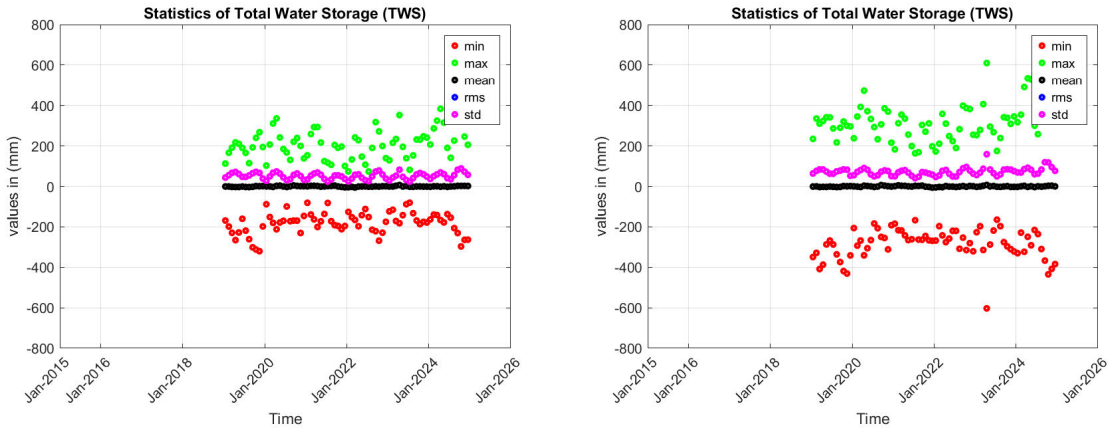

(a) DDK2 solution (b) DDK5 solution

Figure C.3: Comparison of temporal statistical behaviour of GRACE-FO TWS solutions processed with DDK2 and DDK5 filters.

D Additional GLDAS Hydrological Component Results

The following figures present additional GLDAS hydrological model outputs used in the estimation of groundwater storage variations. These components represent the non-groundwater storage contributions removed from the GRACE-FO total water storage observations.
GLDAS provides information about soil moisture and runoff variations, which allows the separation of groundwater-related signals from the total terrestrial water storage variations.

Soil Moisture Layer Variations

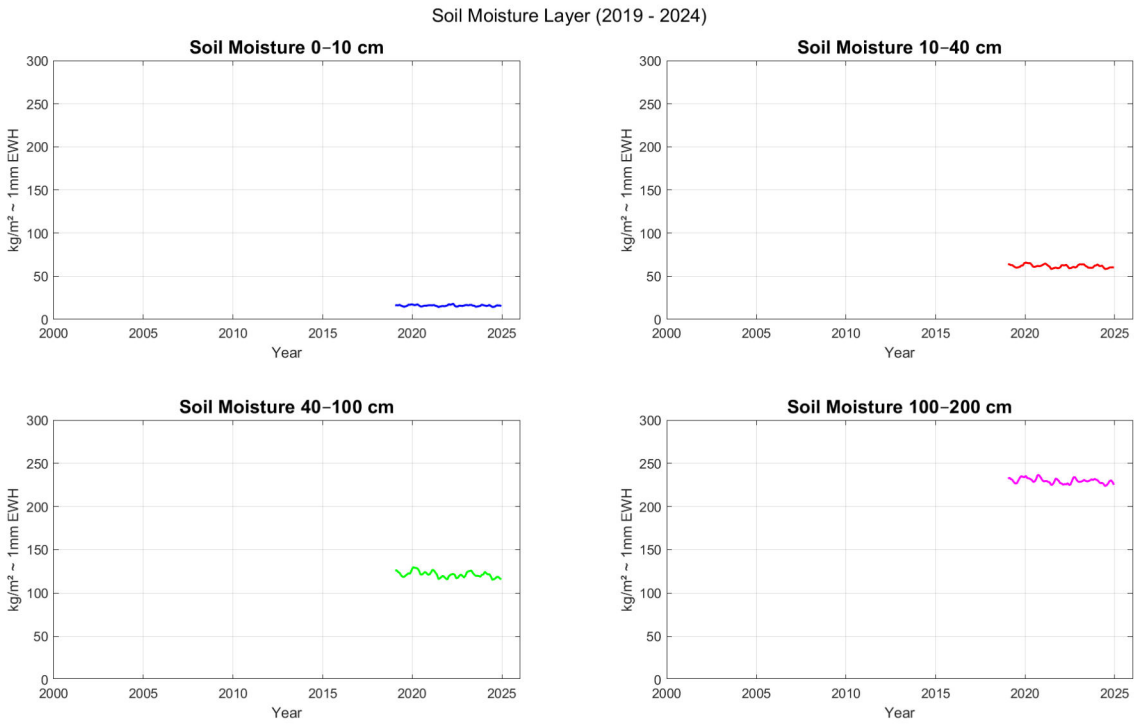

Figure D.1: Temporal variations of GLDAS soil moisture storage at different depth layers over the period 2019–2024. The different layers represent the contribution of near-surface and deeper soil water storage components used for separating groundwater storage variations from GRACE-FO derived total water storage.

Runoff Component Variations

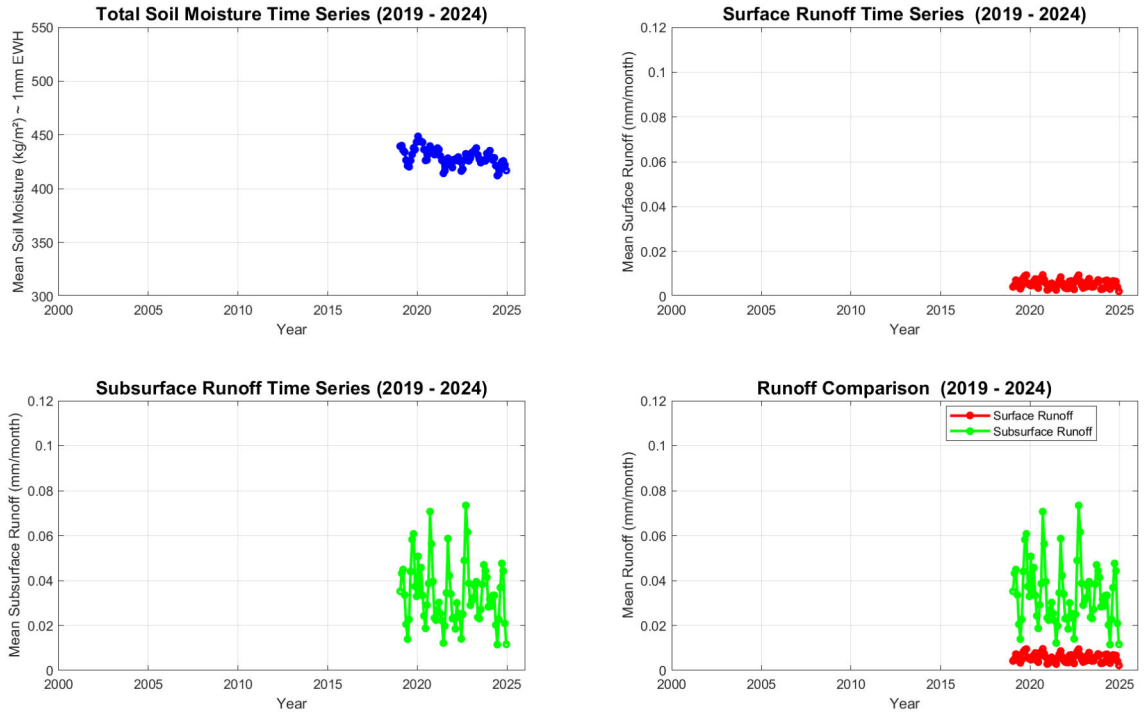

Figure D.2: Temporal variations of GLDAS surface and subsurface runoff components from 2019–2024. These runoff components describe the water loss from the land surface system and are considered during the estimation of groundwater storage anomalies.

Study on Groundwater Changes in Spain and Italy using GRACE, GRACE-FO and GLDAS Data

Swathy Suresh[1]

1 Remote Sensing and Geoinformatics Master of Science (M.Sc.), KIT, Germany
E-Mail: uymsg@student.kit.edu

Abstract

Variations in the Earth's gravity field carry information on the continuous redistribution of mass within the atmosphere, oceans, and terrestrial hydrological systems. This study uses monthly gravity field solutions from the Gravity Recovery and Climate Experiment (GRACE) mission and its successor, GRACE-Follow-On (GRACE-FO), to monitor large-scale Terrestrial Water Storage (TWS) variations, which help evaluate regional water balance and groundwater dynamics.

In this study, TWS variations were estimated over two distinct river basins, specifically the Po Basin in Italy and Ebro basin in Spain using GRACE and GRACE-FO monthly solutions. Temporal gravity field changes were modeled using normalized spherical harmonic coefficients up to degree and order 96. To improve accuracy, low-degree potential coefficients (n = 1,2) were replaced with precise values derived from Satellite Laser Ranging (SLR). Following the formulation of Wahr et al. (1998), these coefficients were converted into Equivalent Water Height (EWH) anomalies, incorporating Load Love Numbers to account for the elastic response of the solid Earth to surface mass loading.

To isolate Groundwater Storage (GWS) variations, hydrological components from the Global Land Data Assimilation System (GLDAS) were utilized. Storage variables, including soil moisture, snow water equivalent, and canopy water, were processed and subtracted from the GRACE-derived TWS anomalies. The resulting hydrological components were analyzed to investigate the spatial and temporal variations of subsurface storage over the study areas. The results demonstrate the capacity of combining satellite gravimetry with land surface models to monitor hidden water resources at a regional scale, providing geodetic information relevant to support sustainable water management and EU CSRD reporting.

Keywords GRACE · GLDAS · Total Water Storage (TWS) · Italy · Spain

KIT Scientific Working Papers
Issue Number 270
ISSN: 2194-1629
DOI: 10.5445/IR/1000191188
Online: June 2026

This document is licensed under the Creative Commons Attribution – Share Alike 4.0 International License (CC BY-SA 4.0):
https://creativecommons.org/licenses/by-sa/4.0/deed.en

1 Introduction

The Earth system undergoes continuous redistribution of mass within the atmosphere, land surfaces, and the oceans. These changes are detected through variations in the Earth's gravity field. The GRACE (Gravity Recovery and Climate Experiment) and GRACE-FO missions deliver monthly gravity field solutions that effectively act as a global scale for observing and quantifying these variations (Dahle et al., 2013).
Temporal variations in the gravity field are described using fully normalized spherical harmonic coefficients ($\bar{C}_{nm}, \bar{S}_{nm}$), which are dimensionless and typically available up to degree and order 96. An important preprocessing step is the replacement of low-degree potential coefficients (particularly degree $n = 1$ and $n = 2$) with more accurate values derived from Satellite Laser Ranging (SLR) data at the beginning of the analysis (Chao and Gross, 1987).
These coefficients are converted into Terrestrial Water Storage (TWS) anomalies and expressed as Equivalent Water Height (EWH) following the approach of Wahr et al. (1998). This conversion uses Load Love Numbers to account for the indirect gravity effects resulting from the elastic deformation of the solid Earth under surface mass loading.
The spatial resolution depends on the chosen maximum degree (L):

- $L = 60$ corresponds to a spatial resolution of roughly 300–400 km.
- $L = 96$ corresponds to a spatial resolution of about 200 km.

Although higher degrees enhance spatial resolution, they introduce more high-frequency noise. Therefore, DDK de-striping filters are applied to reduce correlated errors and improve signal reliability (Swenson and Wahr, 2006; Kusche, 2007; Kusche et al., 2009).
A major challenge in using GRACE data is that it measures total water storage (TWS), which includes soil moisture, surface water, snow, and ice. To estimate Groundwater Storage (GWS), these surface components must be removed using additional datasets. The Global Land Data Assimilation System (GLDAS) provides this information by combining satellite and ground observations within land surface models such as Noah and Catchment, generating gridded estimates for each hydrological component (Rodell et al., 2004).
To estimate groundwater storage (GWS), components such as Soil Moisture (SM), Snow Water Equivalent (SWE), and Canopy Water (CW) are extracted from GLDAS. These variables represent surface and near-surface water storage and are expressed in units directly comparable to GRACE-derived terrestrial water storage (cf. NASA, 2022; Beaudoing and Rodell, 2020). By subtracting these components from total water storage, the remaining signal represents variations in subsurface groundwater storage.

This study compares two European regions:

- **Po River Basin (Italy):** Influenced by glacier melt interacting with groundwater.
- **Ebro River Basin (Spain):** A semi-arid region that depends strongly on groundwater and has no glacier contribution.

The study aims to produce groundwater time series for both basins and analyse them using statistical indicators such as mean, standard deviation (std), and root mean square (RMS).
This work also links geodetic analysis to modern sustainability reporting frameworks. By assessing groundwater changes, the results can support EU CSRD requirements, particularly those addressing climate risk and water management under ESRS standards E1 and E2.

2 Theoretical Aspects

The Gravity Recovery and Climate Experiment (GRACE) satellite mission measures temporal variations in the Earth's gravity field. These variations are primarily caused by mass redistribution within the Earth system, including changes in the atmosphere, oceans, and land water storage. Over continental regions, such variations are mainly associated with terrestrial water storage (TWS), which includes soil moisture, groundwater, surface water, snow, and canopy water (Wahr et al., 1998; Wouters et al., 2014).

2.1 Spherical Harmonic Representation of the Gravity Field

The Earth's gravitational potential at a point $P(r,\theta,\lambda)$ can be represented using a spherical harmonic expansion. This formulation expresses the gravity field in terms of spherical harmonic coefficients and associated Legendre functions (Heiskanen and Moritz, 1967; Torge et al., 2023). The gravitational potential is given by:

$$V(r,\theta,\lambda) = \frac{GM}{r} \sum_{n=0}^{\infty} \left(\frac{a}{r}\right)^n \sum_{m=0}^{n} \left(\bar{C}_{nm}\cos m\lambda + \bar{S}_{nm}\sin m\lambda\right) \bar{P}_{nm}(\cos\theta)\,, \tag{2.1}$$

where:

- GM is the Earth's gravitational constant (Newtons gravitational constant G, and mass of the Earth M),
- a is the Earth's mean radius,
- r is the radial distance from the Earth's center,
- $\bar{C}_{nm}$ and $\bar{S}_{nm}$ are fully normalized spherical harmonic coefficients,
- $\bar{P}_{nm}$ are associated Legendre functions,
- n and m denote the degree and order of the expansion.

Temporal variations in the coefficients $(\Delta\bar{C}_{nm}, \Delta\bar{S}_{nm})$ represent changes in the gravity field (relative to a reference solution), which can be directly related to mass redistribution processes within the Earth system.

2.2 Conversion to Equivalent Water Height

Following the methodology of Wahr et al. (1998), variations in the spherical harmonic coefficients can be converted into equivalent water height (EWH), which expresses mass changes as a layer of water thickness on a sphere of radius a. The relationship is given by:

$$\Delta h^c_{nm} = \frac{a\rho_E}{3\rho_w} \cdot \frac{2n+1}{1+k_n} \Delta\bar{C}_{nm}\,, \qquad \Delta h^s_{nm} = \frac{a\rho_E}{3\rho_w} \cdot \frac{2n+1}{1+k_n} \Delta\bar{S}_{nm}\,, \tag{2.2}$$

where:

- a is the Earth's radius,
- ρ_E is the mean density of the Earth,
- ρ_w is the density of water,
- k_n are load Love numbers accounting for Earth's elastic response,
- $\Delta\bar{C}_{nm}$ and $\Delta\bar{S}_{nm}$ are temporal variations of the Stokes coefficients.

The load Love numbers correct for the deformation of the solid Earth due to surface mass loading, ensuring that the derived water storage estimates are physically consistent (Wahr et al., 1998). The resulting EWH fields represent spatially distributed terrestrial water storage anomalies.

2.3 Components of Terrestrial Water Storage

Terrestrial water storage consists of multiple hydrological components, which together represent the total water stored within the land system:

$$TWS = SM + SWE + SW + GW + CW \tag{2.3}$$

where:

- SM is soil moisture,
- SWE is snow water equivalent,
- SW is surface water,
- GW is groundwater,
- CW is canopy water storage.

GRACE provides an integrated measurement of all these components combined. Therefore, additional datasets (e.g., GLDAS) are required to isolate individual components such as groundwater (Rodell et al., 2004; NASA, 2022).

2.4 Tesseroids for Regional Mass Representation

An alternative approach for modeling gravity effects is the use of tesseroids, which represent mass distributions as spherical volumetric elements. Compared to traditional Cartesian prisms, tesseroids inherently account for the Earth's curvature and provide more accurate results for regional-scale modeling (Heck and Seitz, 2007; Grombein et al., 2013). Tesseroid-based methods are particularly useful in forward and inverse gravity modeling, offering improved numerical stability and computational efficiency (Grombein, 2017). However, in this study, the classical approach of Wahr et al. (1998) is applied to directly convert GRACE spherical harmonic coefficients into terrestrial water storage anomalies.

3 Data

This study uses satellite gravity observations from the GRACE and GRACE Follow-On missions together with hydrological model outputs from the Global Land Data Assimilation System (GLDAS) to analyse terrestrial water storage variations over Italy and Spain.

3.1 GRACE Data

The Gravity Recovery and Climate Experiment (GRACE) and its successor GRACE Follow-On (GRACE-FO) provide monthly gravity field solutions that allow the observation of large-scale mass redistribution within the Earth system. These solutions are distributed as spherical harmonic coefficients representing temporal variations in the Earth's gravity field.

The GRACE data used in this study were obtained from the International Centre for Global Earth Models (ICGEM, 2026) data portal. The ICGEM database provides gravity field solutions generated by several analysis centres including the Center for Space Research (CSR), the German Research Centre for Geosciences (GFZ), and the Jet Propulsion Laboratory (JPL).

In this study, the CSR monthly gravity field solutions were used. These solutions provide global gravity field variations at monthly temporal resolution and are available up to degree and order 96. The spherical harmonic coefficients were truncated at degree and order 96, corresponding to a spatial resolution of approximately 200 km.

To reduce correlated errors and striping patterns commonly present in GRACE gravity solutions, filtered datasets were used. In this study, DDK5 filtered GRACE solutions were applied to suppress noise while preserving the large-scale hydrological signal.
The GRACE dataset covers the time period from 2003 to 2024 and was used to analyse terrestrial water storage variations over the regions of Italy and Spain.

3.2 GLDAS Data

In addition to satellite observations, hydrological data from the Global Land Data Assimilation System (GLDAS, 2025) were used to analyse surface water storage components. GLDAS integrates satellite observations and ground-based measurements with land surface models to simulate hydrological variables and land surface processes.
The GLDAS dataset provides several hydrological components including soil moisture, surface runoff, subsurface runoff, snow water equivalent, and canopy water storage. Soil moisture is provided at four different depth layers representing different levels of the soil column.
The GLDAS data used in this study have a spatial resolution of 0.25° and were used to analyse hydrological behaviour over the regions of Italy and Spain.
It should be noted that GLDAS does not explicitly include groundwater storage. Therefore, differences between GRACE-derived terrestrial water storage estimates and GLDAS surface storage components can be interpreted as groundwater storage variations.

3.3 Data Preprocessing

Before the analysis, both GRACE and GLDAS datasets were processed to ensure consistency and to extract the regions of interest.
For the GRACE dataset, the monthly spherical harmonic coefficients obtained from the CSR RL06 solutions were processed using MATLAB scripts. These scripts were used to read the gravity field coefficients and convert them into equivalent water height (EWH) anomalies following the method described in the theoretical section. The resulting EWH values represent terrestrial water storage anomalies relative to a long-term mean.
To reduce noise and correlated striping errors commonly present in GRACE gravity solutions, DDK5 filtered coefficients were used. These filtered solutions suppress high-frequency noise while preserving large-scale hydrological signals.
After processing the GRACE coefficients, spatial maps of terrestrial water storage anomalies were generated. The analysis was restricted to the study regions corresponding to Italy and Spain.
For the GLDAS dataset, the hydrological variables were extracted from NetCDF files using MATLAB scripts. The variables used in this study include soil moisture, surface runoff, subsurface runoff, snow water equivalent, and canopy water storage. Soil moisture values from the four available depth layers were combined to obtain total soil moisture storage.
The extracted GLDAS variables were averaged over the selected study regions to produce regional time series of hydrological components.
Some standard preprocessing steps commonly applied in GRACE studies were not implemented in this analysis. In particular, the replacement of low-degree coefficients using Satellite Laser Ranging (SLR) solutions was not performed. In addition, leakage correction methods were not applied. These improvements could be considered in future studies.

3.4 Code Implementation and Processing

The analysis of GRACE and GLDAS datasets was carried out using MATLAB scripts developed for automated data acquisition, preprocessing, and analysis.

3.4.1 GLDAS Data Acquisition

GLDAS data were downloaded from the NASA Earthdata portal using an automated MATLAB script. The script reads a text file containing download URLs and filters links corresponding to NetCDF (.nc4) files. Authentication was performed using Earthdata credentials, and the MATLAB function `websave` was used to download the files.

3.4.2 GLDAS Data Processing for Italy and Spain

Provided MATLAB scripts were addapted to process GLDAS datasets for Italy and Spain. These scripts extract hydrological variables such as soil moisture, runoff, snow water equivalent, and canopy water storage.
Soil moisture values from four depth layers were combined to compute total soil moisture storage. Regional subsets were extracted, and averages were computed to generate time series for analysis.

3.4.3 GRACE Data Processing

GRACE spherical harmonic coefficients from the ICGEM database were processed using MATLAB routines. The coefficients were converted into equivalent water height anomalies following the method of Wahr et al. (1998).
These processed data were used to generate spatial maps and time series of terrestrial water storage over Italy and Spain.
The MATLAB scripts provided an efficient workflow for processing both satellite gravity data and hydrological model outputs.

4 Methodology

The methodology of this study focuses on analysing terrestrial water storage variations derived from GRACE satellite observations and comparing them with hydrological variables obtained from the Global Land Data Assimilation System (GLDAS, 2025). The analysis was carried out using MATLAB scripts developed to process both satellite gravity data and hydrological model outputs. The overall workflow consists of data acquisition, preprocessing, conversion to terrestrial water storage, regional extraction, and comparison with hydrological model outputs.
First, monthly GRACE spherical harmonic coefficients were obtained from the International Centre for Global Earth Models (ICGEM) database. The CSR gravity field solutions were selected due to their reliability and global coverage at monthly temporal resolution. To reduce correlated errors and striping effects present in GRACE data, DDK5 filtered spherical harmonic coefficients are used. The spherical harmonic coefficients were then converted into equivalent water height (EWH) anomalies using the formulation proposed by Wahr et al. (1998). These EWH anomalies represent variations in terrestrial water storage relative to a long-term mean.
After computing the EWH values, spatial maps of terrestrial water storage anomalies were generated. The global datasets were spatially subsetted to extract the study regions corresponding to Italy and Spain, enabling the investigation of regional hydrological behaviour.
Hydrological variables from the GLDAS dataset were then extracted for the same study regions. The variables used include soil moisture, surface runoff, subsurface runoff, snow water equivalent, and canopy water storage. Soil moisture values from the four available depth layers were combined to obtain total soil moisture storage.
To estimate groundwater storage variations, the surface water storage components obtained from GLDAS were compared with the GRACE-derived terrestrial water storage anomalies. Since GRACE measures total water storage, the difference between GRACE-derived terrestrial water storage and GLDAS surface components can be interpreted as groundwater storage variations.
Finally, time series and spatial maps were generated to analyse seasonal variability and long-term trends in water storage over Italy and Spain. The results obtained from GRACE observations were compared with GLDAS hydrological variables to investigate the relationship between total water storage and surface water components.

The main processing steps of the methodology can be summarized as follows:

- Acquisition of GRACE and GLDAS datasets
- Preprocessing of GRACE spherical harmonic coefficients
- Conversion of gravity field variations to equivalent water height (EWH)
- Spatial extraction of study regions (Italy and Spain)
- Processing of GLDAS hydrological variables
- Comparison of GRACE-derived TWS with GLDAS components to estimate groundwater storage

5 Results and Discussion

5.1 GRACE-Based Terrestrial Water Storage Analysis

5.1.1 Degree Variance Analysis

The quality of the GRACE spherical harmonic solutions is evaluated using degree variance plots. These plots show the distribution of signal and noise as a function of spherical harmonic degree. The signal variance is highest at lower degrees, indicating that GRACE effectively captures large-scale mass variations. As the degree increases, the signal decreases while the error variance increases, showing that higher-degree coefficients are increasingly dominated by noise.

The intersection between the signal and error curves defines the effective resolution of the GRACE data. In this study, the reliable signal is limited to approximately degree 30–40. Beyond this range, the signal becomes increasingly noisy and less reliable, confirming that GRACE is suitable for large-scale hydrological studies but has limitations in resolving smaller spatial features.

Figure 5.1(a) shows the relative degree variance and error-degree variance for the GRACE solution over Spain in January 2010. The blue curve represents the signal variance, while the red curve represents the error variance. At lower spherical harmonic degrees, the signal variance is significantly higher than the error variance, indicating that GRACE reliably captures large-scale mass variations. As the degree increases, the signal variance decreases rapidly, while the error variance increases steadily.

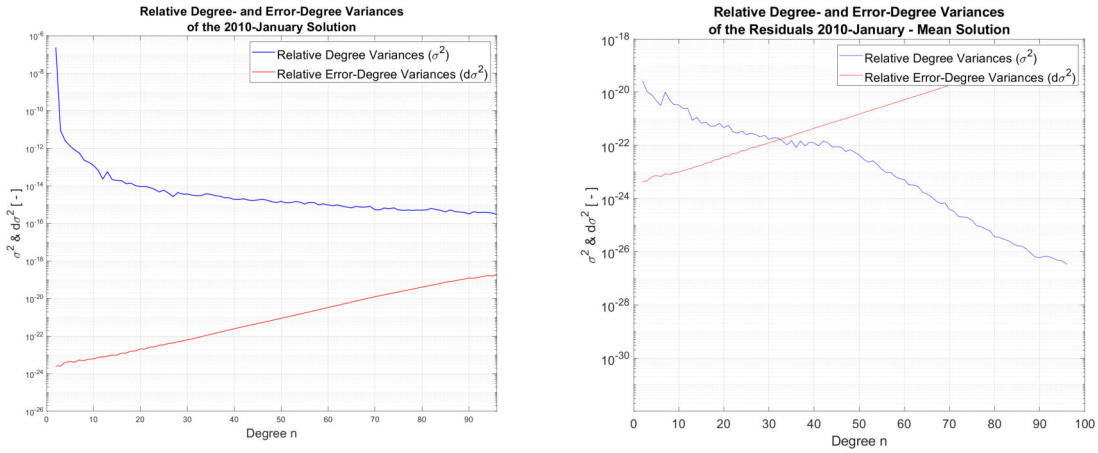

(a) Relative degree variance and error-degree variance. The signal is strongest at lower degrees, while higher degrees are increasingly affected by noise.

(b) Residual degree variance after mean field removal. The reduced signal magnitude shows that temporal gravity variations are small compared to the mean gravity field (a).

Figure 5.1: Degree variance and error-degree variance for the GRACE DDK5 solution in January 2010.

5.1.2 Residual Degree Variance

Figure 5.1(b) shows the residual degree variance after removing the mean gravity field in January 2010. The removal of the mean field significantly reduces the magnitude of the signal, leaving only temporal variations in the gravity field. Compared to the original degree variance, the residual signal is much weaker and decreases more rapidly with increasing spherical harmonic degree.
The residual signal values drop sharply and approach very small magnitudes at higher degrees, while the error variance becomes dominant at lower degrees compared to the original solution. The curves approach each other around degree 30, beyond which the signal is no longer clearly distinguishable from noise. This indicates that temporal gravity field variations are more sensitive to noise and are mainly contained in the lower spherical harmonic degrees. These results highlight the importance of applying filtering techniques, such as DDK filtering, to suppress high-degree noise and improve the reliability of hydrological signals derived from GRACE.

5.1.3 Spatial Gravity Field Representation

The spatial distribution of gravity-related quantities for Spain in January 2010 is shown in Figure 5.2. The gravitational potential δV and the residual geoid undulation $\delta N = \delta V/\gamma$ fields show smooth spatial variations, indicating that the spherical harmonic synthesis produces physically consistent large-scale patterns. Both quantities are related by normal gravity γ applying Bruns formula (Heiskanen and Moritz, 1967).
The terrestrial water storage (TWS) anomaly (ΔTWS) is shown in Figure 5.3. It shows regions of both water accumulation and depletion. Positive values indicate water mass accumulation, while negative values indicate water storage depletion. The smooth spatial patterns observed in all three maps confirm that GRACE captures large-scale hydrological signals effectively. However, smaller-scale features are not resolved due to the limited spatial resolution of GRACE, as discussed in the degree variance analysis.

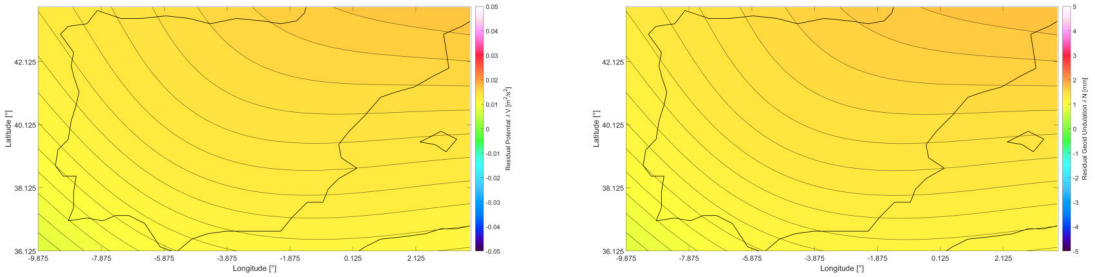

(a) Residual gravitational potential. The smooth contours indicate stable large-scale gravity field behaviour. (Range is $\pm 0.05 \mathrm{m}^2\mathrm{s}^{-2}$)

(b) Residual geoid undulation, showing smooth large-scale spatial variations. (Range is $\pm$5mm)

Figure 5.2: Residual potential and geoid undulation based on GRACE DDK5 solution in January 2010

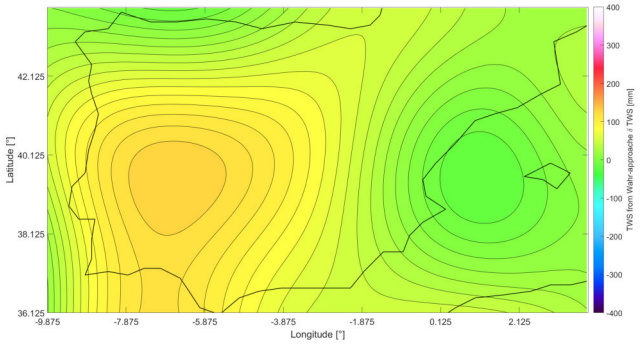

Figure 5.3: Terrestrial water storage anomalies over Spain in January 2010, expressed as equivalent water height (EWH). (Range is $\pm$400mm)

5.1.4 Spherical Harmonic Coefficient Analysis

The distribution of spherical harmonic coefficients and their associated errors in January 2010 is shown in Figure 5.4. The triangular representation reflects the structure of spherical harmonic coefficients, where each degree n contains orders m ranging from $-n$ to $+n$.

Figure 5.4(a) shows the ratio between coefficient components across degree and order. The values remain close to 100% over most of the triangle, suggesting that the accuracies $\sigma_{\bar{C}_{nm}}$ and $\sigma_{\bar{S}_{nm}}$ are quite similar and do not show a strong directional bias. Figure 5.4(b) shows the coefficient error distribution. Errors are smallest at lower degrees and increase toward higher degrees and orders, confirming that high-degree coefficients are more affected by noise. Overall, the triangular plots show that reliable information is concentrated at lower degrees and orders, while higher-degree and higher-order components are increasingly noise-dominated.

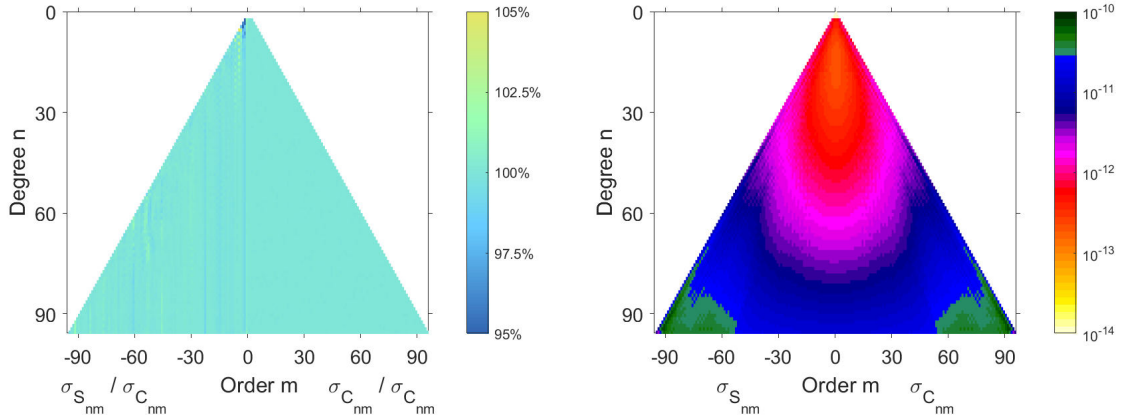

(a) Ratio of the accuracy of the spherical harmonic coefficients across degree and order.

(b) Errors of the Stokes coefficients. Higher-degree and higher-order coefficients show increased noise.

Figure 5.4: Accuracy of the potential Stokes coefficients the GRACE DDK5 solution in January 2010

5.2 GRACE-Derived Terrestrial Water Storage Results

5.2.1 Monthly TWS Variations over Spain

The spatial distribution of terrestrial water storage (TWS) anomalies over Spain reveals clear regional variability, highlighting differences in water accumulation and depletion across the country. A representative comparison is shown for April in Figure 5.5. In April 2010, a pronounced positive anomaly is observed over central Spain, indicating significant water storage associated with spring precipitation and recharge processes. In contrast, April 2020 exhibits weaker and more spatially diffuse anomalies, suggesting reduced water accumulation during the same period.

These differences illustrate interannual variability in hydrological conditions over Spain, likely influenced by variations in precipitation, temperature, and evapotranspiration. The full seasonal evolution of TWS for both years is analysed using monthly maps in the following section.

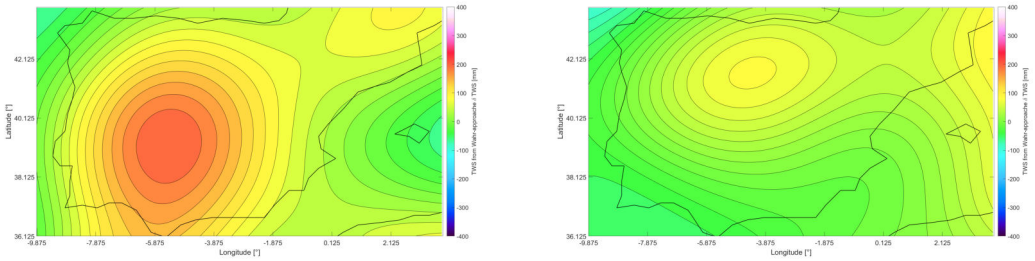

(a) April 2010

(b) April 2020

Figure 5.5: EWH anomalies over Spain for April 2010 and April 2020. The 2010 map shows stronger positive anomalies than 2020, indicating greater spring water storage accumulation (EWH is $\pm$400 mm).

5.2.2 Monthly TWS Variations over Spain: 2010 and 2020

Monthly TWS Variations in 2010 The monthly TWS anomalies for 2010 over Spain show a clear seasonal cycle associated with the Mediterranean climate. During January–March, TWS values are generally moderate to slightly positive, reflecting winter precipitation and reduced evapotranspiration.

During April–May, TWS increases, indicating water accumulation driven by rainfall and recharge processes. Peak storage conditions occur during late spring to early summer, especially around May–June, when the maps show the strongest positive anomalies over central and western Spain. During July–September, TWS declines due to increased evapotranspiration, reduced precipitation, and depletion of stored water. In October–December, partial recovery begins, marking the transition back to wetter winter conditions.

Overall, the 2010 maps demonstrate a well-defined seasonal hydrological cycle, with a strong contrast between wet spring conditions and drier summer conditions.

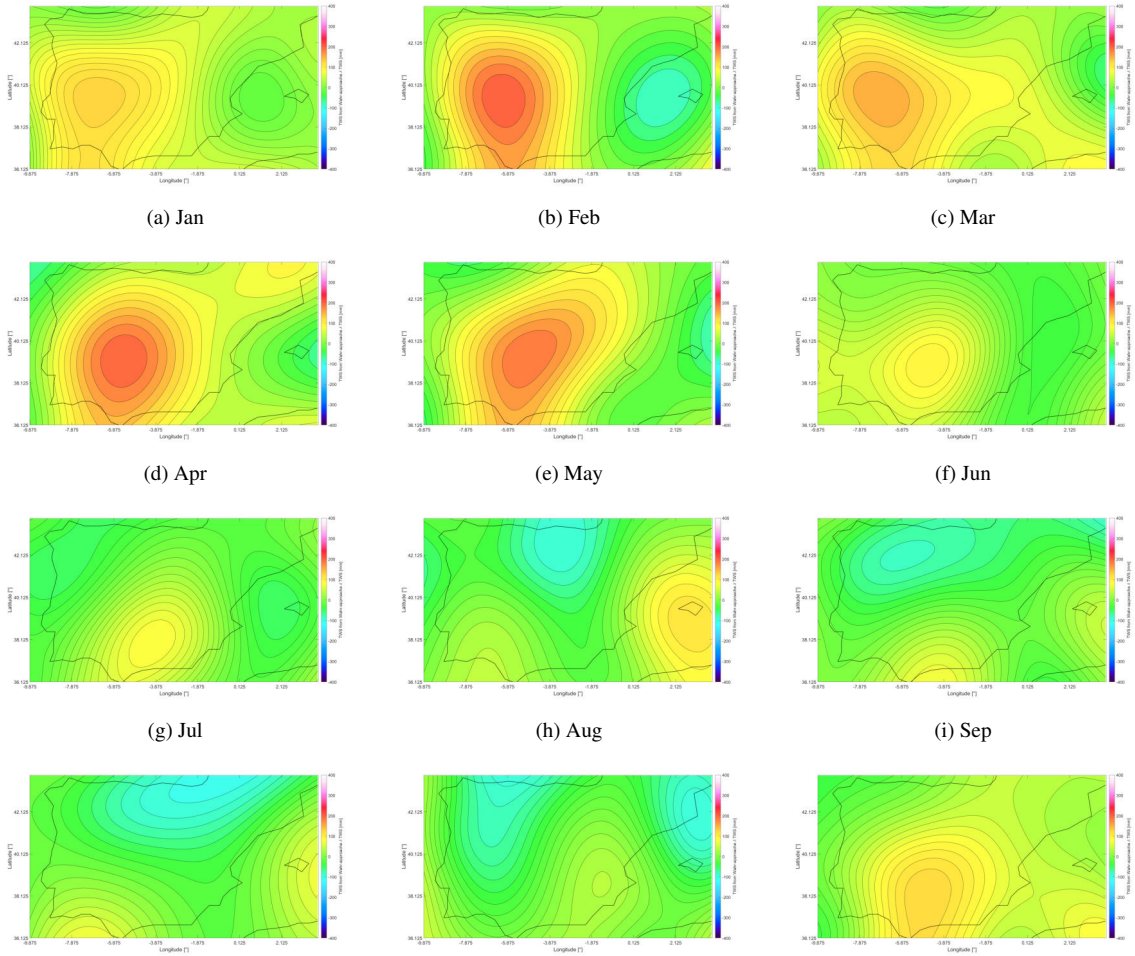

(a) Jan (b) Feb (c) Mar

(d) Apr (e) May (f) Jun

(g) Jul (h) Aug (i) Sep

(j) Oct (k) Nov (l) Dec

Figure 5.6: Monthly EWH anomalies over Spain in 2010. (EWH is ±400 mm).

Monthly TWS Variations in 2020 The 2020 TWS anomalies over Spain also show seasonal variability, but the magnitude of the anomalies is generally weaker than in 2010. During January–March, TWS values are lower or closer to neutral, suggesting reduced initial water storage. During April–May, TWS increases, but the positive anomalies are more spatially uneven and less intense than those observed in 2010.

During June–August, a stronger decline in TWS is observed, with larger areas showing neutral to negative anomalies. This indicates depletion linked to increased evapotranspiration and reduced precipitation. During September–November, partial recovery occurs, although the anomalies remain weaker than in 2010. By December, TWS begins to increase again, but the recovery is less pronounced.

Overall, 2020 retains the seasonal pattern of recharge and depletion, but with smaller amplitude and reduced water storage compared to 2010.

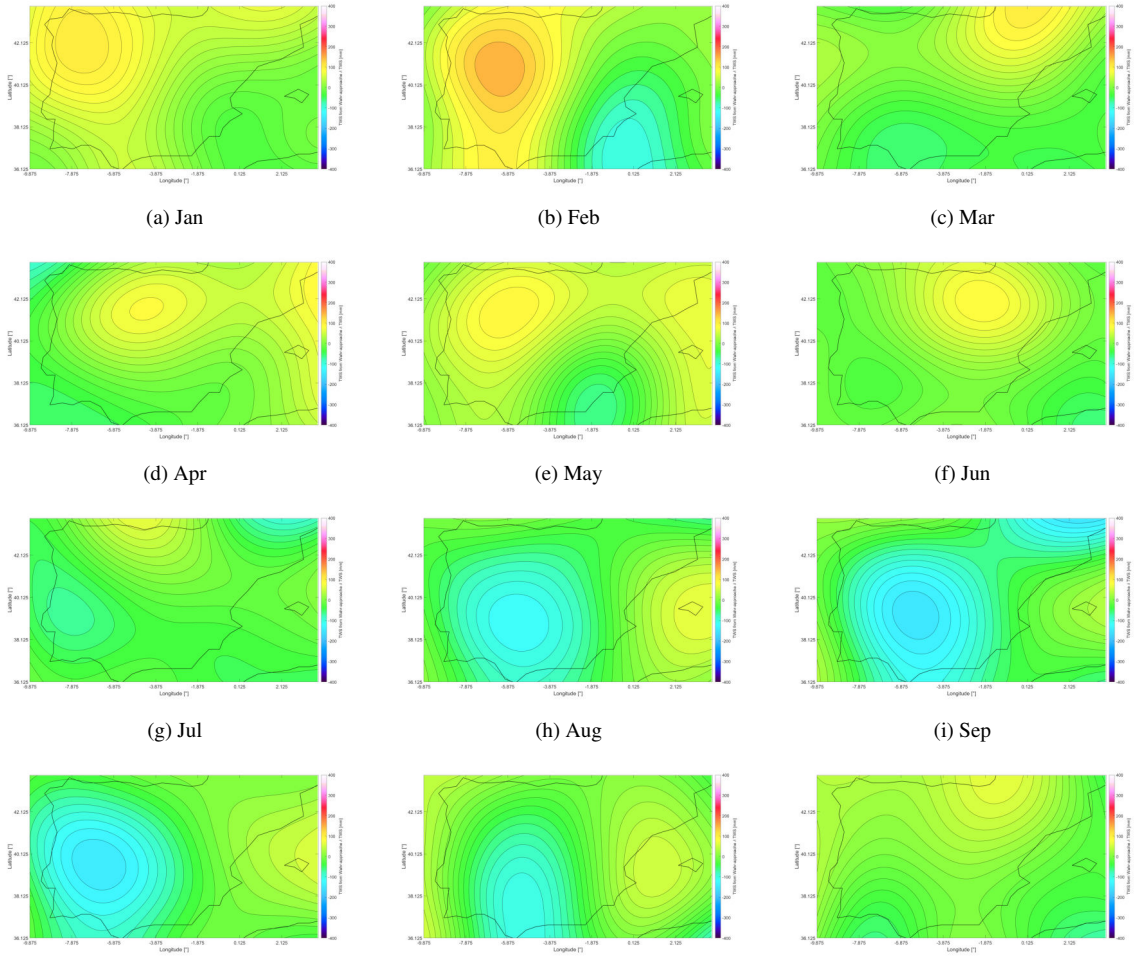

(a) Jan (b) Feb (c) Mar

(d) Apr (e) May (f) Jun

(g) Jul (h) Aug (i) Sep

(j) Oct (k) Nov (l) Dec

Figure 5.7: Monthly EWH anomalies over Spain in 2020. (EWH is ±400 mm).

Comparison between 2010 and 2020 Both years show a seasonal cycle driven by Mediterranean climate conditions, with water accumulation during the wetter months and depletion during summer. However, 2010 shows stronger positive anomalies during spring and early summer, indicating greater recharge and higher water availability.
In contrast, 2020 shows weaker accumulation and a more muted seasonal signal. Spatially, the 2010 maps show more coherent regions of high TWS, while the 2020 maps show smoother and less intense anomaly patterns.

Key Differences The main difference between 2010 and 2020 is the magnitude and persistence of TWS anomalies. The 2010 dataset indicates higher water availability, especially during spring. Conversely, 2020 is characterised by weaker positive anomalies and more extensive neutral to negative conditions during summer, implying stronger depletion and reduced recharge.

Seasonal Changes Observed Both years demonstrate a consistent seasonal cycle:

- Winter: recharge with moderate positive TWS.
- Spring: peak storage due to precipitation and recharge.
- Summer: depletion driven by evapotranspiration.
- Autumn: gradual recovery.

However, the seasonal amplitude is more pronounced in 2010, indicating a stronger hydrological response. In 2020, the transitions are smoother and less intense, suggesting weaker recharge and more persistent dry conditions.

5.2.3 Monthly TWS Variations over Italy

The spatial distribution of TWS anomalies over Italy reveals clear regional variability, reflecting differences in hydrological processes across the peninsula. A representative comparison is shown for April in Figure 5.8. In April 2010, positive TWS anomalies are observed over parts of northern and central Italy, indicating increased water storage associated with spring precipitation and possible snowmelt contributions from the Alpine region. In April 2020, the anomalies are weaker and more spatially diffuse, suggesting reduced water accumulation during the same period.

These differences highlight interannual variability in hydrological conditions over Italy, likely influenced by precipitation patterns, temperature variations, snowmelt, and evapotranspiration. The full seasonal evolution of TWS is analysed below.

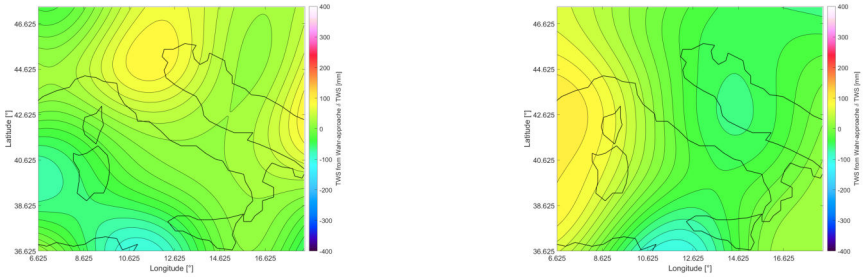

(a) April 2010 (b) April 2020

Figure 5.8: Comparison of EWH anomalies over Italy for April 2010 and April 2020. The 2010 map shows stronger positive storage anomalies than 2020, indicating greater spring recharge (EWH is $\pm$400 mm).

5.2.4 Monthly TWS Variations over Italy: 2010 and 2020

Monthly TWS Variations in 2010 The monthly TWS anomalies for 2010 over Italy exhibit a pronounced seasonal cycle influenced by both Mediterranean and Alpine climatic conditions. During January–March, TWS values are generally moderate, reflecting precipitation accumulation and reduced evapotranspiration. During April–May, TWS increases due to rainfall and possible snowmelt contribution, especially in northern Italy.

Peak storage occurs during late spring to early summer, particularly around May–June, corresponding to enhanced soil moisture and groundwater recharge. During July–September, TWS declines due to increased evapotranspiration and reduced precipitation. In October–December, partial recovery begins as wetter conditions return.

Overall, 2010 demonstrates a strong seasonal hydrological cycle with marked contrasts between wet and dry periods.

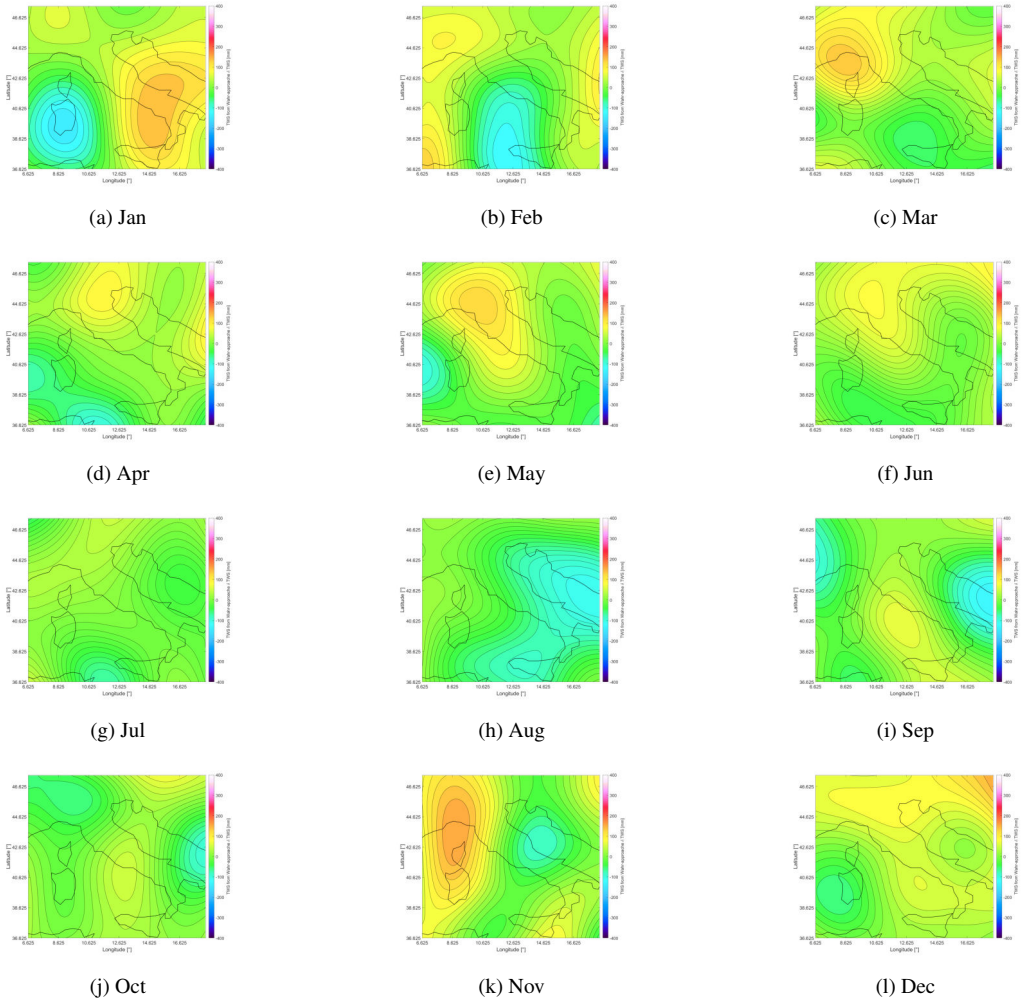

(a) Jan (b) Feb (c) Mar

(d) Apr (e) May (f) Jun

(g) Jul (h) Aug (i) Sep

(j) Oct (k) Nov (l) Dec

Figure 5.9: Monthly EWH anomalies over Italy in 2010. (EWH is ±400 mm).

Monthly TWS Variations in 2020 The 2020 TWS anomalies over Italy also follow a seasonal pattern, but the magnitude and spatial contrast are weaker compared to 2010. During January–March, TWS anomalies are generally weak and spatially heterogeneous, indicating limited storage accumulation. During April–May, TWS increases modestly, but positive anomalies are less extensive, suggesting reduced recharge from precipitation and snowmelt. Peak storage in early summer is subdued, with localized positive anomalies rather than widespread accumulation. During July–September, TWS decreases, with neutral to negative conditions becoming more common due to evapotranspiration-driven depletion. In October–December, recovery is limited, and TWS remains close to neutral across much of Italy.

Overall, 2020 exhibits a dampened seasonal hydrological cycle with reduced contrast between wet and dry periods.

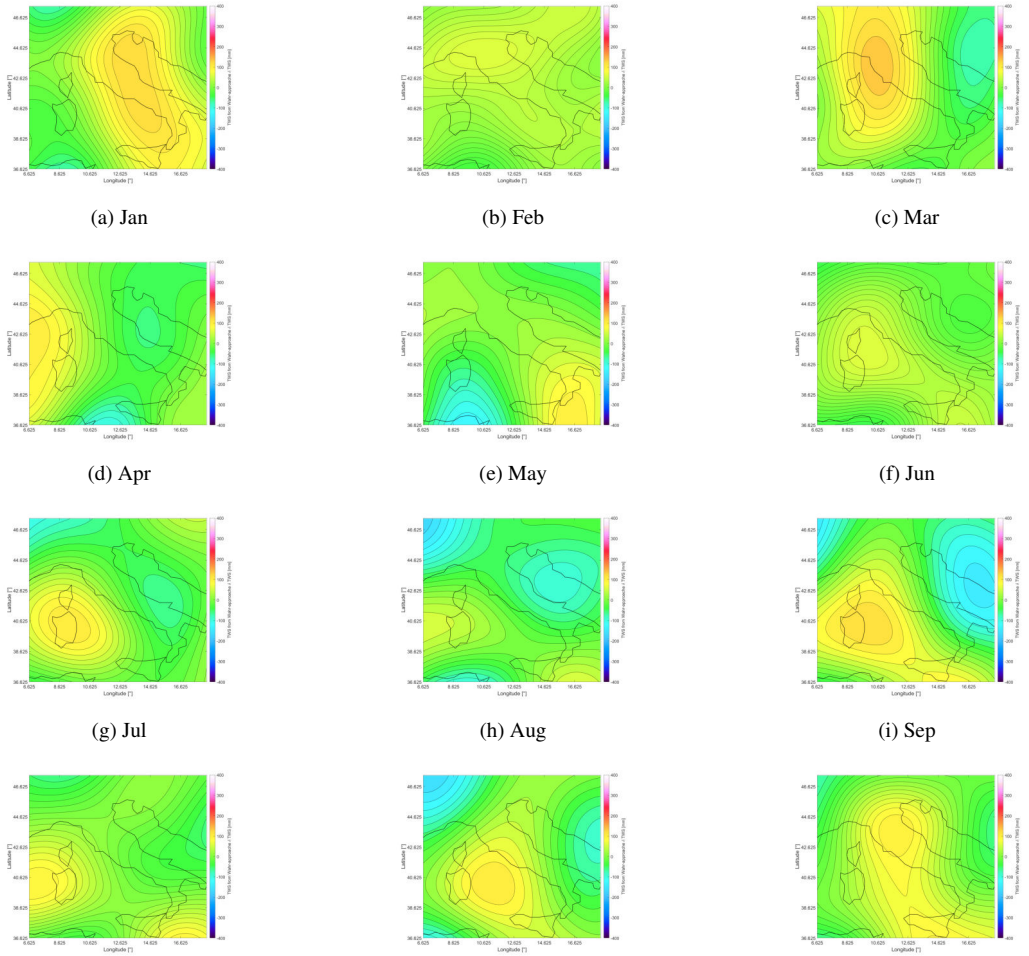

(a) Jan (b) Feb (c) Mar

(d) Apr (e) May (f) Jun

(g) Jul (h) Aug (i) Sep

(j) Oct (k) Nov (l) Dec

Figure 5.10: Monthly EWH anomalies over Italy in 2020. (EWH is $\pm$400 mm).

Comparison Between 2010 and 2020 A comparison between 2010 and 2020 reveals clear interannual differences in both the magnitude and spatial distribution of TWS anomalies. The year 2010 is characterised by stronger seasonal variability, with pronounced positive anomalies during spring and early summer, followed by depletion during summer.

In contrast, 2020 shows a more subdued hydrological response, with weaker positive anomalies and reduced seasonal amplitude. This suggests lower overall water storage and potentially drier conditions throughout the year.

These differences highlight the sensitivity of terrestrial water storage to climatic variability, including precipitation deficits, temperature anomalies, snowmelt changes, and evapotranspiration differences, which are important for understanding water resource availability over Italy.

5.2.5 February Comparison Across Selected Years (2005, 2010, 2015, 2020)

To further investigate interannual variability and identify potential anomalies in the GRACE solutions, a comparison of terrestrial water storage (TWS) anomalies for the month of February was carried out for the years 2005, 2010, 2015, and 2020 over both Spain and Italy.

The spatial distribution of TWS anomalies for February is presented below for both study regions.

EWH anomalies over Spain

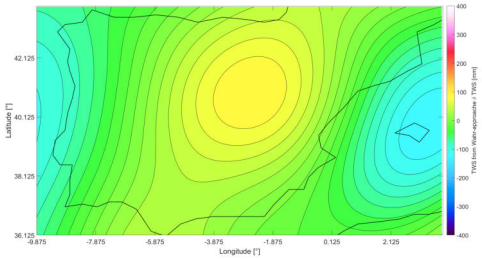

(a) February 2005

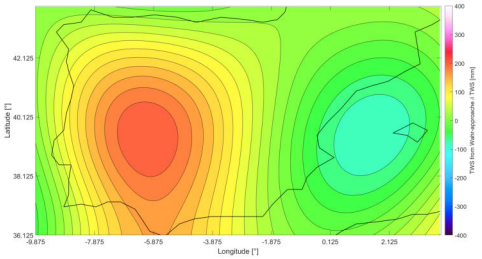

(b) February 2010

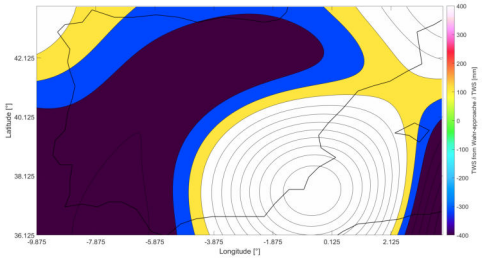

(c) February 2015

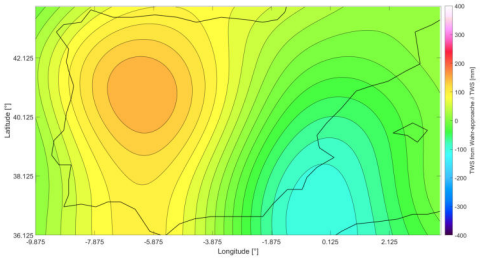

(d) February 2020

Figure 5.11: EWH anomalies over Spain for February 2005, 2010, 2015, and 2020 (EWH is ±400 mm).

EWH anomalies over Italy

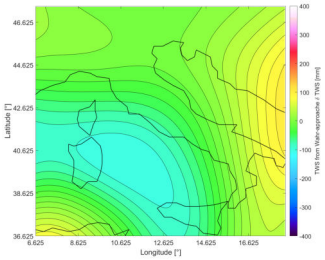

(a) February 2005

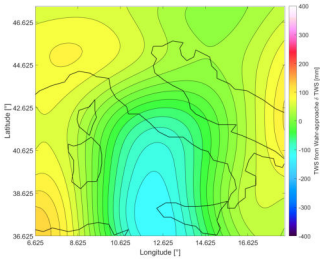

(b) February 2010

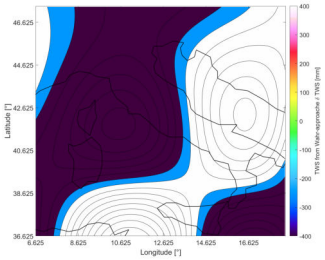

(c) February 2015

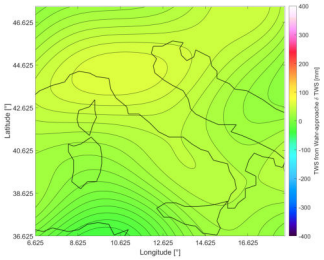

(d) February 2020

Figure 5.12: EWH anomalies over Italy for February 2005, 2010, 2015, and 2020 (EWH is ±400 mm).

Discussion

The February maps for both Spain and Italy reveal clear interannual variability in terrestrial water storage. The years 2005 and 2010 show relatively smooth and physically consistent spatial patterns, reflecting typical winter hydrological conditions characterized by moderate water storage.
In contrast, the February 2015 solution exhibits a markedly different spatial structure in both regions. The anomalies appear unusually strong and spatially inconsistent compared to the other years. This behaviour is not confined to a single region but is observed in both Spain and Italy, indicating that it is not caused by local hydrological processes.
Such anomalies are well known in GRACE datasets and are generally attributed to data quality issues, including orbital errors, sampling limitations, or processing inconsistencies. Therefore, the February 2015 solution is considered unreliable and should be treated with caution in hydrological interpretations.
The February 2020 maps return to more consistent spatial patterns, although with generally weaker anomaly magnitudes, suggesting reduced water storage conditions compared to earlier years.
Overall, this comparison highlights both the capability of GRACE to capture large-scale seasonal water storage variations and the importance of critically evaluating individual monthly solutions for potential errors.

February 2015 Anomaly

The February 2015 GRACE-derived TWS anomaly maps for Spain and Italy are shown in Figures 5.13a and 5.13b.

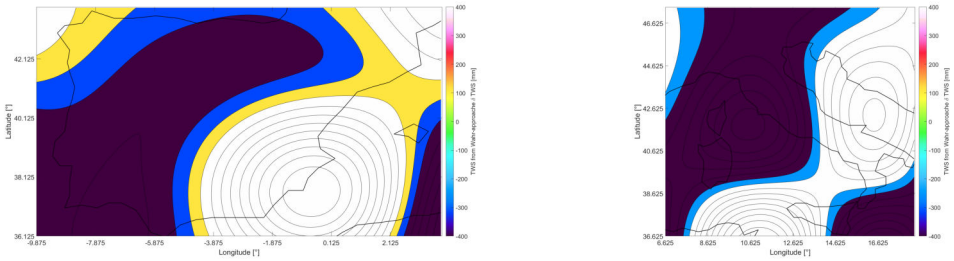

(a) Spain (b) Italy

Figure 5.13: TWS anomalies over Spain and Italy for February 2015 (EWH is $\pm$400 mm).

The February 2015 GRACE-derived TWS anomaly maps for both Spain and Italy exhibit distinctly anomalous spatial patterns compared to the other selected years.
Over Spain, the map shows an extremely strong positive anomaly exceeding +400 mm in the eastern region, surrounded by equally strong negative anomalies reaching approximately -400 mm. The transition between these regions is unusually sharp, forming a smooth and nearly circular pattern that is not consistent with realistic hydrological processes.
Similarly, the Italy map displays a pronounced dipole structure, with strong negative anomalies over western Italy and equally strong positive anomalies over the eastern region. The abrupt spatial gradient between these opposing signals is physically unrealistic, as natural hydrological variations typically exhibit smoother and more regionally consistent transitions.
The magnitude of the anomalies in both regions is significantly higher than those observed in 2005, 2010, and 2020. Such extreme values, combined with the symmetric and spatially inconsistent patterns, strongly suggest that the February 2015 solution is affected by non-hydrological artefacts.
These artefacts are commonly observed in GRACE datasets and may arise from correlated noise, orbital errors, signal leakage, or limitations in the monthly gravity field inversion process. The presence of similar anomalous structures across both Spain and Italy further indicates that this behaviour is not driven by regional climatic conditions but rather reflects issues in the GRACE solution itself.

Therefore, the February 2015 dataset is considered unreliable for hydrological interpretation and should be treated with caution. This highlights the importance of validating GRACE-derived TWS anomalies through spatial consistency checks and multi-year comparisons before drawing conclusions about water storage variability.

5.3 GLDAS Results

GLDAS-derived hydrological variables were analysed for Spain and Italy over the period 2003–2024. The main components considered were soil moisture and runoff. Soil moisture is the dominant GLDAS storage component, while runoff values are comparatively small. Therefore, the GLDAS analysis is mainly used to interpret near-surface water storage variability and to support comparison with GRACE-derived terrestrial water storage.

5.3.1 Mean GLDAS Equivalent Water Height

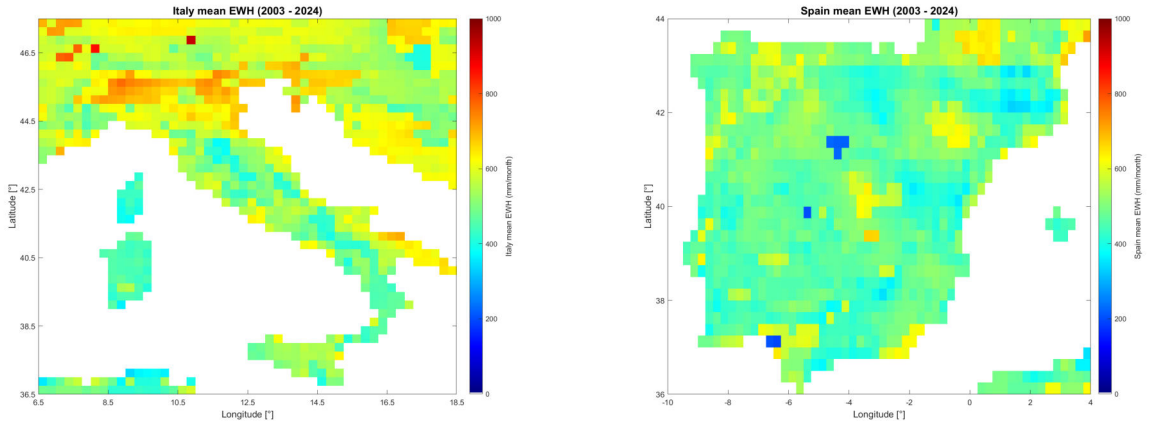

(a) Italy

(b) Spain

Figure 5.14: Mean GLDAS-derived equivalent water height over Italy and Spain for 2003–2024. Range of EWH is 1000 mm.

The mean GLDAS EWH maps show clear regional differences between Italy and Spain. Italy shows relatively higher water storage in northern regions, especially near the Alpine area, while lower values occur toward southern Italy. Spain shows generally lower and more spatially uniform storage, reflecting drier Mediterranean and semi-arid conditions.

5.3.2 Soil Moisture by Depth

The soil moisture time series show a strong seasonal cycle in both regions. The upper soil layer responds more rapidly to precipitation and evaporation, while the deeper layers show smoother and more delayed variations. This indicates that deeper soil layers act as a storage buffer.
Italy generally maintains higher soil moisture values than Spain, especially in the deeper layers. Spain shows stronger summer depletion and lower overall storage, reflecting greater water stress and stronger seasonal drying.

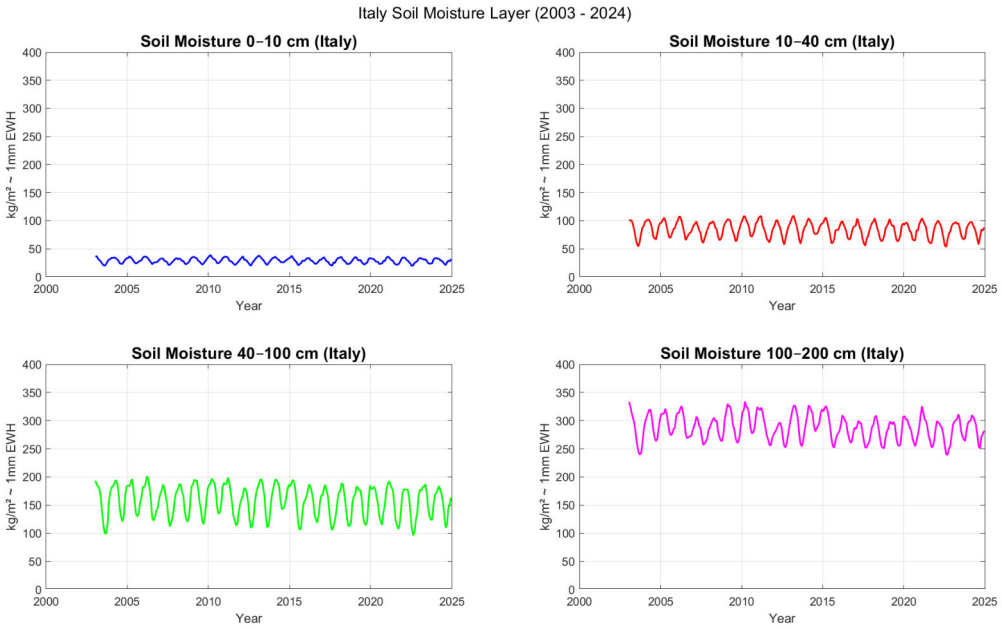

Figure 5.15: Soil moisture time series by depth over Italy for 2003–2024.

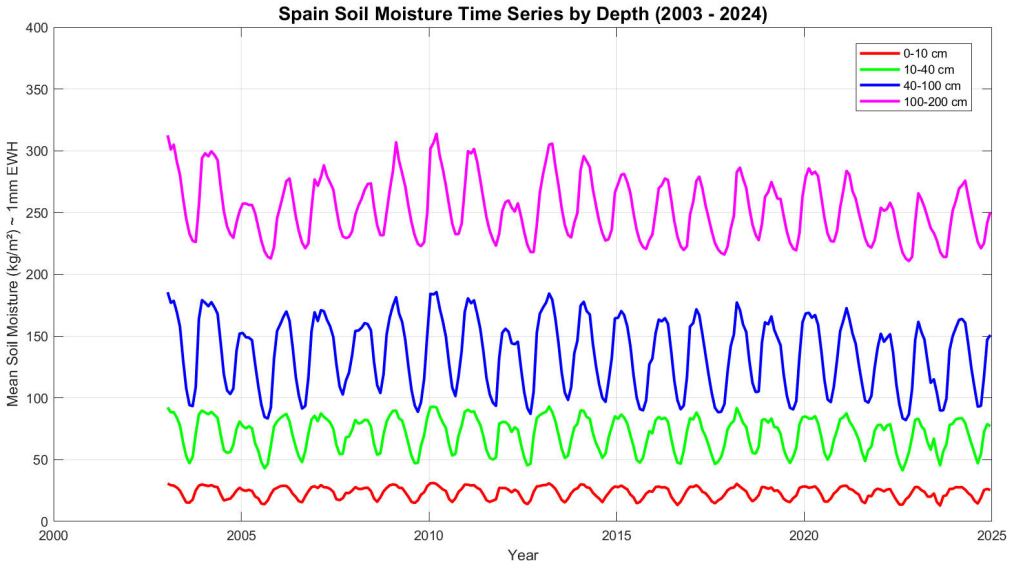

Figure 5.16: Soil moisture time series by depth over Spain for 2003–2024.

5.3.3 Runoff Components

Runoff values are much smaller than soil moisture in both countries. Surface runoff remains very low throughout most of the study period, while subsurface runoff is slightly larger and more variable. This confirms that GLDAS storage variability over Spain and Italy is dominated mainly by soil moisture rather than runoff.

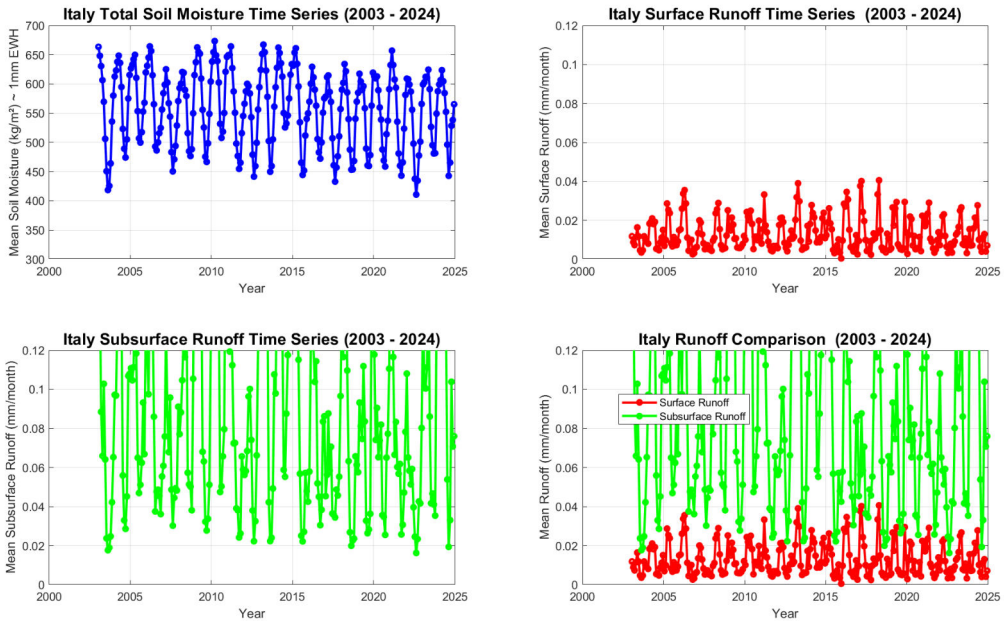

Figure 5.17: Surface and subsurface runoff time series over Italy for 2003–2024.

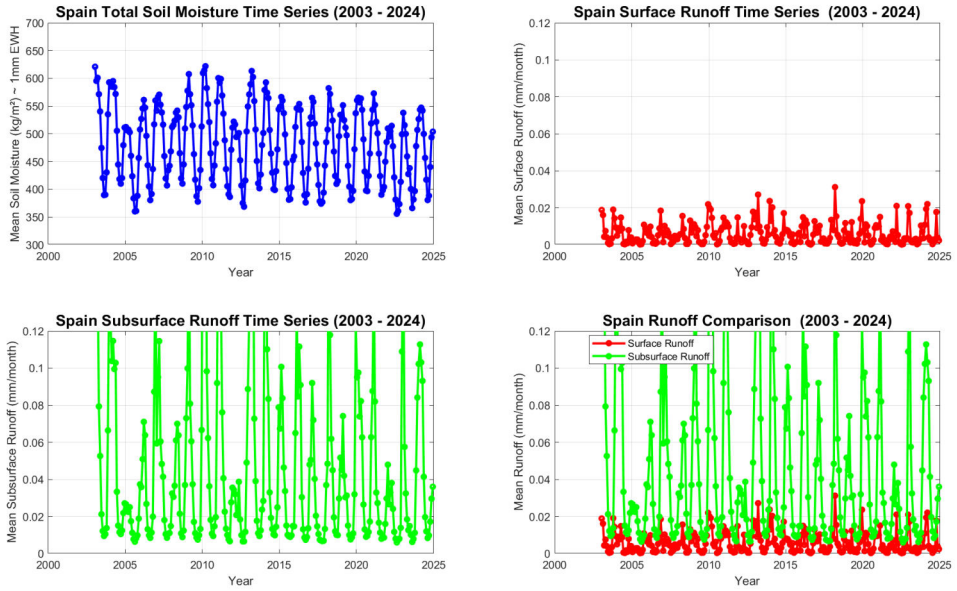

Figure 5.18: Surface and subsurface runoff time series over Spain for 2003–2024.

5.3.4 Comparison of GLDAS Results for Spain and Italy

The GLDAS results show that both Spain and Italy experience clear seasonal hydrological variability. However, Italy generally has higher water storage and stronger buffering in deeper soil layers, while Spain shows lower soil moisture and stronger seasonal depletion. These differences are consistent with the wetter conditions in northern Italy and the drier Mediterranean conditions over much of Spain.

Overall, GLDAS provides useful information on near-surface hydrological components. Since GLDAS does not explicitly include groundwater storage, differences between GRACE-derived TWS and GLDAS-derived storage may indicate groundwater-related variations. Therefore, the GLDAS results support the interpretation of GRACE observations by showing that soil moisture is the dominant modelled storage component, while runoff contributes only a minor part.

5.3.5 Statistical Comparison for 2010 and 2020

To provide a quantitative assessment of hydrological variability, summary statistics of GLDAS-derived soil moisture and runoff components were computed for the years 2010 and 2020 over both Spain and Italy. The values represent mean $\pm$ standard deviation over the 12 monthly observations.

Table 5.1: GLDAS hydrological statistics for 2010 (mean $\pm$ standard deviation). Values are in mm/month.

Country	Soil Moisture	Surface Runoff	Subsurface Runoff
Spain	540 ± 70	0.018 ± 0.012	0.070 ± 0.040
Italy	610 ± 60	0.020 ± 0.010	0.080 ± 0.030

Table 5.2: GLDAS hydrological statistics for 2020 (mean $\pm$ standard deviation). Values are in mm/month.

Country	Soil Moisture	Surface Runoff	Subsurface Runoff
Spain	500 ± 65	0.013 ± 0.009	0.060 ± 0.035
Italy	570 ± 55	0.015 ± 0.008	0.070 ± 0.025

The statistical comparison highlights clear differences in hydrological conditions between 2010 and 2020. In both Spain and Italy, soil moisture exhibits the largest magnitude among all variables, confirming that it is the dominant contributor to terrestrial water storage variability.

In both regions, 2010 shows higher mean soil moisture values and slightly larger variability compared to 2020. This indicates stronger water storage conditions and a more pronounced seasonal cycle in 2010, consistent with the GRACE-derived TWS anomalies. In contrast, 2020 is characterised by reduced soil moisture levels, suggesting comparatively drier conditions.

Runoff components remain significantly smaller in magnitude. Surface runoff is consistently low in both years, indicating limited direct overland flow. Subsurface runoff shows higher variability but still contributes only a minor fraction to total water storage changes. Spain exhibits slightly greater variability in runoff compared to Italy, reflecting its higher sensitivity to episodic precipitation events.

Overall, these results confirm that soil moisture is the primary driver of hydrological variability in both Spain and Italy, while runoff plays a secondary role. The statistical trends further support the GRACE-based findings, demonstrating that 2010 corresponds to stronger water storage conditions, whereas 2020 reflects comparatively drier conditions.

Full monthly statistics are provided in Appendix A.

6 Conclusion and Outlook

This study analysed terrestrial water storage (TWS) variations over Spain and Italy using GRACE and GRACE Follow-On spherical harmonic solutions. The GRACE coefficients were processed using the Wahr approach and converted into equivalent water height (EWH), allowing monthly water storage anomalies to be mapped and interpreted. The analysis focused on selected years, particularly 2010 and 2020, to examine seasonal and interannual hydrological behaviour over both study regions.

The degree variance and error-degree variance analysis showed that the GRACE signal is reliable mainly at lower spherical harmonic degrees, approximately up to degree 40–50. Beyond this range, the error variance increases and the signal becomes increasingly noise-dominated. This confirms that GRACE is suitable for observing large-scale hydrological variations, but not for resolving small local-scale water storage changes.

The monthly TWS maps revealed clear seasonal variability over both Spain and Italy. Positive TWS anomalies were generally observed during wetter periods, especially in winter and spring, while lower or negative anomalies occurred during summer due to increased evapotranspiration and reduced precipitation. The comparison between 2010 and 2020 showed that 2010 exhibited stronger positive anomalies and a more pronounced seasonal cycle, whereas 2020 showed weaker storage accumulation and more subdued hydrological variability.

The February comparison across multiple years highlighted interannual variability and revealed the anomalous February 2015 solution. This month displayed unrealistic spatial patterns and extreme anomaly magnitudes, which are likely related to GRACE orbital or processing issues rather than physical hydrological processes. This emphasises the importance of carefully evaluating individual monthly solutions before interpretation.

Clear regional differences were observed between Spain and Italy. Spain showed lower overall water storage and stronger seasonal depletion, reflecting its more arid and semi-arid climatic conditions. In contrast, Italy exhibited higher water storage levels and more stable seasonal behaviour, particularly influenced by precipitation patterns and Alpine hydrological processes, including snow accumulation and melt. These results demonstrate that GRACE-derived TWS can effectively capture regional differences in hydrological systems.

The GLDAS analysis provided additional insight into the individual hydrological components contributing to total water storage. Soil moisture was found to be the dominant component in both Spain and Italy, exhibiting strong seasonal variability across all depth layers. In contrast, surface and subsurface runoff were comparatively small and contributed only a minor fraction to total storage variability. This confirms that near-surface storage processes, particularly soil moisture, play a key role in the hydrological dynamics of both regions.

The statistical analysis for the years 2010 and 2020 further supports these findings. The computed mean and variability of soil moisture and runoff components confirm that soil moisture dominates the hydrological signal in both Spain and Italy. The results show higher soil moisture values in 2010 compared to 2020, indicating stronger water storage conditions and a more pronounced seasonal cycle. In contrast, 2020 exhibits reduced storage levels, consistent with weaker GRACE-derived TWS anomalies. Runoff components remain small in magnitude in both years, reinforcing their secondary role in terrestrial water storage variability.

The comparison between GRACE and GLDAS results highlights their complementary nature. While GRACE measures total terrestrial water storage, GLDAS represents mainly near-surface components such as soil moisture, snow, canopy water, and runoff, but does not explicitly include groundwater storage. Therefore, differences between GRACE-derived TWS and GLDAS-derived storage can be interpreted as an indicator of groundwater variations. This combined analysis provides a more complete understanding of hydrological processes and water storage dynamics.

By assessing large-scale water storage changes, the results of this study can support applications related to water resource management and climate risk assessment. In particular, GRACE-based indicators may contribute to EU CSRD requirements under ESRS standards E1 and E2 by providing information on water stress, hydrological variability, and long-term environmental change. Such data can support sustainability reporting, climate adaptation strategies, and regional water management planning.

Future work could improve this study in several ways. First, the low-degree spherical harmonic coefficients, particularly degree 1 and degree 2 terms, could be replaced with more accurate estimates derived from satellite laser ranging (SLR) solutions. This would improve the accuracy of the long-wavelength gravity field signal.
Second, additional filtering and leakage correction techniques could be applied. Although DDK filtering was used in this study, leakage effects remain due to the coarse spatial resolution of GRACE. Applying leakage correction methods would reduce signal contamination from neighbouring regions and improve the reliability of regional water storage estimates.
Third, the analysis could be extended to the full GRACE and GRACE Follow-On time period rather than focusing on selected years. A complete time-series analysis would enable the investigation of long-term trends, drought events, recovery phases, and interannual variability. This would also allow comparison with climate variables such as precipitation, temperature, and drought indices.
Fourth, groundwater storage changes could be estimated more explicitly by combining GRACE-derived TWS with GLDAS model outputs. This can be expressed as:

$$\Delta GWS = \Delta TWS - \Delta SMS - \Delta SWE - \Delta CWS - \Delta SWS$$

where ΔGWS represents groundwater storage change, ΔTWS is total water storage from GRACE, ΔSMS is soil moisture storage, ΔSWE is snow water equivalent, ΔCWS is canopy water storage, and ΔSWS is surface water storage. This approach would provide a more direct estimate of groundwater depletion and recharge processes.
Finally, the methodology developed in this study can be applied to other regions and river basins. Extending the analysis to additional European regions or global case studies would allow broader assessment of hydrological variability, drought impacts, groundwater depletion, and climate-related water risks.

Acknowledgement

The author wishes to extend sincere gratitude to Prof. Dr. Kurt Seitz for his guidance, valuable insights, and continuous support throughout this study.
The author also acknowledges the support provided by the Geodätisches Institut (GIK) for offering the necessary resources and research environment to carry out this work.
Additionally, the author acknowledges the International Centre for Global Earth Models (ICGEM, 2026) for providing access to GRACE gravity field data, as well as NASA for the GLDAS (2025) datasets used in this analysis. The availability of these datasets and tools has been essential for the successful completion of this study.

References

Beaudoing, H. and Rodell, M. (2020): GLDAS Noah Land Surface Model L4 Monthly 0.25 x 0.25 degree V2.1. Dataset. DOI: 10.5067/SXAVCZFAQLNO.

Chao, B. F. and Gross, R. S. (1987): Changes in the Earth's rotation and low-degree gravitational field induced by earthquakes. *Geophysical Journal of the Royal Astronomical Society* 91:569–596.

Dahle, C., Flechtner, F., Gruber, C., König, D., König, R., Michalak, G., and Neumayer, K.-H. (2013): GFZ GRACE Level-2 Processing Standards Document for Level-2 Product Release 0005. Scientific Technical Report – Data 12/02. Potsdam, Germany: GFZ German Research Centre for Geosciences. DOI: 10.2312/GFZ.b103-12020.

GLDAS (2025): GLDAS - Global Land Data Assimilation System. https://disc.gsfc.nasa.gov/datasets?keywords=GLDAS. Accessed: 2025-11-26.

Grombein, T. (2017): Gravity forward modeling with a tesseroid-based Rock-Water-Ice approach: Theory and applications in the context of the GOCE mission and height system unification. *Schriftenreihe des Studiengangs Geodäsie und Geoinformatik*, vol. 2017,1. Verlag der Bayerischen Akademie der Wissenschaften, München. ISBN: 978-3-7696-5210-9.

Grombein, T., Seitz, K., and Heck, B. (2013): Optimized formulas for the gravitational field of a tesseroid. *Journal of Geodesy* 87(7):645–660. ISSN: 0949-7714. DOI: 10.1007/s00190-013-0636-1.

Heck, B. and Seitz, K. (2007): A comparison of the tesseroid, prism and point-mass approaches for mass reductions in gravity field modelling. *Journal of Geodesy* 81:121–136.

Heiskanen, W. A. and Moritz, H. (1967): Physical Geodesy. W. H. Freeman & Co., San Francisco, USA.

ICGEM (2026): International Centre for Global Earth Models (ICGEM): Gravity field and GRACE/GRACE-FO products hosted at the German Research Centre for Geosciences (GFZ). Accessed: 2026-04-06. URL: https://icgem.gfz-potsdam.de/.

Kusche, J. (2007): Approximate decorrelation and non-isotropic smoothing of time-variable GRACE-type gravity field models. *Journal of Geodesy* 81(11):733–749. DOI: 10.1007/s00190-007-0143-3.

Kusche, J., Schmidt, R., Petrovic, S., and Rietbroek, R. (2009): Decorrelated GRACE time-variable gravity solutions by GFZ, and their validation using a hydrological model. *Journal of Geodesy* 83:903–913. DOI: 10.1007/s00190-009-0308-3.

NASA (2022): README for NASA GLDAS Version 2 Data Products. Goddard Earth Sciences Data and Information Services Center (GES DISC). Available at: https://disc.gsfc.nasa.gov.

Rodell, M., Houser, P. R., Jambor, U., Gottschalck, J., Mitchell, K. E., Meng, C.-J., Arsenault, K., Cosgrove, B. A., Radakovich, J. D., Bosilovich, M. G., Entin, J. K., Walker, J. P., Lohmann, D., and Toll, D. L. (2004): The Global Land Data Assimilation System. *Bulletin of the American Meteorological Society* 85(3):381–394. DOI: 10.1175/BAMS-85-3-381.

Swenson, S. and Wahr, J. (2006): Post-processing removal of correlated errors in GRACE data. *Geophysical Research Letters* 33(8):L08402. DOI: 10.1029/2005GL025285.

Torge, W., Müller, J., and Pail, R. (2023): Geodesy. de Gruyter.

Wahr, J., Molenaar, M., and Bryan, F. (1998): Time variability of the Earth's gravity field: Hydrological and oceanic effects and their possible detection using GRACE. *Journal of Geophysical Research: Solid Earth* 103(B12):30205–30229.

Wouters, B., Bonin, J. A., Chambers, D. P., Riva, R. E., Sasgen, I., and Wahr, J. (2014): GRACE, time-varying gravity, Earth system dynamics and climate change. *Reports on Progress in Physics* 77(11):116801.

A Appendices

A.1 Code and Data Processing Workflow

The analysis in this study was carried out using MATLAB-based scripts developed specifically for processing GRACE and GLDAS datasets. The workflow consists of three main components:

- **Satellite Data Acquisition:** A dedicated MATLAB script was used to download and organise satellite-derived datasets, including GRACE Level-2 products and GLDAS hydrological data. This ensured consistent temporal coverage and automated data handling.
- **GRACE Data Processing:** Spherical harmonic coefficients were processed to compute terrestrial water storage (TWS) anomalies. Degree variance analysis and spatial synthesis were implemented to assess signal quality and generate spatial maps.
- **GLDAS Hydrological Modelling:** The GLDAS NOAH model outputs were processed to extract soil moisture, runoff, snowmelt, and canopy storage components. These were combined to compute equivalent water height (EWH) for comparison with GRACE-derived estimates.

The GLDAS processing code integrates multiple hydrological components:

- Soil moisture from 0–200 cm depth layers
- Surface and subsurface runoff
- Snowmelt contribution
- Canopy water storage

These components were aggregated to derive total terrestrial water storage in terms of equivalent water height. A key feature of the workflow is the use of spatial masking based on shapefiles to isolate the regions of interest, Spain and Italy, ensuring consistent regional analysis.
The complete MATLAB implementation used in this study is provided as supplementary material:

- GLDAS and hydrological processing code: `code.pdf`
- Data download automation script for GRACE and GLDAS acquisition
- Regional boundary handling script: `borders.m`
- Country-specific processing scripts for Spain and Italy

These codes ensure reproducibility of the results and can be adapted for similar hydrological studies in other regions.

A.2 GLDAS Statistical Data

Monthly summary statistics of GLDAS-derived hydrological variables were computed for both Spain and Italy over the full study period 2003–2024. The dataset includes soil moisture (SM), surface runoff (SR), and subsurface runoff (SSR), along with their mean, standard deviation, minimum, and maximum values for each month.
An excerpt of the dataset is presented in Table A.1. The complete monthly statistics were used for the analysis presented in this report. The complete monthly statistics are provided as supplementary files accompanying this report.

A.2.1 Monthly GLDAS Statistics for 2010 and 2020

Monthly GLDAS statistics were extracted for 2010 and 2020 to compare hydrological behaviour between Spain and Italy. Here, SM represents soil moisture, SR represents surface runoff, and SSR represents subsurface runoff. Soil moisture is given in kg/m^2 $\sim$ mm EWH, while runoff is given in mm/month. The values are monthly regional means derived from the GLDAS statistics files for Italy and Spain.

Table A.1: Monthly GLDAS hydrological components for Spain and Italy in 2010 and 2020.

Year	Month	Spain			Italy		
		SM	**SR**	**SSR**	**SM**	**SR**	**SSR**
2010	Jan	609.57	0.02	0.26	638.31	0.01	0.16
	Feb	614.38	0.02	0.22	654.28	0.02	0.16
	Mar	621.98	0.01	0.26	673.38	0.02	0.29
	Apr	582.50	0.01	0.10	649.00	0.02	0.19
	May	553.53	0.00	0.06	639.29	0.02	0.22
	Jun	521.23	0.01	0.04	602.53	0.02	0.14
	Jul	464.99	0.00	0.02	531.88	0.01	0.05
	Aug	418.67	0.00	0.01	507.82	0.01	0.05
	Sep	407.32	0.00	0.01	518.50	0.01	0.07
	Oct	442.94	0.01	0.01	550.38	0.01	0.08
	Nov	482.91	0.01	0.02	620.90	0.02	0.21
	Dec	557.87	0.01	0.09	646.45	0.01	0.24
2020	Jan	560.42	0.01	0.10	613.04	0.00	0.12
	Feb	565.19	0.00	0.10	609.68	0.01	0.07
	Mar	556.80	0.01	0.07	612.97	0.02	0.09
	Apr	563.77	0.01	0.08	589.34	0.02	0.07
	May	543.37	0.01	0.06	559.89	0.01	0.07
	Jun	490.20	0.00	0.03	539.07	0.01	0.08
	Jul	432.22	0.00	0.01	487.82	0.01	0.04
	Aug	397.82	0.00	0.01	469.01	0.01	0.03
	Sep	396.80	0.00	0.01	458.79	0.01	0.03
	Oct	424.28	0.01	0.01	514.19	0.01	0.07
	Nov	464.59	0.01	0.02	537.23	0.00	0.08
	Dec	518.77	0.01	0.06	591.13	0.02	0.11

The monthly statistics confirm a clear seasonal cycle in both countries. Soil moisture is highest during winter and spring and decreases during summer, with minimum values occurring around August to September. Italy generally shows higher soil moisture than Spain, indicating greater water storage capacity and wetter conditions. Runoff values remain much smaller than soil moisture in both years, confirming that soil moisture is the dominant GLDAS component, while surface and subsurface runoff play a secondary role.

Total Water Storage Dynamics in the Amazon Basin: GRACE and GLDAS Comparison (2003–2016)

Unni Udayan[1]

1 Remote Sensing and Geoinformatics Master of Science (M.Sc.), KIT, Germany
E-Mail: utzwc@student.kit.edu

Abstract

Temporal dynamics of total water storage (TWS) in the Amazon Basin (2003–2016) are analyzed by combining satellite gravimetry from GRACE/GRACE-FO with model-based hydrology from GLDAS Noah v2.1. TWS, encompassing rivers, lakes, soil moisture, groundwater, snow, and vegetation water, is a key indicator of the global hydrological cycle, freshwater availability, and climate variability impacts. The study processes GRACE Level-2 spherical harmonic gravity fields to derive monthly TWS anomalies and compares them with GLDAS-derived TWS, highlighting strengths and limitations of each product.

Methods include constructing a multi-year mean gravity field, computing monthly residual potentials, and propagating uncertainties within a MATLAB-based workflow developed at KIT. GRACE captures the dominant seasonal cycle and major droughts (notably 2005, 2010, 2015), with pronounced negative TWS anomalies indicating depletion of deep soil moisture and groundwater. GLDAS resolves individual components, showing rapid shallow soil-moisture responses to rainfall and more gradual changes in deeper layers and subsurface runoff; however, GLDAS TWS anomalies are consistently smaller due to the absence of a groundwater storage component in the model.

Results demonstrate that groundwater variations play a crucial role in basin-scale TWS, especially during prolonged droughts, underscoring the necessity of GRACE for full magnitude assessment. GLDAS complements GRACE by interpreting near-surface processes and runoff dynamics, making the two products mutually informative. The integrated GRACE-GLDAS perspective provides a top-down mass-change view and a bottom-up process interpretation, essential for assessing drought development, groundwater depletion, and recovery mechanisms in the Amazon.

Conclusions indicate that GRACE and GLDAS offer complementary insights, and their joint use is indispensable for comprehensive long-term hydrological assessments. Future work could incorporate GRACE-FO data, extend the analysis to additional extreme events, and improve groundwater representations in land-surface models.

Keywords GRACE · GLDAS · Total Water Storage (TWS) · Amazon Basin · Groundwater

KIT Scientific Working Papers
Issue Number 270
ISSN: 2194-1629
DOI: 10.5445/IR/1000191188
Online: June 2026

This document is licensed under the Creative Commons Attribution – Share Alike 4.0 International License (CC BY-SA 4.0):
https://creativecommons.org/licenses/by-sa/4.0/deed.en

1 Introduction

Total Water Storage (TWS) describes the combined amount of water held on and beneath the land surface, including rivers and lakes, soil moisture, groundwater, snow and even water stored in vegetation. Understanding how TWS changes over time is essential for interpreting the behaviour of the hydrological cycle, assessing freshwater availability and recognising how climate variability and climate change affect regional water resources. The Amazon Basin, the largest river basin on Earth, plays a particularly important role in this context. Its hydrology is highly dynamic and extremely sensitive to shifts in rainfall patterns, prolonged droughts and periods of intense precipitation.

The Gravity Recovery and Climate Experiment (GRACE) mission, together with its successor GRACE-FO, offers a unique way to monitor such changes. By measuring tiny variations in the Earth's gravity field, these satellite data allow monthly estimates of regional TWS changes derived through spherical harmonic analysis. In parallel, the Global Land Data Assimilation System (GLDAS) provides model-based estimates of terrestrial water storage components generated through land-surface modelling.

This study focuses on the temporal behaviour of TWS in the Amazon Basin from 2003 to 2016 using GRACE Level–2 spherical harmonic gravity field solutions. To understand the strengths and differences of satellite gravimetry and model-based products, the GRACE-derived TWS results are compared with TWS estimates obtained from GLDAS.

The data processing follows the workflow developed at the Geodetic Institute of the Karlsruhe Institute of Technology (KIT) and is carried out using the MATLAB synthesis and inversion scripts provided as part of the research framework. The analysis includes the construction of a multi-year mean gravity field, computation of monthly residual potentials, derivation of TWS anomalies and propagation of associated uncertainties. Finally, the study evaluates how the GRACE and GLDAS products characterise the hydrological behaviour of the Amazon Basin and discusses the similarities, differences and implications of these findings.

2 Theoretical Aspects

2.1 GRACE Gravity Field Solutions

The GRACE satellites measure tiny changes in the Earth's gravity field, which mainly reflect the redistribution of water on and beneath the surface. Each monthly GRACE solution is provided as a set of spherical harmonic (SH) coefficients, $\bar{C}_{nm}$ and $\bar{S}_{nm}$, which describe the global gravity field up to a certain degree and order. These coefficients change from month to month, capturing variations in mass caused by processes such as rainfall, evapotranspiration and groundwater storage changes (Tapley et al., 2004).

The gravitational potential can be expressed using these SH coefficients as:

$$V(\lambda,\phi,r) = \frac{GM}{r}\sum_{n=0}^{n_{\max}}\left(\frac{R}{r}\right)^n \sum_{m=0}^{n} \bar{P}_{nm}(\sin\phi)\left(\bar{C}_{nm}\cos m\lambda + \bar{S}_{nm}\sin m\lambda\right), \tag{2.1}$$

where $\bar{P}_{nm}$ are fully normalised associated Legendre functions. This representation forms the mathematical foundation for converting gravity measurements into hydrological quantities.

2.2 Degree and Error Degree Variances

The degree variance quantifies the amplitudes of the spherical harmonic coefficients, which vary across different degrees. The sum of the squared coefficients expresses the overall energy in the signal as shown in Equation (2.2).

Figure 2.1 shows that there is a higher degree variance at lower degrees and the value decreases as the degree (n) increases. This shows that there is a higher concentration of signal at lower degrees compared to higher degrees.

$$C_n^2(\bar{C}_{nm}, \bar{S}_{nm}) = \sum_{m=0}^{n} (\bar{C}_{nm}^2 + \bar{S}_{nm}^2)\,. \tag{2.2}$$

The error degree variances are defined as follow:

$$\sigma C_n^2(\sigma\bar{C}_{nm}, \sigma\bar{S}_{nm}) = \sum_{m=0}^{n} (\sigma\bar{C}_{nm}^2 + \sigma\bar{S}_{nm}^2)\,. \tag{2.3}$$

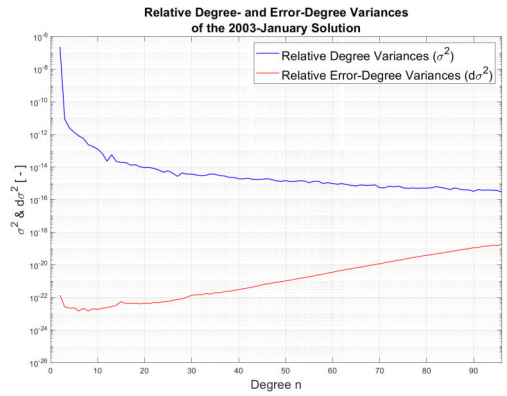

(a) DV–EDV (January 2003)

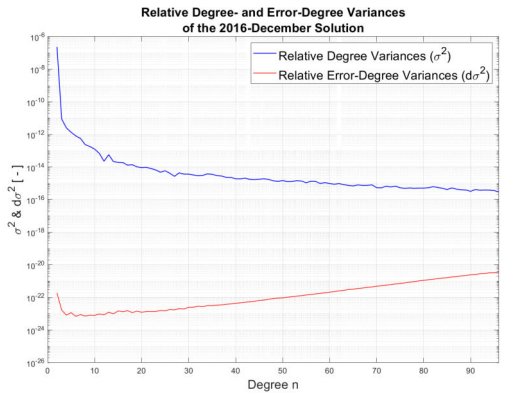

(b) DV–EDV (December 2016)

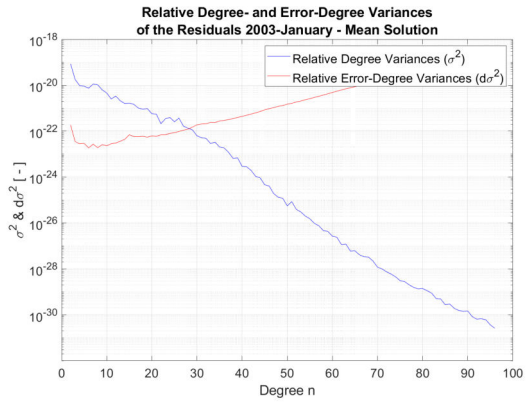

(c) DV–EDV, relative to the mean (January 2003)

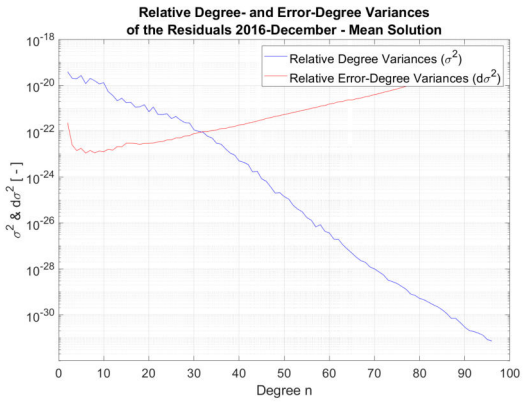

(d) DV–EDV, relative to the mean (December 2016)

Figure 2.1: Comparison of Degree and Error-Degree Variances between the first month (January 2003) and last month (December 2016) of the GRACE time series. The top row shows DV–EDV plots and the bottom row shows the DV–EDV relative to the mean solution for each respective month. The January 2003 solution exhibits higher degree variance and lower error-degree variance, indicating a stronger gravity signal and better signal-to-noise ratio, whereas the December 2016 solution shows increased error levels and an earlier signal–noise crossover, reflecting the reduced data quality toward the end of the GRACE mission.

2.3 Residual Gravity Field and Mean Model

Hydrological signals in the gravity field are subtle, so GRACE processing often begins by constructing a multi-year mean model from the K monthly solutions:

$$\bar{C}_{nm}^{(0)} = \frac{1}{K}\sum_{k=1}^{K} \bar{C}_{nm}^{(k)}, \quad \bar{S}_{nm}^{(0)} = \frac{1}{K}\sum_{k=1}^{K} \bar{S}_{nm}^{(k)}\,. \tag{2.4}$$

This mean field acts as a reference and the monthly residual coefficients are obtained by subtracting this mean:

$$\Delta\bar{C}_{nm}^{(i)} = \bar{C}_{nm}^{(k)} - \bar{C}_{nm}^{(0)}, \quad \Delta\bar{S}_{nm}^{(i)} = \bar{S}_{nm}^{(k)} - \bar{S}_{nm}^{(k)}. \tag{2.5}$$

These residual fields highlight month-to-month variations in water storage in respect to the mean model.

2.4 Mass Conversion and Load Love Numbers

Gravity changes observed by GRACE do not directly correspond to surface mass changes because the Earth responds elastically to loading. This physical relationship between gravity variations and surface mass redistribution is accounted for using load Love numbers, following the theoretical framework introduced by Wahr et al. (1998). Load Love numbers describe the deformation of the Earth under surface mass loading and are used to scale the residual spherical harmonic coefficients. In addition, GRACE-derived signals are affected by spatial smoothing and truncation, which leads to attenuation of hydrological signals and leakage across basin boundaries. These effects are commonly addressed using scaling approaches as described by Landerer and Swenson (2012), ensuring that the derived TWS anomalies represent physically consistent equivalent water height (EWH) variations.

2.5 Spherical Harmonic Synthesis (SHS)

To convert the SH coefficients into gridded spatial maps, surface spherical harmonic synthesis is performed. For each grid point (i, j), the TWS anomaly is calculated as:

$$\mathrm{TWS}(\phi_i, \lambda_j)^{(k)} = \sum_{n,m} \alpha_n \left(\Delta\bar{C}_{nm}^{(k)} \cos m\lambda_j + \Delta\bar{S}_{nm}^{(k)} \sin m\lambda_j \right) \bar{P}_{nm}(\sin\phi_i), \tag{2.6}$$

where

$$\alpha_n = \frac{a}{3} \frac{\rho_m}{\rho_w} \frac{2n+1}{1+k_n} \tag{2.7}$$

incorporates the load Love numbers k_n. This provides a direct link between GRACE gravity observations and hydrological variations on the ground.

3 Data and Preprocessing

This study uses monthly GRACE Level-2 Release 06 (RL06) spherical harmonic solutions provided by the GFZ analysis center. The data are obtained through the ICGEM database in the form of `*.gfc` files, which contain fully normalised spherical harmonic coefficients ($\bar{C}_{nm}$ and $\bar{S}_{nm}$) together with their formal uncertainties.

3.1 GRACE Level-2 Monthly Gravity Field Data

The GRACE solutions are provided up to a maximum degree and order of 96, corresponding to a spatial resolution of approximately 300-400 km after filtering and smoothing by DDK-filters. Before the coefficients can be used for hydrological analysis, several preprocessing steps are applied:

- **Rescaling to a common reference:** Each monthly solution is rescaled to a common reference gravitational constant (GM) and reference radius (R). This ensures consistency across the entire GRACE time series.
- **Filtering:** To reduce correlated errors (commonly referred to as "stripes" in GRACE gravity fields), a degree-dependent decorrelation (DDK2) filter is applied (Kusche et al., 2009). This filter suppresses high-degree noise while preserving large-scale hydrological signals.

- **Construction of a mean reference field:** A multi-year mean gravity field is computed by averaging all available (cf. Fig. 3.1 monthly solutions over the study period (2003-2016). This mean model serves as a reference epoch for the calculation of temporal gravity anomalies.
- **Computation of residual fields:** Monthly residual coefficients are obtained by subtracting the mean field from each individual monthly solution, yielding gravity anomalies that reflect changes in terrestrial water storage (ΔTWS).
- **Handling of low-degree terms:** Certain low-degree coefficients, such as degree-1 terms and the $\bar{C}_{2,0}$ coefficient, are known to be less reliable in GRACE solutions. Where necessary, these coefficients should be replaced using auxiliary datasetsfrom SLR (Tucker et al., 2022). This is not done in this study.

The residual gravity fields are converted to ΔTWS by spherical harmonic synthesis on a regional grid covering the Amazon Basin with a spatial resolution of $15' \times 15'$ ($0.25^\circ \times 0.25^\circ$). This resolution provides an efficient balance between computational cost and the effective spatial resolution of GRACE.
The resulting GRACE ΔTWS fields are physically consistent and suitable for comparison with land surface model outputs.

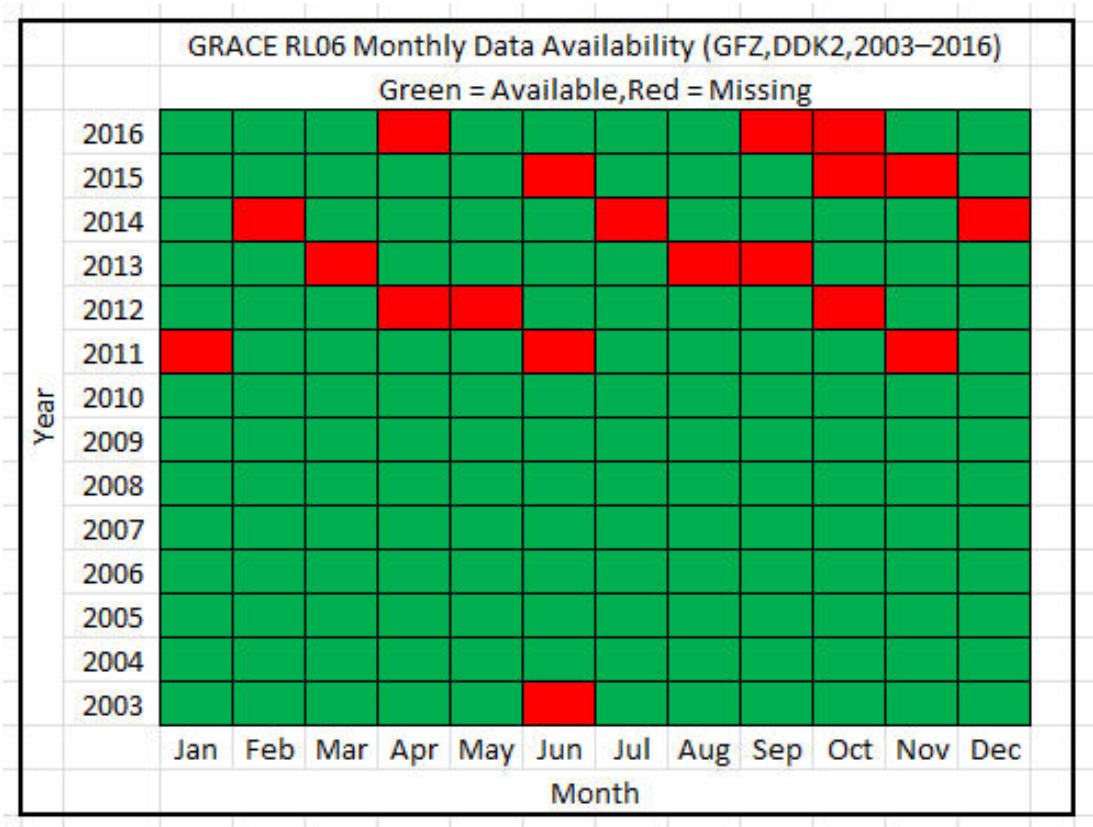

Figure 3.1: Monthly data availability for GRACE RL06 (GFZ, DDK2) from 2003-2016. Green cells indicate months with valid gravity field solutions, while red cells represent missing months without Level-2 data.

3.2 Spatial Domain: Amazon Basin

The analysis focuses on the central Amazon Basin. A regular grid with a spatial resolution of $0.25^\circ \times 0.25^\circ$ is defined over the region:

$$\text{Latitude: } -15^\circ \leq \phi \leq +15^\circ, \qquad \text{Longitude: } -85^\circ \leq \lambda \leq -35^\circ.$$

This spatial domain captures the hydrologically active central basin while remaining computationally efficient for spherical harmonic synthesis and GLDAS processing.
The Amazon Basin spans eight countries (Brazil, Peru, Colombia, Bolivia, Venezuela, Ecuador, Guyana, Suriname) and contains major sub-basins such as the Solimões, Madeira, Negro, Tapajós and Xingu. The basin exhibits strong wet–dry season contrasts driven by the Intertropical Convergence Zone (ITCZ), making it an ideal region for studying seasonal TWS variations with GRACE.

3.3 GLDAS Land Surface Model Data

To complement the GRACE observations, terrestrial water storage (TWS) estimates from the Global Land Data Assimilation System (GLDAS) were used. GLDAS combines observation-based meteorological forcing with land surface models to simulate key components of the terrestrial water cycle (Rodell et al., 2004).
In this study, the GLDAS Noah Land Surface Model version 2.1 monthly products were used. The data were obtained from the NASA Goddard Earth Sciences Data and Information Services Center (GES DISC) and provided in NetCDF format with a spatial resolution of $0.25^\circ \times 0.25^\circ$ and a monthly temporal resolution (Beaudoing and Rodell, 2020). The GLDAS data cover the period 2003-2016, consistent with the GRACE analysis period.
The following GLDAS hydrological components were extracted:

- **Soil moisture** ($\mathrm{kg\,m^{-2}}$) from four soil layers (0-10 cm, 10-40 cm, 40-100 cm and 100-200 cm),
- **Canopy water storage** ($\mathrm{kg\,m^{-2}}$),
- **Snow water equivalent** ($\mathrm{kg\,m^{-2}}$).

These components are summed up and were converted to equivalent water height as the GLDAS-based EWH storage estimates.
Before comparison with GRACE-derived TWS, the GLDAS data were preprocessed using the following steps:

- **Anomaly computation:** Long-term mean values over the study period were removed to obtain monthly TWS anomalies,
- **Spatial subsetting:** The data were masked to the Amazon Basin using a basin shapefile, and only land grid cells within the basin were retained.

GLDAS represents a “bottom-up” estimate of terrestrial water storage based on land surface processes, while GRACE provides an integrated “top-down” measure of total mass change. Comparing both datasets allows the assessment of the consistency between model-based hydrology and satellite-observed water storage variations.

4 Methodology

The methodology consists of four steps which are described briefly in the following.

4.1 Step 1: Building the Multi-Year Mean Gravity Field

The analysis begins by reading all available GRACE GFZ RL06 monthly gravity field solutions for the period 2003-2016. Each monthly solution consists of fully normalised spherical harmonic coefficients and their associated uncertainties. To ensure consistency across the entire time series, all coefficients are rescaled to a common reference system using a fixed geocentrical gravitational constant GM and reference radius R.
Following the approach proposed by Wahr et al. (1998), a multi-year mean gravity field is computed by averaging all monthly solutions. This mean model represents a reference state of the Earth’s gravity field and is later subtracted from each monthly solution to isolate temporal mass variations.

4.2 Step 2: Computing Monthly Residual Gravity Potentials

Monthly gravity anomalies are obtained by subtracting the mean model from each individual monthly solution. The resulting residual spherical harmonic coefficients represent time-variable gravity signals primarily caused by mass redistribution at the Earth's surface.
Using spherical harmonic synthesis, the residual gravitational potential is computed on a regular grid with a spatial resolution of $0.25^\circ \times 0.25^\circ$ over the Amazon Basin. This step converts the spectral representation into spatially continuous gravity anomaly maps. This grid is identical with the GLDAS grid.
In addition:

- Geoid undulations are computed as $\Delta N = V/\gamma(\phi)$, where $\gamma(\phi)$ is the normal gravity on the reference ellipsoid,
- Degree variances are analysed to identify the harmonic degrees that contain the dominant hydrological signal,
- Error Degree Variances are computed to assess how measurement noise propagates across spherical harmonic degrees.

4.3 Step 3: Converting Gravity Variations to Terrestrial Water Storage

To transform gravity anomalies into hydrological quantities, the residual coefficients are converted into surface mass variations using the load Love number formalism. Following the method of Wahr et al. (1998) and Swenson and Wahr (2006), the elastic response of the Earth to surface loading is accounted for by applying degree-dependent Love numbers.
The MATLAB routine `SHS_grid_TWS.mat` is used to generate monthly terrestrial water storage (TWS) anomaly grids in units of equivalent water height.
These diagnostics allow a clear separation between physically meaningful hydrological signals and noise-dominated spectral components.

4.4 Step 4: Statistical Time Series Analysis

For each monthly TWS anomaly map, standard statistical measures are computed, including minimum, maximum, mean, root-mean-square (RMS) and standard deviation. These values are stored to construct a continuous basin-scale TWS time series covering 2003-2016.
The resulting time series captures seasonal variability, interannual trends and extreme hydrological events such as droughts and wet periods in the Amazon Basin.

4.5 Step 5: Comparison with GLDAS-Based Water Storage Estimates

To evaluate the consistency between satellite-based and model-based hydrology, GRACE-derived TWS anomalies are compared with estimates from the GLDAS Noah land surface model. GLDAS provides a "bottom-up" representation of terrestrial water storage based on land surface processes.
The comparison involves the following steps:

1. Extraction of monthly GLDAS water storage components,
2. Conversion to anomalies by removing the long-term mean,
3. Grid selection to match the GRACE spatial resolution,
4. Visual and statistical comparison of spatial patterns and seasonal amplitudes.

This combined analysis highlights agreements and discrepancies between GRACE and GLDAS, particularly regarding groundwater contributions that are not explicitly represented in land surface models.

5 Results and Discussion

This section summarises the key findings from the analysis of GRACE-derived Total Water Storage (TWS) changes over the Amazon Basin, together with the corresponding hydrological components obtained from GLDAS, for the period 2003-2016. To maintain clarity and focus, only selected figures are presented here to illustrate the most relevant large-scale hydrological patterns and extreme events. Additional monthly comparisons are provided in the appendices: Appendix A presents a GRACE-GLDAS comparison for the 2009 flood and Appendix B for the 2010 drought, each using four representative months – January (wet season), April (flood peak), July (post-flood / dry season) and October (transition to the wet season) – to capture the seasonal evolution of basin-scale water storage and runoff processes.

5.1 GRACE-Derived Total Water Storage

The temporal development of TWS across the basin is summarized in Figure 5.1. The time series reveals a pronounced seasonal cycle, with peak water storage typically occurring in April-May and the lowest values in September-October. Well-known drought events in 2005, 2010 and 2015 are clearly reflected as sharp drops in TWS, while years such as 2009, 2012 and 2014 show notable positive anomalies associated with above-average rainfall and high-flow conditions.

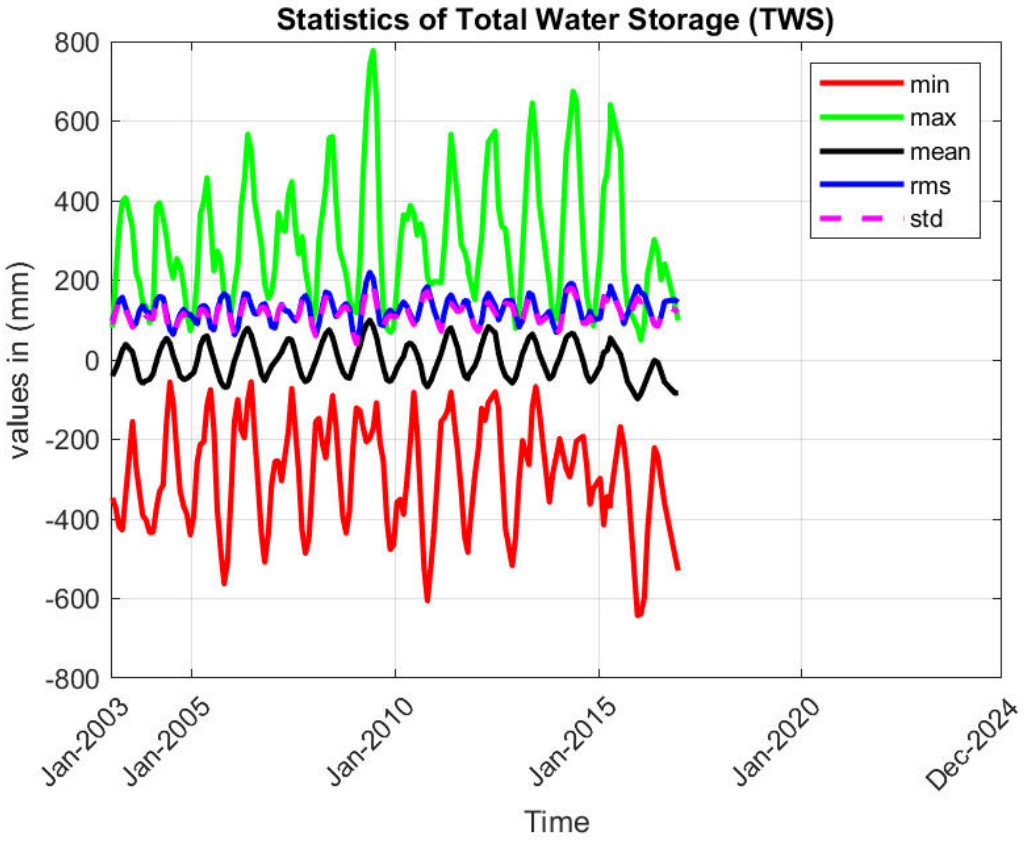

Figure 5.1: Basin-mean GRACE TWS statistics (minimum, maximum, mean, RMS and standard deviation) for 2003-2016.

To demonstrate how GRACE captures hydrological extremes, two contrasting months were selected. Figure 5.2 shows TWS anomaly maps for April 2009, representing a wet, high-water period and October 2010, which corresponds to a severe regional drought. April 2009 exhibits strong positive anomalies associated with widespread flooding, soil saturation and elevated river levels. In contrast, October 2010 displays pronounced negative anomalies linked to the major 2010 megadrought that affected much of central and southern Amazonia.

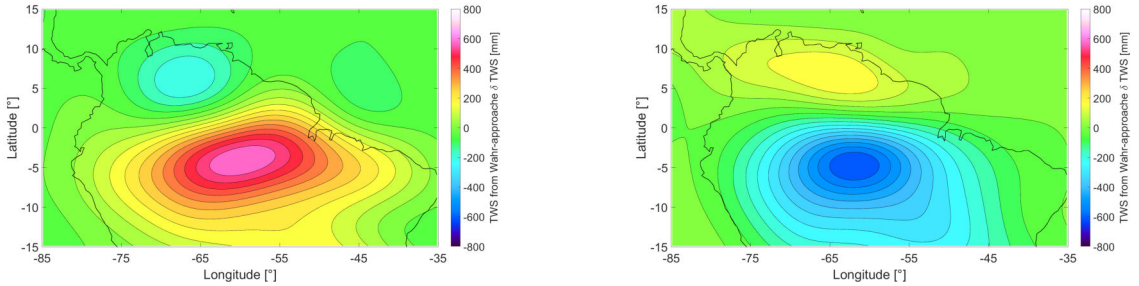

(a) April 2009 – Wet Season / High Water

(b) October 2010 – Severe Drought

Figure 5.2: Representative GRACE TWS anomalies illustrating contrasting hydrological extremes in the Amazon Basin.

To further investigate the interannual variability of basin-scale water storage, the following figures present GRACE-derived TWS anomalies for the months of April and October across all years of the study period (2003-2016). April represents the peak wet or flood season, while October captures the transition toward the wet season following the dry period. Showing these months consistently across years allows a direct comparison of extreme and typical hydrological conditions and highlights the variability and persistence of TWS anomalies under different climatic regimes.

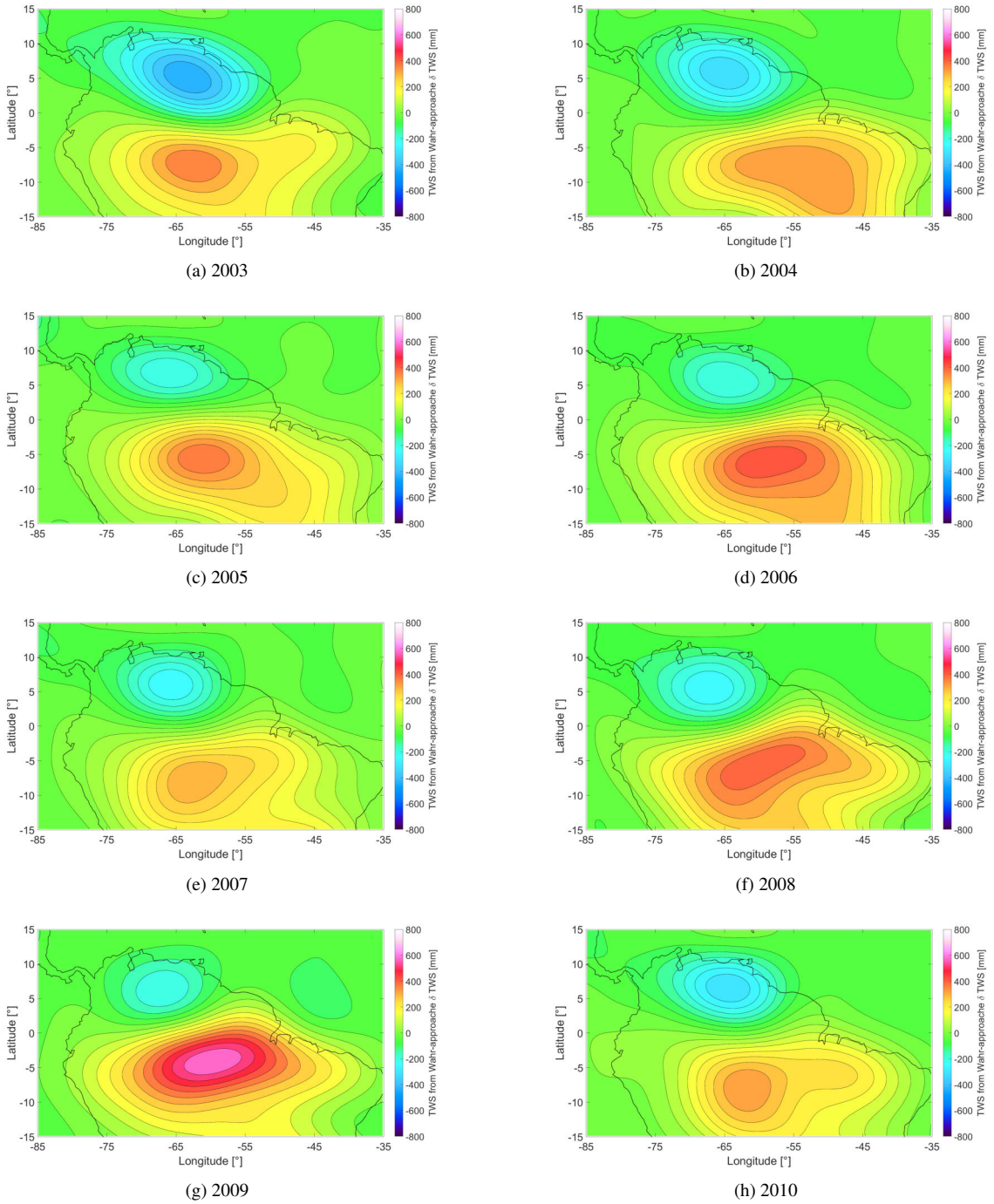

(a) 2003 (b) 2004

(c) 2005 (d) 2006

(e) 2007 (f) 2008

(g) 2009 (h) 2010

Figure 5.3: TWS anomalies in April.

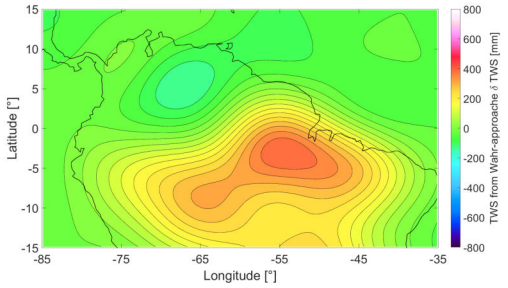

(a) 2011

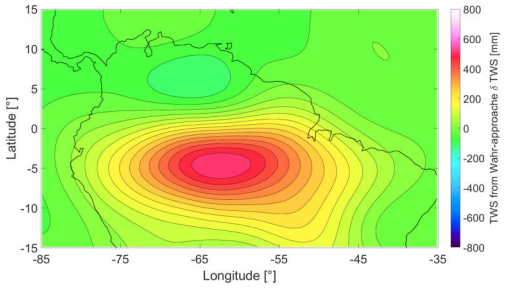

(b) 2012

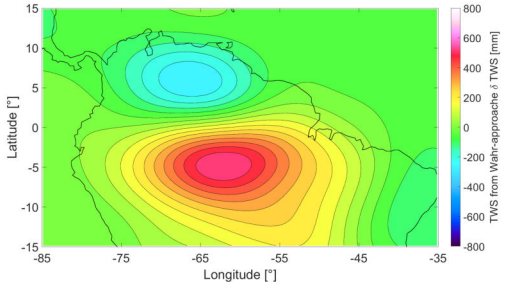

(c) 2013

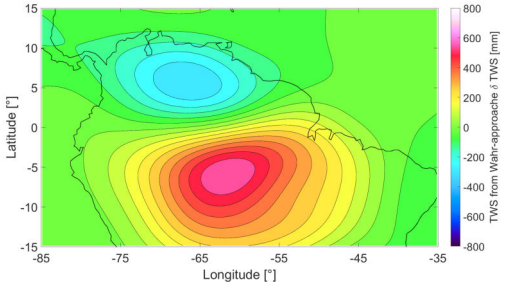

(d) 2014

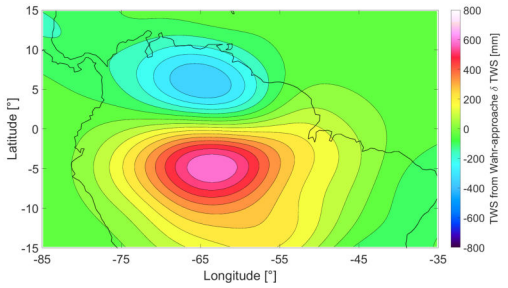

(e) 2015

(f) 2016 (missing)

Figure 5.4: TWS anomalies in April (continued).

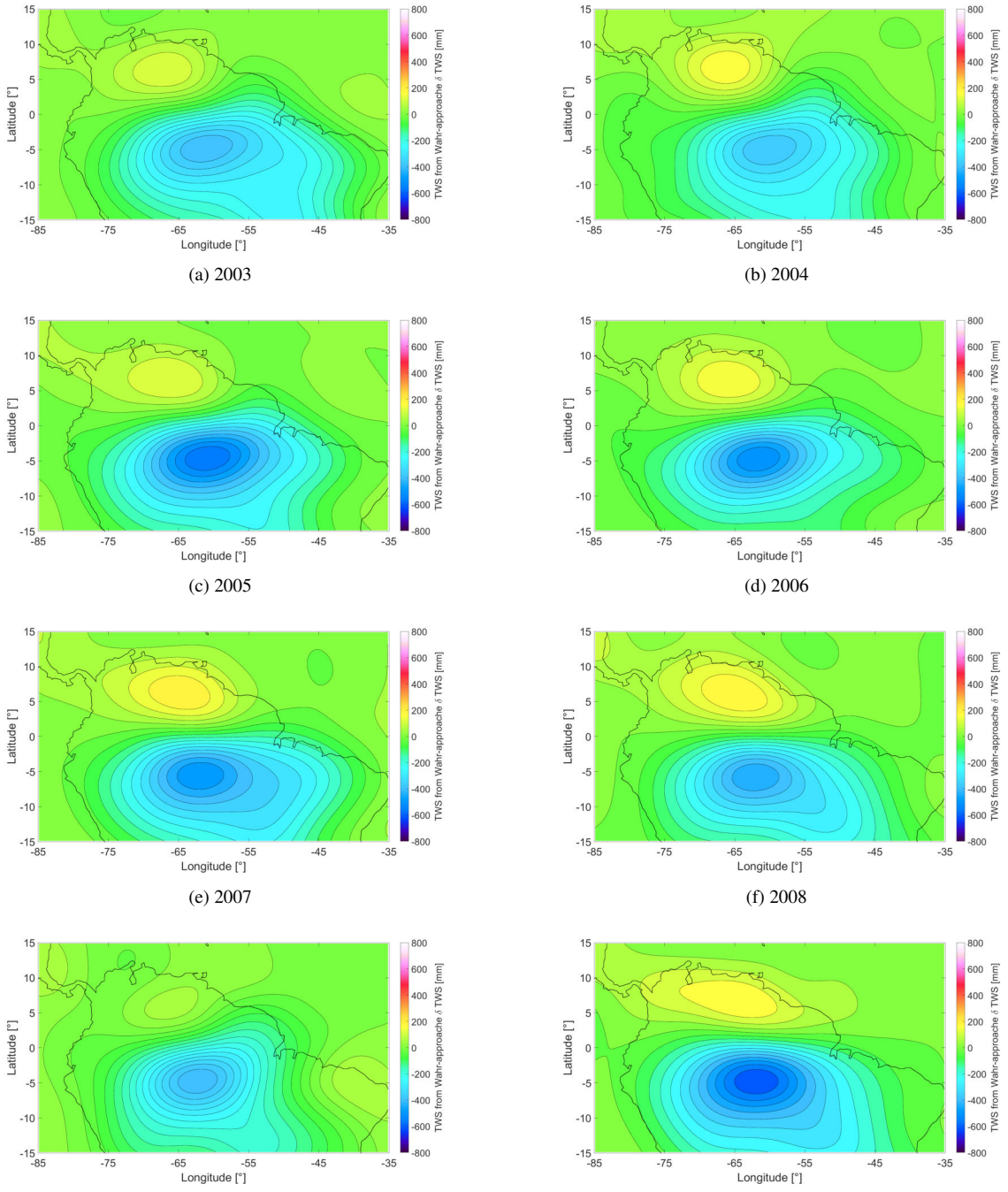

(a) 2003 (b) 2004

(c) 2005 (d) 2006

(e) 2007 (f) 2008

(g) 2009 (h) 2010

Figure 5.5: TWS anomalies in October.

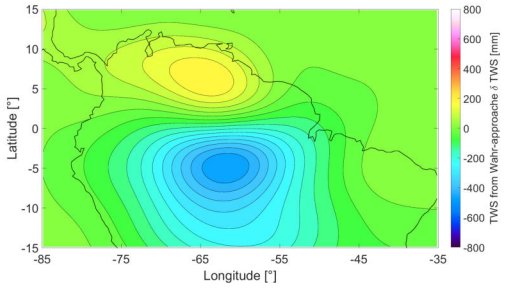

(a) 2011

(b) 2012 (missing)

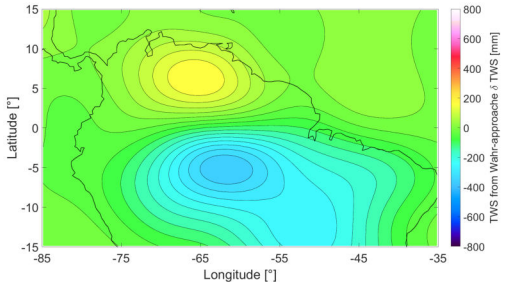

(c) 2013

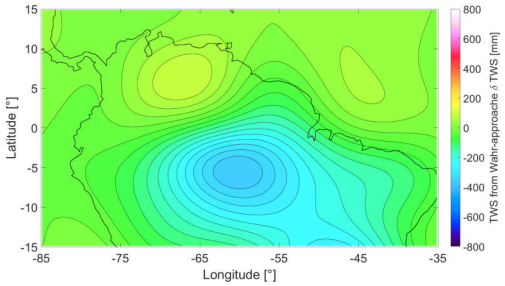

(d) 2014

(e) 2015 (missing)

(f) 2016 (missing)

Figure 5.6: TWS anomalies in October (continued).

5.2 GLDAS Hydrological Components

Figure 5.7 illustrates the multi-year mean terrestrial water storage (EWH) derived from GLDAS for the Amazon Basin. The spatial pattern shows persistently wet conditions across western and central Amazonia, where high soil moisture and continuous groundwater recharge dominate. In contrast, the southeastern parts of the basin appear noticeably drier, consistent with lower rainfall and reduced soil water retention.

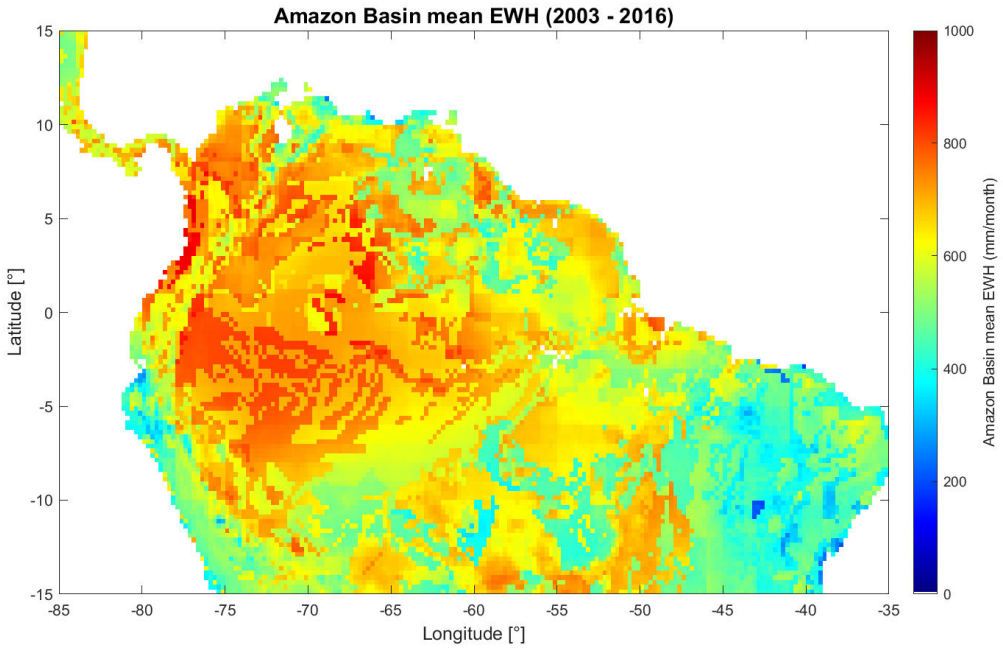

Figure 5.7: Multi-year mean GLDAS-derived terrestrial water storage (EWH) in the Amazon Basin for 2003-2016.

In Figure 5.7 the higher resolution of GLDAS data in the space domain compared to GRACE is visible.
To demonstrate how GLDAS responds to extreme dry conditions, Figure 5.8 presents the soil moisture and total runoff fields for October 2010. Soil moisture levels drop sharply across most of the region, in line with the severe drought detected by GRACE. Runoff values are also greatly reduced, approaching near-zero in many areas, which reflects the widespread depletion of both surface water and subsurface storage during this event.

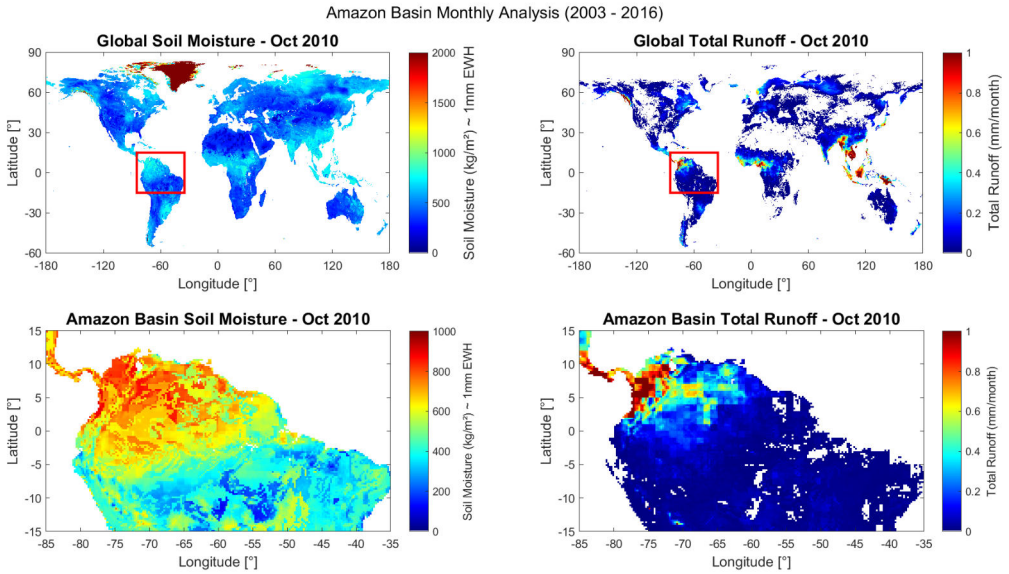

Figure 5.8: GLDAS soil moisture and total runoff during the October 2010 drought. Top: global soil moisture and global total runoff; bottom: Amazon Basin soil moisture and Amazon Basin total runoff. Pay attention to the different scales.

Under high-water conditions, GLDAS captures the expected increase in surface and subsurface runoff following intense rainfall events. Figure 5.9 shows the distribution of these runoff components for April 2009, a typical wet-season month. Subsurface runoff is particularly pronounced in central and western Amazonia, reflecting strong infiltration and deep soil moisture recharge during periods of heavy rainfall and flooding.

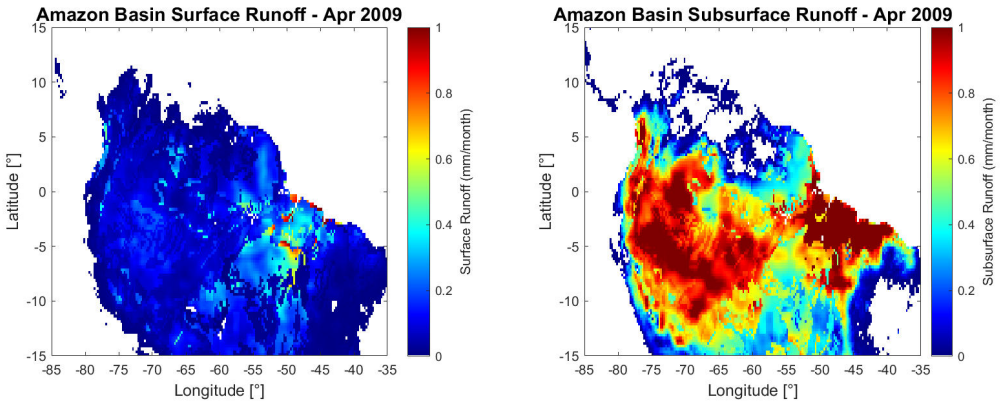

Figure 5.9: GLDAS surface runoff (left) and subsurface runoff (right) for April 2009, representing wet-season conditions and widespread flooding across the Amazon Basin.

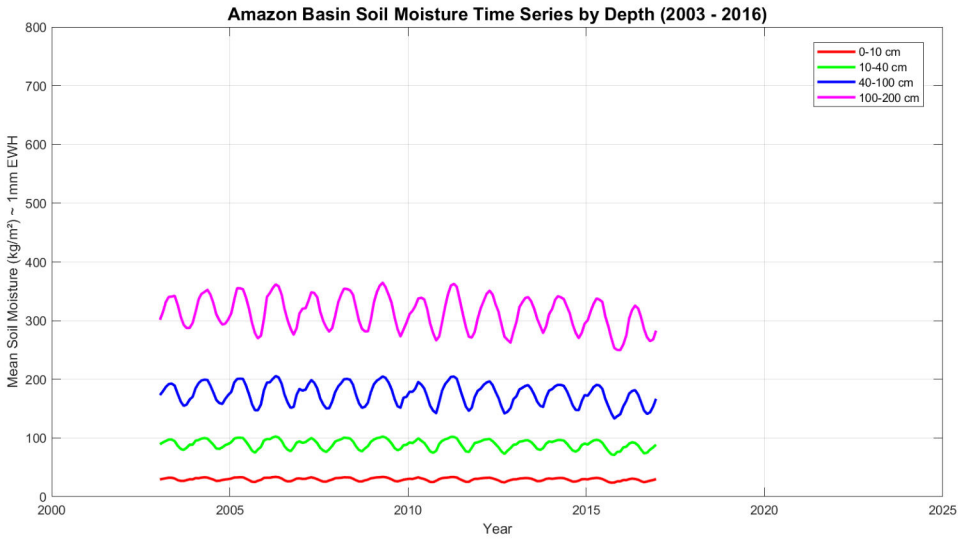

Figure 5.10: Time series of basin-mean GLDAS soil moisture at different depths (0-10, 10-40, 40-100 and 100-200 cm) for the Amazon Basin from 2003 to 2016. Deeper layers show smoother variations and delayed responses compared to shallow soil moisture, indicating longer storage memory.

Figure 5.10 shows the basin-mean GLDAS soil moisture time series for the Amazon Basin at four different depth layers (0-10 cm, 10-40 cm, 40-100 cm and 100-200 cm) during the period 2003-2016. The shallow soil layer (0-10 cm) exhibits strong and rapid seasonal fluctuations, reflecting its direct and immediate response to rainfall and evaporation. With increasing depth, the amplitude of the seasonal cycle increases and the variability becomes higher, indicating hydrological responses in deeper soil layers. The deepest layer (100-200 cm) shows the highest absolute soil moisture values and the strongest short-term variability, demonstrating its large storage capacity and long memory. During dry periods, reductions in shallow soil moisture occur first, while deeper layers respond more gradually, highlighting delayed drainage and sustained groundwater recharge. This depth-dependent behavior explains why GRACE observes prolonged total water storage anomalies during drought events, as deep soil moisture and groundwater contribute significantly to basin-scale water retention and recovery processes.

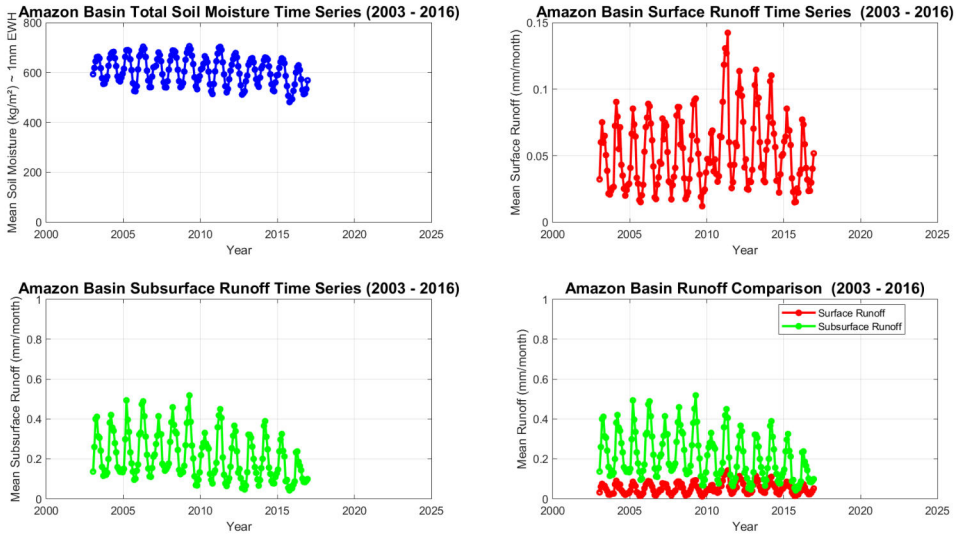

Figure 5.11: Time series of basin-mean GLDAS surface runoff and subsurface runoff for the Amazon Basin during 2003-2016. Subsurface runoff dominates the total runoff signal and shows strong reductions during drought periods.

Figure 5.11 shows the GLDAS-derived time series of total soil moisture, surface runoff and subsurface runoff for the Amazon Basin from 2003 to 2016, together with a direct comparison of runoff components. The total soil moisture exhibits a pronounced seasonal cycle, reflecting the strong wet-dry season contrast in the Amazon, with a slight long-term decline indicating progressive drying during major drought years. Surface runoff responds rapidly to rainfall variability and shows sharp seasonal peaks, but remains relatively low in magnitude, highlighting its short-lived nature. In contrast, subsurface runoff displays larger amplitudes and smoother variations, indicating delayed drainage from deeper soil layers and sustained groundwater contributions. The comparison panel clearly shows that subsurface runoff dominates the total runoff signal throughout the study period, emphasizing the importance of deep soil moisture and groundwater processes in regulating basin-scale hydrology. These results explain why GRACE detects long-lasting TWS anomalies, as deeper water storage components control the persistence and recovery of hydrological extremes such as droughts.

5.3 Comparison of GRACE TWS and GLDAS Soil Moisture and Runoff during the 2005 drought

The comparison between GRACE-derived total water storage (TWS) and GLDAS soil moisture and runoff for 2005 reveals a coherent picture of the evolution of the Amazon drought, while also highlighting fundamental differences between satellite-based and model-based hydrological estimates.

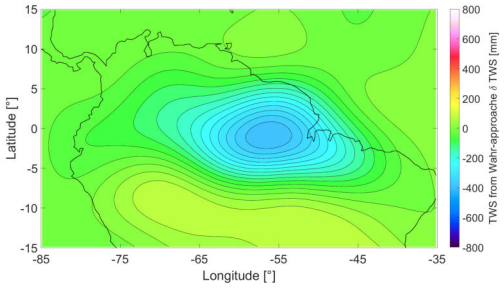

(a) GRACE TWS - January

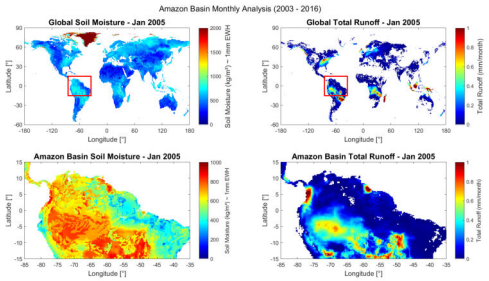

(b) GLDAS Soil Moisture & Runoff - January

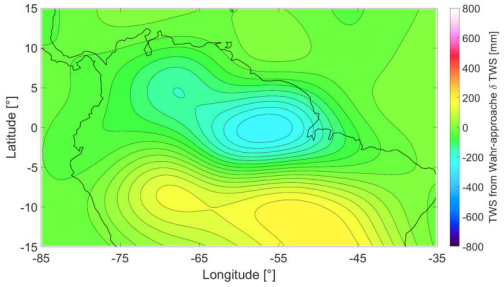

(c) GRACE TWS - February

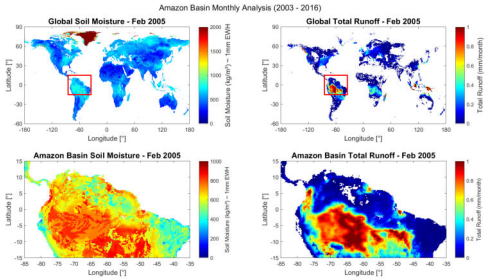

(d) GLDAS Soil Moisture & Runoff - February

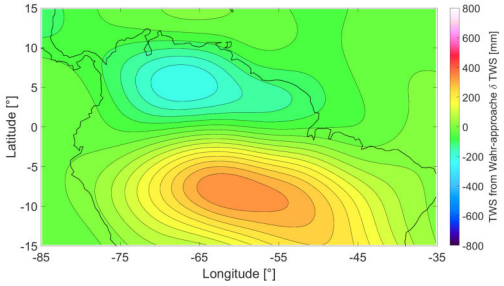

(e) GRACE TWS - March

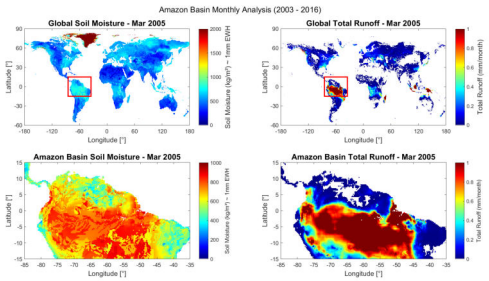

(f) GLDAS Soil Moisture & Runoff - March

Figure 5.12: Comparison of GRACE TWS and GLDAS Soil Moisture and Runoff for the 2005 Amazon Drought (Spring).

During the early months of the year 2005 (January-March, Figure 5.12), GRACE TWS shows slightly positive to near-neutral anomalies over large parts of the Amazon Basin, especially in the southwestern region. This indicates that the basin still retained water from the preceding wet season. In contrast, GLDAS soil moisture is already declining in several regions, while runoff remains generally low. This suggests that rainfall inputs were reduced, but stored water in deeper soil layers and groundwater was still sustaining basin-wide water storage.

From April to June shown in Figure 5.13, a clear transition toward drought conditions is observed. GRACE TWS anomalies decrease rapidly, marking the onset of basin-scale water loss. At the same time, GLDAS shows a strong reduction in soil moisture and a pronounced decrease in runoff, particularly subsurface runoff. This indicates progressive drying of the soil column and reduced drainage to the river system. The consistency in timing between decreasing GRACE TWS and declining GLDAS subsurface runoff confirms the early development of drought conditions.

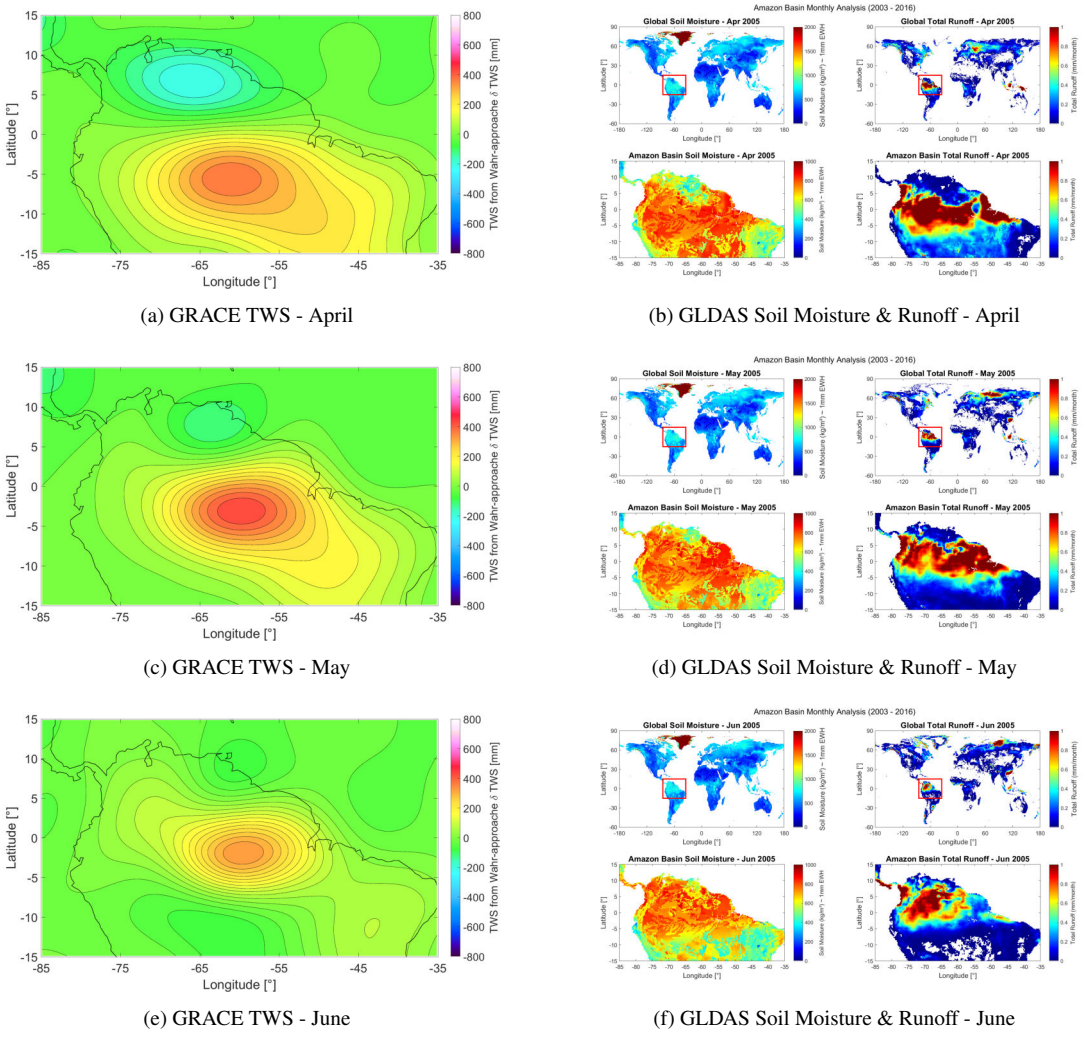

(a) GRACE TWS - April

(b) GLDAS Soil Moisture & Runoff - April

(c) GRACE TWS - May

(d) GLDAS Soil Moisture & Runoff - May

(e) GRACE TWS - June

(f) GLDAS Soil Moisture & Runoff - June

Figure 5.13: Comparison of GRACE TWS and GLDAS Soil Moisture and Runoff for the 2005 Amazon Drought (Summer).

The peak drought phase occurs between July and September as depicted in Figure 5.14. GRACE reveals strong negative TWS anomalies, reaching values of approximately -500 to -600 mm, indicating a substantial depletion of total water storage, including groundwater. GLDAS runoff is near zero across most of the basin during this period and soil moisture reaches its lowest levels. The spatial agreement between severe GRACE TWS deficits and suppressed GLDAS runoff highlights the extreme severity of the drought and the lack of effective recharge during this period.

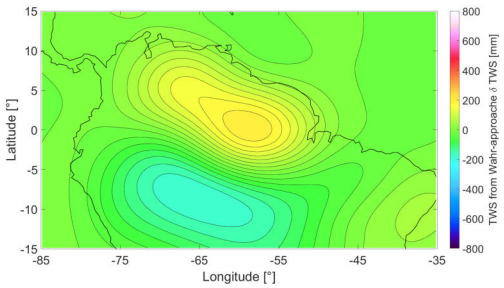

(a) GRACE TWS - July

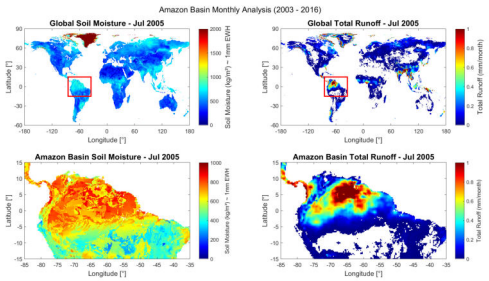

(b) GLDAS Soil Moisture & Runoff - July

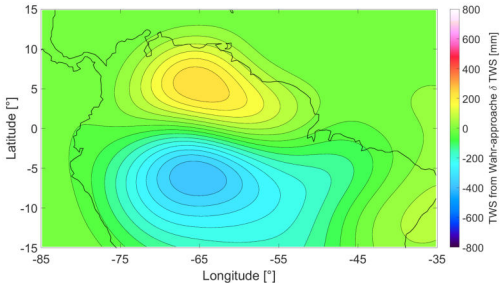

(c) GRACE TWS - August

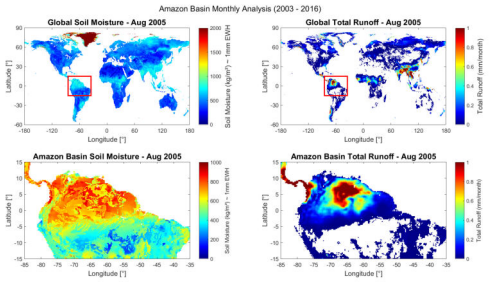

(d) GLDAS Soil Moisture & Runoff - August

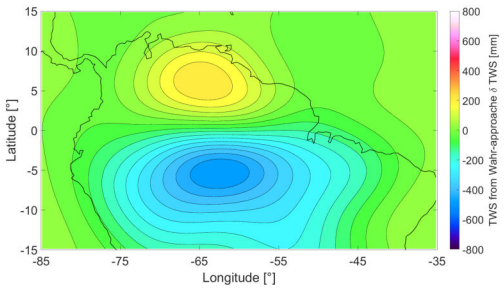

(e) GRACE TWS - September

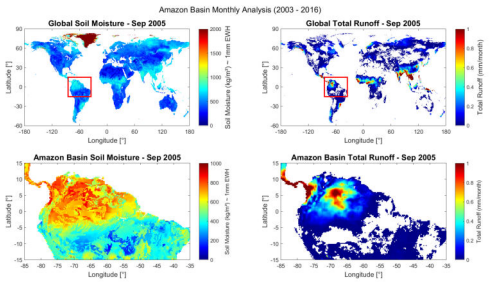

(f) GLDAS Soil Moisture & Runoff - September

Figure 5.14: Comparison of GRACE TWS and GLDAS Soil Moisture and Runoff for the 2005 Amazon Drought (Autumn).

Partial recovery is observed from October to December presented in Figure 5.15. GRACE indicates a gradual increase in TWS in the northern and central Amazon, although large negative anomalies persist in the southwest, reflecting delayed groundwater recovery. GLDAS soil moisture and runoff also show modest increases, consistent with the return of seasonal rainfall. However, runoff recovery is spatially limited, indicating that the hydrological system had not fully returned to normal conditions by the end of the year.

Overall, GRACE captures the integrated response of the hydrological system, including groundwater variations that are not explicitly represented in GLDAS. GLDAS, on the other hand, provides valuable insight into near-surface processes, such as soil moisture depletion and reduced runoff, which explain the physical drivers of the observed GRACE TWS changes. The combined use of GRACE and GLDAS therefore offers a comprehensive understanding of drought evolution, from rainfall deficits and soil drying to long-term groundwater depletion and delayed recovery.

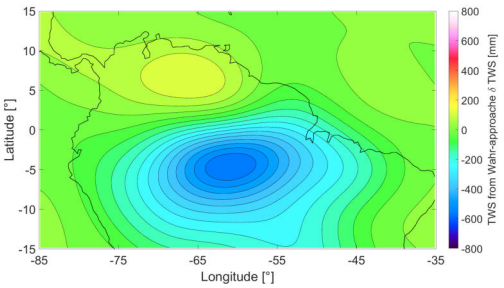

(a) GRACE TWS - October

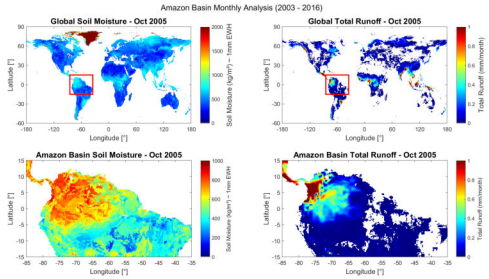

(b) GLDAS Soil Moisture & Runoff - October

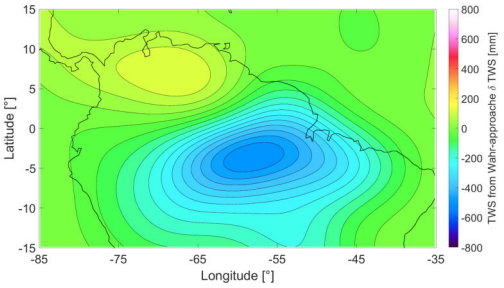

(c) GRACE TWS - November

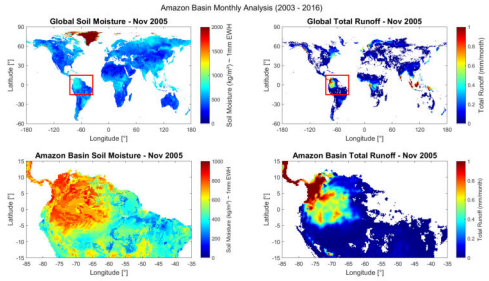

(d) GLDAS Soil Moisture & Runoff - November

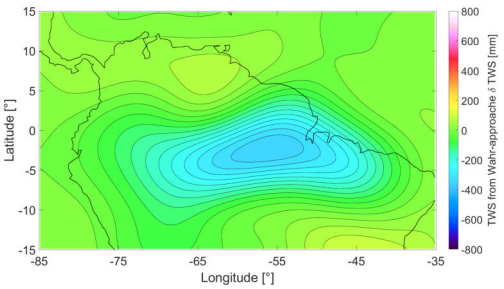

(e) GRACE TWS - December

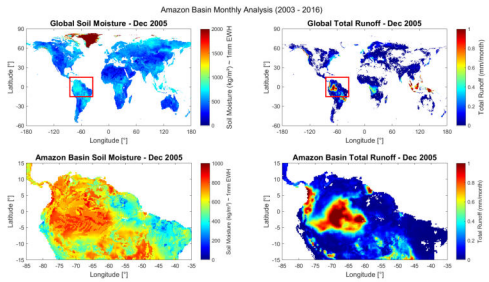

(f) GLDAS Soil Moisture & Runoff - December

Figure 5.15: Comparison of GRACE TWS and GLDAS Soil Moisture and Runoff for the 2005 Amazon Drought (Winter).

6 Conclusion

This study investigated terrestrial water storage (TWS) variability in the Amazon Basin from 2003 to 2016 using GRACE GFZ RL06 gravity field solutions and GLDAS Noah v2.1 land surface model outputs. By combining satellite gravimetry with model-based hydrological components, the analysis provides an integrated view of large-scale water storage changes and the underlying surface and subsurface processes controlling the Amazon hydrological cycle.

GRACE-derived TWS anomalies clearly capture the dominant seasonal cycle and major hydrological extremes, with pronounced storage maxima during the wet season and strong deficits during drought years such as 2005, 2010 and 2015. The 2005 drought, analysed in detail, is characterised by a rapid onset in late boreal spring, a peak water storage deficit during July-September, and a slow recovery toward the end of the year. The magnitude and persistence of the negative TWS anomalies observed by GRACE indicate substantial depletion of deep soil moisture and groundwater (Famiglietti et al., 2011), highlighting the long memory of subsurface water storage in the Amazon Basin.

GLDAS complements these findings by resolving individual hydrological components. Time-series analyses show that shallow soil moisture responds rapidly to rainfall variability, while deeper soil layers and subsurface runoff exhibit smoother variations and delayed responses. During drought periods, GLDAS indicates strong reductions in soil moisture and subsurface runoff, explaining the physical processes leading to declining GRACE TWS.

However, GLDAS-based TWS anomalies are consistently smaller than those observed by GRACE, reflecting the lack of an explicit groundwater storage component in the land surface model.
The comparison demonstrates that groundwater variations play a crucial role in regulating basin-scale water storage, particularly during prolonged droughts. GRACE is therefore essential for capturing the full magnitude of total water storage changes, while GLDAS is most effective for interpreting near-surface hydrological processes and runoff dynamics. Together, GRACE and GLDAS provide complementary and mutually reinforcing perspectives: a top-down observation of integrated mass change and a bottom-up representation of hydrological processes. Their combined use is indispensable for a comprehensive assessment of drought development, groundwater depletion and recovery mechanisms in the Amazon Basin.
Overall, GRACE and GLDAS offer complementary perspectives: GRACE provides a top-down observation of total water storage changes, while GLDAS helps to interpret the physical processes governing surface and near-surface hydrology. Future work could extend this analysis to additional drought and flood events, incorporate GRACE-FO observations and explore improved representations of groundwater storage in land surface models to enhance long-term hydrological assessments of the Amazon Basin.

Acknowledgement

The author wishes to extend his gratitude to Prof. Dr.-Ing. Hansjörg Kutterer, for the Lab Rotation opportunity. Gratitude is also owed to the supervisor, Dr.-Ing. Kurt Seitz, for his valuable guidance and support throughout Lab rotation. His constructive feedback has helped shape the outcome of this study. The author acknowledges the support from Geodätisches Institut (GIK) for providing necessary resources and facilities. Additionally, the author acknowledges ICGEM (GFZ German Research Centre for Geosciences, 2025) and GLDAS (operated by NASA Goddard Space Flight Center) for the data provided for this study.

References

Beaudoing, H. and Rodell, M. (2020): GLDAS Noah Land Surface Model L4 Monthly 0.25 x 0.25 degree V2.1. Dataset. DOI: 10.5067/SXAVCZFAQLNO.

Famiglietti, J. S., Lo, M., Ho, S. L., Bethune, J., Anderson, K. J., Syed, T. H., Swenson, S. C., de Linage, C., and Rodell, M. (2011): Satellites measure recent rates of groundwater depletion in California's Central Valley. *Geophysical Research Letters* 38(3). DOI: 10.1029/2010GL046442.

Kusche, J., Schmidt, R., Petrovic, S., and Rietbroek, R. (2009): Decorrelated GRACE time-variable gravity solutions by GFZ, and their validation using a hydrological model. *Journal of Geodesy* 83:903–913. DOI: 10.1007/s00190-009-0308-3.

Landerer, F. W. and Swenson, S. C. (2012): Accuracy of scaled GRACE terrestrial water storage estimates. *Water Resources Research* 48(4). DOI: 10.1029/2011WR011453.

Rodell, M., Houser, P. R., Jambor, U., Gottschalck, J., Mitchell, K. E., Meng, C.-J., Arsenault, K., Cosgrove, B. A., Radakovich, J. D., Bosilovich, M. G., Entin, J. K., Walker, J. P., Lohmann, D., and Toll, D. L. (2004): The Global Land Data Assimilation System. *Bulletin of the American Meteorological Society* 85(3):381–394. DOI: 10.1175/BAMS-85-3-381.

Swenson, S. and Wahr, J. (2006): Post-processing removal of correlated errors in GRACE data. *Geophysical Research Letters* 33(8):L08402. DOI: 10.1029/2005GL025285.

Tapley, B. D., Bettadpur, S., Watkins, M., and Reigber, C. (2004): The gravity recovery and climate experiment: Mission overview and early results. *Geophysical Research Letters* 31(9):1–4. DOI: 10.1029/2004GL019920.

Tucker, E. S., Nerem, R. S., and Loomis, B. D. (2022): Simulation of a Future SLR Satellite to Improve Low-Degree Gravity Estimates. *Journal of Geophysical Research: Solid Earth* 127(12):e2022JB025743. DOI: https://doi.org/10.1029/2022JB025743.

Wahr, J., Molenaar, M., and Bryan, F. (1998): Time variability of the Earth's gravity field: Hydrological and oceanic effects and their possible detection using GRACE. *Journal of Geophysical Research: Solid Earth* 103(B12):30205–30229.

Appendix

Appendix A: GRACE–GLDAS Comparison During the 2009 Flood

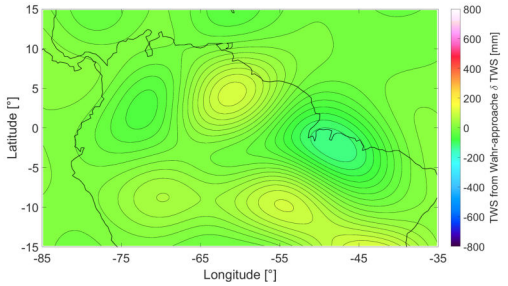

(a) GRACE TWS – January 2009 (Winter)

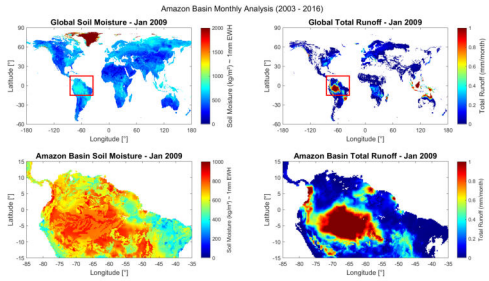

(b) GLDAS Runoff – January 2009

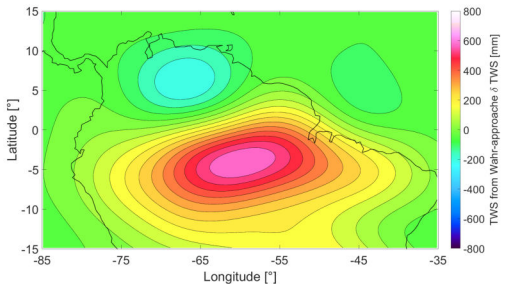

(c) GRACE TWS – April 2009 (Flood peak)

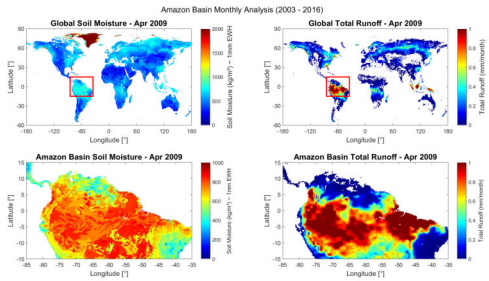

(d) GLDAS Runoff – April 2009

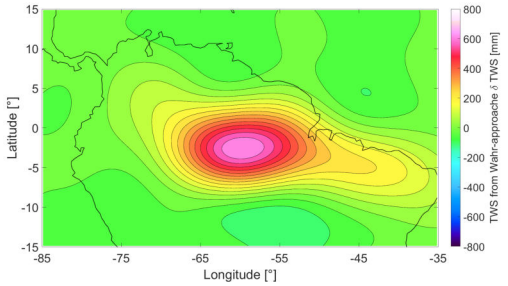

(e) GRACE TWS – July 2009 (Post-flood)

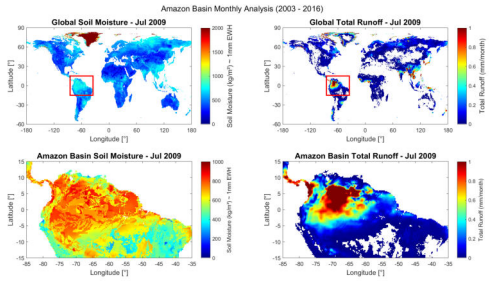

(f) GLDAS Runoff – July 2009

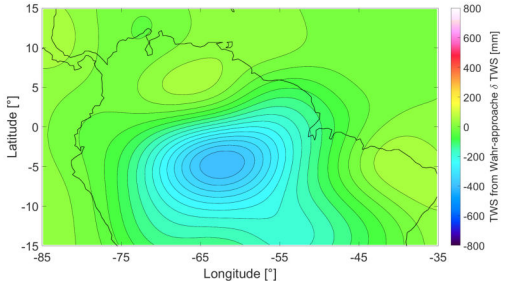

(g) GRACE TWS – October 2009 (Transition)

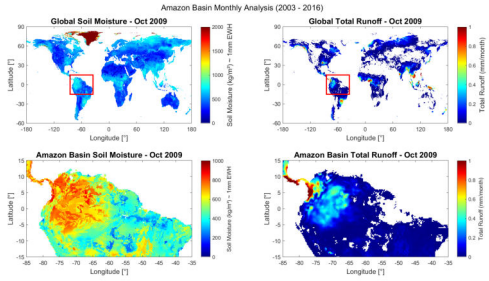

(h) GLDAS Runoff – October 2009

Figure .1: Seasonal comparison of GRACE total water storage (left) and GLDAS runoff (right) during the 2009 Amazon flood. GRACE captures basin-wide water storage accumulation, while GLDAS highlights enhanced surface and subsurface runoff associated with extreme wet conditions.

Appendix B: GRACE–GLDAS Comparison During the 2010 Drought

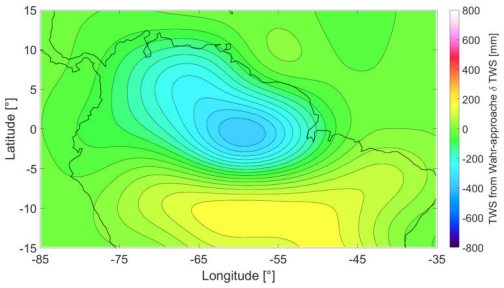

(a) GRACE TWS – January 2010 (Pre-drought)

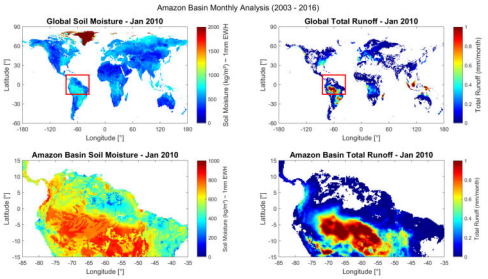

(b) GLDAS Soil Moisture & Runoff – January 2010

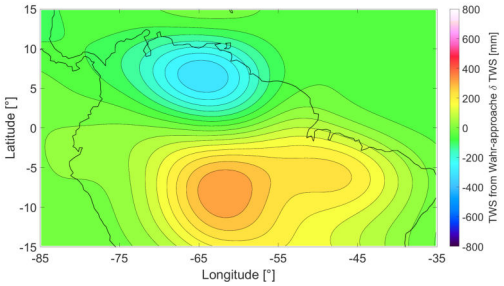

(c) GRACE TWS – April 2010 (Drought onset)

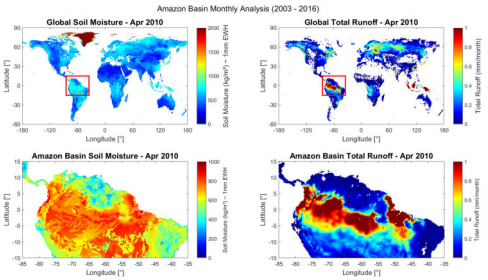

(d) GLDAS Soil Moisture & Runoff – April 2010

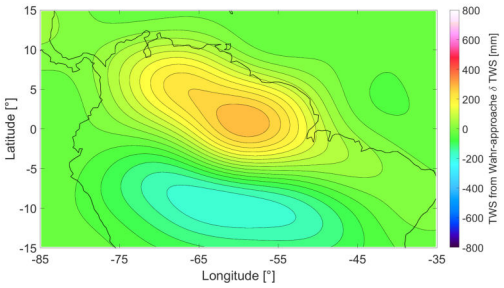

(e) GRACE TWS – July 2010 (Peak drought)

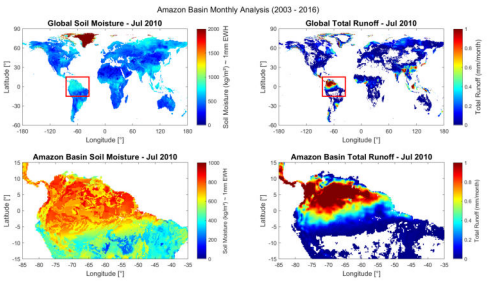

(f) GLDAS Soil Moisture & Runoff – July 2010

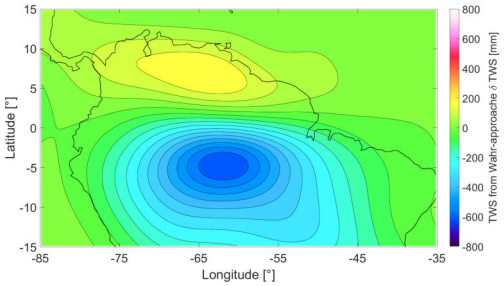

(g) GRACE TWS – October 2010 (Recovery phase)

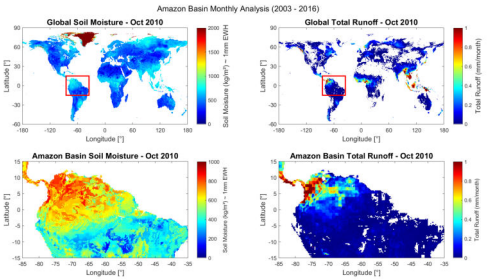

(h) GLDAS Soil Moisture & Runoff – October 2010

Figure .1: Seasonal comparison of GRACE total water storage (left) and GLDAS hydrological variables (right) during the 2010 Amazon drought. GRACE highlights persistent basin-scale water deficits, while GLDAS illustrates rapid soil moisture depletion and suppressed runoff, reflecting drought-driven reductions in rainfall and recharge.

Assessing Loading Effects and Signal Leakage in GRACE-based TWS Estimation over the Amazon Basin (2003-2016)

Unni Udayan[1]

1 Remote Sensing and Geoinformatics Master of Science (M.Sc.), KIT, Germany
E-Mail: utzwc@student.kit.edu

Abstract

This study examined the effects of loading and signal leakage on GRACE-derived terrestrial water storage (TWS) over the Amazon basin for 2003–2016. The goal was to understand how processing choices influenced the magnitude and interpretation of TWS variations. Analysis of loading effects showed that the inclusion of Load Love Numbers ($LLN = 1$) increased TWS amplitudes relative to the rigid Earth case ($LLN = 0$), consistently across time series and spatial maps, while seasonal patterns and spatial distribution were largely unchanged. It was concluded that loading correction mainly modulates signal strength rather than pattern, with Earth deformation due to surface mass changes contributing additional signals that amplified both positive and negative TWS anomalies.

Leakage analysis highlighted the impact of filtering on GRACE data. The DDK2 filter reduced noise but also smoothed part of the original signal, decreasing TWS amplitudes. Scaling factors were applied to effectively compensate for this loss, resulting in significantly larger and more detailed TWS anomalies after scaling, while overall spatial patterns and temporal behavior were preserved. It was shown that leakage correction primarily restored signal strength without introducing artificial changes.

Spatial analyses corroborated these findings for both wet and dry seasons: loading correction and scaling factors were applied to increase TWS anomaly amplitudes, while the general signal structure was preserved. Robustness across years and hydrological conditions was demonstrated.

Overall, loading effects and leakage corrections were found to be essential for accurate interpretation of GRACE-derived water storage. The Earth's elastic response was accounted for by loading correction, and signal loss due to filtering was addressed by scaling factors. It was indicated that ignoring these effects could lead to underestimation of TWS variations and misinterpretation due to aliasing from unresolved high-frequency signals.

In conclusion, a careful combination of loading correction and leakage correction provided a more realistic representation of hydrological changes in the Amazon basin, improving the reliability of GRACE-based studies. Vertical land motion, including Glacial Isostatic Adjustment (GIA), should be considered in future work as it can influence GRACE-based TWS estimates.

Keywords GRACE · GLDAS · Total Water Storage (TWS) · Amazon Basin · Load Love Numbers · Leakage · Scaling Factors

KIT Scientific Working Papers
Issue Number 270
ISSN: 2194-1629
DOI: 10.5445/IR/1000191188
Online: June 2026

This document is licensed under the Creative Commons Attribution – Share Alike 4.0 International License (CC BY-SA 4.0):
https://creativecommons.org/licenses/by-sa/4.0/deed.en

1 Introduction

The Gravity Recovery and Climate Experiment (GRACE) mission has significantly improved our understanding of temporal variations in the Earth's mass distribution. By measuring changes in the distance between two satellites, GRACE provides observations of the Earth's gravity field, which can be interpreted in terms of mass redistribution processes such as terrestrial water storage (TWS), ice mass change or ocean dynamics.

One of the key applications of GRACE data is the estimation of terrestrial water storage changes, commonly expressed as Equivalent Water Height (EWH). However, the interpretation of GRACE-derived signals is not straightforward due to several physical and processing-related effects. Surface mass variations cause elastic deformation of the Earth, known as loading effects, which influence the observed gravity signal. In addition, spatial filtering applied to reduce noise in spherical harmonic solutions introduces signal leakage, leading to attenuation and spreading of the signal across neighboring regions.

This study focuses on the Amazon basin, a region characterized by strong hydrological variability, over the period 2003–2016. The basin is particularly suitable for GRACE-based analysis due to its large water storage changes associated with seasonal cycles, droughts and flood events. Such events have been well documented in previous studies, making the region ideal for analysing large-scale hydrological variations (Tapley et al., 2004; Chen et al., 2010).

To address the challenges in GRACE data interpretation, this study is divided into two main parts. The first part focuses on assessing loading effects using different applications of Load Love Numbers (LLNs), which describe the Earth's elastic response to surface loading (Farrell, 1972). The second part investigates leakage correction using scaling factors derived from hydrological models, following the approach of Landerer and Swenson 2012.

The objective of this work is to analyze how loading effects and leakage corrections influence GRACE-derived TWS estimates and to evaluate their impact on the magnitude, variability and spatial representation of water storage changes.

2 Theoretical Aspects

In this section, the basic theoretical aspects necessary for this study are given.

2.1 GRACE gravity field observations

From the GRACE observations, the temporal variations in Earth's gravity field can be derived in terms of monthly SH models. Variations in the Earth's gravity field caused by mass redistribution lead to small changes in the distance between the satellites. These variations are measured very precisely and used to estimate monthly gravity field models (Tapley et al., 2004). Figure 2.1 illustrates the basic concept of the GRACE mission.

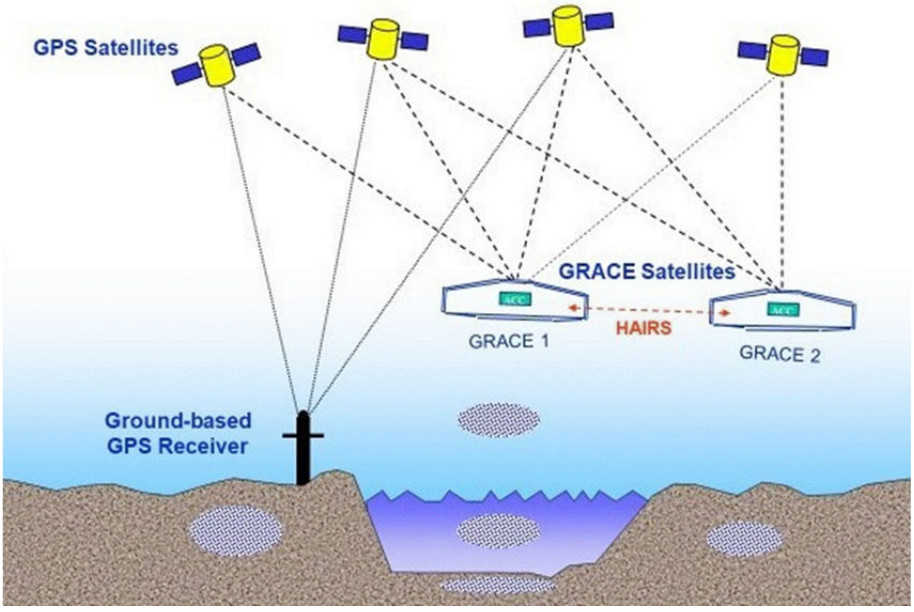

Figure 2.1: Concept of the GRACE satellite mission measuring temporal variations in Earth's gravity field through changes in the distance between two satellites. (Flechtner et al., 2014; Chen et al., 2022)

The Earth's gravitational potential can be described using a spherical harmonic expansion (Heiskanen and Moritz, 1967), which represents the gravity field in theorthonormal basis of the Laplace spherical harmonics with different spatial wavelengths. It can be written as

$$V(\lambda,\phi,r) = \frac{GM}{r}\sum_{n=0}^{n_{\max}}\left(\frac{a}{r}\right)^n \sum_{m=0}^{n} \bar{P}_{nm}(\sin\phi)\left(\bar{C}_{nm}\cos m\lambda + \bar{S}_{nm}\sin m\lambda\right), \tag{2.1}$$

where $\bar{C}_{nm}$ and $\bar{S}_{nm}$ are the fully normalised spherical harmonic coefficients, $\bar{P}_{nm}$ are the fully normalised associated Legendre functions, GM is the Earth's gravitational constant, a is the reference Earth radius and (r,ϕ,λ) are the geocentric spherical coordinates.
Temporal changes in these coefficients correspond to changes in the distribution of mass within the Earth system. By analyzing these variations over time, it is possible to study large-scale processes such as hydrological cycles, ice mass changes and ocean mass variations.

2.2 Conversion from gravity change to water storage

To obtain terrestrial water storage anomalies from GRACE gravity data, the spherical harmonic coefficients must be converted into surface mass variations. This conversion is based on the relationship between gravity changes and mass redistribution (Wahr et al., 1998).
In practice, the gravity variations are transformed into equivalent water height (EWH), which represents the thickness of a water layer that would produce the observed gravity signal. In simplified form, the surface mass anomaly can be expressed as

$$\Delta\sigma(\theta,\lambda) = \frac{a\,\rho_{\text{ave}}}{3\,\rho_w}\sum_{n=2}^{\infty}\frac{(2n+1)}{1+k_n}\sum_{m=0}^{n}\left(\Delta\bar{C}_{nm}\cos m\lambda + \Delta\bar{S}_{nm}\sin m\lambda\right)\bar{P}_{nm}(\sin\phi), \tag{2.2}$$

where a is the Earth radius, ρ_{ave} is the mean Earth density and ρ_w is the density of water. Here, k_n denotes the Load Love Number of degree n, which accounts for the elastic deformation of the Earth due to surface mass loading. The residual terms $\Delta\bar{C}_{nm}$ and $\Delta\bar{S}_{nm}$ represent the temporal variations of the gravitational potential. The summations starts with $n = 2$, because the central term cancels out, and the degree $n = 2$ coefficients are set to zero in the ICGEM (2026) datasets.

This formulation converts gravity variations into equivalent water height anomalies representing terrestrial water storage.

2.3 Load Love Numbers and Earth deformation

When mass accumulates on the Earth's surface, the solid Earth (Lithosphere) responds elastically to the applied load. This response includes both vertical deformation of the crust and changes in the gravitational potential. These effects modify the gravity field observed by satellites.

The Earth's elastic response is described by Load Love Numbers, which quantify how the Earth deforms in response to surface loading. Load Love Numbers are degree-dependent parameters that describe the Earth's elastic response to surface loading and are typically provided as tabulated values, commonly taken from Farrell (1972). When converting GRACE gravity variations to surface mass changes, these Love numbers must be included to separate the contribution of actual mass change from the deformation effect. Earth's Lithosphere responds elastically to surface mass redistribution such as water accumulation or ice loading. When additional mass is applied to the surface, the lithosphere subsides beneath the load and surrounding regions experience horizontal displacement toward the load center. Conversely, when mass is removed, the crust rebounds and horizontal motion occurs away from the unloading region. Figure 2.2 illustrates this elastic response of the Earth to loading and unloading processes.

This elastic response of the Earth is described using Load Love Numbers (Farrell, 1972).

When Load Love Numbers are considered, the conversion from gravity variations to surface mass anomalies becomes

$$\Delta\sigma^C = \frac{a\rho_{\text{ave}}}{3\rho_w}\frac{(2n+1)}{1+k_n}\Delta\bar{C}_{nm}\,, \qquad \Delta\sigma^S = \frac{a\rho_{\text{ave}}}{3\rho_w}\frac{(2n+1)}{1+k_n}\Delta\bar{S}_{nm}\,, \tag{2.3}$$

where k_n is the Load Love Number of degree n.

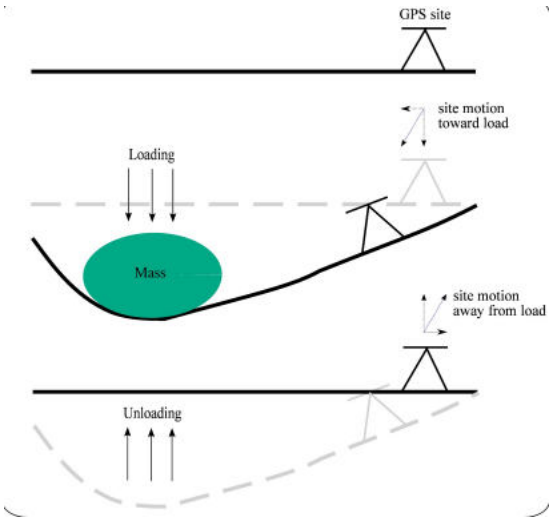

Figure 2.2: Conceptual illustration of elastic loading and unloading of the Earth's crust caused by surface mass redistribution. Surface mass loading produces elastic deformation of the Earth's surface, resulting in subsidence and horizontal motion toward the load, while unloading leads to crustal uplift and motion away from the load. This deformation contributes to gravity variations observed by GRACE satellites. (van Dam, 2017)

In this study, three different configurations are used to evaluate the impact of Load Love Numbers.

The constant scaling term (pre-factor in Equation (2.3)) is defined as

$$\frac{a\rho_{\text{ave}}}{3\rho_w},$$

where a is the mean Earth radius, ρ_{ave} is the average Earth density, and ρ_w is the density of water.

Case 1: No loading correction ($LLN = 0$). The Earth's elastic response is ignored. In the MATLAB implementation, the scale factor is written as

$$Cnm2Dnm(n) = \frac{a\rho_{\text{ave}}}{3\rho_w}(2n+1). \tag{2.4}$$

This equation represents the rigid Earth assumption, where the Earth's deformation is neglected. The term $(2n+1)$ is a degree-dependent scaling factor that arises from the spherical harmonic representation of the Earth's gravity field. It controls how much each harmonic degree contributes to the total signal. Lower degrees represent large-scale variations, while higher degrees represent smaller spatial features, which are amplified by the factor $(2n+1)$.

Case 2: Full loading correction ($LLN = 1$). The Earth's elastic response is included through the Load Love Numbers:

$$Cnm2Dnm(n) = \frac{a\rho_{\text{ave}}}{3\rho_w}\frac{(2n+1)}{1+k_n}. \tag{2.5}$$

Here, k_n represents the Load Love Number of degree n, accounting for the Earth's elastic response to surface mass loading. The factor $(1+k_n)$ modifies the scaling to include deformation effects in addition to the direct mass effect, resulting in a more realistic representation of terrestrial water storage variations.

Case 3: Deformation component ($LLN = 2$). This case represents the isolated contribution of the elastic deformation component, obtained as the difference between the rigid Earth and the loading-corrected cases:

$$Cnm2Dnm(n) = \frac{a\rho_{\text{ave}}}{3\rho_w}(2n+1)\left(\frac{-k_n}{1+k_n}\right). \tag{2.6}$$

This formulation highlights the portion of the signal that arises solely from the Earth's elastic deformation. It quantifies how the inclusion of Load Love Numbers modifies the scaling relative to the rigid Earth assumption.

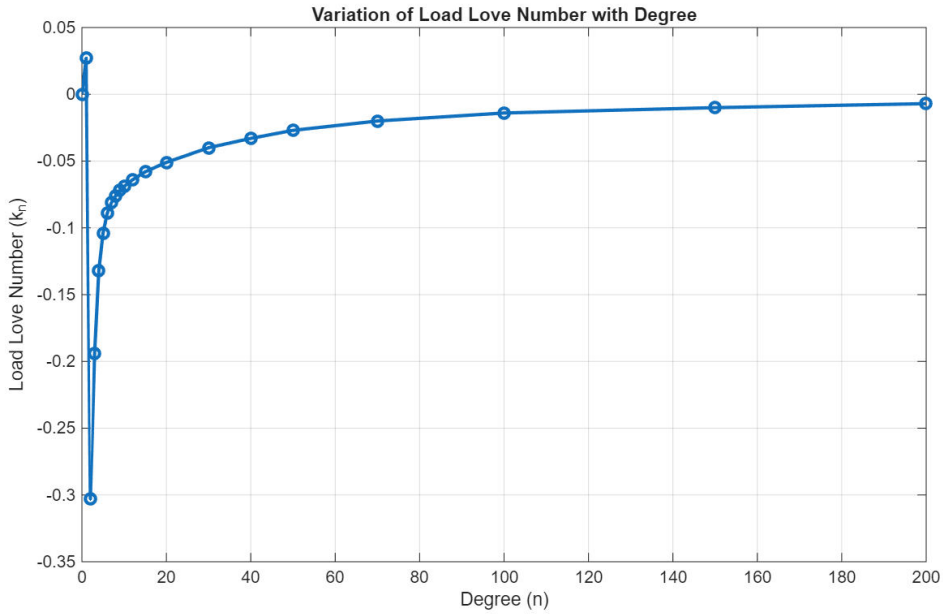

Figure 2.3: Variation of Load Love Number k_n with spherical harmonic degree. The values decrease with increasing degree, indicating that Earth's elastic response is stronger at large spatial scales and weaker at smaller spatial scales (Farrell, 1972).

Figure 2.3 shows the variation of the Load Love Number k_n with spherical harmonic degree. The values decrease with increasing degree and approach zero, indicating that Earth's elastic response is stronger at larger spatial scales and weaker at smaller spatial scales. The negative values of k_n are consistent with the formulation given by Farrell (1972) and reflect the fact that Earth's deformation reduces the gravitational potential associated with surface mass loading.

2.4 Signal leakage in GRACE data

GRACE gravity solutions have a limited spatial resolution of approximately 200–300 km. In addition, filtering techniques are applied to reduce correlated errors in the spherical harmonic coefficients. These filters suppress noise but also smooth the gravity signal.

As a result, signals from one region may spread into neighboring regions. This effect is known as signal leakage and leads to two main problems: the amplitude of the original signal becomes smaller and the spatial distribution of the signal becomes blurred (Swenson and Wahr, 2006).

Leakage effects are particularly important when analyzing hydrological basins or coastal regions, where signals from surrounding areas may influence the estimated water storage changes within the basin.

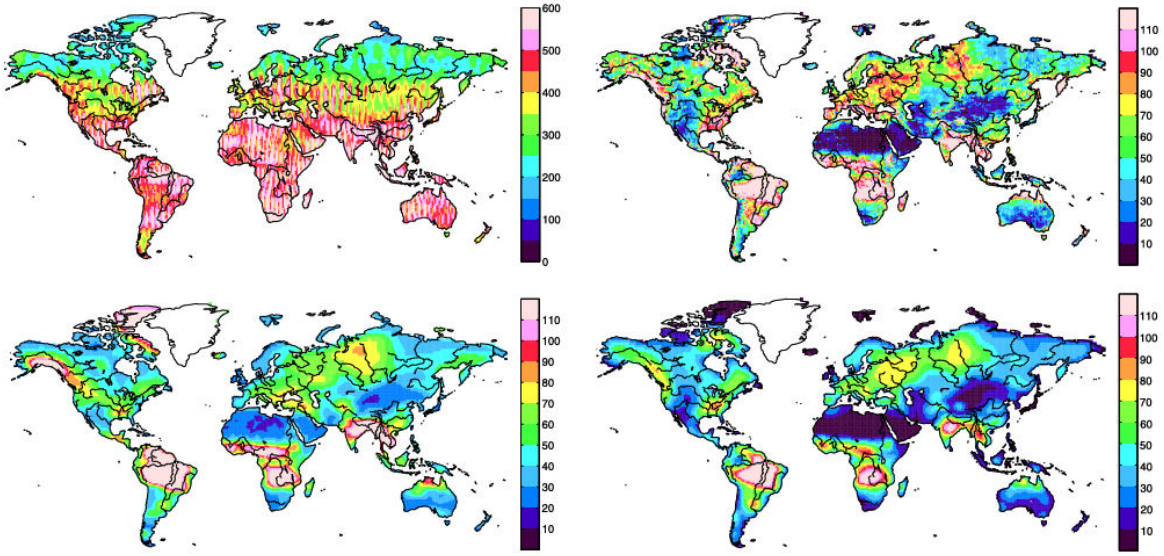

Figure 2.4: Root-mean-square variability of observed (left column: GRACE CSR-RL04) and simulated (right column: GLDAS-NOAH) terrestrial water storage: (top row) unfiltered GRACE TWS and GLDAS-NOAH TWS at $1^\circ \times 1^\circ$ resolution; (bottom row) spectrally truncated at degree and order 60, de-striped after (Swenson and Wahr, 2006), and smoothed with a Gaussian of 300 km width. Note the different color range for the unfiltered GRACE data. Units: mm–H_2O (Landerer and Swenson, 2012, Figure 2)

Figure 2.4 illustrates the impact of spatial filtering on GRACE-derived TWS fields. While filtering techniques such as DDK are essential for reducing correlated noise, they also modify the true geophysical signal. This results in signal attenuation and spatial leakage, where mass variations spread across neighboring regions. As a consequence, the amplitude of TWS variations is systematically underestimated, particularly in regions with strong spatial gradients.

2.5 Leakage Correction Using Scaling Factors

To reduce leakage effects, scaling factors can be applied to GRACE-derived TWS anomalies. Landerer and Swenson (2012) proposed a method to estimate these factors using hydrological model simulations from GLDAS data.

In this approach, water storage fields from a land surface model (e.g., CLM4) are filtered using the same spatial filtering applied to GRACE data. By comparing the original (true) model fields with the filtered ones, a scaling factor is derived that represents the attenuation of the signal caused by filtering.
The corrected GRACE field is computed as

$$g'(x,y,t) = g(x,y,t)\,\alpha(x,y), \tag{2.7}$$

where $g(x,y,t)$ is the filtered GRACE TWS anomaly, $\alpha(x,y)$ is the scaling factor and $g'(x,y,t)$ is the corrected TWS anomaly.
A value of $\alpha(x,y)$ close to 1 indicates minor leakage effects, whereas values significantly greater than 1 indicate stronger signal attenuation and therefore more severe leakage.

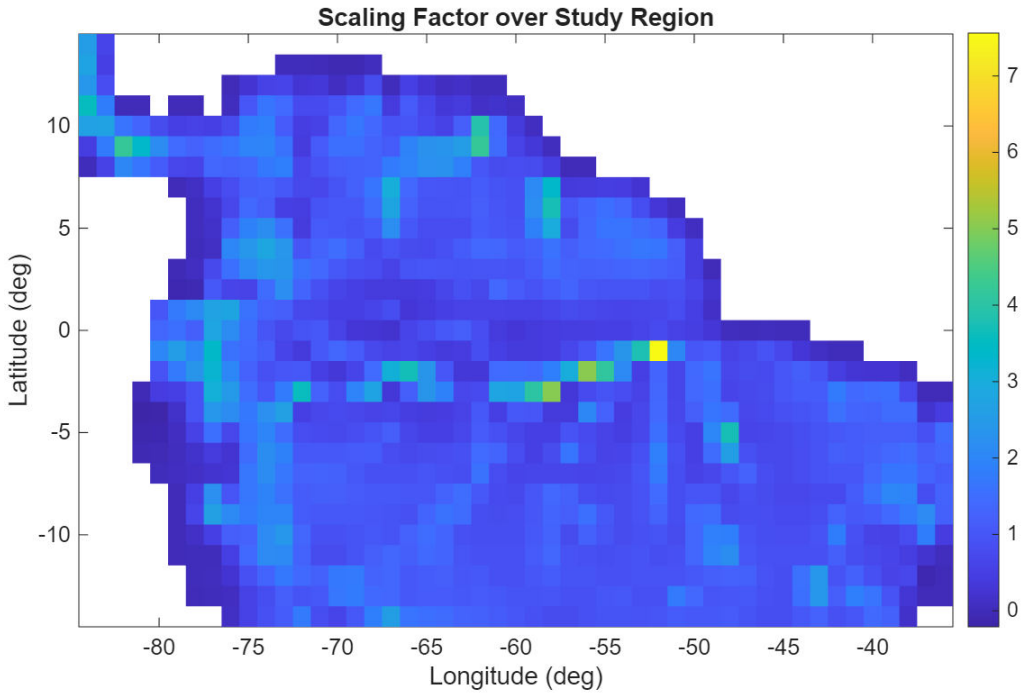

Figure 2.5: Spatial distribution of gain or scaling factors for GLDAS-NOAH monthly TWS variations. (Landerer and Swenson, 2012)

Figure 2.5 shows the spatial distribution of scaling factors used to correct GRACE-derived TWS fields. Values close to one indicate regions where filtering has a minor impact, while larger values highlight areas with strong signal attenuation. These regions typically correspond to areas with high spatial variability or near coastlines, where leakage effects are more pronounced. The application of these scaling factors helps to restore the attenuated signal and improve the accuracy of TWS estimates.
In this study, leakage correction is applied to TWS fields derived using three different Load Love Number formulations. This allows investigation of how leakage correction interacts with loading effects.

- **Case 1:** $LLN = 0$ **with scaling factor**

  In this case, no deformation correction is applied during the conversion from gravity to TWS. The scaling factor is applied directly to the mass-related signal:

$$TWS_0^{corr}(x,y,t) = TWS_{LLN=0}(x,y,t) \cdot \alpha(x,y) \tag{2.8}$$

  This represents leakage correction applied to the uncorrected GRACE signal.

- **Case 2:** $LLN = 1$ **with scaling factor**

  Here, elastic deformation of the Earth is considered using Load Love Numbers. The scaling factor is applied to the deformation-corrected TWS:

$$TWS_1^{corr}(x,y,t) = TWS_{LLN=1}(x,y,t) \cdot \alpha(x,y) \tag{2.9}$$

  This case represents the physically consistent scenario, where both loading effects and leakage are accounted for.

- **Case 3:** $LLN = 2$ **with scaling factor**

  In this case, only the deformation-related component of the signal is considered. The scaling factor is applied to the deformation signal:

$$TWS_2^{corr}(x,y,t) = TWS_{LLN=2}(x,y,t) \cdot \alpha(x,y) \tag{2.10}$$

  Since the deformation signal is smaller in magnitude, the effect of scaling factors is also reduced compared to the previous cases.

By comparing these three cases, it is possible to distinguish between the effects of signal attenuation (leakage) and Earth deformation (loading) and to evaluate their combined impact on GRACE-derived TWS estimates.

3 Data and Preprocessing

This study uses monthly GRACE Level-2 Release 06 (RL06) spherical harmonic solutions provided by the GFZ analysis center (GFZ, 2026). GRACE data products are widely used for analysing mass redistribution processes in the Earth system (Save et al., 2016). The data were obtained from the ICGEM database in `.gfc` format, containing fully normalised spherical harmonic coefficients ($\bar{C}_{nm}$, $\bar{S}_{nm}$) up to degree and order 96.
The analysis covers the period from 2003 to 2016 and focuses on the Amazon basin region (15°S–15°N, 85°W–35°W), which exhibits strong hydrological variability. Figure 3.1 shows the geographical extent of the study area.

Figure 3.1: Map of the Amazon basin showing major rivers and geographical extent of the study area. Source: Wikipedia.

To reduce noise and correlated errors, the DDK2 filter was applied to the spherical harmonic coefficients. All computations were performed on a $1^\circ \times 1^\circ$ spatial grid to ensure consistency with the scaling factor dataset.

For the leakage analysis, scaling factors derived from the CLM4 hydrological model were used. These data are available from the JPL TELLUS project and follow the approach described by Landerer and Swenson (2012). The scaling factor dataset used in this study was provided by the supervisor.
Since these scaling factors are derived from land surface hydrological models, they are only defined over land areas. Ocean mass variations are treated separately in GRACE processing and no corresponding scaling factors are provided for ocean regions.
Therefore, to ensure consistency between the loading-effect analysis and the leakage-correction analysis, all computations were restricted to land grid cells only. A land mask was defined based on the availability of CLM4 scaling factors, where valid values correspond to land and missing values represent ocean areas. This guarantees that both analyses are performed over the same spatial domain.

4 Methodology

The methodology consists of two main components: (i) assessment of loading effects using different Load Love Number (*LLN*) configurations and (ii) correction of signal leakage using scaling factors.

4.1 Computation of TWS

Monthly GRACE coefficients were first rescaled to consistent reference values (GM, R). A mean gravity field was computed and removed from each monthly solution to obtain residual coefficients representing temporal mass variations.
These residuals were transformed into gridded fields using spherical harmonic synthesis and Total Water Storage (TWS) anomalies were computed in terms of equivalent water height (Wahr et al., 1998).

4.2 Loading Effects (Load Love Numbers)

To assess the influence of Earth's deformation, three *LLN* configurations were applied:

- $LLN = 0$: no loading correction (rigid Earth)
- $LLN = 1$: elastic loading included
- $LLN = 2$: deformation-related contribution

For consistency with the leakage-correction analysis, all TWS fields were restricted to land grid cells using a land mask derived from the CLM4 scaling-factor dataset. Statistical evaluations for all *LLN* cases were therefore performed over land areas only.

4.3 Leakage Correction

To reduce signal attenuation caused by filtering, scaling factors (α) were applied to the TWS fields:

$$TWS_{\text{corrected}} = TWS \cdot \alpha \tag{4.1}$$

The correction was applied only over land grid cells, while ocean areas remained unchanged. This ensures that the leakage correction is consistent with the spatial applicability of the scaling factors.
The correction was implemented for all *LLN* cases (0, 1 and 2), allowing comparison between TWS with loading effects only (land-only) and TWS with both loading effects and leakage correction.

4.4 Statistical Analysis

For each configuration, statistical measures (minimum, maximum, mean, RMS and standard deviation) were computed from the gridded TWS fields over land areas. These statistics were analysed as time series to evaluate differences in amplitude and variability between *LLN* configurations and leakage-corrected results.

5 Results

5.1 Assessing Loading Effects

To investigate the influence of surface loading on terrestrial water storage (TWS) estimates, three configurations of loading Love numbers were implemented in the processing workflow. These configurations correspond to $LLN = 0$, $LLN = 1$ and $LLN = 2$, representing different treatments of the Earth's elastic response to surface mass redistribution.
The GRACE spherical harmonic solutions were converted to equivalent water height (EWH) and statistical characteristics of the resulting TWS fields were analysed over the study period. For each configuration, the minimum, maximum, mean, root mean square (RMS) and standard deviation were computed.
To ensure consistency with the leakage-correction analysis, all statistics were computed over land grid cells only. The purpose of this analysis is to evaluate how the inclusion or exclusion of loading corrections affects the magnitude and variability of TWS estimates derived from GRACE data.

5.1.1 Loading Configurations

Three loading scenarios were investigated as explained in Section 2.3:

- $LLN = 0$: Rigid Earth assumption (no loading deformation).
- $LLN = 1$: Full elastic response of the Earth using loading Love numbers.
- $LLN = 2$: Deformation-related contribution associated with loading effects.

5.1.2 Statistics of TWS for $LLN = 0$

Figure 5.1 presents the statistical characteristics of the TWS time series computed without applying loading corrections, restricted to land areas.

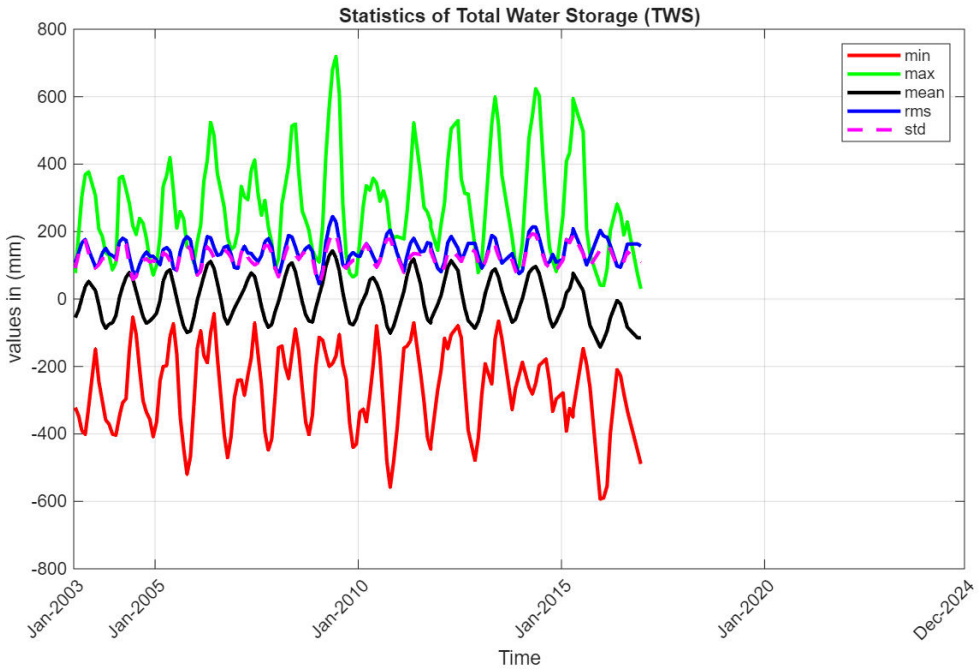

Figure 5.1: Statistical characteristics of terrestrial water storage for $LLN = 0$ (land-only analysis).

A pronounced seasonal cycle is observed, reflecting strong hydrological variability within the Amazon basin. The maximum and minimum values indicate large amplitude variations, while the mean TWS oscillates around zero, as expected for anomaly-based calculations. The RMS and standard deviation follow similar temporal patterns, indicating consistent seasonal variability.

5.1.3 Statistics of TWS for $LLN = 1$

Figure 5.2 shows the statistical characteristics after applying the full loading correction.

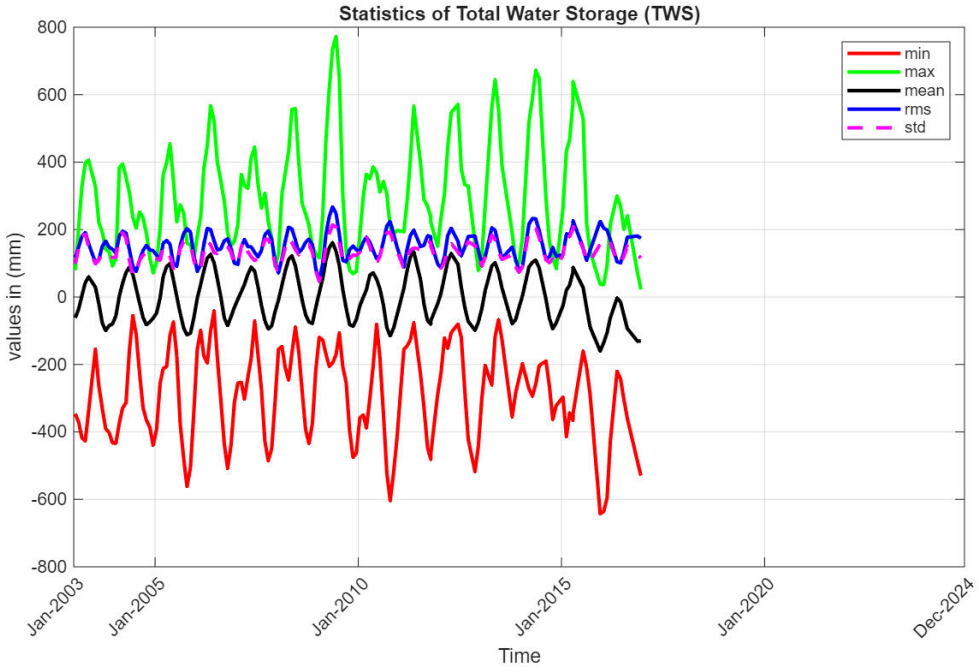

Figure 5.2: Statistical characteristics of terrestrial water storage for $LLN = 1$ (land-only analysis).

Compared to the rigid Earth case ($LLN = 0$), an increase in the amplitude of TWS variations is observed for $LLN = 1$. This is because the elastic response of the Earth contributes additional deformation signals to the gravity field. As a result, both the direct mass effect and the deformation effect are captured, leading to larger maximum and minimum values of TWS. The seasonal pattern remains consistent, but with slightly higher amplitudes.

5.1.4 Statistics of TWS for $LLN = 2$

Figure 5.3 illustrates the statistical characteristics of the deformation-related component.

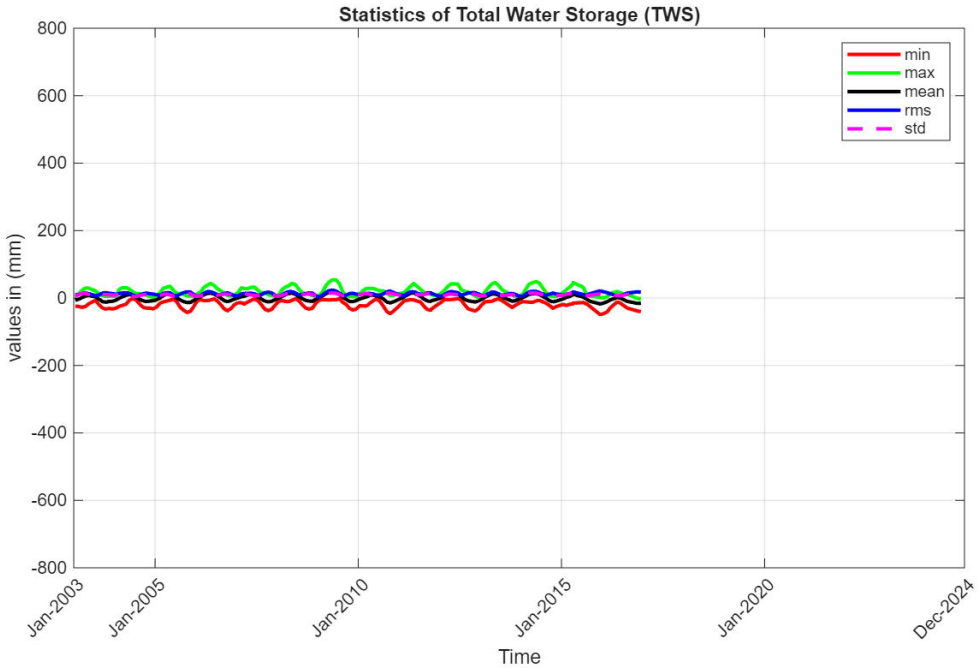

Figure 5.3: Statistical characteristics of terrestrial water storage for $LLN = 2$ (land-only analysis).

In contrast to the previous cases, the magnitude of TWS variations is significantly smaller. This indicates that the deformation-related contribution represents only a fraction of the total TWS signal. However, a clear seasonal pattern is still visible, suggesting that the deformation signal is directly linked to seasonal mass redistribution processes.

Overall, the comparison of the three configurations demonstrates that loading corrections have a measurable impact on the amplitude of TWS estimates, while preserving the temporal behaviour of the signal.

5.2 Spatial Analysis of Loading Effects

To further investigate the spatial impact of loading corrections, selected months representing wet and dry conditions were analysed. April 2009 (wet season) and October 2010 (dry season) were chosen as representative months for the Amazon basin.

Two specific years were selected as illustrative cases:

- April 2009 (flood year)
- October 2010 (drought year)

These cases provide a clear comparison of loading effects under contrasting hydrological conditions. Additional drought years (2005 and 2015) exhibit similar behaviour and are provided in Appendix A.

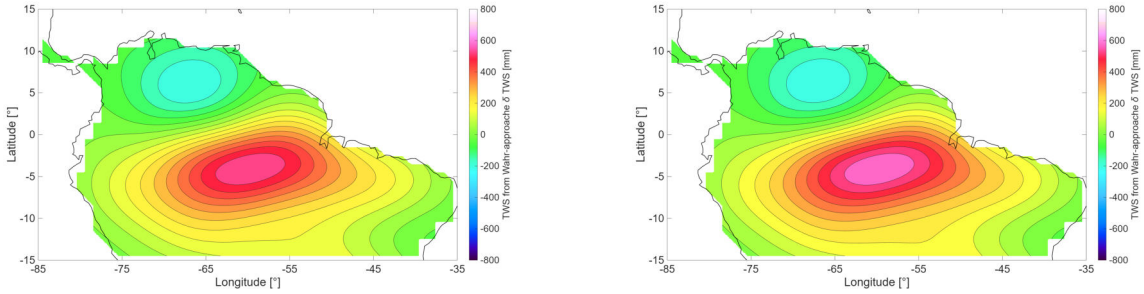

(a) $LLN = 0$ (rigid Earth) (b) $LLN = 1$ (elastic Earth)

Figure 5.4: Spatial distribution of TWS anomalies (EWH) for April 2009.

5.2.1 Wet Season: April 2009

Figure 5.4 shows the spatial distribution of TWS anomalies for April 2009. During the wet season, strong positive TWS anomalies are observed across large parts of the Amazon basin, indicating significant water accumulation. The spatial patterns are nearly identical for both configurations, demonstrating that loading corrections do not alter the distribution of the signal.
However, the amplitude of the TWS anomalies is clearly larger for $LLN = 1$. This indicates that the inclusion of Earth's elastic response enhances the magnitude of the observed water storage variations.

5.2.2 Dry Season: October 2010

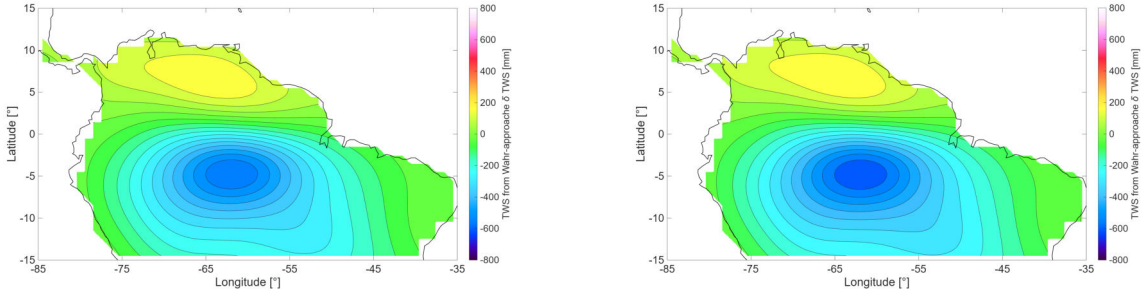

(a) $LLN = 0$ (rigid Earth) (b) $LLN = 1$ (elastic Earth)

Figure 5.5: Spatial distribution of TWS anomalies (EWH) for October 2010.

Figure 5.5 shows the spatial distribution of TWS anomalies for October 2010. In contrast to the wet season, the dry season is characterised by negative TWS anomalies associated with reduced water storage. Similar to the wet season case, the spatial patterns remain consistent between the two configurations.
Nevertheless, the magnitude of the negative anomalies is increased for $LLN = 1$, indicating that loading effects amplify both positive and negative signals. This confirms that Earth's elastic response influences the amplitude of TWS variations without significantly modifying their spatial structure.

5.3 Assessing Leakage Effects

In addition to loading effects, GRACE-derived terrestrial water storage (TWS) estimates are affected by signal leakage caused by spatial filtering. This leads to attenuation of the true signal and spreading of mass variations across neighbouring regions.
In this study, the DDK2 filter was applied to reduce noise, but this smoothing also attenuates part of the original signal, leading to reduced amplitudes in TWS estimates. To compensate for this effect, scaling factors derived

from the CLM4 hydrological model were applied to the TWS fields. These factors restore part of the attenuated signal and provide a more realistic estimate of water storage variations.
To better illustrate the spatial behaviour of leakage correction, Figure 5.6 shows the regional leakage error and the corresponding scaling factors over the Amazon basin.

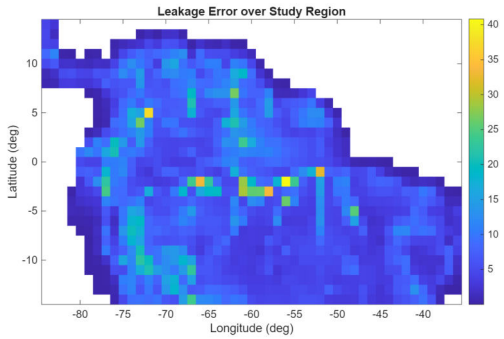

(a) Leakage error over the study region. Units are in mm.

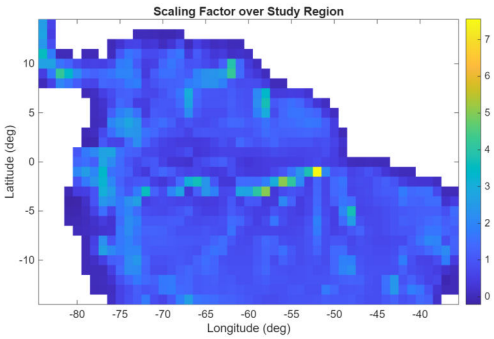

(b) Scaling factor over the study region. (unit less)

Figure 5.6: Spatial distribution of leakage error and scaling factors over the Amazon basin. Regions with larger leakage errors generally correspond to areas with higher scaling factors, indicating where stronger correction is required.

The leakage error is not spatially uniform across the basin. Some regions show relatively small leakage, while others are more strongly affected by signal attenuation. A similar spatial pattern is visible in the scaling factor map, where larger scaling values occur in areas with stronger leakage. This shows that the correction is spatially variable and that stronger amplification is needed in regions where filtering causes greater signal loss.
For each loading configuration ($LLN = 0$, $LLN = 1$ and $LLN = 2$), a comparison was performed between TWS without scaling (uncorrected) and with scaling (leakage-corrected). All computations were restricted to land grid cells to ensure consistency.
The purpose of this analysis is to quantify the impact of leakage correction on the amplitude and variability of TWS estimates.

5.3.1 Statistics of TWS for $LLN = 0$

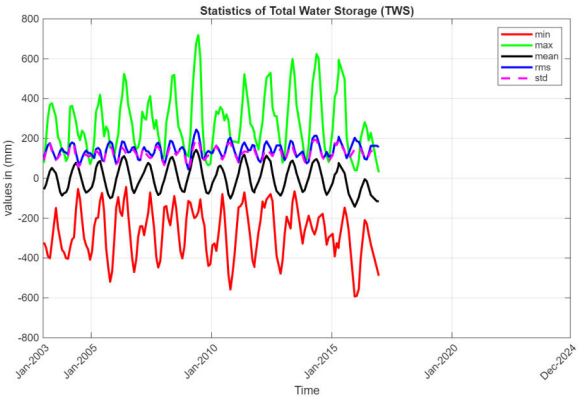

(a) Without scaling

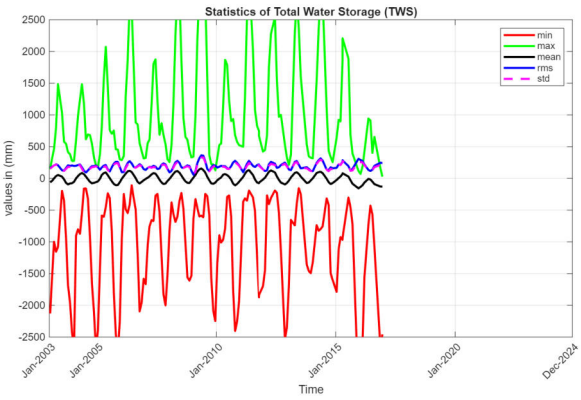

(b) With scaling

Figure 5.7: Comparison of TWS statistics for $LLN = 0$ (land-only analysis).

Figure 5.7 shows the statistical characteristics of TWS for $LLN = 0$, comparing results without and with scaling factors applied over land areas. The application of scaling factors leads to a significant increase in the amplitude of TWS variations. This effect is clearly visible in the extended range of the y-axis in the corrected case, where values increase from approximately ± 800 mm (uncorrected) to about ± 2500 mm after applying scaling factors.

The larger extrema indicate that the original GRACE signal is strongly attenuated due to spatial filtering. The scaling factors compensate for this attenuation and restore a substantial portion of the true hydrological signal. While the amplitude changes considerably, the temporal behaviour of the signal remains consistent. This demonstrates that leakage correction primarily affects the magnitude and spatial resolution of TWS variations, whereas the timing and seasonal patterns remain unchanged.

5.3.2 Statistics of TWS for $LLN = 1$

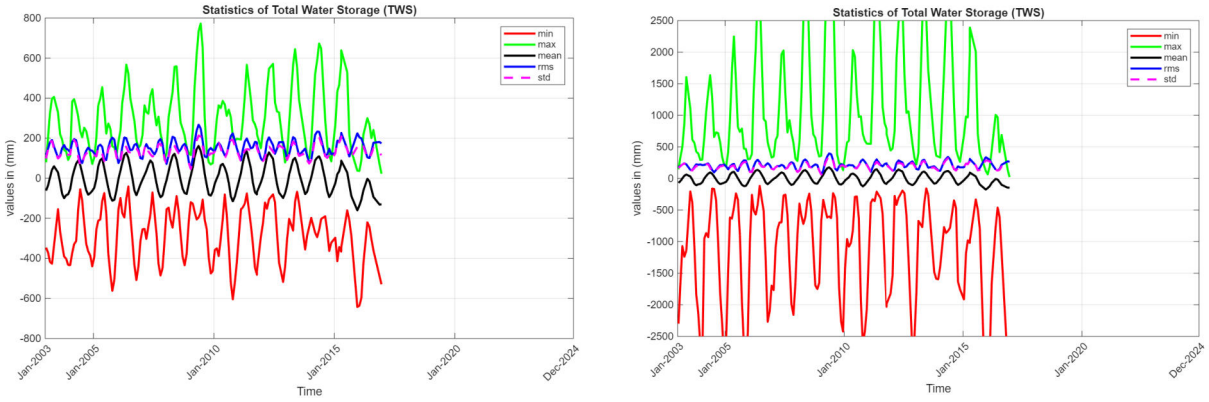

(a) Without scaling

(b) With scaling

Figure 5.8: Comparison of TWS statistics for $LLN = 1$ (land-only analysis).

Figure 5.8 presents the comparison for $LLN = 1$. The behaviour for $LLN = 1$ is consistent with the rigid Earth case. The application of scaling factors leads to a strong increase in the amplitude of TWS variations, which is also reflected in the extended y-axis range (up to approximately ± 2500 mm).
This indicates that leakage correction significantly amplifies the signal by compensating for attenuation caused by GRACE filtering. While the magnitude increases, the temporal pattern remains unchanged, confirming that scaling primarily affects the amplitude of the signal.

5.3.3 Statistics of TWS for $LLN = 2$

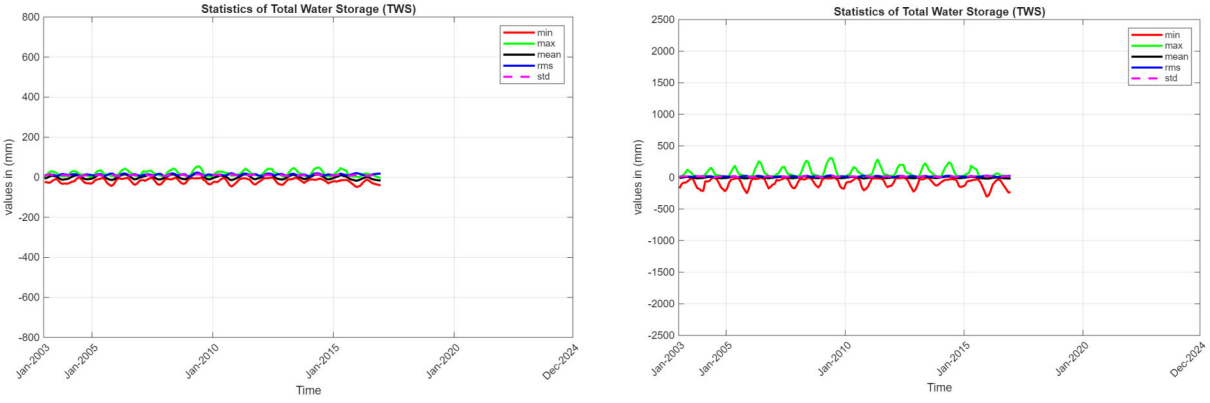

(a) Without scaling

(b) With scaling

Figure 5.9: Comparison of TWS statistics for $LLN = 2$ (land-only analysis).

Figure 5.9 illustrates the comparison for $LLN = 2$. The deformation-related component ($LLN = 2$) shows a similar response to leakage correction. The application of scaling factors increases the amplitude of TWS variations, which is also reflected in the extended y-axis range.

However, compared to $LLN = 0$ and $LLN = 1$, the overall magnitude remains significantly smaller. This indicates that leakage effects influence the deformation signal, but their impact is less pronounced than for the full TWS signal.
The temporal behaviour remains unchanged, confirming that scaling primarily affects the amplitude while preserving the seasonal pattern.

5.4 Spatial Analysis of Leakage Effects

To analyse the spatial impact of leakage correction, representative months from the wet and dry seasons were selected. April 2009 (wet season) and October 2010 (dry season) were chosen to highlight the influence of scaling factors under contrasting hydrological conditions.
The analysis is performed for two loading configurations ($LLN = 0$ and $LLN = 1$), comparing TWS fields computed without scaling (uncorrected) and with scaling (leakage corrected). This allows assessment of leakage effects under both rigid and elastic Earth assumptions.
Two specific years were selected as illustrative cases:

- April 2009 (flood year)
- October 2010 (drought year)

Additional drought years (2005 and 2015) exhibit similar behaviour and are provided in Appendix B.

5.4.1 Wet Season: April 2009

Case 1: No loading correction ($LLN = 0$).

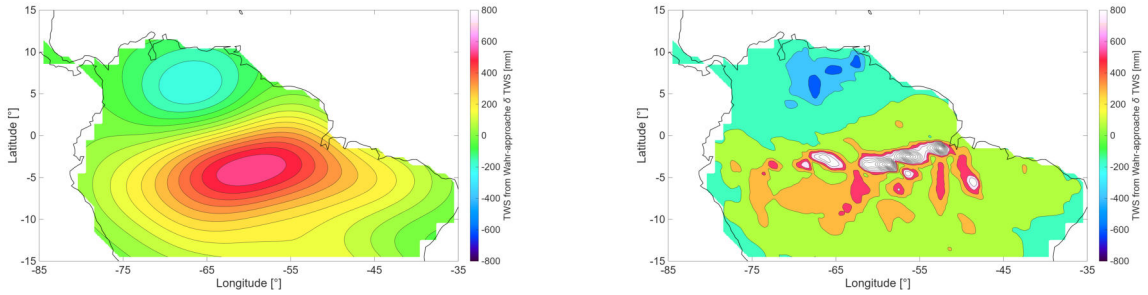

(a) Without scaling (b) With scaling

Figure 5.10: Spatial distribution of TWS anomalies (EWH) for April 2009 ($LLN = 0$).

Figure 5.10 represents the spatial distribution of TWS anomalies for April 2009 under the rigid Earth assumption. Strong positive TWS anomalies are observed across the Amazon basin. After applying scaling, the overall spatial pattern remains similar, but the signal becomes stronger and more detailed. This indicates that the original GRACE data are smoothed due to filtering, and scaling helps to recover the lost signal.

Case 2: Full loading correction ($LLN = 1$).

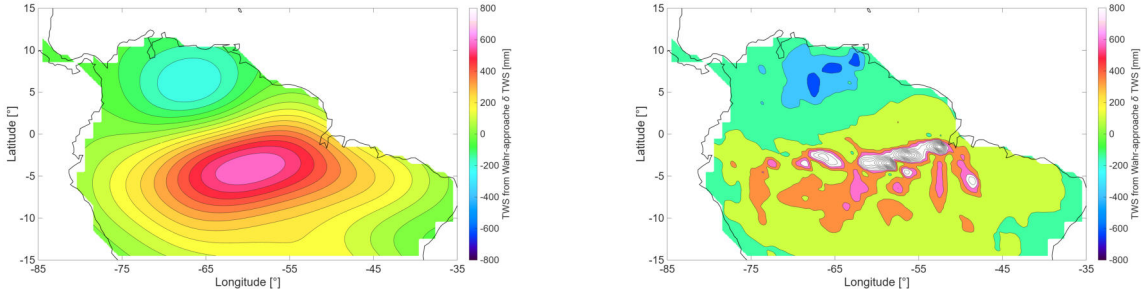

(a) Without scaling (b) With scaling

Figure 5.11: Spatial distribution of TWS anomalies (EWH) for April 2009 ($LLN = 1$).

Figure 5.11 represents the spatial distribution of TWS anomalies for April 2009 with full loading correction. Similar spatial patterns are observed. After applying scaling, the signal becomes stronger and more detailed, with more pronounced positive anomalies. This reflects the combined effect of loading correction and leakage compensation, leading to an improved representation of water storage variations.

5.4.2 Dry Season: October 2010

Case 1: No loading correction ($LLN = 0$).

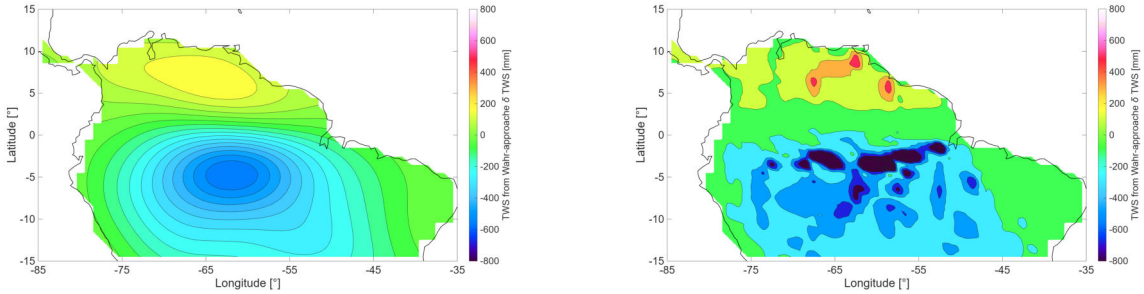

(a) Without scaling (b) With scaling

Figure 5.12: Spatial distribution of TWS anomalies (EWH) for October 2010 ($LLN = 0$).

Figure 5.12 represents the spatial distribution of TWS anomalies for October 2010 under the rigid Earth assumption. During the dry season, negative TWS anomalies dominate the basin. The spatial patterns remain consistent before and after scaling. However, the magnitude of the negative anomalies increases after applying scaling factors, showing that leakage correction helps recover weakened signals.

Case 2: Full loading correction ($LLN = 1$).

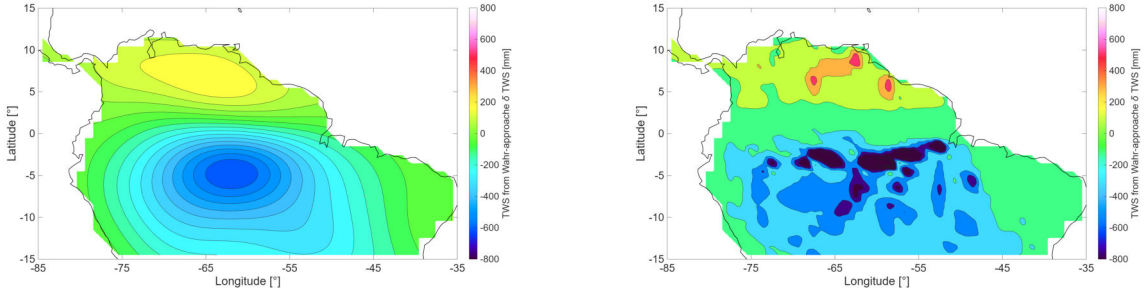

(a) Without scaling (b) With scaling

Figure 5.13: Spatial distribution of TWS anomalies (EWH) for October 2010 ($LLN = 1$).

Figure 5.13 represents the spatial distribution of TWS anomalies for October 2010 with full loading correction. A similar behaviour is observed, where scaling increases the magnitude of negative anomalies while the spatial pattern remains unchanged. This confirms that leakage correction mainly affects the amplitude and the regional spacial pattern of the signal.

6 Conclusion

In this study, the effects of loading and signal leakage on GRACE-derived terrestrial water storage (TWS) over the Amazon basin were analysed for the period 2003 - 2016. The aim was to understand how different processing choices influence the magnitude and interpretation of TWS variations in time and space.

The analysis of loading effects shows that including Load Love Numbers ($LLN = 1$) leads to a noticeable increase in the amplitude of TWS compared to the rigid Earth case ($LLN = 0$). This increase is observed consistently in both time series and spatial maps. However, the seasonal behaviour and spatial distribution of TWS remain largely unchanged. This indicates that loading correction mainly affects the strength of the signal rather than its pattern. The deformation of the Earth due to surface mass changes contributes additional signal, which enhances both positive and negative TWS anomalies.

The leakage analysis highlights the impact of filtering on GRACE data. In this study, the DDK2 filter was applied to reduce noise, but this smoothing also attenuates part of the original signal, leading to reduced amplitudes in TWS estimates. The use of scaling factors effectively compensates for this loss. After applying scaling, the magnitude of TWS anomalies increases significantly and the signals appear more detailed. t the same time, the overall long wavelenth spatial patterns and temporal behaviour remain consistent, regional variations of the signal can be identified now, showing that leakage correction primarily restores signal strength without introducing artificial changes.

The spatial analysis further confirms these findings. For both wet and dry season cases, the application of loading correction and scaling factors enhances the amplitude of TWS anomalies, while the general structure of the signal remains similar. This consistency across different years and hydrological conditions demonstrates the robustness of the results.

Overall, the study shows that both loading effects and leakage correction are essential for accurate interpretation of GRACE-derived water storage. Loading correction accounts for the Earth's elastic response, while scaling factors correct for signal loss caused by filtering. Ignoring these effects can lead to underestimation of TWS variations.

In conclusion, a careful combination of loading correction and leakage correction provides a more realistic representation of hydrological changes in the Amazon basin. These corrections are important for improving the reliability of GRACE-based studies and for better understanding large-scale water storage variability.

Acknowledgement

The author would like to express sincere gratitude to Prof. Dr.-Ing. Hansjörg Kutterer for providing the opportunity to carry out this Lab Rotation. The author is also thankful to the supervisor, Dr.-Ing. Kurt Seitz, for his continuous guidance, support and valuable feedback throughout the course of this work, which greatly contributed to the development of this study.

The author further acknowledges the support of the Geodätisches Institut (GIK) for providing the necessary resources and facilities. Finally, appreciation is extended to ICGEM (GFZ German Research Centre for Geosciences, 2023) for providing the GRACE data used in this analysis.

References

Chen, J. L., Wilson, C. R., and Tapley, B. D. (2010): The 2009 Amazon flood observed from space. *Geophysical Research Letters* 37:L09403. DOI: 10.1029/2010GL042433.

Chen, J., Famiglietti, J. S., Scanlon, B. R., and Rodell, M. (2022): Satellite-based terrestrial water storage changes: Methods, applications, and challenges. *Reviews of Geophysics* 60(1):e2021RG000765. DOI: 10.1029/2021RG000765.

Farrell, W. E. (1972): Deformation of the Earth by surface loads. *Reviews of Geophysics* 10(3):761–797. ISSN: 1944-9208. DOI: 10.1029/RG010i003p00761.

Flechtner, F., Neumayer, K.-H., Dahle, C., Dobslaw, H., Fagiolini, E., Raimondo, J.-C., and Güntner, A. (2014): What can be expected from the GRACE-FO laser ranging interferometer for Earth science applications? *Surveys in Geophysics* 35(5):1009–1031. DOI: 10.1007/s10712-014-9301-8.

GFZ (2026): GRACE-FO – Gravity Recovery and Climate Experiment Follow-On Mission. German Research Centre for Geosciences (GFZ). Accessed: 2026-04-06. URL: https://www.gfz.de/en/section/global-geomonitoring-and-gravity-field/projects/grace-fo-gravity-recovery-and-climate-experiment-follow-on-mission.

Heiskanen, W. A. and Moritz, H. (1967): Physical Geodesy. W. H. Freeman & Co., San Francisco, USA.

ICGEM (2026): International Centre for Global Earth Models (ICGEM): Gravity field and GRACE/GRACE-FO products hosted at the German Research Centre for Geosciences (GFZ). Accessed: 2026-04-06. URL: https://icgem.gfz-potsdam.de/.

Landerer, F. W. and Swenson, S. C. (2012): Accuracy of scaled GRACE terrestrial water storage estimates. *Water Resources Research* 48(4). DOI: 10.1029/2011WR011453.

Save, H., Bettadpur, S., and Tapley, B. D. (2016): High resolution CSR GRACE RL05 mascons. *J. Geophys. Res. Solid Earth* 121:7547–7569. DOI: 10.1002/2016JB013007.

Swenson, S. and Wahr, J. (2006): Post-processing removal of correlated errors in GRACE data. *Geophysical Research Letters* 33(8):L08402. DOI: 10.1029/2005GL025285.

Tapley, B. D., Bettadpur, S., Watkins, M., and Reigber, C. (2004): The gravity recovery and climate experiment: Mission overview and early results. *Geophysical Research Letters* 31(9):1–4. DOI: 10.1029/2004GL019920.

Van Dam, T. (2017): Surface Mass Loading of the Solid Earth: Theory and Examples. EGSIEM Autumn School for Satellite Gravimetry Applications, Potsdam.

Wahr, J., Molenaar, M., and Bryan, F. (1998): Time variability of the Earth's gravity field: Hydrological and oceanic effects and their possible detection using GRACE. *Journal of Geophysical Research: Solid Earth* 103(B12):30205–30229.

Appendix

Appendix A: Additional Spatial Analysis of Loading Effects

To support the results presented in Section 5.2, additional spatial comparisons were carried out for the years 2005 and 2015. These years correspond to major drought events in the Amazon basin and provide further insight into the influence of loading corrections under varying hydrological conditions. In particular, September 2015 is used as a representative dry-season case, as GRACE data for October 2015 are not available.

The same methodology as described in the main analysis was applied, comparing TWS anomalies (EWH) for $LLN = 0$ and $LLN = 1$ during representative wet (April) and dry-season months (September and October).

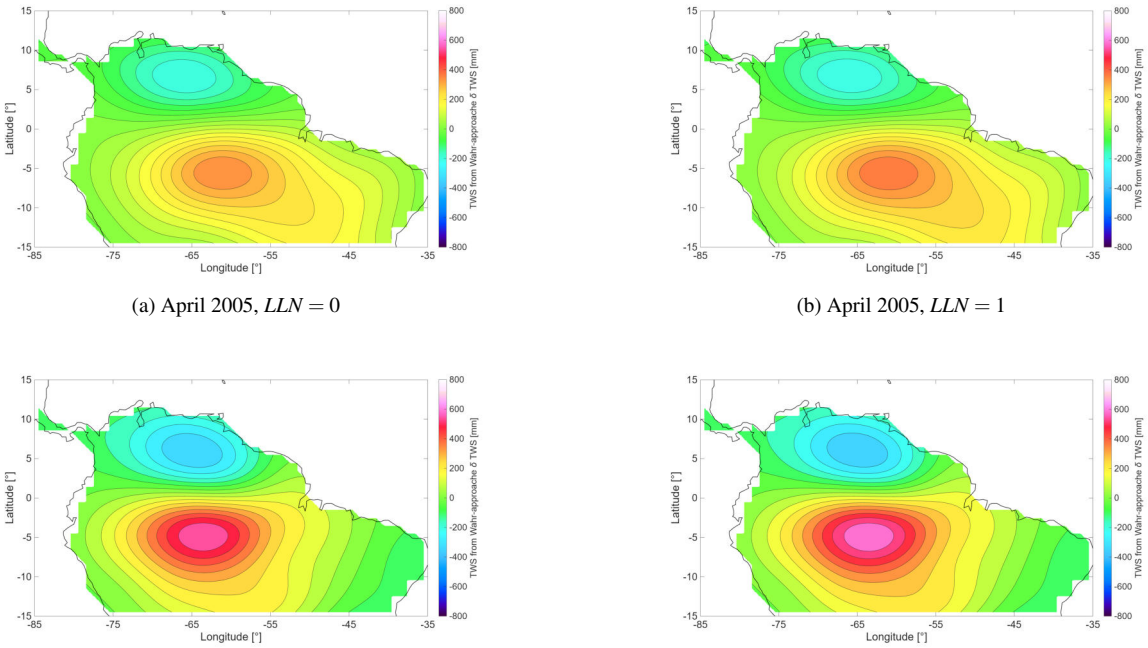

(a) April 2005, $LLN = 0$

(b) April 2005, $LLN = 1$

(c) April 2015, $LLN = 0$

(d) April 2015, $LLN = 1$

Figure .1: Spatial distribution of TWS anomalies (EWH) for April in drought years (2005 and 2015). $LLN = 1$ shows stronger positive TWS values compared to $LLN = 0$, while the spatial pattern remains similar.

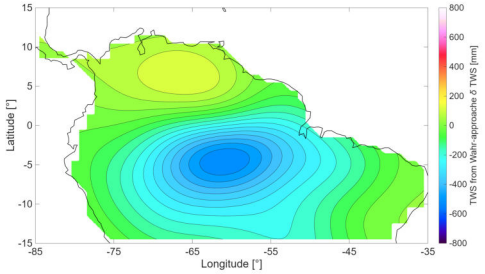

(a) October 2005, $LLN = 0$

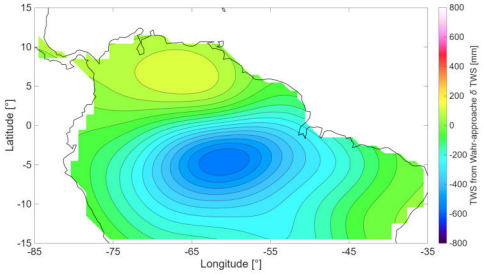

(b) October 2005, $LLN = 1$

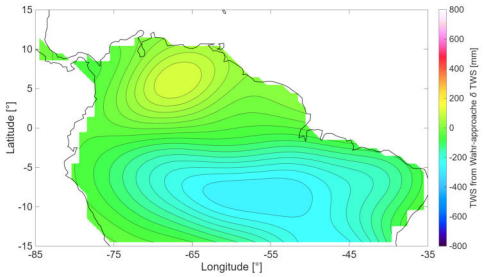

(c) September 2015, $LLN = 0$

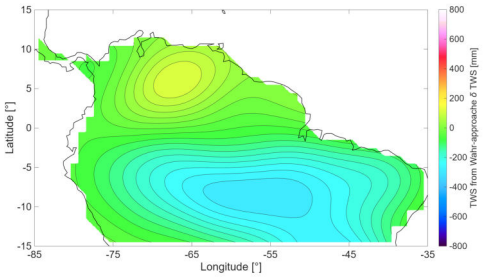

(d) September 2015, $LLN = 1$

Figure .2: Spatial distribution of TWS anomalies (EWH) for October (2005) and September (2015) in drought years. The spatial pattern remains similar, while $LLN = 1$ shows stronger negative TWS values compared to $LLN = 0$.

Appendix B: Additional Spatial Analysis of Leakage Effects

This appendix presents additional spatial comparisons of leakage correction for the Amazon basin using the elastic Earth configuration ($LLN = 1$), to support the results presented in Section 5.4. The results are shown for representative wet (April) and dry-season months (September and October) for the years 2005 and 2015.

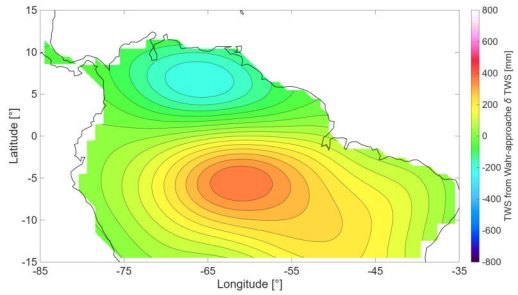

(a) Without scaling

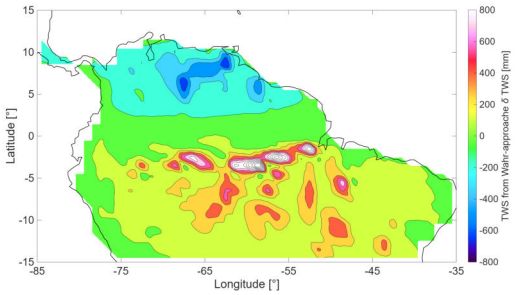

(b) With scaling

Figure .1: Spatial distribution of TWS anomalies (EWH) for April 2005 ($LLN = 1$). Scaling increases the positive TWS values while keeping the same spatial pattern, showing recovery of weakened wet-season signals.

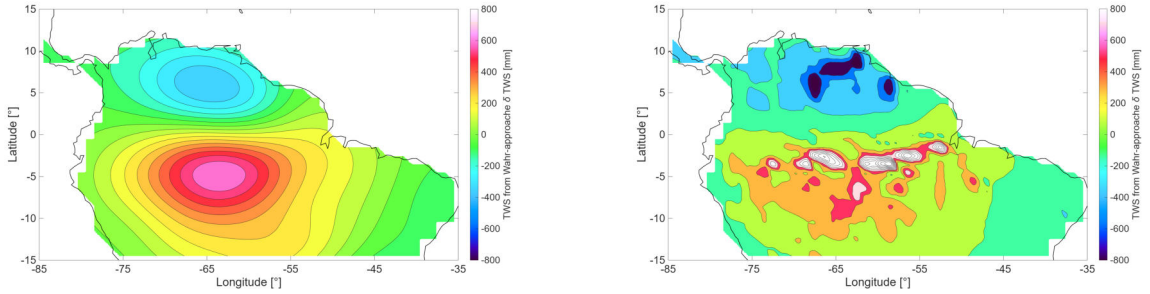

(a) Without scaling (b) With scaling

Figure .2: Spatial distribution of TWS anomalies (EWH) for April 2015 ($LLN = 1$). A similar increase in positive TWS values is seen after scaling, confirming stronger wet-season signals.

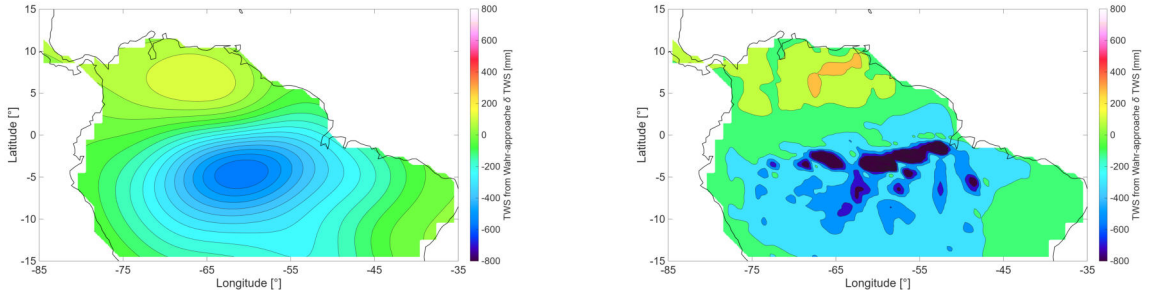

(a) Without scaling (b) With scaling

Figure .3: Spatial distribution of TWS anomalies (EWH) for October 2005 ($LLN = 1$). Scaling increases the negative TWS values while keeping the spatial pattern unchanged, improving dry-season signals.

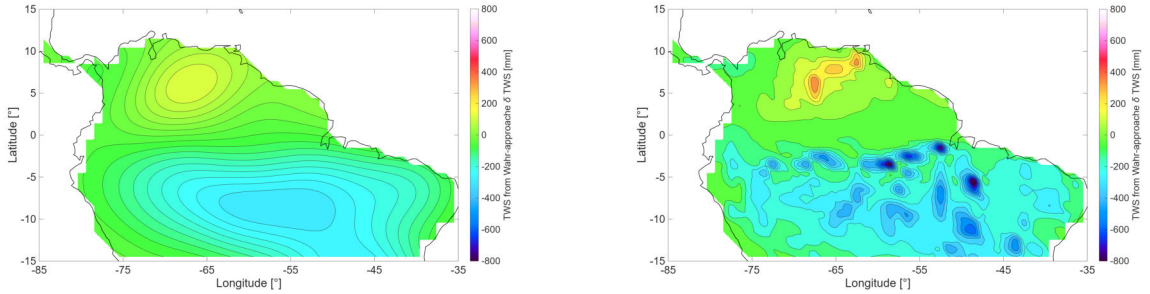

(a) Without scaling (b) With scaling

Figure .4: Spatial distribution of TWS anomalies (EWH) for September 2015 ($LLN = 1$). Scaling strengthens the negative TWS values without changing the pattern, showing consistent behaviour during drought years.

KIT Scientific Working Papers
ISSN 2194-1629

www.kit.edu

KIT – The Research University in the Helmholtz Association